

Materials

FY 2022 Annual Progress Report

Vehicle Technologies Office

(This page intentionally left blank)

Disclaimer

This report was prepared as an account of work sponsored by an agency of the United States government. Neither the United States government nor any agency thereof, nor any of their employees, makes any warranty, express or implied, or assumes any legal liability or responsibility for the accuracy, completeness, or usefulness of any information, apparatus, product, or process disclosed or represents that its use would not infringe privately owned rights. Reference herein to any specific commercial product, process, or service by trade name, trademark, manufacturer, or otherwise does not necessarily constitute or imply its endorsement, recommendation, or favoring by the United States government or any agency thereof. The views and opinions of authors expressed herein do not necessarily state or reflect those of the United States government or any agency thereof.

Acknowledgments

First and foremost, the Principal Investigators (PIs) from industry, academia, and the national laboratories who supplied the content of these reports are to be acknowledged and commended for their outstanding research. It is their work that moves our nation forward to improve and make transportation more affordable, as well as increase energy security.

Thank you to the project managers at the National Energy Technology Laboratory for continued support administering these projects.

We would also like to acknowledge Idaho National Laboratory and Energetics for their help in preparing and publishing this report.

Sarah Ollila

Program Manager
Materials Technology Program
Vehicle Technologies Office

Jerry L. Gibbs

Technology Development Manager
Propulsion Materials
Vehicle Technologies Office

Christopher Schooler

Technology Development Manager
Automotive Metals & Multi-Material Joining
Lightweight Materials
Vehicle Technologies Office

H. Felix Wu, Ph.D.

Technology Development Manager
Carbon Fiber and Polymer Composites
Lightweight Materials
Vehicle Technologies Office

Acronyms and Abbreviations

symbols

α	thermal diffusivity
β	a phase in a metal alloy
ΔT	change in temperature
Δt	change in time
\mathcal{D}	damage parameter
ε	strain
η	viscosity
λ_f	failure point
μ	micron (when referring to size)
μ	viscosity (when used in Darcy's law)
μCT	micro-computed tomography
μm	micrometer
m^3/h	cubic micrometer per hour
$\mu\Omega$	microohm
Θ	designation used for microscale intermetallic precipitates mostly located at the grain boundaries in the as-cast state of aluminum.
Θ'	designation for nanoscale intermetallic precipitates present in the grain interiors of cast aluminum alloy.
ρ	density
σ	standard deviation (when referring to statistical analysis).
σ	stress (or strength, when referring to physical properties).
1D	one-dimensional
1NN	first nearest neighbor
17-4PH	martensitic precipitation-hardening stainless steel with a high concentration of chromium and nickel.
2D	two-dimensional
2NN	second nearest neighbor
2T	Two sheet stack-up
3D	three-dimensional
3DP	three-dimensional printing
3T	Three sheet stack-up

316L	the low carbon version of 316 stainless steel commonly used in chemical and petrochemical industry, in food processing, pharmaceutical equipment, medical devices, in potable water, wastewater treatment, in marine applications and architectural applications near the seashore or in urban areas.
4XT	4X Technologies
5xxx	series designation for aluminum alloyed with magnesium.
6xxx	series designation for aluminum alloyed with magnesium and silicon.
7xxx	series designation for aluminum alloyed with zirconium.
A	
a	absorption rate
Å	angstrom
A	area
A206	aluminum alloy having a high percent of copper (5%) with excellent strength at high temperatures and excellent machinability.
A316L	a chromium-nickel-molybdenum austenitic stainless steel developed to provide improved corrosion resistance to Alloy 304/304L in moderately corrosive environments.
A319	aluminum alloy having a composition of 6% silicon and 3.5% copper alloy with 1.0 iron maximum that has excellent casting and machining characteristics and very good corrosion resistance and weldability.
A356	aluminum alloy with greater elongation, higher strength, and considerably higher ductility than Alloy 356 because of lower iron content that is typically used for airframe castings, machine parts, truck chassis parts, aircraft and missile components, and structural parts requiring high strength.
A380	the most commonly specified aluminum alloy that has the best combination of casting, mechanical, and thermal properties; exhibits excellent fluidity, pressure tightness, and resistance to hot-cracking; and is used for a wide variety of products including chassis for electronic equipment, engine brackets, gearbox cases, household furniture, power, and hand tools.
AA	aluminum alloy
AA	Aluminum Association (when used with a series e.g., AA1100 series)
AA1100	a pure aluminum alloy with excellent forming characteristics and machinability, especially when the alloy is machined in hard temper.
AA1350	a high aluminum content (99.5%) alloy that is highly conductive with good formability used in electronics.
AA4043	a wrought aluminum alloy with good corrosion resistance typically used as filler material for welding of aluminum parts containing high amounts of 4.5% and 6.0% silicon.
AA4047	aluminum silicon brazing or filler alloy with good corrosion resistance.

AA5052	aluminum alloy most suited to forming operations, with good workability and higher strength than that of either 1100 or 3003. Although not heat-treatable, it is stronger than most of the 5xxx series of aluminums.
AA5182	wrought aluminum alloy with good corrosion resistance and weldability containing 4.5% Mg, 0.35% Mn, and the balance aluminum.
AA5356	an alloy in the wrought aluminum-magnesium family (5000 or 5xxx series) used primarily used as welding filler.
AA5754	an alloy in the wrought aluminum -magnesium family (5000 or 5xxx series).
AA6022	heat-treatable low copper precipitation hardenable aluminum sheet alloy containing 0.8% to 1.5% silicon, 0.45% to 0.70% magnesium, and 0.25% zinc.
AA6061	precipitation-hardening aluminum alloy containing 0.8% to 1.2% magnesium and 0.4% to 0.8% silicon as its major alloying elements.
AA6063	aluminum alloy consisting of aluminum, magnesium, and 0.5% silicon used for pipe, railings, furniture, architectural extrusions, irrigation pipes, and transportation.
AA6082	a medium strength alloy with excellent corrosion resistance and the highest strength of the 6000 series alloys used as a structural alloy.
AA610	an aluminum bronze; nominally containing 92% copper and 8% aluminum that is used as an engineering material of medium strength and ductility with a good capacity for being hot worked or cold worked.
AA6111	wrought aluminum alloy that is heat-treatable and possesses high-strength and excellent stretch-forming characteristics containing 0.6% to 1.1% silicon, 0.5% to 1.0% magnesium, 0.1% to 0.45% manganese, 0.5% to 0.9% copper, and 0.15% zinc.
AA6451	aluminum alloy that combined aspects of both AA6111 and AA6016A and is essentially a lower level of copper (<0.4 wt%) version of AA6111 used for production from recycled process scrap.
AA7055	aluminum alloy containing zinc, magnesium, chromium, and copper as hardeners, as well as small amounts of iron, silicon, manganese, and titanium with the highest total strength, good fracture toughness, and a strong ability for fatigue crack propagation with a microstructure that is resistant to intergranular fracture and corrosion.
AA7075	aluminum alloy with strength comparable to many steels, good fatigue strength, and average machinability.
AA7085	a high-strength and high hardenability forging aluminum alloy that has excellent fracture toughness.
ABAQUS or Abaqus	software suite for finite element analysis and computer-aided engineering.
ABL	acrylonitrile-butadiene-lignin
ABS	acrylonitrile-butadiene-styrene
ACMZ	designation for aluminum alloys containing aluminum, copper, manganese, and zirconium.
ACNM	designation for aluminum alloys containing aluminum, cesium, nickel and manganese.
AFA	Alumina-Forming Austenitics or Al ₂ O ₃ -forming austenitic alloys.

AFD	aminophenyl disulfide
Ag	silver
AgCl	silver chloride
AI	artificial intelligence
AISI	American Iron and Steel Institute
Al	aluminum
Al ₄ C ₃	aluminum carbide
Al-Ce-Ni	aluminum alloy demonstrating high mechanical properties at room and elevated temperatures along with good casting properties.
Al ₂ Cu	aluminum-copper (2:1)
Al-Gr	aluminum-graphene
Al ₂ O ₃	aluminum oxide
Al ₃ Ni	nickel aluminide
AlSi10Mg	Traditional cast aluminum alloy used in aerospace and automotive applications because of its light weight, low thermal expansion and good weldability and mechanical properties.
Al ₃ Zr	zirconium aluminide
Alloy 206	structural aluminum castings in the heat-treated temper for applications requiring high-tensile and yield strengths with moderate elongation.
Alloy 380	one of the most commonly specified aluminum alloys with the best combination of casting, mechanical, and thermal properties that exhibits excellent fluidity, pressure tightness, and resistance to hot-cracking and used for a wide variety of products including chassis for electronic equipment, engine brackets, gearbox cases, household furniture, power, and hand tools.
Alloy 6061	a precipitation-hardened aluminum alloy, containing magnesium and silicon as its major alloying elements.
Al ₂ O ₃	aluminum oxide (or alumina)
AM	additive manufacturing or additive manufactured (when referring to processes).
AM60	a castable magnesium alloy with excellent ductility, superior energy absorbing properties, and good strength and castability.
AMT	Advanced Materials for Transportation
ANL	Argonne National Laboratory
AOP	annual operating plan
AP	atmospheric plasma
AP	aerosol-based adhesion promotor
APO	atmospheric plasma-oxidation
APS	Advanced Photon Source
APT	atom probe tomography

Ar	argon
AR	as-cast
AS	advancing side
ASI	Applied Sciences, Inc.
ASM	American Society of Metals
ASTM	American Society for Testing and Materials
ASTM B193	American Society for Testing and Materials standard specification for determination of the electrical resistivity of metallic electrical conductor material.
ASTM B820	American Society for Testing and Materials standard test method for bend testing copper and copper alloy strip samples to determine product formability or the ability to resist cracking when forming a bend around a specific radius.
ASTM B871	American Society for Testing and Materials standard test method for tear testing of aluminum alloy products.
ASTM D256	American Society for Testing and Materials standard for impact testing according to the Izod method for determination of the notched impact resistance of plastics.
ASTM D257	American Society for Testing and Materials standard test method for determining surface resistivity and volume resistivity of insulating materials.
ASTM D412	American Society for Testing and Materials standard used to evaluate the tensile properties of vulcanized thermoset rubber and thermoplastic elastomers.
ASTM D635	American Society for Testing and Materials standard test method for determining the rate of burning for plastics.
ASTM D638	American Society for Testing and Materials standard test method to determine the tensile strength of both reinforced and non-reinforced plastics.
ASTM D2344	American Society for Testing and Materials test standard designed to measure the short-beam strength of high modulus fiber-reinforced polymer matrix composites.
ASTM D3039	American Society for Testing and Materials standard test method for tensile strength of composite materials.
ASTM D3518	American Society for Testing and Materials standard test method for in-plane shear of composite materials.
ASTM D4541	American Society for Testing and Materials standard test method for pull-off strength of coatings using portable adhesion testers.
ASTM D5470	American Society for Testing and Materials standard that measures the steady-state thermal impedance of electrical insulating materials used to enhance heat transfer in electrical and electronic applications.
ASTM D5528	American Society for Testing and Materials standard test method for Mode I fracture toughness of composite materials.
ASTM D6641	American Society for Testing and Materials standard test method for compressive strength of composite materials.
ASTM D7896-19	American Society for Testing and Materials standard test method for thermal conductivity, thermal diffusivity, and volumetric heat capacity of engine coolants and related fluids by a transient hot-wire liquid thermal conductivity method.

ASTM D7905	American Society for Testing and Materials standard test method for Mode II fracture toughness of composite materials.
ASTM E8-16a	American Society for Testing and Materials standard test method for tension testing of metallic materials.
ASTM E162	American Society for Testing and Materials standard for the measurement of surface flammability of materials.
ASTM E290	American Society for Testing and Materials standard test method for determining the ductility of metals through bend testing to provide a visual indication of the material's ductility.
ASTM E662	American Society for Testing and Materials standard test method for specific optical density of smoke generated by solid materials.
ASTM E800	American Society for Testing and Materials standard guide for gases present or generated during fires.
ASTM E831	American Society for Testing and Materials standard test method for linear thermal expansion of solid materials by thermomechanical analysis.
ASTM E1269	American Society for Testing and Materials standard test method for determining specific heat capacity by differential scanning calorimetry.
ASTM E1354	American Society for Testing and Materials standard test method for fire-test-response that measures the response of materials to a controlled level of radiant heat.
ASTM E1461	American Society for Testing and Materials standard test method for the determination of the thermal diffusivity of primarily homogeneous isotropic solid materials.
ASTM E1922	American Society for Testing and Materials standard test method for tensile and compressive translaminar fracture toughness.
ASTM G85	American Society for Testing and Materials test standard for cyclic acidified salt fog (spray) testing.
ASTM G155	American Society for Testing and Materials standard test method that uses a xenon arc lamp to simulate the full spectrum sunlight weathering.
at.%	atomic percent
ATR-FTIR	Attenuated total reflectance – Fourier-transform infrared
AUTO-SMART	Accelent Technologies, Inc. is a product name for a sensor system that assists with vehicle self-sufficiency.
AW-5083 H111	aluminum alloy that is non-heat-treatable containing 4%-4.9% Mg and 0.4%-1.0% Mn with moderate strength, excellent cold forming, welding and spot-welding properties, and good corrosion resistance.
AZ31B	most widely available magnesium grade alloy, high-strength-to-weight ratio with a composition of 2.5% to 3.5% aluminum and 0.7% to 1.3% zinc.
AZ91D	a high-purity magnesium cast alloy that has excellent corrosion resistance, excellent castability, and good strength.
B	
B	boron

BAAM	big area additive manufacturing
BaTiO ₃	barium titanate
BCC or bcc	body-centered cubic
BF	basalt fiber
BiW or BIW	body-in-white
BMS	battery monitoring system
BOF	basic oxygen furnace
BP	budget period
BR	butadiene rubber
B/U	bending/unbending
C	
°C	degrees Centigrade
C	carbon (when referring to chemical elements)
C	compression (when referring to stress-strain relationships)
C _p	specific heat capacity
C11000	copper that has high electrical and thermal conductivity, good corrosion resistance and solderability used for welding fixtures, anodes, bus bar in electrical power installations, ground straps, commutators and current carrying hardware.
Ca	calcium
CaCl ₂	calcium chloride
CA	Composites Automation
CA	cellular automation
CAD	computer-aided design (or drawing)
CADES	Compute and Data Environment for Science
CAE	computer-aided engineering
CALPHAD	<u>CAL</u> culat <u>ion</u> of <u>PHA</u> se <u>D</u> iagrams
CAN	covalent adaptable network
CAN-CFRC	covalent adaptable network-based carbon fiber-reinforced composites
CB	carbon black
CCF	continuous carbon fiber
Cd	cadmium
Ce	cerium
CF	carbon fiber
CF-ABS	carbon fiber-reinforced acrylonitrile-butadiene-styrene
CFC	carbon fiber composite

CFD	computational fluid dynamics
CFR	Code of Federal Regulations
CFRC	carbon fiber-reinforced composite
CFRP	carbon fiber-reinforced polymer
CFR/PC	carbon fiber / polycarbonate
CFTF	Carbon Fiber Technology Facility
CHM	crosshead melt
cm	centimeter
cm/sec	centimeters per second
cm ²	square centimeter
cm ³	cubic centimeter
cm ³ /h	cubic centimeter per hour
cm ³ /min	cubic centimeter per minute
CM	compression molding
CMCV	charge motion control valve
CMOS	complementary metal-oxide semiconductor
CNF	carbon nanofiber
CNG	compressed natural gas
CNT	carbon nanotube
Co	cobalt
CO ₂	carbon dioxide
CO ₂ e/km	carbon dioxide equivalent per kilometer
COF or CoF	coefficient of friction
COMSOL	a cross-platform finite element analysis, solver, and multiphysics simulation software that allows conventional physics-based user interfaces and coupled systems of partial differential equations.
cP	centipoise
CPEC	close proximity electromagnetic carbonization
Cr	chromium
CR	cold-rolled
CRADA	Cooperative Research and Development Agreement
Cr ₂ O ₃	chromium oxide
cSt	centistoke
CT	computed tomography
Cu	copper

CUICAR	Clemson University International Center for Automotive Research
Cu ₂ O	cuprous oxide
Cura	3D slicing software produced by Ultimaker
CUV	crossover utility vehicles
CVD	chemical vapor deposition (or deposited)
CW	cold work
D	
dB	decibels
DC	direct current
DC3D8	a general purpose linear brick element fully integrated (2x2x2 integration points).
DCM	dichloromethane
DE	dynamic epoxy
deal.II	a free, open-source library to solve partial differential equations using the finite element method.
DED	directed energy deposition
DFT	density functional theory
DGEBA	diglycidyl ether of bisphenol A
DIC	digital image correlation
DICTRA	<u>D</u> iffusion- <u>C</u> ontrolled <u>T</u> RANSformations in multicomponent systems, a software diffusion module within Thermo-Calc for accurate simulation of diffusion-controlled reactions in multicomponent alloy systems.
DIN	Deutsches Institut für Normung
DIW	direct ink writing
dL/g	deciliters per gram
DNN	deep neural network
d _o	position of a projection lens
DO ₃	designation for Fe ₃ Si-type ordered phase
DoE	design of experiments (when referring to experimental work)
DOE	U.S. Department of Energy (when referring to the agency)
DP	dual phase
DP590	dual phase steel with low tensile strength (590 MPa) and low yield frequently used in automotive body structure applications requiring high-energy absorption.
DPE	dynamic polyurea/epoxy
DS	degree of shrinkage
DSC	differential scanning calorimetry

E

E'	storage modulus
E _a	energy of crystallization
EAF	electric arc furnace
EBSD	electron backscatter diffraction
ECAP	equal channel angular pressing
EDM	electro-discharge machining
EDS	energy-dispersive spectroscopy
e.g.	abbreviation meaning “for example”
E-EGR	enhanced exhaust gas recirculation
EEERE	Office of Energy Efficiency and Renewable Energy
EGR	exhaust gas recirculation
EIS	electrochemical impedance spectroscopy
EKKcapcast	software for simulating casting processes
ELV	end-of-life vehicle
EM	electromagnetic
EMI	electromagnetic interference
e-motor	electric motor
EoL or EOL	end-of-life
EOLR	end-of-life recycling
EPA	Environmental Protection Agency
Eqn.	equation
E _r	activation energy
Er	erbium
et al.	abbreviation meaning “and others”
eV	electron volt
EV(s)	electric vehicle(s) (when referring to types of vehicles)
<i>ex-situ</i>	off-site or out of place

F

f _c , f _s , and f _p	effective focal length of the optics
FCA US LLC	Fiat Chrysler Automobiles U.S. Limited Liability Company
FCC or fcc	face-centered cubic
FCMF	Fibers and Composites Manufacturing Facility
FDM	fused deposition modeling
FDS	flow-drill screw

Fe	iron
FEA	finite element analysis
FEM	finite element method (or model)
FEV	fuel cell electric vehicle
FIB	focused ion beam
FIFA	flow-induced fiber alignment
FLIR	forward-looking infrared
FMVSS	Federal Motor Vehicle Safety Standard
FOA	Funding Opportunity Announcement
FRP	fiber-reinforced polymer
FSLW	friction stir linear welding
FSP	friction stir processing
F-SPR	friction self-piercing riveting
FST	fire, smoke, and toxicity
FSW	friction stir welding
FTIR	Fourier-transform infrared spectroscopy
Fv	Favimat (a single fiber testing machine)
FVF	fiber volume fraction
FWF	fiber weight fraction
FWHM	full width at half maximum
FY	fiscal year
G	
g	gram(s)
G _{IC}	Mode I interlaminar fracture toughness
g/cc or g/cm ³	grams per cubic centimeter
GCV	generalized cross-validation
GF	glass fiber
GFRP	glass fiber-reinforced polymer
GHG	greenhouse gas
GM	General Motors LLC
GNP	graphene nanoparticles
GPa	gigapascals
GPC	gel permeation chromatography
GREET [®]	<u>G</u> reenhouse gases <u>R</u> egulated <u>E</u> missions and <u>E</u> nergy use in <u>T</u> echnologies

Gridrec	an algorithm for multi-slice tomography
GSAS	General Structure Analysis System
gsm	grams per square meter
GSU	Georgia Southern University

H

h or hr	hour(s)
H ₂	hydrogen
H ₂ O	water
HAADF	high-angle annular dark field
HC340LA	old rolled steel with high yield strength for cold forming
HD	heavy duty
HDG	hot-dip galvanized (or hot-dip galvanizing)
HDI	hexamethylene diisocyanate
HDPE	high density polyethylene
HE-XRD	high-energy x-ray diffraction
HFR	High-rate friction riveting
HIP	hot isostatic pressing
HiVe	high velocity (riveting)
HPDC	high-pressure die-casting
HP-RTM	high-pressure resin transfer molding
HRC	Hardness Rockwell – C scale
HR-TEM	high-resolution transmission electron microscopy
HSLA	high-strength low alloy
Hv	Vickers hardness
HyFi	hybrid fibers
Hz	hertz

I

i.e.	abbreviation for “id est,” a Latin phrase meaning “that is”
i3	five-door urban electric vehicle
I6	inline six (cylinder)
I _G /I _D	Ratio of the intensities of the G band to the D band for Raman spectra
IACMI	Institute for Advanced Composites Manufacturing Innovation
IACS	International Annealed Copper Standard
ICE(V)	internal combustion engine (vehicle)

ICME	integrated computational materials engineering
ICP-OES	inductively coupled plasma - optical emission spectrometer
IEA	International Energy Agency
IFSS	interfacial shear strength
IIHS	Insurance Institute for Highway Safety
ILSS	interlaminar shear strength
IMC	intermetallic compound
IMR	internal mold release
in.	inch
<i>in-situ</i>	on-site or in place
IPC	interpenetrating phase composite
IPF	inverse pole figure
IR	infrared
ISO	International Organization for Standardization
ISO 5660	a test method for assessing the heat release rate and dynamic smoke production rate of specimens exposed in the horizontal orientation to controlled levels of irradiance with an external igniter.

J

<i>J</i>	toughness value
J	joule
J/kg*K	joules per kilogram degree Kelvin
JCP	Joining Core Program

K

<i>k</i>	thermal conductivity
k	permeability content (when used in Darcy's law)
k-factor or k-value	the parameter determining how much linear advance affects the print
K	degree Kelvin
K _{1C}	fracture toughness
K ₂ CO ₃	potassium carbonate
keV	kiloelectron volts
kg	kilogram
kgF	kilogram (force)
kg/hr	kilogram per hour
kg/mol	kilogram per mole
kN	kilonewton

KSII	designation for a lap-shear test, cross-tension sample
Ksi, ksi, and kpsi	kilopound per square inch
KUKA AG	KUKA Aktiengesellschaft Germany (manufacture of robotic systems)
kV	kilovolt
kWh/kg	kilowatt-hour per kilogram
kW/m ²	kilowatt per square meter
L	
L	liter
L	longitudinal
LabVIEW	a graphical programming environment used to develop automated research, validation, and production test systems.
lb.	pound(s)
LBNL	Lawrence Berkeley National Laboratory
LCA	life cycle analysis
LCCF	low-cost carbon fiber
LCI	life cycle inventory
LCS	low carbon steel
LD	light-duty
LFT	long-fiber thermoplastic
Li	lithium
LightMAT	Lightweight Materials Consortium
LiNO ₃	lithium nitrate
LLC	limited liability company
LLNL	Lawrence Livermore National Laboratory
LMCP	Lightweight Metals Core Program
LMP	Larson-Miller Parameter
LPPSC	low pressure precision sand-casting
LSAM TM	Large-Scale Additive Manufacturing
LS-DYNA	advanced, general purpose, multiphysics simulation software package.
LSS	lap-shear strength
LW	lightweight
M	
m	meter (when referring to the measurement)
m	dynamic viscosity of the fluid (when referring to the fluid)

m ²	square meter
M	magnification ratio (when referring to optics)
M	molecular weight (when referring to a material property)
M	molar (when referring to the amount of a substance)
MA	Massachusetts
MA	maleic anhydride
MAS	micro-alloyed steel
MAT	material
MATLAB	<u>MAT</u> rix <u>LAB</u> oratory, a multi-paradigm numerical computing environment and programming language.
MAX	designation for the family of nano-laminated materials for MXenes having the general formula: Mn+1AXn, (MAX) where n = 1 to 4.
M ₂₃ C ₆	phases formed through different heat-treatment of iron-based alloys that can dramatically influence the mechanical properties of materials such as ferritic and austenitic stainless steels.
MCE	multi-cylinder engine
MeOH	methanol
MESC	multifunctional energy storage composites
Mg	magnesium
MgO	magnesium oxide
Mg ₂ Si	magnesium silicide
Mg(OH) ₂	magnesium hydroxide
MgZn ₂	dizinc magnesium
MI	Michigan
MIC	maximal information coefficient
MIL-STD-2031	U.S. Department of Defense test method standard for fire and toxicity test methods and qualification procedure for composite material systems used in hull, machinery, and structural applications inside naval submarines.
min	minute(s)
MJ	mega-joule
MJ/kg	mega-joule per kilogram
ml or mL	milliliter
ML	machine-learning
mm	millimeters
mm ²	square millimeters
mm ³	cubic millimeters

mm/min	millimeters per minute
mm/sec or mms ⁻¹	millimeters per second
MMC	metal matrix composites
Mn	manganese
Mo	molybdenum (when referring to the element)
Mo	Mouromtseff Number (when referring to heat transfer)
MoS ₂	molybdenum disulfide
MOOSE	multiphysics object-oriented simulation environment
MPa	megapascals
MPB	melt pool boundary
MPI	melt pool interior
MQL	minimum quantity lubrication
MR	molecular rebar
MRD	Molecular Rebar Design, LLC
Msi or msi	million pounds per square inch
MSIA	multiscale image analysis
MS/m	megasiemens per meter
MSU	Michigan State University
M-TOW	multi-tow
mV	millivolts
mV/g	millivolt per gram
MW	microwave
mW/cm ²	megawatts per square centimeter
MX or MXene	ceramics first discovered in 2011 that comprise one of the largest families of two-dimensional materials.
MY	model year
N	
N	nitrogen
N	Newton
N ₂	diatomic nitrogen
NaCl	sodium chloride
NaHCO ₃	sodium bicarbonate
Nb	niobium
NbC	niobium carbide
NBR	nitrile butadiene rubber

NCMS	Ni-Cr-Mn-Si
Nd	neodymium
NDE	nondestructive evaluation
Netfabb	software used to prepare three-dimensional files for printing by converting them into 2.5-dimensional slice files, consisting of a list of two-dimensional layers that the 3D printer will create one by one.
NETL	National Energy Technology Laboratory
NHSTA	National Highway Transportation Safety Administration
Ni	nickel
nm	nanometer(s)
NMCFs	nano-, micro-combined fillers
nm/sec	nanometer per second
NMP	N-methylpyrrolidone
NMR	nuclear magnetic resonance
NMVC-R ²	<u>n</u> ano- and <u>m</u> icro-filler <u>r</u> einforced <u>y</u> trimer <u>c</u> omposites made from <u>r</u> ecycled milled carbon fibers.
NN	neural network
NREL	National Renewable Energy Laboratory
NVH	noise, vibration, and harshness
nW/cc	nano Watts per cubic centimeter
O	
O	monatomic oxygen
O ₂	diatomic oxygen
OCP	open circuit potential
OEM	original equipment manufacturer
OM	optical microscopy
OMEGA	<u>O</u> ptimization <u>M</u> odel for reducing <u>E</u> missions of <u>G</u> reenhouse Gases from <u>A</u> utomobiles
OOPB	out of paint booth
OPF	oxidized precursor fiber
OPP	out-of-plane printing
ORNL	Oak Ridge National Laboratory
OSU	The Ohio State University
P	
P (or p)	pressure
P	power

PA	polyamide
PA-6	polyamide 6 (or nylon 6)
PA-66	polyamide 66 (or nylon 66)
PAG	polyalkylene glycol
PALAPREG® P18-03	an unsaturated polyester resin derived from maleic acid and glycols, dissolved in styrene with medium viscosity and high reactivity.
PAN	polyacrylonitrile
PAO	polyalphaolefin
Pa*s	Pascal-seconds
Pb	lead
PC	polycarbonate (when referring to a material)
PC	PrintCast or PrintCasting (when referring to an additive manufacturing process)
PCA	principal component analyses
PCC	Pearson Correlation Coefficient
PDF	probability density function
PE	polyethylene
PECAN	polyester-based covalently adaptable network
PEO	polyethylene oxide
PET	polyethylene terephthalate
PFIB	plasma focused ion beam
PFRP	polymer-fiber-reinforced polymer
PFZ	precipitate-free zones
PHR	parts per hundred resin
PI	principal investigator (when referring to the project)
PI	powder impregnation (when referring to the method)
PLA	polylactic acid
PLC	programmable logic controller
PMCP	Propulsion Materials Core Program
PNNL	Pacific Northwest National Laboratory
PODA	poly(4,4'-oxydianiline terephthalamide
POSS	polyhedral oligomeric silsesquioxanes
PP	polypropylene
PP45SGF	polypropylene glass fiber
ppi	pores per square inch
ppm	parts per million

PPS	pedestrian protection system
PPTA	polyparaphenylene terephthalamide
PS	polymer shielded
psi	pounds per square inch
PμSL	projection micro-stereolithography
PT	plasma treatment
PU	polyurea
PUE	power ultrasonic edge
PUSP	power ultrasonic-based surface processing
PVA	polyvinyl alcohol
PVC	polyvinyl chloride
PVDF	polyvinylidene difluoride
PVP	polyvinylpyrrolidone
PZT	lead zirconate titanate

Q

Q (with number)	quarter (of a year)
Q or q	heat flux
Q	USAXS scattering vector

R

R	resistance
R _a	surface roughness
rad/s	radian per second
RAPID	a photopolymer resin that changes its physical properties when introduced to light.
R&D	research and development
R&DD	research, development, and deployment
RC	recycled content
RC5754	Al alloy belonging to the group of the strain hardening AlMgMn alloys whose strength level is controlled by cold forming and final annealing and used in automotive bodies where a soft, very formable condition is desirable.
rCF	recycled carbon fiber
RE	rare-earth
ReaxFF	reactive force field
ReaxFF MD	reactive force field molecular dynamics
RH	relative humidity

RIVTAC®	a high-speed process supplied by Bollhoff for joining aluminum, steel, plastics, and non-ferrous metals, as well as for mixed joints, multilayer joints, and hybrid joints of these materials
rpm or RPM	revolution(s) per minute
RR	rolling resistance
RR350	an alloy that evolved from a World War II aircraft application by Rolls Royce
RS	retreating side
RSCF	rolling-sliding contact fatigue
RSW	resistance spot weld (or welding)
r/t	radius to thickness ratio
RT	room temperature
RTM	resin transfer mold (or molding)
RVE	representative volume element
S	
s	seconds
S/cm	siemens per centimeter
S/m	siemens per meter
SABC1470	silicon-aluminum-boron coated (grade 1470 steel)
SBIR	Small Business Innovative Research
Sc	scandium
SCB	structured carbon black
SCF	short carbon fibers
SE	secondary electron
SE	shielding effectiveness (when referring to electromagnetic interference)
sec.	second
SECCM	scanning electrochemical cell microscopy
SEM	scanning electron microscope (or microscopy)
SF-TP or SFT	short-fiber-reinforced thermoplastic
ShAPE™	<u>s</u> hear-assisted processing and <u>e</u> xtrusion
SHM	structural health monitoring (when referring to monitoring vehicle conditions)
SHM	simple harmonic motion (when referring to impact testing)
Si	silicon
SiO ₂	silicon oxide
SLIC	sustainable lightweight intelligent composite
SMC	sheet molding compound

S-N	stress-number of cycles
Sn	tin
SNL	Sandia National Laboratories
SO ₃	sulfur trioxide
SOC	state of charge
SOH	state of health
SPD	severe plastic deformation
SPH	smooth particle hydrodynamics
Sr	strontium
SRNL	Savannah River National Laboratory
SS	stainless steel
SSBR	solution styrene-butadiene rubber
SStAC	Stainless Steel Alloy Corrosion (the name of a simulation tool)
STEM	scanning transmission electron microscope (or microscopy)
STQ	solution-treated and quenched
STTR	Small Business Technology Transfer Research
SuRF	Scaleup Research Facility
SUV	sport utility vehicle
T	
t	time
T	temperature (when referring to temperature)
T	tension (when referring to stress-strain relationships)
T	Tesla (when referring to the magnetization field)
T	transverse (when referring to direction)
T _c	creep temperature (when referring to the temperature that materials deform)
T _g	glass transition temperature
T/H	temperature/humidity
T5	temper designation for aluminum that is cooled from an elevated temperature shaping process then artificially aged.
T6	temper designation for aluminum that is heat-treated at a temperature between 325°F and 400°F to increase the strength.
TA	thickening agent
tanδ	loss factor
TCF	Technology Commercialization Fund
TCFE	TCS steel and Fe-alloys database (by Thermo-Calc)

TCI	terephthaloyl chloride
TCP	technology collaboration programs
TCR	temperature coefficient of resistivity
TEA	techno-economic analysis
TEM	transmission electron microscope (or microscopy)
TESPT	bis-(3-triethoxysilylpropyl) tetrasulphane
TFP	tailored-fiber placement
TGA	thermogravimetric analysis
Thermo-Calc	software package for thermodynamic
Ti	titanium
Ti ₃ AlC ₂	titanium alumina carbide
Ti-6Al-4V	a Grade 5 alloy consisting of a two-phase $\alpha+\beta$ titanium alloy with aluminum as the alpha stabilizer and vanadium as the beta stabilizer.
TiB ₂	titanium boride
TiO ₂	titanium dioxide or titania
Ti ₃ C ₂	titanium carbide
Tl	thallium
Tm	thulium
TMD	transition metal dichalcogenide
TMF	thermomechanical fatigue
TMP	thermomechanical processing
TN	Tennessee
Tomopy	<u>T</u> omography- <u>P</u> ython, open-sourced code used to address the needs for image correction and tomographic reconstruction in an instrument independent manner employed at most U.S. synchrotron facilities.
T _p	peak reaction rate temperature
TPC	Technology Collaboration Program
TPM	thermal-pseudo-mechanical
TPU	thermoplastic polyurethane
TRC	Transportation Research Center, Inc
TRL	technology readiness level
TS	tensile strength
TSP	traveling salesman problem
TTT	thermoplastic TCF tape
TuFF	<u>T</u> ailorable <u>u</u> niversal <u>F</u> eedstock for <u>F</u> orming
TYS	tensile yield strength

U

UAM	ultrasonic additive manufacturing
UCB	University of California–Berkeley
UCC	ultraconductive copper
UD	unidirectional
UD-CCM	University of Delaware Center for Composite Materials
UDRI	University of Dayton Research Institute
UHMWPE	ultra-high molecular weight polyethylene
UHSS	ultra-high strength steel
UJ	ultrasonic-based spot-joining
ULVAC ZEM-3	An instrument that simultaneously measures the Seebeck coefficient and electric conductivity of thermoelectric materials.
UMAT	<u>u</u> ser-defined mechanical <u>m</u> aterial behavior - a user subroutine that can be used to define the mechanical constitutive behavior of a material.
U.S.	United States
U.S. DRIVE	U.S. Driving Research and Innovation for Vehicle efficiency and Energy sustainability
USA	United States of America
USAMP	U.S. Automotive Materials Partnership
USW	ultrasonic welding
UTS	ultimate tensile strength
UV	ultraviolet

V

v	velocity
V	vanadium (when referring to the element)
V	volt or voltage (when referring to electricity)
V	volume (when referring to quantity) or wear volume (when referring to wear rate calculations)
V/g	volts per gram
VAC	volts alternating current
VARTM	vacuum-assisted resin transfer molding
VDA	Verband der Automobilindustrie
VFAW	vaporizing foil actuator welding
VIN	vehicle identification number
viz.	“videlicet;” a contraction of the Latin phrase “videre licet,” meaning “it is permitted to see” (synonym: namely).

VMT	vehicle miles traveled
V ₂ O ₅	vanadium oxide
vol. %	volume percent
Vortec L96	an engine produced by General Motors for use in its full-size heavy duty pickup trucks, vans, and SUVs.
VPV	code designation for the equilibrium phase volume fraction.
vs.	versus
VTO	Vehicle Technologies Office
W	
w	weight
W	watts (when referring to electrical energy)
W	tungsten (when referring to the chemical element)
WAIM	water-assist injection-molding
W/mK	watts per meter-Kelvin
W/m°C	watts per meter degree Centigrade
WSU	Washington State University
wt% or wt. %	percent by weight
X	
XGBoost	an optimized distributed gradient boosting library
Xe	xenon
XPS	x-ray photoelectron spectroscopy
XRD	x-ray diffraction
Y	
Y	yttrium
YAG	yttrium-aluminum-garnet
Yb	ytterbium
YS	yield strength
Z	
Zn	zinc
ZOLTEK	a producer of commercial carbon fiber
Zr	zirconium
ZT	ZOLTEK tape

Executive Summary

The Materials Technology subprogram supports the Vehicle Technologies Office's mission to accelerate the deployment of clean energy technology toward achieving net-zero emissions in the transportation sector. The Propulsion Materials research portfolio seeks to develop higher performance materials that can deliver the required electrical, thermal, and strength properties needed to improve efficiency of vehicle powertrains including power electronics. Lightweight Materials research portfolio enables improvements in vehicle efficiency by providing properties that are equal to or better than traditional materials at a lower weight. Because it takes less energy to accelerate a lighter object, replacing cast iron and traditional steel components with lightweight materials, such as advanced high-strength steels, magnesium (Mg) alloys, aluminum (Al) alloys, and fiber-reinforced polymer composites can directly reduce a vehicle's energy consumption. By 2025, the Materials Technology research activities seek to enable a 25% weight-reduction of the glider for light-duty vehicles including body, chassis, and interior as compared to a 2015 baseline at no more than a \$5/lb-saved increase in cost.

Propulsion Materials

In fiscal year (FY) 2022, the Propulsion Materials portfolio began transitioning research from materials for internal combustion engines to focus on materials improvements for electric vehicle powertrain components. The work presented in this report represents the conclusion of efforts in four main areas: (1) use of multiscale modeling to predict corrosion and oxidation of engine components and the material properties needed for future engines; (2) development of new lightweight alloys for high-temperature engine components; (3) additive manufacturing (AM) of powertrain alloys; and (4) lightweight high-efficiency engines for medium duty (MD) vehicles. In addition to these four main thrusts, work was completed on several exploratory projects in novel materials, coatings, processing techniques, and characterization methods relevant to propulsion materials.

The environment within an engine and exhaust system during operation is extremely harsh, with high temperatures and pressures, combustion, and corrosive exhaust gases. This environment corrodes components, including engine intake and exhaust valves, valve seats, and exhaust manifolds. Three projects aim to develop practical and accurate models that can rapidly evaluate corrosion/oxidation of materials—such as stainless steel, nickel-chromium (Ni-Cr) based alloys and cast iron (Fe)—and predict the components performance. These new models will help decrease the time and cost of development as materials are selected for new engines that operate at higher temperatures.

Automotive applications need low-cost, lightweight, high-temperature alloys to enhance efficiencies in systems such as internal combustion engines. One project focuses on increasing the compositional range of the Al-Fe-silicon (Si) system via alloy design and non-equilibrium processing, such as AM. Another effort seeks to develop a fundamental understanding of the features that impart thermal stability to cast Al precipitate microstructures, such as those found in Al-Cu and Al-Cu-Mn-Zr (ACMZ) alloys. Some components, such as exhaust valves, are exposed to even higher temperatures and the development of lower cost, improved wrought-processed Ni-based alloys is needed to achieve the combination of yield and fatigue strengths, oxidation resistance, and cost specific to the operating characteristics and lifetime expectations. Pistons in heavy duty (HD) diesel also have unique requirements and researchers are investigating existing commercial alloys, new developmental alloys, and alloys combined with thermal barrier coatings to enable increased operating temperature while requiring only moderate cost increases. Last, corrosion-resistant coatings are also being evaluated to determine whether the operating temperatures of alloys can be increased by improving cyclic oxidation resistance without impacting the alloy high-cycle fatigue behavior.

AM offers unprecedented possibilities to fabricate unique and complex near-net-shape components leading to significant savings by decreasing tooling and materials cost, accelerating prototype development, offering unique properties, and increasing system efficiency through advanced designs not achievable via conventional fabrication processes. In-depth understanding of the relationship between microstructure and processing parameters could result in unique microstructures and enhanced or geometrically tailored properties for a wide range of powertrain materials and components. Work in this area addresses the specific challenges and opportunities associated with AM for future LD and HD engine and electronic components. Key factors, such as cost, influence of feedstock characteristics, volatilization of species, cooling rates, non-equilibrium phases, materials properties, non-uniform geometry-dependent thermal history, thermal cycling, etc., are assessed for existing and new materials via both modeling and experimental studies.

While the market share of battery electric vehicles is increasing, most MD vehicles are projected to contain conventional or hybrid internal combustion engines well beyond 2030. Improvements in engine efficiency and reductions in powertrain weight have strong leverage to reduce vehicle-related CO₂ emissions for decades to come. Two continuing projects will use advanced materials and weight-savings technologies to demonstrate greater than 15% weight-reduction of the baseline engine while increasing efficiency. Approaches being investigated include development of new high-strength and heat-resistant materials that can be incorporated with novel metal casting and AM processes to produce highly durable engine structures to maximize performance of the materials and systems with minimum mass and cost.

Lightweight Materials

In FY 2022, the lightweight materials portfolio included research in the following three areas: (1) improving the properties and manufacturability of light metals, such as advanced high-strength steel (AHSS), Al alloys, and Mg alloys; (2) reducing the cost of carbon fibers (CFs) and developing Integrated Computational Materials Engineering (ICME) frameworks for manufacturing of polymer composites; and (3) developing novel joining methods to enable multimaterial systems.

Substitution of light metals for mild steel can result in weight-savings of 25%–60% per component, which increases fuel efficiency. However, there are several challenges to the increased use of light metals including material cost, room temperature formability, and corrosion mitigation. In FY 2022, a new core research program focused on the local modification of properties through processing of lightweight metals was launched. Several projects in the Light Metals Core Program are working to lower the cost of Al by enabling the broader use of lower cost alloys which also simplifies manufacturing logistics. Similarly, the use of high-performance Mg alloys in the automotive industry is currently limited due to the addition of costly rare-earth (RE) elements, need for high-temperature forming, and difficulties in corrosion mitigation. Four projects in this report address the challenges that Mg presents; one through alloy development and the other three through novel processing methods that address both formability and corrosion.

Polymer composites also have the potential to reduce component weight by more than 60%. One of the main barriers to widespread implementation is the high cost of CF, which is due in large part to the cost of input material (precursor) and the CF conversion process. In addition to a successfully commercialized plasma-oxidation technology, several projects are addressing this challenge by developing higher throughput conversion of CF, thus further lowering manufacturing costs and increasing production rates. Two projects are investigating potential low-cost CF alternative precursors utilizing ICME models to guide their research to meet DOE's cost targets (no more than \$5 per pound) and four projects are developing alternate or recycled reinforcing fibers. Another challenge to implementation of polymer composites is related to the time required to manufacture components. Three projects are investigating new manufacturing methods including AM and tailored-fiber placement while additional projects are assessing opportunities to functionalize the fibers in automotive components for sensing, part consolidation and energy storage.

The most effective way to reduce the overall weight of a vehicle is to tailor the material selection to each component's needs. However, joining dissimilar materials to create a multimaterial structure is a significant challenge. In FY 2022, the Joining Core Program renewed its efforts by extending joining methods previously developed to additional material pairs, advancing solid-state joining toward industry readiness, investigating surface modifications to improve adhesion and corrosion resistance, and using artificial intelligence for weld quality control. The methods developed in the Joining Core Program include solid-state welding, ultrasonic welding, novel methods for mechanical fastening, and adhesives. Solid-state welding, including an impact welding process investigated by one project, allows for joining materials with vastly different melting temperatures, which is not possible with fusion welding. The portfolio also includes three projects that model the effect of galvanic corrosion on a wide variety of joining methods and material combinations to predict the effect on joint strength and fatigue life and one project that predicts failure of Al to steel joints.

(This page intentionally left blank)

Table of Contents

Vehicle Technologies Office Overview	1
Annual Progress Report.....	1
Organization Chart	2
Materials Technology Program Overview.....	3
Program Introduction	3
Program Goals.....	3
State-of-the-Art	4
Program Organization Matrix.....	5
I Propulsion Materials.....	7
I.1 Powertrain Materials Core Program.....	7
I.1.1 Thrust 1: Lightweight Alloys for Electric Vehicle Propulsion	7
I.1.1.1 Task 1A. Fundamental Studies of Al-Ni Alloys for Improved Electrical Propulsion (Oak Ridge National Laboratory).....	7
I.1.1.2 Task 1B. Higher Temperature Aluminum Alloys and Composites for Lightweight Brake Systems (Oak Ridge National Laboratory).....	14
I.1.1.3 Task 1C. Fundamentals of Fatigue and Creep in Advanced Lightweight Alloys: Cost-Effective Lightweight Alloys for Electric Vehicle Propulsion (Oak Ridge National Laboratory)	20
I.1.1.4 Task 1D. Fundamentals of Corrosion Behavior in Advanced Lightweight Alloys for Electric Vehicle Propulsion (Oak Ridge National Laboratory)	27
I.1.1.5 Task 1E. Lightweight Materials for Improved Electrical Properties (Oak Ridge National Laboratory).....	34
I.1.1.6 Task 1G. Fundamentals of Thermal Properties in Lightweight Alloys for Electric Vehicle Propulsion (Oak Ridge National Laboratory)	40
I.1.1.7 Task 1H. Hybrid Dispersion Strengthened Aluminum Matrix Composites for Higher Efficiency Electric Vehicle Powertrains: Cost-Effective Lightweight Alloys for Electric Vehicle Propulsion (Pacific Northwest National Laboratory)	46
I.1.2 Thrust 2: Materials and Lubricants for Heavy Duty EVs and EV Propulsion	53
I.1.2.1 Task 2A. High-Performance Soft Magnetic Materials for Motor Laminates (Fe-Si) via Shear Rolling (Oak Ridge National Laboratory).....	53
I.1.2.2 Task 2B. Ferrous Alloys for Fatigue-Resistant, Lightweight Geartrains for Heavy Duty Electric Vehicle Systems (Oak Ridge National Laboratory).....	61
I.1.2.3 Task 2C. New Lubricant Strategies for Advanced Thermal Management of Heavy-Duty EVs (Oak Ridge National Laboratory)	66
I.1.2.4 Task 2D. Carbon Nanotube (CNT) Coatings for Superlubricity and Thermal Management of Heavy Duty EVs (Oak Ridge National Laboratory).....	72
I.1.2.5 Task 2E. Solid-Phase Joining and Processing Methods Towards Efficient, Heavy-Duty EV Motors (Pacific Northwest National Laboratory).....	79
I.1.3 Thrust 3: Advanced Processing and Additive Manufacturing for Electric Vehicles.....	88
I.1.3.1 Task 3A. Fundamental Development of Additive Manufactured Alloys for Electric Vehicle Propulsion (Oak Ridge National Laboratory).....	88
I.1.3.2 Task 3B. Fundamentals of Non-Equilibrium Processing for Additive Manufacturing Alloys (Oak Ridge National Laboratory).....	95

I.1.3.3	Task 3C. Advanced Ceramics and Processing for Wireless Charging Systems (Ferrites) (Oak Ridge National Laboratory).....	106
I.1.3.4	Task 3D. Novel, Ultra-High Conductivity Materials (Copper Tape + Carbon Nanotubes) for Electric Vehicles (Oak Ridge National Laboratory).....	113
I.1.3.5	Task 3E. Print Casting of Lightweight Metal Matrix Composites for Battery Enclosures with Impact Resistance and Thermal Management (Oak Ridge National Laboratory).....	122
I.1.3.6	Task 3F. Ultra-Conductor Development for Enhanced EV Performance (Pacific Northwest National Laboratory).....	127
I.1.4	Thrust 4: Advanced Characterization and Computation	134
I.1.4.1	Task 4A. Advanced Characterization – Coordination of Multi-Lab Characterization (Task 4A1) (Oak Ridge National Laboratory).....	134
I.1.4.2	Task 4A. Advanced Characterization – Advanced Characterization of PMCP Research Samples: Characterization of Thermal, Electrical, and Magnetic Properties (Task 4A3) (Oak Ridge National Laboratory).....	141
I.1.4.3	Task 4A. Advanced Characterization – Argonne Advanced Characterization (Task 4A4) (Argonne National Laboratory).....	148
I.1.4.4	Task 4A. Advanced Characterization – Pacific Northwest National Laboratory Advanced Characterization (Task 4A5) (Pacific Northwest National Laboratory)...	155
I.1.4.5	Task 4B. Advanced Computation – Advanced Computational Materials (Task 4B1) (Oak Ridge National Laboratory).....	162
I.1.4.6	Task 4B. Advanced Computation – Machine-Learning Methods for Alloy Design (Task 4B3) (Oak Ridge National Laboratory).....	170
I.1.4.7	Task 4B. Advanced Computation – Life Cycle Analysis (LCA) of EVs GREET® (Task 4B4) (Argonne National Laboratory).....	176
I.2	Modeling of Powertrain Materials.....	183
I.2.1	Next-Generation High-Efficiency Boosted Engine Development (Ford Research and Advanced Engineering).....	183
I.2.2	Low-Mass and High-Efficiency Engine for Medium Duty Truck Applications (General Motors).....	190
I.2.3	Lightweight and Highly Efficient Engines Through Al and Si Alloying of Martensitic Materials (Oak Ridge National Laboratory).....	200
I.2.4	Multiscale Development and Validation of the Stainless Steel Alloy Corrosion (SStAC) Tool for High-Temperature Engine Materials (University of Florida).....	203
II	Lightweight Materials.....	212
II.1	Lightweight Metals Core Program	212
II.1.1	Thrust 1. Selective Processing of Al Sheet Materials (Tasks 1A, 1B, and 1C) (Oak Ridge National Laboratory and Pacific Northwest National Laboratory).....	212
II.1.2	Thrust 2. Selective Processing of Al Castings (Tasks 2A1, 2A2, 2B, and 2C) (Pacific Northwest National Laboratory and Oak Ridge National Laboratory).....	234
II.1.3	Thrust 3. Selective Processing of Mg Castings (Tasks 3A1, 3A2, and 3B) (Pacific Northwest National Laboratory and Oak Ridge National Laboratory).....	259
II.1.4	Thrust 4. Characterization, Modeling, and Life Cycle (Tasks 4A1, 4A2, 4A3, 4C1, and 4C2) (Pacific Northwest National Laboratory, Oak Ridge National Laboratory, and Argonne National Laboratory).....	277

II.2	Light Metals.....	294
II.2.1	ShAPE of Lightweight Alloys for Automotive Components (Pacific Northwest National Laboratory/ Magna International)	294
II.2.2	Developments of a Novel Magnesium Alloy for Thixomolding® of Automotive Components – LightMAT (Oak Ridge National Laboratory).....	301
II.3	Carbon Fiber and Polymer Composites.....	307
II.3.1	Composites Core Program	307
II.3.1.1	High-Temperature Carbon Fiber Carbonization via Electromagnetic Power (Oak Ridge National Laboratory).....	307
II.3.1.2	A Novel Manufacturing Process of Lightweight Automotive Seats – Integration of Additive Manufacturing and Reinforced Polymer Composite (Oak Ridge National Laboratory).....	319
II.3.1.3	Additive Manufacturing for Property Optimization for Automotive Applications (Oak Ridge National Laboratory).....	326
II.3.1.4	3D-Printed Hybrid Composite Materials with Sensing Capability for Advanced Vehicles (Oak Ridge National Laboratory).....	333
II.3.1.5	New Frontier in Polymer Matrix Composites via Tailored Vitrimer Chemistry (Oak Ridge National Laboratory).....	341
II.3.1.6	Adopting Heavy-Tow Carbon Fiber for Repairable, Stamp-Formed Composites (Oak Ridge National Laboratory).....	348
II.3.1.7	Multimaterial, Functional Composites with Hierarchical Structures (Oak Ridge National Laboratory).....	356
II.3.1.8	Layer Time Control for Large-Scale Additive Manufacturing Using High- Performance Computing (Oak Ridge National Laboratory).....	362
II.3.1.9	Ultra-Lightweight, Ductile Carbon Fiber-Reinforced Composites (Oak Ridge National Laboratory).....	376
II.3.1.10	Low-Cost, High-Throughput Carbon Fiber with Large Diameter (Oak Ridge National Laboratory).....	387
II.3.1.11	Carbon Fiber Technology Facility (Oak Ridge National Laboratory).....	394
II.3.1.12	Ultra-Lightweight Thermoplastic Polymer/Polymer Fiber Composites for Vehicles (Pacific Northwest National Laboratory and Oak Ridge National Laboratory).....	416
II.3.1.13	Efficient Synthesis of Kevlar and Other Fibers from Polyethylene Terephthalate (PET) Waste (Pacific Northwest National Laboratory).....	425
II.3.1.14	Additively Manufactured, Lightweight, Low-Cost Composite Vessels for Compressed Natural Gas Fuel Storage (Lawrence Livermore National Laboratory).....	431
II.3.1.15	Biobased, Inherently Recyclable Epoxy Resins to Enable Facile Carbon-Fiber Reinforced Composites Recycling (National Renewable Energy Laboratory)	437
II.3.1.16	Soft Smart Tools Using Additive Manufacturing (Savannah River National Laboratory).....	444
II.3.1.17	Functionally Designed Ultra-Lightweight Carbon Fiber-Reinforced Thermoplastic Composites Door Assembly (Clemson University).....	452
II.3.1.18	Multifunctional Smart Structures for Smart Vehicles (Ford Motor Company).....	458
II.3.1.19	Development of Tailored-Fiber Placement, Multifunctional, High-Performance Composite Material Systems for High-Volume Manufacture of Structural Battery Enclosure (General Motors)	479

II.3.2	Small Business Innovation Research (SBIR).....	493
II.3.2.1	Sustainable Lightweight Intelligent Composites (SLIC) for Next-Generation Vehicles (Newport Sensors, Inc.).....	493
II.3.2.2	Integrated Self-Sufficient, Structurally Integrated Multifunctional Sensors for Autonomous Vehicles (Accellent Technologies, Inc.).....	499
II.3.2.3	Short-Fiber Preform Technology for Automotive Part Production – Phase II (Composites Automation, LLC).....	507
II.3.2.4	Low-Cost Resin Technology for the Rapid Manufacture of High-Performance Fiber-Reinforced Composites (Trimer Technologies, LLC).....	515
II.3.2.5	Flexible, Lightweight Nanocomposites for EMI Shielding Suppression in Automotive Applications (Applied Sciences, Inc.).....	521
II.3.2.6	Conductive Lightweight Hybrid Polymer Composites from Recycled Carbon Fibers (RockyTech Ltd.).....	526
II.3.2.7	Game-Changing Resin/Coating/Adhesive Technology for Lightweight Affordable Composites (Structural Composites, Inc.).....	532
II.3.2.8	Changing the Design Rules of Rubber to Create Lighter Weight, More Fuel-Efficient Tires (Molecular Rebar Design, LLC).....	536
II.3.2.9	Hierarchical Micro/Nano Reinforced Multiscale Hybrid Composites for Vehicle Applications (Advent Innovations, Ltd.).....	543
II.4	Joining of Dissimilar Materials	550
II.4.1	Joining Core Program (JCP)	550
II.4.1.1	Machine-Learning for Automated Weld Quality Control (Pacific Northwest National Laboratory and Oak Ridge National Laboratory).....	550
II.4.1.2	Extending High-Rate Riveting to New Material Pairs (Pacific Northwest National Laboratory).....	567
II.4.1.3	Solid-State Joining of Multimaterial Autobody Parts Toward Industry Readiness (Pacific Northwest National Laboratory and Oak Ridge National Laboratory).....	579
II.4.1.4	Surface Modifications for Improved Joining and Corrosion Resistance (Pacific Northwest National Laboratory, Oak Ridge National Laboratory, and Argonne National Laboratory).....	594
II.4.1.5	Extending Ultrasonic Welding Techniques to New Material Pairs (Oak Ridge National Laboratory).....	615
II.4.2	Multi-Material Joining	621
II.4.2.1	A Hybrid Physics-Based, Data-Driven Approach to Model Damage Accumulation in the Corrosion of Polymeric Adhesives (Michigan State University).....	621
II.4.2.2	High-Strength Steel-Aluminum Components by Vaporizing Foil Actuator Welding (The Ohio State University).....	629
II.4.2.3	Manufacturing Demonstration of a Large-scale, Multi-Material Passenger Vehicle Sub-system (Clemson University).....	634
III	Crosscutting Activities	644
III.1	Lightweight Materials Crosscutting	644
III.1.1	Updated Analysis of the Relationship Between Light-Duty Vehicle Mass, Footprint, and Societal Fatality Risk per Vehicle Mile of Travel (Lawrence Berkeley National Laboratory).....	644

List of Figures

Figure I.1.1.1. APT image of the Al-Ni-Zr alloy heat-treated at 400 °C for 100 h: green, purple, and blue dots represent Al ₃ Ni, Zr, and Al, respectively. Source: ORNL.	9
Figure I.1.1.2. Microstructure evolution of the Al-Ni and Al-Ni-Zr alloys: Microstructure of (a) binary and (b) ternary alloys with various heat-treatment temperatures. (c) Microstructure of as-cast binary alloys with various Ni content. Source: ORNL.	9
Figure I.1.1.3. Microhardness data of the Al-Ni binary and Al-Ni-Zr ternary alloys with respect to (a) heat-treatment-temperature and (b) Ni content: Hv is the Vickers hardness unit (1 Hv \cong 9.8 MPa). Source: ORNL.	10
Figure I.1.1.4. Electrical conductivity of the Al-Ni binary and Al-Ni-Zr ternary alloys with (a) heat-treatment-temperature and (b) Ni content: %IACS is the relative electrical conductivity unit (anneal copper standard). Source: ORNL.	11
Figure I.1.1.5. Effect of adding various microalloying elements to Al-Ni (5-6 wt% Ni) on (a) microhardness and (b) electrical conductivity: Hv is Vickers hardness unit (1 Hv \cong 9.8 MPa) and %IACS is the relative electrical conductivity with respect to anneal copper as standard. Source: ORNL.	11
Figure I.1.1.6. Effect of various microalloying elements on (a) thermal diffusivities of Al-Ni-X alloys and (b) precipitation kinetics in the Al matrix. Source: ORNL.	12
Figure I.1.1.7. Comparison of the microstructure (post-creep) of cast ACMZ alloys with (a) 6 wt% Cu, (b) 9 wt% Cu [1], and (c) creep response of alloys in compression (C) and tension (T) at 300 °C. Source: ORNL.	15
Figure I.1.1.8. (a) ORNL sub-scale brake testing facility. (b) The applied test method simulating heavy truck braking conditions. Source: ORNL.	16
Figure I.1.1.9. Friction coefficient vs. speed for cast iron (baseline) and as-cast Al 9 wt% Cu ACMZ alloy. Source: ORNL.	17
Figure I.1.1.10. Friction coefficient (left y-axis and in blue) along with temperature (right y-axis and in orange) as a function of drag sequence for the entire test sequence (increasing and then decreasing speed). Representative results shown here are for an AM Al-Ce-Ni-Mn alloy in the as-printed state. Source: ORNL.	17
Figure I.1.1.11. Results summarizing wear of brake pad materials for the various Al alloys tested in the heat-treatment conditions of interest. Source: ORNL.	18
Figure I.1.1.12. Worn disc surface profiles measured with laser profilometry. (a) Cast iron baseline worn disc surface profile compared to printed and printed + aged AlCeNiMnZr alloys. (b) Comparison of wear surface profiles of aged ACMZ alloys with 9 wt% and 6 wt% Cu. (c) Comparison of wear surface profiles of as-cast ACMZ alloys with 9 wt% and 6 wt% Cu. Source: ORNL.	18

Figure I.1.1.13. Bright-field scanning transmission electron microscopy images of AM-ACMZ alloy in (a) as-fabricated, and (b) 300 °C, 200 h heat-treated conditions. (c) Minimum creep strain rate vs. applied tensile stress at 300 °C in as-fabricated and heat-treated conditions (e.g., 300 °C/200 h, 350 °C/24 h, 400 °C/6 h, 400 °C/200 h). The solid symbols are for <i>ex-situ</i> tests, while the open symbols for <i>in situ</i> creep tests. (d) Creep resistance of AM-ACMZ alloy compared to other high-temperature Al alloys [2]. T_c is creep temperature. Source: ORNL.....	22
Figure I.1.1.14. (a-c) Phase-specific lattice strain evolution, and (d-f) FWHM of diffraction peaks vs. creep time during the <i>in situ</i> creep tests for the AM-ACMZ alloy in as-fabricated and select heat-treated conditions. The macro strain and creep strain rate results are also shown in (a-c). Source: ORNL.....	22
Figure I.1.1.15. Schematic diagram of the proposed Load Shuffling mechanism to explain load shedding by θ particles during creep. Source: ORNL.....	23
Figure I.1.1.16. (a) Maximum stress vs. cycles to failure of the AM-ACNM alloy during fatigue testing at 350 °C. The horizontal arrow indicates specimen runout at 10^7 cycles and the corresponding stress level is the fatigue limit. The vertical arrows indicate the fatigue limit of wrought Al alloys at 315 °C and 370 °C. (b) Fractograph of a specimen tested at a maximum stress level of 60 MPa showing primary fatigue crack initiation at a Ce-oxide inclusion (yellow box) and multiple secondary cracks (fisheyes). (c) Provides a magnified view of the yellow box in (b), with the energy-dispersive spectroscopy maps in the inset confirming the inclusion as a Ce-oxide particle. Source: ORNL.....	24
Figure I.1.1.17. X-ray tomography reconstruction of a fatigue specimen tested at 60 MPa maximum stress showing (a) porosity inclusions, and (b) corresponding size distribution of pores and inclusions. The equivalent diameter is calculated by assuming the defects are spheres of equivalent volume. (c) Flow chart of the model to predict fatigue limit developed by Zhu et al. [3, 4]. Source: ORNL.....	25
Figure I.1.1.18. Typical Nyquist impedance plots of (a) as-cast and (b) aged Al alloys in a 3.5% NaCl solution. The solution immersion time was 1 h for all measurements. Note the impedance plots with higher-Z(real) and Z(img) values suggesting higher corrosion resistance. Source: ORNL.....	29
Figure I.1.1.19. Averages and standard deviations of $R_2 + R_3$ values in Al alloys in as-cast and aged conditions. Note that higher $R_2 + R_3$ values suggest higher corrosion resistance. Source: ORNL.....	29
Figure I.1.1.20. Typical Nyquist impedance plots of as-cast 319, AM-Al-Ce-Ni-Mn, and AM-Al-Ce-Ni-Mn-Zr alloys in a 3.5% NaCl solution. The solution immersion time was 1 h for all measurements. Source: ORNL.....	30
Figure I.1.1.21. Anodic polarization curves of as-cast 319, AM-Al-Ce-Ni-Mn, and AM-Al-Ce-Ni-Mn-Zr alloys in a 3.5% NaCl solution. The solution immersion time was ~2 h for all measurements. E_p of 319, Al-Ce-Ni-Mn, and Al-Ce-Ni-Mn-Zr are -665, -713 and -552 mV _{SCE} , respectively. Source: ORNL.....	30
Figure I.1.1.22. Two-dimensional corrosion resistance evaluation for as-cast 319 and three AM Al alloys. Note higher x and y values would correspond to higher corrosion resistance. Source: ORNL.....	31

Figure I.1.1.23. Cross-sectional SEM image and EDS maps of as-cast 319 after 168 h immersion in a 3.5% NaCl solution. Source: ORNL. 31

Figure I.1.1.24. Cross-sectional SEM image and EDS maps of AM-Al10SiMg after 168 h immersion in a 3.5% NaCl solution. Source: ORNL. 32

Figure I.1.1.25. Cross-sectional SEM image and EDS maps of AM-AlCeNiMnZr after 168 h immersion in a 3.5% NaCl solution. Source: ORNL. 32

Figure I.1.1.26. Vickers microhardness and electrical conductivity as a function of isochronal treatment temperature for A90 (Al-Zr), A91 (Al-Sn), and A92 (Al-Sn-Zr) alloys. (a) Vickers hardness in MPa showing considerable strengthening from 200 ppm Sn in A91 alloy and interaction of solutes to provide additional strengthening in the Al-Sn-Zr alloy. (b) Eddy current-based electrical conductivity measurements on the same alloys under the same conditions showing an improvement in electrical conductivity for the binary Al-Sn (A91 alloy) and an increase in electrical conductivity for Al-Zr (A90 alloy) and Al-Zr-Sn (A92 alloy) above a temperature of 400 °C. Source: ORNL. 35

Figure I.1.1.27. SEM micrographs for the binary Al-Sn alloy (top) and ternary Al-Sn-Zr alloy (bottom). Three separate heat-treatment conditions are shown for both alloys, homogenized (left), 200 °C isochronal treatment (middle), and 425 °C isochronal treatment (right). Source: ORNL. 36

Figure I.1.1.28. HAADF-STEM image of a Sn-rich particle in Al showing clustering of Sn leading to possible beneficial effects in the properties of the Al-Sn (A91) alloy after isochronal heat-treatment at 200 °C. The particles are likely pure Sn in composition. Source: ORNL. 37

Figure I.1.1.29. Effect of aging time at 200 °C on the properties of Al-Zr (A90), Al-Sn (A91), and Al-Sn-Zr (A92) alloys with (a) Vickers microhardness and (b) electrical conductivity. The property trends are consistent with isochronal trends reported earlier. The hardness values are additive with the higher hardness binary alloy (Al-Sn) having hardness closer to the ternary alloy. The conductivity values are subtractive with the lower conductivity alloy (Al-Zr) having values close to the ternary alloy. Source: ORNL. 37

Figure I.1.1.30. DFT-based binding energy calculations for Zr-X-vacancy in Al, where X represents the elements shown. 1NN and 2NN refer to first and second nearest neighbor positions, respectively. Elements in the shaded pink region prefer binding to Zr in the first nearest neighbor position in the presence of a vacancy. Elements in the shaded light green region prefer the 2NN position, and the L1₂ phase forming elements have a strong preference for being in the 2NN position with Zr in the presence of a vacancy. Sn and Zr strongly prefer interacting in the 1NN position based on these binding energy calculations. Source: ORNL. 38

Figure I.1.1.31. A schematic of overall workflow to predict thermal properties in lightweight alloys. Source: ORNL..... 41

Figure I.1.1.32. Schematic diagram of the step mold and the microstructure of cast pure Al after cooling within each step. The yellow arrow indicates the cooling direction of each sample. Average grain size for each step is denoted at the top right corner of the micrograph. Source: ORNL. 42

Figure I.1.1.33. Thermal and physical properties of as-cast A380 alloys: (a) thermal profiles of various step thicknesses during casting, and (b) microhardness and relative electrical conductivity of specimens cast in various step thicknesses. IACS = International Annealed Copper Standard. Source: ORNL.....	42
Figure I.1.1.34. Effect of heat-treatment temperature on (a) microhardness and (b) electrical conductivity. Hv is Vickers hardness unit ($1 \text{ Hv} \cong 9.8 \text{ MPa}$) and %IACS is the relative electrical conductivity with respect to anneal copper as standard. Presented data only contain isochronal heat-treatment (i.e., after 3 hours). Source: ORNL.....	44
Figure I.1.1.35. Quantitative analysis of experimental data and ML modeling: (a) correlation analysis between process parameters and physical properties, and (b) training result of ML models for predicting electrical conductivity. Source: ORNL.	44
Figure I.1.1.36. Fabrication of AA7075-TiB ₂ composite billet via friction consolidation. (a) Precursor billet made from AA7075 billets and TiB ₂ powder, (b) illustration of friction consolidation process, and (c) AA7075-TiB ₂ composite billet. Source: PNNL.....	48
Figure I.1.1.37. (a) Schematic of step-by-step FSF process and (b) combined friction consolidation and friction stir forging for the fabrication of the composite gear. Source: PNNL.	48
Figure I.1.1.38. SEM images of the <i>in-situ</i> composites: (a) 5 vol.% gravity cast and (b) 10 vol.% squeeze cast. Source: PNNL.	49
Figure I.1.1.39. High-magnification SEM images of the <i>in-situ</i> composites: (a) 5 vol.% gravity cast and (b) 10 vol.% squeeze cast. Source: PNNL.....	49
Figure I.1.1.40. The vertical cross-section images of 7075-TiB ₂ composite billet were made by friction consolidation. (a) Optical image, (b) EDS mapping of titanium showing the mixing zone, (c) Vicker's hardness after T6 post heat-treatment, (d) High-magnification SEM image of the mixing zone, (e) EDS mapping of Al at high-magnification, and (f) EDS mapping of titanium at high-magnification. Source: PNNL.	50
Figure I.1.1.41. Characterization of the composite gear core and teeth. (a) SEM macrograph, distribution of TiB ₂ in (b) core and (c) gear teeth; EDS elemental mapping for (d) Al and (e) Ti, (f) microhardness distribution across the teeth. Source: PNNL.	51
Figure I.1.2.1. Fe-Si Phase Diagram. Source: ORNL [2].	54
Figure I.1.2.2. (a) Example of a drop-cast Fe-Si alloy ingot. (b) Hot-rolled plate produced from an ingot similar to that shown in (a). (c) Tensile properties of Fe-6.5Si-1Cr. Source: ORNL.....	56
Figure I.1.2.3. Examples of Fe-6.5Si- 1Cr (wt%) alloy samples rolled at ~316 °C. (a) Symmetrically rolled, reduction of ~ 15%. (b) Symmetrically rolled, reduction of ~31%. Sample cracked into two during rolling. (c) Asymmetrically rolled, reduction of ~8%. Source: ORNL.	56
Figure I.1.2.4. (a) RT tensile properties of symmetrically and asymmetrically rolled samples. (b) 300 °C tensile properties of hot-rolled and asymmetrically rolled Fe-6.5 wt.% Si- 1Cr. Source: ORNL.	57
Figure I.1.2.5. A schematic showing the workflow of our theoretical/computational approaches that utilize ORNL's high-performance computation resources. Source: ORNL.....	57

Figure I.1.2.6. (a) Quantum Design MPMS3 magnetometer for measuring magnetization from 0.4–400 K using applied fields up to 7 T H curve at Temp.=100 °C. Source: ORNL.....	58
Figure I.1.2.7. (a) Results from magnetic thermogravimetric analysis from a Fe-5Si base alloy. (b) Curie temperature (T _c) superposed on the Fe-Si phase diagram. Dotted lines show ~ Fe-5 wt.% Si composition and the Curie temperature. Source: ORNL.....	59
Figure I.1.2.8. Manufacturing route and activities for design and fabrication of developmental alloys and subsequent machining, testing, and evaluation of RSCF specimens. Source: ORNL.....	63
Figure I.1.2.9. Carburizing simulations showing C content as a function of distance from the surface and time for (a) 16MnCr5 gear steel; and (b) developmental gear steel ORNL-2. Source: ORNL.....	64
Figure I.1.2.10. Surface images of FeMnAlC strips after 20% reduction in a single-pass and 5× reduction with 5% reduction per pass. Source: ORNL.....	64
Figure I.1.2.11. Hardness vs. aging time for FeMnAlC in different starting material conditions (refer to text for meaning of acronyms in legend). Source: ORNL.....	65
Figure I.1.2.12. Multiwall CNTs with different lengths and diameters. Source: ORNL.....	68
Figure I.1.2.13. Organic surface modifications for CNTs. Source: ORNL.....	68
Figure I.1.2.14. Surface-modified CNTs showing stable suspension in a PAG oil. Source: ORNL.....	69
Figure I.1.2.15. Organically modified CNTs showing improved, but still unstable suspension in a PAO oil. Source: ORNL.....	69
Figure I.1.2.16. The addition of 0.5% CNTs increased the thermal conductivity of PAO and PAG base oils by 7%–8% and 8%–10%, respectively. Source: ORNL.....	70
Figure I.1.2.17. A comparison of thermal conductivities of an EV base oil with CNTs in two sizes. The larger CNTs appear to be more effective in improving the thermal conductivity of the oil. Source: ORNL.....	70
Figure I.1.2.18. CNTs deposited on a Type 316 SS disk: (a) SEM top view, with the inset showing the SS disk before and after the CVD process; (b) SEM side view; and (c) HR-TEM images revealing the CNT nanostructure. Source: ORNL.....	73
Figure I.1.2.19. CNT-coated SS demonstrating superlubricity in macroscale sliding under MQL in an ambient environment: (a and b) comparison of friction behavior and worn surface morphology for 100 m sliding at 5,000 cycles for 2.8 hours; (c and d) sustainable superlubricity in elongated sliding tests of 1,000 m at 50,000 cycles for ~28 hours, and 10,500 m at 525,000 cycles for ~12 days, respectively. Source: ORNL.....	75
Figure I.1.2.20. Cross-sectional characterization of the tribofilm on the M2 steel surface after sliding against a CNT-coated 316 SS disk: (a) FIB-SEM images; (b) HR-TEM images; and (c) EDS elemental maps. Source: ORNL.....	76
Figure I.1.2.21. Raman spectra of as-grown CNTs (blue) and the tribofilms on two wear scars on the CNT-coated SS disk (orange) and the M2 tool steel flat (black) after 1,000 m sliding. Source: ORNL.....	77
Figure I.1.2.22. CNT coating grown on Al 6061 alloy surface. Source: ORNL.....	78

Figure I.1.2.23. Schematic of the (a) Al-Cu hybrid rotor and (b) joining of Al to grooved Cu shorting bar. Source: PNNL.	80
Figure I.1.2.24. (a) Coupon stack-up assembly to join five-sheet stacks of Al to shorting bar with the backing plates (inset: schematic of five-sheet stack with grooved Cu shorting bar), (b) single-pass Al-Cu weld, (c) electro-discharge machining cut pullout specimen, and (d) the test fixture in the Instron 5582 to pullout these cut specimen. Source: PNNL.	81
Figure I.1.2.25. (a) Load vs. displacement plot for pullout tests on Al-Cu joints. A custom-made test fixture is shown in the inset. (b) A bar chart showing the maximum load for multiple samples. The Al-Cu fracture after the pullout test is shown in the inset. Source: PNNL.....	82
Figure I.1.2.26. FSW Al-Cu interface. (a) SEM micrograph and (a1) EDS elemental mapping at the interface with uncoated Cu shorting bar. (b) SEM micrograph and (b1) EDS elemental mapping at the interface with Ni-coated Cu shorting bar. (c) SEM micrograph and (c1) EDS elemental mapping on Al-Cu lamella formation near interface. Source: PNNL.	82
Figure I.1.2.27. Conductivity measurement at room temperature: (a) schematic of the sample with voltmeter lead location (inset: Al-Cu FSW samples); and (b) measured electrical resistance for multiple samples. Source: PNNL.	83
Figure I.1.2.28. (a) Top view of polycarbonate boron nitride tool showing the convex scroll shoulder. (b) FSP of Fe-Si alloy. (c) Temperature profile during the processing. Source: PNNL.....	84
Figure I.1.2.29. (a) Optical micrographs of the FSP region. Backscattered electron SEM images of: (b) Base Fe-3 wt% Si, (c) FSP at 750 °C, and (d) FSP at 850 °C. Stress and strain curve for: (e) Fe-3 wt.% Si for base and two different processed conditions; and (f) Fe-4 wt.% Si for base and two different condition samples. Source: PNNL.	84
Figure I.1.2.30. Fractographs showing the fractured surface of tensile-tested: (a-c) Fe-4 wt.% Si base alloy, (d-f) Fe-4 wt.% Si alloy FSP'd at 750 °C, and (g-i) Fe-4 wt.% Si alloy FSP'd at 850 °C. Source: PNNL.	85
Figure I.1.2.31. (a) Hot-rolled plate of Fe 4 wt.% Si alloys after first pass. (b) Hot-rolled plate of Fe 5 wt.% Si alloys after first pass. Source: PNNL.	86
Figure I.1.3.1. Microstructure of as-fabricated (a-c) Al-Ce-Ni-Mn and (d-e) Al-Ce-Ni-Mn-Zr alloys. (a-c) SEM images of Al-Ce-Ni-Mn alloy show Mn-rich, rosette-shaped intermetallic particles (confirmed by the EDS map in the inset); (b) a crack (lower magnification image in the inset) associated with Mn-rich rosettes; and (c) IPF map of the Al-Ce-Ni-Mn alloy shows columnar grain structure. SEM images at (d) lower magnification and (e) higher magnification of the region marked 'e' in (d) show the eutectic structure, while (f) IPF map shows equiaxed grain structure in the AlCeNiMnZr alloy. The inset in (d) shows submicron-sized primary α -Al regions in melt pools. Source: ORNL.	90
Figure I.1.3.2. Summary of (a) hardness as a function of aging at 350 °C for AlCeNiMnZr; (b) the microstructure following aging compared with (c) stress relieved microstructure of Al-Ce-Ni-Mn; and (d) an APT reconstruction showing the presence of nanoscale $Al_3Zr_{1.2}$ precipitates within the FCC-Al matrix. Source: ORNL.....	90
Figure I.1.3.3. Comparison of mechanical properties between Al-Ce-Ni-Mn and Al-Ce-Ni-Mn-Zr showing (a) tensile yield strength as a function of temperature; (b) high-cycle fatigue performance at 350 °C; and (c) tensile creep resistance at 300 °C. Source: ORNL.	91

Figure I.1.3.4. Thermal properties as a function of temperature. Source: ORNL.....	92
Figure I.1.3.5. Electrical resistivity of various AM Al alloys at room temperature. Source: ORNL.	92
Figure I.1.3.6. Schematic flowchart showing the work scope of Task 3B, “Fundamentals of Non-Equilibrium Processing.” Source: ORNL.....	96
Figure I.1.3.7. Phases in cast Al-9.9Ce-4.1Ni after final heat-treatment at (a) 625°C for 2h, (b) 520°C for 20h, (c) 400°C for 200h, and (d) calculated phase amount vs. temperature in Al-9.9Ce-4.1Ni. Source: ORNL.....	98
Figure I.1.3.8. Phases in cast Al-9.6Ce-3.1Ni-0.3Mn after final heat-treatment at (a) 625°C for 2h, (b) 520°C for 20h, (c) 400°C for 200h, and (d) calculated phase amount vs. temperature in Al-9.6Ce-3.1Ni-0.3Mn. Source: ORNL.....	98
Figure I.1.3.9. Phases in cast Al-10.1Ce-2.8Ni-1.2Mn after final heat-treatment at (a) 625°C for 2h, (b) 520°C for 20h, (c) 400°C for 200h, and (d) calculated phase amount vs. temperature in Al-10.1Ce-2.8Ni-1.2Mn. Source: ORNL.	99
Figure I.1.3.10. Phases in the as-cast microstructure of Al-9.9Ce-4.13Ni, Al-9.6Ce-3.1Ni-0.3Mn and Al-10.1Ce-2.8Ni-1.2Mn alloys: (Top) predicted phases from the Scheil solidification model; (Middle) SEM BSE images at low magnification; (Bottom) SEM BSE images at higher magnification identifying individual phase constituents within the microstructures. Source: ORNL.....	100
Figure I.1.3.11. Phases in the as-built microstructure of AM Al-10.5Ce-3.1Ni-1.2Mn: (a-b) STEM images at low and high-magnification; (c) predicted phases from the Scheil solidification model; (d) phase compositions measured from APT analysis. Source: ORNL.....	101
Figure I.1.3.12. Calculated phases in Al-3.7Cu-1.2Ce-0.3Zr (at%) alloys: (a) Solidification reactions and (b) mole fractions of phases predicted by the Scheil model (for interpreting phase stability in as-fabricated microstructure), (c) mole fractions of phases predicted by lever-rule model (for interpreting phase stability in post heat-treated microstructure), and (d) enlarged plot of (c) showing the minor phases. Source: ORNL.....	102
Figure I.1.3.13. Hysteresis loop for Ni _{0.5} Zn _{0.5} Fe ₂ O ₄ showing little hysteresis in an applied magnetic field, which is representative of soft ferrite magnetic materials. Source: ORNL.....	108
Figure I.1.3.14. Magnetic TGA data for (a) Ni _{0.5} Zn _{0.5} Fe ₂ O ₄ and Mg _{0.5} Zn _{0.5} Fe ₂ O ₄ powders with the maximum change in weight, which (b) indicates a Curie temperature of 248 °C for Ni _{0.5} Zn _{0.5} Fe ₂ O ₄ and 83 °C for Mg _{0.5} Zn _{0.5} Fe ₂ O ₄ . Source: ORNL.	108
Figure I.1.3.15. (a) ZnFe ₂ O ₄ structure with 25% doping of Ni (purple) on the Zn (silver) sites that is used for DFT calculations. (b) Magnetic phase diagram for SrFeO _x showing the transitions between magnetic states as a function of temperature and composition. Source: ORNL.....	109
Figure I.1.3.16. Percent of theoretical density as a function of (a) composition and (b) sintering conditions. Source: ORNL.....	110
Figure I.1.3.17. Percent of theoretical density for pellets of Ni _{0.5} Zn _{0.5} Fe ₂ O ₄ sintered at either 1400 °C for 2 hours or 1500 °C for 12 hours with different processing conditions. Source: ORNL.....	110

Figure I.1.3.18. Map, a backscattered scanning electron image with overlays of two different phases in red and orange showing the regions of dense ferrite pieces in a cementitious matrix. Source: ORNL.	111
Figure I.1.3.19. Schematic flowchart showing the work scope of Task 3B, “Fundamentals of Non-Equilibrium Processing.” Source: ORNL.	115
Figure I.1.3.20. Typical SEM images of CNT and Cu coated tapes after each processing step. The inset of (b) displays the rougher surface morphology of thin Cu and rolling marks on the thick Cu tape substrates. Source: ORNL.	117
Figure I.1.3.21. Cross-sectional Z-contrast STEM images of Cu/CNT/Cu samples on (a)12 μm and (b) 28 μm Cu substrates. The inset of (b) shows the CNT lattice planes. Source: ORNL.	117
Figure I.1.3.22. Comparison of resistivity as a function of temperature (275 K to 400 K) for single CNT layer UCC architectures prepared with PVP and without PVP in the electrospinning solutions. Plots display significantly reduced resistivity as compared to reference Cu substrates. Source: ORNL.	118
Figure I.1.3.23. Comparison of current density of single CNT layer UCC architectures of the same samples presented in Figure I.1.3.4.4. Plot displays increased ampacity as compared to reference Cu substrates. The inset of the left panel shows typical photographs of the test samples before and after the measurements. Source: ORNL.	119
Figure I.1.3.24. Energy diagram showing the density of states for semiconducting (11,0) and nitrogen and Cu-doped semiconducting CNTs. Source: ORNL.....	120
Figure I.1.3.25. Process for synthesizing IPC materials using the PC technique. The reinforcing lattice is printed using a laser powder bed fusion process, filled with liquid metal using pressure die-casting, and then post-processed to optimize the properties. Source: ORNL.	123
Figure I.1.3.26. Results of HIP conditions of ASTM F3318 – 18 (100 MPa at 510-530°C for 3 hours), on a vacuum infiltrated PC sample with 30 volume% 316L stainless steel lattice with balance of cast A356 Al. The HIP post-processing procedure mitigates the porosity in the A356 matrix but also closes the interfaces between the constituents. The upper left image is a 2-inch diameter PC pipe section produced with vacuum infiltration highlighting the poor infiltration quality observed with the original vacuum infiltration process at larger scales. This porosity is being mitigated by adopting a high-integrity high-pressure casting process. Source: ORNL.....	125
Figure I.1.3.27. Conceptual model of PC sheet prototype for EV battery containment. Note the option of integral cooling channels and features in the diecast portion that enable modularity and thermal management, both key aspects identified by industry in FY 2022 discussions. Source: ORNL.	125
Figure I.1.3.28. Electrical conductivity of AA1100-only wires (without graphene additives) manufactured via ShAPE™ at varying extrusion temperatures and forces. Source: PNNL.....	130
Figure I.1.3.29. Electrical conductivity and TCR of AA1100-only (control) and Al/GNP samples with 0.1 wt.% GNPs manufactured at an extrusion temperature of 450 °C different extrusion forces. Source: PNNL.....	131
Figure I.1.3.30. ShAPE™ tooling and process development resulting in 3–5 m long Al/GNP wires with a diameter of 2.5 mm. Process development was optimized to ensure smooth wire surfaces which is crucial for property uniformity. Source: PNNL.....	132

Figure I.1.4.1. Thrust 4 coordination of the multi-lab characterization. Researchers identify an EV material problem to be solved and propose work. Upon successful review and ranking, funds are awarded with advanced characterization (and computation) and analyses ensuing. Discussions and meetings occur often between researchers at the national laboratories through hybrid meetings and email. Results are converted into research products with the goal of their application within future EVs. Source: ORNL.	135
Figure I.1.4.2. (a) Backscattered electron image of a commercial cementitious iron spinel. (b) PCA of the EDS map from the same region showing two different phases. (c) PCA of Raman map from the same region. Source: ORNL.....	138
Figure I.1.4.3. (a) Average Raman spectra from the two spinel phases shown in Figure I.1.4.1.2(c). (b) Raman spectra acquired from various ferrite compositions made from materials originating from a commercial supplier. Source: ORNL.....	138
Figure I.1.4.4. Bright-field STEM micrographs of AM Al-Cu-Mn-Zr: (a) as-fabricated; (b) crept for 210 h at 45 MPa and 300 °C; (c) aged 350 °C for 24 h, and then crept for 1010 h at 43 MPa and 300 °C; and (d) aged 400 °C for 6 h, and then crept for 866 h at 38 MPa and 300 °C. Insets show the detail of precipitate/dislocation interactions. Source: ORNL.....	139
Figure I.1.4.5. (a) Thermtest THW L1 Hot-Wire system at ORNL to measure thermal conductivity of liquids with (b) examples of thermal conductivity measurements on polyalphaolefin (PAO) based lubricants with and without modified carbon nanotube additions. Source: ORNL.	143
Figure I.1.4.6. Temperature gradient established across a steel-steel interface in an infrared image. The temperature line profile shows the measured temperature drop. Source: ORNL.....	144
Figure I.1.4.7. Electrical resistivity measurement methods. From left to right: 4-point probe (ZEM-3); Eddy current probe, Inline 4-point probe [4], and 4-point knife edge method [5]. Source: ORNL.	144
Figure I.1.4.8. (a) Electrical resistivity of printed commercial Al-Si, developmental Al-Cu, and developmental Al-Ce alloys vs. cast commercial alloy 319 and pure Al. (b) Electrical resistivity of model and developmental cast Al-Ni alloys. Source: ORNL.	145
Figure I.1.4.9. Thermal diffusivity of cast Al-Ni alloys from Task 1A. Source: ORNL.	145
Figure I.1.4.10. Example of RT electrical resistivity of a set of five cast Al-Ni samples for each heat-treatment condition from Task 1A. Source: ORNL.	146
Figure I.1.4.11. (a) Photograph and (b) corresponding schematic drawing of synchrotron XRD arrangement for the study of ShAPE-processed Al specimens received from PNNL. Source: ANL... ..	149
Figure I.1.4.12. Experimental setup showing the diffraction and tomography detectors at beamline 1-ID in the APS, where the x-ray beam path is marked in white with a solid line showing the incident beam and dashed lines representing the transmitted/diffracted beams. Source: ANL.....	150
Figure I.1.4.13. Synchrotron XRD patterns of (a) the Al-Control sample, (b) the Al-Gr measured across height direction, and (c) the Al-Gr sample measured along length direction. Source: ANL... ..	151
Figure I.1.4.14. (a) Photograph of cylindrical Cu ultra-conductor sample mounted horizontally on sample holder; and (b) schematic drawing of synchrotron X-ray diffraction arrangement for the study. Source: ANL.....	152

Figure I.1.4.15. Synchrotron XRD patterns of samples Cu-171 (top) and Cu-184 (bottom) measured at different spots along length direction. Source: ANL.....	153
Figure I.1.4.16. Compositions of the AFA alloys produced at ORNL. Source: ORNL	153
Figure I.1.4.17. (a) HE-XRD spectra of the AFA alloys with two different compositions in two different states (i.e., as-cast and crept). (b) 3D μ -CT reconstructions of the as-cast and crept conditions of one alloy, color coded by feature (pore/precipitate) volume. Source: ANL.....	154
Figure I.1.4.18. TEM bright-field montages of NCMS alloy oxidized in dry air vs. wet air for 500 hours at 950 °C. Source: PNNL.....	158
Figure I.1.4.19. APT analysis of NCMS alloy oxidized in dry air vs. wet air for 500 hours at 950 °C showing elemental segregation differences. Source: PNNL.	158
Figure I.1.4.20. Deformed micropillars from (a) on/near MPB and (b) away from MPB with the corresponding stress-strain graphs in (c). Source: PNNL.....	159
Figure I.1.4.21. SEM images and EDS maps of the Al ₂ O ₆ -5 vol.% TiB ₂ composite. Color code for the EDS maps – blue: aluminum; teal: titanium; pink: manganese; yellow: copper; lime: iron; and dark blue: boron. Source: PNNL.....	159
Figure I.1.4.22. Change in grain size of Fe-3 % Si alloy from base alloy as a function of friction stirred processing temperature. Source: PNNL.	160
Figure I.1.4.23. (a) Atomistic modeling of nitrogen-doped CNTs based on the experimental XPS data. (b) Density of states of (11,0) semiconducting CNTs with Cu or N dopants. Source: ORNL.	164
Figure I.1.4.24. Calculated electronic conductivity for (a) inverse of resistivity ρ , and (b) charge carrier density (n_c) of (11,10) semiconducting CNTs with N doping. Source: ORNL.	165
Figure I.1.4.25. Prediction of thermal conductivity of (a) Al-3Ni (N7) and (b) Al-3Ni-0.45Zr (N8) using SEM as an initial input for thermal conductivity prediction in FEM. (c) The prediction agrees with the measured data. Source: ORNL.....	166
Figure I.1.4.26. Synthetic microstructure of N8 \times 1200 created using (a) CA; (b) experimental SEM image; (c) vertically aligned microstructure; and (d) analyzed pattern using two-point statistics in which the color plot shows the microstructure is vertically aligned with the similarly sized columnar structure. Source: ORNL.....	167
Figure I.1.4.27. (a, b) Comparison of energies calculated from fitted cluster expansion with DFT results. (c) Experimental phase diagram and calculated A2-B2 phase boundary (red) and B2-DO ₃ (blue). Source: ORNL.....	169
Figure I.1.4.28. Framework of designing new alloys based on high-throughput ML: (a) CALPHAD-based thermochemical information is augmented as scientific features in ML models. The models are trained with experimental data. (b) The DoE approach is used to narrow down the search space for hypothetical alloy compositions from high-dimensional composition space. Scientific features of such alloys are calculated by high-throughput computational thermodynamics with high-performance computing. (c) Hypothetical alloys are subjected to virtual experiments by using the trained ML models. (d) Ideal alloy compositions are extracted by imposing screening conditions and statistical analysis. Source: ORNL.	171
Figure I.1.4.29. Physics-augmented ML training: (a) top 15 input features ranked by MIC analysis and (b) training result of ML models that incorporate scientific features. Source: ORNL...	172

Figure I.1.4.30. Creep-rupture time of experimental (closed circles) and hypothetical (open squares) alloys with various creep stress conditions. LMP is used to represent the rupture time. Filled triangle represents the ideal alloy composition extracted from hypothetical alloys at 250 MPa. The rupture time of the ideal alloy is projected to 170 and 100 MPa via ML predictions. Source: ORNL.....	174
Figure I.2.1.1. The project development approach and work streams. Source: Ford.	184
Figure I.2.1.2. Composite oil pan. Source: Ford/ORNL.	185
Figure I.2.1.3. Oil pan images. Source: Ford/ORNL.	185
Figure I.2.1.4. Conventional and AM oil cooler designs. Source: Ford.....	186
Figure I.2.1.5. Weight-saving design elements enabled by AM sand cores. Source: Ford.	186
Figure I.2.1.6. AM sand core design elements. Source: Ford.	187
Figure I.2.1.7. Valvetrain system comparison. Source: Ford.	187
Figure I.2.1.8. Path to 15% Weight-Reduction. Source: Ford.....	189
Figure I.2.2.1. Cylinder head system. Source: GM.....	191
Figure I.2.2.2. Engine block system. Source: GM.	191
Figure I.2.2.3. Valvetrain system. Source: GM.....	191
Figure I.2.2.4. (a) Induction and (b) EGR systems. Source: GM.....	192
Figure I.2.2.5. (a) Fuel and (b) coolant pump sys. Source: GM.....	192
Figure I.2.2.6. Complete PHASE 2 engine system. Source: GM.	193
Figure I.2.2.7. S-N fatigue data of LPPSC and baseline 319 alloy cylinder heads tested at 250 °C. Source: GM.	194
Figure I.2.2.8. AM printed PHASE 2 pistons. Source: ORNL.....	194
Figure I.2.2.9. S-N fatigue data of AM printed and cast Al pistons tested at 300 °C. Source: GM. ..	195
Figure I.2.2.10. (a) New cast steel crank casting design and (b) a PHASE 2 crank. Source: GM.	195
Figure I.2.2.11. S-N fatigue data of cast tell cranks in various conditions compared with the forged baseline cranks. Source: GM.....	196
Figure I.2.2.12. Through process modeling approach flow for a cast Al block. Source: GM.	197
Figure I.2.2.13. Casting process simulation and casting quality (e.g., porosity) prediction in cast steel crank. Source: GM.	197
Figure I.2.2.14. CET simulation for cast Al alloy solidified under an average cooling rate of 5-10 K/s, with or without random nucleation. Source: OSU.	198
Figure I.2.2.15. CAE simulation of AM grain structure. Laser speed of 1.5M/S and thermal properties of AISi10 alloy used. Top row shows thermal profile, bottom figures show individual grains. Source: OSU.	198
Figure I.2.4.1. (a) SEM micrographs of 21-2N corroded in Ar-20O ₂ atmosphere. (b) A graph of the hardness values. (c) The EDS line scan elemental composition from the scale/alloy interface into the alloy. Source: University of Wisconsin-Madison.	204

Figure I.2.4.2. (a) TGA curves for 21-2N corroded in dry CO ₂ at 700 °C for 3, 10, and 50 hours. (b) TEM/EDS cross-section analysis of the oxide formed on 21-2N after 10 hours in the TGA. Source: University of Wisconsin-Madison.....	205
Figure I.2.4.3. (a) Polyhedral structure of a conventional MnCr ₂ O ₄ unit cell showing the vectors of travel for each vacancy mediated oxygen migration. (b) Nudged elastic band method profile illustrating the migration barrier heights for each vacancy mediated oxygen migration mechanism. Source: University of Florida.....	206
Figure I.2.4.4. (a) A schematic of the migration mechanism for an oxygen split ‘dumbbell’ interstitial in MnCr ₂ O ₄ . (b) Migration barrier height for the mechanism. Source: University of Florida.....	207
Figure I.2.4.5. (a) Comparison between experimental and calibrated simulation oxidation rates showing the growth rate of each oxide where the Mn ₃ O ₄ experimental thickness at the 1925 hour (marked as red) is possibly due to surface spallation. (b) The growth rate of the total oxide. The root-mean-square percentage error between the experiment and the simulation is 12.14%. Source: University of Florida.....	208
Figure I.2.4.6. Oxide growth with time for Orders 1-5 from Table I.2.4.1. (a), (b), (c), and (d) show the growth of MnCr ₂ O ₄ , Cr ₂ O ₃ , Mn ₃ O ₄ , and the total oxide, respectively. Source: University of Florida.....	209
Figure I.2.4.7. Numerical results of pit corrosion compared with the solution from [1]. The pit growth kinetics for (a) a single pit and (b) multiple pits. Source: Idaho National Laboratory.....	210
Figure I.2.4.8. (a) Outward oxide growth predicted by the SStAC tool (with the oxide in red) and the temperature profile for a 2D axisymmetric simulation, and (b) a 3D solution. Source: University of Florida.....	210
Figure II.1.1.1. Thrust and project structure of the LMCP. Source: PNNL.....	213
Figure II.1.1.2. Thrust 1 and project structure of the LMCP. Source: PNNL.....	214
Figure II.1.1.3. (a) Variable wall thickness extrusion. (b) Extruded tubing with locally modified properties. (c) Flat strip with locally modified properties. Source: PNNL.....	215
Figure II.1.1.4. Design and system integration of equipment for controlling wall thickness during ShAPE. Source: PNNL.....	217
Figure II.1.1.5. Wall thickness transitioning from 1 mm to 2 mm, and then back to 1 mm. Source: PNNL.....	218
Figure II.1.1.6. Al 6061 tubing manufactured by ShAPE with regions processed at different temperatures to locally modify strength, elongation, and microstructure in a single material. Source: PNNL.....	219
Figure II.1.1.7. Al 5182 strip rolled to a uniform thickness of 0.9 mm from a tube having a variable wall thickness of 1 mm and 2 mm. A 64% difference in toughness is achieved for different regions of a single strip. Source: PNNL.....	220
Figure II.1.1.8. Effect of interdendritic spacing in the bulk vs. partially remelted pool boundary regions: (a) a quantitative comparison of the interdendritic spacing; and (b) a schematic diagram of the mechanism of deformation in the two different regions. Knapp et al. [5].....	221

Figure II.1.1.9. Effect of aging on the deposited (a) Al 5356, (b) Al 4047, and (c) Al 4043 materials. Solution heat-treatment was done at 535 °C for four hours and aging was done at 160 °C for up to 24 hours. Lines show average of three measurements and filled regions indicate ± 1 standard deviation. Source: ORNL.....	222
Figure II.1.1.10. Improved bending stiffness from a modified sheet: (a) Al 4047 deposited on a 6111 sheet and an unmodified 6111 sheet after bend test, and (b) load-displacement curve showing improvement in bending stiffness. Source: ORNL	223
Figure II.1.1.11. r/t for base alloys and the highest formable processed conditions for each alloy. A lower r/t indicates a higher formability. Bars represent the as-received material, while lines represent the processed material. The inset shows the formability improvements in the 6111 alloy. Source: PNNL	223
Figure II.1.1.12. Press brake bending setup used to bend 7055-T6 sheets. (a) Press brake machine and its dies. (b) Brittle fracture of unprocessed 7055-T6 sample and a 90-degree bent FSP 7055-T6 sample. (c) Side view of FSP 7055-T6 showing 90-degree bend without any cracks and top view of FSP 7055-T6 bent sample with crown side on tension without any crack. Source: PNNL	224
Figure II.1.1.13. Robotic integration of FSP. (a) FSP tool attached to the PNNL robot. (b) High-speed linear FSP runs. (c) Circular FSP run. Source: PNNL	224
Figure II.1.1.14. (a) Inverted bending setup with DIC strain mapping capability. (b) Thickness strain map showing the strain distribution on the bent surface after failure. Source: PNNL	225
Figure II.1.1.15. (a) Induction heating coil integrated into the roller B/U device and (b) location of the two heating zones. Source: PNNL	226
Figure II.1.1.16. Side view of the roller B/U process showing the top roller movement and changing angles of depression of (a) 4.5 ° and (b) 12.0 °. (c) Temperature distribution on the sheet during the roller bending-unbending processing of 6111 sheet. Source: PNNL.....	226
Figure II.1.1.17. Color map shows the hardness (as HRF) distribution on the sheet after the roller B/U process. The temperature plot shows the temperature rise during the process for the corresponding hardness locations. Dashed rectangles show the samples extracted for bend testing and the pictures show the top surfaces of the bent samples, where cracking is visible in the failed samples. Source: PNNL	227
Figure II.1.1.18. (a) Setup used for laser modification. (b) Temperature profiles obtained at the bottom surface of the sample during a single-pass and a 7-pass thermal treatment at a laser power of 350W. Source: ORNL	228
Figure II.1.1.19. (a) Load vs. displacement obtained using bend testing of an untreated 2.5-mm-thick 7075-T6 sample and a laser-treated 2.5-mm-thick 7075-T6 sample. Note the significant decrease in loads and the increase in displacement of the punch observed in the treated sample. (b) Optical images of the tested samples showing the improved bending observed in the treated sample. Source: ORNL	228
Figure II.1.1.20. Half of the sheet used in the laser heating model: (a) temperature distribution within the sheet and (b) the predicted temperature histories (solid line) of AA70756 alloy with P=350W compared with actual measured temperatures (triangles) for identical process conditions. T and B are the top and bottom center of the sample. Source: ORNL.....	229

Figure II.1.1.21. The edge view of two of the sheared samples with the sample movement direction (S) marked in green arrows and ultrasound direction (U) marked in red colors for manual stage and motorized stages. Source: ORNL.	229
Figure II.1.1.22. (a) PUE setup using motorized stage. (b) Plan view of edge modified samples. (c) Edge view of modified samples. In these experiments, the ultrasonic movement was parallel to the edge and sample movement direction (or longitudinal direction). Source: ORNL.	230
Figure II.1.1.23. (a) Half dog bone geometry used for tensile testing of samples. (b) The samples after tensile test show typical splitting type failure for as-sheared sample and the more ductile shear type failure for the samples after PUE modifications. Source: ORNL.	230
Figure II.1.1.24. (a) Tensile load-displacement curves, (b) engineering stress-strain curve with strains recorded from strain-gauge, and (c) stress-strain curve using crosshead displacement with stiffness correction. Source: ORNL.	231
Figure II.1.2.1. Thrust and project structure of the LMCP. Source: PNNL.	235
Figure II.1.2.2. Three projects within the LMCP Thrust 2. Source: PNNL and ORNL.	237
Figure II.1.2.3. Premium HPDC Aural-5 alloy: (a) cross-sectional microstructure; (b) shrinkage porosity in the middle area; (c) dendritic structures, Al-Si eutectic phase, second-phase particulates; and (d) refined eutectic Si. Source: PNNL.	239
Figure II.1.2.4. (a) Acicular Mg ₂ Si phase present in HPDC Aural-5. (b) Acicular phases refined and uniformly distributed after FSP. Source: PNNL.	240
Figure II.1.2.5. (a) A schematic showing the experimental setup used for <i>in situ</i> diffraction experiments at the beamline. (b) A photograph showing the corresponding specimen with the crosshairs indicating the general position of the region interrogated by the high-energy X-ray beam. Source: PNNL.	241
Figure II.1.2.6. (a) Schematic of PNNL's Joule-heating experimental setup. (b) Thermal map of the HPDC A380 plate sample during local heat-treatment showing the approximate locations of the tensile test samples by the dashed lines that were machined after aging for mechanical testing. Source: PNNL.	242
Figure II.1.2.7. Four-point bending fatigue testing: (a) schematic of testing configuration and (b) comparison of the stress for the number of cycles to failure plot for HPDC and FSP specimens at R =0.1 along the weld direction. Source: PNNL.	244
Figure II.1.2.8. Tear toughness testing: (a) geometry of tear test specimen of FSP'd Aural-5; (b) comparison of load-displacement curve; and (c) comparison of unit propagation energy. Source: PNNL.	244
Figure II.1.2.9. Ultrasonic processing regions on 3-mm-thick A380 diecast Al alloy sheets, made with different process conditions. The PUSP process load was set at 100 lb., with process power varied in the range of 100–300W. Fatigue specimens were cut from the processed sheets and are presently in testing. Source: ORNL.	245
Figure II.1.2.10. Four-point bending test design and setup to ensure uniform bending stresses to cover the regions treated by PUSP and the adjacent regions with process residual stresses. Source: ORNL.	246

Figure II.1.2.11. (a) Four-point bending fatigue testing results of PUSP-processed Alloy A380 under different process conditions where the maximum load = 1000N and R = 0.1. (b) “No PUSP” processed base material samples (C-2 and C-3) along with other samples. Source: ORNL..	246
Figure II.1.2.12. Surface microstructure refinements by PUSP under different process power levels and 100 lb. process load: (a) and (b) are the cross-sectional view of the PUSP-processed region near the top surface of the A380; (c) through (e) are high-magnification views of the processed region under three different process power levels taken near the red squares in (a) and (b); and (f) is the high-magnification view of the base metal. Source: ORNL.	248
Figure II.1.2.13. Effect of ultrasonic vibration amplitude (energy) on the surface residual stress distribution. Source: ORNL.	249
Figure II.1.2.14. Simulation results for the effect of PUSP on the reduction of high stress at a corner location under bending stress. Source: ORNL.	249
Figure II.1.2.15. Optical micrographs show (a) the dendritic microstructure of the control casting and (c) the globular microstructure of the ultrasonicated casting. Scanning electron micrographs show (b) the needle-like β -Al ₅ FeSi particles in the control casting and (d) the rectangular β -Al ₅ FeSi particles in the ultrasonicated casting. Source: PNNL.	250
Figure II.1.2.16. (a) Engineering stress is plotted vs. engineering strain for tensile specimens extracted from the control casting (dendritic microstructure) and ultrasonicated casting (globular microstructure). Solid lines indicate specimens with porosity levels <1%. (b) This single frame from a ProCAST casting simulation shows molten Al being poured into a graphite mold initially at RT. Source: PNNL and ORNL.	251
Figure II.1.2.17. Demonstration of deposition of 5356 wire on A356 cast ingot with hybrid manufacturing: (a-c) deposition of multiple layers with only final machining; (e-f) similar deposition of multiple layers with machining between each layer. Part height is 10 mm tall after final machining. Source: ORNL.	253
Figure II.1.2.18. Relationship between Vickers hardness and YS for the deposited materials. Source: ORNL.	253
Figure II.1.2.19. Annotated photograph of the laser hot-wire deposited and machined 4047 rivet tab on HPDC Aural-5 plate. Source: ORNL.	254
Figure II.1.3.1. Primary thrust areas for Project 3A, “Surface Modification for Improving Corrosion Properties,” and Project 3B, “Improving Local Thermomechanical Treatments for Improving Mechanical Behavior of Mg Alloys.” Source: PNNL.	260
Figure II.1.3.2. Schematics and photos of three reactive surface processes: (a) direct plasma jet treatment, (b) two-step plasma coating, and (c) Li-salt loading + thermal CO ₂ treatment. Source: ORNL.	261
Figure II.1.3.3. Scanning transmission electron microscopy image (upper left) and its Mg, O, and C EDS maps of a P1-coated AZ91D sample in cross-sectional perspective. Source: ORNL.	263
Figure II.1.3.4. Comparison of (a) impedance spectra and (b) H ₂ collection volume in uncoated and Si-O-C layer deposited (e.g., P1- and P8-coated) AZ91D samples. The exposed surface area for H ₂ collection measurements was 0.833 cm ² for all samples. Source: ORNL.	263
Figure II.1.3.5. Comparison of (a) impedance spectra and (b) polarization curves in untreated and Li-salt loaded + CO ₂ thermal treated AZ91D samples. Source: ORNL.	264

Figure II.1.3.6. (a) Variation of deposited coating thickness and deposit weight with gas temperature at gas pressure of 2 MPa. (b) Variation of deposited coating thickness and deposit weight with gas temperature at gas pressure of 6.5 MPa. (c) Variation of deposited coating thickness and deposit weight with gas pressure at gas temperature of 400 °C. Source: PNNL.....	266
Figure II.1.3.7. (a) Polished bare AZ91 and Zn-coated surfaces before the corrosion test and (b) the surfaces after the corrosion test. (c) Total volume of H ₂ collected over 350 hours. Source: PNNL.	267
Figure II.1.3.8. (a) Wear test data of bare AM60 and AZ91 substrate and Zn coating. (b) Post-wear-tested surface profile of AZ91 substrate and Zn-coated AZ91. Source: PNNL.	267
Figure II.1.3.9. (a) AM60 automotive part and (b) the selected regions from the part (highlighted by the yellow dotted line in (a) used for cold spray. Cold spray was performed on three different sub-components with different curved surfaces, marked as A, B, and C. Images of the curved Mg alloy sub-components (c) before cold spray and (d) after cold spray. (e) Cross-section image of sub-component B. Source: PNNL.	269
Figure II.1.3.10. Fatigue results for (a) AZ91 and (c) AM60 in as-cast and FSP conditions along with micro-CT results (b and d). Source: PNNL.	270
Figure II.1.3.11. Fatigue-failure as a function of porosity fraction for Mg alloys in various conditions. Source: PNNL.	271
Figure II.1.3.12. Pictures of the (a) curved plates, (b) processed plates, (c) defect-free longitudinal section, and (d) uniform hardness from the flat to the curved regions. Source: PNNL.	271
Figure II.1.3.13. (a) YS vs. elongation for various non-RE Mg alloys. (b) YS as a function of Ca content in wt.%. Source: PNNL.....	272
Figure II.1.3.14. Pictures of (a) the groove in AM60, (b) the press fitted Ca-added Mg alloy in the groove, (c) the processing strategy that was implemented, and (d) the cross-section showing the defect-free processed section consisting of AM60 and the Ca-added Mg alloy. (e) A tensile property summary for the as-cast and FSP for both the AM60 and Ca-added Mg alloy. Source: PNNL.	273
Figure II.1.3.15. (a) Friction surfacing setup; (b) top; and (c) side views of a deposit. (d) Cross-section showing defect-free, solid deposit. Source: PNNL.....	274
Figure II.1.4.1. STEM images of (a) the Al7055 base alloy with white arrows highlighting the Mg ₂ Zn precipitates in the grain interiors and grain boundaries, and (b) the 7055 alloy stir zone microstructure after friction stir processing. (c-e) The APT reconstruction revealing the change in element distribution before and after FSP. Source: PNNL.....	280
Figure II.1.4.2. (a) The USAXS experimental setup at beamline 9-ID-C [3] with all the beam paths shown in red and in incident x-ray beam entering through the ‘slits.’ (b) WAXS patterns of the two boundary formability cases with the peak positions of all the major phases (e.g., Al, MgZn ₂ , Al ₃ Zr) indicated below the spectra. Note that the high-formability samples show less intense/absence of MgZn ₂ and Al ₃ Zr peaks (i.e., lower phase fractions). (c) (q) vs. (q) plots from the SAXS analysis for both the boundary cases showing the decrease in feature sizes of the precipitates/dispersoids (e.g., peaks shifting to a higher [q] value) from the low formability sample to a high-formability sample due to FSP treatment. Source: ANL.	281

Figure II.1.4.3. (a) Calculated solid fraction (f_s) and main phases as a function of temperature during cooling using a back diffusion model at a constant cooling rate of 1.37°C/s for alloy A356a1. (b) Secondary dendrite arm spacing [mm] distribution within the entire casting for alloy A356a2. Here the dimensions on the simulated mold are approximately $4.76\text{ cm} \times 4\text{ cm}$ in the x- and z-directions, respectively. Source: ORNL.....	283
Figure II.1.4.4. (a) Comparison of phase volume fraction of the main precipitate phases in the selected alloys under equilibrium conditions (solid infill) and under Scheil solidification conditions (hatched infill). (b) Demonstration of simulated Mg_2Si size in Al 4043 during a simulated 828K heating for 1000 seconds. Source: ORNL.....	284
Figure II.1.4.5. (a) Dependence of water adsorption energy on coverage of the pure and doped Mg surfaces. The coverage unit is ML, which is calculated as the ratio of the number of adsorbates to all available sites on the surface; and (b) the H_2O absorption configuration. (c) Dependence of energy on the surface atom displacements away from the surface. The energy profiles for displacing Mg and dopants X are in solid and dashed lines, respectively. (d) Detachment energy of the hydrated dopant. Source: PNNL.....	285
Figure II.1.4.6. (a) E-chip double-tilt heating holder for TEM; inset shows well-oriented θ' precipitate at 200°C to illustrate capability of the holder. (b) Electropolished alloy disk, with thin grain areas located within squares. (c) SEM image of that same area, with the suggested PFIB cut and location on the heater holes indicated. Source: ORNL.....	286
Figure II.1.4.7. SPH simulation results: (a) temperature distribution on a cross-section in the direction normal to the weld line and (b) simulated reaction forces on the FSP tool where the Z force denotes the plunging force. Source: PNNL.....	287
Figure II.1.4.8. Longitudinal residual stress prediction at the center of the plate for the (a) flat and (b) curved plates. Source: PNNL.....	288
Figure II.1.4.9. (a) Mises effective stress distribution and (b) equivalent plastic strain distribution assigned to a tube before quenching. Example plots of (c) temperature drop and (d) compressive hoop stress during quenching. Source: PNNL.....	289
Figure II.1.4.10. Comparison of GHG emissions for primary and secondary Al. Source: ANL.....	290
Figure II.2.1.1. ShAPE machine installed in PNNL's Solid-Phase Processing Laboratory. Source: PNNL.....	295
Figure II.2.1.2. (a) Extruded profiles manufactured using a porthole die integrated with the ShAPE process. (b) Schematic of porthole die integrated with a rotating billet. (c) Porthole die assembly with surface features to assist material flow. (d) Back side of porthole die head showing port exits and square mandrel Source: PNNL.....	296
Figure II.2.1.3. Extrusions made from Al 6063 industrial scrap by ShAPE using porthole die configurations producing (a) circular, (b) square, (c) trapezoid, and (d) two-cell trapezoidal profiles. Source: PNNL.....	297
Figure II.2.1.4. SE image montage of a trapezoidal extrudate cross-section in the as-extruded condition without voids or weld seam defects. (b-g) Microstructure at various locations showing highly refined and uniform grain size and crystallographic orientation indicating weak texture. Locations b, c, e, and g are at the expected weld seam location and show no bonding or texture defects. (M.U.D. stands for multiple of uniform density.) Source: PNNL.....	298

Figure II.2.2.1. Schematic of the approach used in the project. Source: ORNL.	303
Figure II.2.2.2. Schematic showing the three characteristics of interest for alloys used in the thixomolding process. Source: ORNL.....	303
Figure II.2.2.3. Melting range and % elongation of experimental alloys. Source: ORNL.....	304
Figure II.2.2.4. Visual evaluation of corrosion tested coupons: (a) AM60B control and (b) Alloy #1. Source: FCA US LLC.....	305
Figure II.2.2.5. (a) Remnants from cast billet. (b) Section from an extrusion. Source: ORNL.	305
Figure II.2.2.6. (a) Yield strengths of Alloy #1 and Alloy #6 in the as-cast and extruded conditions and (b) percent elongation to failure of Alloy #1 and Alloy #6 in the as-cast and extruded conditions. Source: ORNL.....	306
Figure II.3.1.1. Carbonization in one-step of a 300k ribbon of commodity grade OPF using two EM-powered furnaces set-up inline. Source: ORNL.	310
Figure II.3.1.2. Picture of a continuous sample of 300k filaments ribbon coming out of the HTC before the split. The yellow tags delimit the processing conditions. Minor damage can be noticed in the center left of the sample. Source: ORNL.	311
Figure II.3.1.3. Random resistance measurements of the continuous batch sample. Most of the values are in the 1Ω range or below, as shown in the pictures. This value is typical of fiber that has been processed at 1200°C or higher. (Note: the unknown number of filaments between the probes is a limitation of the accuracy of this method.) Source: ORNL.....	312
Figure II.3.1.4. (a) Damage of moderate importance coming out of the HTC furnace which might randomly create a filament jam in the cavity of the furnace. This damage is systematically exacerbated by the splitter (not shown) and (b) results in a ‘Gordian knot’ that fails to pass through the winder. Source: ORNL.	313
Figure II.3.1.5. Carbonization in one-step. Two tows of 50k filaments of commodity grade OPF using two EM-powered furnaces setup inline. Source: ORNL.....	313
Figure II.3.1.6. Carbonization in one-step of four tows of 50k filaments of commodity grade OPF using two EM-powered furnaces set-up inline. Source: ORNL.....	315
Figure II.3.1.7. Example of a damaged areas. (a) Metallic part of the cavity partially covered with dark soot showing obvious pitting and the signature of undesirable arcing. (b) Molten metal (in yellow) on top of damaged insulation. Source: ORNL.....	316
Figure II.3.1.8. Type K thermocouples of 1/16 in. (~1.6mm) were used to probe the process. This thermocouple experienced two levels of damage: (1) the tip melted during the process; and (2) the tip could no longer travel through the bore after the process cooled down and broke during the replacement procedure. The thermocouples in similar locations were replaced with Type B that failed in a comparable manner. Source: ORNL.....	316
Figure II.3.1.9. Example of two custom components (from the same manufacturer) tested for their forward voltage gain (S_{21}) for (a) the first component and (b) the second component. Source: ORNL.	317
Figure II.3.1.10. The AM-CM process: (a) binder jetting of metal specimens with custom designs, (b) BAAM of composite preforms, and (c) compression overmolding of composite on top of the metal inserts to obtain the hybrid panels. Source: ORNL.	321

Figure II.3.1.11. Stress-strain characteristics of polymer composite perpendicular to the bead and along the bead directions: (a) 20 wt.% CF/ABS and (b) 40 wt.% CF/PA66. (c) Stress-strain characteristics of 316L stainless steel infiltrated with bronze. Source: ORNL.....	322
Figure II.3.1.12. (a) Tensile testing of metal composite overmolded specimens. (b) Stress-strain curves obtained from DIC. Source: ORNL.....	323
Figure II.3.1.13. (a) Sub-component design evolution through multiple iterations. (b) Optimized sub-component design, resultant displacement, and stress contours. Source: ORNL.....	324
Figure II.3.1.14. (a) Design evolution of seatback frame through multiple iterations. (b) The optimized seatback frame design, resultant displacement, and stress contours. Source: ORNL. ...	325
Figure II.3.1.15. Toolpaths for lattice-based bumper designs: (a) discontinuous toolpaths generated in Cura and (b) continuous toolpaths generated using an ORNL slicer. Source: ORNL...	327
Figure II.3.1.16. Full-scale multimaterial lattice-based bumper. Source: ORNL.....	328
Figure II.3.1.17. (a) Load cases and deflection requirement for a door arm rest. (b) Topology-optimized design. (c) Shell-based design. (d) Strut-based design. Source: ORNL.....	328
Figure II.3.1.18. (a) Boundary conditions applied on the armrest design, and resultant displacement via FEA for applied (b) vertical load and (c) horizontal load. Source: ORNL.....	329
Figure II.3.1.19. (a) Strut-based armrest design. (b) In-plane slicing and toolpath for 3D printing. (c) In plane printed armrest design. Source: ORNL.	329
Figure II.3.1.20. (a) - (b) OPP of door armrest. (c) - (d) The toolpath planning for OPP wrapping. Source: ORNL.	330
Figure II.3.1.21. Workflow of the ML-based inverse design framework. (a) Mechanical properties as inputs. (b) Design with lattice gene types and material combinations. (c) Computer-aided design model leading to the printed bumper. (d) Experimental validation of mechanical properties. Source: UCB.	331
Figure II.3.1.22. Setup and benchmark of the simulation framework. (a) Configuration for test samples. (b) and (c) Comparison between experiments and numerical responses for low- and high-strain rates. Source: UCB.	331
Figure II.3.1.23. Inverse design using ML. (a) Venn diagram showing the design space by materials and lattice combinations. (b) Configuration for compliant cells and rigid cells. (c) Isometric of the Gene 2 configuration. (d) Stress-strain curves for low and high loading rates. Source: UCB.....	332
Figure II.3.1.24. Schematic modification of the fibers with silane treatment methods and the testing protocols for evaluating composite fabricated test samples to determine adhesion strength. Source: ORNL.	335
Figure II.3.1.25. (a) Schematic representation of the thermal aging process in CF-epoxy composites. (b) Thermal cycling protocol for CF-epoxy composites during the aging process. (c) Extent of deterioration of tensile strength of epoxy composites after thermal cycling. Source: ORNL.	336

- Figure II.3.1.26. FEA simulations comparing the stress-strain test results and the interfacial strength and toughness measurement for 5 wt% p-CF, a-CF, and s-CF/epoxy composites. (a) First-principals stress (top image) and strain (bottom image) contours for the s-CF/epoxy composite. (b) The FEA simulation of a 3D-printed sandwich structure and epoxy only prepared for a piezoelectric sensor embedment protocol. Source: ORNL..... 337
- Figure II.3.1.27. (a) 3D-printing of epoxy and continuous CF was initially achieved with the modified Hyrel attachment; however, results were not ideal and backpressure flows are still a problem. (b) A new co-extrusion assembly was designed to have both the fiber and epoxy matrix under the same pressure environment. Source: ORNL..... 338
- Figure II.3.1.28. (a) Raman mapping of MoS₂ distribution into PVDF at 8% and 11%. Note the poor distribution at higher concentrations of the 2D nanomaterial. (b) The properties of the 3D-printed PDF-MOS₂ piezoelectric sensors showing concentration-dependent differences between commercial and modified filler materials. Source: UNT..... 339
- Figure II.3.1.29. Illustration of traditional processes for thermoset and dynamic vitrimers. (a) Conventional epoxy-based on permanently crosslinked networks cannot be reprocessed or recycled after cure. (b) DE consisting of dynamic covalent bonds, as part of the crosslinked network, can be reprocessed or recycled only at high temperatures and a long annealing time, but it lacks repeated recyclability. (c) DPE with exchangeable bonds has a controllable network reconfiguration, possesses a relatively low glass transition temperature, and can be reprocessed or recycled at least six times at a moderate temperature and short annealing time after curing. Source: ORNL..... 342
- Figure II.3.1.30. Synthesis and thermomechanical properties of DE and DPE. (a) Synthesis of crosslinked DPE resin by reacting isocyanate and epoxy with AFD (each chemical structure is in red, blue, and black, respectively). (b) FTIR spectra of epoxy (black), PU (red), and DPE (blue) samples. (c) Dynamic mechanical analysis curves obtained for different weight ratios of PU to epoxy representing $\tan \delta$ versus temperature. (d) Representative tensile stress-strain curves for three different weight ratios of PU to epoxy resins for 1:2 (pink), 1:1 (blue), and 2:1 (red). Source: ORNL..... 344
- Figure II.3.1.31. Reprocessing by hot-pressing. (a) Traditional epoxy samples crosslinked by unexchangeable bonds resulting in broken pieces. (b) Tested DE specimens reprocessed at the same hot-pressing condition as traditional epoxy resulting in a compact film. (c) Pristine DPE samples after testing that were hot-pressed (reprocessed) to obtain a recycled compact film which was easily cut to dumbbell-shaped specimens. (d) Summarized tensile strength values of reprocessed DE (green) and PU/epoxy samples (blue) (data are represented as mean \pm SEM). (e) FTIR spectra of dynamic samples before and after reprocessing. Source: ORNL..... 345
- Figure II.3.1.32. Demonstration of CFRP manufacturing by both prepregs and stamping: (a) Preparation of CFRP from a vitrimer of DPE resin and (b) CM and stamping of the cured multilayered CFRP sheet via thermoforming technique reshaped to a 3D form (top and bottom views of the multilayered 3D composite sheet). (c) Representative stress-strain curves obtained from the tensile tests for conventional epoxy composites (black), DE composites (green), and DPE composites (blue), respectively. (d) A DPE composite with a crack in the middle after the flexural test and fully repaired after being hot-pressed at 160 °C for 5 min. (e) Interlaminar shear strength (ILSS) retention measured after repairing the cracked sample from each cycle's short-beam shear tests for up to six cycles of both DPE and DE CFRPs. Source: ORNL..... 346

Figure II.3.1.33. Refluxing 45 wt.% CF-PP composite: (a) CF-PP strips in xylene solvent before refluxing; and (b) the remaining CF-PP sample after refluxing and washing with xylene solvent. Source: UNT.....	350
Figure II.3.1.35. Tensile test data for the CF-PP composites: (a) results for samples prepared using different fabrication techniques; and (b) stress-strain results for the novel multilayered CF-PP laminates that were hot-pressed at different molding pressures. Source: UNT.	351
Figure II.3.1.36. DSC thermograms of (a-c) N6,6 and (d-f) PP-CF composites for fiber-loading ratios of 10, 20 and 30 vol.%. Source: ORNL.	353
Figure II.3.1.37. Kissinger plot for the (a) N6,6-CF and (b) PP-CF composites. Source: ORNL.	354
Figure II.3.1.38. CF-PP laminate stack prior to consolidation. Source: ORNL.	354
Figure II.3.1.39. (a) Stress vs. strain plot summarizing the tensile properties of the uniaxial composite. (b) CF-PP composite laminate showing composite mode failure. Source: ORNL.....	354
Figure II.3.1.40. Schematic illustrating the test setup for characterizing the electromechanical properties of the composite beams. A permanent magnet shaker was used to input vibrations at the base of the beams while the voltage was measured using a digital multimeter. Source: ORNL.	357
Figure II.3.1.41. (a) Output voltages of the composite beams with different concentrations of BaTiO ₃ and different accelerations input. (b) The average sensitivity of the composites with different concentrations of BaTiO ₃ . Source: ORNL.	358
Figure II.3.1.42. (a) One representative sample illustrating the noise floor voltage and voltage outputs plotted as a function of acceleration for the 3.5 wt.% BaTiO ₃ sample to calculate the resolution. (b) The resolution values calculated for all composites with varying BaTiO ₃ concentrations. Source: ORNL.	358
Figure II.3.1.43. Scatter plots showing the voltage generated and power density as a function of circuit resistance for (a) 0.5 wt.%, (b) 3.5 wt.%, and (c) 4 wt.% BaTiO ₃ composites. Source: ORNL.	359
Figure II.3.1.44. Scatter plots showing the voltage generated and power density as a function of circuit resistance for (a) 0.5 wt.%, (b) 3.5 wt.%, and (c) 4 wt.% BaTiO ₃ composites. Source: ORNL.	359
Figure II.3.1.45. (a) Schematic of the electrospinning process on a CF mat. (b) SEM image showing homogenous deposition of nanofibers in random orientations on the CFs. (c) A higher magnification SEM image of the nanofibers on the CF surface. Source: ORNL.	360
Figure II.3.1.46. (a) Schematic showing the fabrication process of combining two layers of nanofiber coated CFs and testing it in the transverse direction. (b) Transverse tensile test results comparing the bare CFs with nanofiber coated CFs under various processing conditions. Source: ORNL.	360
Figure II.3.1.47. (a) The LSAM™ and (b) 3D printing of a shuttle in process at Local Motors. Source: Thermwood Corporation and ORNL.	363
Figure II.3.1.48. Failures in large-scale 3D printing: (a) debonding between layers due to overcooling and (b) material collapse due to the too high temperature of layers. Source: Thermwood Corporation and ORNL.	364

Figure II.3.1.49. Failures in large-scale 3D printing: (a) debonding between layers due to overcooling and (b) material collapse due to the too high temperature of layers. Source: Thermwood Corporation and ORNL.	365
Figure II.3.1.50. Dimensions and the printed structure of a hexagon. Source: ORNL.	366
Figure II.3.1.51. Thermal images in °C of a hexagon from an IR camera during the 3D printing process. (a) Top view. (b) Side view. Source: ORNL.	367
Figure II.3.1.52. Process of progressive material activation for the hexagon geometry (Case 2). Source: ORNL.	368
Figure II.3.1.53. Heat transfer behavior of (a) isotropic and (b) anisotropic materials. Source: ORNL.	370
Figure II.3.1.54. Local coordinate system aligned with the printing (fiber) direction. Source: ORNL.	370
Figure II.3.1.55. Thermal conductivity in the three principal directions of printed CF-PC. Source: ORNL.	371
Figure II.3.1.56. Heat transfer behavior of (a) isotropic and (b) anisotropic materials. Source: ORNL.	371
Figure II.3.1.57. Local coordinate system aligned with the printing (fiber) direction. Source: ORNL.	372
Figure II.3.1.58. Optimal layer time of each layer from the 10 th layer to the 61 st layer for (a) Case 1; (b) Case 2 and (c) Case 3. Source: ORNL.	373
Figure II.3.1.59. Cross-section point presenting the most optimal layer time with the trend of optimization results. Source: ORNL.	373
Figure II.3.1.60. Layer temperature prediction for the 130 seconds layer time case. Source: ORNL.	374
Figure II.3.1.61. Result of the additional optimization process for the 130 seconds layer time case. Source: ORNL.	374
Figure II.3.1.62. (a) Schematic of the large-area high-resolution projection stereolithography system. (b) Large-area high-resolution projection stereolithography system with a large format printing vat. (c) Optical path diagram of the infinity-corrected projection design. (d) Current optical system setup with adjustable projection area/resolution. Source: ORNL.	378
Figure II.3.1.63. (a) Block diagram of the processing and control schematic. Blue line: File processing; Red line: 24V power circuit; Green line: Analog or digital signals; Orange line: Power circuit for motors. (b) Diagram of the printing process. Source: ORNL.	379
Figure II.3.1.64. (a) Schematic of the large-scale (50 cm), high-resolution (50 μm) vase designed in nTopology and sliced into layers with each layer split into 5 × 7 sub-sections. (b) An illustration outlining the optimization of the scan path. (c) Comparison of the scanning time cost between conventional and optimized paths, where k=20 refers to the circle pattern in (a), and k=6 refers to a more general pattern in (b). The scanning speed dramatically increases for the large volume structure with the hollowed inner. Source: ORNL.	380

Figure II.3.1.65. Printable feature size range of different AM techniques in one hour. The maximum printable size is normalized according to the throughput of the methods. Estimated throughput: two-photon 0.22 $\mu\text{m}^3/\text{h}$; moving optics: 500 cm^3/h , P μ SL 1 cm^3/h , FDM 30 cm^3/h , BAAM 45400 cm^3/h . Source: ORNL.....	380
Figure II.3.1.66. (a) Extruded pattern with programmed fiber orientations. (b) The schematic of the compression process of beads with an oval and flat shape. (c) Captured images from cured beads before and after compression. The histogram shows the orientation distribution of the fibers. (d) Printed hollowed car bumper with localized fiber orientation. Source: ORNL.....	382
Figure II.3.1.67. (a) Measured stiffness of printed CFRPs with varying fiber-loading and lengths. (b) Mechanical property map of fiber-reinforced composites printed via SLA. Source: ORNL.....	383
Figure II.3.1.68. (a) As-fabricated large-scale hierarchical CFRP truss-lattice materials (e.g., strut radius = 150 μm). (b) As-fabricated large-scale CFRP plate-lattice materials. (c) As-fabricated large size high-resolution Voronoi vase made of CFRP. The vase is designed to have gradient unit cell size and strut thickness along its height direction. Source: ORNL.....	384
Figure II.3.1.69. Hollowed car bumper design with a lattice structure. Source: ORNL.....	384
Figure II.3.1.70. (a) 3D printed hollowed car bumper with a length of 110 cm. (b) Each half (~55 cm) was printed separately and bonded together to make a full-size (110 cm) bumper. Source: ORNL.....	385
Figure II.3.1.71. CF manufacturing process and cost analysis. Source: ORNL.....	395
Figure II.3.1.72. Embodied energy for PAN and coal pitch precursor and CF manufacturing. Source: ORNL.....	397
Figure II.3.1.73. Multiscale R&D approach. Source: ORNL.....	398
Figure II.3.1.74. Pitch material from different sources. Source: ORNL.....	400
Figure II.3.1.75. (a) Pelletization process. (b) Pelletized pitch material. Source: ORNL.....	400
Figure II.3.1.76. Melt-blowing of pitch precursor at bench scale and scaleup including microscopy images of the produced fiber. Source: ORNL.....	401
Figure II.3.1.77. Melt-spinning of pitch precursor at bench scale and scaleup including SEM images of the produced fiber. Source: ORNL.....	401
Figure II.3.1.78. Optical microscopy images of the nylon fiber samples (for illustration purposes only). Source: ORNL.....	402
Figure II.3.1.79. Optimized pin configuration of the heated pin die system. Dual pin configurations were set to +45, -45, +45, and -45, respectively. Fiber was weaved through the pin system as shown. This pin configuration and weave pattern was found to optimally impregnate the CF tow. Source: FCMF.....	403
Figure II.3.1.80. Thermoplastic tape impregnation process. This system was designed for the impregnation of wide tow (+350K) TCF. Source: FCMF.....	403
Figure II.3.1.81. Molten polymer coated TCF being kneaded in the pin/kneading die. Notice how the heated pins knead in the polymer into the TCF to completely impregnate it to make TTT. Source: FCMF.....	405

Figure II.3.1.82. Take-up system collecting the TCF thermoplastic impregnated tape. The TTT is wrapped about a cardboard tube clamped on a chuck to collect it. The chuck is further connected to a clutch that adjusts torque to maintain tension constant inline. Source: FCMF.....	405
Figure II.3.1.83. Image enhancement for void analysis on two layers of <i>in-situ</i> consolidated CF-PP tape. Image processing program outlines edges of tape to exclude voids outside of the tape region. Source: FCMF.....	406
Figure II.3.1.84. Flexural load vs. displacement for TCF thermoplastic tape. Source: FCMF.	407
Figure II.3.1.85. Zoomed microscopic image of the failed sample demonstrating crack initiation on the thin side and along the tension surface. Source: FCMF.....	408
Figure II.3.1.86. Bar graph comparing flexural strengths of different samples. Source: FCMF.	408
Figure II.3.1.87. Bar graphs comparing flexural modulus of different samples. Source: FCMF.....	409
Figure II.3.1.88. Representative curves of load vs. displacement for ILSS of TCF thermoplastic tape. Source: FCMF.....	409
Figure II.3.1.89. (a) Side view of failed sample showing failure mode was ductile with crack initiation from the bottom side (tension). (b)Top view of bottom surface crack (tension side). Source: FCMF.	410
Figure II.3.1.90. Bar graphs comparing flexural modulus of different samples. Source: FCMF.....	410
Figure II.3.1.91. (a) Failed tensile sample specimen the failure can be due to crack propagation from matrix rich region. (b) Failed sample with the halves separated. Source: FCMF.....	411
Figure II.3.1.92. Bar graph representing tensile modulus with the average value and standard deviation. Source: FCMF.....	411
Figure II.3.1.93. Bar graph depicting tensile strength for tested specimen with the average value and standard deviation. Source: FCMF.	412
Figure II.3.1.94. Representative curves for tensile load vs. displacement for three samples. Source: FCMF.	412
Figure II.3.1.95. Comparison on the IFSS of polymer matrix and polymer fiber with different treatment methods: (a-c) similar material system (e.g., PE-PE, PP-PP); (d-f) dissimilar material system (PP-PE). Note: PT means plasma treatment, AP means aerosol-based adhesion promotor, PT+PEO means grafting of polyethylene oxide after plasma treatment, and MA means maleic anhydride polypropylene sizing. Source: PNNL.....	418
Figure II.3.1.96. (a) Stress-strain curves for non- and fiber-treated composites with PP fabrics and an HDPE matrix; and (b-c) maximum principal strain field and failure morphology at a nominal strain of 0.6. Source: PNNL.	418
Figure II.3.1.97. (a-b) CM for the fabrication of hat-shaped low-density polyethylene reinforced by woven UHMWPE fabrics; (c) temperature profiles for the entire molding process measured from three embedded thermocouples; and (d) standard deviation of temperatures among thermocouples during molding. Source: PNNL.	419
Figure II.3.1.98. (a) Morphology in the gauge area of an UHMWPE-HDPE composite after peak load, (b) plastic deformation and damage of HDPE matrix, (c) UHMWPE fiber breakage at edge, and (d-e) failure morphologies of penetrated self-reinforced PP twill composites and twill CFRPs after impact loading. Source: PNNL.....	420

Figure II.3.1.99. Melting peaks for as-spun, 1st drawn, 2nd drawn, and 3rd drawn PP fibers. Source: ORNL.....	421
Figure II.3.1.100. Investigation of dimensional stability for polyolefin fibers at high temperatures. Source: ORNL.....	422
Figure II.3.1.101. Mechanical properties of reinforcing PP fibers drawn at various draw ratios. Source: ORNL.....	422
Figure II.3.1.102. The overall hot-press process to fabricate ultra-lightweight thermoplastic polymer/polymer fiber composites using PP fiber reinforcement and chemically modified PP matrix. Source: ORNL.....	423
Figure II.3.1.103. Direct depolymerization of PET waste and concerted repolymerization. Source: PNNL.....	426
Figure II.3.1.104. Synthesis of PPTA through the acid chloride route, formed from terephthalic acid monomer obtained through PET hydrolysis. Source: PNNL.....	427
Figure II.3.1.105. (a) Initial reaction method (e.g., Method 1) near completion which yielded low molecular weight (inherent viscosity = 3.01 dL/g). (b) Improved reaction method (e.g., Method 2) near completion yielded higher molecular weight (inherent viscosity = 4.8 dL/g). Commercially sourced TCI was used in each case. Source: PNNL.....	428
Figure II.3.1.106. Inherent viscosity of PPTA (0.5% w/v in sulfuric acid) synthesized by either Method 1 or Method 2 and using either PET-derived or commercially sourced TCI. The shaded zone (4-5 dL/g) represents inherent viscosity suitable for fiber spinning. Source: PNNL.....	428
Figure II.3.1.107. Synthesis of PODA aramid polymer. Source: PNNL.....	429
Figure II.3.1.108. (a) Liquid 18 wt.% PPTA dope solution in 99.9% purity H ₂ SO ₄ at 90 °C. (b) The same dope solidified at 50 °C (in oil bath) upon cooling. Source: WSU.....	429
Figure II.3.1.109. Schematic of an AM-CNG storage vessel concept. (a) External rigid structural layers of the vessel: load-bearing resin filaments (blue) filled with short and continuous CF (white). (b) Continuous filament material is applied to the midbody yielding maximum hoop strength. (c) Short-fiber extrusion used to fabricate complex end caps. Flexible and cross- linkable polymer compositions reinforced with nanoplatelets shown in (b) and (c) will be printed to serve as the inner layers of a vessel (yellow and blue layers represent the inner gas barrier and transition to structural layers, respectively). Source: LLNL.....	433
Figure II.3.1.110. Project schedule. Source: LLNL.....	434
Figure II.3.1.111. Cutaway view of a 4-in. diameter by 6 in. long scaled CNG tank design that will be implemented in this project via an AM process. The tank consists of three material 'zones' (e.g., liner, midbody, topcoat) – all of which will be chemically contiguous and printed in the same process operation. Source: LLNL.....	434
Figure II.3.1.112. Mathematically derived layer solutions for the cylindrical region of the midbody of the tank, which were generated using optimization tools in the LLNL Code NIKE-3D. These non-obvious solutions have been validated to show decreased compliance with decreased volume fraction fiber vs. standard wind geometries. Source: LLNL.....	435
Figure II.3.1.113. Project overview. Source: NREL.....	438

Note: STGE = sorbitol tetraglycidal ether; BDGE = butanediol diglycidyl ether; MHPA = methylhexahydrophthalic anhydride; MHHPA = methylhexahydro dimethyl phthalic ester	439
Figure II.3.1.114. PECAN resin chemistry in which bioderived epoxies and anhydrides are combined to a crosslinked network and can be recycled with methanol. Source: NREL.	439
Figure II.3.1.115. Dynamic mechanical analysis results and coupons for the (a) first, (b) second, and (c) third lives of the PECAN-CFRCS demonstrating consistent or enhanced properties across lives.. Source: WSU.	440
Figure II.3.1.116. Properties of the PECAN CFRC relative to steel. Source: NREL.	440
Figure II.3.1.117. A comparison of alternative fiber reinforcements for (a) a PECAN CFRC versus (b) a PECAN-based polyethylene reinforced composite. (c) Potential accessible phase space through reformulation of PECAN-CFRCS. Source: NREL.	442
Figure II.3.1.118. PECAN CFRC thermoforming demonstration. (a) Digital drawing the thermoforming mold with multiple different geometries alongside the (b) top and (c) side view of the thermoformed CFRC. Source: NREL.	442
Figure II.3.1.119. Diagram of 3D printing equipment for CCF composites: Source: SRNL.....	446
Figure II.3.1.120. (a) The process for coating the CNTs and micrographs of the CCF filament with an optimized homogeneous coating of CNTs; (b) the scaled-up CNT coating line; and (c) a close-up view of the fiber roller. Source: SRNL.....	447
Figure II.3.1.121. (a) 300 feet of CNT-coated CCF filament on six rolls, and (b) larger rolls of 3,000 feet of CNT-coated CCF after scaleup. Source: SRNL.	447
Figure II.3.1.122. Short-beam shear data showing a 20% increase in shear strength and 250 microns longer displacement for breakage with the microwave-annealed coupon. Source: SRNL..	448
Figure II.3.1.123. Thermal transfer data of thermal pucks. Source: SRNL.	449
Figure II.3.1.124. (a) Thermoplastic prepreg forming tool geometry for concept demonstration and (b) sub-component tool parts geometry (dimensions in mm). Source: SRNL.....	449
Figure II.3.1.125. TEA and LCA scenarios, processes, and identified scope. Source: SRNL.....	450
Figure II.3.1.126. Single score energy analysis comparing the three different tooling options. CFC and machined-metal tooling are 84% and 154% more energy-intensive to produce, respectively, over the SRNL 3D-printed CF tooling. Source: SRNL.	450
Figure II.3.1.127. Comparison of energy consumed per cubic meter for the annealing of CF soft tooling. SRNL's 3D-printed tooling shows an order of magnitude less energy usage per cubic meter. Source: SRNL.	451
Figure II.3.1.128. Overview of (a) tooling installation trials for (b) inner beltline stiffener. Source: Clemson University.....	454
Figure II.3.1.129. Process flow for stamping: heating, transport and forming of material. Source: Clemson University.....	454
Figure II.3.1.130. Trials showing visual appearance of sample as a function of tool temperature. Source: Clemson University.....	454
Figure II.3.1.131. (a) Formed inner beltline part on the heated tool. (b) Post-processed parts being evaluated. Source: Clemson University.....	455

Figure II.3.1.132. Overview of manufacturing progress on the inner panel part. Source: Clemson University.....	456
Figure II.3.1.133. Overview of progress on static testing fixture and dynamic tests planed. Source: Clemson University.....	456
Figure II.3.1.134. Project task breakdown. Source: Ford Motor Company.....	459
Figure II.3.1.135. Task list for component design work stream. Source: Ford Motor Company.	459
Figure II.3.1.136. CAD rendering of instrument panel cross car beam with relative placement of the steering column sub-assembly. Source: Ford Motor Company.	461
Figure II.3.1.137. Business and weight-savings assessment of the cross car beam design concept at the end of BP1. Source: Ford Motor Company.....	461
Figure II.3.1.138. Flexural strength and flexural modulus of PA66/MXene composites. Source: Ford Motor Company.....	462
Figure II.3.1.139. (a) (b) Wall thickness variation along the length of the (c) demonstrator part used for process development. Source: Ford Motor Company.....	464
Figure II.3.1.140. Occurrence of thick-section voids in the corners of the demonstrator part (a) without added cooling and (b) with added cooling. Source: Ford Motor Company.....	465
Figure II.3.1.141. Progression of hot runner degree of hollow after water-assist is turned on. (a) A seven-second pack sample. (b) A ten-second pack sample. Source: Ford Motor Company.....	465
Figure II.3.1.142. Jig design to form M-TOW into AM attachment points. Source: Ford Motor Company.....	466
Figure II.3.1.143. M-TOW preforms produced in support of injection overmolding studies. Source: Ford Motor Company.....	466
Figure II.3.1.144. Printed circuitry on decorative film. Source: Ford Motor Company.	467
Figure II.3.1.145. Film distortion near the injection gate. Source: Ford Motor Company.....	467
Figure II.3.1.146. (a) Revised printed circuit design and (b) physical prototype for surface mounting of electrical componentry. Source: Ford Motor Company.	468
Figure II.3.1.147. Preliminary over-injection molding shots with no ink washout or electrical component debonding. Source: Ford Motor Company.....	468
Figure II.3.1.148. Close-up of inserts placed in the molding tool. Source: Ford Motor Company.....	469
Figure II.3.1.149. Finished part after injection-molding showing the location of attachment points. Source: Ford Motor Company.	469
Figure II.3.1.150. Design of pick-and-place fixture (blue) and end-of-arm (dark grey). Source: Ford Motor Company.....	470
Figure II.3.1.151. The pick-and-place fixture and end-of-arm tooling picking up tow and hardpoints. Source: Ford Motor Company.....	470
Figure II.3.1.152. The pick-and-place robot automation cell. Source: Ford Motor Company.	471
Figure II.3.1.153. Close-up of end-of-arm. Source: Ford Motor Company.	471

Figure II.3.1.154. (a) Initial design concept to retrofit existing robot cell with (b) the over-mold transfer table. Source: Ford Motor Company.....	472
Figure II.3.1.155. Revised tasks and milestones for the AM tooling workstream. Source: Ford Motor Company.....	472
Figure II.3.1.156. XGBoost 'weight' predictions for individual cycles for three consecutive trials (orange line) and empirical data (blue dots). Source: Ford Motor Company.	474
Figure II.3.1.157. XGBoost 'part volume' prediction for individual cycles for three consecutive trials (orange line) and empirical data (blue dots). Source: Ford Motor Company.....	475
Figure II.3.1.158. Model input features ranked by importance for predicting 'weight.' Source: Ford Motor Company.....	476
Figure II.3.1.159. Model input features ranked by importance for predicting 'part volume.' Source: Ford Motor Company.....	476
Figure II.3.1.160. Tensile testing results for 40CF/PA66 and 30Cf/10BF/PA66 specimens Source: Ford Motor Company.....	477
Figure II.3.1.161. The fiber length distribution for virgin pellets, 0 wt.% RC, shredded granulate, 33 wt.% RC, 67 wt.% RC, and 100 wt.% RC samples. Source: Ford Motor Company.	477
Figure II.3.1.162. NMR spectroscopy of neat PA66 pellets and 100% RC samples of 30CF/10BF/PA66 showing the ¹³ C spectra at (a) low ppm, (b) high ppm, and (c) the ¹ H NMR spectra. Source: Ford Motor Company.	478
Figure II.3.1.163. Lattice materials included in this mechanical property study. Source: GM.....	481
Figure II.3.1.164. Tensile stress-strain curves for Lattice materials at different carbon-to-glass fiber ratios. Source: GM.....	481
Figure II.3.1.165. Tensile stress-strain curves for hybrid materials at different types of carbon and glass fibers. Source: GM.	482
Figure II.3.1.166. Draping tool for experiments. Source: GM.	483
Figure II.3.1.167. (a) 2D fabric pattern. 3D draped geometry from (b) simulation and (c) experimental result. Source: GM.	483
Figure II.3.1.168. Configurations studied using the lattice preform: (1) slits; and (2) no slits. Source: GM.....	483
Figure II.3.1.169. (a) 2D preform design with no-slit and (b) the draped preform design with no-slit. Source: GM.	484
Figure II.3.1.170. Geometry of the HP-RTM mold used for experiments. Source: GM.....	484
Figure II.3.1.171. Comparison of pressure profile from the experiments and simulations. Source: GM.....	485
Figure II.3.1.172. Multiscale framework for structural performance of composites. Source: GM....	486
Figure II.3.1.173. Enhanced RVE model of hybrid fiber composite. Source: GM.	486
Figure II.3.1.174. Comparison of experimental and RVE results for the hybrid fiber composite. Source: GM.....	486

Figure II.3.1.175. Stress-strain and resistance relationship of a composite with an embedded carbon tow sensor. Source: GM 487

Figure II.3.1.176. Impact test setup and resistance results for undamaged and damaged samples. Source: GM..... 488

Figure II.3.1.177. Samples with embedded 3K sensor tow (copper rivets for electric terminals). Source: GM..... 488

Figure II.3.1.178. Two-part NN. Source: GM..... 489

Figure II.3.1.179. Comparison of NN-based multiscale model with experimental results. Source: GM..... 490

Figure II.3.1.180. Geometry of the baseline battery enclosure for the GM model Cadillac Lyriq. Source: GM..... 490

Figure II.3.1.181. Mini-battery enclosure design. Source: GM. 491

Figure II.3.2.1. (a) SLIC bumper beam. (b) Cross section schematic of SLIC bumper beam. Source: Newport Sensors, Inc. 495

Figure II.3.2.2. Specimen fabrication. Source: Newport Sensors, Inc..... 496

Figure II.3.2.3. The simultaneous piezo and strain amplifier. Source: Newport Sensors, Inc. 496

Figure II.3.2.4. (a) Experimental test setup showing the universal testing machine clamping the specimen. (b) Plots of strain-gauge resistance change vs. strain, and stress vs. strain. Source: Newport Sensors, Inc. 497

Figure II.3.2.5. (a) Specimen after tensile test showing failure at top. (b) Time history chart of piezoelectric charge showing micro-crack sign signal before failure at sensor located at top. Source: Newport Sensors, Inc. 497

Figure II.3.2.6. SMART layer sensors. Source: Accellent Technologies, Inc..... 500

Figure II.3.2.7. System test setup. Source: Accellent Technologies, Inc..... 501

Figure II.3.2.8. Voltage impulse received upon an impact with a golf club: (a) golf club and (b) voltage impulse curves. Source: Accellent Technologies, Inc..... 502

Figure II.3.2.9. Voltage impulse received upon an impact with a prosthetic leg: (a) prosthetic leg and (b) voltage impulse. Source: Accellent Technologies, Inc. 503

Figure II.3.2.10. The dimension and design of the skateboard. Source: Accellent Technologies, Inc. 504

Figure II.3.2.11. MESC battery arrangement. Source: Accellent Technologies, Inc. 505

Figure II.3.2.12. SEM of T800 prepreg recycled fiber from Vartega: (a) and (b) as received; and (c) after additional pyrolysis process. Source: Composites Automation, LLC. 510

Figure II.3.2.13. TuFF processing using recycled T-800 from Vartega: (a) TuFF material processing; (b) 24 layer TuFF prepreg; (c) C-scan of bladder molded TuFF material; and (d) micrograph showing high-quality material for tensile testing. Source: Composites Automation, LLC. 511

Figure II.3.2.14. SEM of recycled T-800 TuFF composite failed tensile surface showing fiber clusters. Source: Composites Automation, LLC. 512

Figure II.3.2.15. (a) Electrospinning apparatus for the TuFF2-CA process line. (b) SEM of 0.1 gsm PVA e-spun fibers on T800 TuFF preform. Source: Composites Automation, LLC.....	513
Figure II.3.2.16. (a) Non-isothermal DSC scans for different heating rate. (b) Fraction of conversion vs. time predictions for isothermal cure temperatures ranging from 80 °C to 150 °C. Source: Composites Automation, LLC.	513
Figure II.3.2.17. (a) Viscosity as a function of temperature for a heating ramp of 2 °C/minute and (b) micrograph of TuFF T800/M77 snap-cure resin. Source: Composites Automation, LLC.....	514
Figure II.3.2.18. Dielectric cure monitor data from the molding of a 28-mm-thick composite part demonstrating a 90-second cure time. Source: Trimer Technologies, LLC.	519
Figure II.3.2.20. Pultruded profiles using Trimer’s resin system for (a) carbon and (b) fiberglass. Source: Trimer Technologies, LLC.....	520
Figure II.3.2.21. Weight comparison between two braided harnesses: (a) traditional copper plated metal harness and (b) 40% lighter PVC/CNF composite fabricated by ASI. Source: ASI.	523
Figure II.3.2.22. SEM images of the PAN/CNF nonwoven veils. Notice the hybrid multiscale composite structure created by the PAN macroscopic CFs that are wrapped by CNF, which themselves are surrounded by nano-sized CB. Source: ASI.	524
Figure II.3.2.23. (a) Covalent surface functionalization of rCF with carbon nanofiller to form highly stable NMCF. SEM images of (b) freshly prepared NMCF and (c) recycled NMCF from NMVC-R ² . Due to the strong covalent bonding between CF micro-fillers and carbon-based nanofillers, NMCF is stable even after a series of solution and solid-state processing under heat. Source: RockyTech Ltd.	527
Figure II.3.2.24. (a) Tensile stress-strain curves of various vitrimers. (b) Tensile and conductive properties of NMVC-R ² made of vitrimers and NMCFs in comparison with CFRP made with unmodified rCF. SEM images of (c) the surface and (d) the cross-section of the NMVC-R ² . Source: RockyTech Ltd.	528
Figure II.3.2.25. (a) Closed-loop recycling of NMVC-R ² through solution-phase depolymerization and repolymerization. (b) Tensile stress-strain curves of recycled NMVC-R ² in comparison with the original sample. Source: RockyTech Ltd.	529
Figure II.3.2.26. Alignment of microscale rCF (unmodified) through FIFA: (a) The image of 1' x 3' panel of CFRP with aligned short carbon fibers; (b, c) SEM images of the CFRP along the fiber direction showing successful fiber alignment through the FIFA method. Source: RockyTech Ltd.	529
Figure II.3.2.27. EMI-SE of CFRP samples consisting of unmodified rCF: (a) without fiber alignment; and (b) with fiber alignment, as shown in Figure II.3.2.6.4(b). Source: RockyTech Ltd. .	530
Figure II.3.2.28. Impact test results (ASTM D256). Source: SCI.....	535
Figure II.3.2.29. (a) The basis from literature for the tested ‘gray’ and ‘green’ tire tread compounds. (b) A rendition of the differences between a conventional ‘black’ and high silica ‘green’ tire treads. Source: MRD.....	537
Figure II.3.2.30. Flow diagram of most experiments performed by MRD during the course of Phase I. Source: MRD.	538
Figure II.3.2.31. Spider graph demonstrating materials property changes with nonfunctional MR in a ‘gray’ tire tread compound. Source: MRD.	539

Figure II.3.2.32. Annotated transmission electron microscope image of MR dispersed in a ‘gray’ tire tread compound. Source: MRD.	539
Figure II.3.2.33. Spider graph demonstrating materials property changes with nonfunctional MR in a ‘green’ tire tread compound. Source: MRD.	539
Figure II.3.2.34. Graphic showing theorized mechanism of organosilane bonding between MR and the polymer matrix. Source: MRD.....	540
Figure II.3.2.35. Plot demonstrating simultaneous improvement in reinforcement (100% modulus) and RR (Tan δ at 60 °C). Source: MRD.	540
Figure II.3.2.36. Plot demonstrating simultaneous improvement in reinforcement (100% modulus) and R (Tan δ at 60 °C). Source: MRD.....	541
Figure II.3.2.37. Conceptual design of proposed multiscale hybrid composite for vehicle applications. Source: Advent.....	544
Figure II.3.2.38. Solution-spinning system. Source: GSU.....	546
Figure II.3.2.39. Fiber diameter before and after strain-hardening. Source: GSU.	546
Figure II.3.2.40. Composite specimen manufacturing. Source: Advent.....	547
Figure II.3.2.41. Composite specimen tensile testing. Source: Advent.....	547
Figure II.4.1.1. A summary of two sheet thick weld stack-ups in terms of materials, thicknesses, and surface treatments. Source: ORNL.....	552
Figure II.4.1.2. Two approaches to establish associations among process parameters, weld attributes, and weld performance. Source: PNNL/ORNL.....	552
Figure II.4.1.3. The expendable unified ML model. Source: ORNL.....	553
Figure II.4.1.4. A summary list of data distribution of the 40 weld stack-ups (~99% of usable Al-steel weld data set from GM). Source: ORNL.....	554
Figure II.4.1.5. Mean absolute accuracy of ML predicted (a) peak load; (b) extension at the break; and (c) total energy for all 40 Al-steel weld stack-ups. Source: ORNL.....	556
Figure II.4.1.6. A comparison between ML predictions and experimentally measured mean value and standard deviation of peak load for (a) GM’s 40 Al-steel weld stack-ups, as well as for individual welds of different weld stack-ups, including (b) 0.8-mm-thick AA X626 with 0.9-mm-thick HDG LCS, (c) 1.2-mm-thick AA 6022 with 1.2-mm-thick HDG LCS, (d) 1.1-mm-thick AA 5754 with 2.0-mm-thick HDG HSLA 340, and (e) 1.0-mm-thick AA X610 with 1.2-mm-thick HDG CR210B2. Source: ORNL.....	557
Figure II.4.1.7. ML model predicted the peak load of ~ 90% independent test welds on the 1.2-mm-thick AA6022 and 1.4-mm-thick bare LCS with a more than 80% accuracy. Source: ORNL.	558
Figure II.4.1.8. Importance scores of the independent variables determined based on comprehensive ML analysis of 40 weld stack-ups. Source: ORNL.....	558

Figure II.4.1.9. (a) Flowchart showing the application of the fully trained ML model for weld design to identify weld attributes/conditions for meeting joint target performance. (b1) and (b2) Identification of a set of weld variables to achieve the performance target: peak load ≥ 750.0 N and total energy ≥ 14.5 J for welds made by 1.2-mm-thick 6022 with 2.0-mm-thick HDG LCS and 1.1-mm-thick 6022 with 2.0-mm-thick HDG LCS (e.g., a material combination not yet tested experimentally). Source: ORNL.....	559
Figure II.4.1.10. Principal components of the five coach peel performance metrics (peak load, total energy, extension at break, extension at peak load, energy up to peak load) constructed for (a) AA6022/LCS and X626/LCS RSW joints, and (b) classification of RSW joints as optimal and non-optimal using the k-means clustering method. Source: PNNL.....	561
Figure II.4.1.11. The smoothed ‘ideal’ hardness curve demonstrating the ideal hardness distribution across the width of the RSW joints developed for comparison of RSW weld structure metrics. Source: PNNL.....	562
Figure II.4.1.12. The smoothed ‘ideal’ hardness curve demonstrating the ideal hardness distribution across the width of the RSW joints developed for comparison of RSW weld structure metrics. Source: PNNL.....	563
Figure II.4.1.13. (a) Principal components of the five coach peel performance metrics (e.g., peak load, extension at peak load, extension at break, energy up to peak load, total energy) constructed for Stack-up 2C RSW joints, and (b) the distribution of variable minimal depth of the variables from the Random Forest model. Source: PNNL.....	564
Figure II.4.1.14. (a) Lap-shear strength of Al5052/CFRP-PA66 combination with various PT parameters on CFRP-PA66. (b) Fracture morphology after the lap-shear failure showed residual black CFRP PA66 was evident on all failure surfaces. Source: PNNL.....	568
Figure II.4.1.15. (a) Average surface roughness vs. laser treatment parameters. (b1) Microscale computation with the consideration of real material surface morphology. (b2) Nominal shear strength vs. interfacial strength/adhesive strength for an adhesively bonded metal joint. (c1) SEM of AA380. (c2) Al grains of laser-ablated AA380. (c3) Atomic percentage of surfaces treated with different laser powers from GM. Source: PNNL.....	569
Figure II.4.1.16. The properties of ABL-based adhesives: (a) tensile strength of adhesive films; (b) LSS results with Al 6061 as the substrate; (c) surface energy for adhesive films; (d) fracture surface for lap-shear samples; (e) SEM of adhesives; (e-1) control sample; and (e-2) with addition of TA. Source: ORNL.....	570
Figure II.4.1.17. (a) Lap-shear load-displacement curves of DP590 steel plates to AA5052-H32 and AA6061-T6 plates along with AA5052-H32/AA6061-T6 to PA66 composite plates. (b) Testing results for the various surface treatments on lap-shear loading in the AA6061-T6 joints. Source: PNNL.....	571
Figure II.4.1.18. Load-displacement curves for AA6061-T6 joints with and without adhesive/plasma application. Source: PNNL.....	571
Figure II.4.1.19. (a) Schematic of HiVe process set-up and dimensions. (b) Finite element mesh for HiVe simulations. Source: PNNL.....	572
Figure II.4.1.20. (a) Optimized die design. (b) Corresponding experimental cross-section. (c) Comparison of load-displacement curves. Source: PNNL.....	572

Figure II.4.1.21. Experimental setup showing the diffraction geometry in transmission mode at beamline 1-ID through APS. The x-ray beam path is marked in white with a solid line showing the incident beam and dashed line showing two diffracted beams. Source: ANL.....	573
Figure II.4.1.22. (a) Total scan area covered by the measurement array of spots (e.g., ~30 rows along x and ~20 columns along y) marked in red. Note that it covers both the joined and substrate areas. (b) 2D diffraction pattern acquired from the substrate region of the Al/Al joint. (c) Corresponding 1D diffraction pattern obtained by azimuthally integrating the 2D pattern in (b). Source: ANL.....	573
Figure II.4.1.23. Lattice parameter map from the measurement array overlaid on an optical micrograph of the Al/Al rivet. Source: ANL.....	574
Figure II.4.1.24. (a) The AA6061-DP590 joint processed via HFR. (b) Optical microscopy image of the cross-section of AA6061-DP590 HFR joint with an M42 rivet. (c) The smoothed 'ideal' hardness curve demonstrating the ideal hardness distribution across the width of the RSW joints developed for a comparison of RSW weld structure metrics. (d) Lap-shear performance comparison of the joints. Source: PNNL.....	575
Figure II.4.1.25. (a) Experimental and simulated load vs. displacement lap-shear test results. (b, c) Equivalent plastic strain distributions at peak load for the case: (b) without bonding; and (c) with a metallurgical bonded interface. (d) Experimental failure morphology showing a rivet bonded with DP590. Source: PNNL.....	576
Figure II.4.1.26. Material arrangements for the four material stacks to be joined and characterized. Source: PNNL.....	580
Figure II.4.1.27. Overview of project approach. Source: ORNL.....	580
Figure II.4.1.28. Load per unit width vs. crosshead displacement plot for 3T FSLW joints: (a) lap-shear, (b) T peel, and (c)-(d) bar chart compilation of several tested samples. Source: PNNL.....	581
Figure II.4.1.29. (a) Load per width vs. crosshead displacement plot for 3T FSLW joints showing the effect of the dwell on joint strength. (b) Top view of the weld without the pilot hole. (c) Top view of the plate with the pilot hole. Source: PNNL.....	582
Figure II.4.1.30. Comparison of welding time (including plunge-in and traverse time) per plunging speed for (a) plunge-in time and (b) "strength of joint. Source: PNNL.....	583
Figure II.4.1.31. 6111-6022 stack FS welded U-Peel (a) and (a1) testing set-up, welding scheme (b) Seam A, (b1) Seam B, (b2) Seam C, (c) loading direction, (d) load vs. displacement plot. Source: PNNL.....	584
Figure II.4.1.32. Curve welding on (a) 7055-7055-6022 stack and (b) 6111-6111-6022 stack with a macrograph of cross-sections. (c) FSLW of demonstration stamped part (inset: ~ 500 mm long weld without any surface defect). Source: PNNL.....	585
Figure II.4.1.33. (a) A schematic of the test sample used for the single-edge notch bending fracture tests. (b) Lap-joint load-displacement plots from the two simulations, with and without the weld fracture test data, as compared to the lap-shear test data. Source: PNNL.....	586
Figure II.4.1.34. The T-Peel load-displacement plots from the two simulations, with and without dwell time at the exit hole, as compared to the experimental data from a sample with no dwell time. Source: PNNL.....	586

Figure II.4.1.35. Simulation results of U-Peel joint under KSII-type loading. (a) Von-Mises stress distributions just before fracture. (b) Bottom and top sheets after complete fracture of the joint. Source: PNNL.	587
Figure II.4.1.36. (a) Experimental and simulated load vs. displacement lap-shear test results. (b, c) Equivalent plastic strain distributions at peak load for the case: (b) without bonding; and (c) with a metallurgical bonded interface. (d) Experimental failure morphology showing a rivet bonded with DP590. Source: PNNL.....	588
Figure II.4.1.37. Summary of mechanical joint performances for Al7055-CFRC F-SPR joints. (a) Load vs. displacement curves from lap-shear tensile testing. (b) Load vs. displacement curves from cross-tension testing. (c) S-N curve from fatigue testing, showing Al fracture after fatigue testing. Source: ORNL.....	589
Figure II.4.1.38. Temperature distribution for a two-dimensional axisymmetric model and Mises stress plot showing the rivet shape under different plunging depths. ILD stands for interlocking distance. Source: ORNL.....	590
Figure II.4.1.39. The stress plot for different die shapes. ILD indicates the interlocking distance between the rivet and the bottom sheet. Source: ORNL.....	590
Figure II.4.1.40. Summary of mechanical joint performances for Al7055-DP980 F-SPR joints. (a) Load vs. displacement curves from lap-shear tensile testing. (b) Load vs. displacement curves from cross-tension testing. Source: ORNL.....	591
Figure II.4.1.41. New F-SPR weld system with C-frame for joining of demonstration parts. Source: ORNL.	592
Figure II.4.1.42. (a) Continuous wave laser system at ORNL. (b) A Nyquist impedance plot of baseline 600 grit finish (grey squares) and 75, 100, and 150W laser-treated Al7075. Source: ORNL.	596
Figure II.4.1.43. (a) New AP system integrated with a robotic system at ORNL. (b) A Nyquist impedance plot for baseline Al7075. (c) A Nyquist impedance plot for AP-treated Al7075. Source: ORNL.	598
Figure II.4.1.44. Depth profiles by XPS: (a) and (c) show the baseline Al7075 (control); (b) and (d) show the open-air plasma-treated Al7075. Source: ORNL.....	599
Figure II.4.1.45. (a) SEM image with chemical element maps. (b) Cross-section SEM image for open-air plasma-treated Al7075. (c) Elemental depth file. Source: ORNL.....	600
Figure II.4.1.46. High-magnification STEM image for open-air plasma-treated Al7075 with chemical element maps. Note: ADF = annular dark field; BF = bright field. Source: ORNL.	601
Figure II.4.1.47. (a) Characterization setup showing the diffraction geometry in reflection mode. The x-ray beam path is marked in red with a solid line showing the incident beam and a dashed line showing the diffracted (reflected) beam. Note that the sample is inclined at an angle of 75 degrees to the beam direction. (b) An example of a one-dimensional diffraction pattern for the oxide layer shown in white along with the stick patterns/peak positions of various expected oxide species. Source: ANL.	602
Figure II.4.1.48. (a) SEM image with chemical element maps. (b) Cross-section SEM image for open-air plasma-treated Al7075. (c) Elemental depth file. Source: ORNL.....	603

Figure II.4.1.49. (a) Comparison of a representative joint of AA6061 plate joined to AA6061 plate before and after corrosion. (b) Comparison of a representative joint of DP590 plate joined to AA6061 plate (without a rivet) before and after corrosion showing white corrosion product on the surface. Source: PNNL.	604
Figure II.4.1.50. Pre- and post-SECCM measurements showing cross-sectional optical images of two different rivet samples: (a) Al6061-Al6061 with a steel rivet and (b) Al6061-Al6061 with an Al7075 sacrificial rivet. Source: PNNL.....	604
Figure II.4.1.51. Corrosion potential values across an interface for (a) Al6061-Al6061 steel rivet (dotted line) and (b) Al6061-DP590 steel rivet. Source: PNNL.	605
Figure II.4.1.52. (a) Simple rivet geometry and (b) pre- and post-plasma-treated surface current density of Al6061 and Al5052 sheet for a range of rivet-to-sheet ratio. Source: PNNL.	606
Figure II.4.1.53. (a) Simple rivet geometry and (b) pre- and post-plasma-treated surface current density of Al6061 and Al5052 sheet for a range of rivet-to-sheet ratio. Source: PNNL.	607
Figure II.4.1.54. The main components of XP0012 and XP5005 adhesives. Source: PNNL.	608
Figure II.4.1.55. (a) Vibrational peak assignment of uncured and cured XP0012 adhesive. Peak change at the interface of (b) XP0012/CFRP-PA66, and (c) XP0012/Al6061. Source: PNNL.....	608
Figure II.4.1.56. XP5005 adhesive on (a) CFRP-PA66 and (b) Al6061 surfaces. Source: PNNL.	609
Figure II.4.1.57. NBR-lignin adhesive on (a) CFRP-PA66 and (b) Al6061 surfaces. Source: PNNL...	609
Figure II.4.1.58. Chemical interaction diagram of (a) XP0012, (b) XP5005, and (c) NBR-lignin adhesives on CFRP-PA66 and Al6061 surfaces. Source: PNNL.....	610
Figure II.4.1.59. Corrosion potential values across an interface for (a) Al6061-Al6061 steel rivet (dotted line) and (b) Al6061-DP590 steel rivet. Source: PNNL.	611
Figure II.4.1.60. SEM, atomic map, and EBSD images of laser-ablated Al380 cross-section. Source: PNNL.	612
Figure II.4.1.61. Peak lap-shear tensile load as a function of ultrasonic energy on single-joint (a) Al-Mg and (b) Al-steel coupons. Source: ORNL.	617
Figure II.4.1.62. (a) Representative microstructure at the Al-Mg USW joints showing IMC at the interface. (b) The average IMC thickness as a function of welding energy of Al-Mg USW joints. Source: ORNL.	617
Figure II.4.1.63. Chemical composition of Al-steel joint interface at the center of the joint. Source: ORNL.	617
Figure II.4.1.64. Measured sonotrode vibration amplitude during the (a) first and (b) third USW although the power setting was identical. Source: ORNL.	618
Figure II.4.1.65. (a) Predicted and (b) measured temperature history showing a higher temperature occurred when making the first USW joint. Source: ORNL.....	618
Figure II.4.1.66. Reference single-joint strength and strength of each joint in large coupons of Al-Mg. Source: ORNL.	619
Figure II.4.1.67. Reference single-joint strength and strength of each joint in large coupons of Al-steel. Source: ORNL.	619

Figure II.4.2.1. Details for the thermos- and vibration experiment: (a) sample treatment, (b) loading profile, (c) example of loading test results, and (d) changes in constitutive behavior under uniaxial loading. Source: Michigan State University.	623
Figure II.4.2.2. Validation of the model outputs to experimental data for the thermo + vibration + mechanical testing for tensile and cyclic conditions. Source: Michigan State University.....	623
Figure II.4.2.3. Validation of the model outputs to experimental data for the thermo + fatigue + mechanical testing for tensile and cyclic conditions. Source: Michigan State University.....	624
Figure II.4.2.4. Validation of trio-aging against experimental data for the thermo + hydrolysis + UV + mechanical testing at (a) 45°C and (b) 60°C. Source: Michigan State University.....	625
Figure II.4.2.5. V Validation of model prediction for hydrolysis experimental data at (a) 60°C, (b) 80°C, and (c) 95°C. Source: Michigan State University.....	626
Figure II.4.2.6. Final prototype component with Al painted gray and steel black. Source: The Ohio State University.....	631
Figure II.4.2.7. Testing of prototype welds: (a) the regions where welds were cut, (b) project participants Y. Mao and J. Wright holding the welded sub-components, (c) a VFAW sub-component, and (d) the failure loads of prototype welds compared to the baseline. Source: The Ohio State University.....	631
Figure II.4.2.8. A process flow for manufacturing the baseline and prototype components. Source: The Ohio State University.....	632
Figure II.4.2.9. Systems approach with multiple simulation-validation loops at various component scales. (For the purpose of illustration only; details not intended to be readable) Source: Clemson University.....	635
Figure II.4.2.10. Baseline BiW breakdown by sub-assembly. Source: Clemson University.....	637
Figure II.4.2.11. Baseline BiW breakdown by 12 global load cases. Source: Clemson University....	638
Figure II.4.2.12. Conceptual designs – summary, assessment, and downselection. Source: Clemson University.....	638
Figure II.4.2.13. Process for modeling metal composite transition joints. Source: Clemson University.....	640
Figure II.4.2.14. Stress distributions of composite-fiber loops for three-layer transition joint. Source: Clemson University.....	640
Figure II.4.2.15. CFRP-AA samples: (a) longitudinal tensile sample; (b) longitudinal compression sample; (c) shear sample; (d) and (e) three-point bending sample; and (f) transverse tensile sample. Source: The Ohio State University.	641
Figure II.4.2.16. Schematics of pure CFRP samples: (a) longitudinal tensile sample; (b) longitudinal compression sample; and (c) shear sample. Source: The Ohio State University.	641
Figure II.4.2.17. UAM process modifications: (a) spindle speed increaser; (b) fiber alignment device; and (c) runway welding surface. Source: The Ohio State University.....	642
Figure III.1.1.1. Total number of U.S. crash fatalities, and distribution by crash type, by year. Source: NHTSA Fatality Analysis Reporting System.....	645

Figure III.1.1.2. Percent of fatalities in all crashes and pedestrian crashes, by vehicle type and year. Source: NHTSA Fatality Analysis Reporting System..... 646

Figure III.1.1.3. Distribution of registered vehicles from a sample state by vehicle type and year. Source: Experian Vehicles in Operation..... 647

Figure III.1.1.4. Distribution of production-weighted estimated test weight of MY 2019 LD vehicles by vehicle type. Source: U.S. EPA. 648

Figure III.1.1.5. Distribution of production-weighted footprint of MY 2019 LD vehicles by vehicle type. Source: U.S. EPA. 648

List of Tables

Table I.1.1.1.1. Alloy Compositions Analyzed by ICP-OES.	8
Table I.1.1.4.1. Nominal Chemical Compositions of Al Alloys Used in this Task [1]	28
Table I.1.1.6.1. Nominal Composition (wt.%) of A380 Alloy Used in this Task.	41
Table I.1.1.6.2. T5 Heat-Treatment Schedule for Cast Alloy 380 in this Task.....	43
Table I.1.2.2.1. Composition of Commercial Gear Steels 16MnCr5 and 8620 in Use in Europe and the U.S., and a High Mn Low-Density Austenitic Steel Under Evaluation in the Present Work.	62
Table I.1.2.3.1. Proposed Organically Modified CNTs vs. the State-of-the-Art Dispersant-Suspended CNTs.....	67
Table I.1.3.1.1. Comparison of Measured Alloy Composition Between the Al-Ce-Ni-Mn and Al-Ce-Ni-Mn-Zr Alloys.....	89
Table I.1.3.2.1. Phases in the AM AL-10.5Ce-3.1Ni-1.2Mn	101
Table I.1.3.2.2. Compositions of the Intermetallic Phases in Atomic Percent for All Conditions, Locations, and Phase Type with the Average Values and Standard Deviations in Parentheses.....	103
Table I.1.3.4.1. Comparison of the Properties of Single-Walled CNTs vs. Cu	114
Table I.1.4.1.1. Thrust 4A1 “Funded Advanced Characterization Projects” in FY 2022.....	136
Table I.1.4.2.1. Thrust 4A3-22 Characterization Capabilities and Related Testing Requests from the Thrust 1–3 Development Tasks in FY 2022.....	142
Table I.1.4.3.1. ShAPE-processed Al Ultra-Conductor Samples Characterized by Synchrotron X-ray Diffraction at APS.....	150
Table I.1.4.3.2. ShAPE-processed Cu Ultra-Conductor Samples Characterized by Synchrotron X-ray Diffraction at the APS	152
Table I.1.4.4.1. NCMS Alloy Composition	156
Table I.1.4.4.2. Al-Ce-Ni-Mn Alloy Composition	157
Table I.1.4.5.1. Thrust 4B1 Funded Advanced Computation Projects in FY 2022	163
Table I.1.4.5.2. Substitutional Energy (Stability) and Average Magnetic Moments (<mag.>) for A- and B-Site Doping of Mg and Ni in ZnFe ₂ O ₄ . Source: ORNL.....	168
Table I.1.4.6.1. Description of Different Types of Alloy Features Considered in this Task	172
Table I.1.4.6.2. List of Top 30 Features Based on MIC Analysis Between Input Features and AFA Creep	173
Table I.1.4.6.3. Number of Hypothetical Alloys Determined by Combinatorial Design from Experimental Data and Grid Spacing (H and L Denote Heavy and Light Elements, Respectively)....	173
Table I.1.4.7.1. Recycled Steel Content of New Vehicles.....	178
Table I.1.4.7.2. Recycled Al Content of New Vehicles	179
Table I.2.1.1. Original vs. Updated Weight-Reduction Status Relative to the Baseline Engine.....	188

Table I.2.2.1. Comparison of Measured and Predicted New Technologies to Baseline L96 Engine at Weighted Average GEM Cycle Operating Points	193
Table I.2.4.1. The Order of Oxides Used for This Study	208
Table II.1.1.1. Summary of Measured Material Properties	221
Table II.1.2.1. Composition of HPDC Aural-5 Plates	239
Table II.1.2.2. Summary of Tensile Properties of HPDC Aural-5 Before and After FSP	243
Table II.1.2.3. Summary of Tensile Test Results of Locally Heat-treated (Followed by Aging) HPDC A380.....	252
Table II.1.3.1. Corrosion Reaction Resistance Values of Untreated and N ₂ Plasma-Treated AZ91D Samples Performed at ORNL.....	262
Table II.1.3.2. Corrosion Reaction Resistance Values of Plasma Si-O-C Coatings Deposited on AZ91D Samples Performed at ORNL.....	264
Table II.1.3.3. Corrosion Reaction Resistance Values of Untreated and Li-Salt Loaded + CO ₂ Thermal Treated AM60 Samples Performed at ORNL.....	264
Table II.1.3.4. Wear Volume and Rates of Untreated and Li Salt Loaded + CO ₂ Thermal Treated AZ91D Samples. Wear Measurements Performed with A 6 mm Si ₃ N ₄ Ball with 1 N, 200 mm/s and A 5000 Cycle Performed at PNNL	265
Table II.1.3.5. CP-Zn Cold Spray Trials Performed at PNNL	265
Table II.1.3.6. Adhesion Test Data Following the ASTM D4541 Standard Performed at PNNL	268
Table II.1.3.7. Selected Friction Surfacing Processing Conditions and Quality Results by PNNL.....	274
Table II.1.4.1. Thrust 4 – Characterization, Modeling, and Life Cycle Projects Funded in FY 2022. 279	
Table II.2.1.1. Process Parameters for ShAPE Extrusion of Al 6063 Industrial Scrap using a Porthole Die.....	296
Table II.2.1.2. Tensile Properties of 2-mm-thick Round Tubing Extruded by ShAPE from Al 6063 Industrial Scrap Compared to ASTM [13] and ASM [14] Standards. Note: * = Total Elongation.....	297
Table II.2.2.1. Die-Casting Alloys, Compositions, and Mechanical Properties.....	304
Table II.3.1.1.1. Phased Approach to HTC Project.....	309
Table II.3.1.1.2. Mechanical Properties of a Continuous Sample Fully Carbonized with the LTC and HTC EM-Powered Furnaces.....	311
Table II.3.1.1.3. Mechanical Properties of Two Tows of 50k Filaments Simultaneously Processed with LTC and HTC Devices Inline That Are EM-Powered and Maintained Constant for All Samples with the Main Variable Among the Samples Being the Total Residence Time (LTC + HTC).....	314
Table II.3.1.1.4. Density of the Samples Reported In Table II.3.1.1.3 With an Average Density of the HTC Samples of ~1.76 g/cc.....	314
Table II.3.1.6.1. FY 2022 Milestone Summary	349
Table II.3.1.8.1. Three Cases with Different Layer Times.	366
Table II.3.1.8.2. Experimental Conditions for 3D Printing.....	366

Table II.3.1.8.3. Parameters for Simulation.....	367
Table II.3.1.10.1. Carbon Fiber from Plasma Oxidized Steam-Stretched Dralon 3.3 dtex Precursor*	390
Table II.3.1.10.2. Carbon Fiber from Plasma Oxidized but Non-Steam-Stretched Dralon 3.3 dtex Precursor*	390
Table II.3.1.10.3. Carbon Fiber from Dralon 5.5 dtex Precursor Conventionally Processed*	391
Table II.3.1.10.4. Carbon Fiber from Steam-Stretched Dralon 5.5 dtex Precursor*	391
Table II.3.1.10.5. MTR20798 Dralon 5.5 dtex Plasma Oxidized, Conventionally Carbonized Group 1*	392
Table II.3.1.10.6. MTR20798 Dralon 5.5 dtex Plasma Oxidized, Conventionally Carbonized Group 2*	392
Table II.3.1.11.1. Alternative Precursor and Advanced Conversion Processing Estimated Reduced Cost and Embodied Energy	396
Table II.3.1.11.2. Task 3 Milestones, Task Descriptions, and Status	399
Table II.3.1.11.3. Properties of Nylon-6 Precursor Spools	402
Table II.3.1.11.4. Properties of Textile Carbon Fiber.....	404
Table II.3.1.11.5. ExxonMobil™ PP3155 PP Homopolymer Properties.....	404
Table II.3.1.11.6. Average Fiber Weight and Fiber Volume Percentages for All Material Plates Produced Where the Overall FWF Was 36.23% and FVF Was 24.74%.....	406
Table II.3.1.11.7. Flexural Testing Values for TCF Thermoplastic Tape	407
Table II.3.1.11.8. ILSS Values Obtained for TCF Thermoplastic Tape.....	409
Table II.3.1.11.9. Tensile Strength and Modulus Values for TCF Thermoplastic Tape Composite ...	411
Table II.3.1.11.10. Calculation of Theoretical Tensile Strength and Modulus Using Rule of Mixture	412
Table II.3.1.12.1. FY 2022 PNNL Milestones	417
Table II.3.1.12.2. FY 2022 ORNL Milestones	421
Table II.3.1.15.1. Techno-economic and Supply Chain Analyses Results for the PECAN-CFRCs Across Multiple Lives	441
Table II.3.1.16.1. Project Milestones and Status	446
Table II.3.1.16.2. Short-Beam Shear Data Comparison.....	448
Table II.3.1.17.1. Project Participants.....	453
Table II.3.1.18.1. Milestones For Task 1 Work Stream Activities.....	460
Table II.3.1.19.1. Materials, Process, and Features for the Demonstration Battery Enclosure Assembly.....	490
Table II.3.2.2.1. Peak Frequency due to Various Object Impacts.....	503
Table II.3.2.2.2. Important Characteristics of the Skateboard	505

Table II.3.2.3.1. Recycled T-800 Tuff Composite Comparison to Continuous Fiber Mechanical Properties 512

Table II.3.2.4.1. Comparison of Trimer’s RTM Polymer with Current Low-Cost Rapid-Cure Resins .. 516

Table II.3.2.4.2. Material Properties from Vacuum-Assisted Resin Transfer Molding E-Glass Composites..... 518

Table II.3.2.5.1. Effect of Carbon Loading and Shear Conditions on the Electrical Resistivity of a Hybrid PVC/Carbon Compound..... 523

Table II.3.2.5.2. Effect of CNF and Areal Weight on the Sheet Resistivity and Shielding Effectiveness of Nonwoven Samples..... 524

Table II.3.2.7.1. Test Objectives and Summary of Most Promising Candidates..... 534

Table II.3.2.8.1. Changes in Reinforcement with Silane-Functionalized MR vs. Incumbent Reinforcing Filler Silica 541

Table II.3.2.9.1. Summary of Tensile Test Results 548

Table II.4.1.1.1. Stack-up Nomenclature by PNNL Used with the Corresponding Materials (and Thicknesses) for Model Building..... 560

Table II.4.1.3.1. Summary of Mechanical Joint Performances for F-SPR Al7055-Al7055 Joints..... 587

Table II.4.1.4.1. Summary of EIS Impedance for Baseline, Laser-treated, and Open-air Plasma-treated Al7075..... 597

Table II.4.1.4.2. Impedance Values on the Before and After Plasma-treated Al5052 Alloy..... 603

Table II.4.2.3.1. Project Partner Organizations..... 635

Table II.4.2.3.2. Planned Full-scale Glider Structural Validation Plan..... 636

Table II.4.2.3.3. Stiffnesses for Concept 1 vs. Baseline Performance..... 639

Table II.4.2.3.4. Experimental Data from CFRP-AA Testing..... 642

Table II.4.2.3.5. Experimental Data from CFRP Testing..... 642

(This page intentionally left blank)

Vehicle Technologies Office Overview

Vehicles move our national economy. Annually, vehicles transport 18 billion tons of freight—about \$55 billion worth of goods each day¹—and move people more than 3 trillion vehicle miles.² Growing our economy requires transportation, and transportation requires energy. The transportation sector accounts for approximately 30% of total U.S. energy needs³ and the average U.S. household spends over 15% of its total family expenditures on transportation,⁴ making it, as a percentage of spending, the costliest personal expenditure after housing. Transportation is critical to the overall economy, from the movement of goods to providing access to jobs, education, and healthcare.

The transportation sector has historically relied heavily on petroleum, which supports over 90% of the sector's energy needs today,⁵ and, as a result, surpassed electricity generation to become the largest source of CO₂ emissions in the country.⁶ The Vehicle Technologies Office (VTO) will play a leading role to decarbonize the transportation sector and address the climate crisis by driving innovation within and deployment of clean transportation technologies.

VTO funds research, development, demonstration, and deployment (RDD&D) of new, efficient, and clean mobility options that are affordable for all Americans. VTO leverages the unique capabilities and world-class expertise of the National Laboratory system to develop new innovations in vehicle technologies, including: advanced battery technologies; advanced materials for lighter weight vehicle structures and better powertrains; energy-efficient mobility technologies and systems (including automated and connected vehicles as well as innovations in connected infrastructure for significant systems-level energy efficiency improvement); combustion engines to reduce greenhouse gas (GHG) and criteria emissions; and technology integration that helps demonstrate and deploy new technology at the community level. Across these technology areas and in partnership with industry, VTO has established aggressive technology targets to focus RDD&D efforts and ensure there are pathways for technology transfer of federally supported innovations into commercial applications.

VTO is uniquely positioned to accelerate sustainable transportation technologies due to strategic public-private research partnerships with industry (e.g., U.S. DRIVE, 21st Century Truck Partnership) that leverage relevant expertise. These partnerships prevent duplication of effort, focus DOE research on critical RDD&D barriers, and accelerate progress. VTO advances technologies that assure affordable, reliable mobility solutions for people and goods across all economic and social groups; enable and support competitiveness for industry and the economy/workforce; and address local air quality and use of water, land, and domestic resources.

Annual Progress Report

As shown in the organization chart (below), VTO is organized by technology area: Batteries R&D; Electrification R&D; Materials Technology R&D; Decarbonization of Offroad, Rail, Marine, and Aviation; Energy-Efficient Mobility Systems; and Technology Integration. Each year, VTO's technology areas prepare an Annual Progress Report (APR) that details progress and accomplishments during the FY. VTO is pleased to submit this APR for FY 2022. The APR presents descriptions of each active project in FY 2022, including funding, objectives, approach, results, and conclusions.

¹ Bureau of Transportation Statistics, DOT, Transportation Statistics Annual Report 2020, Table 4-1, <https://www.bts.gov/tsar>.

² Davis, Stacy C., and Robert G. Boundy. Transportation Energy Data Book: Edition 39. Oak Ridge National Laboratory, 2021, <https://doi.org/10.2172/1767864>. Table 3.8 Shares of Highway Vehicle-Miles Traveled by Vehicle Type, 1970-2018.

³ Ibid. Table 2.2 U.S. Consumption of Total Energy by End-use Sector, 1950-2018.

⁴ Ibid. Table 11.1 Average Annual Expenditures of Households by Income, 2019.

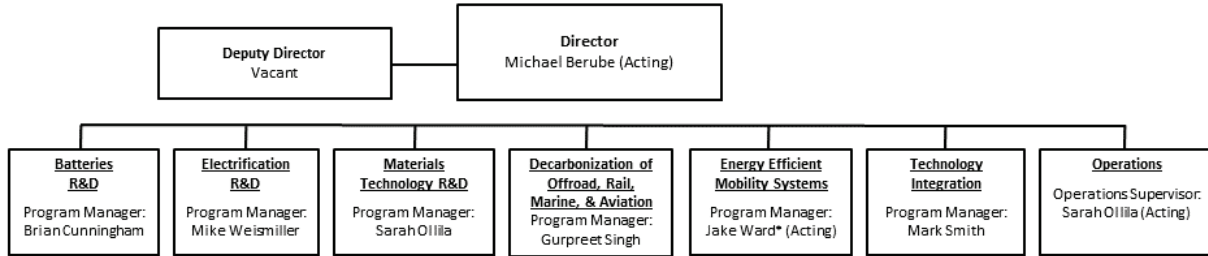
⁵ Ibid. Table 2.3 Distribution of Energy Consumption by Source and Sector, 1973 and 2019.

⁶ Environmental Protection Agency, Draft U.S. Inventory of Greenhouse Gas Emissions and Sinks, 1990-2019, Table 2-11. Electric Power-Related Greenhouse Gas Emissions and Table 2-13. Transportation-Related Greenhouse Gas Emissions.

Organization Chart

Vehicle Technologies Office Federal Staff

September 2022



**based at NETL-Pittsburgh*

Materials Technology Program Overview

Program Introduction

The Materials Technology subprogram supports the DOE/EERE goals of achieving 100% decarbonization of the transportation sector by 2050. This ambitious goal will be realized through the increased deployment of electric and hydrogen fuel cell vehicles. Materials play an important role in increasing the efficiency of electric vehicles through weight reduction as well as enabling additional functionality such as faster charging and new sensing technologies. Lighter weight vehicle structures and electric drivetrains will require fewer batteries to achieve the same range, which in turn reduces battery cost, material needs, and reduces the GHG emissions from battery production. Functional materials with improved properties such as electrical conductivity, thermal conductivity, and unique sensing capabilities will enable innovations in charging and autonomous vehicles. The materials and manufacturing methods used to make vehicles also contribute to GHGs and the Materials Technology subprogram supports research, development, and deployment to increase recyclability and reduce the overall embodied energy of vehicles. The Materials Technology subprogram accomplishes its technical objectives through research programs with academia, National Laboratories, and industry.

The Propulsion Materials portfolio is closely aligned with other VTO subprograms to identify critical materials needs for next-generation high-efficiency powertrains for both HD and LD vehicles. Strategies for achieving high-efficiency powertrains includes addressing key challenges in electrical conductivity, thermal conductivity, magnetic materials, and high-temperature operation currently limiting advances in electric powertrains and wireless charging. The Powertrain Materials Core Program is a national laboratory consortium that targets critical powertrain components based on thermal loading, structural, and electrical requirements and utilizes an ICME approach to link advanced characterization to high-performance computing methods to accelerate development of new material families. In FY 2022, the program has partnered with the Electrification subprogram to focus new materials development efforts on challenges facing power electronics for electric vehicles.

The Lightweight Materials team works closely with industry through the U.S. DRIVE partnership to understand LD vehicle structural weight-reduction goals and to identify technical challenges that prevent the deployment of lightweight materials. The most promising and likely approach for lightweighting is a multimaterial structure, which focuses on the use of the right material for the application. The Lightweight Materials research portfolio addresses significant technology gaps for each family of structural materials: Mg, AHSS, Al, and polymer composites. Gaps include raw material costs, formability, manufacturing cycle time, ability to model and predict failure, corrosion mitigation, and incorporation of new materials into manufacturing plants. In addition, research efforts investigate dissimilar material joining in order to enable the reliable assembly of these multimaterial systems.

Program Goals

The Materials Technology subprogram supports the VTO's mission to accelerate the deployment of clean energy technology toward achieving net-zero emissions in the transportation sector. Lighter vehicles with more efficient powertrains reduce energy use, decrease GHG emissions, and save consumers money. The structural and powertrain systems that we target to improve are limited by materials performance. By improving the properties of powertrain and structural materials, we can enable a significant improvement in energy efficiency for future vehicles. Increasing the thermal and electrical conductivity of low-cost materials will enable increased electric vehicle efficiency while improving properties in structural materials, such as stiffness, strength, joinability, and crash-energy absorption—all with lower cost, will accelerate the deployment of lightweight materials in the automotive market. The specific performance and cost targets for the Materials

Technology subprogram are to enable a 25% weight-reduction for LD vehicle gliders including body, chassis, and interior as compared to a 2015 baseline at no more than a \$5/lb.-saved increase in cost by 2025.

State-of-the-Art

Automakers are seeking to improve fuel economy, increase electric vehicle range, or reduce battery size while improving or maintaining vehicle performance and safety. Lighter weight vehicle structures and electric drivetrains will require fewer batteries to achieve the same range, which in turn reduces battery cost, material needs, and reduces the GHG emissions from battery production. Functional materials with improved properties such as electrical conductivity, thermal conductivity, and unique sensing capabilities will enable innovations in charging and autonomous vehicles. For structural components, the market is shifting from traditional steel components to lighter weight materials such as AHSSs, Al alloys, Mg alloys, and polymer composites.

To support the transition to all electric light-duty vehicles by 2035, research is needed to increase efficiency and decrease manufacturing cost of electrified powertrains. Development of new alloys with improved electrical/mechanical properties and enhanced resistance to corrosion/oxidation of components operating in harsh environments such as electrical bus bars, lightweight gears, underbody suspension, and brakes will address the future properties needs of electric and hydrogen fuel cell vehicles. Expanded development and characterization of materials supporting electrification such as lightweight conductors, ferrites, and high-Si-steels are also important for challenging components such as inverters, motors, and gear-train. However, inadequate databases, modeling, and design tools are significant barriers for further development of new materials. By evaluating existing computational tools and identifying gaps that must be overcome to achieve seamless integration across multiple-length scales and increasing understanding of the basic behavior of the material (effects of solute at the atomistic level, microstructural development, microstructure/property relationships, fracture and failure mechanisms, durability, temperature-dependent behavior, etc.), more accurate design tools and predictive models can be established. Characterization and multiscale computational materials methods will accelerate discovery and early-stage development of cutting-edge materials and innovative production techniques like AM for lighter and more efficient powertrains.

AHSS is the most mature lightweight material in terms of widespread use in industry due to its compatibility with existing manufacturing infrastructure and vehicle materials. Application of third-generation high-strength steel has the potential to reduce component weight by up to 25%, particularly in strength-limited designs. However, technical challenges remain to improve weldability and weight-reduction is dependent on the ability to maintain stiffness at reduced gauges. Al continues to see steady growth in market share in the automotive industry⁷ despite issues of material cost, room temperature (RT) formability, and limitations within the existing manufacturing infrastructure. This is due to the 40% weight-savings that can be achieved with Al along with the well-established domestic supply chain. Mg has the potential to significantly reduce vehicle component weight by 55% or greater; however, there are several significant technical barriers preventing increased use of this material in vehicle designs. Mg has high raw material costs and price volatility, relatively low specific stiffness, difficulty in forming sheet at low temperatures, low ductility of finished components, and a limited alloy set, among other challenges. CF and other polymer composites have the potential to reduce component weight by more than 60%. The main barriers to widespread use are the high cost to manufacture the CF, lack of high-volume composite manufacturing methods, and a need for reliable predictive tools for both part design and performance prediction.

When combinations of the above lightweight materials are used, the resulting multimaterial structures have challenges of their own. Traditional joining methods used in automotive assembly, such as resistance spot-welding and riveting, are inefficient for joining of dissimilar metals and for some combinations, infeasible. In the near-term, friction stir scribe welding and resistance spot riveting are showing promising advances for the

⁷ Giampieri, A., J. Ling-Chin, Z. Ma, A. Smallbone, and A. P. Roskilly, 2020, "A review of the current automotive manufacturing practice from an energy perspective," *Appl. Energy*, Vol. 261, Art. 114074.

joining of AHSS and Al (the more mature lightweight metals). An additional challenge posed by multimaterial structures is the increased risk of corrosion due to galvanic coupling. As the barriers to introduction of Mg and CF are overcome, breakthroughs in joining technology will also be necessary.

Program Organization Matrix

The Materials Technology subprogram is led by Program Manager, Sarah Ollila.

- Propulsion Materials focuses on:
 - Materials for Electric Vehicle Powertrain Components (Jerry Gibbs) – which includes addressing key challenges in electrical conductivity, thermal conductivity, magnetic materials, and high-temperature operation.
- Lightweight Materials consists of three research portfolios:
 - Light Metals (Christopher Schooler) – which includes research on property improvement and processing advances for AHSS, Al, and Mg.
 - Polymer Composites (Felix Wu) – which includes research on low-cost production of CF, novel processing methods for polymer composites, and predictive performance models of CF and other fiber-reinforced or hybrid composites.
 - Joining of Dissimilar Materials (Christopher Schooler) – which includes research on solid-state, mechanical, and chemical joining methods, as well as galvanic corrosion mitigation.

All the activities within the Materials Technology subprogram utilize computational methods for material discovery, prediction of structure, understanding failure mechanisms including corrosion, and the effects of processing on properties.

(This page intentionally left blank)

I Propulsion Materials

I.1 Powertrain Materials Core Program

I.1.1 Thrust 1: Lightweight Alloys for Electric Vehicle Propulsion

I.1.1.1 Task 1A. Fundamental Studies of Al-Ni Alloys for Improved Electrical Propulsion (Oak Ridge National Laboratory)

Dongwon Shin, Principal Investigator

Oak Ridge National Laboratory
Materials Science and Technology Division
1 Bethel Valley Rd.
Oak Ridge, TN 37830
E-mail: shind@ornl.gov

J. Allen Haynes, PMCP Consortium Manager

Oak Ridge National Laboratory
Materials Science and Technology Division
1 Bethel Valley Rd.
Oak Ridge, TN 37830
E-mail: haynesa@ornl.gov

Jerry Gibbs, DOE Technology Development Manager

U.S. Department of Energy
E-mail: jerry.gibbs@ee.doe.gov

Start Date: November 1, 2021	End Date: September 30, 2023	
Project Funding (FY 2022): \$230,000	DOE share: \$230,000	Non-DOE share: \$0

Project Introduction

This task will investigate the effect of two key factors on the electrical conductivity and high-temperature stability in cast Al-Ni alloys: the volume fraction of the key intermetallic phase of nickel aluminide (Al_3Ni) and the associated interfacial structure (Al/ Al_3Ni). The volume fraction of Al_3Ni will be varied with different amounts of nickel (Ni), and select minor alloying elements (e.g., zirconium [Zr], titanium [Ti], and iron [Fe]) will be added to investigate their propensity to be segregated at the Al/ Al_3Ni interface, as well as their aluminide formation. This task will utilize advanced characterization (e.g., atom probe tomography [APT]/scanning tunneling electron microscopy) and computation (e.g., first-principles density functional theory calculations) to correlate experimentally measured electrical conductivity and hardness with the observed distribution of key intermetallic and Al/ Al_3Ni interface structures.

Objectives

This task aims to understand the effect of the volume fraction of key intermetallic (Al_3Ni) and interfacial (Al/ Al_3Ni) structures on the electrical conductivity and high-temperature stability of cast Al-Ni alloys.

Approach

Experiments were designed to investigate the effect of interfacial structure (Al/ Al_3Ni) and the amount of Al_3Ni in Al-Ni alloys. Four different microalloying elements were added in Ni-containing aluminum (Al) alloys to modify the Al/ Al_3Ni interface structure: Ti, vanadium (V), Zr, and Fe. These microalloying elements were anticipated to segregate at the Al/ Al_3Ni interface based on previously observed results for Zr and scandium [1, 2]. The prepared alloys contain 5-6 wt% of Ni, near the Al-rich eutectic composition in the binary Al-Ni

system. The effect of the various amount of Al₃Ni was investigated for the Al-Ni binary and Al-Ni-Zr ternary alloys. Nickel contents between 2 and 6 wt%, compositions within the hypoeutectic region in the Al-Ni binary system, were used to vary the amount/density of the Al₃Ni intermetallic phase.

Once the alloys were synthesized, heat-treatment was carried out at 300, 350, 400, and 450°C for 200 hours. Microstructure analysis and physical property measurements were carried out using a suite of advanced characterization facilities at Oak Ridge National Laboratory (ORNL). We used Vickers hardness with a 5 kgf load for microhardness measurements, the eddy current method for electrical conductivity measurements, and laser flash analysis for thermal diffusivity measurements. The microstructure and the evolution of intermetallic microfibers were analyzed by scanning electron microscopy (SEM). Atomic scale composition analysis was carried out by APT to investigate the segregation of microalloying elements at the interface between the microfiber and Al matrix.

Results

All alloys were prepared by the electric arc melting method under an argon atmosphere, followed by casting into chilled copper molds. The bulk compositions were then analyzed by an inductively coupled plasma-optical emission spectrometer (ICP-OES). The ICP-OES result of all investigated alloy compositions is summarized in Table I.1.1.1.1.

Table I.1.1.1.1. Alloy Compositions Analyzed by ICP-OES.

System	Al, wt%	Ni, wt%	Zr, wt%	Ti, wt%	V, wt%	Fe, wt%	Si, wt%
Al-Ni	Bal	1.92	0	0	0.01	0.03	0.01
Al-Ni	Bal	3.76	0	0	0	0.03	0.02
Al-Ni	Bal	4.68	0	0	0	0.033	0.022
Al-Ni-Zr	Bal	2.09	0.45	0	0	0.03	0.02
Al-Ni-Zr	Bal	3.73	0.4	0	0	0.03	0.02
Al-Ni-Zr	Bal	5.7	0.41	0	0	0.032	0.02
Al-Ni-Ti	Bal	5.98	0	0.31	0	0.034	0.021
Al-Ni-V	Bal	5.69	0	0	0.3	0.032	0.2
Al-Ni-Fe	Bal	4.89	0	0	0	0.52	0.02

The relationship between microstructure evolution and two experimental factors (i.e., Ni content and microalloying elements) was investigated by APT and SEM. Figure I.1.1.1.1 presents the APT image of the Al/Al₃Ni interface in an Al-Ni-Zr alloy heat-treated at 400°C for 100 hours. The APT analysis, conducted under a supporting Advanced Characterization Project within Powertrain Materials Core Program Thrust 4A, reveals for the analyzed interface, Zr segregates between the Al matrix and the Al₃Ni intermetallic. The segregation of microalloying elements at the Al/Al₃Ni interface has been reported to delay the spheroidization and the coarsening of Al₃Ni during heat-treatment [2].

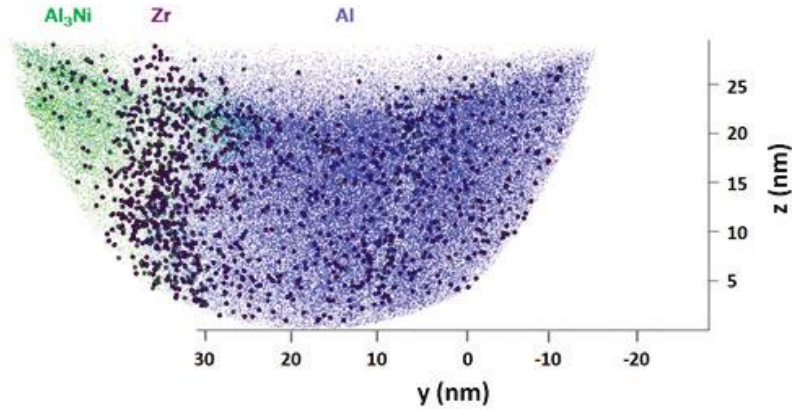


Figure I.1.1.1. APT image of the Al-Ni-Zr alloy heat-treated at 400 °C for 100 h: green, purple, and blue dots represent Al₃Ni, Zr, and Al, respectively. Source: ORNL.

In the as-cast condition, Al₃Ni in the eutectic phase has the rod-like shape of microstructures, which is the main strengthening phase in the Ni-containing Al alloys. At elevated temperatures, the rod-like shape coarsens and spheroidizes, which reduces the strength of alloys. Figure I.1.1.1.2(a) and Figure I.1.1.1.2(b) are SEM images that present the microstructure evolution of Al₃Ni with isothermal heat-treatment for 200 h at various temperatures in the Al-Ni binary alloy and Al-Ni-Zr ternary alloy, respectively. These microstructures show the degree of spheroidization and coarsening of the rod-like Al₃Ni phase varies as a function of heat-treatment temperature for both alloys; however, a significant difference in the degree of spheroidization between the binary and ternary alloy is not observed. The effect of various Ni content on the microstructures of the Al-Ni binary alloys is presented in Figure I.1.1.1.2(c). The dark grey regions represent the Al matrix, whereas the bright grey areas are the eutectic phase composed of the Al matrix and Al₃Ni intermetallics. The SEM images show the increasing amount of eutectic phase with the increasing Ni content in the alloy. Since the eutectic phase has a constant volume fraction of Al₃Ni, increasing the eutectic phase amount results in increased Al₃Ni intermetallic.

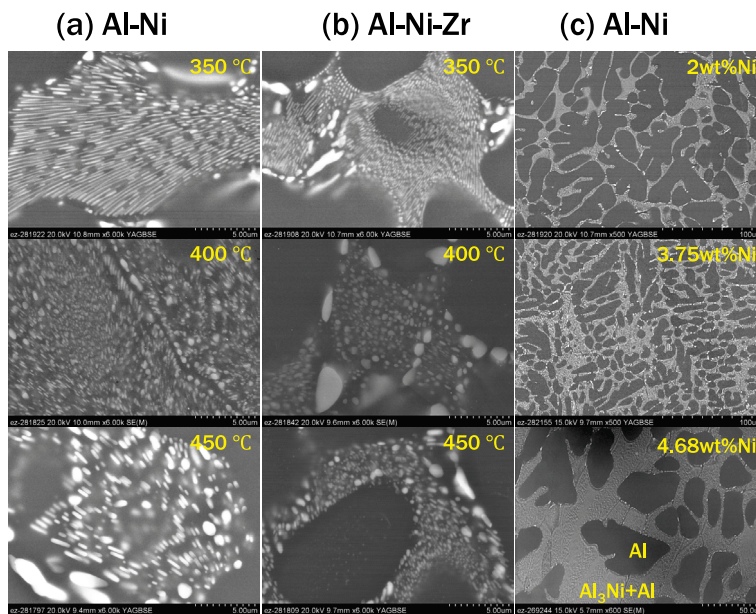


Figure I.1.1.2. Microstructure evolution of the Al-Ni and Al-Ni-Zr alloys: Microstructure of (a) binary and (b) ternary alloys with various heat-treatment temperatures. (c) Microstructure of as-cast binary alloys with various Ni content. Source: ORNL.

Figure I.1.1.1.3(a) shows the microhardness of Al-Ni (blue) and Al-Ni-Zr (red) alloys with respect to heat-treatment temperature. With the heat-treatment process, the ternary alloys show a substantial increase in hardness. Although the addition of Zr in the Al-Ni alloys does not appear to result in a significant suppression in spheroidization and coarsening of the Al_3Ni intermetallic, its effect on alloy microhardness is substantial. The surge of hardness in the ternary alloys is attributed to the coherent precipitate formation, i.e., $\text{L}_{12}\text{-Al}_3\text{Zr}$ in the Al matrix. It should be noted L_{12} precipitates are too small to be observed by SEM. As such, the microstructure analysis of L_{12} will be performed with APT in FY 2023. The significance of spheroidization and coarsening of Al_3Ni intermetallic on microhardness is also presented in Figure I.1.1.1.3(a). The binary alloys (i.e., blue lines) show a decreasing trend of microhardness with increasing heat-treatment temperatures. The spheroidization and coarsening of Al_3Ni intermetallic are the primary causes of the hardness loss with increasing heat-treatment temperature. The comparison of the hardness data between the alloys with two different Ni contents (i.e., 2 wt% and 3.76 wt% Ni) also supports this argument. The degree of hardness loss is more severe in Al-3.76Ni alloy than in Al-2Ni alloy since the vol.% Al_3Ni is higher in the Al-3.76Ni alloy. The effect of Ni content on microhardness is presented in Figure I.1.1.1.3(b). A noticeable increase in microhardness is observed for both 300°C and 450°C in Al-Ni alloys; however, the hardness increase caused by Ni content is not substantial for the Al-Ni-Zr alloys. This result indicates the precipitation-hardening of Al_3Zr , although the volume fraction is small, is the dominant strengthening mechanism.

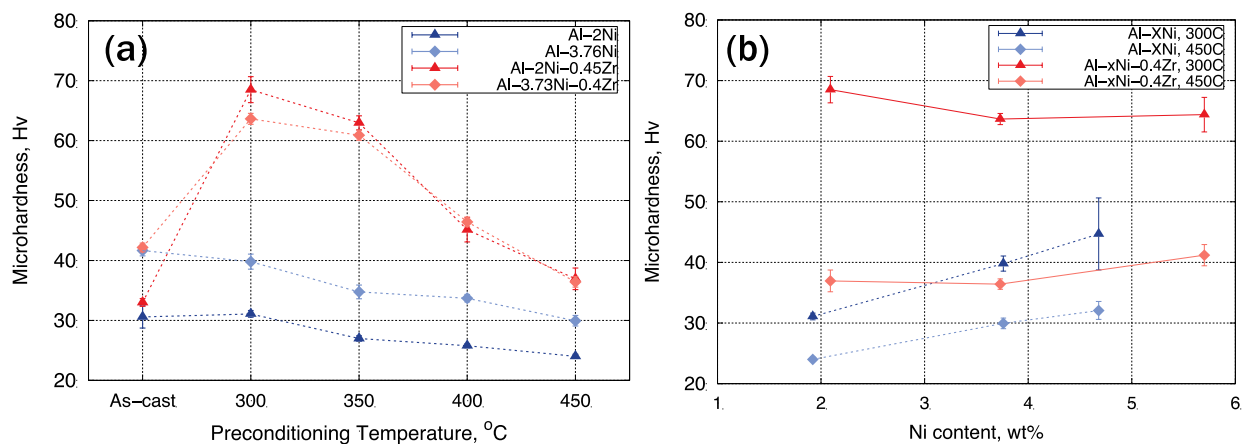


Figure I.1.1.3. Microhardness data of the Al-Ni binary and Al-Ni-Zr ternary alloys with respect to (a) heat-treatment-temperature and (b) Ni content: Hv is the Vickers hardness unit ($1 \text{ Hv} \cong 9.8 \text{ MPa}$). Source: ORNL.

Whereas the significance of spheroidization and coarsening of Al_3Ni intermetallic on microhardness is not negligible, its effect is not substantial on electrical conductivity. Figure I.1.1.1.4(a) presents the electrical conductivity change over various heat-treatment temperatures. Electrical conductivity data of the binary alloys in Figure I.1.1.1.4(a) reveal heat-treatment temperature is insignificant on electrical conductivity, even though the significant morphology change of Al_3Ni was observed over various heat-treatment temperatures, as shown previously in Figure I.1.1.1.2(a). Figure I.1.1.1.4(a) also shows the significant increase in electrical conductivity of the Al-Ni-Zr ternary alloy, which has a similar microstructure evolution as the Al-Ni binary alloy over various heat-treatment temperatures. This result is attributed to the Zr solubility in the Al matrix. Electrical conductivity in metal is inversely proportional to solute content [3]. After casting, the ternary alloys have the maximum solubility of Zr, which results in significant electron scattering within the Al matrix; however, the Zr solute depletes from the Al matrix and forms Al_3Zr precipitates during the heat-treatment process. Higher heat-treatment temperature yields a faster depletion rate, thus increasing electrical conductivity by a higher amount. In addition, the volume fraction of Al_3Ni influences electrical conductivity, as shown in Figure I.1.1.1.4(b). The higher Ni content yields a higher volume fraction of Al_3Ni , which results in more electron scattering at the interface between the Al matrix and Al_3Ni intermetallic. Therefore, electrical conductivity decreases with increasing volume fraction of Al_3Ni .

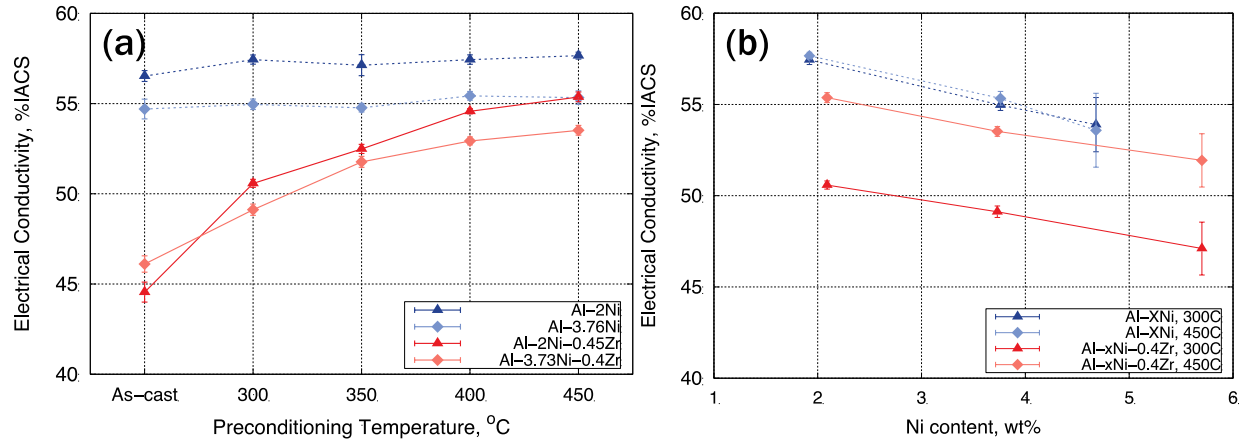


Figure I.1.1.4. Electrical conductivity of the Al-Ni binary and Al-Ni-Zr ternary alloys with (a) heat-treatment-temperature and (b) Ni content: %IACS is the relative electrical conductivity unit (anneal copper standard). Source: ORNL.

The relation between the various microalloying elements (i.e., Fe, Zr, Ti, and V) and physical properties (i.e., microhardness and electrical conductivity) is presented in Figure I.1.1.1.5. All alloys in Figure I.1.1.1.5 have similar Ni content (i.e., 5-6 wt%) to isolate the effect of microalloying elements from other sources of contributions, e.g., vol.% Al_3Ni . Figure I.1.1.1.5(a) shows the microalloying elements (i.e., Fe, Ti, and V) other than Zr do not have an increase in hardness after heat-treatment. The result indicates precipitation-hardening also did not occur for the alloys containing Fe, Ti, or V, likely due to sluggish kinetics of the solute transport (i.e., not forming precipitate) or fast kinetics (i.e., precipitates were already coarsened). The interface structure (Al/ Al_3Ni) modification by microalloying elements and its effect on microhardness can be observed in Figure I.1.1.1.5(a). The hardness reduction rate of the alloys containing Fe, Ti, and V is like the Al-Ni binary alloys. This trend suggests adding microalloying elements in Al-Ni alloys has an insignificant effect on delaying the spheroidization and coarsening of Al_3Ni , which is consistent with microstructure observations.

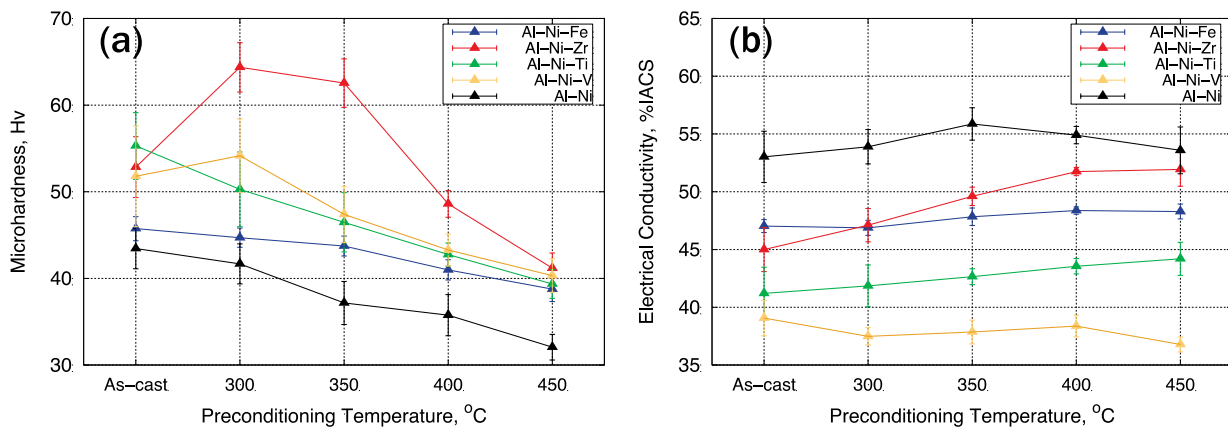


Figure I.1.1.5. Effect of adding various microalloying elements to Al-Ni (5-6 wt% Ni) on (a) microhardness and (b) electrical conductivity: Hv is Vickers hardness unit ($1 \text{ Hv} \cong 9.8 \text{ MPa}$) and %IACS is the relative electrical conductivity with respect to anneal copper as standard. Source: ORNL.

Figure I.1.1.1.5(b) presents the effect of various microalloying elements on electrical conductivity. All alloys with microalloying elements have lower electrical conductivity than the Al-Ni binary alloy due to the solubility of microalloying elements in the Al matrix. With increasing preconditioning temperature, minimal changes in electrical conductivity appear for the alloys including Fe, Ti, and V. The result indicates the solubility change of the microalloying elements (i.e., Fe, Ti, and V) in the Al matrix is insignificant for the given heat-treatment

conditions because precipitation formation reduces the solubility of the microalloying element in the Al matrix which is a significant factor in electrical conductivity. This interpretation is consistent with the qualitative analysis of the microhardness data in Figure I.1.1.1.5(a).

Figure I.1.1.1.6(a) presents the effect of various microalloying elements on thermal diffusivities. The data are presented with respect to the tracer diffusivity of microalloying elements in the Al matrix [4].

Figure I.1.1.1.6(a) shows a slight variation in thermal diffusivities of the alloys containing Fe and V over various heat-treatment temperatures. This result suggests the Fe-containing alloy might have reached the equilibrium from supersaturation at the lowest heat-treatment temperature (300°C/200 h). In contrast, the V-containing alloy remains supersaturated even at the highest heat-treatment temperature (450°C/200 h). On the other hand, Zr- and Ti-containing alloys show increasing thermal diffusivity with the heat-treatment temperature increase, indicating the solute is depleting from supersaturation to an equilibrium state.

The time-temperature-transformation diagram was calculated using TC-PRISMA and presented in Figure I.1.1.1.6(b), assuming the equilibrium phases as precipitates. The time-temperature-transformation diagram at 100 hours shows the $\text{Al}_{13}\text{Fe}_4$ phase precipitates below 250°C, while no precipitation occurs for the Al_{21}V_2 up to 400°C. These results indicate the minor Fe and V solubility change in the Al matrix during the heat-treatment between 300 and 450°C. Since the solubility of microalloying elements is the dominant mechanism for electrical conductivity and thermal diffusivity, little change in thermal diffusivity is expected for the alloys containing V and Fe. These calculation results agree with the experimental observation of thermal diffusivity given in Figure I.1.1.1.6(a). Further verification of the microstructure evolution and kinetic mechanism will be performed with APT.

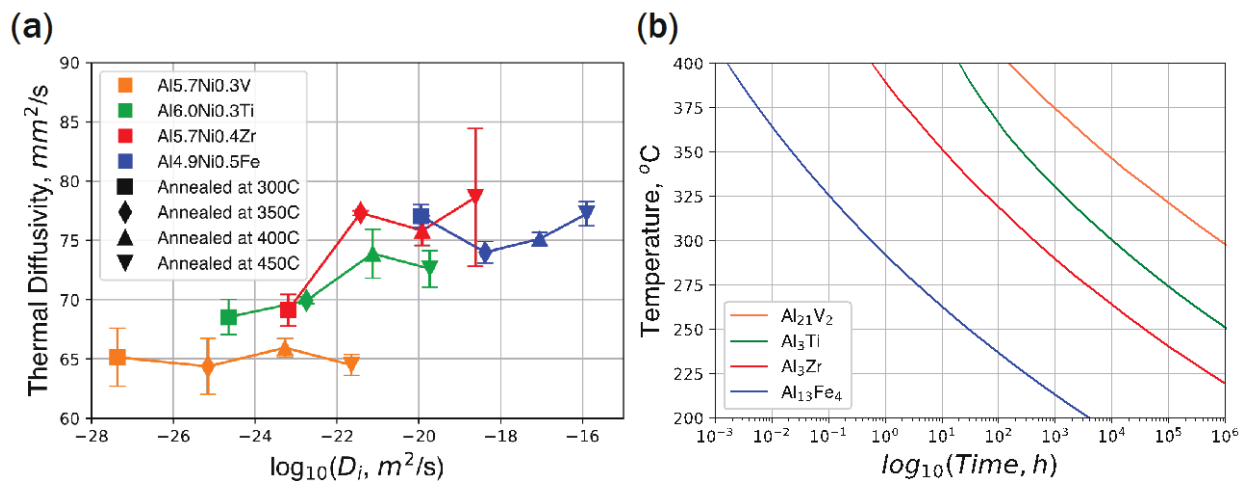


Figure I.1.1.6. Effect of various microalloying elements on (a) thermal diffusivities of Al-Ni-X alloys and (b) precipitation kinetics in the Al matrix. Source: ORNL.

Conclusions

An experimental investigation was performed to reveal the effect of the volume fraction of Al_3Ni and interfacial structure (Al/ Al_3Ni) on microhardness and electrical conductivity. APT observed the segregation of microalloying elements at the Al/ Al_3Ni interface; however, no significant effect of solute additions was observed in delaying the spheroidization of the Al_3Ni . The experimental results indicate precipitation induced by microalloying elements is the dominant mechanism for both hardness and conductivity in ternary Al-Ni-X alloys.

Key Publications

1. Harsha Gunda, N. S., R. A. Michi, M. F. Chisholm, A. Shyam, and D. Shin, 2023, “First-principles study of Al/Al₃Ni interfaces,” *Comput. Mater. Sci.*, Vol. 217, Art. 111896. <https://doi.org/10.1016/j.commatsci.2022.111896>.

References

1. Suwanpreecha, C., J. Perrin Toinin, R. A. Michi, P. Pandey, D. C. Dunand, and C. Limmaneevichitr, 2019, “Strengthening mechanisms in Al-Ni-Sc alloys containing Al₃Ni microfibers and Al₃Sc nanoprecipitates,” *Acta Mater.*, Vol. 164, pp. 334–346. <https://doi.org/10.1016/j.actamat.2018.10.059>.
2. Pandey, P., S. K. Makineni, B. Gault, and K. Chattopadhyay, 2019, “On the origin of a remarkable increase in the strength and stability of an Al-rich Al-Ni eutectic alloy by Zr addition,” *Acta Mater.*, Vol. 170, pp. 205–217. <https://doi.org/10.1016/j.actamat.2019.03.025>.
3. Klemens, P. G., and R. K. Williams, 1986, “Thermal conductivity of metals and alloys,” *Inter. Metals Rev.*, Vol. 31, No. 1, pp. 197–215. <https://doi.org/10.1179/imtr.1986.31.1.197>.
4. Andersson, J.-O., T. Helander, L. Höglund, P. Shi, and B. Sundman, 2002, “Thermo-Calc & DICTRA, computational tools for materials science,” *Calphad*, Vol. 26, No. 2, pp. 273–312. [https://doi.org/10.1016/S0364-5916\(02\)00037-8](https://doi.org/10.1016/S0364-5916(02)00037-8).

Acknowledgements

The authors would like to thank R. Michi, K. Hanson, T. Muth, D. McClurg, J. Poplawsky, and H. Wang of ORNL for contributing to the experimental work.

I.1.1.2 Task 1B. Higher Temperature Aluminum Alloys and Composites for Lightweight Brake Systems (Oak Ridge National Laboratory)

Amit Shyam, Principal Investigator

Oak Ridge National Laboratory
Materials Science and Technology Division
1 Bethel Valley Rd.
Oak Ridge, TN 37830
E-mail: shyama@ornl.gov

J. Allen Haynes, PMCP Consortium Manager

Oak Ridge National Laboratory
Materials Science and Technology Division
1 Bethel Valley Rd.
Oak Ridge, TN 37830
E-mail: haynesa@ornl.gov

Jerry Gibbs, DOE Technology Development Manager

U.S. Department of Energy
E-mail: jerry.gibbs@ee.doe.gov

Start Date: November 1, 2021	End Date: September 30, 2022	
Project Funding (FY 2022): \$270,000	DOE share: \$270,000	Non-DOE share: \$0

Project Introduction

This task focuses on development and implementation of lightweight alloys and lightweight metal matrix composites (MMCs) for rear brake systems in electric vehicles (EVs). A suite of properties and testing schemes that are applicable for brake systems were evaluated for new compositions and existing higher temperature lightweight alloys. The wear resistance and temperature limit of lightweight Al brakes are lower than their cast iron counterparts. The thermal conductivity and specific heat are also different. If the wear resistance and upper temperature limit of Al alloys can be pushed higher, these alloy systems could be useful for brake rotor applications, especially rear brakes for EV powertrains, which typically experience less severe conditions than front brakes. EV powertrains have hybrid mechanical and regenerative braking options and, therefore, the mechanical braking material demands are expected to be less severe and the lightweight alloy systems are expected to have potential to displace higher density cast iron in some scenarios. Lightweight alloy brake rotors could add up to >25 lbs. per vehicle considering there are two rear brake rotors per vehicle. Also, since brake rotors are reciprocating mass, the impact is even more significant compared to lightweighting of stationary components. Along with reduced demands on mechanical braking in EVs, new generations of Al alloys with improved temperature capability provide renewed possibility for lightweighting of brake rotors for EVs, as either monolithic alloys or as the matrix for composite brake materials. The FY 2022 first year effort for this task focused on evaluating lightweight alloys in the most severe conditions first—combining monolithic Al alloys with brake testing under HD truck braking conditions. Alloys tested were the Al-Cu (cast) and Al-Ce-Ni (additive) alloy systems for brake rotor applications. Out-year efforts will apply compositing approaches and will expand studies to evaluate lower demand (e.g., MD and LD) braking conditions.

Objectives

This task will aid the understanding and development of higher temperature Al alloys and related composites for lightweight brake systems that can be deployed in EVs. Specific objectives from the first year of this task are as follows:

- To revive sub-scale brake testing capability at ORNL

- To apply Al alloys and MMCs for lightweight brake systems.

Approach

It is relevant to understand the brake requirements for EVs where regenerative braking is possible. Sub-scale brake testing capability that can measure the friction coefficient, wear behavior, and temperature of disk specimen during simulated brake testing was re-established at ORNL. A suite of monolithic high-temperature lightweight alloys with different heat treatments, along with baseline cast iron specimens, were identified for brake testing under HD braking conditions (the most severe combination). The wear resistance, temperature limit, thermal conductivity, and specific heat of lightweight Al brakes are different from their cast iron counterparts. If the wear resistance and upper temperature limit of Al alloys can achieve an adequate threshold, such alloys could be useful for lightweighting of rear brake rotors for EVs as either monolithic brake rotor materials or higher temperature matrices for MMC rotors. Improvements in the testing methods and the alloys were identified based on the FY 2022 results. New alloys, compositing approaches, and testing conditions will be implemented in FY 2023 along with a refined understanding of brake requirements for EVs.

Results

The creep properties of two candidate brake rotor cast alloy materials—ACMZ alloys with 6 wt% and 9 wt% Cu—were tested at 300°C. Cross-section SEM, inverse pole figure (IPF), and Kernel average maps (KAM) for 6 wt% and 9 wt% Cu alloy concentrations of strain around grain boundaries and particles are shown in Figure I.1.1.2.1(a) and Figure I.1.1.2.1(b), respectively. Creep rates shown in Figure I.1.1.2.1(c) indicate higher deformation in the 9 wt% Cu alloys (compared to 6 wt% Cu) and in tension (compared to compression) as reported by Bahl, et.al. [1].

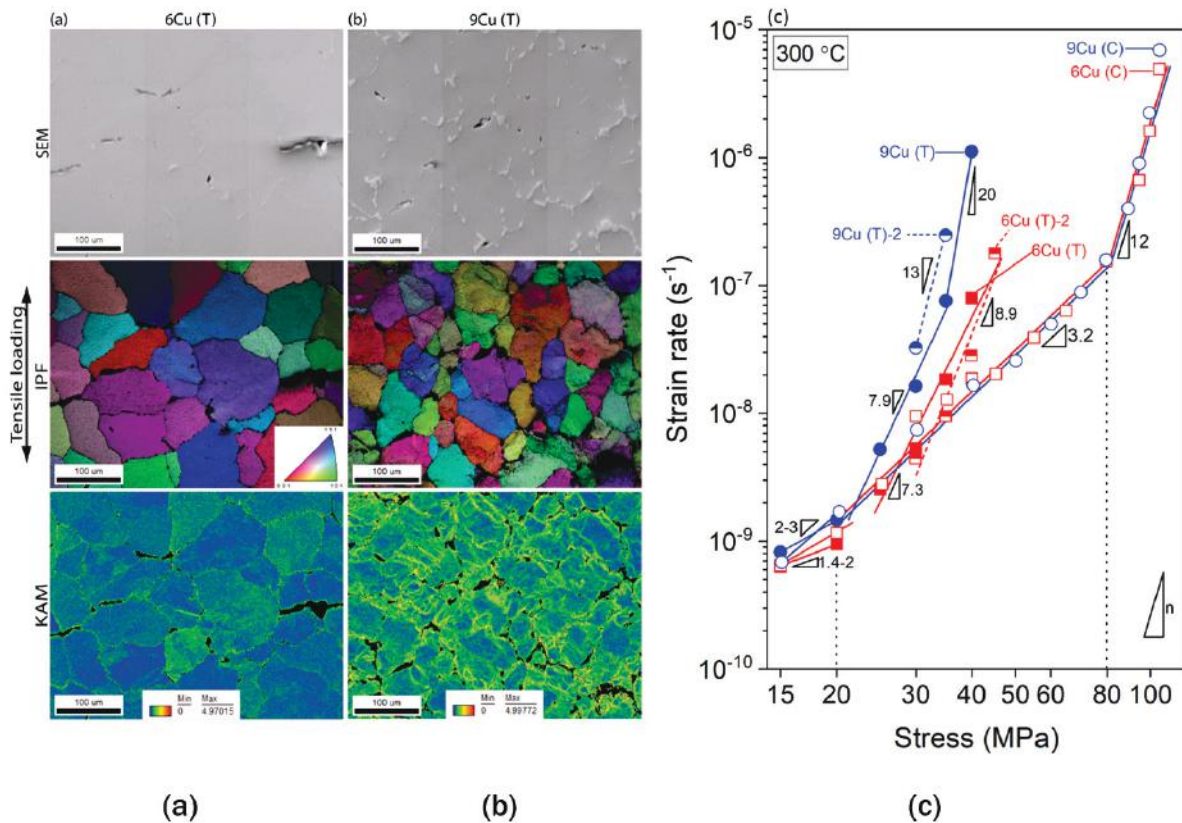


Figure I.1.1.7. Comparison of the microstructure (post-creep) of cast ACMZ alloys with (a) 6 wt% Cu, (b) 9 wt% Cu [1], and (c) creep response of alloys in compression (C) and tension (T) at 300 °C. Source: ORNL.

The same cast alloys were machined into discs and tested in the as-cast and aged conditions in the ORNL sub-scale brake testing facility. Moreover, additively manufactured (AM) Al-Ce-Ni alloy discs were also tested in the as-printed and aged conditions. Figure I.1.1.2(a) shows an image of the sub-scale test facility along with the method applied for testing shown in Figure I.1.1.2(b). Specimen discs were 5 inches in diameter with a thickness of 0.5-0.625 inches. A JURID 539™ brake pad material for HD vehicles was applied at a load level resulting in 1 MPa contact pressure. Five repetitive drags (20 seconds each) were applied for each test speed at constant load in the following sequence of speeds: 2 m/s → 6 m/s → 9.6 m/s → 15 m/s → 9.6 m/s → 6 m/s → 2 m/s. Temperature of the test specimen was measured in situ with an infrared sensor. Friction coefficient was measured during the test and wear-tracks on the specimen were quantified with laser profilometry.

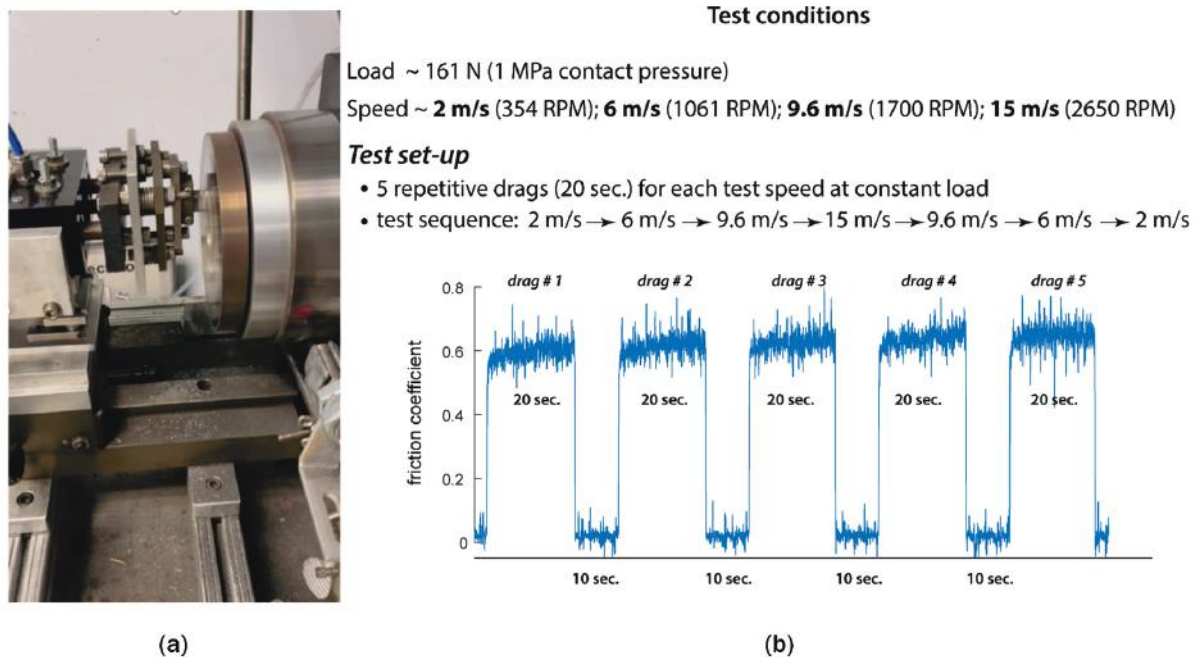


Figure I.1.1.8. (a) ORNL sub-scale brake testing facility. (b) The applied test method simulating heavy truck braking conditions. Source: ORNL.

Test results on friction coefficient as a function of test speed for Al-9 wt% Cu ACMZ alloy (in the as-cast state) along with baseline cast iron alloy is reported in Figure I.1.1.2.3. While cast iron tests enter the desired friction coefficient band for braking (0.35-0.5) as test speed is increased, the Al alloy starts in the band but exits the band at higher brake testing speeds (>10 m/s).

The frictional performance of the ACMZ alloy disc with 9 wt% Cu alloy met the minimum friction coefficient requirement for braking, which is > 0.35, and had no ‘fade’ at high speeds albeit with increased friction. The effect of test speed on the friction coefficient and specimen temperature for the five drags per test for an AM Al-Ce-Ni-Mn alloy in the as-printed state is shown in Figure I.1.1.2.4. This alloy is a modified version of another printable high-temperature alloy developed by ORNL, whose properties were reported on recently [2]. Specimen temperatures increase steadily as the test speed is increased. For the highest speed of 15 m/s (2650 RPM), a temperature as high as 370°C was measured. Friction coefficients for the various test conditions varied between 0.3–0.7 for this alloy under the monitored test conditions.

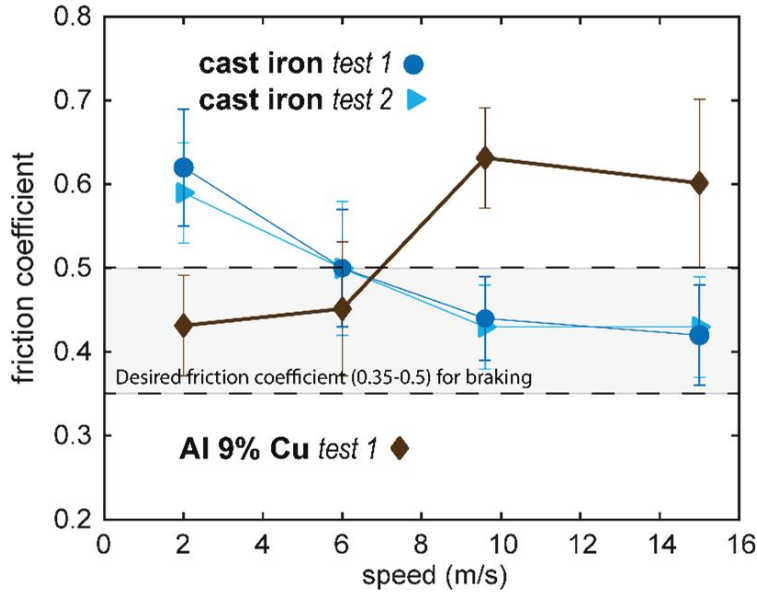


Figure I.1.1.9. Friction coefficient vs. speed for cast iron (baseline) and as-cast Al 9 wt% Cu ACMZ alloy. Source: ORNL.

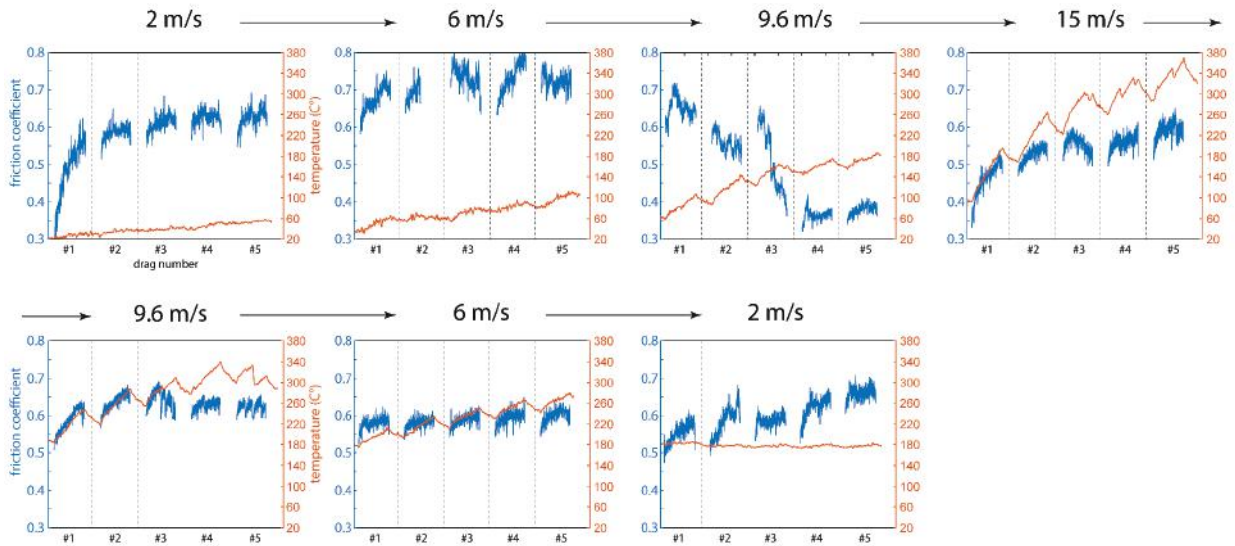


Figure I.1.1.10. Friction coefficient (left y-axis and in blue) along with temperature (right y-axis and in orange) as a function of drag sequence for the entire test sequence (increasing and then decreasing speed). Representative results shown here are for an AM Al-Ce-Ni-Mn alloy in the as-printed state. Source: ORNL.

For the test conditions reported, the HD brake pad material (JURID 539™) experienced severe wear and the results for wear degradation are summarized in Figure I.1.1.2.5. Under conditions where the cast iron material resulted in no pad height or mass loss, the Al alloys resulted in a pad height loss (for the as-cast Al-9%Cu ACMZ alloy) of less than 1 mm (1000 μm) and less than ~500 mg of pad mass loss (for the aged Al-6%Cu ACMZ alloy). Severe wear marks on the brake pad material are also evident in the images shown in Figure I.1.1.2.5. Within the Al alloy family, the wear resistance was poor under these test conditions and could be loosely ranked as follows: as-printed AlCeNiMnZr > aged AlCeNiMnZr > aged cast ACMZ > as-cast ACMZ. These rankings roughly correlated with the hardness values of the investigated alloys. The softest alloy tested, the as-cast ACMZ alloy with 6 wt% Cu, generated wear debris so rapidly the test needed to be

stopped within tens of seconds. The severe wear of the brake pad material in these preliminary tests confirmed the choices of brake pad material will need optimization for future testing of lightweight alloys, and this will be an area of emphasis in FY 2023. In addition, compositing approaches (with a hard and wear-resistant ceramic as reinforcement) will almost certainly be necessary for the application of lightweight alloys for brake rotor applications in the most severe braking conditions, such as those reported in this study.

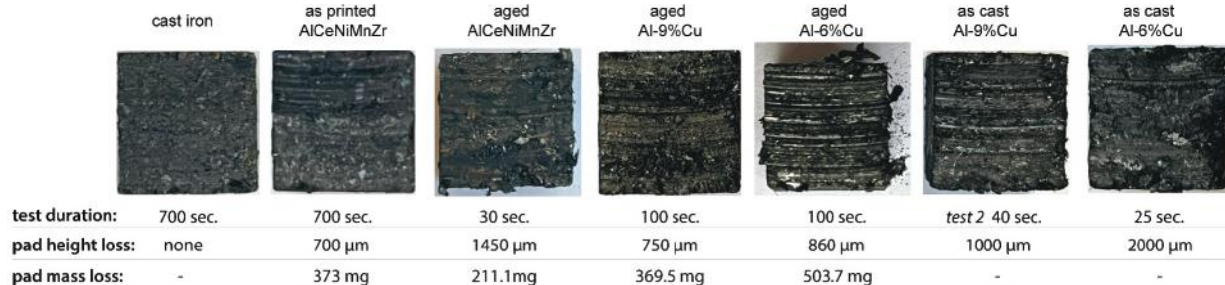


Figure I.1.1.11. Results summarizing wear of brake pad materials for the various Al alloys tested in the heat-treatment conditions of interest. Source: ORNL.

Besides the rapid wear in the pad material during Al alloy testing, the discs themselves had severe surface damage as shown by the results in Figure I.1.1.2.6. The worn surfaces of the discs were profiled with a laser profilometer. While the cast iron disc specimen in Figure I.1.1.2.6(a) showed no wear depth, the as-printed alloy and the aged, printed alloy showed a maximum wear depth of around 100 μm and 40 μm , respectively. Note the test duration was shorter for the aged material due to severe wear in the brake pad material. The aged cast ACMZ alloys had a maximum wear depth of approximately 50 μm shown in Figure I.1.1.2.6(b) and the as-cast alloy, which had lower hardness, had a higher maximum wear depth of > 100 μm shown in Figure I.1.1.2.6(c).

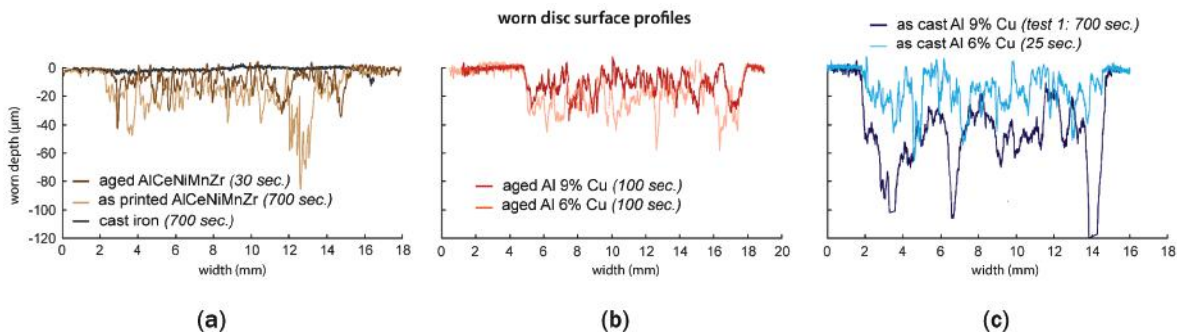


Figure I.1.1.12. Worn disc surface profiles measured with laser profilometry. (a) Cast iron baseline worn disc surface profile compared to printed and printed + aged AlCeNiMnZr alloys. (b) Comparison of wear surface profiles of aged ACMZ alloys with 9 wt% and 6 wt% Cu. (c) Comparison of wear surface profiles of as-cast ACMZ alloys with 9 wt% and 6 wt% Cu. Source: ORNL.

Overall, results confirmed these test conditions, which simulated HD vehicle braking conditions (and pads), were unacceptably severe for monolithic Al alloys as disc specimens. Test conditions will be adjusted in FY 2023 to represent and investigate LD and MD EV regenerative braking conditions.

Conclusions

- Creep tests were performed on ACMZ alloys with 6 wt% and 9 wt% Cu in tension and compression. The lower copper alloy had improved creep response and the tensile creep rates were higher than compressive creep rates for the same alloy.

- An ORNL sub-scale brake testing facility was revived, and several tests were completed on baseline cast iron alloys and cast and printed Al alloys of interest.
- The frictional performance of the ACMZ alloy disc with 9 wt% Cu alloy met the minimum friction coefficient requirement for braking >0.35 and had no ‘fade’ at high speeds. Within the Al alloy family, the wear resistance could be loosely ranked as follows: as-printed AlCeNiMnZr $>$ aged AlCeNiMnZr $>$ aged cast ACMZ $>$ as-cast ACMZ.
- Both the brake pad material and brake discs themselves showed rapid wear under the testing conditions selected for all candidate Al alloys tested. The testing conditions simulated HD vehicles and were too severe for Al discs. Future test conditions will be adjusted to investigate LD and MD EV rear braking conditions.

Key Publications

1. Bahl, S., J. U. Rakhmonov, C. Kenel, D. C. Dunand, and A. Shyam, 2022, “Effect of grain boundary θ -Al₂Cu precipitates on tensile and compressive creep properties of cast Al-Cu-Mn-Zr alloys,” *Mater. Sci. Eng. A*, Vol. 840, Art. 142946. <https://doi.org/10.1016/j.msea.2022.142946>.

References

1. Bahl, S., J. U. Rakhmonov, C. Kenel, D. C. Dunand, and A. Shyam, 2022, “Effect of grain boundary θ -Al₂Cu precipitates on tensile and compressive creep properties of cast Al-Cu-Mn-Zr alloys,” *Mater. Sci. Eng. A*, Vol. 840, Art. 142946. <https://doi.org/10.1016/j.msea.2022.142946>.
2. Michi, R. A., K. Sisco, S. Bahl, Y. Yang, J. D. Poplawsky, L. F. Allard, R. R. Dehoff, A. Plotkowski, and A. Shyam, 2022, “A creep-resistant additively manufactured Al-Ce-Ni-Mn alloy,” *Acta Mater.*, Vol. 227, Art. 117699. <https://doi.org/10.1016/j.actamat.2022.117699>.

Acknowledgements

T. Grejtak, J. Qu, S. Bahl, J. A. Haynes, D. McClurg, A. Plotkowski, and J. Meier of ORNL are acknowledged for their contribution to this effort. J. Rakhmonov, C. Kenel, and D. C. Dunand of Northwestern University are acknowledged for creep testing results and collaboration.

I.1.1.3 Task 1C. Fundamentals of Fatigue and Creep in Advanced Lightweight Alloys: Cost-Effective Lightweight Alloys for Electric Vehicle Propulsion (Oak Ridge National Laboratory)

Sumit Bahl, Principal Investigator

Oak Ridge National Laboratory
Materials Science and Technology Division
1 Bethel Valley Rd.
Oak Ridge, TN 37830
E-mail: bahls@ornl.gov

J. Allen Haynes, PMCP Consortium Manager

Oak Ridge National Laboratory
Materials Science and Technology Division
1 Bethel Valley Rd.
Oak Ridge, TN 37830
E-mail: haynesa@ornl.gov

Jerry Gibbs, DOE Technology Development Manager

U.S. Department of Energy
E-mail: jerry.gibbs@ee.doe.gov

Start Date: November 1, 2022	End Date: September 30, 2023	
Project Funding (FY 2022): \$270,000	DOE share: \$270,000	Non-DOE share: \$0

Project Introduction

Creep (static loading) and fatigue (dynamic loading) are important failure modes in lightweight Al alloys. Recent advancements in manufacturing including AM, hybrid manufacturing, and ultra-large high-pressure die-casting have motivated the development of new Al alloys that are compatible with and take advantage of modern manufacturing processes for improved performance in EV applications. Lightweight conductors, particularly dilute Al alloys, are known to be prone to creep at higher currents. Emerging trends indicate new deformation and failure mechanisms in Al alloys produced by advanced manufacturing methods, typically related to unique microstructures and/or flaws. Concurrently, there is increasing realization of the importance of materials sustainability by utilizing feedstocks with higher proportions of secondary recycled Al alloys, which is likely to impact the creep and fatigue behavior by introduction of increased or additional intermetallic content due to certain impurities in the recycle stock. This task focuses on relating the microstructural features to creep and fatigue-failure mechanisms in cast and printed Al alloys for EV applications, including structural body parts, electrical conductors, brake systems, etc.

Objectives

This task will aid the understanding and development of creep and fatigue-resistant Al alloys for deployment in EV applications. Specific objectives from the first year of this task are as follows:

- Characterize creep behavior, fatigue properties, and identify microstructural features responsible for failure of printed lightweight alloys under those conditions.
- Apply in situ testing via neutron diffraction to obtain phase-specific insights into alloy deformation mechanisms.
- Provide input for alloy design and processing modifications for enhancement of creep and fatigue properties.

Approach

AM has enabled a new class of Al alloys with a high-volume fraction ($\sim > 10$ vol.%) of nanoscale intermetallic particles, exhibiting improved mechanical properties compared to their conventionally manufactured counterparts [1]. Two Al alloys within this class of alloys developed at ORNL are Al-9Cu-0.5Mn-1Zr (Al-Cu-Mn-Zr) and Al-10.5Ce-3.1Ni-1.2Mn (Al-Ce-Ni-Mn) in research co-sponsored by the VTO and the AMO. The ACMZ alloy is strengthened by ~ 10 vol.% of nanoscale equilibrium θ -Al₂Cu particles and a small volume fraction < 0.5 vol.% of metastable θ' -Al₂Cu precipitates. The creep properties of ACMZ alloys were measured *ex-situ* and *in-situ* via neutron diffraction to examine the role of θ particles on creep behavior in the temperature range of 300°–400°C. The Al-Ce-Ni-Mn (ACNM) alloy family is a near-eutectic composition strengthened by a mixed population of Ce-, Ni-rich intermetallic particles with a total volume fraction of ~ 35 vol.%. The high-cycle fatigue properties of the alloy were characterized at 350°C. Crack initiation/propagation mechanisms were identified by fractography, and theoretical models were applied to predict the fatigue life.

Results

The creep properties of the AM-ACMZ alloy were tested at 300°C in the as-fabricated condition and after preconditioning the alloy for various time/temperature combinations prior to creep testing (e.g., 300°C/200 h, 350°C/24 h, 400°C/6 h, 400°C/200 h) under both *ex-situ* testing and *in-situ* via neutron diffraction conditions. Figure I.1.1.3.1(a) and Figure I.1.1.3.1(b) show microstructures of the AM-ACMZ alloy in the initial as-fabricated condition and after 300°C/200 h heat-treatment, respectively. The as-fabricated microstructure comprises finer θ particles at the grain boundaries, as well as in the intragranular regions. The θ particles coarsen after heat-treatment and are mainly present at grain boundaries. The results of creep strain rate versus (vs.) applied tensile stress are shown in Figure I.1.1.3.1(c) with closed symbols for the *ex-situ* tests and open symbols for the *in situ* tests. The creep resistance of the AM-ACMZ alloy is highest in the as-fabricated condition and reduces after heat treatments due to coarsening of θ -Al₂Cu particles, which is the major strengthening phase in this laser powder bed printed version of the alloy. The creep resistance inversely scales with the intensity of the heat-treatment. An increase in temperature and/or time of the heat-treatment leads to greater coarsening of the θ particles and a consequent reduction in creep resistance. The as-fabricated AM-ACMZ alloy exhibits superior creep performance as compared to other high-temperature Al alloys, including the cast counterpart of the ACMZ alloy, as shown in Figure I.1.1.3.1(d).

The creep rates measured during the *in situ* creep tests (e.g., open symbols) are like those measured during the *ex-situ* tests (e.g., closed symbols). Figure I.1.1.3.2 shows phase-specific lattice strain evolution vs. creep time in α -Al matrix and θ particles of as-fabricated, 350°C/24 h, and 400°C/6 h heat-treated conditions measured with neutron diffraction. The most striking result of the *in situ* creep tests is that lattice strain in the θ phase decreases continuously with creep time, while that of the α -Al remains stable or increases slightly, basically indicating an unexpected shedding of load by the harder θ particles. Figure I.1.1.3.2 also shows full width at half maximum (FWHM) of the diffraction peaks. The FWHM of the θ phase decreases with creep time in the as-fabricated condition but remains constant for the heat-treated conditions. The decrease in the FWHM of the θ particles in the as-fabricated condition is likely due to coarsening of the particles and concomitant strain relaxation during creep, which would have occurred prior to testing for particles in the heat-treated conditions resulting in their stable FWHM values.

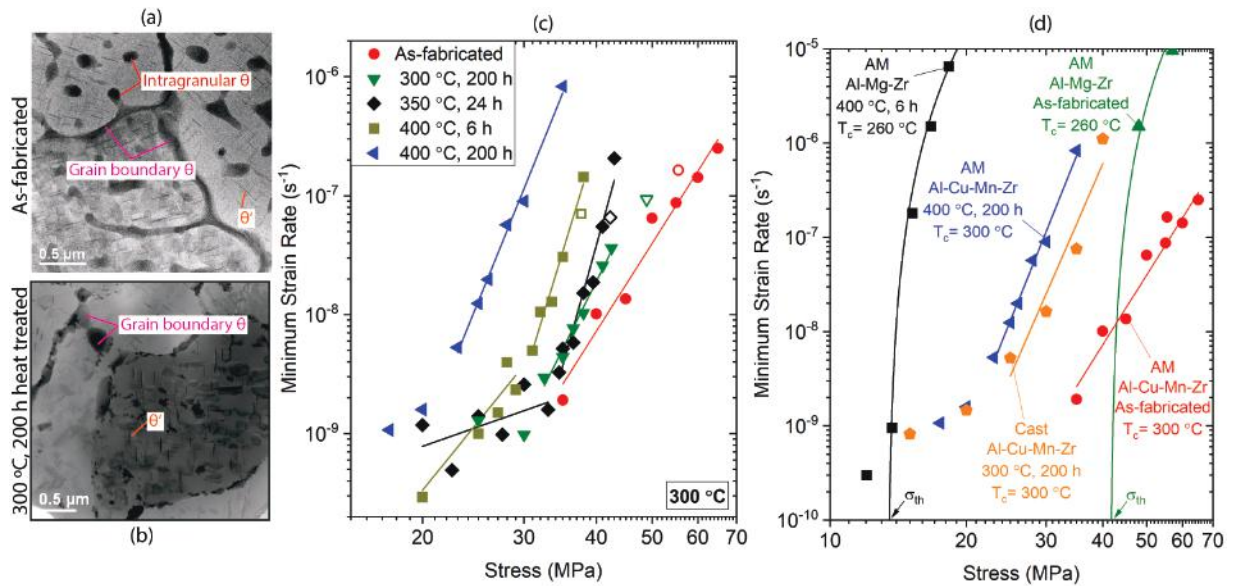


Figure I.1.1.13. Bright-field scanning transmission electron microscopy images of AM-ACMZ alloy in (a) as-fabricated, and (b) 300 °C, 200 h heat-treated conditions. (c) Minimum creep strain rate vs. applied tensile stress at 300 °C in as-fabricated and heat-treated conditions (e.g., 300 °C/200 h, 350 °C/24 h, 400 °C/6 h, 400 °C/200 h). The solid symbols are for *ex-situ* tests, while the open symbols for *in situ* creep tests. (d) Creep resistance of AM-ACMZ alloy compared to other high-temperature Al alloys [2]. T_c is creep temperature. Source: ORNL.

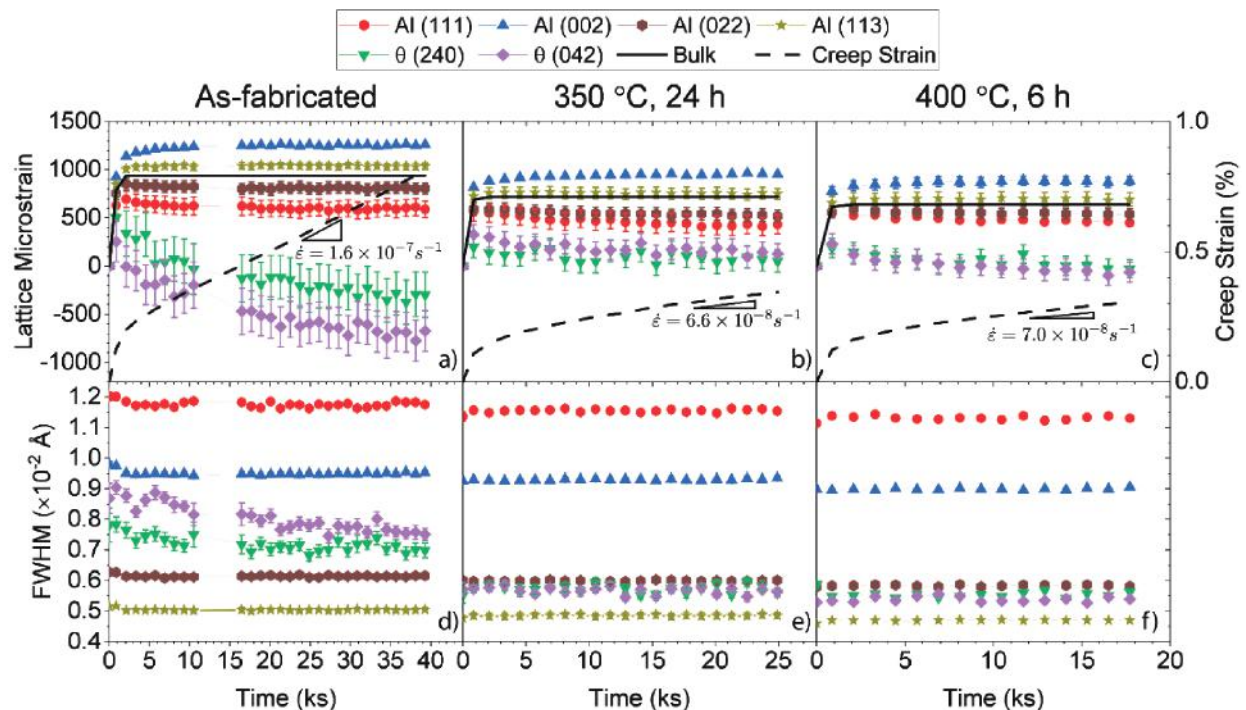


Figure I.1.1.14. (a-c) Phase-specific lattice strain evolution, and (d-f) FWHM of diffraction peaks vs. creep time during the *in situ* creep tests for the AM-ACMZ alloy in as-fabricated and select heat-treated conditions. The macro strain and creep strain rate results are also shown in (a-c). Source: ORNL.

The mechanism proposed for the load shedding by θ particles is schematically explained in Figure I.1.1.3.3. The lattice strain at the start of creep deformation is similar in the α -Al and θ phases for the as-fabricated condition, as shown in Figure I.1.1.3.2, indicating some load transfer to θ particles from the Al grains, which is stage I of deformation, as shown in Figure I.1.1.3.3. With further deformation, θ particles coarsen, particularly those at alloy grain boundaries, and develop soft precipitate-free zones (PFZs) around them devoid of the much finer metastable θ' precipitates. These soft PFZs near grain boundaries then begin to shed load to the stronger grain interior. Since the θ particles are enveloped inside the PFZs, these particles also shed load, which is stage II of deformation. As the PFZs continue to widen with time, it leads to a gradual increase in load shedding (or decrease in lattice strain) by θ particles. This mechanism is a new discovery and we have termed this two-way load transfer initially from Al grains to grain boundary θ particles at beginning of creep followed by transfer back from the particles to the grain during later stages of creep as ‘Load Shuffling.’ This Load Shuffling discovery underscores the exclusive capability of neutron diffraction to provide fundamental insights into creep deformation mechanisms by distinguishing the time-dependent strain responses of each specific alloy constituent, which offers significant implications in guiding design of future alloys with improved creep resistance.

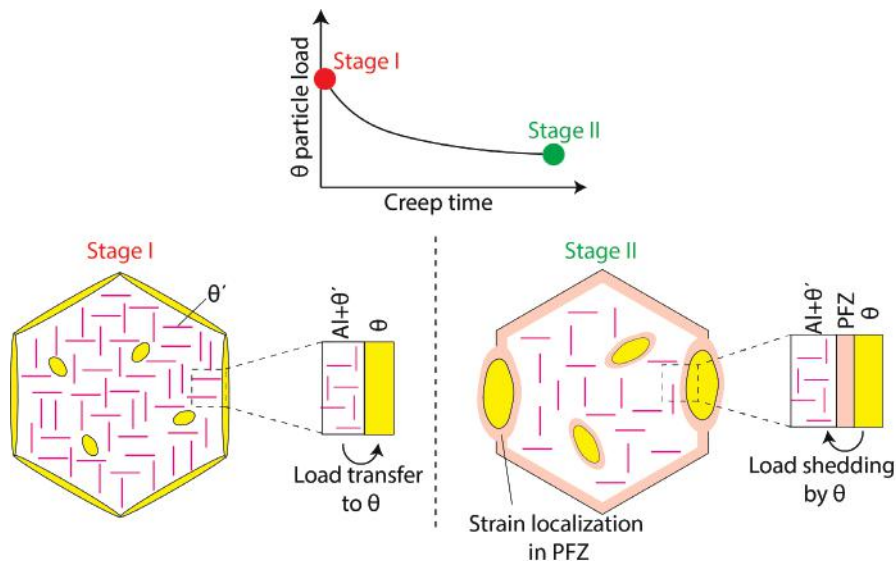


Figure I.1.1.15. Schematic diagram of the proposed Load Shuffling mechanism to explain load shedding by θ particles during creep. Source: ORNL.

Transitioning to the fatigue studies of the AM-ACNM alloy, Figure I.1.1.3.4(a) shows the maximum stress vs. cycles to failure during high-cycle fatigue testing at 350°C. The fatigue strength of the printed alloy at 350°C is comparable to the most fatigue-resistant wrought Al alloys at 315°C. The excellent fatigue resistance is due to a high-volume fraction (~35 vol.%) of thermally stable Ce-, Ni-rich intermetallic particles, which significantly strengthens the alloy at elevated temperatures, and optimizes the printing process to minimize porosity. The SEM fractographs after fatigue-failure are shown in Figure I.1.1.3.4(b) and Figure I.1.1.3.4(c), respectively, for a sample tested at a maximum stress of 60 MPa. The primary fatigue crack initiated at an inclusion close to the specimen surface, as shown in the yellow box of Figure I.1.1.3.4(b). The energy-dispersive spectroscopy elemental maps in the inset of Figure I.1.1.3.4(c) confirm that it is a Ce-oxide inclusion. The fractograph also shows multiple sub-surface, secondary crack initiation sites resembling ‘fisheyes’ as marked in Figure I.1.1.3.4(b).

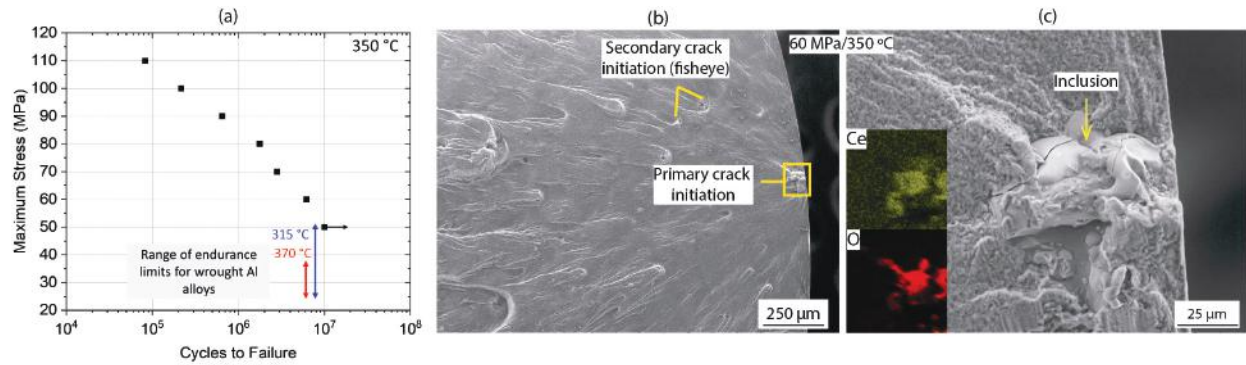


Figure I.1.1.16. (a) Maximum stress vs. cycles to failure of the AM-ACNM alloy during fatigue testing at 350 °C. The horizontal arrow indicates specimen runout at 10^7 cycles and the corresponding stress level is the fatigue limit. The vertical arrows indicate the fatigue limit of wrought Al alloys at 315 °C and 370 °C. (b) Fractograph of a specimen tested at a maximum stress level of 60 MPa showing primary fatigue crack initiation at a Ce-oxide inclusion (yellow box) and multiple secondary cracks (fisheyes). (c) Provides a magnified view of the yellow box in (b), with the energy-dispersive spectroscopy maps in the inset confirming the inclusion as a Ce-oxide particle. Source: ORNL.

The size distributions of the inclusions and porous defects in the ACNM alloy were measured by x-ray computed tomography; the results are shown in Figure I.1.1.3.5. The largest oxide inclusions are larger in size as compared to the largest pores, which is consistent with fatigue crack initiation occurring at the inclusions. Fatigue-failure has been commonly associated with porosity in printed lightweight alloys. This study demonstrates that when AM processing parameters are optimized to initially minimize porosity, fatigue cracks initiate at the larger oxide inclusions, acting as the weaker links in the microstructure. This result demonstrates pathways toward further improvements in fatigue performance by reducing oxide inclusions next in either the powder feedstock or those that result from feedstock handling and printing, while also minimizing porosity. The presence of multiple fisheye secondary cracks shown in Figure I.1.1.3.4(b) indicates that in the AM-ACNM alloy: (i) fatigue crack initiation is relatively easy; (ii) fatigue life is dominated by propagation of small fatigue cracks; and (iii) fatigue limit is associated with non-propagating small fatigue cracks. A linear elastic fracture mechanics threshold-based model developed by Zhu et al. [3, 4] was applied to predict the fatigue life in the present case. The flow chart of the model is shown in Figure I.1.1.3.5(c). The experimentally determined distributions of pores and inclusions shown in Figure I.1.1.3.5(b) were used to create a random array of defect distribution in a volume. The mode I stress intensity factor range (ΔK_I) was calculated for each defect for an applied stress amplitude. If the maximum value of the stress intensity factor in the sample volume exceeded the threshold stress intensity factor (ΔK_{th}) (assumed equal to $0.5 \text{ MPa}\sqrt{\text{m}}$), the sample failed. A new random array of defects was generated in the volume with the same experimentally determined overall distribution, and the process was repeated for a lower stress amplitude decreased by an amount δ . If no failure occurred, the process was repeated with a new array of defects at a stress amplitude increased by the amount δ . A statistical value of the fatigue limit was determined by repeating the process for a specified number of tests, N . The model assumes pores and inclusions are equivalent regions for fatigue crack initiation; in other words, the matrix-inclusion interface is debonded. The assumption is reasonable as the debonded inclusions provide a traction free surface similar to pores. The model predicted a fatigue limit of $58 \pm 7 \text{ MPa}$ in reasonable agreement with the experimental value of 50 MPa.

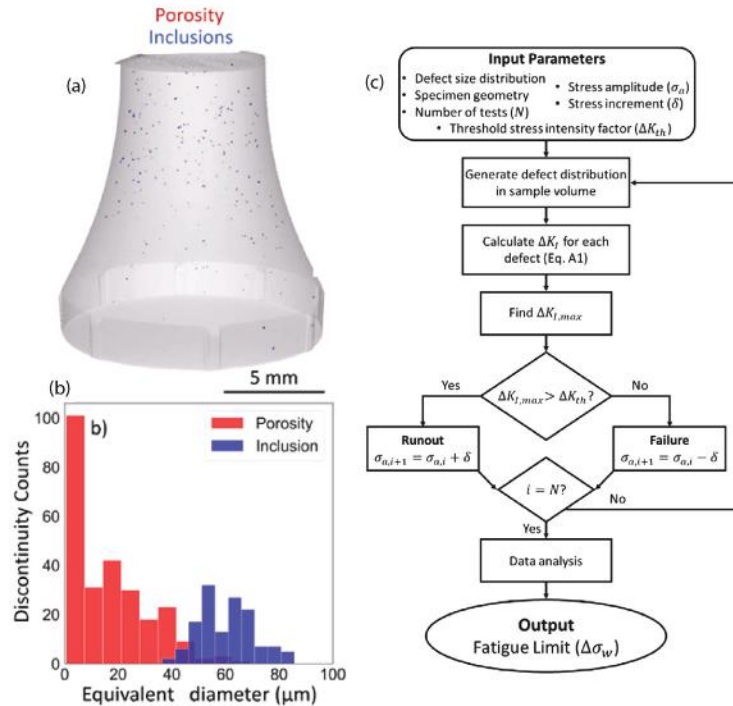


Figure I.1.1.17. X-ray tomography reconstruction of a fatigue specimen tested at 60 MPa maximum stress showing (a) porosity inclusions, and (b) corresponding size distribution of pores and inclusions. The equivalent diameter is calculated by assuming the defects are spheres of equivalent volume. (c) Flow chart of the model to predict fatigue limit developed by Zhu et al. [3, 4]. Source: ORNL.

Conclusions

- *In situ* creep experiments via neutron diffraction unexpectedly revealed in an AM Al-9Cu-0.45Mn-1Zr alloy, harder intermetallic particles of θ -Al₂Cu phase shed load to the softer Al matrix.
- A new mechanism has been proposed (and recently published in a peer reviewed journal [5]) to explain the discovery of load shedding by the θ -Al₂Cu phase. The θ particles at the grain boundaries coarsen and develop surrounding soft PFZs during creep. At the start of creep deformation with no PFZs, θ particles effectively carry load from the Al grain. Once PFZs form at grain boundaries, they shed load to the stronger Al grain and since the θ particles are embedded inside the PFZs, the particles also shed load. This newly identified two-way transfer of load between grain boundary θ particles and Al grain has been termed ‘Load Shuffling’ by this research team.
- The high-cycle fatigue properties of an AM Al-10.5Ce-3.1Ni-1.2Mn alloy were measured at 350°C. The alloy exhibits excellent fatigue limit of 50 MPa at 350°C, which is comparable to that of wrought Al alloys at 315°C and represents a substantial improvement in temperature resistance for a lightweight alloy.
- The defect population of the AM-ACNM alloy consists of pores and oxide inclusions, with the latter being larger in size. As a result, primary fatigue cracks initiated at near-surface inclusions. A linear elastic fracture mechanics-based model is applied to reasonably predict the experimentally measured fatigue limit.

Key Publications

1. Bahl, S., J. U. Rakhmonov, C. Kenel, D. C. Dunand, and A. Shyam, 2022, “Effect of grain boundary θ -Al₂Cu precipitates on tensile and compressive creep properties of cast Al-Cu-Mn-Zr alloys,” *Mater. Sci. Eng. A*, Vol. 840, Art. 142946. <https://doi.org/10.1016/j.msea.2022.142946>.

2. Michi, R. A., S. Bahl, C. M. Fancher, K. Sisco, L. F. Allard, K. An, D. Yu, R. R. Dehoff, A. Plotkowski, and A. Shyam, 2023, “Load shuffling during creep deformation of an additively manufactured Al-Cu-Mn-Zr alloy,” *Acta Mater.*, Vol. 244, Art. 118557. <https://doi.org/10.1016/j.actamat.2022.118557>.
3. Michi, R. A., K. Sisco, S. Bahl, Y. Yang, J. D. Poplawsky, L. F. Allard, R. R. Dehoff, A. Plotkowski, and A. Shyam, 2022, “A creep-resistant additively manufactured Al-Ce-Ni-Mn alloy,” *Acta Mater.*, Vol. 227, Art. 117699. <https://doi.org/10.1016/j.actamat.2022.117699>.
4. Rakhmonov, J. U., S. Bahl, A. Shyam, and D. C. Dunand, 2022, “Cavitation-resistant intergranular precipitates enhance creep performance of θ' -strengthened Al-Cu based alloys,” *Acta Mater.*, Vol. 228, Art. 117788. <https://doi.org/10.1016/j.actamat.2022.117788>.

References

1. Michi, R. A., A. Plotkowski, A. Shyam, R. R. Dehoff, and S. S. Babu, 2021, “Towards high-temperature applications of aluminum alloys enabled by additive manufacturing,” *Int. Mater. Rev.*, Vol. 67, No. 3, pp. 1–48. <https://doi.org/10.1080/09506608.2021.1951580>.
2. Griffiths, S., J. R. Croteau, M. D. Rossell, R. Erni, A. De Luca, N. Q. Vo, D. C. Dunand, and C. Leinenbach, 2020, “Coarsening- and creep resistance of precipitation-strengthened Al-Mg-Zr alloys processed by selective laser melting,” *Acta Mater.*, Vol. 188, pp. 192–202. <https://doi.org/10.1016/j.actamat.2020.02.008>.
3. Yi, J. Z., X. Zhu, J. W. Jones, and J. E. Allison, 2007, “A probabilistic model of fatigue strength controlled by porosity population in a 319-type cast aluminum alloy: Part II. Monte-Carlo simulation,” *Metall. Mater. Trans. A Phys. Metall. Mater. Sci.*, Vol. 38, No. 5, pp. 1123–1135. <https://doi.org/10.1007/s11661-006-9069-2>.
4. Zhu, X., J. Z. Yi, J. W. Jones, and J. E. Allison, 2007, “A probabilistic model of fatigue strength controlled by porosity population in a 319-type cast aluminum alloy: Part I. Model development,” *Metall. Mater. Trans. A Phys. Metall. Mater. Sci.*, Vol. 38, No. 5, pp. 1111–1122. <https://doi.org/10.1007/s11661-006-9070-9>.
5. Michi, R. A., S. Bahl, C. M. Fancher, K. Sisco, L. F. Allard, K. An, D. Yu, R. R. Dehoff, A. Plotkowski, and A. Shyam, 2023, “Load shuffling during creep deformation of an additively manufactured Al-Cu-Mn-Zr alloy,” *Acta Mater.*, Vol. 244, Art. 118557. <https://doi.org/10.1016/j.actamat.2022.118557>.

Acknowledgements

All of the coauthors, including R. A. Michi, J. U. Rakhmonov, A. Shyam, A. Plotkowski, D. C. Dunand, C. Kenel, C. M. Fancher, K. Sisco, L. F. Allard, K. An, D. Yu, R. R. Dehoff, Y. Yang, and J. D. Poplawsky are acknowledged for their contributions. The research was co-sponsored by the VTO and the AMO. The *in situ* creep experiments used resources of the Spallation Neutron Source at ORNL sponsored by the U.S. Department of Energy’s Scientific User Facilities Division, Office of Basic Energy Sciences.

I.1.1.4 Task 1D. Fundamentals of Corrosion Behavior in Advanced Lightweight Alloys for Electric Vehicle Propulsion (Oak Ridge National Laboratory)

Jiheon Jun, Principal Investigator

Oak Ridge National Laboratory
Materials Science and Technology Division
1 Bethel Valley Rd.
Oak Ridge, TN 37830
E-mail: junj@ornl.gov

J. Allen Haynes, PMCP Consortium Manager

Oak Ridge National Laboratory
Materials Science and Technology Division
1 Bethel Valley Rd.
Oak Ridge, TN 37830
E-mail: haynesa@ornl.gov

Jerry Gibbs, DOE Technology Development Manager

U.S. Department of Energy
E-mail: jerry.gibbs@ee.doe.gov

Start Date: November 1, 2021	End Date: September 30, 2023	
Project Funding (FY 2022): \$185,000	DOE share: \$185,000	Non-DOE share: \$0

Project Introduction

Aqueous corrosion resistance of Al alloys is one of the key performance aspects to be considered when these lightweight alloys are used in EVs. This task was initiated to evaluate aqueous corrosion behavior of new higher performance developmental Al alloys designed at ORNL, including alloys for three-dimensional (3D) printing, in comparison to commercial Al alloys. By studying and understanding their corrosion behavior, these new developmental alloys and their associated manufacturing and heat-treatment processes can be appropriately evaluated for potential application as future lightweight powertrain materials, including battery enclosures for EVs.

Objectives

This task aims to provide understanding of the corrosion behavior of new cast and additively manufactured (AM) Al alloys developed at ORNL, including direct comparison with relevant commercial Al alloys in 3.5% NaCl solution. This comparison will facilitate the prediction of corrosion performance of advanced lightweight alloys considered as future automotive powertrain materials and aid relevant industries to select corrosion-compatible Al alloys for manufacturing of EV components.

Approach

Corrosion resistance was comprehensively evaluated by multiple electrochemical techniques in short-term (< 3 h) exposures and long-term (~168 h) immersion tests. The corrosive media used for all electrochemical measurements and immersion tests at RT was 3.5% NaCl solution open-to-air. Electrochemical measurements, including electrochemical impedance spectroscopy and polarization, used platinum wire counter and saturated calomel reference electrodes. For most impedance spectra, a circuit model was used to determine $R_2 + R_3$ values relevant to corrosion resistance in $\text{ohm}\cdot\text{cm}^2$. SEM equipped with energy-dispersive spectroscopy (EDS) was used to investigate the nature of the corrosion attack and microstructural features after immersion testing.

The chemical compositions of the Al alloys used in this task are summarized in Table I.1.1.4.1. The higher copper (Cu) ACMZ cast Al alloys (from ORNL) as well as two Cu-containing commercial Al alloys, 319 and RR350, were tested in as-cast and aged conditions. Three AM Al alloys were tested, including the commercial Al10SiMg alloy, but only the AM-Al-Ce-Ni-Mn received the 450°C, 2 h heat-treatment.

Table I.1.1.4.1. Nominal Chemical Compositions of Al Alloys Used in this Task [1]

Category	Cast or AM alloys	Weight percents								
		Cu	Ce	Mn	Ni	Zr	Si	Mg	Fe	Al
Commercial Compositions	319 (as-cast and aged*)	~3.5	-	-	-	-	~6	-	<1	Bal.
	AM-Al10SiMg (as-printed)	-	-	-	-	-	~10	~0.4	-	
	RR350 (as-cast and aged*)	~5	-	~0.2	~1.5	~0.2	<0.1	-	<0.1	
ORNL Higher Cu ACMZ	6Cu (as-cast and aged*)	~6	-	~0.5	-	~0.2	<0.1	-	<0.1	
	7Cu (as-cast and aged*)	~7	-	~0.5	-	~0.2	<0.1	-	<0.1	
	8Cu (as-cast and aged*)	~8	-	~0.5	-	~0.2	<0.1	-	<0.1	
ORNL Printed	AM-Al-Ce-Ni-Mn**	-	~9	~1	~4	-	-	-	-	
	AM-Al-Ce-Ni-Mn-Zr (as-printed)	-	~9	~0.5	~4	~1	-	-	-	

*Aged condition: two-step heat treatments of 550 °C, 5 h solution treatment + 240 °C, 5 h aging treatment in air,

**heat-treated in air at 450 °C for 2 h

Results

Figure I.1.1.4.1 compares the typical impedance spectra of the cast Al alloys, including the two commercial alloys (319, RR350) and the three developmental alloys (6Cu, 7Cu, and 8Cu ACMZ), each in the as-cast and aged conditions, as shown in Figure I.1.1.4.1(a) and Figure I.1.1.4.1(b), respectively, in the same x and y scales in $\text{ohm}\cdot\text{cm}^2$. Overall, the impedance magnitudes decreased slightly in aged conditions for most alloys, indicating that corrosion resistance was slightly decreased after aging. In the as-cast conditions, 6Cu, 7Cu, and 8Cu ACMZ alloys exhibited larger impedances than RR350 and 319 alloys, suggesting better corrosion resistance in the former group. However, this trend was not observed in the aged alloys, where impedances of the ACMZ and commercial alloys were more mixed.

The $R_2 + R_3$ values were determined from impedance data fitting of all cast alloys, which enabled statistical comparisons of $R_2 + R_3$, using averages and standard deviations, as presented in Figure I.1.1.4.2. The data indicates the as-cast 6Cu and 7Cu ACMZ alloys had higher corrosion resistance than the other cast alloys. However, after aging, all higher Cu ACMZ alloys showed very similar $R_2 + R_3$ values. From the data comparison, it is presumed the three higher Cu ACMZ alloys, in both as-cast and aged conditions, would exhibit corrosion resistance comparable to or slightly better than the two commercial Al alloys (319 and RR350).

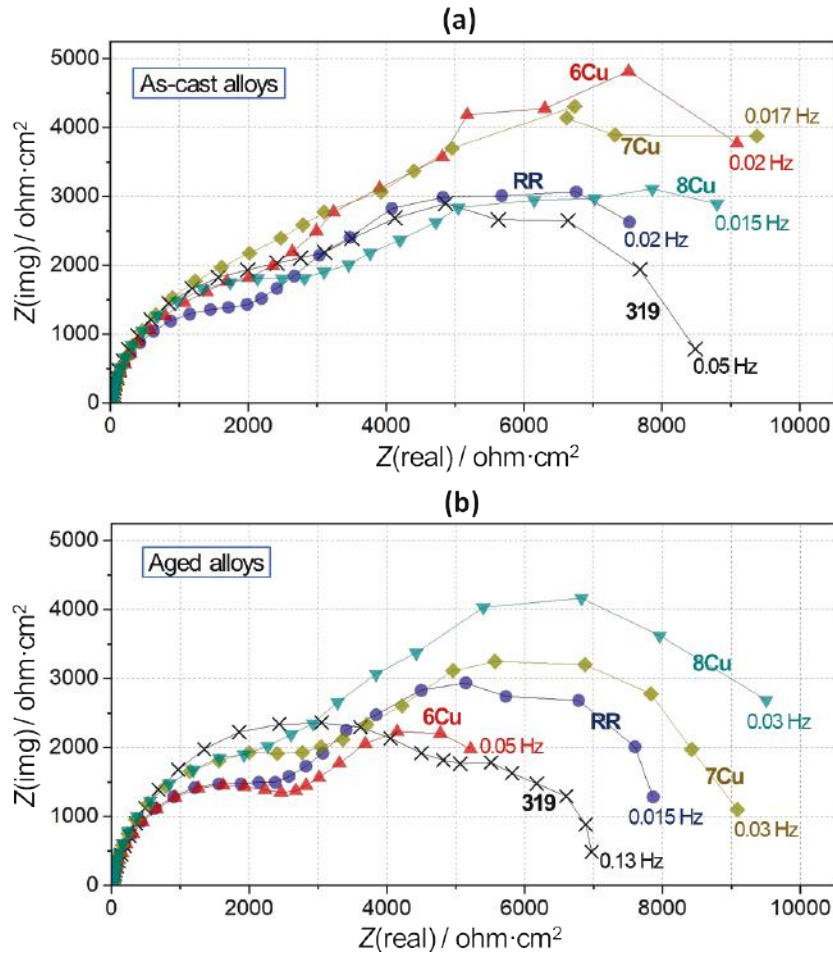


Figure I.1.1.18. Typical Nyquist impedance plots of (a) as-cast and (b) aged Al alloys in a 3.5% NaCl solution. The solution immersion time was 1 h for all measurements. Note the impedance plots with higher- $Z(\text{real})$ and $Z(\text{img})$ values suggesting higher corrosion resistance. Source: ORNL.

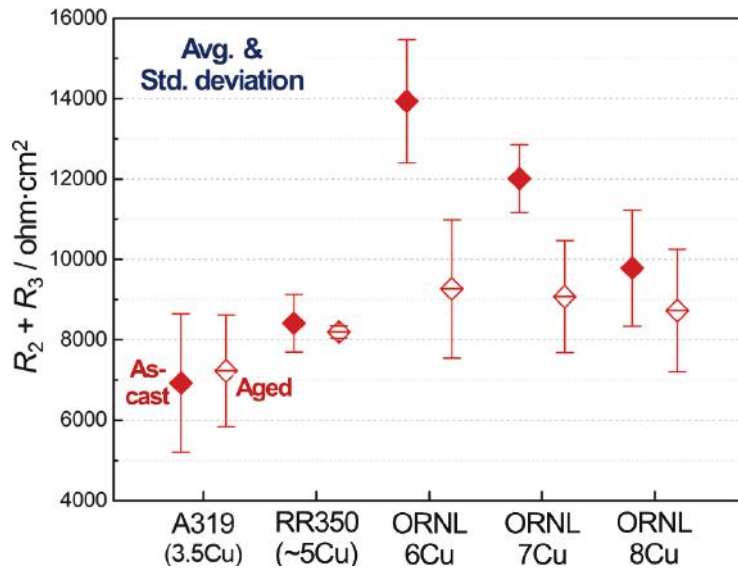


Figure I.1.1.19. Averages and standard deviations of $R_2 + R_3$ values in Al alloys in as-cast and aged conditions. Note that higher $R_2 + R_3$ values suggest higher corrosion resistance. Source: ORNL.

Figure I.1.1.4.3 shows typical impedance spectra of as-cast 319, heat-treated AM-Al-Ce-Ni-Mn, and as-printed AM-Al-Ce-Ni-Mn-Zr. The impedance magnitude was distinctively higher in AM-Al-Ce-Ni-Mn-Zr than the others, indicating superior corrosion resistance under these conditions. Comparison of typical anodic polarization curves of as-cast 319, AM-Al-Ce-Ni-Mn, and AM-Al-Ce-Ni-Mn-Zr are compared in Figure I.1.1.4.4. Pitting potential (noted as E_p in the figure), where anodic corrosion current increased sharply, was higher in AM-Al-Ce-Ni-Mn-Zr, implying the alloy was more resistant to the initiation of pitting corrosion attacks than the other two alloys. For multiple anodic polarization data, the difference of pitting and corrosion potentials ($E_p - E_{corr}$), which is defined as approximate passivity, were also compared. The corrosion potential values, without any polarization, were collected before the anodic polarizations. The greater $E_p - E_{corr}$ becomes, the higher the resistance to corrosion.

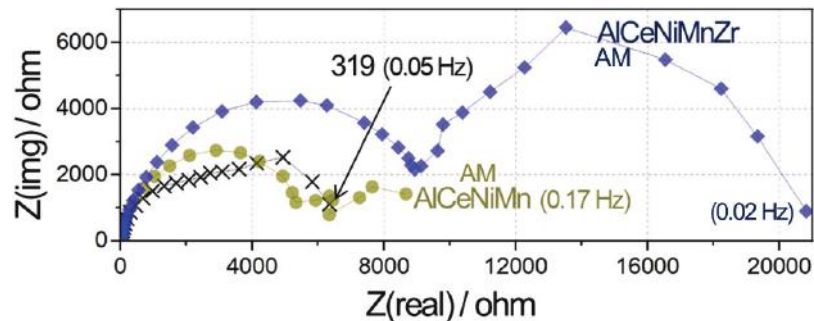


Figure I.1.1.20. Typical Nyquist impedance plots of as-cast 319, AM-Al-Ce-Ni-Mn, and AM-Al-Ce-Ni-Mn-Zr alloys in a 3.5% NaCl solution. The solution immersion time was 1 h for all measurements. Source: ORNL.

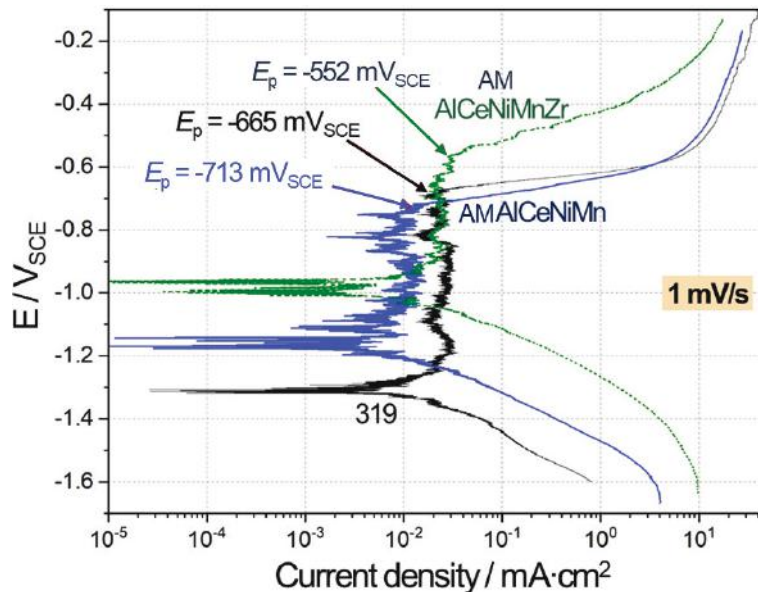


Figure I.1.1.21. Anodic polarization curves of as-cast 319, AM-Al-Ce-Ni-Mn, and AM-Al-Ce-Ni-Mn-Zr alloys in a 3.5% NaCl solution. The solution immersion time was ~ 2 h for all measurements. E_p of 319, Al-Ce-Ni-Mn, and Al-Ce-Ni-Mn-Zr are -665, -713 and -552 mV_{SCE} , respectively. Source: ORNL.

To assess two separate types of corrosion measurement data more comprehensively, $R_2 + R_3$ and $E_p - E_{corr}$ values were plotted on x and y axes, respectively, as presented in Figure I.1.1.4.5. In this plot, the upper right corner, where both $R_2 + R_3$ and $E_p - E_{corr}$ values are large, represents higher corrosion resistance. The averages and standard deviations of the four Al alloys in this plot suggest developmental AM-AlCeNiMnZr and commercial AM-Al10SiMg have higher corrosion resistance than AM-Al-Ce-Ni-Mn and as-cast 319.

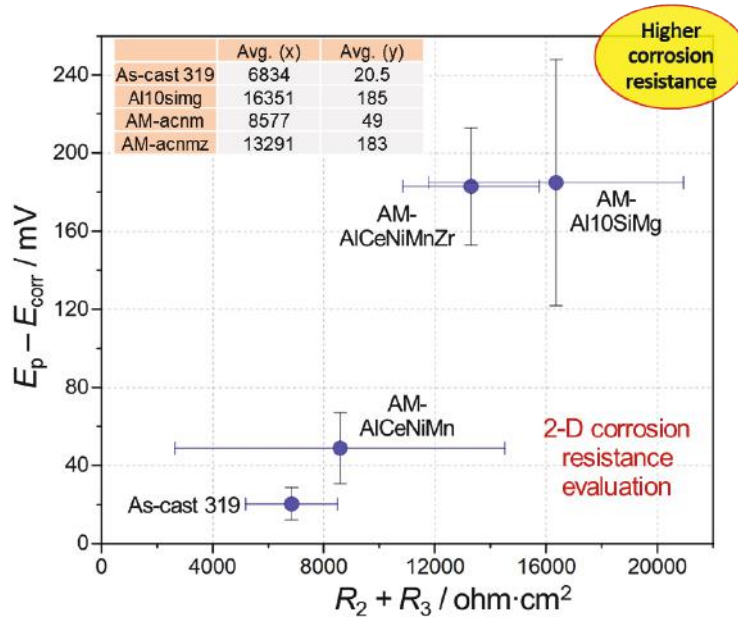


Figure I.1.1.22. Two-dimensional corrosion resistance evaluation for as-cast 319 and three AM Al alloys. Note higher x and y values would correspond to higher corrosion resistance. Source: ORNL.

Figure I.1.1.4.6 shows a SEM image of a metallographic cross-section of as-cast 319 alloy after 168 h immersion testing and reveals the deep corrosion attack after long-term testing. The attack reached a depth of at least 450 μm and the reaction products were Al-lean and O-rich as shown by the elemental maps, indicating the commercial alloy suffered quite a severe localized attack. From this SEM image and EDS elemental maps, no specific microstructural features were correlated to the path of the corrosion attack.

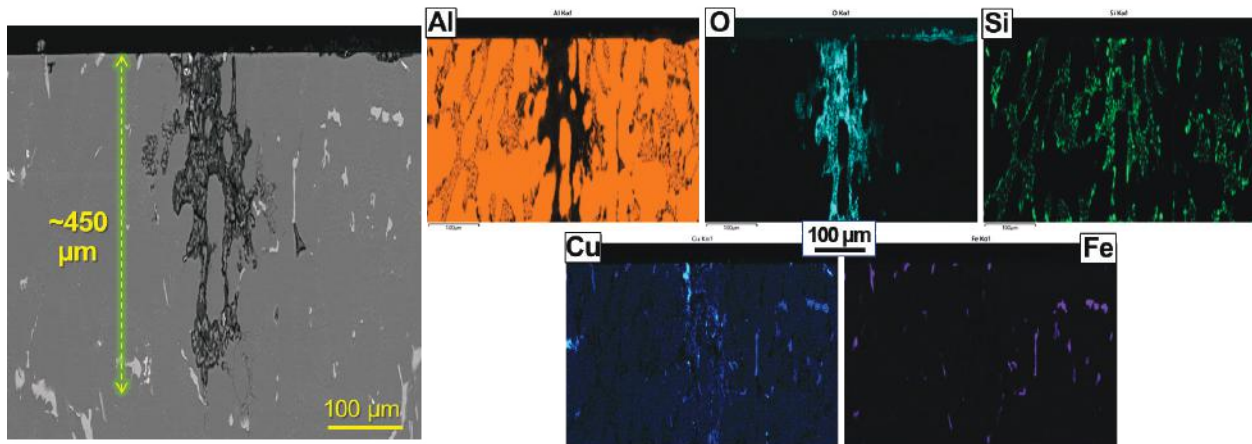


Figure I.1.1.23. Cross-sectional SEM image and EDS maps of as-cast 319 after 168 h immersion in a 3.5% NaCl solution. Source: ORNL.

Cross-sectional SEM image and EDS elemental maps for AM-Al10SiMg are presented in Figure I.1.1.4.7. Unlike the as-cast 319, the commercial AM-Al10SiMg exhibited a relatively shallow corrosion attack ($<15 \mu\text{m}$ in-depth). Other cross-sectional regions did not reveal any significant attacks in the same sample. Figure I.1.1.4.8 shows similar SEM images and EDS maps for AM-AlCeNiMnZr, which also exhibited a relatively shallow attack ($\sim 13 \mu\text{m}$ in-depth). These results indicate both of the printed Al alloys, one Al-Si based and one Al-Ce-Ni based, were more corrosion-resistant than as-cast commercial 319 in these long-term ($\sim 168 \text{ h}$) immersion tests.

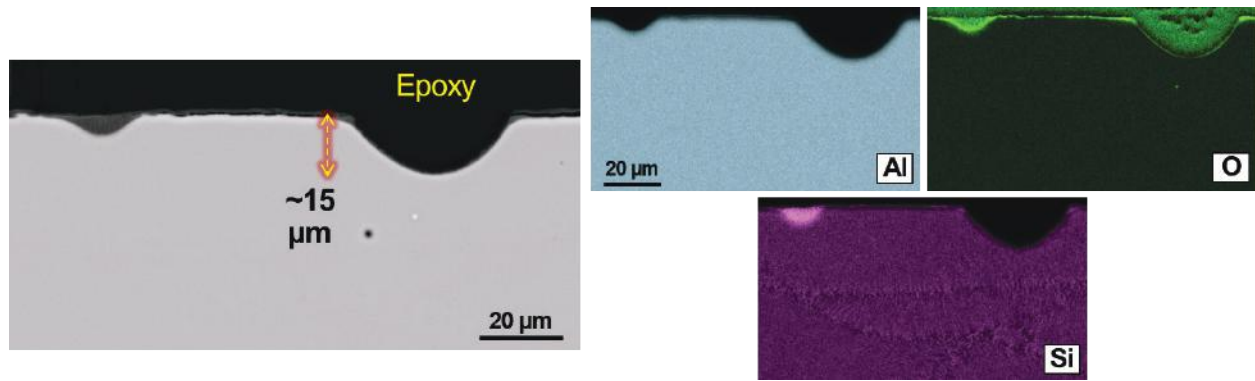


Figure I.1.1.24. Cross-sectional SEM image and EDS maps of AM-Al10SiMg after 168 h immersion in a 3.5% NaCl solution. Source: ORNL.

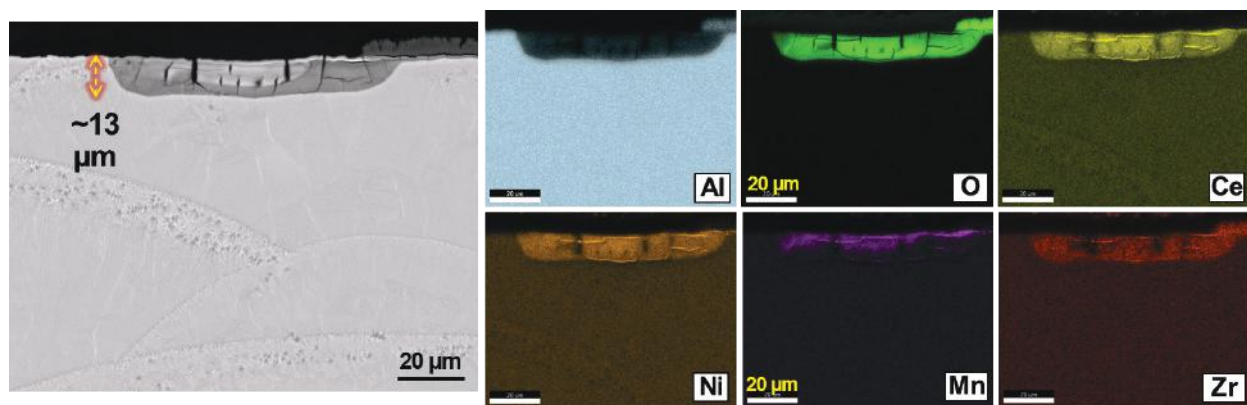


Figure I.1.1.25. Cross-sectional SEM image and EDS maps of AM-AlCeNiMnZr after 168 h immersion in a 3.5% NaCl solution. Source: ORNL.

The trends of the short-term corrosion performance data, as shown in Figure I.1.1.4.5, also indicated that both AM-Al10SiMg and AM-AlCeNiMnZr have much better corrosion resistance than as-cast 319. The long-term corrosion resistance from Figure I.1.1.4.6, Figure I.1.1.4.7, and Figure I.1.1.4.8, respectively, agrees with this short-term electrochemical data, highlighting the consistency of trends identified by the corrosion evaluation methods in this task. Each method of testing has thus far indicated corrosion resistance of the two AM Al alloys would be an improvement over the commonly used automotive cast alloy 319.

Conclusions

- In short-term electrochemical evaluation, as-cast ACMZ 6Cu and 7Cu Al alloys showed higher corrosion resistance than as-cast commercial alloys 319 and RR350. In aged conditions, however, the difference in corrosion resistance was not as prominent. In both the as-cast and aged conditions, the developmental higher Cu cast ACMZ alloys are considered to exhibit higher or at least comparable corrosion resistance, as compared to 319 and RR350.
- Corrosion evaluation from two separate types of electrochemical studies suggested higher corrosion resistance of AM-Al10SiMg and AM-AlCeNiMnZr in short-term (< 3h) corrosion exposure as compared to as-cast alloy 319.
- Long-term (~168 h) exposure caused a much deeper corrosion attack (~450 μm) in as-cast 319 than those observed in AM-Al10SiMg and AM-AlCeNiMnZr (< 15 μm depth of attack). Characterization results after long-term immersion tests agree with electrochemical evaluation data from short-term exposures.

- Both of the printed alloy families—one Al-Si based and one Al-Ce-Ni based—appear to have superior corrosion resistance to cast alloy 319, a commonly used commercial alloy for automotive applications. Although more work is necessary, these laboratory results under limited conditions suggest printed Al alloys may offer equal or improved corrosion resistance to classes of automotive Al alloys that have been deployed for decades.

Key Publications

1. Jun, J., 2022, “Task 1D-22: Fundamentals of Corrosion Behavior in Advanced LW Alloys for EV Propulsion,” PMCP VTO Mid-year Program Review, Virtual, Washington, DC, USA, 24 March 2022.
2. Jun, J., A. Shyam, J. A. Haynes, and Y. Su, 2021, “Effect of Copper Contents on Corrosion of High-Performance ACMZ Cast Aluminum Alloys,” invited oral presentation, Materials Science & Technology (MS&T) 2021, Virtual, Columbus, OH, USA, 22 October 2021.
3. Kiosidou, L., J. Srinivasan, P. J. Noell, and E. J. Schindelholz, 2022, “On the nature of critical potentials for aluminum repassivation,” Oral Presentation at 242nd ECS Meeting, Atlanta, GA, USA, 11 October 2022.

References

1. Bahl, S., X. Hu, E. Hoar, J. Cheng, J. A. Haynes, and A. Shyam, 2020, “Effect of copper content on the tensile elongation of Al-Cu-Mn-Zr alloys: Experiments and finite element simulations,” *Mater. Sci. Eng. A*, Vol. 772, Art. 138801. <https://doi.org/10.1016/j.msea.2019.138801>.

Acknowledgements

The authors thankfully acknowledge the contributions and support from A. Shyam, A. Plotkowski, S. Bahl, D. McClurg, and J. Wade at ORNL.

I.1.1.5 Task 1E. Lightweight Materials for Improved Electrical Properties (Oak Ridge National Laboratory)

Amit Shyam, Principal Investigator

Oak Ridge National Laboratory
Materials Science and Technology Division
1 Bethel Valley Rd.
Oak Ridge, TN 37830
E-mail: shyama@ornl.gov

J. Allen Haynes, PMCP Consortium Manager

Oak Ridge National Laboratory
Materials Science and Technology Division
1 Bethel Valley Rd.
Oak Ridge, TN 37830
E-mail: haynesa@ornl.gov

Jerry Gibbs, DOE Technology Development Manager

U.S. Department of Energy
E-mail: jerry.gibbs@ee.doe.gov

Start Date: November 1, 2021	End Date: September 30, 2023	
Project Funding (FY 2022): \$300,000	DOE share: \$300,000	Non-DOE share: \$0

Project Introduction

Conduction of electricity in a battery electric vehicle (BEV) is dominated by copper (Cu) components. A BEV motor itself may have more than a mile of Cu wire in the stator windings. Overall, a BEV can have hundreds of pounds of Cu in various components. Compared to Cu wires, Al wires provide a lower cost and lighter option for transportation conductors, such as wiring, stators, busbars, and connectors. At the same time, Al wires are susceptible to galvanic corrosion, non-conductive oxide formation, and creep—particularly at higher currents. This task will focus on designing Al alloy compositions with improved balance of properties in wire form as compared to Cu wires. A fundamental conflict exists between electrical and mechanical properties of wires, as microstructural features that improve one are often detrimental to the other, and vice versa. In this task, we will pursue co-optimization of the mechanical and electrical properties of Al alloys for BEV automotive and freight applications through compositional, processing, and heat-treatment innovations.

Objectives

This task will develop new Al alloy compositions with the balance of properties in wire form that make them more competitive with Cu wires. Specific objectives from the first year of this task are as follows:

- Develop Al alloy families replacing Cu for EVs applications delivering economic and weight-savings opportunities.
- Develop microstructure-electrical and -mechanical property relationships that help to guide the development of such Al alloys.

Approach

A conflict exists between the mechanical and electrical properties of Al alloys [1]. In this task, which is in Year 1, we started by identifying the microstructural features that help break the tradeoff in mechanical and electrical properties in Al alloys. Dilute binary and ternary alloys are of interest, such as Al-Zr, Al-Sn, and Al-Sn-Zr alloy systems. Fundamental understanding of the microstructure-electrical and mechanical property relationships and tradeoffs were emphasized and an alloy design framework was established. Electrical

resistivity measurement equipment was purchased and calibrated for the Al alloys of interest. Advanced computational and characterization efforts towards understanding the favorable properties of the Al-Sn-Zr alloy system—and its corresponding binary alloys—were initiated. Longer term, this task will focus on designing Al alloy compositions with improved balance of properties in wire form as compared to Cu wires for BEV applications.

Results

In the early portion of FY 2022, a new capability was established to measure electrical conductivity in Al alloys through eddy current-based instrumentation. Alloy ingots were cast for the evaluation of mechanical and electrical properties. Three alloys designated A90, A91, and A92 were cast at NanoAl, the industry collaborator to ORNL in this task. A90 is a binary Al-Zr alloy, A91 is a binary Al-Sn alloy, and A92 is a ternary Al-Sn-Zr alloy. The concentration of tin (Sn) was low at ~200 ppm by atomic concentration. All alloys were homogenized at 640°C for 24 hours, water quenched, and then a series of isochronal treatments were conducted on individual specimens for three hours each from 150°C to 550°C in 25°C increments, followed by a water quench. Following each isochronal treatment, Vickers microhardness and electrical conductivity values were measured.

Figure I.1.1.5.1 summarizes the trends in Vickers hardness, which was converted to MPa as shown in Figure I.1.1.5.1(a), and electrical conductivity, which is shown as MS/m in Figure I.1.1.5.1(b), as a function of isochronal treatment temperature. For the binary Al-Zr alloy (A90), the Vickers hardness remains nearly constant at 200 MPa up to 400°C, after which the hardness value modestly increases to 250 MPa. The Vickers hardness value in the Al-Sn binary alloy (A91) reaches a peak value of 300 MPa around 200°C and then decreases back to ~200 MPa at 500°C. The ternary Al-Sn-Zr alloy (A92) shows the most unexpected results for hardness with values remaining nearly constant near 300 MPa up to 200°C and dropping in hardness until 350°C and then a peak value of about 450 MPa at 425°C.

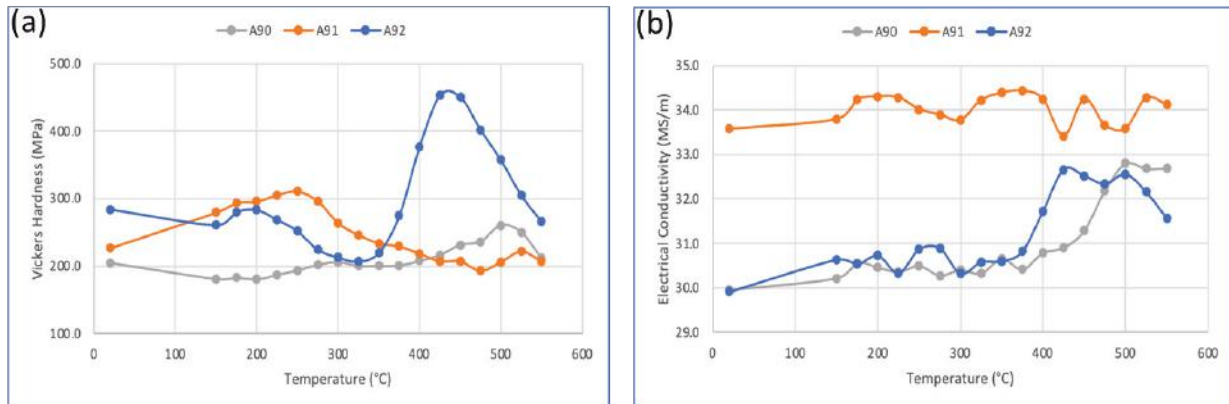


Figure I.1.1.26. Vickers microhardness and electrical conductivity as a function of isochronal treatment temperature for A90 (Al-Zr), A91 (Al-Sn), and A92 (Al-Sn-Zr) alloys. (a) Vickers hardness in MPa showing considerable strengthening from 200 ppm Sn in A91 alloy and interaction of solutes to provide additional strengthening in the Al-Sn-Zr alloy. (b) Eddy current-based electrical conductivity measurements on the same alloys under the same conditions showing an improvement in electrical conductivity for the binary Al-Sn (A91 alloy) and an increase in electrical conductivity for Al-Zr (A90 alloy) and Al-Zr-Sn (A92 alloy) above a temperature of 400 °C. Source: ORNL.

Note the two results in Figure I.1.1.5.1(a). First, the microhardness can be increased by ~100 MPa by adding 200 ppm of Sn because the A91 alloy has a peak microhardness value that is 100 MPa higher than pure Al. Second, the ternary alloy has a peak microhardness value of 450 MPa, indicating an interaction between the Zr and Sn solutes. The latter result will be explored further with a first-principles calculation-based approach. Figure I.1.1.5.1(b) shows distinct trends in the electrical conductivity measurements for the same three alloys

under the same conditions of exposure. The binary Al-Zr alloy (A90) demonstrates a monotonic increase in electrical conductivity with temperature with the rate increasing further at 400°C and the value peaking at 500°C. The ternary Al-Sn-Zr (A92) alloy showed a similar trend as the binary Al-Zr; both had a peak electrical conductivity of ~33 MS/m. The binary Al-Sn alloy (A91) showed a distinctly higher electrical conductivity value of ~34 MS/m that remained nearly constant with the isochronal treatment temperature. When mechanical and electrical properties are considered together, the peak aged ternary alloy (A92) appears to possess the best combination of properties and deserves further study to identify the microstructural features that lead to optimized properties.

SEM images for binary Al-Sn (A91) and ternary Al-Sn-Zr (A92) alloys are shown in Figure I.1.1.5.2. The top row images are for the Al-Sn alloy with different heat-treatment conditions: as-homogenized on left, 200°C isochronal heat-treatment in the middle, and 425°C isochronal heat-treatment on right. The bottom row images are for the ternary Al-Sn-Zr alloy in the same conditions. The images in Figure I.1.1.5.2 indicate the presence of large grains resulting from ingot processing. The Al-Sn alloy grain boundaries are decorated by brighter contrast—due to a heavier atomic number—particles, and/or continuous films, and chemical analysis confirmed these regions are rich in Sn. The structure of the particles also indicated incipient melting, further confirming particles rich in Sn, as it melts at ~225°C in Al, which is much lower than the homogenization treatment. This is important to understand, since such Sn-rich films at the grain boundaries are likely to embrittle the binary Al alloy. Surprisingly, the ternary alloy did not possess a conspicuous grain boundary film, although the local grain boundary areas were observed with etch pits or particle decoration. The lack of grain boundary film rich in Sn in the ternary alloy also indicates a possible chemical reaction and interaction between the Sn and Zr atoms that was indicated earlier. Finally, the reduction in grain boundary particles suggests the potential for improvement in ductility of the ternary alloy as compared to the binary alloy. Ductility measurements will be performed in FY 2023.

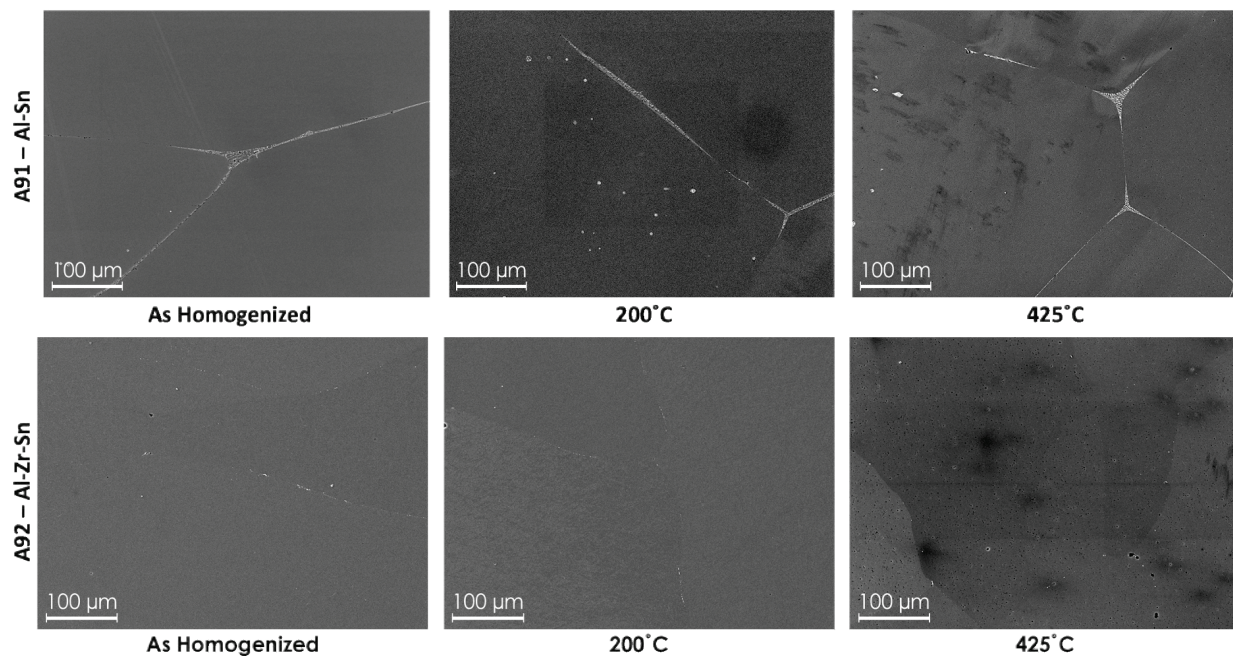


Figure I.1.1.27. SEM micrographs for the binary Al-Sn alloy (top) and ternary Al-Sn-Zr alloy (bottom). Three separate heat-treatment conditions are shown for both alloys, homogenized (left), 200°C isochronal treatment (middle), and 425°C isochronal treatment (right). Source: ORNL.

The Al-Sn binary A91 alloy was observed with High-Angle Annular Dark Field – Scanning Transmission Electron Microscopy (HAADF-STEM). As shown in Figure I.1.1.5.3, Sn-rich particles (confirmed by chemical analysis) were observed in the $\langle 001 \rangle$ orientation of the matrix after 200°C isochronal aging. The particles are likely pure Sn, are coherent with the matrix and about 2–3 nm in diameter. Such refined Sn particles explain the strengthening of the Al matrix by addition of only 200 ppm of Sn and may also explain the minimal decrease in the electrical conductivity for the Al-Sn A91 alloy, as shown in Figure I.1.1.5.1.

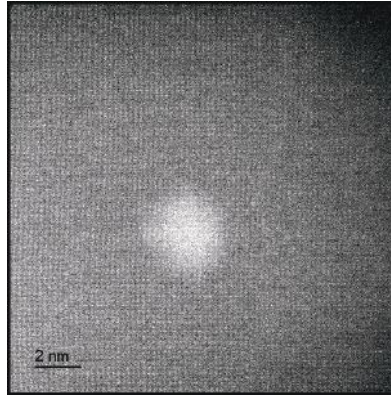


Figure I.1.1.28. HAADF-STEM image of a Sn-rich particle in Al showing clustering of Sn leading to possible beneficial effects in the properties of the Al-Sn (A91) alloy after isochronal heat-treatment at 200°C. The particles are likely pure Sn in composition. Source: ORNL.

Following homogenization at 640°C for 24 hours, aging curves were generated for the three alloys (e.g., Al-Zr or A90, Al-Sn or A91, Al-Zr-Sn or A92) at 200°C for up to 100 hours of exposure. The effect of aging time on Vickers microhardness and electrical conductivity for the three alloys is shown in Figure I.1.1.5.4. The binary Al-Sn alloy shows properties nearly comparable to the ternary alloy, likely because of rapid formation of Sn clusters reported in the HAADF-STEM imaging. At the same time, the Sn clusters are small enough to not be especially detrimental to electrical conductivity as the values remain nearly constant at 35 MS/m. The Al-Zr binary alloy performs poorly under the examined conditions with simultaneously low hardness values and electrical conductivity. The poor performance of the Al-Zr alloy is due to Zr solutes remaining in solution at 200°C and not providing effective strengthening while at the same time being detrimental for electron flow. The ternary Al-Zr-Sn alloy behaves like the binary Al-Sn alloy in terms of microhardness but like the Al-Zr alloy in terms of electrical conductivity.

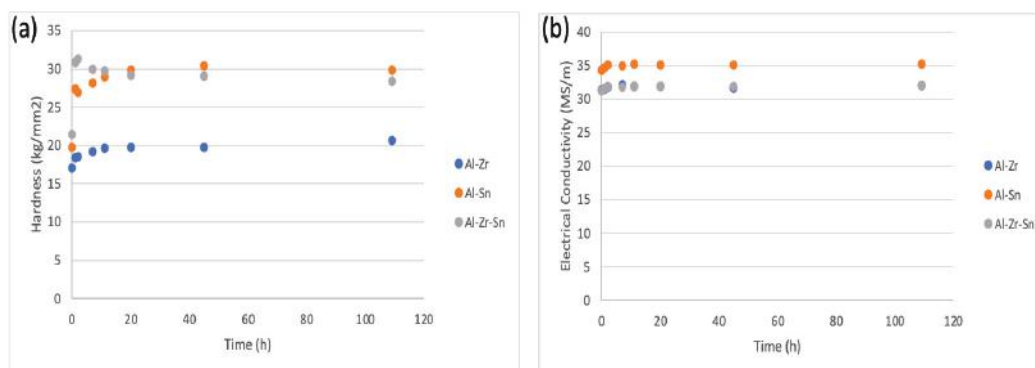


Figure I.1.1.29. Effect of aging time at 200°C on the properties of Al-Zr (A90), Al-Sn (A91), and Al-Sn-Zr (A92) alloys with (a) Vickers microhardness and (b) electrical conductivity. The property trends are consistent with isochronal trends reported earlier. The hardness values are additive with the higher hardness binary alloy (Al-Sn) having hardness closer to the ternary alloy. The conductivity values are subtractive with the lower conductivity alloy (Al-Zr) having values close to the ternary alloy. Source: ORNL.

Several results presented earlier indicate the interaction between the Zr and Sn atoms. Recently, a first-principles database has been reported for binding energies of various solutes in Al in the presence of Cu, Si, and Mg solutes with and without vacancies [2]. Density functional theory (DFT)-based binding energy calculations were performed in FY 2022 for several solutes in the presence of Zr and vacancy in Al, the results are summarized in Figure I.1.1.5.5. Note the DFT calculations were performed on the Eagle High-Performance Computing cluster at the National Renewable Energy Laboratory. Comparisons are performed for the binding energy values in the first nearest neighbor (1NN) and second nearest neighbor (2NN) positions. Results for binding of elements in the presence of Zr are significantly different from previous results reported where Cu, Si, and Mg were primary solutes. Elements in the shaded pink region of Figure I.1.1.5.5 prefer binding to Zr in the 1NN position in the presence of a vacancy. Elements in the shaded light green region of Figure I.1.1.5.5 prefer the 2NN position and the $L1_2$ structure (or Al_3X) forming elements have a strong preference for being in the 2NN position with Zr in the presence of a vacancy (e.g., Zr, Ti). Sn and Zr strongly prefer interacting in the 1NN position based on the binding energy calculations. The presented results provide a fundamental basis for possible interaction between Zr and Sn atoms in Al in the presence of vacancies that result from homogenization and such interactions will be explored further in FY 2023 through advanced characterization and computational techniques.

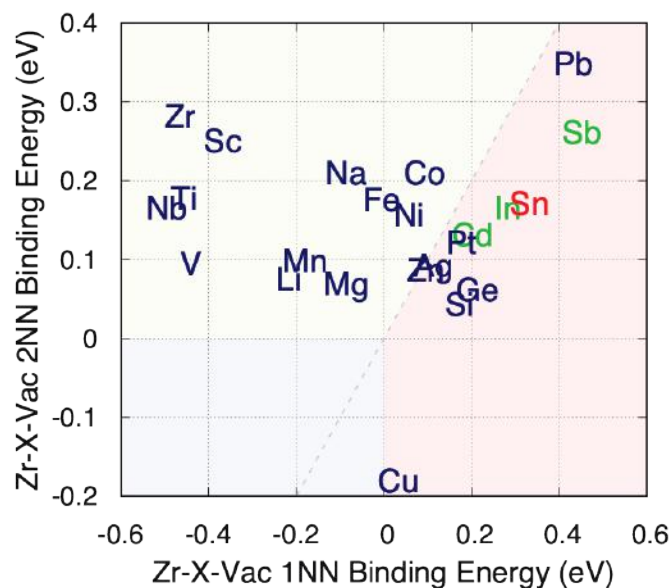


Figure I.1.1.30. DFT-based binding energy calculations for Zr-X-vacancy in Al, where X represents the elements shown. 1NN and 2NN refer to first and second nearest neighbor positions, respectively. Elements in the shaded pink region prefer binding to Zr in the first nearest neighbor position in the presence of a vacancy. Elements in the shaded light green region prefer the 2NN position, and the $L1_2$ phase forming elements have a strong preference for being in the 2NN position with Zr in the presence of a vacancy. Sn and Zr strongly prefer interacting in the 1NN position based on these binding energy calculations. Source: ORNL.

Conclusions

- Dilute Al-Zr, Al-Sn, and Al-Zr-Sn alloy ingots were fabricated and homogenized to study the isochronal and isothermal evolution of Vickers microhardness and electrical conductivity of these cast alloys.
- It was demonstrated that Sn atoms are particularly beneficial for strengthening Al on a per atom basis, and the addition of Sn solute atoms led to only a marginal decrease in electrical conductivity of the alloys, a significant result. Sn atoms formed small clusters upon aging at an intermediate temperature of 200°C and these were likely the microstructural constituent that provided beneficial electrical and mechanical properties.

- The ternary Al-Zr-Sn alloy showed an outstanding balance of electrical and mechanical properties following heat-treatment at 425°C. Sn and Zr atoms interact strongly with each other according to DFT calculations performed in this study. This interaction is hypothesized to be the reason for improved mechanical and electrical response of the ternary Al-Sn-Zr alloy.

References

1. Wang, Y., L. Zhu, G. Niu, and J. Mao, 2021, “Conductive Al alloys: The contradiction between strength and electrical conductivity,” *Adv. Eng. Mater.*, Vol. 23, No. 5, Art. 2001249. <https://doi.org/10.1002/adem.202001249>.
2. Peng, J., S. Bahl, A. Shyam, J. A. Haynes, and D. Shin, 2020, “Solute-vacancy clustering in aluminum,” *Acta Mater.*, Vol. 196, pp. 747–758. <https://doi.org/10.1016/j.actamat.2020.06.062>.

Acknowledgements

The authors thankfully acknowledge the contributions of N. Vo from NanoAl (now a part of Steel Dynamics, LLC). In addition, D. Shin, A. Haynes, J. Meier, L. Allard, S. Bahl, and D. McClurg of ORNL are acknowledged for their contributions to this effort as well.

I.1.1.6 Task 1G. Fundamentals of Thermal Properties in Lightweight Alloys for Electric Vehicle Propulsion (Oak Ridge National Laboratory)

Dongwon Shin, Principal Investigator

Oak Ridge National Laboratory
Materials Science and Technology Division
1 Bethel Valley Rd.
Oak Ridge, TN 37830
E-mail: shind@ornl.gov

J. Allen Haynes, PMCP Consortium Manager

Oak Ridge National Laboratory
Materials Science and Technology Division
1 Bethel Valley Rd.
Oak Ridge, TN 37830
E-mail: haynesa@ornl.gov

Jerry Gibbs, DOE Technology Development Manager

U.S. Department of Energy
E-mail: jerry.gibbs@ee.doe.gov

Start Date: November 1, 2021	End Date: September 30, 2023	
Project Funding (FY 2022): \$285,000	DOE share: \$285,000	Non-DOE share: \$0

Project Introduction

This task aims to achieve optimal thermal conductivities of cast lightweight alloys for BEVs via heat-treatment processes while maintaining/exceeding mechanical properties targets. Chill casting was used as a surrogate fabrication method for die-casting, which is a process currently used for manufacturing numerous housing and heat transfer components for BEVs. Various heat-treatment routes from the design of experiments approach are being performed in a (semi) high-throughput manner within the context of data analytics. Electrical conductivities of heat-treated samples were measured as a surrogate property to thermal conductivity. The hardness of all the samples is being measured to quickly screen mechanical properties. Machine-learning (ML) models are being trained to predict electrical conductivities and hardness of aluminum (Al) alloys as a function of heat-treatment. Heat-treatment conditions will be virtually optimized to maximize electrical conductivities while maintaining mechanical properties by rapidly interrogating the digital-twin. Finally, designed hypothetical heat-treatment conditions are being experimentally validated.

Objectives

This project aims to establish a workflow using ICME that can be used to optimize heat-treatment conditions of cast lightweight alloys to improve thermal conductivities while maintaining/exceeding target mechanical properties.

Approach

An experimental investigation was conducted to reveal the effect of various process parameters on microhardness and thermal conductivity. In particular, we focused on three process parameters: cooling rate in the mold during casting, heat-treatment temperature, and duration after casting. To simultaneously vary the cooling rate during casting in each heat, we used a low carbon steel step mold with four thicknesses of 4, 10, 20, and 40 mm. The unique thickness of each step determines the cooling rate during casting; thus, four different cooling rates were investigated from one cast ingot. A380 alloy was used for these casting experiments. The chemistry of A380 is presented in Table I.1.1.6.1.

Table I.1.1.6.1. Nominal Composition (wt.%) of A380 Alloy Used in this Task.

Al	Cu	Mg	Fe	Sn	Ni	Zn	Mn	Si
82.25	3.5	0.1	1.3	0.35	0.5	3	0.5	8.5

After casting and heat-treatment, all samples were subjected to physical property measurement (i.e., hardness, electrical conductivity). Vickers hardness with 5 kgf load was used to measure microhardness. The eddy current method was used for electrical conductivity measurements. It should be noted that electrical conductivity measurement is often used as a surrogate for thermal conductivity because it is much simpler to measure and the two properties in a metal are typically proportional to each other, according to Wiedemann-Franz law [1]. The overall workflow of the present study is presented in Figure I.1.1.6.1.

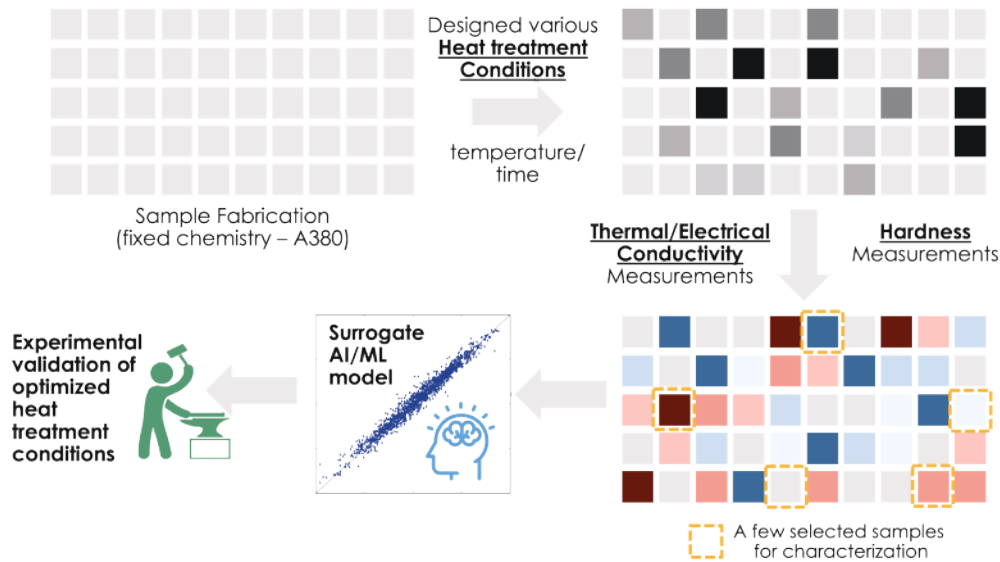


Figure I.1.1.31. A schematic of overall workflow to predict thermal properties in lightweight alloys. Source: ORNL.

Results

Different cooling rates contribute to differences in key microstructure features such as micro-segregation and grain and/or intermetallic particle size. Pure Al was cast with a step mold to investigate the relationship between cooling rate and grain size without micro-segregation. Figure I.1.1.6.2 shows the schematic diagram of the step mold used for this task. The step mold was designed to represent the various casting conditions used for BEV component suppliers, such as multiple cooling rates and thicknesses of molds. Hence, the knowledge obtained in this task can be applied to the industry sector regarding trends in physical properties and microstructure evolutions. The electron backscattered diffraction texture analysis of a pure Al cast ingot is presented on the right side of Figure I.1.1.6.2. Roman numerals (e.g., i, ii, iii, iv) correspond to the 4, 10, 20, and 40 mm step thicknesses, respectively. The difference in thicknesses of the steps gives rise to distinct differences in cooling rate. Thinner thickness induces a higher cooling rate. Neighboring colors present different grains with differing orientation, so the grain size differences are clearly visible. The average grain size for each step was analyzed. The results show average grain size decreases with a higher cooling rate, and grains were elongated in the general direction of heat flow to the mold wall during cooling.

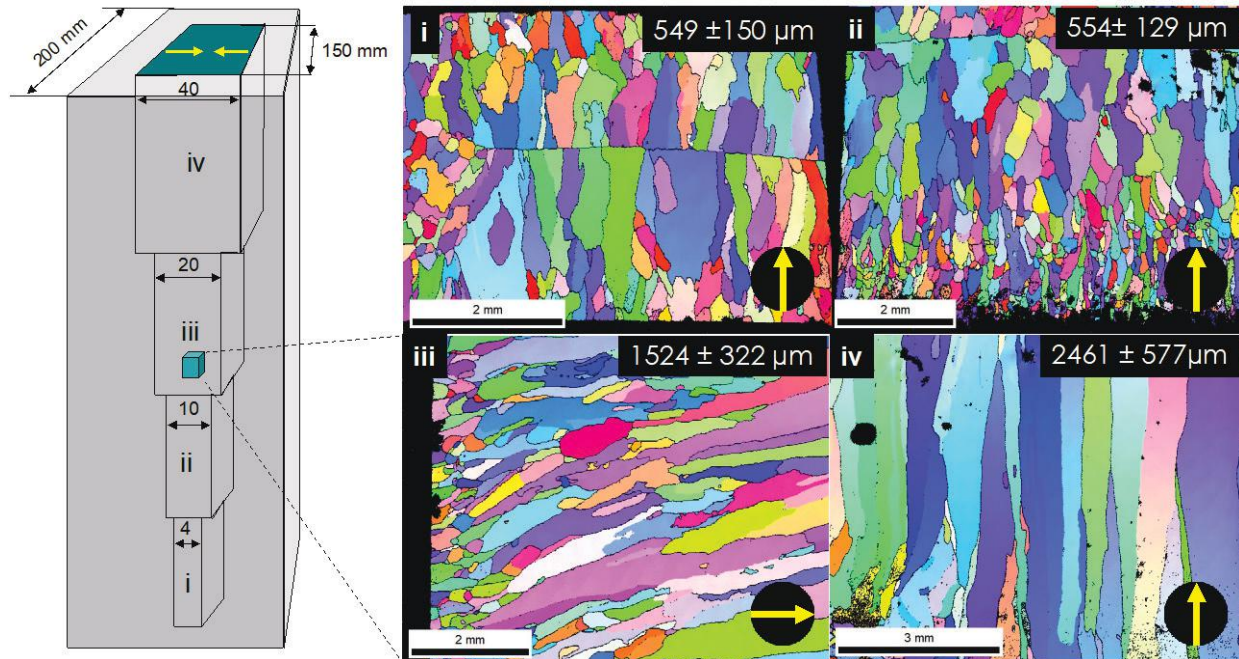


Figure I.1.1.32. Schematic diagram of the step mold and the microstructure of cast pure Al after cooling within each step. The yellow arrow indicates the cooling direction of each sample. Average grain size for each step is denoted at the top right corner of the micrograph. Source: ORNL.

The A380 alloy, which is a commercial alloy commonly used for die-casting of non-structural vehicle components, was prepared by casting into the same step mold to investigate the effect of various cooling rates on microhardness and electrical conductivity. Casting was conducted by melting and homogenizing the A380 alloy melt at 680°C (i.e., 50°C above the liquidus temperature). The mold was preheated at 70°C to reduce porosity formation during casting. Figure I.1.1.6.3(a) shows the temperature profile of each step during casting. The solidification rates for 10, 20, and 40 mm steps were analyzed as 9.0, 3.5, and 1.1°C/s. These results confirm what was anticipated; the step thickness determines the cooling rate (i.e., a faster cooling rate with a thinner step thickness). The solidification rate of 4 mm step could not be analyzed due to the limits of thermocouple response time.

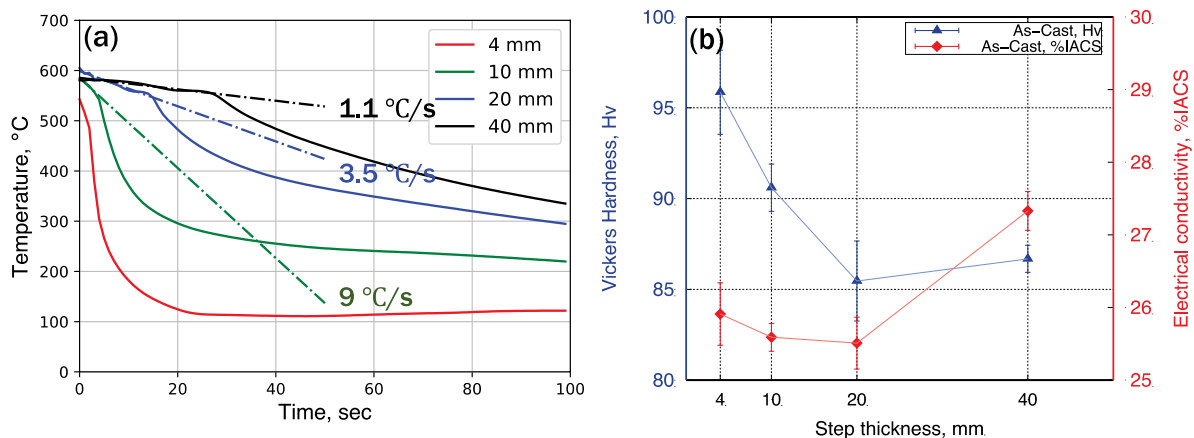


Figure I.1.1.33. Thermal and physical properties of as-cast A380 alloys: (a) thermal profiles of various step thicknesses during casting, and (b) microhardness and relative electrical conductivity of specimens cast in various step thicknesses. IACS = International Annealed Copper Standard. Source: ORNL.

After casting, specimens were prepared from each step by electrical discharge machining to measure microhardness and electrical conductivity. The effect of various step sizes on the A380 physical properties is presented in Figure I.1.1.6.3(b). Microhardness decreases by more than 10 H_v (98 MPa) with increasing step thickness from 4 to 20 mm; however, the change in electrical conductivity is insignificant. On the other hand, further increasing the step thickness does not reduce the hardness, whereas a noticeable increase (2% IACS) of electrical conductivity was observed. The result indicates it is indispensable to tradeoff microhardness for the increase in thermal conductivity when the cooling rate is the only controlling factor. To improve the thermal conductivity of the alloy while maintaining microhardness, an additional process such as heat-treatment is essential.

Various heat treatments were performed to affect the microstructure and physical properties of the A380 alloy specimens. Table I.1.1.6.2 summarizes the heat-treatment processes used in this task. Eighteen different heat-treatment conditions were applied to specimens cut from the 10, 20, and 40 mm steps so that they had near identical mold cooling rates for each set of specimens.

Table I.1.1.6.2. T5 Heat-Treatment Schedule for Cast Alloy 380 in this Task

Step Thickness, mm	Duration, h	Temperature, °C	Step Thickness, mm	Duration, h	Temperature, °C
4	0.5	150, 250	20	0.5	100, 150, 200, 250
	1.5	150, 250		1.5	100, 150, 200, 250
	5	530		3	100, 150, 200, 250
	6	150, 250		5	530
				6	100, 150, 200, 250
10	0.5	100, 150, 200, 250	40	0.5	100, 150, 200, 250
	1.5	100, 150, 200, 250		1.5	100, 150, 200, 250
	3	100, 150, 200, 250		3	100, 150, 200, 250
	5	530		5	530
	6	100, 150, 200, 250		6	100, 150, 200, 250

Figure I.1.1.6.4(a) shows the microhardness data of A380 after being heat-treated for 3 hours over various temperatures. The samples cast in 10, 20, and 40 mm thicknesses are presented in blue, red, and green. At each aging temperature, the sample cast in the thinner step (e.g., 10 mm) has higher hardness values than those in the thicker steps (e.g., 20 mm). The electrical conductivity data in Figure I.1.1.6.4(b) presents an opposite trend. The data in blue (i.e., 10 mm) appears to have the lowest electrical conductivity over the full temperature range. This result reveals the tradeoff effect between microhardness and electrical conductivity, related to the varying cooling rates during casting, remains even after 3 hours of heat-treatment. In addition, Figure I.1.1.6.4 also presents the possibility of minimizing the tradeoff effect between microhardness and electrical conductivity by using an optimum heat-treatment condition. As can be seen in Figure I.1.1.6.4(a), peak hardness for cast A380 appears at the aging temperature of 200°C for each step thickness. Electrical conductivity at 200°C, as given in Figure I.1.1.6.4(b), is also high compared to those at 100 and 150°C. These experimental data suggest the potential of co-optimizing microhardness and electrical conductivity by searching for optimum heat-treatment conditions for specific alloy compositions and casting methods. Correlation between a processing parameter and a physical property was performed to quantitatively analyze the effect of processing parameters on physical properties with an open-source data analytics front-end code called ASCENDS [2].

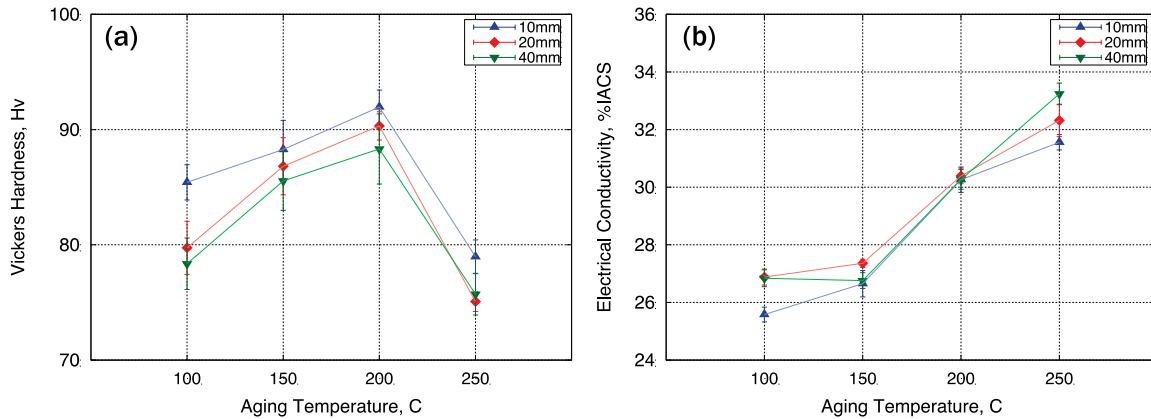


Figure I.1.1.34. Effect of heat-treatment temperature on (a) microhardness and (b) electrical conductivity. Hv is Vickers hardness unit ($1 \text{ Hv} \cong 9.8 \text{ MPa}$) and %ACS is the relative electrical conductivity with respect to anneal copper as standard. Presented data only contain isochronal heat-treatment (i.e., after 3 hours). Source: ORNL.

Pearson Correlation Coefficient (PCC) was used for the correlation analysis as it measures both the strength and direction of linear relations. Correlation analysis results are presented in Figure I.1.1.6.5(a). The step thickness shows a negative correlation relation with microhardness. The result is consistent with the qualitative analysis with as-cast samples, where a thinner step yields higher microhardness. Moreover, the strong negative PCC strength in Figure I.1.1.6.5(a) indicates the casting effects remain even after various heat-treatment processes. Electrical conductivity shows a strong positive relation with heat-treatment temperature. This trend is also consistent with isochronal data presented in Figure I.1.1.6.4(b). Based on the experimental electrical conductivity measurement, a preliminary ML model was trained using the Random Forest algorithm. The training results are presented in Figure I.1.1.6.5(b). Relatively high accuracy ($R^2=0.859$) was achieved by using only three input features: step thickness, heat-treatment temperature, and duration. The preliminary result shows the feasibility of using ML models to search for ideal heat-treatment conditions to maximize electrical conductivities of diecast Al alloys, while still maintaining adequate mechanical properties.

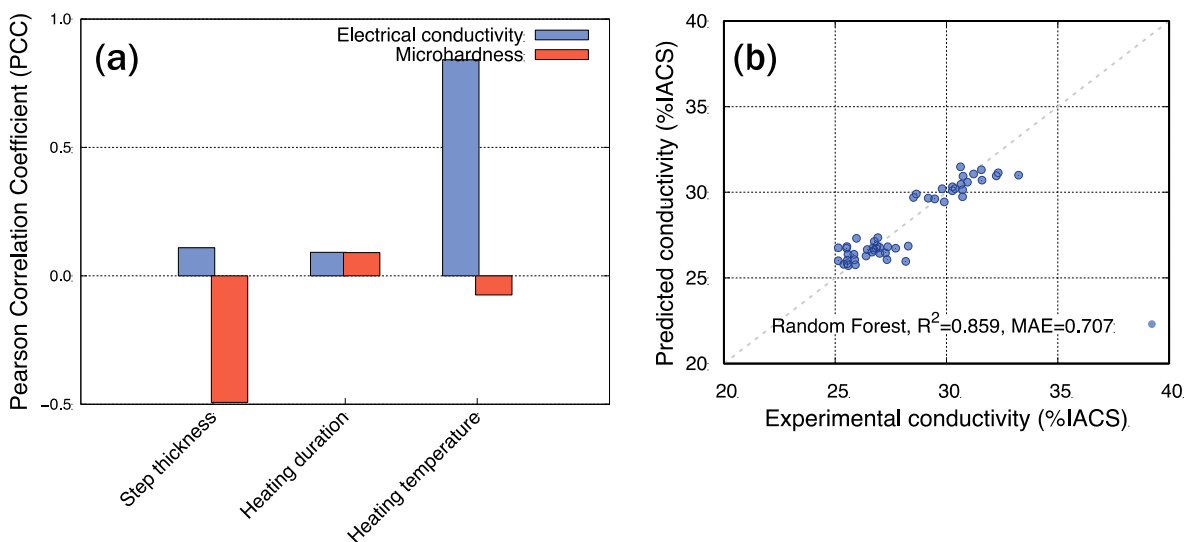


Figure I.1.1.35. Quantitative analysis of experimental data and ML modeling: (a) correlation analysis between process parameters and physical properties, and (b) training result of ML models for predicting electrical conductivity. Source: ORNL.

Conclusions

This experimental investigation was carried out to reveal the effect of processing parameters (i.e., step thickness, heat-treatment duration, and temperature) on physical properties (i.e., microhardness and electrical conductivity) of pure cast Al and a commercial cast Al alloy. Quantitative analysis based on PCC showed mold step thickness during casting yields a substantial effect on microhardness, while the impact is insignificant on electrical conductivity. On the other hand, heat-treatment temperature is the highest correlated factor for electrical conductivity. The difference in correlation strength between microhardness and electrical conductivity with a key processing parameter such as heat-treatment indicates the possibility of improving electrical conductivities further while maintaining mechanical properties. Moreover, the high accuracy of the preliminary ML training results supports the feasibility of using a digital-twin approach as a surrogate for fabrication processes. Scientific features such as equilibrium phase fractions and compositions will be considered as input features to couple physics in the training of future ML models. Experiments with other commercial diecast alloy compositions, such as A383 and Aural 5, will be conducted in FY 2023.

References

1. Kittel, C., and P. McEuen, 1996, *Introduction to Solid-State Physics. Eighth Edition*. Wiley, New York, NY, USA.
2. Lee, S., J. Peng, A. Williams, and D. Shin, 2020, “ASCENDS: Advanced data SCiENce toolkit for Non-Data Scientists,” *J. Open-Source Softw.*, Vol. 5, No. 46, Art. 1656. <https://doi.org/10.21105/joss.01656>.

Acknowledgements

The authors would like to thank K. Hanson, T. Muth, and H. Wang of ORNL for contributing to the experimental work for this project.

I.1.1.7 Task 1H. Hybrid Dispersion Strengthened Aluminum Matrix Composites for Higher Efficiency Electric Vehicle Powertrains: Cost-Effective Lightweight Alloys for Electric Vehicle Propulsion (Pacific Northwest National Laboratory)

Mert Efe, Principal Investigator

Pacific Northwest National Laboratory
902 Battelle Blvd.
Richland, WA, 99352
E-mail: mert.efc@pnnl.gov

J. Allen Haynes, PMCP Consortium Manager

Oak Ridge National Laboratory
Materials Science and Technology Division
1 Bethel Valley Rd.
Oak Ridge, TN 37830
E-mail: haynesa@ornl.gov

Jerry Gibbs, DOE Technology Development Manager

U.S. Department of Energy
E-mail: jerry.gibbs@ee.doe.gov

Start Date: November 1, 2021	End Date: September 30, 2023	
Project Funding (FY 2022): \$330,000	DOE share: \$330,000	Non-DOE share: \$0

Project Introduction

Al MMCs offer several advantages in powertrain applications compared to their cast iron or steel counterparts. Weight-savings—particularly the reduction of unsprung weight—and the mass-compounding effect on adjacent components, such as suspension arms and springs with lighter designs, are among the most significant benefits. Lower wear and corrosion rates are also possible with Al MMCs. Despite these advantages, commercial applications of Al composites in internal combustion engine vehicle powertrains have been very limited [1]. The higher cost of materials and processing, difficulty in machining, non-uniform microstructures, higher heat transfer to the adjacent components, and limited strength have been the challenges limiting the widespread application of MMCs [1, 2].

The automotive landscape has radically changed in recent years with the dawn of EVs. In a modern EV powertrain, the differential/transmission element is the second-heaviest component after the motors and inverters; and the brake system is the fourth heaviest after the wheels and tires. Forty percent of weight-savings is possible when steel and cast iron parts in these components are replaced by Al-MMC parts. This could translate into ~ 16 miles (26 km) range increase in a typical 2-ton, 350-mile (1800 kg, 560 km) range EV, assuming 10% weight-savings correspond to 7% increase in range [3]. Moreover, lower wear and corrosion rates of Al-MMC brake rotors may reduce non-exhaust particle emissions from the brake system, which constitutes 59% of road particulate matter emissions [4]. The lower corrosion rate of Al also correlates well with the longer maintenance interval of an EV, as-cast-iron brake rotors are prone to rusting. In addition, energy harvesting in electric/hybrid vehicle operation decreases the amount of energy that must be dissipated by the mechanical brakes by as much as 40%. This can allow for much lower brake temperatures and enable the usage of Al MMCs. Benefits of Al alloys and composites in EV powertrains are also supported by recent interest from automotive industry through multiple research studies and applications [2, 5, 6].

This project addresses the previous challenges associated with Al MMCs and investigates sustainable, lower cost MMCs with matching performance to cast iron or steels. Titanium diboride (TiB₂) is chosen as the reinforcement particle for its lower cost and better wettability with an Al matrix. TiB₂ has been used as a grain refiner of Al alloys, which potentially enables recyclability of Al-TiB₂ composites as grain refiner master alloys. Lower cost is also achieved by novel, near-net shape-processing routes, where compositing of nano- and micron-sized TiB₂ particles into the Al matrix and shaping of the component occurs simultaneously.

Objectives

The two main objectives of this project are:

1. Developing a hybrid-Al-MMC containing micron-sized TiB₂ particles for wear resistance and sub-micron-sized TiB₂ particles for strengthening.
2. Developing a processing method to reinforce the outer layer of the composite with the micron-sized particles while maintaining a uniform distribution of sub-micron-sized particles in the matrix.

While composites containing either micron- or nano-sized particulate reinforcements have been previously demonstrated and are well-established [1, 7], the novelty and uniqueness of this project is in the hybrid composite approach containing multiple particle types, where the size of the particulates depend on the function at a given location in the composite part. The compositing processes are also novel in achieving final shape of the components while maintaining the desired microstructure.

Approach

The two main objectives of this project are:

1. Melting and casting route for cast Al-MMC (liquid-phase processing) to replace cast iron in applications such as brake discs.
2. Solid-phase processing route for wrought Al-MMC to replace steels in high-strength applications such as gears and electric motor rotors and stators.

To demonstrate the potential of MMCs, an *in-situ*, hybrid-Al composite brake rotor will be produced by combining stir-and-squeeze casting techniques, and the wear rates will be benchmarked with cast iron. A hybrid-Al composite gear will be produced by combining friction consolidation and forging of Al alloy powder and TiB₂ powder, and the strength improvements will be reported.

In FY 2022, the cast composite was produced by halide salt reactions with molten Al, which is a well-known process for the *in-situ* formation of sub-micron-sized TiB₂ particles inside an Al matrix [7]. The Al A206 alloy was selected as the matrix for its high-temperature strength. The alloy was melted in a clay-graphite crucible coated with zirconia, and the melt was covered with a continuous flow of argon. Temperature was brought to 850°C, and then a homogenous mixture of pre-heated potassium hexafluoro titanate salt and potassium tetrafluoroborate halide salts were added slowly to the melt. The melt was continuously stirred with a graphite stir rod and impeller coated with zirconia for one hour just below the surface of the molten metal (stirring speed was determined by the appearance of the melt and was set as high as possible without causing a vortex effect—around 120 rpm). Stirring started one minute prior to adding the salts and continued throughout the reaction. After one hour reaction time, the liquid salt was poured off and the solid dross was skimmed. The MMC melt was then cast through a 15 pores per square inch (ppi) filter, into an either pre-heated graphite mold or squeeze cast into a disc-shaped steel mold at 90 MPa pressure.

For the solid-phase processing route, high-strength AA7075-TiB₂ composite billet was produced via friction consolidation and the near-net shape composite gear was produced via friction stir forging. Alloy 7075 was selected for its high RT strength. The fabrication process of AA7075-TiB₂ composite billet via friction consolidation is shown in Figure I.1.1.7.1. At first, 12 non-through holes were drilled in an AA7075 billet and filled with compacted TiB₂ powders. Then, this precursor billet was placed in a billet sleeve and processed via friction consolidation. A scroll-faced H-13 tool steel rotating friction consolidation die was pushed onto the

billet to generate heat and plastic deformation. The hot billet was plasticized under the rotating die while the added TiB_2 powder was stirred and dispersed through the AA7075 matrix.

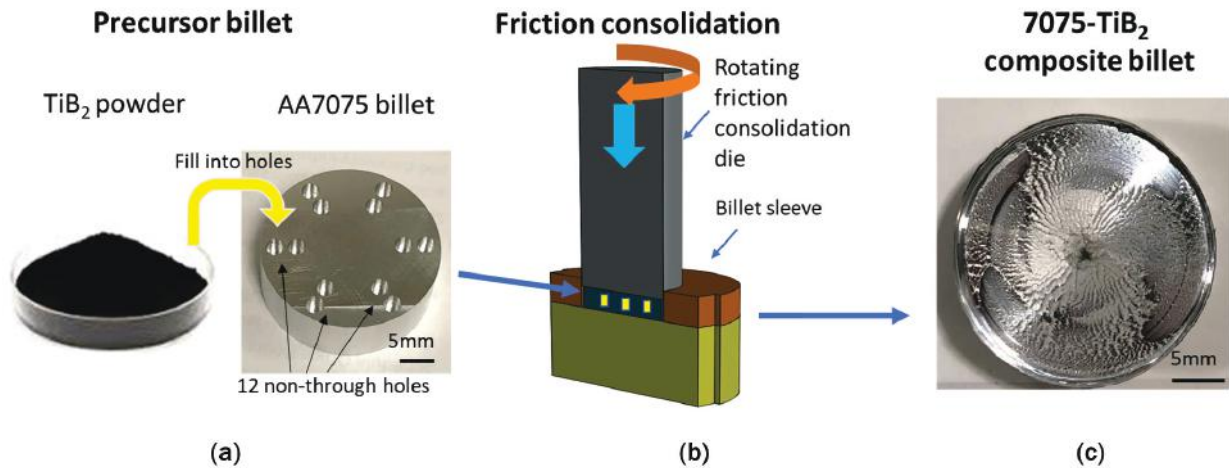


Figure I.1.1.36. Fabrication of AA7075- TiB_2 composite billet via friction consolidation. (a) Precursor billet made from AA7075 billets and TiB_2 powder, (b) illustration of friction consolidation process, and (c) AA7075- TiB_2 composite billet. Source: PNNL.

Figure I.1.1.7.2(a) illustrates step-by-step friction stir forging (FSF) process of making a gear. Process initiates with inserting a solid billet in a hollow die (14, 8, or 6 teeth) then clamped it properly in the work deck followed by plunging and forging to the desired shape. For the composite gear, AA5083 alloy was used as the matrix for the initial trials. The 5083- TiB_2 composite billet was first obtained by friction consolidation of the powders and then friction forged in billet form with a 32 mm diameter and 21 mm height, as shown in Figure I.1.1.7.2(b). The forging process used friction stir welding tool made of hardened H13 tool steel that consists of flat shoulder (32 mm diameter) and three flats-threaded pin (19 mm diameter). FSF work performed in position control mode in an ultra-high-precision friction stir welding machine.

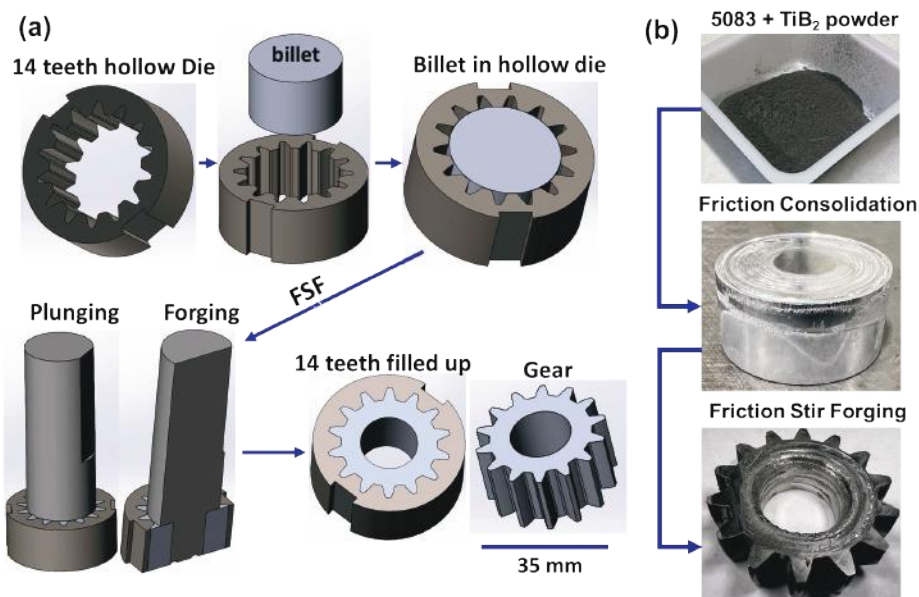


Figure I.1.1.37. (a) Schematic of step-by-step FSF process and (b) combined friction consolidation and friction stir forging for the fabrication of the composite gear. Source: PNNL.

Results

The halide salt reaction with molten Al route was successful in producing *in-situ* A206-TiB₂ composites. Figure I.1.1.7.3 compares the microstructures of 5 vol.% and 10 vol.% A206-TiB₂ composites obtained by SEM. Porosity is minimal in both composites. The 5 vol.% composite had a lower solidification rate due to the gravity casting into the graphite mold. The lower cooling rate results in larger grain size and accumulation of TiB₂ and other phases to the grain boundaries. The 10 vol.% composite, on the other hand, has much smaller grain size due to the squeeze casting and faster solidification rate. The distribution of TiB₂ and other phases appear to be more uniform, however it contains significantly higher fraction of reaction by-products and needle-like Al₃Ti intermetallics confirmed by EDS performed in SEM. The 10 vol.% composite had higher viscosity due its higher salt content (3:1 volume ratio of salts to molten metal) and it was challenging to filter and skim the molten material.

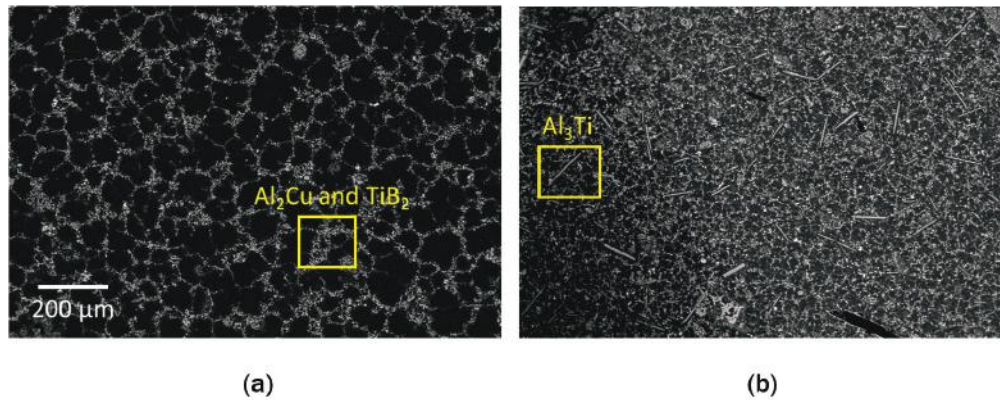


Figure I.1.1.38. SEM images of the *in-situ* composites: (a) 5 vol.% gravity cast and (b) 10 vol.% squeeze cast. Source: PNNL.

Figure I.1.1.7.4 shows high-magnification SEM images of the *in-situ* composites. Average TiB₂ particle size in both composites is sub-micrometer, yet 10 vol.% composite has slightly smaller TiB₂ particles. This is likely due to the different salt content, stir casting parameters, and solidification rates. Distribution of TiB₂ particles is more homogeneous in the 10 vol.% composite, whereas grain interiors are almost free of TiB₂ particles in the 5 vol.% composite. Both composites have Al₂Cu precipitates at the grain boundaries, typical to A206 alloy and its high copper content. FY 2023 work will focus on addition of micron-sized particles into the *in-situ* composites, squeeze casting them into the brake rotor shape, and testing of the wear properties in PNNL's brake tester.

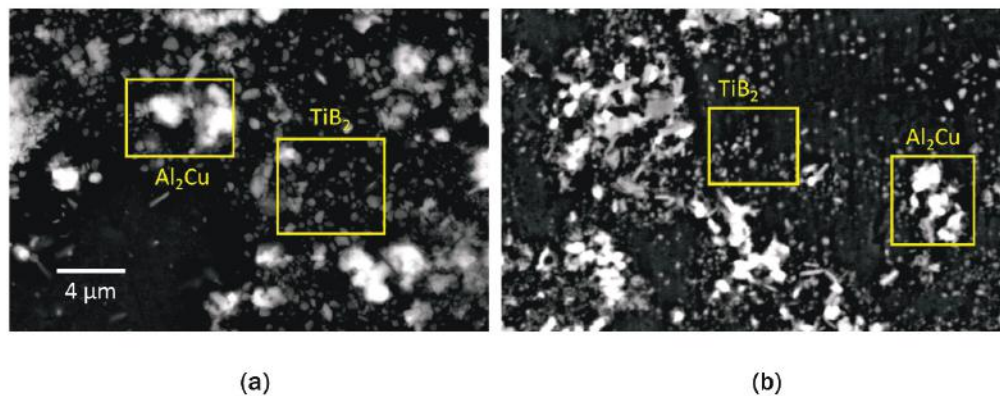


Figure I.1.1.39. High-magnification SEM images of the *in-situ* composites: (a) 5 vol.% gravity cast and (b) 10 vol.% squeeze cast. Source: PNNL.

It was possible to mix the TiB_2 powders into the Al billet with the friction consolidation technique. Optical microscopy image in Figure I.1.1.7.5(a) shows the extent of the processed region (mixing zone) in the 7075- TiB_2 composite. Figure I.1.1.7.5(b), EDS shows the upper region is rich in Ti, which indicates the TiB_2 powder has been successfully dispersed in this mixing zone. Titanium has not been detected in the lower region that is only 7075 base metal. Figure I.1.1.7.5(c) shows the hardness of the sample after T6 heat-treatment. Average hardness at the 7075- TiB_2 mixing zone is $203 \pm 10\text{HV}$ and the maximum hardness is $\sim 240\text{HV}$, which is 33% higher than 7075-T6 alone ($181 \pm 2\text{HV}$). Figure I.1.1.7.5(d) reveals the morphology of TiB_2 particles at high magnification. Figure I.1.1.7.5(e) and Figure I.1.1.7.5(f) show the particles were uniformly dispersed in the 7075 matrix with a size range from 100 nm to 5 μm . Based on the EDS result, the estimated content of TiB_2 is about 6.8wt% ($\sim 5 \text{ vol.}\%$).

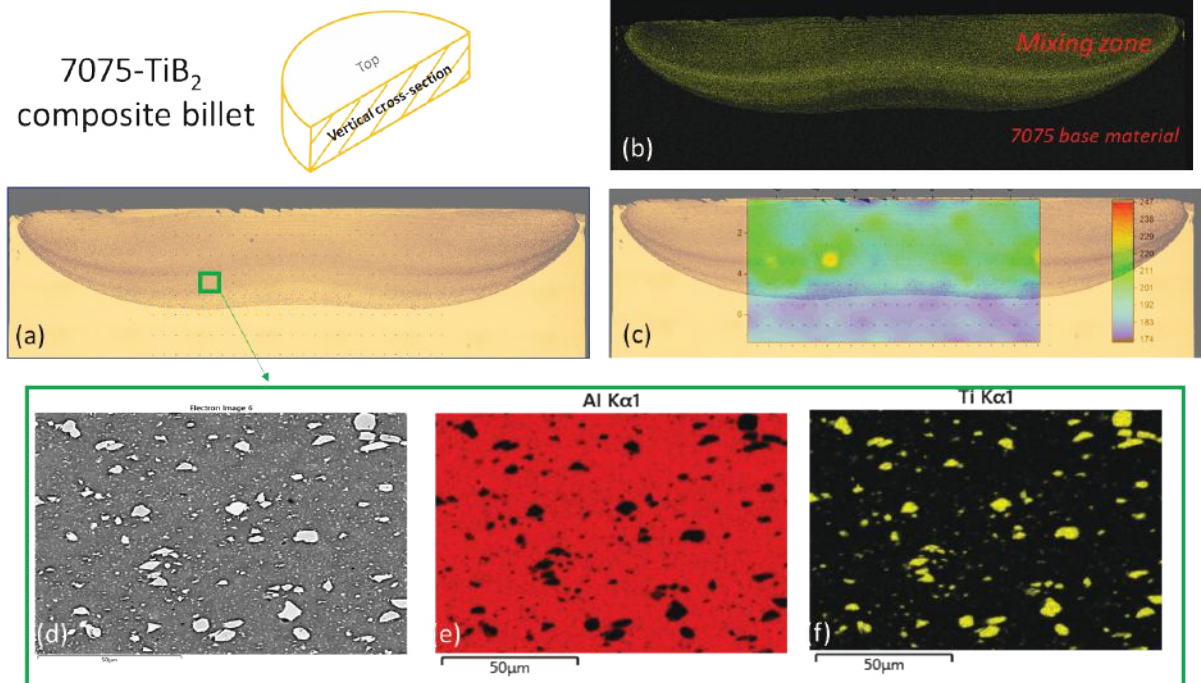


Figure I.1.1.40. The vertical cross-section images of 7075- TiB_2 composite billet were made by friction consolidation. (a) Optical image, (b) EDS mapping of titanium showing the mixing zone, (c) Vicker's hardness after T6 post heat-treatment, (d) High-magnification SEM image of the mixing zone, (e) EDS mapping of Al at high-magnification, and (f) EDS mapping of titanium at high-magnification. Source: PNNL.

With successful compositing of TiB_2 with Al, friction consolidation and forging processes are combined to produce a near-net shape composite gear. In this case, the starting material was the powder precursor. Alloy powder (AA5083 + 10 vol.% TiB_2) was first friction consolidated, then followed by FSF to obtain the composite gear with 14 teeth as shown in Figure I.1.1.7.2(b). SEM/EDS has been performed at the teeth and core of the gear samples shown in Figure I.1.1.7.6 to see the distribution of TiB_2 . SEM macrograph of one tooth with core is shown in Figure I.1.1.7.6(a). Figure I.1.1.7.6(b) and Figure I.1.1.7.6(c) are the magnification SEM pictures. Homogenous and uniform distribution of TiB_2 is clearly seen across the matrix in both core and gear teeth. EDS elemental mapping for Al, as observed in Figure I.1.1.7.6(d), and Ti, as can be seen in Figure I.1.1.7.6(e), confirms the uniform distribution of TiB_2 in the matrix. Microhardness distribution across the gear teeth ($\sim 115 \pm 10 \text{ Hv}$) exhibits significant amount of improvement ($\sim 51\%$) compared to base AA 5083 ($\sim 76 \pm 5\text{Hv}$), Figure I.1.1.7.6(f). FY 2023 work will focus on production of gears from the 7075 powders with higher fraction of micron-sized TiB_2 at the teeth and measuring the strength of composite at various locations.

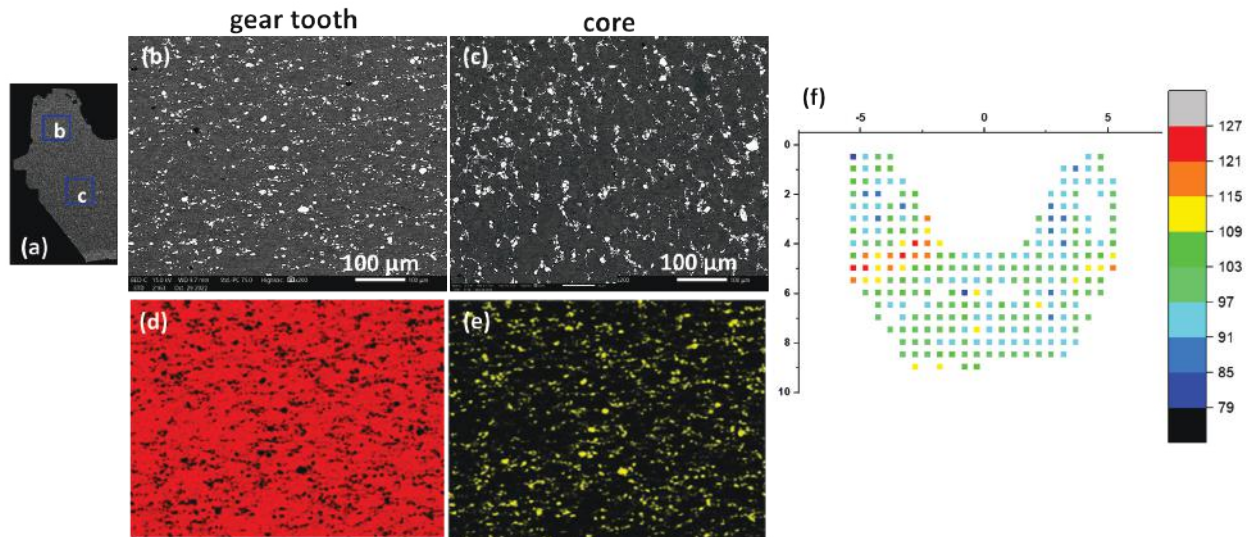


Figure I.1.1.41. Characterization of the composite gear core and teeth. (a) SEM macrograph, distribution of TiB_2 in (b) core and (c) gear teeth; EDS elemental mapping for (d) Al and (e) Ti, (f) microhardness distribution across the teeth. Source: PNNL.

Conclusions

This project addresses previous challenges associated with MMCs and develops alternative, cost-effective processing methods. Composites with sub-micron and micron-sized TiB_2 particle reinforcements are demonstrated by liquid-phase and solid-phase processing approaches.

For the liquid-phase route, the *in-situ* TiB_2 -A206 composites are produced through reaction of the halide salts with the molten Al. The composites are then cast with either gravity or squeeze casting. The final composite microstructure depends on the casting technique and the volume fraction of TiB_2 . Faster solidification rates with squeeze casting distribute the particles uniformly, with majority of the particles in sub-micron size range.

For the solid-phase processing route, TiB_2 powder is successfully mixed with the Al alloy powders. The consolidated billet is then forged into a gear shape. The distribution of TiB_2 is uniform after both processes, with particle sizes ranging from 100 nm to 5 μm . TiB_2 reinforcements results in ~ 30%–50% hardness increase compared to the base material, which should translate into higher strength for the composites.

Key Publications

1. Efe, M., J. P. Choi, X. Li, H. Das, G. Grant, and D. Herling, 2023, “Recyclable Aluminum MMC for EV Powertrain Applications,” Accepted for Presentation at the TMS 2023 Annual Meeting, 19–23 March 2023, San Diego, CA, USA.

References

1. Rohatgi, P. K., N. Gupta, and A. Daoud, 2008, “Synthesis and processing of cast metal matrix composites and their applications,” in: *ASM Handbook v15: Casting*, ASM International, Materials Park, OH, USA. pp. 1149-1164.
2. Carney, D., 2020, “Lightweight aluminum brakes for EVs are Continental’s aim,” DesignNews website, Available at: <https://www.designnews.com/automotive/lightweight-aluminum-brakes-evs-are-continentials-aim> (last accessed 6 December 2022).
3. Bull, M., 2011, “Mass reduction performance of PEV and PHEV vehicles,” *Proceedings of 22nd International Technical Conference on the Enhanced Safety of Vehicles (ESV)*, 13–16 June 2011, Washington, D.C., USA, Paper 11-0346.

4. Air Quality Expert Group, 2019, “Non-exhaust emissions from road traffic,” Report prepared for U.S. Department for Environment, Food and Rural Affairs. Available at: https://uk-air.defra.gov.uk/assets/documents/reports/cat09/1907101151_20190709_Non_Exhaust_Emissions_types_et_Final.pdf (last accessed 6 December 2022).
5. Rettig, M., et al., 2020, “Aluminum brake disc,” *Proceedings of EuroBrake 2020*, 16–19 June 2020, Online, Paper EB2020-MDS-010.
6. Shrestha, S., R. Francis, and A. Smith, 2020, “RELIABLE: Wear-resistant lightweight aluminium brakes for vehicles,” *Proceedings of EuroBrake 2020*, 16–19 June 2020, Online, Paper EB2020-EBS-032.
7. Pramod, S. L., S. R. Bakshi, and B. S. Murty, 2015, “Aluminum-based cast *in situ* composites: A review,” *J. Mater. Eng. Perform.*, Vol. 24, No. 6, pp. 2185–2207. <https://doi.org/10.1007/s11665-015-1424-2>.

Acknowledgments

The authors would like to thank PNNL staff members D. Herling and G. Grant for their support and technical directions and discussion. We commend Dr. X. Li and Dr. H. Das of PNNL for their leadership and help in the friction consolidation and forging tasks. We thank Dr. J.-P. Choi of PNNL for his support in the casting task. Cast composites were manufactured and characterized by Loukus Technologies, Inc., Calumet, MI. We thank Dr. A. Loukus and Mr. S. Kastamo of Loukus Technologies for their collaboration and technical discussions. Dr. X. Ma and Mr. A. Ortiz of PNNL also are acknowledged for their help in the composite characterization.

I.1.2 Thrust 2: Materials and Lubricants for Heavy Duty EVs and EV Propulsion

I.1.2.1 Task 2A. High-Performance Soft Magnetic Materials for Motor Laminates (Fe-Si) via Shear Rolling (Oak Ridge National Laboratory)

Govindarajan Muralidharan, Principal Investigator

Oak Ridge National Laboratory
Materials Science and Technology Division
1 Bethel Valley Rd.
Oak Ridge, TN 37830
E-mail: muralidhargn@ornl.gov

J. Allen Haynes, PMCP Consortium Manager

Oak Ridge National Laboratory
Materials Science and Technology Division
1 Bethel Valley Rd.
Oak Ridge, TN 37830
E-mail: haynesa@ornl.gov

Jerry Gibbs, DOE Technology Development Manager

U.S. Department of Energy
E-mail: jerry.gibbs@ee.doe.gov

Start Date: November 1, 2021	End Date: September 30, 2023	
Project Funding (FY 2022): \$250,000	DOE share: \$250,000	Non-DOE share: \$0

Project Introduction

This task seeks to develop and demonstrate new iron(Fe)-silicon(Si) steels that enable higher power density electric motors. The Fe-Si steels that are widely used to make motor laminates for EV motors typically contain 2.5–3.5 wt% silicon. There is rapidly growing interest from motor manufacturers to increase motor speed to improve power density. High-speed motors incur losses in the magnetic cores due to changing magnetic fields. Widely used Fe-(2.5–3.5)Si steel must be rolled to extremely thin sheets (0.35 mm or less) and laminated into motor cores to reduce such losses. However, the use of thin sheets decreases the stacking factor and substantially increases manufacturing complexity and cost. Increasing the resistivity of Fe-Si steels is an alternate approach to achieve reduced losses in higher speed electric motors. Higher amounts of silicon in the steel increases its electrical resistance, improving magnetic properties and reducing losses. For example, Si steels with 6.5% Si have a high-resistivity and permeability, low-eddy current losses and hysteresis losses, (especially at higher frequencies), and almost zero magnetostriction [1]. However, as the Si content increases, the material becomes extremely brittle and is very difficult to cold roll into thin sheets. This embrittlement has been the primary deterrent in the use of higher silicon Fe-Si steels in motor laminates. Availability of an Fe-Si steel with higher Si content that can be cold-rolled and stamped will facilitate its use in motor core laminates, thereby increasing the efficiency and power density of electric motors, and hence, the range of EVs.

Objectives

The objective of Task 2A is to develop higher Si steels (5–6.5 wt.% Si) that can be produced using traditional manufacturing routes, to include warm-shear rolling and cold rolling, and which can be stamped to form laminates that enable higher power density electric motors for EVs.

Approach

The limited ductility of Fe-Si steels with higher Si contents is primarily due to ordering reactions that occur in Fe-Si alloys with higher Si levels, as shown in the phase diagram in Figure I.1.2.1.1. One or more ordered phases designated as B2 (Fe-Si type) and DO₃ (Fe₃Si type) can form in Fe-(6–6.5 wt.%) Si alloys depending on alloy composition, temperature, and processing history. The vertical line shown in the figure represents the alloy composition Fe-6.5 wt.% Si. As shown in Figure I.1.2.1.1, this alloy is likely to show the presence of A2 (disordered Body-Centered Cubic structure), B2, or B2 + DO₃ at equilibrium, depending on the temperature and thermal-mechanical processing history [1,2]. The types of intermetallic phases and the degree of ordering present in the alloys determines strength and ductility. In particular, it has been shown that the formation of the DO₃ phase during cooling can be responsible for the brittle behavior of Fe-6.5 wt.% Si alloy at RT.

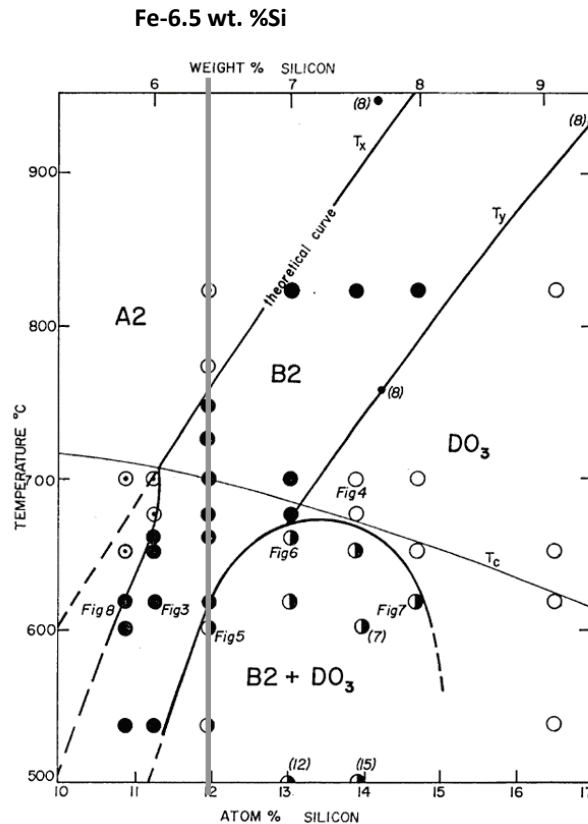


Figure I.1.2.1. Fe-Si Phase Diagram. Source: ORNL [2].

Several approaches have been used to improve RT ductility in Fe-6.5 wt.% Si alloys [1]. Previous work has shown rapid or splat quenching can suppress the formation of the DO₃ phase, thereby making the alloy more ductile. However, splat quenching can be achieved only in very thin and narrow ribbons, hence making it difficult and expensive to subsequently fabricate larger components. Other techniques, such as chemical vapor deposition to siliconize or hot dipping of a ductile Fe-3.2 wt.% Si sheet followed by diffusion annealing, have been used to make thin sheets of high-Si steel, but these approaches can be complex and expensive.

The current project uses two parallel and potentially synergistic approaches to enable the development of higher Si, Fe-Si steels. The first approach will be to develop a thermal-mechanical processing route consisting of hot and warm rolling, which has recently shown to be effective in achieving softening of Fe-6.5 wt.% Si alloys, thereby increasing RT ductility and enabling cold rolling [3]. ORNL has a unique mill employing heated rolls that can be heated up to ~300°C and can perform both symmetric and asymmetric (shear) rolling. Shear rolling has been shown to result in grain refinement, improving uniformity of microstructure, and texture

modification in steels, aluminum (Al) alloys, titanium, and magnesium alloys, thus making it attractive for this application [4]. The use of heated rolls eliminates the potentially detrimental roll quenching effect that happens when preheated sheets are rolled using cold rolls. The second approach is the addition of various alloying elements (X) to modify the stability of the intermetallic phases in Fe-Si-X alloys. Recent work has shown the addition of certain elements, including some rare earths, can reduce the degree of intermetallic ordering, thereby increasing RT ductility. Selection of alloying elements were initially guided by previous work in the literature and are being refined using first-principles calculations as outlined below.

Results

Alloy Processing

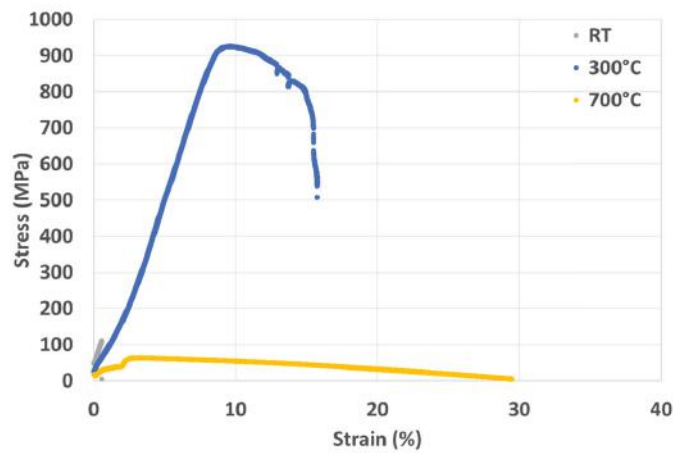
Experiments were designed to evaluate the effect of symmetric rolling at 300°C on the strength and ductility at 300°C and at RT. Several experimental Fe-(5–6.5) wt.% S-Xi alloys where X denotes alloying elements (e.g., chromium [Cr]) were arc-melted and fabricated in the form of drop castings of typical size measuring between 0.5–1 in. square and 3–4 in. long, as observed in Figure I.1.2.1.2(a). Alloying elements were selected from examples in the literature [5]. These ingots were homogenized at 1100°C followed by hot-rolling to a thickness of ~0.25 in., as observed in Figure I.1.2.1.2(b). Specimens were machined for mechanical testing from the rolled plate, also as shown in Figure I.1.2.1.2(b). Tensile tests were performed in the hot-rolled condition to evaluate strength and ductility at 300°C and 700°C. Figure I.1.2.1.2(c) shows the results from these tests on a hot-rolled Fe-6.5Si-1Cr alloy. Samples were subsequently heat-treated in the temperature range of 700–800°C and rolled both symmetrically and asymmetrically at ~316°C. Figure I.1.2.1.3(a) and Figure I.1.2.1.3(b) show examples of Fe-6.5 wt.% Si-1 Cr specimens symmetrically rolled to reductions of ~15% and 31%, respectively, with the specimen rolled to ~31% cracking during rolling. Figure I.1.2.1.3(c) shows a sample of the same alloy that was asymmetrically rolled to a reduction of ~8%.

Tensile samples were machined from the rolled material shown in Figure I.1.2.1.3. It was found that the tensile samples fabricated from the symmetrically rolled sample with ~15% reduction, as shown in Figure I.1.2.1.3(a), were extremely brittle and fractured before testing. Figure I.1.2.1.4(a) compares the tensile properties at RT obtained from the symmetrically rolled Fe-6.5 wt.% Si- 1Cr sample with ~ 31% reduction, the asymmetrically rolled Fe-6.5 wt.% Si- 1Cr sample with ~ 8% reduction that showed < 1% strain-to-failure, and an Fe-(5–6.5) wt.% Si-X1 alloy (Alloy A) where X1 is an alloying element different from Cr, asymmetrically rolled ~ 20% reduction at the same temperature that showed a significantly higher strain-to-failure of ~7%. Other higher Si alloys in this study have shown strain-to-failure of >20% and an invention disclosure is being submitted on these alloys and associated processing steps. These results suggest a certain minimum amount of deformation may be required to achieve benefits from warm asymmetric rolling. It is also likely that different alloys may respond differently to asymmetric rolling, while certain alloys may be more favorably affected by the asymmetric rolling process. Figure I.1.2.1.4(b) compares the tensile behavior at 300°C of the hot-rolled Fe-6.5 wt.% Si- 1Cr sample and the asymmetrically rolled Fe-6.5 wt.% Si- 1Cr sample with ~8% reduction. Note the asymmetrically warm-rolled sample shows lower strength and comparable ductility, indicating softening of the alloy due to warm, asymmetrical rolling. Further experiments are underway to evaluate the effect of larger reductions during asymmetric rolling on the RT ductility of this alloy.



(a)

(b)



(c)

Figure I.1.2.2. (a) Example of a drop-cast Fe-Si alloy ingot. (b) Hot-rolled plate produced from an ingot similar to that shown in (a). (c) Tensile properties of Fe-6.5Si-1Cr. Source: ORNL.



(a)

(b)

(c)

Figure I.1.2.3. Examples of Fe-6.5Si-1Cr (wt%) alloy samples rolled at $\sim 316^\circ\text{C}$. (a) Symmetrically rolled, reduction of $\sim 15\%$. (b) Symmetrically rolled, reduction of $\sim 31\%$. Sample cracked into two during rolling. (c) Asymmetrically rolled, reduction of $\sim 8\%$. Source: ORNL.

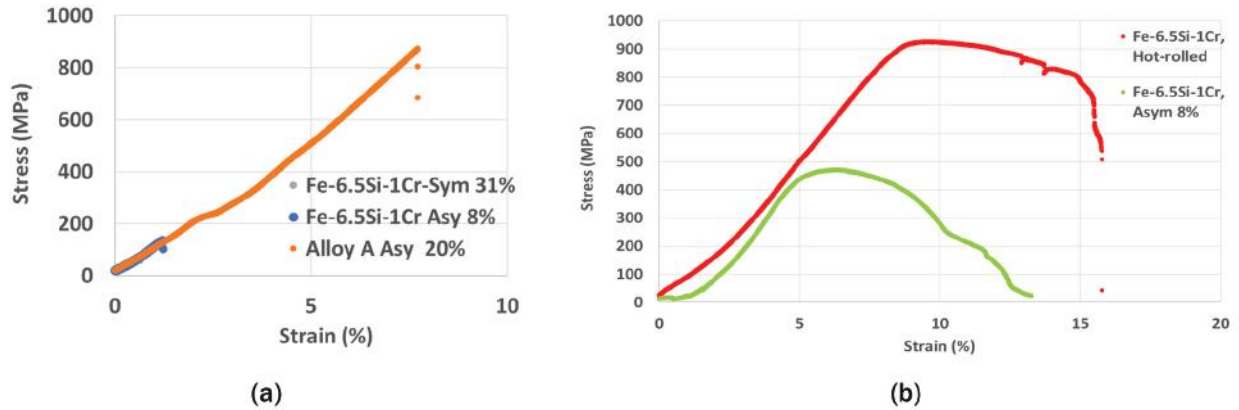


Figure I.1.2.4. (a) RT tensile properties of symmetrically and asymmetrically rolled samples. (b) 300 °C tensile properties of hot-rolled and asymmetrically rolled Fe-6.5 wt.% Si- 1Cr. Source: ORNL.

Computational Modeling

In this supporting Thrust 4 project, an effort was initiated to seek alloying element additions to modify thermodynamic stabilities of the B2 phase using first-principles DFT-based theoretical approaches. The DFT part of the calculations were performed using the Vienna Ab-initio Simulation Package, and a particle-swarm optimization-based algorithm was employed to further explore competing phases for a given composition. Specifically, we utilized our developed computational materials platform that combines materials database searches, first-principles calculations, and global structure search algorithms [6, 7]. Figure I.1.2.1.5 shows a schematic of a workflow developed for the project. This method was used to calculate the effect of changing the metal-to-silicon ratio (M:Si in $(M)_xSi_{1-x}$) on the properties of the B2 phase, where M included various transition metals. We focused on a high-dopant system as a model system, where the metal concentration of most stable M-Si systems ranged between 0.3 and 0.75, depending on the metals being studied. Results from two example calculations, additions of Cr and nickel (Ni), are shown in Figure I.1.2.1.5. The addition of Cr shows the presence of a maximum in the unit cell volume at $x \sim 0.5$, whereas this maximum is not observed with the addition of Ni. The most promising elements that show the largest effects will be considered for alloying element additions.

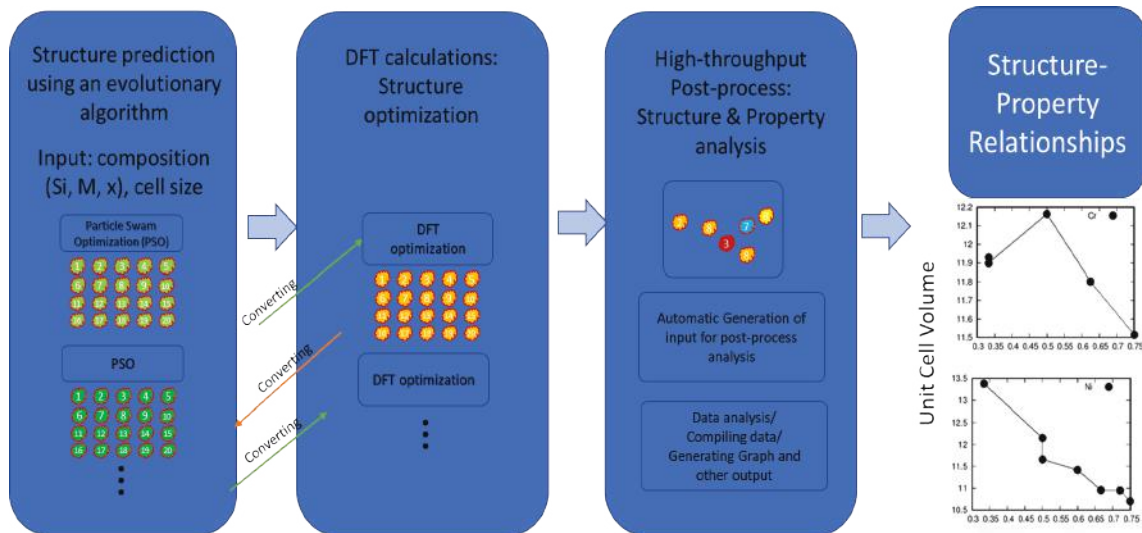
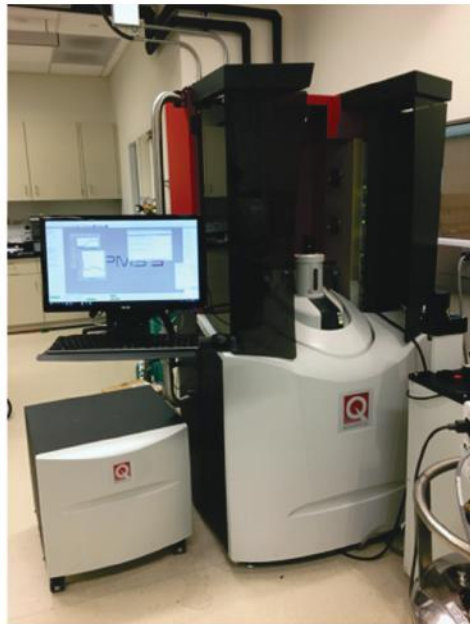


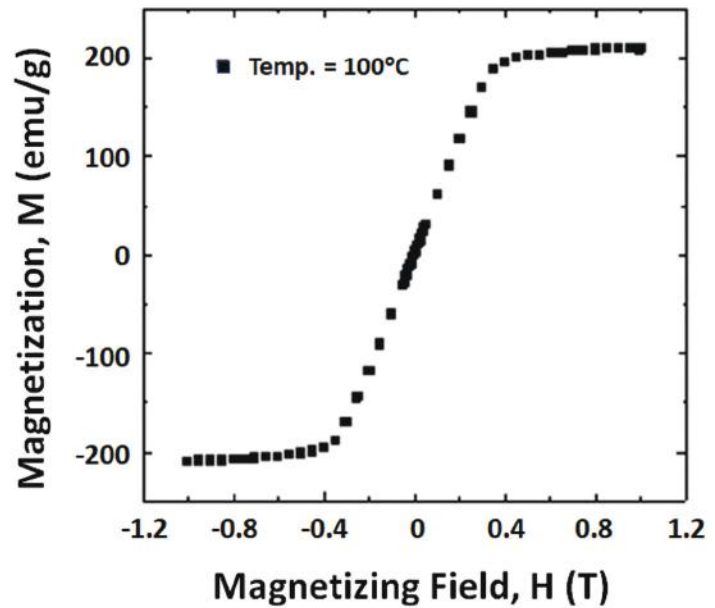
Figure I.1.2.5. A schematic showing the workflow of our theoretical/computational approaches that utilize ORNL's high-performance computation resources. Source: ORNL.

Magnetic Measurements

Magnetic measurements of selected developmental alloys were performed using squid magnetometry in a Quantum Design MPMS3 cryostat, as observed in Figure I.1.2.1.6(a). Measurements were performed as a function of temperature, and isothermal magnetization measurements were performed at 100°C (373 K). These field-dependent magnetization measurements revealed a magnetization at a field of 1T of 208emu/g at 373 K and 215 emu/g at 273 K, as can be seen in Figure I.1.2.1.6(b). The saturation magnetic moment of this alloy is consistent with that of data for Fe-Si alloys in the literature [1]. Thermal analysis measurements were also performed to determine the Curie temperature T_C of the alloy. These measurements were performed using the thermogravimetric analysis approach. Specifically, the apparent weight of the sample, w , is measured as a function of temperature, while the sample is kept in proximity to a permanent magnet. In the configuration utilized, the permanent magnet is placed above the sample, while the ferromagnetic sample is pulled upward towards the permanent magnet. Thus, the measured weight (e.g., ‘apparent weight’) is lower than the true weight of the sample when the sample is attracted towards the permanent magnet. The attraction of the sample to the magnet decreases rapidly at T_C , thus allowing the Curie temperature to be determined from the temperature-derivative of the apparent weight where a maximum is observed. For the Fe-5 wt.% Si-based alloy used in this measurement, the Curie temperature was found to be 717°C, as shown in Figure I.1.2.1.7(a), which is consistent with data in the literature for an alloy of this composition, as observed in Figure I.1.2.1.7(b) [8], thereby providing evidence the targeted Si content was achieved for this alloy.



(a)



(b)

Figure I.1.2.6. (a) Quantum Design MPMS3 magnetometer for measuring magnetization from 0.4–400 K using applied fields up to 7 T H curve at Temp.=100°C. Source: ORNL.

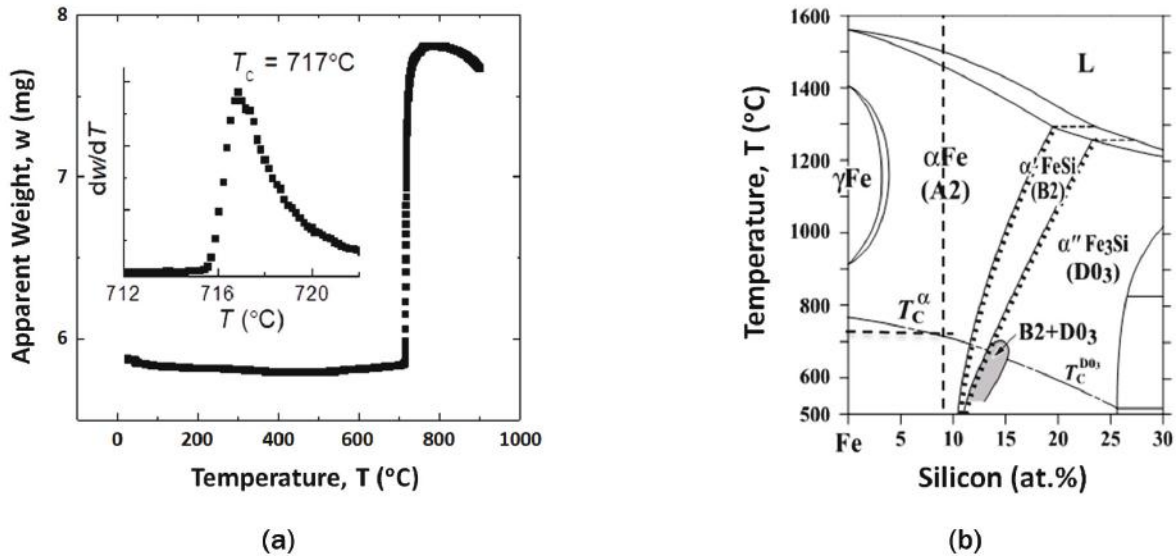


Figure I.1.2.7. (a) Results from magnetic thermogravimetric analysis from a Fe-5Si base alloy. (b) Curie temperature (T_c) superposed on the Fe-Si phase diagram. Dotted lines show \sim Fe-5 wt.% Si composition and the Curie temperature. Source: ORNL.

Conclusions

The effect of processing sequences, including hot-rolling and warm symmetric and asymmetric rolling, on the strength and ductility of several experimental Fe-(5-6.5) wt.% Si-X alloys, where X denotes alloying element additions, were evaluated in this work. It was found that:

- A reduction of \sim 8% in a warm asymmetric rolling process resulted in softening of an Fe-6.5 wt.% Si- 1Cr alloy at 300°C.
- RT ductility was improved by asymmetric rolling, but the magnitude of improvement was dependent on alloy composition and extent of warm rolling. Further work is ongoing to evaluate the effect of processing conditions on further improving the RT ductility.
- First-principles computational modeling was initiated to identify alloying element additions that would modify the disorder-order transition temperatures in these alloys.
- Magnetic measurements on a Fe-5 wt.% Si-based alloy showed magnetization values and Curie temperatures consistent with the composition of the alloy.

References

1. Ouyang, G., X. Chen, Y. Liang, C. Macziewski, and J. Cui, 2019, "Review of Fe-6.5 wt%Si high silicon steel—A promising soft magnetic material for sub-kHz application," *J. Magn. Mater.*, Vol. 481, pp. 234–250. <https://doi.org/10.1016/j.jmmm.2019.02.089>.
2. Swann, P. R., L. Granas, and B. Lehtinen, 1975, "The B2 and DO₃ ordering reactions in iron–silicon alloys in the vicinity of the curie temperature," *Met. Sci. J.*, Vol. 9, pp. 90–96. <https://doi.org/10.1179/030634575790445279>.
3. Fu, H., Z. Zhang, Q. Yang, and J. Xi, 2011, "Strain-softening behavior of an Fe–6.5wt.%Si alloy during warm deformation and its applications," *Mat. Sci. and Eng. A.*, Vol. 528, pp. 1391–1395. <https://doi.org/10.1016/j.msea.2010.10.093>.
4. Vincze, G., F. J. P. Simoes, and M. C. Butuc, 2010, "Asymmetrical rolling of aluminum alloys and steels: A review," *Metals*, Vol. 10, No. 9, Art. 1126. <https://doi.org/10.3390/met10091126>.

5. Yu, X., Z. Zhang, and J. Xi, 2016, “Effects of rare-earth elements doping on ordered structures and ductility improvement of Fe–6.5wt.%Si alloy,” *Mater. Lett.*, Vol. 184, pp. 294–297. <https://doi.org/10.1016/j.matlet.2016.08.074>.
6. Huhn, W. P., B. Lange, V. W-z Yu, M. Yoon, and V. Blum, 2020, “GPU-acceleration of all-electron electronic structure theory using localized numeric atom-centered basis functions,” *Comp. Phys. Comm.*, Vol. 254, Art. 107314. <https://doi.org/10.1016/j.cpc.2020.107314>.
7. Yu, V. W.-z., J. Moussa, P. Kus, A. Marek, P. Messmer, M. Yoon, H. Lederer, and V. Blum, 2021, “GPU-acceleration of the ELPA2 distributed eigensolver for dense symmetric and hermitian eigenproblems,” *Comp. Phys. Comm.*, Vol. 262, Art. 107808. <https://doi.org/10.1016/j.cpc.2020.107808>.
8. Kubaschewski, O., 1993, *Phase Diagrams of Binary Iron Alloys*, ASM International, Materials Park, OH, USA. pp. 380–381.

Acknowledgements

The authors would like to acknowledge the following ORNL staff: Dr. M. Yoon for leading the computational modeling sub-task; Dr. A. May for leading the magnetic measurements sub-task; K. Hanson, D. Moore, and G. Cox for materials processing; and K. Hedrick and I. Stinson for mechanical testing. The authors also wish to acknowledge Dr. T. Ros and C. Cliffs for guidance in this work.

I.1.2.2 Task 2B. Ferrous Alloys for Fatigue-Resistant, Lightweight Geartrains for Heavy Duty Electric Vehicle Systems (Oak Ridge National Laboratory)

Dean Pierce, Principal Investigator

Oak Ridge National Laboratory
Materials Science and Technology Division
1 Bethel Valley Rd.
Oak Ridge, TN 37830
E-mail: piercedt@ornl.gov

J. Allen Haynes, PMCP Consortium Manager

Oak Ridge National Laboratory
Materials Science and Technology Division
1 Bethel Valley Rd.
Oak Ridge, TN 37830
E-mail: haynesa@ornl.gov

Jerry Gibbs, DOE Technology Development Manager

U.S. Department of Energy
E-mail: jerry.gibbs@ee.doe.gov

Start Date: November 1, 2021 End Date: September 30, 2023
Project Funding (FY 2022): \$230,000 DOE share: \$230,000 Non-DOE share: \$0

Project Introduction

This task aims to develop new steel alloys and evaluate existing steels for applications in drivetrain components, such as gears in future HD EVs. Goals of this project will be to develop or identify steels that substantially reduce weight of components and/or increase the efficiency of power transmission in electrified drivetrains, particularly of HD vehicles, leading to fuel- and freight-efficiency increases and reductions in GHG emissions. The task is focused on steel due to the durability and longevity demands of HD vehicle drivetrains, where vehicles are often required to operate up to 1,000,000 miles. Materials development is focused on improving certain key manufacturing and performance attributes of steel over existing commercial gear and drivetrain steels, such as AISI 8620 and 16MnCr5. Some of the important attributes of gear steels are: (1) surface hardness after carburizing or nitriding; (2) core strength and toughness; (3) high-cycle fatigue resistance; (4) response to nitriding and/or carburizing; (5) reduced mass or density; (6) surface tribological properties to reduce friction; and (7) thermal transport properties that can influence temperature at the contacting surfaces. Manufacturing considerations will also inform alloy development decisions in order to ensure the developed materials can be cast, processed, and machined in an efficient and cost-effective manner. This task has sought input from users of gears in government sectors to ensure the task remains focused on the critical technical barriers.

Objectives

The objectives of this task are to identify existing steels and develop new, innovative steels that can substantially reduce weight and increase efficiency of power transmissions in the drivetrains of HD EVs and lead to fuel- and freight-efficiency increases. The existing low alloy martensitic carburizing steels most widely used for gears are 8620 in the U.S. and 16MnCr5 in Europe. The low alloy content of 8620 and 16MnCr5, listed in Table I.1.2.2.1, make them cost-effective materials for gears. Note that additional developmental martensitic steels are under investigation, but their compositions are not permitted to be disclosed at this time. New steels for gear applications must be similarly inexpensive, enable substantial manufacturing savings, and result in exceptional performance improvements to offset any raw material cost increases.

Table I.1.2.2.1. Composition of Commercial Gear Steels 16MnCr5 and 8620 in Use in Europe and the U.S., and a High Mn Low-Density Austenitic Steel Under Evaluation in the Present Work.

	Steel Class	Mn	Cr	Si	C	Ni	Al	Mo	Fe
16MnCr5	Martensitic	1.15	0.95	0.25	0.16	-	-	-	Bal.
8620	Martensitic	0.8	0.5	0.25	0.205	0.55	-	0.2	Bal.
ORNL-2	Martensitic	Disclosure of these compositions are not permitted at this time.							Bal.
ORNL-4	Martensitic	Disclosure of these compositions are not permitted at this time.							Bal.
ORNL-5	Martensitic	Disclosure of these compositions are not permitted at this time.							Bal.
FeMnAlC	Austenitic	31	-	0.85	1.06	-	8.48	0.51	Bal.

Approach

The project currently has two main sub-tasks. Sub-task 1 is focused on developing novel martensitic steels that will reduce gear weight and have potential to enable more efficient power transmission in drivetrains relative to the existing martensitic gear steels. Sub-task 2 is focusing on evaluating an existing low-density (6.67 g cm^{-3}) austenitic steel for gear applications.

Sub-task 1

The developmental martensitic steels in Sub-task 1 have been designed using computational thermodynamics with several concurrent objectives:

1. Exhibit properties that enable reduced gear weight, leading to lower reciprocating mass and improved vehicle efficiency.
2. Enable increased surface hardness after carburizing over existing gear steels (e.g., 8620 and 16MnCr5).
3. Incorporate an affordable alloying strategy that reduces the barrier for industry adoption of new materials.

In Objective 2 above, we hypothesize that by significantly increasing the surface hardness and wear resistance of the gear, it can improve fatigue strength, which could result in additional performance and endurance benefits. These additional benefits may include improved efficiency by enabling the use of lower viscosity gear oil to a reduction in churning losses. As such, improved overall vehicle efficiency increases may be realized through lighter weight gears (Objective 1) and reduced drivetrain losses (Objective 2). To confirm the hypothesis outlined above, the developmental alloys will be fabricated into rolling-sliding contact fatigue (RSCF) specimens (roller and ring) and tested in a RSCF testing rig at ORNL to simulate gear contact, which is depicted in Figure I.1.1.6.1.. The developmental alloys will be compared to baseline gear steels under typical gear simulation conditions previously developed at ORNL [1].

The activities and processes required in Sub-task 1 to design, fabricate, process, and evaluate steels under relevant gear conditions are non-trivial. The major activities required are shown schematically in Figure I.1.2.2.1 and include alloy design, arc melting, forging cylindrical arc metals into pancake-shaped pucks, heat-treating the material to achieve high hardness, machining and grinding the RSCF specimens, carburizing or nitriding the surface, performing a final grinding after carburizing or nitriding to achieve final dimensions and required surface roughness, performing the RSCF testing, and then characterizing the wear surface and pitting of the rollers of the baseline steels and developmental steels. In order to reduce the complexities and accelerate this process, ORNL has melted alloys with carbon (C) content that mimic the expected surface C content after carburizing. This enables ORNL to test the wear and fatigue properties of the surface of the new alloys, allowing for the elimination of the gas carburizing and ‘final machining and grinding after carburizing’ steps to accelerate the research. The RSCF specimens are being machined in FY 2023 Quarter 1 (Q1) and testing is planned for FY 2023 Q2. In parallel, ORNL is conducting modeling simulations of the carburizing process of the new developmental alloys, and experimental carburizing trials in FY 2023 will be informed by these simulations.

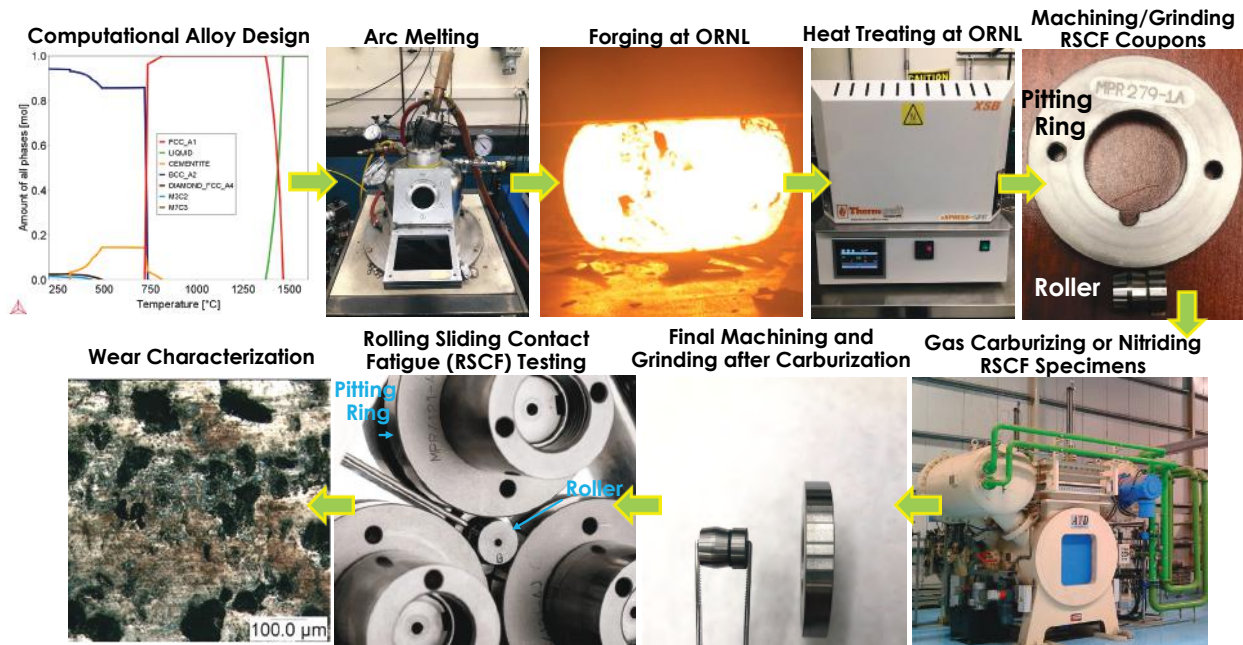


Figure I.1.2.8. Manufacturing route and activities for design and fabrication of developmental alloys and subsequent machining, testing, and evaluation of RSCF specimens. Source: ORNL.

Sub-task 2

Sub-task 2 is focused on evaluating an existing a high-manganese, low-density austenitic steel referred to as FeMnAlC (composition provided in Table I.1.2.2.1), for gear applications—specifically, the aim is to evaluate the RSCF behavior. Although high in raw material cost, the FeMnAlC alloy has 15% lower density than typical martensitic steel, providing immediate and tangible weight-savings benefits over 8620 and 16MnCr5. The FeMnAlC alloys also have excellent castability and ductility in the cast or solution-treated condition. It is therefore possible that this alloy may have the necessary suite of characteristics to be cast into blanks and/or manufactured into final shape by gear-rolling [2]. Both casting and gear-rolling are cost- and energy-efficient processes. Although it is not the intent of this work to evaluate the suitability of these manufacturing routes for the FeMnAlC alloy, the possibility of these routes could enable this alloy to reduce the manufacturing steps and carbon intensity associated with more traditional gear manufacturing routes and potentially offset the higher raw materials costs of the alloy, thereby making the alloy more attractive to industry for gear applications. A primary goal of Sub-task 2 is to fabricate RSCF specimens of the FeMnAlC alloy and test them under relevant gear-operating conditions [1], and then compare the performance of FeMnAlC to existing steels 8620 and 16MnCr5. Since FeMnAlC alloys without surface modification have exhibited similar wear behavior to carburized 8620 steels under other wear conditions, RSCF testing of the FeMnAlC alloy without a carburized or nitrided surface is anticipated to occur in FY 2023. Carburizing or nitriding of the surface will be explored in FY 2023 if needed to increase the surface hardness.

Results

Sub-task 1

Small cylindrical 500 g ingots of the new alloys were arc-melted, axially forged at 1150°C into pucks using the process shown in Figure I.1.2.2.1, annealed, and then heat-treated to a hardness greater than 60 HRC at ORNL. RSCF specimens are currently being machined and are expected to be ready for testing in Q2 FY 2023. Results from simulations of the carburizing process on ORNL-2 are provided in Figure I.1.2.2.2(a) and Figure I.1.2.2.2(b), respectively, which show the predicted C content as a function of depth from the surface for different carburizing times at 930°C for the baseline gear steel 16MnCr5 and a developmental gear steel ORNL-2, respectively. The developmental alloy exhibits different predicted C diffusion kinetics. Refinement of the carburizing parameters for the developmental alloys is ongoing.

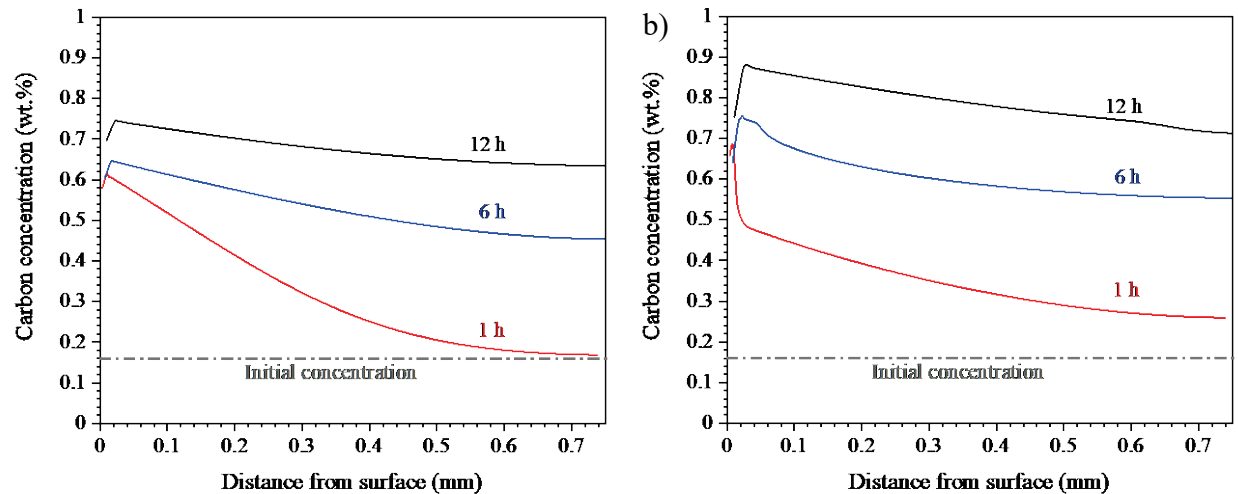


Figure I.1.2.9. Carburizing simulations showing C content as a function of distance from the surface and time for (a) 16MnCr5 gear steel; and (b) developmental gear steel ORNL-2. Source: ORNL.

Sub-task 2

Aging studies of the FeMnAlC alloy were conducted for various material starting conditions, including the as-cast condition (AR), AR+cold-rolled (CR), AR+solution-treated and quenched (STQ)+CR, AR+STQ, and AR+CR+STQ. Samples of the FeMnAlC steel in the STQ condition could be cold-rolled 20% in a single-pass without cracking and a 5 \times reduction was achieved using 5% deformation per pass, as can be seen from the surface images shown in Figure I.1.2.2.3. All conditions demonstrated an increase in hardness with aging time at 575°C, as provided in Figure I.1.2.2.4, with hardness peaking in the range of 37–44 HRC. One or more of these conditions will be selected for RSCF specimen fabrication and testing of FeMnAlC without surface modification in FY 2023. Reference [3] indicates the abrasive wear resistance of FeMnAlC steels without surface modification is comparable to carburized 8620 steels but could be increased with increasing C content. As such, carburizing simulations of the FeMnAlC alloy will be conducted to inform experimental carburizing trials in FY 2023.

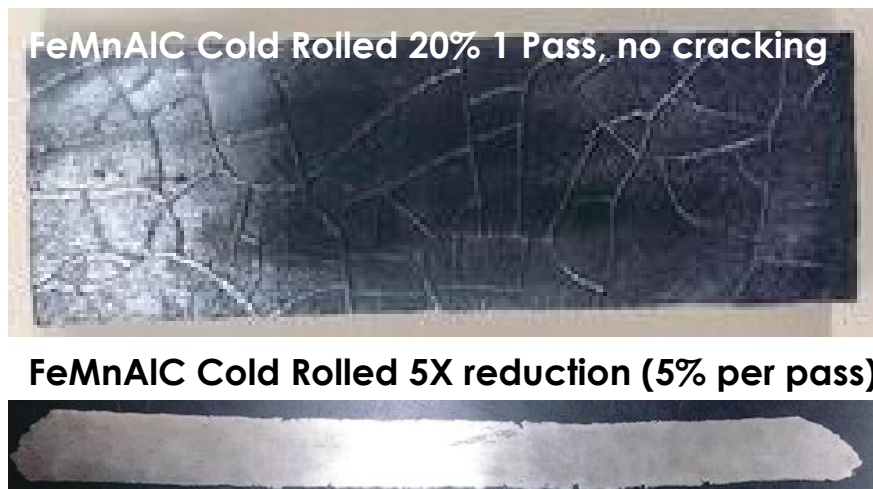


Figure I.1.2.10. Surface images of FeMnAlC strips after 20% reduction in a single-pass and 5 \times reduction with 5% reduction per pass. Source: ORNL.

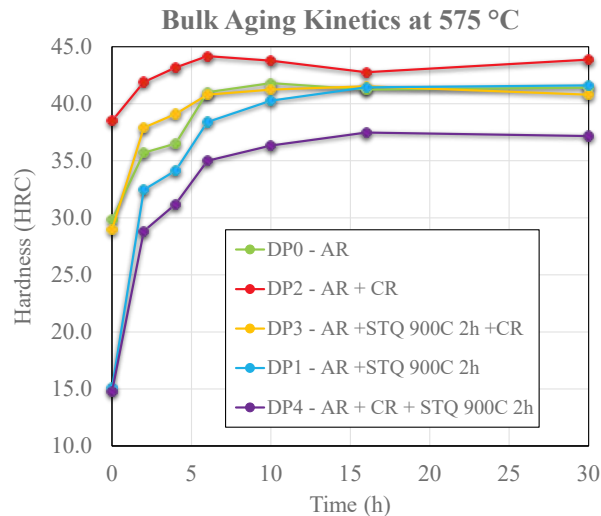


Figure I.1.2.11. Hardness vs. aging time for FeMnAlC in different starting material conditions (refer to text for meaning of acronyms in legend). Source: ORNL.

Conclusions

Two sub-tasks are being explored in Task 2B. Sub-task 1 is focused on designing, fabricating, and evaluating novel developmental martensitic steel alloys for gear applications. Computational thermodynamics was used to design steel compositions with potential for reducing gear weight and increasing the efficiency of power transmission through the gears. The steels have been arc-melted and forged. Carburizing simulations indicate the new developmental alloys respond differently to carburizing, and these simulations will inform experimental carburizing studies in FY 2023. RSCF specimens are currently being fabricated and testing is planned for FY 2023 to confirm improved properties in simulated gear operation over existing commercial gear steels. In Sub-task 2, ORNL is focusing on evaluating an existing low-density, age-hardenable austenitic steel for gear applications with potential for 10%–15% weight-savings over typical commercial gear steels. Initial rolling, heat-treating, and aging studies have been conducted to identify suitable processing conditions for gears. RSCF specimens of this alloy are also being fabricated and testing is planned for FY 2023.

Key Publications

1. Pierce, D., 2022, “Steel for improved gear performance,” ORNL Invention Disclosure No. 81941488.

References

1. Stump, B. C., Y. Zhou, M. B. Viola, H. Xu, R. J. Parten, and J. Qu, 2018, “A rolling-sliding bench test for investigating rear axle lubrication,” *Tribol. Int.*, Vol. 121, 450–459. <https://doi.org/10.1016/j.triboint.2018.01.058>.
2. Khodaei, A., 2015, “Gear-rolling for the production of high-grade gears,” M.S. Thesis, KTH Royal Institute of Technology, Stockholm, Sweden. Available at: <https://www.diva-portal.org/smash/get/diva2:853448/FULLTEXT01.pdf> (last accessed 31 January 2023).
3. Buckholz, S. A., 2013, “The influence of aluminum and carbon on the abrasion resistance of high-manganese steels,” M.S. Thesis, Missouri University of Science and Technology, Rolla, MO, USA. Available at: <https://www.proquest.com/docview/1434157862> (last accessed 31 January 2023).

Acknowledgements

The following ORNL staff are acknowledged and thanked for their important contributions to this task: R. Pillai for performing the carburizing simulations; J. Qu for guidance on the RSCF testing; I. Stinson for machining; D. Heidel for arc melting and heat-treating; and K. Hanson for rolling.

I.1.2.3 Task 2C. New Lubricant Strategies for Advanced Thermal Management of Heavy-Duty EVs (Oak Ridge National Laboratory)

Jun Qu, Principal Investigator

Oak Ridge National Laboratory
Materials Science and Technology Division
1 Bethel Valley Rd.
Oak Ridge, TN 37830
E-mail: quejn@ornl.gov

J. Allen Haynes, PMCP Consortium Manager

Oak Ridge National Laboratory
Materials Science and Technology Division
1 Bethel Valley Rd.
Oak Ridge, TN 37830
E-mail: haynesa@ornl.gov

Jerry Gibbs, DOE Technology Development Manager

U.S. Department of Energy
E-mail: jerry.gibbs@ee.doe.gov

Start Date: November 1, 2021 End Date: September 30, 2022
Project Funding (FY 2022): \$230,000 DOE share: \$230,000 Non-DOE share: \$0

Project Introduction

The electric motor in an EV rotates at 15,000 rpm and future motors may rotate up to 30,000 rpm. The copper winding on the e-motor gets very hot and is cooled by a lubricant. Currently, increasing heat transfer efficiency is the primary challenge for e-motor oils to allow higher current for higher torque output. The excellent thermal conductivity (2800–6000 W/mK, 10× higher than copper) and self-lubricating nature of carbon nanotubes (CNTs) presents an opportunity for them to be used as oil additives for thermal and frictional management. However, CNTs have poor oil suspendability and tend to aggregate and precipitate, and thus, lose their uniform heat transfer enhancement. In this task, we are covalently functionalizing the surface of CNTs using organics to enable stable suspension of CNTs in e-motor oils for improved heat transfer during lubrication. The organics on the CNT surfaces are expected to not only prevent the aggregation of CNTs, but also improve their oleophilicity for uniform oil dispersion. In addition, the self-lubricating nature of CNTs is expected to provide effective friction reduction and wear protection to allow the use of lower viscosity fluids for more rapid convection (more efficient heat transfer) and lower hydrodynamic drag (energy savings). A significant portion of this annual operating plan task is committed to a cooperative research and development agreement (CRADA) with Valvoline (NFE-22-09129), which launched on June 13, 2022.

Objectives

This task intends to gain fundamental understanding and develop new lubricant strategies—specifically organic-modified CNTs as novel additives for EV fluids—to enable superior lubricity, heat transfer, and sustainability for HD EVs.

Approach

The heat transfer capability of a fluid can be evaluated using the Mouromtseff Number (Mo):

$$Mo = \rho^a \kappa^b C_p^d / \mu^e \quad (1)$$

where ρ , k , C_p , and m represent the density, thermal conductivity, specific heat capacity, and dynamic viscosity of the fluid, respectively.

The most straightforward approach to increasing heat transfer capacity is reducing the oil viscosity, but this would inevitably increase the risk of wear, requiring more effective wear protection of the surfaces. Another approach is to use additives with higher thermal conductivity. The focus here is to investigate covalently functionalized multiwall CNTs as potential additives for lubricating oils to improve both heat transfer efficiency and tribological performance.

CNTs are ideal for heat transfer applications, since they possess exceptional thermal conductivity of 2800–6000 W/mK, which is one order of magnitude higher than that of metallic copper (385 W/mK), and a specific heat capacity of 0.7 J/gK, which is twice that of copper [1]. Compared with commonly used nanoparticles, CNTs have high aspect ratios to potentially build a network of channels for higher heat flux. In addition, CNTs are self-lubricating, and thus, would possibly allow the use of lower viscosity oils for more efficient heat dissipation. While CNTs have been previously explored as additives to heat transfer fluids in limited literature studies [2, 3], these investigations encountered great difficulties in suspending CNTs in lubricating oils. Dispersants appear to help, but the experimentally measured thermal conductivity of a fluid containing CNTs was significantly lower than the theoretical value. Our approach is to apply organic modifications to the CNT surface to facilitate dispersion and suspension of CNTs in EV fluids [4]. Similar surface functionalization had achieved stable suspension of metallic and ceramic nanoparticles in lubricating oils in our previous work [5, 6, 7]. Table I.1.2.3.1 compares the proposed organically modified CNTs against the state-of-the-art dispersant-suspended CNTs in heat transfer fluids.

Table I.1.2.3.1. Proposed Organically Modified CNTs vs. the State-of-the-Art Dispersant-Suspended CNTs

	CNTs dispersed by surfactant	Organically modified CNTs
Organic-CNT Bonding	Weaker electrostatic interaction at the CNT-dispersant interface	Stronger covalent bonding at the CNT-organic interface
CNT-CNT Interaction	CNTs in bundles suspended by dispersant	Individual CNTs suspended by the organic layer
Path of Heat Flux	Isolated CNT bundles	Global or local CNT network(s)

The work scope for this task includes: (1) identification of suitable CNT types and sizes; (2) CNT surface modification; (3) materials characterization; (4) suspendability of organically modified CNTs; (5) thermophysical testing; (6) tribological testing; and (7) data analysis.

Results

CNT Types and Sizes

Multiwall CNTs were reported to provide more enhancement in heat transfer than single-wall CNTs, and therefore, are the focus of this study. Several multiwall CNTs with different lengths and diameters, as shown in Figure I.1.2.3.1, have been acquired as candidates for surface modifications.

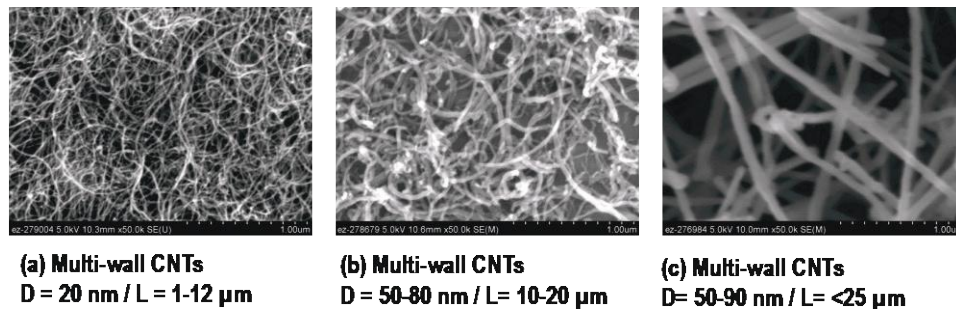
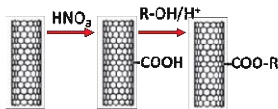


Figure I.1.2.12. Multiwall CNTs with different lengths and diameters. Source: ORNL.

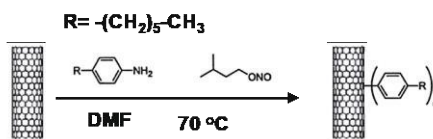
Organic Modification of CNTs

This sub-task is developing unique organic surface modifications for CNTs to allow stable suspension and dispersion in EV fluids. Research is in progress using different synthesis approaches, including esterification, diazonium coupling, and organic peroxides-based modification, as illustrated in Figure I.1.2.3.2.

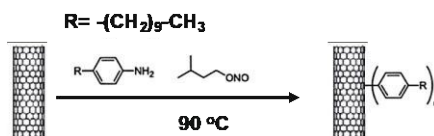
1. Acid treatment + Esterification



2. Diazonium coupling reaction



3. Diazonium coupling reaction (Solvent free)



4. Organic peroxide pathways

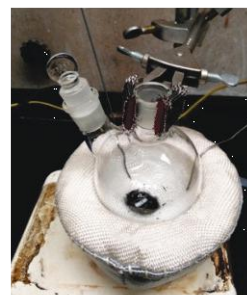
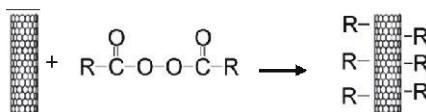


Figure I.1.2.13. Organic surface modifications for CNTs. Source: ORNL.

Suspendability of Organically Modified CNTs in Oils

The initial efforts to demonstrate organically modified CNTs has delivered encouraging results. Figure I.1.2.3.3 compares suspension of CNTs in a polar polyalkylene glycol (PAG) base oil. While the unmodified CNTs appeared to be dispersed and suspended in the PAG oil immediately after sonication, they precipitated and settled on the bottom of the vial after 26 days of storage. In contrast, the two types of organically modified CNTs showed stable dispersion and suspension even after 52 days. Suspension of CNTs in a non-polar polyalphaolefin (PAO) base oil was more challenging, as shown in Figure I.1.2.3.4. The unmodified CNTs clearly precipitated after only 3 days. The organic modification seemed to slow down the settling but will require further improvements for long-term stable suspension in non-polar PAO oils.

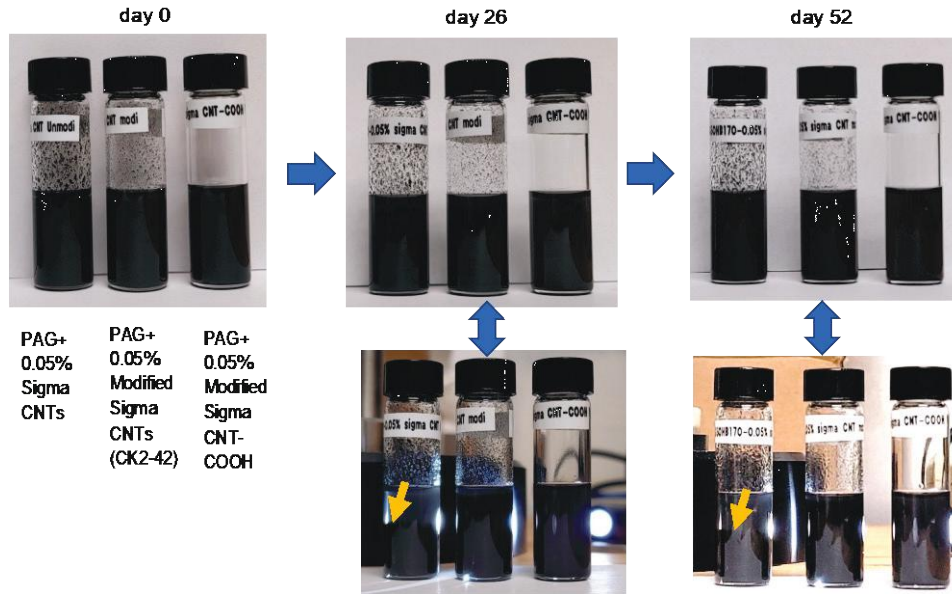


Figure I.1.2.14. Surface-modified CNTs showing stable suspension in a PAG oil. Source: ORNL.

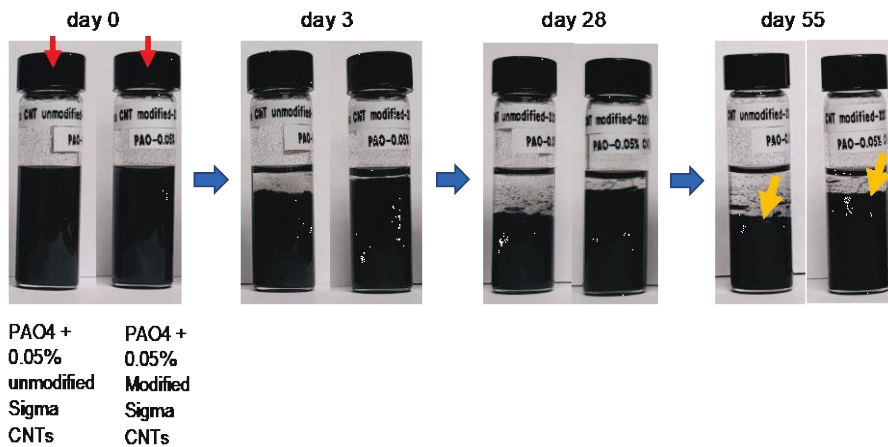


Figure I.1.2.15. Organically modified CNTs showing improved, but still unstable suspension in a PAO oil. Source: ORNL.

Oil Thermal Conductivity Enhancement by CNTs

Thermal conductivity of lubricants with and without CNTs was measured using a Transient Hot-Wire Liquid Thermal Conductivity Meter using the procedure defined in American Society for Testing and Materials (ASTM) standard D-7896-19. Preliminary results of adding 0.5% unmodified CNTs to the PAO and PAG base oils showed 7%–8% and 8%–10% improvement in thermal conductivity, respectively, as shown in Figure I.1.2.3.5. The thermal conductivities of an EV base oil with and without CNTs are compared in Figure I.1.2.3.6. The CNT size clearly has a significant influence on thermal conductivity of the modified oils. The addition of 0.25 wt.% of CNTs of 50–90 nm diameter and 10–25 μm length increased the thermal conductivity of the oil by 19%. In contrast, using smaller CNTs of 20 nm diameter and 1–12 μm length at the same 0.25% concentration increased the thermal conductivity of the oil by only 3%. Further investigation is under way to confirm the trend that larger CNTs provide better performance and to begin to understand the mechanisms behind this experimental observation for further optimization.

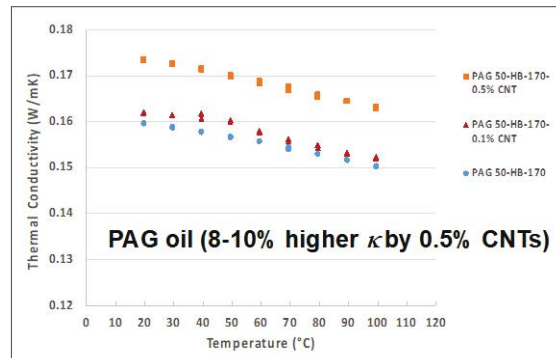
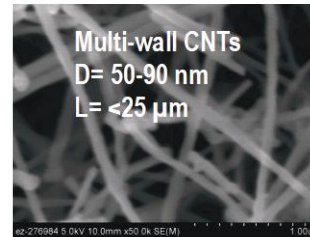
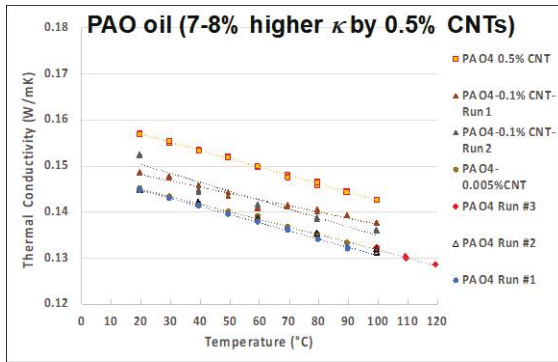
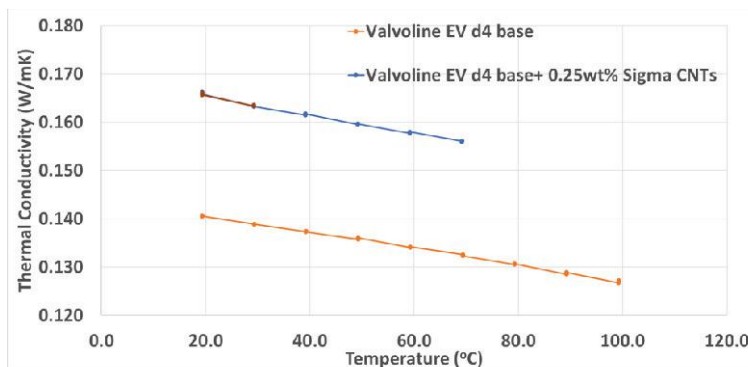
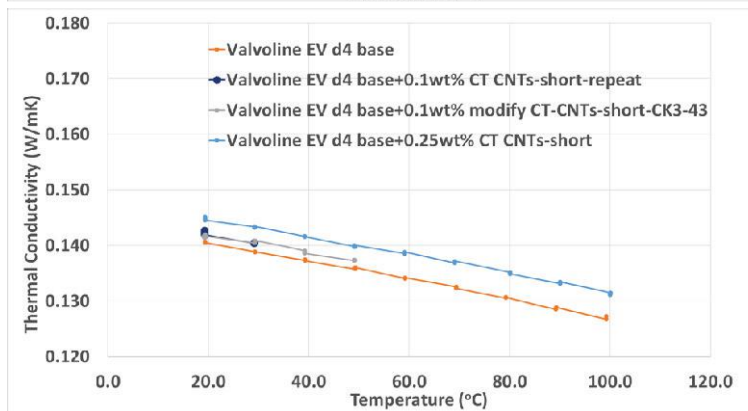
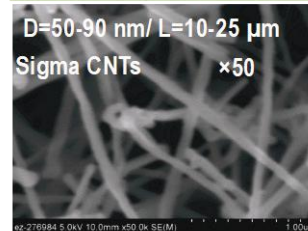


Figure I.1.2.16. The addition of 0.5% CNTs increased the thermal conductivity of PAO and PAG base oils by 7%–8% and 8%–10%, respectively. Source: ORNL.



Larger CNTs increased the oil thermal conductivity by 19%



Smaller CNTs increased the oil thermal conductivity by 3%

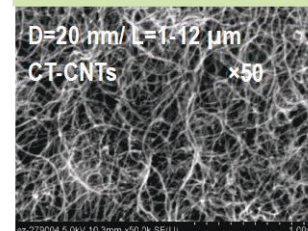


Figure I.1.2.17. A comparison of thermal conductivities of an EV base oil with CNTs in two sizes. The larger CNTs appear to be more effective in improving the thermal conductivity of the oil. Source: ORNL.

Conclusions

CNTs possess 10× higher thermal conductivity than copper and would be ideal additives for enhancing the heat transfer capacity of EV fluids. Compared with commonly used nanoparticles, CNTs have high aspect ratios to potentially create a network of channels for higher heat flux within a lubricant fluid. Additionally, CNTs are self-lubricating, and thus, would possibly allow the use of lower viscosity oils for more efficient heat dissipation. However, CNTs cannot be dispersed or suspended in oils without help. This study is developing organic surface modifications for CNTs to allow stable oil suspension and subsequently increase the thermal conductivity of the EV fluid. Proof-of-concept has been achieved for functionalized CNTs in a polar PAG oil and improvement was observed in a non-polar PAO oil. Initial results showed as much as 19% increased thermal conductivity by adding 0.25% CNTs to an EV base oil. Larger CNTs seemed to be much more effective than smaller CNTs in increasing the oils' heat transfer. Further development and fundamental investigation are underway in collaboration with Valvoline under a new CRADA agreement.

Key Publications

1. Qu, J., 2022, "CNTs for EV friction and thermal management," *2nd STLE Tribology and Lubrication for E-Mobility Conference*, 30 November–2 December 2022, San Antonio, TX, USA.
2. Qu, J., 2022, "Ionic and nano lubricant additives for ICE, rear axle, and e-motor," *Valvoline International R&D Annual Meeting*, 31 October–2 November 2022, Lexington, KY, USA (invited keynote).
3. Qu, J., C. Kumara, H. Wang, and H. M. Meyer, "Materials, lubricants, and cooling for heavy duty electric vehicles," Project ID mat237, *DOE VTO Annual Merit Review*, 21–23 June 2022, Washington, DC, USA.

References

1. Muratov, V. B., O. O. Vasil'ev, L. M. Kulikov, V. V. Garbuz, Y. V. Nesterenko, and T. I. Duda, 2012, "Thermodynamic properties of multiwalled carbon nanotubes," *J. Superhard Mater.*, Vol. 34, No. 3, pp. 173–178. <https://doi.org/10.3103/S1063457612030045>.
2. Chen, L., and H. Xie, 2009, "Silicon oil based multiwalled carbon nanotubes nanofluid with optimized thermal conductivity enhancement," *Colloids Surf. A Physicochem. Eng. Asp.*, Vol. 352, No. 1, pp. 136–140. <https://doi.org/10.1016/j.colsurfa.2009.10.015>.
3. Nanda, J., C. Maranville, S. C. Bollin, D. Sawall, H. Ohtani, J. T. Remillard, and J. M. Ginder, 2008, "Thermal conductivity of single-wall carbon nanotube dispersions: Role of interfacial effects," *J. Phys. Chem. C*, Vol. 112, No. 3, pp. 654–658. <https://doi.org/10.1021/jp711164h>.
4. Qu, J., and C. Kumara, "Organic-modified carbon nanotubes as lubricant additives for improved heat transfer and lubricity," ORNL Invention Disclosure # 202004711, 20 August 2020.
5. Kumara, C., and J. Qu, 2022, "Metal nanoparticles as lubricant additives," U.S. Patent #11,370,988, 28 June 2022.
6. Kumara, C., D. N. Leonard, H. M. Meyer, H. M. Luo, B. L. Armstrong, and J. Qu, 2018, "Palladium nanoparticles enabled ultra-thick tribofilm with unique composition," *ACS Appl. Mater. Interfaces*, Vol. 10, No. 37, pp. 31804–31812. <https://doi.org/10.1021/acsami.8b11213>.
7. Kumara, C., H. M. Luo, D. N. Leonard, H. M. Meyer, and J. Qu, 2017, "Organic-modified silver nanoparticles as lubricant additives," *ACS Appl. Mater. Interfaces*, Vol. 9, No. 42, pp. 37227–37237. <https://doi.org/10.1021/acsami.7b13683>.

Acknowledgements

The authors would like to acknowledge the support of the co-PI, C. Kumara, and their ORNL collaborator, H. Wang. Technical support from our CRADA partner, Valvoline, as well as from our co-PIs—J. Bonta, N. Ren, E. Murphy, and R. England—is also acknowledged.

I.1.2.4 Task 2D. Carbon Nanotube (CNT) Coatings for Superlubricity and Thermal Management of Heavy Duty EVs (Oak Ridge National Laboratory)

Jun Qu, Principal Investigator

Oak Ridge National Laboratory
Materials Science and Technology Division
1 Bethel Valley Rd.
Oak Ridge, TN 37830
E-mail: quejn@ornl.gov

J. Allen Haynes, PMCP Consortium Manager

Oak Ridge National Laboratory
Materials Science and Technology Division
1 Bethel Valley Rd.
Oak Ridge, TN 37830
E-mail: haynesa@ornl.gov

Jerry Gibbs, DOE Technology Development Manager

U.S. Department of Energy
E-mail: jerry.gibbs@ee.doe.gov

Start Date: November 1, 2021	End Date: September 30, 2022	
Project Funding (FY 2022): \$240,000	DOE share: \$240,000	Non-DOE share: \$0

Project Introduction

Parasitic frictional loss in EVs consumes 6% of the energy. Critical EV components—including the electric motor (e-motor), inverter, and battery—require more efficient cooling to allow higher power output. This project intends to develop a CNT coating for potential applications to EV powertrains for friction and thermal management. This CNT coating possesses superlubricity (e.g., friction coefficient <0.01) in macroscale sliding in an ambient environment, and thus, it is a compelling candidate for improved mechanical efficiency of e-motor bearings and e-axle gears. The CNT coating can also potentially be used to improve the heat dissipation in the EV system by taking advantage of the exceptionally high thermal conductivity (e.g., $>10\times$ higher than aluminum) of CNTs and much increased surface area by $>100\times$. One application of immediate interest is heat exchangers. This study proposes to develop the CNT coating specifically for application to EV powertrain alloys, determine the sustainability of superlubricity, demonstrate the feasibility of enhanced heat transfer capacity, and gain fundamental understanding to enable improved design, manufacturing, and cost of deployable coatings for advanced friction and thermal management.

Objectives

This task intends to gain fundamental understanding and develop CNT-based coatings for EV powertrain components for enhanced frictional and thermal management.

Approach

This study proposes to develop novel coatings composed of CNTs for friction and thermal management specifically for EVs. These CNT coatings were recently invented at ORNL in a proof-of-concept seed money project funded by ORNL. The coating process is based on chemical vapor deposition (CVD) using a low-cost precursor (e.g., ethanol), and thus, has few geometric restrictions, is low-cost, and is readily scalable.

Superlubricity, a phenomenon defined as a surface with a coefficient of friction (COF) below 0.01 [1, 2], was limited to the microscale in controlled environments in earlier literature and has recently been realized for

macroscale sliding of ceramic and carbon surfaces lubricated by water and other polar fluids. However, there is a lack of reports on superlubricity for the most common bearing system (i.e., steel-steel contact in non-polar oil lubrication). The CNT coating being developed in this study is intended to function as sacrificial, running-in coating to generate superlubricity for macroscale steel-to-steel sliding under minimum quantity lubrication (MQL) in the ambient environment. Such a superlubricity coating could be applied to the e-motor bearings and e-axle gears for improved mechanical efficiency. In addition to friction reduction, the wear protection by the CNT coating could also enable the use of lower viscosity e-motor/e-axle lubricants, leading to a higher heat transfer capacity. The CNT coating could also be used for EV cooling, specifically of the e-motor and inverter, by taking advantage of the exceptionally high thermal conductivity of CNTs (2800–6000 W/mK, compared with 88–251 W/mK for Al alloys), and much increased surface area (by 100× to 1,000×). Growing CNTs on the fins of the e-motor heat exchanger and/or radiator is anticipated to improve the air-to-fin and/or liquid-to-solid heat transfer. The work scope for this year included CNT coating development, materials characterization, bench scale tribological testing, thermophysical testing, and data analysis.

Results

CNTs Synthesis and Morphology

A type 316 stainless steel (SS) disk (10 mm in diameter) was used as a substrate to deposit CNTs with a ‘catalyst-free’ CVD process [3] using an in-house CVD setup. The inset in Figure I.1.2.4.1(a) shows a Type 316 SS disk before and after the CVD process. The entire surface appears black after the process, which typically indicates good CNT coating coverage. Figure I.1.2.4.1(a) and Figure I.1.2.4.1(b), respectively, show the top and side views of the array of CNTs with vertical alignment on the SS surface. The length of the deposited CNTs is 20–30 μm and average diameters are in the range of 40–50 nm. However, the deposited length and diameter of the CNTs can be controlled by the carbon source and CVD process parameters. High-resolution transmission electron microscopy (HR-TEM) images in Figure I.1.2.4.1(c) clearly show they are multiwall CNTs. Graphitic interlayers with parallel lattice fringes are clearly visible in the higher magnification images.

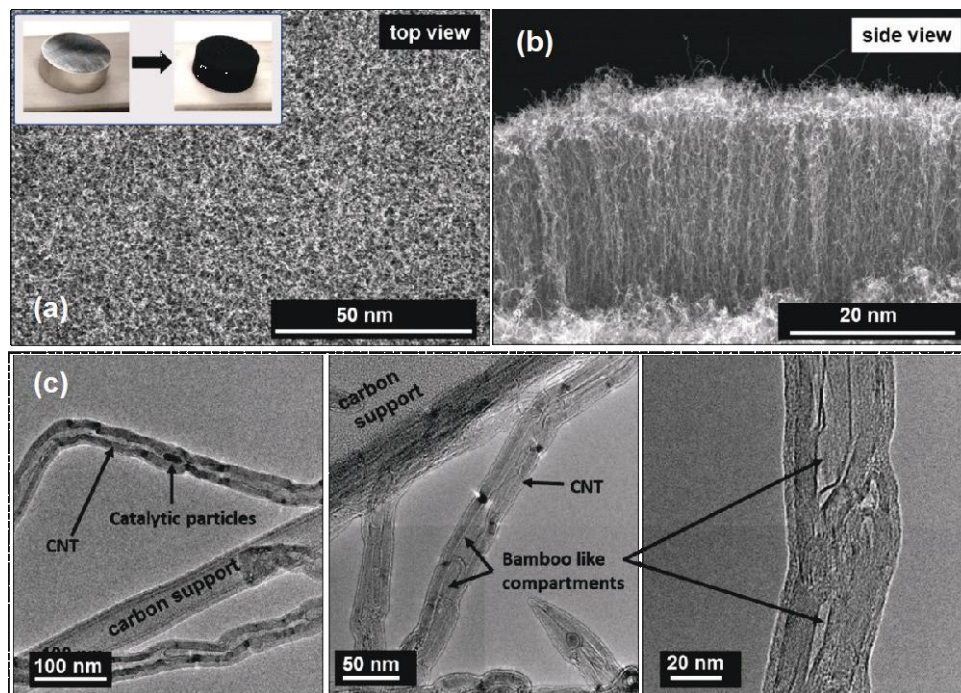


Figure I.1.2.18. CNTs deposited on a Type 316 SS disk: (a) SEM top view, with the inset showing the SS disk before and after the CVD process; (b) SEM side view; and (c) HR-TEM images revealing the CNT nanostructure. Source: ORNL.

Superlubricity Behavior

Disk-on-flat reciprocating sliding tests were conducted under MQL. The lubricant was polyalphaolefin 4 cSt base oil. Only one droplet (~0.05 mL) of oil was used in each test. A Type 316 SS disk, with or without the CNT coating, was rubbing against an M2 tool steel flat. Tests were carried out at RT under a constant 100 N load at 0.5 Hz oscillation with a 10 mm stroke for sliding distances of 100, 1,000, or 10,500 m. Three forms of SS disks were tested: (a) bare disk as polished; (b) CNT-coated by the above-described CVD process; and (c) heat-treated by going through a similar CVD process, but without introducing the carbon source. At least two repeat tests were carried out for each material at each testing condition. Figure I.1.2.4.2(a) compares the friction behavior for 100 m of sliding at 5,000 cycles for 2.8 hours under MQL. The COF of all tests with or without the CNT coating started in the range of 0.05–0.15, confirming the boundary lubrication regime as predicted by the oil film thickness and lambda ratio calculation.

The COF for the bare SS disk (e.g., Control 1) started high and fluctuated in the range of 0.15–0.4. Such a high COF (>0.2) indicated scuffing damage, which was later confirmed by the worn surface morphology. The heat-treated SS disk performed substantially better with the COF in the range of 0.1–0.2, which may be attributed to the oxide film from the heat-treatment. In contrast, the CNT-coated SS disk, after a short running-in period with a COF in the range of 0.05–0.1, produced an ultra-low steady-state COF of 0.003–0.007 throughout the 100 m sliding. Elongated tests of sliding distances of 1,000 m at 50,000 cycles for 27.8 hours and 10,500 m at 525,000 cycles for 12.15 days were conducted and demonstrated sustainable superlubricity, as shown in Figure I.1.2.4.2(c) and Figure I.1.2.4.2(d), respectively. Only one droplet of oil was used for each 1,000 m test and an additional one droplet of oil was supplied every 3 days to compensate for oil evaporation during the 10,500 m test. In the two 1,000 m tests, the steady-state COF was 0.007 and 0.003, respectively. In the 10,500 m test, the COF stabilized at about 0.002. It should be stressed once again that, unlike the literature reported superlubricity that generally requires flooded lubrication for a hydrodynamic effect or a special-controlled gas environment, this CNT coating demonstrated superlubricity in macroscale sliding under MQL in the ambient environment, which is quite remarkable.

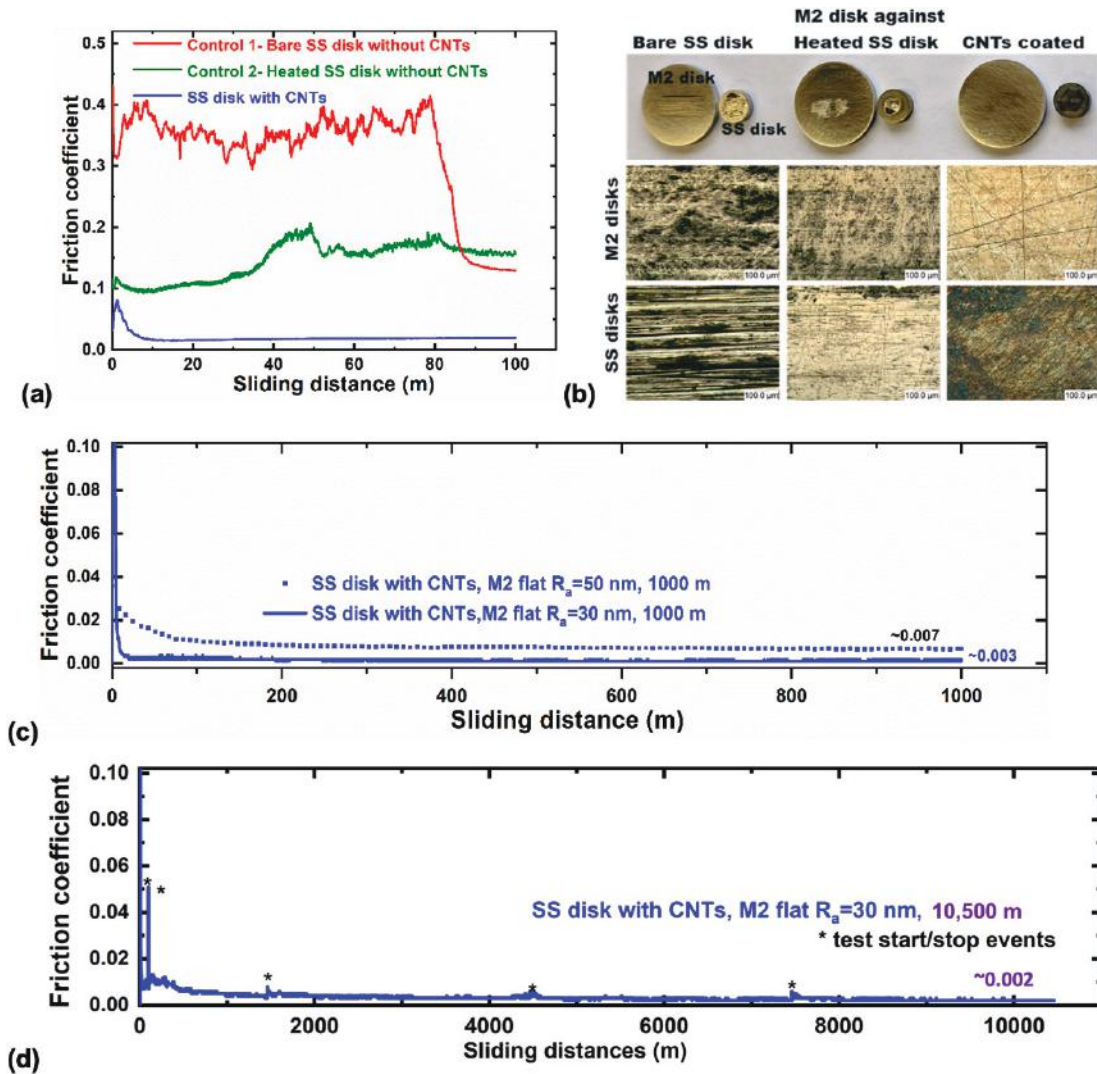


Figure I.1.2.19. CNT-coated SS demonstrating superlubricity in macroscale sliding under MQL in an ambient environment: (a and b) comparison of friction behavior and worn surface morphology for 100 m sliding at 5,000 cycles for 2.8 hours; (c and d) sustainable superlubricity in elongated sliding tests of 1,000 m at 50,000 cycles for ~28 hours, and 10,500 m at 525,000 cycles for ~12 days, respectively. Source: ORNL.

Worn Surface Characterization

The worn surfaces are shown in Figure I.1.2.4.2(b). The wear scars on the bare SS disks show clear signs of scuffing damage. Using the heat-treated SS disks reduced the severity of surface damage. In contrast, negligible wear or surface damage was observed on the CNT-coated SS disks and their counter M2 steel surfaces. EDS analysis suggested a carbon-rich tribofilm on the contact areas, which is likely a result of transfer and smearing of the fractured CNTs. Figure I.1.2.4.3(a) shows a focused ion beam (FIB) SEM lifted cross-section of the M2 tool steel flat tested against a CNT-coated SS disk after 100m of sliding. The tribofilm appears to enclose some nanoparticles, possibly wear debris, and fills the valleys to make the surface smoother. Figure I.1.2.4.3(b) displays the HR-TEM images near the interlayer, in the middle, and near the top surface of the tribofilm. The darker particles are likely iron oxides based on lattice spacing measurement. The lighter region probably is carbon-based according to the EDS analysis, as observed in Figure I.1.2.4.3(c), but its lattice spacing could not be accurately determined because the crystalline lattices were fractured and scattered and mixed with the amorphous phase. It appears this tribofilm is dominated by carbonaceous materials in the bottom zone and contains an increasing amount of iron oxide nanoparticles towards the top surface. The

Raman spectra of the as-grown CNTs and the carbon contents in the tribofilms are shown in Figure I.1.2.4.4. The intensity ratio of the G to D bands (I_G/I_D) indicates the degree of disorder in the graphene structure. The I_G/I_D ratio of the as-grown CNTs is about 1.5. The carbon signal on both the worn surfaces shows characteristics similar to graphene oxides with a reduced I_G/I_D ratio (0.55), indicating the graphene structure became more disordered after testing. In addition, the G band became broader and shifted to a higher frequency after the sliding test, which correlates well with the compressed carbon-rich film on the contact surface as peak shift to a higher frequency often is associated with compressive residual stress. The Raman spectra of the tribofilms on the worn SS disk and its counter M2 steel flat seem very similar, suggesting the carbon film being formed at the contact interface and possibly transferred back and forth between the two surfaces.

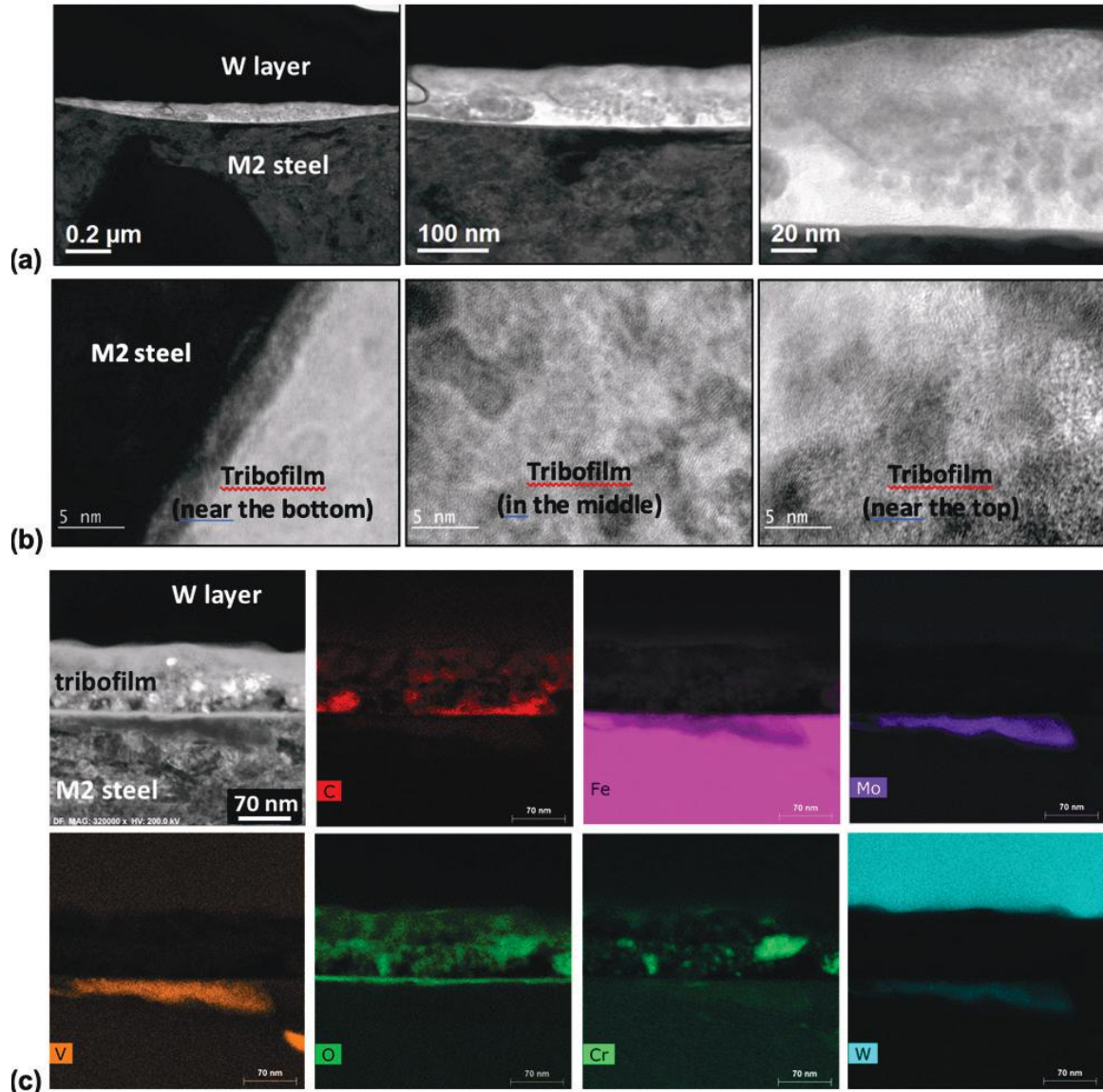


Figure I.1.2.20. Cross-sectional characterization of the tribofilm on the M2 steel surface after sliding against a CNT-coated 316 SS disk: (a) FIB-SEM images; (b) HR-TEM images; and (c) EDS elemental maps.

Source: ORNL.

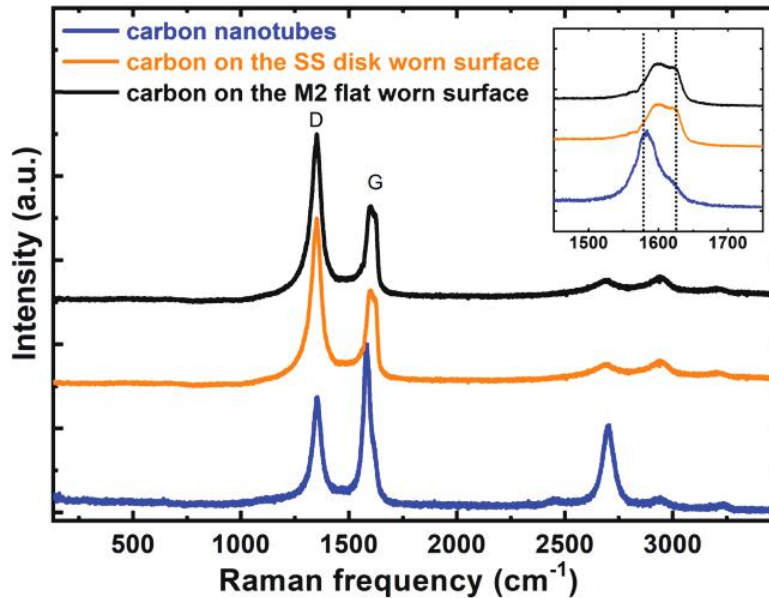


Figure I.1.2.21. Raman spectra of as-grown CNTs (blue) and the tribofilms on two wear scars on the CNT-coated SS disk (orange) and the M2 tool steel flat (black) after 1,000 m sliding. Source: ORNL.

Hypothetic Mechanisms for Superlubricity

Multiwall CNTs are essentially cylindrical structures consisting of rolled-up sheets of graphene. It is hypothesized that CNTs fractured into small graphene flakes at the contact interface during the initial running-in period of the tribotest. The continued thermomechanical stresses would further mix the graphene flakes (individual or clustered) with the metallic wear debris (off the steel surface during running-in) at the interface, oxidize them, and deposit them onto the contact area to form a tribofilm. Such a hypothesis is supported by the tribofilm characterization results in Figure I.1.2.4.3 and Figure I.1.2.4.4. Since the contact areas on both the 316 stainless and M2 tool steel disks were covered by a graphene-containing tribofilm, the actual sliding pair became graphene-graphene, which presumably had very low shear resistance and thus led to superlubricity. This is similar to the superlubricity performance previously observed for a graphene-coated ceramic-ceramic contact in boundary lubrication [4]. The presence of oil, despite MQL, is necessary in achieving superlubricity by preventing scuffing, aligning the graphene flakes in forming the tribofilm, and protecting the tribofilm from wear.

Applicability and Limitations

While superlubricity behavior was observed for the CNT coating, it is understood the coating's tribological performance could be significantly influenced by the bearing materials, contact geometry, lubricant chemistry, as well as operation conditions such as temperature and gas environment. Therefore, the reported superlubricity behavior and mechanisms here simply set a scientific basis for future studies on the applicability and limitations of such a CNT coating for specific applications.

CNT Coating for Improving Heat Transfer

The CNT coating possesses a high thermal conductivity and high surface area and thus is ideal for heat dissipation. One potential application is heat sinks, which are commonly made of aluminum (Al). However, growing CNTs on the Al surface is rather challenging due to CVD deposition temperatures. By tailoring the CVD process parameters, initial feasibility of depositing on Al has been demonstrated. As shown in Figure I.1.2.4.5, an array of vertically aligned CNTs was successfully grown on an Al alloy 6061 surface with nominally 100% surface coverage. The CVD processing temperature had to be 600°C or slightly above, which has potential to be too high for most Al alloys because the heat-treatment temperature for Al alloys is up to 525°C. The impact of the CVD process at 600°C on the thermophysical and mechanical properties of the Al alloys will be investigated.

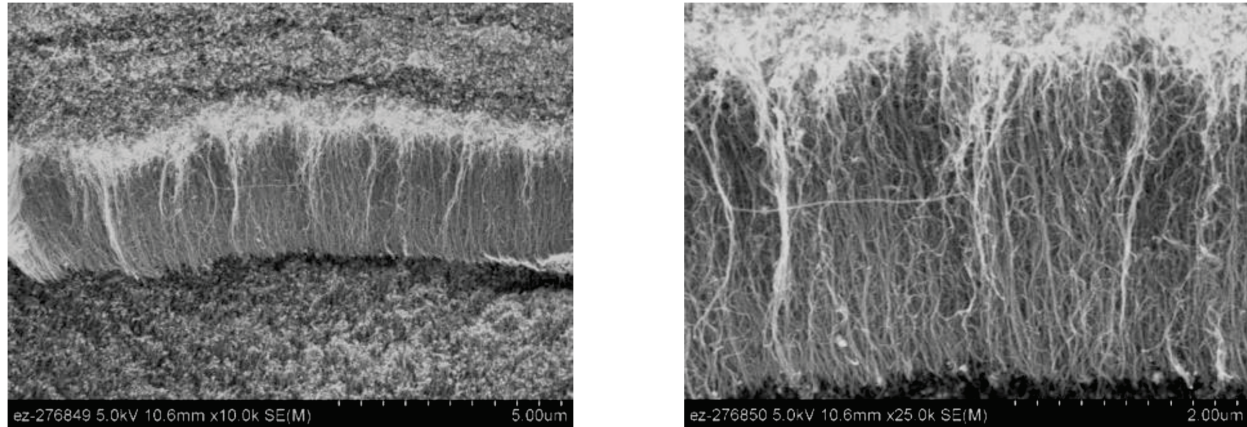


Figure I.1.2.22. CNT coating grown on Al 6061 alloy surface. Source: ORNL.

Conclusions

A coating composed of vertically aligned CNTs is being developed for frictional and thermal management for potential EV applications. This CNT coating, when used for running-in, has demonstrated superlubricity COF of 0.001–0.007 in macroscale sliding under MQL in the ambient environment. This was 95%–99% friction reduction compared with the uncoated baseline. While the CNT coating was quickly removed during running-in, the fractured CNTs created a tribofilm containing graphene and graphene oxide. The ultra-low shear resistance of the in situ formed graphene-graphene contact interface is believed to be responsible for the superlubricity performance. It was observed that the graphene-containing tribofilm, once established, could accommodate changes in sliding conditions and sustain in extended sliding (e.g., 10,500 m or 525,000 cycles for 12 days) even without additional CNT supply. This CNT coating also has potential in improving heat transfer by taking advantage of its high thermal conductivity and surface area.

Key Publications

1. Kumara, C., M. J. Lance, and J. Qu, 2023, “Macroscale superlubricity by a sacrificial carbon nanotube coating,” *Mater. Today Nano*, accepted for publication.
2. Qu, J., 2022, “CNTs for EV friction and thermal management,” *2nd STLE Tribology and Lubrication for E-Mobility Conference*, 30 November–2 December 2022, San Antonio, TX, USA.
3. Qu, J., C. Kumara, H. Wang, and H. M. Meyer, “Materials, lubricants, and cooling for heavy duty electric vehicles,” Project ID mat237, *DOE VTO Annual Merit Review*, 21–23 June 2022, Washington, DC, USA.

References

1. Shinjo, K., and M. Hirano, 1993, “Dynamics of friction: Superlubric state,” *Surf. Sci.*, Vol. 283, pp. 473–478. [https://doi.org/10.1016/0039-6028\(93\)91022-H](https://doi.org/10.1016/0039-6028(93)91022-H).
2. Müser, M. H., 2015, “Theoretical studies of superlubricity,” In Gnecco, E., and E. Meyer (eds.), *Fundamentals of Friction and Wear on the Nanoscale*, pp. 209–232. Springer Cham, Switzerland.
3. Kumara, C., J. Qu, and P. A. Menchhofer, 2020, “Superlubricity coating containing carbon nanotubes,” U.S. Patent Application 17/090,216, 5 November 2020.
4. Liu, Y., J. Li, X. Ge, S. Yi, H. Wang, Y. Liu, and J. Luo, 2020, “Macroscale superlubricity achieved on the hydrophobic graphene coating with glycerol,” *ACS Appl. Mater. Interfaces*, Vol. 12, pp. 18859–18869. <https://doi.org/10.1021/acsami.0c01515>.

Acknowledgements

The authors would like to acknowledge the support of the co-PI, C. Kumara, and their ORNL collaborators: H. Wang, H. Meyer, and M. Lance. Technical support from K. Cooley also is acknowledged.

I.1.2.5 Task 2E. Solid-Phase Joining and Processing Methods Towards Efficient, Heavy-Duty EV Motors (Pacific Northwest National Laboratory)

Piyush Upadhyay, Principal Investigator

Pacific Northwest National Laboratory
Energy Processes & Materials Division
902 Battelle Blvd.
Richland, WA 99354
E-mail: piyush.upadhyay@pnnl.gov

J. Allen Haynes, PMCP Consortium Manager

Oak Ridge National Laboratory
Materials Science and Technology Division
1 Bethel Valley Rd.
Oak Ridge, TN 37830
E-mail: haynesa@ornl.gov

Jerry Gibbs, DOE Technology Development Manager

U.S. Department of Energy
E-mail: jerry.gibbs@ee.doe.gov

Start Date: November 15, 2021	End Date: September 30, 2023	
Project Funding (FY 2022): \$244,000	DOE share: \$244,000	Non-DOE share: \$0

Project Introduction

The purpose of this task is to develop solid-phase, processing-based manufacturing technologies to produce high-performance dissimilar joints and materials to improve EV electric motors (e-motors), resulting in a lower cost, higher efficiency, and reduced weight. This task uses friction stir derived joining and processing techniques to explore technical feasibility of producing: (1) high-strength, high conductivity Al-Cu joints; and (2) high-formability, high-resistivity, low-coercivity, and high-Si steel for rotor cores. These two sub-tasks are described below.

Sub-task 1: Al-Cu Friction Stir Welding (FSW) Joint Development

High-power induction motor rotors are made entirely of either Al or Cu. The process of die-casting Al rotors is cost-effective and has gradually improved since first being developed a century ago. However, Al is 60% less electrically conductive than Cu. EV motors made from Cu can result in large efficiency improvements along with reduced motor package size and weight, which leads to a longer range between charging. However, the weight and cost of Cu and the high cost of die-casting as compared to Al still represent challenges for commercialization of Cu rotors. One approach is to replace the thick Cu end caps with lightweight Al, while retaining Cu shorting bars for improved conductivity throughout the steel core. Reduction of overall mass of the rotor (e.g., reduced inertia) can also increase durability, especially when operated at a higher rpm. However, significant challenges exist in manufacturing this hybrid assembly. The loss of electrical conductivity and mechanical strength at the Al-Cu transition region/interface is a primary challenge. This challenge is due to vastly different melting points, high-temperature flow stresses, persistent oxide layers and coefficient of thermal expansion mismatch. The Al-Cu interface created by both fusion and solid-state methods contains brittle intermetallic compounds (IMCs) that can negatively impact electrical conductivity and mechanical strength at the joint. Proper control of thickness and composition of the IMC layer is critical for consistent mechanical and electrical performance. This task intends to leverage solid-phase, processing-based technological expertise at PNNL to enable low-weight Al-Cu hybrid rotors.

Sub-task 2: : Friction Stir Processing (FSP) of Fe-Si Steel

Rolled laminate sheets of ferromagnetic (Fe-2%–3% Si) material is used as a magnetic core for induction rotors and stators. The current manufacturing technology begins with cold rolling of hot-rolled strips followed by batch annealing and temper rolling. Subsequently, strip blanks are stamped and the laminations are subjected to annealing treatments. These steps are followed to ensure the electrical and magnetic properties are optimized. The need is to have a high-magnetic permeability, high-saturation induction, low-coercivity, and low-eddy current loss. A roadblock to increasing efficiency is the gauge thickness of laminations. To minimize electrical conduction and thereby minimize core loss through maximizing magnetic flux density, the laminations are kept as thin as possible (e.g., 0.35 mm or thinner). This leads to increased manufacturing costs. One solution is to decrease resistivity by increasing the Si content of steel. An increased Si content has been shown to produce a good balance of high-saturation magnetization, high electrical resistivity, and low Fe loss. However, conventionally manufactured high-Si steel is brittle and has poor formability, leading to higher rejection rates and blanking tool costs. Significant cost-savings could be achieved if high-Si steel can be produced with better formability.

Objectives

The goal of Task 1 is to mature friction stir techniques to fabricate relevant Al-Cu coupons with co-optimized mechanical strength and electrical conductivity for Al-Cu hybrid rotors. Experimental trials will include the fabrication of coupon level microstructural and mechanical characterization. Task 2 will develop FSP methods to produce high-Si steel from cast/rolled billet. The aim is to produce highly refined grains and heal any porosity present in high-Si steels towards increased resistivity and formability performance. Experimental trials will include coupon level microstructural and mechanical property characterization.

Approach**Sub-task 1: Al-Cu FSW Joint Development**

Our approach will use novel Al-Cu interface geometries, tool design, and welding parameters to produce and study a large set of Al-Cu-bonded joints. Developmental work will first occur at the linear coupon level. End cap construction is typically made of multiple stacks of thin sheets (as opposed to single monolithic plate) in order to ensure hole tolerances are met during stamping/waterjet cutting operation. For this rotor construction, five stacked Al sheets (2 mm each) are to be bonded to vertically arranged Cu shorting bars. Mechanical and electrical testing of the joints are performed as the welding process is matured and benchmarked against the overcasting method. The overall construction of the induction motor rotor is shown in Figure I.1.2.5.1.

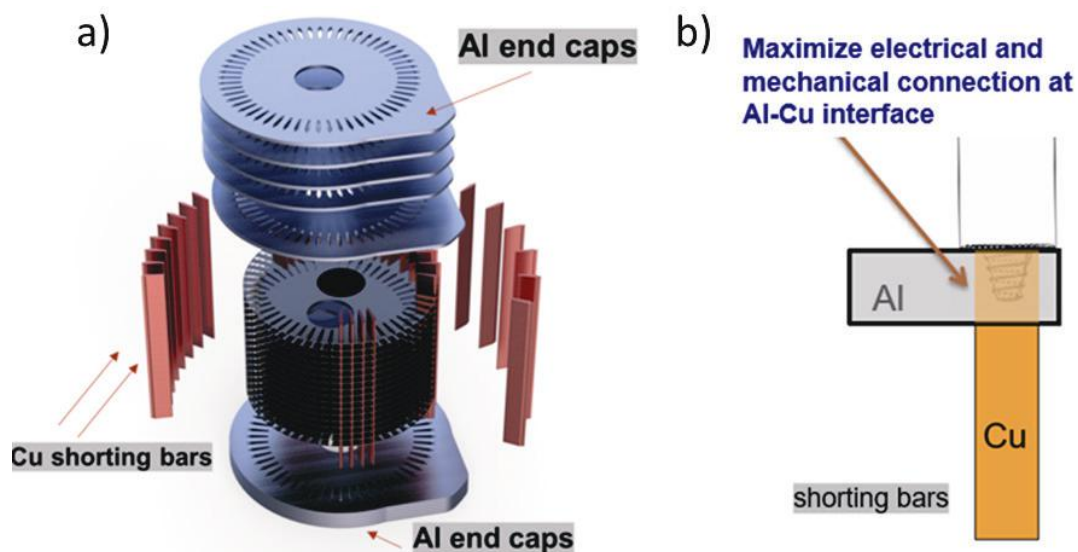


Figure I.1.2.23. Schematic of the (a) Al-Cu hybrid rotor and (b) joining of Al to grooved Cu shorting bar.

Source: PNNL.

Sub-task 2: Al-Cu FSP of Fe-Si Steel

This task will evaluate FSP of Fe-Si (3%–6.5%). Process parameters, tooling, and thermal management will be optimized towards higher formability of high-Si electrical steels. This task will perform systematic developmental work with microstructural, mechanical, and electrical characterization towards the goal of producing high-formability, high-Si steel.

Results

Sub-task 1: Al-Cu FSW Joint Development

A series of trials has been conducted in this study to demonstrate successful joints of five-sheet stack of 2-mm-thick 6061 Al alloy with Cu shorting bar with reasonable joint strength and other physical properties. For the trials, key factors are different tool geometry, welding scheme (single-pass, double pass), and different design of Cu shorting bars with Ni coating and without coating. While the double pass, Al-Cu joints performed well; manufacturing Al-Cu rotor using double pass method requires twice the welding time and two sets of fixturing. So, we are focused on evaluating effectiveness of single-pass approach. Figure I.1.2.5.2 summarizes the Al-Cu stack-up configuration, image of single-pass weld without any surface defect, electro-discharge machining cut pullout tensile specimen, and the fixture for the pullout tests. A custom-designed fixture was fabricated for the pull test that avoided any bending on the stack-up.

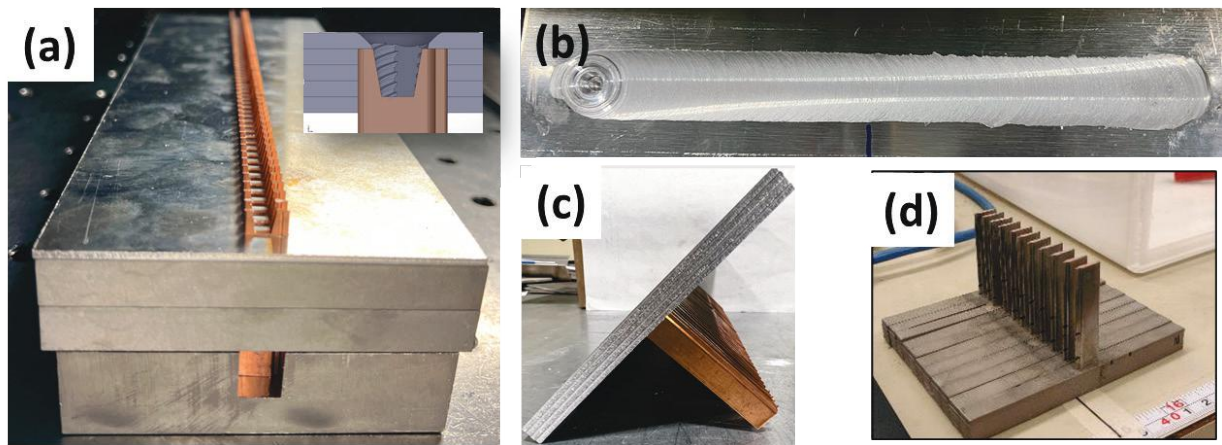


Figure I.1.2.24. (a) Coupon stack-up assembly to join five-sheet stacks of Al to shorting bar with the backing plates (inset: schematic of five-sheet stack with grooved Cu shorting bar), (b) single-pass Al-Cu weld, (c) electro-discharge machining cut pullout specimen, and (d) the test fixture in the Instron 5582 to pullout these cut specimen. Source: PNNL.

After iterative development, process parameter combination of 800 rpm, welding speed of 100 mm/min and plunge depth of 9.5 mm was downselected and multiple samples were tested. Typical load vs. displacement plot and bar chart of peak loads prior to fracture are plotted in Figure I.1.2.5.3(a) and Figure I.1.2.5.3(b), respectively. Average pullout load of single-pass Al-Cu joint is 2381 ± 50 N (8 samples). This strength is comparable to preliminary data from General Motors. For die-casted Al-Cu samples Cu shorting bar fractures were mostly interfacial during pullout testing, as observed in the inset of Figure I.1.2.5.3(b). Sample-to-sample variation in the pullout load is minimal and significantly lower than that for Die-casting method. Nevertheless, the pullout strength of double pass joints, which is being explored in a separate CRADA project, is higher than the single-pass approach so far. However, the single-pass approach is more desirable as it can reduce production time and offer simpler fixturing. Additional process development including tool design and parameter adjustment is planned to further improve the joint strength.

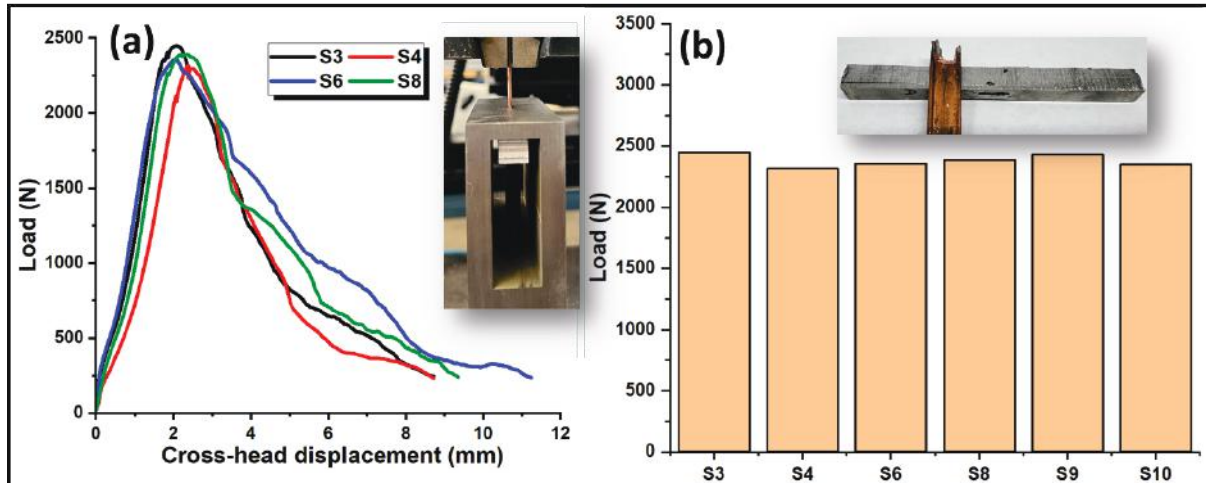


Figure I.1.2.25. (a) Load vs. displacement plot for pullout tests on Al-Cu joints. A custom-made test fixture is shown in the inset. (b) A bar chart showing the maximum load for multiple samples. The Al-Cu fracture after the pullout test is shown in the inset. Source: PNNL.

Ni-coated Cu shorting bars are used to enhance the bonding between Al-Cu and manage the IMC formation at the interface for Die-casting method. SEM and EDS analyses have been done at the FSW interface for both Al-uncoated Cu and Al-Ni-coated Cu joints to understand the IMC formation. As shown in Figure I.1.2.5.4(a), the interface shows an intimate bonding between Al-Cu, and EDS elemental mapping indicates some extent of diffusion with a formation of oxide layer at the interface, as shown in Figure I.1.2.5.4(a1). An interface with Ni-coated Cu indicates the presence of a non-uniform and interrupted Ni layer between the Al/Cu attributing sound joint, as observed in Figure I.1.2.5.4(b) and Figure I.1.2.5.4(b1), respectively. Fragmented Cu particles are embedded in the Al side, as can be seen in Figure I.1.2.5.4(b). This is due to the shear deformation during high-speed welding that results in the breaking and dispersing of Cu particles. Lamellar flow pattern near the interface, as shown in Figure I.1.2.5.4(c) and Figure I.1.2.5.4(c1), suggests well mixing between Al and Cu during the FSW. It should be noted here that SEM/EDS analysis is not able to resolve any IMC layer at the Al-Cu interface. Several research studies have highlighted type, thickness, and distribution of the formation of IMCs at the FSW Al-Cu interface [1–4]. There are reports on the formation of Al_2Cu , Al-Cu type IMCs and a wide range of IMC layer thickness at the interface from $18\ \mu\text{m}$ – $1.7\ \mu\text{m}$ [1–5]. However, Muthu et al. [5] reported a nano-scaled continuous IMC layer enhanced the joint performance. It is plausible that a nano-scaled IMC layer may be present in the Al-Cu joint in this case since bulk plasticization of copper was avoided in this work.

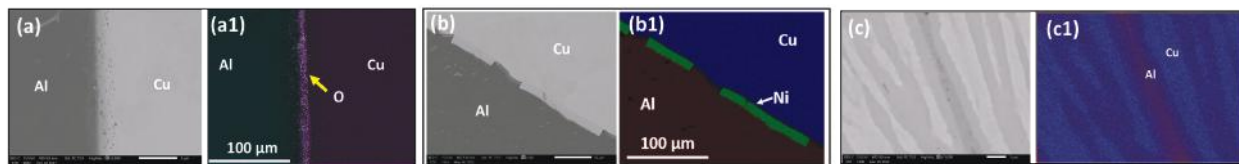


Figure I.1.2.26. FSW Al-Cu interface. (a) SEM micrograph and (a1) EDS elemental mapping at the interface with uncoated Cu shorting bar. (b) SEM micrograph and (b1) EDS elemental mapping at the interface with Ni-coated Cu shorting bar. (c) SEM micrograph and (c1) EDS elemental mapping on Al-Cu lamella formation near interface. Source: PNNL.

Electrical resistance was measured across the Al-Cu interface using a four-point testing method at RT. To standardize voltmeter lead distance and cross-sectional area, the specimens were machined to have identical cross-sections ($11.0\ \text{mm} \times 6.5\ \text{mm}$), as shown in the inset of Figure I.1.2.5.5(a). A low-noise Keithley 6221 DC power supply was used to supply test currents of 0.1 A, and a Keithley 2182A nanovoltmeter was used in

parallel to measure the corresponding voltage drops. Both the power supply and nanovoltmeter were interfaced through the delta configuration to supply currents with alternating polarities and to eliminate contact resistance/thermoelectric artifacts during measurement. Sample temperatures were measured using a Teledyne A655sc forward-looking non-contact infrared camera. The voltmeter leads were located equidistant from the center of the Al bars and into the Cu bars at same distances from the end joined to Al base. Voltage drop was measured at two locations per sample, shown in Figure I.1.2.5.5(a). Electrical performance was represented as the electrical resistance measured across the measurement locations as well as resistance-per-length at RTs for all samples as shown in Figure I.1.2.5.5(b).

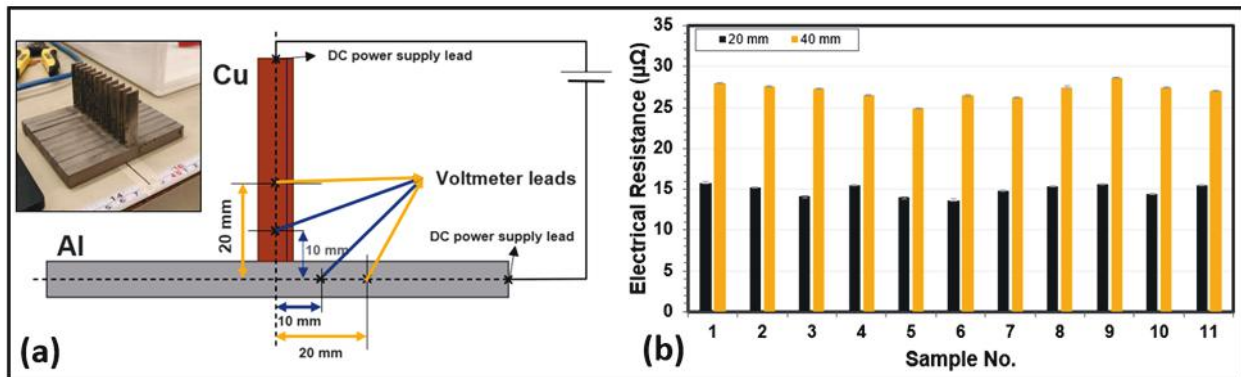


Figure I.1.2.27. Conductivity measurement at room temperature: (a) schematic of the sample with voltmeter lead location (inset: Al-Cu FSW samples); and (b) measured electrical resistance for multiple samples.

Source: PNNL.

Results show the electrical resistances measured across the Al-Cu samples with similar dimensions across identical measurement locations vary between 13.95–15.80 $\mu\Omega$ for the shorter measurement distances of 20 mm, and from 24.89–28.59 $\mu\Omega$ for measurements across 40 mm. These variations in sample resistances are larger than the standard deviations in the measurements seen per sample, which are two orders of magnitude lower and on the order of 0.08–0.09 $\mu\Omega$. This indicates the material behavior is different across the different samples in a statistically significant manner. However, it must be noted that these differences account not only for the weld characteristics, but also for any features—such as pores, cracks, grain size distribution, precipitate density, etc.—in the Al and Cu specimens used to make the weld. This is evident when we examine the resistance-per-length for the samples. If the differences in the weld alone are the source of the variation between the samples, we would expect to see the same resistance-per-length even when the measurements are made at different samples, such as 20 vs. 40 mm. However, the current measurements show a difference of 0.02–0.1 $m\Omega/m$ for measurements across 20 mm and 40 mm, showing that the additional features account for the differences in the electrical resistance. As such, additional testing methods are being developed currently to account for only the variations brought by the weld conditions imposed. This includes decreasing the measurement distances across where voltage drop data is collected. We are working on more trials with different combination of parameters to understand this phenomenon more effectively. We are also planning to send a few samples to our collaborators at General Motors to perform independent measurements to benchmark the electrical measurements.

Sub-task 2: Al-Cu FSP of Fe-Si Steel

In FY 2022, we focused on the linear FSP of the Fe-3 wt.% Si and Fe-4 wt.% alloys to create a baseline for understanding the FSP behavior of Fe-Si steel. In FY 2023, we will focus on higher Si content steel (e.g., Fe-5 wt.% Si-Fe-6.5 wt.% Si). A prior effort at PNNL has demonstrated Fe-Si alloys can be friction stir processed at lower processing temperatures. All FSP work was performed at processing temperatures of 750°C, 800°C, 825°C, and 850°C to understand the effect of processing temperature on mechanical properties. The near-constant temperature during processing was obtained with the help of a temperature control mode developed at PNNL. A custom-made convex scroll shoulder polycarbonate boron nitride tool, as shown in

Figure I.1.2.5.6(a), was used for the FSP. FSP is a high-temperature process, and hence, Fe-Si alloys are susceptible to oxidation during processing. Argon gas was used as a shielding atmosphere to minimize surface oxidation. Figure I.1.2.5.6(b) shows a typical FSP run. The temperature during processing measured at the tool shoulder was plotted in Figure I.1.2.5.6(c), indicating the temperature is fairly constant during the entire processing length barring the plunge-in and extract location.

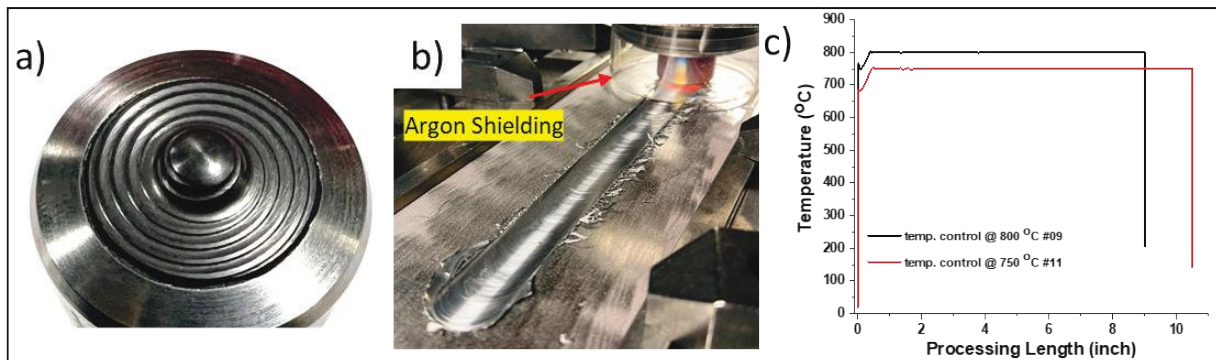


Figure I.1.2.28. (a) Top view of polycarbonate boron nitride tool showing the convex scroll shoulder. (b) FSP of Fe-Si alloy. (c) Temperature profile during the processing. Source: PNNL.

The overall processed region is shown by the low magnification overview presented in the optical micrograph in Figure I.1.2.5.7(a). The intense plastic deformation and frictional heating results in a typical basin-shaped nugget region. To understand the microstructural changes and estimation of mechanical properties, samples were extracted from this nugget region. The microstructures before and after the FSP were compared by the backscattered electron micrographs presented in Figure I.1.2.5.7(b-d). The Fe-3Si base alloy consists of large grains of $\sim 144 \mu\text{m}$. A significant grain refinement can be observed in the nugget region after FSP. Within the FSP microstructure, the higher temperature processing (e.g., 850°C) results in a larger grain size ($\sim 21 \mu\text{m}$) when compared with the 750°C processed microstructure ($\sim 12 \mu\text{m}$). The resultant mechanical properties are presented in Figure I.1.2.5.7(e) and Figure I.1.2.5.7(f), respectively. The difference in the strength of FSP samples when compared with the base is obvious, albeit small. The increase in strength can be expected due to the refinement in the microstructure. Notably, an improvement in the ductility can also be observed in the FSP samples—especially for Fe-4 wt.% Si. These observations require further analysis to achieve a better understanding of the mechanism involved during the processing of these alloys.

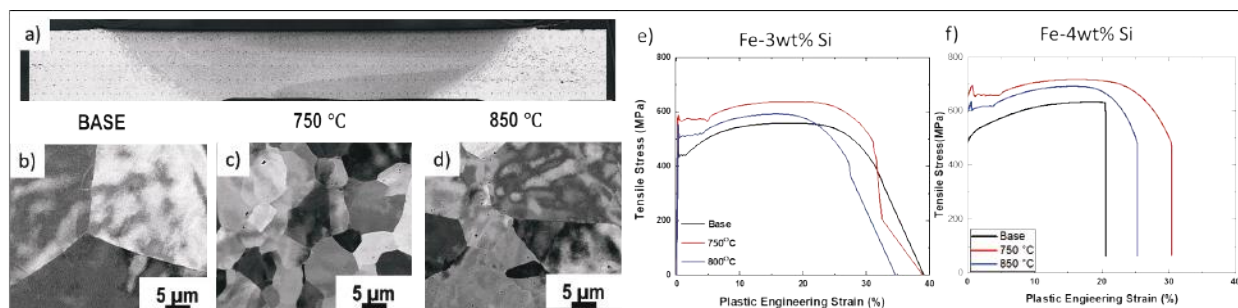


Figure I.1.2.29. (a) Optical micrographs of the FSP region. Backscattered electron SEM images of: (b) Base Fe-3 wt% Si, (c) FSP at 750°C , and (d) FSP at 850°C . Stress and strain curve for: (e) Fe-3 wt.% Si for base and two different processed conditions; and (f) Fe-4 wt.% Si for base and two different condition samples. Source: PNNL.

The fractured surface of Fe-4 wt.% Si alloys generated during the uniaxial tensile testing were examined by SEM and are shown in Figure I.1.2.5.8. The low magnification fractography in Figure I.1.2.5.8(a), Figure I.1.2.5.8(d), and Figure I.1.2.5.8(g), respectively, show the overall fracture geometry and appearance. Fractographic surfaces reveal cleavage fractures across the crystallographic planes containing river-like features. The characteristic steps and ledge, as shown in Figure I.1.2.5.8(b) and Figure I.1.2.5.8(c), are indicative of an intergranular fracture. In contrast, the alloys FSP at 750°C and 850°C temperatures show elongated dimples of varying sizes distributed throughout the fractured surfaces. These fractured surfaces are indicative of large plastic deformation prior to fractures, and hence, are indicative of ductile fractures. Given the topographical features of the failed surface are governed by the microstructure of the alloy, it can be correlated that while the base alloy microstructure was brittle, FSP has shown improvement in the ductility of the Fe-Si alloys.

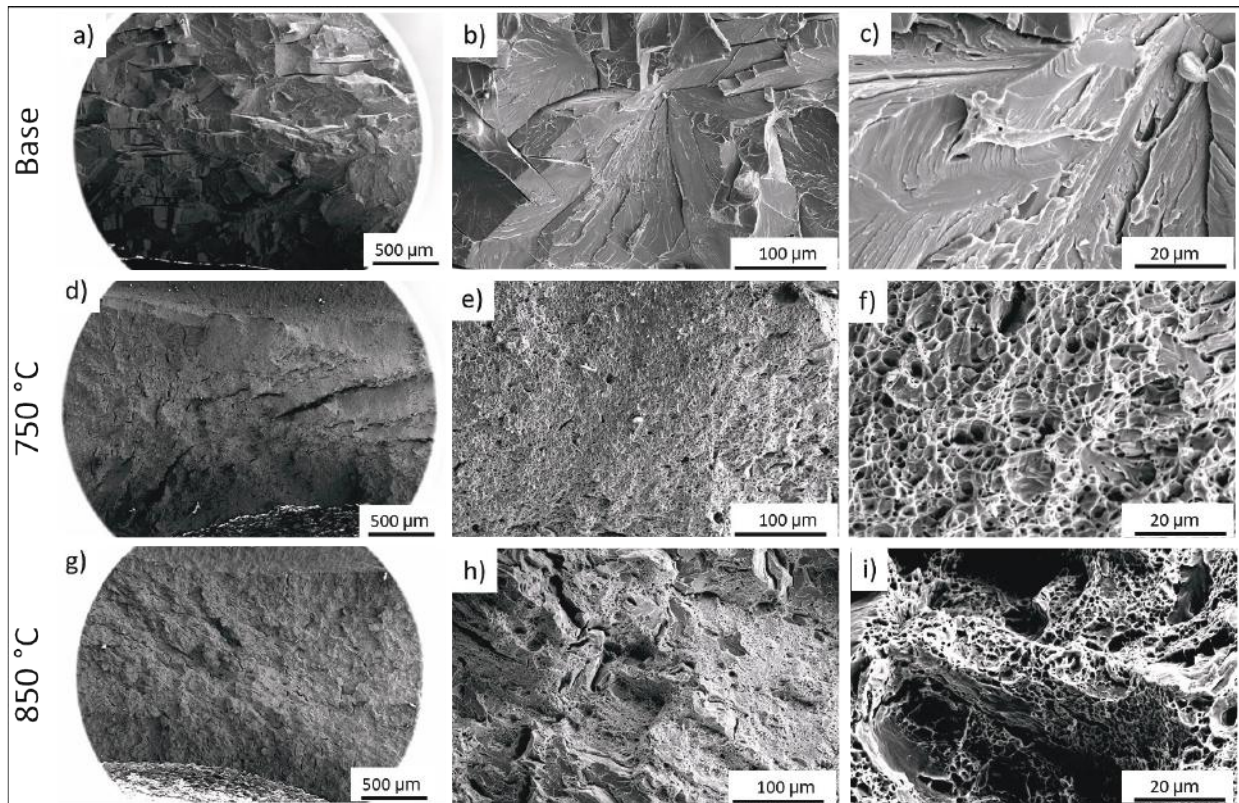


Figure I.1.2.30. Fractographs showing the fractured surface of tensile-tested: (a-c) Fe-4 wt.% Si base alloy, (d-f) Fe-4 wt.% Si alloy FSP'd at 750 °C, and (g-i) Fe-4 wt.% Si alloy FSP'd at 850 °C. Source: PNNL.

The increase in the Si content results in the formation of ordered B2 phases making the subsequent rolling of the Si steel difficult [6]. Hot rolling of alloys containing both 4 wt.% Si and 5 wt.% Si was performed to validate this. Hot rolling was performed after soaking the alloys at 900°C for an hour with a 5% reduction in thickness per pass. Figure I.1.2.5.9 shows images of rolled plates after the first pass. Crack formation is evident in the Fe 5 wt.% Si alloys after a single-pass, as shown in Figure I.1.2.5.9(b), while Fe-4 wt.% Si showed no crack. The crack in the Fe 5 wt.% Si alloy after a single-pass of hot-rolling was intergranular.

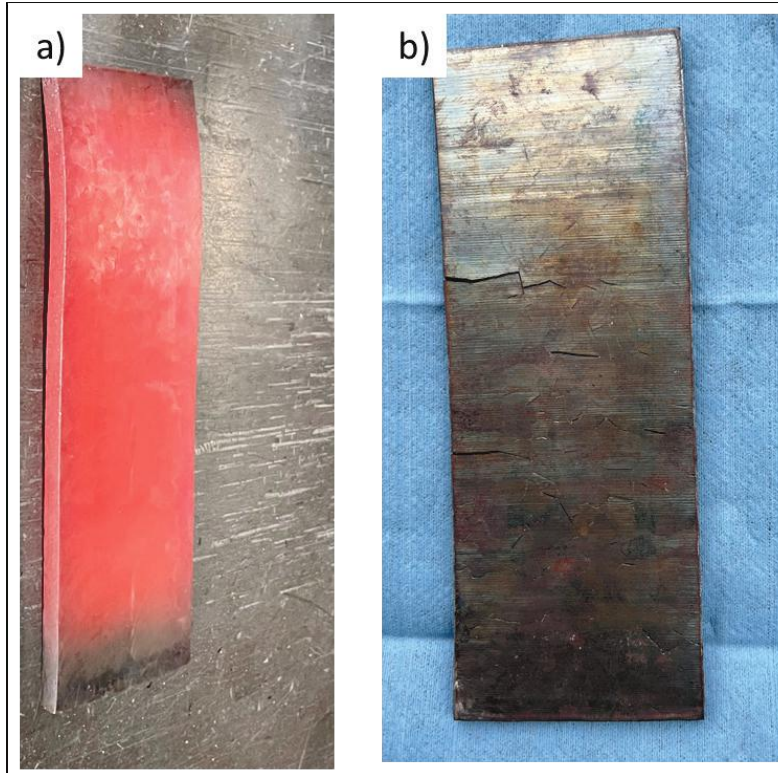


Figure I.1.2.31. (a) Hot-rolled plate of Fe 4 wt.% Si alloys after first pass. (b) Hot-rolled plate of Fe 5 wt.% Si alloys after first pass. Source: PNNL.

The microstructural and mechanical property response substantiate that after FSP, the ductility of the alloy has improved. Next, we intend to perform the FSP of the Fe 5 wt.% Si alloy and do subsequent hot rolling. Furthermore, the Shear-Assisted Processing and Extrusion (ShAPE™) route is also being explored.

Conclusions

Single-pass FSW of a five-sheet stack of Al with Ni-coated and uncoated Cu shorting bar successfully demonstrated. Pullout strength of the joints are comparable to diecast Al-Cu. SEM/EDS elemental mapping shows well bonded interface between Al-Cu and presence of non-uniform Ni layer for Al-Ni coated Cu joint. However, SEM/EDS analysis is not able to resolve any IMC layer at the interface. Electrical resistance measurement shows some variation across the weld length. The microstructural analyses of the Fe-Si alloys show grain refinement occurs during FSP. The subsequent mechanical property assessment points out that while the base alloy showed brittle fracture during tensile testing, the FSP'd alloys demonstrated features of typical ductile fracture. Furthermore, strength and ductility improvements were also observed in FSP'd samples when compared with the base alloys.

References

1. Saeid, T., A. Abdollah-zadeh, and B. Sazgari, 2010, "Weldability and mechanical properties of dissimilar aluminum-copper lap joints made by friction stir welding," *J. Alloys Compd.*, Vol. 490, Nos. 1–2, pp. 652–655. <https://doi.org/10.1016/j.jallcom.2009.10.127>.
2. Galvão, I., J. C. Oliveira, A. Loureiro, and D. M. Rodrigues, 2011, "Formation and distribution of brittle structures in friction stir welding of aluminium and copper: Influence of process parameters," *Sci. Technol. Weld. Join.*, Vol. 16, No. 8, pp. 681–689. <https://doi.org/10.1179/1362171811Y.0000000057>.
3. Carvalho, G. H. S. F. L., I. Galvão, R. Mendes, R. M. Leal, and A. Loureiro, 2019, "Friction stir welding and explosive welding of aluminum/copper: Process analysis," *Mater. Manuf. Process.*, Vol. 34, No. 11, pp. 1243–1250. <https://doi.org/10.1080/10426914.2019.1644452>.

4. Bhattacharya, T. K., H. Das, S. S. Jana, and T. K. Pal, 2017, “Numerical and experimental investigation of thermal history, material flow, and mechanical properties of friction stir welded aluminium alloy to DHP copper dissimilar joint,” *Int. J. Adv. Manuf. Technol.*, Vol. 88, pp. 847–861. <https://doi.org/10.1007/s00170-016-8820-0>.
5. Felix Xavier Muthu, M., and V. Jayabalan, 2015, “Tool travel speed effects on the microstructure of friction stir welded aluminum-copper joints,” *J. Mater. Process. Technol.*, Vol. 217, pp. 105–113. <https://doi.org/10.1016/j.jmatprotec.2014.11.007>.
6. Ouyang, G., X. Chen, Y. Liang, C. Macziewski, and J. Cui, 2019, “Review of Fe-6.5 wt% Si high silicon steel—A promising soft magnetic material for sub-kHz application,” *J. Magn. Magn. Mater.*, Vol. 481, pp. 234–250. <https://doi.org/10.1016/j.jmmm.2019.02.089>.

Acknowledgements

The authors acknowledge the contributions of the following PNNL staff members: the welding, processing, and data analysis activities were supported by H. Das and S. Shukla in association with M. Pole, X. Ma, and B. Gwalani; the mechanical testing was performed by T. Roosendaal, R. Seffens, and E. Nickerson; the electrical conductivity testing was performed by K. Kappagantula and A. Nittala; the metallography and hardness testing was performed by A. Guzman and M. Blazon; and the hot-rolling was performed by M. Rhodes and R. Seffens. The authors also are thankful to B. Carlson and J. Agapiou for the material and technical support and discussion for sub-task 1.

I.1.3 Thrust 3: Advanced Processing and Additive Manufacturing for Electric Vehicles

I.1.3.1 Task 3A. Fundamental Development of Additive Manufactured Alloys for Electric Vehicle Propulsion (Oak Ridge National Laboratory)

Alex Plotkowski, Principal Investigator

Oak Ridge National Laboratory
Materials Science and Technology Division
1 Bethel Valley Rd.
Oak Ridge, TN 37830
E-mail: plotkowskij@ornl.gov

J. Allen Haynes, PMCP Consortium Manager

Oak Ridge National Laboratory
Materials Science and Technology Division
1 Bethel Valley Rd.
Oak Ridge, TN 37830
E-mail: haynesa@ornl.gov

Jerry Gibbs, DOE Technology Development Manager

U.S. Department of Energy
E-mail: jerry.gibbs@ee.doe.gov

Start Date: November 1, 2021	End Date: September 30, 2023	
Project Funding (FY 2022): \$450,000	DOE share: \$450,000	Non-DOE share: \$0

Project Introduction

Automotive companies are seeking to apply the technical potential of AM to EV powertrain systems. Although Al alloys are desirable for their high-specific strength, good corrosion resistance, and high electrical and thermal conductivities, few conventional Al alloys are well-suited for production with AM processes. This lack of alloy feedstock selection has limited application of AM for EVs, preventing automotive companies from taking advantage of the geometric complexity in AM that may offer weight-reduction and increased efficiency. The purpose of this task is to develop new Al alloys that are suitable for AM of EV components. Previous research at ORNL has successfully developed new AM Al alloys with significantly improved properties for higher temperature operations. The digital metallurgy lessons learned from those previous efforts are applied here to help develop a design philosophy for AM Al alloys that are suitable for EVs, targeting applications with simultaneous and competing requirements for high-strength and electrical/thermal conductivity.

Objectives

The objective for this task is to measure critical material properties for EV-related applications in ORNL-designed AM Al alloys and benchmark these properties against commercially available AM alloys.

Approach

The key challenge addressed in this project is the development of alloys with exceptional combinations of mechanical and electrical/thermal properties. AM processing, and specifically the laser powder bed fusion processing used in this research, characteristically results in very high cooling rates during solidification. This unique processing behavior enables the design of new alloys with novel microstructures and property combinations, in addition to the well-known opportunity to print complex geometries. Therefore, the approach of this task is to design new alloys that are both processable via AM and form desirable microstructures and combinations of properties. Previous ORNL research investigated a range of possible alloy chemistries, with the most promising results found for Al-Ce-Ni-based alloys. That research showed that an Al-Ce-Ni-Mn alloy

exhibited exceptional mechanical performance, particularly for high-temperature creep resistance. However, the AM processing window for this alloy was narrow, and the RT ductility was low, necessitating a high-temperature annealing heat-treatment (450°C, 2 h) prior to post-processing and testing. In FY 2022, we sought to improve the printability of this alloy and further improve its mechanical performance. We then characterized this alloy for thermophysical and electrical properties and compared the results against baseline AM alloys (e.g., commercially available AlSi10Mg and previously researched Al-Cu-Mn-Zr). These results provide significant insight into the relationship between alloy composition, processability, microstructure evolution, and key properties.

Results

Our previous work demonstrated the excellent thermal stability and mechanical properties of an Al-Ce-Ni-Mn alloy [1]. However, the alloy also experienced cracking during removal of samples from the AM build plate, necessitating a high-temperature annealing heat-treatment (450°C, 2h) for further processing and testing. That heat-treatment tended to coarsen the microstructure of the alloy with a corresponding detrimental effect on the properties. To improve the processability and properties of the alloy, two changes were made to the composition: (1) the manganese (Mn) content was reduced to avoid formation of damaging Mn-rich intermetallic phases and (2) zirconium (Zr) was added to refine the grain structure, which has been shown to reduce hot-tearing susceptibility [2] and act as a precipitation strengthener [3]. The composition of the new alloy is compared against the previous composition in Table I.1.3.1.1.

Table I.1.3.1.1. Comparison of Measured Alloy Composition Between the Al-Ce-Ni-Mn and Al-Ce-Ni-Mn-Zr Alloys

Alloy	Al	Ce	Ni	Mn	Zr	Si	Fe
Al-Ce-Ni-Mn [1]	Balance	10.50	3.09	1.18	-	0.12	0.18
Al-Ce-Ni-Mn-Zr	Balance	7.53	4.72	0.5	0.65	0.054	0.12

Figure I.1.3.1.1 shows representative details of the as-fabricated microstructure of the two alloys. SEM and EDS show that the Al-Ce-Ni-Mn alloy tends to produce Mn-rich intermetallic particles during processing. Evaluation of a representative fracture surface shows that the crack location is strongly correlated to the location of these particles. By comparison, the Al-Ce-Ni-Mn-Zr alloy, with lower Mn content, does not contain the same intermetallic particles in the as-fabricated microstructure. The new alloy also exhibits Al₃Zr cuboidal particles located near the center of equiaxed face-centered cubic (FCC) Al grains, which is evidence of effective grain refinement during solidification due to the addition of Zr. Electron backscatter diffraction of the two alloys shows a more refined and equiaxed grain structure in the AlCeNiMnZr alloy.

Based on previous results from ORNL [4, 5] and in the literature [3, 6], the Zr content in the alloy was expected to enable hardening through the precipitation of L1₂ Al₃Zr nanoparticles. A heat-treatment study was performed, and the hardness was measured following various treatment times at 350°C, as observed in Figure I.1.3.1.2(a). An initial decrease in hardness was observed, likely due to relaxation of any residual stress or plastic deformation from the as-fabricated state, followed by an increase in hardness up to 24 h. A heat-treatment of 350°C for 8 h was selected for subsequent characterization and testing. For this condition, the initial microstructure has partially spheroidized and coarsened, as shown in Figure I.1.3.1.2(b), but to a much lesser extent than the Al-Ce-Ni-Mn alloy subjected to the original higher temperature annealing heat-treatment, as can be seen in Figure I.1.3.1.2(c). Additionally, as shown by the APT data in Figure I.1.3.1.2(d), nanoscale Al₃Zr precipitates have formed, which explains the increase in hardness following heat-treatment.

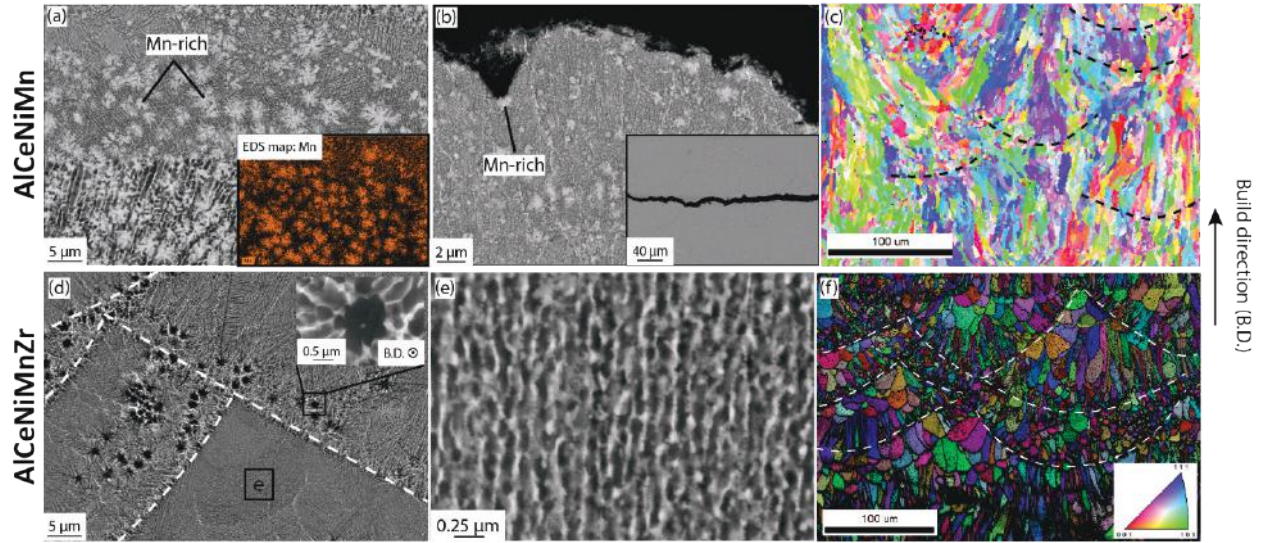


Figure I.1.3.1. Microstructure of as-fabricated (a-c) Al-Ce-Ni-Mn and (d-e) Al-Ce-Ni-Mn-Zr alloys. (a-c) SEM images of Al-Ce-Ni-Mn alloy show Mn-rich, rosette-shaped intermetallic particles (confirmed by the EDS map in the inset); (b) a crack (lower magnification image in the inset) associated with Mn-rich rosettes; and (c) IPF map of the Al-Ce-Ni-Mn alloy shows columnar grain structure. SEM images at (d) lower magnification and (e) higher magnification of the region marked 'e' in (d) show the eutectic structure, while (f) IPF map shows equiaxed grain structure in the AlCeNiMnZr alloy. The inset in (d) shows submicron-sized primary α -Al regions in melt pools. Source: ORNL.

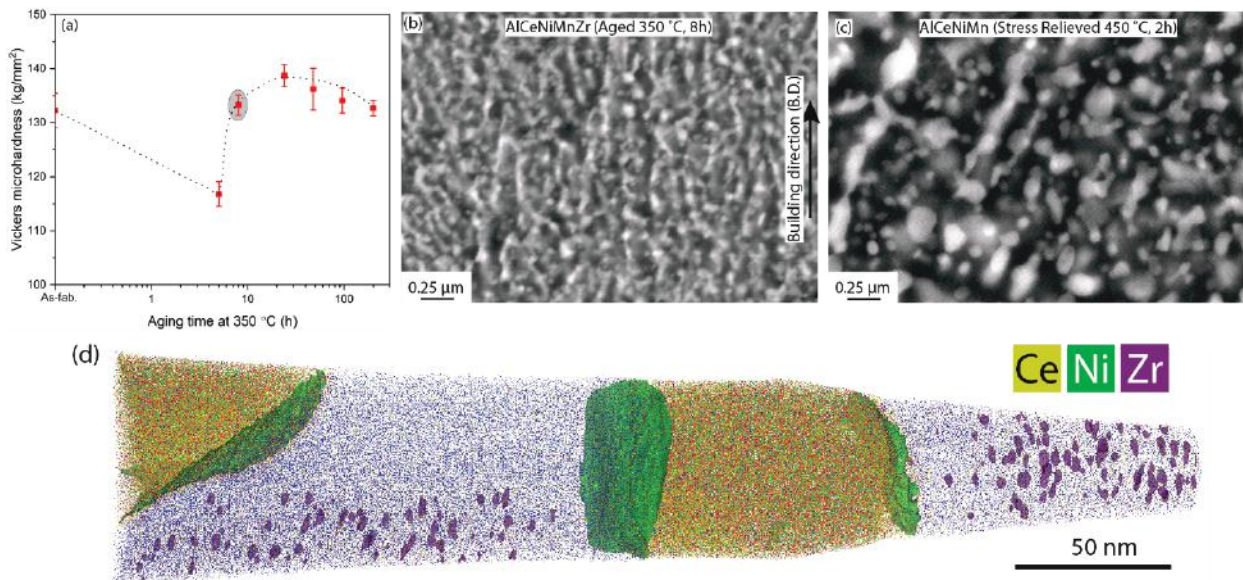


Figure I.1.3.2. Summary of (a) hardness as a function of aging at 350 °C for AlCeNiMnZr; (b) the microstructure following aging compared with (c) stress relieved microstructure of Al-Ce-Ni-Mn; and (d) an APT reconstruction showing the presence of nanoscale Al_3ZrL_{12} precipitates within the FCC-Al matrix. Source: ORNL.

The mechanical properties of the two alloys are compared in Figure I.1.3.1.3. The yield strength was measured as a function of temperature using a 30-min hold time before testing. The AlCeNiMnZr alloy shows approximately the same as-fabricated yield strength as the Al-Ce-Ni-Mn alloy but is much stronger following precipitation heat-treatment. The RT strengthening effect may be explained by the Al_3Zr precipitation during heat-treatment, but, interestingly, this effect diminished at higher temperatures, where the alloy has approximately the same yield strength in both the as-fabricated and heat-treated conditions. Both cases for AlCeNiMnZr show better high-temperature strength than the Al-Ce-Ni-Mn alloy because of the retention of the refined intermetallic structure by reducing the coarsening that occurs during the higher temperature annealing treatment of the Zr-free alloy. Figure I.1.3.1.3(b) shows high-cycle fatigue data for 350°C. Both alloys perform well compared to conventional cast and wrought Al alloys. For intermediate and high-stress levels, the AlCeNiMnZr alloy performs better than Al-Ce-Ni-Mn, but fatigue was not sensitive to heat-treatment. Both alloys exhibit similar fatigue limits (defined as $>10^7$ cycles) as this regime is dominated by the defect or inclusion structure, which may not be significantly different in the two alloys. Finally, Figure I.1.3.1.3(c) shows the tensile creep behavior at 300°C. Both alloys compare favorably against a variety of benchmark higher temperature cast Al alloys. Retention of the refined intermetallic structure for the AlCeNiMnZr alloy in this case has a significant influence, providing a substantial increase in creep resistance compared to Al-Ce-Ni-Mn.

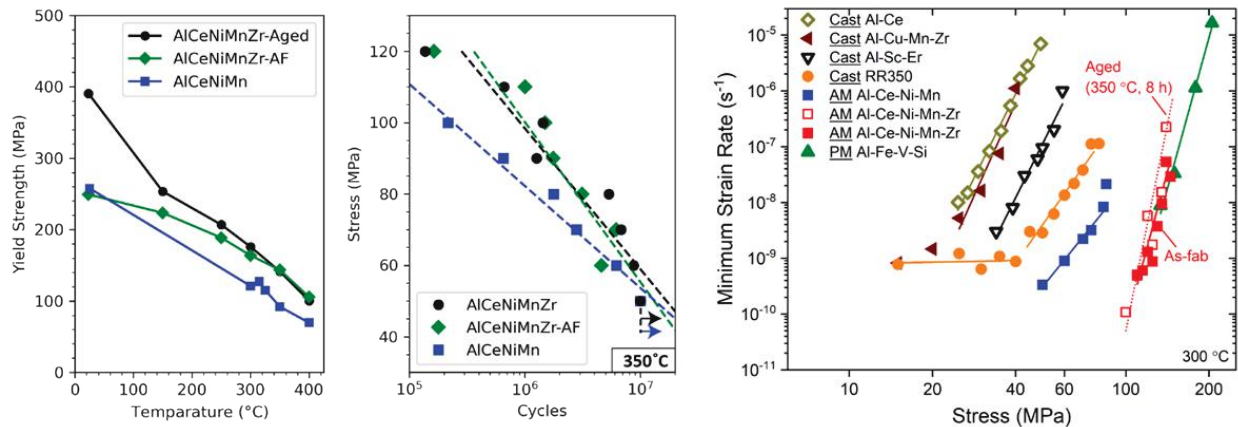


Figure I.1.3.3. Comparison of mechanical properties between Al-Ce-Ni-Mn and Al-Ce-Ni-Mn-Zr showing (a) tensile yield strength as a function of temperature; (b) high-cycle fatigue performance at 350 °C; and (c) tensile creep resistance at 300 °C. Source: ORNL.

The thermophysical properties of the AlCeNiMnZr alloy were measured and compared against reference AM alloys (e.g., commercial AlSi10Mg and ORNL's Al-Cu-Mn-Zr [7], known as ACMZ). Figure I.1.3.1.4 shows the specific heat, thermal diffusivity, and thermal conductivity of these printed alloys as a function of temperature. As is usually the case, the exceptional mechanical properties of AlCeNiMnZr comes at the expense of the thermal performance. The additions of moderate amounts of heavy elements (Ce and Ni) tended to increase the density, ρ (2.91 g/cm³ compared to 2.67 g/cm³ for AlSi10Mg). The specific heat, c_p , was lower than that of AlSi10Mg or ACMZ, although it increased with heat-treatment. The thermal diffusivity, α , was highest for AlSi10Mg and lower for as-fabricated AlCeNiMnZr. ACMZ and heat-treated AlCeNiMnZr had a similar intermediate thermal diffusivity. Similar trends were observed for thermal conductivity, which may be calculated as $k = \alpha\rho c_p$.

Electrical resistivity was also measured at RTs for the same set of alloys and conditions, as observed in Figure I.1.3.1.5. Similar trends were observed for the thermal conductivity, in which AlSi10Mg had the lower electrical resistivity, as-fabricated AlCeNiMnZr had the highest, and heat-treated AlCeNiMnZr and ACMZ were similar and in between. Interestingly, both the thermal and electrical conductivity of AlCeNiMnZr were significantly higher in the heat-treated case than the as-fabricated condition, meaning that the heat-treatment

has the effect of simultaneously increasing mechanical and thermal/electrical performance. The reason for this effect is that Zr has a much larger detrimental effect on conductivity when in solution in the FCC-Al matrix than it does when forming Al_3Zr precipitates. However, the strengthening effect of the precipitates is much larger than that of solution strengthening.

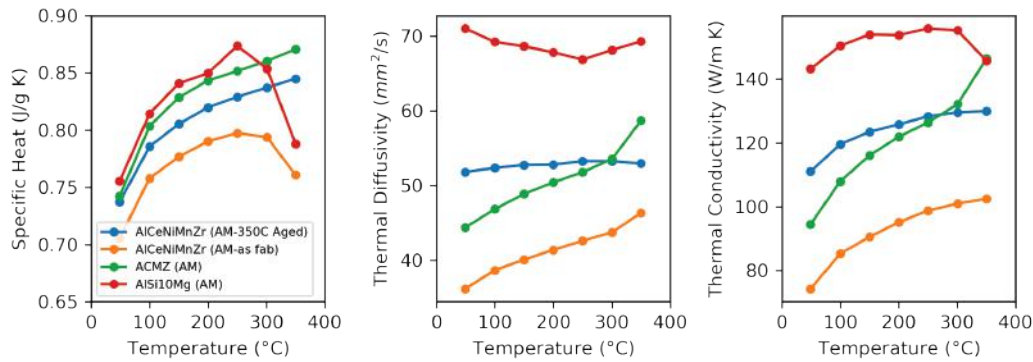


Figure I.1.3.4. Thermal properties as a function of temperature. Source: ORNL.

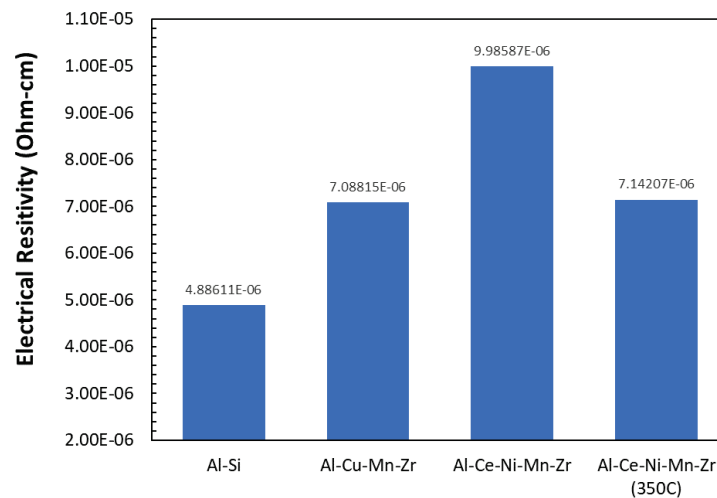


Figure I.1.3.5. Electrical resistivity of various AM Al alloys at room temperature. Source: ORNL.

Conclusions

Research in this task has demonstrated that new Al alloys may be tailored for AM feedstock and may thus result in superior mechanical properties relative to conventionally processed alloys. In particular, high-temperature strength, creep, and fatigue resistance may be achieved. For EV applications, however, a combination of mechanical and electrical/thermal performance is often required. Most microstructural features that increase strength tend to reduce conductivity, and this trend was observed here, in which the high-performance AlCeNiMnZr alloy had lower thermal and electrical conductivity than the commercially available AlSi10Mg alloy. However, additional trends were also observed that provide a path forward to design AM Al alloy with exceptional combinations of mechanical and electrical/thermal performance. The Zr content in the AlCeNiMnZr alloy was observed to provide greater strength following heat-treatment to form nanoscale Al_3Zr L_{12} precipitates, while simultaneously increasing electrical and thermal conductivity compared to the as-fabricated conditions. At the same time, the addition of Zr was shown to improve additive manufacturability compared to a previously designed Al-Ce-Ni-Mn alloy. These results suggest that pursuing Zr additions, or similar tri-aluminide forming elements (such as Sc, Er, or V) may be a viable approach for designing high-performance AM Al alloys for EV applications.

Key Publications

1. Bahl, S., A. Plotkowski, K. Sisco, D. N. Leonard, L. F. Allard, R. A. Michi, J. D. Poplawsky, R. Dehoff, and A. Shyam, 2021, “Elevated temperature ductility dip in an additively manufactured Al-Cu-Ce alloy,” *Acta Mater.*, Vol. 220, Art. 117285. <https://doi.org/10.1016/j.actamat.2021.117285>.
2. Bahl, S., K. Sisco, Y. Yang, F. Theska, S. Primig, L. F. Allard, R. A. Michi, C. Fancher, B. Stump, R. Dehoff, A. Shyam, and A. Plotkowski, 2021, “Al-Cu-Ce(-Zr) alloys with an exceptional combination of additive processability and mechanical properties,” *Addit. Manuf.*, Vol. 48, Art. 102404. <https://doi.org/10.1016/j.addma.2021.102404>.
3. Hu, X., S. Bahl, A. Shyam, A. Plotkowski, B. Milligan, L. Allard, J. A. Haynes, Y. Ren, and A. Chuang, 2022, “Repurposing the θ (Al₂Cu) phase to simultaneously increase the strength and ductility of an additively manufactured Al-Cu alloy,” *Mater. Sci. Eng. A*, Vol. 850, Art. 143511. <https://doi.org/10.1016/j.msea.2022.143511>.
4. Michi, R. A., S. Bahl, C. M. Fancher, K. Sisco, L. F. Allard, K. An, D. Yu, R. R. Dehoff, A. Plotkowski, and A. Shyam, 2022, “Load shuffling during creep deformation of an additively manufactured Al-Cu-Mn-Zr alloy,” *Acta Mater.*, Vol. 244, Art. 118557. <https://doi.org/10.1016/j.actamat.2022.118557>.
5. Michi, R. A., A. Plotkowski, A. Shyam, R. R. Dehoff, and S. S. Babu, 2022, “Towards high-temperature applications of aluminum alloys enabled by additive manufacturing,” *Int. Mater. Rev.*, Vol. 67, No. 3, pp. 298–345. <https://doi.org/10.1080/09506608.2021.1951580>.
6. Michi, R. A., J. Simpson, S. Bahl, Q. Campbell, P. Brackman, A. Plotkowski, R. Dehoff, J. Haynes, Q. Qang, and A. Shyam, 2023, “Additively manufactured Al-Ce-Ni-Mn alloy with improved elevated-temperature fatigue resistance,” *Addit. Manuf.*, Vol. 66, Art. 103477. <https://doi.org/10.1016/j.addma.2023.103477>.
7. Michi, R. A., K. Sisco, S. Bahl, L. F. Allard, K. B. Wagner, J. D. Poplawsky, D. N. Leonard, R. R. Dehoff, A. Plotkowski, and A. Shyam, 2022, “Microstructural evolution and strengthening mechanisms in a heat-treated additively manufactured Al-Cu-Mn-Zr alloy,” *Mater. Sci. Eng. A*, Vol. 840, Art. 142928. <https://doi.org/10.1016/j.msea.2022.142928>.
8. Michi, R. A., K. Sisco, S. Bahl, Y. Yang, J. D. Poplawsky, L. F. Allard, R. R. Dehoff, A. Plotkowski, and A. Shyam, 2022, “A creep-resistant additively manufactured Al-Ce-Ni-Mn alloy,” *Acta Mater.*, Vol. 227, Art. 117699. <https://doi.org/10.1016/j.actamat.2022.117699>.
9. Perrin, A., S. Bahl, D. N. Leonard, R. Michi, K. Sisco, A. Plotkowski, A. Shyam, R. Dehoff, D. Shin, and Y. Yang, 2022, “Phase stability in cast and additively manufactured Al-rich Al-Cu-Ce alloys,” *J. Alloys Compd.*, Vol. 926, Art. 166984. <https://doi.org/10.1016/j.jallcom.2022.166984>.
10. Plotkowski, A., K. Sisco, S. Bahl, A. Shyam, Y. Yang, L. Allard, P. Nandwana, A. M. Rossy, and R. R. Dehoff, 2020, “Microstructure and properties of a high-temperature Al-Ce-Mn alloy produced by additive manufacturing,” *Acta Mater.*, Vol. 196, pp. 595–608. <https://doi.org/10.1016/j.actamat.2020.07.014>.
11. Poplawsky, J. D., R. A. Michi, L. F. Allard, S. Bahl, A. J. Plotkowski, and A. Shyam, 2022, “Using θ' interfaces as templates for planar L12 precipitation in Al-Cu-Mn-Zr alloys,” *Addit. Manuf. Lett.*, Vol. 3, Art. 100086. <https://doi.org/10.1016/j.addlet.2022.100086>.
12. Shyam, A., A. Plotkowski, S. Bahl, K. Sisco, L. F. Allard, Y. Yang, J. A. Haynes, and R. R. Dehoff, 2020, “An additively manufactured Al-Cu-Mn-Zr alloy microstructure and tensile mechanical properties,” *Materialia*, Vol. 12, Art. 100758. <https://doi.org/10.1016/j.mtla.2020.100758>.
13. Sisco, K., A. Plotkowski, Y. Yang, D. Leonard, B. Stump, P. Nandwana, R. R. Dehoff, and S. S. Babu, 2021, “Microstructure and properties of additively manufactured Al-Ce-Mg alloys,” *Sci. Rep.*, Vol. 11, Art. 6953. <https://doi.org/10.1038/s41598-021-86370-4>.

14. Yang, Y., S. Bahl, K. Sisco, M. Lance, D. Shin, A. Shyam, A. Plotkowski, and R. R. Dehoff, 2020, “Primary solidification of ternary compounds in Al-rich Al-Ce-Mn alloys,” *J. Alloys Compd.*, Vol. 844, Art. 156048. <https://doi.org/10.1016/j.jallcom.2020.156048>.

References

1. Michi, R. A., K. Sisco, S. Bahl, Y. Yang, J. D. Poplawsky, L. F. Allard, R. R. Dehoff, A. Plotkowski, and A. Shyam, 2022, “A creep-resistant additively manufactured Al-Ce-Ni-Mn alloy,” *Acta Mater.*, Vol. 227, Art. 117699. <https://doi.org/10.1016/j.actamat.2022.117699>.
2. Martin, J. H., B. D. Yahata, J. M. Hundley, J. A. Mayer, T. A. Schaedler, and T. M. Pollock, 2017, “3D printing of high-strength aluminium alloys,” *Nature*, Vol. 549, pp. 365–369. <https://doi.org/10.1038/nature23894>.
3. Croteau, J. R., S. Griffiths, M. D. Rossell, C. Leinenbach, C. Kenel, V. Jansen, D. N. Seidman, D. C. Dunand, and N. Q. Vo, 2018, “Microstructure and mechanical properties of Al-Mg-Zr alloys processed by selective laser melting,” *Acta Mater.*, Vol. 153, pp. 35–44. <https://doi.org/10.1016/j.actamat.2018.04.053>.
4. Bahl, S., K. Sisco, Y. Yang, F. Theska, S. Primig, L. F. Allard, R. A. Michi, C. Fancher, B. Stump, R. Dehoff, A. Shyam, and A. Plotkowski, 2021, “Al-Cu-Ce(-Zr) alloys with an exceptional combination of additive processability and mechanical properties,” *Addit. Manuf.*, Vol. 48, Art. 102404. <https://doi.org/10.1016/j.addma.2021.102404>.
5. Theska, F., Y. Yang, K. D. Sisco, A. Plotkowski, and S. Primig, 2022, “On the high-temperature stability of the Al₈Cu₃Ce intermetallic in an additively manufactured Al-Cu-Ce-Zr alloy,” *Mater. Charact.*, Vol. 191, Art. 112109. <https://doi.org/10.1016/j.matchar.2022.112109>.
6. Agrawal, P., S. Gupta, S. Thapliyal, S. Shukla, R. S. Haridas, and R. S. Mishra, 2021, “Additively manufactured novel Al-Cu-Sc-Zr alloy: Microstructure and mechanical properties,” *Addit. Manuf.*, Vol. 37, Art. 101623. <https://doi.org/10.1016/j.addma.2020.101623>.
7. Shyam, A., A. Plotkowski, S. Bahl, K. Sisco, L. F. Allard, Y. Yang, J. A. Haynes, and R. R. Dehoff, 2020, “An additively manufactured Al-Cu-Mn-Zr alloy microstructure and tensile mechanical properties,” *Materialia*, Vol. 12, Art. 100758. <https://doi.org/10.1016/j.mtla.2020.100758>.

Acknowledgements

The authors acknowledge the contributions of the following ORNL team members for this sub-task: A. Shyam, R. Dehoff, S. Bahl, R. Michi, Y. Yang, J. Poplawsky, A. Perrin, and L. Allard.

I.1.3.2 Task 3B. Fundamentals of Non-Equilibrium Processing for Additive Manufacturing Alloys (Oak Ridge National Laboratory)

Ying Yang, Principal Investigator

Oak Ridge National Laboratory
Materials Science and Technology Division
1 Bethel Valley Rd.
Oak Ridge, TN 37830
E-mail: yangying@ornl.gov

J. Allen Haynes, PMCP Consortium Manager

Oak Ridge National Laboratory
Materials Science and Technology Division
1 Bethel Valley Rd.
Oak Ridge, TN 37830
E-mail: haynesa@ornl.gov

Jerry Gibbs, DOE Technology Development Manager

U.S. Department of Energy
E-mail: jerry.gibbs@ee.doe.gov

Start Date: November 1, 2021	End Date: September 30, 2023	
Project Funding (FY 2022): \$225,000	DOE share: \$225,000	Non-DOE share: \$0

Project Introduction

AM of lightweight alloys offers unique opportunities to produce distinct microstructures that cannot be achieved from conventional casting methods, as a result of the high cooling rates and heterogeneous cooling conditions in AM melt pools [1]. The relationships between process parameters, heat transfer, and microstructural evolution, however, are often convoluted and poorly understood. The ability to understand and control microstructural evolution in AM processing has the potential to revolutionize the design and control of microstructures and properties of AM alloys. This task is dedicated to addressing two major challenges in AM Al alloys. The first is limited knowledge of microstructural evolution (specifically phase stability) for materials fabricated via non-equilibrium processing conditions. The second is that newly designed AM alloys have limited phase diagram and thermodynamic property information. The lack of baseline knowledge in these new classes of Al alloys is a barrier to accurate analysis and prediction of how kinetic factors affect the phase stability and phase transformations in non-equilibrium processing conditions.

The alloy systems investigated herein are an emerging class of AM Al alloys designed by ORNL [2]. These alloys are primarily based on the Al-Ce eutectic system [3], but also include variants based on aluminum-nickel (Al-Ni) [4] and aluminum-copper (Al-Cu) [5, 6] near-eutectic systems. They were designed to resist hot-cracking/hot-tearing based on the principle that the narrow solidification temperature range and large volume fraction of terminal eutectics can better fill the interdendritic regions that are typical initiation sites for hot-tearing/cracking. Apart from inherent resistance to hot tearing, the rapid solidification conditions associated with laser powder bed AM processing also refines the eutectic structures, resulting in improved mechanical properties in these binary eutectic systems. To further enhance the high-temperature strength, ternary eutectic alloys based on Al-M-Ce (M=Ni, Cu, Mn, Mg), as well as quaternary alloys of Al-Ni-Mn-Ce [2] and Al-Cu-Ce-Zr [7], are currently under investigation at ORNL for applications such as lightweight rear brakes for EVs. However, there are no thermodynamic databases in the literature for these two quaternary systems. Therefore, in FY 2022, we developed thermodynamic databases for the Al-Ni-Mn-Ce and Al-Cu-Ce-Zr systems. Calculated results from these two databases for investigated alloys are presented in the Results

section and compared to experimental microstructural characterization. In the comparison of the heat-treated microstructure of the Al-Cu-Ce-Zr alloy with that of Al-Cu-Ce alloy, the zirconium (Zr) addition was found to greatly slow the coarsening of intermetallic phases [7]. Because the Zr addition did not introduce new phases, its beneficial role is assumed to be related to kinetic factors. New work on measuring the diffusion coefficients of Al, copper (Cu), cerium (Ce), and Zr in Al FCC structure was initiated in FY 2022 in collaboration with the University of Maryland to understand the coarsening kinetics. However, due to delays in the subcontracting process, this work is still ongoing in FY 2023. Therefore, in this document we will only report thermodynamic calculation results for phase stability in the Al-Cu-Ce-Zr and Al-Ni-Mn-Ce alloys. The measurement of diffusion coefficients in the Al-Cu-Ce-Zr alloy will be reported in FY 2023. The work scope of this task is schematically shown in Figure I.1.3.2.1.

Fundamentals of Non-Equilibrium Processing for AM Alloys

Develop thermodynamic and kinetic knowledge for designing light weight AM materials.

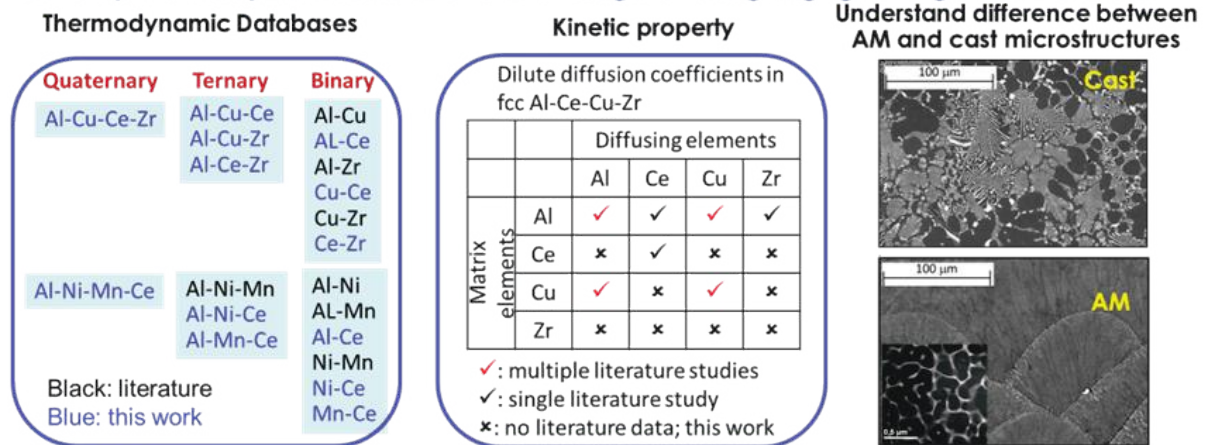


Figure I.1.3.6. Schematic flowchart showing the work scope of Task 3B, “Fundamentals of Non-Equilibrium Processing.” Source: ORNL.

Objectives

The objective of this task is to develop fundamental knowledge of phase stability, thermodynamics, and kinetics for the newly designed AM Al-Ni-Mn-Ce and Al-Cu-Ce-Zr alloys in order to better understand and control microstructural evolution under non-equilibrium AM processing conditions of lightweight alloys.

Approach

Computer coupling of phase diagrams and thermo-chemistry (i.e., the Calculation of Phase Diagrams [CALPHAD] approach) [8], was used to develop thermodynamic databases of the Al-Ni-Mn-Ce and Al-Cu-Ce-Zr systems. The status of constituent binary and ternary systems is summarized in Figure I.1.3.2.1. With the developed thermodynamic databases, two types of calculations were performed, where the first is the solidification path following the Scheil model [9, 10] to predict the phases formed during the AM solidification process. This model was used to describe the solidification process under relatively fast cooling rates. The second type of calculation is the equilibrium phase calculation using the lever-rule model to predict phases formed during post heat treatments. The calculation results were then compared with a suite of microstructural characterization results from conventional casting and AM alloys, including SEM, STEM, and APT. The STEM and APT studies were conducted to support this task as part of two Powertrain Materials Core Program, Thrust 4, Advanced Characterization Projects. Where the modeling results conflict with experimental results, thermodynamic databases are being refined to accommodate the new cast phase results. Our results suggested the Scheil model can be used to predict phase stability in both cast and AM solidification conditions; however, the size and morphology of phases in both conditions are quite different. This would

require including kinetic factors to better understand the microstructural evolution in AM. A Cellular Automata modeling framework is currently under development for this purpose.

Results

Effect of Mn Addition on Phase Stability in Al-Rich Cast Al-Ni-Ce Alloys

Phase analysis of AM Al-Ce-Ni alloys has identified phases not predicted from reported ternary liquidus projections of the system in the literature. The presence of a small amount of manganese (Mn) contamination in these alloys called into question whether these phases arose from the non-equilibrium processing conditions of AM, or because of the small additions of Mn that drastically shifted the phase stability of the system. Therefore, we investigated the Mn addition on the phase stability of three conventionally cast alloys: Al-10.1Ce-2.8Ni-1.2Mn, Al-9.6Ce-3.1Ni-0.3Mn, and Al-9.9Ce-4.1Ni, all in wt%. The alloy compositions were chosen to keep Ni+Mn constant, with the assumption that Mn substitutes with Ni in the quaternary phases due to their similar atomic size. The first alloy's composition is to mimic the composition of the AM Al-10.5Ce-3.1Ni-1.2Mn alloy; the second alloy contains a much smaller amount of Mn to study the intermediate phase equilibrium, and the third alloy is the corresponding Al-Ce-Ni ternary. Phase analysis confirmed that minute levels of Mn substituting for Ni in the system drastically shifts the liquidus projection toward the Al-rich corner of the ternary phase diagram such that the eutectic Al_3Ni phase is suppressed entirely in favor of the $\text{Al}_{23}\text{Ni}_6(\text{Ce},\text{Mn})_4$ phase. The experimental data was then used to refine the CALPHAD modeling of the liquidus projection and isothermal sections for the quaternary system Al-Ce-Ni-Mn.

Figure I.1.3.2.2(a, b, c) show the phases in cast Al-9.9Ce-4.1Ni with the final heat-treatment at 620°C for 2h, 520°C for 20h, and 400°C for 200h, respectively. In all three temperatures, the phases presented in the microstructure are the same, (Al)-Matrix, $\text{Al}_{11}\text{Ce}_3$ and Al_3Ni . Figure I.1.3.2.2(d) plotted the calculated amount of equilibrium phases vs. temperature in this alloy using thermodynamic description published in the literature [11], showing good agreement between experimental and calculation results.

Figure I.1.3.2.3(a, b, c) show the phases in cast Al-9.6Ce-3.1Ni-0.3Mn with the final heat-treatment at 620°C for 2h, 520°C for 20h, and 400°C for 200h, respectively. At 620°C, this alloy has equilibrium phases of (Al)-Matrix, $\text{Al}_{11}\text{Ce}_3$, and $\text{Al}_{23}\text{Ni}_6(\text{Ce},\text{Mn})_4$. At temperatures below 540°C, the $\text{Al}_{23}\text{Ni}_6(\text{Ce},\text{Mn})_4$ phase transforms into the Al_3Ni phase, leading to the coexistence of the (Al)-Matrix, $\text{Al}_{11}\text{Ce}_3$, $\text{Al}_{23}\text{Ni}_6(\text{Ce},\text{Mn})_4$, and Al_3Ni at 400°C. The absence of Al_3Ni in the 520°C sample is probably due to an inadequate amount of Al_3Ni detected. The results from this alloy suggested that a small amount of Mn (0.3wt%) can greatly promote the stability of $\text{Al}_{23}\text{Ni}_6(\text{Ce},\text{Mn})_4$ and completely suppress the formation of Al_3Ni from liquid. Utilizing the newly obtained experimental results, we incorporated Mn into thermodynamic modeling of the $\text{Al}_{23}\text{Ni}_6(\text{Ce},\text{Mn})_4$ phase. After incorporating these thermodynamic database improvements, the calculated phase amounts as a function of temperature are plotted in Figure I.1.3.2.3(d) and agree with the experimental results very well.

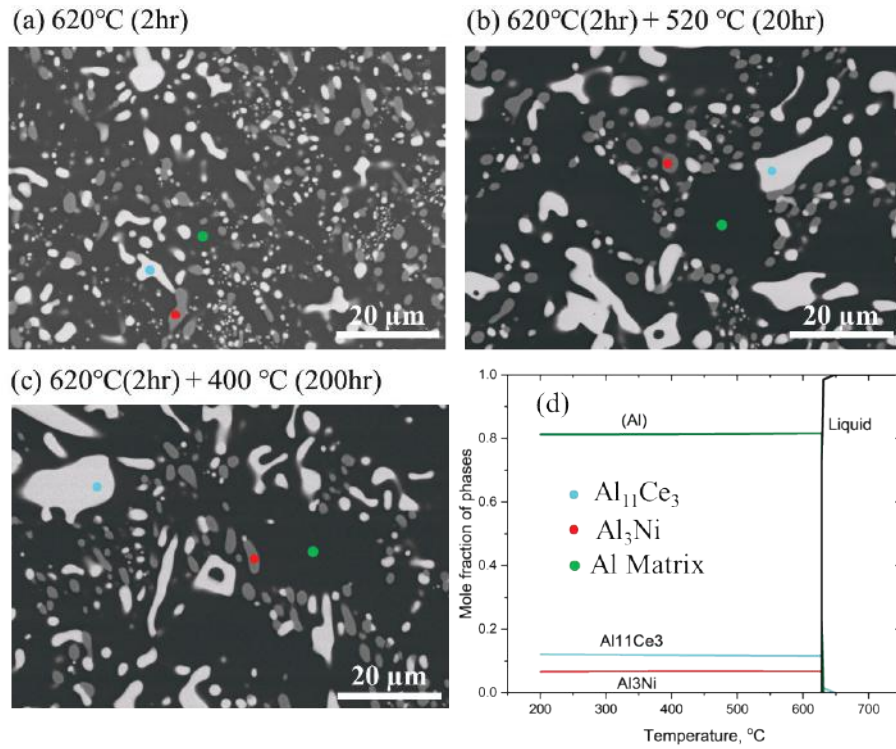


Figure I.1.3.7. Phases in cast Al-9.9Ce-4.1Ni after final heat-treatment at (a) 625°C for 2h, (b) 520°C for 20h, (c) 400°C for 200h, and (d) calculated phase amount vs. temperature in Al-9.9Ce-4.1Ni. Source: ORNL.

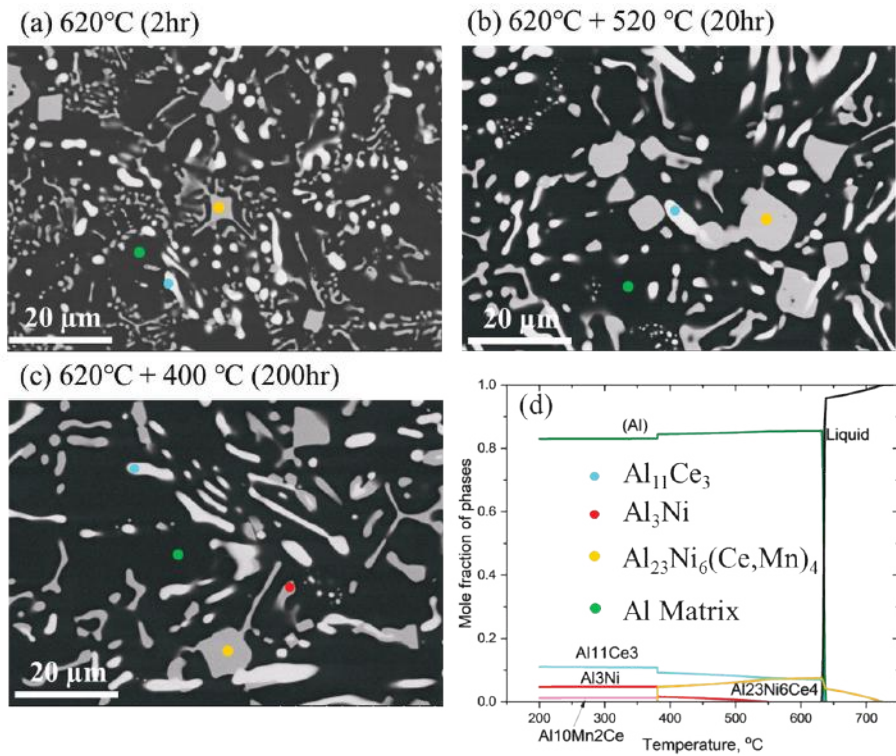


Figure I.1.3.8. Phases in cast Al-9.6Ce-3.1Ni-0.3Mn after final heat-treatment at (a) 625°C for 2h, (b) 520°C for 20h, (c) 400°C for 200h, and (d) calculated phase amount vs. temperature in Al-9.6Ce-3.1Ni-0.3Mn. Source: ORNL.

Figure I.1.3.2.4(a, b, c) show the phases in Al-10.1Ce-2.8Ni-1.2Mn with the final heat-treatment at 620°C for 2h, 520°C for 20h, and 400°C for 200h, respectively. The addition of 1.2 wt% Mn greatly stabilized the Al₁₀Mn₂Ce and Al₂₀Mn₂Ce phases, both of which were emanated from the Al-Mn-Ce ternary. At 620°C, this alloy has equilibrium phases of (Al)-Matrix, Al₁₁Ce₃, Al₂₀Mn₂Ce, and Al₂₃Ni₆(Ce,Mn)₄. At temperatures below 600°C, the Al₂₀Mn₂Ce phase transforms into Al₁₀Mn₂Ce phase, leading to coexistence of the (Al)-Matrix, Al₁₁Ce₃, Al₂₃Ni₆(Ce,Mn)₄, and Al₁₀Mn₂Ce at 520°C and 400°C. The transformation seemed not complete at 400°C for 200h as a small amount of Al₂₀Mn₂Ce was observed in the sample. We incorporated Ni into thermodynamic modeling of the Al₁₀Mn₂Ce and Al₂₀Mn₂Ce phases, utilizing the newly obtained experimental results. The calculated phase amounts as a function of temperature are plotted in Figure I.1.3.2.4(d), which reasonably agrees with the experimental results.

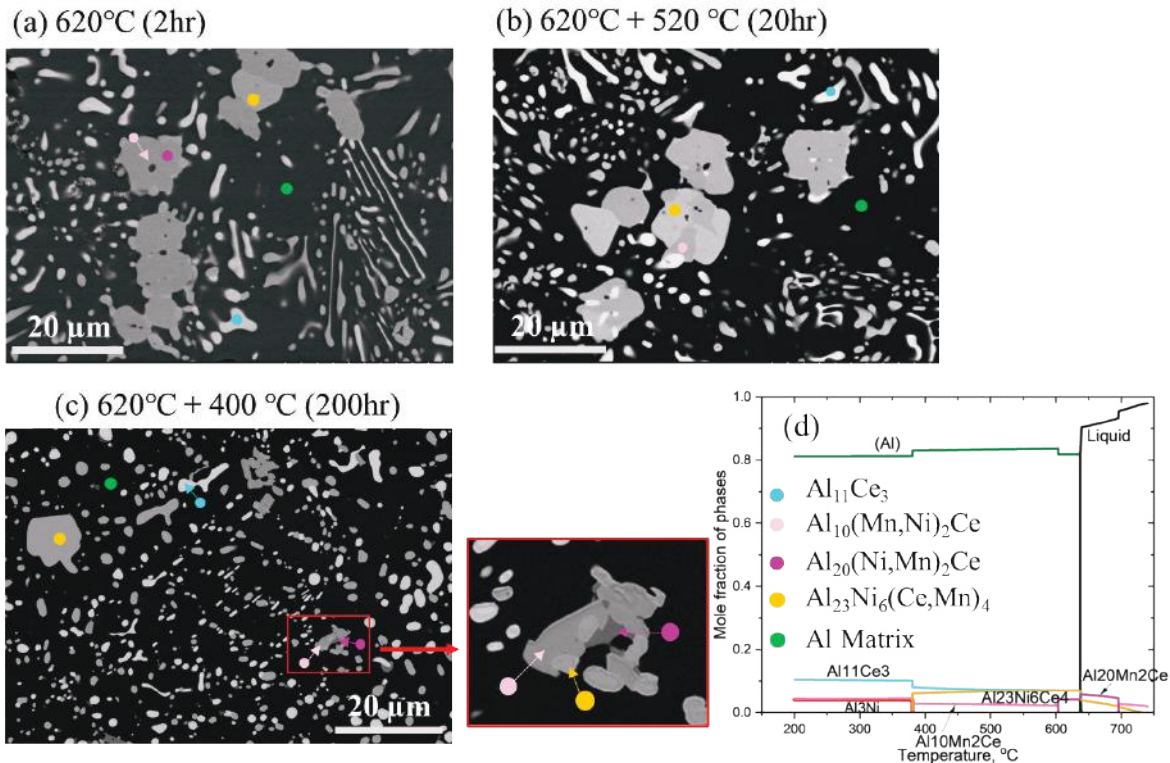


Figure I.1.3.9. Phases in cast Al-10.1Ce-2.8Ni-1.2Mn after final heat-treatment at (a) 625°C for 2h, (b) 520°C for 20h, (c) 400°C for 200h, and (d) calculated phase amount vs. temperature in Al-10.1Ce-2.8Ni-1.2Mn. Source: ORNL.

With the newly obtained thermodynamic models for phases in the Al-Ce-Ni-Mn quaternary, we calculated the solidification paths of the three cast alloys using the Scheil model, which are plotted in the top row of graphs in Figure I.1.3.2.5. The comparison shows that without Mn addition, the ternary alloy has the smallest solidification temperature range, and the phases present in the as-cast microstructure are (Al) matrix, Al₁₁Ce₃, and Al₃Ni. With a small amount of Mn addition (0.3 wt%), the primary solidification shifted from Al₁₁Ce₃ to Al₂₃Ni₆(Ce,Mn)₄ and melting temperature increased from ~650°C to ~725°C. The phases presented in the as-cast microstructure are (Al) matrix, Al₁₁Ce₃, Al₂₃Ni₆(Ce,Mn)₄, and Al₃Ni. The amount of Al₃Ni is much less because of the reduced amount of liquid within the final eutectic reaction of Liq→(Al)+Al₁₁Ce₃+Al₃Ni. With an increase to 1.18 wt% Mn, the primary solidification phase becomes Al₁₀Mn₂Ce and the melting temperature is further increased to ~780°C. The phases present in the as-cast microstructure are (Al) matrix, Al₁₀Mn₂Ce, Al₂₀Mn₂Ce, Al₁₁Ce₃, Al₂₃Ni₆(Ce,Mn)₄, and Al₃Ni. The predicted primary phases and other phases present in the microstructure are in good agreement with the observed phases in the SEM images of the alloy as shown in the middle (e.g., low-magnification) and bottom (e.g., high-magnification) rows of Figure I.1.3.2.5.

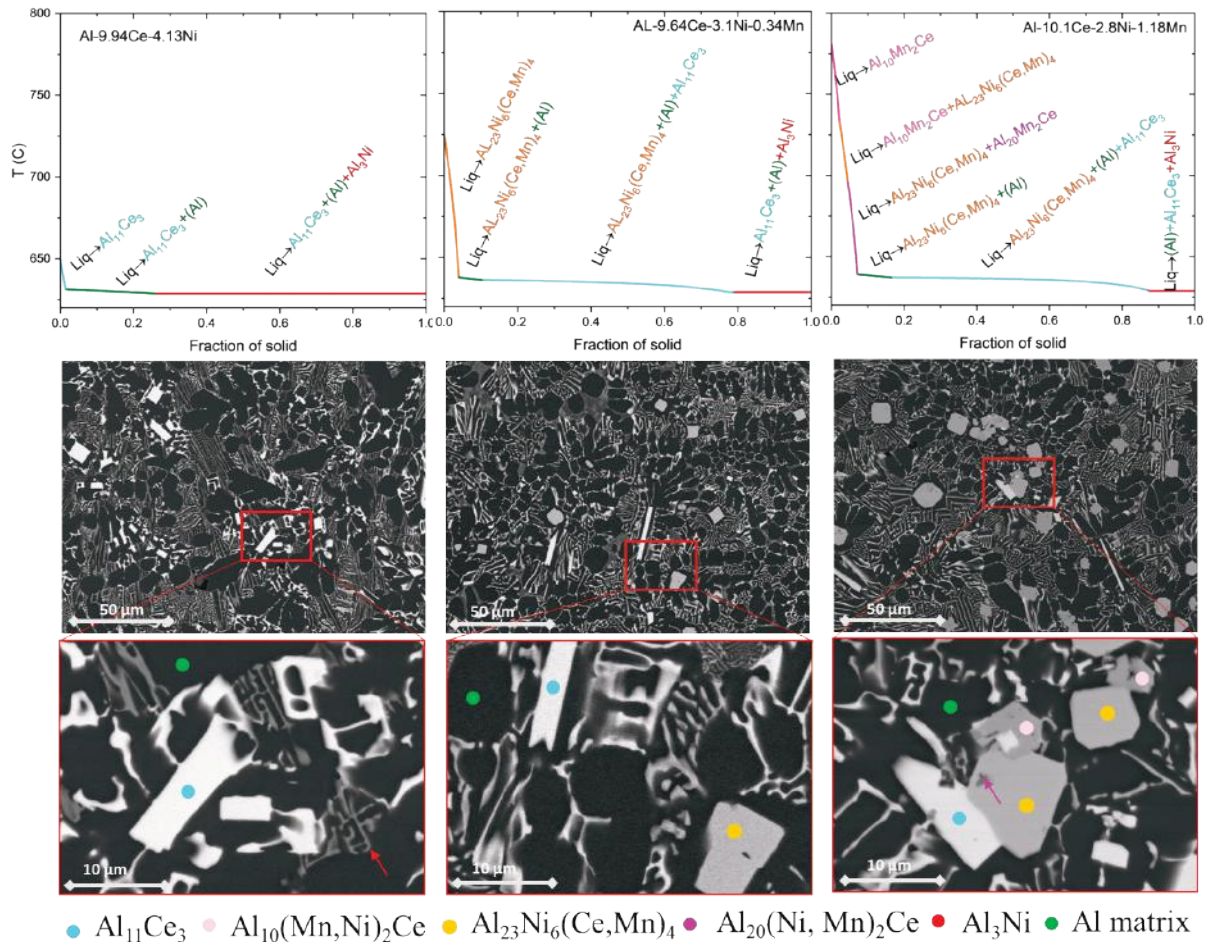


Figure I.1.3.10. Phases in the as-cast microstructure of Al-9.9Ce-4.13Ni, Al-9.6Ce-3.1Ni-0.3Mn and Al-10.1Ce-2.8Ni-1.2Mn alloys: (Top) predicted phases from the Scheil solidification model; (Middle) SEM BSE images at low magnification; (Bottom) SEM BSE images at higher magnification identifying individual phase constituents within the microstructures. Source: ORNL.

The phases in the AM Al-10.5Ce-3.1Ni-1.2Mn are shown in the STEM image in Figure I.1.3.2.6(a, b). The phase compositions were measured using APT due to the fine scale of the phase size. The following five phases were observed in the AM microstructure: (Al) matrix, $\text{Al}_{11}\text{Ce}_3$, $\text{Al}_{10}\text{Mn}_2\text{Ce}$, $\text{Al}_{20}\text{Mn}_2\text{Ce}$, and $\text{Al}_{23}\text{Ni}_6(\text{Ce},\text{Mn})_4$ with the properties shown in Table I.1.3.2.1. These five phases were also predicted from the Scheil solidification modeling results as shown in Figure I.1.3.2.6(c). The agreement between experimental and modeling results suggested the phases formed from AM are the same as those from the conventional cast method. However, the size and morphology and distribution of phases, which are not only dependent on thermodynamics but also kinetics, are very different by comparing Figure I.1.3.2.5 and Figure I.1.3.2.6. Cellular Automata modeling, which incorporates the currently developed thermodynamics information with kinetics modeling, is in progress to simulate the temporal evolution of size, morphology, and distribution of phases.

It was concluded from the results of this study of the effect of Mn addition on phase stability of Al-Ce-Ni alloys that there is vast potential for using minute additions of the alloying element Mn to drastically alter and manipulate phase stability and microstructure in Al-Ce-Ni systems.

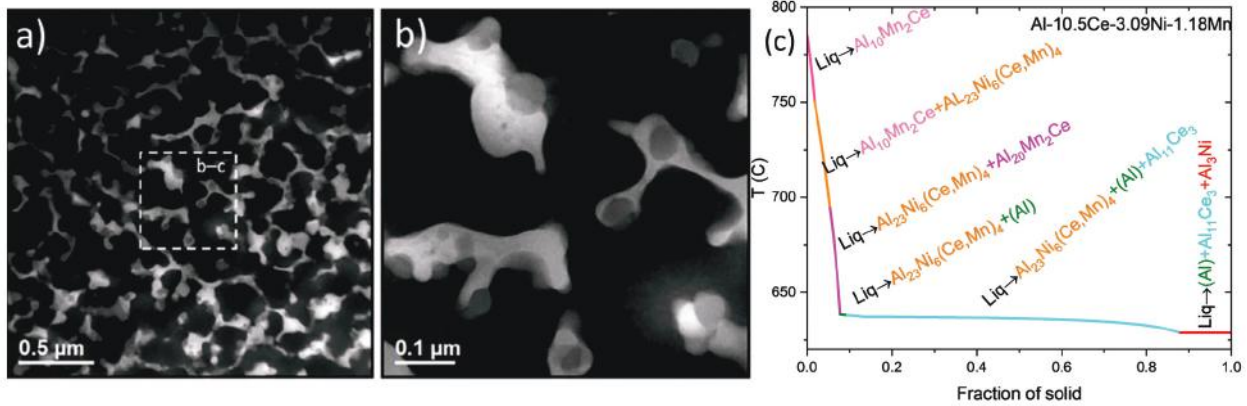


Figure I.1.3.11. Phases in the as-built microstructure of AM Al-10.5Ce-3.1Ni-1.2Mn: (a-b) STEM images at low and high-magnification; (c) predicted phases from the Scheil solidification model; (d) phase compositions measured from APT analysis. Source: ORNL.

Table I.1.3.2.1. Phases in the AM AL-10.5Ce-3.1Ni-1.2Mn

	(Al)-Matrix	Al ₁₁ Ce ₃	Al ₁₀ Mn ₂ Ce	Al ₂₀ Mn ₂ Ce	Al ₂₃ Ni ₆ Ce ₄
Al	Balance	74.54±1.17	75.53±1.96	86.77±1.95	70.50±0.61
Ni	0.07±0.10	0.14±0.07	2.71±0.28	0.22±0.15	17.95±0.33
Si	0.004±0.005	0.22±0.12	0.49±0.08	0.18±0.11	0.48±0.10
Mn	0.10±0.06	0.27±0.14	12.99±0.86	7.41±1.59	2.63±0.15
Ce	0.02±0.03	24.76±1.40	8.29±0.73	5.076±0.70	8.44±0.23
Mg	0.004±0.007	0.08±0.08	0.005±0.007	0.344±0.36	0.01±0.01

Effect of Zr on Phase Stability in Al-rich Al-Cu-Ce-Zr Quaternary

Phase analysis has identified that most phases are the same for the additive manufactured Al-Cu-Ce and Al-Cu-Ce-Zr alloys except for a small amount of primary Al₃Zr phase in the quaternary alloys. A thermodynamic database of the Al-Cu-Ce-Zr system was developed in this study based on prior work on the modeling of Al-Cu-Ce alloys [12]. This database was then used to predict the solidification path of the AM Al-3.7Cu-1.2Ce-0.3Zr (at%) alloy. This alloy follows a complex sequence of solidification reactions as shown in Figure I.1.3.2.7(a). The Al₃Zr is the first phase solidified from liquid because of the high liquidus temperature and limited solubility of Zr in the Al primary liquidus line. Once the Al₃Zr is formed, the liquid composition runs across the peritectic ridge of Liquid+Al₃Zr→(Al)-matrix and moves to the primary Al phase region. The solidification path is then primarily made up of three reactions: Liquid →Al matrix, Liquid →Al matrix+Al₄Ce, and Liquid →Al matrix+Al₈Cu₃Ce. The Al₄Ce phase has been reported as a high-temperature stable intermetallic in the Al-Ce system and therefore forms as the first solidified intermetallic phase early during solidification. The next solidified intermetallic, Al₈Cu₃Ce, appears stable over a wide solidification range between 620 and 550°C. This intermetallic phase has been observed only recently in our Al-Cu-Ce ternary alloys. Around 550°C, Al₈Cu₄Ce and Al₆₈Cu₁₅Zr₁₇ are expected to form through a ternary eutectic reaction but in negligible amounts and within narrower temperature ranges. Below 550°C and 500°C, due to segregation-induced high solute contents in the liquid-phase, the solidification reactions become more complicated with additionally formed Al₂Cu-θ and Si. The relative mole fractions of phases in the as-cast microstructure are plotted in Figure I.1.3.2.7(b); Al₈Cu₃Ce, (Al,Cu,Si)₄Ce (Al₄Ce-type), and Al₂Cu-θ are all expected in high mole fractions. The presence of these phases in the as-fabricated Al-3.7Cu-1.2Ce-0.3Zr (at%) alloy was validated by the APT analysis results in Table I.1.3.2.2. In the current Al-Cu-Ce-Zr alloy, Cu and a

small amount of impurity silicon (Si) were also present in the Al sublattice of Al_4Ce . While the Al_4Ce phase has been observed only at the melt pool boundary (MPB), its presence away from the MPB cannot be excluded due to the limited volumes acquired by APT needles. The absence of other minor phases predicted from the solidification simulation such as $\text{Al}_8\text{Cu}_4\text{Ce}$, $\text{Al}_{68}\text{Cu}_{15}\text{Zr}_{17}$ and Si could either be because of their negligible phase fractions in the microstructure or because the AM cooling is too fast to allow complete solute segregation, which is essential for the final complex solidification reactions to occur.

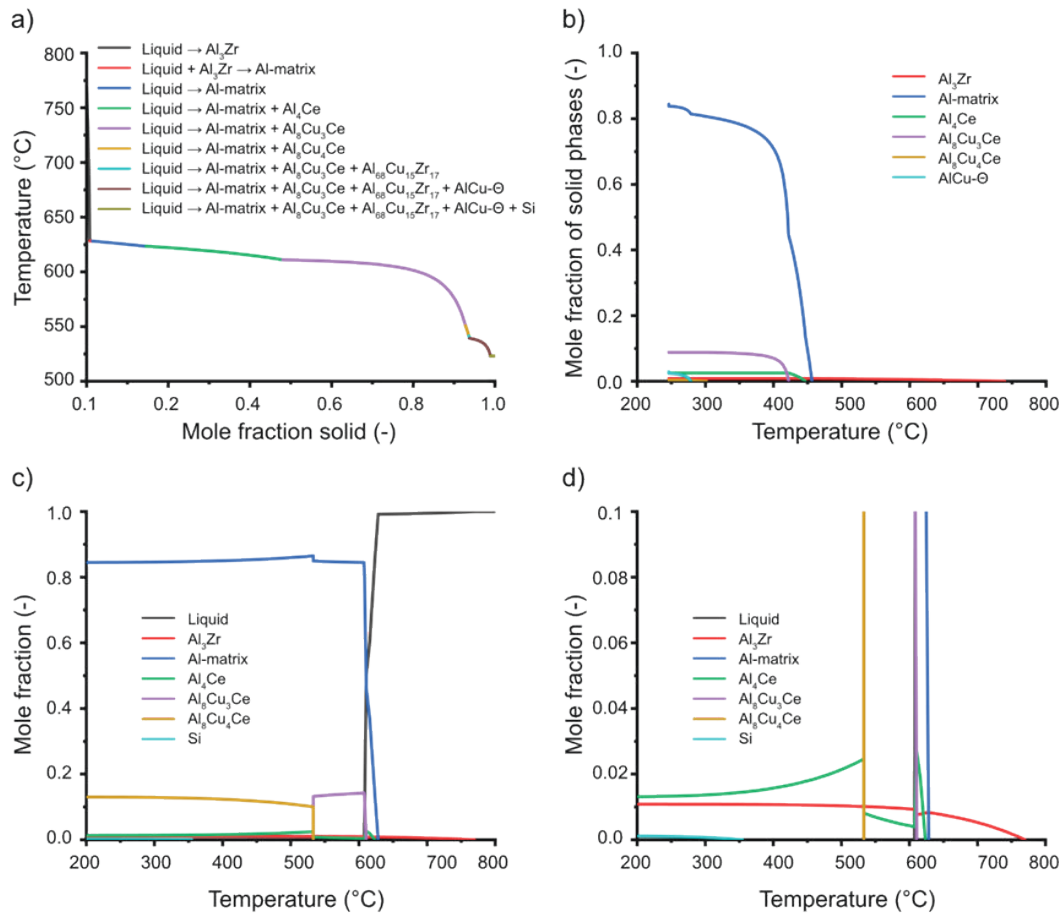


Figure I.1.3.12. Calculated phases in Al-3.7Cu-1.2Ce-0.3Zr (at%) alloys: (a) Solidification reactions and (b) mole fractions of phases predicted by the Scheil model (for interpreting phase stability in as-fabricated microstructure), (c) mole fractions of phases predicted by lever-rule model (for interpreting phase stability in post heat-treated microstructure), and (d) enlarged plot of (c) showing the minor phases. Source: ORNL.

Figure I.1.3.2.7(c) shows the calculated equilibrium mole fractions of phases in the Al-3.7Cu-1.2Ce-0.3Zr (at%) alloy, which can help to assess phase transformations during heat-treatment. It shows that above 620°C, this alloy is expected to melt, whereas Al_3Zr and Al_4Ce are expected to form between 620 and 600°C. Below 600°C, $\text{Al}_8\text{Cu}_3\text{Ce}$ is formed in addition to the (Al)-matrix and Al_4Ce . Around 530°C, the phase transformation $\text{Al}_8\text{Cu}_3\text{Ce} \rightarrow \text{Al}_8\text{Cu}_4\text{Ce}$ is expected, which may be accompanied by the formation of secondary, nanoscale Al_3Zr precipitates. While synchrotron X-ray diffraction in our previous work shows that this phase transformation takes place in the Al-Cu-Ce ternary alloy, Zr additions inhibit this transformation in the Al-Cu-Ce-Zr quaternary alloy. The underlying mechanisms can be attributed to slow diffusion caused by Zr segregation at Al/ $\text{Al}_8\text{Cu}_3\text{Ce}$ interfaces. Finally, below 350°C, Si and $\text{Al}_{68}\text{Cu}_{15}\text{Zr}_{17}$ are expected with negligible mole fractions. Figure I.1.3.2.7(d) provides an enlarged region of Figure I.1.3.2.7(c) to allow closer observation of low mole fraction phases.

This work suggested that adding a small amount of Zr can form Al_3Zr during solidification, which acts as a grain refiner. It can also slow down or even inhibit the phase transformation from Al_8Cu_3Ce to Al_8Cu_4Ce , as well as the coarsening of intermetallic phases. To understand the beneficial role of Zr on coarsening resistance and inhibiting phase transformation, experimental measurement of diffusion coefficients of elements in the Al-Cu-Ce-Zr FCC structure is currently in progress, which will provide better understanding of the kinetic effects of Zr additions.

Table I.1.3.2.2. Compositions of the Intermetallic Phases in Atomic Percent for All Conditions, Locations, and Phase Type with the Average Values and Standard Deviations in Parentheses

Condition	Location	Al	Cu	Ce	Zr	Si	Residual	Type
As-fabricated	Away	71.1 (2.4)	19.5 (1.6)	8.5 (0.7)	0.2 (0.1)	0.4 (0.1)	< 0.1	Al_8Cu_3Ce
	From	67.8 (1.2)	32.1 (1.2)	< 0.1	< 0.1	< 0.1	< 0.2	Al_2Cu-O
	MPB	79.1 (5.1)	19.7 (3.1)	0.1 (0.3)	0.3 (0.6)	0.5 (1.2)	< 0.4	Al_3Cu-O''
	At	71.1 (1.5)	20.7 (1.2)	7.8 (0.7)	0.1 (0.2)	0.2 (0.3)	< 0.1	Al_8Cu_3Ce
	MPB	69.3 (1.3)	30.6 (1.4)	< 0.1	< 0.1	< 0.1	< 0.1	Al_2Cu-O
Heat-treated	Away	49.9 (1.9)	16.5 (1.9)	21.4 (1.8)	11.9 (1.2)	11.9 (1.2)	< 0.1	$(Al,Cu,Si)_4Ce$
	From	67.1 (1.1)	21.1 (0.4)	9.5 (0.3)	0.5 (0.1)	0.5 (0.1)	< 0.4	Al_8Cu_3Ce
	MPB	72.8 (1.8)	3.4 (0.9)	2.0 (1.0)	0.9 (0.3)	0.9 (0.3)	< 0.1	Al_3Zr
	At	67.9 (0.8)	22.0 (0.5)	9.2 (0.3)	0.4 (0.1)	0.4 (0.1)	< 0.3	Al_8Cu_3Ce
	MPB	69.0 (2.7)	1.5 (1.2)	1.2 (0.4)	0.3 (0.3)	0.3 (0.3)	< 0.1	Al_3Zr

Conclusions

This task investigated the phase stability and solidification paths of Al-Ni-Mn-Ce and Al-Cu-Ce-Zr alloys using a strategically coupled approach of thermodynamic modeling and experimental study. The developed thermodynamic models for these two quaternary systems have been validated by the newly obtained experimental data. The results from the Al-Ni-Mn-Ce system showed that a small amount of Mn addition (~0.3wt%) can shift the primary phase from $Al_{11}Ce_3$ to $Al_{23}Ni_6Ce_4$, and for an increased level of Mn (~1.2wt%), the primary phase will be shifted to $Al_{10}Mn_2Ce$. This work has demonstrated the powerful potential for using minute levels of specific alloying elements, such as Mn, to drastically alter the solidification pathways, phase stability, and microstructure in Al-Ce-Ni alloys. The results from the Al-Cu-Ce-Zr system suggested that a small amount of Zr addition will form the primary Al_3Zr phase, which served as grain refiner. The beneficial role of Zr primarily lies in the kinetic inhibition on phase transformation and grain growth. For both alloy systems, we found that despite the much more refined microstructure, the phases present in the AM alloy are similar to those in the cast alloy, suggesting the current AM processing conditions have a major role in refining microstructure but can still maintain or approach the local equilibrium conditions at the solid-liquid interface of eutectic solidification in this alloy family. The validated thermodynamic models for the Al-Ni-Mn-Ce and Al-Cu-Ce-Zr system will be used in Cellular Automaton modeling to simulate the temporal evolution of the phase size, morphology, and distribution under different cooling conditions.

Key Publications

1. Bahl, S., K. Sisco, Y. Yang, F. Theska, S. Primig, L. F. Allard, R. A. Michi, C. Fancher, B. Stump, R. Dehoff, and A. Shyam, 2021, “Al-Cu-Ce(-Zr) alloys with an exceptional combination of additive processability and mechanical properties,” *Addit. Manuf.*, Vol. 48, Part 8, Art. 102404. <https://doi.org/10.1016/j.addma.2021.102404>.
2. Michi, R. A., K. Sisco, S. Bahl, Y. Yang, J. D. Poplawsky, L. F. Allard, R. Dehoff, A. Plotkowski, and A. Shyam, 2022, “A creep-resistant additively manufactured Al-Ce-Ni-Mn alloy,” *Acta Mater.*, Vol. 227, Art. 117699. <https://doi.org/10.1016/j.actamat.2022.117699>.
3. Perrin, A., S. Bahl, D. N. Leonard, R. Michi, K. Sisco, A. Plotkowski, A. Shyam, R. Dehoff, D. Shin, and Y. Yang, 2022, “Phase stability in cast and additively manufactured Al-rich Al-Cu-Ce alloys,” *J. Alloys Compd.*, Vol. 926, Art. 166984. <https://doi.org/10.1016/j.jallcom.2022.166984>.
4. Perrin, A., R. A. Michi, K. D. Sisco, A. Plotkowski, A. Shyam, R. Dehoff, and Y. Yang, 2023, “Effect of Mn on phase equilibria in Al-rich Al-Ce-Ni alloys,” in preparation for publication.
5. Theska, F., Y. Yang, K. D. Sisco, A. Plotkowski, and S. Primig, 2022, “On the high-temperature stability of the Al₈Cu₃Ce intermetallic in an additively manufactured Al-Cu-Ce-Zr alloy,” *Mater. Charact.*, Vol. 191, Art. 112109. <https://doi.org/10.1016/j.matchar.2022.112109>.

References

1. Frazier, W. E., 2014, “Metal additive manufacturing: A review,” *J. Mater. Eng. Perform.*, Vol. 23, No. 6, pp. 1917–1928. <https://doi.org/10.1007/s11665-014-0958-z>.
2. Michi, R. A., A. Plotkowski, A. Shyam, R. R. Dehoff, and S. S. Babu, 2022, “Towards high-temperature applications of aluminium alloys enabled by additive manufacturing,” *Int. Mater. Rev.*, Vol. 67, No. 3, pp. 298–345. <https://doi.org/10.1080/09506608.2021.1951580>.
3. Plotkowski, A., O. Rios, N. Sridharan, Z. Sims, K. Unocic, R. T. Ott, R. R. Dehoff, and S. S. Babu, 2017, “Evaluation of an Al-Ce alloy for laser additive manufacturing,” *Acta Mater.*, Vol. 126, pp. 507–519. <https://doi.org/10.1016/j.actamat.2016.12.065>.
4. Rödler, G., F. G. Fischer, J. Preußner, V. Friedmann, C. Fischer, A. Weisheit, and J. H. Schleifenbaum, 2021, “Additive manufacturing of high-strength eutectic aluminium-nickel alloys—Processing and mechanical properties,” *J. Mater. Process. Technol.*, Vol. 298, Art. 117315. <https://doi.org/10.1016/j.jmatprotec.2021.117315>.
5. Wang, Z., X. Lin, L. Wang, Y. Cao, Y. Zhou, and W. Huang, 2021, “Microstructure evolution and mechanical properties of the wire+ arc additive manufacturing Al-Cu alloy,” *Addit. Manuf.*, Vol. 47, Art. 102298. <https://doi.org/10.1016/j.addma.2021.102298>.
6. Shyam, A., Plotkowski, S. Bahl, K. Sisco, L. F. Allard, Y. Yang, J. A. Haynes, and R. R. Dehoff, 2020, “An additively manufactured Al-Cu-Mn-Zr alloy microstructure and tensile mechanical properties,” *Mater.*, Vol. 12, Art. 100758. <https://doi.org/10.1016/j.mtla.2020.100758>.
7. Bahl, S., K. Sisco, Y. Yang, F. Theska, S. Primig, L. F. Allard, R. A. Michi, C. Fancher, B. Stump, R. Dehoff, and A. Shyam, 2021, “Al-Cu-Ce(-Zr) alloys with an exceptional combination of additive processability and mechanical properties,” *Addit. Manuf.*, Vol. 48, Art. 102404. <https://doi.org/10.1016/j.addma.2021.102404>.
8. Kaufman, L., and H. Bernstein, 1970, *Computer Calculation of Phase Diagrams with Special Reference to Refractory Metals*, Academic Press, New York, NY, USA.
9. Scheil, E., 1942, “Bemerkungen zur schichtkristallbildung,” *Int. J. Mater. Res.*, Vol. 34, No. 3, pp. 70–72. <https://doi.org/10.1515/ijmr-1942-340303>.

10. Chen, S. L., Y. Yang, S. W. Chen, X. G. Lu, and Y. A. Chang, 2009, „Solidification simulation using Scheil model in multicomponent systems,” *J. Phase Equilib. Diffus.*, Vol. 30, No. 5, pp. 429–434. <https://doi.org/10.1007/s11669-009-9568-0>.
11. Wang, H., Z. Li, Z. Chen, and B. Yang, 2016, „Thermodynamic optimization of the Ni-Al-Ce ternary system,” *J. Phase Equilib. Diffus.*, Vol. 37, No. 2, pp. 222–228. <https://doi.org/10.1007/s11669-015-0447-6>.
12. Perrin, A., R. A. Michi, K. D. Sisco, A. Plotkowski, A. Shyam, R. Dehoff, and Y. Yang, 2023, “Effect of Mn on phase equilibria in Al-rich Al-Ce-Ni alloys,” in preparation for publication.

Acknowledgements

Research was sponsored by the DOE-EERE VTO Propulsion Materials Program. Collaborations from A. Plotkowski, A. Shyam, A. Perrin, S. Bahl, R. A. Michi, D. Leonard, K. Sisco, and R. Dehoff of ORNL are acknowledged.

I.1.3.3 Task 3C. Advanced Ceramics and Processing for Wireless Charging Systems (Ferrites) (Oak Ridge National Laboratory)

Beth Armstrong, Principal Investigator

Oak Ridge National Laboratory
Materials Science and Technology Division
1 Bethel Valley Rd.
Oak Ridge, TN 37830
E-mail: armstrongbl@ornl.gov

J. Allen Haynes, PMCP Consortium Manager

Oak Ridge National Laboratory
Materials Science and Technology Division
1 Bethel Valley Rd.
Oak Ridge, TN 37830
E-mail: haynesa@ornl.gov

Jerry Gibbs, DOE Technology Development Manager

U.S. Department of Energy
E-mail: jerry.gibbs@ee.doe.gov

Start Date: November 1, 2021	End Date: September 30, 2023	
Project Funding (FY 2022): \$290,000	DOE share: \$290,000	Non-DOE share: \$0

Project Introduction

Wireless charging is a critical technology to enable a broader spectrum of the future transportation sector to transition to EVs. While wired charging works for plugging in cars at night or while not in use, wireless charging is needed for transportation applications, such as with heavy vehicles, where on-road time needs to be maximized [1] and there can be localized high-load scenarios, such as very steep grades. Minimizing charging time is made possible through dynamic wireless charging, where vehicles are charged as they drive. While this concept has been shown for buses and delivery trucks, new materials are required for both on-road (transmitting) and on-vehicle (receiving) wireless charging devices to improve the function, relative mass, and durability of current systems [2, 3]. One major area for materials development is in the ferrite core as it is typically the heaviest component in a high-power wireless charging pad [4]. The tunability of this class of advanced ceramic materials provides a strong framework and opportunity for developing new chemistries to meet the variable electric drive design space. It also enables flexibility in the processing of unique and/or composite architectures. Current ferrite parts have been dominated by simple, planar geometries and are too heavy and cumbersome to be effectively utilized on the vehicle side of such charging systems.

By combining ORNL's suite of relevant capabilities and expertise—including ceramic synthesis, processing, wireless charging system design, and characterization—new hybrid material systems and advanced architectures may be realized. A systematic approach will be utilized to evaluate and determine baseline property sets of the current state-of-the-art commercial ceramic materials. A new compositional array of materials will be designed and synthesized using guidance from computational predictions and targeted advancements over the baseline materials in the desired suite of processing, mechanical, physical, and magnetic properties.

Initially, simple geometries will be fabricated using traditional ceramic processing methods to develop an understanding of the baseline sintering behavior needed for the architecture–property relationship. This will better enable the design of potentially complex novel wireless structures. This will require more advanced

ceramic processing methods, such as AM. Materials and designs will be characterized by collaborators at ORNL, including the electric drive team at the National Transportation Research Center and the Basic Energy Sciences–Materials Sciences and Engineering Division team in the Materials Science and Technology Division. The eventual more complex ceramic architectures will be printed in collaboration with the AM team at the Manufacturing Demonstration Facility.

Objectives

This project aims to develop tunable and lighter weight advanced ceramic materials (ferrites), as well as the appropriate processing methods for the fabrication of dynamic wireless charging systems for heavy vehicle applications. This project will determine mechanical, physical, and magnetic properties that are critical to wireless charging applications; baseline existing materials against these metrics; and begin fabrication of bulk structures in order to pursue these aims.

Approach

This research task is taking place in four main sub-tasks: (1) determine properties of interest; (2) baseline existing materials; (3) optimize composition and processing; and (4) characterization and testing.

Determining properties of interest and baselining materials provided a route to start investigating pathways to new, advanced ceramics for wireless charging systems. The properties of interest were determined from a literature search and discussions with motor/power electronics designers and a commercial ferrite powder supplier. The existing materials were characterized according to the properties of interest to obtain a materials baseline for the current state-of-the field. With this information, we will be able to optimize the composition and processing to develop new materials that are well-suited for wireless charging systems. These materials will be characterized and tested to ensure adequate performance and provide feedback for further optimization of both composition and processing.

Results

To understand advanced ceramics and processing for wireless charging systems, the first three tasks were to determine: (1) the current state of magnetic ceramic materials, (2) the techniques needed to characterize magnetic ceramic materials, and (3) the materials needs as defined by motor and power electronics designers. Over the course of an initial literature review and several discussions with collaborators, the following key parameters were identified: (a) low-cost, (b) high-saturation flux density, (c) low power loss, (d) operation at high frequencies (85–150 kHz), (e) high Curie temperature ($>100^{\circ}\text{C}$), and (f) low relative permeability (1500–3000). Of these parameters, Curie temperature and relative permeability were selected as the two key measurable parameters to benchmark materials. These parameters were selected because Curie temperature indicates maximum operational temperature conditions and relative permeability defines the magnetic response to an applied field. Spinel ferrites and hexaferrites were chosen as the first starting material systems because they have both high operational frequencies and diverse chemical systems that would yield tunable compositions and properties.

To create a baseline property database, ferrite powders with a variety of compositions were obtained from a commercial vendor, Steward Advanced Materials, and compared with existing fabricated wireless charging components, Magment and Ferroxcube 3C95. For each powder sample and component material, the structure and morphology were characterized using X-ray diffraction and SEM, respectively. Initial magnetic measurements were performed to determine the magnetic permeability and Curie temperature. Magnetic permeability is determined from the hysteresis loop and is determined by the rate of change of the magnetic moment in an applied magnetic field. A representative hysteresis loop of $\text{Ni}_{0.5}\text{Zn}_{0.5}\text{Fe}_2\text{O}_4$ is shown in Figure I.1.3.3.1 and illustrates high-magnetic permeability due to the low hysteresis as evident by the small gap in the hysteresis loop on the cycling of the applied magnetic field. The Curie temperature is determined by performing thermogravimetric analysis (TGA) measurements in the presence of a magnetic field. A strong magnet is placed above the sample, and when the sample is magnetized, it appears to be lighter because it is attracted to the magnet above; however, at the Curie temperature, the sample is demagnetized and appears to have an increased mass since it is no longer attracted to the magnet. When no magnetic field is applied there is

no change in the mass of the sample on heating. The Curie temperature is assigned as the temperature at which change in weight is at a maximum. Magnetic TGA measurements for $\text{Ni}_{0.5}\text{Zn}_{0.5}\text{Fe}_2\text{O}_4$ and $\text{Mg}_{0.5}\text{Zn}_{0.5}\text{Fe}_2\text{O}_4$ are shown in Figure I.1.3.3.2. The Curie temperature for the $\text{Ni}_{0.5}\text{Zn}_{0.5}\text{Fe}_2\text{O}_4$ powder is 248°C and 83°C for the $\text{Mg}_{0.5}\text{Zn}_{0.5}\text{Fe}_2\text{O}_4$ powder, highlighting the significant difference in Curie temperature just by switching the composition from Ni to Mg. The magnetic data shows that $\text{Ni}_{0.5}\text{Zn}_{0.5}\text{Fe}_2\text{O}_4$ meets the Curie temperature requirements outlined by motor and power electronics designers, but the Curie temperature for $\text{Mg}_{0.5}\text{Zn}_{0.5}\text{Fe}_2\text{O}_4$ is less than 100°C and is therefore too low.

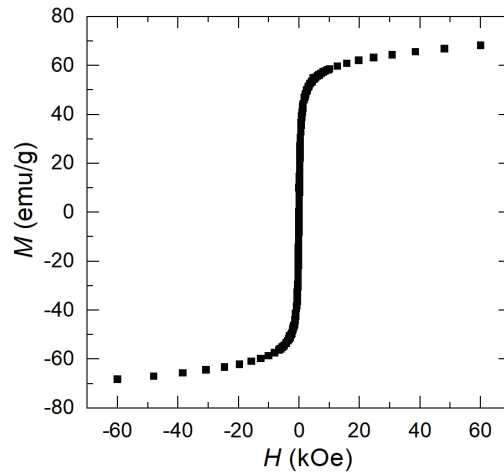


Figure I.1.3.13. Hysteresis loop for $\text{Ni}_{0.5}\text{Zn}_{0.5}\text{Fe}_2\text{O}_4$ showing little hysteresis in an applied magnetic field, which is representative of soft ferrite magnetic materials. Source: ORNL.

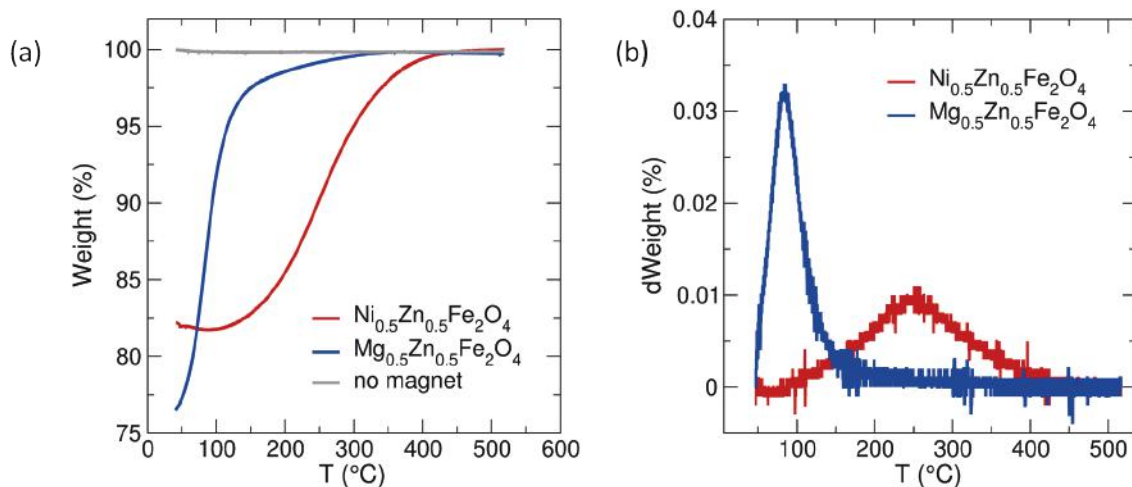


Figure I.1.3.14. Magnetic TGA data for (a) $\text{Ni}_{0.5}\text{Zn}_{0.5}\text{Fe}_2\text{O}_4$ and $\text{Mg}_{0.5}\text{Zn}_{0.5}\text{Fe}_2\text{O}_4$ powders with the maximum change in weight, which (b) indicates a Curie temperature of 248°C for $\text{Ni}_{0.5}\text{Zn}_{0.5}\text{Fe}_2\text{O}_4$ and 83°C for $\text{Mg}_{0.5}\text{Zn}_{0.5}\text{Fe}_2\text{O}_4$. Source: ORNL.

Due to the depth of the compositional space for ferrite materials, modeling efforts to streamline and downselect candidate systems were initiated. Additional task support from a computational materials project under PMCP Thrust 4B has funded efforts to explore the compositional space of spinel ferrites to simulate and predict how composition effects the magnetic properties of ferrite materials and to guide future synthesis efforts by determining which elements yield favorable properties when doped into the spinel structure. This work is done by testing the stability and determining the magnetic properties of spinel structures with a range of doping compositions and concentrations. Figure I.1.3.3.3(a) shows the ZnFe_2O_4 structure with 25% doping

of Ni (purple) on the Zn (silver) site. Additional calculations can be performed on this structure to determine the magnetic properties as a function of temperature, as well as composition, to create magnetic phase diagrams like the one shown in Figure I.1.3.3(b) for SrFeO_x , which shows the transitions between different magnetic states as a function of temperature and oxygen concentration [5]. These modeling efforts help to understand how dopants and composition affect magnetic properties. This information can be used as we move toward making more complex architectures.

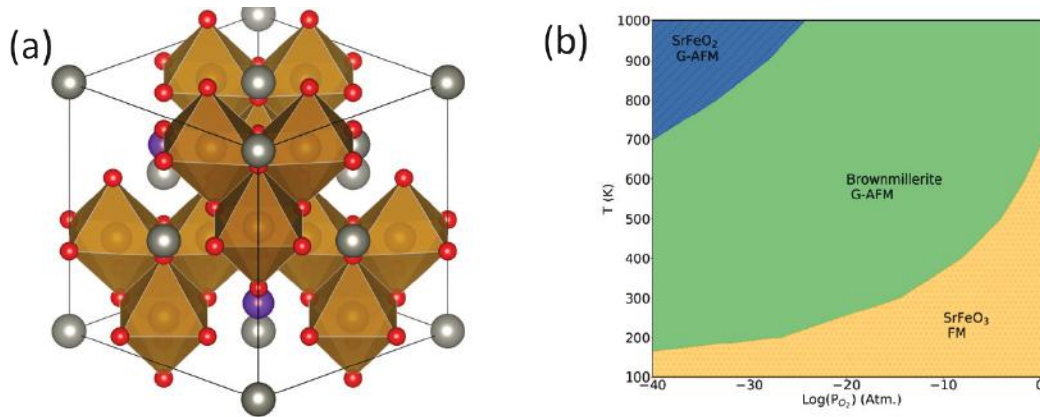


Figure I.1.3.15. (a) ZnFe_2O_4 structure with 25% doping of Ni (purple) on the Zn (silver) sites that is used for DFT calculations. (b) Magnetic phase diagram for SrFeO_x showing the transitions between magnetic states as a function of temperature and composition. Source: ORNL.

Once the initial baseline properties were determined from the powder samples, the fabrication of dense ceramic compacts was performed. Dense structures were chosen to maximize the magnetic properties because current ferrite cores are fabricated as single-phase dense components with aligned grains. By fabricating these simple structures, we were able to understand how the concentration, as well as the composition, of dopants influenced densification and optimize densification and fabrication conditions. The ferrite powders were compressed into pellets and sintered to achieve a bulk compact similar to the dense plates used in current wireless charging testing and applications. In performing the densification studies, the ability to densify the pellets was highly dependent upon the composition and the concentration of the dopants in the powders. All densities shown were determined using the Archimedes method. Initial studies for samples sintered at 1200°C for two hours are shown in Figure I.1.3.3.4(a). The concentration of Ni in the ferrite structure significantly affects the densification, with the $\text{Ni}_{0.5}\text{Zn}_{0.5}\text{Fe}_2\text{O}_4$ pellets having an average density of 3.406 g/cm^3 (63.69% of the theoretical density) and the $\text{Ni}_{0.8}\text{Zn}_{0.2}\text{Fe}_2\text{O}_4$ pellets having a higher average density of 4.086 g/cm^3 (76.25% theoretical density) for the same sintering conditions. The composition of the dopant is also shown to have a large effect on the densification of the compact, with the $\text{Mg}_{0.5}\text{Zn}_{0.5}\text{Fe}_2\text{O}_4$ pellets having an average density of 4.496 g/cm^3 (92.68% theoretical density) for the same concentration of dopants as the $\text{Ni}_{0.5}\text{Zn}_{0.5}\text{Fe}_2\text{O}_4$ pellets. An increase of 28.99 in the percentage of theoretical density is obtained only by exchanging Mg for Ni in the structure. To understand the role of temperature and time on the sintering of the ferrite powders, the $\text{Ni}_{0.5}\text{Zn}_{0.5}\text{Fe}_2\text{O}_4$ powders were heat-treated with additional sintering conditions, as shown in Figure I.1.3.3.4(b). The density increased as a function of sintering temperature and time, with the highest densities achieved being 4.115 g/cm^3 (77.70% theoretical density) and 4.088 g/cm^3 (76.41% theoretical density) from the samples sintered for 12 hours at 1450°C and 1500°C , respectively.

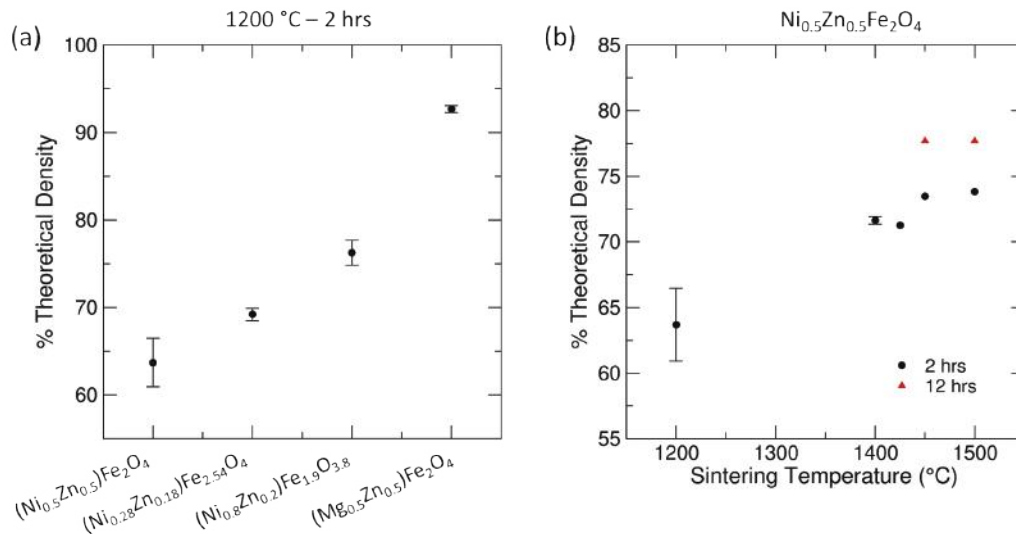


Figure I.1.3.16. Percent of theoretical density as a function of (a) composition and (b) sintering conditions. Source: ORNL.

To increase the density of the $\text{Ni}_{0.5}\text{Zn}_{0.5}\text{Fe}_2\text{O}_4$ compacts beyond 77.70% theoretical density, additional processing steps were tested. By testing different processing steps, the optimum processing conditions could be determined for use in fabricating future architectures. These processing steps included sieving the powders to remove large particles, humidifying the powders in water to increase bonding between particles, and grinding and repressing the pellets. For the $\text{Ni}_{0.5}\text{Zn}_{0.5}\text{Fe}_2\text{O}_4$ pellets, a large increase in the density was observed when the powders were sieved before pressing the pellets for both sintering conditions of 1400°C for two hours and 1500°C for 12 hours, as observed in Figure I.1.3.3.5. This indicated that the particle size distribution within the powders is critical to achieving higher density components. By sieving the powders, a final density of 4.597 g/cm³ (85.96% theoretical density) was achieved for the pellets sintered at 1400°C for two hours. This means that by sieving the powders, a higher density can be achieved without heating to 1500°C or holding at temperature for 12 hours. By sieving powders and heating to 1500°C for 12 hours, a density of 4.798 g/cm³ (89.73% theoretical density) is achieved and can be increased above 90% theoretical density with additional processing steps, such as humidifying powders and repressing parts.

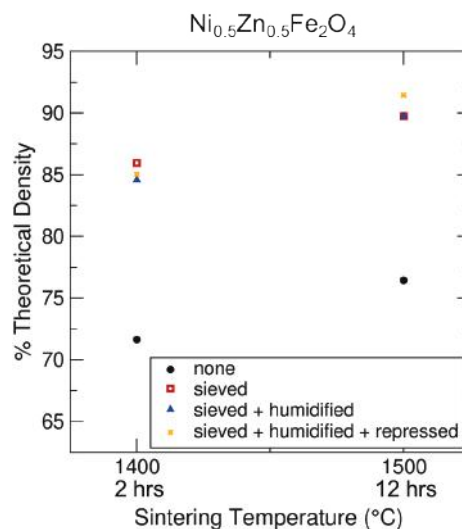


Figure I.1.3.17. Percent of theoretical density for pellets of $\text{Ni}_{0.5}\text{Zn}_{0.5}\text{Fe}_2\text{O}_4$ sintered at either 1400 °C for 2 hours or 1500 °C for 12 hours with different processing conditions. Source: ORNL.

While additional processing steps were utilized to create higher density ceramic materials, studies performed with additional support from a supporting project within Powertrain Materials Core Program Thrust 4A characterized the composition and structural grain morphology of commercially obtained sintered ceramic ferrite materials using electron probe X-ray microanalysis / Raman mapping. This work highlighted three important results: (1) the commercial ferrite component, Magment, is not 100% dense; (2) it is not single-phase; and (3) the grain orientation is not completely aligned. Instead, it contains pieces of recycled ferrite materials embedded in a cementitious matrix as shown in Figure I.1.3.3.6. This contradicts the previous assumption that high densities are necessary to achieve the magnetic strengths needed for these applications and that alignment of the grains correlates to magnetic dipole alignment. This realization enables research strategies for lightweighting these structures that can allow addition of voids or porosity, or even the introduction of a lighter weight secondary phase creating a more durable composite structure. It also enables the use of mixed ferrite phases in a composite architecture to tune the magnetic properties as application demands are identified.

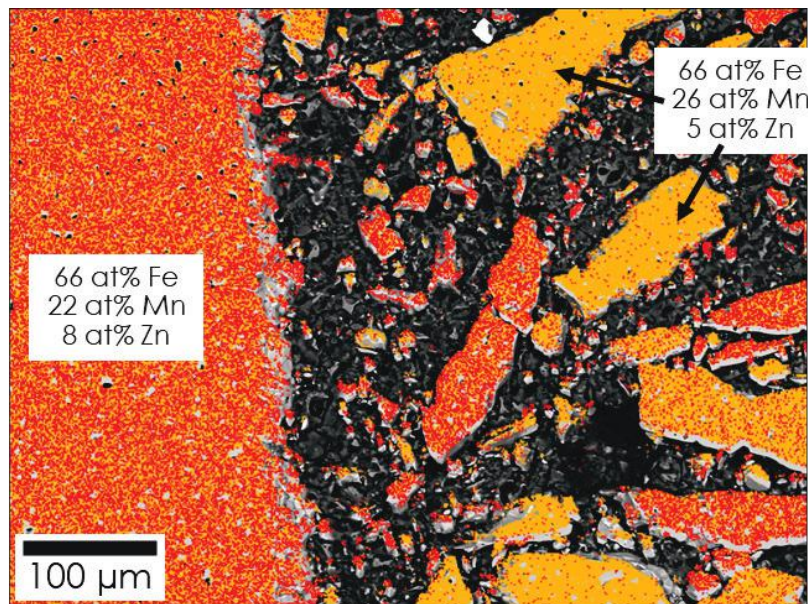


Figure I.1.3.18. Map, a backscattered scanning electron image with overlays of two different phases in red and orange showing the regions of dense ferrite pieces in a cementitious matrix. Source: ORNL.

Conclusions

Initial literature reviews and discussions with collaborators identified several parameters of interest and determined that the Curie temperature and relative permeability of the material were the first key parameters to focus on to develop materials for wireless BEV charging applications. Ferrite powders were obtained from a commercial vendor, characterized, and compared with existing wireless charging materials. Magnetic hysteresis measurements and TGA were used to characterize the magnetic properties of the materials. Once the initial powders were characterized, bulk structures were fabricated. The sintering conditions were found to depend upon the sample compositions. Additional processing steps were used to improve the sintering of materials. Using sieving powders to remove larger particles was found to have a significant effect on sintering. These results combined with those from the Thrust 4 projects show clear areas for future work to advance design of both future ceramic magnetic materials and their processing pathways. Modeling efforts are providing a method to predict ferrite compositions to guide and focus the synthesis strategy for new materials for wireless charging applications. Results from electron probe X-ray microanalysis / Raman mapping of existing commercial materials show that not all commercial products are dense compacts, opening new opportunities for possible lightweighting and property enhancing efforts.

Key Publications

1. Bullock, S. E., B. L. Armstrong, V. R. Cooper, M. S. Kesler, and R. D. McAuliffe, 2022, “Additive printing of ferrite magnetic structure for wireless charging,” ORNL Invention Disclosure 202205148, 8 September 2022.
2. McAuliffe, R. D., and B. L. Armstrong, 2023, “The role of ferrites in wireless charging for electric vehicles,” in preparation.

References

1. Lukic, S., and Z. Pantic, 2013, “Cutting the cord: Static and dynamic inductive wireless charging of electric vehicles,” *IEEE Electr. Mag.*, Vol. 1, No. 1, pp. 57–64. <https://doi.org/10.1109/MELE.2013.2273228>.
2. Jang, Y. J., Y. D. Ko, and S. Jeong, 2012, “Optimal design of the wireless charging electric vehicle,” *2012 IEEE International Electric Vehicle Conference*, 4–8 March 2012, Greenville, SC, USA. pp. 1–5. <https://doi.org/10.1109/IVEC.2012.6183294>.
3. Thurston, A., 2022, “‘Magnetisable concrete’ trialed for non-stop charging of EVs,” *The Energyst*, 7 January 2022 [Online]. Available at: <https://theenergyst.com/magnetisable-concrete-trialled-for-non-stop-charging-of-evs/> (last accessed 31 January 2023).
4. Mohammad, M., S. Choi, and M. E. Elbuluk, 2019, “Loss minimization design of ferrite core in a DD-coil-based high-power wireless charging system for electrical vehicle application,” *IEEE Trans. Transp. Electrification*, Vol. 5, No. 4, pp. 957–967. <https://doi.org/10.1109/TTE.2019.2940878>.
5. Ferreira, T., S. Achatya, Y. Li, D. S. Parker, A. S. Sefat, and V. R. Cooper, 2021, “Unintended consequence of topochemical reduction of SrFeO₃ to SrFeO₂: Design of infinite layered oxides,” *Phys. Rev. Mater.*, Vol. 5, Art. 123401. <https://doi.org/10.1103/PhysRevMaterials.5.123401>.

Acknowledgements

The authors would like to acknowledge Steward Advanced Materials for providing commercial ferrite powders for baselining properties, D. May for assistance in measuring the magnetic properties of ferrite powders and compacts, and M. Mohammad for discussions on design requirements for wireless charging pads. The authors would also like to acknowledge A. Haynes, T. Watkins, D. Shin, and J. Gibbs for their programmatic guidance on this project.

I.1.3.4 Task 3D. Novel, Ultra-High Conductivity Materials (Copper Tape + Carbon Nanotubes) for Electric Vehicles (Oak Ridge National Laboratory)

Tolga Aytug, Principal Investigator

Oak Ridge National Laboratory
Chemical Sciences Division
1 Bethel Valley Rd.
Oak Ridge, TN 37830
E-mail: aytugt@ornl.gov

J. Allen Haynes, PMCP Consortium Manager

Oak Ridge National Laboratory
Materials Science and Technology Division
1 Bethel Valley Rd.
Oak Ridge, TN 37830
E-mail: haynesa@ornl.gov

Jerry Gibbs, DOE Technology Development Manager

U.S. Department of Energy
E-mail: jerry.gibbs@ee.doe.gov

Start Date: May 21, 2021	End Date: September 30, 2022	
Project Funding (FY 2022): \$370,000	DOE share: \$370,000	Non-DOE share: \$0

Project Introduction

This project focuses on the design, study, and evaluation of scalable and high-throughput synthesis approaches and material technologies for the fabrication of a new class of high-performance copper (Cu)-based tape conductors (i.e., ultra conductive copper (UCC) composites). These novel tape composites have higher electrical conductivity than pure Cu to enable significant improvement in the efficiency of most on- and off-board electrical conduction applications for EVs. The new concepts and methods developed within this project are expected to contribute to meeting the DOE VTO 2025 performance and cost targets. After over a decade of global research and development efforts to develop UCC composites elsewhere, the most promising of these are composed of one-dimensional (1D) carbon nanotubes (CNT) and Cu, but the RT performance of these composites is inconsistent, and the synthetic methods are not reproducible or scalable to commercially viable levels.

The core problem being addressed is that power losses associated with the electrical resistance of Cu adversely impact and limit the efficiency and performance of all electric devices. The remarkable ballistic electrical transport characteristics offered by CNTs (the charge carriers can travel over approximately 500 nm in nanotubes without scattering) offer the opportunity to measurably improve the electrical and thermal conductivity of a Cu matrix composite vs. pure Cu conductors, as well as imparting additional CNT-enabled benefits, including lower weight, better flexibility, and improved thermal management, as observed in Table I.1.3.4.1.

Table I.1.3.4.1. Comparison of the Properties of Single-Walled CNTs vs. Cu

	Cu	CNT
Electrical Conductivity	59.6 MS/m	100 MS/m
Thermal Conductivity	400 W/m-K	4000 W/m-K
Current Density	10^6 A/cm ²	10^8 A/cm ²

To date, a few promising ultra-conducting Cu-CNT composites have been reported with conductivities increased by $\geq 30\%$ compared with the International Annealed Cu Standard and ampacities up to ~ 100 times higher than Cu [1–4]. However, all these technologies are only capable of being demonstrated on very short (i.e., μm – mm) sample sections and are not scalable to practically useful lengths. To our knowledge, there are presently no viable competing technologies commercially available to produce such advanced conductors to simultaneously provide consistently increased conductivity, higher current density, and improved mechanical properties in a scalable manner. Numerous processes have been explored to prepare Cu-CNT composites. The most common approaches to form layered Cu-CNT structures include powder metallurgical wire processing routes such as spark plasma sintering, hot-pressing, deformation-based processing techniques and electrochemical processing methods. All other technologies are based on either CNT-fibers, which do not enable conductivity levels comparable to pure Cu, or on covetic processes based on introduction of carbon particles into a molten metal under forced convection and high electric field [5,6]. However, the field of covetics is very new and the results are controversial [7,8]. To date, there have been very few reports on improved conductivity in such covetic Cu materials; the issues related to fundamental understanding of the potential mechanism(s) of metal-carbon bonding and inconsistent performance characteristics have not been resolved. Some possible reasons for the weak performance for longer material lengths include employment of low-quality/purity CNTs, lack of controlled CNT alignment along the direction of the current flow, limited wettability and inhomogeneous distribution of CNTs on and into the metal matrix, and a poor fundamental understanding of Cu-CNT interactions affecting bulk electrical transport properties [2]. Furthermore, most of the previous UCC-type processing strategies have been unstable, with research either demonstrating inconsistent results, or being limited to unscalable laboratory processing techniques, rendering them unsuitable for large-scale commercial development into affordable, practical conductors. It should be noted that the ORNL UCC materials are not related to covetic technologies.

Objectives

Cost and size are the key barriers to achieving the technical research and development targets of the Electrical and Electronics Technical Team 2025 electric traction drive system. This necessitates more energy-efficient power delivery through the development of improved conductors able to provide enhanced electrical conductivity, higher current carrying capacity (i.e., ampacity), and better mechanical strength. Such conductors can improve energy utilization through reduced ohmic losses, transport power with smaller size and/or lightweight wires/cables, and enable better thermal management across system components, potentially resulting in immense cumulative technological and economic value in all energy sectors ranging from on- and off-board components in electric drive vehicles to power grid systems, as well as interconnects to electronic devices and motors.

The overall objective of this project is to demonstrate a novel technological platform, designed around scalable, cost-effective, and commercially viable processing methods to produce UCC conductors for most electrified powertrain components (i.e., converters, batteries, wiring, interconnects, busbars, charging systems, etc.) while enabling much needed reduced weight/volume, higher power density, and improved reliability and thermal characteristics. These ultra conductive metal composites will exhibit improved electrical conductivity, ampacity, and mechanical strength, all exceeding that of pure Cu by as much as 10%. This new composite conductor couples the excellent properties of CNTs, such as light weight, high-strength, and good conductivity. The research and development effort combines ORNL's strengths in theory and simulations,

nanomaterial research, electron microscopy, and scalable material processing with novel methods to produce scalable assemblies of Cu-CNT multilayer composites. Specific research and development efforts in FY 2022 included: (1) establishing critical design inputs for prototype fabrication; (2) theoretical and computational modeling of the complex parameter spaces of CNTs and metal coatings to support experimental work for improved electrical transport properties of UCCs; and (3) establishing key processing needs and purchasing and beginning to establish necessary tools for prototype-scaleup (> 50 cm).

Approach

Our overall approach is to couple theoretical and experimental efforts to enable the design, reproducible assembly, and scaling of CNT-Cu multilayer composites that have electrical conductivity and ampacity exceeding that of pure Cu and current Cu-CNT composites. To achieve this, two interrelated and equally important tasks are being pursued: (1) the development of controllable processing techniques for the design and scalable, reproducible fabrication of advanced multilayer composites; and (2) theory-guided optimization for high-performance Cu-CNT multilayer composites. The second activity was supported by the program's Advanced Characterization and Computational Thrust (Thrust 4), via a project entitled "Materials by Design for Novel, Ultra-High Conductive Materials Using First-Principles Computational Approaches," led by ORNL staff member Mina Yoon. Using first-principles atomistic calculations, the aim of the Thrust 4 project is to establish a fundamental understanding and structure-property relationship between materials parameters and macroscale performance, which will guide experimental efforts for improved electrical transport properties. With the aid from this Thrust 4 project, we have identified the influence of nitrogen and Cu doping on the electronic properties of semiconducting CNTs and confirmed that semiconducting CNTs can transform into metallic tubes through doping.

The unique fabrication approach begins with formulating stable CNT dispersions via solution methods for the deposition of a directionally aligned, uniform network of CNT coatings on the surface of commercial Cu tapes. Following CNT deposition via solution methods in a manner that intentionally aligns the CNTs along the direction of the current flow, and along the length of the Cu substrate tape (which can be scaled to be continuous), samples were heat-treated to remove all organic chemicals related to the solution binders from the CNT matrix and Cu surface. Subsequent deposition of thin Cu overlayers by industry standard (i.e., high-volume capable) sputter deposition techniques, followed by thermal treatment processes, enables high percolation conductivity throughout the entire CNT/metal matrix ensemble, as shown in Figure I.1.3.4.1. The result is a thin continuous network of highly conductive CNTs embedded beneath the sputtered Cu, such that both surfaces of the UCC tape are only Cu. It should be noted that a flexible substrate surface with low reactivity, such as a Cu tape, is necessary for these solution methods to successfully deposit and align a continuous network of CNTs along the desired axis (which means this general method is not designed to coat aluminum conductors, which form a very persistent passive oxide layer on their surfaces). The sequence of manufacturing methods selected for this UCC technology is based on methods previously adopted, developed, and used for commercial manufacturing of higher temperature superconducting tapes, which have been scaled to continuous manufacturing processes.

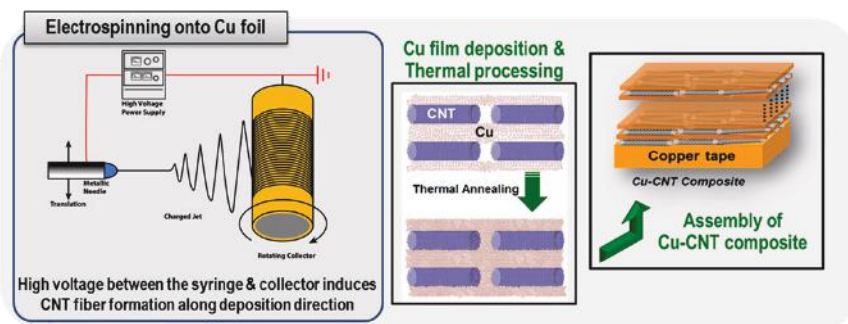


Figure I.1.3.19. Schematic flowchart showing the work scope of Task 3B, "Fundamentals of Non-Equilibrium Processing." Source: ORNL.

Samples were characterized by SEM for investigation of microstructures and to evaluate alignment of the nanotube networks deposited. Cross-sectional microstructures of samples were studied by Z-contrast STEM. Specimen preparation was carried out by FIB methods, and STEM images were recorded using a Nion UltraSTEM operating at 200 kV. Electrical conductivity of the UCC composites was characterized in the temperature range from 4 K to 400 K using a physical property measurement system. Ampacity measurements (i.e., defined as maximum current that a conductor can carry continuously under the conditions of use) were conducted using a custom-built 4-point transport probe under controlled vacuum in 1 atm of ambient helium gas. Owing to its inertness and high thermal conductivity, helium was used as a heat transfer medium to prevent heat-induced damage to spring-loaded voltage contacts during measurements. Although all dimensions of the test structures were carefully determined using an optical microscope and a micrometer, based on errors that may be associated with the equipment used to measure geometrical factors (sample width, distance between the voltage contacts, and substrate thickness), a generous estimation of uncertainty of 5% and 9% was calculated for the resistivity values on 28 and 12 μm Cu substrates, respectively.

Results

An industrially scalable electrospinning approach was selected to incorporate CNTs on Cu tape platforms. The combined effects of the electric field and mechanical forces result in alignment of the deposited nanotube networks along the long axis of the Cu tape, demonstrating an effective and scalable nanofiber templating strategy. To achieve a well-aligned fiber array on Cu tapes, as observed in Figure I.1.3.4.2(a), a suitable collector rotating speed of 1,500 rpm was selected and the CNT solution was spun by applying a specific positive voltage between the rotating collector and the dispensing needle at RT. The electrospinning mixture, which contained the single-wall CNTs, was prepared in a dimethylformamide and polyvinylpyrrolidone (PVP, 10 wt.%) solution. After electrospinning, the coated Cu tapes were then treated at 600 °C in a vacuum furnace for 2 h at a pressure of 1×10^{-4} Torr. Thermal treatment in a vacuum ensures the effective removal of PVP and residual surfactant/organic solvents from the CNT matrix while preventing oxidation of the Cu and CNTs, as can be seen in Figure I.1.3.4.2(b). Subsequent deposition of thin Cu overlayers (100-200 nm) using a 2 in. diameter high-purity (99.999%) Cu target by industry standard sputter deposition techniques, followed by thermal treatment to anneal and densify the deposited Cu, enables high percolation conductivity throughout the entire CNT/metal matrix ensemble. The latter process not only enables a void-free, dense Cu overlayer but also facilitates Cu diffusion into the network of deposited CNTs and prevents oxidation of both components. No substrate heating was employed during the Cu depositions. This leads to condensed and smaller grain Cu overlayer structure on the CNTs, as shown in Figure I.1.3.4.2(c), which eventually evolves into larger Cu grains due to grain growth during annealing, forming a very thin, dense, continuous, and conformal Cu coating over the CNT layers, as observed in Figure I.1.3.4.2(d). Note that two different thicknesses of Cu tapes were used in our studies, a 12 μm battery foil, which has a visibly rough surface morphology, and a 28 μm rolled Cu, whose surface is flatter than the 12 μm tape, but has visible rolling marks, as shown in Figure I.1.3.4.2. The influence of the two different substrate surface morphologies can be seen from Figure I.1.3.4.2, where both the CNT and Cu layers exhibit excellent topographical coverage on both platforms.

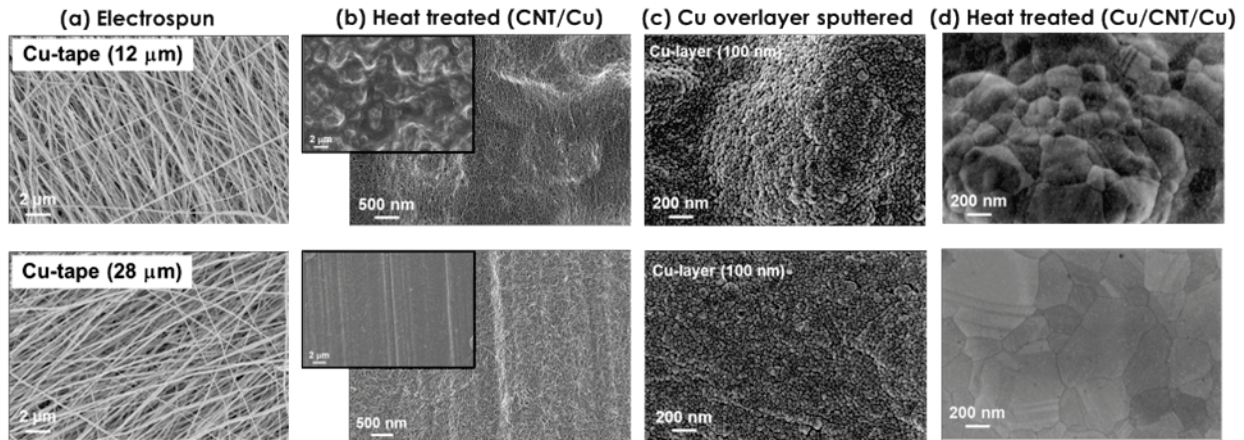


Figure I.1.3.20. Typical SEM images of CNT and Cu coated tapes after each processing step. The inset of (b) displays the rougher surface morphology of thin Cu and rolling marks on the thick Cu tape substrates.

Source: ORNL.

A series of ‘Z-contrast’ cross-sectional STEM analyses, as observed in Figure I.1.3.4.3, were conducted on the fully processed Cu/CNT/Cu composites, as shown in Figure I.1.3.4.2(d), in order to obtain more detailed information related to thickness and adhesion between Cu and CNT layers, as well as to examine possible doping effects. The higher-Z elements (Cu with $Z = 29$) appear brighter than the lower-Z elements (C with $Z = 6$) when the cross-sectional images are taken in high-angle annular dark field (HAADF) imaging mode. However, the results in Figure I.1.3.4.3 are presented in annular bright-field imaging mode, in which the contrast was essentially reversed from the HAADF mode, thus revealing brighter CNT layers and darker regions of Cu. Cross-sectional images on both Cu tapes display evenly dispersed CNT layers in between the two Cu layers as well as a dense, homogeneous Cu microstructure and good interfacial adhesion characteristics between the Cu and CNT layers. The annular bright-field imaging mode also clearly shows the diffusion of Cu inside the CNT matrix (i.e., dark regions infiltrating into the CNT layer) as well as graphitic structures (i.e., wavy stripes) associated with the nanotubes in the inset of Figure I.1.3.4.3(b).

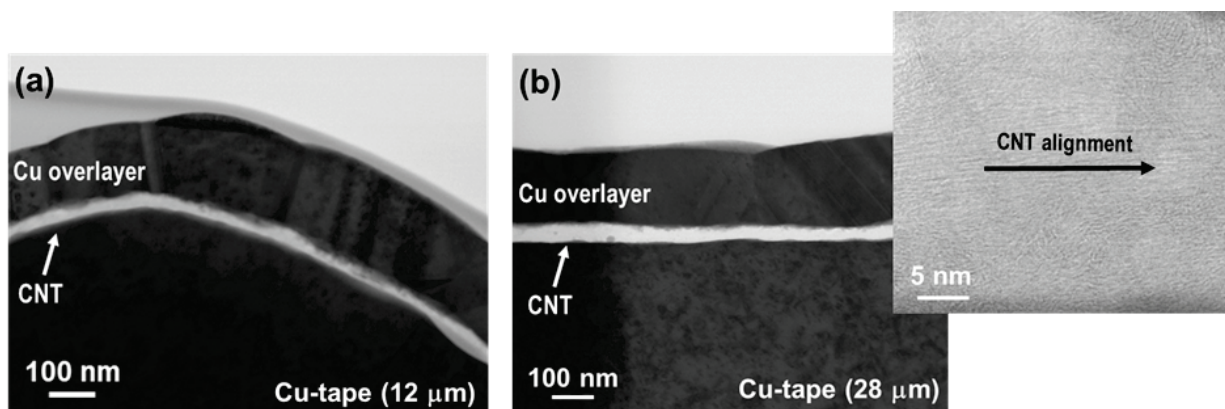


Figure I.1.3.21. Cross-sectional Z-contrast STEM images of Cu/CNT/Cu samples on (a) 12 μm and (b) 28 μm Cu substrates. The inset of (b) shows the CNT lattice planes. Source: ORNL.

Using a physical property measurement system, temperature-dependent electrical properties of single-layer Cu/CNT/Cu samples on both thin and thick Cu platforms was measured at various temperatures ranging from 275–400 K. The plots shown in Figure I.1.3.4.4 also include data for reference Cu substrates treated under the same processing conditions (e.g., temperature and time) that the Cu/CNT/Cu samples undergo, where the electrospinning was conducted without PVP incorporated CNT dispersions. Results shown in Figure I.1.3.4.4

for both thicknesses of Cu tapes verified reduction of electrical resistivity by $\sim 6\%$ – 7% for the UCC composite specimens that were prepared with PVP based CNT dispersions, over the entire temperature range compared to that of the reference pure Cu samples. Importantly, the temperature coefficient of resistivity (TCR) values calculated from the slope of the $\rho/\rho(300\text{K})$ curves for all UCC samples (for $28\ \mu\text{m}$ Cu: $3.82 - 3.84 \times 10^{-3}/\text{K}$ and for $12\ \mu\text{m}$ Cu: $3.79 \times 10^{-3}/\text{K}$) were lower than the reference Cu samples (for $28\ \mu\text{m}$ Cu: $3.87 \times 10^{-3}/\text{K}$ and for $12\ \mu\text{m}$ Cu: $3.82 \times 10^{-3}/\text{K}$). This electrical behavior is remarkable and can be attributed to the lower TCR of CNTs [3,9]. However, also note that the advantages in electrical performance of the composite are less significant without PVP formulation (reduced to only 2% – 3% improvement), the reasons for which are explained below.

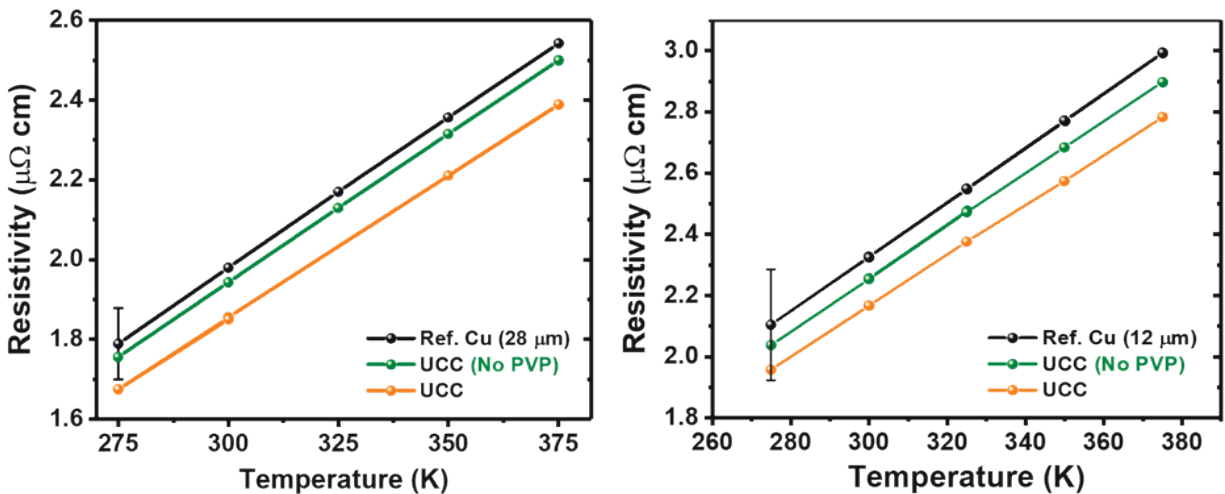


Figure I.1.3.22. Comparison of resistivity as a function of temperature (275 K to 400 K) for single CNT layer UCC architectures prepared with PVP and without PVP in the electrospinning solutions. Plots display significantly reduced resistivity as compared to reference Cu substrates. Source: ORNL.

Similar trends in performance can also be observed from the evaluation of the same samples' current carrying capacity (i.e., ampacity), as shown in Figure I.1.3.4.5. Both plots display two distinct regimes of the increase in current density: a nearly current independent regime where the resistivity is nearly constant with current and an exponential transition regime toward ultimate failure (i.e., burnout). In the former regime, the resistivity of the material increases because of the current-induced Joule-heating. In the latter regime, higher current densities further increased the temperature of the conductor, which in turn accelerated Cu diffusion, eventually leading to failure of the test specimens at higher currents (see inset). As displayed in the figure, while all composite samples demonstrated increased ampacity compared with the Cu reference, a notably larger improvement was exhibited by samples with PVP formulation (14% – 15% increase in ampacity vs. only 6% without PVP). Ampacity Also displayed in the right panel are the exponential fits [$y = y_0 + A\exp(R.x)$] to current density curves that reveal decreased rate (R) of increase in resistivity at higher temperatures than pure Cu. Accordingly, this behavior is most likely related to the increased activation energy for Cu diffusion in carbon-added Cu materials. In fact, through experimental and theoretical studies, the suppression of the surface and grain boundary Cu diffusion, especially at high temperatures, due to increased Cu diffusion activation energy in carbon-doped Cu composites and its impact on the realization of a high ampacity for Cu–CNT composites, has been verified [3, 10, 11]. The observed reduction in TCR and R values should be highly beneficial for electrical device applications requiring higher current and higher temperature operation, including fast charging.

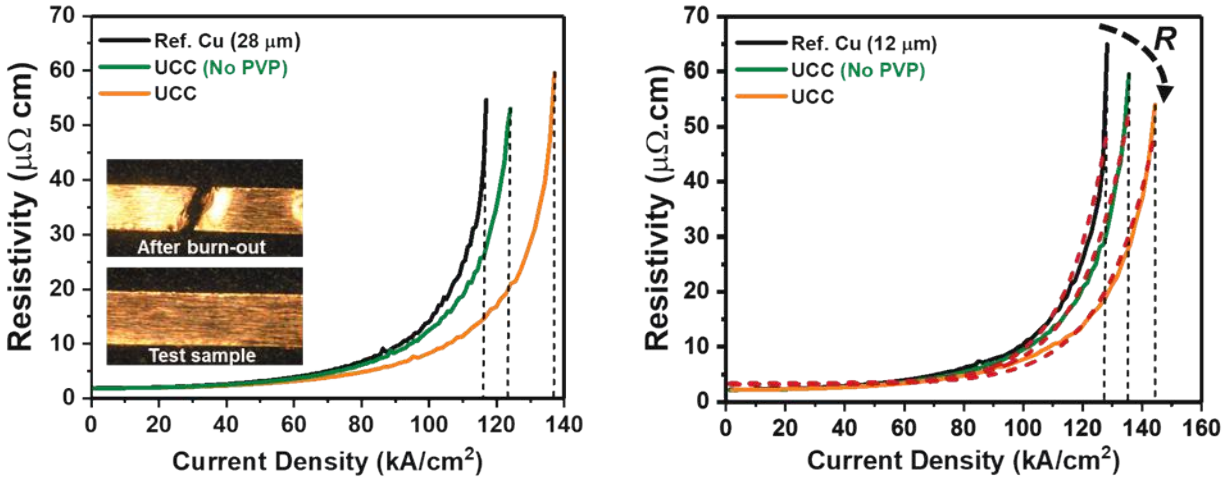


Figure I.1.3.23. Comparison of current density of single CNT layer UCC architectures of the same samples presented in Figure I.1.3.4.4. Plot displays increased ampacity as compared to reference Cu substrates. The inset of the left panel shows typical photographs of the test samples before and after the measurements.

Source: ORNL.

Next, a series of computational material studies were initiated this year to begin to understand the influence of PVP to improve the electrical properties of UCCs. First-principles density functional theory calculations were conducted, and we have identified mechanisms that explain the favorable influence of both nitrogen and Cu doping on the electronic properties of semiconducting CNTs. We have also confirmed that semiconducting CNTs transform into metallic tubes through doping. Note that nitrogen doping of the CNTs is associated with the chemical nature of PVP and Cu doping is correlated with the vacuum-induced volatility and diffusion of Cu atoms from the underlying Cu substrate into the CNT matrix, as shown in Figure I.1.3.4.3. Hence, doping CNTs with nitrogen and Cu (both electron donors) increases the electron density of the nanotubes and enhances their metallic properties. This is particularly important because the synthetic production methods of CNTs generally yield one-third of CNTs in metallic and two-thirds in semiconducting nature. Figure I.1.3.4.6 shows the density of states in undoped semiconducting CNTs compared to nitrogen and Cu-doped semiconducting tubes. While semiconducting tubes show a large energy gap around Fermi level, doping with either nitrogen and Cu significantly enhances the density of states near the Fermi level, indicating an increased number of conduction electrons and, hence, improved electronic transport properties of semiconducting CNTs. These observations are consistent with other reports on nitrogen-doped CNTs [12, 13].

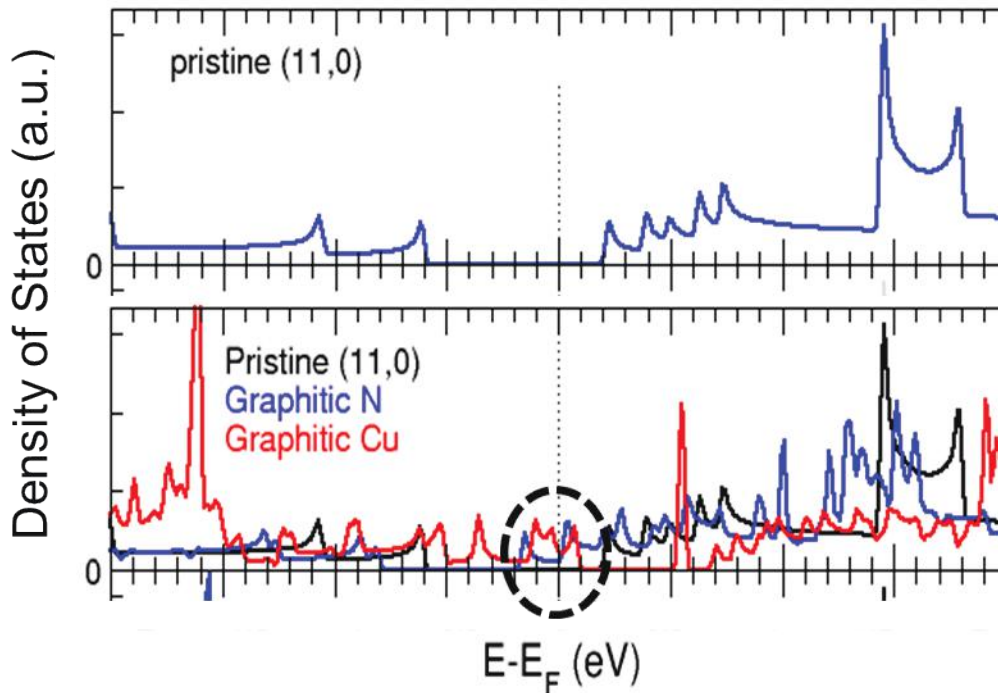


Figure I.1.3.24. Energy diagram showing the density of states for semiconducting (11,0) and nitrogen and Cu-doped semiconducting CNTs. Source: ORNL.

Conclusions

Advanced low resistive loss materials are needed to increase power density and reduce cost while improving efficiency and reliability of most on- and off-board electrical conduction applications for EVs. Under this multiyear project, using scalable, cost-effective, and commercially viable processing methods, we have demonstrated the feasibility of a novel materials/computational modeling platform that can facilitate the design and scalable fabrication of advanced ultra-conducting copper composite materials for a broad range of industrial applications. The benefits that will be gained from this research are expected to help meet the US DOE VTO 2025 performance targets and can lead to reduced weight/volume, as well as improved reliability, efficiency, and thermal characteristics for all electrified power train components. Specific accomplishments include: (1) established the viability of industrially scalable processing techniques for CNT deposition – electrospinning; (2) verified good interfacial characteristics between Cu and CNT layers through detailed planar and cross-sectional microstructural analyses; (3) demonstrated that theoretical modeling can support and better explain experimental efforts and observations, with these simulation efforts supported by a project in collaboration with the program’s Advanced Characterization and Computational Thrust (Thrust 4); and (4) demonstrated decreased resistivity (> 6%–7%) and increased ampacity (> 14%–15%) over pure Cu with all composite samples demonstrating lower TCR than reference Cu.

Key Publications

1. Aytug, T., “Advanced Processing and Additive Manufacturing for EV Propulsion: Novel, Ultra-High Conductivity Composites for EVs,” 2022 DOE VTO Annual Merit Review, 22 June 2022, Washington, DC, USA.

References

1. Stillman, H., and M. Burwell, 2013, “Ultraconductive Copper Wire: Overview of Worldwide Research and Development,” International Copper Association, Copper 2013 International Conference, 1–4 December 2013, Santiago, Chile.

2. Lee, D. F., M. Burwell, and H. Stillman, 2015, "Priority Research Areas to Accelerate the Development of Practical Ultraconductive Copper Conductors," ORNL/TM-2015/403, September 2015, Oak Ridge National Laboratory, Oak Ridge, TN, USA. Available at: <https://info.ornl.gov/sites/publications/files/Pub58011.pdf> (last accessed 20 January 2023).
3. Subramaniam, C., T. Yamada, K. Kobashi, A. Sekiguchi, D. N. Futaba, M. Yumura, and K. Hata, 2013, "One hundredfold increase in current carrying capacity in a carbon nanotube–copper composite," *Nat. Commun.*, Vol. 4, Art. 2202. <https://doi.org/10.1038/ncomms3202>.
4. Subramaniam, C., A. Sekiguchi, T. Yamada, D. N. Futaba, and K. Hata, 2016, "Nanoscale, planar, and multi-tiered current pathways from a carbon nanotube–copper composite with high conductivity, ampacity, and stability," *Nanoscale*, Vol. 8, No. 7, pp. 3888–3894. <https://doi.org/10.1039/C5NR03762J>.
5. Forrest, D. R., I. Jasiuk, L. Brown, P. Joyce, A. Mansour, and L. Salamanca–Riba, 2012, "Novel Metal Matrix Composites with Integrally-Bound Nanoscale Carbon," *Nanotech 2012*, 18 June 2012, Santa Clara, CA, USA, CRC Press, Boca Raton, FL, USA.
6. Brown, L., P. Joyce, D. Forrest, and J. Wolk, 2011, "Physical and Mechanical Characterization of a Nanocarbon Infused Aluminum Matrix Composite," Proceedings of the SAMPE Fall Technical Conference, 17-20 October 2011, Ft. Worth, TX, USA.
7. De Groh III, H. C., and U. (Balu) Balachandran, 2018, "Conductivity of Copper–Carbon Covetic Composite," NASA/TM—2018-219790, National Aeronautics and Space Administration, Hampton, VA, USA. Available at: <https://ntrs.nasa.gov/archive/nasa/casi.ntrs.nasa.gov/20180003330.pdf> (last accessed 20 January 2023).
8. Bakir, M., and I. Jasiuk, 2017, "Novel metal-carbon nanomaterials: A review on covetics," *Adv. Mater. Lett.*, Vol. 8, No. 9, pp. 884–890. <https://doi.org/10.5185/amlett.2017.1598>.
9. Sun, S., W. Mu, M. Edwards, D. Mencarelli, L. Pierantoni, Y. Fu, K. Jeppson, and J. Liu, 2016, "Vertically aligned CNT-Cu nanocomposite material for stacked through-silicon-via interconnects," *Nanotechnology*, Vol. 27, No. 33, Art. 335705. <https://doi.org/10.1088/0957-4484/27/33/335705>.
10. Liu, C.-L., 2002, "Screening beneficial dopants to Cu interconnect by modeling," *Appl. Phys. Lett.*, Vol. 80, No. 5, pp. 763–765. <https://doi.org/10.1063/1.1445471>.
11. Kinloch, I. A., J. Suhr, J. Lou, R. J. Young, and P. M. Ajayan, 2018, "Composites with carbon nanotubes and graphene: An outlook," *Science*, Vol. 362, No. 6414, pp. 547–553. <https://doi.org/10.1126/science.aat7439>.
12. Barzegar, H. R., E. Gracia-Espino, T. Sharifi, F. Nitze, and T. Wågberg, 2013, "Nitrogen doping mechanism in small diameter single-walled carbon nanotubes: Impact on electronic properties and growth selectivity," *J. Phys. Chem. C*, Vol. 117, No. 48, pp. 25805–25816. <https://doi.org/10.1021/jp409518m>.
13. Wang, H., T. Maiyalagan, and X. Wang, 2012, "Review on recent progress in nitrogen-doped graphene: Synthesis, characterization, and its potential applications," *ACS Catal.*, Vol. 2, No. 5, pp. 781–794. <https://doi.org/10.1021/cs200652y>.

Acknowledgements

The author would like to acknowledge the support provided by J. Gibbs, DOE Technology Development Manager for the Electric Drive Technologies Program, VTO, DOE-EERE. The author also recognizes and appreciates the support of A. Haynes, ORNL Powertrain Materials Core Program Manager. The significant contributions from K. Li, M. McGuire, M. Yoon, A. Lupini, and F. List to the project are also acknowledged.

I.1.3.5 Task 3E. Print Casting of Lightweight Metal Matrix Composites for Battery Enclosures with Impact Resistance and Thermal Management (Oak Ridge National Laboratory)

Derek Splitter, Co-Principal Investigator

Oak Ridge National Laboratory
Buildings and Transportation Science Division
2360 Cherahala Blvd.
Knoxville, TN 37932
E-mail: splitterda@ornl.gov

Sebastien Dryepondt, Co-Principal Investigator

Oak Ridge National Laboratory
Materials Science and Technology Division
1 Bethel Valley Rd.
Oak Ridge, TN 37830
E-mail: dryepondtsn@ornl.gov

J. Allen Haynes, PMCP Consortium Manager

Oak Ridge National Laboratory
Materials Science and Technology Division
1 Bethel Valley Rd.
Oak Ridge, TN 37830
E-mail: haynesa@ornl.gov

Jerry Gibbs, DOE Technology Development Manager

U.S. Department of Energy
E-mail: jerry.gibbs@ee.doe.gov

Start Date: November 1, 2021 End Date: September 30, 2023
Project Funding (FY 2022): \$290,000 DOE share: \$290,000 Non-DOE share: \$0

Project Introduction

This task seeks to understand how the AM of a reinforcing metal network combined with metal casting and infiltration of lower melting temperature alloys such as Al, a process termed PrintCasting (PC), can be developed to create lightweight metal-metal composite structures that increase energy absorption without significantly affecting thermal conductivity and overall weight. A key advantage of the PC method is that it leverages AM control over the reinforcing phase mesostructure. Therefore, the geometry and spatial distribution of the reinforcing constituent can be precisely controlled to create composites with geometries that realize improved energy absorbing behavior, as well as other tailored mechanical and thermal properties, with capability for locally controlled and varied properties across a component. It has been demonstrated that high levels of energy absorption can be achieved by creating a reinforcement geometry that converts the applied tensile load into local compression of the more brittle cast Al matrix [1]. The printed reinforcement geometry is patterned with a topology designed to be bending dominated, which upon axial loading collapses the reinforcement mesh, compressing the lightweight alloy matrix trapped in between. The project has potential to provide solutions to overcome key barriers related to battery containment and thermal management. This novel concept also offers significant cross-cutting opportunities, as evidenced by its being licensed for non-transportation industries.

Objectives

This project aims to create AM metal-metal composites for battery enclosures with high-energy absorption and tailorable local mechanical, acoustic, and thermal properties. Potential broader applications include energy absorption under tensile loading for scenarios that include impulse loading, blast containment, and load-bearing structures, all of which are conditions relevant to battery containment in EVs. The objective is to understand the geometric factors, bonding, material selection, manufacturing, cost, and scaling aspects that enable development of multimaterial hybrid systems suitable to high demand, long-duration EV battery containment applications, such as electric freight trucks.

Approach

A powerful feature of metal AM is the ability to directly print net-shaped structures with high levels of architectural complexity, but most additive processes are limited to a single feedstock resulting in monolithic materials. In the hybrid approach of PC materials developed by ORNL the capabilities of AM are leveraged with the lower cost and more rapid processing offered by conventional casting. Specifically, the local control over composition is achieved through the AM portions by changing the printed lattice size and/or geometry, enabling gradients in composition. Subsequently, the printed, complex, reinforcement lattice is overcast and melt-infiltrated with a lower melting point, lightweight alloy—in this study a cast Al alloy A356. The lightweight cast A356 alloys have lower ductility due to casting porosity and experience brittle failure under tension but can undergo very large plastic deformation under compression, whereas the AM reinforcement lattice (printed from stainless alloy 316L or Ti6Al4V) exhibits very high-strength and tensile ductility.

The A356/316L or Ti64/Al material systems are known to form brittle Fe-Al or Ti-Al IMCs when fused together [2], which motivated design of the novel PC hybrid processing strategy. This approach combines AM of the higher melting point material lattice with casting of the lower melting point alloy to eliminate liquid-phase mixing of the two alloys and thus avoids intermetallic formation, as highlighted in Figure I.1.3.5.1.

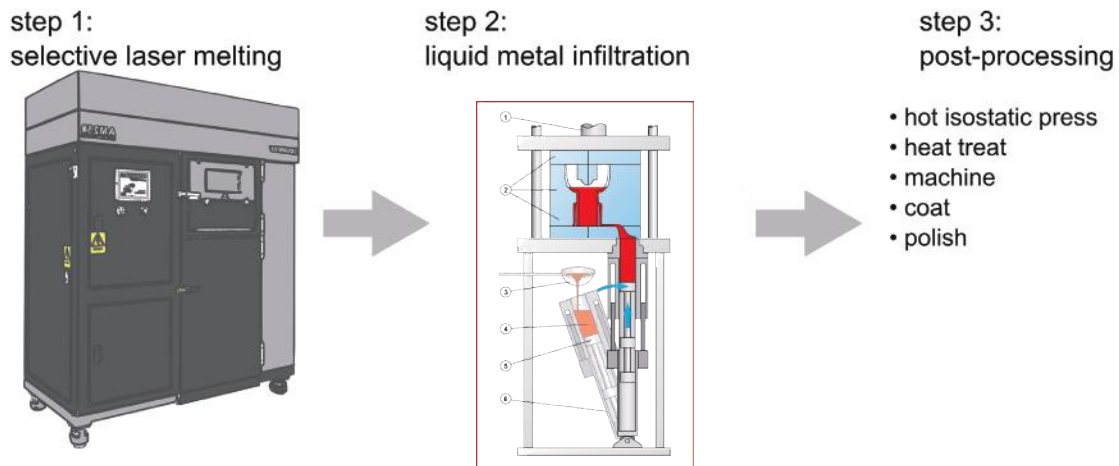


Figure I.1.3.25. Process for synthesizing IPC materials using the PC technique. The reinforcing lattice is printed using a laser powder bed fusion process, filled with liquid metal using pressure die-casting, and then post-processed to optimize the properties. Source: ORNL.

The result of the PC process is an interpenetrating phase composite (IPC) in which the two constituents form continuous and interconnected networks but do not fuse and form Al-based intermetallics at the interfaces. It has been shown that an interpenetrating morphology can enable unique mechanical and thermal properties in a nonlinear blending of the properties of the constituents [1, 3–5]. More specifically, it has been shown [1] that fracture toughness can be increased by interconnecting the more ductile phase in a brittle/ductile system, which further improves energy absorption. The goal of this project is to leverage these unique properties of PC materials for EV battery containment systems, where PC materials can exceed the individual material energy

absorption performance criteria of the individual PC constituents (monolithic Al or stainless steel); yet the PC material can be nearly 50% thinner than monolithic Al members and more than 2X more thermally conductive than stainless steel [6]. These properties not only improve impact resistance, but also allow for smaller EV battery assembly sizes and weight reductions from material properties alone.

The potential advantage of the PC approach to battery containment is highlighted by the fact that a known critical technology gap in EV battery containment is weight management. The battery containment enclosure is often the single heaviest component in an EV, which typically can exceed 110–160 kilograms itself (compromising up to 6%–10% of total light-duty EV vehicle mass). Thus, improvement in structural performance and weight-savings afforded by optimizing material properties also has the potential to greatly reduce vehicle mass, thus demonstrating a pathway to improved energy efficiency and lower battery demand or improved vehicle range.

Results

The initial task effort, which began in FY 2022, centered around defining whether PC materials were appropriate materials possibilities for EV battery containment applications. Several discussions occurred with OEMs concerning off-highway and light, medium, and HD trucks. Overwhelmingly, the feedback and key issues presented in these discussions were thermal management (cooling and conduction) and impact resistance, which are crucial areas for further development for battery containment. Feedback indicated that PC materials were a possible fit for battery confinement as the materials performance was found to be well tailored to the material performance demands being examined by manufacturers for future EV powertrains. One area of discussion and challenge for improvement was scalability and the approach/technology for infiltration during casting. Thus, FY 2022 task efforts were directed towards manufacturing and scaleup of the PC methodology.

The metal infiltration aspect of IPC has been found to be a critical area of needed research. Specifically, significant porosity was observed in the infiltrated cast Al constituent in PC materials in the previous generation of research for lightweight pistons. Simulation results and measurements also indicated the metal-metal interfaces of PC materials is critical to energy absorption [1]. Specifically in PC materials, we discovered that slip between the matrix and reinforcement constituents at the interface is beneficial (strain-to-failure increases and load sharing stress reversal results), but porosity in the matrix material is not beneficial because it reduces the matrix strength. Previously, in FY 2021, we observed that hot isostatic pressing (HIP) closed the matrix material pores (desirable for strength), but also improved the bonding of the cast matrix phase to the AM produced reinforcement phase (undesirable for energy absorption), as observed in Figure I.1.3.5.2.

Thus, through HIP processing PC materials became stronger but more brittle with reduced energy absorption, which is less desirable for battery enclosures. Since EV battery containment requires energy absorption and strength, different casting technologies have been explored in FY 2022. Through conversations with industry, it was determined that high-integrity versions of high-pressure die-casting (HPDC) offered the potential to reduce intra-matrix porosity while maintaining some interface slip. The HPDC process can produce tons of casting pressure vs. only 1 atmosphere of pressure in vacuum gravity casting, the method previously used for IPC. Additionally, HPDC also lends itself well to economies of scale, geometric complexity, and scale desired by industry.

Discussions with industry provided insights into lean flexible manufacturing options which are currently in the final contracting phase (with a U.S. foundry) for commissioning fabrication of a PC battery containment prototypes using high-integrity die-casting of Al over 316L stainless steel lattices produced at ORNL by laser powder bed fusion. Specifically, the conceptual rendering of the opportunities and approach for PC materials from pressure die-casting infiltration is seen in Figure I.1.3.5.3.

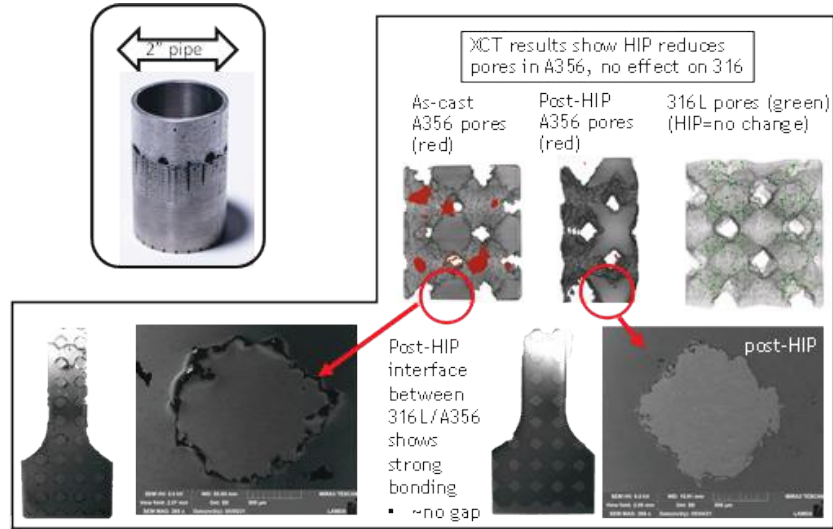


Figure I.1.3.26. Results of HIP conditions of ASTM F3318 – 18 (100 MPa at 510-530°C for 3 hours), on a vacuum infiltrated PC sample with 30 volume% 316L stainless steel lattice with balance of cast A356 Al. The HIP post-processing procedure mitigates the porosity in the A356 matrix but also closes the interfaces between the constituents. The upper left image is a 2-inch diameter PC pipe section produced with vacuum infiltration highlighting the poor infiltration quality observed with the original vacuum infiltration process at larger scales. This porosity is being mitigated by adopting a high-integrity high-pressure casting process. Source: ORNL.

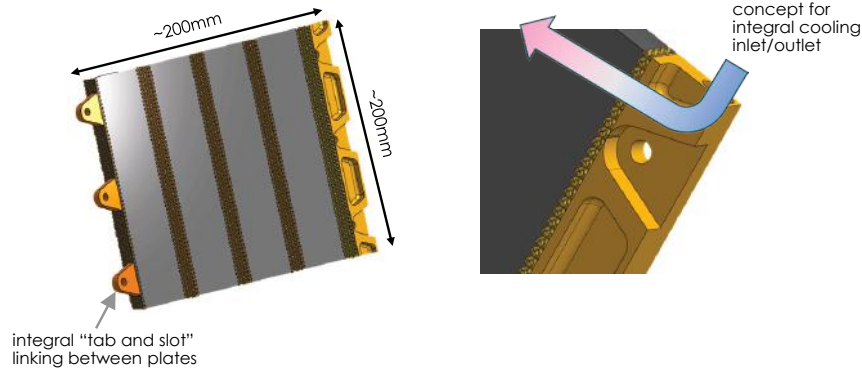


Figure I.1.3.27. Conceptual model of PC sheet prototype for EV battery containment. Note the option of integral cooling channels and features in the diecast portion that enable modularity and thermal management, both key aspects identified by industry in FY 2022 discussions. Source: ORNL.

The conceptual process of the HPDC PC approach highlights the ability to add integral features such as internal cooling channels and higher-resolution support structures that are currently not feasible with vacuum infiltration processes. Moreover, the significant pressure increase (i.e., tons vs. 1 atm) will be engineered to improve infiltration and reduce porosity with industry partners who are experts in complex pressure die-casting approaches and have access to specific casting modeling tools, such as the EKKcapcast software. Progress in FY 2022 has included confirming with multiple industry sources that PC materials were a potential fit for battery enclosures with improved thermal management and impact resistance, defining the new work scope, envisioning and engineering the prototype geometry, finding vendors with suitable capabilities, and arranging the associated contracting. Future work will be focused on the fabrication and characterization of the IPC prototype to further refine the design of the high-performance IPC battery containment. It is also worth noting that potential integration of sensors in the IPC battery enclosure to monitor the battery life has been discussed with industrial partners.

Conclusions

Research and analysis to understand the properties and potential of PC metal-metal composites for EV battery containment was conducted. Initial work focused on industry input and design opportunities. Feedback indicated that the innovative PC material has potential to be of great value for higher performance multi-purpose battery containment; however, improvements in manufacturing and scaling need to be demonstrated. We contracted a supplier of high-integrity die-castings who has contributed to designing a prototype and to resolving known areas of materials performance improvements, particularly porosity reduction in the cast Al constituent. Work scope and prototype geometries of interest were defined, and associated contracting is underway. The resulting scalable prototype from this effort will be evaluated and compared to previous smaller scale PC material efforts. It is anticipated that significant performance and scalability of manufacturing improvements could be afforded using HPDC for matrix infiltration in PC metal-metal composite structures.

Key Publications

1. Allen, J., J. Cheng, X. Hu, D. Splitter, and A. Shyam. 2022. “Modeling Hypervelocity Impacts in Additively Manufactured Interpenetrating Composites.” The Minerals, Metals & Materials Society 2022 Annual Meeting & Exhibition, Feb 2022.

References

1. Cheng, J., M. Gussev, J. Allen, X. Hu, A. R. Moustafa, D. A. Splitter, and A. Shyam, 2020, “Deformation and failure of PrintCast A356/316 L composites: Digital image correlation and finite element modeling,” *Mater. Des.*, Vol. 195, Art. 109061. <https://doi.org/10.1016/j.matdes.2020.109061>.
2. Hofmann, D. C., J. Kolodziejska, S. Roberts, R. Otis, R. P. Dillon, J. O. Suh, Z. K. Liu, and J. P. Borgonia, 2014, “Compositionally graded metals: A new frontier of additive manufacturing,” *J. Mater. Res.*, Vol. 29, No. 17, pp. 1899–1910. <https://doi.org/10.1557/jmr.2014.208>.
3. Moustafa, A. R., R. B. Dinwiddie, A. E. Pawlowski, D. A. Splitter, A. Shyam, and Z. C. Cordero, 2018, “Mesostructure and porosity effects on the thermal conductivity of additively manufactured interpenetrating phase composites,” *Addit. Manuf.*, Vol. 22, pp. 223–229. <https://doi.org/10.1016/j.addma.2018.05.018>.
4. Pawlowski, A. E., Z. C. Cordero, M. R. French, T. R. Muth, J. K. Carver, R. B. Dinwiddie, A. M. Elliott, A. Shyam, and D. A. Splitter, 2017, “Damage-tolerant metallic composites via melt infiltration of additively manufactured preforms,” *Mater. Des.*, Vol. 127, pp. 346–351. <https://doi.org/10.1016/j.matdes.2017.04.072>.
5. Poole, L. L., M. Gonzales, M. R. French, W. A. Yarberr III, A. R. Moustafa, and Z. C. Cordero, 2020, “Hypervelocity impact of PrintCast 316L/A356 composites,” *Int. J. Impact Eng.*, Vol. 136, Art. 103407. <https://doi.org/10.1016/j.ijimpeng.2019.103407>.
6. French, M. R., A. Pawlowski, A. Shyam, D. A. Splitter, A. M. Elliott, J. K. Carver, W. A. Yarberr, Z. C. Cordero, 2017, “Hypervelocity impact of additively manufactured A356/316L interpenetrating phase composites,” ORNL, Oak Ridge, TN, USA. Available at: https://www.researchgate.net/profile/Zack-Cordero/publication/319311101_Hypervelocity_impact_of_additively_manufactured_A356316L_interpenetrating_phase_composites/links/59a319a3aca2726b9028585e/Hypervelocity-impact-of-additively-manufactured-A356-316L-interpenetrating-phase-composites.pdf (last accessed 29 December 2022).

Acknowledgements

The authors would like to thank X. Hu, J. Cheng, J. Allen, and M. Gussev of ORNL for their valuable assistance in data collection, analysis, and computational efforts. The authors also acknowledge Falcon Lakeside Manufacturing for their detailed discussion with us on HPDC.

I.1.3.6 Task 3F. Ultra-Conductor Development for Enhanced EV Performance (Pacific Northwest National Laboratory)

Keerti S. Kappagantula, Principal Investigator

Pacific Northwest National Laboratory
Energy & Environment Directorate
902 Battelle Blvd.
Richland, WA 99354
E-mail: ksk@pnnl.gov

Darrell Herling, PNNL PMCP Program Manager

Pacific Northwest National Laboratory
Energy & Environment Directorate
902 Battelle Blvd.
Richland, WA 99354
E-mail: darrell.herling@pnnl.gov

J. Allen Haynes, PMCP Consortium Manager

Oak Ridge National Laboratory
Materials Science and Technology Division
1 Bethel Valley Rd.
Oak Ridge, TN 37830
E-mail: haynesa@ornl.gov

Jerry Gibbs, DOE Technology Development Manager

U.S. Department of Energy
E-mail: jerry.gibbs@ee.doe.gov

Start Date: November 15, 2022	End Date: September 30, 2023	
Project Funding (FY 2022): \$400,000	DOE share: \$400,000	Non-DOE share: \$0

Project Introduction

In this project, we are developing Al and Cu conductors with enhanced electrical performance for use as EV electrical components, such as motor windings, busbars, connectors, and cables in order to demonstrate the potential for reduced energy loss and GHG emissions, all while improving EV range. Electrical components in EVs are traditionally made using alloys with high electrical conductivity, such as electrolytic tough pitch Cu (C11000) and oxygen-free, high conductivity Cu (C10100) alloys. Additionally, high electrical conductivity Al alloys, such as AA1350 or AA1100, are also used to promote vehicle lightweighting because of their low-density even though they demonstrate only 60% of the electrical conductivity of C11000. Enhancing EV performance through the use of materials with better electrical properties—in particular, higher electrical conductivity and current density, as well as a lower TCR compared to commercial alloys—will lead to significantly improved energy savings.

Recent work at Pacific Northwest National Laboratory (PNNL) shows that manufacturing metal composites with nanocrystalline additives such as graphene using a shear-based solid-phase processing technique called shear-assisted processing and extrusion (ShAPE™) can enhance electrical conductivity both at RT and elevated operating temperatures, as well as at a lower TCR compared to commercial conductor grade Cu and Al alloys [1]. Such composites, when demonstrating enhanced electrical properties compared to the base metals, are colloquially referred to as ‘ultra-conductors.’

While demonstrating enhanced electrical performance in ShAPE™-synthesized metal-graphene composites is a significant step forward in ultra-conductor development, there are barriers to using these composites to manufacture commercial-scale EV electrical components. Over the past two years, our conversations with more than 20 motor and EV electrical component manufacturers have revealed that to motivate easy market adoption of ultra-conductors, performance metrics should be at least 10% higher than that of existing commercial conductors at operating temperatures. Additionally, the composite manufacturing process, ShAPE™, must be scaled-up to synthesize bulk metal composites at industrially significant volumes while preserving the enhanced electrical conductivity.

At the beginning of the project, the Cu and Al composite samples were manufactured to have largest dimensions of ~2-m-length and 2–3 mm diameter [2]. This must be extended to manufacturing bar-stock with dimensions and volumes matching those generally used by windings and component manufacturers in processing set-ups. Finally, there are several post-processing steps (e.g., rolling, stamping, annealing, machining) used in manufacturing EV components using rod-, bar- or sheet-stock, depending on the final product forms. Such thermomechanical processing can alter the microstructures of the ShAPE™ ultra-conductors and could be detrimental to electrical, mechanical, and corrosion behavior. There is a gap in ultra-conductor literature on the effects of machining and forming operations on composite performance. Understanding these effects of post-processing and accounting for them during component manufacturing is essential to ensure the performance enhancements developed in the bulk-scale ShAPE™ composite are preserved in the final parts manufactured from the ultra-conductor bar-stock.

Objectives

Based on the gaps identified in the roadmap for adoption of ShAPE™ ultra-conductors at the commercial scale, the following objectives were developed for the current project:

1. Demonstrate 10% enhanced conductivity at operating temperatures in Cu ultra-conductors and Al ultra-conductors manufactured using ShAPE™ technology.
2. Scaleup ultra-conductor manufacturing using ShAPE™ in sufficient quantities of 5-mm diameter rods that are necessary for making EV components, such as windings and cables.
3. Determine the effects of post-processing techniques (such as drawing and annealing) on the electrical and mechanical behavior of the bulk-scale ShAPE™-synthesized ultra-conductors.

Approach

This project is progressing along two simultaneous tracks encompassing three tasks. Track 1 focuses on Al and Cu ultra-conductor development using ShAPE™. Here, we are evaluating the effect of nanocrystalline carbon additives (e.g., graphene, reduced graphene oxide) on electrical and mechanical properties; namely electrical conductivity, TCR, ultimate tensile strength, yield strength and % elongation of C10100, C11000, and AA1100. We are also identifying composite formulations demonstrating enhanced performance compared to market standards, apt for commercial applications in this track. Track 2 focuses on ultra-conductor component manufacturing process development. Here, we are determining optimal precursor configurations, ShAPE™ manufacturing parameters, tooling, product forms, and post-processing treatments required for making EV components such as motor windings, wires, and cables using the ultra-conductors developed in Track 1. In this track, we are benchmarking scaled-up, ultra-conductor performance against commercial product performance by testing the electrical and mechanical performance of the ShAPE™ samples.

Composite Synthesis

AA1100, C11000, and C10100 were used as feedstock materials and embedded with CVD graphene for Cu matrix and reduced graphene oxide nanoparticles (GNP) for Al matrix composites. CVD graphene consists of monolayer graphene sheets deposited on C11000 foils to about 20–30 μm thickness. GNPs are in the form of flakes 2–8 μm long with an average flake thickness of > 3 nm. Billets with an average diameter of ~250 mm were assembled with the metal feedstock and relevant quantities of the graphene additives. ShAPE™ was used to manufacture composite wires (2.5 mm diameter) using the

metal/graphene billets. During the ShAPE™ process, a rotating die impinges on the stationary metal/graphene billet. At the billet-die interface, owing to the mechanical energy applied by the tool as well as the friction being generated, the billet is heated and plasticized. Subsequently, the billet material flows through the die hole to form the extrudate wires. During extrusion, forces are measured via load cells attached to the frame of the machine, while temperature of the deforming material is measured via a thermocouple attached to the face of the extrusion die.

Over the first two-quarters of FY 2022, Al-only samples were made initially at different process conditions to identify their effect on electrical conductivity and TCR. The process parameters resulting in the highest electrical conductivity and TCR were noted for further experimental development. Subsequently Al/GNP and Cu/graphene samples were manufactured with varying graphene/GNP content as part of Track 1 using the previously determined ShAPE™ process parameters. In Track 2, billet ring and extrusion die dimensions were designed to manufacture >3 m long wires suitable for post-processing into lower-gauge wires via cold-drawing. Electrical conductivity along the wires was determined to identify property evolution in samples without and with graphene additives. Process conditions and tool designs were optimized to obtain uniform diameters of samples during ShAPE™ owing to its implications on conductivity and TCR measurements.

The diameters of the extruded wires were measured with a Keyence LS-7601 optical micrometer. The wire surface was cleaned with isopropanol and dried, and the diameter of the sample is initially measured using the optical micrometer calibrated using a 0.1000-in. National Institute of Standards and Technology-certified gauge pin. The diameter of the wire sample was measured at five points along its length, by recording the maximum and minimum diameter values at each point. The local average diameter at these points was calculated, which was used to estimate the global average of the diameter of the wire. The deviation of the local cross-sectional area from the global average was calculated; as per ASTM B193, diameter variation should be such that globally the variability in the cross-sectional area of the wire is within 0.75%. Samples whose diameter variation results in >0.75% variability in cross-sectional area were regarded as defective and not tested further.

Electrical Property Measurement

The volume resistivity was measured using Ohm's law normalized over the specimen length and cross-sectional area. Ohm's law states that the current flowing is directly proportional to the voltage/potential difference applied across the metallic conductor, at constant sample temperature. The proportionality constant is termed the 'resistance.' Electrical conductivity testing was performed per ASTM B193 using a Keithley 2182A nanovoltmeter, Keithley 2260B-30-72 bench power supply, and a Teledyne FLIR thermal camera. In this setup, two pairs of electrical leads are connected across the wire sample: the DC power supply leads that provide current are in series while the nanovoltmeter leads that measure the voltage drop are in parallel. The Keithley 6221 power supply and Keithley 2182A nanovoltmeter are combined to generate extremely low currents (<105 mA) for measuring precise voltage drops across specimen lengths at RT ($20 \pm 0.5^\circ\text{C}$). The delta method is used during testing where test current polarities are reversed at preset frequencies to eliminate the noise from thermoelectric voltages and contact resistances. The setup is controlled using LabView graphical user interface designed by Keithley, to set parameters of test current, resistance measurement modes, and data acquisition time and sampling rate. Depending on the length of the segment, multiple test runs were executed along the wire length and the average electrical conductivity and standard error were calculated accordingly. To measure the TCR of the samples, the Keithley 2260B power supply was used in conjunction with the 2182A nanovoltmeter. The brass leads served as current supply leads, while simultaneously holding the sample wire taut. DC currents were passed through the wire samples and wire temperature was measured by the infrared camera. The DC current heats the specimen wire through Joule-heating. The current levels were maintained for at least five minutes after a target wire temperature was reached within $\pm 0.5^\circ\text{C}$ for achieving thermal equilibrium. At steady-state temperature corresponding to a DC current level, voltage drop across the wire was measured for 100 seconds to determine electrical resistivity. Following this, the resistivity of the sample was plotted as a function of steady-state temperatures. The TCR of a sample was then determined as per ASTM B193.

Results

Track 1 – Ultra-Conductor Material Development

Figure I.1.3.6.1 shows the electrical conductivity of AA1100-only wires manufactured via ShAPE™ at different temperature and forces applied during extrusion. Note the temperature is provided on y-axis and extrusion forces are tracked on the x-axis. Electrical conductivity magnitude is scaled on the color bar attached to the right of the plot indicating the variation of values corresponding to the different colors. The standard error in measurement for all the values shown in the plot below were between 0.01 and 0.03% International Annealed Copper Standard (IACS). A clear pattern in the evolution of the electrical conductivity is not readily evident from the figure below. Electrical conductivity of all the samples was seen to be within 1% IACS difference ranging from 58.87% IACS on the lower end to 59.61% IACS on the higher end. While these values may be different with statistical significance in many instances, given that the variability was low even at different processing conditions, the prime conclusion from this exercise was that AA1100 conductivity was relatively stable despite the material being processed at varying temperatures. Similar results were seen for AA1100 wires manufactured via hot extrusion [3].

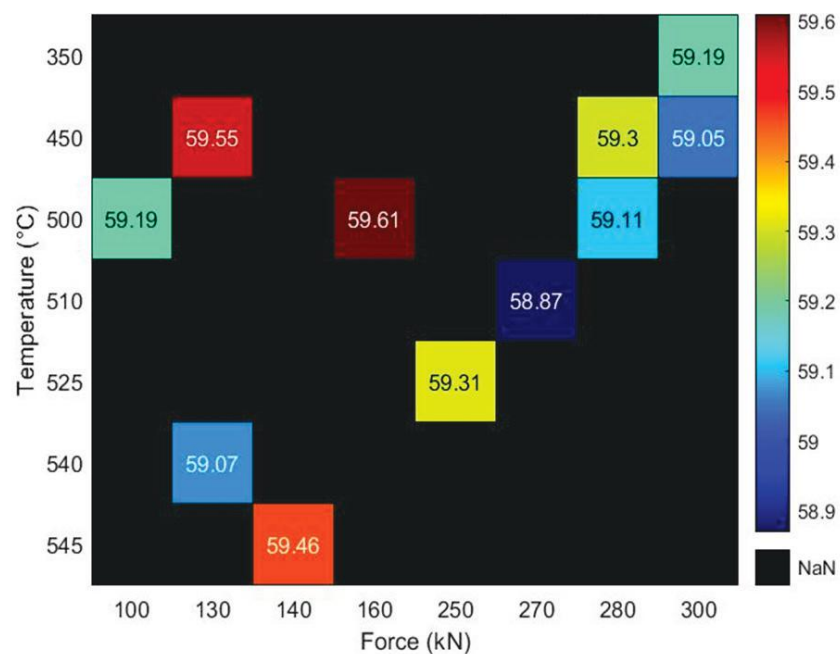


Figure I.1.3.28. Electrical conductivity of AA1100-only wires (without graphene additives) manufactured via ShAPE™ at varying extrusion temperatures and forces. Source: PNNL.

While not presented here, please note that similar trend as electrical conductivity was seen in the TCR variation of the AA1100-only wires. TCRs of these wires varied between $4.3\text{--}4.4 \times 10^{-3}\text{°C}^{-1}$, which was not a significant variation and corresponded with the TCR of AA1100 reported in literature [3]. Subsequently, Al/GNP samples were manufactured via ShAPE™ with 0.1 wt.% GNP content at 450–500°C to evaluate their effect on TCR of the composites. Figure I.1.3.6.2 shows the electrical conductivity of TCR of Al-only and Al/GNP composites with 0.1 wt.% GNP additives processed at 450°C and 130 kN, which were conditions resulting in higher electrical conductivity than those seen in Figure I.1.3.6.1. It is important to note here that Al/GNP samples were not processed at 500°C, even though the AA1100-only sample showed the highest conductivity of 59.61 %IACS at this process condition, since it is suspected based on literature evidence that Al and carbon from the GNP may reach to form an intermetallic, Al_4C_3 at this temperature, which is insulative—and therefore detrimental—to conductivity enhancement in Al matrix. When 0.1 wt.% GNP was added to the Al matrix, the TCR was lowered (by 5%) from 4.34°C^{-1} to 4.16°C^{-1} . However, when the Al/GNP composites were extruded a higher extrusion force of ~250 kN (compared to the 130 kN used to manufacture

the samples previously), the TCR of the Al/GNP wires decreased by >7% to $4.04^{\circ}\text{C}^{-1}$. Note that AA1100-only control samples demonstrated similar electrical conductivity and TCR at both the processing conditions of $450^{\circ}\text{C}/130\text{ kN}$ and $450^{\circ}\text{C}/230\text{ kN}$. These results suggest a direct relationship between process conditions such as extrusion forces and temperatures (and the shear forces imparted on the composite during processing), which is not evident for the control sample, implying the differences may be attributed to graphene evolution during ShAPE™ processing. Currently, microstructural characterization is ongoing, which we believe can shed light on the factors affecting the TCR of the composites.

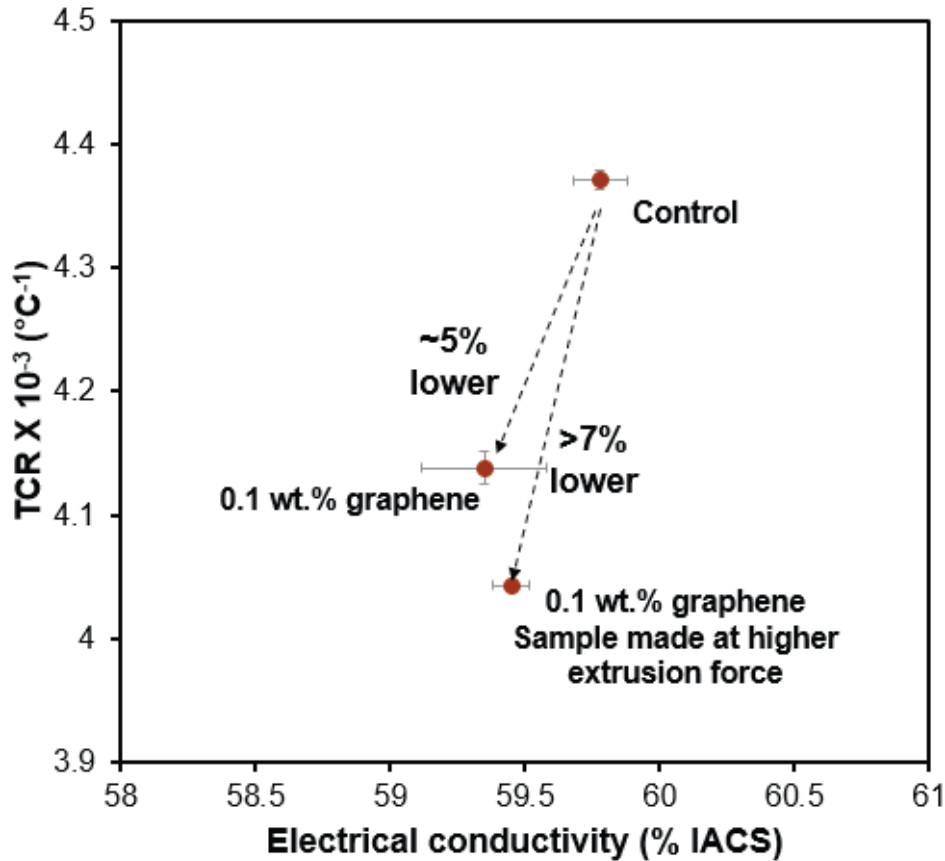


Figure I.1.3.29. Electrical conductivity and TCR of AA1100-only (control) and Al/GNP samples with 0.1 wt.% GNPs manufactured at an extrusion temperature of 450°C different extrusion forces. Source: PNNL.

Track 2 – Ultra-Conductor Component Development

In Track 2, ShAPE™ tooling, such as die and billet ring dimensions as well as the thermocouple locations, were modified to accommodate longer billets while maintaining the extrusion ratios of the tooling used previously. Subsequently, 3–5 m long ShAPE™ wires with an average diameter of 2.5 mm were produced. Process parameters were optimized to eliminate rough wire surfaces, particularly the striations, as shown in Figure I.1.3.6.3, and other extrusion patterns seen at times in previous ShAPE™ samples. Considering these composites were manufactured with ~0.25 wt.% GNP, which is ~2.5× the GNP content of specimens in Track 1, they demonstrate electrical conductivity of ~59% IACS while their TCR was ~4.3–4.4°C⁻¹. Currently, efforts are underway to manufacture Al/GNP wires at different extrusion forces in order to achieve lower TCR values that were seen in the Track 1 results.

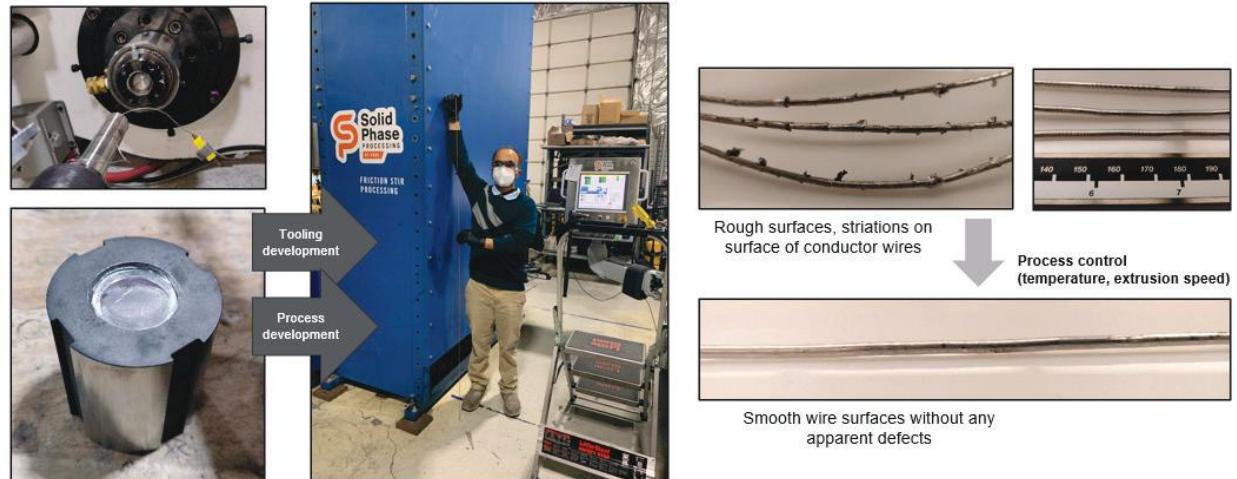


Figure I.1.3.30. ShAPE™ tooling and process development resulting in 3–5 m long Al/GNP wires with a diameter of 2.5 mm. Process development was optimized to ensure smooth wire surfaces which is crucial for property uniformity. Source: PNNL.

Conclusions

In FY 2022 efforts for this project, Al-only wires with a diameter of 2.5 mm were manufactured at various temperatures and extrusion forces via the ShAPE™. Results showed that process temperatures and forces did not significantly affect the electrical conductivity of AA1100 ShAPE™ wires. Subsequently, Al/graphene wires were manufactured, also via ShAPE™, using 0.1 wt.% reduced graphene oxide additives. Electrical performance testing showed that when the wires were extruded at 4 mm/min, the TCR of the composites was 5% lower than the Al-only samples; however, when the composites were extruded at more than double the tool traverse rates, the TCR was lowered by 7%. These results showed that extrusion speeds, and consequently the shear forces applied to the composites, affected the electrical properties of the composites, which was not evident in the Al-only samples, implying the differences were present due to the evolution of the graphene additives during ShAPE™. In addition to the material development efforts, tooling and process development was also carried out to enable the synthesis of 3–5 m long ShAPE™ Al/graphene composite wires. Process development was designed to manufacture composite wires with smooth surfaces, free of striations, to maintain uniform electrical properties along the entire length of the wires.

Key Publications

1. Frazier, W. E., B. Gwalani, J. A. Silverstein, J. D. Escobar, and K. S. Kappagantula, 2022, “Microstructure-sensitive calculations of metal nanocomposite electrical conductivity,” *International Materials, Applications, & Technologies 2022 (IMAT 2022)*, 12–15 September 2022, New Orleans, LA, USA.
2. Kappagantula, K. S., A. K. Nittala, X. Li, W. Choi, and N. Overman, 2023, “Bulk-scale friction-extruded aluminum wires with enhanced conductivity,” Manuscript submitted to *Adv. Mater.*
3. Ma, B., J. Thomas, Z. Zhang, B. Gwalani, K. S. Kappagantula, and D. Singh, 2023, “Characterization of ShAPE-processed ultra-conductors via synchrotron x-rays micro-beam diffraction,” Manuscript submitted to *Mater. Lett.*
4. Nepal, K., K. N. Subedi, D. A. Drabold, and K. S. Kappagantula, 2022, “Electrical conduction in aluminum with graphite and graphene impurities,” *Materials Science & Technology 2022 (MS&T 2022)*, 9–12 October 2022, Pittsburgh, PA, USA.

5. Nittala, A. K., M. R. E. Rabby, J. A. Silverstein, B. Gwalani, and K.S. Kappagantula, 2023, “Synthesis of aluminum/graphene composites with enhanced electrical properties through shear-assisted processing and extrusion,” Minerals, Metals, & Materials Society 2023 (TMS 2023), 19–23 March 2023, San Diego, CA, USA.
6. Subedi, K. N., K. S. Kappagantula, F. F. Kraft, A. K. Nittala, and D. A. Drabold, 2022, “Electrical conduction processes in aluminum: Defects and phonons,” *Phys. Rev. B*, Vol. 105, No. 10, Art. 104114. <https://doi.org/10.1103/PhysRevB.105.104114>.
7. Subedi, K. N., K. Nepal, C. Ugwumadu, K. S. Kappagantula, and D. A. Drabold, 2023, “Electronic transport in copper-graphene composites,” *Appl. Phys. Lett.*, Vol. 122, Art. 031903. <https://doi.org/10.1063/5.0137086>.

References

1. Li, X., C. Zhou, N. Overman, X. Ma, N. Canfield, K. S. Kappagantula, J. Schroth, and G. Grant, 2021, “Copper-carbon composite wire with a uniform carbon dispersion made by friction extrusion,” *J. Manuf. Process.*, Vol. 65, pp. 397–406. <https://doi.org/10.1016/j.jmapro.2021.03.055>.
2. Kappagantula, K., 2022, *CABLE Big Idea Workshop 2022*, 20–21 July 2022, Chicago, IL, USA.
3. Nittala, A., 2022, “Development of high-performance aluminum conductors: A study of additive and process influence on electrical performance,” Ph.D. Dissertation, April 2022, Ohio University, Athens, OH, USA. Available at: https://etd.ohiolink.edu/apexprod/rws_etd/send_file/send?accession=ohiou1643855576553448&disposition=inline (last accessed 26 January 2023).

Acknowledgements

The authors appreciate the efforts of M. R. E. Rabby on ShAPE process design, A. Nittala for the conductor design and property characterization, N. Overman for the microstructural characterization efforts, and A. Guzman for the sample preparation efforts. The authors also acknowledge the collaboration with Argonne National Laboratory (ANL) via the Thrust 4 project and for D. Singh’s leadership, as well as the work completed by B. Ma and J. Thomas on characterizing aluminum and copper ultra-conductors using the Advanced Photon Source (APS). PNNL is operated by the Battelle Memorial Institute for DOE under contract number DE-AC06-76LO1830.

I.1.4 Thrust 4: Advanced Characterization and Computation

I.1.4.1 Task 4A. Advanced Characterization – Coordination of Multi-Lab Characterization (Task 4A1) (Oak Ridge National Laboratory)

Thomas R. Watkins, Co-Principal Investigator

Oak Ridge National Laboratory
Materials Science and Technology Division
1 Bethel Valley Road
Oak Ridge, TN 37830
E-mail: watkinstr@ornl.gov

J. Allen Haynes, Co-Principal Investigator

Oak Ridge National Laboratory
Materials Science and Technology Division
1 Bethel Valley Road
Oak Ridge, TN 37830
E-mail: haynesa@ornl.gov

Jerry Gibbs, DOE Technology Development Manager

U.S. Department of Energy
E-mail: jerry.gibbs@ee.doe.gov

Start Date: October 1, 2019 End Date: September 30, 2023
Project Funding (FY 2022): \$450,000 DOE share: \$450,000 Non-DOE share: \$0

Project Introduction

This report describes the activities performed during the fourth year of Thrust 4A1, “Advanced Characterization,” under the Powertrain Materials Core Program (PMCP) consortium occurring at ORNL. The report also covers the coordination of Thrust 4, “Multi-Lab Characterization,” efforts amongst the three consortium labs: ORNL, PNNL, and ANL. These activities are sponsored by the DOE-EERE VTO PMCP.

In FY 2022, which was the fourth year of the consortium’s five-year program, the PMCP’s mission pivoted from a focus on internal combustion engines to a 100% focus on EVs. Three new long-term materials development thrusts were initiated—each thrust with multiple development tasks—Thrust 1: “Lightweight Alloys for EV Propulsion;” Thrust 2: “Materials & Lubricants for Heavy Duty EVs;” and Thrust 3: “Advanced and AM for EVs.” The goal of the PMCP is to accelerate the design, development, demonstration, and deployment of new, cost-effective advanced materials solutions for EV powertrains via a modern ICME approach. The properties of these new materials are targeted to enable improvements in electric motor efficiency, component lightweighting, improved thermal management, and durability enhancement for future EVs. To support this goal, Thrust 4, which includes both advanced characterization (Thrust 4A) and advanced computation (Thrust 4B), undergirds the development tasks within the three development thrusts (Thrusts 1, 2, and 3) by providing tools and expertise from within the national laboratory consortium that is able to acquire deeper understanding of materials structure and properties, and thus insight into the design and development of superior future materials for LD, MD, and HD EV powertrain applications. This unique programmatic support model was created within the PMCP and has recently been adopted by other programs.

Objective

The overall objective for Thrust 4A is to provide advanced characterization support projects for Thrusts 1, 2, and 3 of the PMCP in order to obtain data and scientific understanding that will be applied to the development

of new materials for future advanced EVs. Thrust 4A1 covers the advanced characterization activities at ORNL and also coordinates the Thrust 4 research activities across all three consortium labs.

Approach

Coordination of the multi-lab characterization activities are accomplished first with dedicated funding for advanced characterization after internal proposal, review, and award of Thrust 4 projects to support specific development tasks from Thrusts 1–3, and second with ad-hoc and regularly scheduled meetings amongst the PMCP task PIs and the Thrust 4 project researchers. These dedicated Thrust 4 research funds are intended to enable advanced characterization (and computation) to more effectively support the science and development objectives of the program task. Thus, any task principal investigator from any lab within Thrusts 1, 2, and 3 can request advanced characterization support from defined Thrust 4 resources and staff at any of the three labs through a standardized multi-lab proposal review process. Therein, two-page proposals are submitted, reviewed, and ranked by a review committee. Thrust 4 support projects are then awarded to high-ranked proposals as funds allow, as observed in Figure I.1.4.1.1. In FY 2022, 15 of 16 Thrust 4 proposals were approved for advanced characterization projects across the three consortium labs: ORNL, ANL, and PNNL. Table I.1.4.1.1 lists all Thrust 4 projects awarded across the PMCP in FY 2022.

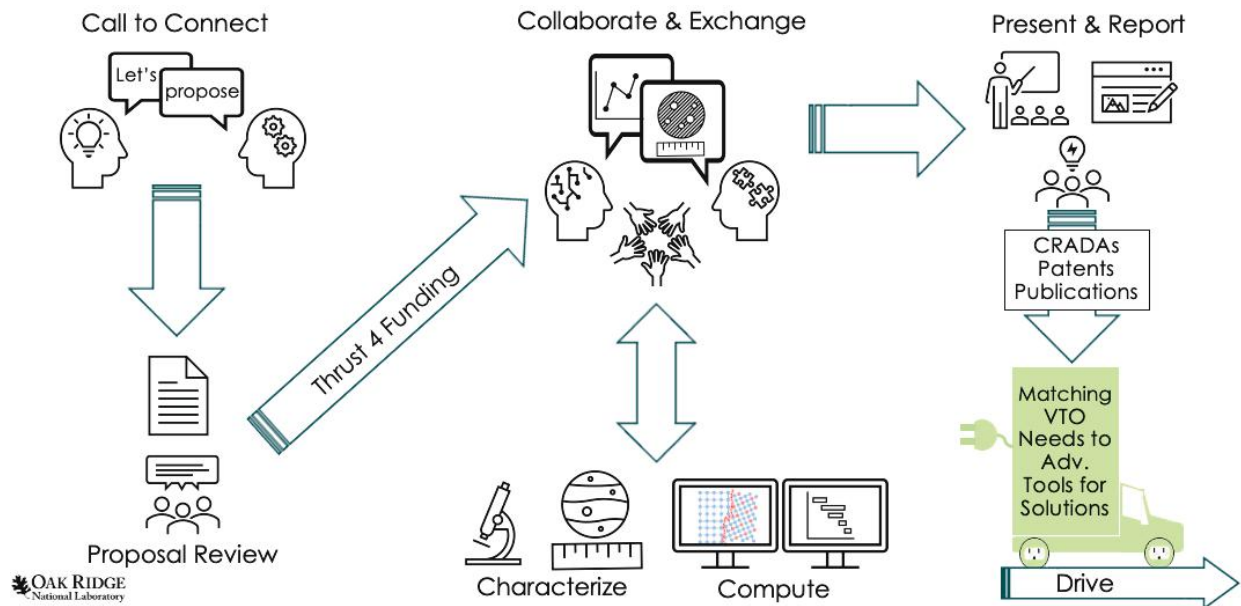


Figure I.1.4.1. Thrust 4 coordination of the multi-lab characterization. Researchers identify an EV material problem to be solved and propose work. Upon successful review and ranking, funds are awarded with advanced characterization (and computation) and analyses ensuing. Discussions and meetings occur often between researchers at the national laboratories through hybrid meetings and email. Results are converted into research products with the goal of their application within future EVs. Source: ORNL.

Table I.1.4.1.1. Thrust 4A1 “Funded Advanced Characterization Projects” in FY 2022

Thrust	Task Lab	Task	Thrust 4A1 Lab	Tool	Project #: Description
1*	ORNL	Lightweight (LW) Materials for Improved Electrical Properties	ORNL	APT	22-6: Measure precipitate composition, size, number density, and volume fraction related to mechanical & electrical properties in Al-(Fe)-Zr-Sn Alloys
1	ORNL	LW Materials for Improved Electrical Properties	ORNL	STEM	22-11: Same as above, but with STEM
1	PNNL	Hybrid Dispersion Strengthened Al Matrix Composites for Higher Efficiency EV Powertrains	PNNL	STEM and APT	22-19: Determine the particle size and chemistry of nano-sized reinforcement particles in an aluminum matrix that controls mechanical and tribological behaviors
2**	ORNL	Carbon NanoTube Coatings for Superlubricity & Thermal Management of HD EVs	ORNL	X-ray Photoelectron Spectroscopy (XPS)	22-5: Characterize the nature of the carbon bonding to an aluminum substrate and correlate to heat transfer and superlubricity performances
2	ORNL	Ferrous Alloys for Fatigue-Resistant, LW Geartrains for HD EV Systems	ORNL	STEM and APT	22-16: Investigation of near-surface microstructure in nitrided and carburized low-density steels
2	PNNL	Solid-phase joining and processing methods towards efficient, HD EV motors	PNNL	STEM, APT, and Atomic Force Microscopy	22-21: Characterize phase, composition, precipitate, and inclusions type and distributions, which could enhance formability and maintain magnetic properties
2	ORNL	High-Performance Soft Magnetic Materials for Motor Laminates (Fe-Si) Via Shear Rolling	ANL	APS, synchrotron X-ray Diffraction (XRD)	22-22: Determine the phases as a function of temperature and composition
2	ORNL	High-Performance Soft Magnetic Materials for Motor Laminates (Fe-Si) Via Shear Rolling	ORNL	Spallation Neutron Source and XRD	22-23: Determine the phases as a function of heat-treatment and composition
3***	ORNL	Advanced Ceramics and Processing for Wireless Charging Systems (ferrites)	ORNL	Raman Microscopy & Electron MicroProbe	22-9: Map phase, grain orientation and composition across the microstructure of ferrites
3	ORNL	Fundamentals of Non-Equilibrium Processing for AM Alloys	ORNL	SEM & STEM	22-2: Characterize the crystal structure of phases in AM and Cast Al alloys
3	ORNL	Fundamentals of Non-Equilibrium Processing for AM Alloys	ORNL	APT	22-3: Compositional analysis of phases within an ultrafine nanoscale eutectic microstructure

Thrust	Task Lab	Task	Thrust 4A1 Lab	Tool	Project #: Description
3	PNNL	Ultra-conductor Development for Enhanced EV Performance	ANL	APS, Synchrotron XRD	22-10: Identify the crystal structure and strain state of shear-processed nanocarbon in bulk Cu & Al
3	ORNL	Fundamental Development of Additive Manufactured Alloys for EV Propulsion	ORNL	STEM	22-12: Identify key microstructural features controlling the thermophysical properties of aluminum alloys
3	ORNL	Fundamental Development of Additive Manufactured Alloys for EV Propulsion	ORNL	APT	22-13: Same as above
3	PNNL	Ultra-Conductor Development for Enhanced EV Performance	PNNL	STEM & APT	22-17: Identify the structure and chemical composition of the graphene additives & their interface within the Al matrix

*1. Lightweight Alloys for EV Propulsion; **2. Materials & Lubricants for Heavy Duty EVs; ***3. Advanced and Additive Manufacturing for EVs.

Following are examples of the technical approach of two selected Thrust 4A1 projects from FY 2022. Briefly, **Project 22-9** analyzes and compares Raman and EDS elemental maps acquired from the same locations on polished cross-sections of sintered ferrite samples. Through principal component analyses (PCAs) of both techniques, the local phase and composition of the ferrites were determined for specific combinations of sources, materials, and processing conditions. **Project 22-12** examines microstructural changes resulting from the preparation conditions, aging conditions, and creep treatments using STEM. Each of the two representative FY 2022 projects are described in more detail below.

Results

Project 22-9: Characterization of Processing and Structure Impacts on Ferritic Materials supports the development of *Task 3C: Advanced Ceramics and Processing for Wireless Charging Systems*. The parent task is developing advanced magnetic ceramics for future LD and HD vehicle wireless charging applications. A commercially available ferrite wireless charging material for dynamic wireless charging was obtained, sectioned, and characterized using the techniques highlighted in the approach section. This baseline ferrite material is a cementitious-based iron spinel for potential use in roadways with a transmitting charging system. Figure I.1.4.1.2 highlights a region of this material that was analyzed in Project 22-9 using both EDS and Raman spectroscopy. Two iron (Fe)-spinel phases were found with slightly differing manganese (Mn) and zinc (Zn) content, as shown by the red and orange phases in the PCA analysis of the EDS map in Figure I.1.4.1.2(b). The PCA of the Raman spectroscopy map from the same region is presented in Figure I.1.4.1.2(c). The red phase map is 66 at% Fe, 22 at% Mn, and 8 at% Zn, whereas the orange phase map shows 66 at% Fe, 26 at% Mn, and 5 at% Zn. Figure I.1.4.1.3 provides the average Raman spectra acquired from the two phases in Figure I.1.4.1.2(c). The different Raman spectra from these two phases indicate changes in the octahedral site of the spinel. The prominent peak at 620 cm^{-1} is the A1 g mode associated with the octahedral cation Fe. The shoulder is likely due to the Zn substituting for Fe and occupying some of these octahedral sites in the lattice.

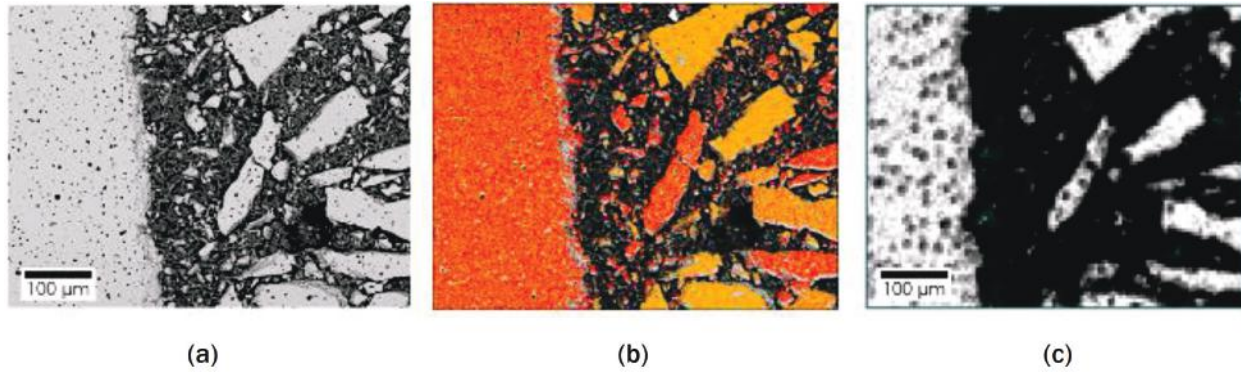


Figure I.1.4.2. (a) Backscattered electron image of a commercial cementitious iron spinel. (b) PCA of the EDS map from the same region showing two different phases. (c) PCA of Raman map from the same region. Source: ORNL.

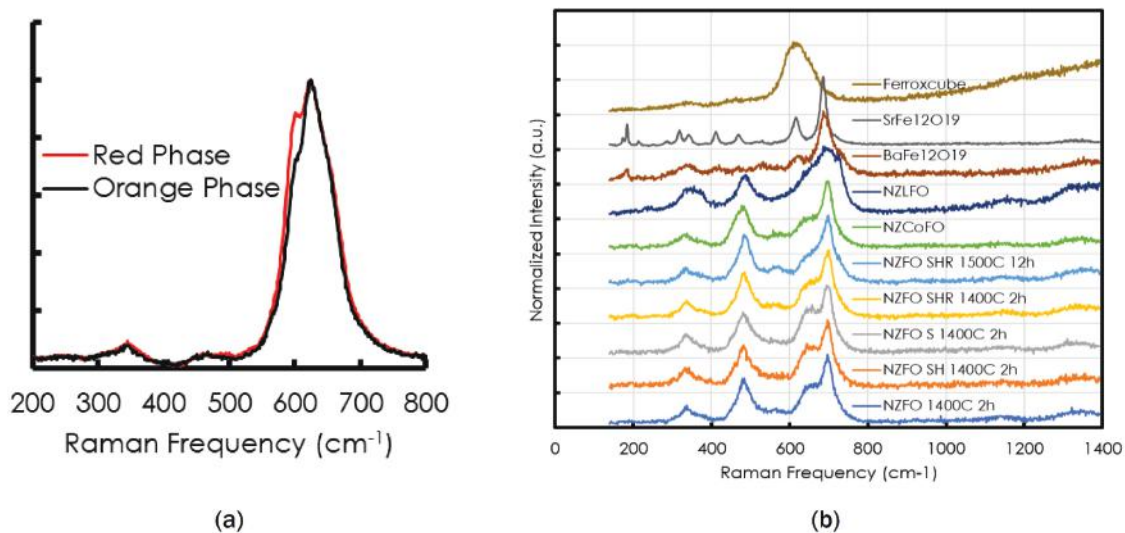


Figure I.1.4.3. (a) Average Raman spectra from the two spinel phases shown in Figure I.1.4.1.2(c). (b) Raman spectra acquired from various ferrite compositions made from materials originating from a commercial supplier. Source: ORNL.

Interestingly, this work highlighted three important results. This ferrite material is not 100% dense and is not single-phase. In addition, the grain orientations are not completely aligned. This contradicts the previous assumption that high densities are necessary to achieve the magnetic strengths needed for these applications and that grain alignment correlates to magnetic dipole alignment. This discovery suggests that new research pathways wherein lightweighting can occur—particularly for the vehicle side of the charging couple—with the addition of voids or porosity or even the introduction of a lighter weight secondary phase can create a more durable composite structure. Also, the use of mixed ferrite phases in a composite architecture to tune the magnetic properties as application demands was identified. To examine this more closely, an array of alternative ferrite compositions was identified from a literature review and supplied in collaboration with a commercial ferrite powder supplier. These powders were pressed into simple pellets for benchmark studies. Baseline Raman spectra were then collected, as shown in Figure I.1.4.1.3(b). The spectra all exhibit Raman peaks associated with the spinel phase. Further analyses of these samples are in progress.

Project 22-12: STEM Investigations of Microstructure-Thermophysical Properties Correlations in Al Alloys supports the development of *Task 3A: Fundamental Development of Additive Manufactured Alloys for EV Propulsion*. The STEM method is being used for precipitate analysis (e.g., crystal structure, microchemistry, size, spatial distributions) under various heat-treatment conditions in a creep-resistant Al-Cu-Mn-Zr alloy fabricated by laser powder bed fusion AM methods to establish microstructure-thermophysical property correlations. Figure I.1.4.1.4 exhibits the as-fabricated microstructure showing θ' -Al₂Cu precipitates, dislocation distributions, and grain boundaries. After creep and aging, and followed by creep testing at 300 – 400°C, the alloy microstructures were discovered to be similar, with particles distributed along the grain boundaries and a lower volume fraction of θ' -Al₂Cu precipitates distributed in the matrix as compared to the as-fabricated microstructure shown in Figure I.1.4.1.4(b) and Figure I.1.4.1.4(c), respectively. In addition, multiple dislocations and dislocation tangles are noted at and between the θ' -Al₂Cu precipitates. In Figure I.1.4.1.4(c), the microstructure contains other spherical particles in the grain interiors, likely the ~10–100 nm diameter particles with various enrichments of copper (Cu), Mn, and zirconium (Zr) that form during the pre-creep heat-treatment. Some of these grain interior particles may also be L₁₂-Al₃Zr precipitates that have coarsened during the creep test via pipe diffusion of Zr atoms. The samples aged at 400°C, both at 6 h, as shown in Figure I.1.4.1.4(d), and 200 h (not shown), have clear PFZs around the grain boundaries and an overall reduction in the number of particles on the grain boundaries when compared to the as-fabricated and 350°C, 24 h microstructures, as captured in Figure I.1.4.1.4(a) and Figure I.1.4.1.4(b), respectively. These PFZs likely developed during the pre-creep heat-treatment and increased in size as the creep tests progressed. In the 400°C heat-treated samples, dislocation tangles are concentrated in the grain interiors around the ~10–100 nm diameter particles enriched in Cu, Mn, and Zr. These (and other) microstructural developments during aging and creep testing have led to ORNL proposing a new load shuffling mechanism [1], which explains the mechanical property behavior of these AM alloys. Therein, the transfer of load moves first from the Al grains to the refined grain boundary θ particles at the onset of deformation (e.g., limited PFZs), and then the load transfers back from the grain boundary particles to the Al grains after the growth of surrounding lower strength PFZs during creep.

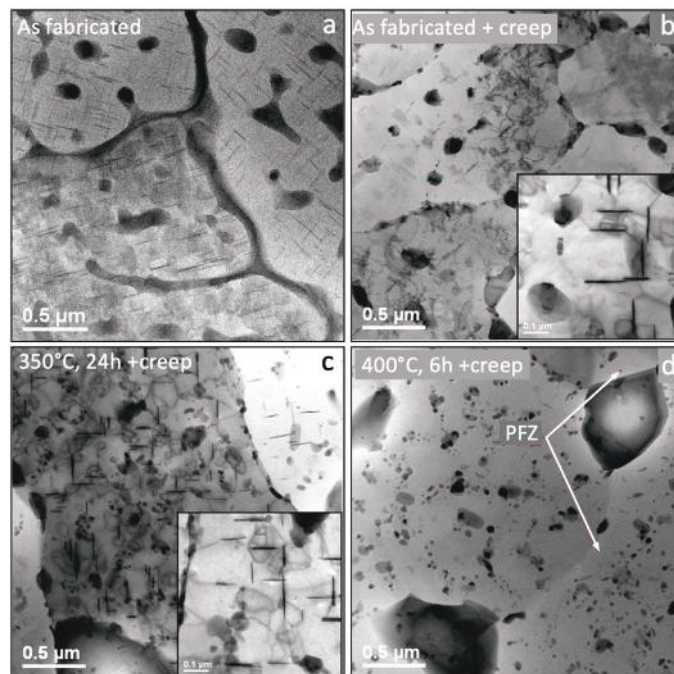


Figure I.1.4.4. Bright-field STEM micrographs of AM Al-Cu-Mn-Zr: (a) as-fabricated; (b) crept for 210 h at 45 MPa and 300 °C; (c) aged 350 °C for 24 h, and then crept for 1010 h at 43 MPa and 300 °C; and (d) aged 400 °C for 6 h, and then crept for 866 h at 38 MPa and 300 °C. Insets show the detail of precipitate/dislocation interactions. Source: ORNL.

Conclusions

Understanding the behavior of alloy systems under various processing and use conditions requires a suite of advanced materials characterization techniques to clarify chemical, microstructural, and phase changes as a function of time, elevated temperature, pressure/loading, and other conditions. Coordination of this suite of advanced characterization capabilities and expertise across three national laboratories is managed through Thrust 4.

Examples of FY 2022 Thrust 4A1 projects highlighted here are essential for accomplishing the mission of accelerated materials development for future advanced EVs under the PMCP. Here, Raman spectroscopy and EDS mapping are critical techniques for understanding the local phases and compositions present on sintered ferrites and provided important findings that commercially available materials are not a single-phase or high density materials as previously expected, opening new opportunities for both lightweighting and tailoring the magnetic properties of the ferrite materials. Similarly, high-resolution aberration-corrected STEM imaging allowed direct imaging of crystalline phases, precipitates, dislocations, and chemical information in potential future EV alloys and has elucidated a new load shuffling mechanism. The combination of advanced characterization tools from the national labs provides for these two examples of essential, unique, and timely discovery, as well as deeper scientific understanding, which enable more rapid development of the next-generation of advanced powertrain materials for light-, medium-, and HD EVs.

Key Publications

1. Michi, R. A., S. Bahl, C. M. Fancher, K. Sisco, L. F. Allard, K. An, D. Yu, R. R. Dehoff, A. Plotkowski, and A. Shyam, 2022, "Load shuffling during creep deformation of an additively manufactured Al-Cu-Mn-Zr alloy," *Acta Mater.*, Vol. 244, Art. 118557. <https://doi.org/10.1016/j.actamat.2022.118557>.

References

1. Michi, R. A., S. Bahl, C. M. Fancher, K. Sisco, L. F. Allard, K. An, D. Yu, R. R. Dehoff, A. Plotkowski, and A. Shyam, 2022, "Load shuffling during creep deformation of an additively manufactured Al-Cu-Mn-Zr alloy," *Acta Mater.*, Vol. 244, Art. 118557. <https://doi.org/10.1016/j.actamat.2022.118557>.

Acknowledgements

The authors would like to thank Steward Advanced Materials for providing the ferrite powder samples. The authors also acknowledge the contributions of their ORNL team members for this sub-task: B. Armstrong, M. Lance, L. Allard, A. Shyam, and A. Plotkowski.

I.1.4.2 Task 4A. Advanced Characterization – Advanced Characterization of PMCP Research Samples: Characterization of Thermal, Electrical, and Magnetic Properties (Task 4A3) (Oak Ridge National Laboratory)

Hsin Wang, Co-Principal Investigator

Oak Ridge National Laboratory
Materials Science and Technology Division
1 Bethel Valley Road
Oak Ridge, TN 37830
E-mail: wangh2@ornl.gov

J. Allen Haynes, Co-Principal Investigator

Oak Ridge National Laboratory
Materials Science and Technology Division
1 Bethel Valley Road
Oak Ridge, TN 37830
E-mail: haynesa@ornl.gov

Jerry Gibbs, DOE Technology Development Manager

U.S. Department of Energy
E-mail: jerry.gibbs@ee.doe.gov

Start Date: October 1, 2021 End Date: September 30, 2023
Project Funding (FY 2022): \$180,000 DOE share: \$180,000 Non-DOE share: \$0

Project Introduction

Electrical and thermophysical properties of materials used in EV powertrains are important because: (1) they provide key materials processing quality controls and performance parameters; and (2) they are used in vehicle design, modeling, and simulation of components. Task 4A3 is focusing on test setup and validation of state-of-the-art methods for characterization of electrical and thermal properties of key EV-related materials. Testing standards and metrology are emphasized, especially for advanced conductors and new alloys produced by modern casting and AM processes.

Objective

There are two main objectives for this task. The first objective is supporting the various development tasks within Thrusts 1–3 by characterizing the thermal and electrical properties of the materials being studied and developed in those tasks. The second objective is contributing to the integral materials development strategies of the PMCP via the scientific and technical understanding developed in these characterization studies.

Approach

The Year One approach to this new characterization task included the following tasks:

1. A program-wide characterization seminar was held in the first quarter of FY 2022 to familiarize the multi-laboratory team with the available instruments and testing capabilities available to the Thrust 1–3 PIs.
2. A survey of electrical and thermophysical testing needs across the new development tasks within the three development thrusts was conducted to prioritize schedules and resources.
3. Working with the Thrust 1–3 PIs to establish appropriate testing protocols, specimen specifications, and baseline materials properties for each related task was completed.

4. Testing of the electrical and thermal properties of the Thrust 1–3 materials was performed, data analysis was conducted, and a report was prepared.

Results

In the first quarter of FY 2022, an online seminar was held to survey the materials testing needs of Thrust 1–3. Existing characterization capabilities were presented to the PIs PMCP tasks. Feedback was collected in terms of the necessary characterization instrument to be used and the temperature ranges needed for the specific materials. The number of specimens (e.g., test matrix) and anticipated schedules were provided by the various PIs to define the time and effort required and to outline the annual characterization priorities and schedule. Table I.1.4.2.1 shows the Task 4A3 characterization capabilities requested by nine of the development tasks and lists their specific materials of interest for characterization. Table I.1.4.2.1 also includes two recently acquired instruments for electrical (e.g., eddy current) and thermal conductivity (e.g., hot-wire) measurements and a newly constructed thermal interface resistance system setup using a load frame and infrared camera.

Table I.1.4.2.1. Thrust 4A3-22 Characterization Capabilities and Related Testing Requests from the Thrust 1–3 Development Tasks in FY 2022.

ORNL Instrument Name	Function	Temperature Range	Support Thrust 1–3 Tasks	Material
Netzsch FLA457	Thermal Diffusivity	RT-1100 °C	1G-22, 3A-22 1F-22 2A2	Al-Cu, Al-Si Alloys Aluminum (Al) Steel Alloys
Netzsch Dil 402	Thermal Expansion	RT-2200 °C	3C-22	Ferrites
Netzsch DSC 404	Heat Capacity	RT-1650 °C	1G-22, 3A-22 1F-22 2A2	Al-Cu, Al-Si Alloys Al Alloys Steel alloys
ULVAC ZEM-3	Electrical Conductivity	RT-800 °C	3C-22	Ferrites
ULVAC ZEM-5	Electrical Conductivity	RT-1200 °C	1E-22	Al-Ce Alloys
Signatone Probe Station	Electrical Conductivity	RT-450 °C	1G-22, 3A-22 1A-22	Al-Cu, Al-Si Alloys Al-Ni Alloys
Ecopia HMS3000	Electrical Conductivity	77K, 300K	1F-22	Aluminum
TPS1500 - Hot Disk	Thermal Conductivity	RT	1A-22	Al Cast Ingots
TPS 3500 - Hot Disk	Thermal Conductivity	-35 °C–200 °C		
Thermtest THW L1*	Thermal Conductivity	RT-350 °C	2C-22	Lubricants
Eddy Current Probe*	Electrical Conductivity	RT	1A-22	Al-Cu, Al-Si Alloys
Interface Resistance*	Thermal Resistance	RT-200 °C	2D-22	Interface Material

*New equipment acquired in FY 2022 as well as a special setup using existing instrumentation.

Improvement in thermal conductivity in EV lubricants can enhance heat transfer and has potential to enable better temperature control of vehicle components, such as motors and other rotating parts. New FY 2022 Task 2C, *New Lubricant Strategies for Advanced Thermal Management of HD EVs*, is evaluating the addition of surface-modified carbon nanotubes (CNTs) to EV lubricants in order to improve the thermal management capabilities of those fluids. A new hot-wire thermal conductivity system was purchased by ORNL in FY 2022, which follows the methods of ASTM D7896-19 [1] to measure liquid thermal conductivity over the temperature range of 35°C to 350°C. The instrument and hot-wire heater/probe are shown in Figure I.1.4.2.1(a). Novel lubricant formulations with modified CNT additives prepared in Task 2C are being tested using this system. Thermal conductivity as a function of temperature for various modified lubricants is shown in Figure I.1.4.2.1(b). A total of 10 baseline liquids and modified liquids were measured in FY 2022. A significant influence of suspended CNT additions on lubricant thermal conductivity was confirmed.

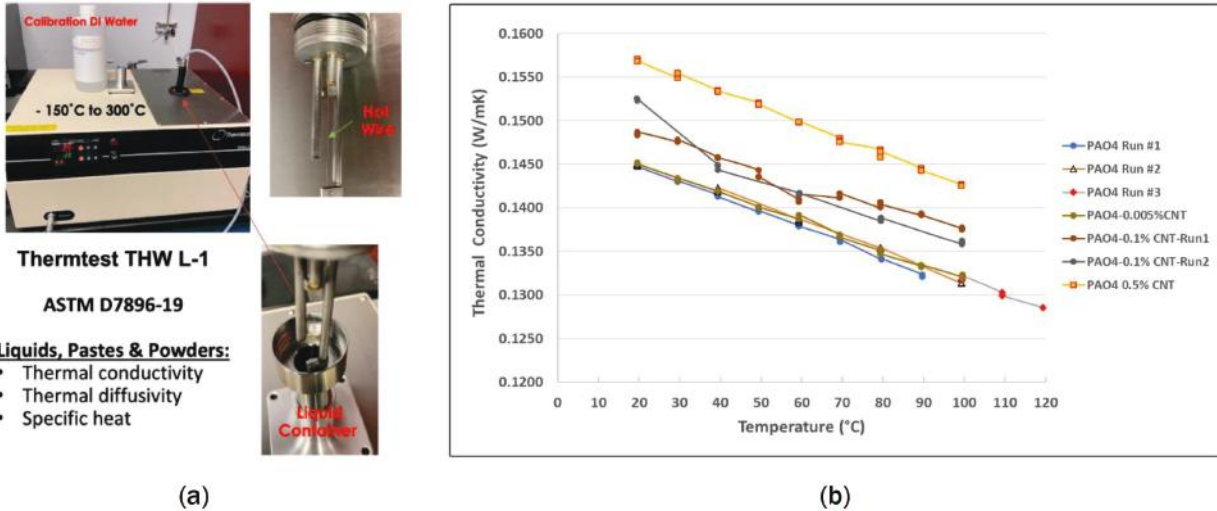


Figure I.1.4.5. (a) Thermtest THW L1 Hot-Wire system at ORNL to measure thermal conductivity of liquids with (b) examples of thermal conductivity measurements on polyalphaolefin (PAO) based lubricants with and without modified carbon nanotube additions. Source: ORNL.

Interface thermal resistance is a very important property that affects heat transfer and removal from numerous EV-related components and devices. Task 2D, *CNT Coatings for Superlubricity and Thermal Management of HD EVs*, has a very specific requirement for this measurement between an Al and stainless steel interface. A Thermal Resistance Measurement System was designed and built at ORNL that incorporates a servomotor driven mechanical load frame, following ASTM D5470-17 [2], to apply a constant load to compress the samples. An infrared camera, FLIR SC7000, was used to monitor the temperature of the specimens and the interface. The system also uses an AlN heater to apply heat from the top and an Al cooling plate at the bottom to remove the heat. As a result, a stable temperature gradient is established after ~30 minutes. The temperature drop, ΔT , at the interface with cross-section area A , is measured along with the temperature gradient ($\Delta T/\Delta X$) on either side of the interface. The heat flux, Q , is calculated from the known thermal conductivity of both materials. Interface resistance under specific pressure is calculated using:

$$\text{Thermal conductivity } k = -Q/(A\Delta T/\Delta x) \quad (1)$$

$$\text{Thermal Interface Resistance } R = \Delta T/(Q/A) \quad (2)$$

Figure I.1.4.2.2 is a typical infrared image of a pair of samples under a stable temperature gradient. The temperature drop is shown in the temperature line profile. A series of interface materials were tested under identical conditions and thermal interface resistance of these materials were compared. These results are not yet cleared for public distribution due to intellectual property procedures.

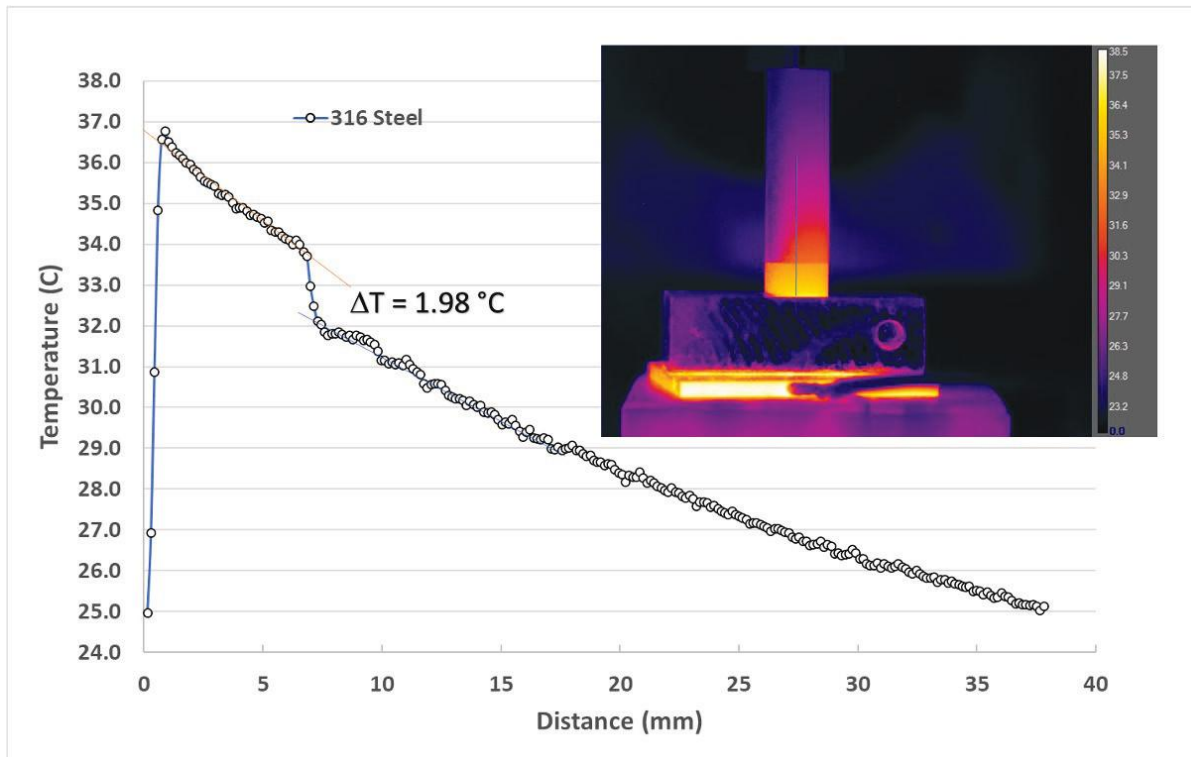


Figure I.1.4.6. Temperature gradient established across a steel-steel interface in an infrared image. The temperature line profile shows the measured temperature drop. Source: ORNL.

Electrical conductivity/resistivity is also a focus of the PMCP and related measurements were requested by six development tasks across Thrusts 1–3, as shown previously in Table I.1.4.2.1. Two techniques were used: (1) a 4-point probe method for electrical resistivity using ULVAC ZEM-3; and (2) an eddy current probe method for non-magnetic materials, particularly using Al. The ZEM-3 probe measurement arrangement is shown in Figure I.1.4.2.2. Two nickel electrodes in contact with a bar or cylinder specimen provided the current contacts. Two thermocouples with a tip size of 0.5 mm have contacted the specimen. Voltage is measured from the same wire of each thermocouple. The spacing between the contacts varies from 3–8 mm and is carefully measured using a digital microscope. The specimen temperature is the average of the two thermocouples. The eddy current method [3] employs a probe, as shown in Figure, that is pressed against the sample surface for a few seconds. Electrical conductivity is measured using various appropriate known standards as calibration. More than 100 specimens were measured in FY 2022 using these two techniques. Several examples of such measurement results are shown in Figure I.1.4.2.4(a) and Figure I.1.4.2.4(b), respectively, where the electrical resistivities of various cast or printed creep-resistant commercial, developmental, and model Al alloys were measured and compared to pure Al.

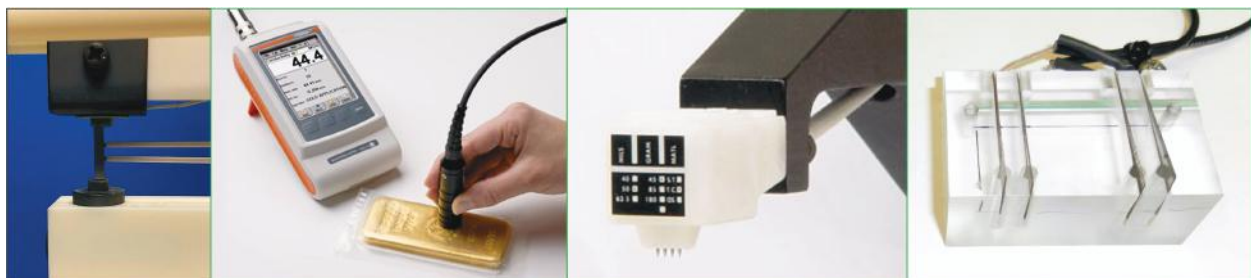


Figure I.1.4.7. Electrical resistivity measurement methods. From left to right: 4-point probe (ZEM-3); Eddy current probe, Inline 4-point probe [4], and 4-point knife edge method [5]. Source: ORNL.

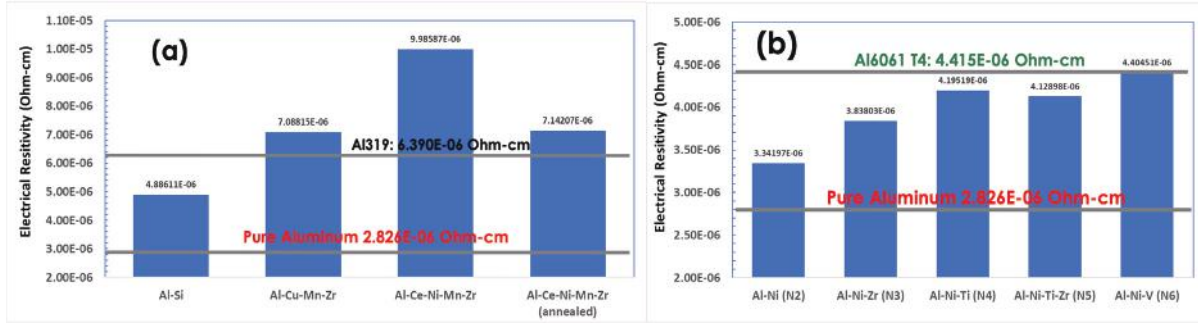


Figure I.1.4.8. (a) Electrical resistivity of printed commercial Al-Si, developmental Al-Cu, and developmental Al-Ce alloys vs. cast commercial alloy 319 and pure Al. (b) Electrical resistivity of model and developmental cast Al-Ni alloys. Source: ORNL.

Thermal diffusivity, specific heat, and thermal expansion testing were requested by six different developmental tasks. These are typically thermophysical properties following ASTM E1461 [6], E831 [7], and E1269 [8]. Figure I.1.4.2.5 shows a typical thermal diffusivity vs. temperature plot of example materials from Task 1A, *Fundamental Studies of Al-Ni Alloys for Improved Electrical Properties*. In this case, a series of Al-Ni-X alloys were measured to 400°C. The base Al-Ni alloy shows a change of slope at 350°C, likely a Curie transition. When Ti, Zr, and V were added, the thermal diffusivity dropped 10%–20% and a transition was not observed in the tested temperature range. Overall, more than 120 specimens prepared from various Al alloys were measured for electrical and thermal properties in FY 2022.

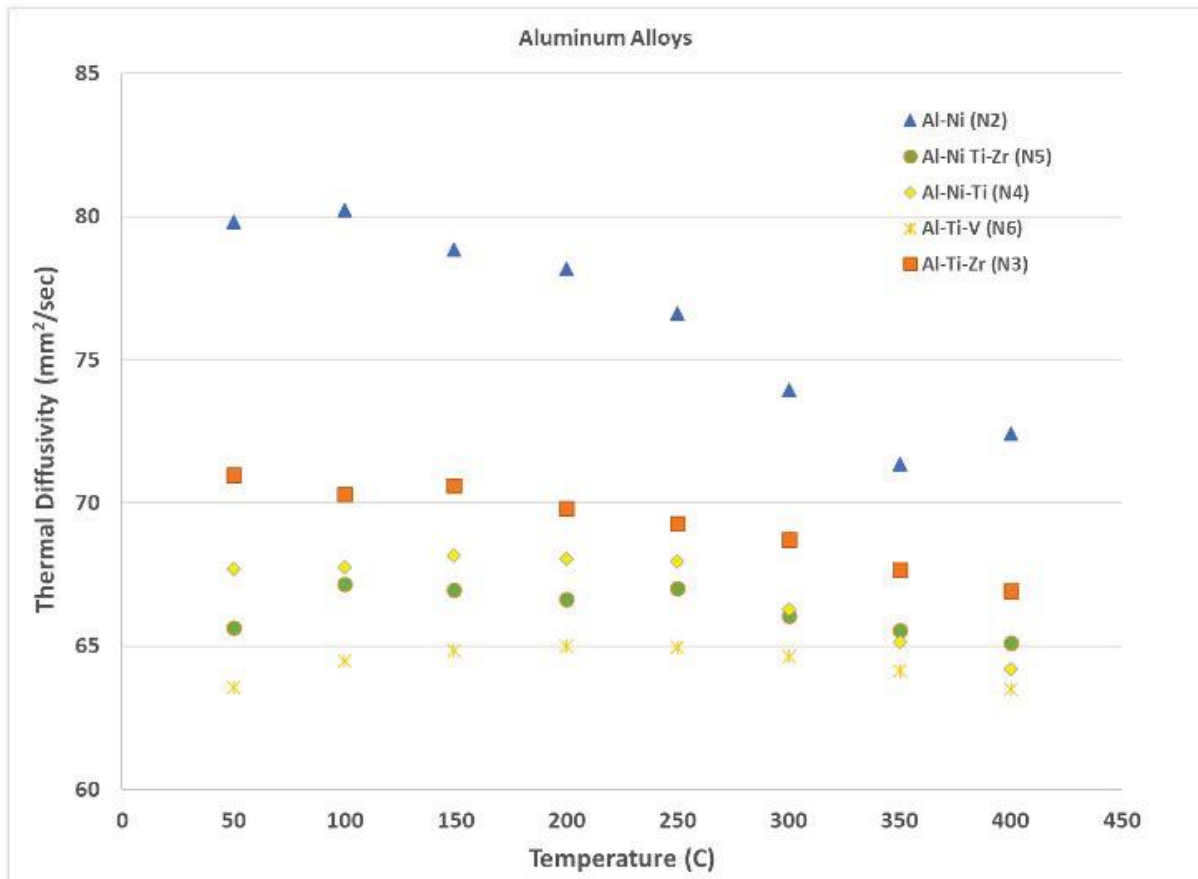


Figure I.1.4.9. Thermal diffusivity of cast Al-Ni alloys from Task 1A. Source: ORNL.

Figure I.1.4.2.6 shows a plot of raw data measured by ZEM-3 to determine the electrical resistivity of a cast Al-Ni alloy after four different heat-treatment 200-hr annealing temperatures. Each annealing temperature prepared five specimens from different parts of the cast ingot. Five measurements were performed on each specimen. A total of 100 electrical resistivity measurements were carried out on this alloy after the various heat treatments. One of the purposes of generating a large amount of consistently collected properties data is to enable a property database for ML and optimization of future cast Al alloys to optimize mechanical properties with thermal and/or electrical properties.

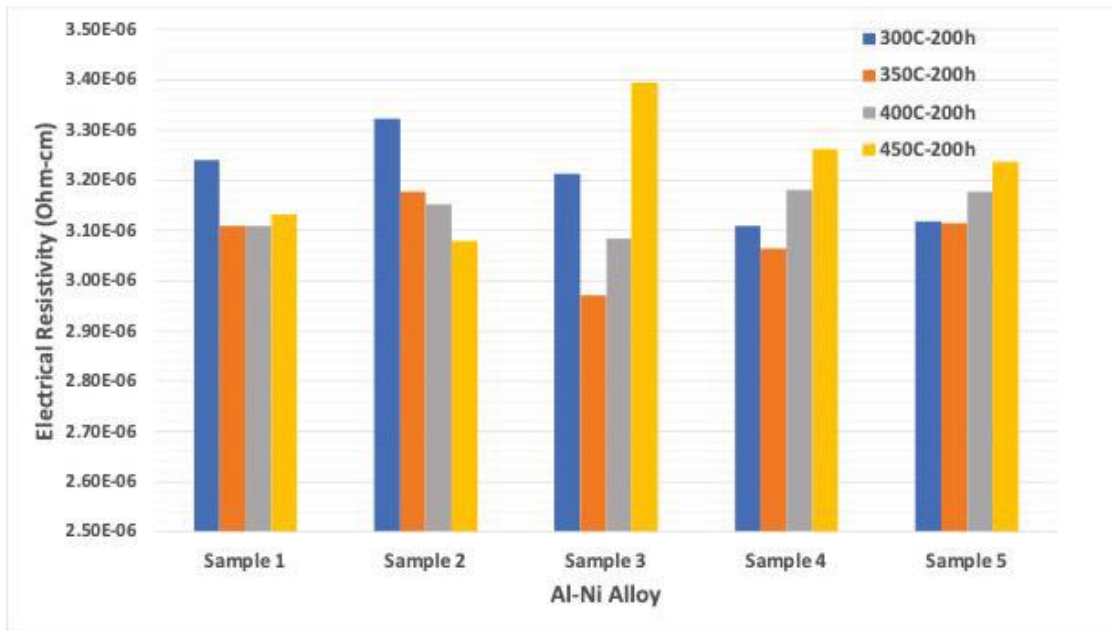


Figure I.1.4.10. Example of RT electrical resistivity of a set of five cast Al-Ni samples for each heat-treatment condition from Task 1A. Source: ORNL.

Metrology for electrical conductivity was another important topic for this task. Several tasks within the program are focused on development of ultra-high conductivity materials. For example, Task 3D, *Novel, Ultra-High Conductivity Materials for EVs*, is developing ultra-conducting tape-based composites combining copper tape and carbon nanotubes. Measurements become more challenging when the specimens are much smaller than standard requirements, and when they have very low electrical resistivities. This task, along with the International Energy Agency Advanced Materials for Transportation organization, planned a virtual workshop in the 3rd Quarter of FY to invite experts in this field for an in-depth discussion on this topic.

Conclusions

In FY 2022, which was year one, Task 4A3 worked closely with the Thrust 1–3 developmental task PIs after presenting characterization capabilities and surveying the related characterization needs across the program team. Testing of electrical and thermal properties began in the second quarter with nine different PMCP Tasks providing materials. In addition to the materials properties, a collaborative relationship with the task PIs was established whereby the understanding developed in these characterization studies was applied to support materials design goals. Materials properties were collected in some cases to support understanding of the influences of materials processing parameters and for a database for development of ML tools for microstructure-properties correlations of cast Al alloys. In the cases where tasks identified new testing needs, two new test systems—a hot-wire thermal conductivity for fluids and an eddy current probe for resistance measurements in non-magnetic materials—were acquired, while a third system for thermal interface analysis was designed and built-in-house at ORNL. A DOE VTO workshop on ultra-high conductivity materials has been planned for the first quarter of FY 2023. Data analysis, reporting, and publications with the Thrust 1–3 PIs are underway.

References

1. ASTM D7896-19, 2019, “Standard Test Method for Thermal Conductivity, Thermal Diffusivity, And Volumetric Heat Capacity of Engine Coolants and Related Fluids by Transient Hot-Wire Liquid Thermal Conductivity Method,” ASTM International, West Conshohocken, PA, USA.
2. ASTM D5470-17, 2017, “Standard Test Method for Thermal Transmission Properties of Thermally Conductive Electrical Insulation Materials,” ASTM International, West Conshohocken, PA, USA.
3. ASTM E1004, 2017, “Standard Test Method for Determining Electrical Conductivity Using the Electromagnetic (Eddy Current) Method,” ASTM International, West Conshohocken, PA, USA.
4. ASTM F1529 – 97, 1997, “Standard Test Method for Sheet Resistance Uniformity Evaluation by Inline Four-Point Probe with the Dual-Configuration Procedure,” ASTM International, West Conshohocken, PA, USA.
5. ASTM C611-21, 2021, “Standard Test Method for Electrical Resistivity of Manufactured Carbon and Graphite Articles at RT,” ASTM International, West Conshohocken, PA, USA.
6. ASTM E1461-13, 2022, “Standard Test Method for Thermal Diffusivity by the Flash Method,” ASTM International, West Conshohocken, PA, USA.
7. ASTM E831-19, 2019, “Standard Test Method for Linear Thermal Expansion of Solid Materials by Thermomechanical Analysis,” ASTM International, West Conshohocken, PA, USA.
8. ASTM E1269-11(2018), 2018, “Standard Test Method for Determining Specific Heat Capacity by Differential Scanning Calorimetry,” ASTM International, West Conshohocken, PA, USA.

Acknowledgements

The authors would like to acknowledge the collaboration on this report with the Thrust 1-3 researchers: S. Kwon, A. Shyam, D. Shin, J. Qu, C. I. Gamaralalage, A. Plotkowski, D. Pierce, and R. Michi. The authors would also like to thank S. Curlin and D. McClurg for their help with the electrical and thermal properties measurements.

I.1.4.3 Task 4A. Advanced Characterization – Argonne Advanced Characterization (Task 4A4) (Argonne National Laboratory)

Dileep Singh, Principal Investigator

Argonne National Laboratory
Applied Materials Division
9700 South Cass Ave.
Lemont, IL 60439
E-mail: dsingh@anl.gov

J. Allen Haynes, PMCP Consortium Manager

Oak Ridge National Laboratory
Materials Science and Technology Division
1 Bethel Valley Rd.
Oak Ridge, TN 37830
E-mail: haynesa@ornl.gov

Jerry Gibbs, DOE Technology Development Manager

U.S. Department of Energy
E-mail: jerry.gibbs@ee.doe.gov

Start Date: October 1, 2021

End Date: September 30, 2023

Project Funding (FY 2022): \$310,000

DOE share: \$310,000

Non-DOE share: \$0

Project Introduction

As part of Thrust 4A for Advanced Characterization support of the PMCP consortium, this report entails the synchrotron x-ray characterizations performed during FY 2022 for two specific projects:

- *Synchrotron x-ray characterizations for understanding the structure and strain state of solid-phase processed nanocarbon in bulk metal (Cu, Al) composites that are produced by shear-assisted processing and extrusion (ShAPETM) method developed at PNNL. ShAPE-processed ultra-high conductivity materials, also known as ultra-conductors, contain minute amounts of nanoscale crystalline carbon additive, such as graphene or carbon nanotubes incorporated into a Cu or Al base metal matrix via ShAPE. The ShAPE ultra-conductors exhibit enhanced electrical properties when compared to their parent (Cu/Al) materials.*

Several nanocarbon features of interest in ShAPE-processed ultra-conductor nanocomposites, such as nanocarbon morphology, topology, defect density, and interfacial integration with the surrounding metal can affect the electrical properties of the conductors. Previous modeling work has shown that these features are crucial in developing high-mobility charge carrier pathways in ultra-conductors [1]. Since the nanocarbon infused into metal matrix by ShAPE is in far-from-equilibrium conditions, the ultra-conductor composites and nanocarbon structures dispersed in them are rather unique. Laboratory XRD systems provide insufficient signal to noise resolution for probing nanocarbon structures. Thus, it requires high-intensity synchrotron x-ray source to resolve structural fingerprints of these carbon nanostructures infused in the metals for developing a comprehensive understanding of the nanostructure formation/distribution in the material. A high-intensity focused beam synchrotron x-ray, which was available at the beamline Sector 33-ID at the APS at ANL, was used for the investigation of nanocarbon structures infused in the metal matrixes in ShAPE-processed ultra-conductors.

- Fe-based castable Alumina-Forming Austenitic (AFA) alloys could potentially be used in automotive engine parts due to their high oxidation and creep resistance.* The overarching goal of this project was to study the fundamental mechanisms governing the enhanced creep properties of AFA alloys developed at ORNL. The correlative electron microscopy and APT studies by PNNL showed that a slight change in composition results in a significant change in the amount of Laves phases and precipitation characteristics of multiple intermetallic phases, which in turn results in a considerable change in creep resistance. The use of synchrotron x-rays was to complement these observations and to confirm the underlying mechanisms for observed improved creep resistance.

Objectives

The overall objective for Thrust 4A is to provide advanced characterization support projects for Thrusts 1, 2, and 3 of the PMCP in order to obtain data and scientific understanding that will be applied to the development of new materials for future advanced EVs. In Task 4A4, this objective is accomplished utilizing the high-intensity focused beam synchrotron x-rays at the APS to carry out μ -diffraction, μ -tomography, and phase studies of new materials for future advanced EVs.

Approach

ShAPE-processed Cu and Al Ultra-conductors

A high-intensity synchrotron X-ray beamline Sector 33-ID at APS, which was designed for focused beam diffraction studies of ShAPE-processed Al and Cu ultra-conductors, was utilized. Using focused beam micro-diffraction, we successfully resolved structural features with peak intensities that are three orders of magnitude weaker when compared to the prime diffraction peaks. For ShAPE-processed Al conductors, large attenuation length ($\approx 500 \mu\text{m}$ for 15 keV photons) allows adequate intensity for carrying out transmission XRD investigation. Transmission synchrotron XRD provides the advantage of increased probing or interaction volume between x-ray beam and the specimen under investigation, as shown in Figure I.1.4.3.1.

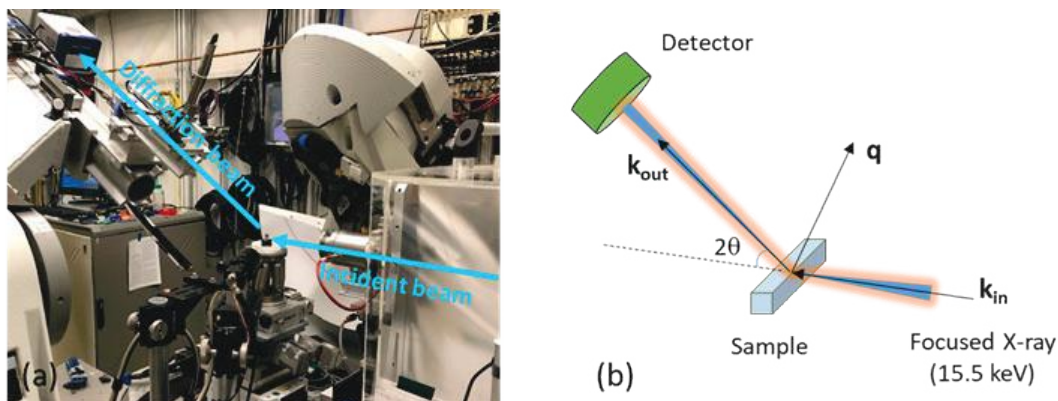


Figure I.1.4.11. (a) Photograph and (b) corresponding schematic drawing of synchrotron XRD arrangement for the study of ShAPE-processed Al specimens received from PNNL. Source: ANL.

Two ShAPE-processed Al thin bar specimens made at PNNL were investigated by high-energy focused beam synchrotron x-ray for diffraction. Sample preparation condition and the dimensional parameters of these two samples are listed in Table I.1.4.3.1. The ‘Al-Control’ sample was processed by ShAPE without adding carbon source, while the “Al-Graphene” was processed by ShAPE with reduced graphene oxide additives. An AA1100-series alloy was used as the parent material. An incident synchrotron beam energy of 15.5 keV was focused on the samples with a spot size of $\approx 20 \mu\text{m}$. We probed the ShAPE Al conductors at different locations across the height/thickness direction and along the length direction for information regarding distribution uniformity of nanocarbon structures. For ShAPE-processed Cu conductors, their attenuation length is substantially smaller ($\approx 30 \mu\text{m}$ for 20 keV photons). A focused synchrotron x-ray beam does not provide adequate intensity to penetrate through ShAPE Cu ultra-conductor specimens of 2-mm-diameter received from PNNL. Thus, we conducted micro-diffraction with a 20 keV beamline focused at $\approx 20 \mu\text{m}$ below the sample

surface in reflection mode and measured at different locations along the length direction to probe the distribution uniformity of nanocarbon features infused in the Cu matrix by ShAPE process. Such an experimental setup enabled the reliable measurement with good statistics of small satellite peaks of orders of magnitude weaker when compared to the prime Cu diffraction peaks. With graphitic carbon infused in Cu ultra-conductors by the ShAPE process, we observed a peak split associated with graphitic nanocarbon structures infused in a Cu matrix, as well as the Cu_2O diffraction peaks associated with surface oxidation of ShAPE Cu ultra-conductors. Our experiments demonstrated that synchrotron XRD technique is an effective and reliable approach for the characterization of nanocarbon structures and their distribution in the ShAPE-processed Al and Cu ultra-conductors.

Table I.1.4.3.1. ShAPE-processed Al Ultra-Conductor Samples Characterized by Synchrotron X-ray Diffraction at APS

Sample ID	Description	Height (mm)	Width (mm)	Length (mm)
Al-Control	Al-control sample without carbon addition produced by ShAPE	1.35	1.15	30.3
Al-Graphene	Al ultra-conductor produced by ShAPE with 0.1 wt.% reduced graphene oxide as carbon source in feedstock	1.35	1.10	33.2

AFA Alloys

HE-XRD was used to determine the amount of minor phases (i.e., Laves and other intermetallic phases, such as carbides) as a function of location, and x-ray micro-computed tomography (μ -CT) was employed to determine the change in distribution of pore and precipitate characteristics (i.e., size and shape). The HE-XRD and μ -CT experiments were performed at the 1-ID-E beamline in the APS using a monochromatic x-ray beam of energy of 71.676 keV. The experimental setup at the beamline is shown in Figure I.1.4.3.2. A probe volume of approximate dimensions of $0.2 \times 1 \times 1 \text{ mm}^3$ was used at specific locations along the crept/fractured sample for both characterizations. The diffraction measurement involved a 360° rotation of the sample while being exposed to the x-ray beam to acquire several two-dimensional diffraction patterns; a summed diffraction pattern from the 36 frames was used for the analysis in the General Structure Analysis System, GSAS-II, software. This step was performed to ensure sufficient information about the minor phases is captured for the analysis. As can be seen in Figure I.1.4.3.2, the μ -CT detector was placed closer to the sample (nominally 150 mm) as compared to the x-ray detector. Several radiographs were acquired using a complementary metal-oxide semiconductor (CMOS) camera while rotating the specimen from 0° to 360° and were reconstructed using the Gridrec algorithm in the TomoPy software package to obtain the cross-sectional slices needed for the 3D reconstruction of the probed volume. The measurement yielded a pixel resolution of $1.17 \mu\text{m}$, and therefore, a single voxel volume of $1.61 \mu\text{m}^3$.

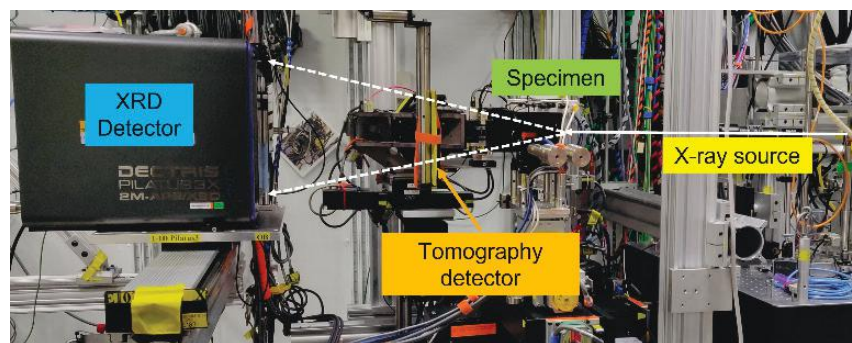


Figure I.1.4.12. Experimental setup showing the diffraction and tomography detectors at beamline 1-ID in the APS, where the x-ray beam path is marked in white with a solid line showing the incident beam and dashed lines representing the transmitted/diffracted beams. Source: ANL.

Results

ShAPE Ultra-conductors

We successfully conducted transmission diffraction investigation with ShAPE-processed Al conductor samples and the results are shown in Figure I.1.4.3.3. With such an experimental arrangement, an XRD pattern is measured at a spot which is the average across the width direction at the spot. To investigate material uniformity of the received specimens, we collected diffraction patterns at three different positions across the height direction. The ‘top,’ ‘middle,’ and ‘bottom’ positions separated by 400 μm were measured with each sample, as illustrated by the insets shown in Figure I.1.4.3.3(a) and Figure I.1.4.3.3(b). In addition to the prime peaks associated with Al, we observed small peaks of intensities that are about three orders of magnitude weaker in intensity. These small peaks are associated with an intermetallic phase and exist in the AA1100 series alloys [1] used as starting materials for making ‘Al-Control’ and aluminum-graphene (‘Al-Gr’) samples by ShAPE-processing. XRD patterns shown in Figure I.1.4.3.3(c) were measured at nine different spots along the length direction with two adjacent spots separated by 200 μm . All diffraction patterns of ‘Al-Control’ and ‘Al-Gr’ samples produced by the ShAPE process are virtually the same as shown in Figure I.1.4.3.3, indicating that the ShAPE process samples are uniform with respect to the length scale of our investigations. We observed no difference in the diffraction patterns of the ‘Al-Control’ and the ‘Al-Gr’ sample under this investigation. Since reduced graphene oxide was used as feedstock for incorporation into the ‘Al-Gr’ sample made by ShAPE-processing, it is possible that the graphene in the resulting ‘Al-Gr’ sample exists in the form of single- or multilayer (no more than a few layers) graphene.

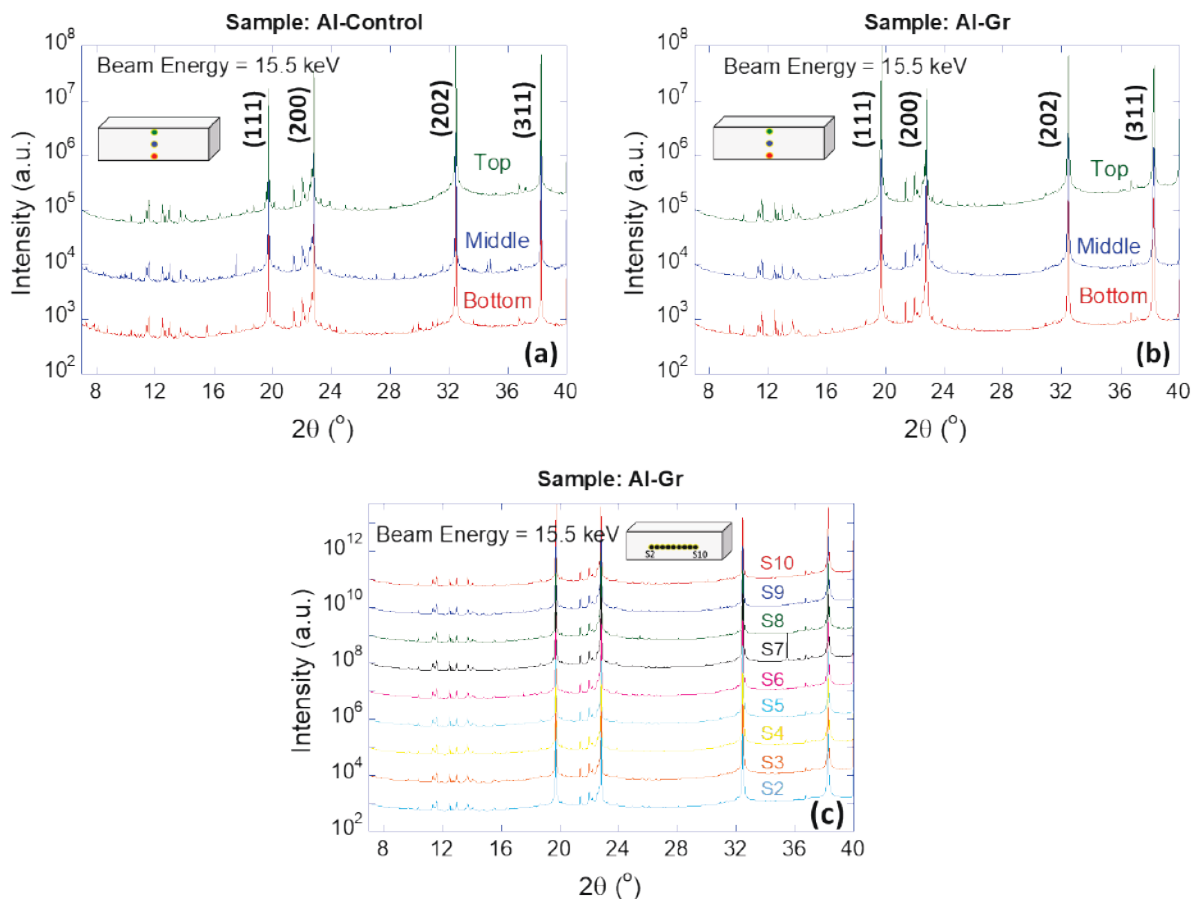


Figure I.1.4.13. Synchrotron XRD patterns of (a) the Al-Control sample, (b) the Al-Gr measured across height direction, and (c) the Al-Gr sample measured along length direction. Source: ANL.

ShAPE-processed Cu ultra-conductors with graphitic carbon and CVD graphene as carbon sources, respectively, in the starting materials were investigated. Both samples contained ≈ 100 ppm carbon and were produced by ShAPE-processing with oxygen-free high conductivity Cu as a parent material. As listed in Table I.1.4.3.2, these two cylindrical specimens, as received from PNNL, are 2.0 mm in diameter and approximately 12.5 mm long. The Cu-171 ultra-conductor sample was produced by ShAPE-processing with graphitic carbon in the feedstock, while a Cu-184 ultra-conductor sample was produced by ShAPE-processing with CVD graphene as a carbon source in the feedstock. A synchrotron x-ray beam of 20.0 keV photon energy was used for this experiment. Due to the small attenuation length in the Cu materials, an incident beam was focused at ≈ 20 μm below the surface of the cylindrical specimens, which were mounted horizontally on a specimen holder, as observed in Figure I.1.4.3.4(a). For 20.0 keV synchrotron x-ray beam, the attenuation length in Cu samples is ≈ 30 μm . A schematic drawing of the sample with respect to the measurement beam is illustrated in Figure I.1.4.3.4(b).

Table I.1.4.3.2. ShAPE-processed Cu Ultra-Conductor Samples Characterized by Synchrotron X-ray Diffraction at the APS

Sample ID	Description	Diameter (mm)	Length (mm)
Cu-171	Cu ultra-conductor produced by ShAPE with graphitic carbon in feedstock	2.0	12.5
Cu-184	Cu ultra-conductor produced by ShAPE with CVD graphene in feedstock	2.0	12.5

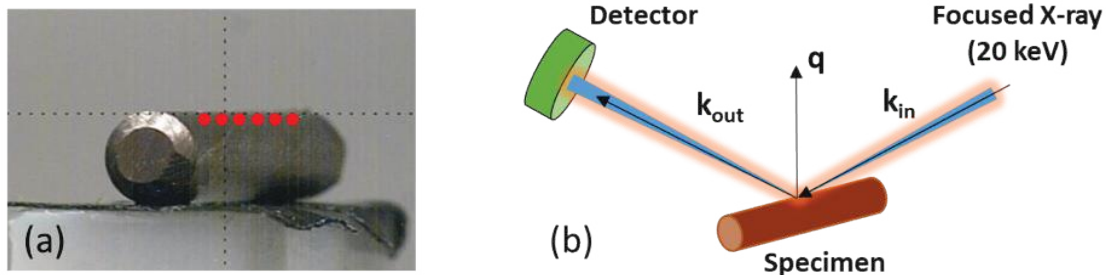


Figure I.1.4.14. (a) Photograph of cylindrical Cu ultra-conductor sample mounted horizontally on sample holder; and (b) schematic drawing of synchrotron X-ray diffraction arrangement for the study. Source: ANL.

Measurements were conducted at six different locations along the length direction with two adjacent locations separated by 500 μm . X-ray diffraction patterns of sample Cu-171 and Cu-184 are shown in Figure I.1.4.3.5.. In addition to the prime Cu peaks, we observed small peaks that are ≈ 3 orders of magnitude lower in intensity associated with infused graphite (at $2\theta \approx 11^\circ$) and Cu_2O (at $2\theta \approx 14^\circ$ and $\approx 23^\circ$). The Cu_2O diffraction peaks are due to surface oxidation at RT under ambient atmosphere [2]. Distribution of Cu_2O phase is uniform, as shown in the top of Figure I.1.4.3.5.. In contrast, peak shape and intensity of graphite (002) peak varies from location to location possibly indicating a non-uniform distribution of graphitic carbon in sample Cu-171. The peak split and variation in relative intensity suggesting that the topological structure of graphitic carbon infused by ShAPE-processing is also varying. It is possible that additional ShAPE process optimization is required to produce a graphitic carbon containing ultra-conductor sample with enhanced uniformity.

When compared with these diffraction patterns of sample Cu-171, as shown in the top of Figure I.1.4.3.5., we observed that much weaker peaks for sample Cu-184 were associated with Cu_2O (111) and Cu_2O (220) at $2\theta \approx 14^\circ$ and $2\theta \approx 23^\circ$, respectively. No diffraction peaks associated with graphite (at $2\theta \approx 11^\circ$) was observed. This suggests that the CVD graphene exists in ShAPE Cu ultra-conductor in the form of single- or multilayer graphene after ShAPE process. We observed small Cu_2O diffraction peaks at some locations, but not at other locations, as shown in the bottom of Figure I.1.4.3.5..

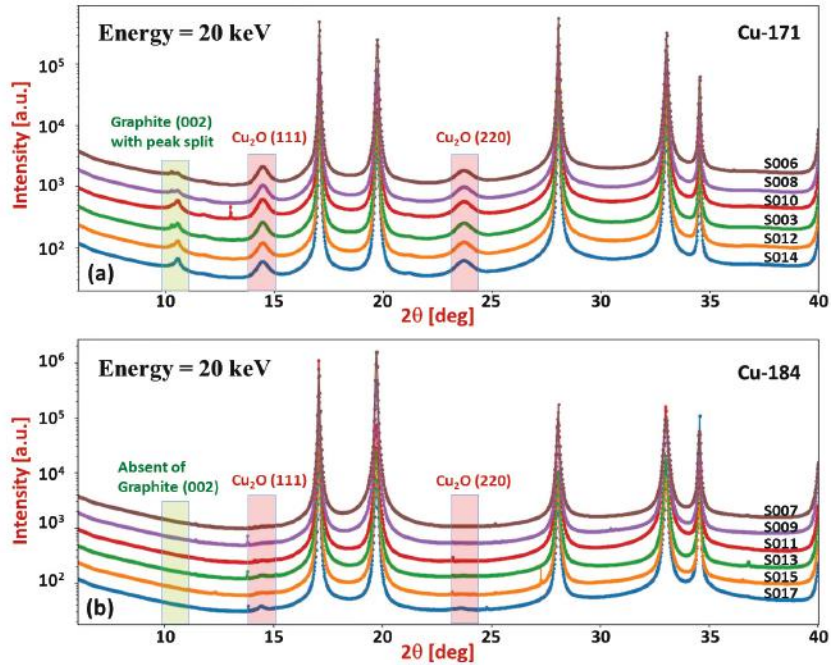


Figure I.1.4.15. Synchrotron XRD patterns of samples Cu-171 (top) and Cu-184 (bottom) measured at different spots along length direction. Source: ANL.

AFA Alloys

The HE-XRD patterns and μ -CT reconstructions for both of ORNL’s AFA alloy compositions, as shown in Figure I.1.4.3.6, in their as-cast and crept states are shown in Figure I.1.4.3.7(a) and Figure I.1.4.3.7(b), respectively. Figure I.1.4.3.7(a) shows a clear difference in phase content of the Laves and other intermetallic phases—seen as a difference in peak intensity—in line with the microscopy results from PNNL. The amounts of detrimental intermetallic phases and carbides (e.g., Laves, B2, NbC, $M_{23}C_6$) in AFA5 were lower than those in AFA2. This was achieved by balancing key alloying elements (i.e., Nb, Ni, Mo), which supported the increased creep resistance in AFA5. Figure I.1.4.3.7(b) shows the typical size and distribution of features (pores and/or precipitates) in sample AFA5. The smaller size features are observed to be more in number as compared to large size features in both the as-cast and crept states, in addition to the number density and size of these features seen to increase after creep testing. AFA5 with lower alloying element content showed slower coarsening of the observed features during creep testing than those in AFA2 (not shown in the figure), which were also consistent with the increased creep resistance in AFA5. μ -CT also allows for quantification of the feature density and morphologies as a function of alloy composition and test conditions, as shown in Figure I.1.4.3.7(b), which makes it a versatile tool in comparing the alloys post-creep testing and/or with varying alloy compositions.

Alloy	Composition, wt.%																			Remarks	
	Fe	Ni	Cr	Al	Cu	Mn	Mo	Nb	Si	Ti	W	Zr	Y	C	B	N	S	O	P		
AFA2	Nominal	47.69	25	15	4	0.5	2	2	1	1	0.2	1	0.1	0.1	0.4	0.01	-	-	-	-	Target
	Analyzed	48.04	25.01	15.06	3.81	0.48	1.92	2.05	0.76	0.96	0.19	1.15	0.11	0.027	0.40	0.0075	<0.0020	0.0008	0.0012	<0.0050	VA02-2 (#21347)
AFA5	Nominal	51.69	22	17	4	-	2	1	0.6	0.5	-	0.5	0.1	0.1	0.5	0.01	-	-	-	-	Target
	Analyzed	51.15	22.2	17.43	3.91	<0.01	1.97	1.05	0.62	0.44	<0.01	0.54	0.11	0.039	0.51	0.0113	<0.0020	0.0008	0.0005	0.0075	VA05-2 (#21349)

Figure I.1.4.16. Compositions of the AFA alloys produced at ORNL. Source: ORNL

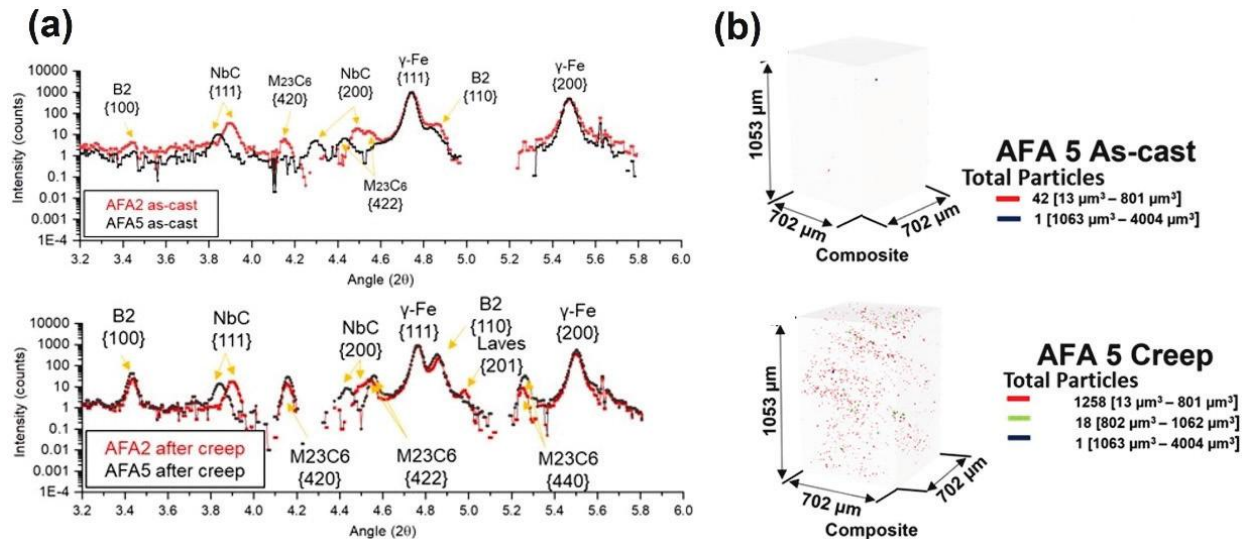


Figure I.1.4.17. (a) HE-XRD spectra of the AFA alloys with two different compositions in two different states (i.e., as-cast and crept). (b) 3D μ -CT reconstructions of the as-cast and crept conditions of one alloy, color coded by feature (pore/precipitate) volume. Source: ANL.

Conclusions

Synchrotron XRD is effective in characterizing nanocarbon structures and their distribution in the ShAPE-processed Al and Cu ultra-conductors. Graphene carbon structures infused into Al and Cu ultra-conductors produced by ShAPE process are uniformly distributed when compared to samples made with graphitic carbon in the feedstock, which could lead to enhanced electrical conductivity.

ORNL's AFA alloys in their as-cast and crept states were characterized using HE-XRD and μ -CT. The results showed that by tuning the alloying elements the detrimental intermetallic phases could be reduced, leading to enhanced creep resistance. These results corroborated with microscopy observations.

Key Publications

Two journal publications are currently being drafted on the work reported here.

References

- Gwalani, B., M. Pole, K. E. Whalen, S. Li, B. T. O'Callahan, J. Tao, A. K. Nittala, and K. Kappagantula, 2021, "Evaluating Effects of Shear Processing on 2D Crystalline Materials in 3D Metal Matrices," PNNL-32102. Pacific Northwest National Laboratory, Richland, WA, USA.
- Choudhary, S., J. V. N. Sarma, S. Pande, S. Ababou-Girard, P. Turban, B. Lepine, and S. Gangopadhyay, 2018, "Oxidation mechanism of thin Cu films: A gateway towards the formation of single oxide phase," *AIP Adv.*, Vol. 8, Art. 055114. <https://doi.org/10.1063/1.5028407>.

Acknowledgements

The task leads for the ultra-conductors and AFA alloys projects from PNNL were K. Kappagantula and B. Gwalani, respectively. Their valuable insights and providing samples is greatly appreciated. Contributions by B. Ma and Z. Zhang (ultra-conductors) and J. Thomas, A. Chuang, and R. Kamath (AFA alloys) at ANL in conducting the APS experiments and data analysis is also acknowledged. Helpful discussions with Y. Yamamoto and T. R. Watkins (ORNL) and A. Devraj (PNNL) are appreciated as well. This research used resources of the APS, which is a DOE-SC user facility operated for the DOE-SC by ANL under Contract No. DE-AC02-06CH11357.

I.1.4.4 Task 4A. Advanced Characterization – Pacific Northwest National Laboratory Advanced Characterization (Task 4A5) (Pacific Northwest National Laboratory)

Arun Devaraj, Principal Investigator

Pacific Northwest National Laboratory
Physical Metallurgy Division
902 Battelle Blvd.
Richland, WA 99354
E-mail: arun.devaraj@pnnl.gov

J. Allen Haynes, PMCP Consortium Manager

Oak Ridge National Laboratory
Materials Science and Technology Division
1 Bethel Valley Rd.
Oak Ridge, TN 37830
E-mail: haynesa@ornl.gov

Jerry Gibbs, DOE Technology Development Manager

U.S. Department of Energy
E-mail: jerry.gibbs@ee.doe.gov

Start Date: October 1, 2019

End Date: September 30, 2023

Project Funding (FY 2022): \$340,000

DOE share: \$340,000

Non-DOE share: \$0

Project Introduction

This report summarizes the FY 2022 progress on advanced microstructural characterization of materials conducted at PNNL for the PCMP as follows:

- *Project 1: Advanced characterization of oxide formed on Ni-Cr-Mn-Si (NCMS) alloy.* Ni-Cr based alloys are promising for propulsion applications. However, the atomic scale mechanisms of high-temperature oxidation of these alloys, especially in the presence of water vapor, is still not well understood. Hence, this project was focused on advanced characterization of oxides formed on NCMS alloys during high-temperature oxidation both with and without moisture using advanced microstructural characterization capabilities at PNNL.
- *Project 2: Nanomechanical testing of additively manufactured Al-Ce-Ni-Mn alloy.* Laser powder bed fusion-based AM was shown to be a promising method by ORNL to fabricate creep-resistant Al-RE alloys (e.g., Al-Ce-Ni-Mn) with stable microstructures up to 400°C. As creep testing of these alloys at high temperatures show that void coalescence and failure initiation occur along the MPB in the microstructure, understanding how the local mechanical behavior of the MPB influences the global properties of the AM alloy is crucial. Hence, this Thrust 4 project was focused on analyzing the influence of microstructural heterogeneity on nanomechanical properties of laser powder bed fusion AM Al-Ce-Ni-Mn alloys.

Projects 3 and 4, which are described below, are currently ongoing. Additional work is being conducted on both in FY 2023:

- *Project 3: Advanced characterization of Al₂O₃-TiB₂ composites:* For developing hybrid dispersion strengthened Al matrix composites for cost-effective lightweight alloys for EV propulsion, the Al₂O₃-TiB₂ composites were produced through *in-situ* reactions of titanium (Ti) and boron containing halide salts with the molten Al₂O₃ alloy. The microstructure of such *in situ* formed composites needs to be understood and optimized to best engineer these composites and achieve optimum mechanical

properties. This task is focused on revealing the microstructure of *in situ* Al206-TiB₂ composites using advanced characterization.

- **Project 4: Advanced characterization of friction stir processed Fe-Si alloys:** Rolled sheet laminates of ferromagnetic (Fe-2-3 wt% Si) material are used as a magnetic core for induction rotors and stators. However, the current manufacturing technology for Fe-Si steels is costly and leads to high rejection rates due to the low formability of high-Si-containing alloys. Significant cost-savings could be achieved if high-Si steel can be produced with better formability. Therefore, solid-phase processing-based manufacturing technologies are being explored at PNNL to produce high-performance Fe-Si steels for low-cost, efficient, and lightweight EV motors. The focus of this task is to use advanced characterization to analyze the microstructure of friction stir processed Fe-Si alloys for high-formability, high-resistivity, and low-coercivity high silicon steel for rotor cores.

Objectives

The overall objective for Thrust 4A5 is to provide advanced characterization support for Thrusts 1, 2, and 3 of the PMCP in order to obtain data and scientific understanding that will be applied to the development of new materials for future advanced EVs.

Approach

Specific approaches for each task are described in the sections that follow.

Project 1: Advanced characterization of oxide formed on NCMS alloy.

Rectangular (20 × 10 × 1.5 mm) coupons of model NCMS alloys, as observed in Table I.1.4.4.1, were received from ORNL and investigated. Before exposure, the specimens were ground to a 600-grit finish and ultrasonically cleaned in acetone and methanol. Samples were exposed in automated cyclic rigs at ORNL in 1 h cycles in dry air and air + 10% H₂O (wet air) flowing at 500 cm³.min⁻¹ (velocities of 0.60-0.68 cm.s⁻¹) between 80 and 500 h. The specimens were heated to the test temperature in the aforementioned atmosphere and kept at temperature for 1 h before cooling to RT over 10 min. After oxidation, cross-sections were prepared, Cu-plated, and mounted in conductive epoxy mounts for metallographic analyses. The mounted samples were ground to a 1200 grit finish using silicon carbide grinding paper and subsequently polished with diamond paste to a 1 μm surface finish. The final polishing step was made using colloidal silicon oxide (SiO₂) slurry. The microstructures of the oxidized samples were analyzed first using SEM. Samples for TEM and APT were then prepared from the oxide layer through a site-specific lift-out process using dual beam FIB SEM [1]. Detailed TEM and APT analyses were conducted to analyze the structure and composition of the multilayered oxides. The APT measurements were carried out using a local electrode atom probe system equipped with a 355 nm wavelength ultraviolet laser. Analyses were performed using the Integrated Visualization and Analysis Software.

Table I.1.4.4.1. NCMS Alloy Composition

Composition	Ni	Cr	Mn	Si
wt.%	76.86	21.17	1.43	0.50
at.%	74.32	23.11	1.48	1.01

Project 2: Nanomechanical testing of additively manufactured Al-Ce-Ni-Mn alloy.

One sample of Al-Ce-Ni-Mn alloy with dimensions of 5 × 5 × 2 mm from the as-processed laser powder bed fusion AM Al-Ce-Ni-Mn alloy from ORNL was sectioned and polished using standard metallographic techniques [2]. The elemental composition of the Al-Ce-Ni-Mn alloy is given in Table I.1.4.4.2. The specimen was then mounted on a standard SEM stub using fast-curing conductive silver paste. Cylindrical micropillars of dimensions 5 μm diameter and 10 μm height (1:2 aspect ratio) were milled into the cross-section of the bulk specimen using the xenon ions of a plasma FIB microscope. To avoid any damage on the surface, the pillar surfaces were subjected to a final cleaning step using 100 picoamp current and 30 kilovolt voltage. One pillar was milled targeting the MPBs and one within the melt pool interiors (MPIs) to obtain a comparison of their

mechanical properties. Micro-compression tests at ambient temperature were then performed *in situ* using the PI89 picoindenter. The pillars were deformed with a flat-punch diamond indenter tip in a displacement controlled mode at a constant rate of 50 nm/sec. Live deformation videos were captured using the SEM, and the resulting load vs. displacement data were converted into engineering stress vs. strain curves. The compliances induced from the base of the micropillars (e.g., substrate effect) and the indenter tip were subtracted from the displacement recorded by the picoindenter. These corrected displacements were then used to calculate the actual strains during testing. Material-specific parameters, such as yield strength (YS) and ultimate tensile stress (UTS) from each pillar test were then calculated.

Table I.1.4.4.2. Al-Ce-Ni-Mn Alloy Composition

Element	Al	Ce	Ni	Mn
Composition (wt.%)	84.92	10.50	3.09	1.18

Project 3: Advanced characterization of Al206-TiB2 composites.

Composites containing 5 vol. % in situ formed TiB₂ dispersions in Al206 alloy obtained from Task 1H members at PNNL were metallographically polished. The microstructure was characterized by SEM and EDS. Based on the SEM-EDS results, specific regions were selected for preparing TEM and APT samples using a FIB microscope.

Project 4: Advanced characterization of friction stir processed Fe-Si alloys.

Sectioned samples of Fe - 3 wt.% Si alloys were obtained from the Task 2E team members at PNNL in the form of cast billet and friction stir processed alloys with peak temperatures from 750–850°C in 25°C increments. All samples were metallographically polished. SEM backscattered electron imaging of the samples was conducted to analyze the variation in microstructure as a function of the friction stir processed peak temperature. Specific regions from the microstructure were identified for FIB-based sample preparation for TEM and APT. Similar studies are currently under progress for Fe - 6 wt.% Si alloys.

Results

Project 1: Advanced characterization of oxide formed on NCMS alloy.

TEM bright-field images of NCMS alloy after oxidation in dry air and wet air are shown in Figure I.1.4.4.1. In dry air, a columnar grain microstructure was observed below the MnCr₂O₄ layer and equiaxed grains closer to the alloy-oxide interface. In wet air, only equiaxed grains were formed and were slightly finer than in dry air. An increase in Cr₂O₃ grain size from the alloy-oxide interface toward the gas/oxide interface was measured, with a slightly larger increase in dry air than in wet air. The median grain sizes were 420 ± 222 μm and 301 ± 125 μm in dry and wet air, respectively. In addition, on top of the multi-layered Cr₂O₃ scale, a single-layered MnCr₂O₄ scale was observed and measured to be about 600 and 900 nm thick in wet and dry air, respectively. Figure I.1.4.4.2 displays the 3D atomic maps from the APT analyses performed at the SiO₂/Cr₂O₃ interface in dry air and at the alloy/Cr₂O₃ interface in wet air. The clear presence of Siⁿ⁺, Mnⁿ⁺, and Oⁿ⁺ at the Cr₂O₃ grain boundaries in dry air oxidized alloy is evident. However, no grain boundary or SiO₂ precipitate could be isolated in wet air, as seen with the presence of Ni derivatives (Niⁿ⁺, NiO_xHⁿ⁺) from the underlying alloy. Such detailed comparison of TEM and APT results from dry air and wet air oxidized alloy is now permitting a comprehensive understanding of elemental transport pathways occurring during high-temperature oxidation.

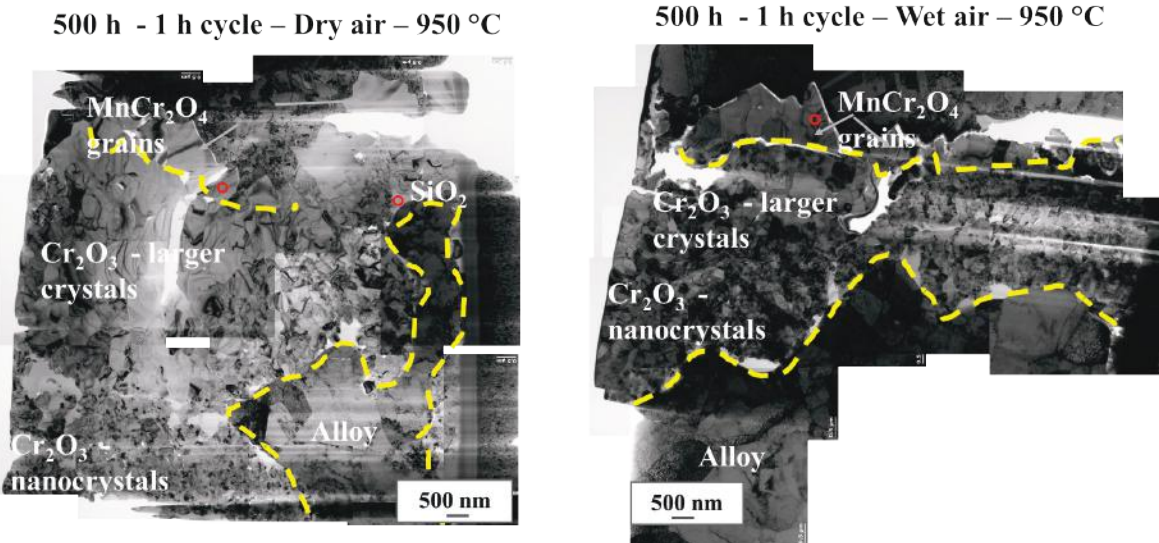


Figure I.1.4.18. TEM bright-field montages of NCMS alloy oxidized in dry air vs. wet air for 500 hours at 950 °C. Source: PNNL.

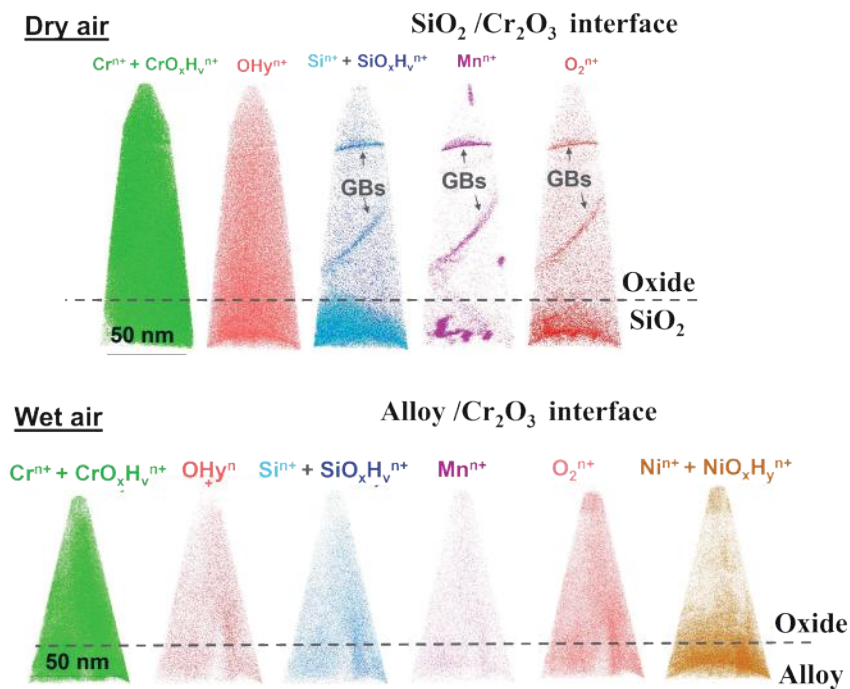


Figure I.1.4.19. APT analysis of NCMS alloy oxidized in dry air vs. wet air for 500 hours at 950 °C showing elemental segregation differences. Source: PNNL.

Project 2: Nanomechanical testing of additively manufactured Al-Ce-Ni-Mn alloy.

A comparison of the SEM image of the deformed micropillars and the stress vs. strain curves for both the tested pillars on/near MPBs vs. away from the MPBs, are shown in Figure I.1.4.4.3(a–c). The calculated YS at 2% strain is 310 MPa for pillar 1 (MPB) and 493 MPa for pillar 2 (MPI), respectively, highlighting the weaker melt pool boundaries. The MPBs can thus be considered as a contributing factor to the heterogeneity at a small-scale and justify the observed cracking along the MPBs at a bulk-scale for Al-Ce-Ni-Mn alloy. This study highlights that understanding the local nanomechanical properties of MPBs in AM alloys may be critical

for developing processing conditions and post-fabrication heat treatments that can then be optimized to avoid property heterogeneities in the microstructures.

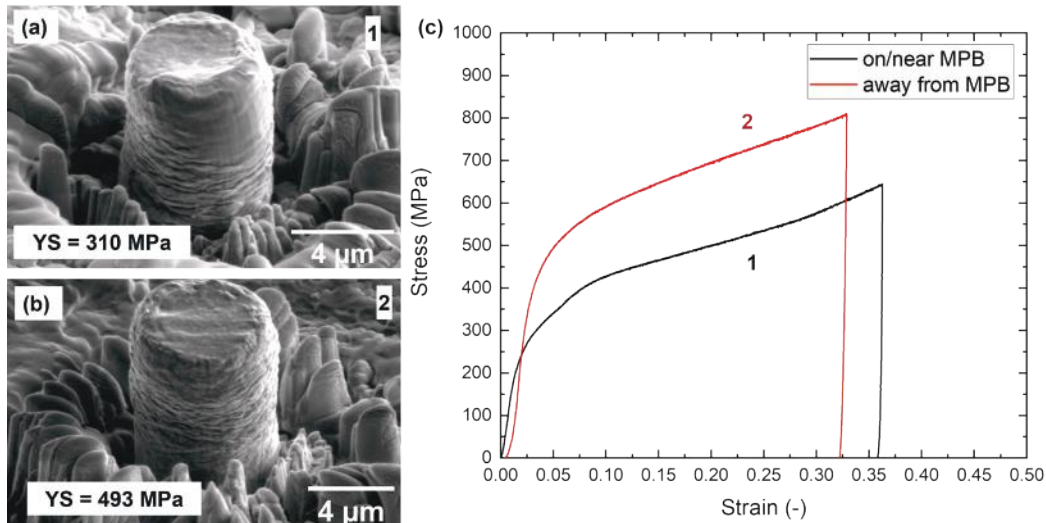


Figure I.1.4.20. Deformed micropillars from (a) on/near MPB and (b) away from MPB with the corresponding stress-strain graphs in (c). Source: PNNL.

Project 3: Advanced characterization of Al206-TiB₂ composites.

From SEM imaging of the 5 vol.% TiB₂ composite, it was seen to have minimal amount of dross and Al₃Ti intermetallic particles, as observed in Figure I.1.4.4.4.. The cleanliness of the as-cast product was due to lower TiB₂, which reduced the viscosity at the molten state. The majority of the TiB₂ are accumulated at the grain boundaries, while some ~ 100 nm sized dispersions are also present inside the grains. Large Al₂Cu precipitates are also present at the grain boundaries. The clustering of particles is likely due to the slow cooling rates associated with the gravity casting method used in this sample.

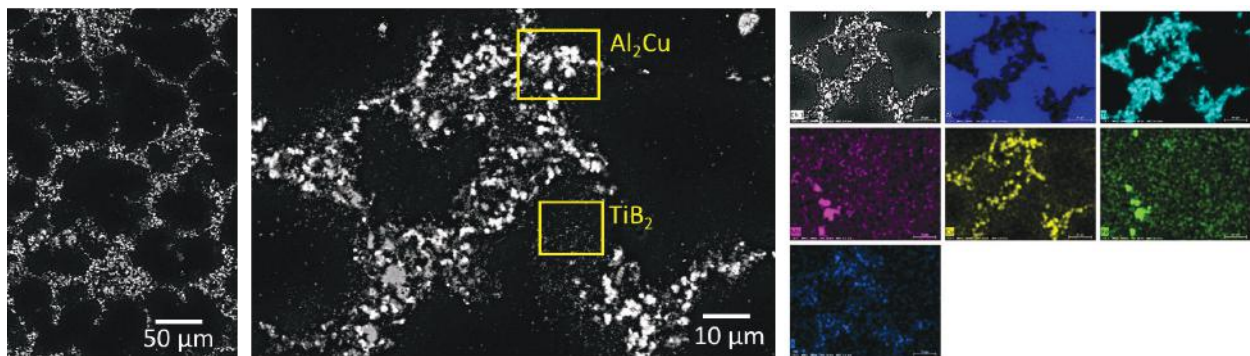


Figure I.1.4.21. SEM images and EDS maps of the Al₂₀₆-5 vol.% TiB₂ composite. Color code for the EDS maps – blue: aluminum; teal: titanium; pink: manganese; yellow: copper; lime: iron; and dark blue: boron. Source: PNNL.

The high-resolution TEM study will start after the composite production work is finalized. The results obtained in the initial SEM study will serve as a guideline for the TEM study. Particular regions-of-interest with sub-micron-sized TiB₂ particles and their interfaces with the Al₂Cu precipitates will be studied in the future using TEM and APT.

Project 4: Advanced characterization of friction stir processed Fe-Si alloys.

Linear friction stir processed Fe-3(wt.%) Si alloy at various peak temperatures were metallographically polished to analyze the change in microstructure. The microstructures of the as-cast base alloy—denoted as BASE and after friction stir processing at various peak temperatures—were analyzed using backscattered electron imaging in a SEM, as observed in Figure I.1.4.4.5. The base Fe-3 wt.% Si alloy has large grains with an average grain size of 144 μm . A high degree of grain refinement was observed in the nugget region formed by friction stir processing. Within the friction stir processed microstructure, the higher temperature processing (850°C) results in a larger grain size (~21 μm) when compared with 750°C processed microstructure (~12 μm). This clear change in grain size also leads to a corresponding change in the mechanical properties. Next steps include analyzing the microstructure of higher Si compositions up to 6 wt.% Si. Selected friction stir processed Fe-Si samples that perform at two extreme ends of formability characteristics will be downselected for additional advanced characterization. FIB-SEM, TEM, and APT will be conducted on these samples at different regions-of-interest. In addition, magnetic domain measurements using magnetic atomic force microscopy will also be used to directly correlate microstructure to local magnetic properties.

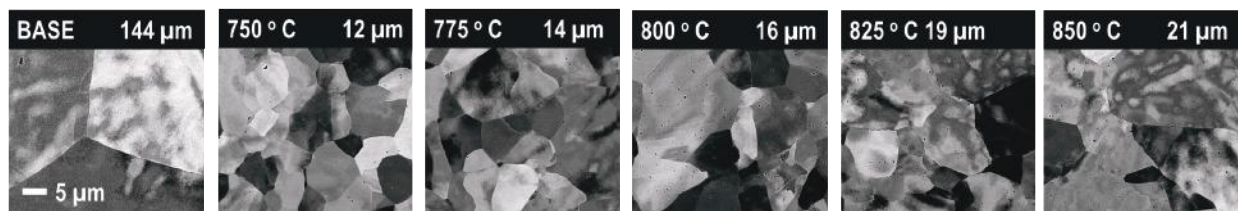


Figure I.1.4.22. Change in grain size of Fe-3 % Si alloy from base alloy as a function of friction stirred processing temperature. Source: PNNL.

Conclusions

Across all four tasks, advanced microstructural characterization is revealing key atomic scale insights on processing-microstructure-mechanical property relationships and material degradation mechanisms for materials relevant to PMCP. This synergy between advanced characterization conducted under Thrust 4 and material development activities conducted in Thrusts 1 to 3 can help design next-generation materials with extraordinary properties for future EVs.

Key Publications

1. Ajantiwalay, T., R. Michi, C. Roach, A. Shyam, A. Plotkowski, and A. Devaraj, 2022, “Influence of microstructural heterogeneities on small-scale mechanical properties of an additively manufactured Al-Ce-Ni-Mn alloy,” *Addit. Manuf. Lett.*, Vol. 3, Art. 100092. <https://doi.org/10.1016/j.addlet.2022.100092>.
2. Gwalani, B., J. Liu, S. Lambeets, M. Olszta, J. Poplawsky, A. Shyam, and A. Devaraj, 2022, “Rapid assessment of interfacial stabilization mechanisms of metastable precipitates to accelerate high-temperature Al alloy development,” *Mater. Res. Lett.*, Vol. 10, No. 12, pp. 771–779. <https://doi.org/10.1080/21663831.2022.2102947>.
3. Liu, J., R. Kannan, D. Zhang, T. Liu, P. Nandwana, and A. Devaraj, 2022, “Multiscale characterization of supersolidus liquid-phase sintered H13 tool steel manufactured via binder jet additive manufacturing,” *Addit. Manuf.*, Vol. 56, Art. 102834. <https://doi.org/10.1016/j.addma.2022.102834>.

References

1. Devaraj, A., D. E. Perea, J. Liu, L. M. Gordon, T. J. Prosa, P. Parikh, D. R. Diercks, S. Meher, R. P. Kolli, Y. S. Meng, and S. Thevuthasan, 2018, “Three-dimensional nanoscale characterisation of materials by atom probe tomography,” *Int. Mater. Rev.*, Vol. 63, No. 2, pp. 68–101. <https://doi.org/10.1080/09506608.2016.1270728>.
2. Michi, R. A., K. Sisco, S. Bahl, Y. Yang, J. D. Poplawsky, L. F. Allard, R. R. Dehoff, A. Plotkowski, and A. Shyam, 2022, “A creep-resistant additively manufactured Al-Ce-Ni-Mn alloy,” *Acta Mater.*, Vol. 227, No. 117699. <https://doi.org/10.1016/j.actamat.2022.117699>.

Acknowledgements

The task leads for the ultra-conductors and AFA alloys projects from PNNL were K. Kappagantula and B. Gwalani, respectively. Their valuable insights and providing samples is greatly appreciated. Contributions by B. Ma and Z. Zhang (ultra-conductors) and J. Thomas, A. Chuang, and R. Kamath (AFA alloys) at ANL in conducting the APS experiments and data analysis are also acknowledged. Helpful discussions with Y. Yamamoto and T. R. Watkins (ORNL) and A. Devraj (PNNL) are appreciated as well. This research used resources of the APS, which is a DOE-SC user facility operated for by ANL under Contract No. DE-AC02-06CH11357.

For project 1, the key contributors were R. Pillai and M. Romedenne from ORNL, as well as S. Lambeets, M. Wirth, and C. Roach from PNNL. For project 2, the key contributors were R. Michi, A. Shyam, and A. Plotkowski from ORNL, as well as T. Ajantiwalay and C. Roach from PNNL. For project 3, the key contributor was M. Efe. The composites were manufactured and characterized at Loukus Technologies, Inc., in Calumet, MI, by A. Loukus and S. Kastamo. For project 4, the key contributors were H. Das, S. Shukla, M. Pole, X. Ma, B. Gwalani, P. Upadhyay, S. Lambeets, and T. Liu at PNNL. For T4 coordination in PMCP, contributions from T. Watkins and A. Haynes from ORNL and D. Herling from PNNL are acknowledged.

I.1.4.5 Task 4B. Advanced Computation – Advanced Computational Materials (Task 4B1) (Oak Ridge National Laboratory)

Dongwon Shin, Principal Investigator

Oak Ridge National Laboratory
Materials Science and Technology Division
1 Bethel Valley Rd.
Oak Ridge, TN 37830
E-mail: shind@ornl.gov

J. Allen Haynes, PMCP Consortium Manager

Oak Ridge National Laboratory
Materials Science and Technology Division
1 Bethel Valley Rd.
Oak Ridge, TN 37830
E-mail: haynesa@ornl.gov

Jerry Gibbs, DOE Technology Development Manager

U.S. Department of Energy
E-mail: jerry.gibbs@ee.doe.gov

Start Date: November 1, 2021	End Date: September 30, 2022	
Project Funding (FY 2022): \$370,000	DOE share: \$370,000	Non-DOE share: \$0

Project Introduction

This report describes FY 2022 activities in Thrust 4B within the VTO PMCP, which aims to rapidly develop and deliver new materials and manufacturing solutions via an ICME framework that enables both powertrain efficiency advancements and weight reductions over the full range of on-road vehicle classes. The program pivoted all research from a focus on internal combustion engines to a new focus on EVs in FY 2022.

Thrust 4 is a unique programmatic research strategy that was initiated in FY 2019 at the launch of the five-year PMCP consortium and is intended and structured to elevate emphasis and access to the unique world-class computational and characterization capabilities of the PMCP's three national laboratories. Thrust 4A focuses on advanced characterization and Thrust 4B on advanced computational materials/ICME. Development tasks within the three development thrusts (i.e., Thrusts 1–3) of the PMCP submit Thrust 4 project proposals annually to compete for Thrust 4 capabilities to support specific research objectives or to address specific scientific problems within the development tasks.

Task 4B, “Advanced Computational Materials,” is designed to provide ICME research capabilities to the development tasks within the PMCP's three development thrusts. Once Thrust 4 project awards are made, the Task 4B project staff are integrated into their sponsoring development tasks and provide a range of computational capabilities within these teams, including computational thermodynamic and kinetic simulation approaches (e.g., CALPHAD), high-throughput first-principles DFT calculations, and phase-field, finite element, crystal plasticity, and modern data analytics.

Objectives

The objective is to integrate computational and characterization capabilities within an ICME framework to foundationally undergird materials design that support sub-tasks within Tasks 1–3. The goal is to apply advanced ICME methodologies by combining predictive and advanced characterization tools for alloy behavior to accelerate materials design from technology readiness level (TRL) 1 to 4.

Approach

Task PIs within Thrusts 1–3 request support from Thrust 4 projects at the three laboratories through a standardized request form, after which a small committee reviews, ranks, and awards Thrust 4 projects. Thrust 4 provides the majority of funding for each project, with some defined fraction of cost-sharing from the sponsoring task. Thrust 4 projects are typically intended as one-year support efforts with specifically defined goals and are funded in the range of \$25–100K.

Results

Selected example results, which are denoted as * in Table I.1.4.5.1, from specific projects within Thrust 4B are presented as brief vignettes on the following pages to provide examples of progress and results in FY 2022.

Table I.1.4.5.1. Thrust 4B1 Funded Advanced Computation Projects in FY 2022

Thrust 4 Project No.	Tasks	Task PI	Project PI	Thrust 4B Project Title
22-01*	3D-22	Tolga Aytug	Mina Yoon	Materials by Design for Novel, Ultra-High Conductive Materials Using First-Principles Computational Approaches
22-07*	1G-22	Dongwon Shin	Yousub Lee	Finite Element Simulations Combined with ML to Predict Thermal Conductivities of Al Alloys
22-08	1G-22	Dongwon Shin	Eva Zarkadoula	Molecular Dynamics Simulations of Precipitate Evolution in Lightweight Alloys: Al-Mg-Zn
22-14	1E-22	Amit Shyam	Dongwon Shin	First-Principles Study of Solute-Vacancy Clustering in Al-Zr(Fe) Alloys
22-15*	3C-22	Beth Armstrong	V. Cooper S. Bullock	Composition and Phase Prediction of Ferritic Material Properties
22-18*	2A-22	Muralidharan Govindarajan	Mina Yoon	Alloying Element Effects on the Stability of Fe-Si Intermetallic Phases
22-20	1A-22	Dongwon Shin	Adrian Sabau	Microstructure Prediction During Casting of Al-Ni alloys

* Selected task.

Project 4B:22-01: Materials by Design for Novel, Ultra-High Conductive Materials Using First-Principles Computational Approaches (Project PI: Mina Yoon, ORNL)

Development task supported: *Task: 3D-22: Novel, Ultra-High Conductivity Materials (Cu tape + CNTs) for EVs (Task PI: Tolga Aytug, ORNL)*

This project aims to support the development of Task 3D in designing and manufacturing ultra conductive Cu-CNT composites with significantly improved electrical conduction properties by providing first-principles atomistic calculations that support the explanation of experimental results in the parent development task. In particular, the energetics, electronic, and transport properties of Cu-CNT composites functionalized with N have been investigated.

Figure I.1.4.5.1(a) shows the atomistic modeling of nitrogen-doped CNTs based on the XPS data. Depending on various parameters, such as the type of N/Cu dopants incorporated into the CNTs and the type of CNTs (e.g., metallic or semiconducting tubes), the electronic density of state changes drastically near the Fermi level. Figure I.1.4.5.1(b) summarizes the density of state as a function of the various parameters. We also identified the dopants and their configurations expected to improve the electronic transport properties. In particular, Cu and N dopants increase the electronic densities of (11,0) – semiconducting nanotubes. Consequently, the appropriately doped CNTs transition from semi-metallic to metallic behavior. However, including pyrrolic N, as shown in Figure I.1.4.5.1(b), seems detrimental to the electrical conductivity as it generates localized electronic states.

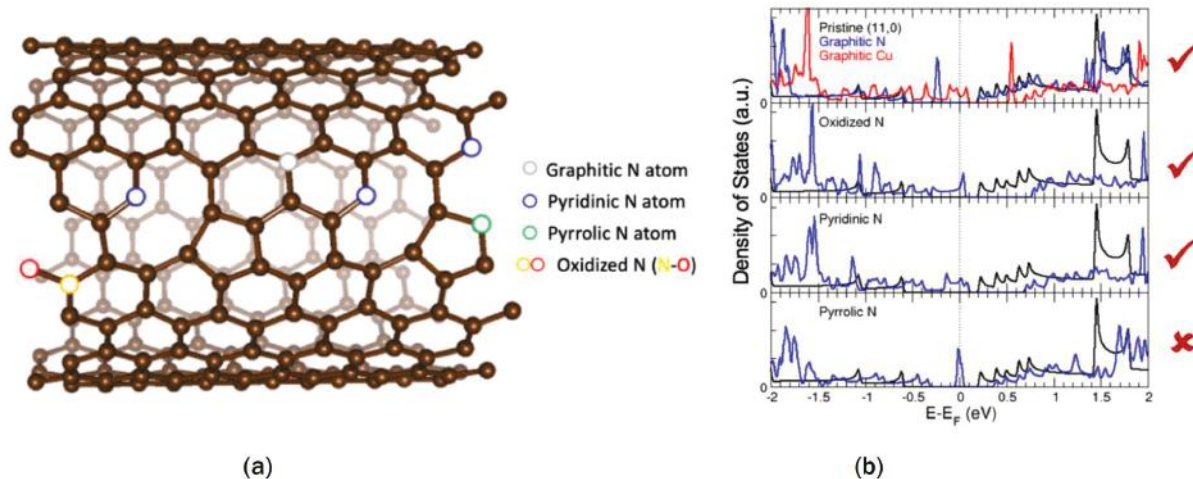


Figure I.1.4.23. (a) Atomistic modeling of nitrogen-doped CNTs based on the experimental XPS data. (b) Density of states of (11,0) semiconducting CNTs with Cu or N dopants. Source: ORNL.

We further investigated the electrical conductivity of CNTs by solving the Boltzmann equation that accounts for incorporating electron-phonon coupling based on first-principles calculations [1]. Special attention was paid to the dependence on doping. We studied both metallic (5,5) and semiconducting (11,0) CNTs. The electrical conductivity of (5,5) CNTs was as high as 7×10^7 S/m, consistent with experimental data ranging from 10^6 to 10^7 S/m for pure CNTs. Figure I.1.4.5.2 shows the temperature-dependent electrical resistivity of (11,0) semiconducting CNTs with nitrogen dopant and changes in charge carrier density. Our calculations show that nitrogen doping can significantly decrease the electrical resistivity of (11,0) CNTs. These calculations are consistent with experimental data showing that the electrical conductivity of nanotube-containing Cu-based ultra conductive composites, mixed with a significant amount of semiconducting CNTs, was significantly increased when a nitrogen-rich binder was used during composite processing.

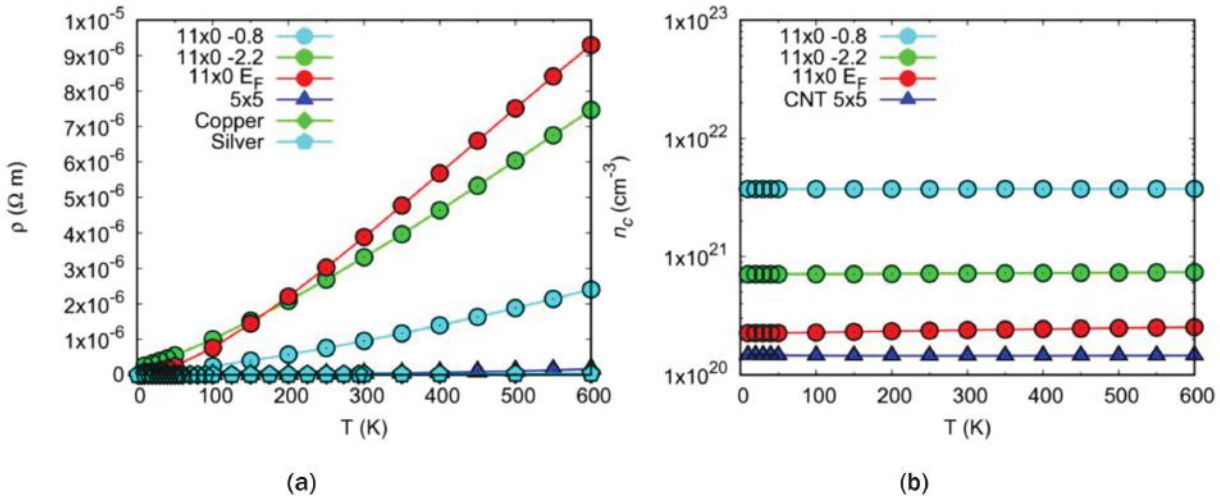


Figure I.1.4.24. Calculated electronic conductivity for (a) inverse of resistivity ρ , and (b) charge carrier density (n_c) of (11,10) semiconducting CNTs with N doping. Source: ORNL.

Project 4B:22-7: Finite Element Simulations Combined with ML to Predict Thermal Conductivities of Al Alloys (Project PI: Yousub Lee, ORNL)

Development task supported: Task 1G-22-Fundamentals of Thermal Properties in Lightweight Alloys for EV Systems (Task PI: Dongwon Shin, ORNL)

The quantitative understanding of various microstructural features of precipitates in cast Al-alloys and the thermal conductivities of cast Al-alloys is not established yet. The objectives of this task are to: (1) provide a quantitative understanding of the correlation between precipitate features and thermal properties; (2) create a reliable surrogate model for extended application through high-throughput finite element method (FEM) and data analytics using high-performance computing; and (3) provide design/optimization guidance for the experiment to acquire desired thermal properties.

The approaches used in this project included constructing a framework using open-source FEM code, object-oriented finite element 2 by the National Institute of Standards and Technology for thermal conductivity prediction, cellular automata [2] for the generation of a synthetic microstructure, and two-point statistics for comparison of characteristic features of the microstructure to link to ML.

The thermal conductivity of cast Al-3Ni (N7) and Al-3Ni-0.45Zr (N8) was predicted using oriented finite element 2 and the results are shown in Figure I.1.4.5.3(a) and Figure I.1.4.5.3(b), respectively, and validated in Figure I.1.4.5.3(c) with an experimentally measured thermal diffusivity, α ($\alpha = k/\rho C_p$) from Task 1A-22. The same microstructure from different magnifications of $\times 500$, $\times 1200$, and $\times 6000$ shows distinctive morphologies in Figure I.1.4.5.3(a) and Figure I.1.4.5.3(b), respectively. Nevertheless, the predicted thermal conductivities were in the acceptable error range, regardless of magnification, in the same material except for one at N7, $\times 6000$. The outlier of thermal conductivity predicted in Figure I.1.4.5.3(c) results from the $3\times$ difference in area fraction of the eutectic phase (e.g., vs. 5% at N7, $\times 500$ and $\times 1200$ vs. 15% at N7, $\times 6000$). It indicates that the area fraction should be kept constant for correct prediction in the same microstructure.

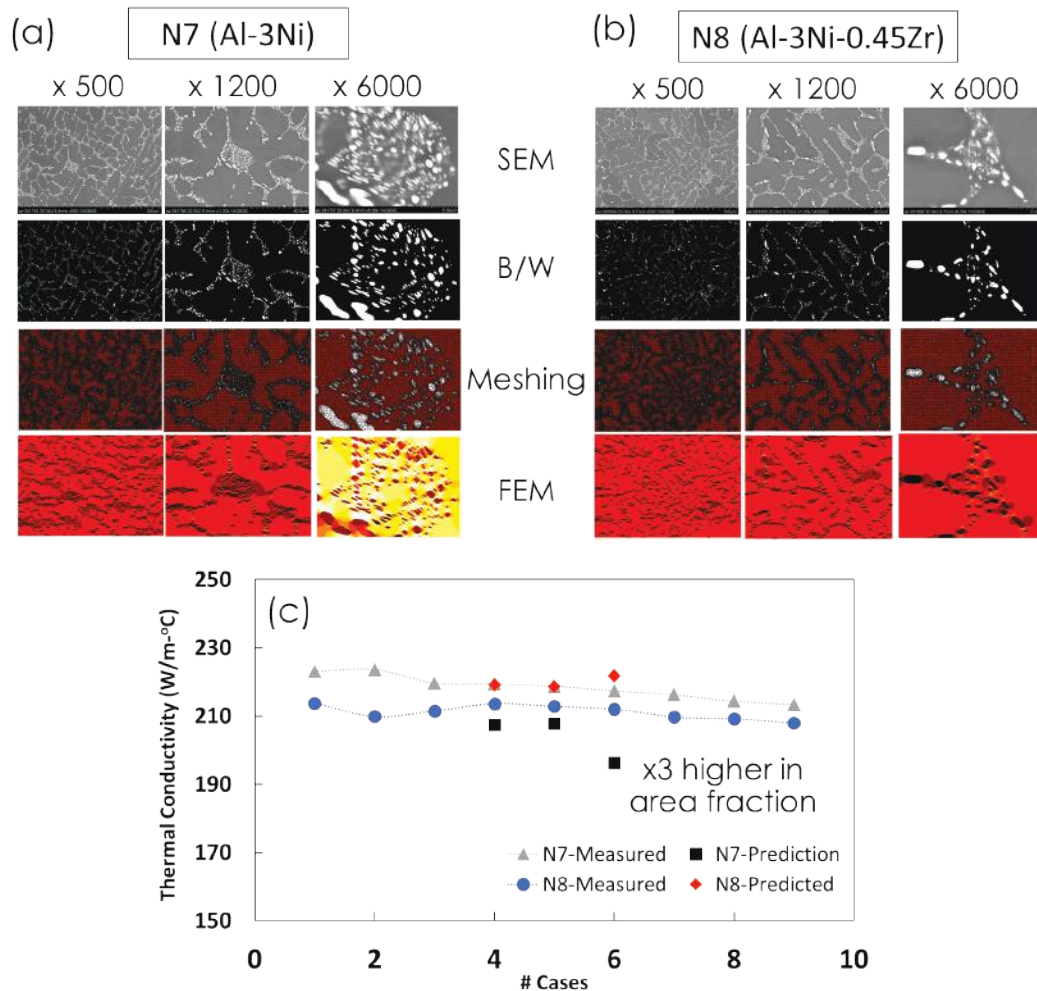


Figure I.1.4.25. Prediction of thermal conductivity of (a) Al-3Ni (N7) and (b) Al-3Ni-0.45Zr (N8) using SEM as an initial input for thermal conductivity prediction in FEM. (c) The prediction agrees with the measured data. Source: ORNL.

We have used cellular automata to create a synthetic microstructure in Figure I.1.4.5.4(a) for the corresponding SEM image of N8, $\times 1200$ in Figure I.1.4.5.4(b). With this method, any microstructures can be designed and created as input for FEM. The microstructure looks similar between Figure I.1.4.5.4(a) and Figure I.1.4.5.4(b), but the comparison is qualitative, so it is unclear. Thus, the similarity of the microstructures will need to be statistically confirmed. The integrated analysis using the synthetic microstructure in Figure I.1.4.5.4(c) and the two-point statistics in Figure I.1.4.5.4(d) can be a potential option for statistical quantification for various features of eutectic microstructures in cast Al-alloys.

The results showed that the thermal conductivity of cast Al-alloys is predictable using FEM simulation. The discrepancy in prediction is potentially attributed to the unknown actual thermal conductivity of the eutectic regions. Thus, further investigation (e.g., the interface effect between eutectic and matrix due to segregation or porosity) will be conducted to improve the prediction accuracy. The synthetic microstructure was successfully generated using cellular automata. Two-point statistics were tested as an option for statistical quantification of the microstructure. Principal component analysis, an unsupervised statistical technique using two-point statistics as an input for the dimensional reduction in ML, will be used to find a correlation between microstructure and thermal conductivity.

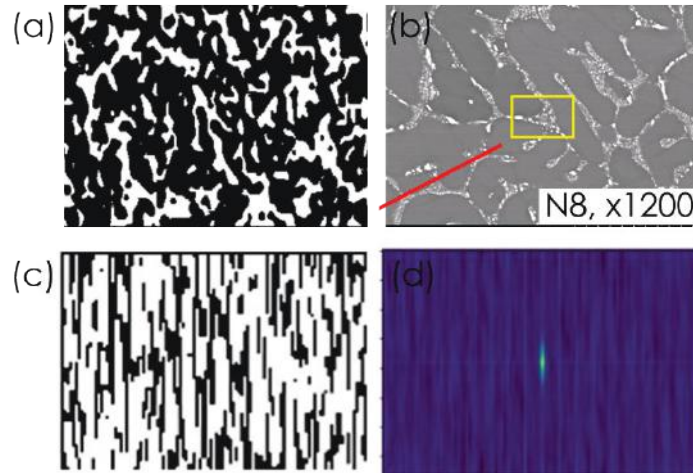


Figure I.1.4.26. Synthetic microstructure of N8 \times 1200 created using (a) CA; (b) experimental SEM image; (c) vertically aligned microstructure; and (d) analyzed pattern using two-point statistics in which the color plot shows the microstructure is vertically aligned with the similarly sized columnar structure. Source: ORNL.

Project 4B:22-15: Composition and Phase Prediction of Ferritic Material Properties (Project PIs: Valentino Cooper and Steve Bullock, ORNL)

Development task supported: *Task 3C-22: Advanced Ceramics and Processing for Wireless Charging Systems (ferrites) (Task PI: Beth Armstrong, ORNL)*

The overarching goal of this task is to employ computation and theoretical methods to support the discovery and design of new ferrite-based magnetic materials (in Task 3C) for wireless charging systems. A key premise is to understand how doping of ferrite ceramics can be used to increase the permeability and Curie temperature of these materials while potentially minimizing the electrical loss at the operating frequency of 85 kHz. Initial efforts in this project have focused on understanding the solubility limits and preferred doping sites of magnesium (Mg) and nickel (Ni) in ZnFe_2O_4 . These preliminary results are intended to be correlated with—and validated by—experimental efforts in development Task 3C. They will be the basis for large-scale, high-throughput calculations designed to understand which metal cations can be substituted within these ceramic materials and their consequences on the magnetic behavior and transition temperatures. Ultimately, this task will assist in establishing a set of potential materials that are ferromagnetic and stable at operating temperatures of inductive charging magnets and guide the parallel Task 3C effort of synthesizing ferrites for wireless charging.

First-principles DFT calculations were used in this project to explore Mg and Ni doping within the ZnFe_{24} ferrite end-member compound. The substitutions were examined at the 25% and 50% levels on the A- and 25% level on the B-sites, each in a $2 \times 2 \times 2$ AB_2O_4 unit cell. A dopant level of 25% on the A-site resulted in substituting two zinc (Zn) cations, while the corresponding B-site 25% configuration would involve replacing four iron (Fe) cations. We assume a reference of the ground state binary oxides for each case to compute the stability or likelihood of substitution. While the initial studies have focused on Mg and Ni substitutions, we have also identified a range of 2+ and 3+ ions suitable for substitution on the A- and B-sites. Subsequent calculations to examine the stability phase diagrams of these materials are pending.

Table I.1.4.5.2 lists the substitutional energy (stability) for replacing Mg and Ni on the Zn (A-site) and Fe (B-site) in ZnFe_2O_4 . Here, we observe that both Mg and Ni are slightly unstable on the A-site for both the 25% and 50% configurations, as indicated by the small positive energies. It is worth noting that DFT is a 0K approach and that these very small energies suggest that at RT, one can expect a sizable number of A-site substitutions. In contrast, we find that both Mg and Ni are significantly more stable on the B-site. This could be commensurate with the fact that ionic radii of both Mg (0.72) and Ni (0.56 HS, 0.6 LS) in the 3+ state are

similar to Fe^{3+} (0.55 HS, 0.645 LS) in octahedral coordination. These results suggest that the nominal compositions of AFe_2O_4 may be more Fe-deficient than expected if Mg and Ni preferentially substitute for Fe rather than Zn. A second explanation could be that Fe in these systems would also populate the A-sites. To better understand this possibility, additional calculations are underway to explore the possibility of Fe substituting for Zn in the presence of the dopants. We note that the experimental Raman spectra of the commercially available ferrite wireless charging materials studied in Task 4A indicates the presence of other ions, likely Zn, populating the Fe octahedral sites. Such a substitution would have consequences for the magnetic behavior—especially if the Fe ions now sit in a tetrahedral coordinated site and are thus subject to a significantly different crystal field splitting. Additionally, these calculations suggest the need to perform Mossbauer experiments on the current materials, as this can indicate the populations of Fe in an octahedral or tetrahedral environment. Nevertheless, in all cases, we see that the substitution of either non-magnetic Mg or magnetic Ni ions has minimal impact on the average moment ($\langle \text{mag} \rangle$) of Fe on the B-sites of these materials.

Table I.1.4.5.2. Substitutional Energy (Stability) and Average Magnetic Moments ($\langle \text{mag} \rangle$) for A- and B-Site Doping of Mg and Ni in ZnFe_2O_4 . Source: ORNL

Atom Substituted	A (Zn)- 25%	A (Zn)- 50%	B (Fe) - 25%
Mg			
stability (eV/f.u.)	0.024	0.048	-0.857
$\langle \text{mag} \rangle$ Fe	4.083	4.085	3.93753
Ni			
stability (eV/f.u.)	0.062	0.142	-0.971
$\langle \text{mag} \rangle$ Fe site	4.082	4.074	4.069
$\langle \text{mag} \rangle$ Ni site	1.76	1.60	0.945

Project 4B:22-15: Composition and Phase Prediction of Ferritic Material Properties (Project PIs: Valentino Cooper and Steve Bullock, ORNL)

Development task supported: *Task 3C-22: Advanced Ceramics and Processing for Wireless Charging Systems (ferrites) (Task PI: Beth Armstrong, ORNL)*

This project aims to develop a first-principles approach to describe the structural transition in the Fe-Si-X system, where X is an alloying element. Fe-Si with higher silicon (Si) levels (5 wt.%–6.5 wt.%) is a promising soft-magnet material. One of the drawbacks of Fe-Si alloys with higher Si is the formation of ordered B2 or D0_3 phases [3], which increases the brittleness of the Fe-Si alloy, making it difficult to roll into motor electric laminates at RT. A possible way to avoid the formation of the B2 phase is to change the A2-B2 transition temperature by introducing a third element in the alloy such that the A2-B2 transition, and resultant brittle behavior, can be avoided in the alloy through appropriate thermal-mechanical treatment. It is important that the choice of the alloying element should not result in a reduction of the magnetization per volume, Curie temperature, or electrical resistivity.

To investigate the problem, we have developed a DFT-based approach to calculate the order-disorder transition boundaries. The A2-B2 structural transition was modeled using a statistical mechanics approach where interaction between atomic components of the alloy placed in lattice sites was expanded over clusters, widely known as the cluster expansion approach. The energies of a small set of ordered components were calculated using DFT calculations, as observed in Figure I.1.4.5.5(a). In the current calculation, 213 ordered structures were used in fitting, and the agreement is very reasonable as can be seen from a comparison of calculated and fitted energies presented in Figure I.1.4.5.5(b). It is worth mentioning that the expansion should be accurate for a small concentration of Si, approximately 14%, only. The fitted effective cluster interaction values were used in a Monte-Carlo model to calculate the A2-B2 and the B2- D0_3 phase boundaries as a function of temperature.

As seen in Figure I.1.4.5.5(c), the A2-B2 transition was not accurately reproduced in the current Monte-Carlo calculations. In our future work, we intend to calculate the Fe-Si thermodynamic potential at fixed Si concentrations and temperatures within the cluster variation approximation to improve the accuracy.

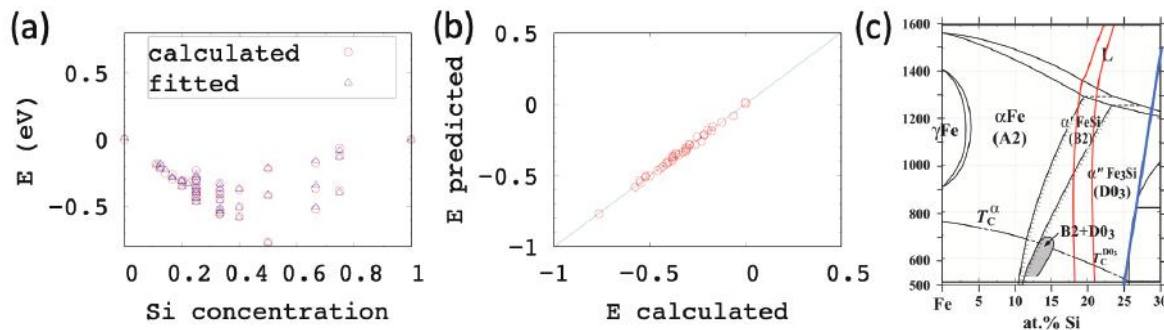


Figure I.1.4.27. (a, b) Comparison of energies calculated from fitted cluster expansion with DFT results. (c) Experimental phase diagram and calculated A2-B2 phase boundary (red) and B2-D0₃ (blue).

Source: ORNL.

The successful development of this methodology to predict the phase boundaries in this system would then allow the calculation of the effect of various third elements on the relative stabilities of the disordered and ordered phases. For example, shifting the calculated B2-D0₃ boundary to higher Si levels would eliminate the formation of the D0₃ phase at the Si levels of interest, thereby improving the ductility and enabling the RT processing of the resulting alloy.

Conclusions

Utilizing advanced computation to generate simulated data can provide insight into understanding the behavior of alloy systems under various processing and operating conditions relevant to automotive applications. A suite of ICME methods is coordinated in Thrust 4.

Examples of FY 2022 Thrust 4B1 projects highlighted here are essential for accomplishing the mission of accelerated materials development for future advanced EVs under the PMCP. DFT approach was used to explain improved electronic conductivities of Cu:CNT-doped with nitrogen (4B:22-1), FEM simulations to predict thermal conductivities of Al-Ni alloys as a function of microstructures (4B:22-7), DFT calculations to investigate the stability and magnetic properties of zinc ferrites doped with Mg and Ni (4B:22-15), and another example of an atomistic simulation that correlates DFT-driven phase stability of Fe-Si alloy with the thermomechanical process. Combined with Thrust 4A1 advanced characterization projects, the advanced modeling and simulation projects within Thrust 4B1 provide support to main development tasks that accelerate the discovery of advanced materials for EVs and elucidate underlying mechanisms.

References

1. Zhou, J.-J., J. Park, I.-T. Lu, I. Maliyov, X. Tong, and M. Bernardi, 2021, "Perturbo: A software package for *ab-initio* electron-phonon interactions, charge transport and ultrafast dynamics," *Comput. Phys. Comm.*, Vol. 264, Art. 107970. <https://doi.org/10.1016/j.cpc.2021.107970>.
2. Sayama, H., 2013, "PyCX: A Python-based simulation code repository for complex systems education," *Complex Adapt. Syst. Model.*, Vol. 1, No. 2, pp. 1–10. <https://doi.org/10.1186/2194-3206-1-2>.
3. Kubaschewski, O., 1993, *Phase Diagrams of Binary Iron Alloys (Monograph Series on Alloy Phase Diagrams, Vol. 9)*, Okamoto, H., (ed.), ASM International, Materials Park, OH, USA. p. 380.

Acknowledgements

This research used resources of the Oak Ridge Leadership Computing Facility at ORNL, which is supported by DOE-SC under contract DE-AC05-00OR22725.

I.1.4.6 Task 4B. Advanced Computation – Machine-Learning Methods for Alloy Design (Task 4B3) (Oak Ridge National Laboratory)

Dongwon Shin, Co-Principal Investigator

Oak Ridge National Laboratory
Materials Science and Technology Division
1 Bethel Valley Rd.
Oak Ridge, TN 37830
E-mail: shind@ornl.gov

Yukinori Yamamoto, Co-Principal Investigator

Oak Ridge National Laboratory
Materials Science and Technology Division
1 Bethel Valley Rd.
Oak Ridge, TN 37830
E-mail: yamamotoy@ornl.gov

J. Allen Haynes, PMCP Consortium Manager

Oak Ridge National Laboratory
Materials Science and Technology Division
1 Bethel Valley Rd.
Oak Ridge, TN 37830
E-mail: haynesa@ornl.gov

Jerry Gibbs, DOE Technology Development Manager

U.S. Department of Energy
E-mail: jerry.gibbs@ee.doe.gov

Start Date: November 1, 2021	End Date: September 30, 2022	
Project Funding (FY 2022): \$150,000	DOE share: \$150,000	Non-DOE share: \$0

Project Introduction

A data analytics framework was implemented to design advanced alloys in multicomponent and multiphase systems. With ORNL's AFA stainless steel, experimental data have been consistently accumulated for over a decade. In this framework, we trained surrogate ML models to predict the creep-rupture life of AFA alloys as a function of elemental alloy chemistry and creep test conditions (e.g., stress, temperature). We have augmented the raw experimental AFA dataset, which consists of only chemical composition and test conditions, with synthetic microstructural information (e.g., phase fraction, degree of supersaturation) by exercising an ICME approach in a high-throughput manner. The trained ML models were interrogated to predict the creep-rupture life of a large set of hypothetical alloys, populated using the design of experiments (DoE) approach. The statistical analysis of the predicted creep dataset via the present ML approach provides a reduced search space for superior new AFA alloy compositions.

Objectives

This project aims to identify improved potential alloy chemistries of AFA alloys (up to 17 alloying elements) using the ML approach. From the ML models trained with alloy chemistry and synthetic microstructural information, it is possible to rapidly explore high-dimensional, multicomponent AFA alloy compositional space to identify new AFA alloys for which creep properties under a window of specific conditions are predicted to be better than existing creep properties.

Approach

The overview of the workflow used in this task is presented in Figure I.1.4.6.1. First, surrogate ML models were trained, as shown in Figure I.1.4.6.1(a), where raw AFA experimental data were augmented with scientific features, such as phase fractions and phase compositions to correlate the creep-rupture life of AFA with microstructural information [1]. The synthetic scientific features were obtained by the CALculation PHase of Diagrams (CALPHAD) method, which is an effective method to explore the phase stabilities of multicomponent systems [2]. Afterward, hypothetical AFA alloy compositions were populated by the DoE approach, as observed in Figure I.1.4.6.1(b). Due to the massive number of required calculations, the Compute and Data Environment for Science (CADES), which is a cloud computing service similar to Amazon Web Services at ORNL, was utilized to calculate the scientific features (i.e., thermochemical information) of hypothetical alloys. Figure I.1.4.6.1(c) illustrates the prediction of the creep-rupture life of hypothetical alloys through the interrogation of the ML models. Five independent ML models were used for the predictions to ascertain the convergence between the models. Lastly, the composition space for hypothetical alloys with high creep-rupture life was statistically analyzed after imposing a screening condition (e.g., top x% creep life) on the predicted dataset, as can be seen in Figure I.1.4.6.1(d). We used the Gaussian fitting to extract alloy compositions anticipated to possess higher creep.

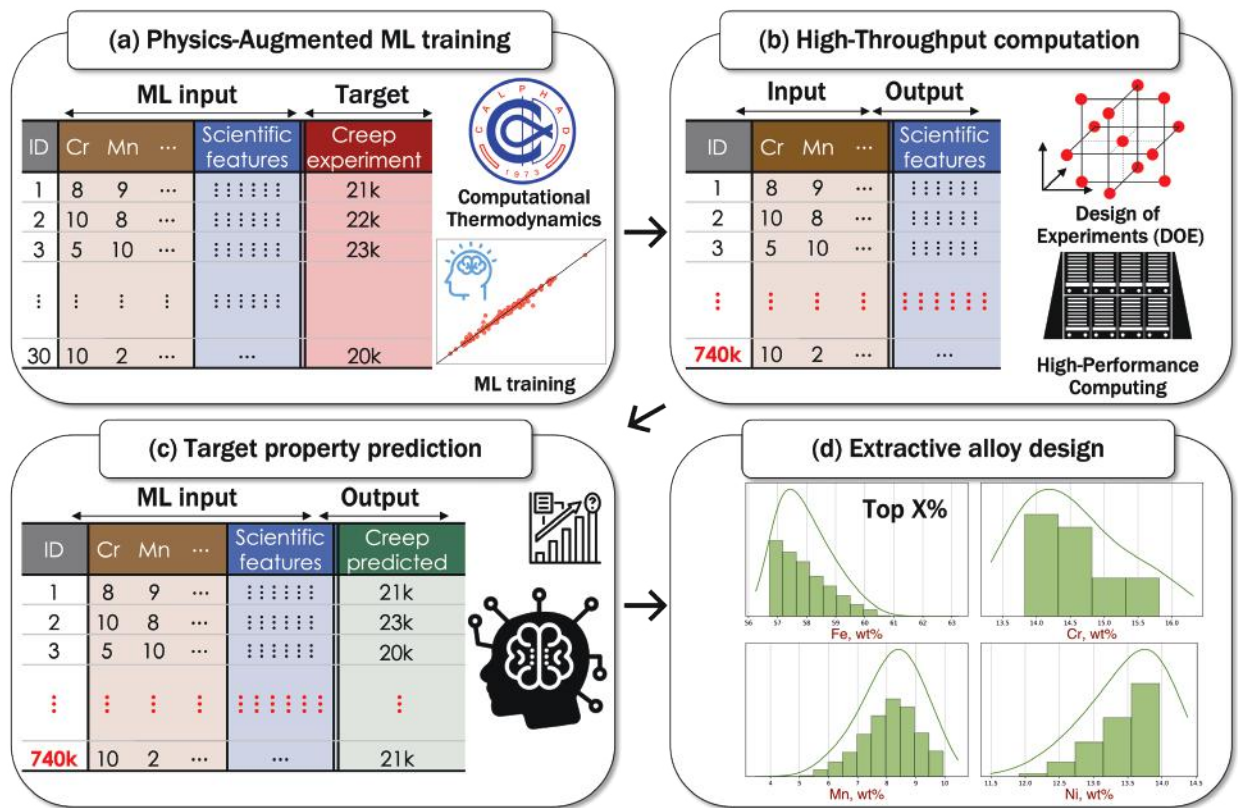


Figure I.1.4.28. Framework of designing new alloys based on high-throughput ML: (a) CALPHAD-based thermochemical information is augmented as scientific features in ML models. The models are trained with experimental data. (b) The DoE approach is used to narrow down the search space for hypothetical alloy compositions from high-dimensional composition space. Scientific features of such alloys are calculated by high-throughput computational thermodynamics with high-performance computing. (c) Hypothetical alloys are subjected to virtual experiments by using the trained ML models. (d) Ideal alloy compositions are extracted by imposing screening conditions and statistical analysis. Source: ORNL.

Results

We implemented two types of features: (1) experimental features and (2) synthetic/scientific features. Experimental features include the conditions for manufacturing alloys and creep testing, such as bulk composition, solutionizing temperature (T1), creep stress, and creep testing temperature (T2). Synthetic features include thermochemical information, such as the equilibrium phase volume fraction (VPV) and the phase composition of austenite (X_FCC) at creep testing conditions. We have used the TCFe11 computational thermodynamics database as implemented in the Thermo-Calc software package. The suggestions of AFA domain experts determined the key scientific features to be emphasized. The alloy features and their descriptions are summarized in Table I.1.4.6.1.

Table I.1.4.6.1. Description of Different Types of Alloy Features Considered in this Task

Features	Description
Experimental Features Stress T1, T2 dT Nb/C {Element}_at.	Creep testing stress Solutionizing, creep testing temperature Temperature difference between T1 and T2 The ratio between Nb and C in atom fraction Elemental composition in atom fraction
Synthetic (Scientific) Features T2_VPV_{Phase} T2_X_FCC_Fe_{Element} d_VPV_{Phase}	The volume fraction of a phase at T2 Composition of an element in the austenite phase at T2 Degree of supersaturation (volume fraction difference at T1 and T2)

Correlation analysis between each feature and the creep-rupture life was conducted based on the maximal information coefficient (MIC) [3], which identifies both linear and nonlinear relations between a feature and creep-rupture life that can provide insight into identifying impactful features of creep resistance. Figure I.1.4.6.2(a) presents the top 15 highly correlated input features. As anticipated, creep testing conditions (i.e., stress and temperature, or T2) are identified as higher impact features. The top five highly correlated features include the phase fraction of the BCC_B2 phase. This finding is consistent with the domain knowledge that AFA creep resistivity is highly sensitive to the formation of the BCC_B2 phase [4]. Notably, the role of domain experts is critical in more effectively interpreting correlation analyses, as quantitative correlation analyses may contain statistical bias. For instance, the B content in austenite (T2_X_FCC_Fe_B) appeared as the most impactful feature; however, the amount of B in AFA alloys is too small (less than 3 ppm) to be considered important according to the domain experts. We trained random forest ML models with 23 experimental and 42 scientific features; high accuracy was achieved ($R^2=0.91$), as shown in Figure I.1.4.6.2(b). The top 30 alloy features and their MIC ranks in training ML models are listed in Table I.1.4.6.2.

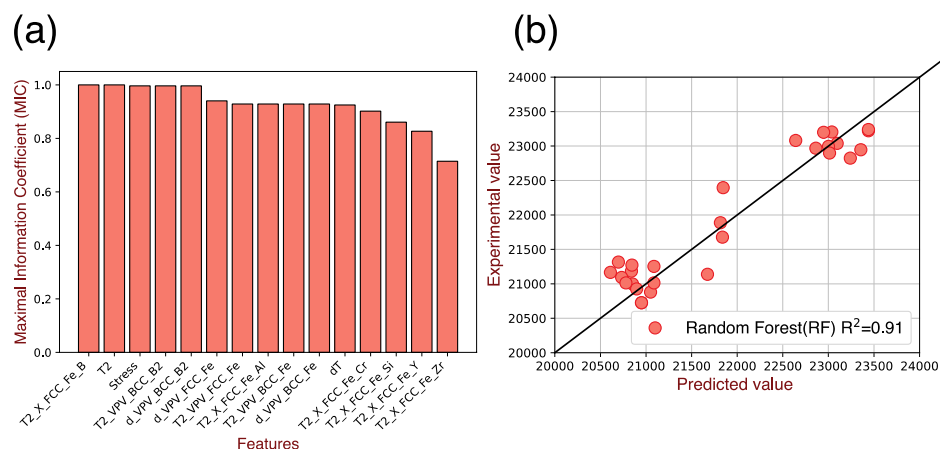


Figure I.1.4.29. Physics-augmented ML training: (a) top 15 input features ranked by MIC analysis and (b) training result of ML models that incorporate scientific features. Source: ORNL.

Table I.1.4.6.2. List of Top 30 Features Based on MIC Analysis Between Input Features and AFA Creep

MIC Rank	Features	MIC Rank	Features	MIC Rank	Features
1	T2_X_FCC_Fe_B	11	dT	21	T2_X_FCC_Fe_Ti
2	T2	12	T2_X_FCC_Fe_Cr	22	T2_X_FCC_Fe_Nb
3	Stress	13	T2_X_FCC_Fe_Si	23	T2_X_FCC_Fe_Cu
4	T2_VPV_BCC_B2	14	T2_X_FCC_Fe_Y	24	T2_X_FCC_Fe_P
5	d_VPV_BCC_B2	15	T2_X_FCC_Fe_Zr	25	T2_VPV_M2B_CB
6	d_VPV_FCC_Fe	16	T2_X_FCC_Fe_C	26	T2_X_FCC_Fe_Fe
7	T2_VPV_FCC_Fe	17	T2_VPV_FCC_Cu	27	T2_X_FCC_Fe_V
8	T2_X_FCC_Fe_Al	18	d_VPV_FCC_Cu	28	T2_X_FCC_Fe_Mn
9	T2_VPV_BCC_Fe	19	T2_X_FCC_Fe_W	29	d_VPV_M2B_CB
10	d_VPV_BCC_Fe	20	T2_X_FCC_Fe_Ni	30	T2_VPV_C14_LAVES

T2 and Stress are the creep testing temperature and stress; VPV and X represent volume fraction and mole fraction, respectively. The detailed description of features is given in Table I.1.4.6.1.

Hypothetical alloy compositions were populated to explore the high-dimensional compositional space of AFA alloys. Table I.1.4.6.3 summarizes the composition range of experimental data for each element. We implemented an evenly spaced grid with a combinatorial method, using two different grid spacings to account for the differing effect of heavy and light elements on creep-rupture time. The numbers of hypothetical alloys based on various grid spacing schemes are listed in Table I.1.4.6.3. The ideal compositional grid spacing suggested by domain experts is 0.002 wt.% for light elements (i.e., boron and carbon) and 0.05 wt.% for heavy elements (i.e., elements with an atomic number of 7 or greater). However, this grid spacing generates over 10^{12} hypothetical alloys, which is daunting to calculate corresponding synthetic features, even with the modern high-performance computing capability. Next, we considered the coarse-to-fine grid approach to effectively reduce the number of hypothetical alloys. The initial grid spacing of 0.02 wt.% and 0.5 wt.% were used for light and heavy elements, respectively. Once the ideal alloy composition range was determined, as can be seen in Figure I.1.4.6.1(c) and Figure I.1.4.6.1(d) above, finer grid spacing was introduced for smaller search space (e.g., 0.02 wt.% and 0.1 wt.% for light and heavy elements).

Table I.1.4.6.3. Number of Hypothetical Alloys Determined by Combinatorial Design from Experimental Data and Grid Spacing (H and L Denote Heavy and Light Elements, Respectively)

Type	Experimental Composition Range, wt%										Number of Hypothetical Alloys	Grid Spacing, wt.%
	Fe (H)	Cr (H)	Mn (H)	Ni (H)	Cu (H)	Al (H)	Nb (H)	Mo (H)	W (H)	C (L)		
Max	62.74	15.81	9.95	13.97	3.10	2.56	1.03	0.15	0.15	0.21	1.14x10 ¹²	H: 0.05, L: 0.002
											4.43x10 ⁹	H: 0.1, L: 0.02
Min	56.72	13.83	4.00	11.91	2.81	2.40	0.59	0.00	0.00	0.09	1.00x10 ⁶	H: 0.3, L: 0.02
											7.40x10 ⁵	H: 0.5, L: 0.02
Composition range of Si(H), V(H), Ti(H), Y(H), Zr(H), B(L), and P(H) are not included.											6.12x10 ³	H: 1, L: 0.02

From the combinatorial design of hypothetical alloys, over 700,000 hypothetical alloys were selected. This set of alloys has a composition precision of 0.5 wt.% for each element (0.02 wt.% for light elements), which is within the composition range of industrial stainless steel alloys [5]. The creep-rupture life of the hypothetical alloys was predicted for five different creep testing conditions: 100, 150, 170, 200, and 250 MPa for creep stress; 923, 956, 976, 990, and 1023 K for creep testing temperature, respectively. Figure I.1.4.6.3 presents the creep-rupture life of experimental data (e.g., ground-truth) and hypothetical alloys predicted by ML models. We use Larson-Miller Parameters (LMP) to represent the rupture time:

$$LMP = T * (20 + \ln(t_{rupture})) \quad (1)$$

where T is the creep testing temperature in Kelvin and $t_{rupture}$ is the rupture time in 1 hour.

The composition distribution of the top 30% of the hypothetical alloys at a selected simulated creep testing condition was analyzed to extract the alloy compositions with the highest predicted potential for superior creep resistance. An example of the extracted alloys is presented in Figure I.1.4.6.3. The alloy composition was extracted at a creep testing condition of 250 MPa with 923 K. Then, the LMP of the alloy at different creep testing conditions (170 MPa with 976 K and 100 MPa with 1023 K) was predicted. The results indicate the alloy with predicted high LMP at 250 MPa is also likely to have high LMP at lower stress levels. As future opportunities emerge for studies of this type of alloy, these predictions will be used to define experimental validation experiments for the most promising AFA compositions.

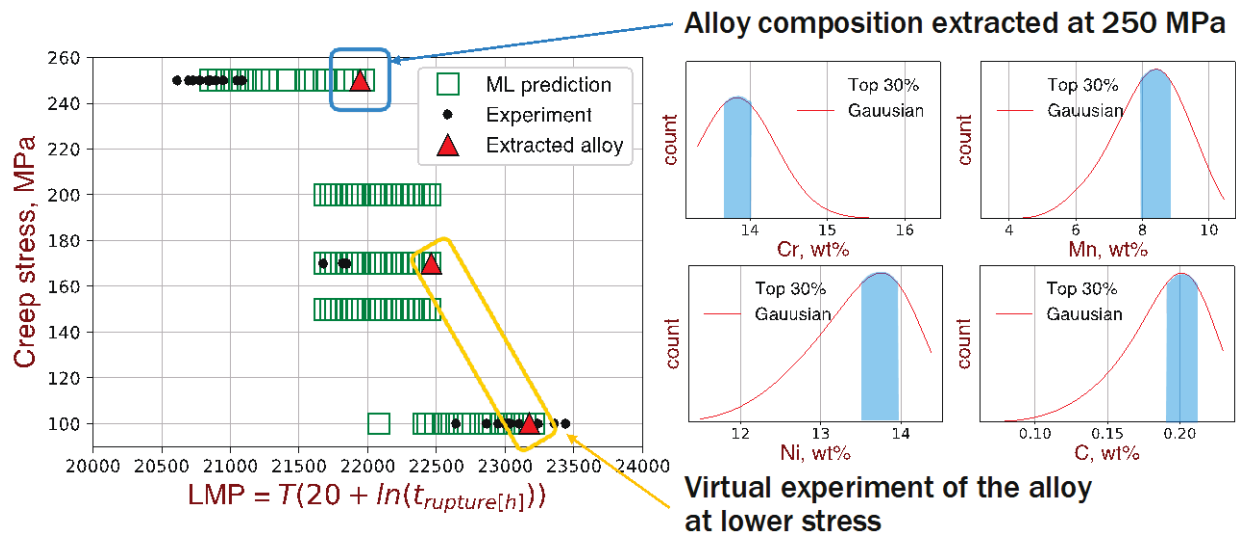


Figure I.1.4.30. Creep-rupture time of experimental (closed circles) and hypothetical (open squares) alloys with various creep stress conditions. LMP is used to represent the rupture time. Filled triangle represents the ideal alloy composition extracted from hypothetical alloys at 250 MPa. The rupture time of the ideal alloy is projected to 170 and 100 MPa via ML predictions. Source: ORNL.

Conclusions

A modern data analytics workflow that leverages highly consistent experimental data and a high-throughput ICME approach to identify the chemistry of advanced high-temperature alloys has been established. We have used an example of ORNL's multi-decade AFA alloys experimental dataset and have developed a computational thermodynamics approach to training ML models that can predict creep properties, represented as the LMP, as a function of alloy chemistry, testing conditions, and microstructural information. Over 700,000 hypothetical AFA alloys were generated to predict their creep properties, and we have calculated microstructural information via high-throughput computational thermodynamic calculations. The distribution of individual elemental compositions has been analyzed computationally, of which creep properties were

predicted to exceed existing experimental results. The demonstrated workflow is anticipated to be of value for predicting the properties of other alloys by rapidly exploring high-dimensional compositional space when high-fidelity experimental data and physics-informed features obtained from ICME approaches are available.

Key Publications

1. Peng, J., Y. Yamamoto, M. P. Brady, S. Lee, J. A. Haynes, and D. Shin, 2021, “Uncertainty quantification of machine-learning predicted creep property of alumina-forming austenitic alloys,” *J. Mater.*, Vol. 73, pp. 164–173. <https://doi.org/10.1007/s11837-020-04423-x>.

References

1. Shin, D., Y. Yamamoto, M. P. Brady, S. Lee, and J. A. Haynes, 2019, “Modern data analytics approach to predict creep of high-temperature alloys,” *Acta Mater.*, Vol. 168, pp. 321–330. <https://doi.org/10.1016/j.actamat.2019.02.017>.
2. Ågren, J., 1996, “Calculation of phase diagrams: CALPHAD,” *Current Opin. Solid-State Mater. Sci.*, Vol. 1, No. 3, pp. 355–360. [https://doi.org/10.1016/S1359-0286\(96\)80025-8](https://doi.org/10.1016/S1359-0286(96)80025-8).
3. Reshef, D. N., Y. A. Reshef, H. K. Finucane, S. R. Grossman, G. McVean, P. J. Turnbaugh, E. S. Lander, M. Mitzenmacher, and P. C. Sabeti, 2011, “Detecting novel associations in large data sets,” *Science*, Vol. 334, No. 6062, pp. 1518–1524. <https://doi.org/10.1126/science.1205438>.
4. Yamamoto, Y., M. L. Santella, M. P. Brady, H. Bei, and P. J. Maziasz, 2009, “Effect of alloying additions on phase equilibria and creep resistance of alumina-forming austenitic stainless steels,” *Metall. Mater. Trans. A*, Vol. 40, No. 8, pp. 1868–1880. <https://doi.org/10.1007/s11661-009-9886-1>.
5. Padilha, A. F., and P. R. Rios, 2002, “Decomposition of austenite in austenitic stainless steels,” *ISIJ Int.*, Vol. 42, No. 4, pp. 325–327. <https://doi.org/10.2355/isijinternational.42.325>.

Acknowledgements

The authors would like to thank J. Peng for the discussion on high-throughput computational thermodynamics calculations and M. B. Brady for his insight on selecting scientific feature selections for the training of the ML models.

I.1.4.7 Task 4B. Advanced Computation – Life Cycle Analysis (LCA) of EVs GREET® (Task 4B4) (Argonne National Laboratory)

Christopher P. Kolodziej, Co-Principal Investigator

Argonne National Laboratory
Energy Systems & Infrastructure Analysis Division
9700 S. Cass Avenue
Lemont, IL 60439
E-mail: ckolodziej@anl.gov

Jared Kelly, Co-Principal Investigator

Argonne National Laboratory
Energy Systems & Infrastructure Analysis Division
9700 S. Cass Avenue
Lemont, IL 60439
E-mail: jckelly@anl.gov

Michael Wang, Co-Principal Investigator

Argonne National Laboratory
Energy Systems & Infrastructure Analysis Division
9700 S. Cass Avenue
Lemont, IL 60439
E-mail: mqwang@anl.gov

J. Allen Haynes, PMCP Consortium Manager

Oak Ridge National Laboratory
Materials Science and Technology Division
1 Bethel Valley Rd.
Oak Ridge, TN 37830
E-mail: haynesa@ornl.gov

Jerry Gibbs, DOE Technology Development Manager

U.S. Department of Energy
E-mail: jerry.gibbs@ee.doe.gov

Start Date: November 1, 2021 End Date: September 30, 2022
Project Funding (FY 2022): \$100,000 DOE share: \$100,000 Non-DOE share: \$0

Project Introduction

Many technical options are being examined to help decarbonize the transportation sector. However, a holistic examination of GHG emissions from vehicle production, operation, and end-of-life (EOL) is required to ensure these technologies are not shifting the GHG burden from one source to another along the vehicle life cycle. This is especially important as vehicle GHG emission standards and vehicle electrification begin to result in significant reductions to GHG emissions. The GHGs Regulated Emissions and Energy use in Technologies (GREET®) model developed at ANL with DOE support can analyze the impact of various materials used in vehicle production on the life cycle for GHG emissions. The influence of substituting lightweight materials to reduce vehicle weight, and thus vehicle battery demand, is of particular interest in this study.

ANL has been developing the GREET[®] model since 1994 with an initial focus on energy production and consumption in the transportation sector. From the beginning, the vehicle cycle (i.e., life cycle burden of materials used within the vehicle), as well as the fuel-cycle, were included to have a complete, cradle-to-grave view of the vehicle life cycle. The vehicle cycle analysis is included in GREET2, as GREET1 is primarily used for fuel-cycle analysis. In GREET2, ANL characterized the energy and material inputs associated with many important vehicle materials and identified the composition of the components associated with several powertrains across multiple vehicle classes. ANL has since updated and expanded those material characterizations, as well as the vehicle powertrain options. ANL has not, until now, updated the modeling approach for treating material recycling.

ANL has been working with the International Energy Agency (IEA) to expand the GREET model for LCA of vehicle technologies to geographic areas outside the United States, working with seven IEA transportation technology collaboration programs (TCPs), including the Advanced Materials for Transportation (AMT) TCP. The globalization of the DOE-funded GREET model through the IEA GREET+ Extension project by ANL, IEA, and its seven transportation TCPs will help illustrate a holistic, consistent comparison of different vehicle technologies in different world regions.

This project for the VTO PMCP expanded ‘GREET2’—the vehicle cycle module of the GREET LCA model—to address key issues affecting vehicle cycle GHG emissions of these powertrain technologies by using different materials to achieve vehicle lightweighting (see <https://greet.es.anl.gov/> for the GREET model and its publications). ANL and DOE will use the expanded GREET2 model for IEA’s GREET+ Extension project so global LCA of vehicle technologies by IEA and the seven IEA TCPs can benefit from the most advanced version of GREET2.

Objectives

- Investigate differences in recycling rates and recycled content for major automotive materials.
- Collect data on major global differences in automotive material recycling rates and recycled content.
- Investigate LCA methodologies for the treatment of recycled materials.
- Augment GREET’s current method of the recycling content approach with an appropriate method that considers recycling at the end of product life.
- Investigate factors limiting the levels of recycled steel and aluminum (Al) going into new vehicles.
- Support the IEAs AMT TCP in the development of GREET+ and examine vehicle LCA studies from other countries compared to the United States.

Approach

A critical element of any LCA is the life cycle inventory (LCI) data. The LCI in GREET is composed of thousands of data values, supported by references. To perform any updates to GREET2, a thorough literature review is necessary. If newer data is available to update the GREET LCI, those updates can be incorporated into the following year’s version of GREET. However, it is important that the new values have a high degree of fidelity and can be properly cited. A more detailed categorization of the information can become available over time. In this case, the new data can add granularity to the GREET LCA results. However, it can also require a larger effort to carry that level of granularity into the rest of the GREET LCI.

Results

Research of Virgin vs. Recycled Steel and Aluminum in New Vehicles

In GREET2, the shares of virgin and recycled materials (e.g., steel, Al, lead, nickel, magnesium) going into a vehicle are input parameters. For steel used in manufacturing a new vehicle, 26.4 wt.% is recycled steel, based on a 2012 reference [1]. For Al, the recycled content is 11 wt.% for wrought Al and 85 wt.% for cast Al, both taken from a 1998 reference [2]. Since these references have become somewhat dated, a concerted effort was made in FY 2022 to verify if those recycled content numbers are still representative of today’s new vehicle

manufacturing. However, there are several challenges in finding the recycled content of materials going into new vehicles. Vehicle manufacturers typically do not know the exact recycled content of the steel or Al received from their suppliers. In addition, steel and Al suppliers typically do not keep track of what materials are sent to the automotive industry vs. other industries (e.g., construction, appliances).

Steel used in vehicles is manufactured using either a Basic Oxygen Furnace (BOF) or an Electric Arc Furnace (EAF) with a typical recycled steel content of 25-35 wt.% and >80 wt.%, respectively [3]. A large amount of the 25–30 million tons of steel used annually by the U.S. automotive industry is supplied by BOF steelmakers. In comparison, approximately 71% of the world’s steel for all end uses is made using BOF. Zhu et al. explains that flat products are the most sensitive to defects due to contamination from tramp elements (such as Cu) in recycled steel, so all primary BOF steel is assumed to be used for production of slab to maintain the highest possible purity in flat intermediate products [4]. This means the large flat exterior pieces of vehicle steel (body-in-white, hood, doors, etc.) would likely be composed almost entirely of BOF steel (approx. 94 wt.%) with a recycled content of 25 wt%–35 wt%. Conversely, more internal steel vehicle components could be acquired from EAF with a recycled steel content of > 80 wt.% [5]. Table I.1.4.7.1 provides a comparison.

Table I.1.4.7.1. Recycled Steel Content of New Vehicles

Source	Steel	
GREET2, 2021	26.4 wt%	
Hua, 2022 [5]	25 wt% - 35 wt% (BOF)	>80 wt% (EAF)

For the international expansion of GREET to GREET+ through the IEA, this project also examined the recycled steel content of vehicles in Europe and East Asia. In Europe, Arcelor Mittal Luxembourg, which only produces steel from EAF, reported an overall recycled steel content of 95 wt.%, while Arcelor Mittal Belgium and Arcelor Mittal Poland, which only produce steel from BOF, reported a recycled steel content of 15 wt.% and 23.5 wt.%, respectively [6]. However, it is not possible to clearly identify the automotive steel recycled content since these are values for all steel produced for all industries from those steel plants. In Japan, Nakamura et al. described the recycled steel content of a typical car to be 29 wt.% in 2012 [7].

During FY 2022, a great deal of information was identified regarding the types of steel used for vehicles, typical recycled contents of BOF and EAF steels, and limitations on the recycled steel content entering new steel. However, there was not a recent report available that clearly gave a single value of recycled steel weight percent going into new vehicles. Future work will examine the possibility of categorizing the recycled content of multiple types of BOF and EAF steel used in vehicles, as opposed to one ‘steel’ value in current GREET2.

Fortunately, for automotive Al production in the U.S., a recent report by the Aluminum Association (AA) provided detailed information regarding recycled Al content specific to the automotive industry, categorizing the recycled content of three types of Al products [8]. The recycled content was 80 wt.% for diecast products, 72.4 wt.% for extruded products, and 24 wt.% for sheet products. There was no information provided in the report on the breakdown between pre-consumer and post-consumer scrap for diecast Al recycled content. However, for extruded Al product, most of the recycled content came from pre-consumer scrap. The recycled content for sheet Al product came entirely from pre-consumer scrap. In GREET2, Al is categorized by ‘wrought Al’ (11 wt.% recycled content) and ‘cast Al’ (85 wt.% recycled content) based on a 1998 reference [2]. Extrusion and sheet Al are categories of wrought Al, but at this point GREET2 only specifies between cast and wrought Al. The current value of cast Al recycled content in GREET2 is similar to the value given in the recent AA report, as shown in Table I.1.4.7.2. However, the AA’s 2022 report indicates higher recycled Al content in extrusions and sheets than what is currently indicated in GREET2 for general ‘wrought’ Al. Given the more detailed breakdown of types of wrought Al in the AA report, it is possible to categorize wrought Al in GREET2 into extrusions and sheet in future work. For the 2022 release of GREET2, wrought Al recycled content was increased commensurate with the balance of extruded and sheet Al in a typical new vehicle.

Table I.1.4.7.2. Recycled Al Content of New Vehicles

Source	Cast Al	Wrought Al	
GREET2, 2021	85 wt.%	11 wt.% (1998 reference)	
GREET2, 2022	80 wt.%	35.1 wt.%	
AA, 2022	80 wt.%	72.4 wt.% (extrusion)	24 wt.% (sheet)

In Europe, Jaguar Land Rover in the United Kingdom has worked with the world’s largest Al recycler and automotive Al sheet manufacturer, Novelis, since 2016 to incorporate a newly developed alloy product called RC5754 into the body panels of the Jaguar XE [9]. Novelis’ RC5754 has a recycled content of at least 75 wt.%, of which post-consumer scrap accounts for 25 wt.% and pre-consumer scrap accounts for 50 wt.%. This is a significant increase in automotive Al sheet recycled content compared to the 24 wt.% recycled content stated in the AA report. To make this increase in recycled content, Novelis and Jaguar Land Rover developed the automotive industry’s first closed-loop recycling agreement, including a dedicated round-trip railway service to deliver material between Novelis locations in Germany and the United Kingdom. Closed-loop recycling means the scrap from a given product or process is recycled back into the same product. This Novelis Al product, RC5754, is currently only available in Europe. However, in North America, Novelis and Ford developed the world’s largest closed-loop recycling system for Ford’s Al-body pickup trucks, resulting in Ford recycling more than 90% of its Al scrap [9].

Like Al, the largest limitation to increasing the recycled Al content of new vehicles is the commingling of post-consumer Al scrap with scrap from other alloys, which brings together Al of different alloy types. This limits the suitability of this scrap in the end-product (whether cast or wrought Al). Closed-loop recycling offers a large advantage to increasing the recycled content of new Al because the scrap is well controlled, and its characteristics are known.

Research of EOL Vehicle Recycling and Disposal

When a vehicle reaches its EOL, its components and materials can be reused, recycled, recovered (i.e., energy from combustion), incinerated, or landfilled. Processing of an end-of-life vehicle (ELV) is categorized by four stages:

- Removal of hazardous materials (fluids, batteries, etc.)
- Dismantling vehicle for reuse or resale parts
- Vehicle hulk shredding
- Automotive shredder residual sorting.

The energy inputs and GHG emissions from processing an ELV consist of transport, disassembly, shredding, crushing, and sorting. Currently, ELV GHG emissions contribute a small percentage of life cycle GHG emissions, being 1% for internal combustion engine vehicles (ICEV), 3% for BEVs and 7% for fuel cell EVs [10]. Absolute EOL emissions for a BEVs (3.4 g CO₂e/km) are approximately 2× higher than that of an ICEV (1.4 g CO₂e/km), while that of a fuel cell EVs is approximately 9× higher (12.1 g CO₂e/km) than that of an ICEV. As the production and operation vehicle life cycle GHG emissions continue to reduce, the percentage contribution from these EOL GHG emissions could double over the next several years.

In the material breakdown of a typical ELV, 70 wt.% is ferrous metals (steel and iron) and 4 wt.% is non-ferrous metals (e.g., Al, copper, zinc) [11]. In GREET2, the total metals composition of a new internal combustion engine-powered conventional vehicle is 77 wt.%, which is consistent with the ELV data, with a small difference in the composition of ferrous metals (61.8 wt.%) and non-ferrous metals (15.2 wt.%). Part of the reason for the difference is that ELVs represent dated vehicle designs and metal compositions, while the makeup of a new vehicle in GREET represents recent advancements in vehicle material designs (e.g., use of Al for lightweighting). The average ELV contains 4.9 gallons of total fluids—2.7 gallons of fuel; 1.0 gallon of oil;

0.7 gallon of coolant; 0.3 gallon of transmission fluid; and smaller quantities of brake fluid, air conditioning refrigerant, gear oil, and windshield washer fluid. Many recycling centers will convert these fluids with high calorific value to energy by using a boiler for heat or electricity.

In the United States, there are no ELV federal regulations on recycling minimum requirements. However, many states have laws regarding handling of mercury switches, tires, and lead acid batteries. Despite no federal ELV recycling regulation, the economics of ELV recycling drives the recycling-and-recovery rate of ELVs in the U.S. to 85%–95% [11]. The United States, Japan, and Europe are the largest automotive recyclers and exporters of ferrous scrap in the world. Europe and Japan have regulations for minimums on ELV reuse, recycling, and recovery. Japan has a 99% ELV recovery-and-recycling ratio, while Europe requires $\geq 85\%$ reuse/recycle and $\geq 95\%$ reuse/recovery. In the United States, the ELV recycling rate is 96% for steel and 91% for Al [12, 13].

Added LCA Recycled Material Allocation Method to GREET

The GREET model has historically utilized the Recycled Content (RC) Method, often also called the Cutoff Approach, which considers the recycled material content going into producing a new product (e.g., vehicle) when determining the embodied environmental burdens of a material. However, in an LCA there are other approaches for evaluating and allocating the burdens associated with the production of primary or virgin materials and of secondary (e.g., recycled) materials. In addition to the RC Method, is the End-of-Life Recycling (EOLR) Method, also called the Avoided Burden Approach. Both approaches are International Organization for Standardization (ISO)-compliant and frequently applied to LCA. These two methods of considering material recycling are the most widely used, and thus the addition of the EOLR Method was an important augmentation of the GREET model that allows LCA practitioners to consider two perspectives on how material lifetimes and recycling can be treated.

For detailed information on these two methods of accounting for recycled materials, one can examine the work of Frischknecht [14] and Johnson et al. [15], which provide detailed perspectives on each, as well as additional context for further allocation approaches. In reality, RC into new product and recycling rate at EOL are not exclusive, but LCAs typically decide on one approach or the other to be conservative and to not double count the benefits of recycling. Briefly, Frischknecht identifies that the RC method “*accounts for environmental impacts at the time they occur*” [14], whereas the EOLR method operates under the basic assumption that material will likely be recycled and thereby avoid significant future resource consumption and pollutant emissions. Thus, the RC method may be thought of as characterizing the system as it currently is (i.e., it identifies how much recycled material goes into the product today), while the EOLR method may be considered prospective (i.e., it identifies the likely recycled material derived from the product in the future). Both offer important perspectives in the LCA space; Frischknecht notes that each is considered as ISO-compliant [14].

The mathematical formulation of these two methods is presented in our technical report [16]. In short, the recycled content assumed in the RC method and that assumed in the EOLR method are the main drivers of difference observed in their respective application. Further, if these two values are equal, then the two approaches yield the same results, subject to some temporal assumptions.

IEA Advanced Materials for Transportation TCP Support

During the past FY, this project has supported the DOE involvement in the IEA AMT TCP. One of the key deliverables was updated web content to describe the role of LCA in the TCP. Additionally, ANL participated in the AMT TCP project on GREET+ extension in IEA. At the request of the DOE technology development manager during the AMT TCP meeting, this project investigated the limiting factors to increasing the recycled steel and Al content of new vehicles, as well as international percentages of RC in new vehicles and ELV processing and recycling.

Conclusions

Research has identified new information regarding the RC of steel and Al in new vehicles, even relatively new materials that are allowing for higher RC. However, the categorization of the information provided does not match the current framework of how GREET2 classifies steel and Al, prompting consideration of how to incorporate the new information into the GREET2 framework. A review of ELV processing has identified the key processing steps involved and the recycling rates of steel and Al. Using that information, GREET2 was updated to include the EOLR method as an alternative approach to the RC method that already existed in GREET2.

Key Publications

1. Kelly, J. C., and C. P. Kolodziej, 2022, “Addition of End-of-Life Recycling Methodology to GREET® 2022 for Steel and Aluminum,” ANL Technical Memo, October 2022.

References

1. Keoleian, G., S. Miller, R. De Kleine, A. Fang, and J. Mosley, 2012, “Life Cycle Material Data Update for GREET Model,” Center for Sustainable Systems, University of Michigan, Report No. CSS12-12, 9 July 2012. Available at: <https://greet.es.anl.gov/files/greet2-lca-update> (last accessed 26 January 2023).
2. Weston, R. F., 1998, “Life Cycle Inventory Report for the North American Aluminum Industry” Aluminum Association, Arlington, VA, USA.
3. World Auto Steel, n.d., “Life Cycle Thinking,” [Online]. Available at: <https://www.worldautosteel.org/life-cycle-thinking/> (last accessed 26 January 2023).
4. Zhu, Y., K. Syndergaard, and D. R. Cooper, 2019, “Mapping the annual flow of steel in the United States,” *Environ. Sci. Technol.*, Vol. 53, No. 19, pp. 11260–11268. <https://doi.org/10.1021/acs.est.9b01016>.
5. Hua, N. P., J. C. Kelly, G. M. Lewis, and G. A. Keoleian, 2022, “Regional analysis of aluminum and steel flows into the American automotive industry,” *J. Ind. Ecol.*, Vol. 26, pp. 1318–1332. <https://doi.org/10.1111/jiec.13268>.
6. Thomas, J. S., and J. P. Birat, 2013, “Methodologies to measure the sustainability of materials – Focus on recycling aspects,” *Metall. Res. Technol.*, Vol. 110, No. 1, pp. 3–16. <https://doi.org/10.1051/metal/2013054>.
7. Nakamura, S., Y. Kondo, K. Matsubae, K. Nakajima, T. Tasaki, and T. Nagasaka, 2012, “Quality- and dilution losses in the recycling of ferrous materials from end-of-life passenger cars: Input-output analysis under explicit consideration of scrap quality,” *Environ. Sci. Technol.*, Vol. 46, No. 17, pp. 9266–9273. <https://doi.org/10.1021/es3013529>.
8. Wang, J., “The Environmental Footprint of Semi-Fabricated Aluminum Products in North America: A Life Cycle Assessment Report,” Aluminum Association Report, January 2022. [Online]. Available at: https://www.aluminum.org/sites/default/files/2022-01/2022_Semi-Fab_LCA_Report.pdf (last accessed 26 January 2023).
9. Novelis, 2016, “Novelis Aluminum Drives Sustainability,” [Online]. Available at: <https://www.novelis.com/wp-content/uploads/2020/04/8.5-x-11-Novelis-Auto-Sustainability-Factsheet-Final.pdf> (last accessed 26 January 2023).
10. Schwarz, L., B. Stumper, M. Bargende, S. Dreyer, et al., 2019, “Environmental Assessment of the End-of-Life Phase of Alternative and Conventional Propulsion Systems in the Context of Life Cycle Assessment,” SAE Technical Paper 2019-01-5013. <https://doi.org/10.4271/2019-01-5013>.
11. Automotive Recyclers Association, “Car Recycling: Ultimate Guide to the Automotive Recycling Industry,” [Online]. Available at: <https://www.junkcarmedics.com/blog/car-recycling/> (last accessed 26 January 2023).

12. American Iron and Steel Institute and Steel Manufacturers Association, 2021, “Determination of Steel Recycling Rates in the United States,” 27 July 2021, [Online]. Available at: <https://www.steel.org/aisi-and-sma-steel-recycling-rates-report-final-07-27-2021> (last accessed 26 January 2023).
13. Kelly, S., and D. Apelian, 2016, “Automotive Aluminum Recycling at End-of-Life: A Grave-to-Gate Analysis,” Center for Resource Recovery-and-Recycling (CR3), Metal Processing Institute, Worcester Polytechnic Institute, Worcester, MA, USA. Available at: <https://www.aluminum.org/sites/default/files/2021-10/Final-Report-Automotive-Aluminum-Recycling-at-End-of-Life-A-Grave-to-Gate-Analysis.pdf> (last accessed 26 January 2023).
14. Frischknecht, R., 2010, “LCI modeling approaches applied on recycling of materials in view of environmental sustainability, risk perception, and eco-efficiency,” *Int. J. LCA*, Vol. 15, No. 7, pp. 666–671. <https://doi.org/10.1007/s11367-010-0201-6>.
15. Johnson, J. X., C. A. McMillan, and G. A. Keoleian, 2013, “Evaluation of life cycle assessment recycling allocation methods: The case study of aluminum,” *J. Ind. Ecol.*, Vol. 17, No. 5, pp. 700–711. <https://doi.org/10.1111/jiec.12050>.
16. Kelly, J. C., and C. P. Kolodziej, 2022, “Addition of End-of-Life Recycling Methodology to GREET® 2022 for Steel and Aluminum,” ANL Technical Memo, October 2022.

Acknowledgements

The authors would like to thank T. Maani of ANL for his significant contribution in this work to identify information about recycled steel and Al content.

I.2 Modeling of Powertrain Materials

I.2.1 Next-Generation High-Efficiency Boosted Engine Development (Ford Research and Advanced Engineering)

Michael Shelby, Principal Investigator

Ford Motor Company
Research and Innovation Center
2101 Village Road
Dearborn, MI 48121
E-mail: mshelby@ford.com

Jerry Gibbs, DOE Technology Development Manager

U.S. Department of Energy
E-mail: jerry.gibbs@ee.doe.gov

Start Date: October 1, 2019

End Date: December 31, 2022

Project continuation evaluated annually

Project Funding (FY 2022): \$10,000,000 DOE share: \$7,566,730 Non-DOE share: \$2,433,270

Project Introduction

The next-generation high-efficiency engine development project is a 39-month research and development effort funded by DOE-EERE VTO. The goal of the project is to combine advanced combustion system technologies, thermal management strategies, and advanced materials to demonstrate a turbocharged gasoline engine with peak efficiency exceeding the best of today's hybrid EVs engines. While the market share of BEVs is increasing, most LD vehicles are projected to use conventional or hybrid EV powertrains well beyond 2030. Improvements in engine efficiency and reductions in powertrain weight have strong leverage to reduce vehicle-related carbon dioxide emissions for decades to come. This project develops engine efficiency and weight-saving technologies that enable competitive, profitable internal combustion engines, targeting the highest production volume powertrains.

The project team consists of Ford Motor Company, FEV North America, and ORNL. Each partner brings strengths to this collaboration, and the combined knowledge in powertrain, combustion, component design, analytical development, and manufacturing will ensure a successful project.

Objectives

The objective of this project is to develop an engine with advanced combustion technologies capable of achieving $\geq 23\%$ fuel efficiency improvement relative to a baseline 2016-model-year 3.5L V6 EcoBoost F150. The engine will be compliant with applicable U.S. Environmental Protection Agency emissions standards. The fuel economy improvement will be demonstrated via engine dynamometer testing coupled to vehicle drive-cycle simulations. Advanced materials and weight-saving technologies will also be used to demonstrate the capability of $\geq 15\%$ weight-reduction of the baseline engine. These targets are particularly challenging given that the baseline engine is already a lightweight, downsized boosted engine.

FY 2022 objectives are as follows:

- Continue single-cylinder engine (SCE) dynamometer studies supporting calibration optimization
- Complete fabrication, assembly, and test prep of the first multi-cylinder engine (MCE)
- Complete evaluation of the weight-savings and study additional weight-reduction actions.

Approach

To achieve the goals of the project, work will be divided into several overlapping workstreams as illustrated in Figure I.2.1.1. The technology selection process will be strongly guided by analytical tools, including 3D flow and combustion modeling, as well as structural and thermal analysis. Key items related to engine efficiency, outlined in the blue dotted circles of Figure I.2.1.1, were demonstrated and developed using research SCEs. The final status of the fuel economy and weight targets will be demonstrated via dynamometer testing of a complete MCE—circled in yellow in Figure I.2.1.1—along with the regulatory drive-cycle simulations.

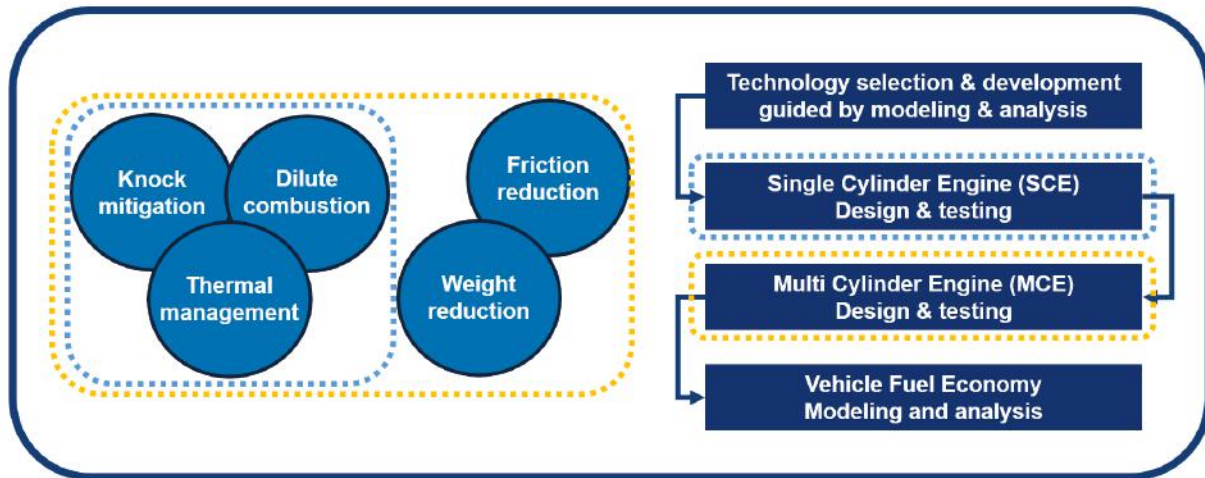


Figure I.2.1.1. The project development approach and work streams. Source: Ford.

This report will emphasize the materials aspects of the project. A second report has been prepared for the DOE Decarbonization of Offroad, Rail, Marine, and Aviation program's annual report focusing on the combustion and efficiency portions of the project.

Results

Work during this reporting period has been focused in three areas: (1) completing the weight assessment relative to the 15% reduction target, (2) investigating additional weight-reduction actions, and (3) completing assembly and test preparation of the MCE. Weight-reduction actions have included material selection, manufacturing techniques, and architecture design decisions. This report will cover an example of each in the sections below and conclude with an overall assessment relative to the project goals.

Material Selection: Structural Composite Oil Pan

As a part of the weight-reduction target for this project, a composite oil pan was designed in collaboration with ORNL as a composite demonstration component. The oil pan was chosen because it has several design requirements that demonstrate suitability of the chosen material and process to other components. The pan must be lightweight, easy to manufacture, and durable to the chemical, thermal, and mechanical boundary conditions present on the engine. The oil pan is also long and has a deep draw, which are challenging characteristics for some manufacturing processes.

The engine oil pan has been designed considering the material properties of composites to provide the structural capabilities needed for the powertrain system and reduced mass compared to conventional materials. The single-piece component, as shown in Figure I.2.1.2, is designed for an oil capacity of six quarts and a complete perimeter seal. In addition, it is a structural component of the powertrain providing a mechanical connection between the engine and the transmission. This mounting interface enhances the stiffness of the powertrain assembly for superior noise, vibration, and harshness characteristics. The pan also saves weight by providing a direct mounting location for the air conditioning compressor.

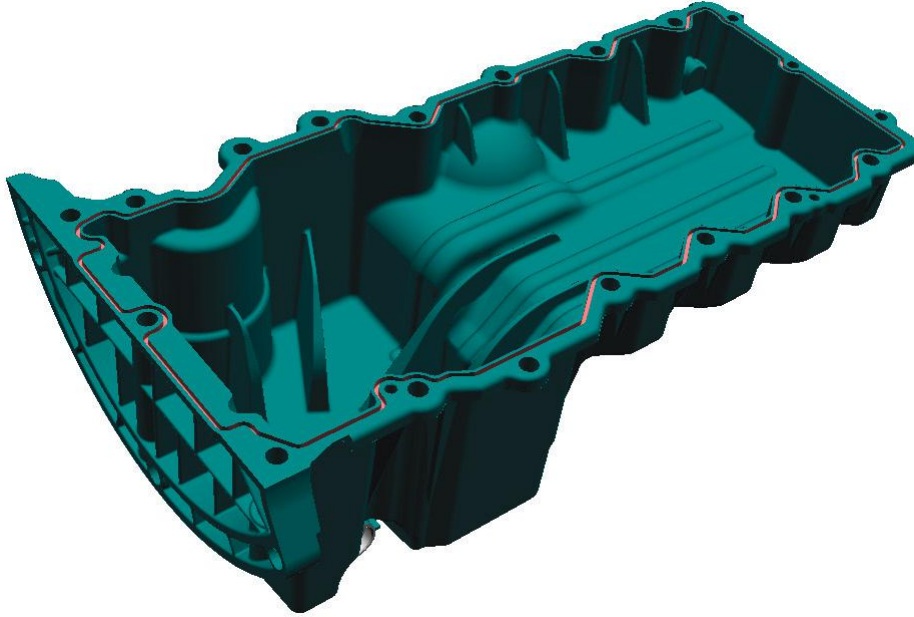


Figure I.2.1.2. Composite oil pan. Source: Ford/ORNL.

Extrusion-compression molding of Solvay's Amodel® PXM-18179, a highly filled glass fiber and recycled CFs polyphthalamide, was selected for manufacturing the oil pan. This material and process features high-heat deflection temperature, high-flexural modulus, and high-tensile strength, as well as excellent creep resistance and low moisture absorption.

For extrusion-compression molding, pellets of thermoplastic material reinforced with fibers are fed into a low shear extruder, which is used to plasticate the composite material into a 'charge.' This charge is then transferred to a fast-acting press for the compression/consolidation process. AM is then used to make the bellhousing insert on the back of the pan, saving tremendous time and machining hours as the features of this area are complex and difficult to mold. Final pans were completed in the third quarter of 2022 and are shown in Figure I.2.1.3. Weight-savings, relative to an Al part, are estimated to be 2.0 kg.



Figure I.2.1.3. Oil pan images. Source: Ford/ORNL.

Material Techniques: AM Heat Exchangers

An Al oil cooler was designed and printed at Ford Advanced Manufacturing Center out of AlSi10Mg Al material, as observed in Figure I.2.1.4. The printed design consists of triply periodic minimal surface interior geometry enabled by AM. This geometry is not feasible using conventional stacked plate heat exchangers. The part was developed to demonstrate a design that pushes the limits on wall thickness to minimize component weight, reduce pressure drop through the cooler, and improve cooling capability. A 400 g weight-reduction was accomplished with the printed part. Early assessments of the printed part on a thermal flow test rig demonstrated a 50% reduction in pressure drop with slightly reduced heat transfer performance.

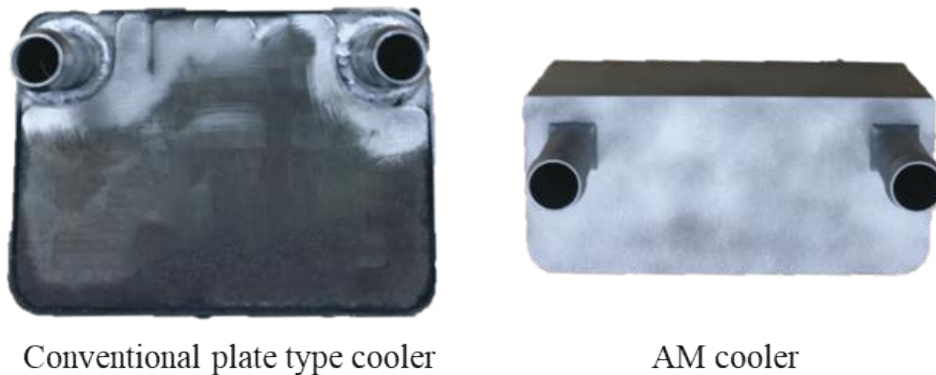


Figure I.2.1.4. Conventional and AM oil cooler designs. Source: Ford.

Material Techniques: AM Cylinder Block Casting Cores

Prototype cylinder head and block castings for this project were manufactured using AM sand cores. The cylinder head was designed to take advantage of weight-saving features enabled by using such cores, while the cylinder block was initially engineered using design rules for die-casting.

Directly printing sand cores using an AM process enables casting features that are not possible with traditional sand cores or with die-casting. Re-entrant features are possible, such as those shown in Figure I.2.1.5. Using AM to produce the sand cores also eliminates the need for draft angles because there is no need to remove the core from a mold. Multiple cores can often be integrated into one core, which reduces the risk of core shift and enables reduced wall thicknesses in some areas.

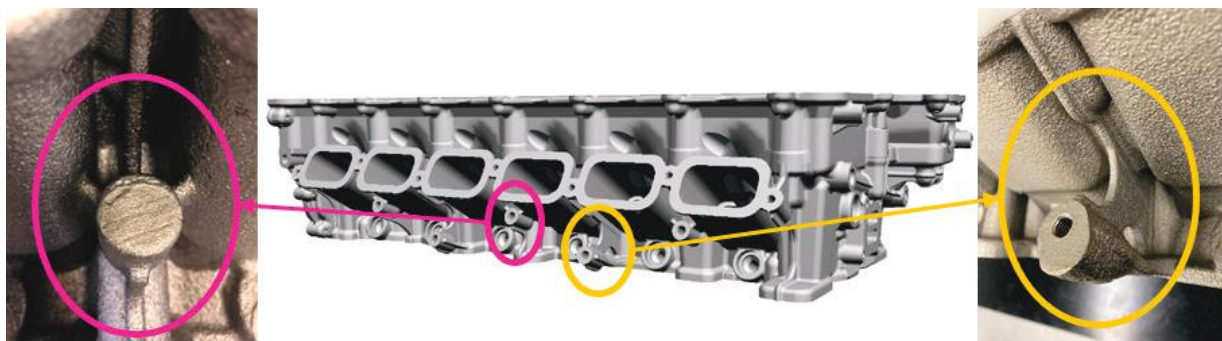


Figure I.2.1.5. Weight-saving design elements enabled by AM sand cores. Source: Ford.

After demonstrating the manufacturing feasibility of these features on the cylinder head, a second design effort was conducted applying these features to the block. The redesigned block eliminated several unused bolt bosses, recontoured the block deck to remove unneeded material, reduced ribbing and draft angles, and cored out excess material from several areas. These items combined to reduce the mass of the engine by 2.2% relative to the original diecast component. Figure I.2.1.6 shows the AM sand core design elements.

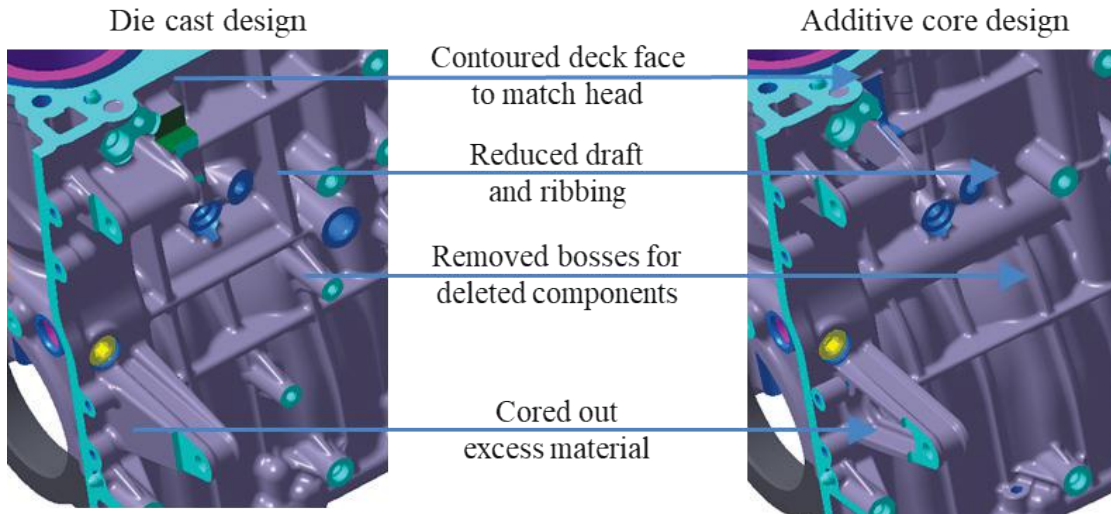


Figure I.2.1.6. AM sand core design elements. Source: Ford.

Architecture Design: Inline Engine with UniAir Valvetrain

To meet the target of improving fuel economy by 23%, several new technologies were added to the engine that were not included in the baseline. In most cases, these new technologies increased the engine weight, thus making the weight target more challenging to achieve. Moving to an inline architecture allowed the addition of Schaeffler’s UniAir valve actuation system on the intake valves while contributing to a 1.5% reduction in the engine weight, as shown in Figure I.2.1.7. In this case, the additional weight of the UniAir actuators was more than offset by the reduction in cam drive complexity, elimination of variable cam timing actuators, and reduced number of cam shafts.

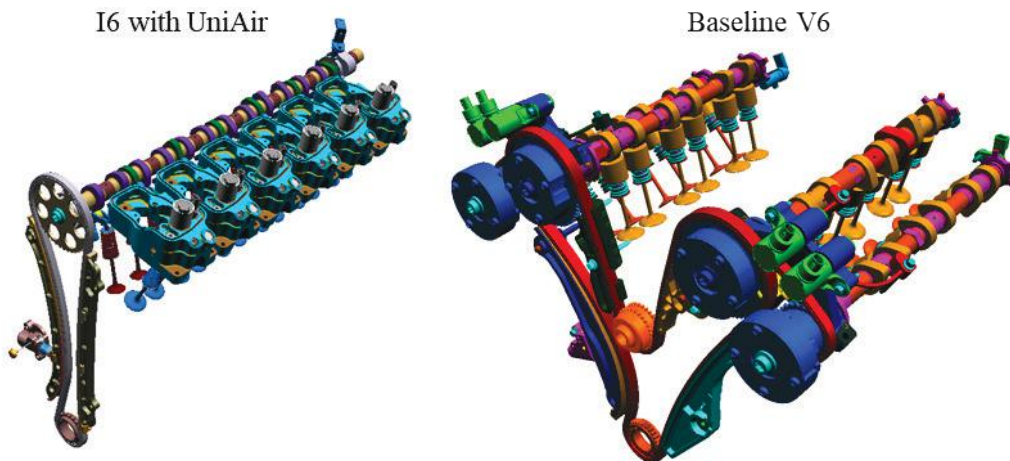


Figure I.2.1.7. Valvetrain system comparison. Source: Ford.

Overall Weight-Reduction Status

All MCE components are now available and have been weighed. The total engine weight, assuming a passive pre-chamber ignition system, has been calculated based on these individual component measurements. The current prototype 3.7L engine achieved a 4.3% weight-reduction relative to the 2016 model year 3.5L V6 EcoBoost engine baseline. Therefore, additional weight actions are required to achieve the 15% reduction target. Table I.2.1.1 compares the current weight-reduction status (e.g., ‘Updated % Weight-Reduction’) to the expected weight-reduction laid out in the project proposal (e.g., ‘Original % Weight-Reduction’). The original plan was projected to achieve the 15% target, but as Table I.2.1.1 highlights, some areas of the current engine

design did not provide the expected benefit or were heavier than originally planned. It is difficult to apportion the overall engine weight into the items listed in Table I.2.1.1, but three items account for a majority of the shortfall to the target:

1. The boost system complexity was increased to facilitate higher boost pressures for more aggressive miller valve timings, which resulted in a weight penalty for the boost system instead of the expected weight benefit.
2. The engine stroke was increased to improve thermal efficiency, which resulted in a significant increase in the weight of the engine block and crankshaft.
3. The engine architecture shift to an inline engine did not result in the anticipated weight-reduction. This can be partially attributed to the long stroke and the required crankshaft structure.

Table I.2.1.1. Original vs. Updated Weight-Reduction Status Relative to the Baseline Engine

Proposed Actions	Original % Weight-Reduction	Updated % Weight-Reduction	Comments
Engine Architecture	2.8	0.9	Shift from a 'V' to an 'I' engine architecture.
Advanced Materials	2.7	3.1	CFs compression-molded oil pan, front cover, engine mounts. Additive titanium connecting rods. Composite rear seal carrier, exhaust gas recirculation mixer.
Exhaust Manifolds	3.6	2.7	Integrated into head in lieu of cast steel manifolds.
Single Bank Exhaust	3.5	4.4	Fewer catalysts bricks, sensors, and pipes.
Optimized Cylinder Head	1.2		Additive cores. Updated % weight-reduction captured under engine architecture.
Variable Valvetrain	1.3	-0.1	Deleted intake cams, variable cam timing actuators, sensors and add UniAir.
Optimized Cylinder Block	0.8	2.2	Additive cores to optimize block for weight.
Plasma Transferred Wire Arc	1.2	1.4	Plasma Transferred Wire Arc in lieu of cast iron bore liners.
Battery Optimization	3.4	3.3	Replace 12V lead acid battery with Li-ion battery.
Exhaust Gas Recirculation System	-3.3	-3.9	Baseline does not have an exhaust gas recirculation system.
Engine Thermal Actions	-1.8	-2.7	Addition of piston cooling jets, intake runner spacer, and advanced cooling system.
Long Stroke	-2.7	-5.8	Deck height increase up to 20 mm, additional crank structure to accommodate long stroke.
Boost System	2.4	-1.3	2.4% reduction for a single turbo boost system.
Net Weight-Savings	15.1	4.3	

Further weight reductions have been investigated using additional design optimizations that specifically target component weight. These items were not incorporated into the MCE hardware to avoid additional prototype costs but are in line with other actions that have been demonstrated in the current prototype. These weight-reduction actions provided an additional 5.3% weight benefit without degrading fuel efficiency. The status of the engine weight-reduction, with these items included, is captured in the '3.7L I6 – Weight Actions' column of Figure I.2.1.8 and consists of the following items:

- Reduced crankshaft weight (hollow main bearing journals)

- Composite intake manifold
- Magnesium cam carrier and UniAir bricks
- Catalyst system inlet and exhaust downpipe optimization with a reduced number of bolted connections.

A path to achieve the 15% weight-reduction target is possible but requires additional weight actions; some have the potential to impact the engine fuel efficiency or performance objectives. Therefore, additional data is needed to evaluate these potential tradeoffs further. For example, one path to achieve the 15% weight-reduction target would be to utilize a single twin-scroll turbocharger instead of the current dual turbocharger boost system. This action would likely limit the early intake valve closing knock benefit and could degrade the engine's full load performance. The status of the engine weight-reduction with a twin-scroll boost system is shown in the '3.7L I6 – Further Study' column of Figure I.2.1.8. The following items are example actions that have been studied and would increase the weight-reduction benefit to achieve the 15% target:

- Single twin-scroll turbocharger boost system that achieves the weight target with reduced performance
- Exhaust gas recirculation cooler and flow enhancement throttle delete
- Reduced peak engine speed
- Reduced engine stroke.

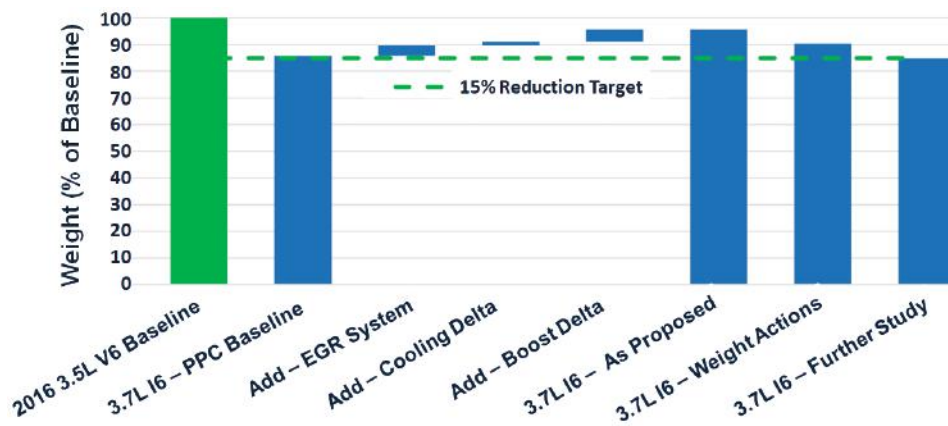


Figure I.2.1.8. Path to 15% Weight-Reduction. Source: Ford.

Conclusions

Simultaneously meeting the fuel economy and weight targets of this project presents many materials-related challenges. In the third year of this project, we have completed manufacturing and assembly of the prototype engine. This report provides examples of weight-reduction through material selection, manufacturing techniques, and engine architecture design. Also included is a detailed weight comparison of the target and actual weight-reduction in several categories. Additionally, several actions have been identified beyond those included in the project proposal that would be required to reach the 15% weight-reduction target. These efforts directly support the mass reduction and efficiency improvement goals of the project.

Acknowledgments

The author would like to thank our partners at FEV North America and ORNL for their collaboration and support, as well as our National Energy Technology Project Manager, Ralph Nine, for his continued guidance.

I.2.2 Low-Mass and High-Efficiency Engine for Medium Duty Truck Applications (General Motors)

Qigui Wang, Co-Principal Investigator

General Motors, LLC.
30003 Fisher Brothers Road
Warren, MI 48093
E-mail: qigui.wang@gm.com

Ed Keating, Co-Principal Investigator

General Motors, LLC.
28755 Louis Chevrolet Road
Warren, MI 48093
E-mail: ed.keating@gm.com

Jerry L. Gibbs, DOE Technology Development Manager

U.S. Department of Energy
E-mail: jerry.gibbs@ee.doe.gov

Start Date: October 1, 2019 End Date: December 31, 2023
Project Funding (FY 2022): \$2,474,679 DOE share: \$1,187,339 Non-DOE share: \$1,287,340

Project Introduction

Today's transportation vehicle customers are demanding that manufacturers produce engines with lower weight and improved efficiency to reduce fuel consumption, emissions, and costs associated with vehicle use, while maintaining or even increasing engine performance. Thus, developing the next-generation of high-efficiency, very-low-emission internal combustion engines requires a combination of new combustion strategies, advanced materials, and new materials processing techniques to further increase engine efficiency and reduce weight.

Objectives

The objective of this collaborative project between GM, ORNL, The Ohio State University (OSU), Michigan Technological University (MTU), and ECK Industries Inc. (ECK) is to develop an advanced MD truck engine equipped with advanced materials and combustion technologies capable of achieving $\geq 10\%$ fuel efficiency improvement and $\geq 15\%$ engine weight-reduction when compared to the 2015 Model Year GM L96 VORTEC 6.0L V8 engine compliant with applicable U.S. Environmental Protection Agency emission standards with performance demonstrated via simulation coupled with an engine dynamometer test.

Approach

This project is proposed as a large-scale engine design and demonstration enabled by an advanced materials and manufacturing development program, with a comprehensive plan spanning a period of four years in two phases. The project begins with engine architecture design and analysis activities, advanced materials and manufacturing process development, and downselection. It culminates in an engine-test cell evaluation with optimal materials and manufacturing solutions supporting final vehicle simulation. The final engine-test will verify engine weight-reduction and performance to the objectives of the Funding Opportunity Announcement (FOA) [1].

Several advanced combustion technologies will be investigated including stoichiometric combustion, increased compression ratio, aggressive exhaust gas recirculation (EGR) dilution, and load point optimization. High-strength and heat-resistant materials will be developed and incorporated with novel metal casting and AM

processes to produce highly durable engine structures to maximize performance of the materials and systems with minimum mass and cost. The opportunity to include advanced materials and manufacturing in conjunction with a high potential combustion system and engine technologies also creates the chance to revisit the most appropriate engine specification to realize the desired efficiencies while reducing engine weight cost-effectively. A focus will be on the most cost-effective solution to promote wide market acceptance using the right materials in the right place and right process for the right parts. Single- and multimaterial solutions for key engine components will be investigated. ICME [2, 3] and CAE tools will be fully utilized to accelerate both engine design and material and manufacturing solution development and optimization.

Results

Based on our PHASE 1 research and development initiatives, advanced combustion and materials technologies have been developed and downselected for the proposed MD truck engine capable of meeting the requirements.

Task 3.1. Design and Build Engines to Facilitate Test Cell Evaluation of Proposed Medium Duty Truck Solution Incorporating Components

Sub-task 3.1.1

Design of the PHASE 2 engine cylinder head and block was completed, as shown in Figure I.2.2.1 and Figure I.2.2.2, which has incorporated the relevant advanced combustion and materials technologies developed in PHASE 1, such as dual-ignition, uniform combustion cooling, and charge motion control, etc.

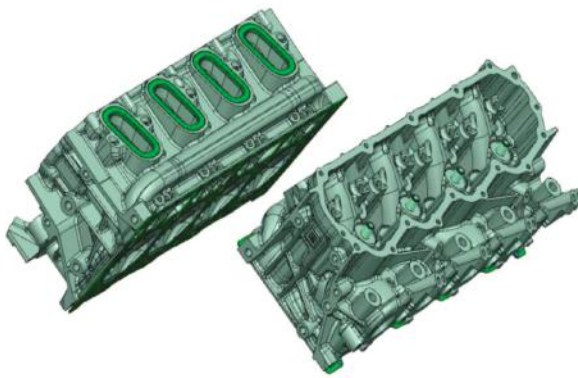


Figure I.2.2.1. Cylinder head system. Source: GM

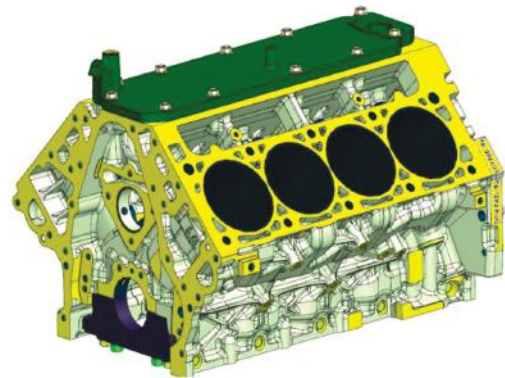


Figure I.2.2.2. Engine block system. Source: GM

Sub-tasks 3.1.2 – 3.1.3

Figure I.2.2.3 shows the design completion of the valvetrain, while Figure I.2.2.4(a) shows the induction and Figure I.2.2.4(b) shows the exhaust systems that enable the Atkinson cycle strategies, the enhanced E-EGR, and variable induction system strategies.

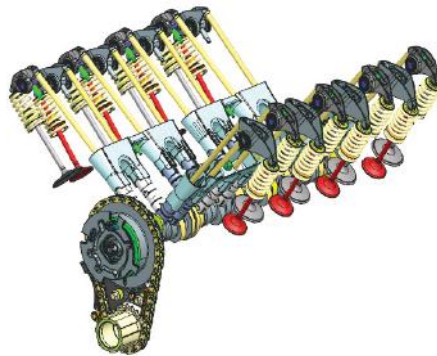


Figure I.2.2.3. Valvetrain system. Source: GM.

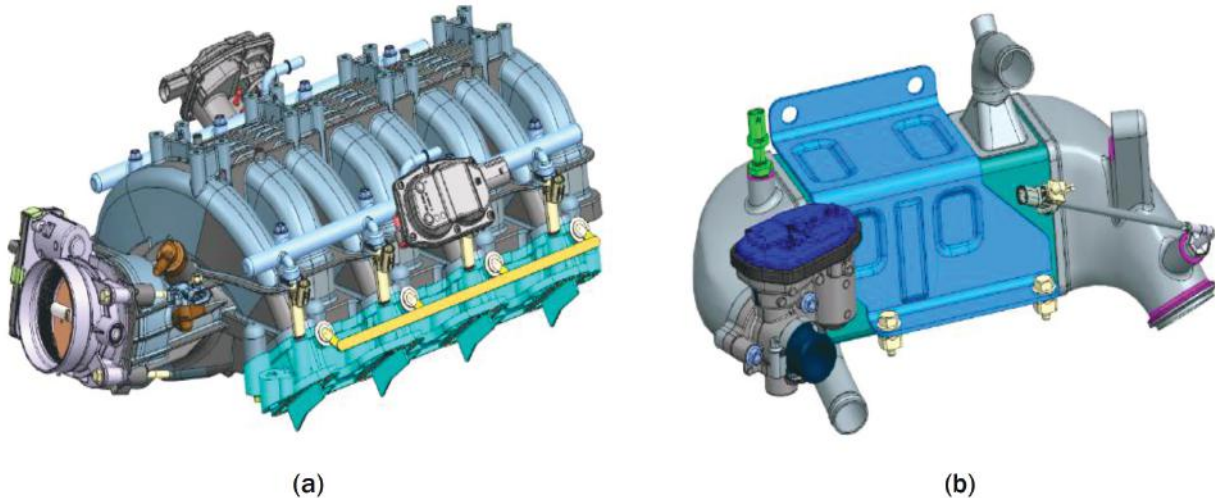


Figure I.2.2.4. (a) Induction and (b) EGR systems. Source: GM.

Sub-tasks 3.1.4 – 3.1.8

Figure I.2.2.5 shows the design completion of the fuel and coolant pump systems capable of ‘ultra’ high-pressure fuel injection and advanced combustion cooling enhancement. Figure I.2.2.6 shows the design of the PHASE 2 engine completed with integration of all the advanced combustion and materials technologies developed for this project. With the developed material solutions, the PHASE 2 engine mass is more than 15% lighter than the baseline engine, while the engine displacement increased from 6.0 L to 6.6 L. Table I.2.2.1 compares the PHASE 1 engine fuel economy improvement measured from various advanced combustion technologies with the CAE model predictions. It can be noted that the reported fuel economy improvement of 9.1% is on track to meet or exceed the project target of 10% once the pre-chamber spark plug benefit is added.

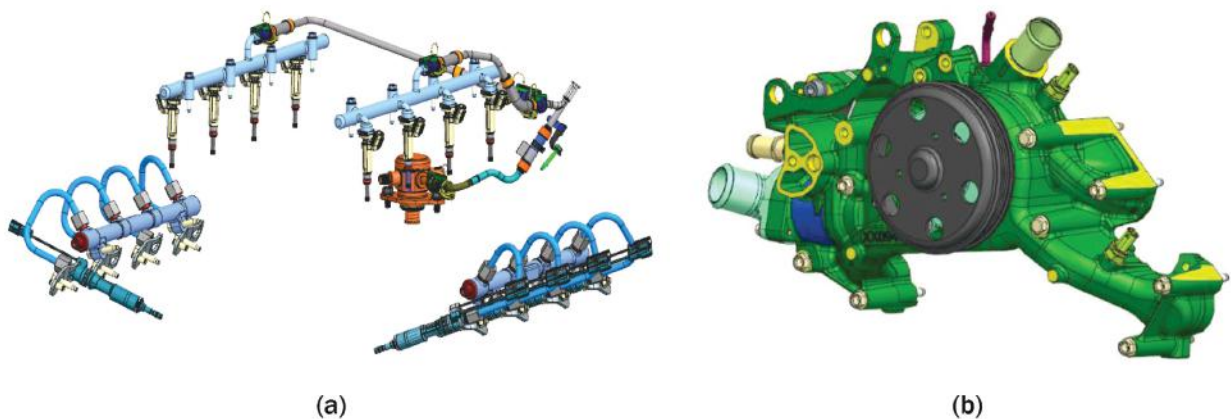


Figure I.2.2.5. (a) Fuel and (b) coolant pump sys. Source: GM.

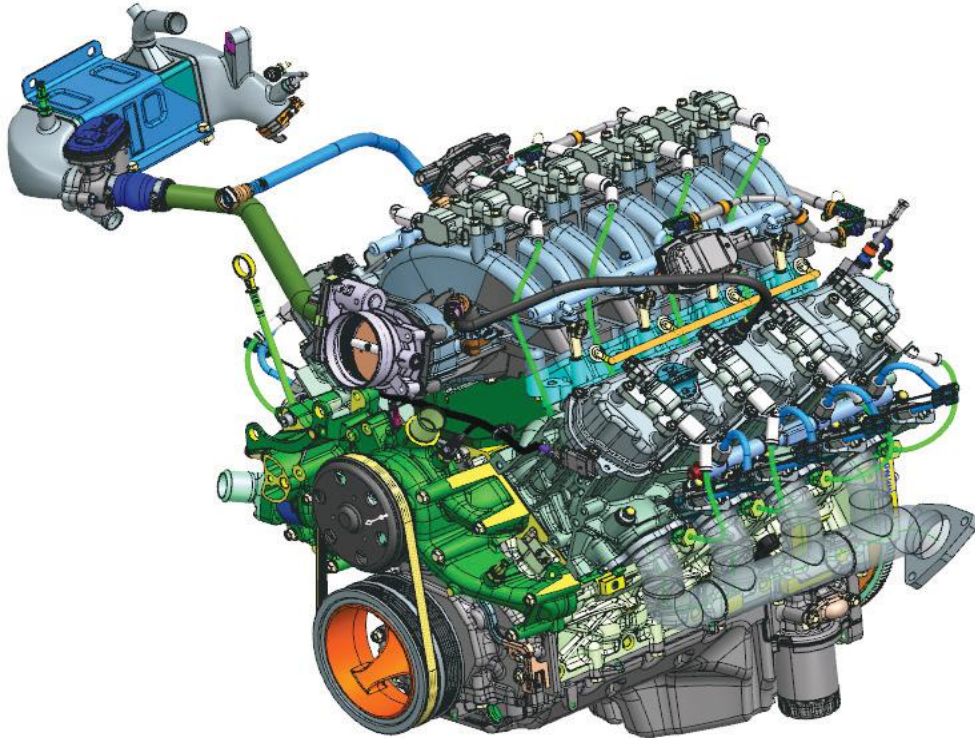


Figure I.2.2.6. Complete PHASE 2 engine system. Source: GM.

Table I.2.2.1. Comparison of Measured and Predicted New Technologies to Baseline L96 Engine at Weighted Average GEM Cycle Operating Points

Measured Weighted Fuel Economy Improvement		Predicted Weighted Fuel Economy Improvement from Simulation	
L96 Baseline		L96 Baseline	
PHASE 1	0.7%	PHASE 1	
Charge Motion Control Valve (CMCV)	2.8%	PHASE 1 + CMCV	4.4%
E-EGR	1.8%	E-EGR	4.3%
Full Authority Cylinder Deactivation	1.3%	Full Authority Cylinder Deactivation	1.3%
UHP Direct Fuel Injection + PFI	2.5%	UHP Direct Fuel Injection	1.8%
Passive Pre-Chamber Ignition	TBD	Passive Pre-Chamber Ignition	2.8%
TOTAL	9.1%	TOTAL	14.6%

Task 3.2. Demonstration of the Highest Payoff Materials and Manufacturing Solutions for Key Engine Components for the Proposed Medium Duty Truck Engine

Sub-tasks 3.2.1 – 3.2.2

A novel low pressure precision sand-casting (LPPSC) process has been developed for casting a high-quality Al cylinder head and engine block through a comprehensive casting process simulation and multiscale defect and microstructure modeling, gating, and riser system, as well as LPPSC process parameter optimization, as shown in Figure I.2.2.7. The fatigue strength of the LPPSC heads at 250°C has improved by at least 20% compared with the baseline heads.

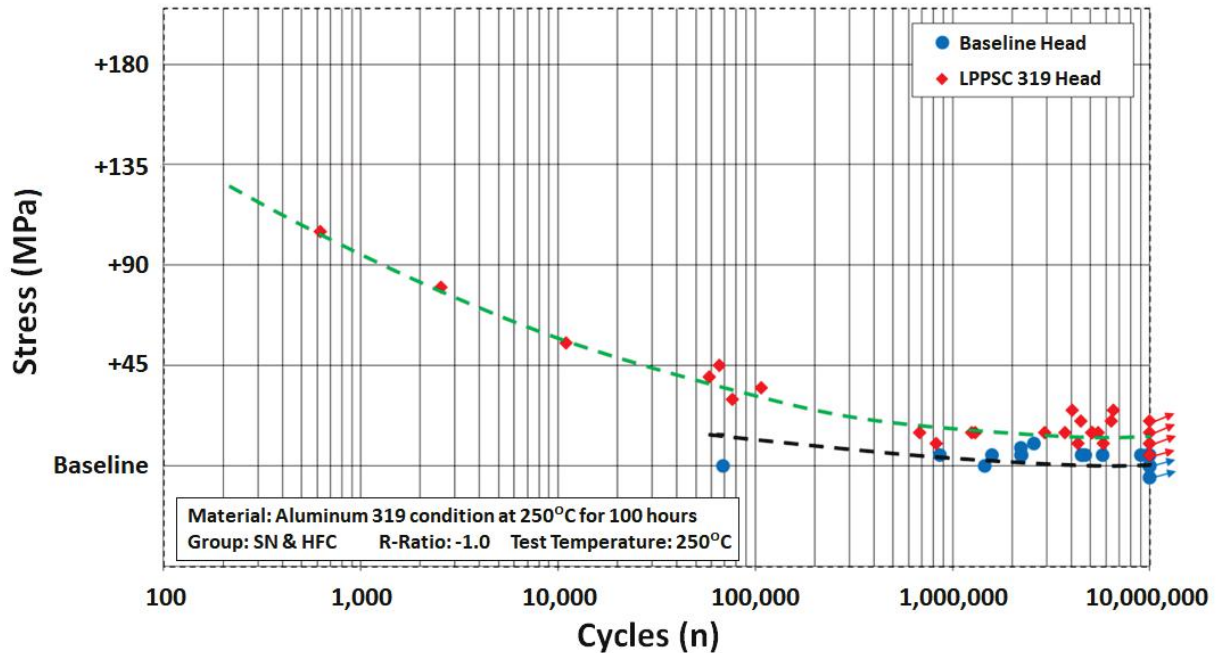


Figure I.2.2.7. S-N fatigue data of LPPSC and baseline 319 alloy cylinder heads tested at 250 °C. Source: GM.

Sub-task 3.2.3

The PHASE 2 piston has been designed and printed with ORNL's Al-Ce based DuAlumin-3D alloy, as shown in Figure I.2.2.8. The PHASE 2 AM piston is ~11g lighter than cast Al production piston. CAE durability analysis indicates that the AM piston design exceeds the piston safety factor (PSF) requirements. Figure I.2.2.9 shows stress-life (S-N) and staircase fatigue testing of both AM and cast Al pistons. The high-cycle fatigue (10^7 cycles) strength of the AM pistons at 300°C is improved by at least 50% in comparison with the cast Al production pistons.



Figure I.2.2.8. AM printed PHASE 2 pistons. Source: ORNL.

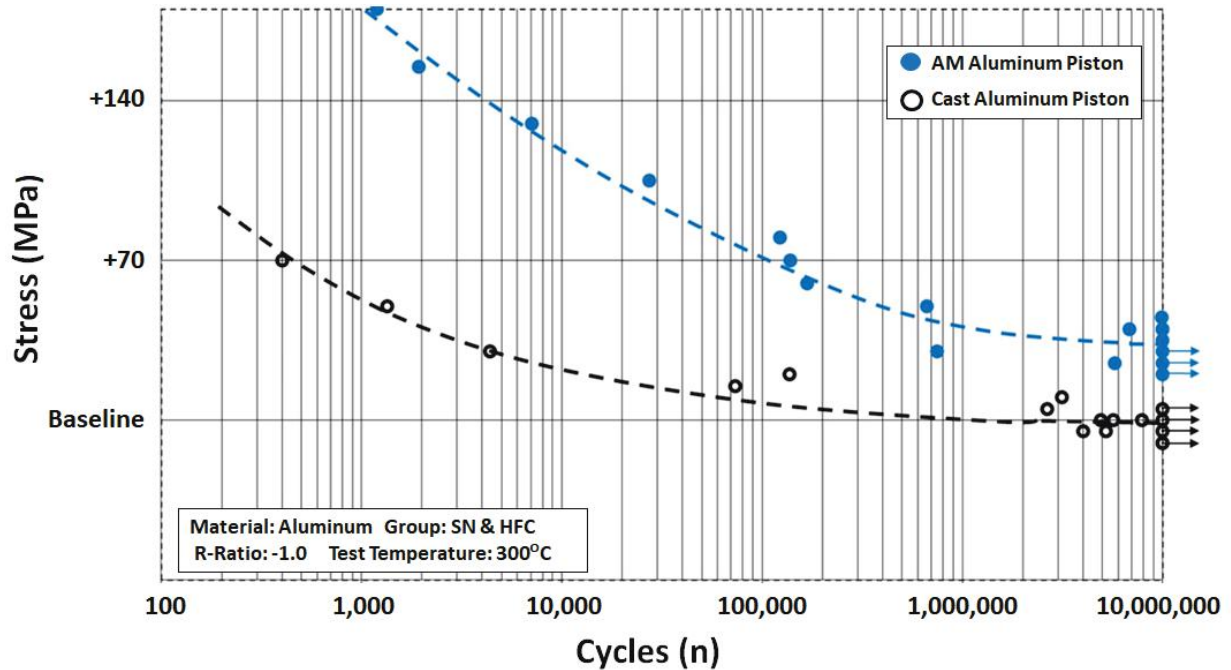


Figure I.2.2.9. S-N fatigue data of AM printed and cast Al pistons tested at 300 °C. Source: GM.

Sub-task 3.2.4

A new design of chills, gating, and riser system has produced high-quality cast steel cranks with minimum microporosity in PHASE 2, as shown in Figure I.2.2.10. Fatigue performance of the PHASE 2 cast steel cranks with the new gating system (e.g., the 2nd set cranks) is much improved in comparison with the cranks made in PHASE 1 (e.g., the 1st set cranks) particularly in the high-cycle fatigue regime (e.g., > 300,000 cycles), as observed in Figure I.2.2.11. The PHASE 2 steel cranks have similar fatigue performance of the forged steel baseline cranks. After HIP, the PHASE 1 cranks show better fatigue performance than the forged ones. It is believed that the PHASE 2 cranks should do the same after HIP, indicating that the cast steel alloy developed in the project has inherent advantages over the baseline forged steels.

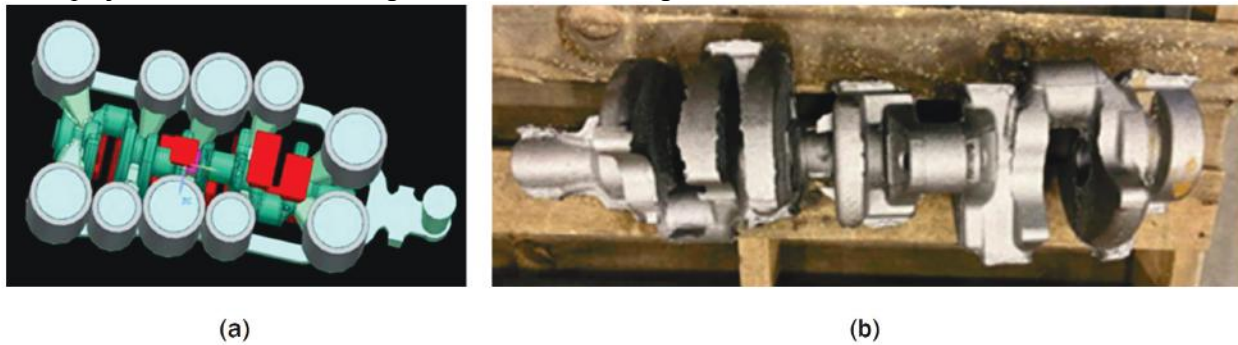


Figure I.2.2.10. (a) New cast steel crank casting design and (b) a PHASE 2 crank. Source: GM.

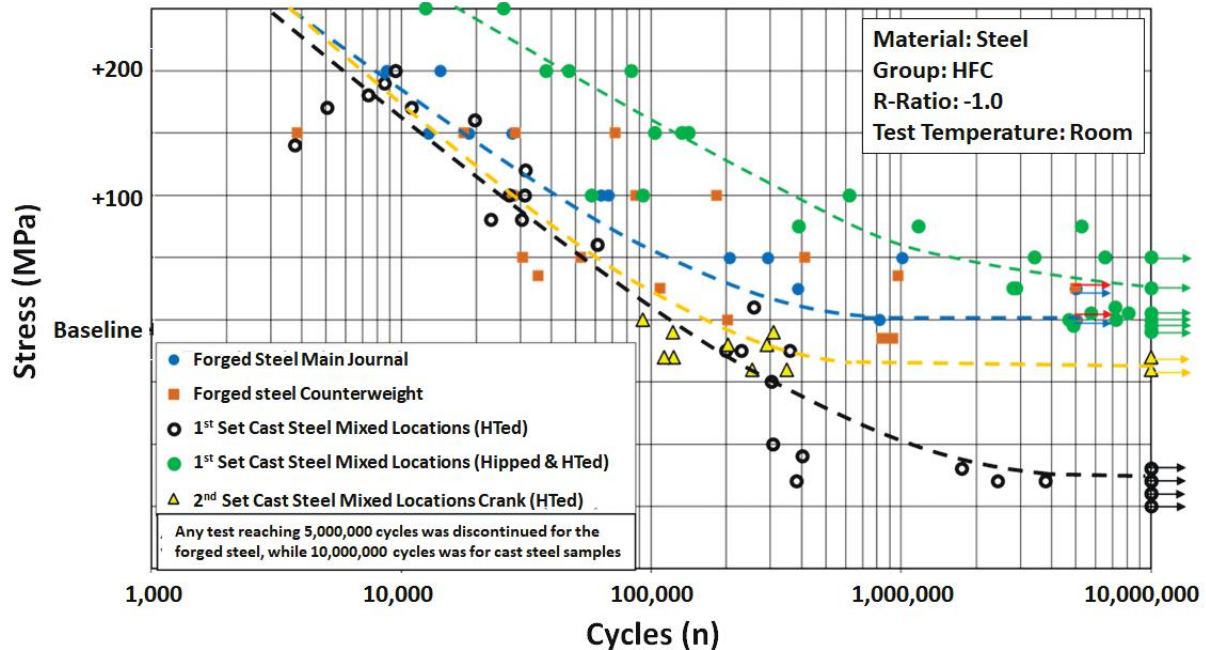


Figure I.2.2.11. S-N fatigue data of cast steel cranks in various conditions compared with the forged baseline cranks. Source: GM.

Sub-task 3.2.5

Through process modeling and local materials property simulation by following the ICME approach that has been continuously conducted on the PHASE 2 cast Al cylinder head and engine block, the cast steel and nodular iron cranks, as well as the cast and AM Al pistons, were all built to ensure their designs met the necessary performance and durability requirements. Figure I.2.2.12 shows the through process modeling approach flow for the LPPSC Al engine block. After the block casting geometry and gating/riser system is optimized, the comprehensive casting process modeling is carried out to simulate the mold filling and solidification. With the modeling capabilities developed at GM for multiscale defects (e.g., porosity and oxides) and microstructure simulation, nodal-based microstructure (e.g., the secondary dendrite arm spacing) and defect population (e.g., porosity volume fraction and sizes) are predicted throughout the entire block casting. Based on the simulated defect and microstructure from casting process modeling, location-specific material properties (e.g., tensile and fatigue properties) can then be predicted and incorporated in the CAE performance and durability analysis of the block casting. Similarly, the through process modeling and ICME approach has been applied to other castings such as cast steel crankshaft.

Figure I.2.2.13 shows an example of using casting process modeling capability in crank casting gating/riser system optimization.

Modeling of AM and cast Al microstructure has been continuing at OSU using the cellular automaton (CA) technique. In this Budget Period, a cast Al microstructure simulation has been focused on columnar to equiaxed transition (CET). Modeling of AM microstructure has been carried out in a simulating grain structure. Figure I.2.2.14 shows an example of the CET simulations of Al-8.6%Si-0.32%Mg-0.44%Fe-0.22%Mn alloy during casting solidification. Figure I.2.2.15 shows an example of AM grain microstructure evolution for a vertical multi-pass build case.

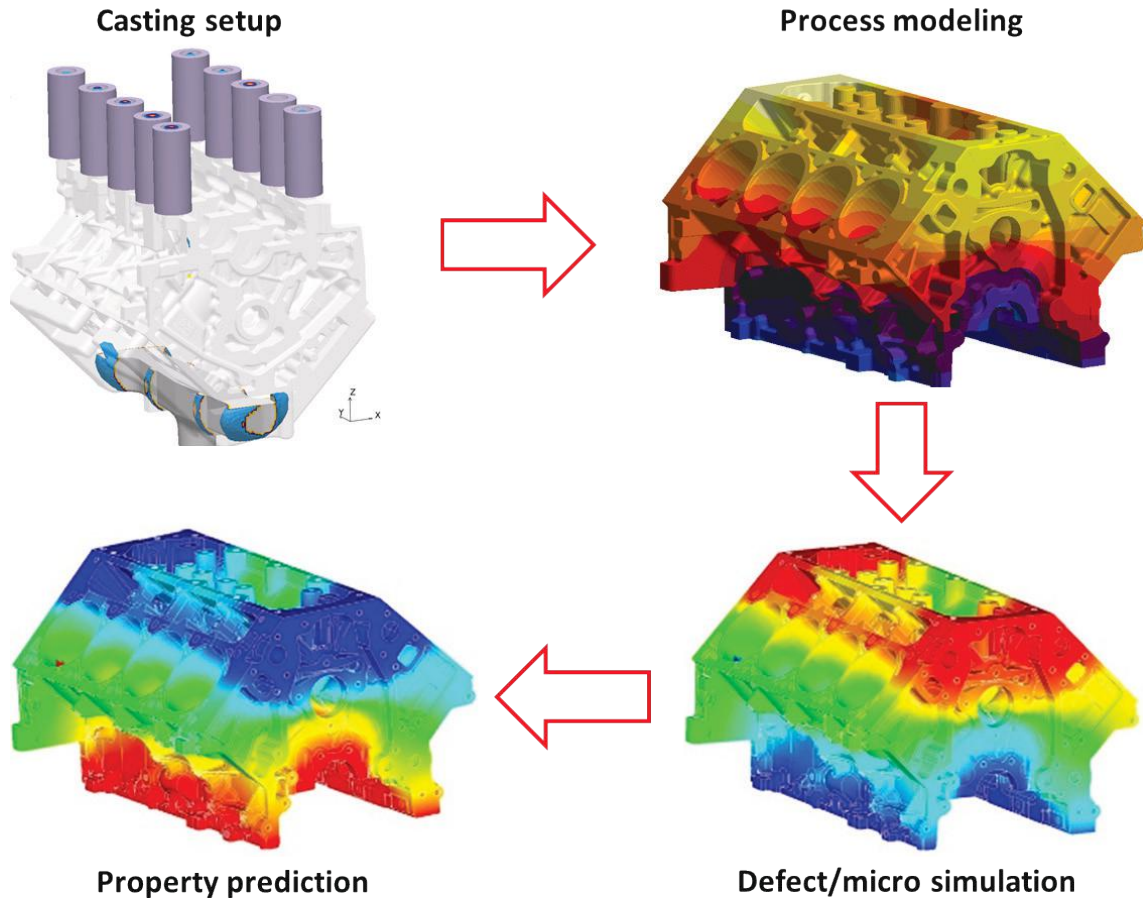


Figure I.2.2.12. Through process modeling approach flow for a cast Al block. Source: GM.

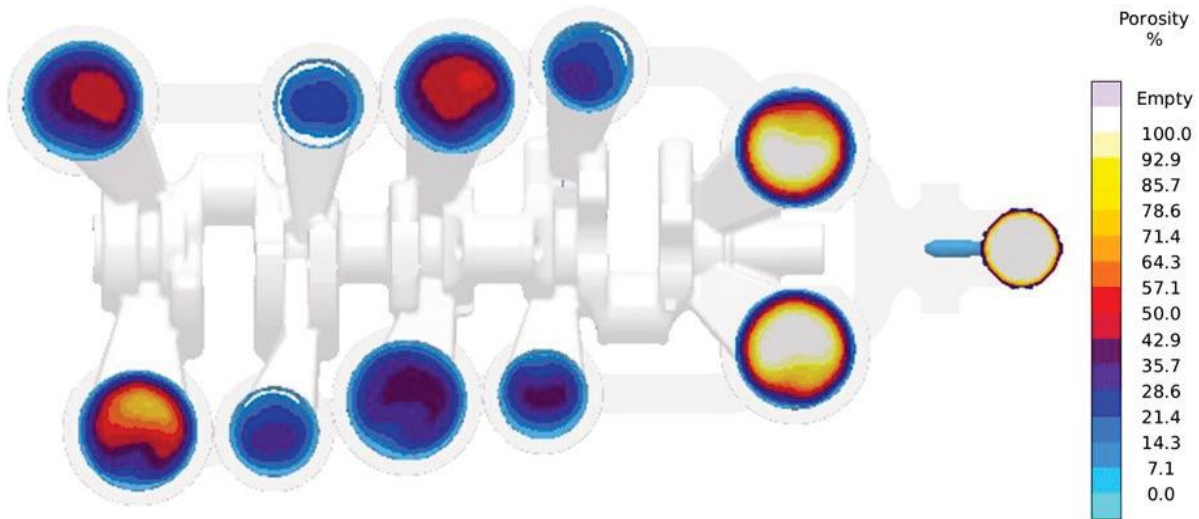
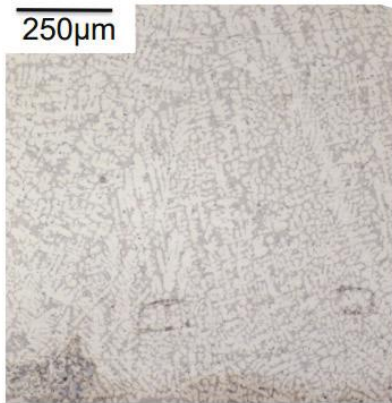


Figure I.2.2.13. Casting process simulation and casting quality (e.g., porosity) prediction in cast steel crank. Source: GM.

Est. average cooling rate 5-10K/s



With random nucleation

Without random nucleation

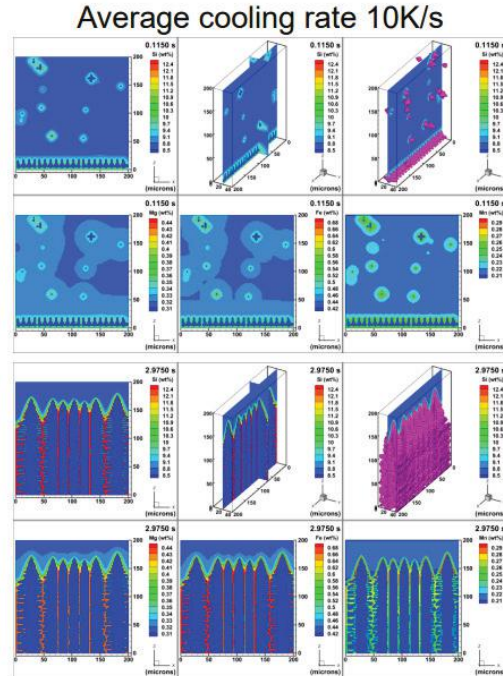


Figure I.2.2.14. CET simulation for cast Al alloy solidified under an average cooling rate of 5-10 K/s, with or without random nucleation. Source: OSU.

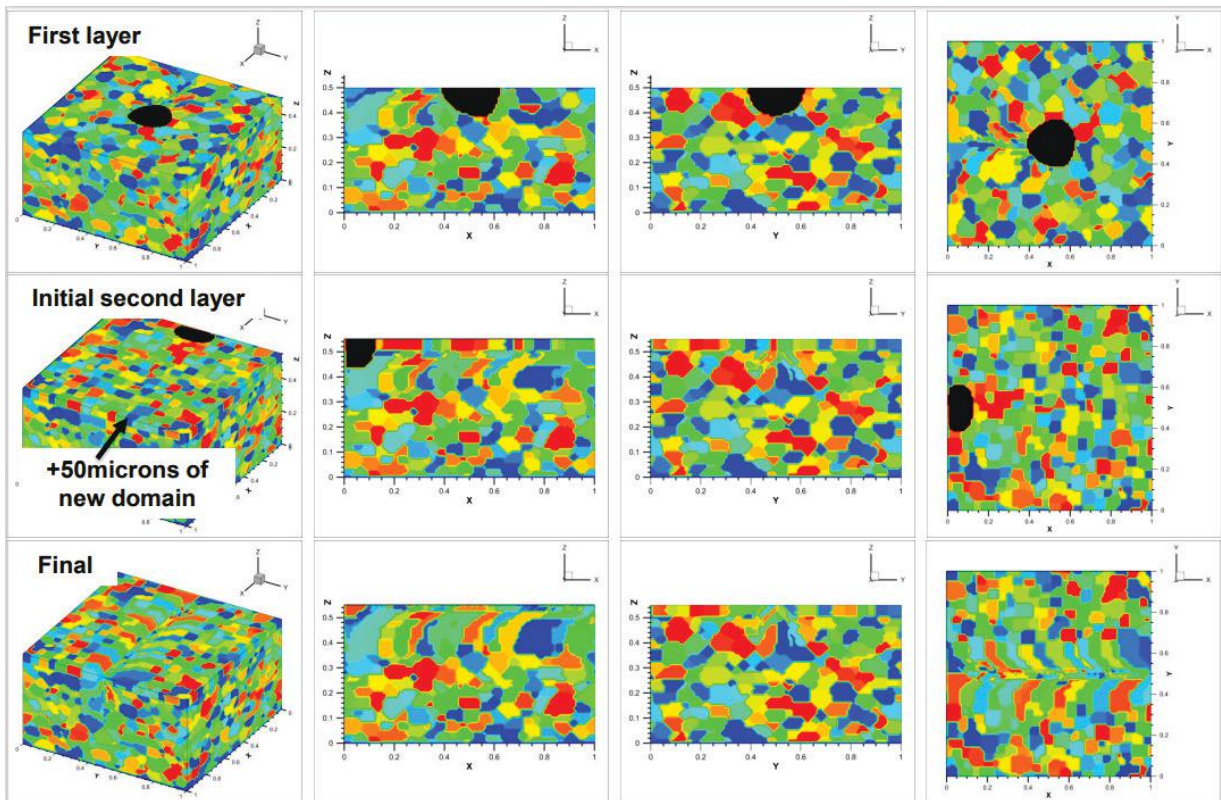


Figure I.2.2.15. CAE simulation of AM grain structure. Laser speed of 1.5M/S and thermal properties of AISi10 alloy used. Top row shows thermal profile, bottom figures show individual grains. Source: OSU.

Conclusions

PHASE 2 engine design has been completed with incorporation of advanced combustion and materials technologies developed in PHASE1. Based on the technology development and verification computationally and experimentally, the designed PHASE2 engine should be able to achieve the FOA objective of 10% fuel economy improvement and 15% mass reduction. ICME approach has been used in the project to link materials, manufacturing and system design into a holistic computational framework to enable the design and manufacturing of key engine parts with location-specific microstructure and material property modeling.

Key Publications

1. Moodispaw, M. P., B. Chen, A. A. Luo, and Q. Wang, 2022, “Achieving metallurgical bonding in aluminum/steel bimetallic castings,” *CastExpo and Metalcasting Congress, 23–26 April 2022, Columbus, OH, USA*, Paper 22-040, American Foundry Society Transactions.

References

1. DOE-EERE, 2019, “Fiscal Year 2019 Advanced Vehicle Technologies Research Funding Opportunity Announcement,” DE-FOA-0002014, Washington, D.C., USA. Available at: <https://eere-exchange.energy.gov/FileContent.aspx?FileID=25f7a4dd-9874-4ace-9606-2ab52fe9cc18>. last accessed 6 February 2023.
2. National Research Council, 2008, *Integrated Computational Materials Engineering: A Transformational Discipline for Improved Competitiveness and National Security*, The National Academies Press, Washington, D.C., USA. <https://doi.org/10.17226/12199>.
3. Wang, Q. G., P. Jones, Y. Wang, and D. Gerard, 2011, “Advances in computational tools for virtual casting of aluminum components,” in: Allison, J. E., P. M. Collins, and G. Spanos (eds.), *Proceedings of the 1st World Congress on ICME*, TMS 2011, pp. 217–222. <https://doi.org/10.1002/9781118147726.ch30>.

Acknowledgments

The PIs would like to thank DOE-EERE VTO for the opportunity to work on this important project, especially Dr. S. Khan, Mr. J. Gibbs, and Mr. R. Nine at DOE for their project oversight. The PIs are also very grateful to Mr. S. Campbell (contract manager at GM) and the GM project and management team; Dr. A. Shyam and his team at ORNL; Prof. A. Luo and his team at OSU, Prof. P. Sanders and his team at MTU, and Mr. D. Weiss and his team at ECK Industries, Inc., for their extreme support and dedication to the project.

I.2.3 Lightweight and Highly Efficient Engines Through Al and Si Alloying of Martensitic Materials (Oak Ridge National Laboratory)

Yong-Ching Chen, Co-Principal Investigator

Cummins Technical Center
1900 McKinley Avenue
Columbus, IN 47201
E-mail: yong-ching.c.chen@cummins.com

Dean Pierce, Co-Principal Investigator

Oak Ridge National Laboratory
1 Bethel Valley Road
Oak Ridge, TN 37831
E-mail: piercedt@ornl.gov

Jerry L. Gibbs, DOE Technology Development Manager

U.S. Department of Energy
E-mail: jerry.gibbs@ee.doe.gov

Start Date: May 1, 2019	End Date: October 31, 2023	
Project Funding (FY 2022): \$1,625,000	DOE share: \$625,000	Non-DOE share: \$1,000,000

Project Introduction

This project began as a joint two-year project funded by the DOE VTO LightMAT Program between ORNL and Cummins to develop and engine-test a new steel alloy for pistons in advanced, higher efficiency diesel engines. The project brings expertise from both organizations to enable rapid development and specific optimization of the alloy's properties for the unique requirements of the piston application. The project was divided into Phase 1—focused on laboratory-scale alloy development—and Phase 2—focused on scaling the developed alloy, manufacturing a piston from the new alloy, and then engine-testing the full-scale piston. Work in both phases of the project is being completed jointly by Cummins and ORNL, but ORNL executed the majority of the alloy development in Phase 1 while Cummins is primarily responsible for the majority of efforts relating to piston manufacture and engine-testing in Phase 2. The project is currently in Phase 2. An extension of one-year with an additional \$125,000 in funds to ORNL and an additional \$80,000 cost-share commitment by Cummins was approved by VTO in FY 2021. Cummins has exceeded their cost-share commitment of \$580,000 and has spent \$742,473 as of October 30, 2022. Cummins expects the total in-kind contribution for the project to be ~\$1,000,000 at the end of the project. Some delays to the project have been incurred—mostly related to the supply chain for manufacturing prototype pistons for engine-testing—and a no-cost extension has been submitted to extend the project end date to October 31, 2023.

The current piston materials for medium and HDDEs are quenched and tempered 4140 martensitic steel and grade 38MnVS6 micro-alloyed steel (MAS). These materials are cost-effective and have high-strength and acceptable oxidation resistance at temperatures up to ~500°C. A primary pathway to increase the efficiency of internal combustion engines involves increasing both peak cylinder pressure and combustion gas temperature. However, 4140 and MAS are currently operating at their temperature limits, which prevents further increases in efficiency by increasing combustion gas temperatures and pressures. Thus, new piston materials are required to overcome this barrier to increasing MD and HD diesel engine efficiency. Additional barriers to implementing new piston materials are cost and manufacturability. Some commercially available candidate materials that may possess the necessary elevated temperature properties are too expensive or have poor weldability and/or machinability resulting in additional costs and technical barriers.

Objectives

The objectives of this project are to develop and engine-test new steel alloys for diesel engine pistons capable of higher temperature. A new steel alloy must exhibit sufficient fatigue strength and oxidation resistance to be able to operate at peak temperatures of 600°C for extended periods of time. Furthermore, elevated-temperature strength, oxidation resistance, and thermal conductivity are often in conflict with one another, and significant attention in this project has focused on how to balance these competing properties. An alloy must also be friction weldable to a piston-skirt material of 4140 or MAS and have reasonably good machining characteristics. In addition, the raw material cost of the new steel can only be incrementally greater than 4140 or MAS. The developmental steel must also demonstrate a higher TRL to enable the alloy to be commercially scaled and implemented in a relatively rapid timeframe, meaning the alloy should be similar enough to existing materials that it can be manufactured and processed with existing processes and equipment at steel mills and piston manufacturers. Therefore, while innovative alloying strategies are being pursued in this project, radical departures from current or candidate commercial materials have been carefully avoided in this three-year project. Cummins and ORNL have defined internal targets for strength, thermal conductivity, oxidation resistance, and cost for the new alloys.

Approach

This project is focused on the development of new higher temperature steel alloys for piston materials. We have selected 4140 steel as the baseline alloy along with one additional commercial alloy, designated 'Alloy C,' with higher heat resistance that may be suitable for 600°C operation in piston materials. These baseline alloys were used to evaluate performance improvements of the new developmental alloys. This project used computational alloy design methods to better facilitate identification of alloy chemistries that were expected to possess the necessary mechanical and oxidation properties for piston applications operating at 600°C. Once alloy compositions were identified, the alloys were arc-melted, processed by hot-rolling, heat-treated, tested, and characterized. Testing included elevated-temperature tensile testing, oxidation testing, thermal diffusivity measurements, and measurements of the coefficient of thermal expansion for select alloys. Samples were also aged at high temperatures for long periods of time to simulate thermal exposure during engine operation, and then tensile tested at elevated temperatures to evaluate each alloy's resistance to aging. High-cycle rotating beam fatigue testing was performed on lab melted ingots of the developmental alloy. Microstructures were characterized by optical microscopy.

An iterative alloy development process was used, in which small batches of material were melted and tested based on computational guidance, and the experimental results used to guide the development of the next batch(es) of alloys. This process has resulted in an improved understanding of alloying effects on properties relevant to piston materials, continuous optimization, and downselection of promising alloy chemistries and processing routes. The same tests were performed on Alloy 4140 and Alloy C as were also used in the developmental alloys to directly compare and assess any improvement over the well-established commercial alloys. Computational fluid dynamics software was employed to evaluate how properties such as alloy thermal conductivity affect piston temperature distributions under expected engine operating conditions, and to evaluate how predicted surface temperatures will change from alloy to alloy.

For the final phase of this project, a new developmental alloy was downselected and then scaled-up at an external vendor in order to make sufficient amounts of material for fabrication of piston prototypes with a piston manufacturer. The prototype pistons are currently in the process of being manufactured in Q4 FY 2022 and will undergo welding and machining trials. The new developmental alloy from this LightMAT project will be used for the piston crown and rotary friction welded to a piston-skirt comprised of MAS. High-cycle rotating beam fatigue testing at elevated temperatures also will be performed on the scaled-up developmental steel material to understand how it compares to the lab melted steel previously tested.

Results

The data generated in this project are proprietary and only certain details are available for public disclosure. Some delays to the project have been incurred due to the Covid-19 pandemic. The following important results and achievements have occurred in FY 2022:

- Cummins and ORNL, working with external steel melting and forging shops, melted and rotary forged an 1800 lb. ingot of the new development steel. The forged round bar was cut into pucks for subsequent processing into piston crowns.
- The pucks were machined closer to piston dimensions (pre-machined pucks). Cummins and ORNL worked with a heat-treatment shop to develop an industrial heat-treatment procedure for the developmental alloy (pre-machined pucks). 60+ pre-machined pucks of the developmental alloy were heat-treated and subsequently provided to the piston supplier, MAHLE, for prototype piston manufacture.
- MAHLE, Cummins, and ORNL are in the process of fabricating the piston prototypes, with manufacturing occurring at a MAHLE facility.
- Cummins and ORNL, working with MAHLE, have performed modeling of predicted temperature and stresses the piston would be exposed to during engine-testing to ensure safe operation.

Conclusions

In FY 2022, Cummins and ORNL melted and forged an 1800 lb. ingot, fabricated pre-machined pucks from the forged bar, developed a heat-treatment procedure and heat-treated the pucks, and are in the process of fabricating prototype piston crowns from the pucks with MAHLE. These developmental crowns will be friction welded to piston skirts, consisting of microalloyed steel, by MAHLE for full-scale engine-testing by Cummins. A split engine-test (e.g., three developmental alloy pistons and three baseline 4140 pistons) is planned at Cummins for Q2 FY 2023. The project has submitted a no-cost extension to extend the project end date to October 31, 2023, to give ample time to characterize engine tested pistons and to complete any remaining project tasks.

Key Publications

1. Invention disclosure submitted by Cummins and ORNL in FY 2021.
2. Patent application submitted by Cummins and ORNL in FY 2021.

Acknowledgments

The following ORNL personnel are acknowledged for their contributions to this project: G. Muralidharan, A. Haynes, T. Muth, I. Stinson, G. Cox, D. Moore, D. Heidel, K. Hanson, V. Cox, H. Wang, A. Trofimov, K. Hedrick, and G. Garner. The following Cummins personnel are acknowledged for their contributions as well: C. Trobaugh, Q. Ma, J. Zhou, H. Savage, B. Wang, W. D. McNulty, J. Wright, and D. E. Richardson. The following MAHLE personnel are acknowledged for their contributions: D. Gabriel and E. D. Rejowski.

I.2.4 Multiscale Development and Validation of the Stainless Steel Alloy Corrosion (SStAC) Tool for High-Temperature Engine Materials (University of Florida)

Michael Tonks, Principal Investigator

University of Florida
100D Rhines Hall
Gainesville, FL 32611
E-mail: michael.tonks@ufl.edu

Jerry L. Gibbs, DOE Technology Development Manager

U.S. Department of Energy
E-mail: jerry.gibbs@ee.doe.gov

Start Date: May 1, 2019 End Date: October 31, 2023
Project Funding (FY 2022): \$1,625,000 DOE share: \$625,000 Non-DOE share: \$1,000,000

Project Introduction

The environment within an engine cylinder during operation is extremely harsh, with high temperatures, combustion, and corrosive exhaust gases. This environment corrodes engine components, including exhaust valves and exhaust valve seats. Current engine materials, such as stainless steels, resist corrosion during normal operation. However, as new engines are pushed to higher temperatures, the material can undergo microstructure evolution that sensitizes it to corrosion, resulting in premature failure.

Companies that design and build engine parts do not typically employ models of corrosion; rather, they employ standard temperature ranges and allowable fuels for which each alloy can be employed when making material selection decisions for a specific part and customer. These standards are based on conservative physical properties of the alloy and on successful deployment history. This reliance on conservative standards can result in over-design and increased cost. In addition, if a new advanced engine design results in conditions significantly different from the deployment history, these standards may not be applicable. This can lead to a vastly increased time and cost of development.

Objectives

The goal of this project is to create a simulation tool to assist in part design, reducing costs by eliminating the need for conservative material selection, and enabling alloy optimization to improve corrosion resistance. Thus, it will help reduce costs for existing engines and will assist in the material selection and engine design for the engines of the future, reducing development time by years. To meet our stated goal, have developed the SStAC tool, which:

- Can model corrosion of valve steels in an engine environment at temperatures up to 800°C
- Can simulate the corrosion of an engine valve in 1D for a fast estimate of the corrosion rate and in 2D and 3D for more detailed simulations that represent the valve geometry and predict the precise location and rate of corrosion
- Was implemented using the Multiphysics Object-Oriented Simulation Environment (MOOSE)
- Employs a corrosion model that is being developed to describe the fundamental mechanisms of corrosion, including the impact of microstructure and alloy composition.

At the completion of the project, the SStAC tool will be able to predict the corrosion rate of engine valves with no more than 10% error.

Approach

The SStAC tool is being developed using a combination of macroscale model development, mesoscale, and atomic scale simulations to define the impact of microstructure on alloy corrosion, and an experimental campaign to inform and validate the models. This work is being carried out during three BPs. BP1 ended in February 2020 and our primary focus was the development of an initial corrosion model. BP2 ended in February 2021 and focused on the creation of the SStAC tool using the MOOSE framework. BP3 began in March 2021 and encompassed the completion and preliminary validation of the SStAC tool. The tasks for BP 3 were:

- Task 3.1 – Third Experimental Campaign
- Task 3.2 – Validate and Apply the Mesoscale Model
- Task 3.3 – Validation and Release of the SStAC Tool.

Results

Task 3.1 – Third Experimental Campaign

The corrosion experiments in dry and wet CO₂ showed the formation of Mn-rich oxide layers. Mn diffusion from the alloy substrate to the oxide/metal interface has been identified as being the rate-limiting step in 21-2N corrosion. However, Mn is FCC stabilized and its depletion induces the nucleation and growth of a body-centered cubic (BCC) layer at the oxide/metal interface, growing into the alloy. Since the BCC phases are known to be less ductile than FCC, there is a potential risk of alloy embrittlement or oxide spallation under thermal cycling. To investigate the effect of the Mn depletion region on the mechanical properties, such as hardness, of the alloy near the scale/alloy interface, a 21-2N sample was corroded in Ar-20O₂ atmosphere for 100 hours and nano-indentation near the oxide/metal interface was performed. Figure I.2.4.1(a) shows the cross-section of 21-2N sample with indents near oxide/metal interface and gradually reaching 20 μm away from the oxide/metal interface. Figure I.2.4.1(b) shows the hardness values as a function of the distance from scale/alloy interface where the value decreases to ~ 3 GPa in the bulk area compared to values of 4.5–5 GPa in the Mn-depleted region close the scale/alloy interface. Figure I.2.4.1(c) shows an EDS line scan near the oxide/metal interface of Mn, Cr, and Fe wt.% composition.

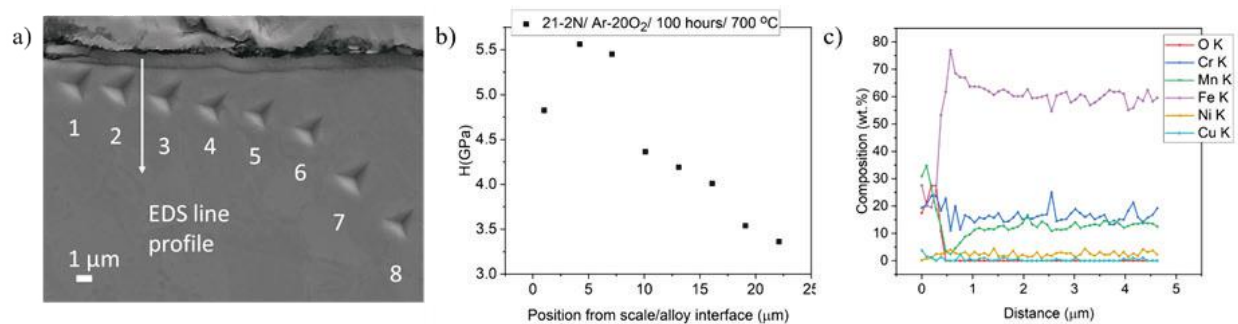


Figure I.2.4.1. (a) SEM micrographs of 21-2N corroded in Ar-20O₂ atmosphere. (b) A graph of the hardness values. (c) The EDS line scan elemental composition from the scale/alloy interface into the alloy.

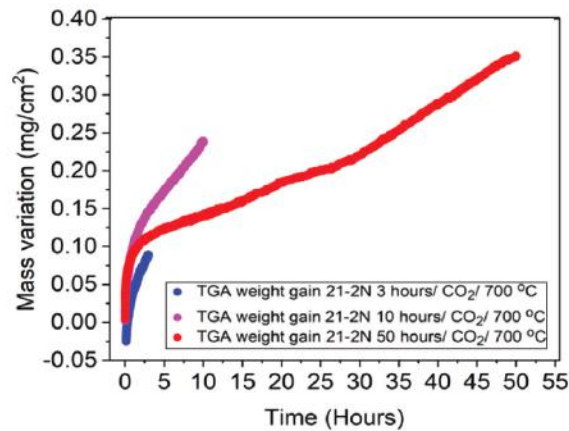
Source: University of Wisconsin-Madison.

It appears that the BCC phase is indeed harder than the region deeper into the substrate. It would be interesting to study the possible spallation of the oxide under thermal cycling induced by the growth of the harder—and likely more brittle—BCC phase underneath the oxide.

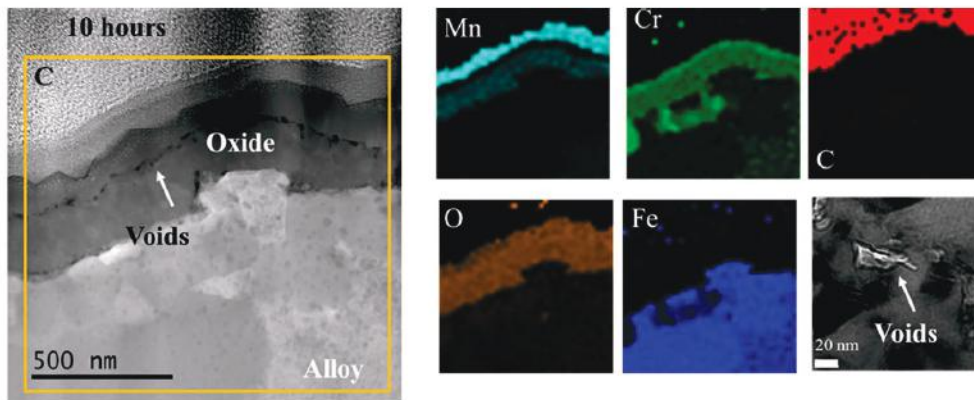
TGA was performed on a 21-2N alloy in dry CO₂ for 3, 10, and 50 hours at 700°C to study the oxidation rate continuously at low exposure. TGA was relatively complex to perform because of the very small sample size and the relatively high oxidation rate at the beginning of exposure induced by the high Mn reactivity. TGA results are presented in Figure I.2.4.2(a) as mass gain per unit area for the three different exposure times. The

data does not exactly line up for all three samples due to the scatter in the sample geometry. Nevertheless, a rapid increase in weight gain is observed, likely because of high Mn-rich oxide growth. As exposure time increases, the Mn-rich oxide transforms into a more protective MnCr_2O_4 spinel, and the oxidation rate decreases. It is worth noting that the weight gain in TGA after 50 hours of exposure is like the one obtained after 50 hours in the corrosion furnace on bulk samples. This makes the TGA data reliable and comparable to the previous weight gain curves obtained on the bulk samples.

Figure I.2.4.2(b) shows the TEM/EDS cross-sectional analysis of the sample corroded for 10 hours in TGA. The outer Mn oxide and inner MnCr spinel are observed after 10 hours exposure in TGA. There is also evidence of voids at Mn and Cr oxide interface—most probably Mn diffuses through the MnCr spinel and a thin chromia layer forms between the inner MnCr spinel and the outer Mn_3O_4 oxide. This mechanism is the same as that determined for the bulk samples. Consequently, the corrosion mechanism of small samples in the TGA is comparable to the bulk samples in the corrosion furnace tube. A continuous oxide layering is observed very early on—as early as after 10 hours of exposure. Hence, a protective oxide forms extremely fast on the 21-2N alloy and a layered oxide layer grows homogeneously on the sample. This is likely different in 23-8N, which would likely form non-continuous oxide formation and patches of non-protective oxide growth.



(a)



(b)

Figure I.2.4.2. (a) TGA curves for 21-2N corroded in dry CO_2 at 700°C for 3, 10, and 50 hours. (b) TEM/EDS cross-section analysis of the oxide formed on 21-2N after 10 hours in the TGA.

Source: University of Wisconsin-Madison.

Task 3.2 – Validate and Apply the Mesoscale Model

Atomic Scale Development

The atomistic simulation campaign has completed its work on defect thermodynamics and kinetics in the MnCr_2O_4 oxide phase. The most crucial advancements made since the previous year include a thorough analysis of interstitial defect sites and the identification of an interstitial mechanism that is favorable for bulk diffusion of oxygen. Furthermore, we have made progress in evaluating the migration energy barriers of point defects in the Cr_2O_3 , Mn_3O_4 , and Fe_2O_3 phases that have also been identified in the layered oxide structure by our experimental collaborators.

Figure I.2.4.3 illustrates the three possible oxygen vacancy migration pathways in MnCr_2O_4 spinel. The oxygen can migrate between the shared edge of two Cr octahedra, along the edge of a Mn tetrahedron, or through a structural vacancy between the corners of a Mn tetrahedron and a Cr octahedron. Our investigation finds that the pathway that includes the structural vacancy has a significantly lower barrier height of just 2.1 eV relative to the octahedral pathway at 3.3 eV or the tetrahedral pathway at 3.2 eV. Additionally, we find that the charge state-of-the oxygen vacancy has a negligible effect on the overall barrier height. The 1^+ state was considered due to its lower formation energy relative to the neutral state at the valence edge of the bandgap. No other charge states showed any region of favorability.

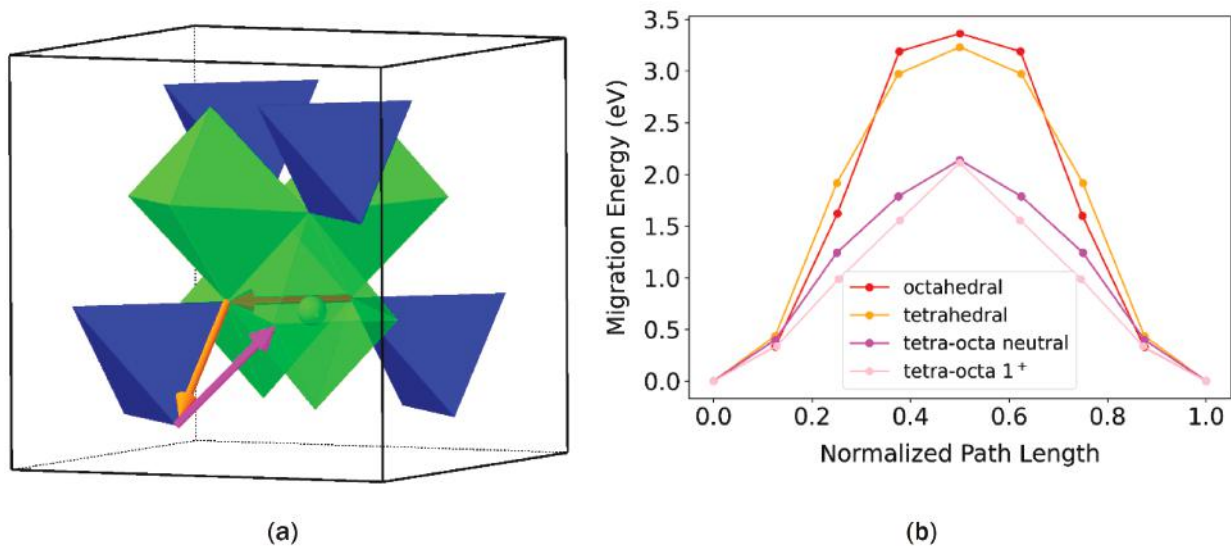


Figure I.2.4.3. (a) Polyhedral structure of a conventional MnCr_2O_4 unit cell showing the vectors of travel for each vacancy mediated oxygen migration. (b) Nudged elastic band method profile illustrating the migration barrier heights for each vacancy mediated oxygen migration mechanism. Source: University of Florida.

Figure I.2.1.4. illustrates an interstitial mechanism by which oxygen can diffuse through the MnCr_2O_4 lattice. Our investigation found that oxygen interstitial defects are significantly more favorable than cationic interstitial defects—especially when they occupy a split ‘dumbbell’ type configuration. This mechanism can occur when one of the oxygens in a dumbbell arrangement migrates to a neighboring oxygen lattice site, knocking the existing oxygen off its position and creating another dumbbell on the adjacent lattice site. The barrier height associated with this mechanism is 1.9 eV. When forming the interstitial oxygen defect, the neutral charge state is favored throughout the bandgap, and was thus the only charge state considered for migration. Given the small 0.2 eV difference in barrier height between this mechanism and the aforementioned vacancy mediated one, it is clear that oxygen may migrate along either path, which suggests a higher overall mobility for oxygen.

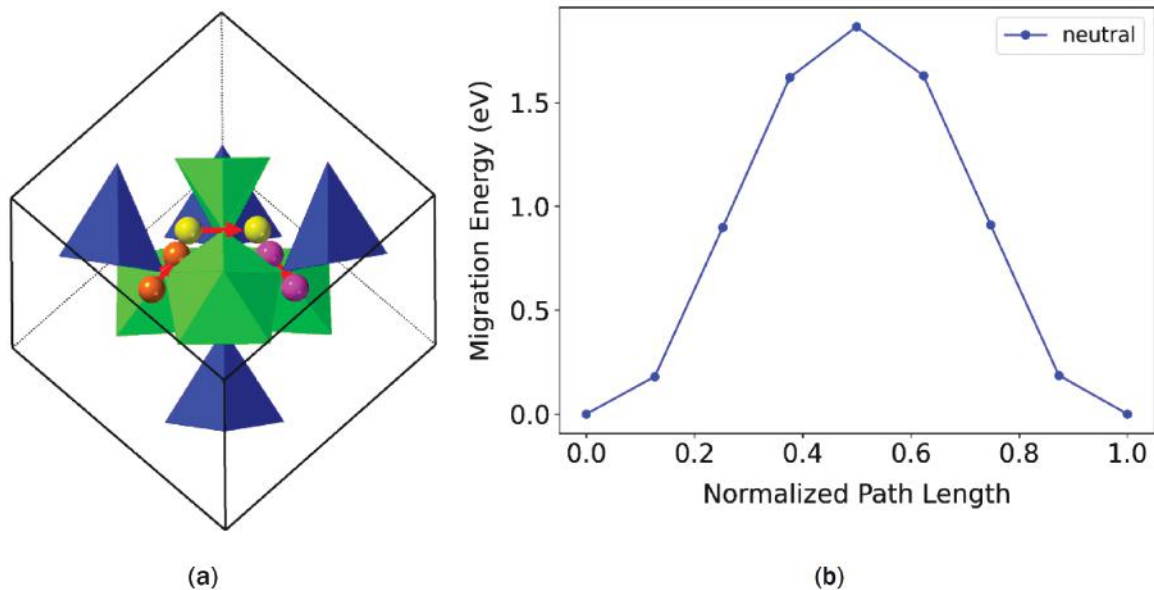


Figure I.2.4.4. (a) A schematic of the migration mechanism for an oxygen split 'dumbbell' interstitial in MnCr_2O_4 . (b) Migration barrier height for the mechanism. Source: University of Florida.

Current work on Cr_2O_3 has been focused on validating the methods using native Cr vacancy mediated mechanisms, but future work that will be more valuable for model development will consider the migration of substituted cationic species, such as Mn or Fe in the Cr_2O_3 lattice. This will help us to understand the kinetic barriers that contribute to the oxide layer ordering atop the steel substrate. We have identified likely cationic migration pathways and are interested in exploring if those same paths are favored for substituted cationic species.

Mesoscale Model Development

An electrochemical phase-field model has been developed to investigate the oxidation mechanisms of the 21-2N valve stainless steel alloy exposed to CO_2 at 973 K. Three oxide phases observed in oxidation experiments are included in the model: (1) Mn_3O_4 , (2) Cr_2O_3 , and (3) MnCr_2O_4 . The sensitivity of the oxidation processes to the values of the diffusion mobilities was examined. We find that both inward oxygen and outward metal diffusion are important for oxidation. The oxidation rate is calibrated against experimental data by modifying the following sensitive mobilities:

$$M_{\text{Cr}}^{\text{Cr}_2\text{O}_3}, M_{\text{Cr}}^{\text{MnCr}_2\text{O}_4}, M_{\text{O}}^{\text{MnCr}_2\text{O}_4}, M_{\text{Mn}}^{\text{MnCr}_2\text{O}_4}.$$

The comparison between the calibrated and the experimental oxidation rate is shown in Figure I.2.4.5. The root-mean-square percentage error of MnCr_2O_4 , Cr_2O_3 , and Mn_3O_4 growth rate between the simulation and experiment are 17.46%, 26.70%, and 44.25%, respectively.

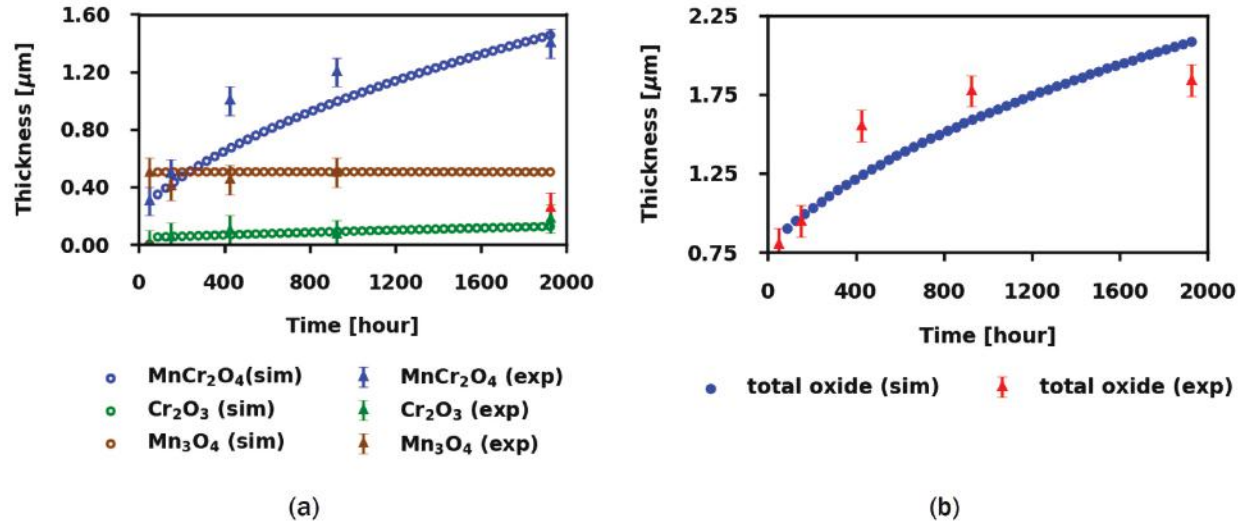


Figure I.2.4.5. (a) Comparison between experimental and calibrated simulation oxidation rates showing the growth rate of each oxide where the Mn_3O_4 experimental thickness at the 1925 hour (marked as red) is possibly due to surface spallation. (b) The growth rate of the total oxide. The root-mean-square percentage error between the experiment and the simulation is 12.14%. Source: University of Florida.

Table I.2.4.1. The Order of Oxides Used for This Study

Order Label	Inner Oxide	Middle Oxide	Outer Oxide
Order 1	MnCr_2O_4	Cr_2O_3	Mn_3O_4
Order 2	MnCr_2O_4	Mn_3O_4	Cr_2O_3
Order 3	Cr_2O_3	MnCr_2O_4	Mn_3O_4
Order 4	Cr_2O_3	Mn_3O_4	MnCr_2O_4
Order 5	Mn_3O_4	MnCr_2O_4	Cr_2O_3

In 1D simulation, like is used for the simulation from Figure I.2.4.5, the order of the oxides directly impacts the oxide growth, since an oxide layer can only grow if metal and O ions arrive at the oxide interfaces. Therefore, we investigated how the order of the initial oxide layers changes the oxide growth. Table I.2.4.1 lists the labels we used for five possible orders of the three oxide layers. The oxides have the same $0.1 \mu\text{m}$ initial length. We find that Cr_2O_3 serves as a barrier to outward Mn diffusion, as shown in Figure I.2.4.6. Moreover, coating the alloy with Cr_2O_3 could be used to limit oxidation.

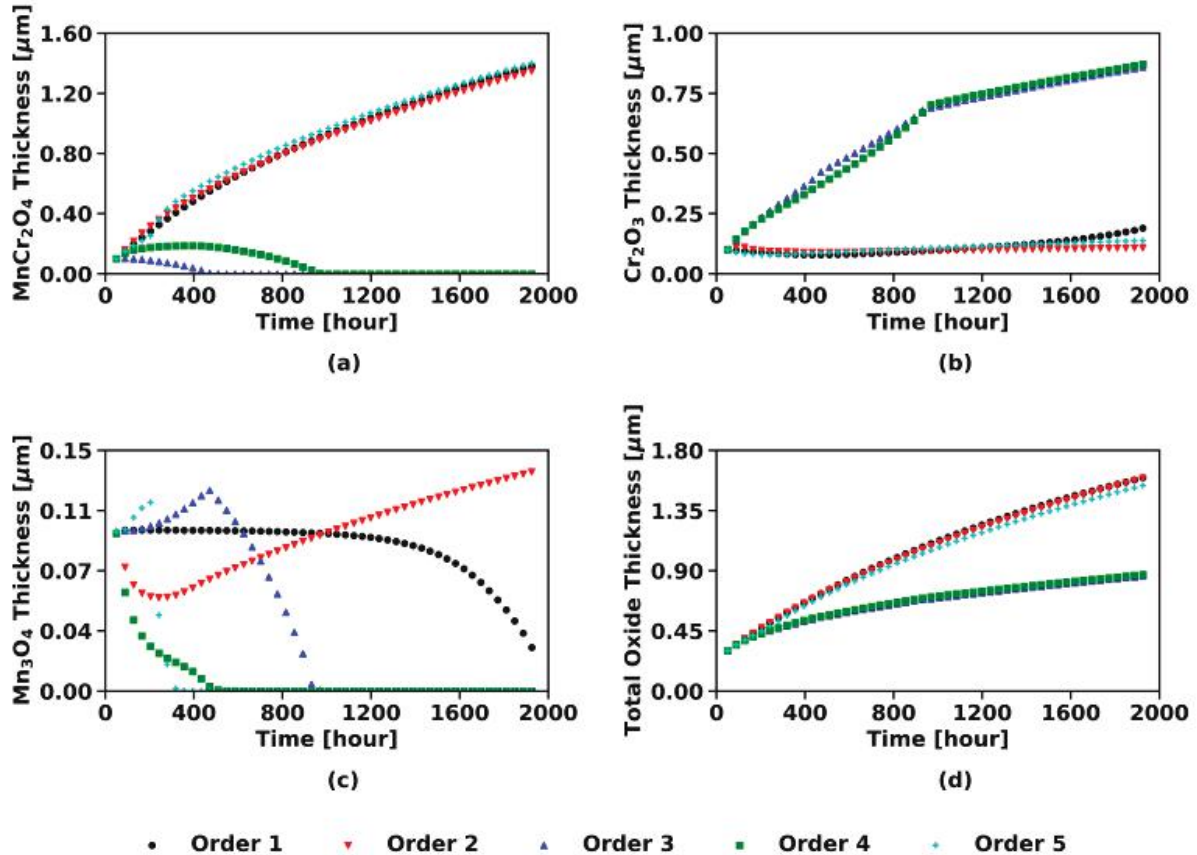


Figure I.2.4.6. Oxide growth with time for Orders 1-5 from Table I.2.4.1. (a), (b), (c), and (d) show the growth of MnCr_2O_4 , Cr_2O_3 , Mn_3O_4 , and the total oxide, respectively. Source: University of Florida.

Task 3.3 – Validation and Release of the SStAC

The SStAC tool has been developed in the MOOSE framework. In the tool, the level set method is used to represent the moving interface. The interface location is updated by solving a level set evolution equation. The level set method is used in conjunction with the extended FEM to introduce solution discontinuity at the interface. The interfacial constraints are weakly enforced via a penalty method. The velocity extension procedure based on the nearest node projection is implemented. The proposed algorithm is fulfilled by the unique multi-app capability of MOOSE.

Accelerated foil corrosion tests were simulated to predict corrosion morphologies with the goal of demonstrating the viability of the approach in multi-dimensions and benchmarking against results from a published experimental and numerical study [1]. The results of growth of a single isolated pit and multiple pits are shown in Figure I.2.4.7. MOOSE's numerical results of real-time pit growth are consistent with the numerical solution from the literature.

Finally, we applied our method to an engine valve problem. The temperature on the exterior was obtained from the literature. The outward corrosion was considered. The corrosion velocity is proportional to the temperature and has a cutoff value of 920K. Both 2D axisymmetric and fully 3D valve problems were simulated as shown in Figure I.2.4.8. The unique capabilities of our computational framework include: (1) setting different properties for base metal and oxide materials; (2) solving fully multiphysics problems including mechanics, thermal and mass diffusion; and (3) massive parallel computing that is dimension agnostic. The codes, input files, and documentation are available to the public on Github (<https://github.com/jiangwen84/sstac>).

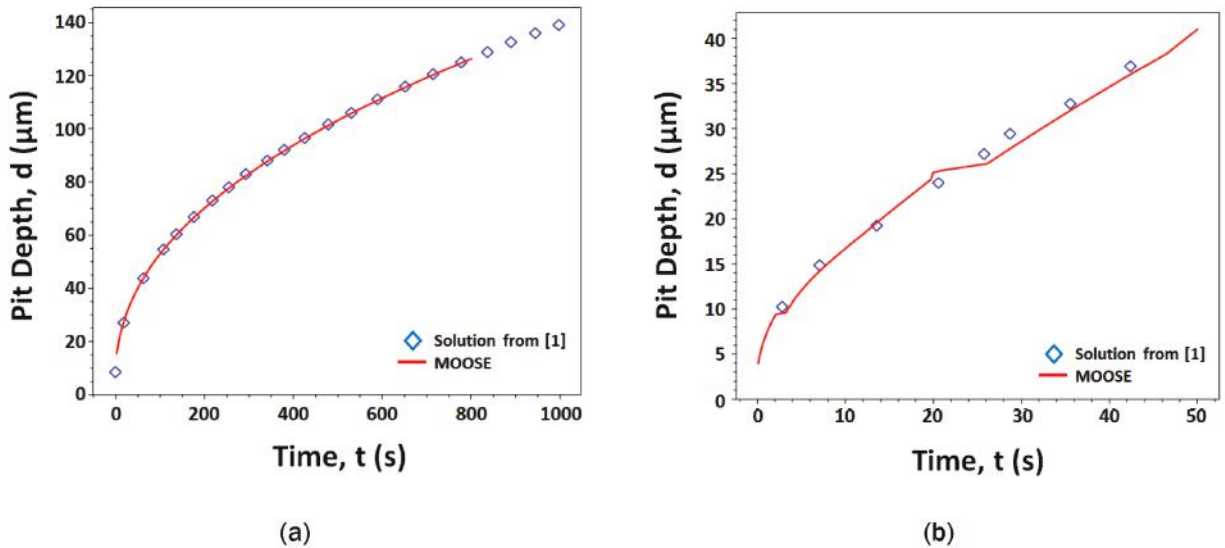


Figure I.2.4.7. Numerical results of pit corrosion compared with the solution from [1]. The pit growth kinetics for (a) a single pit and (b) multiple pits. Source: Idaho National Laboratory.

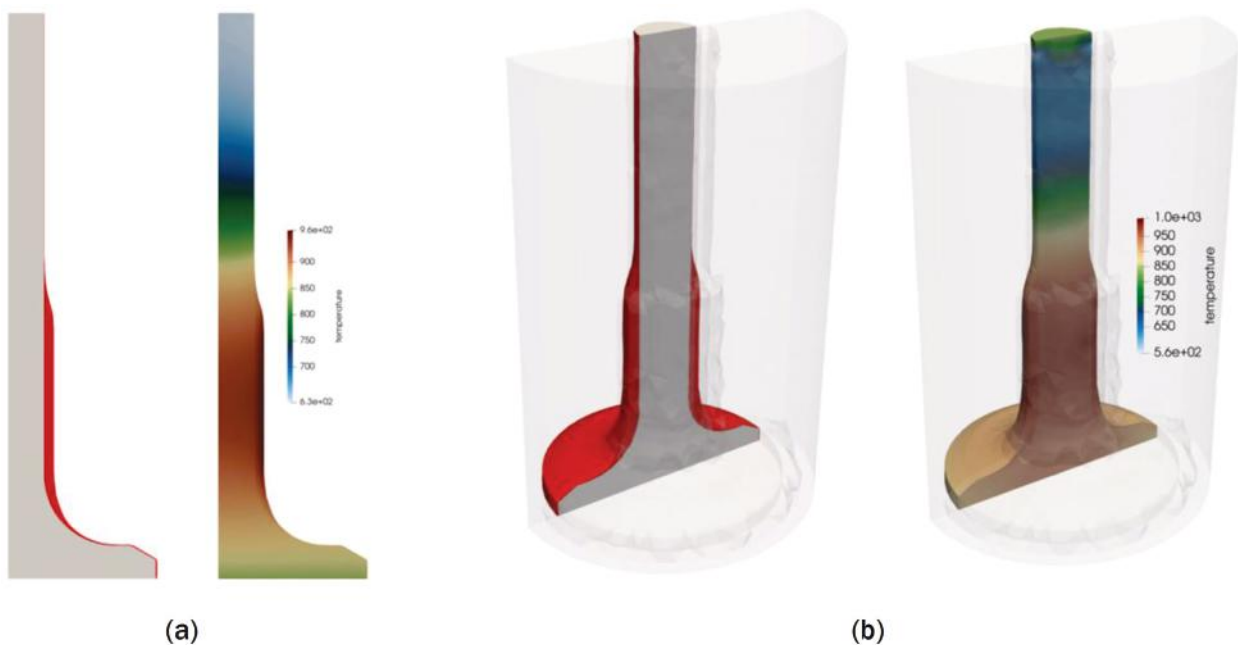


Figure I.2.4.8. (a) Outward oxide growth predicted by the SStAC tool (with the oxide in red) and the temperature profile for a 2D axisymmetric simulation, and (b) a 3D solution. Source: University of Florida.

Conclusions

We have completed our development of the SStAC tool and released it on Github.com. It can model the corrosion of 21-2N valve steels exposed to CO_2 with greater than 10% accuracy, compared to the results from our furnace tested samples. We have also completed our mesoscale model that represents the detailed corrosion mechanisms and used it to show the impact of oxide layer order on the corrosion behavior. Atomistic simulations were used to provide property values for the SStAC tool and for the mesoscale model.

Key Publications

1. Ullberg, R. S., X. Wu, M. R. Tonks, and S. R. Phillpot, 2023, “Energetics and diffusion kinetics of point defects in MnCr₂O₄ Spinel from first principles,” *J. Phys. Chem. Solids*, Vol. 181, Art. 111519.
<https://doi.org/10.1016/j.jpcs.2023.111519>.
2. Wu, X., I. Abdallah, W. Jiang, R. S. Ullberg, S. R. Phillpot, A. Couet, J. H. Perepezko, and M. R. Tonks, 2023, “A phase-field study of stainless steel oxidation from high-temperature carbon dioxide exposure,” *J. Comp. Mater. Sci.*, Vol. 218, Art. 111996.
<https://doi.org/10.1016/j.commatsci.2022.111996>.
3. Abdallah, I., T. Kim, X. Wu, L. Bailly-Salins, M. Elbakhshwan, M. Carroll, M. R. Tonks, J. H. Perepezko, and A. Couet, 2022, “Oxidation kinetics and microstructure evolution of high Mn stainless steel alloy in CO₂ at 700°C,” *Corros. Sci.*, Vol. 195, Art. 110013.
<https://doi.org/10.1016/j.corsci.2021.110013>.

References

1. Duddu, R., 2014, “Numerical modeling of corrosion pit propagation using the combined extended finite element and level set method,” *Comput. Mech.*, Vol. 54, pp. 613–627.
<https://doi.org/10.1007/s00466-014-1010-8>.

II Lightweight Materials

II.1 Lightweight Metals Core Program

II.1.1 Thrust 1. Selective Processing of Al Sheet Materials (Tasks 1A, 1B, and 1C) (Oak Ridge National Laboratory and Pacific Northwest National Laboratory)

Darrell Herling, Co-Principal Investigator

Pacific Northwest National Laboratory
902 Battelle Blvd.
Richland, WA 99354
E-mail: darrell.herling@pnnl.gov

Scott Whalen, Co-Principal Investigator (Project 1A)

Pacific Northwest National Laboratory
902 Battelle Blvd.
Richland, WA 99354
E-mail: scott.whelen@pnnl.gov

Alex Plotkowski, Co-Principal Investigator (Project 1B)

Oak Ridge National Laboratory
Materials Science and Technology Division
1 Bethel Valley Rd.
Oak Ridge, TN 37830
E-mail: plotkowskiaj@ornl.gov

Mert Efe, Co-Principal Investigator (Project 1C1, Thrust 1 Lead)

Pacific Northwest National Laboratory
902 Battelle Blvd.
Richland, WA 99354
E-mail: mert.efes@pnnl.gov

Govindarajan Muralidharan, Co-Principal Investigator (Project 1C2)

Oak Ridge National Laboratory
Materials Science and Technology Division
1 Bethel Valley Rd.
Oak Ridge, TN 37830
E-mail: muralidhargn@ornl.gov

Christopher Schooler, DOE Technology Development Manager

U.S. Department of Energy
E-mail: christopher.schooler@ee.doe.gov

Start Date: October 1, 2020 End Date: September 30, 2023
Project Funding (FY 2022): \$1,300,000 DOE share: \$1,300,000 Non-DOE share: \$0

Project Introduction

The Light Metals Core Program (LMCP), led by PNNL, is an integrated effort between PNNL, ORNL, and ANL. The overall program aims to develop and demonstrate scalable, cost-effective processing methods to locally enhance the properties of Al and Mg alloys to enable broader implementation of lightweight alloys in vehicles. Focused collaborative research thrusts have been established to develop local property modification strategies for each targeted metal system: (1) high-strength Al sheet and tube (Thrust 1); (2) Al castings (Thrust 2); and (3) Mg castings (Thrust 3). Figure II.1.1.1 provides a brief description of these thrusts and how the principal manufacturing methodologies interact with each other and the support thrusts on characterization and modeling, as well as the transition to higher TRLs.

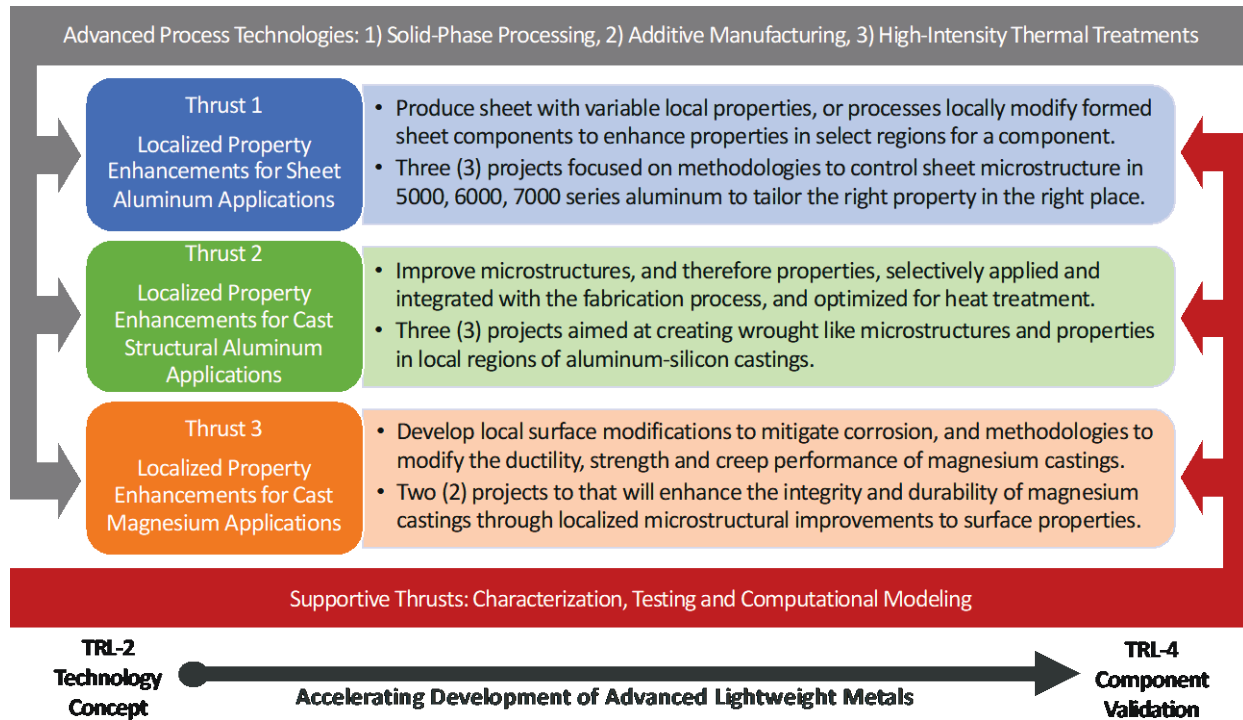


Figure II.1.1.1. Thrust and project structure of the LMCP. Source: PNNL.

The technical goal of the program is to demonstrate that components and assemblies composed of commercially available alloys can be selectively modified to exhibit locally enhanced properties and deliver high materials performance in the most needed locations. This approach allows for significant improvements in manufacturability, structural efficiency, and weight-savings in next-generation vehicles. Furthermore, the approach enables the right properties in the right locations and provides the opportunity to decrease the number of metal alloys required for new vehicle manufacture, reducing the challenges that automakers face today in managing supply chains, assuring sufficient materials sustainability, and efficiently recycling scrap metal.

The following report describes the FY 2022 technical efforts and results of Thrust 1, “Localized Property Enhancements for Sheet Aluminum Applications.” Wrought Al that is stamped or formed into components represent a material category that makes up the largest percentage of the glider in most designs. High-strength Al sheet and extrusions offer the opportunity to significantly reduce the weight of the glider through down-gauging and the replacement of steel structures. However, multiple science and engineering challenges prevent more widespread use of high-strength Al. These challenges include the natural tradeoffs between high-strength, ductility, stiffness, joining, and durability. High-strength Al can suffer from low ductility, which in turn leads to poor RT formability and poor energy absorption during crash deformation. Aligning with the overarching goal of the LMCP consortium, Thrust 1 seeks to address these challenges by developing cost-

effective and scalable methodologies to locally modify Al sheets and tubes so the right property is in the right place.

Objectives

The main objective of Thrust 1 is to solve challenges associated with the high-strength Al by local improvements in the properties and/or geometry. Thrust 1 has four projects, as shown in Figure II.1.1.2. Project 1A (PNNL) aims to demonstrate the feasibility of PNNL's ShAPE technology for producing automotive components with locally modified properties and thickness variations along the length. Components are envisioned to be in the form of tubular extrusions or rolled flat for subsequent stamping. Project 1B (ORNL) aims to (1) generate an understanding of the properties of additively deposited Al and the interaction of the deposited material with the underlying Al sheet alloys, and (2) demonstrate that the local stiffness and strength of a formed sheet can be enhanced using the Form-and-Print approach. Projects 1C1 (PNNL) and 1C2 (ORNL) have a common goal of improving formability of age- or work-hardened Al sheets. The goal is to reduce the bending radius over thickness ratio (r/t) and total ductility at failure for the processed region of the sheet metal, which will be a performance indicator for its general use in automotive applications demanding high local formability, such as stamping, deep drawing, hemming, riveting, edge stretchability, etc. Targeted applications for all of these projects include energy transfer structures, such as the A-B-C pillars or cross-body structures, and inner and outer closure panels and their reinforcement members.

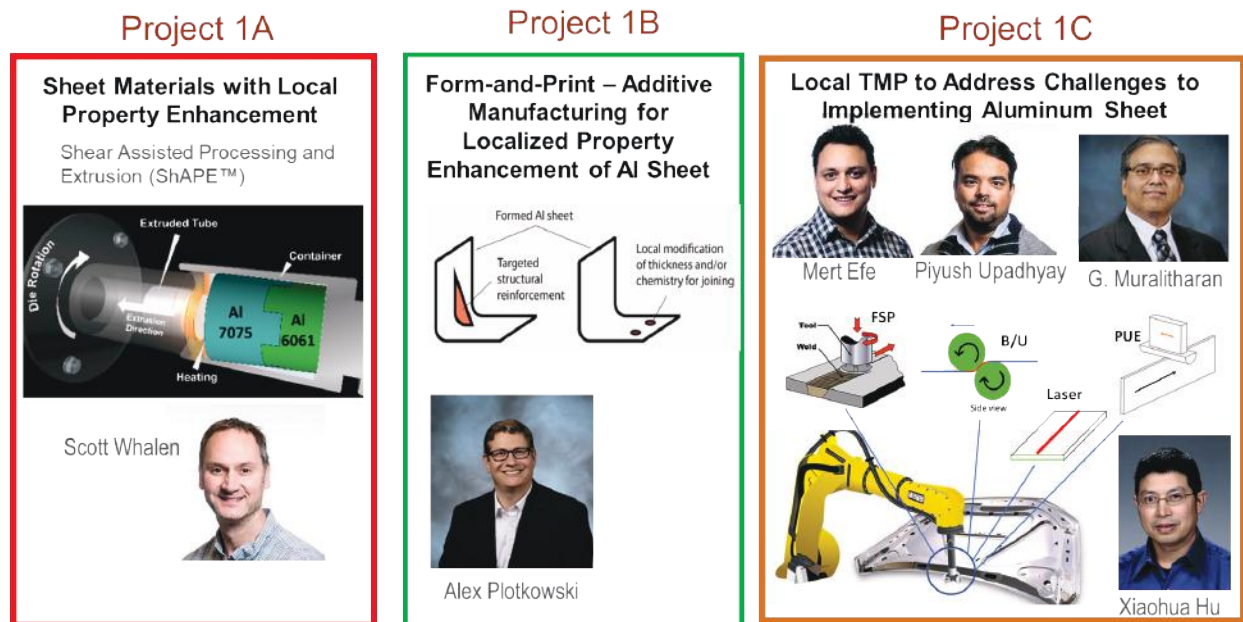


Figure II.1.1.2. Thrust 1 and project structure of the LMCP. Source: PNNL.

Approach

Project 1A: Sheet Materials with Local Property Enhancements

This project is developing the ShAPE technology and associated post-processing techniques for fabricating Al components with material properties that vary along the length. Figure II.1.1.3 shows the primary tasks that were pursued in FY 2022 and are described in detail below. The feedstock materials that were investigated include Al 5182/6061/6111 for variable wall thickness, Al 6061/6082 for selectively modified extrusions, and Al 5182 for selectively modified strip. These materials were identified during conversations with Tier 1 and OEM companies. General advantages of ShAPE, as compared to conventional extrusion, include *in situ* homogenization of as-cast billets, extreme microstructural refinement, variable hardening response to heat-treatment, and the ability to tune thermomechanical conditions during the extrusion process at specific locations. The three primary tasks associated with this project are as follows:

- **Task 1 – Variable Wall Thickness:** Develop tooling, fixtures, articulating the third axis, system integration, and process parameters to demonstrate variable wall thickness extrusion, as shown in Figure II.1.1.3(a).
- **Task 2 – Locally Modified Extrusion:** Control thermomechanical conditions during extrusion to create regions with a different precipitation-hardening response, as shown in Figure II.1.1.3(b).
- **Task 3 – Locally Modified Strip:** Roll strip from Al 5182 extrusions fabricated with variable wall thickness using the approach in Task 1. This will result in a flat strip with a uniform thickness having location-specific properties due to differing extents of cold work across the strip, as shown in Figure II.1.1.3(c).

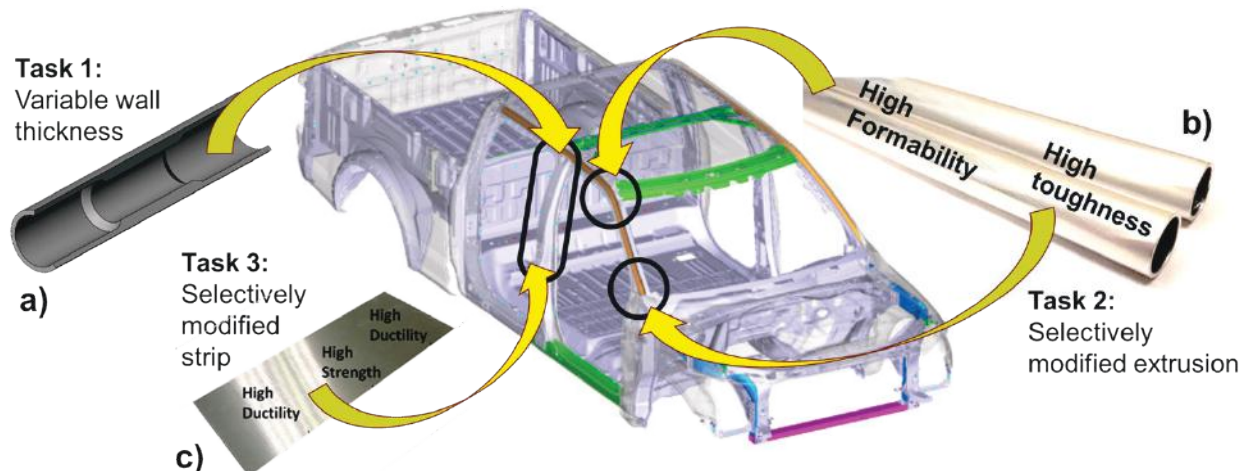


Figure II.1.1.3. (a) Variable wall thickness extrusion. (b) Extruded tubing with locally modified properties. (c) Flat strip with locally modified properties. Source: PNNL.

Project 1B: Form-and-Print – Additive Manufacturing for Localized Property Enhancement for Al Sheet

To facilitate the deposition of material on the formed sheet, a Mazak VTC-800G system was used, which uses wire-fed laser hot-wire directed energy deposition (DED) for material deposition and can perform machining operations as part of the manufacturing process. The Mazak system also allows for the deposited material to be machined to the necessary geometric specifications. Three different wire feedstock Al alloys were chosen for investigation as deposits (e.g., Al 4043, Al 4047, Al 5356) due to their wide commercial availability and recyclability. Deposits of these alloys were made and characterized to obtain an understanding of the process-structure-property relationships of these alloys as additive feedstock for thin sheet substrates. Based on the characterized properties, demonstration parts were made to show the potential for increases in bending stiffness resulting from the locally deposited materials.

Project 1C: Local Thermomechanical Processing (TMP) to Address Challenges to Implementing Al Sheet

This joint project of PNNL and ORNL aims to develop new TMP methods for improving the local formability of commercial Al sheets relevant to body-in-white and closure applications. The approach is to start with an age- or work-hardened sheet and improve its formability only where needed, without losing the high-strength elsewhere. During FY 2022, research work focused on 6111-T6, 6451-T6, 7055-T6, 7075-T6, and 7085-T76 alloys. 6xxx series were selected for their use in closure panels and support members, whereas 7xxx series were selected for their potential application in structural frame members. The 6xxx sheets were provided courtesy of Ford Motor Company and Novelis. The 7xxx sheets were purchased through commercial vendors.

PNNL is developing two methods for the local formability improvements. The first method is FSP. Intense plastic deformation and heating during FSP results in dynamic recrystallization and refined grains, which further results in local softening at certain processing parameters [1]. FSP development is conducted on a high-

precision FSW robot machine (supplied by TTI, USA) located at PNNL. In FY 2022, robotic integration of the process was completed.

The second PNNL method is the roller bending/unbending (B/U) process, which employs rolls that clamp to the blank and travel on the sheet to continuously bend and unbend the sheet locally without changing its final shape and thickness. Spacing between the rolls is adjustable to accommodate different sheet thicknesses and to change the level of deformation. A compact apparatus was developed for this method, which can be integrated to a robot as an end-effector. In FY 2022, a 5-kW capacity commercial induction heating system was also integrated to the process that enabled simultaneous deformation and heating during B/U.

ORNL is developing two approaches including (a) local heat-treatment to induce softening via laser heating and (b) localized modification using ultrasonic processing. The purpose of laser heating is to heat regions-of-interest to a temperature that would coarsen or dissolve strengthening precipitates, thereby reducing strength, increasing ductility, and improving formability in the treated zones prior to bending or shearing operations of high-strength sheet alloys in those zones. Heat transfer models were developed to predict the temperature profile of the laser heating. Experimentally measured temperature profiles were used to calibrate the thermal models of laser processing, which was performed using a TRUMPF laser system.

Power ultrasonic actuators, when pressed on a metallic material, can induce acoustic plastic softening, reduce the contact friction coefficient, and promote phase transformation and recrystallization. Recent research at ORNL on ultrasonic-assisted indentation and self-piercing riveting has shown up to 50% localized softening. The current work aims to increase the edge quality of trimmed Al sheet alloys by burr smoothing and damage elimination of edge surface and sub-surface through pre-treatment with a power ultrasonic actuated hemispherical probe. The edge formability will also be significantly improved by this edge quality enhancement. Previous high-fidelity simulations by Hu et al. [2] indicated that edge formability can also be improved by removing plastic strains during local heating of the deformed area. In this project, lab-scale shearing of AA6111-T6 Al alloy sheets was performed and ultrasonic edge modification was conducted on the edges of the sheared samples using different processing conditions (e.g., variations in ultrasonic power).

Testing efforts were coordinated between PNNL and ORNL to measure and benchmark the performance of the processed sheets. Bend testing, according to the ASTM E290 standard, was conducted on two modules. The first module used a 90° bending angle for low formability alloys, such as 7xxx, while the second module used a 180° bending angle knife edge die for high-formability alloys, such as 6xxx. Samples which were 25-mm-wide were cut from the as-received and processed sheets using a hand shear tool with the processed region at the center. Bending pins/mandrels with fixed radii were attached to the module for bend testing. Pins with progressively smaller radii were used to gradually reduce the r/t ratio until a fracture was observed. For each pin size, a different sample was used, and tests were repeated two to four times to pinpoint the minimum bend radius before cracking. The ASTM B820-18 standard was used to determine if a sample had failed. An optical stereoscope with a magnification of 34× was used to determine if microcracks appeared on the surface, which established the minimum bending radius. Orange peeling or a rough surface were not considered as a failure, and bending radii for all the tests was measured after testing with the same stereomicroscope. During FY 2022, a VDA inverted fixed radius bending module was also developed and integrated with a digital image correlation (DIC) system to measure the fracture strains and maximum bend angles. Half dog bone tensile testing was developed for the edge stretchability evaluations. Standard hardness and tensile testing accompanied the formability tests to measure the overall mechanical properties of the as-received and processed sheets.

Results

Project 1A: Sheet Materials with Local Property Enhancements

Task 1 Progress

To control wall thickness during ShAPE extrusion, the position of a tapered mandrel must be precisely controlled within the die throat as the rotating die plunges into the billet. A system controlling the tapered mandrel position during extrusion was fully designed and integrated with the ShAPE machine, as shown in Figure II.1.1.4. The system consists of a linear servo actuator integrated with the crosshead, control system, ram stem, translating mandrel, and billet container that accommodates the moving mandrel.

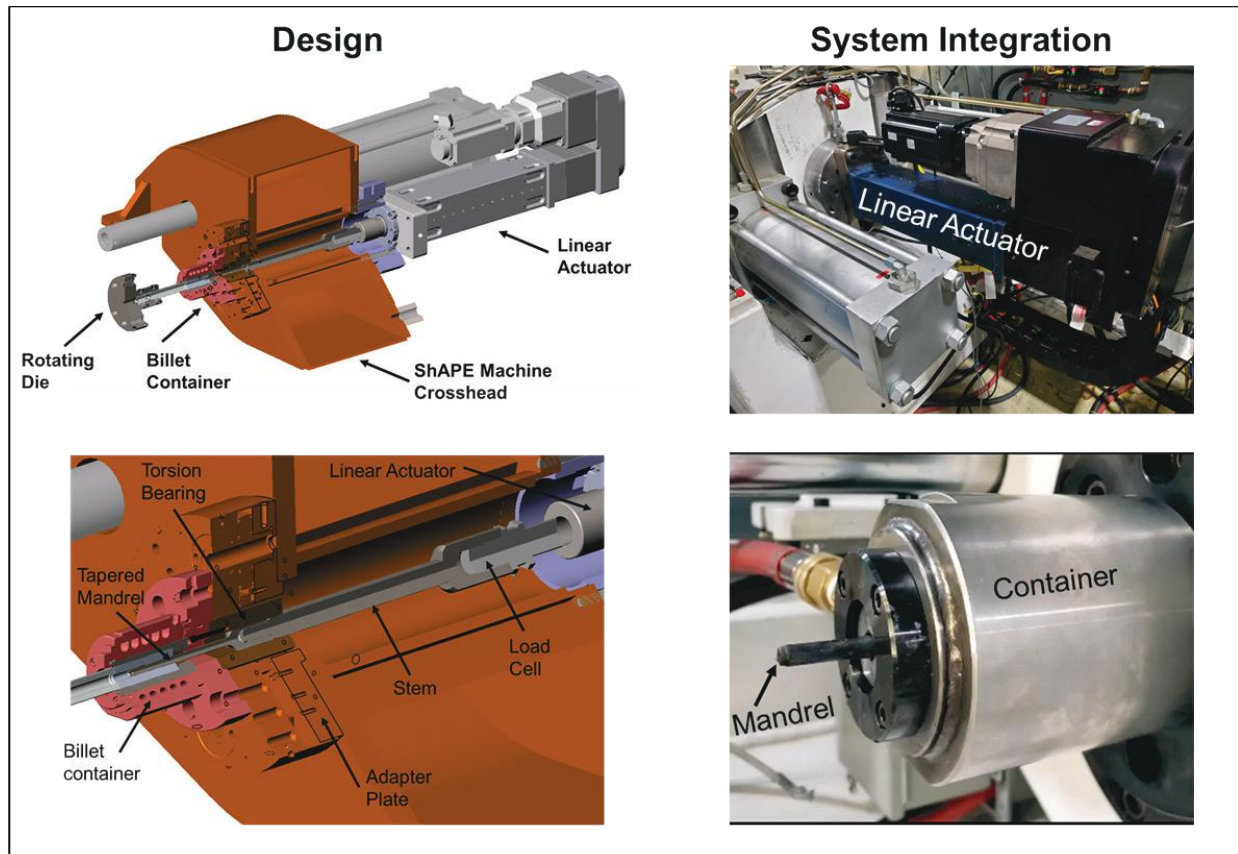


Figure II.1.1.4. Design and system integration of equipment for controlling wall thickness during ShAPE.
Source: PNNL.

The system shown in Figure II.1.1.4 was used to extrude Al 6061, Al 6111, and Al 5182 with a 12 mm outer diameter and a wall thickness that transitioned from 1 mm to 2 mm, and then back to 1 mm along the length of the extrusion. Figure II.1.1.5 shows transverse cross-sections for each alloy and thickness region. The embedded table shows wall thickness is stable across the three alloys investigated. For 6xxx alloys, which are strengthened by precipitation-hardening, variable wall thickness can be used to modify local stiffness or formability characteristics. For 5xxx alloys, which are strengthened by working, extruded tubing can be slit and rolled to a uniform thickness to form strips with different extents of strain-hardening.

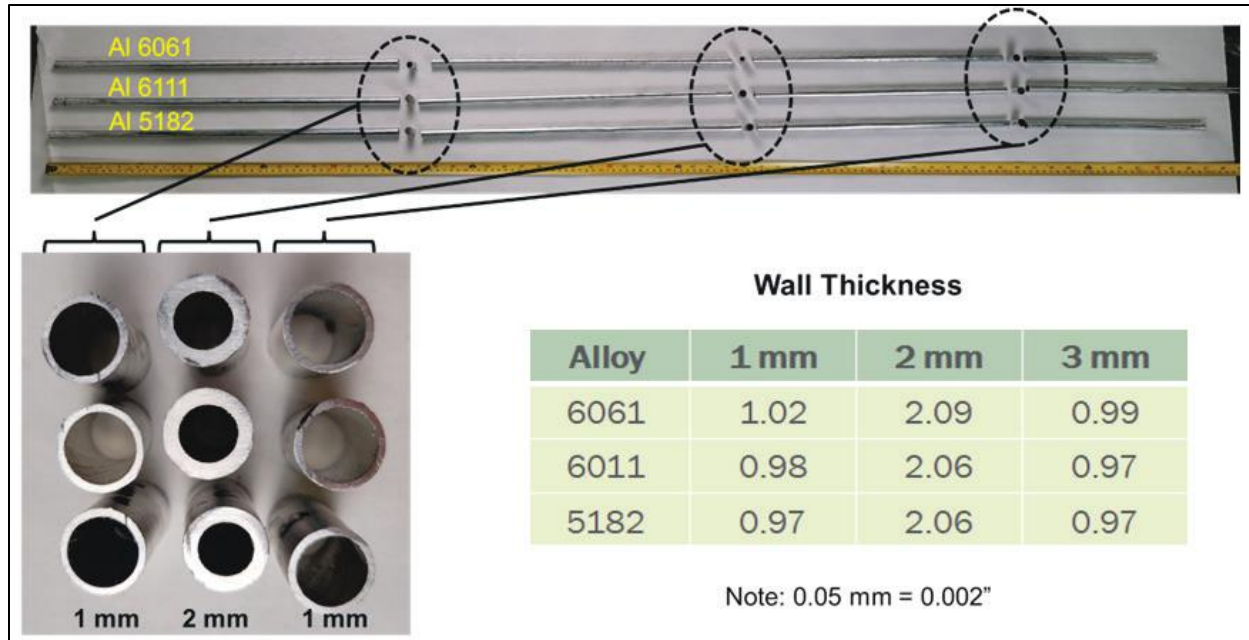


Figure II.1.1.5. Wall thickness transitioning from 1 mm to 2 mm, and then back to 1 mm. Source: PNNL.

Task 2 Progress

A unique feature of ShAPE extrusion as compared to conventional extrusion is the ability to prescribe the process temperature by controlling the revolutions per minute (rpm). For 6xxx alloys, this enables manipulation of second-phase solutionization during extrusion, which in turn affects precipitation during artificial aging after extrusion. Figure II.1.1.6 shows an Al 6061 tube where rpm = 60 achieved a die temperature of 440°C for the first meter of the extrusion, and rpm = 200 achieved 520°C for the second meter of the extrusion. Both sections were artificially aged to the T5 condition by heat-treating in air at 175°C for eight hours and subsequently tensile tested. The plot and micrographs show that microstructural features (e.g., grain size and second-phase distribution) and mechanical properties (e.g., strength and elongation) can be locally modified along a single extrusion as a function of process temperature. The transition length from one property region to another can be controlled by modulating ram speed and rotational speed. Transition lengths as short as 2.5 inches between steady-state regions (e.g., regions of constant process temperature) have been accomplished by sharply, and simultaneously, increasing rotational speed and decreasing ram speed.

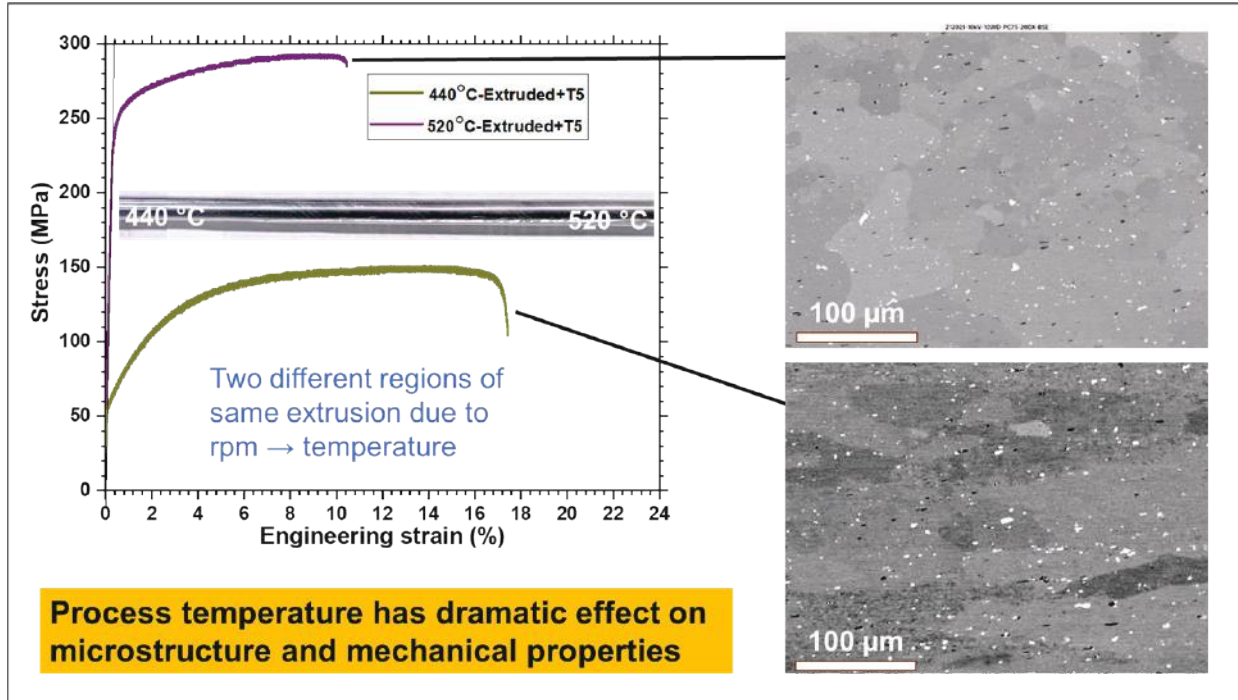


Figure II.1.1.6. Al 6061 tubing manufactured by ShAPE with regions processed at different temperatures to locally modify strength, elongation, and microstructure in a single material. Source: PNNL.

Task 3 Progress

The Al 5182 tube shown in Figure II.1.1.5 was slit and rolled to a uniform thickness of 0.9 mm. This resulted in one region having 10% cold work (CW) transitioning to a second region with 55% CW and then back to 10% CW. Two sub-scale ASTM-E8 tensile specimens were extracted by electron discharge machining from the 10% CW and 55% CW regions. Figure II.1.1.7 compares the stress vs. strain curves for the 10% CW and 55% CW regions show that toughness (e.g., energy absorption) is 64% higher for the region that was 1-mm-thick prior to rolling. Thus, for possibly the first time, a single strip of Al alloy with uniform thickness has been fabricated with locally modified strength, ductility, and toughness. Table A and Table B in Figure II.1.1.7 compare the 10% CW and 55% CW ShAPE-rolled material with the handbook values for conventionally rolled Al 5182 showing a similar strength with a higher elongation for the ShAPE-rolled material.

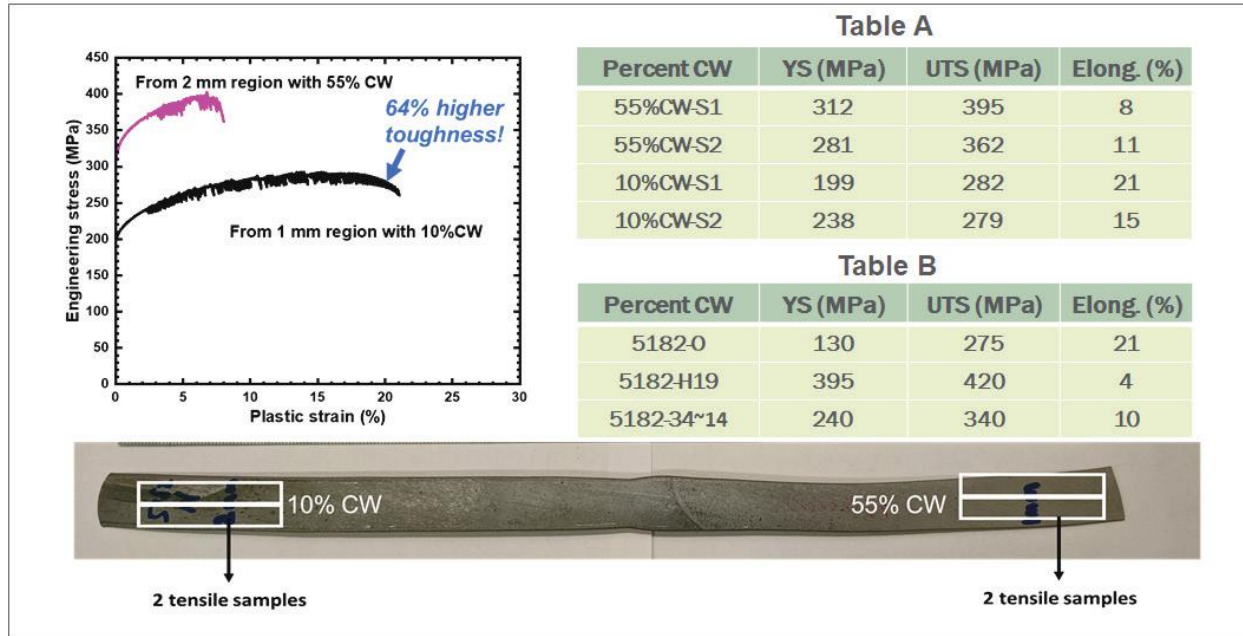


Figure II.1.1.7. Al 5182 strip rolled to a uniform thickness of 0.9 mm from a tube having a variable wall thickness of 1 mm and 2 mm. A 64% difference in toughness is achieved for different regions of a single strip. Source: PNNL.

Project 1B: Form-and-Print – Additive Manufacturing for Localized Property Enhancement for Al Sheet

Project 1B (ORNL) Progress

Table II.1.1.1 shows the material properties that were measured for the three alloys of interest: (1) Al 4043 (e.g., Al with 4.5 wt.% - 6 wt.% Si), (2) Al 4047 (e.g., Al with 11 wt.% - 12 wt.% Si); and (3) Al 5356 (e.g., Al with 4.5 wt.% - 5.5 wt.% Mg, <0.25 wt.% Si). These materials are all available as welding wire and the properties of the materials themselves are not widely available due to the weld properties being largely dependent on the mixture of the base metal and the wire. Published work by Kannan et al. [3] on this task described the additional analysis of hot-cracking susceptibility for a variety of commercial weld wires under different DED processing conditions. To obtain the mechanical properties, blocks of material were deposited on a substrate and sub-scale SS-J3 tensile specimens were extracted from the block [4]. Five repetitions were done for each sample, and the means and standard deviations are reported below.

Some values for Al 4043 deposited through other processes were found in the literature. In Knapp et al. [5], it was shown that the properties of the laser hot-wire DED material were comparable to those of arc-welded Al 4043. The Al 4043 deposits were measured to have 99.3% theoretical density via the Archimedes method, indicating that the laser hot-wire DED process can deposit the investigated alloys with properties that are reasonably representative of other processes. The measured properties are reported in Table II.1.1.1. Importantly, the range of alloys deposited had expectedly different properties. Al 4047 had the highest YS, but lower ductility (i.e., elongation at failure). Conversely, Al 5356 had higher ductility, but lower YS. Having a tradeoff between ductility and strength can be useful from an engineering perspective because it can allow for different types of local property modification.

Table II.1.1.1. Summary of Measured Material Properties

Alloy	Hardness (HV)	YS (MPa)	Tensile Strength (MPa)	Elongation at Failure (%)
Al 4043	49±7	89±9	154±5	18±2
Al 4047	70±3	125±3	189±5	14±2
Al 5356	59±4	97±3	190±7	26±1

In addition to the bulk mechanical properties of the deposited material, the deformation behavior of the deposited material, the substrate, and the interface between the two were investigated. Localized deformation behavior of Al 4043 deposited on a wrought Al 6061 alloy was characterized using DIC to observe the spatial distribution of deformation during tensile testing; this work was recently published in Knapp et al. [5]. It was found that the interface between the substrate and the deposited material was stronger than the deposited material, which indicates the local modification of the material via the described deposition strategies is not creating a weak point at the interface. All the observed deformation occurred near the fusion zone boundaries in a partially remelted zone. This was confirmed using optical and electron microscopy to characterize the deformed samples. Figure II.1.1.8(a) shows the difference in the interdendritic spacing, an important microstructure feature that influences deformation behavior, in the bulk of the deposited layer (denoted as ‘Layer’) and in the partially remelted zone near the MPB (denoted as ‘MPB’). Figure II.1.1.8(b) shows a schematic of how the partially remelted zones occur in a perpendicular fashion to the build direction and a description of how this might affect the motion of dislocations in the material.

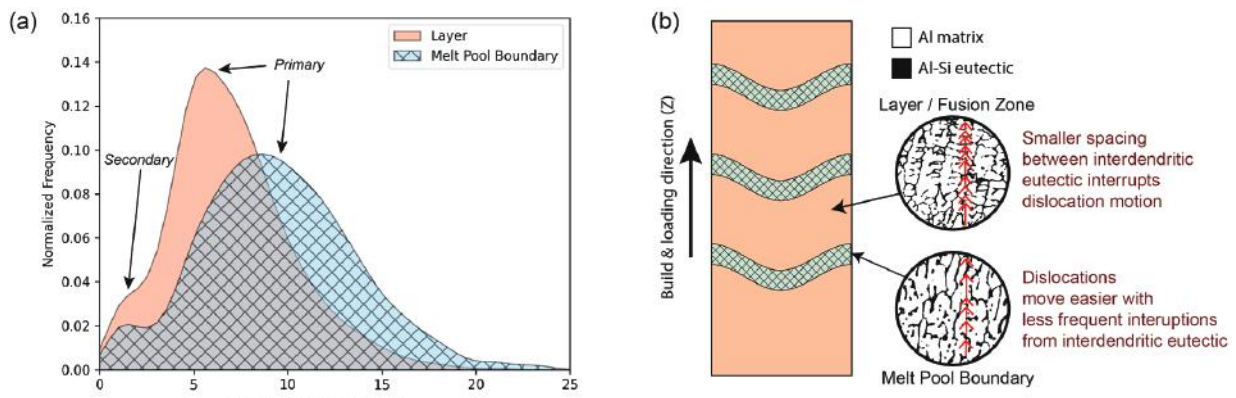


Figure II.1.1.8. Effect of interdentritic spacing in the bulk vs. partially remelted pool boundary regions: (a) a quantitative comparison of the interdentritic spacing; and (b) a schematic diagram of the mechanism of deformation in the two different regions. Knapp et al. [5]

One solution to avoiding localized deformation in the partially remelted zones would be to apply a high-temperature heat-treatment to the part after printing to reduce the heterogeneity of the microstructure. To understand how the different deposited materials responded to heat-treatment, hardness curves during an aging process were measured for deposited material in the as-deposited and heat-treated conditions. The high-temperature heat-treatment was done at a common solution heat-treatment temperature for Al-Si-Mg alloys (e.g., 535°C) and is therefore referred to as a solution heat-treatment. Though none of the investigated wire compositions are conventionally heat-treatable, thermodynamic Scheil solidification calculations showed there could be an increase in Mg₂Si-strengthening precipitates due to solute segregation compared to the equilibrium condition. Figure II.1.1.9 shows the effect of aging on the three different wire materials (e.g., Al 4043, Al 4047, Al 5356) under both the direct age and solution heat-treated conditions. For all materials, the properties of the solution-treated parts were always lower than the direct-aged samples. There was also a larger increase in hardness in response to aging for the Al 4043 and Al 5356 wire in the direct-aged material. The effect of the as-built microstructure on aging behavior is particularly noticeable in the Al 4043 material, where

the direct-aged sample increased in hardness after four hours of heat-treatment, while the solution-treated sample did not respond to aging. Further investigation is needed to quantify the change in homogeneity in the sample due to solution heat-treatment, but the decrease in properties initially indicates it is undesirable to solution heat-treat as a post-processing step. The ability to omit a high-temperature heat-treatment has the potential to enable more rapid and less costly localized processing.

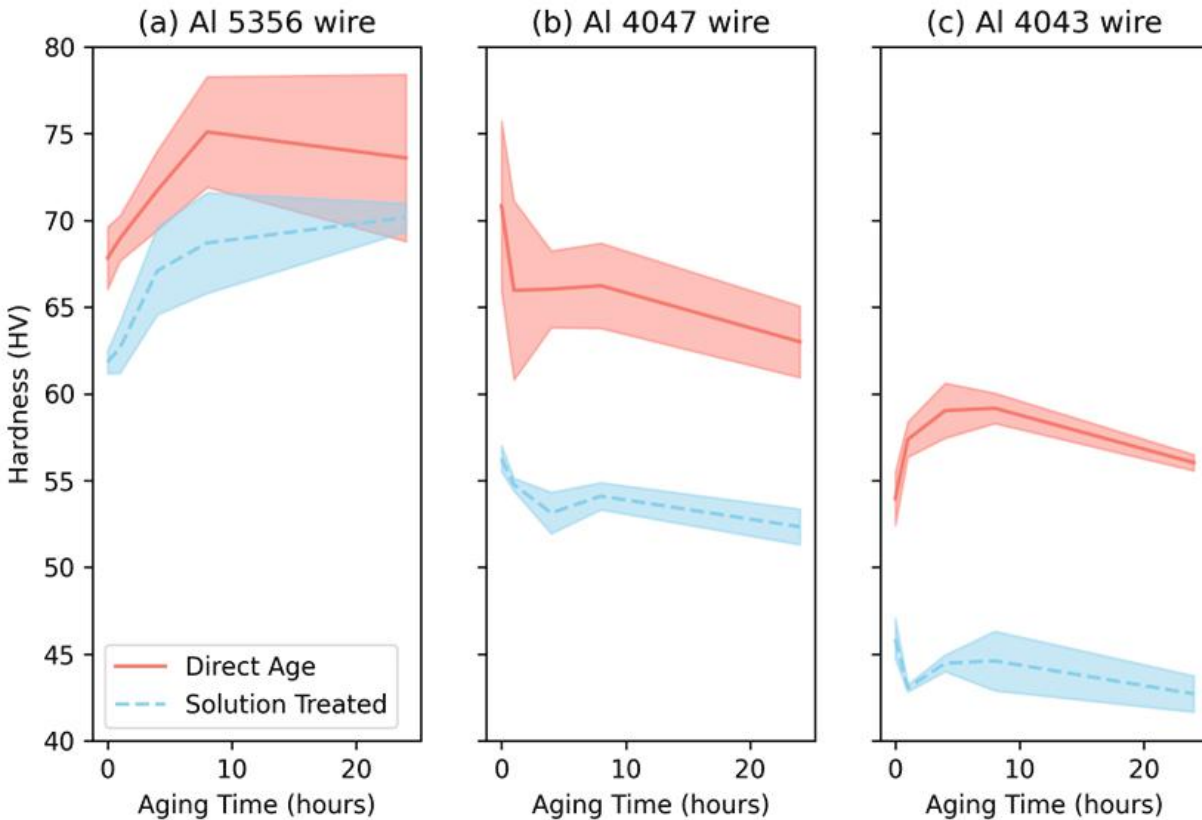


Figure II.1.1.9. Effect of aging on the deposited (a) Al 5356, (b) Al 4047, and (c) Al 4043 materials. Solution heat-treatment was done at 535 °C for four hours and aging was done at 160 °C for up to 24 hours. Lines show average of three measurements and filled regions indicate ± 1 standard deviation. Source: ORNL.

Once the properties of the deposited material were better understood, the properties of a locally modified formed sheet were investigated. Due to the importance of panel stiffness in crashworthiness, bending stiffness was chosen as a property of interest to improve. To improve the stiffness of a plate, three 50-mm-long passes of Al 4047 were added to the center of a 6 in. \times 6 in. sheet of 2-mm-thick 6111 Al. Coupons for bend testing were cut from the modified sheet and from an identical unmodified 6111 sheet. Figure II.1.1.10(a) shows the geometry of the modified and unmodified test coupons after bend testing. Figure II.1.1.10(b) shows the results of the bend testing. The modified sheet showed a 25% improvement in bending stiffness at low levels of deformation and peaked at a 50% increase in bending stiffness as compared to the unmodified sheet at 2 mm of deformation. Around 3 mm of deformation, the deposited material fractured, and the overall stiffness of the sheet decreased significantly. The overall toughness of the modified and unmodified sheet remained approximately the same, indicating the local modification could be applied to increase bending stiffness of the sheet at low levels of deformation. Such a strategy is attractive as local stiffening could enable a potential down-gauge of the overall sheet thickness.

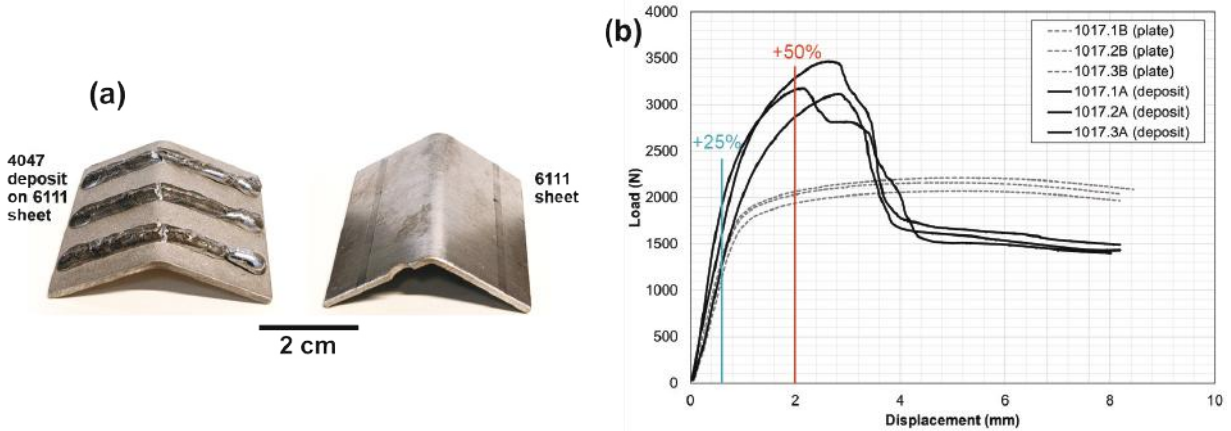


Figure II.1.1.10. Improved bending stiffness from a modified sheet: (a) Al 4047 deposited on a 6111 sheet and an unmodified 6111 sheet after bend test, and (b) load-displacement curve showing improvement in bending stiffness. Source: ORNL.

Project 1C: Local TMP to Address Challenges to Implementing an Al Sheet

Project 1C1 (PNNL) Progress

FSP and roller B/U were both successful in improving the formability of the Al sheets as measured by the r/t ratio (e.g., a lower r/t indicates higher formability). Figure II.1.1.11 summarizes the r/t of 7xxx and 6xxx alloys before and after processing. The inset shows a dramatic improvement in formability where the as-received 6111 sheet in T6 temper fails with cracking at $r/t = 1.2$, it is possible to bend the same material over itself after processing with $r/t = 0.36$. FSP achieved formability improvements of > 20% in 7075, > 36% in 7055, 41% in 7085, and 70% in 6111. B/U achieved > 60% formability improvement in 6111. Strikingly, both FSP and B/U achieved T4 level formability in the locally processed region of the 6111-T6 sheet, where the remainder of the sheet remained in its T6 temper strength.

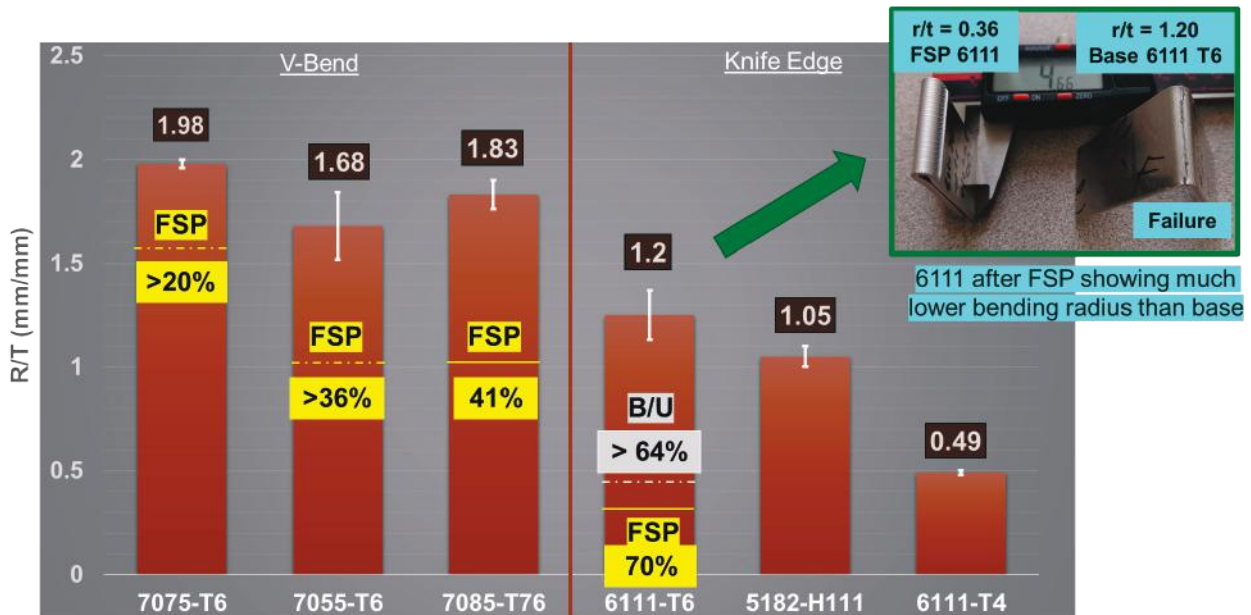


Figure II.1.1.11. r/t for base alloys and the highest formable processed conditions for each alloy. A lower r/t indicates a higher formability. Bars represent the as-received material, while lines represent the processed material. The inset shows the formability improvements in the 6111 alloy. Source: PNNL.

To prove viability for manufacturing, FSP 7055-T6 sheets were subjected to press brake bending at a bending radius of 10 mm. To make a 90-degree bend in the 7055-T6, the sheets are typically heated to 170°C. However, for this testing, all the bending was done at RT. Figure II.1.1.12 shows a sudden brittle fracture in the unprocessed sheet while the FSP sample was successfully bent in both directions (e.g., crown in tension and compression) without any cracks. This provides confidence selective processing can enable shaping of 7xxx at RT.

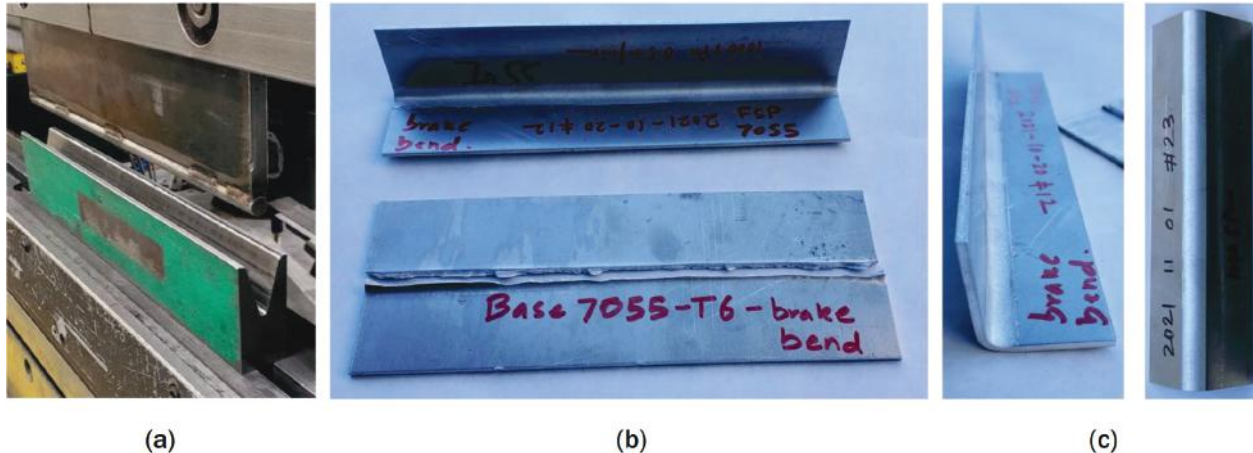


Figure II.1.1.12. Press brake bending setup used to bend 7055-T6 sheets. (a) Press brake machine and its dies. (b) Brittle fracture of unprocessed 7055-T6 sample and a 90-degree bent FSP 7055-T6 sample. (c) Side view of FSP 7055-T6 showing 90-degree bend without any cracks and top view of FSP 7055-T6 bent sample with crown side on tension without any crack. Source: PNNL.

FSP of sheet Al has also been demonstrated in the friction stirred welding robot at a viable welding speed, as shown in Figure II.1.1.13. All the FSP runs in the Al sheet demonstrating local formability improvements were straight linear runs. Robotic FSP runs at high-speed enable the demonstration of formability improvements in curved regions. To this end, a 250 mm diameter circular FSP region was produced in a 2-mm-thick 6111-T6 sheet. For demonstration purposes, a plunge depth of 1 mm was used such that ~50% of sheet was processed. Due to limited robot stiffness, a circular welding path was implemented near the center of the robot table. For the liner paths, a welding speed of ~5 m/min is possible for a 1 mm plunge depth in a 6111 sheet.

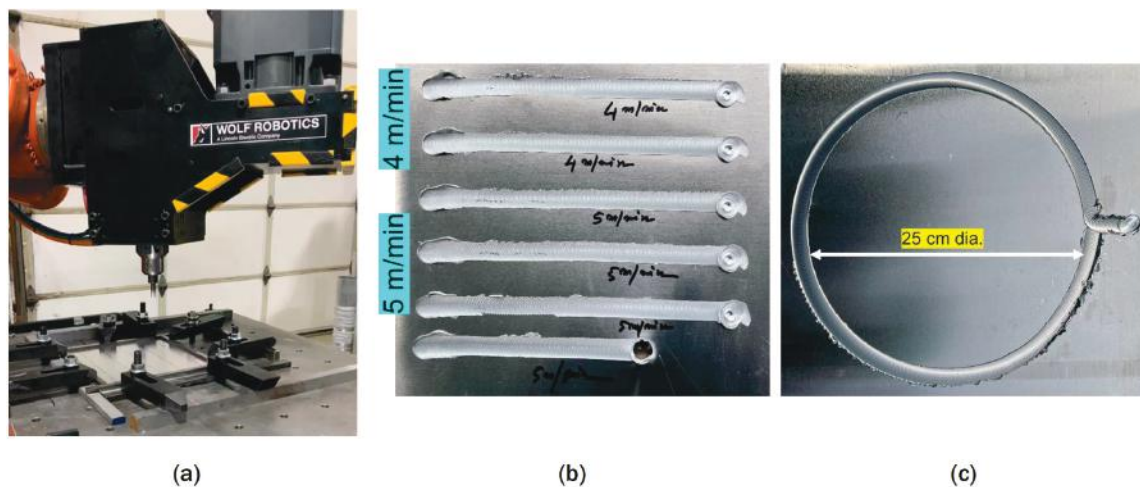


Figure II.1.1.13. Robotic integration of FSP. (a) FSP tool attached to the PNNL robot. (b) High-speed linear FSP runs. (c) Circular FSP run. Source: PNNL.

Natural aging behavior of the processed sheets were studied, especially for the 7xxx alloys known to rapidly age at RT. Sheets were tensile-tested at certain times after processing and kept in a -60°C freezer in between the testing. Tensile testing right after processing confirmed the bend testing results where the processed sheets have significant softening and ductility gain compared to the base materials. Alloys 7055 and 7075 rapidly harden and regain strength with time and lose their formability after two weeks. Alloys 7085 and 6111, on the other hand, retain their formability even after three months from processing.

Inverted bending setup with DIC integration was successfully designed and built according to VDA 238-100 testing standard for an Instron testing frame, as shown in Figure II.1.1.14. The span of the supports could be controlled to vary the amount of plastic strain during bending and control the bending rate. The knife edge shaped punch had a fixed radius of 0.38 mm, which is smaller than the pin sizes used for prior bend testing. This allows the more formable 5xxx and 6xxx series samples to fracture on the VDA setup to establish maximum bend angle and fracture strain. The test is inverted so the DIC cameras could be focused on the bending surface to record and analyze strain evolution over the entire test up to fracture in real-time. Initial trials on the FSP 7075 sheet showed failure at $\sim 100^{\circ}$ of bending angle at ~ 0.28 average thickness true strain over the full bent surface.

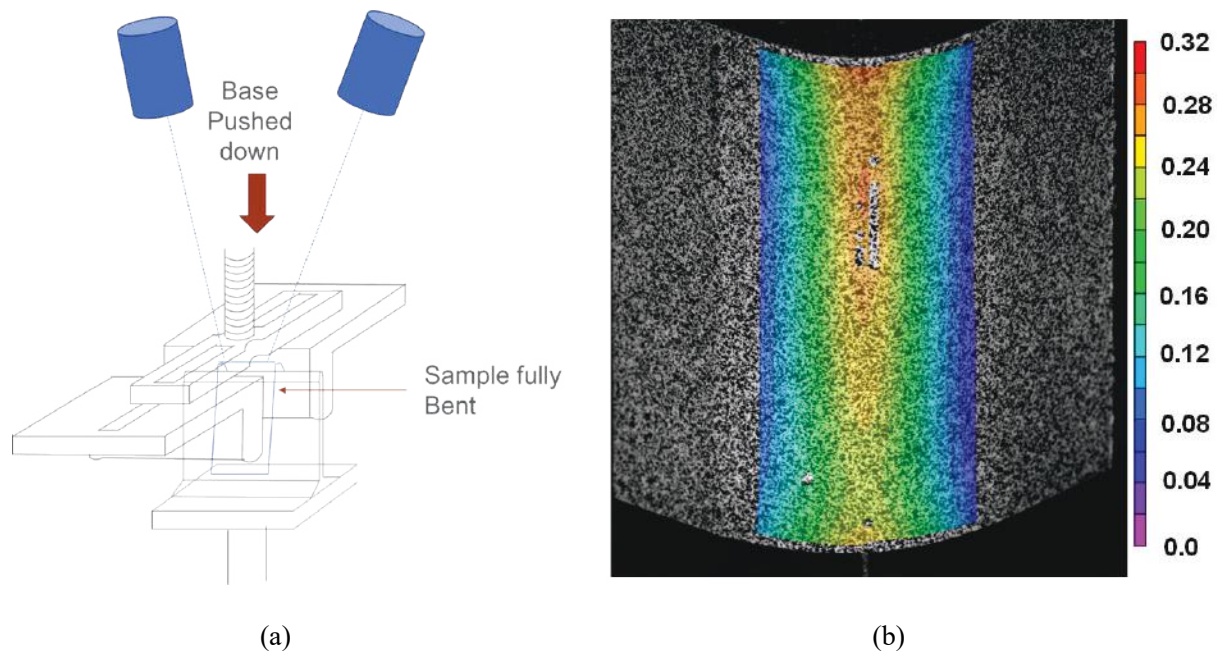


Figure II.1.1.14. (a) Inverted bending setup with DIC strain mapping capability. (b) Thickness strain map showing the strain distribution on the bent surface after failure. Source: PNNL.

Electrical heating in the form of induction heating was integrated to the roller B/U device with an automatic drive motor system. Figure II.1.1.15(a) shows the B/U setup with the induction coil integration while feeding a sheet and Figure II.1.1.15(b) shows the location of the heating zones. Al 5052-H32 sheets were first deformed without heating to measure the strain-hardening effects. 6111-T6 sheets were then processed under simultaneous heating and deformation to show temperature variation along the processed zone with hardness measurements to measure the mechanical properties.

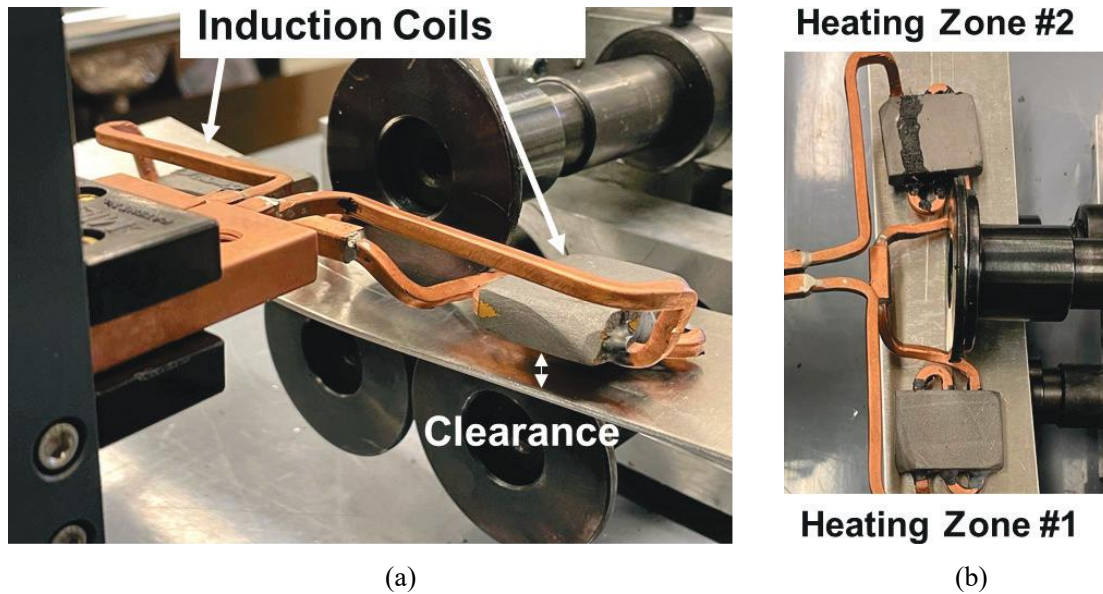


Figure II.1.1.15. (a) Induction heating coil integrated into the roller B/U device and (b) location of the two heating zones. Source: PNNL.

Initial B/U tests on the 5052-H32 were conducted at RT with a roller angle depression of 4.5° , 6.2° , and 12.0° . Figure II.1.1.16(a) and Figure II.1.1.16(b) shows the 4.5° and 12.0° angle of depression of a 5052-H32 sheet and the severity of the B/U process. The hardness was measured along the rolled portion of the sheet, which showed an increase in Rockwell hardness F-scale (HRF) from 64.9 ± 1.7 to 70.1 ± 1.2 after the 12.0° roller depression. This suggests a significant strain-hardening was achieved. The hardness of the sheet at 12.0° was very similar to the 4.5° and 6.2° angles, which suggests more severe depression angles might be needed to induce higher strain-hardening into the sheet metal to see an appreciable change in hardness.

Figure II.1.1.16(c) shows the temperature distribution on the 6111 sheet during processing recorded by a thermal camera. The top part first enters under the induction coils, and therefore, reaches the maximum temperature. As the sheet is moving, the temperature decreases and reaches almost a steady state. The temperature increase of up to 450°C causes softening in the sheet, most likely due to solutionization or coarsening of the precipitates, which in turn results in the formability increase.

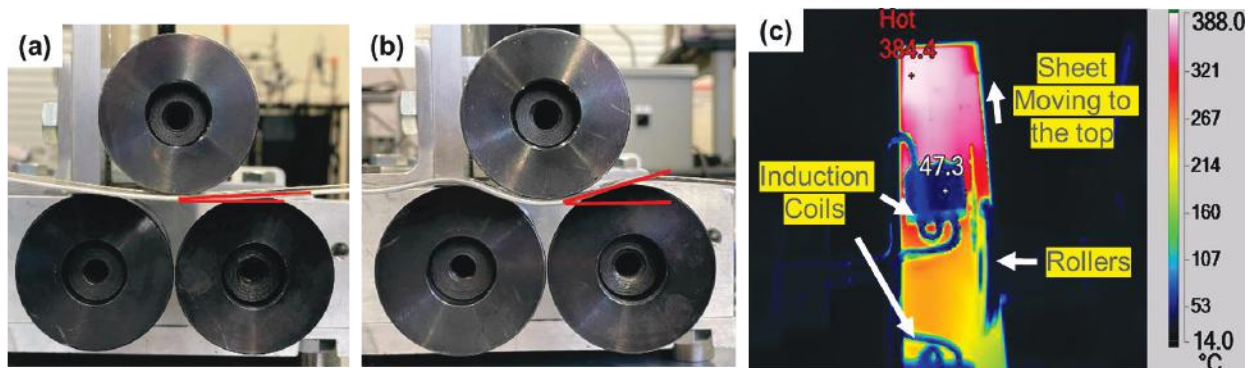


Figure II.1.1.16. Side view of the roller B/U process showing the top roller movement and changing angles of depression of (a) 4.5° and (b) 12.0° . (c) Temperature distribution on the sheet during the roller bending-unbending processing of 6111 sheet. Source: PNNL.

Figure II.1.1.17 shows the corresponding hardness distribution on the sheet. There is a direct correlation between the temperature rise and the level of softening. The hardness gradually decreases toward the entry, and the entry region (left side of image) has the lowest hardness, where the temperature was the highest. The exit region (right side of image) is processed last, and the temperature was lowest, and therefore, the sheet has its original T6 hardness. Bending samples extracted from various locations in the sheet were tested at a constant r/t of 0.45. The samples with the lower hardness can be bent successfully at $r/t = 0.45$ without any failure, whereas the samples with the higher hardness fail with cracking at the same ratio. Indeed, unprocessed T6 samples of the same alloy have a critical r/t of 1.2, below this ratio they cannot accommodate the bending radius and fail by cracking. Therefore, the processed samples that can be bent at $r/t = 0.45$ indicate their formability is increased by at least 60% with the roller B/U process.

Finally, a preliminary cost and feasibility analysis was completed for the two processes developed in this project. A report detailing the calculation of cost-savings was submitted. Potential cost-savings are possible when softer Al sheet components in T4 temper are replaced with thinner—yet stronger—Al sheets with T6 temper, assuming the T6 sheets with local processing has the same or better formability as compared to T4 temper. The material, and hence, the cost-savings are due to ~ 17% down-gauging with strength benefits of T6-temper sheets, which offsets the cost increase due to the additional processing.

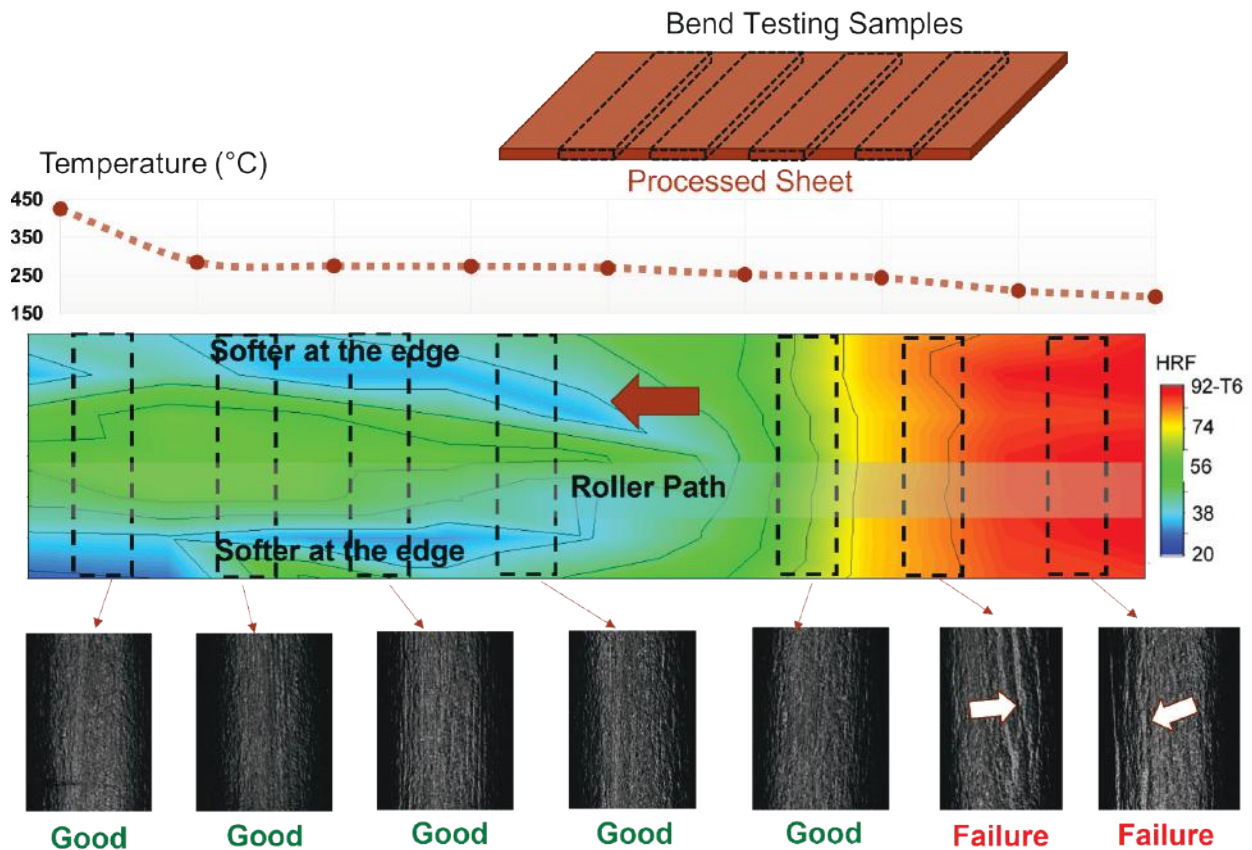


Figure II.1.1.17. Color map shows the hardness (as HRF) distribution on the sheet after the roller B/U process. The temperature plot shows the temperature rise during the process for the corresponding hardness locations. Dashed rectangles show the samples extracted for bend testing and the pictures show the top surfaces of the bent samples, where cracking is visible in the failed samples. Source: PNNL.

Project 1C2 (ORNL) Progress

Figure II.1.1.18 shows the setup used for sample positioning underneath the laser beam and for temperature logging. The laser was allowed to travel along a straight-line path on the top surface of the sample, as shown in Figure II.1.1.18(a). A thermocouple was placed in contact with the bottom surface of the sample, directly underneath the path of the laser. Figure II.1.1.18(b) shows the typical temperature profiles obtained at a power level of 350W during a single-pass treatment and a 7-pass treatment of 2.5-mm-thick 7075-T6 samples. Maximum temperatures of $\sim 160^{\circ}\text{C}$ were obtained at the bottom surface of the sample at the sampling rate of 10 Hz used in these experiments.

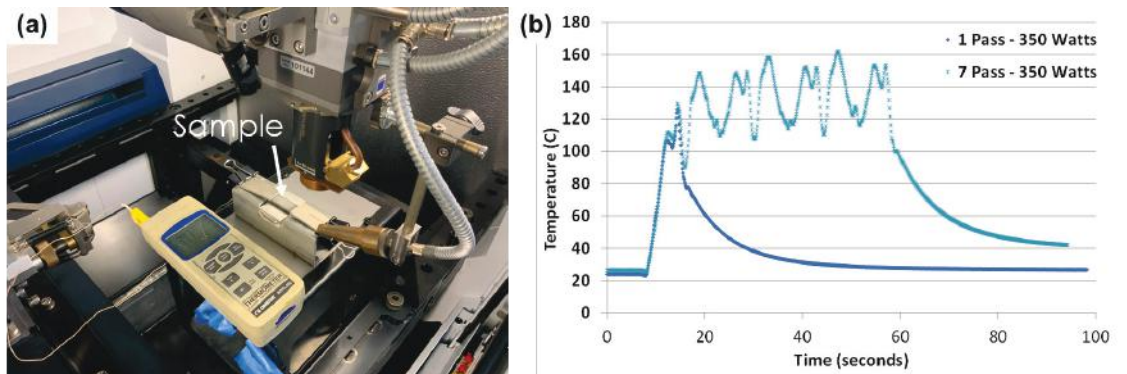


Figure II.1.1.18. (a) Setup used for laser modification. (b) Temperature profiles obtained at the bottom surface of the sample during a single-pass and a 7-pass thermal treatment at a laser power of 350W. Source: ORNL.

Figure II.1.1.19(a) shows the load vs. elongation curve obtained during the bend test using a punch of radius 2.35 mm on an untreated 2.5-mm-thick 7075-T6 sheet, and a 2.5-mm-thick 7075-T6 sheet laser-treated at a power level of 350W. Load vs. elongation curves show a drop in load in the untreated sample indicating cracking. The treated samples did not exhibit this drop in load, suggesting no cracking. This indicates localized laser processing enables significant improvements in the bending behavior of a high-strength 7075-T6 sheet to a radius to sheet thickness of ~ 0.94 . This is an encouraging result as it exceeds the milestone criterion of having an r/t less than 2.0. Figure II.1.1.19(b) shows the optical images of the bend-tested samples confirming the 7075-T6 treated sheet could be bent successfully, thus indicating improvement formability. Experiments are ongoing to understand the microstructural evolution achieved using the processing conditions used in the experiments completed to date, and to enable the development of processing conditions to further improve the r/t ratios.

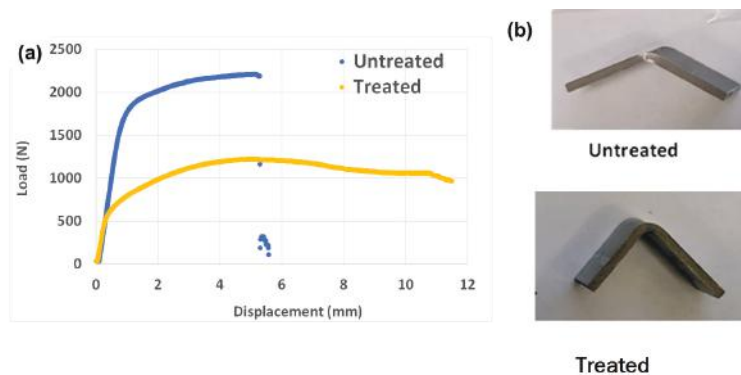


Figure II.1.1.19. (a) Load vs. displacement obtained using bend testing of an untreated 2.5-mm-thick 7075-T6 sample and a laser-treated 2.5-mm-thick 7075-T6 sample. Note the significant decrease in loads and the increase in displacement of the punch observed in the treated sample. (b) Optical images of the tested samples showing the improved bending observed in the treated sample. Source: ORNL.

Based on the local laser heating geometry, an Abaqus heat transfer model was developed for an Al sheet of $100 \times 12.7 \times 2.5 \text{ mm}^3$ as the length, width, and thickness, respectively. A ring heat source model with an inner diameter of 1.98 mm and an outer diameter of 0.7 mm was used where the heat (q) input per unit area was assumed to be homogeneously distributed within the ring: $q = aP/A$, where P is the laser power, A is the area of the ring, and a is the laser absorption rate. To save computation time, only half of the model was considered, which assumed mirror symmetry with reference to the width \times thickness plane, as shown in Figure II.1.1.20. Eight node hexahedral thermal elements (DC3D8) were used with the meshing denser at the top surface and mid-plane of the sheet, which are directly under the laser illumination, as shown in Figure II.1.1.20(a). Figure II.1.1.20(b) shows a comparison between the predicted temperature histories and the measured temperatures at the bottom of the sheet at $a=0.12$, $P=350 \text{ W}$, a laser scan speed $v=5$ inches per minute, and a laser waiting time $t_w=1 \text{ s}$ between laser scans. The convective heat transfer of the sheet surface with the ambient air (25°C or 298 K) is considered for the cooling. In the current work, the convection coefficient of $200 \text{ W}/(\text{m}^2\cdot\text{K})$ is used to lump sum the effect of the air cooling and cooling from the clamps. The thermal parameters for the AA6111-T6 alloy, such as heat transfer coefficient and heat capacity values, were taken from the literature. As seen in Figure II.1.1.20, slight differences are observed between the measured peak temperatures and predicted temperatures and further work is ongoing to resolve these differences. This model will then be used to identify optimum processing conditions to obtain the desired process temperatures and local bendability.

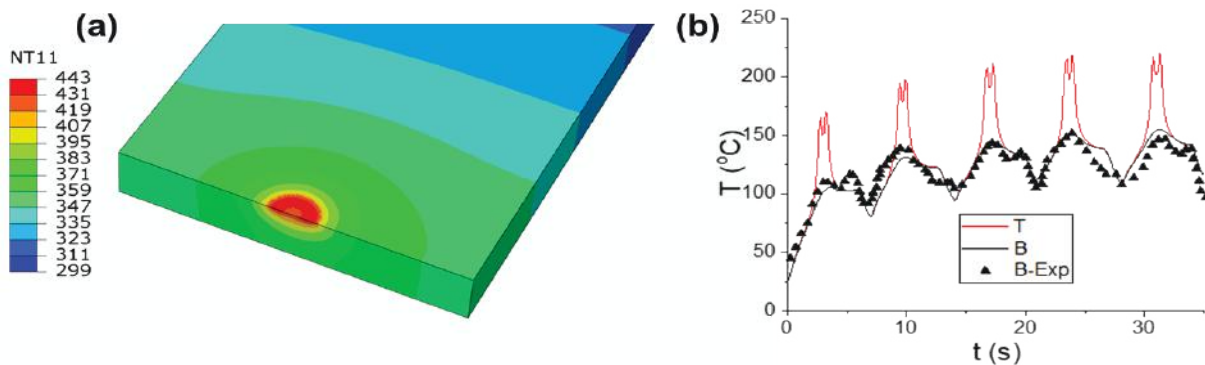


Figure II.1.1.20. Half of the sheet used in the laser heating model: (a) temperature distribution within the sheet and (b) the predicted temperature histories (solid line) of AA70756 alloy with $P=350\text{W}$ compared with actual measured temperatures (triangles) for identical process conditions. T and B are the top and bottom center of the sample. Source: ORNL.

Power ultrasonic edge (PUE) modification was performed by applying ultrasonic power through a sonotrode with a load of 300 N on the sheared edges of the previously sheared samples. The sample was moved under the sonotrode either manually or using a motor with the sample movement always parallel to the sample length, as shown in Figure II.1.1.21. The total process time was ~ 4 seconds. After shearing, PUEs were first performed on six of the samples with six different ultrasonic power levels measuring 0.1 to 0.35 kW. For manual stage motion, the ultrasound (U) direction was perpendicular to the stage movement (i.e., in the transverse (T) direction of the sample), as shown in Figure II.1.1.21. Using the manual stage, only 25 to 30 mm of the edge of the sample could be modified in 4 s.

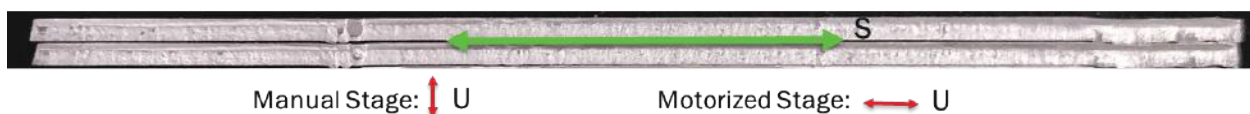


Figure II.1.1.21. The edge view of two of the sheared samples with the sample movement direction (S) marked in green arrows and ultrasound direction (U) marked in red colors for manual stage and motorized stages. Source: ORNL.

To ensure a larger modification length, a motorized stage set was acquired, as shown in Figure II.1.1.22(a), and used in subsequent experiments. Here, PUE was performed with the ultrasonic vibration direction parallel to the stage movement (i.e., in a longitudinal (L) direction of the sample). PUEs were performed on eight samples with six ultrasonic conditions, as shown in Figure II.1.1.22(b). The edge conditions of the eight samples are provided in Figure II.1.1.22(c) with eight different ultrasonic energies which range from 0.1 to 1 kW.

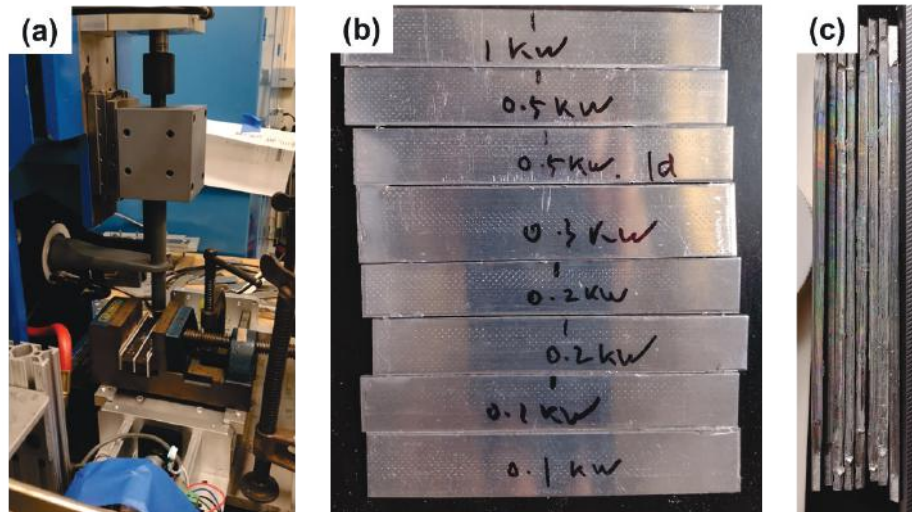


Figure II.1.1.22. (a) PUE setup using motorized stage. (b) Plan view of edge modified samples. (c) Edge view of modified samples. In these experiments, the ultrasonic movement was parallel to the edge and sample movement direction (or longitudinal direction). Source: ORNL.

To assess the effect of PUE on edge stretchability, five modified samples were selected to be cut into tensile samples with a half dog bone shape, with a geometry as shown in Figure II.1.1.23(a), in the following descriptions: (1) sheared, non-edge modified; (2) sheared, edge modified with 100 W ultrasound transverse to the sample length direction (100W T); (3) sheared, edge modified with 300 W ultrasound transverse to the sample length direction (300W T); (4) sheared, edge modified with 100 W ultrasound longitudinal to the sample length direction (100W L); and (5) sheared, edge modified with 300 W ultrasound longitudinal to the sample length direction (300W L). We chose the samples of ultrasonic power below 300 W because the sonotrode goes too deep into the material with higher power. The samples after tensile testing are shown in Figure II.1.1.23(b).

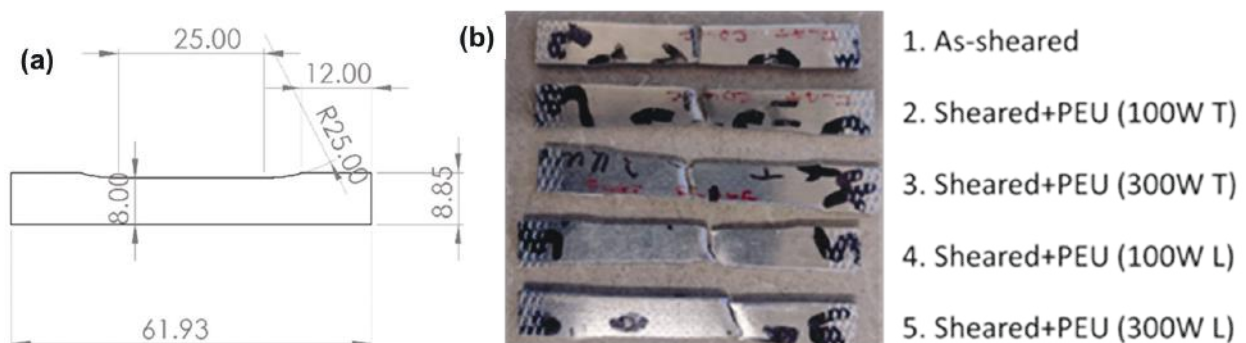


Figure II.1.1.23. (a) Half dog bone geometry used for tensile testing of samples. (b) The samples after tensile test show typical splitting type failure for as-sheared sample and the more ductile shear type failure for the samples after PUE modifications. Source: ORNL.

As expected, the as-sheared sample exhibited shear splitting type failures [2] and samples with PUE shear exhibiting a ductile shear type failure mode. These results are shown in the load-displacement curves in Figure II.1.1.24(a) and the engineering stress-strain curves are shown in Figure II.1.1.24(b) and Figure II.1.1.24(c). Note that Figure II.1.1.24(b) shows the stress-strain curves from the strain-gauge measurement. Since the strain-gauge slipped during testing of sample 2, the strains were not recorded after the slip. From the load-displacement curve, shown in Figure II.1.1.24(a), and the stress-strain curve calculated from it with a stiffness correction [6], shown in Figure II.1.1.24(c), this sample demonstrated an elongation of around 13%, which is much higher than the as-sheared sample. Edge modification using PUE resulted in significant improvements of elongations between 27% to 75% which exceeds the 25% target set in the project milestone.

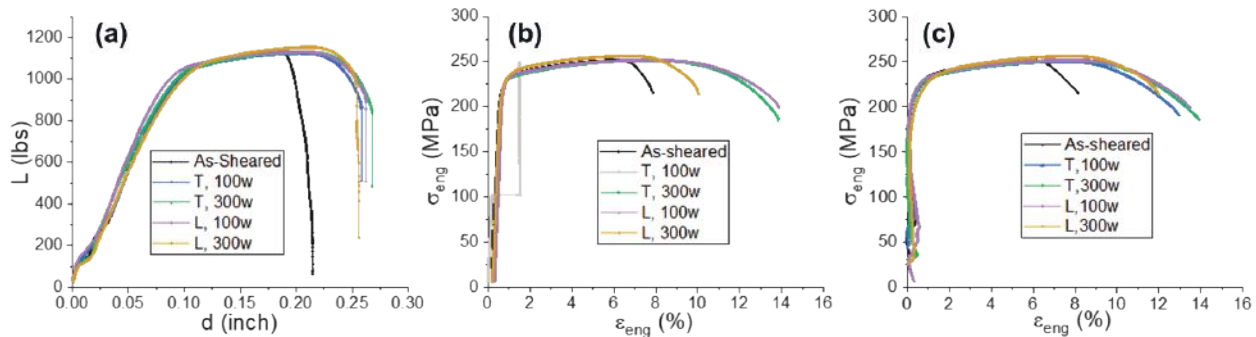


Figure II.1.1.24. (a) Tensile load-displacement curves, (b) engineering stress-strain curve with strains recorded from strain-gauge, and (c) stress-strain curve using crosshead displacement with stiffness correction.

Source: ORNL.

Conclusions

During FY 2022, each project in Thrust 1 achieved their goals in selectively modifying an Al sheet and tube properties and geometries.

Project 1A demonstrated locally modified properties could be achieved during ShAPE extrusion and after subsequent rolling of ShAPE-extruded tubing:

- A system was designed and integrated with the ShAPE machine for extruding round tubing with wall thickness tailored along the length of an extrusion. This was shown for Al 6061, Al 6111, and Al 5182 where wall thickness varied from 1 mm to 2 mm and then back to 1 mm.
- Al 6061 tubing was processed with the first meter at 440°C and the second meter at 520°C. This resulted in strength and elongation differing substantially in a single extrusion after T5 heat-treatment.
- Al 5182 tubing with variable wall thickness was rolled flat to achieve a strip with locally modified CW ranging from 10% to 55%. This resulted in toughness differing by 64% within a single strip of material.

Project 1B gained significant understanding of the behavior of laser hot-wire AM Al alloys deposited onto an Al sheet via the Form-and-Print approach. While the partially remelted zone between layers in the deposited materials has some effect on localized deformation of the as-deposited material, a solution heat-treatment generally weakened the material. Furthermore, compared with an unmodified sheet, up to a 50% increase in the localized bending stiffness of a 6111 sheet with deposited 4047 material was demonstrated. With an improved understanding of the material behavior and a successful demonstration of the improved localized properties, future work conducted by Project 1B will focus on expanding the understanding and possible applications of the Form-and-Print approach.

Project 1C showed the feasibility of various techniques in improving the local formability and edge stretchability of the high-strength Al sheets in their T6 temper:

- FSP achieved formability improvements of > 20 percent in 7075, >36 percent in 7055, 41 percent in 7085, and 70 percent in 6111 as measured by the r/t ratio in the bend tests. Local formability of 6111 was on T4 temper level, while the rest of the sheet remained in T6 temper. Robotic integration of the process was completed with demonstration of high-speed runs of up to 5 m/min and two-dimensional patterns.
- With the addition of induction heating, B/U also achieved > 60% improvement in the formability by B/U and heating the sheets simultaneously. It was possible to control the level of deformation and heating independently, and process temperatures up to 450°C were demonstrated.
- The inverted VDA testing gave the strain distributions on the bent sheets and enabled calculation of the thickness strains just before the fracture.
- Laser thermal treatments were successful in the local softening of a 2.5-mm-thick 7075-T6 sheet. Bending experiments show laser processing allows for bending a high-strength 7075-T6 sheet to a $r/t \sim 0.94$, thereby exceeding the milestone criterion of $r/t < 2.0$.
- A thermal model is under development to predict sheet temperatures achieved during laser processing. Further validation is required to improve accuracy of the preliminary models.
- PUE modification showed up to 75% improvement in tensile elongation of edge sheared 6111-T6 samples.

Key Publications

Project 1A

1. Komarasamy, M., L. Li, B. S. Taysom, A. Soulam, G. Grant, D. R. Herling, and S. A. Whalen, 2022, "Coextrusion of aluminum alloys via shear-assisted processing and extrusion," In: Eskin, D. (ed.), *Light Metals 2022*, Springer, Cham, Switzerland. pp. 308–313. https://doi.org/10.1007/978-3-030-92529-1_43.
2. Komarasamy, M., S. Whalen, and B. Milligan, 2022, "Manufacturing components with variable properties via solid-phase processing," Provisional Patent Filed.
3. Komarasamy, M., S. Whalen, and B. Milligan, 2022, "Shear-assisted extrusion assemblies and methods," U.S. Patent Application.
4. Milligan, B., B. S. Taysom, X. Ma, and S. Whalen, 2023, "Solutionization via severe plastic deformation: Effect on natural aging in an Al-Mg-Si-(Mn) alloy," In: Broek, S. (ed.), *Light Metals 2023*, Springer, Cham, Switzerland. in process.
5. Milligan, B., X. Ma, B. S. Taysom, and S. Whalen, 2022, "Solutionization via severe plastic deformation: Effect of temperature and quench method in a ShAPE-processed Al-Mg-Si alloy," Preprint (Under Review), *Social Science Research Network*. <https://doi.org/10.2139/ssrn.4231970>.
6. Taysom, B. S., and S. Whalen, 2022, "Apparatus for variable wall thickness during ShAPE extrusion," U.S. Patent Application.

Project 1B

1. Kannan, R., G. L. Knapp, P. Nandwana, R. Dehoff, A. Plotkowski, B. Stump, Y. Yang, and V. Paquit, 2022, "Data mining and visualization of high-dimensional ICME data for additive manufacturing," *Integr. Mater. Manuf. Innov.*, Vol. 11, pp. 57–70. <https://doi.org/10.1007/s40192-021-00243-2>.
2. Knapp, G. L., M. Gushev, A. Shyam, T. Feldhausen, and A. Plotkowski, 2022, "Microstructure, deformation, and fracture mechanisms in Al-4043 alloy produced by laser hot-wire additive manufacturing." *Addit. Manuf.*, Vol. 59, Art. 103150. <https://doi.org/10.1016/j.addma.2022.103150>.

Project 1C

1. Balusu, K., K. S. Choi, H. Das, A. Samanta, P. Upadhyay, S. Jana, and A. Soulam, 2022, “On the utility of the thermo-pseudo-mechanical model’s residual stress prediction capability for the development of friction stir processing,” Preprint (Under Review), *Int. J. Adv. Manuf. Technol.*
<https://doi.org/10.21203/rs.3.rs-2176313/v1>.
2. Nasim, W., H. Das, S. S. Kulkarni, A. Rohatgi, D. R. Herling, G. J. Grant, P. Upadhyay, and M. Efe, 2022, “Local thermomechanical processing for improving formability of high-strength aluminum sheets,” *SAE Technical Papers*, Paper No. 2022-01-0244. <https://doi.org/10.4271/2022-01-0244>.
3. Nasim, W., H. Das, P. Upadhyay, and M. Efe, 2022, “Improving local formability of 6xxx and 7xxx aluminum alloy sheets using friction stir processing,” *Int. J. Adv. Manuf. Technol.*, Vol. 124, pp. 2957–2967. <https://doi.org/10.1007/s00170-022-10569-6>.

References

1. Ma, Z. Y., 2008, “Friction stir processing technology: A review,” *Metall. Mater. Trans. A Phys. Metall. Mater. Sci.*, Vol. 39, pp. 642–658. <https://doi.org/10.1007/s11661-007-9459-0>.
2. Hu, X. H., X. Sun, and S. F. Golovashchenko, 2014, “Predicting tensile stretchability of trimmed AA6111-T4 sheets,” *Comput. Mater. Sci.*, Vol. 85, pp. 409–419.
<https://doi.org/10.1016/j.commatsci.2014.01.015>.
3. Kannan, R., G. L. Knapp, P. Nandwana, R. Dehoff, A. Plotkowski, B. Stump, Y. Yang, and V. Paquit, 2022, “Data mining and visualization of high-dimensional ICME data for additive manufacturing,” *Integr. Mater. Manuf. Innov.*, Vol. 11, pp. 57–70. <https://doi.org/10.1007/s40192-021-00243-2>.
4. Gussev, M., J. T. Busby, K. G. Field, M. A. Sokolov, and S. E. Gray, 2015, “Role of scale factor during tensile testing of small specimens,” In: Sokolov, M. A., and E. Lucon (Eds.), *Small Specimen Test Techniques: 6th Volume, 29–31 January 2014, Houston, TX, USA*, ASTM International, West Conshohocken, PA, USA. <https://doi.org/10.1520/STP157620140013>.
5. Knapp, G. L., M. Gussev, A. Shyam, T. Feldhausen, and A. Plotkowski, 2022, “Microstructure, deformation, and fracture mechanisms in Al-4043 alloy produced by laser hot-wire additive manufacturing.” *Addit. Manuf.*, Vol. 59, Art. 103150. <https://doi.org/10.1016/j.addma.2022.103150>.
6. Hu, X., K. S. Choi, X. Sun, Y. Ren, and Y. Wang, 2016, “Determining individual phase flow properties in a quench and partitioning steel with *in situ* high-energy XRD and multiphase elasto-plastic self-consistent method,” *Metall. Mater. Trans. A Phys. Metall. Mater. Sci.*, Vol. 47, pp. 5733–5749.
<https://doi.org/10.1007/s11661-016-3373-2>.

Acknowledgments

PNNL, ORNL, and ANL thank the DOE-EERE VTO for their support through the LMCP. The Project 1A PI commends PNNL staff members B. Milligan, M. Komarasamy, and B. S. Taysom for their excellent task leadership on this project. The Project 1B PI acknowledges the contributions of the ORNL team members for this sub-task: G. Knapp, T. Feldhausen, A. Shyam, D. Brown, M. Paramanathan, S. Graham, and S. Hawkins. P. Upadhyay served as the co-PI of the PNNL Project 1C1, while X. Hu served as the co-PI of the ORNL Project 1C1. These Project 1C1 PIs also thank past and current PNNL staff members W. Nasim, H. Das, and A. Ortiz for their excellent contributions. The Project 1C2 PIs acknowledge ORNL staff members K. Faraone and R. Miller for the laser modification experiments, J. Chen for their assistance with the ultrasonic experiments, and K. Hedrick and S. Hawkins for the mechanical testing.

II.1.2 Thrust 2. Selective Processing of Al Castings (Tasks 2A1, 2A2, 2B, and 2C) (Pacific Northwest National Laboratory and Oak Ridge National Laboratory)

Glenn J Grant, LMCP Program Manager, Principal Investigator (Thrust 2)

Pacific Northwest National Laboratory
902 Battelle Blvd.
Richland, WA 99352
E-mail: glenn.grant@pnnl.gov

Saumyadeep Jana, Co-Principal Investigator (Project 2A1)

Pacific Northwest National Laboratory
902 Battelle Blvd.
Richland, WA 99352
E-mail: saumyadeep.jana@pnnl.gov

Zhili Feng, Co-Principal Investigator (Project 2A2)

Oak Ridge National Laboratory
1 Bethel Valley Rd.
Oak Ridge, TN 37831
E-mail: fengz@ornl.gov

Aashish Rohatgi, Co-Principal Investigator (Project 2B)

Pacific Northwest National Laboratory
902 Battelle Blvd.
Richland, WA 99352
E-mail: aashish.rohatgi@pnnl.gov

Alex Plotkowski, Co-Principal Investigator (Project 2C)

Oak Ridge National Laboratory
1 Bethel Valley Rd.
Oak Ridge, TN 37831
E-mail: plotkowskij@ornl.gov

Christopher Schooler, DOE Technology Development Manager

U.S. Department of Energy
E-mail: christopher.schooler@ee.doe.gov

Start Date: October 1, 2020 End Date: September 30, 2023
Project Funding (FY 2022): \$1,450,000 DOE share: \$1,450,000 Non-DOE share: \$0

Project Introduction

The LMCP, led by PNNL, is an integrated effort between PNNL, ORNL, and ANL. The overall program aims to develop and demonstrate scalable, cost-effective processing methods to locally enhance the properties of Al and Mg alloys to enable broader implementation of lightweight alloys in vehicles. The technical goal is to demonstrate that components and assemblies composed of commercially available alloys can be selectively modified to exhibit locally enhanced properties and deliver high materials performance in the most needed locations. This approach allows for significant improvements in manufacturability, structural efficiency, and weight-savings in next-generation vehicles. Furthermore, the approach enables the right properties in the right locations and provides the opportunity to decrease the number of metal alloys required for new vehicle manufacture, which reduces the challenges automakers face today in managing supply chains, and assures sufficient materials sustainability, and efficiently recycling scrap metal.

New processing methodologies could allow high-strength Al sheet materials over 450 MPa yield stress to reach ductility over 15% or forming bend radii $< 2 \times$ thickness. Local processing of cast parts can produce regions on a casting that will show $> 5 \times$ fatigue life or doubling of the endurance limit stress. Inherent to the research plan is an underpinning science theme to understand the behavior of microstructure evolution during manufacturing and the resulting material performance in-service. Recognizing metal microstructures are process dependent, controlling and optimizing the right microstructure will lead to desired property (ductility, strength, fatigue, corrosion resistance, etc.) in the right location of the components. Focused collaborative research thrusts have been established to develop local property modification strategies for each targeted metal system: high-strength Al sheet, Al castings, and Mg castings. Figure II.1.2.1 provides a brief description of these thrusts and how the principal manufacturing methodologies interact, as well as transition to higher TRLs. Within those thrusts, individual projects explore and develop the science and process engineering to create spatially tailored properties in alloys and assemblies of target metal systems. A fourth, cross-cutting thrust provides overarching support in testing, characterization, and modeling.

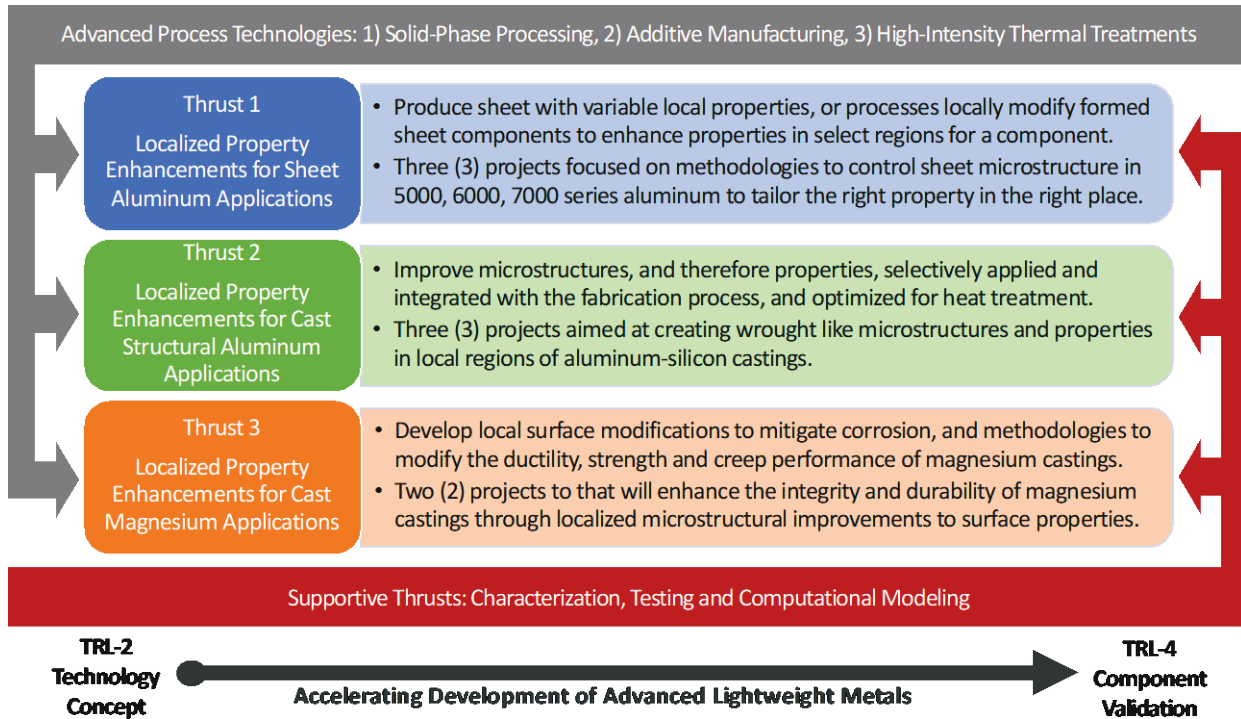


Figure II.1.2.1. Thrust and project structure of the LMCP. Source: PNNL.

The following report describes the FY 2022 technical efforts and results of Thrust 2, “Selective Processing of Aluminum Castings.” Al cast parts offer excellent opportunities for vehicle lightweighting, a reduced part count, and lowered assembly costs. However, there are science and engineering challenges with the application of castings in automotive body/chassis structures, including local ductility in the regions where castings are attached to other structures; fatigue in stressed members; and the sometimes-inverse relationship between castability (fluidity) and strength. To enable further integration of lightweight castings into the body-in-white (BIW), this thrust proposes to develop processes to locally modify cast parts so single castings can satisfy the varying property requirements at different locations of the component.

Cast microstructures are inherently less homogeneous than the wrought materials, and their properties (e.g., fatigue, fracture performance, ductility, strength) are usually defined by local microstructural characteristics, such as porosity; second-phase distribution and morphology; and dendrite size and morphology. Castings are especially prone to durability challenges due to near-surface microstructural inhomogeneities. Through the development of manufacturing approaches to locally customize, optimize, and/or repair microstructures in the component to meet specific application performance requirements, it will become possible to consider Al castings for a much wider range of applications and to reduce wall thicknesses in existing cast parts to enable additional weight-savings. In addition, local thermomechanical processing (TMP) may be able to bring alloys with high impurity content, like those with a high content of recycled feedstock, back to high property levels needed by designers.

HPDC Al alloys provide a potential route to achieve lightweighting by using a large, thin-wall and intricately shaped castings as structural members in a car body, replacing multiple joined structures and assemblies with single complex castings. However, for HPDC components to reliably perform as structural members, they need to demonstrate a good combination of strength, ductility, fracture toughness, and in certain situations, energy absorption and/or high-fatigue properties. Most general purpose HPDC Al alloys contain dendritic microstructure, acicular Si particles, and IMCs (β -FeSiAl (FeSiAl₅), and Al₁₅(MnFe)₃Si₂, etc.) that negatively impact the strength and ductility of HPDC Al alloys, hampering their acceptance as structural car body components [1, 2]. Work in Thrust 2 addresses these challenges by investigating TMP techniques, such as FSP and power ultrasonic surface processing (PUSP) to locally alter the microstructure of HPDC components, remove casting defects, and help achieve better mechanical properties.

In recent U.S. Department of Energy funded research, the front and rear sub-frames in a multimaterial lightweight vehicle were designed to be produced from cast Al welded to extruded Al sections [3]. In the same work, the rear control arms were designed to be made of cast Al [4]. However, as-cast microstructures are typically dendritic, are inherently less homogeneous, and may contain porosity resulting in lower mechanical performance compared to wrought materials. Some enhancement in as-cast properties can be achieved through microstructural refinement by increasing the local cooling rate (e.g., by using chills) and/or enhancing the nucleation rate in the melt (e.g., by adding grain refiners). However, the use of chills is not always practical and grain refiners are limited in how small of a grain size they can efficiently produce. Furthermore, castings are often heat-treated to achieve high strength. However, heat treatments that require solutionizing at elevated temperatures are not always feasible in cases where the presence of entrapped gas porosity can create blistering, such as in HPDC.

AM offers unique advantages compared to the casting of components, including generally faster cooling rates to achieve more refined microstructures and improved properties, as well as a broader range of geometric freedom. However, using AM to create a large quantity of monolithic structures would be significantly more costly and time-consuming compared to casting the same parts. The Thrust 2 Cast-and-Print project looks to combine the economic benefits of casting with AM by selectively using AM to locally modify geometry or chemistry of cast parts. This approach is significantly different than existing additive techniques, because the ‘substrate’ for the AM process is not discarded after printing due to being an actual part. Thrust 2 endeavors to overcome many of the challenges limiting greater use of Al castings in automotive structures. While Al casting

technology is well-developed, many scientific and technical challenges remain, and performance improvements are possible that can enable greater weight-savings, fewer separate parts, more RC, and lower embedded carbon in vehicle manufacturing and end-use.

Objectives

Thrust 2 will seek to enhance the local properties in cast Al components through three projects: (1) using FSP or PUSP to create local regions of improved microstructure that exhibit better fatigue performance, and to fix locally defected microstructures at cold shots or in locations where die filling is challenging; (2) using an integrated high-intensity thermomechanical approach that combines ultrasonics, Joule-heating, and high-pressure waterjet peening to modify local microstructures for enhanced strength, fatigue resistance, and ductility; and (3) using an AM Cast-and-Print process to locally improve microstructures and/or add structural features.

Thrust 2 is comprised of three individual projects, as shown in Figure II.1.2.2. Project 2A is a collaborative project between PNNL and ORNL (e.g., 2A1, 2A2) investigating FSP and PUSP to locally improve the strength, ductility, and fatigue performance of HPDC Al alloys in thin-walled castings. Project 2B (PNNL) focuses on high-intensity thermomechanical and thermal treatments to improve the properties of thicker wall (e.g., > 2 mm) Al structural castings, and Project 2C (ORNL) focuses on using AM to make cast parts with local AM additions.

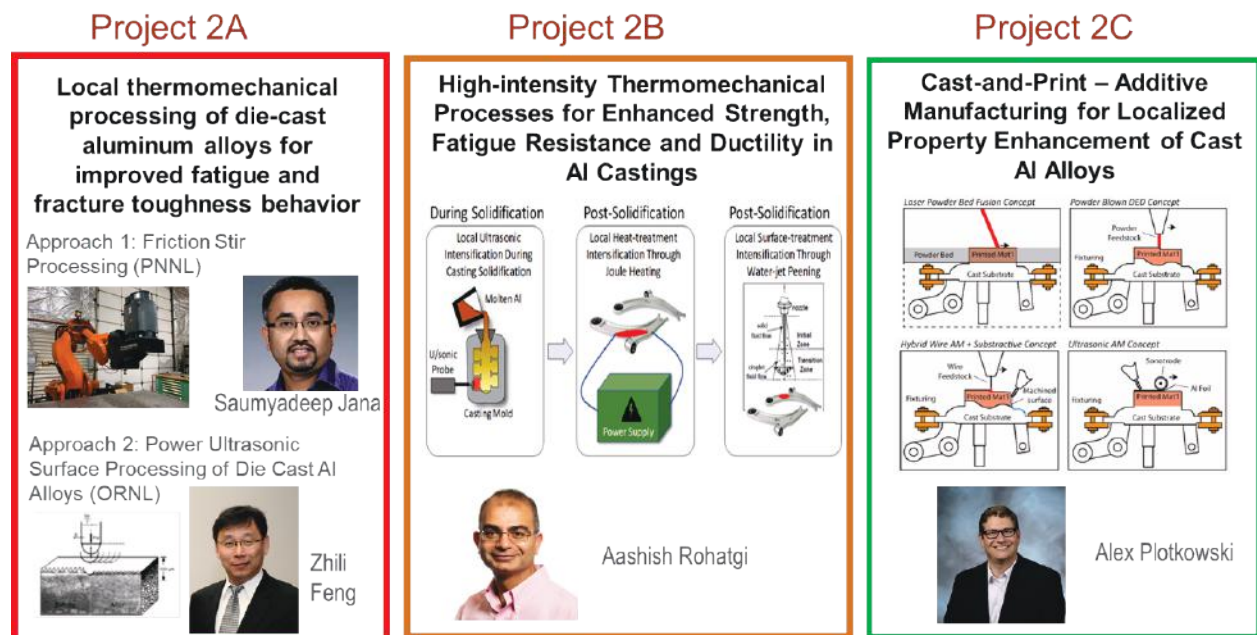


Figure II.1.2.2. Three projects within the LMCP Thrust 2. Source: PNNL and ORNL.

Project 2A1: FSP of Diecast Al Alloys

The objective of Project 2A1 is to investigate the effectiveness of FSP, a TMP method, to locally modify the microstructure of thin-walled HPDC Al alloy plates. Selective local processing of the HPDC component can be carried out to remove defects/other microstructural features responsible for mechanical property depression, especially in areas prone to failure [5, 6]. In addition, as more recycled Al is considered in the feedstocks of casting alloys, impurities and higher levels of iron will reduce the mechanical performance of the as-cast parts. Local FSP processing has an opportunity to modify the microstructure to bring back lost performance and enable higher recycle content in cast alloys.

This project develops the FSP process and evaluates the improved mechanical performance through coupon level mechanical testing. Two HPDC Al alloys are investigated in this study: (1) high-Fe containing A380; and (2) low Fe containing Aural-5. The objectives of this project are to: (1) demonstrate that FSP can reduce/remove casting porosity and achieve microstructural refinement in an HPDC Al alloy of choice; and (2) demonstrate the combined effect of microstructural refinement together with the elimination of casting porosity results in improved mechanical properties (e.g., strength, ductility) in an FSP-processed HPDC Al alloy.

Project 2A2: Power Ultrasonic Surface Processing of Diecast Al Alloys

The objective of Project 2A2 is to explore and develop PUSP technology to enhance surface properties of cast Al alloys for auto body structures. Specifically, the research and development focuses on: (1) near-surface local property enhancement at critical regions, such as load transfer locations, high-stress locations, and stress concentration points within complex diecast components; and (2) one-sided processing to improve the local microstructure of thin-wall complex geometries, such as difficult to reach locations in diecast components.

Project 2B: High-Intensity Thermomechanical Processes

The objectives of Project 2B are to: (1) improve the UTS and ductility of cast Al alloys; and (2) increase the local fatigue life of cast Al alloys. Project 2B focuses on thicker-walled, permanent mold cast parts. As-cast microstructures are typically dendritic, inherently less homogeneous, and may contain porosity, resulting in lower mechanical performance as compared to the wrought materials. Some enhancement in as-cast properties can be achieved through microstructural refinement by increasing the local cooling rate (e.g., by using chills) and/or enhancing the nucleation rate in the melt (e.g., by adding grain refiners). However, the use of chills is not always practical, and grain refiners are limited in how small a grain size can efficiently be produced. Furthermore, castings are often heat-treated to achieve high strength. However, heat treatments that require solutionizing at elevated temperatures are not always feasible in cases where the presence of entrapped gas porosity can create blistering, such as in HPDCs. Consequently, while Al casting technology is well-developed, many scientific and technical challenges remain. This project will develop advanced approaches to locally modify Al castings, and thereby satisfy the varying property requirements at different locations within the cast components.

Project 2C: Cast-and-Print: Additive Manufacturing for Localized Property Enhancement of Al Castings

The objective of Project 2C, the Cast-and-Print task, is to develop an understanding of the process-property-structure relationships that occur during the AM of material onto an existing cast Al part. It is necessary to understand the complexities of deposition on various geometries and how widely available wire feedstock for welding behaves during AM. Through the expansion of understanding of the Cast-and-Print approach, this task aims to enable a novel approach to the future design of lightweight automotive structural components.

Approach

Project 2A1: FSP of Diecast Al Alloys

In FY 2021, a general purpose HPDC A380 alloy was selected for local microstructural modification through FSP. In particular, the effect of FSP was studied on cast porosity and the modification of acicular Si- and Fe-containing particles. Microstructural characterization along with quasi-static and dynamic mechanical property evaluation indicates promising results for the viability of the FSP method. Higher fatigue life and tensile properties were demonstrated after FSP, even though the HPDC diecast plate had a die-skin ~0.5 mm in thickness with a lower defect density and a highly refined microstructure.

In FY 2022, premium HPDC alloy Aural-5 has been selected to evaluate the effect of FSP on this class of alloy. Aural-5 is a low Fe (~0.09 wt.%) containing alloy, with the chemical composition listed in Table II.1.2.1.. Aural-5 is commercially used by automobile companies on several structural components, such as rear rails for the Jaguar Land Rover, the front shock towers for GM, and multiple components for Porsche. Figure II.1.2.3 shows the casting defects in Aural-5, which are mostly noted in the form of shrinkage porosity, as shown in Figure II.1.2.3(b), and are concentrated near the mid-wall, as shown in Figure II.1.2.3(a). Since Aural-5 is modified strontium (Sr), it has refined dendritic microstructure at the die-wall, as shown in

Figure II.1.2.3(c), refined eutectic Si particles, as shown in Figure II.1.2.3(d), and large 2nd phase particulates present in between the dendritic microstructure, marked by the red arrows in Figure II.1.2.3(c).

Table II.1.2.1. Composition of HPDC Aural-5 Plates

Al	Si	Mg	Mn	Fe	Ti	Sr
Balance (wt. %)	6.88	0.25	0.56	0.09	0.06	125 ppm

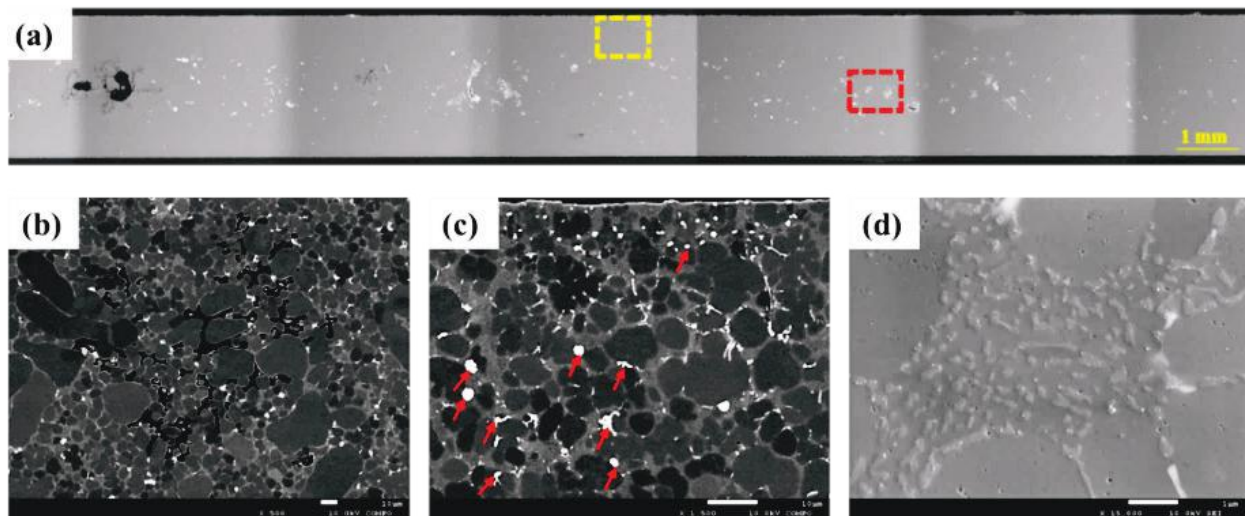


Figure II.1.2.3. Premium HPDC Aural-5 alloy: (a) cross-sectional microstructure; (b) shrinkage porosity in the middle area; (c) dendritic structures, Al-Si eutectic phase, second-phase particulates; and (d) refined eutectic Si. Source: PNNL.

For processing of HPDC Aural-5 plate, FSP was carried out using a tool rotational speed of 1,200 rpm and a traverse velocity of 0.7 m/min. Only single-pass processing was required for the processing of Aural-5 plates. The microstructure of the Aural-5 plate both before and after FSP is compared in Figure II.1.2.4. The Aural-5 alloy in as-cast condition shows the presence of acicular Mg_2Si phase along the inter-dendritic regions, as shown in Figure II.1.2.4(a). However, FSP leads to a breakdown of such acicular Mg-rich phases, and thus, the second-phase particles are uniformly and homogeneously distributed throughout the FSP microstructure, as shown in Figure II.1.2.4(b). In addition, FSP removes casting porosity, and the processed matrix appears to be 100% dense.

Multiple miniature-sized tensile specimens were extracted from the process zone to locally compare mechanical properties at different areas of the FSP region. Typically, a FSP nugget can be divided into three zones: (1) the advancing side, (2) the middle side, and (3) the retreating side that show some characteristic microstructural features. Uniform property across all the zones is desirable and confirms process optimization. For effective comparison, miniature tensile coupons were also extracted from the HPDC Aural-5 plate, along the die-skin and mid-wall areas. Additionally, four-point bending fatigue tests, and tear toughness tests were conducted on HPDC Aural-5 alloy both before and after FSP to evaluate the role of FSP on mechanical properties of this premium low Fe containing Al alloy.

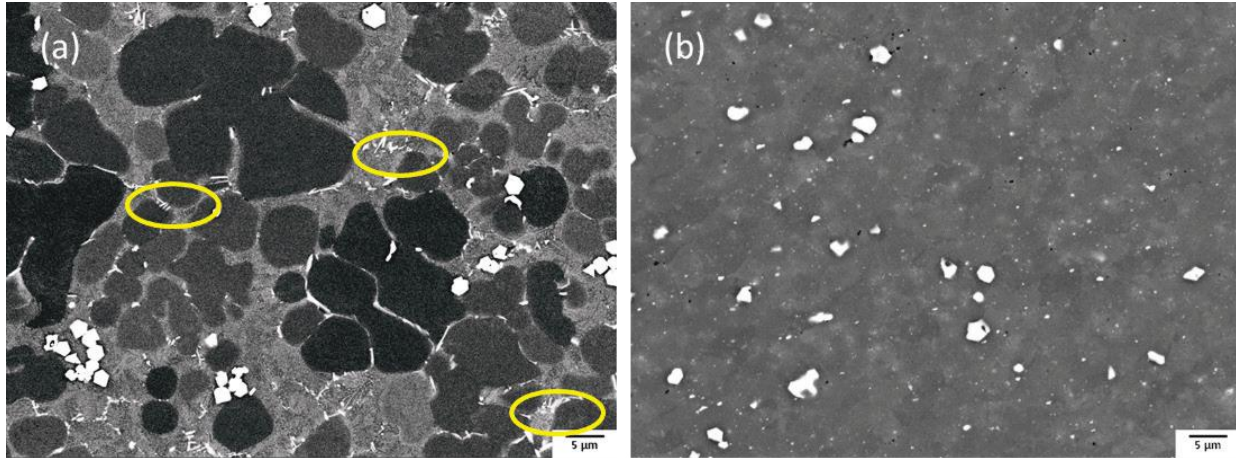


Figure II.1.2.4. (a) Acicular Mg_2Si phase present in HPDC Aural-5. (b) Acicular phases refined and uniformly distributed after FSP. Source: PNNL.

Project 2A2: Power Ultrasonic Surface Processing of Diecast Al Alloys

The PUSP method is a relatively new concept in the early stages of development. The underlying physics of PUSP suggest it has the potential to achieve local near-surface microstructural modifications at low normal loads to the part surface, which will be essential for single-side processing in some complex-shaped automotive body components, particularly thin-wall diecast components that may be prone to deformation at higher normal loads. The second potential advantage of PUSP is its ability to create compressive surface residual stresses. It is known that compressive surface residual stress induced by laser shot peening has led to significant improvement of fatigue life of Al alloy structures for aerospace applications.

Project 2A2's approach is to explore and develop PUSP technology to improve local properties of cast Al alloys for auto body structures. Specifically, the task is pursuing understanding of how surface property enhancements of diecast Al imposed by surface-treatment with power ultrasonics can enable increased durability and fatigue life. During PUSP of the surface, highly localized heating and severe plastic deformation occur, which closes solidification porosity, refines the microstructure, and generates compressive residual stresses within a specific volume determined by processing conditions and material properties. In addition, the acoustic plastic softening effect is being investigated to reduce the required process load for one-side processing of a thin-wall or difficult to reach surfaces, enabling integration with robotic auto body structure assembly systems.

This project is employing both experimental process development and physics-based computational simulation methods. The multiscale modeling effort is designed to support process development by simulating heat generation, plastic deformation, and residual stresses, as well as the resulting microstructure, residual stress affected by PUSP, and enhanced durability or fatigue life of body structure components.

The physics-based computational modeling framework integrates three types of analyses leading to the prediction of the fatigue life of parts that have been locally treated by PUSP. First, a previously developed ultrasonic joining process model [7] was refined and applied to ultrasonic processing by means of the thermomechanical FEM. The process model is being applied to determine the effects of sonotrode geometry and processing conditions to impart surface deformation and vibrational heating. Transient temperature, plastic strain, and stresses from the process model are used as inputs for future recrystallization and microstructure simulations. Fatigue performance simulations are being used to connect the process, microstructure changes, and residual stresses to the improvement in fatigue life by ultrasonic processing.

Project 2B: High-Intensity Thermomechanical Processes

This project is divided into three main tasks where each task will develop a different processing approach that may be used to improve the local properties of cast Al automotive components at different stages of the manufacturing process. The first task will enhance the initial casting stage by applying local ultrasonic intensification during casting with the goal of refining the as-cast microstructure. Ultrasonic-induced microstructural refinement has been attributed to mechanisms, such as enhanced heterogeneous nucleation and the fracture of dendrites [8–11] and the ultrasonically refined microstructure is expected to improve the as-cast strength, ductility, and fatigue life of the casting [11, 12]. The second task will enhance the heat-treatment stage by applying local thermal intensification with the goal of strengthening the as-cast microstructure. Thermal intensification will be applied through Joule-heating and is expected to accelerate atomic scale diffusion processes, which will decrease the time and/or temperatures required for post-solidification heat treatments. The third task will enhance the surface-treatment stage by applying local waterjet peening to impart deep residual compressive stresses, which are expected to improve the fatigue life of the casting. In industrial practice, one or more of these three techniques could be applied to produce high-performance Al castings where the local properties have been enhanced to meet the local property requirements.

During FY 2022, the primary focus of this work was to characterize the microstructure and mechanical properties of samples cast with and without ultrasound (Task 1), and to develop the Joule-heating-based local heat-treatment method (Task 2) to improve the mechanical properties.

For Task 1, A356+Fe (i.e., A356 Al with added Fe content) was cast in a graphite mold at RT. A 20 kHz, 13-mm-diameter ultrasound probe made of Ti6Al4V was used to apply local ultrasonic intensification during casting. Control castings were fabricated without ultrasonication; the ultrasound probe was not powered in this case but was inserted to ensure similar local solidification conditions as the sonicated castings. SEM was used to quantify the size and shape of the β -Al₃FeSi intermetallic particles in specimens sectioned from the castings. Tensile specimens were extracted from the castings, heat-treated to a T6 temper, and tested to measure the local strength and ductility. X-Ray CT was conducted to quantify the porosity. Thermodynamic and casting simulations of A356 were conducted using ProCAST software to predict phase evolution during solidification, the thermophysical properties, and temperature throughout the casting. *In situ* beamline experiments were conducted at the APS, as shown and described in Figure II.1.2.5, where diffraction and the radiography data of molten A356 were collected during solidification, both with and without ultrasound.

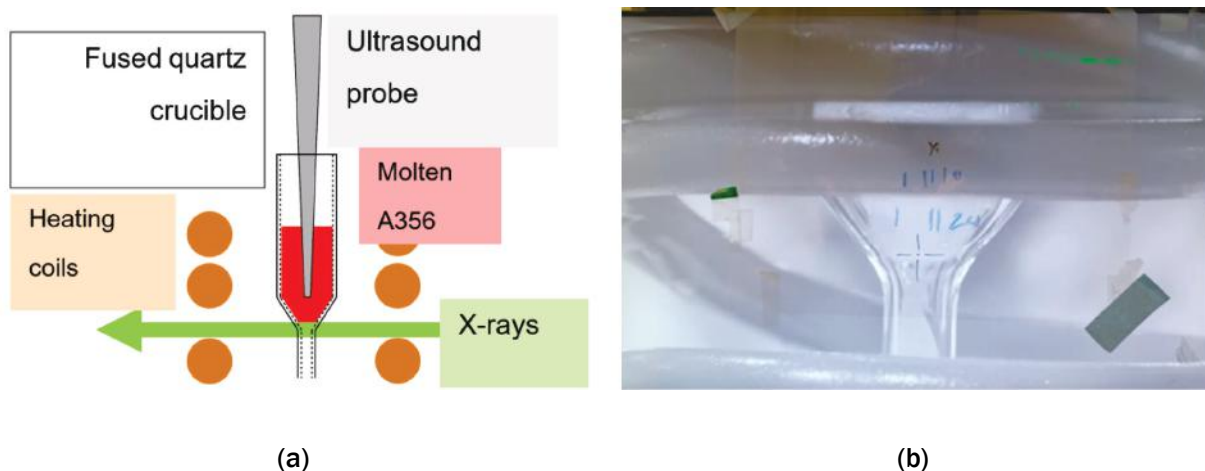


Figure II.1.2.5. (a) A schematic showing the experimental setup used for *in situ* diffraction experiments at the beamline. (b) A photograph showing the corresponding specimen with the crosshairs indicating the general position of the region interrogated by the high-energy X-ray beam. Source: PNNL.

For the Task 2 Joule-heating experiments, an A380 HPDC alloy plate was heat-treated (solutionized) locally by PNNL's Joule-heating method, whereby the sample was heated and its temperature controlled by controlling the electrical current flowing through it. Figure II.1.2.6(a) shows a schematic of PNNL's setup where a $\sim 50 \times 50 \times \sim 3.5$ mm test sample is clamped between two electrodes. Samples were solutionized for various temperature-time combinations, quenched in water, and then artificially aged at 155°C in a conventional furnace for 18 hours. The solutionization temperature was selected as 490°C , which was based on the literature. Some as-quenched samples showed tiny blisters suggesting the temperature-time needed to be optimized to minimize/avoid blistering. Therefore, the solutionization time was limited to 8 mins. to minimize blistering. The samples were then machined to 2.5 mm thickness and miniature tensile test samples, as shown schematically in Figure II.1.2.6(b), were cut by waterjet machining. Thus, the physical location of a tensile sample in the heat-treated plate is associated with the local temperature it experienced during Joule-heating. The tensile samples were tested at a constant strain rate of 0.001/s and the strain was measured through PNNL's custom micro-3D DIC system.

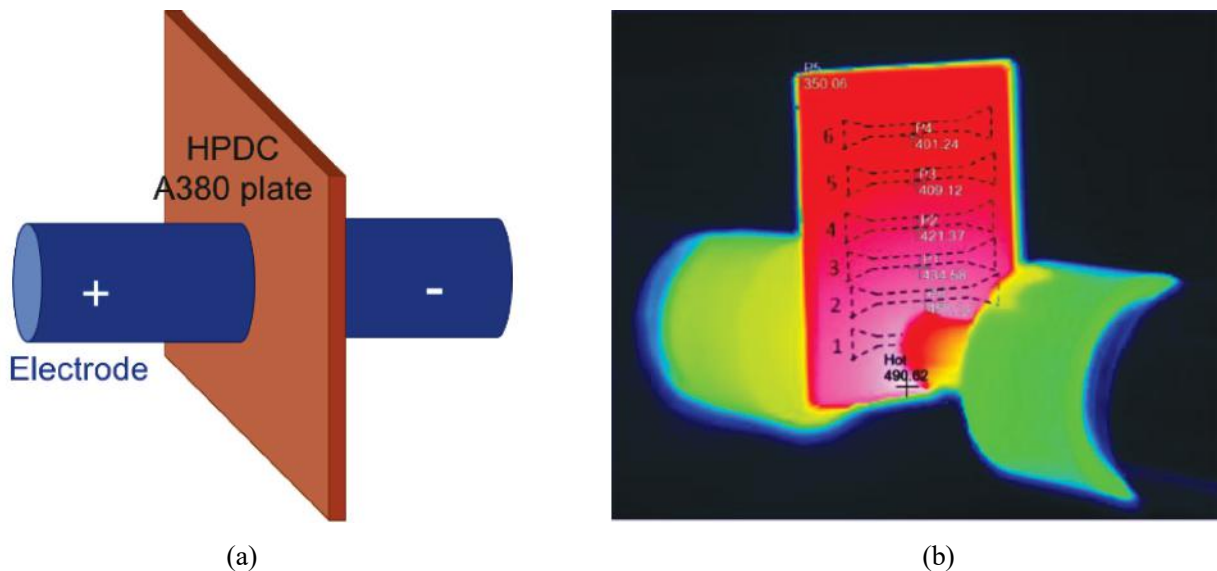


Figure II.1.2.6. (a) Schematic of PNNL's Joule-heating experimental setup. (b) Thermal map of the HPDC A380 plate sample during local heat-treatment showing the approximate locations of the tensile test samples by the dashed lines that were machined after aging for mechanical testing. Source: PNNL.

Project 2C: Cast-and-Print: AM for Localized Property Enhancement of Al Castings

The laser hot-wire AM additive process was used for this task—specifically the Mazak VTC-800G system—that heats the feedstock wire using resistive heating and then melts the heated wire using a laser to deposit it onto the build area. Additionally, the Mazak VTC-800G is a hybrid manufacturing system, meaning it also has capabilities to use subtractive manufacturing to machine deposit material to a given specification. This approach was chosen due to the process only needing access to the top surface of the part and being able to produce geometries to a specific tolerance.

Parts were manufactured from several Al-Si and Al-Mg wire feedstock alloys, namely Al alloys 4043 (Al with 4.5 wt% - 6 wt% Si), 4047 (Al with 11 wt% - 12 wt% Si), and 5356 (Al with 4.5 wt% - 5.5 wt% Mg and <0.25 wt% Si), deposited onto cast alloy A356 (Al with 0.3 wt% - 0.45 wt% Mg and 6.5 wt% - 7.5 wt% Si). The selection of these feedstock alloys came from an analysis of the hot-cracking susceptibility of various commercially available Al alloy wires, which is described in Kannan et al. [13] A previous analysis of the recyclability of the chosen wires also showed material added using Cast-and-Print would not adversely affect the recycling stream for Al-Si-Mg cast alloys, such as the A356 series of cast Al alloys. Coupon-scale parts were manufactured for characterization of the material properties via optical microscopy, hardness testing, and

tensile testing. Demonstrations of the Cast-and-Print approach were also conducted to show examples of the potential utility for automotive applications.

Results

Project 2A1: FSP of Diecast Al Alloys

Table II.1.2.2 summarizes the tensile test results carried on miniature samples extracted from a FSP'd Aural-5 plate. Miniature samples in an as-cast condition are also included. 'AS' and 'RS' refer to the advancing and retreating locations of the FSP region, respectively. Tensile properties are better along the die-wall region, based on the location-specific tensile property data. A major difference is noted with percent elongation to failure and YS. Such difference can be attributed to denser and refined microstructure observed along the die-wall region of HPDC Aural-5 plates. After FSP, an increase in YS and percent elongation over the HPDC condition is noted due to the modification of the cast microstructure. Based on the average YS of the mid-wall (~117 MPa) and the average YS of the middle-FSP region (~137 MPa), an increase of ~17% in YS could be achieved due to FSP modification of the cast microstructure. The average percent elongation to failure for the mid-wall and die-wall HPDC samples were found to be 6% and 10%, respectively. After FSP, the average percent elongation to failure for the AS, middle, and RS samples increases to 14.5%, 14.4%, and 13.7%, respectively, which corresponds to a greater than 20% improvement in percent elongation over the mid-wall section, as well as over the die-wall section of the as-received Aural 5 casting.

Table II.1.2.2. Summary of Tensile Properties of HPDC Aural-5 Before and After FSP

Test Condition	YS (MPa)	UTS (MPa)	Percent Elongation
Die-Wall	128.7 ± 10.2	235.5 ± 16.2	9.9 ± 2.1
Mid-Wall	117.2 ± 9.9	196.8 ± 30.5	6.0 ± 2.5
FSP-AS	132.5 ± 7.1	227.9 ± 2.7	14.5 ± 4.2
FSP-Middle	136.7 ± 7.6	242.0 ± 8.7	14.4 ± 2.7
FSP-RS	136.3 ± 1.8	226.9 ± 0.6	13.7 ± 3.7

Subsequently, high-cycle bending fatigue properties have been evaluated in HPDC and FSP'd conditions at various stress levels in a four-point bending configuration. Fatigue tests were carried out on an MTS uniaxial servo-controlled testing frame at a 10 Hz loading frequency using a stress ratio of $R = 0.1$. Figure II.1.2.7 shows the S-N plots of the HPDC and FSP'd Aural-5 specimens, which compares the high-cycle fatigue properties of HPDC vs. FSP conditions at various maximum bending stress. At any applied stress value, the FSP'd specimens demonstrated a higher fatigue life than the HPDC specimens. As an example, ~300% improvement of fatigue life was observed for the FSP specimen in comparison with a HPDC condition at 325 MPa. Moreover, at a lower stress level of 250 MPa, the FSP specimen did not fail after $\sim 2.0 \times 10^6$ cycles indicating more than 500% improvement. At 225 MPa stress level, the FSP-driven fatigue life improvement is more than 200%. Therefore, the target fatigue property improvement of more than 10% could be achieved after FSP modification.

Due to a thin section of the Aural-5 plates, tear toughness is measured instead of plain strain fracture toughness (K_{IC}). Based on the ASTM B871 standard, the details of specimen geometry are shown in Figure II.1.2.8(a). The specimens are pin-loaded and the load-displacement curve is captured for both HPDC and FSP'd Aural-5, as shown in Figure II.1.2.8(b). The area under the curve represents the tear initiation and propagation energy. After FSP modification, it requires 44% more energy to tear FSP'd Aural-5 than HPDC specimens. FSP was, thus, able to improve tear toughness by more than 15% as compared to the HPDC condition.

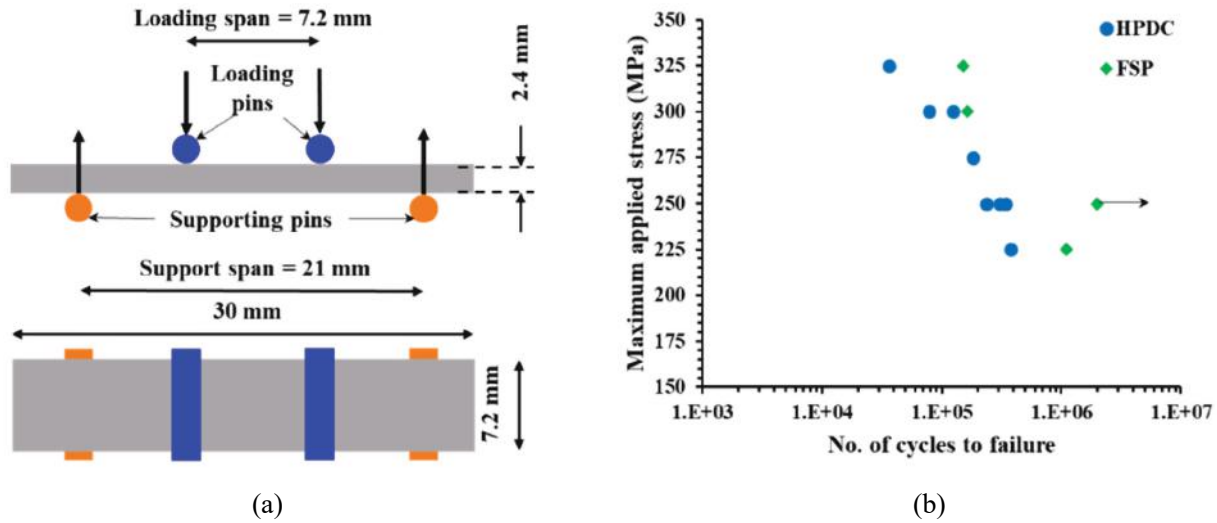


Figure II.1.2.7. Four-point bending fatigue testing: (a) schematic of testing configuration and (b) comparison of the stress for the number of cycles to failure plot for HPDC and FSP specimens at R = 0.1 along the weld direction. Source: PNNL.

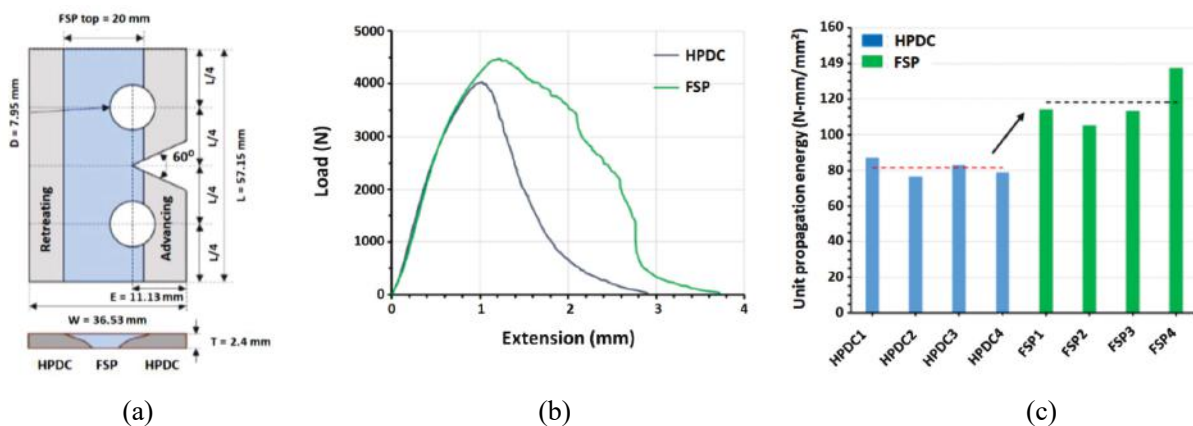


Figure II.1.2.8. Tear toughness testing: (a) geometry of tear test specimen of FSP'd Aural-5; (b) comparison of load-displacement curve; and (c) comparison of unit propagation energy. Source: PNNL.

Project 2A2: Power Ultrasonic Surface Processing of Diecast Al Alloys

The research and development in FY 2022 centered on demonstrating the feasibility of PUSP to use a targeted process load of 200–300 lbs. to achieve the formation of compressive surface residual stresses, as well as meaningful surface microstructure refinement. Diecast Al alloys A380 and Aural 5 were processed by PUSP under a wide range of process parameters and tool designs, assisted by process modeling.

Two significant milestones toward the project goal of surface modification and performance enhancement of complex cast body structures were achieved in FY 2022. First, the PUSP processing load was reduced to 100–200 lbs. by more effectively utilizing the unique acoustic softening phenomenon. The required load is 5%–10% of the typical load required for other complementary solid-state processes, such as FSP. Such significant reduction of the normal load during solid-state microstructural modification processing is necessary to enable a one-sided surface-treatment process and for some particularly thin-walled cast components. The low load reduces or eliminates the need to have opposing surface access for back side anvil support to sustain the processing load for thin-walled or complex geometry cast parts. The combined features of low load and

one-side processing offers a potential solution to a major hurdle for the auto industry to apply localized surface modification processes for property improvement to thin-wall and complex geometry components.

Second, the processing method was advanced from a spot surface modification used in FY 2021 to a linear surface modification in the first quarter of FY 2022. Transition to linear treatments greatly improved both the surface finish and the microstructural uniformity and the anticipated residual stress profile as compared to spot processing. Linear surface modification allowed for the production of surface-treated cast A380 blocks for fatigue testing. Figure II.1.2.9 shows an example of the PUSP-processed blocks for fatigue testing. Each plate was approximately 10 in. long and 5 in. wide, with three processed regions approximately 2.5–5 in. long. PUSP process parameters were systemically varied in producing these regions. The fatigue test utilized four-point bend test techniques designed specifically for investigating the surface microstructure modification and residual stress effects. The finite element model, as shown in Figure II.1.2.10, was used to define how to apply uniform bending stress to both the region processed by PUSP (e.g., ~5 mm wide) and the adjacent base metal where the residual stress from PUSP may still exit (e.g., ~8 mm on each side).

Figure II.1.2.11(a) highlights the effect of PUSP on the fatigue life of Alloy 380 under different conditions. As shown in the figure, the effect of PUSP is highly dependent on the processing conditions. For both the process conditions of R1-B and R2-B, the improvement in fatigue lives exceeded two times that of the baseline material without PUSP treatment. The specimen photographs in Figure II.1.2.11(b) also show the failure location of each of the fatigue-tested plate specimens. The processed regions are indicated by arrows on the broken samples in the figure. The locations of failure were also indicative of the effect of PUSP. Samples B-1 and B-2 (repeating samples under the R1-B process conditions), which had considerably higher fatigue lives, had the failure location outside of the processed region, about 8-10 mm away from the PUSP-processed region.

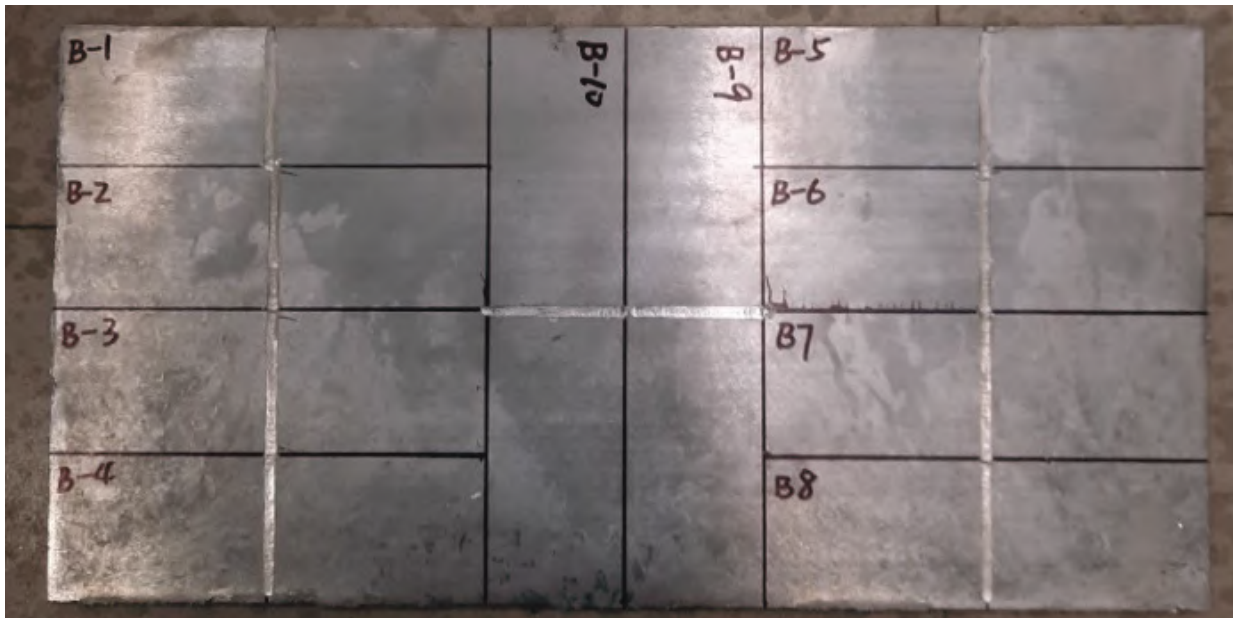


Figure II.1.2.9. Ultrasonic processing regions on 3-mm-thick A380 diecast Al alloy sheets, made with different process conditions. The PUSP process load was set at 100 lb., with process power varied in the range of 100–300W. Fatigue specimens were cut from the processed sheets and are presently in testing.

Source: ORNL.

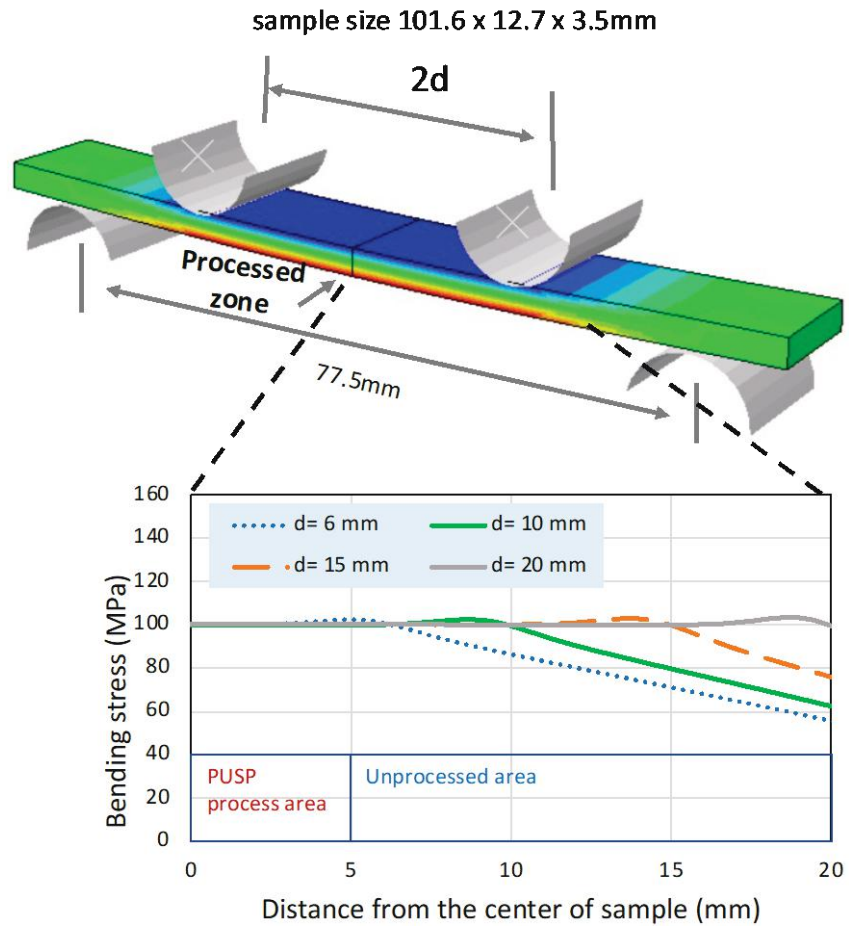


Figure II.1.2.10. Four-point bending test design and setup to ensure uniform bending stresses to cover the regions treated by PUSP and the adjacent regions with process residual stresses. Source: ORNL.

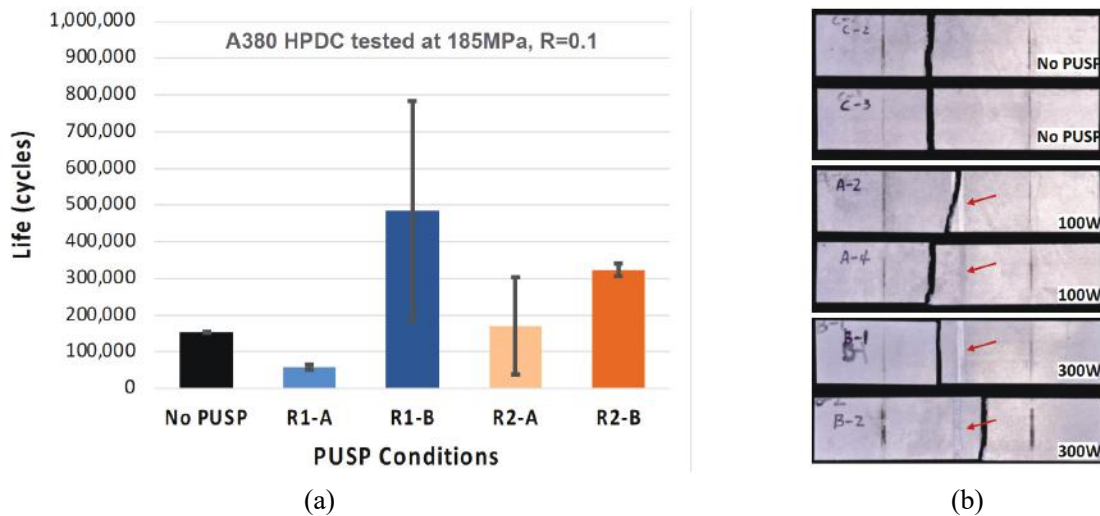


Figure II.1.2.11. (a) Four-point bending fatigue testing results of PUSP-processed Alloy A380 under different process conditions where the maximum load = 1000N and R = 0.1. (b) “No PUSP” processed base material samples (C-2 and C-3) along with other samples. Source: ORNL.

The SEM cross-sectional images in Figure II.1.2.12 confirm the near-surface microstructure refinement by PUSP processing on Alloy A380. The low load PUSP processing resulted in noticeable surface microstructure refinement of the diecast microstructure, including the breakdown of diecast solidification eutectic structures, the refinement of strengthening phases/particles, and the closing of near-surface solidification pores. Under the process power of 100–500 W investigated thus far; the extent of microstructure refinement increases with the increase of ultrasonic power. On the other hand, the depth of the microstructure refinement zone was approximately 50 μm and was insensitive to the ultrasonic power applied.

A finite element numerical model [14] was utilized to investigate the process conditions on the generation of surface heat, the effect of acoustic softening, and the surface residual stress distribution as a result of PUSP. The PUSP simulation results were used to assist the process development, especially on the formation of compressive surface residual stress, which is one of the key factors enhancing the durability and performance of diecast body structures. Figure II.1.2.13 shows an example of the simulation results—the effect of vibration amplitude, which is directly related to the process power or energy input—has a strong influence on the surface residual stress distribution. The simulation was performed on a flat coupon, like the one in Figure II.1.2.11. The simulation results suggest there is a threshold ultrasonic power level above which compressive surface residual stress develops. This was consistent with the fatigue testing results shown in Figure II.1.2.11. Under the relatively low power level (100W), the fatigue lives of PUSP-processed materials were lower than the non-processed base metal. At 300W, PUSP improved the fatigue lives by $> 2\times$.

The PUSP process model was applied to investigate the benefits of PUSP on stress concentration locations of diecast autobody structure components. The simulation results are shown in Figure II.1.2.14, for a corner location under bending stress from structural load of BIW. The simulation results suggest PUSP would substantially reduce the high-stress concentration at the corner of the structure under the bending stress load. Such simulation results are being considered for PUSP processing in the high-stress locations in prototypical diecast body structures, with experiments planned for FY 2023.

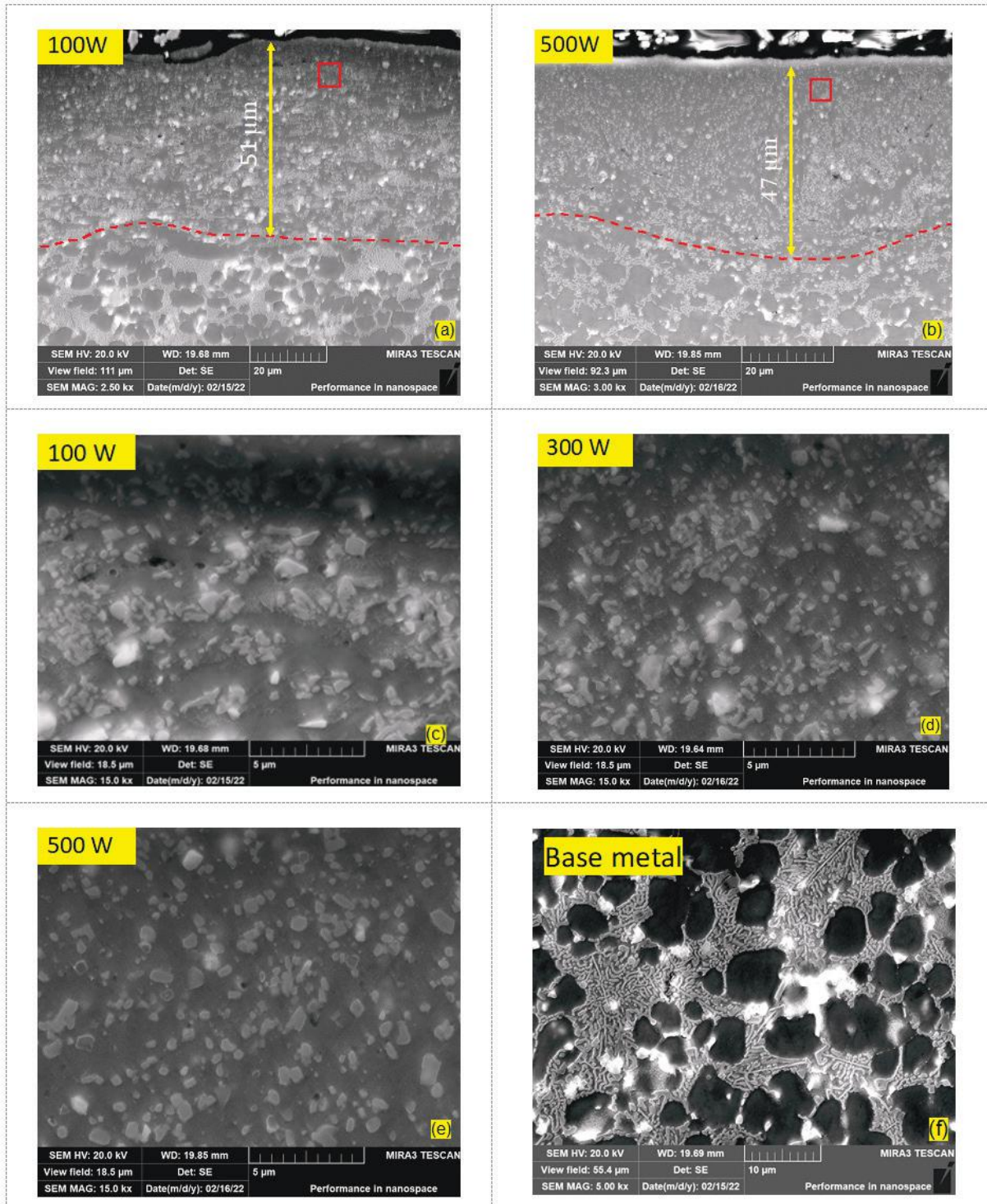


Figure II.1.2.12. Surface microstructure refinements by PUSP under different process power levels and 100 lb. process load: (a) and (b) are the cross-sectional view of the PUSP-processed region near the top surface of the A380; (c) through (e) are high-magnification views of the processed region under three different process power levels taken near the red squares in (a) and (b); and (f) is the high-magnification view of the base metal. Source: ORNL.

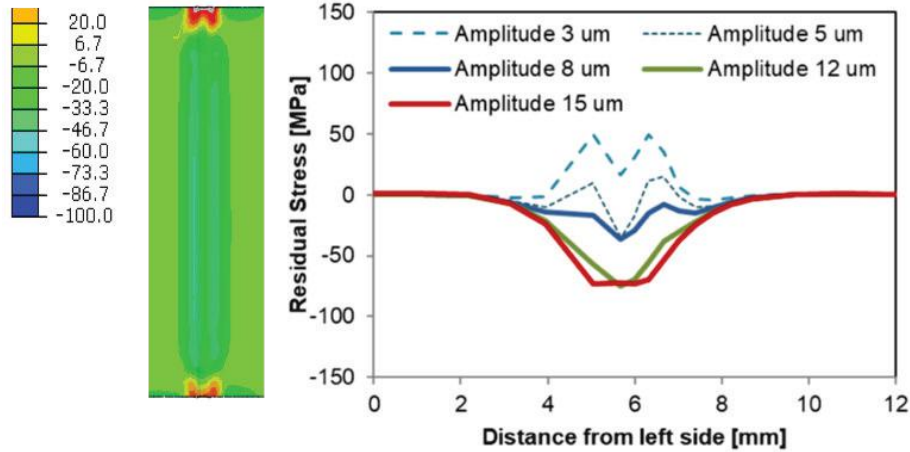


Figure II.1.2.13. Effect of ultrasonic vibration amplitude (energy) on the surface residual stress distribution. Source: ORNL.

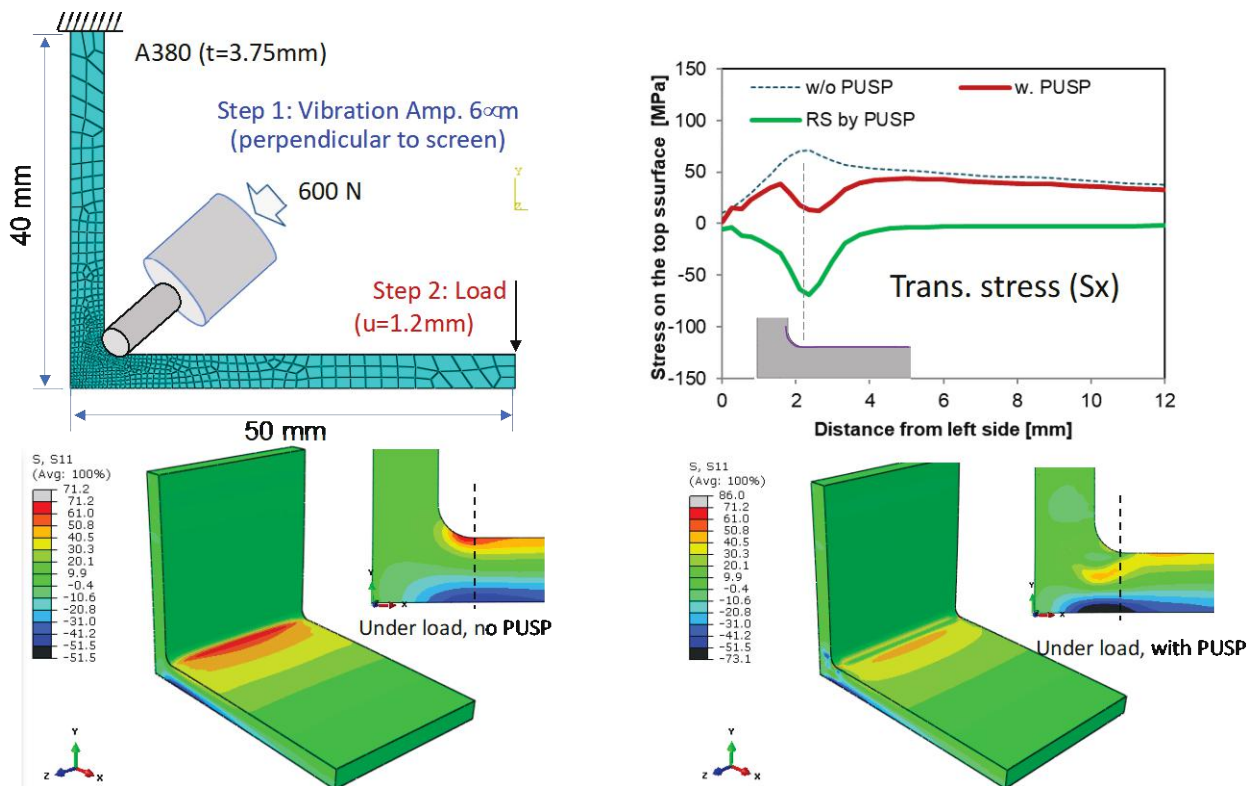


Figure II.1.2.14. Simulation results for the effect of PUSP on the reduction of high stress at a corner location under bending stress. Source: ORNL.

Project 2B: High-Intensity Thermomechanical Processes

Task 1: For the casting experiments, the average cooling rate during solidification was $\sim 2^{\circ}\text{C/s}$, which is similar to the cooling rates associated with permanent mold casting techniques (e.g., ~ 0.1 to 1°C/s). Previously, ultrasound was demonstrated to transform the microstructural morphology from dendritic to globular and reduce the average grain size by 74% [15].

Figure II.1.2.15(a) and Figure II.1.2.15(c) show examples of the dendritic microstructure of the control casting (without ultrasound) and the globular microstructure (with ultrasound). The application of ultrasound also transformed the morphology of the intermetallic β -Al₅FeSi phase particles from needle-like and an aspect ratio of 14, to rectangular and an aspect ratio of 6, as shown in Figure II.1.2.15(b) and Figure II.1.2.15(d), respectively. Typically, β -Al₅FeSi particles are deleterious to the overall strength and ductility of the alloy since their needle-like morphology makes them a source of stress concentration. The rectangular morphology of the ultrasonically modified β -Al₅FeSi particles is expected to have a less pronounced stress concentration than the needle-like morphology. Thus, by reducing the aspect ratio of the β -Al₅FeSi intermetallic needle-like phase, ultrasound technique could reduce the stress risers in the microstructure and improve the overall strength and ductility of Fe-rich Al alloys.

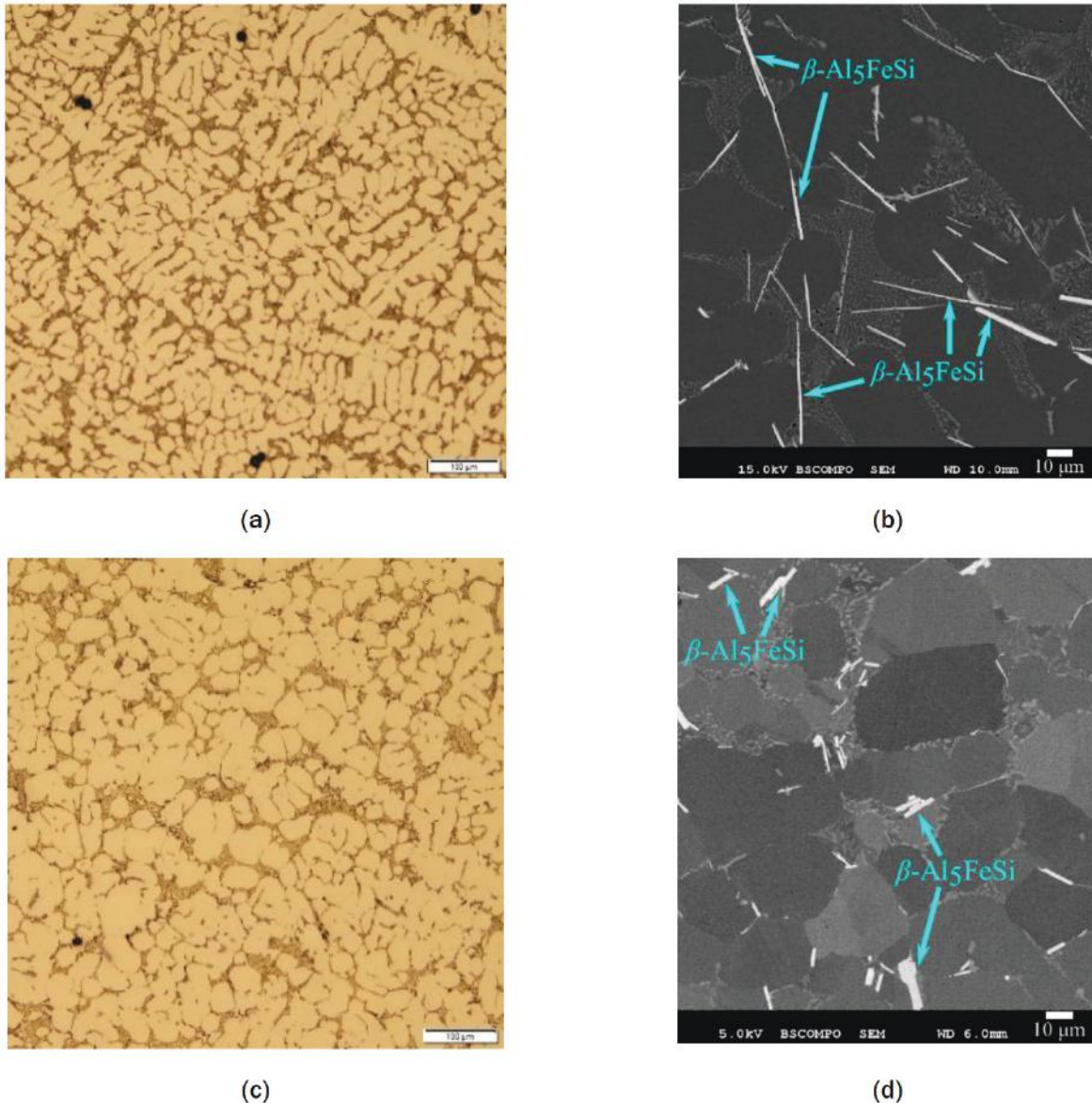


Figure II.1.2.15. Optical micrographs show (a) the dendritic microstructure of the control casting and (c) the globular microstructure of the ultrasonicated casting. Scanning electron micrographs show (b) the needle-like β -Al₅FeSi particles in the control casting and (d) the rectangular β -Al₅FeSi particles in the ultrasonicated casting. Source: PNNL.

Tensile specimens were extracted from the control casting (e.g., dendritic microstructure) and from the ultrasonicated casting (e.g., globular microstructure). When considering all the tensile specimens tested, the average UTS between the two microstructures is the same, but the globular microstructure of the ultrasonicated casting has 88% greater elongation at rupture compared to the dendritic microstructure of the control casting. Due to non-optimal casting process parameters, the porosity was not consistent throughout either casting. The porosity of individual tensile specimens ranged from 0.33% to 2.94%. High porosity levels can decrease strength and ductility, which therefore makes it difficult to correlate mechanical properties to the microstructure. To mitigate the potential influence of porosity on mechanical properties, if we only consider tensile specimens with porosity < 1%, the globular microstructure had 10% greater UTS (e.g., 201 MPa compared to 220 MPa) and 200% greater elongation at rupture (1.51% elongation compared to 0.50% elongation), as shown in Figure II.1.2.16(a). This means that the globular microstructure of the ultrasonicated casting has greater ductility and UTS compared to the dendritic microstructure of the control casting, and the enhancements are more pronounced/apparent in castings with low porosity. Using videos of casting experiments as an input, casting simulations were performed to estimate the temperature and solid-phase fraction of the alloy during casting. A still image from one of the casting simulations is shown in Figure II.1.2.16(b). *In situ* diffraction and radiography experiments conducted at the APS generated data that are currently being analyzed. This data will offer deeper insights into the mechanisms that control ultrasonically induced grain refinement and will enable optimization of ultrasonic melt processing to produce high-performance castings.

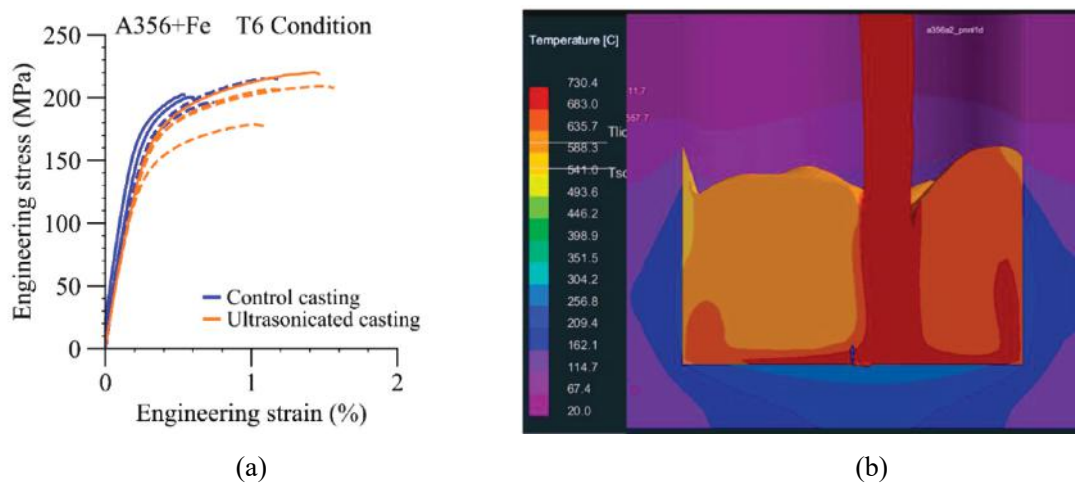


Figure II.1.2.16. (a) Engineering stress is plotted vs. engineering strain for tensile specimens extracted from the control casting (dendritic microstructure) and ultrasonicated casting (globular microstructure). Solid lines indicate specimens with porosity levels <1%. (b) This single frame from a ProCAST casting simulation shows molten Al being poured into a graphite mold initially at RT. Source: PNNL and ORNL.

Task 2: Figure II.1.2.16(b) shows the temperature distribution in a locally Joule-heated sample as imaged by an infrared thermal camera. The heat generated by Joule-heating of the plate under the electrodes is conducted to the rest of the sample, generating a thermal gradient. As expected, the highest temperature (e.g., 490°C) is obtained adjacent to the electrodes and gradually decreases with increasing distance away from the electrodes, reaching ~350°C at a location diagonally across from the electrode, as shown in Figure II.1.2.16(b). Table II.1.2.3 compares the mechanical properties of the heat-treated and as-cast samples. Location #1 is directly under the electrode and experiences the highest temperature during solutionization, while Location #6 is the farthest from electrode and experiences the lowest temperature. As an example, for a 490°C target solutionization temperature, sample locations and their corresponding approximate temperatures are as follows: #1 – 490°C; #2 – 450°C; #3 – 435°C; #4 – 420°C; #5 – 410°C; and #6 – 400°C.

Table II.1.2.3. Summary of Tensile Test Results of Locally Heat-treated (Followed by Aging) HPDC A380

Sample Location	*490 °C – 2 min.		*490 °C – 4 min.		*490 °C – 8 min.		*450 °C – 8 min.		As-Cast
See Figure II.1.2.16(b)	UTS	%el	UTS	%el	UTS	%el	UTS	%el	273.1 ± 16.9 MPa 2.7 ± 1.2% (average of 10 samples)
1	308.0	1.76	219.6	0.72	231	0.7	285.8	1.82	
2	260.8	1.01	290.2	2.22	229	0.5	243.3	1.65	
3	297.4	2.05	273.0	2.45	179	0.3	228.0	1.72	
4	269.1	1.83	270.0	3.32	215	1.0	208.0	1.32	
5			267.0	4.01	176	0.9	197.0	1.31	
6	260.2	2.01	265.0	3.66	168	0.9	229.3	1.61	

* Temperature refers to the maximum measured temperature value, i.e., adjacent to the electrode.

Project 2C: Cast-and-Print: AM for Localized Property Enhancement of Al Castings

The depositions made in FY 2021 were done on the Mazak model VC-500, whereas the depositions done in FY 2022 were done on a more recent model, the Mazak VTC-800G. While both systems use laser hot-wire AM combined with subtractive machining capabilities, the hardware is slightly different. In particular, the build head configuration changed, including the shielding gas flow and the laser spot geometry. These changes resulted in oxidation of the feedstock during deposition when using similar processing parameters to those used in FY 2021.

Figure II.1.2.17(a-c) shows the effect oxidation build-up has on the print quality. The layer of oxide that formed on the surface led to insufficient wetting of the liquid metal on the previously deposited surface. Ultimately, the balling led to a large amount of porosity in the final part. As a temporary strategy to allow deposition progress while addressing the oxidation issue, a machining operation was added between each layer to provide a flat surface for the deposition of each new layer. As shown in Figure II.1.2.17(d-f), the interlayer machining operation significantly reduced the lack-of-fusion porosity occurring due to the oxide layer. The final machining yielded a part with no surface porosity or large lack-of-fusion defects and demonstrates the capability of the hybrid process to yield complex geometries with a machined surface finish. Several blocks of deposited material were made for the 4043, 4047, and 5356 alloys, using the interlayer machining approach to minimize porosity in the printed parts. Sub-scale tensile specimens (SS-J3 type) were cut from the deposited blocks to measure the YS of the deposited material. Several single-pass deposits were also made for each material so properties could be compared between single-layer and multilayer deposits. Because the single-pass deposits were not large enough to extract tensile specimens, the hardness-YS relationship from Tiryakioğlu et al. [16], $\sigma_y = 3 \times HV - 80$, was used to back-calculate tensile properties from the hardness of the single-pass deposits. Conversely, the same relationship was applied to determine hardness values for the multi-pass deposits tensile tests for comparison. The resulting material properties are shown in Figure II.1.2.18.

Regarding YS, the 4043 wire is the weakest of the materials. Comparatively, the 4047 and 5356 wires both had reasonably high YS of greater than 100 MPa. Based on the measured properties, 4047 was chosen as the default material to use moving forward in the project. However, the 5356 wire also could be considered for certain applications, because it has a slight tradeoff in strength for an increase in ductility compared to the deposited 4047 wire (14% elongation at failure for the 4047 and 26% elongation at failure for the 5356, as measured from SS-J3 tensile specimens of deposited alloys).

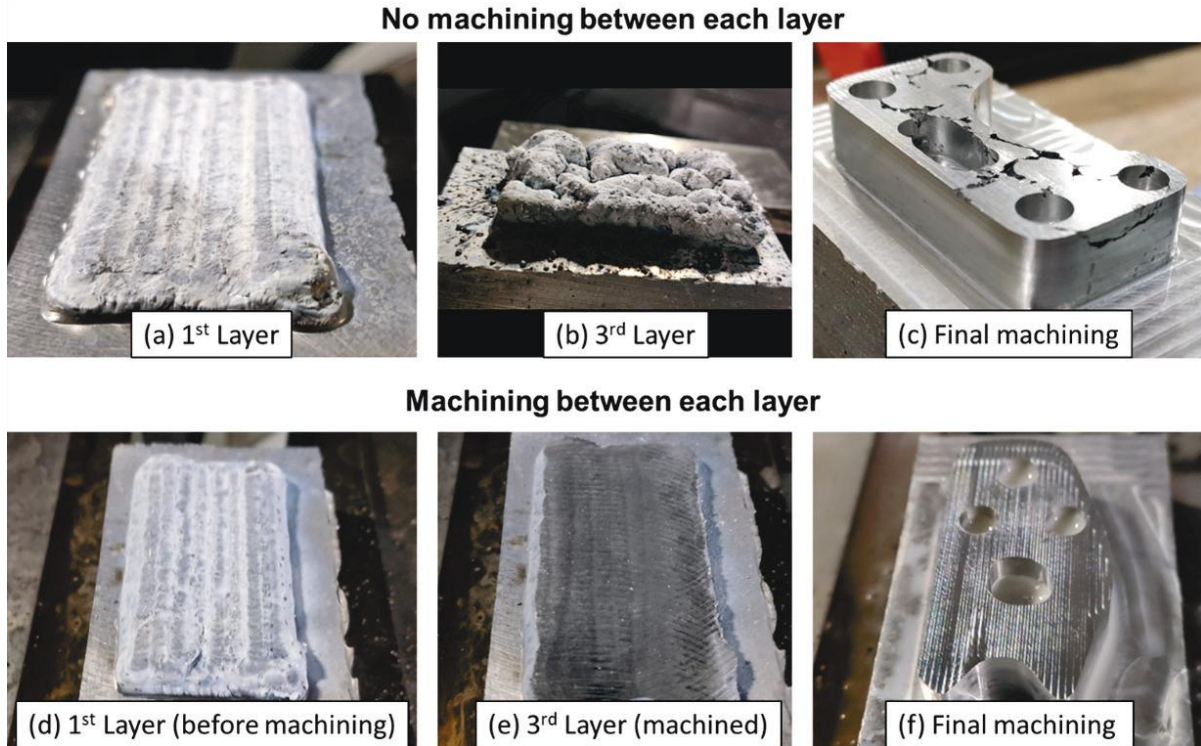


Figure II.1.2.17. Demonstration of deposition of 5356 wire on A356 cast ingot with hybrid manufacturing: (a-c) deposition of multiple layers with only final machining; (e-f) similar deposition of multiple layers with machining between each layer. Part height is 10 mm tall after final machining. Source: ORNL.

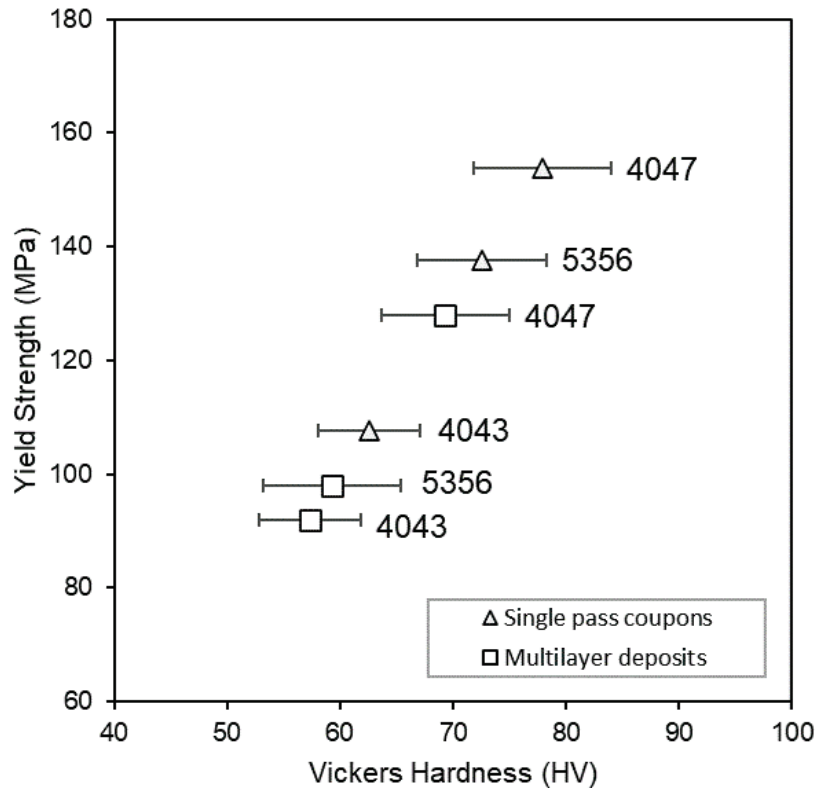


Figure II.1.2.18. Relationship between Vickers hardness and YS for the deposited materials. Source: ORNL.

With a better understanding of the mechanical properties of the materials of interest, potential applications of the Cast-and-Print to assist in joining of vehicle parts were assessed. After discussions with industry collaborators, it was determined that an interesting application of the Cast-and-Print technology would be to add rivet ‘tabs’ to HPDC plates of Aural-5. Due to the relatively high strength of the HPDC plates compared to cast Al alloys, self-piercing rivets are not a practical method of joining thicker sections. Because it was demonstrated that the interface between the deposited material and the substrate was strong [17], deposited tabs of material easier to rivet were hypothesized to facilitate riveting as a joining method for larger, thicker section (2–5 mm) Aural-5 castings where it would otherwise be impractical.

Once representative HPDC Aural-5 sheets were received from the industrial partner, process parameter development for successful deposition of Al4047 material on the new substrate material was conducted. Until this point, the cast substrate was always a larger block at least 25-mm-thick, so new process parameters had to be determined for deposition on the 2-mm-thick Aural-5 sheets to avoid melting through the sheet. This ultimately resulted in the successful deposition of a rivet tab, as shown in Figure II.1.2.19. Though a single bead of deposit is several millimeters wide, the ability of the hybrid process to use machining allowed for a thin, 2-mm tab to be machined. Further characterization of the tab and additional testing will be done in FY 2023, including characterization of the porosity in the tab via microscopy.

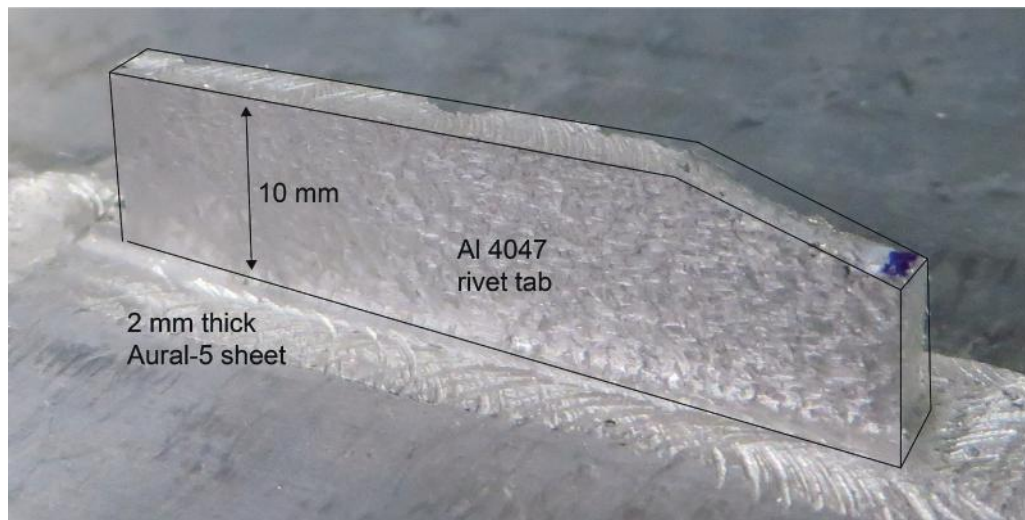


Figure II.1.2.19. Annotated photograph of the laser hot-wire deposited and machined 4047 rivet tab on HPDC Aural-5 plate. Source: ORNL.

Conclusions

Project 2A1: FSP of Diecast Al Alloys

During FY 2021, FSP was evaluated as a TMP technique to locally induce microstructural changes in a thin-wall HPDC A380 alloy. Two to ten times higher fatigue life and increased yield and elongation performance was demonstrated after FSP. This performance increase in some cases exceeded the performance of even the die-wall (skin) region known to have improved microstructures in HPDC materials.

During FY 2022, FSP was carried out on HPDC Aural-5 alloy in flat plate geometry. Aural-5 is a premium quality HPDC Al alloy, and it was fabricated by the high vacuum die-casting method. As a result, the porosity content was measured to be minimal. Additionally, since this alloy was Sr-modified, it shows a highly refined eutectic Si particle size and distribution. Reduction in Fe content, and use of higher Mn led to exclusion of detrimental β -AlFeSi phase that lowers tensile properties in an HPDC Al alloy. Therefore, a good combination of alloy chemistry—together with casting process improvement—led to a diecast alloy that shows improved tensile properties. Despite this high-performance starting point, when FSP is applied to Aural-5 plate, further

improvement in tensile properties was observed. The most noted improvement occurred in tensile ductility and increased yield after FSP was applied to Aural-5 alloys. Microstructural examination of the FSP condition reveals refinement and homogeneous distribution Mg_2Si phase, which could be one of the major reasons behind enhanced tensile ductility. With increased YS and tensile ductility, higher toughness is also noted because of FSP. A tear toughness test conducted on both diecast and FSP'd Aural-5 alloy, indicates > 40% higher energy required to fracture FSP'd plates. This has significant implication for energy absorption in crash conditions and may be important when using cast materials in parts of the BIW expected to undergo high-energy events.

High-cycle fatigue behavior of FSP'd Aural-5, however, shows limited improvement after FSP, potentially due to the excellent microstructure near-surface in Aural 5 HPDC castings. Further analysis and modeling are underway through a recently selected Thrust 4, "Advanced Characterization" project. This project will develop models of as-cast and thermomechanically modified materials and the effects on fatigue behavior of FSP microstructures.

Project 2A2: PUSP of Diecast Al Alloys

The following accomplishments have been made in FY 2022:

- Achieved the targeted PUSP process load of 250~300 lbs. This is essential for future single-side localized processing of cast Al component surfaces with a robotic system and some thin-wall die-cast components.
- Demonstrated significant near-surface microstructure refinement by PUSP at low loads.
- Identified the process conditions by process simulations for compressive surface residual stress and microstructure refinements.
- Demonstrated over 2× fatigue life improvement by PUSP on diecast A380 Al alloy.

Project 2B: High-Intensity Thermomechanical Processes

Ultrasonic and Joule-heating based high-intensity processing techniques are being developed to enhance the mechanical performance of Al castings. *Ex-situ* and *in-situ* local ultrasonication experiments, supported by numerical simulations, were performed on A356 Al alloys and their microstructures and mechanical properties were characterized. HPDC A380 Al was subject to local heat-treatment using Joule-heating and its mechanical properties characterized. The following conclusions were reached:

- The application of ultrasound reduced the aspect ratio of the brittle $\beta-Al_5FeSi$ phase from 14 to approximately six and changed the morphology from needle-like to rectangular plate-like.
- For tensile specimens with less than 1% porosity, the globular microstructure of the ultrasonicated casting had 10% greater UTS and 200% greater elongation at rupture than the dendritic microstructure of the control casting.
- Further development of the ultrasonic-assisted casting process could increase the amount of Fe tolerated in cast Al alloys used in automotive applications and enable cheaper, recycled alloys to be used.
- Local solution heat-treatment of HPDC A380 Al alloy for as short as 2 mins., followed by age hardening, increased the local strength by ~13%, relative to the as-cast state.
- Higher solution temperatures and times lead to blistering that counteracts against age hardening.
- With higher quality casting (i.e., lower entrapped gas porosity, such as in vacuum die-casting), the weakening effect of blistering is expected to be reduced and it may be possible to obtain even higher local strengthening with short heat-treatment time.

Project 2C: Cast-and-Print: AM for Localized Property Enhancement of Al Castings

The work done during FY 2022 on this task showed the chosen approach to the Cast-and-Print process can create a variety of features and materials on multiple form factors of cast substrates. Further understanding of the properties of the 4043, 4047, and 5356 deposits via laser hot-wire methods were determined and several demonstrations of the utility of the hybrid manufacturing process were shown. Both the 4047 and 5356 wires produced deposits with greater than 100 MPa YS. By applying this process knowledge, the Cast-and-Print process was used to successfully print the rivet tabs, which provides a platform for further analysis of the rivet tab performance in FY 2023.

Key Publications**Project 2A1**

1. Balusu, K., K. S. Choi, H. Das, A. Samanta, P. Upadhyay, S. Jana, and A. Soulam, 2022, "On the utility of the thermo-pseudo-mechanical model's residual stress prediction capability for the development of friction stir processing," *Int. J. Adv. Manuf. Technol.*, preprint. 25 October 2022. <https://doi.org/10.21203/rs.3.rs-2176313/v1>.
2. Jana, S., A. Samanta, H. Das, and G. J. Grant, G.J., 2022, "Friction stir processing: A thermomechanical processing tool to locally improve tensile and fatigue properties," *2022 Die-Casting Congress & Tabletop*, 13–15 September 2022, Lexington, Kentucky, USA.
3. Samanta, A., R. J. Seffens, H. Das, A. D. Guzman, T. J. Roosendaal, D. Garcia, M. Song, G. J. Grant, and S. Jana, 2022, "Microstructure-refinement-driven enhanced tensile properties of high-pressure diecast A380 alloy through friction stir processing," *J. Manuf. Process.*, Vol. 78, pp. 352–362. <https://doi.org/10.1016/j.jmapro.2022.04.027>.
4. Samanta, A., H. Das, G. J. Grant, and S. Jana, 2022, "Effect of tool design and pass strategy on defect elimination and uniform, enhanced tensile properties of friction stir processed high-pressure diecast A380 alloy," *Mater. Sci. Eng. A*, Vol. 861, Art. 144388. <https://doi.org/10.1016/j.msea.2022.144388>.
5. Samanta, A., H. Das, D. Garcia, R. J. Seffens, T. J. Roosendaal, A. Guzman, G. J. Grant, and S. Jana, 2022, "Microstructural modification of a high-pressure diecast A380 alloy through friction stir processing and its effect on mechanical properties," In: *Light Metals 2022*, TMS 2022 Annual Meeting & Exhibition, 27 February–3 March 2022, Anaheim, CA, USA. pp. 766–771. https://doi.org/10.1007/978-3-030-92529-1_101.
6. Samanta, A., H. Das, G. J. Grant, and S. Jana, 2022, "Friction stir processing-based local microstructure modification to improve high-cycle fatigue properties of high-pressure diecast aluminum alloy," *Materials Science and Technology (MS&T22) Technical Meeting and Exhibition*, 9–12 October 2022, Pittsburgh, PA, USA.
7. Samanta, A., H. Das, G. J. Grant, and S. Jana, 2023, "Enhanced tensile and tear toughness properties of thin-wall vacuum-assisted high-pressure diecast aural-5 alloy by friction stir processing," *TMS 2023 Annual Meeting & Exhibition*, 19–23 March 2023, San Diego, CA, USA.

Project 2A2

1. Jana, S., and Z. Feng, 2022, "LMCP P2A – Solid-Phase Processing of Aluminum Castings," *DOE-EERE VTO 2022 Annual Merit Review Meeting*, 21–23 June 2022, Washington D.C, USA.

Project 2B

1. Rader, K. E., et al., 2023. "Improving the mechanical properties of cast aluminum via ultrasonication-induced microstructural refinement," *Light Metals 2023*. Accepted for publication.

Project 2C

1. Kannan, R., G. L. Knapp, P. Nandwana, R. Dehoff, A. Plotkowski, B. Stump, Y. Yang, and V. Paquit, 2022, "Data mining and visualization of high-dimensional ICME data for additive manufacturing," *Integr. Mater. Manuf. Innov.*, Vol. 11, No. 1, pp. 57–70. <https://doi.org/10.1007/s40192-021-00243-2>.

2. Knapp, G. L., M. Gussev, A. Shyam, T. Feldhausen, and A. Plotkowski, 2022, “Microstructure, deformation, and fracture mechanisms in Al-4043 alloy produced by laser hot-wire additive manufacturing,” *Addit. Manuf.*, Vol. 59, Part A, Art. 103150.
<https://doi.org/10.1016/j.addma.2022.103150>.

References

1. Sigworth, G. K., and R. J. Donahue, 2021, “The metallurgy of aluminum alloys for structural high-pressure die-castings,” *Int. J. Met.*, Vol. 15, pp. 1031–1046. <https://doi.org/10.1007/s40962-020-00535-x>.
2. Hartlieb, M., 2013, “Aluminum alloys for structural die-casting,” *Diecast. Eng.*, Vol. 57, No. 3, pp. 40–43. Available at: https://www.mercalloy.com/site_media/pdfs/NADCA_-_Aluminum_Alloys_for_Structural_Die_Casting.pdf. (Last accessed 6 February 2023).
3. Zaluzec, M., D. Wagner, T. W. Skrzek, and J. Conklin, 2015, “MMLV: Project overview,” SAE Technical Paper 2015-01-0407, *SAE 2015 World Congress & Exhibition*, SAE International, Warrendale, PA, USA. <https://doi.org/10.4271/2015-01-0407>.
4. Betrancourt, S., X. Chen, J. Wallace, C. Flanigan, D. A. Wagner, V. Kiridena, J. L. Conklin, R. M. Carpenter, and J. Logsdon, 2015, “MMLV: Chassis design and component testing,” SAE Technical Paper 2015-01-1237, *SAE 2015 World Congress & Exhibition*, SAE International, Warrendale, PA, USA. <https://doi.org/10.4271/2015-01-1237>.
5. Nakata, K., Y. G. Kim, H. Fujii, T. Tsumura, and T. Komazaki, 2006, “Improvement of mechanical properties of aluminum die-casting alloy by multi-pass friction stir processing,” *Mater. Sci. Eng. A*, Vol. 437, No. 2, pp. 274–280. <https://doi.org/10.1016/j.msea.2006.07.150>.
6. Jana, S., R. S. Mishra, J. B. Baumann, and G. Grant, 2009, “Effect of stress ratio on the fatigue behavior of a friction stir processed cast Al-Si-Mg alloy,” *Scr. Mater.*, Vol. 61, No. 2, pp. 992–995. <https://doi.org/10.1016/j.scriptamat.2009.08.011>.
7. Huang, H., J. Chen, Y. C. Lim, Z. L. Feng, X. H. Hu, J. H. Cheng, and X. Sun, 2019, “Heat generation and deformation in ultrasonic welding of magnesium alloy AZ31,” *J. Mater. Process. Tech.*, Vol. 272, pp. 125–136. <https://doi.org/10.1016/j.jmatprotec.2019.05.016>.
8. Wang, F., D. Eskin, J. Mi, C. Wang, B. Koe, A. King, C. Reinhard, and T. Connolley, 2017, “A synchrotron X-radiography study of the fragmentation and refinement of primary intermetallic particles in an Al-35 Cu alloy induced by ultrasonic melt processing,” *Acta Mater.*, Vol. 141, pp. 142–153. <https://doi.org/10.1016/j.actamat.2017.09.010>.
9. Zhang, Z., Wang, C., Koe, B., Schleputz, C. M., Irvine, S., and Mi, J. 2021. “Synchrotron X-ray imaging and ultrafast tomography in situ study of the fragmentation and growth dynamics of dendritic microstructures in solidification under ultrasound,” *Acta Mater.*, Vol. 209, Art. 116796. <https://doi.org/10.1016/j.actamat.2021.116796>.
10. Khalifa, W., Tsunekawa, Y., and Okumiya, M. 2008. “Effect of ultrasonic melt treatment on microstructure of A356 aluminum cast alloys,” *Int. J. Cast Met. Res.*, Vol. 21, No. 1–4, pp. 129–134. <https://doi.org/10.1179/136404608X361819>.
11. Puga, H., J. Barbosa, S. Costa, S. Ribeiro, A. M. P. Pinto, and M. Prokic, 2013, “Influence of indirect ultrasonic vibration on the microstructure and mechanical behavior of Al-Si-Cu alloy,” *Mater. Sci. Eng. A*, Vol. 560, pp. 589–595. <https://doi.org/10.1016/j.msea.2012.09.106>.
12. Eskin, G. I., 2001, “Broad prospects for commercial application of the ultrasonic (cavitation) melt treatment of light alloys,” *Ultrason. Sonochem.*, Vol. 8, pp. 319–325. [https://doi.org/10.1016/S1350-4177\(00\)00074-2](https://doi.org/10.1016/S1350-4177(00)00074-2).

13. Kannan, R., G. L. Knapp, P. Nandwana, R. Dehoff, A. Plotkowski, B. Stump, Y. Yang, and V. Paquit, 2022, “Data mining and visualization of high-dimensional ICME data for additive manufacturing,” *Integr. Mater. Manuf. Innov.*, Vol. 11, pp. 57–70. <https://doi.org/10.1007/s40192-021-00243-2>.
14. Huang, H., Chen, J., Cheng, J., Lim, Y. C., Hu, X., Feng, Z., & Sun, X. (2020). Surface engineering to enhance heat generation and joint strength in dissimilar materials AZ31 and DP590 ultrasonic welding. *Int. J. Adv. Manuf. Technol.*, Vol. 111, No. 11, pp. 3095–3109. <https://doi.org/10.1007/s00170-020-06341-3>.
15. Grant, G. J., S. Jana, Z. Feng, A. Rohatgi, and A. Plotkowski, 2022, “II.1.8, Light Metals Core Program: Thrust 2 – Selective Processing of Al Castings,” In: Kleinbaum, S., J. L. Gibbs, and H. F. Wu (Eds.), *Materials FY 2021 Annual Progress Report*, VTO, DOE/EE-2615, August 2022, pp. 240–259.
16. Tiryakioğlu, M., J. Campbell, and J. T. Staley, 2003, “On macrohardness testing of Al–7 wt.% Si–Mg alloys: II. An evaluation of models for hardness–yield strength relationships,” *Mater. Sci. Eng. A*, Vol. 361, No. 1–2, pp. 240–248. [https://doi.org/10.1016/S0921-5093\(03\)00514-8](https://doi.org/10.1016/S0921-5093(03)00514-8).
17. Knapp, G. L., M. Gussev, A. Shyam, T. Feldhausen, and A. Plotkowski, 2022, “Microstructure, deformation, and fracture mechanisms in Al-4043 alloy produced by laser hot-wire additive manufacturing,” *Addit. Manuf.*, Vol. 59, Part A, Art. 103150. <https://doi.org/10.1016/j.addma.2022.103150>.

Acknowledgments

Project 2A1

The author gratefully acknowledges the help and technical support from the following individuals during the execution of this project: A. Samanta, R. Seffens, A. Guzman, and T. Roosendaal. Technical discussions with G. Grant, D. Gotthold, D. Herling and Z. Feng are gratefully acknowledged. Finally, the author extends his sincere thanks to the DOE Technology Manager, S. Kleinbaum, for her support of the LMCP Program.

Project 2A2

The author acknowledges contributions from J. Chen, H. Huang, J. Wang, Y. Li, Y. Chae Lim, J. Cheng, X. Hu, and J. Allen of the ORNL project team. The author also acknowledges the support from General Motors and Ford Motor Company in providing the diecast materials and prototype diecast body structure components.

Project 2B

This project, and the LMCP program, is a collaborative effort across several DOE national laboratories. The authors are thankful for technical discussions with A. Sabau, A. Plotkowski, and T. Watkins at ORNL; and D. Singh, J. Thomas, A. Chaung, P. Kenesei, K. Fezzaa, and A. Deriy at ANL. Technical contributions of the PNNL staff supporting this research are gratefully acknowledged. In particular, the authors are grateful to K. Rader and M. Efe for leading the experimental tasks on ultrasonic processing and heat-treatment, respectively. K. Rader was assisted by J. Helgeland and J. Darsell in the ultrasonic process development and casting experiments; K. Balusu and A. Soulami led the thermal modeling effort; X. Ma contributed to the overall project coordination and A. Guzman and N. Canfield assisted with metallography and microscopy. The authors also acknowledge discussions with D. Weiss at ECK Industries and T. Skrzek pertaining to Al casting practice and approaches to implement new processing techniques in industrial applications.

Project 2C

The authors acknowledge the contributions of the ORNL team members for this sub-task: G. Knapp, T. Feldhausen, A. Shyam, D. Brown, M. Paramanathan, S. Graham, and A. Plotkowski.

II.1.3 Thrust 3. Selective Processing of Mg Castings (Tasks 3A1, 3A2, and 3B) (Pacific Northwest National Laboratory and Oak Ridge National Laboratory)

Vineet V. Joshi, Co-Principal Investigator (Project 3A1)

Pacific Northwest National Laboratory
900 Battelle Blvd.
Richland, WA 99354
E-mail: vineet.joshi@pnnl.gov

Mageshwari Komarasamy, Co-Principal Investigator (Project 3A2)

Pacific Northwest National Laboratory
900 Battelle Blvd.
Richland, WA 99354
E-mail: mageshwari.komarasamy@pnnl.gov

Jiheon Jun, Co-Principal Investigator (Project 3B)

Oak Ridge National Laboratory
1 Bethel Valley Rd.
Oak Ridge, TN 37831
E-mail: junj@ornl.gov

Christopher Schooler, DOE Technology Development Manager

U.S. Department of Energy
E-mail: christopher.schooler@ee.doe.gov

Start Date: October 1, 2020 End Date: September 30, 2023
Project Funding (FY 2022): \$1,100,000 DOE share: \$1,100,000 Non-DOE share: \$0

Project Introduction

HPDC is generally used to fabricate cast Mg components. Almost 90% of the Mg cast components are currently manufactured via the HPDC process. The main advantages of the process are that it is fast, economical, and can produce complex components. However, the cast components have about 1.5–4% porosity area fraction in AZ91 and AM60 Mg alloys. The presence of pores negatively affects static, cyclic, and damage-tolerant properties. The current solution is to employ vacuum-assisted HPDC or the super-vacuum die-casting process, which has been shown to reduce porosity. In the current project, local thermomechanical processing will be employed to locally modify the microstructure and properties. Furthermore, corrosion is a major hindrance to widespread Mg usage. More robust corrosion protection approaches for Mg castings will result in increased adoption in vehicle components with corresponding lightweighting benefits. Automotive manufacturers and tier one suppliers will not increase adoption of lightweight Mg alloy castings without more robust corrosion resistance, as well as improved mechanical properties. The development of processes to locally enhance such properties in cast surfaces is a highly challenging fundamental and applied research topic with strong academic, national laboratories, and industry interest. National laboratories have world-class advanced characterization facilities combined with cutting-edge materials and processing science capabilities beyond that available at a given company.

Objectives

This project has two main objectives: (1) the improvement of localized corrosion properties (e.g., Project 3A); and (2) the improvement of localized mechanical properties (e.g., Project 3B), as shown in Figure II.1.3.1.

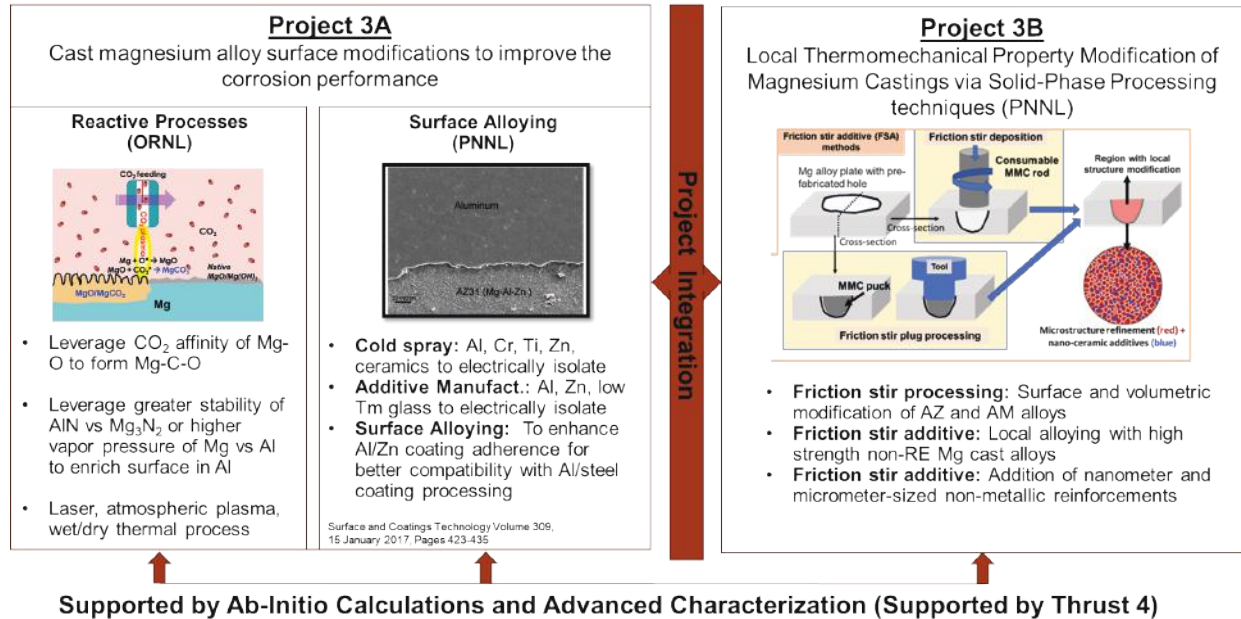


Figure II.1.3.1. Primary thrust areas for Project 3A, “Surface Modification for Improving Corrosion Properties,” and Project 3B, “Improving Local Thermomechanical Treatments for Improving Mechanical Behavior of Mg Alloys.” Source: PNNL.

Projects 3A1 (Reactive Processes – ORNL) and 3A2 (Surface Alloying – PNNL)

The objective is to perform localized surface modification in cast Mg components that will improve their overall corrosion performance. The end-goal of the project is to improve corrosion resistance, eliminate or minimize corrosion-induced fatigue, minimize galvanic coupling for faying surfaces, and if needed, improve surface receptivity for subsequent top coating processes on Mg castings. In this multi-laboratory collaborative effort, we plan to accomplish these goals by employing a multi-faceted approach that relies on replacing the corrosion susceptible MgO-Mg(OH)₂ native film—either directly or indirectly—by modifying the alloy surface composition. To accomplish this, processing strategies and techniques are being developed that are guided by improved fundamental understanding of the underlying mechanisms using *ab-initio* methods, advanced electrochemical potential measurement and microstructural characterization techniques. The effort will focus on HPDC AM60 and AZ91 alloy families and may also consider additional processes or alloys based on automotive manufacturer and tier 1 supplier inputs.

Projects 3B (Thermomechanical Property Modification – PNNL)

The goal is to perform localized enhancement of the mechanical properties, such as ductility and fatigue properties, of HPDC cast Mg components using FSP and friction stir additive methods. The project will develop ways for localized microstructure modification, measure the change in resultant properties, and demonstrate the property modification on either AZ91 or AM60 Mg cast components.

Approach

Project 3A1

In FY 2022, this task investigated three reactive surface-treatment processes. Two are based on an open-air plasma jet, while the remaining one is based on a wet alkali metal salt loading plus subsequent thermal treatments in a carbon dioxide (CO₂) environment. These processes were downselected from an array of processes initially investigated in year one (FY 2021) including (1) an Nd-YAG laser that was not continued in FY 2022; (2) an open-air nitrogen (N₂) plasma, in which two versions were downselected to continue in FY 2022; and (3) a lithium (Li) salt loading plus thermal CO₂ treatment that was downselected to continue in FY 2022. Schematics and photos of the three processes selected for further development in FY 2022 are presented in Figure II.1.3.2. Two versions of an open-air N₂ plasma process, one with and one without a

precursor feeder, were used for plasma-based surface modification and coating processes, respectively. In the direct plasma jet processes, which are shown in Figure II.1.3.2(a), ionized gas molecules (i.e., plasma) physically collide on the Mg alloy surfaces where reactions between the Mg, lab-air, and ionized gas are promoted to form a protective reaction layer. In the plasma coating process, which is shown in Figure II.1.3.2(b), a plasma jet is used in two steps where a modified organosilicon precursor is injected with plasma jet in the second stage to form a Si-O-C coating on the Mg alloy surface. Additionally, the third FY 2022 method, wet preloading of LiNO_3 salt and subsequent CO_2 thermal treatment, which is shown in Figure II.1.3.2(c), was also studied to form a Li-O-C rich Mg compound layer as a corrosion barrier. Advanced multiscale characterization techniques were employed to characterize the surfaces before and after coating/modification. Wear testing was also used to study wear performance of the surface-modified Mg alloys and to compare to the unmodified surface condition.

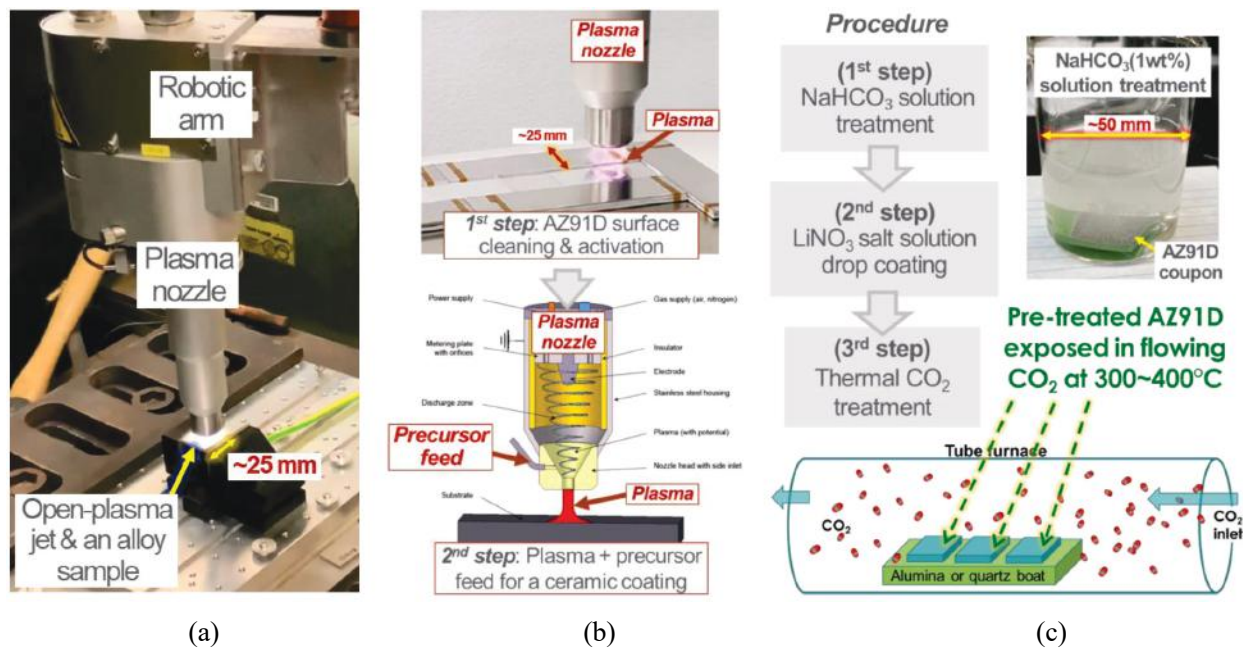


Figure II.1.3.2. Schematics and photos of three reactive surface processes: (a) direct plasma jet treatment, (b) two-step plasma coating, and (c) Li-salt loading + thermal CO_2 treatment. Source: ORNL.

Two common HDPC commercial Mg alloys—AZ91D (Mg-9Al-1Zn-0.5Mn) and AM60 (Mg-6Al-0.5Mn-0.2Zn)—were obtained from a commercial vendor as substrates for surface modification. To assess their corrosion resistance, 3.5 wt.% NaCl solutions open-to-air at RT were used for typical electrochemical and H_2 collection measurements. For electrochemical measurements, including electrochemical impedance spectroscopy (EIS) and polarization, a platinum wire counter and saturated calomel reference electrodes were used. For most impedance spectra, two equivalent circuit models were used to determine R_2 or $R_2 + R_3$ values that are relevant to corrosion resistance in $\text{ohm}\cdot\text{cm}^2$.

Project 3A2

A surface modification technique, namely cold spray, was utilized for surface coating/alloying Mg alloys with Al and Zn, respectively. Commercially procured (CP) Zn and Al6061 are coated on top of cast Mg-alloys using the cold spray method. Successfully doing so will completely change the corrosion characteristics of the alloy. This will also make it more amenable to conventional conversion or plasma electrolytic and epoxy electro-coat techniques, as well as mitigate the challenges associated with joining Mg cast components with Al or steel components. To evaluate corrosion properties of coating Al and Zn with respect to substrate, electrochemical properties were measured of surface-modified cast Mg alloys at the microscopic level, as well as the macroscale. Long-term corrosion tests were also performed using an immersion test method and

corrosion progress was tracked by collecting H₂ gas. Mechanical properties of the coatings were evaluated by performing wear test and adhesion test of the coating. The optimized coating process parameter was finally utilized on a section of an actual AZ91D HDPC cast part.

Project 3B

In FY 2022, coupon level microstructural modification of AZ91 and AM60 alloys, curved plate processing, and local alloying via groove processing and friction surfacing was achieved. For FSP, tool rotational speed and traverse rate were varied to obtain a processing temperature in the range of 400–450°C. Furthermore, single and overlapping processing runs were carried out on both AZ91 and AM60 alloys. The processing runs that exhibited a defect-free surface were subjected to tensile and fatigue property characterization. Fatigue property analysis in a stress-controlled configuration with the fatigue ratio (e.g., ratio of maximum to minimum stress) of R=0.1 was completed in the as-cast and as-processed conditions. Prior to testing, the fatigue samples were analyzed with X-ray micro-CT to measure the porosity fraction in the gauge section. Curved plate processing was implemented using a robotic platform, which required optimizing the processing conditions to obtain a defect-free processed region. Microscopy and mechanical property characterization of the curved region were also performed. Local alloying via groove FSP and friction surfacing was implemented as well. A groove was fabricated in a Mg alloy, press fitted with a calcium (Ca)-added Mg alloy, and subsequently processed via FSP for seamless incorporation. For friction surfacing, a consumable rod was made from a Ca-added Mg alloy in both as-cast and homogenized conditions (e.g., 480°C for 24 hours). Rod rotational speed, traverse rate, and forge force were optimized to obtain a good deposit. Both variants of the locally alloyed material were subjected to microscopic analysis to investigate the quality of the alloyed region.

Results

Project 3A1

Table II.1.3.1 summarizes the corrosion reaction resistance data from EIS data fitting for the direct N₂ plasma-treated and untreated AZ91D. Higher corrosion reaction resistance is associated with slower Mg corrosion in the samples. Corrosion reaction resistance data, R_2 or $R_2 + R_3$, indicate five overlaps of the N₂ plasma treatment produced improved corrosion resistance as compared to the untreated AZ91D (~1.6× of the untreated). It is presumed that the single-pass and three overlap N₂ plasma treatments compared in Table II.1.3.1 resulted in removal of the native oxide layer (i.e., a surface-cleaning effect), so corrosion resistance was reduced as compared to the untreated samples. This suggests effective surface modification of AZ91D by N₂ plasma treatment occurs after removal of the native oxide layer by sufficient overlap of the plasma jet, followed by a more protective and unique plasma-induced oxide that grows as the number of plasma passes increases. Therefore, process optimization of the N₂ plasma surface-treatment should be further investigated to find an optimum condition to achieve the highest corrosion resistance in the least amount of processing time. One advantage of the plasma treatment process is its potential for a rapid pace surface-treatment for large or complex surfaces.

Table II.1.3.1. Corrosion Reaction Resistance Values of Untreated and N₂ Plasma-Treated AZ91D Samples Performed at ORNL

AZ91D Sample	Untreated 600 grit SiC finish	N ₂ plasma, 1 pass (single)	N ₂ plasma, 3 passes (3 overlap)	N ₂ plasma, 5 passes (5 overlap)
Corrosion Reaction Resistance (ohm-cm ²)	~2600 (Avg.)	447	1106	4129

For plasma-assisted Si-O-C layer deposition, an industrial partner (Plasmatreat USA, CA) performed various coating conditions. Two coating processes, designated as P1 and P8 coatings, were downselected based on their initial corrosion performance studies. Figure II.1.3.3 shows a scanning transmission electron microscopy image and its Mg, O, and C EDS maps of a P1-coated AZ91D sample in a cross-sectional perspective where a Si-O-C coating with ~200 nm in thickness is observed to be uniformly deposited on the AZ91D substrate.

Impedance spectra and H₂ collection data are presented in Figure II.1.3.4 for uncoated, P1-coated, and P8-coated AZ91D samples. Compared to uncoated AZ91D, P1- and P8-coated AZ91D samples exhibited much greater impedance values, which implies the coated samples had higher corrosion resistance, as shown in Figure II.1.3.4(a). Moreover, both the P1- and P8-coated AZ91D samples produced lower H₂ compared to uncoated AZ91D, indicating the coated samples had lower corrosion rates. The corrosion reaction resistance values of P1- and P8-coated AZ91D samples, as summarized in Table II.1.3.2, are significantly higher ($> 2 \times 10^4 \text{ ohm}\cdot\text{cm}^2$) than the uncoated AZ91D ($\sim 2600 \text{ ohm}\cdot\text{cm}^2$). From the data, the corrosion reaction resistance of the P1- and P8-coated samples are at least a factor of 9 or greater. These results clearly indicate a plasma-deposited Si-O-C layer offers improved corrosion protection for AZ91D substrates.

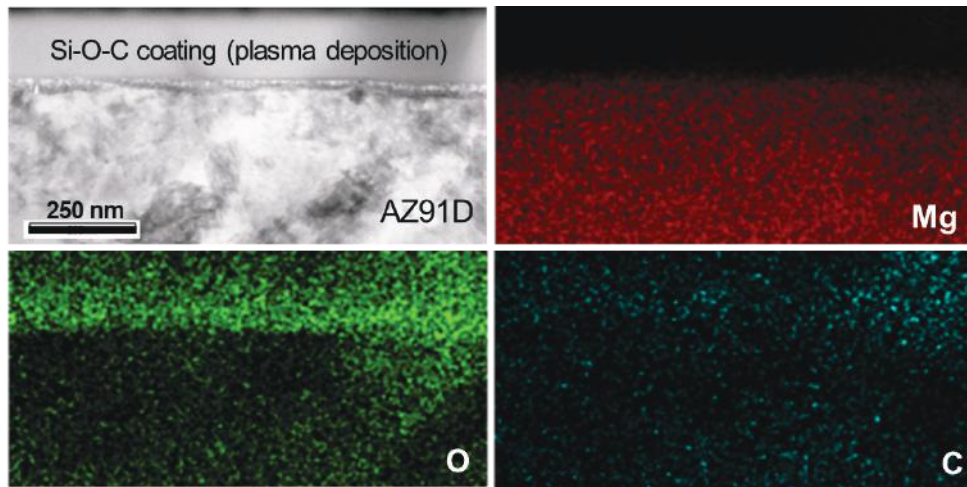


Figure II.1.3.3. Scanning transmission electron microscopy image (upper left) and its Mg, O, and C EDS maps of a P1-coated AZ91D sample in cross-sectional perspective. Source: ORNL.

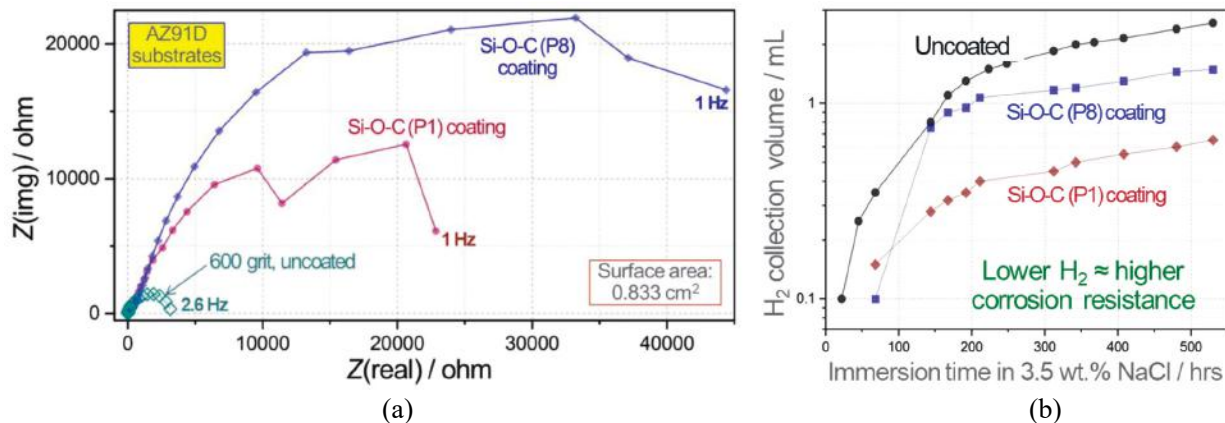


Figure II.1.3.4. Comparison of (a) impedance spectra and (b) H₂ collection volume in uncoated and Si-O-C layer deposited (e.g., P1- and P8-coated) AZ91D samples. The exposed surface area for H₂ collection measurements was 0.833 cm² for all samples. Source: ORNL.

Table II.1.3.2. Corrosion Reaction Resistance Values of Plasma Si-O-C Coatings Deposited on AZ91D Samples Performed at ORNL

AZ91D Samples	Uncoated 600 grit SiC Finish	Si-O-C (P1) Coating	Si-O-C (P8) Coating
Corrosion Reaction Resistance ($\text{ohm}\cdot\text{cm}^2$)	~2600 (Avg.)	~21000 and ~22110 (2 data)	~43260 and ~45900 (2 data)

For wet Li-salt loaded + thermal CO_2 treated AZ91D samples, electrochemical evaluations were performed using EIS and polarization as presented in Figure II.1.3.5. The impedance values of the Li-2.5-2.5 sample (i.e., treated with 2.5% NaHCO_3 and 2.5% LiNO_3 solutions before thermal CO_2 treatment) were much greater than untreated AZ91D, as shown in Figure II.1.3.5(a). In the polarization measurements, the Li-2.5-2.5 sample showed passive-like anodic current (e.g., the near vertical region in the potential vs. current plot) before an increase of anodic current at higher potential, as shown in Figure II.1.3.5(b), indicating that the treated sample would be more resistant to anodic Mg corrosion than the untreated samples. These results strongly suggest the effectiveness of wet Li-salt loading + CO_2 thermal treatment in improving corrosion resistance of AZ91D substrate. A similar treatment was also performed on AM60. As summarized in Table II.1.3.3, the corrosion reaction resistance value of the Li-2.5-1.0 sample (i.e., treated with 2.5% NaHCO_3 and 1% LiNO_3 solutions) is almost 10 \times higher than untreated AM60 samples. Based on this, wet Li-salt loading + CO_2 thermal treatment is also considered as an effective corrosion protection method that should be further studied and developed for the AM60 class of Mg alloys.

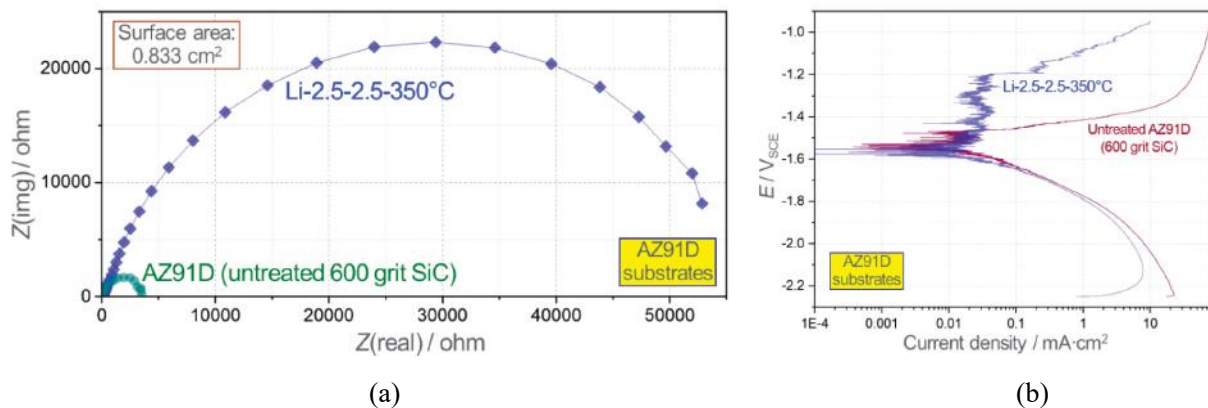


Figure II.1.3.5. Comparison of (a) impedance spectra and (b) polarization curves in untreated and Li-salt loaded + CO_2 thermal treated AZ91D samples. Source: ORNL.

Table II.1.3.3. Corrosion Reaction Resistance Values of Untreated and Li-Salt Loaded + CO_2 Thermal Treated AM60 Samples Performed at ORNL

AM60 Sample	600 grit SiC Finish	Li 2.5-1.0
Corrosion Reaction Resistance ($\text{ohm}\cdot\text{cm}^2$)	~2340 (Avg.)	~22690

For selected wet Li-salt loaded + thermal CO_2 treated AZ91D samples, surface wear volume and rate measurements were performed by PNNL collaborators. The summarized results in Table II.1.3.4 indicate wet Li-salt loading + CO_2 thermal treated AZ91D surfaces had improved wear resistance as compared to the untreated sample, with approximately 20% reduction in wear.

Table II.1.3.4. Wear Volume and Rates of Untreated and Li Salt Loaded + CO₂ Thermal Treated AZ91D Samples. Wear Measurements Performed with A 6 mm Si₃N₄ Ball with 1 N, 200 mm/s and A 5000 Cycle Performed at PNNL

AZ91D Sample	Wear Volume (mm ³)	Wear Rate (mm ³ /N-m)	Change in Wear Rate With Respect to Untreated (%)
600 Grit SiC Finish	~0.161	1.35×10 ⁻³	0% (Baseline)
Li 2.5-1.0	~0.128	1.07×10 ⁻³	-21%
Li 2.5-2.5	~0.126	1.05×10 ⁻³	-22%

Project 3A2

A solid-phase surface modification technique using coatings is being utilized to improve corrosion properties. Cold spray coating trials were performed on AZ91 HDPC cast coupons. Zn coating was performed on top of an AZ91 Mg-substrate with varying deposition parameters, such as gas temperature and pressure, to obtain the desired coating properties. Coating process parameters are given in Table II.1.3.5. Two trials were conducted wherein CP-Zn powders were spray-coated on top of Mg alloy coupons at gas pressures in the range of 2.0 – 6.5 MPa and temperatures in the range of 150 – 400°C. In Trial 1, particles were not sieved, and the average particle size was 6.5 μm. However, in Trial 2, particles were sieved, and the average particle size was 35 μm. In addition, particles were dried at 120°C for 1 hour in Trial 2. Other process parameters, such as spray angle and carrier gas, were kept the same in both trials. In the case of Trial 1, the coating porosity was approximately 1–2%; however, significantly lower porosity was observed in the Trial 2 coatings (less than 1%). Detailed microstructure, corrosion, and mechanical properties of the coatings were characterized in the Trial 2 samples.

Table II.1.3.5. CP-Zn Cold Spray Trials Performed at PNNL

Cold Spray Settings	Trial #1	Trial #2
Powder Size	Average particle size: 6.5 μm (Powders were not sieved)	Average particle size: 35 μm Particle size range: 20–53 μm
Heat-Treatment of Powders	None	Dried at 120 °C for 1 hour
Spray Angle	1 pass at 45-degree spray angle and 10 passes at 90-degree spray angle	1 pass at 45-degree spray angle and 10 passes at 90-degree spray angle
Gas Temperature (°C)	150–400	150–400
Gas Pressure (MPa)	2–6.5	2–6.5
Cold Spray Gas	Nitrogen	Nitrogen
Porosity	~1–2%	<1%

Coating efficiency was estimated by measuring coating thickness and weights of all the deposited samples. Figure II.1.3.6 shows the coating thickness with varying gas temperature and pressure. Coating thickness and weight increases with increasing gas temperature at fixed pressures of 2 MPa and 6.5 MPa are shown in Figure II.1.3.6(a) and Figure II.1.3.6(b), respectively. Furthermore, Figure II.1.3.6(c) shows the variation of coating thickness with varying gas pressure at a fixed temperature of 400°C. Data indicates maximum coating efficiency is obtained between gas pressures of 3–4.5 MPa.

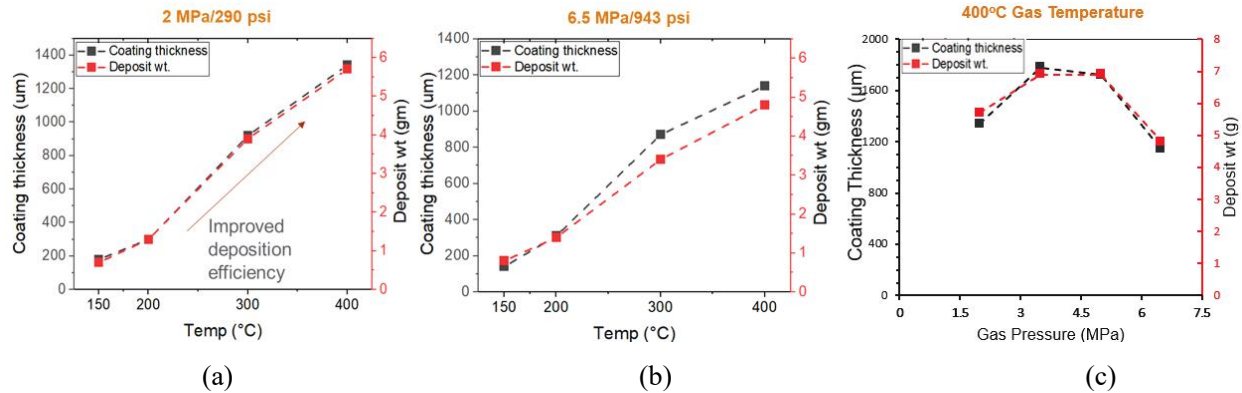


Figure II.1.3.6. (a) Variation of deposited coating thickness and deposit weight with gas temperature at gas pressure of 2 MPa. (b) Variation of deposited coating thickness and deposit weight with gas temperature at gas pressure of 6.5 MPa. (c) Variation of deposited coating thickness and deposit weight with gas pressure at gas temperature of 400 °C. Source: PNNL.

Corrosion performance was evaluated on an AZ91 substrate and an AZ91 substrate coated with Zn. Square shaped samples (both substrate and coating) with 15 mm × 15 mm (2.25 cm²) dimensions were polished with up to 1200 grit paper before immersion tests. Corrosion tests were performed using an immersion test method and corrosion progress was tracked by collecting H₂ gas. NaCl solution with 0.6 wt.% was used as the corrosion medium. Figure II.1.3.7(a) and Figure II.1.3.7(b), respectively, show the sample surfaces before and after the tests, as well as the hydrogen collection setup. H₂ gas was collected up to 338 h immersion time. After 338 h of immersion in NaCl solution, the AZ91 substrate appears to be severely corroded; however, the Zn-coated surface shows negligible corrosion. Figure II.1.3.7(c) shows the immersion time vs. the total volume of H₂ gas collected. A very high-volume of H₂ gas collected in the bare AZ91 substrate as compared with the treated (coated with Zn) substrate. From the H₂ collection data, it can be concluded that a 4500% reduction of H₂ gas evolution in the Zn-coated sample is observed compared with the bare substrate, which indicates significant improvement of corrosion properties in treated substrates.

Wear tests were performed on an AZ91 substrate and a Zn coating on top of an AZ91 substrate. Wear volume and wear rate of substrate and coating are calculated and shown in Figure II.1.3.8(a). Figure II.1.3.8(b) shows the surface height profile of post wear test samples. Relatively higher wear volume and wear rate is observed in the substrate material. The data shows greater than 50% improvement in wear resistance in the Zn-coated AZ91 substrates as compared with the uncoated AZ91 substrate material.

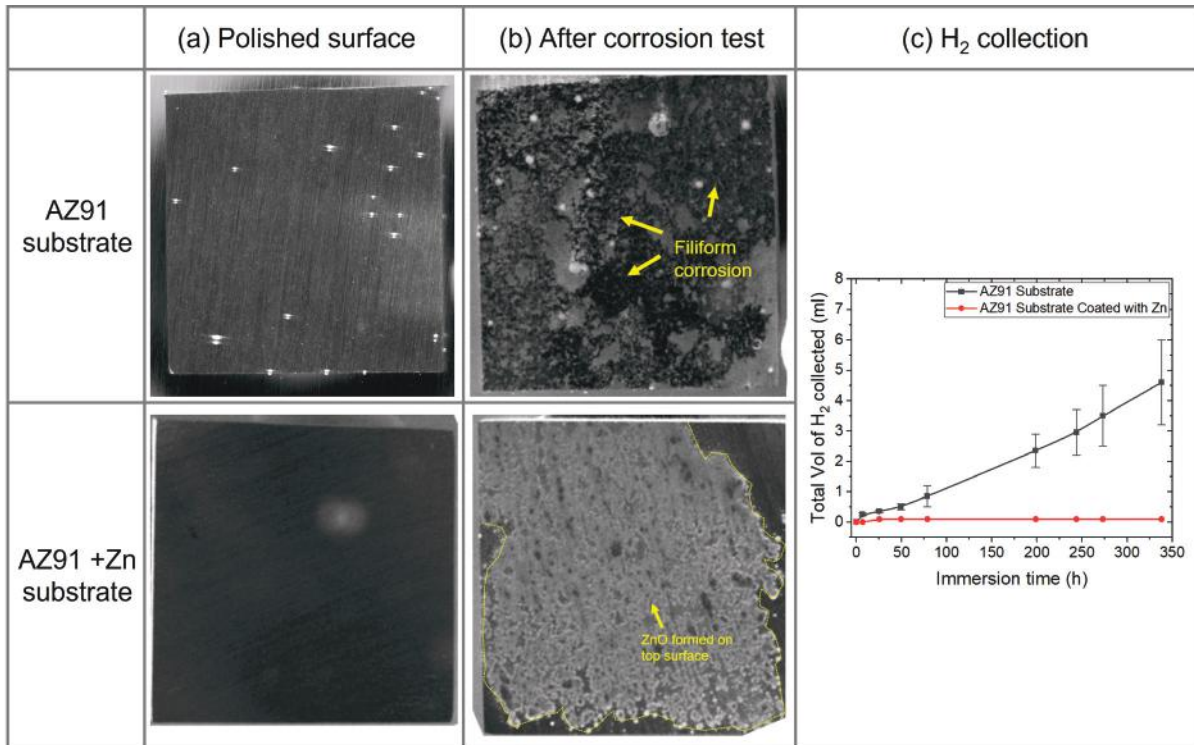


Figure II.1.3.7. (a) Polished bare AZ91 and Zn-coated surfaces before the corrosion test and (b) the surfaces after the corrosion test. (c) Total volume of H₂ collected over 350 hours. Source: PNNL.

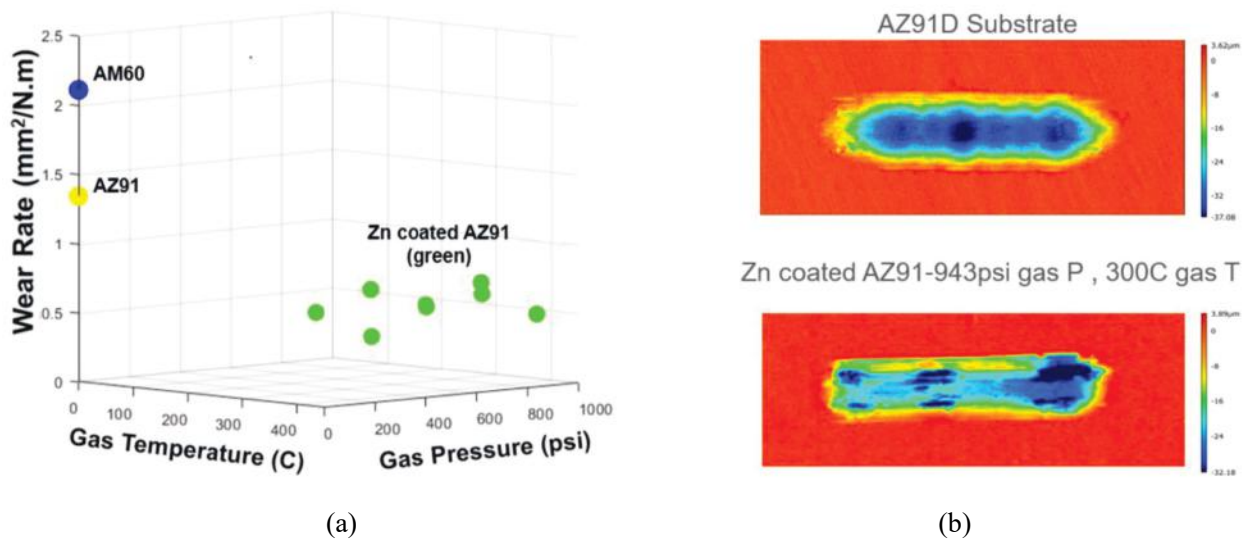


Figure II.1.3.8. (a) Wear test data of bare AM60 and AZ91 substrate and Zn coating. (b) Post-wear-tested surface profile of AZ91 substrate and Zn-coated AZ91. Source: PNNL.

A bond strength evaluation was performed on the Zn-coated samples. Gas temperature and pressure were varied in the range of 150–400°C and 1.5–6.5 MPa, respectively. A substrate with a 1 in. × 1 in. area was coated for the bond strength evaluation. Bond strength of the Zn coatings was evaluated by following the ASTM D4541 testing method. Table II.1.3.6 shows the bond strength values of Zn-coated samples. The measured average bond strength for coating deposited at 150°C, 200°C, 300°C, and 400°C gas temperature, respectively, is 29.9, 30.8, 30.4, and 32.0 MPa, respectively.

Table II.1.3.6. Adhesion Test Data Following the ASTM D4541 Standard Performed at PNNL

Sample Nos.	Gas Temperature (°C)	Gas Pressure (MPa)	Bond Strength (MPa)	Average Bond Strength (MPa)	Standard Dev. (MPa)
1	150°C	2.0	34.57	28.9	5.0
2		3.5	24.91		
3		5.0	27.38		
4	200°C	2.0	33.18	30.8	3.8
5		3.5	33.15		
6		5.0	31.57		
7		6.5	25.22		
8	300°C	3.5	26.27	30.4	3.4
9		3.5	32.26		
10		5.0	33.90		
11		6.5	29.16		
12	400°C	2.0	29.16	32.0	2.5
13		3.5	34.54		
14		5.0	33.49		
15		6.5	30.78		

Cold spray was performed on an AM60 automotive component, where sub-parts of the component were used for Zn coating. Surfaces were polished with a 600 grit finish before performing cold spray coating. Figure II.1.3.9(a) shows the larger component, while the yellow highlighted section (e.g., sub-component) shows what was used for coating. The sub-component, sectioned in three regions—namely A, B, and C—is shown in Figure II.1.3.9(b). Coatings were performed at a gas temperature of 400°C and a pressure of 3.5 MPa with a nozzle distance of 25 mm. The first pass was deposited at a 45° nozzle spray angle. Following this, the next 10 passes were deposited at a 90° nozzle spray angle. Figure II.1.3.9(c) and Figure II.1.3.9(d), respectively, show the curved surfaces both before and after coating. Very uniform coating thickness was achieved in all three sub-components with unique surface curvatures and without any defects. Figure II.1.3.9(e) shows the cross-section of sub-component B with a uniform coating and an average thickness of 1.2 mm.

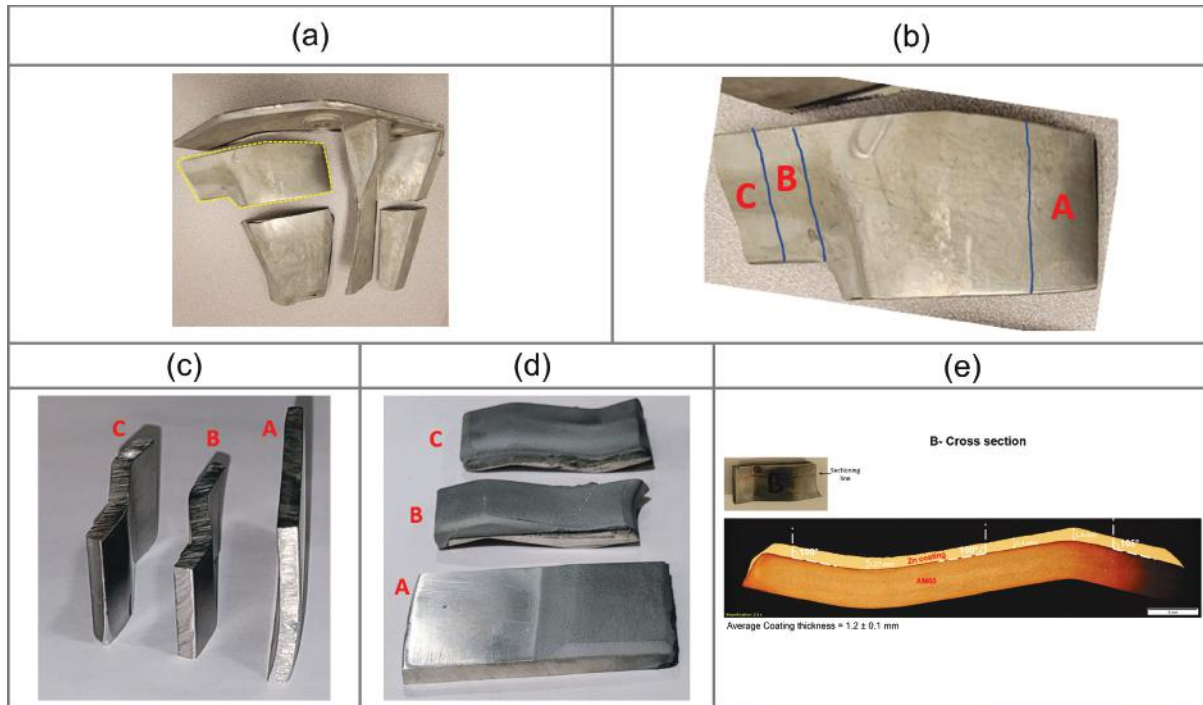


Figure II.1.3.9. (a) AM60 automotive part and (b) the selected regions from the part (highlighted by the yellow dotted line in (a) used for cold spray. Cold spray was performed on three different sub-components with different curved surfaces, marked as A, B, and C. Images of the curved Mg alloy sub-components (c) before cold spray and (d) after cold spray. (e) Cross-section image of sub-component B. Source: PNNL.

Project 3B

The key results presented in this FY 2022 report are from local property modification using FSP and local alloying using friction stir alloying/deposition methodologies. FSP of both flat and curved coupons were fabricated and the results are presented. Furthermore, initial results from local alloying of Ca-added Mg alloy onto a Mg plate via groove processing and friction surfacing are also presented. The summary of fatigue testing results for both AZ91 and AM60 alloys in as-cast and FSP conditions is presented in Figure II.1.3.10. In the HPDC condition, fatigue lives with and without the skin, which is a surface layer with a fine microstructure, were similar. The inset in Figure II.1.3.10(a) shows backscattered electron imaging of the skin. In both alloys, the FSP condition outperformed the HPDC material, as shown in Figure II.1.3.10(a) and Figure II.1.3.10(c), respectively. This is due to porosity elimination and coarse intermetallic refinement during FSP. The average porosity of the HPDC material was ~1.4% and ~2.5% for the AZ91 and AM60, respectively. As shown in the micro-CT analysis in Figure II.1.3.10(b) and Figure II.1.3.10(d), respectively, the FSP material had significantly reduced porosity in the range of 0.6%–0.001%, depending on the processing conditions. The extent of defect elimination possible via FSP is significant. This study further adds to the available literature where cast material with low porosity fraction showed improvement in fatigue properties.

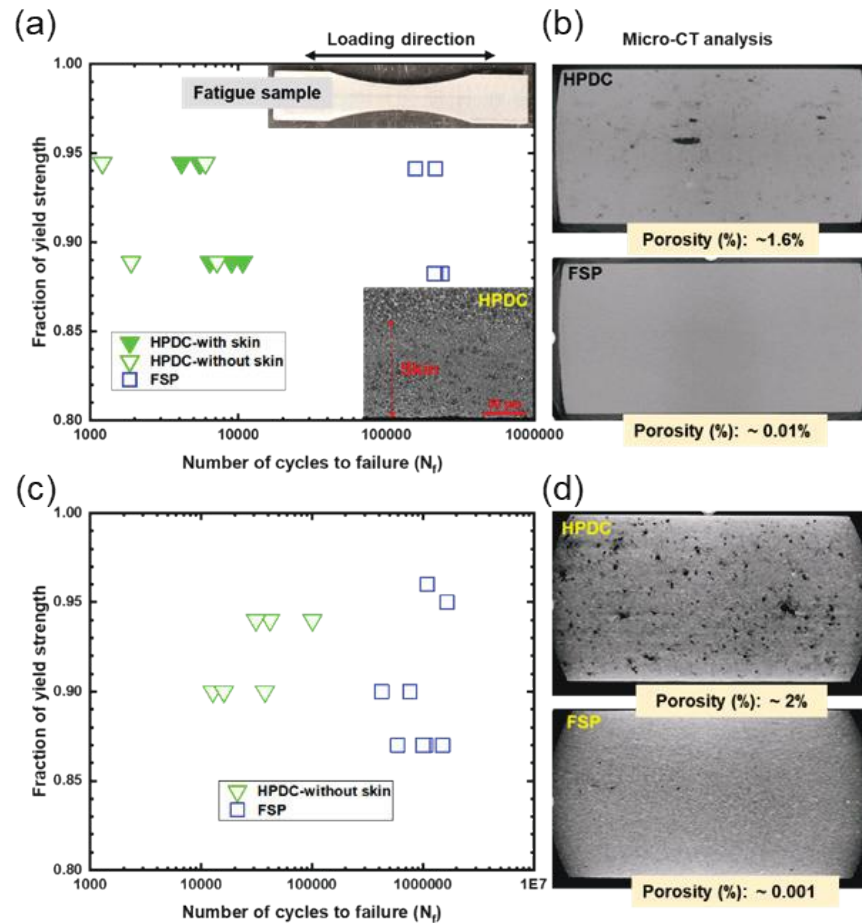


Figure II.1.3.10. Fatigue results for (a) AZ91 and (c) AM60 in as-cast and FSP conditions along with micro-CT results (b and d). Source: PNNL.

Figure II.1.3.11 summarizes fatigue-failure lives as a function of the porosity fraction. Remnant porosity- and microstructure-controlled failure in both alloys occurred above and below 0.01% porosity, respectively. Furthermore, most of the FSP samples that had <0.01% porosity did not fail even after 2×10^6 fatigue cycles. This provides an understanding of the extent of defect reduction needed to have improved fatigue lives. Note these samples were run at different stress levels and the distinction is made based on fractographic analysis.

As a pathway to demonstrate local property modification at the component level, FSP of curved sections was performed. A summary of the key results is presented in Figure II.1.3.12. A picture of the plate with a 15° curvature and a picture of the plate after FSP are shown in Figure II.1.3.12(a) and Figure II.1.3.12(b), respectively. The contrast is due mainly to the curvature, as shown in the inset in Figure II.1.3.12(b) and did not have any surface processing flaws. A defect-free cross-section with an average porosity of 0.07% in the processed region was observed, as shown in Figure II.1.3.12(c). In addition to obtaining a defect-free processed region, mechanical property investigations were conducted to understand the local strength of the curved region in comparison to the flat region. As shown in Figure II.1.3.12(d), a uniform hardness across the curved processed region was noted. A higher hardness towards the bottom of the analyzed region is due to the thermomechanically affected zone, which extended from the flat to the curved region. The curved plate processing was conducted on a robotic FSP platform, which required a complete parametric study to obtain defect-free processing with improved performance. This is not covered in this report for brevity.

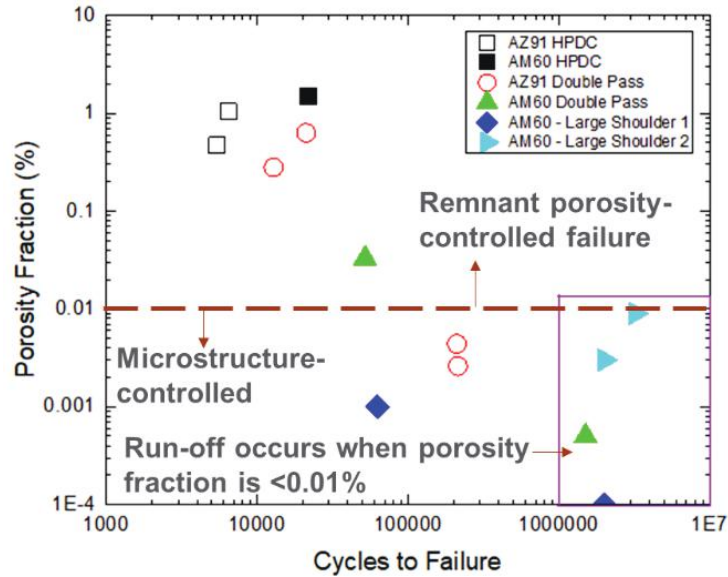


Figure II.1.3.11. Fatigue-failure as a function of porosity fraction for Mg alloys in various conditions. Source: PNNL.

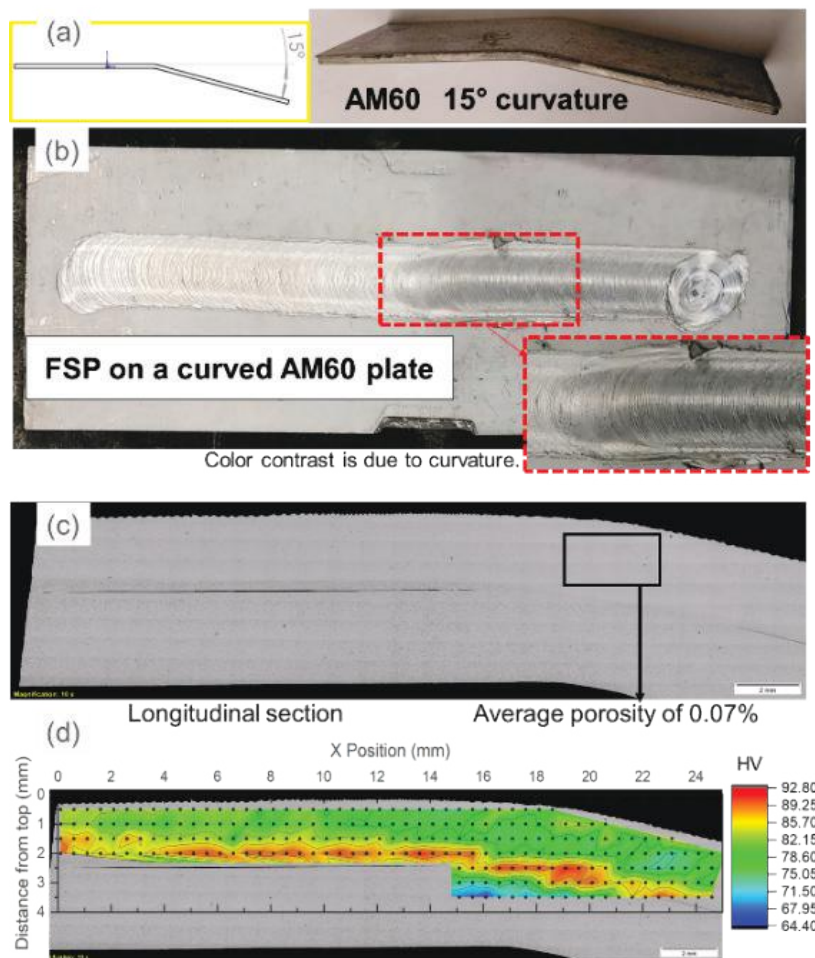


Figure II.1.3.12. Pictures of the (a) curved plates, (b) processed plates, (c) defect-free longitudinal section, and (d) uniform hardness from the flat to the curved regions. Source: PNNL.

Strength improvement due to microstructural refinement can only be to a certain extent. If a location regularly undergoes higher stress, it may need to have further reinforcements. The proposed solution is to locally alloy the region with higher strength Mg alloys via solid-phase techniques. An exhaustive literature search for non-RE added Mg alloys that exhibited higher strength than AM60 was carried out and the summary of the results are presented in Figure II.1.3.13(a). Thermomechanically processed Ca-added Mg alloys outperformed many other alloys with YS reaching above 300 MPa while exhibiting more than 5% elongation. Furthermore, strength as a function of Ca addition was documented to downselect the compositions for local alloying, as shown in Figure II.1.3.13(b). The compositions selected for this work are AM60 with 3 wt.% Ca and AM60 with 4 wt.% Ca to maximize strength without reducing elongation due to the presence of coarse Ca-based intermetallic phases.

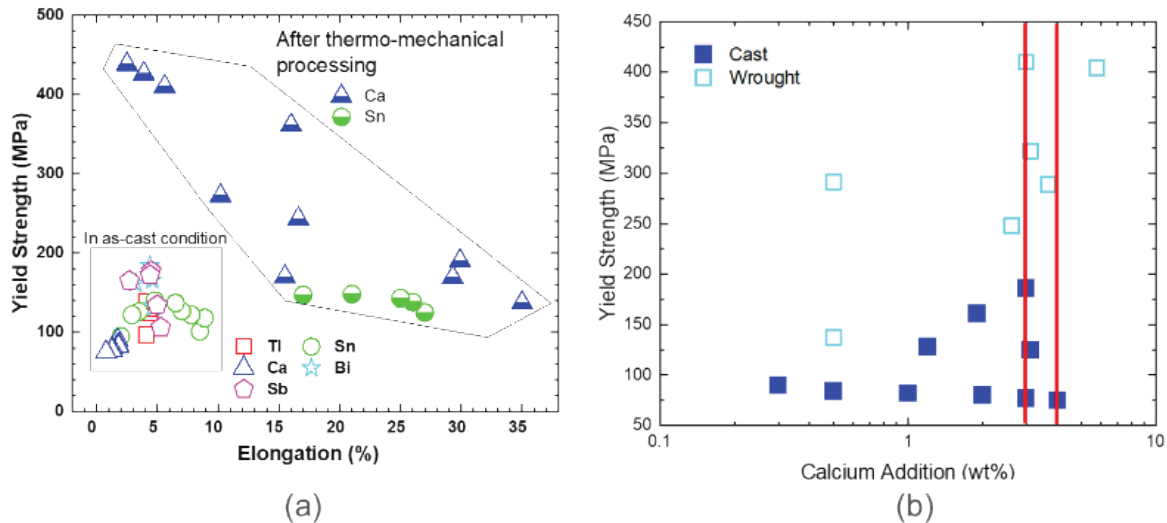


Figure II.1.3.13. (a) YS vs. elongation for various non-RE Mg alloys. (b) YS as a function of Ca content in wt.%. Source: PNNL.

As stated above, local alloying was carried out via groove FSP, as shown in Figure II.1.3.14(a), and friction surface deposition, as shown in Figure II.1.3.14(b). A gradual alternating raster process was employed, which is shown in Figure II.1.3.14(c), while the result of the processed cross-section is given in Figure II.1.3.14(d). The processed region was defect-free and a gradual transition from AM60 to Ca-added Mg alloy was noted. A tensile property summary in the as-cast and FSP is shown for both AM60 and the Ca-added Mg alloy in Figure II.1.3.14(e). A general observation is that the FSP has significantly improved the elongation. The Ca-added Mg alloy failed in the elastic region ($\sim 2\%$ strain) in the as-cast condition but exhibited plastic deformation in the processed condition. Furthermore, the YS of processed Ca-added Mg alloy is more than twice that of the AM60 alloy. Another point to note is that the YS of the gradual alloying was in between the processed AM60 and the Ca-added AM60, which indicates the proposition of locally increasing the strength is working; however, fine-tuning the extent of dilution will have to be controlled to further increase the strength.

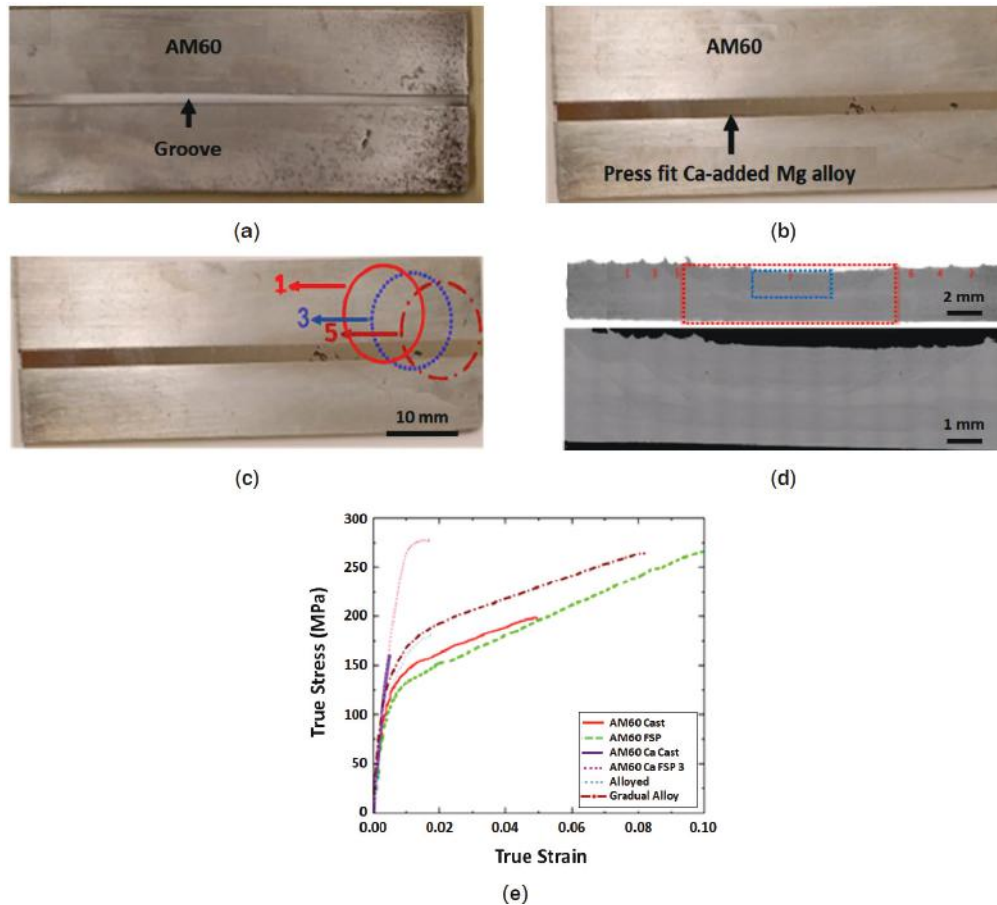


Figure II.1.3.14. Pictures of (a) the groove in AM60, (b) the press fitted Ca-added Mg alloy in the groove, (c) the processing strategy that was implemented, and (d) the cross-section showing the defect-free processed section consisting of AM60 and the Ca-added Mg alloy. (e) A tensile property summary for the as-cast and FSP for both the AM60 and Ca-added Mg alloy. Source: PNNL.

The second local alloying method implemented was friction surfacing; key initial results are presented in Figure II.1.3.15. The setup where the interaction between the Ca-added Mg tool/rod and the substrate generates heat and plasticizes the material, which is then deposited onto the surface, is shown in Figure II.1.3.15(a). Table II.1.3.7 summarizes key efforts in making this method work since no published literature exists on Mg friction surfacing. The literature is also notably limited for depositing a stronger material (Ca-added Mg alloy) onto a weaker substrate (AM60). As noted in Table II.1.3.7, rods of Ca-added Mg alloy were tested in both an as-cast and homogenized condition on various Mg and Al substrates. Substrates of various strength were used to induce heating and consequent plasticization of the rods because Ca-added Mg alloy had higher hardness in the as-cast condition. Finally, after homogenization that reduced the strength of the rod, successful deposits were obtained on AM60 substrate, an example is presented in Figure II.1.3.15(b) and Figure II.1.3.15(c), respectively. The height of deposit was around 4 mm and the cross-section in Figure II.1.3.15(d) displays the defect-free, solid deposit. Tensile and fatigue property characterization of this deposit in as-deposited and aged conditions are underway. Overall, demonstration of the proposed concepts was successful and shows promising initial results.

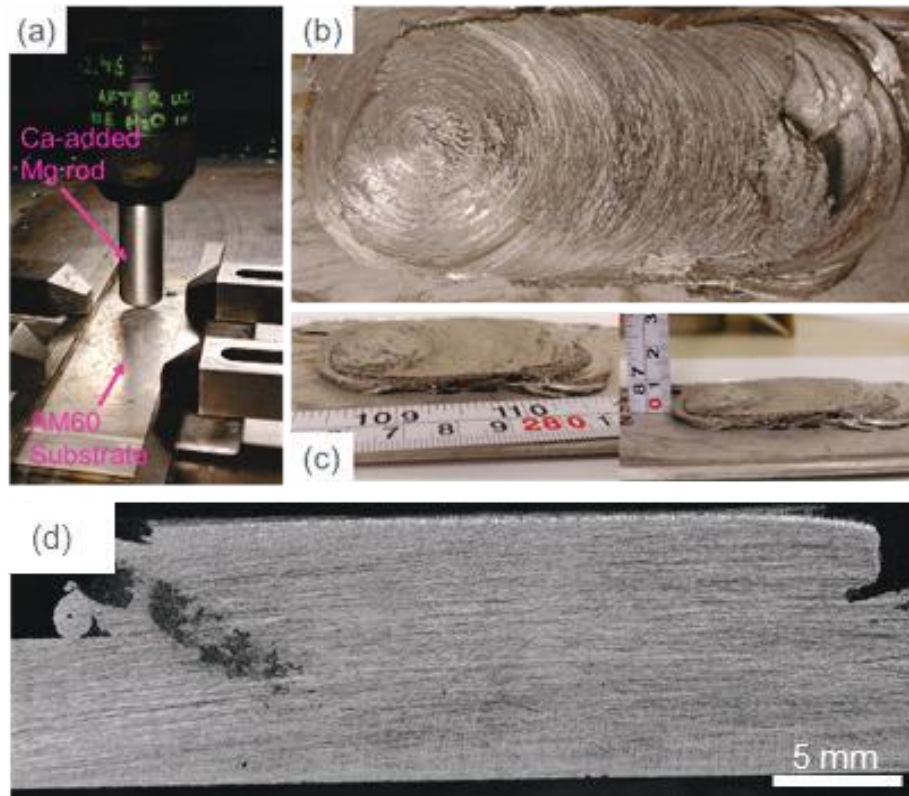


Figure II.1.3.15. (a) Friction surfacing setup; (b) top; and (c) side views of a deposit. (d) Cross-section showing defect-free, solid deposit. Source: PNNL.

Table II.1.3.7. Selected Friction Surfacing Processing Conditions and Quality Results by PNNL

No.	Rod Condition	Substrate	Rotation speed (RPM)/traverse rate (mm/min)/force (N)	Quality
1	As-Cast	AM60 Groove	1500/50/2500	<ul style="list-style-type: none"> Poor surface finish Tearing of substrate.
2	As-Cast	AZ91 Groove	1500/65/300	<ul style="list-style-type: none"> Poor surface finish Reduced tearing.
3	As-Cast	AA7075 Flat Plate	1500/65/2500	<ul style="list-style-type: none"> No successful alloying.
4	As-Cast	AA5083 Flat Plate	1600/65/5000	<ul style="list-style-type: none"> No successful alloying Minor deformation of feed rod.
5	Homogenized	AM60 Flat Plate	1250/30/2500	<ul style="list-style-type: none"> First layer did not adhere well Subsequent layers had a very smooth and uniform surface.
6	Homogenized	AM60 Flat Plate	1500/30/2500	<ul style="list-style-type: none"> Smooth surface finish Non-uniform layer height.
7	Homogenized	AM60 Flat Plate	1900/30/2500	<ul style="list-style-type: none"> Layer height was very large, but also varied within a single track Rough surface finish.

Conclusions

Project 3A1

- Direct N₂ plasma treatment on AZ91D was effective in corrosion protection (reducing corrosion by ~1.6×), but only after five plasma passes. Lower numbers of plasma passes decreased the corrosion resistance of AZ91D, presumably due to removal of the native surface oxide. Further process optimization will be required to achieve the highest corrosion resistance.
- Plasma-deposited Si-O-C layers, resulting from the two-step plasma treatment process with an organosilicon precursor, were highly effective in increasing the corrosion resistance of AZ91D Mg alloy substrate and reduced corrosion rates by ~1/9 or further.
- Wet Li-salt loading and CO₂-thermal treated AZ91D and AM60 Mg alloy samples exhibited higher corrosion resistance (by ~1/9) as supported by EIS and polarization measurements. Wet Li-salt loading and CO₂ thermal treatment was also effective in increasing surface wear resistance of AZ91D Mg alloy substrates.

Project 3A2

- Cold spray coatings of Zn powders were deposited onto Mg alloy substrates at a range of 3.5–6.5 MPa gas pressure and 150–400°C gas temperature.
- Long-term immersion corrosion tests indicate significant improvement of corrosion properties in Zn-coated substrate compared with bare substrate.
- Greater than 50% improvement in wear rate was observed in Zn-coated substrates as compared to uncoated substrates.
- The measured average adhesive bond strength for coating deposited at 150°C, 200°C, 300°C, and 400°C, respectively, gas temperature is 29.9 MPa, 30.8 MPa, 30.4 MPa, and 32.0 MPa, respectively. Several adhesive tests ended with failure of the substrate before failure of the coatings.
- The optimized deposition parameters were employed to demonstrate cold spray coating capability of curved automotive parts in PNNL. Zinc powders deposited on AM60 curved parts showed negligible porosity and uniform thickness.

Project 3B

- FSP of HPDC AM60 and AZ91 alloys led to a notable increase in fatigue due to elimination of casting defects and refinement of coarse secondary phase precipitates.
- Curved regions were successfully processed via FSP and achieved a porosity fraction of 0.07% compared to ~2.5% in the as-cast condition. Hardness was uniform across the flat and curved processed regions.
- Local alloying via FSP of a groove filled with Ca-added Mg yielded a ~30% increase in YS compared to as-cast AM60 and an increase in elongation to failure from 4.5% to 8%.
- Friction surfacing was shown as an alloying alternative to produce fully dense Ca-added Mg alloys on an AM60 substrate.

Key Publications

1. Garcia, D., H. Das, X. Ma, T. Roosendaal, V. Joshi, D. Herling, M. Komarasamy, and G. Grant, “Exploring the microstructure-property relationship of Mg-Al-Mn alloys enhanced via friction stir processing,” In: Maier, P., S. Barela, V. M. Miller, and N. R. Neelameggham (eds.), *Magnesium Technology 2022*, The Minerals, Metals & Materials Series, Springer, Cham, Switzerland. https://doi.org/10.1007/978-3-030-92533-8_33.

2. Jun, J., Y. C. Lim, Y.-F. Su, A. Sy, R. Robinson, and D. Pappas, 2023, “Open-air plasma-assisted Si-O-C layer deposition on AZ91D Mg alloy for corrosion mitigation,” In: Barela, S., A. Leonard, P. Maier, N. R. Neelameggham, and V. M. Miller (eds.), *Magnesium Technology 2023*, The Minerals, Metals & Materials Series, Springer, Cham, Switzerland. https://doi.org/10.1007/978-3-031-22645-8_13.
3. Jun, J., Y.-F. Su, D. Pappas, A. Sy, R. Robinson, and Y. C. Lim, 2022, “Corrosion protection of AZ91D Mg alloy by open-air plasma-assisted deposition of silane based coating,” [Online]. Available at: <https://ssrn.com/abstract=4192666> (last accessed 1 February 2023).
4. Jang, G. G., J. Jun, S. Yeom, M. Yoon, Y.-F. Su, J. Wade, M. S. Stephens, and J. K. Keum, 2023, “Atmospheric pressure plasma treatment of magnesium alloy for enhanced coating adhesion and corrosion resistance,” *Coatings*, Vol. 13, No. 5, Art. 897. <https://doi.org/10.3390/coatings13050897>.
5. Jang, G. G., S. Yeom, J. K. Keum, M. Yoon, H. Meyer III, Y.-F. Su, and J. Jun, 2023, “Formation of carbon and oxygen rich surface layer on high-purity magnesium by atmospheric carbon dioxide plasma,” *J. Magnes. Alloy*, Vol. 11, No. 1, pp. 88–99. <https://doi.org/10.1016/j.jma.2022.10.008>.
6. S. Niverty, R. Kalsar, A. J. Naccarelli, T. J. Eden, X. Ma, N. Overman1, R. Prabhakaran, G. Grant, D. Herling, V. V. Joshi, “Bond Coat Assisted Enhancement in Microstructural, Mechanical and Corrosion Behavior of AZ91 Magnesium Alloy Cold Spray-Coated with Aluminum Alloys” (Manuscript under preparation).
7. S. Niverty, R. Kalsar, G. Grant, D. Herling, V. V. Joshi, “Cold Sprayed Coatings of Commercially Pure Zinc for Enhancing the Corrosion Performance of Magnesium Alloys” (Manuscript under preparation).

References

1. Rettberg, L. H., J. B. Jordon, M. F. Horstemeyer, and J. W. Jones, 2012, “Low cycle fatigue behavior of diecast Mg alloys AZ91 and AM60,” *Metall. Mater. Trans. A Phys. Metall. Mater. Sci.*, Vol. 43, No. 7, pp. 2260–2274. <https://doi.org/10.1007/s11661-012-1114-8>.
2. Lim, Y. C., J. Jun, D. N. Leonard, Y. Li, J. Chen, M. P. Brady, and Z. Feng, 2022, “Study of galvanic corrosion and mechanical joint properties of AZ31B and carbon-fiber reinforced polymer joined by friction self-piercing riveting,” *J. Magnes. Alloy*, Vol. 10, No. 2, pp. 400–410. <https://doi.org/10.1016/j.jma.2021.05.003>.

Acknowledgments

The authors from PNNL recognize D. Garcia, X. Ma, H. Das, A. Guzman, T. Roosendaal, R. Seffens, M. Rhodes, R. Kalsar, S. Niverty, V. Prabhakaran, C. B Smith, D. Graff, and G. G. Neuenschwander for their processing and/or characterization activities for this project. The authors from ORNL recognize Y. C. Lim, G. G. Jang, A. Plotkowski, and J. Wade.

II.1.4 Thrust 4. Characterization, Modeling, and Life Cycle (Tasks 4A1, 4A2, 4A3, 4C1, and 4C2) (Pacific Northwest National Laboratory, Oak Ridge National Laboratory, and Argonne National Laboratory)

Arun Devaraj, Co-Principal Investigator (Project 4A1)

Pacific Northwest National Laboratory
902 Battelle Blvd.
Richland, WA 99354
E-mail: arun.devaraj@pnnl.gov

Thomas Watkins, Co-Principal Investigator (Project 4A2)

Oak Ridge National Laboratory
1 Bethel Valley Rd.
Oak Ridge, TN 37831
E-mail: watkinstr@ornl.gov

Dileep Singh, Co-Principal Investigator (Project 4A3)

Argonne National Laboratory
9700 South Cass Ave.
Lemont, IL 60439
E-mail: dsingh@anl.gov

Jeffrey S. Spangenberg, Co-Principal Investigator (Project 4C1)

Argonne National Laboratory
9700 South Cass Ave.
Lemont, IL 60439
E-mail: jspangenberg@anl.gov

Ayoub Soulami, Co-Principal Investigator (Project 4C2)

Pacific Northwest National Laboratory
902 Battelle Blvd.
Richland, WA 99354
E-mail: ayoub.soulami@pnnl.gov

Christopher Schooler, DOE Technology Development Manager

U.S. Department of Energy
E-mail: christopher.schooler@ee.doe.gov

Start Date: October 1, 2020 End Date: September 30, 2023
Project Funding (FY 2022): \$1,150,000 DOE share: \$1,150,000 Non-DOE share: \$0

Project Introduction

This report describes the activities performed during FY 2022 in the Characterization, Computation, and Life Cycle activity under Thrust 4 within the DOE VTO LMCP. The goal of the LMCP, which was launched in October 2020, is to combine multiscale modeling, rapid measurement of properties (i.e., high-throughput testing), and novel processing technologies (i.e., solid-phase processing, AM, and high-intensity thermal treatment) to locally control material properties. Three materials development thrusts are included in the LMCP: Thrust 1 – Selective Processing of Al Sheet; Thrust 2 – Selective Processing of Al Castings; and Thrust 3 – Localized Property Enhancement for Cast Mg Alloys. Thrust 4 supplements and supports the advanced characterization, computational modeling, and life cycle needs of the various tasks within the three materials development thrusts. Advanced characterization activities include STEM, APT, synchrotron x-rays, neutron scattering, and other capabilities. The advanced characterization is a multi-laboratory effort involving ANL, PNNL, and ORNL. In FY 2022, PNNL conducted the STEM and APT studies. Beamline proposals have been submitted to ANL’s APS for accessing synchrotron x-rays for diffraction experiments. The modeling task includes high-performance computing, DFT, smooth particle hydrodynamics (SPH), multiscale modeling for understanding solidification, thermodynamic models, process models, and micro-macro FEM for bendability. Modeling tasks have been conducted both at PNNL and ORNL; residual stress characterization, prediction, and optimization tasks have been conducted at PNNL; and material life cycle studies have been conducted at ANL. This report will cover the results from the Thrust 4 efforts conducted at PNNL, ORNL, and ANL across all three of the following tasks: (1) advanced characterization and modeling; (2) residual stress characterization, prediction, and optimization; and (3) material life cycle in the first year of this project.

Objectives

The objectives of this project are to (1) bring together advanced microstructural characterization, local mechanical testing, and predictive modeling to help establish processing-microstructure-property/performance relationships; (2) characterize, predict, and optimize residual stresses introduced by the local processing approaches used to achieve intentionally heterogeneous microstructure; and (3) study recyclability of intentionally heterogeneous Al and Mg alloys.

Approach

The approach in this thrust is to leverage the unique combinations of experimental and computational science capabilities and expertise at these three national laboratories in advanced characterization, modeling, residual stress studies, and material life cycle assessments. The LMCP PIs from Thrusts 1–3, all propose, compete, and obtain access to advanced characterization capabilities and modern computational tools and expertise through an internal proposal review process, issued twice in each financial year. During the review process of the Thrust 4 requests, emphasis is placed on cross-national laboratory collaborations, especially integrating advanced characterization with computational studies from PNNL, ORNL, and ANL.

The access to advanced characterization and computation—as well as residual stress studies and material life cycle expertise enabled through Thrust 4—provides a unique opportunity to accelerate the development of Al- and Mg-based lightweight alloys with an intentionally heterogeneous microstructure. Table II.1.4.1 provides all the advanced characterization, computation projects, residual stress, and life cycle projects funded and executed in FY 2022. The ‘Results’ section focuses on describing the progress of selected subprojects from each of the three primary projects.

Table II.1.4.1. Thrust 4 – Characterization, Modeling, and Life Cycle Projects Funded in FY 2022

Project	Subproject Title	Relevant Thrust and Project	Lab Ownership
1. Advanced Characterization and Modeling	APT of precipitates in additively manufactured Al alloy	1B	ORNL
	Thermodynamic and process modeling to understand factors affecting the melting and solidification of Al alloys during AM processing	1B & 2C	ORNL
	Advanced characterization of microstructure-mechanical property relationship in FSP Al 7055	1C	PNNL & ANL
	Geometry optimization forming a high-performance computing model that provides strategic locations of local property modifications resulting in successful RT stamping/forming	1C	ORNL
	To understand the composition, size, and spatial distribution of strengthening precipitates formed after local thermal treatments of Al Alloy 7075	1C	ORNL
	Precipitate evolution in Al 6111 during Friction Stir and Bend/Unbend processing	1C	PNNL & ORNL
	ORNL's high-fidelity ultrasonic process modeling tool to guide the transition of power ultrasonic-based surface processing process development from lab flat coupons to the complex-shaped 3D high-pressure diecast body parts	2A	ORNL
	Macro-micro FEM for improved fatigue behavior of friction stir processed A380 castings	2A	PNNL & ORNL
	Casting simulations for ultrasonic casting process of A356 alloys	2B	PNNL & ORNL
	Understanding the bond strength at meso-scale at the interface of Zn-Zn particles and Zn-AZ91 substrate after cold spray using in situ RT micropillar compression and micro-tension test	3A	PNNL
	Understanding spherical particle deformation and flattening behavior during cold spray of commercially pure Al and Al6061 alloy on Mg-substrates using SPH modeling	3A	PNNL
2. Residual Stress Characterization, Prediction, and Optimization	SPH simulation of heat generation during FSP of AA7075	4	PNNL
	Modeling of the quenching/distortion during ShAPE tube extrusion		
3. Material Life Cycle	Material life cycle studies	4	ANL

Results

Project 1 – Advanced Characteristics and Modeling

This task brought together the capabilities and expertise in advanced microstructural characterization and computational modeling at PNNL, ORNL, and ANL for supporting requests under various subprojects from Thrusts 1–3. Results from a subset of these projects are described below.

Project 1.1 – Advanced Characterization of Microstructure-Mechanical Property Relationship in FSP 7055 Al Alloy

PNNL researchers in Thrust 1, Project C, successfully processed Al 7055 alloys using high-speed FSP. It is known that the stir zones after FSP reduced the load to the yield point in the bend tests. The focus of this sub-task was to apply advanced microstructural characterization of nanoscale precipitates in a base Al 7055 alloy and FSP stir zone using aberration-corrected STEM and APT at PNNL to establish the FSP-microstructure-mechanical property relationships relative to the stir zones. A newly procured PFIB system at PNNL was instrumental in fabricating Gallium contamination-free TEM and APT samples of these Al alloys.

Figure II.1.4.1(a) and Figure II.1.4.1(b) show STEM images for the base Al 7055 and after friction stir processing, highlighting the presence of a high density of $MgZn_2$ precipitates in base alloy, which gets destabilized after FSP. Few Al_3Zr precipitates were observed after FSP. Also following FSP, the number density of the $MgZn_2$ precipitate was observed to decrease considerably as evident in the APT results in Figure II.1.4.1(c) through Figure II.1.4.1(e). This reduction in the precipitate number density led to an increase in bendability of the alloy locally at the friction stir processed zone. Thus, advanced characterization revealed the reasoning for the reduced load to yield point during bend tests after FSP.

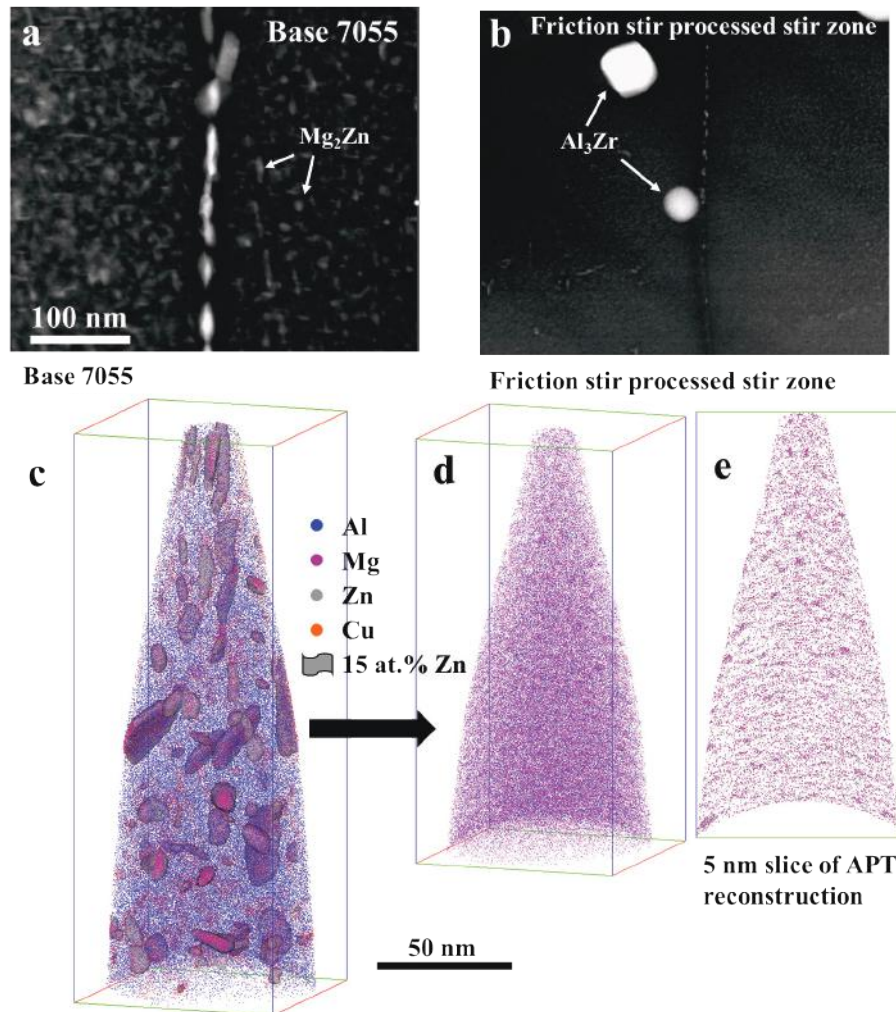


Figure II.1.4.1. STEM images of (a) the Al7055 base alloy with white arrows highlighting the Mg_2Zn precipitates in the grain interiors and grain boundaries, and (b) the 7055 alloy stir zone microstructure after friction stir processing. (c-e) The APT reconstruction revealing the change in element distribution before and after FSP. Source: PNNL.

Project 1.2 – Characterization of Precipitate Size Distribution in FSP Al Alloys Using Small Angle X-Ray Scattering (SAXS)

Al7085-T6 and 7055-T6 alloy sheets (e.g., 2.5-mm-thick) were subjected to FSP with the aim of improving local formability. Preliminary bendability tests conducted at PNNL showed that a combination of thermomechanical variables resulted in higher formability [1]. A significant factor in determining the formability of the Al alloy systems in question is the nature of the precipitates/dispersoids present [2]. Therefore, with an aim of characterizing the volume fraction and size distribution of the precipitates/dispersoids in a statistically significant sample volume, SAXS experiments in transmission mode were conducted at beamline 9-ID-C in the APS [3]. An x-ray beam of size $0.5 \text{ mm} \times 0.5 \text{ mm}$, with an energy of 21 keV, was used to perform the measurements on samples extracted from different regions in the processed alloy plate (e.g., stir zone, heat affected zone, base metal). The experimental setup at the beamline is shown in Figure II.1.4.2(a). Ultra-small angle x-ray scattering (USAXS), SAXS, and wide-angle x-ray scattering (WAXS) measurements were performed sequentially using three separate detectors to cover at least four decades in (q) (e.g., reciprocal space vector), translating to a feature size range of angstrom to μm in real space.

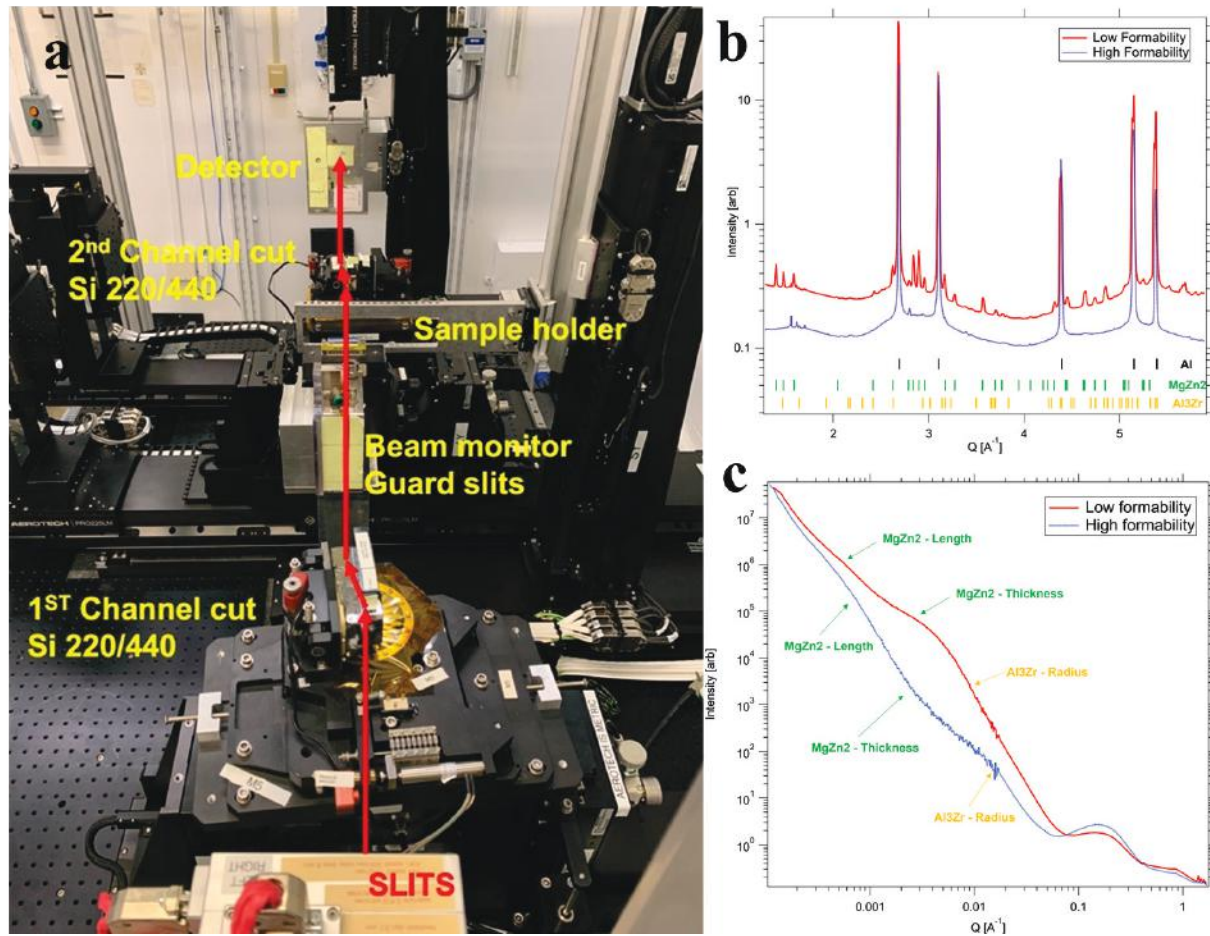


Figure II.1.4.2. (a) The USAXS experimental setup at beamline 9-ID-C [3] with all the beam paths shown in red and in incident x-ray beam entering through the 'slits.' (b) WAXS patterns of the two boundary formability cases with the peak positions of all the major phases (e.g., Al, MgZn2, Al3Zr) indicated below the spectra. Note that the high-formability samples show less intense/absence of MgZn2 and Al3Zr peaks (i.e., lower phase fractions). (c) (q) vs. (q) plots from the SAXS analysis for both the boundary cases showing the decrease in feature sizes of the precipitates/dispersoids (e.g., peaks shifting to a higher $[q]$ value) from the low formability sample to a high-formability sample due to FSP treatment. Source: ANL.

The data pre-processing and stitching the USAXS+SAXS+WAXS data to obtain a single $I(q)$ vs. (q) for a given sample was performed by the beamline staff using the Nika and Indra software packages in an IgorPro environment. SAXS analysis involving the multi-variable fitting of the $I(q)$ vs. (q) plot to obtain the particle size distribution was performed using the Irena software package in an IgorPro environment. An initial guess of the approximate particle size and shape is required for the SAXS analysis. Correlative STEM and APT performed at PNNL [4] showed the presence of spherical Al_3Zr dispersoids and platelet-like $MgZn_2$ precipitates. Further, the approximate precipitate sizes were obtained from image analysis of the STEM micrographs and found to be – $MgZn_2$ (thickness ~ 20 nm, length ~ 50 nm) and Al_3Zr (radius ~ 5 nm).

The WAXS patterns, as shown in Figure II.1.4.2(b), were used to identify the phases present in the samples extracted from the FSP zone of the Al7085 samples. Two boundary cases are used here as examples—ones with the highest and lowest formability in the present sample matrix. The major phases present were Al, Al_3Zr , and $MgZn_2$ with a tiny fraction of unindexed peaks suspected to be from Al_2Zr , $Mg_2Al_4Zn_3$, or oxide phases. The sample with the highest formability showed a significantly smaller volume fraction of precipitates/dispersoids compared to the lowest formability, which agrees well with the conclusions drawn using the STEM/APT results in [4].

The above WAXS information is further used for the SAXS analysis. The $I(q)$ vs. (q) curves for the cases used in the WAXS analysis are shown in Figure II.1.4.2(c). On the $I(q)$ vs. (q) plots, the larger mean feature sizes of the precipitates/dispersoids (e.g., thickness and length of $MgZn_2$, radius of Al_3Zr) are seen as peaks in the lower (q) region. The high-formability sample is seen to have lower mean feature sizes, as observed by the higher (q) value that is indicated by the arrows in Figure II.1.4.2(c), than the lower formability sample. This provides additional justification for the observation of an increase in formability/bendability after the FSP treatment. Further, the unmarked peaks in the high (q) region are suspected to arise from a core-shell nature of either the Al_3Zr or $MgZn_2$ seen to occur due to the sluggish diffusion of the heavier element and will be investigated in detail in the future.

For the next step, FSP samples with different process parameters at different process affected zones will be sourced from PNNL and characterized to understand the variation of precipitate size distribution with the thermomechanical variables. This will further aid the FSP process optimization and enable increase in site-specific formability for end application [4]. The process-structure relationships and the fundamental insights obtained from the various characterization tools are planned to be synthesized into a manuscript for publication in a high-impact journal. A conference abstract is planned to be sent to the Minerals, Metals, and Materials Society (TMS) 2023 to present a poster regarding the results of this study.

Project 1.3 – Casting Simulations for Ultrasonic Casting Process of A356 Alloys

This project supports the development of the ultrasonic casting process at PNNL under Project 2B. The project goal was to guide casting experiments at PNNL by the prediction of baseline solidification and ensuing microstructure variables without applied ultrasonic energy. Casting simulations were conducted at ORNL matching the specific geometry, alloy, and process parameters used at PNNL. ORNL simulations provided baseline microstructure data and fundamental knowledge that complemented the laboratory-scale casting experiments and post-mortem mechanical properties and microstructure evaluations conducted at PNNL for ultrasonic casting development. Two A356 alloy compositions were considered. The Al material database (CompuTherm) and microstructure model in ProCAST [5,6] were used to conduct the thermodynamic simulations for both alloys, based on a back diffusion model for a constant cooling rate of 1.37°C/s and the Scheil model. A full set of material properties and process conditions were generated. The quantitative phase evolution during solidification is shown in Figure II.1.4.3(a) and is critical for the development of an ultrasonic-based casting process as the application of the ultrasonic field is likely to affect the local composition. Further, process simulations offer insight on solidification patterns (i.e., the distribution of the baseline microstructure in the entire casting), which can be used to identify areas wherein the ultrasonic probe would be more effective for microstructure alteration, as observed in Figure II.1.4.3(b).

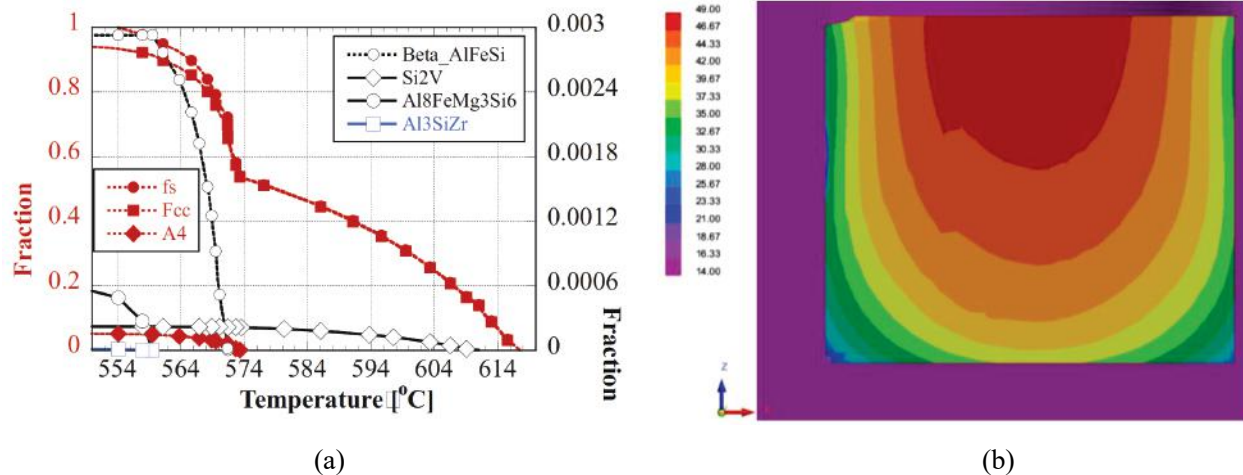


Figure II.1.4.3. (a) Calculated solid fraction (f_s) and main phases as a function of temperature during cooling using a back diffusion model at a constant cooling rate of 1.37°C/s for alloy A356a1. (b) Secondary dendrite arm spacing [mm] distribution within the entire casting for alloy A356a2. Here the dimensions on the simulated mold are approximately $4.76\text{ cm} \times 4\text{ cm}$ in the x - and z -directions, respectively. Source: ORNL.

Project 1.4 – Thermodynamic and Process Modeling to Understand Factors Affecting the Melting and Solidification of Al Alloys During AM Processing

In FY 2021, an ORNL computational support thrust was focused on implementing a process model that could predict an approximate thermal history for various points in the substrate and deposit during the ‘Form-and-Print’ and ‘Cast-and-Print’ processes. Because phase development in an alloy is dependent on the thermal history, having a process model was a necessary first step. Because the implementation of the process model was largely completed, the focus in FY 2022 was on developing the thermodynamic databases needed to leverage that thermal data for phase development in the alloy.

In FY 2021, an ORNL computational support thrust was focused on implementing a process model that could predict an approximate thermal history for various points in the substrate and deposit during the ‘Form-and-Print’ and ‘Cast-and-Print’ processes. The focus in FY 2022 was on developing the thermodynamic databases needed to leverage that thermal data for phase development in the structure resulting from the layered addition of a dissimilar Al alloy by laser hot-wire AM. During this process, the deposition of multiple layers results in thermal cycling, as previously deposited layers are reheated and cool between each layer. Additionally, the deposition of dissimilar material adds an additional complexity of a composition gradient across the part as the material in the substrate is mixed with the deposited material. This project leverages computational models to approximate the thermal cycles experienced during the process with the goal of predicting aspects of solidified alloy properties using thermodynamic and kinetic models.

The dissimilar alloys chosen were Al 4043, Al 4047, and Al 5356, which are to be deposited on cast or wrought Al-Si-Mg alloys. Phase prediction of the substrate material, mixed composition in the first layer, and deposit material requires an Al-Si-Mg thermodynamic database and kinetic parameters. From researching the literature on simulations within the Al-Si-Mg, the work of Povoden-Karadeniz et al. [7] was found to provide a significant starting point for implementing a thermodynamic database compatible with the Pandat software.

Next, an analysis of the expected phase fractions in each of the dissimilar Al 4043, Al 4047, and Al 5356 alloys was performed. Phase composition was evaluated at equilibrium, as well as under Scheil solidification conditions—typically more representative of AM conditions. These results, as shown in Figure II.1.4.4(a), indicate the expected results that the Mg_2Si precipitate only forms in low phase fractions due to limiting amounts of either Si or Mg, but also that the solute segregation due to fast cooling rates, represented by the Scheil solidification calculation, increases the potential amount of Mg_2Si in all cases. This supports those

different responses to heat-treatment that may occur for alloys in the as-built condition. Initial work was also done on developing the kinetic parameters for the alloy systems, although work is still ongoing to gather the experimental data needed to validate these results. A demonstration of the simulated Mg_2Si precipitate radius over time for Al 4043 alloy is shown in Figure II.1.4.4(b), where the thermal conditions were determined based on the time the first deposition layer spends above $550^\circ C$ in a representative wall with 25 layers. Post-processing heat treatments were simulated under a variety of conditions for deposits of the Al 4043, Al 4047, and Al 5356 alloys. Future work will focus on the characterization of those datasets to calibrate the parameters of the kinetic parameters for the Al-Si-Mg system for use of the precipitation model as a predictive tool.

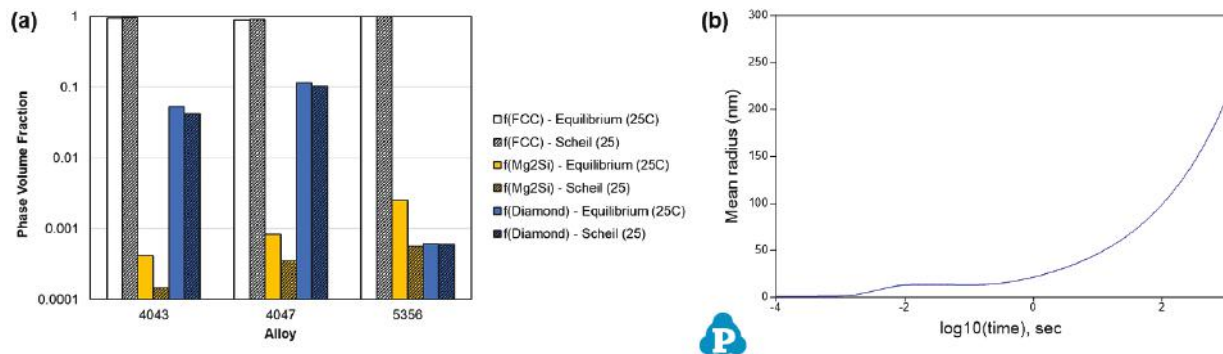


Figure II.1.4.4. (a) Comparison of phase volume fraction of the main precipitate phases in the selected alloys under equilibrium conditions (solid infill) and under Scheil solidification conditions (hatched infill). (b) Demonstration of simulated Mg_2Si size in Al 4043 during a simulated 828K heating for 1000 seconds. Source: ORNL.

Project 1.5 – High-Performance Computing for DFT Studies of Cast Mg Local Corrosion Mitigation

To provide insight into the understanding of the corrosion mechanisms of Mg alloys and designing corrosion-resistant Mg alloys, it is necessary to investigate the effect of dopants on the corrosion mechanism of Mg surfaces. Here we investigated the effect of dopants—including Zn, Al, and Ce—on the initial stages of water adsorption and surface atoms dissolution at the atomic scale. DFT [8, 9] calculations were performed using Vienna Ab-initio Simulation Package [10-13] with the generalized gradient approximation of Perdew-Burke-Ernzerhof functional for the exchange-correlation potential and the projector augmented wave potential.

To analyze the effect of the dopants and adsorbed H_2O on Mg corrosion, we compared energies needed to remove a single Mg species on pure and doped surfaces with and without H_2O . The adsorption of up to six water molecule clusters on the surfaces was considered in this work to understand the effect of dopants on the interactions between adsorbed water molecules (e.g., hydrogen bonding). The stability of water molecules is increasing with coverage on all surfaces besides the MgCe surface, as shown in Figure II.1.4.5(a) and Figure II.1.4.5(b), due to hydrogen bonding between adsorbed water molecules, which is about 0.24 eV. However, the stability of water molecules increased with coverage (1/30 monolayer [ML]) is smaller than 0.24 eV, suggesting the interactions of water molecules with the surface decreases at high coverage. Dependence of water adsorption energy on the coverage of the Mg-Zn and Mg-Al surfaces are comparable and the trend of that are similar on the pure Mg surface, but approximately 0.05 eV less stable than the two doped surfaces. The relative stability of the water clusters remained the same order as a single water molecule—they are more stable on the MgCe surface, followed by the Mg-Zn and Mg-Al surfaces, and are the least stable on the pure Mg surface.

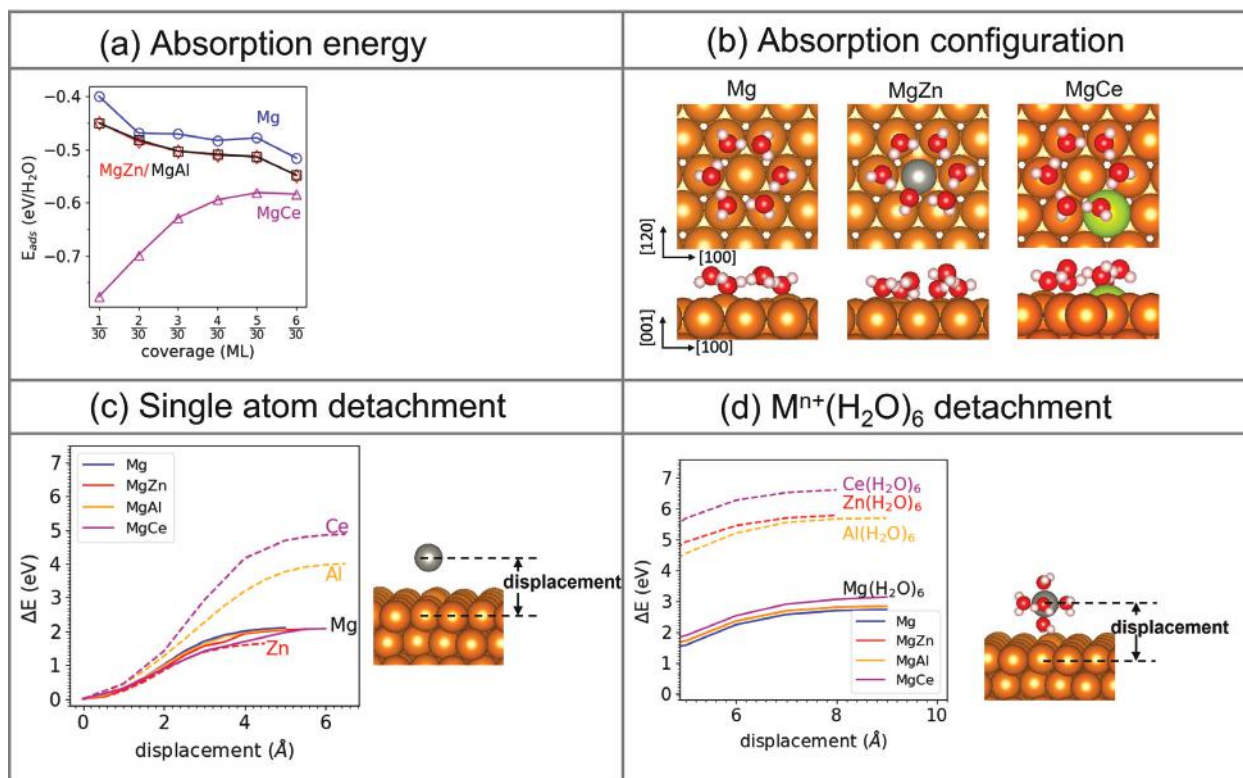


Figure II.1.4.5. (a) Dependence of water adsorption energy on coverage of the pure and doped Mg surfaces. The coverage unit is ML, which is calculated as the ratio of the number of adsorbates to all available sites on the surface; and (b) the H_2O absorption configuration. (c) Dependence of energy on the surface atom displacements away from the surface. The energy profiles for displacing Mg and dopants X are in solid and dashed lines, respectively. (d) Detachment energy of the hydrated dopant. Source: PNNL.

The dissolution of surface atoms is one of the primary indications of metal surface corrosion. The dissolution of surface atoms is investigated on clean surfaces and water-adsorbed surfaces. On clean surfaces, a single surface atom (e.g., Mg or dopant atom X) was removed from the surface up to the distance between the atom and surface of 6.5 \AA , as indicated in Figure II.1.4.5(c) and Figure II.1.4.5(d), respectively. It shows that Mg next to the dopant is slightly less costly to be removed than surface Mg on a pure Mg surface, suggesting that dopant destabilizes the surface Mg atoms next to the dopant. In addition, the stability of Mg and dopants are noticeably different—Zn is less stable than Mg, but the other two dopants are much more stable than Mg.

On the water-adsorbed surfaces, hydrated metal species ($M^{n+} \cdot (H_2O)_6$) were removed and placed above the surfaces by 3 \AA . It shows that the hydrated $Mg^{2+} \cdot (H_2O)_6$ is less costly to be removed from the Mg surface with dissolution energy of 0.55 eV, than a hydrated dopant species. The dopants, Zn and Al, reduced this energy further by 0.15 and 0.11 eV, respectively. These results suggest that on the doped surfaces, Mg is easier to leave the surface than the Zn or the Al. In other words, in aqueous environments, the role of dopants in prohibiting the corrosion of the surface is not through stabilizing the surface Mg atoms next to the dopants. In addition, it is less costly to remove hydrated Mg and Al species than a single atom; however, it is more costly to remove a hydrated Zn than a single Zn atom, suggesting that unlike Al, Zn stabilize the surface in aqueous environment.

Project 1.6 – In Situ TEM to Study Precipitate Evolution in Al 6111 Alloy

To obtain the desired formability, Al sheets are processed at high strains and temperatures (e.g., 300–500°C) in narrow processed zones (e.g., 6–12 mm wide), which results in dynamically recrystallized and solutionized microstructures. However, solutionization and reprecipitation of these Al alloys can be quite complicated when undergoing simultaneous deformation and heating. Understanding the individual effects of strain and temperature to obtain the desired microstructure is critical in selecting the process parameters to achieve the desired formability. The *in situ* TEM technique to be employed in this support project is ideal to monitor the microstructural changes at high temperatures and quantifying their kinetics, which will be key in designing the process parameters and understanding the role of microstructural features controlling the mechanical behavior.

Figure II.1.4.6 illustrates the ORNL-PNNL sample preparation process developed for preparing Al lamellae for *in situ* heating. The double-tilt holder with an E-chip installed is shown in Figure II.1.4.6(a). The inset in the figure shows an θ' -Al₂Cu precipitate at 8M \times and 200°C that was oriented precisely down a $\langle 110 \rangle$ Al zone axis, illustrating the precision and stability of the holder required for our experiments. Electrical current flows via the outer two contacts through the gold leads on the chip, and only the tiny center membrane at the tip of the arrow heats up. Figure II.1.4.6(b) shows a SEM image of an electropolished 3-mm Al 6111 disk, where the edges of the hole in the disk are electron transparent. Bright-field TEM is used to orient the grains in the foil. Figure II.1.4.6(c) is the SEM image of a portion of Area 3 with a single grain; the dotted line is the suggested cut line for the PFIB processing. The circles are sized and positioned relative to the thin grain (i.e., ‘lamella’) to indicate where the cut lamella should be placed on the E-chip so that the thin edge extends over a hole in the heater membrane, providing the best for imaging precipitate structures. Some PFIB-related problems were encountered initially related to the attaching of the PFIB sample to the heater membrane. Remedial procedures have been implemented to mitigate the preparation problems; a second round of sample preparation is presently underway.

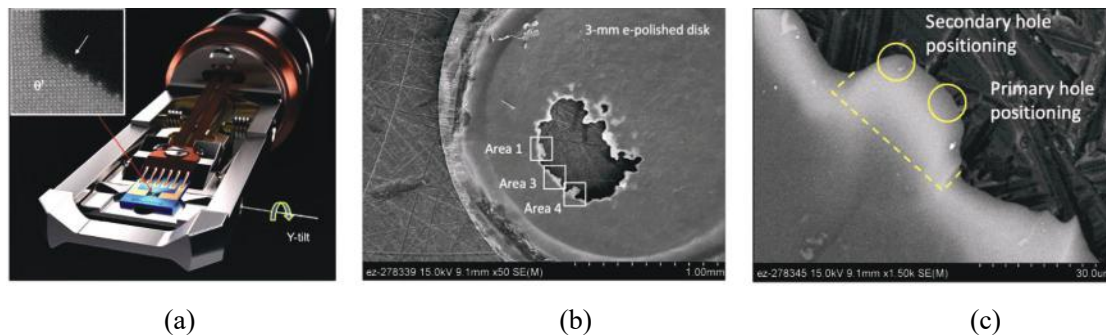


Figure II.1.4.6. (a) E-chip double-tilt heating holder for TEM; inset shows well-oriented θ' precipitate at 200 °C to illustrate capability of the holder. (b) Electropolished alloy disk, with thin grain areas located within squares. (c) SEM image of that same area, with the suggested PFIB cut and location on the heater holes indicated. Source: ORNL.

Project 2 – Residual Stress Characterization, Prediction, and Optimization for Hybrid Property Assemblies

The aim of this task is to investigate residual stresses resulting from locally modified properties and provide support to other projects in the various Thrusts 1–3. The approach proposed in this project will combine the continuum-level models to predict the residual stresses, dimensional instability, and latent defects; with experimental measurements of the extent of residual stresses caused by the local enhancement methods. During FY 2021, predictive modeling tools to simulate residual stresses during FSP of Al alloys were developed and validated. FY 2022 focused on upgrading the simulation tools to improve their accuracy and make them applicable to Mg alloys and curved plates. Additionally, simulation models were developed to predict residual stresses and distortion during ShAPE tube extrusion.

Project 2.1 – SPH Simulation of Heat Generation during FSP of AA7075

While computationally efficient, heat source models like the thermal-pseudo-mechanical (TPM) model implemented in FEM suffer from inaccuracies. An approach to use the accurate heat generation prediction from SPH in the FEM was proposed as a solution. This SPH-FEM coupling procedure [14] was verified in a previous effort. The SPH simulation of FSP on AA7075 has been carried out, and the accuracy of the heat generation has been validated using experimental data.

SPH simulation was set-up for FSP on a 2.5-mm-thick AA7075-T6 plate. While the process parameters and tool geometry matched that of the experiment, the simulated plate in the planar dimensions was much smaller. The plate was only long enough so that the simulation reached a steady-state condition. Figure II.1.4.7(a) shows the simulated temperature fields in the steady state. The maximum temperatures were around 500°C, just like those observed in the experiments. Figure II.1.4.7(b) shows the various forces on the FSP tool during the simulation. The Z force, which is the force in the plunging direction, is around 10 kN in the steady-state and matches the observed value. The accuracy of the temperature and tool force predictions validates the SPH simulation and qualifies its use within the coupled SPH-FEM approach.

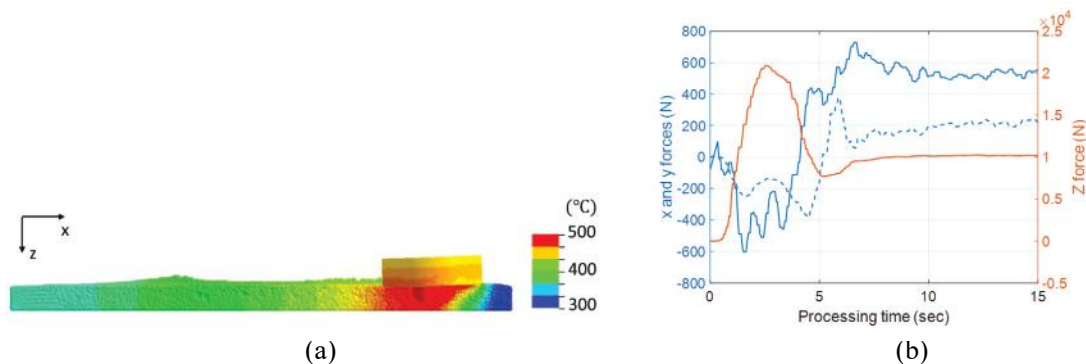


Figure II.1.4.7. SPH simulation results: (a) temperature distribution on a cross-section in the direction normal to the weld line and (b) simulated reaction forces on the FSP tool where the Z force denotes the plunging force. Source: PNNL.

The TPM model was used to simulate the residual stresses in the Mg alloys while the SPH-FEM was being developed. Previously, the TPM model was only applied to wrought Al alloy plates. In this report, the required model modifications to both the heat generation model and the hardness evolution model were made so that FSP on cast Mg alloys can be simulated. In addition, the TPM model was modified and applied to curved plates.

The heat generation equation in the TPM model was modified by multiplying it with a calibration factor ζ [15]. The calibration factor was set for each FSP condition so that the simulated maximum temperatures at the steady state match the experimentally observed values. ζ was found to be 0.95 and 0.72 for Mg alloys, AZ91 and AM60, respectively. The simulated temperatures now match the experimentally observed value of around 420–430°C. The material microstructure evolution model was modified to incorporate observations for Mg alloys. AZ91 involved no hardness change, but in AM60, the stir hardness increased by 20%–40% [16]. So, in the model for AM60, as the tool moves, the hardness in the stir zones increases. For the curved plate, the movement of the heat source was modified to follow the curve. Figure II.1.4.8(a) and Figure II.1.4.8(b) show the longitudinal residual stress prediction at the center of the plate for the flat and curved plates, respectively. The curved plate is just the flat plate bent by 15° in the middle. The residual stress distribution average through the thickness is similar, but the surface stresses differ. In the bent plate, the stresses on the top surface are larger, and the stresses on the bottom surface are smaller when compared to the flat plate. These differences demonstrate the need for residual stress simulation on curved plates and components.

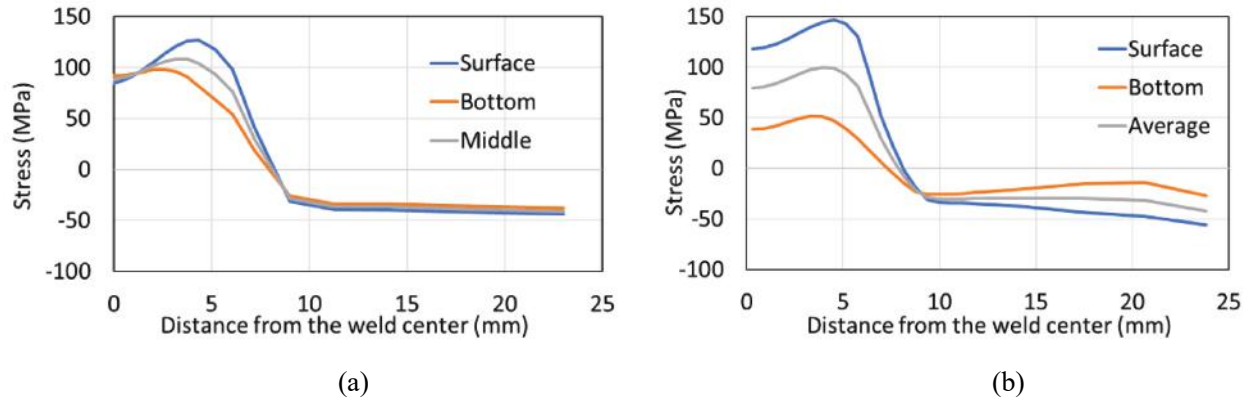


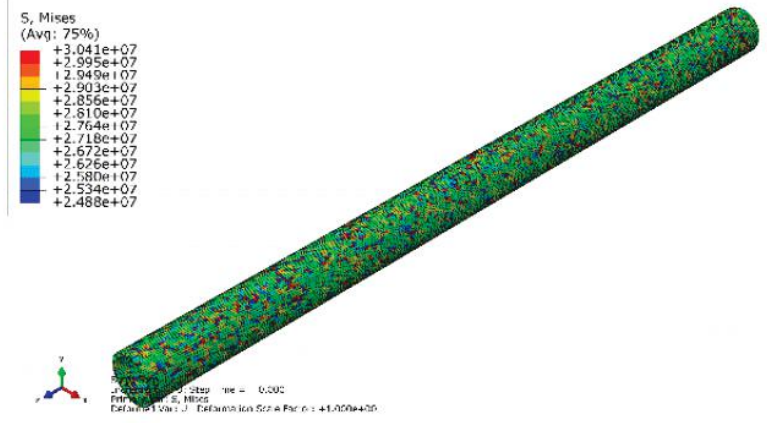
Figure II.1.4.8. Longitudinal residual stress prediction at the center of the plate for the (a) flat and (b) curved plates. Source: PNNL.

In the future, residual stress prediction and residual stress characterization of actual components will be the priority. Additional tasks include validating the residual stresses predicted by the SPH-FEM approach using experimental data. SPH-FEM approach will also be modeled to predict distortion.

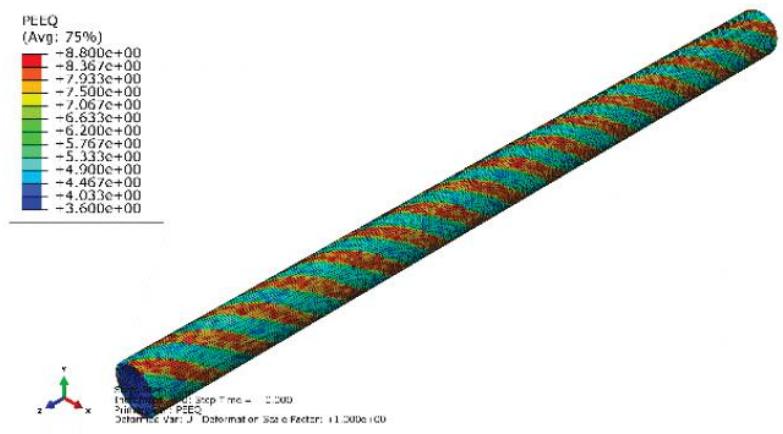
Project 2.2 – Modeling of the Quenching/Distortion During ShAPE Tube Extrusion

ShAPE can fabricate thin-walled tubing whose microstructure and bulk properties are uniquely tailored along the length of the extrusion. However, waviness/distortion is often observed during water quenching on the ShAPE extrusion tube, probably due to the residual stresses evolved during the process. This work aims to identify the possible sources for the tube distortion observed during quenching and to suggest solutions to avoid it.

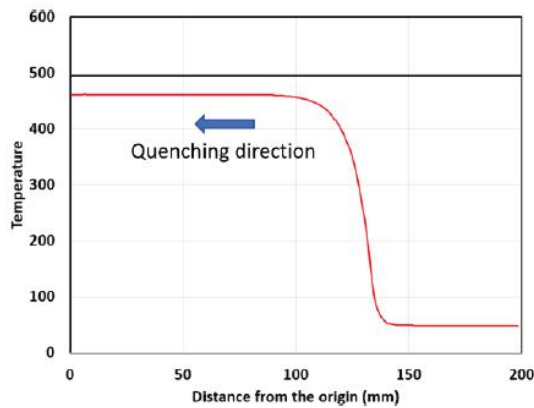
In FY 2022, modeling works were performed to understand the roles/evolutions of residual stresses during the extrusion/quenching process. The SPH simulations were first performed to find how the residual stresses/strains are distributed in the tube from the extrusion process. The observed stress/strain distributions were then assigned to the tube as initial conditions before quenching simulations to examine their effects. Figure II.1.4.9(a) and Figure II.1.4.9(b) show an example of the Mises effective stress distribution and equivalent plastic strain distribution assigned to the tube based on the SPH simulation results. The finite element simulations were then conducted systematically for various conditions to examine the stress evolutions. Figure II.1.4.9(c) and Figure II.1.4.9(d) show the example plots for temperature drop and compressive hoop stress evolving during quenching. While the tube distortion is not clearly seen from the simulations yet, these compressive stresses appear to be associated with the tube distortion effects, and their strength levels were also observed to depend on the initial simulation conditions. This indicates that tube distortion may depend on the process conditions of ShAPE and quenching. Future works would be to find the simulation conditions that show the tube distortion and then to suggest possible processing conditions that can prevent the tube distortion.



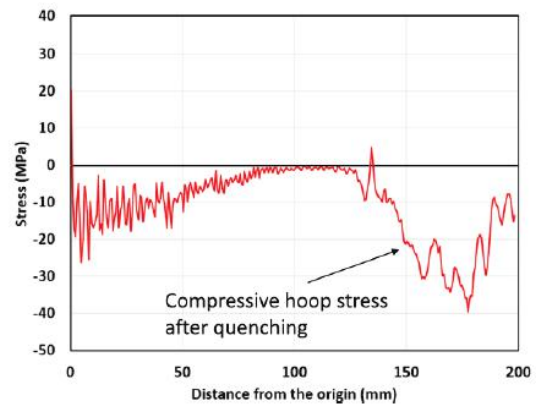
(a)



(b)



(c)



(d)

Figure II.1.4.9. (a) Mises effective stress distribution and (b) equivalent plastic strain distribution assigned to a tube before quenching. Example plots of (c) temperature drop and (d) compressive hoop stress during quenching. Source: PNNL.

Project 3 – Material Life Cycle

It is uncommon for materials and products to be developed with much thought to sustainability and recyclability. The LMCP has deliberately provided focus on this area during the development process, and this is to be commended. It is important to keep in mind that one of the main purposes of the program is to lightweight for vehicle efficiency. Without considering the sustainability of the manufacturing and EOL management, it is hard to understand the overall effect the materials can have on sustainability.

This program's overall objective is to save energy. The objective of this project, within the program, is to ensure awareness of all the direct and indirect factors that contribute to energy savings and to develop techniques and tools to measure our progress.

First, an understanding of the energy requirements using virgin materials in parts and assemblies needs to be understood. Simply replacing a steel part with an identical Al part will not necessarily meet performance requirements. The energy needed to make parts using RC needs to be defined as well. Consequences of using new materials or combining multiple parts into a single larger part need to be understood as well. For example, connection points between parts or dissimilar metals can make recycling more difficult or create issues with contamination. There must be a feedback loop between the EOL processing and recycling to the manufacturing design. Many times, a change in manufacturing materials or design can have a negative affect at EOL and it takes the EOL processors to convey the cause to the manufacturer.

The team went on several tours of auto shredders and downstream metal recovery facilities. The process of how Al and Mg are recovered from a vehicle for recycling is understood, but it should be mentioned that there is not one single way that materials are processed, nor is there a single place where these products are sold back to the market. In fact, many paths have been found to take recovered Al, some are domestic, and some are overseas. The goal is to recover as much metal as possible for recycling because primary Al requires much more energy to produce and generates nearly $5 \times$ as much GHG emissions, as indicated in Figure II.1.4.10. Auto shredders recover approximately 95% of the available Al from the vehicles. Ideally, the metal recovered from end-of-life vehicles go back into new vehicle manufacturing, but if it not, there is still a great benefit because it obviates the need to mine as much Al to produce those other—presumably lower quality—products.

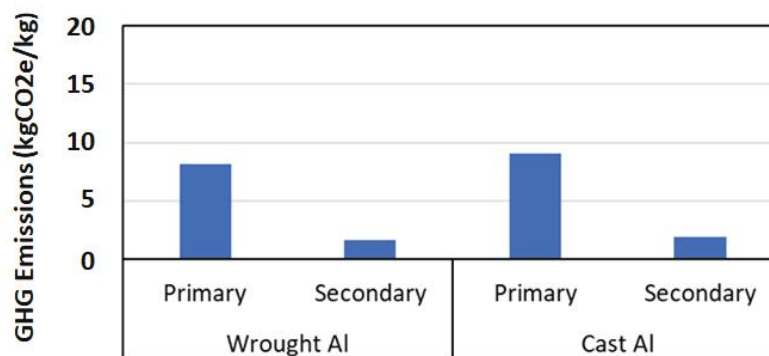


Figure II.1.4.10. Comparison of GHG emissions for primary and secondary Al. Source: ANL.

Al content in vehicles has increased from 6.3% in 1995 to 10.5% in 2017, but so has the number of alloys, both cast and wrought. This large number of alloys makes it difficult to exploit the most benefit from recycling. Most importantly, due to the amount of silicon in cast alloys, most of the recycled Al ends up in cast products. It should be noted that new EVs do not use the large quantity of cast Al for engine blocks and transmissions housings.

Much of this project relies on conversations with stakeholders and the LMCP thrust teams. The main findings during meetings and interactions with the teams demonstrated that it is possible to increase the amount of

lightweight metals in vehicles while reducing the number of alloys. This can be achieved by manufacturing parts with local treatments to provide different performance requirements using the same alloy. This reduces the need for different alloys and connection point, etc. In addition, manufacturing techniques being studied can reduce the amount of unnecessary material where it is not needed. Other major findings from stakeholders include the fact that other countries will commonly pay metal recyclers more for the material. This is not ideal because we would prefer these materials stay within the United States so we can enjoy the benefits from recycling Al and providing a steadier supply chain. It was also found that removing alloying elements from Al during the remelting process is difficult and expensive so dilution with virgin material is required. This limits the amount of recycle content that can be in a melt. As mentioned before, most recovered materials end up as feed for cast alloys. If fewer alloys were used in vehicles, in general, it would make it easier for recyclers to target specific alloys, or groups of alloys using technologies such as X-ray fluorescence to detect/eject separation systems. A success that may not be as challenging to reach would be to have wrought and cast separable using these technologies. Then there would be more recycled wrought material for reuse.

Conclusions

Across all six subprojects under Project 1, advanced microstructural characterization is revealing key atomic scale insights on processing-microstructure-mechanical property relationships for Al and Mg alloys relevant to the LMCP. This synergy between advanced characterization conducted under Thrust 4 and the material development activities conducted in Thrusts 1 to 3 can help design next-generation lightweight metals with intentionally heterogeneous microstructure with extraordinary properties for automotive applications.

Key modeling capabilities—such as the TPM model, SPH, and FEMs, as well as the experimental methods—have now been developed to predict and evaluate residual stresses in friction stir processed alloys under Project 2.

Finally, the material life cycle task under Project 3, is ensuring that various thrusts from 1–3 have a positive impact on energy and environment. There are a lot of factors that come into play when determining this impact. The team has, and will continue to, communicate, and learn from the many stakeholders. This is a dynamic industry, and it is important to look for unintended consequences of making changes both at the beginning and end of a product's life. To help ease the visualization of both good and bad impacts, this team will develop a spreadsheet that will estimate the cost and environmental impacts and then will suggest changes that can be made at the EOL of products with intentionally heterogeneous microstructure.

Key Publications

1. Balusu, K., L. Li, K. S. Choi, and A. Soulam, 2022. "Coupling smoothed particle hydrodynamics with FEM to simulate residual stresses from friction stir processing," *Proceedings of the ASME 2022 International Mechanical Engineering Congress and Exposition*. Volume 9: Mechanics of Solids, Structures, and Fluids; Micro- and Nano-Systems Engineering and Packaging; Safety Engineering, Risk, and Reliability Analysis; Research Posters, 30 October–3 November 2022, Columbus, OH, USA. <https://doi.org/10.1115/IMECE2022-93695>.
2. Balusu, K., K. S. Choi, H. Das, A. Samantha, P. Upadhyay, S. Jana, and A. Soulam, 2022, "On the utility of the thermal-pseudo-mechanical model's residual stress prediction capability for the development of friction stir processing," *Int. J. Adv. Manuf. Technol.*, under review. <https://doi.org/10.21203/rs.3.rs-2176313/v1>.
3. Pang, Q., M. Song, R. Kalsar, V. V Joshi, and P. V Sushko, 2022, "Water adsorption and surface atom detachment on Zn-, Al-, Ce-doped Mg surfaces," in Maier, P., S. Barela, V. M. Miller, and N. R. Neelameggham (Eds.), *Magnesium Technology 2022*, pp. 291–292. https://doi.org/10.1007/978-3-030-92533-8_48.
4. Pang, Q., M. Song, R. Kalsar, V. V Joshi, and P. V Sushko, 2023, "Water adsorption and surface atom dissolution on Zn-, Al-, Ce-doped Mg surfaces," under preparation.

References

1. Wahaz, N., H. Das, P. Upadhyay, and E. Mert, 2023, “Improving local formability of 6xxx and 7xxx aluminum alloy sheets using friction stir processing,” *Int. J. Adv. Manuf. Technol.*, Vol. 124, pp. 2957–2967. <https://doi.org/10.1007/s00170-022-10569-6>.
2. Marlaud, T., A. Deschamps, F. Bley, W. Lefebvre, and B. Baroux, 2010, “Evolution of precipitate microstructures during the retrogression and re-ageing heat-treatment of an Al–Zn–Mg–Cu alloy,” *Acta Mater.*, Vol. 58, No. 14, pp. 4814–4826. <https://doi.org/10.1016/j.actamat.2010.05.017>.
3. Ilavsky, J., F. Zhang, R. N. Andrews, I. Kuzmenko, P. R. Jemian, L. E. Levine, and A. J. Allen, 2018, “Development of combined microstructure and structure characterization facility for *in situ* and *operando* studies at the Advanced Photon Source,” *J. Appl. Crystallogr.*, Vol. 51, No. 3, pp. 867–882. <https://doi.org/10.1107/S160057671800643X>.
4. Devaraj, A., A. Soulami, T. Watkins, D. Singh, J. Spangenberg, and S. Kleinbaum, 2021, “Light Metals Core Program – Thrust 4 – Characterization, Modeling, and Life Cycle (Pacific Northwest National Laboratory,” in Kleinbaum, S., J. L. Gibbs, and H. F. Wu (Eds.), *Materials FY 2021 Annual Progress Report*, DOE-EERE VTO, pp. 276–287.
5. Guo, J., and M. T. Samonds, 2007, “Alloy thermal physical property prediction coupled computational thermodynamics with back diffusion consideration,” *J. Phase Equilibria Diffus.*, Vol. 28, pp. 58–63. <https://doi.org/10.1007/s11669-006-9005-6>.
6. Guo, J., and M. T. Samonds, 2004, “Property prediction with coupled macro-micromodeling and computational thermodynamics,” *Proceedings of MCSP6*, Kaohsiung, Taiwan, pp. 157–164.
7. Povoden-Karadeniz, E., P. Lang, P. Warczok, A. Falahati, W. Jun, and E. Kozeschnik, 2013, “CALPHAD modeling of metastable phases in the Al–Mg–Si system,” *Calphad*, Vol. 43, pp. 94–104. <https://doi.org/10.1016/j.calphad.2013.03.004>.
8. Hohenberg, P., and W. Kohn, 1964, “Inhomogeneous electron gas,” *Phys. Rev.*, Vol. 136, No. 3B, pp. B864–B871. Available at: <https://journals.aps.org/pr/pdf/10.1103/PhysRev.136.B864> (last accessed 1 March 2023).
9. Kohn, W., and L. J. Sham, 1965, “Self-consistent equations including exchange and correlation effects,” *Phys. Rev.*, Vol. 140, No. 4A, pp. A1133–A1138. Available at: <https://journals.aps.org/pr/pdf/10.1103/PhysRev.140.A1133> (last accessed 1 March 2023).
10. Kresse, G., and J. Furthmüller, 1996, “Efficient iterative schemes for *ab-initio* total energy calculations using a plane-wave basis set,” *Phys. Rev. B Condens. Matter.*, Vol. 54, No. 16, pp. 11169–11186. Available at: <https://journals.aps.org/prb/pdf/10.1103/PhysRevB.54.11169> (last accessed 1 March 2023).
11. Kresse, G., and J. Furthmüller, 1996, “Efficiency of *ab-initio* total energy calculations for metals and semiconductors using a plane-wave basis set,” *Comput. Mater. Sci.*, Vol. 6, No. 1, pp. 15–50. [https://doi.org/10.1016/0927-0256\(96\)00008-0](https://doi.org/10.1016/0927-0256(96)00008-0).
12. Kresse, G., and J. Hafner, 1993, “*Ab-initio* molecular dynamics for liquid metals,” *Phys. Rev. B Condens. Matter.*, Vol. 47, No. 1, pp. 558–561. Available at: <https://journals.aps.org/prb/pdf/10.1103/PhysRevB.47.558> (last accessed 1 March 2023).
13. Kresse, G., and J. Hafner, 1994, “*Ab-initio* molecular dynamics simulation of the liquid-metal-amorphous-semiconductor transition in germanium,” *Phys. Rev. B Condens. Matter.*, Vol. 49, No. 20, pp. 14251–14269. Available at: <https://journals.aps.org/prb/pdf/10.1103/PhysRevB.49.14251> (last accessed 1 March 2023).
14. Balusu, K., L. Li, K. S. Choi, and A. Soulami, 2022. “Coupling smoothed particle hydrodynamics with FEM to simulate residual stresses from friction stir processing,” *Proceedings of the ASME 2022 International Mechanical Engineering Congress and Exposition*. Volume 9: Mechanics of Solids,

Structures, and Fluids; Micro- and Nano-Systems Engineering and Packaging; Safety Engineering, Risk, and Reliability Analysis; Research Posters, 30 October–3 November 2022, Columbus, OH, USA.
<https://doi.org/10.1115/IMECE2022-93695>.

15. Balusu, K., K. S. Choi, H. Das, A. Samantha, P. Upadhyay, S. Jana, and A. Soulami, 2022, “On the utility of the thermal-pseudo-mechanical model’s residual stress prediction capability for the development of friction stir processing,” *Int. J. Adv. Manuf. Technol.*, under review. <https://doi.org/10.21203/rs.3.rs-2176313/v1>.
16. Iwaszko, J., K. Kudia, K. Fila, and M. Strzelecka, 2016, “The effect of FSP on the microstructure and properties of AM60 magnesium alloy,” *Arch. Metall. Mater.*, Vol. 61, No. 3, pp. 1209–1214.
<https://doi.org/10.1515/amm-2016-0254>.

Acknowledgments

For Project 1.1, contributions from M. Song, C. Roach, T. Ajantiwalay, H. Das, M. Efe, and P. Upadhyay are acknowledged. For Project 1.2, R. R. Kamath, J. Thomas, A. Chuang, J. Ilavsky at ANL are acknowledged for data collection, pre-processing, and analysis at APS beamline; P. Upadhyay, and H. Das at PNNL are gratefully acknowledged for providing the FSP A1-7085/7055 samples; and T. Ajantiwalay, C. Roach, J. Escobar, and M. Olszta at PNNL are acknowledged for the correlative TEM and APT results. This research used resources of the APS; a DOE–Office of Science user facility operated by ANL under Contract No. DE-AC02-06CH11357. The ORNL and PNNL team members for Project 1.3 included A. Sabau, K. E. Rader, and A. Rohatgi. For Project 1.4, the contributions of ORNL team members G. Knapp, Y. Yang, and A. Plotkowski are acknowledged. Contributions from Q. Pang, P. Sushko, R. Kalsar, and V. Joshi are acknowledged for Project 1.5. The contributions for Project 1.6 include L. Allard, M. Efe, P. Upadhyay, B. Gwalani, and A. Yu from ORNL and PNNL are acknowledged. Project 2 contributions from PNNL team members K. Balusu, L. Li, K. S. Choi, and A. Soulami are acknowledged as well.

II.2 Light Metals

II.2.1 ShAPE of Lightweight Alloys for Automotive Components (Pacific Northwest National Laboratory/ Magna International)

Scott Whalen, Co-Principal Investigator

Pacific Northwest National Laboratory
902 Battelle Blvd.
Richland, WA 99354
E-mail: scott.whalen@pnnl.gov

Massimo DiCiano, Co-Principal Investigator

Magna Services of America, Inc. (Magna R&D)
750 Tower Dr.
Troy, MI 48098
E-mail: massimo.diciano@magna.com

Christopher Schooler, DOE Technology Development Manager

U.S. Department of Energy
E-mail: christopher.schooler@ee.doe.gov

Start Date: January 1, 2019 End Date: September 30, 2022
Project Funding (FY 2022): \$2,005,000 DOE share: \$1,005,000 Non-DOE share: \$1,000,000

Project Introduction

Lightweight automotive components made from aluminum (Al) alloys offer 25% weight-savings as compared to state-of-the-art high-strength steel components. Additionally, components made from 100% secondary Al offer >50% energy savings and >90% CO₂ savings during the manufacturing process as compared to conventional extrusion, since the use of primary Al during recycling can both be eliminated [1–2]. For this CRADA between the PNNL and Magna Services of America, Inc., Research and Development (Magna R&D), ShAPE is being developed to convert Al scrap directly into a sub-scale EV battery support structure and chassis components. Extruded Al EV battery structures provide a commercialization opportunity based on equal, or improved performance, at a reduced cost as compared to conventional extrusions.

The potential cost reduction and environmental benefits associated with the use of cast feedstock comprised of 100% secondary Al scrap are well-established [1–4]. However, the use of secondary scrap without the addition of a significant percentage of primary Al has not developed into an industry process due to fundamental material challenges associated with intermetallic dispersion [5] and uniform microstructure [6]. These process limitations have been overcome using severe plastic deformation (SPD) techniques [7], such as equal channel angular pressing (ECAP) [8]; however, although successful from a scientific standpoint, ECAP and other SPD processes are not scalable to an industrial level. The ShAPE process combines the microstructural advantages of SPD with the scalability of a conventional extrusion process to offer a unique technology for converting secondary Al directly into automotive components. This report highlights the most noteworthy progress made towards this goal in FY 2022.

Objectives

The goal of this Magna R&D/PNNL project is to demonstrate the feasibility of using PNNL's ShAPE technology to manufacture Al alloy extrusions using feedstock comprised from 100% secondary Al. It is envisioned that by using the ShAPE process, feedstock comprised of 100% secondary Al can be used to fabricate cross-members, engine cradles, roof rails, and EV battery support structures with reduced cost and environmental impact.

Approach

The scope of work in FY 2022 focused on developing the ShAPE extrusion process for noncircular, multicellular, cross-sections using a porthole bridge die. Magna R&D was primarily responsible for supplying feedstock material, porthole tool fabrication, process modeling, and testing. PNNL was primarily responsible for tool design, fixture fabrication, process development, microstructural characterization, publication, and project reporting. Figure II.2.1.1 shows PNNL's first-of-a-kind ShAPE machine, which is the manufacturing platform utilized for this project.



Figure II.2.1.1. ShAPE machine installed in PNNL's Solid-Phase Processing Laboratory. Source: PNNL.

Unlike conventional extrusion where the billet is pressed against the die using a strictly linear motion, the ShAPE extrusion process superimposes a rotational shear force by spinning the die or billet. The ShAPE process is described in detail elsewhere [9–12]; however, the basic operation is briefly described here for convenience. Contact between the billet and rotating die generates frictional heating at the die/billet interface along with heating within a thin layer of deforming material below the die face due to plastic deformation. The extent of heat generation and depth of the deformation zone is controlled by regulating rotational speed, motor torque, and ram speed. As a result, the heat required to soften the material is entirely derived by the process and billet pre-heating in a separate furnace is not required. As the temperature increases, material plastically flows inward toward the extrusion orifice through individual spiral grooves machined into the die face. Upon exiting the grooves, the flow streams consolidate prior to entering the extrusion orifice where the material then flows between the mandrel and weld chamber to form a tube.

Results

The primary goal in FY 2022 was to demonstrate that ShAPE can extrude Al 6063 industrial scrap with adequate mechanical properties using a porthole die, manufacturing circular, noncircular, and noncircular multiwall profiles. Figure II.2.1.2 shows the extruded profiles manufactured in FY 2022 using the porthole die configuration, as well as a diagram of the process and pictures of the porthole tooling.

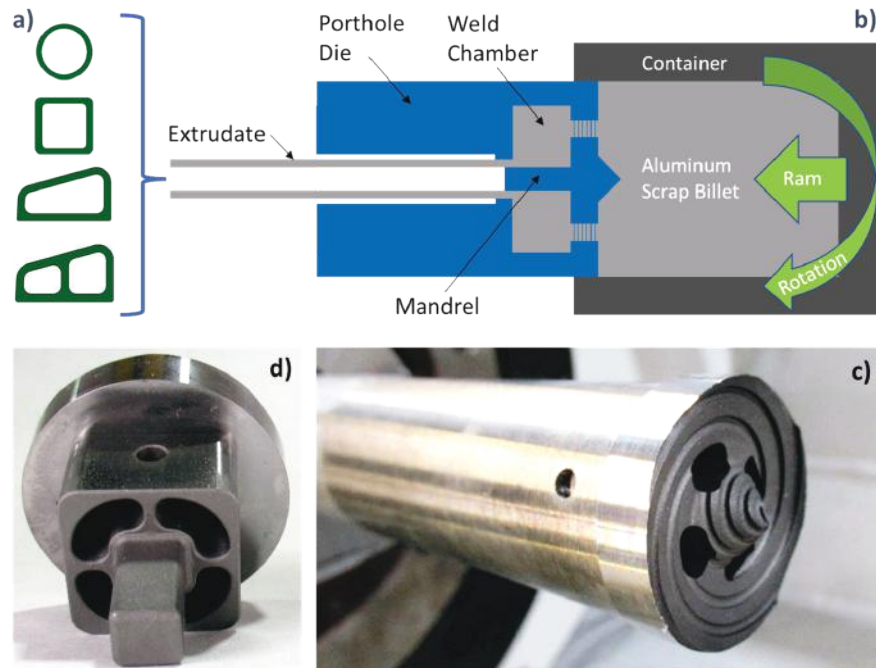


Figure II.2.1.2. (a) Extruded profiles manufactured using a porthole die integrated with the ShAPE process. (b) Schematic of porthole die integrated with a rotating billet. (c) Porthole die assembly with surface features to assist material flow. (d) Back side of porthole die head showing port exits and square mandrel
Source: PNNL.

To demonstrate extrusion of Al 6063 industrial scrap by ShAPE, Magna R&D provided PNNL with cast billets comprised of 100% industrial scrap, collected from a Magna manufacturing facility. Cast billets were provided to PNNL in the unhomogenized condition. PNNL extruded these cast billets using porthole tooling designed by PNNL (round and square) and Magna R&D (trapezoidal and 2-cell trapezoidal), all of which were fabricated by Magna R&D. Multiple extrusions were performed for the process conditions shown in Table II.2.1.1. Water quenching was incorporated near the die exit to achieve ‘die quench’ as is typical for industry. The circular, square, trapezoidal, and two-cell trapezoidal profiles had a nominally 2 mm wall thickness with the characteristic diameter of each profile having these dimensions—12.7 mm circular, 13.9 mm square, and 18.1 mm trapezoidal and two-cell trapezoidal. After extrusion, 150 mm long sections were cut from the round tubes and artificially aged at 177°C for eight hours to achieve a T6 temper. No solution heat-treating was performed prior to artificial aging to discover if die quenching was achieved during ShAPE extrusion of castings made from Al 6063 industrial scrap. The 150 mm long tubular specimens were fitted with tapered pugs on each end per ASTM E8 and pulled at Magna on an Instron 8802 load frame with a 25-kN load cell at a rate of 0.02 mm/s, with a 25-mm mechanical extensometer measuring displacement of the gauge length.

Table II.2.1.1. Process Parameters for ShAPE Extrusion of Al 6063 Industrial Scrap using a Porthole Die

Extrudate Profile	Billet Diameter (mm)	Extrusion Ratio	Die Rotation (rpm)	Die Face Temperature (°C)	Ram Force (kN)	Ram Speed (mm/min)
Round	31.8	11.4	55	460	610	120
Square	31.8	11.0	40	490	720	120
Trapezoid	38.1	9.1	30	510	390	10
2-Cell Trapezoid	38.1	7.9	40	500	370	10

Extrudates shown in Figure II.2.1.3 were approximately one meter long, manufactured from 10 cm long billets. Round extrusions were investigated initially to (1) solve engineering challenges associated with integrating a rotating billet into the ShAPE process and (2) demonstrate that Al could be separated into ports and recombined while rotating the billet. The circular profile and surface appearance for round tubing are shown in Figure II.2.1.3(a). The weld chamber and mandrel were then modified to produce the square profile shown in Figure II.2.1.3(b). Next, the port configuration, mandrel geometry, and weld chamber were redesigned to form an asymmetric trapezoidal profile. HyperXtrude simulations were performed to check that all regions of the extrudate had nominally the same velocity to promote weld seam closure and avoid curling. The trapezoidal profile and surface appearance are shown in Figure II.2.1.3(c). Finally, the trapezoidal mandrel was modified to form an internal web, thereby generating the two-cell profile shown in Figure II.2.1.3(d). With systematically increasing complexity, the ShAPE process has demonstrated the ability to extrude noncircular, asymmetric, multicellular profiles from Al 6063 industrial scrap. For all profiles, wall thickness varied by less than $\pm 5\%$ along the extrudate length, which is typical of conventional extrusion. In fact, YS (246.9 ± 10.4 MPa), UTS (270.8 ± 9.6 MPa), and uniform elongation ($16.5 \pm 2.4\%$) all exceeded industry standards [13,14], as shown in Table II.2.1.2. Notably, the ShAPE elongation results are for uniform elongation and the industry standards are for total elongation. This suggests that ShAPE-extruded material has exceptional elongation compared to the industry standard since uniform elongation gives lower values than total elongation. Surface roughness was measured to be $R_a = 4.93 \mu\text{m} \pm 0.40 \mu\text{m}$ as the average of 40 line-scans per face on each of the four exterior surfaces of the trapezoidal profile.

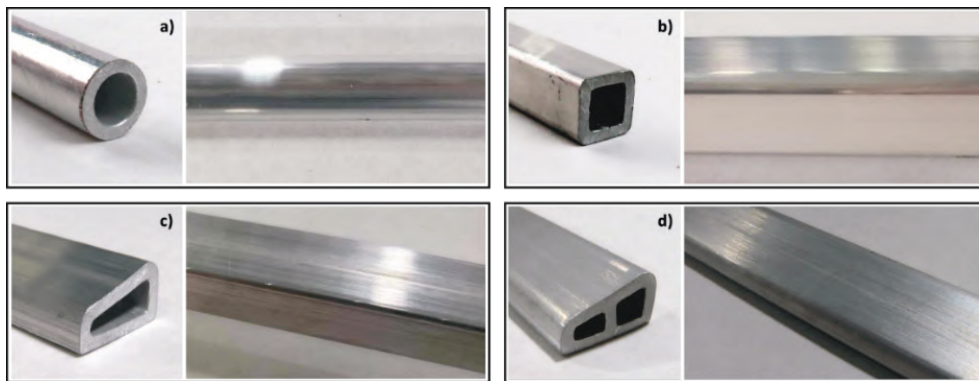


Figure II.2.1.3. Extrusions made from Al 6063 industrial scrap by ShAPE using porthole die configurations producing (a) circular, (b) square, (c) trapezoid, and (d) two-cell trapezoidal profiles. Source: PNNL.

Table II.2.1.2. Tensile Properties of 2-mm-thick Round Tubing Extruded by ShAPE from Al 6063 Industrial Scrap Compared to ASTM [13] and ASM [14] Standards. Note: * = Total Elongation

Property	ShAPE Al 6063 Scrap	T6 ASTM Min. [13]	T6 ASM Typ. [14]
Yield Strength (MPa)	247 ± 10	170	205
Ultimate Strength (MPa)	271 ± 10	214	241
Elongation (%)	16.5 ± 2.4	8*	12*

Table II.2.1.2 shows that the yield and ultimate strengths for ShAPE-extruded 6063 castings, subsequently heat-treated to the T6 condition, are significantly higher than conventionally extruded 6063 in the T6 condition, per the ASTM and American Society for Metals (ASM) standards. This demonstrates that the Mg_2Si strengthening phase is driven into solution during extrusion and that press quenching was effective in minimizing Mg_2Si reprecipitation and coarsening. As such, this work validates that ShAPE can extrude 6063 casting made from 100% secondary Al, without solution heat-treatment, with properties adequate for applications where conventionally extruded 6063 is a candidate.

A microstructural analysis of the trapezoidal profile in the as-extruded condition is presented in Figure II.2.1.4, illustrating the microstructural refinement achieved for ShAPE-extruded Al 6063 industrial scrap using a porthole die. The SEM secondary electron (SE) image montage presented in (a) shows full consolidation free of macro-level voids or weld seam defects, (b, c, e) and (g) show electron backscatter diffraction data collected midway through the wall thickness, and (d) and (f) show data at the inner and outer surfaces of the profile, respectively. The microstructure is highly refined and equiaxed with average grain sizes statistically similar for each location. The average grain size for all locations was $6.7\ \mu\text{m}$ with a standard deviation of $4.6\ \mu\text{m}$. Grain size examined through the wall thickness had no statistical variation. The IPF shown in Figure II.2.1.4 are parallel to the extrusion axis (Z). Pole figure plots are shown for the $\{001\}$ planes and illustrate texture development. Local texture depends on the location examined across the extrudate profile, which suggests deformation gradients exist within the workpiece during processing. SEM images from the entire SE montage were examined for evidence of incomplete weld seam fusion. This search revealed that all areas were fully recrystallized; no weld seam defects were detected.

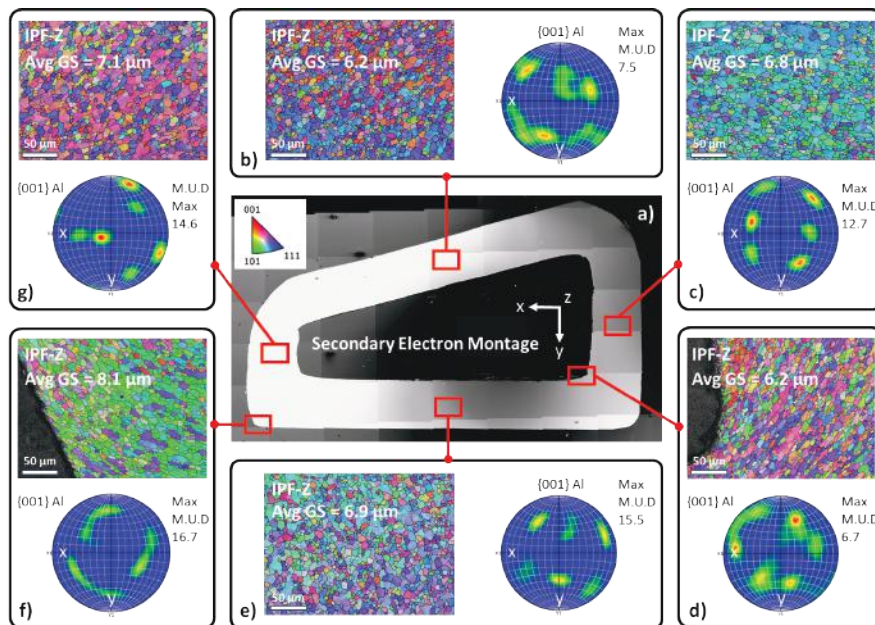


Figure II.2.1.4. SE image montage of a trapezoidal extrudate cross-section in the as-extruded condition without voids or weld seam defects. (b-g) Microstructure at various locations showing highly refined and uniform grain size and crystallographic orientation indicating weak texture. Locations b, c, e, and g are at the expected weld seam location and show no bonding or texture defects. (M.U.D. stands for multiple of uniform density.) Source: PNNL.

Conclusions

The joint PNNL/Magna R&D project team demonstrated the feasibility of manufacturing extrusions via ShAPE comprised of 100% Al 6063 secondary Al using unhomogenized cast billet feedstock. Tensile properties exceeding the ASTM minimum standard and ASM typical values for a T6 temper suggest that ShAPE-extruded castings have viable properties for automotive applications where Al 6063 is of interest. Porthole extrusion dies were integrated with the rotating ShAPE process to extrude noncircular, asymmetric, multicellular profiles relevant to automotive components.

Key Publications

1. Taysom, B. S., Md. Reza-E-Rabby, X. Ma, M. DiCiano, T. Skaszek, and S. A. Whalen, 2022, "Fabrication of aluminum alloy 6063 tubing from secondary scrap with shear-assisted processing and extrusion," in Eskin, D. (ed.), *TMS 2022 Light Metals*, The Minerals, Metals & Materials Series. Springer, Cham, Switzerland. pp. 294–300. https://doi.org/10.1007/978-3-030-92529-1_41.

2. Whalen, S. A., Md. Reza-E-Rabby, C. A. Lavender, and B. S. Taysom, 2022, “Devices and methods for performing shear-assisted extrusion, extrusion feedstocks, extrusion processes, and methods for preparing metal sheets,” U.S. Patent 11,383,280, granted 12 July 2022.
3. Whalen, S. A., B. S. Taysom, N. R. Overman, Md. Reza-E-Rabby, Y. Qiao, T. Richter, T. Skaszek, and M. DiCiano, 2023, “Porthole die extrusion of aluminum 6063 industrial scrap by shear-assisted processing and extrusion,” *Manuf. Lett.*, under review.
4. Whalen S. A., N. Overman, B. S. Taysom, Md. Reza-E-Rabby, T. Skaszek, and M. DiCiano, 2023, “Shear-assisted processing and extrusion of unhomogenized aluminum alloy 6063 castings with high iron content,” in Broek, S. (ed.), *TMS 2023 Light Metals*, The Minerals, Metals & Materials Series. Springer, Cham, Switzerland. pp.327–332. https://doi.org/10.1007/978-3-031-22532-1_45.

References

1. Mulholland, E., 2016, “Aluminum Extrusion EPD Background Report,” Aluminum Extruders Council, September 19, 2016. [Online] Available at: <https://www.apexextrusions.ca/cms/wp-content/uploads/2018/08/LEED-V4-Industry-Aluminum-Background-EPD-LCA-LEED-V4-2.pdf> (last accessed 1 March 2023).
2. Bushi, L., T. Skaszek, and T. Reabum, 2019, “New ultralight automotive door life cycle assessment,” *Int. J. Life Cycle Assess.*, Vol. 24, pp. 310–323. <https://doi.org/10.1007/s11367-018-1515-z>.
3. Ab Rahim, S. N., M. A. Lajis, and S. Ariffin, 2015, “A review of recycling aluminum chips by hot extrusion process,” *Procedia CIRP*, Vol. 26, pp. 761–766. <https://doi.org/10.1016/j.procir.2015.01.013>.
4. Wan, B., W. Chen, T. Lu, F. Liu, Z. Jiang, and M. Mao, 2017, “Review of solid-state recycling of aluminum chips,” *Resour. Conserv. Recycl.*, Vol. 125, pp. 37–47. <https://doi.org/10.1016/j.resconrec.2017.06.004>.
5. Chiba, R., T. Nakamura, and M. Kuroda, 2011, “Solid-state recycling of aluminum alloy swarf through cold profile extrusion and cold rolling,” *J. Mater. Process. Technol.*, Vol. 211, No. 11, pp. 1878–1887. <https://doi.org/10.1016/j.jmatprotec.2011.06.010>.
6. Guley, V., N. B. Khalifa, and A. E. Tekkaya, 2010, “Direct recycling of 1050 aluminum alloy scrap material mixed with 606 aluminum alloy chips by hot extrusion,” *Int. J. Mater. Form.*, Vol. 3, pp. 853–856. <https://doi.org/10.1007/s12289-010-0904-z>.
7. Azushima, A., R. Kopp, A. Korhonen, D. Y. Yang, F. Micari, G. D. Lahoti, P. Groche, J. Yanagimoto, N. Tsuji, A. Rosochowski, and A. Yangida, 2008, “SPD processes for metals,” *CIRP Ann. – Manuf. Technol.*, Vol. 57, No. 2, pp. 716–735. <https://doi.org/10.1016/j.cirp.2008.09.005>.
8. Haase, M., N. B. Khalifa, A. E. Tekkaya, and W. Z. Misiolek, 2012, “Improving mechanical properties of chip-based aluminum extrudates by integrated extrusion and equal channel angular pressing (iECAP),” *Mater. Sci. Eng. A*, Vol. 539, pp. 194–204. <https://doi.org/10.1016/j.msea.2012.01.081>.
9. Lavender, C. A., V. V. Joshi, G. J. Grant, S. Jana, S. A. Whalen, J. T. Darsell, and N. R. Overman, 2019, “System and process for formations of extrusion products,” U.S. Patent 10,189,063, granted 29 January 2019.
10. Whalen, S. A., N. Overman, V. Joshi, T. Varga, D. Graff, and C. Lavender, 2019, “Magnesium alloy ZK60 tubing made by ShAPE™,” *Mat. Sci. Eng. A*, Vol. 755, No. 7, pp. 278–288. <https://doi.org/10.1016/j.msea.2019.04.013>.
11. Taysom, B. S., N. Overman, M. Olszta, Md. Reza-E-Rabby, T. Skaszek, M. DiCiano, and S. A. Whalen, 2021, “Shear-assisted processing and extrusion of enhanced strength aluminum alloy tubing,” *Int. J. Mach. Tools Manuf.*, Vol. 169, Art. 103798. <https://doi.org/10.1016/j.ijmachtools.2021.103798>.

12. Whalen, S. A., M. Olszta, Md. Reza-E-Rabby, T. Roosendaal, T. Wang, D. Herling, B. S. Taysom, S. Suffield, and N. Overman, 2021, “High-speed manufacturing of aluminum alloy 7075 tubing by ShAPE,” *J. Manuf. Process.*, Vol. 71, pp. 699–710. <https://doi.org/10.1016/j.jmapro.2021.10.003>.
13. ASTM B221M-21, 2021, *Standard Specification for Aluminum and Aluminum Alloy Extruded Bars, Rods, Wire, Profiles, and Tubes (Metric)*, ASTM International, West Conshohocken, PA, USA.
14. ASM Handbook Volume 2: Properties and Selection of Aluminum Alloys, 2019, “6063 Extrusion Alloy,” Weritz, A. K., and J. G. Kaufman (ed.), ASM International, Novelty, OH, USA.

Acknowledgments

PNNL and Magna R&D thank the DOE VTO LightMAT Program for supporting this project. Report approved for unlimited release PNNL-33707.

II.2.2 Developments of a Novel Magnesium Alloy for Thixomolding® of Automotive Components – LightMAT (Oak Ridge National Laboratory)

Govindarajan Muralidharan, Co-Principal Investigator

Oak Ridge National Laboratory
1 Bethel Valley Rd.
Oak Ridge, TN 37831
E-mail: muralidhargn@ornl.gov

Bryan Macek, Co-Principal Investigator

Stellantis (FCA US LLC)
1000 Chrysler Dr.
Auburn Hills, MI 48326
E-mail: bryan.macek@stellantis.com

Nathan Sanko, Co-Principal Investigator

Leggera Technologies
87 Northpointe Dr.
Orion Township, MI, 48359
E-mail: nathan@leggaretech.com

Christopher Schooler, DOE Technology Development Manager

U.S. Department of Energy
E-mail: christopher.schooler@ee.doe.gov

Start Date: February 1, 2020	End Date: September 30, 2023	
Project Funding (FY 2022): \$200,000	DOE share: \$100,000	Non-DOE share: \$100,000

Project Introduction

Mg alloy die-castings are increasingly used in the automobile industry to achieve cost-effective mass reduction, especially in systems where multiple components can be integrated into a single thin-wall die-casting. However, there is only one die-caster in North America capable of producing die-castings of the size needed for components, such as instrument panel structures, liftgate inner panels, swing gate inner panels, and similar components, thus making it difficult to negotiate competitive pricing and creating a supply chain risk. Furthermore, there are several component quality restrictions in thin-walled Mg die-castings, including variability in dimensional accuracy, part-to-part variation in mechanical properties, and porosity in the final part, which has limited the continued growth of diecast components in the automobile industry.

An alternative to die-casting is the process of thixomolding. Widely used in the electronics industry, the thixomolding process has begun to make inroads into the automobile industry (e.g., 2018 Jeep Wrangler spare tire carrier) as a competing process to die-casting for producing complex thin-wall Mg components.

While the thixomolding process is similar to the die-casting process in that hot metal is injected into a die, it differs in at least one significant aspect. While the die-casting process relies on filling a mold at high speeds with the alloy in the completely molten state, the thixomolding process fills a mold with a thixotropic alloy in a semi-solid slurry state at a temperature between the liquidus and solidus temperatures. Ideally, the material should be ~30%–65% solid rather than being completely liquid at the beginning of the injection process. Advantages of the thixomolding process over die-casting include a finer grain structure, lower porosity, improved dimensional accuracy, improved part-to-part consistency, improved mechanical properties

(particularly ductility in the component), the ability to reduce wall thickness for mass savings, and longer tool life due to lower process temperatures.

Although thixomolding offers improved mechanical properties over diecast Mg components, the mechanical properties obtained in the thixomolded parts are still not sufficient to broadly enable application in components where both strength and ductility are key requirements (e.g., crash critical components exposed to high-impact velocities and powertrain or chassis components subjected to high levels of cyclic loading). Currently, the mechanical properties are limited by the alloys being used, which are the same alloys used in the die-casting process. Thus, there is a need for the development of new alloys, which can achieve high strength with improved ductility for use in components fabricated by the thixomolding process.

Objectives

The objective of this project is to develop one or more novel Mg alloys more suitable for thixomolding automotive structural components than the current die-casting alloys used for this process. For this project, ORNL will assist Fiat Chrysler Automobiles U.S. LLC (FCA US LLC) and Leggera Technologies in the development of up to two new Mg alloys optimized for the thixomolding process with improved mechanical properties when compared to current die-casting alloys. The primary interest is in improving ductility and fatigue strength, as these are properties that are critical for use in body and chassis structural applications. Since good corrosion resistance is also desirable for this application, this property will also be considered when evaluating promising alloy compositions. Additionally, suitability for heat-treatment to further improve YS, tensile strength, and corrosion performance is of interest, since this capability is not available in current die-casting alloys.

Approach

In consultation with Leggera Technologies, FCA US LLC will establish the desired thixomolding processing parameters, target strength, ductility, and corrosion performance requirements of the new alloy. To understand the relationship between thixomolding process conditions, alloy composition, microstructure, and properties of the current alloys, ORNL will perform a baseline study of two industry standard Mg alloys suitable for thixomolding in collaboration with industrial partners. ORNL has initiated microstructural characterization of an existing thixomolded component fabricated with AM60 using OM and SEM and X-ray microchemical analysis to understand the effect of alloy composition and processing conditions on the microstructural evolution during the thixomolding process and its effect on strength and ductility. The goal of this work is to determine which alloying element additions will result in microstructural modifications that increases both the strength and ductility in the final thixomolded product.

Based on correlations developed in this part of the work, the team will initiate new alloy development by identifying favorable microstructural characteristics for the target mechanical properties. ORNL will establish the feasibility of using computational thermodynamic models to predict the observed microstructure and to simulate the effect of selected alloying element additions on the solidification behavior. ORNL will also identify alloy compositions that have the potential to be successfully fabricated using the thixomolding process, while having the desired microstructure in the final thixomolded component. Laboratory-scale heats will be fabricated at ORNL, and the as-cast microstructure and tensile properties of the alloys will be evaluated to identify the required type and amount of alloying element additions. One or two alloys will be downselected for alloy ingot and chip production for use in the thixomolding process, and a prototype component will be produced by Leggera Technologies. FCA US LLC will coordinate and complete material characterization tests for one new material from samples excised from the component produced by Leggera Technologies and will supervise computer-assisted engineering card development to support component modeling. Finally, FCA US LLC will conduct simulated component structural evaluation using the new properties developed for the computer-assisted engineering card. Figure II.2.2.1 provides a schematic of the approach used in the project.

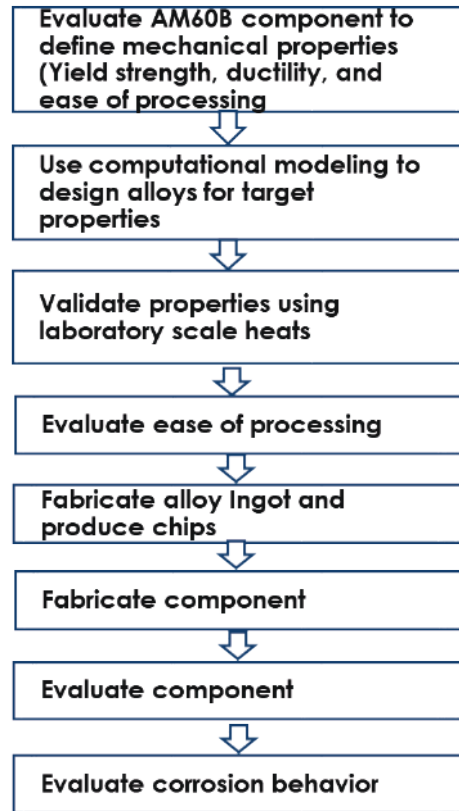


Figure II.2.2.1. Schematic of the approach used in the project. Source: ORNL.

The aim of the alloy development effort used in this project was to develop new alloys for use in the thixomolding process that balance three major characteristics: (1) ease of processing; (2) strength; and (3) ductility. An alloy such as AZ91D exemplifies ease of processing, but at the cost of ductility. AM60B has good ductility and strength, but better processing characteristics are desirable for use in the thixomolding process. Table II.2.2.1 shows the nominal compositions of the alloys, their RT YS, and ductilities [1–4]. Figure II.2.2.2 schematically shows the three required characteristics of the alloys and the current status of properties of AM60B and AZ91D. For the alloy development effort, ease of processing was characterized by the liquidus, solidus, and the melting range (e.g., defined as the difference between the liquidus and solidus) [5]. AZ91D has a significantly greater melting range and lower solidus when compared to AM60B, which was associated ease of processing. Hence, lower solidus and wider melting range were targeted for the new alloys.

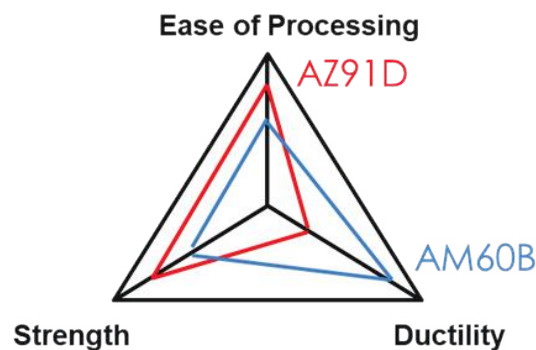


Figure II.2.2.2. Schematic showing the three characteristics of interest for alloys used in the thixomolding process. Source: ORNL.

Table II.2.2.1. Die-Casting Alloys, Compositions, and Mechanical Properties

Alloy	Mg	Al	Zn	Mn	Sr	YS (MPa)	% Elongation
AM60B	Bal.	6	0.2	0.3	0	121	16
AZ63A	Bal.	6	3	0.15	0	130	5
AJ52	Bal.	5	0	0.4	2	126	9
AZ91D	Bal.	9	0.7	0.3	0	158	6

Results

In the previous year of the project, several promising alloys were identified based on their liquidus, solidus, and melting range, and laboratory-scale heats were cast for evaluation. Tensile properties were measured in the as-cast condition and promising alloys were identified in a patent application [1]. Based on the calculated melting range and ductility obtained in the as-cast condition, two alloys—Alloy #1 and Alloy #6—were identified with a melting range close to that of AZ91D and with percent elongation to failure better than that of AZ91D, as shown in Figure II.2.2.3.

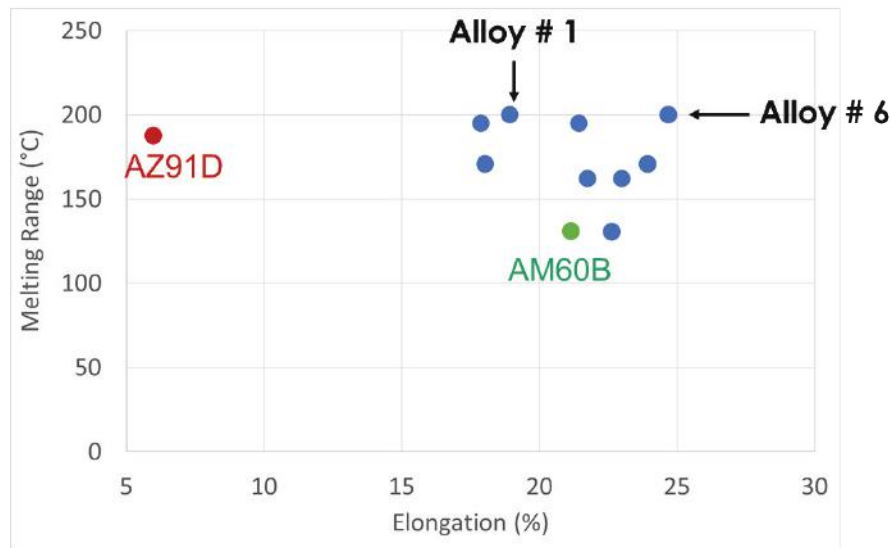


Figure II.2.2.3. Melting range and % elongation of experimental alloys. Source: ORNL.

Alloy coupons were also tested for their corrosion resistance using ASTM G85 Annex 2 testing protocol, which is a cyclic acidified salt spray tests, with a target duration based on 10 years of service. The coupons were treated using a standard pre-treatment and powder coat prior to testing. Figure II.2.2.4 shows a visual comparison of the control and the new Alloy #1 after five weeks of testing, which clearly shows the combination of properties in the new Alloy #1 produces better corrosion performance than the baseline AM60B when subjected to similar protective coatings and testing conditions.



Figure II.2.2.4. Visual evaluation of corrosion tested coupons: (a) AM60B control and (b) Alloy #1. Source: FCA US LLC.

A total of 12 billets of the two downselected alloys—Alloy #1 and Alloy #6—were cast using a 9.5 in. diameter vertical permanent mold. These castings had to be extruded into a shape compatible with the machine used to manufacture chips that could be used for the thixomolding process. The castings produced were turned and sectioned in 9 in. diameter \times 30 in. long extrusion billets. Extrusions measuring 5.0 in. wide \times 3.5 in. tall were produced using the machined billets to facilitate their use in downstream processes. Tensile specimens were extracted from the remnants of the castings, as observed in Figure II.2.2.5(a), and from sections obtained from the extrusions, as indicated in Figure II.2.2.5(b). It was anticipated that the grain size in the extrusions would be more similar to those obtained after thixomolding, and hence, the properties obtained from the extrusions could be used as a guidance for the properties that would be achieved in the thixomolded part [3].



Figure II.2.2.5. (a) Remnants from cast billet. (b) Section from an extrusion. Source: ORNL.

Figure II.2.2.6(a) shows the yield strengths of Alloy #1 and Alloy #6 in the as-cast and extruded condition. As can be observed from the figure, the yield strengths of both alloys increase after extrusion due to its finer grain structure. Yield strengths after extrusion of ~ 140 MPa and ~ 180 MPa of Alloy #1 and Alloy #6, respectively, are greater than that of AM60B. Elongations to failure of the two alloys are $\sim 11\%$ and 16% for Alloy #1 and Alloy #6, respectively as shown in Figure II.2.2.6(b), with Alloy #6 showing values comparable to that of AM60B. It should be recalled that both alloys have a melting range that would likely improve the processability in the thixomolding process. Extrusions from both alloys are awaiting chipping and part fabrication.

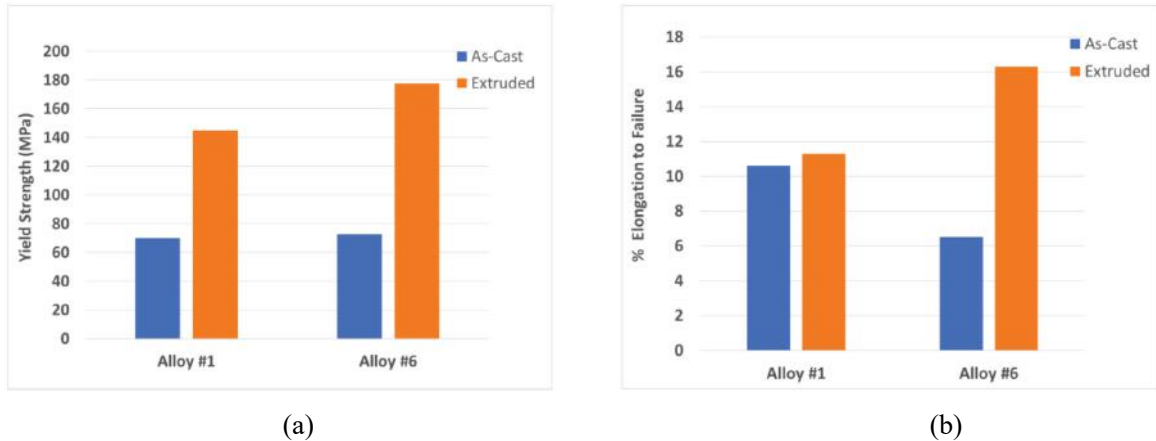


Figure II.2.2.6. (a) Yield strengths of Alloy #1 and Alloy #6 in the as-cast and extruded conditions and (b) percent elongation to failure of Alloy #1 and Alloy #6 in the as-cast and extruded conditions. Source: ORNL.

Conclusions

New alloys required for thixomolding applications have to balance ease of processing, strength and ductility. Computational modeling was used to identify promising alloys that would have better processing characteristics than the current baseline alloy AM60B while retaining strength and ductility. Two promising alloy compositions were identified and scaled-up to industrial scale castings. Castings were extruded in preparation for fabrication of chips to be used for thixomolding components. Mechanical testing of extruded materials with a microstructure similar to that expected in a thixomolded part showed good strength and ductility for the new alloys. Future work will fabricate a component and evaluate microstructure and properties.

Key Publications

1. Muralidharan., G., B. Macek, and N. Sanko, 2022, “New magnesium alloys for thixomolding applications,” Provisional Patent Application 63/433,077, filed 16 December 2022.

References

1. Luo, A. A., 2013, “Magnesium casting technology for structural applications,” *J. Magnes. Alloy*, Vol. 1, No. 1, pp. 2–22. <https://doi.org/10.1016/j.jma.2013.02.002>.
2. Patel, H. A., D. L. Chen, S. D. Bhole, and K. Sadayappan, 2010, “Microstructure and tensile properties of thixomolded magnesium alloys,” *J. Alloys Compd.*, Vol. 496, No. 1–2, pp. 140–148. <https://doi.org/10.1016/j.jallcom.2010.02.042>.
3. Avedesian, M. M., and H. Baker (eds.), 1999, *Magnesium and Magnesium Alloys*, ASM International, Materials Park, OH, USA.
4. Moosbrugger, C. (ed.), 2017, *Engineering Properties of Magnesium Alloys*, ASM International, Materials Park, OH, USA.
5. Czerwinski, F., 2004, “Processing features of thixomolding magnesium alloys,” *Die-Casting Engineer*, Vol. 48, No. 6, pp. 52–58.

Acknowledgments

The authors would like to acknowledge J. Caris and N. Farkas of Magnesium USA for their assistance with the alloy scaleup and extrusions. The authors also would like to thank the following from ORNL: R. Davies and A. Haynes for their support; K. Hedrick for mechanical property measurements; and V. Cox and C. Duggan for metallography.

II.3 Carbon Fiber and Polymer Composites

II.3.1 Composites Core Program

II.3.1.1 High-Temperature Carbon Fiber Carbonization via Electromagnetic Power (Oak Ridge National Laboratory)

Felix L. Paulauskas, Principal Investigator

Chemical Sciences Division
Oak Ridge National Laboratory
1 Bethel Valley Rd.
Oak Ridge, TN 37831
E-mail: paulauskasfl@ornl.gov

Rich Davies, Composites Core Program Manager

Oak Ridge National Laboratory
Materials Science and Technology Division
1 Bethel Valley Rd.
Oak Ridge, TN 37831
E-mail: daviesrw@ornl.gov

H. Felix Wu, DOE Technology Development Manager

U.S. Department of Energy
E-mail: felix.wu@ee.doe.gov

Start Date: November 17, 2020 End Date: June 30, 2023
Project Funding (FY 2022): \$2,000,000 DOE share: \$2,000,000 Non-DOE share: \$0

Project Introduction

HTC of polymer fiber via EM power is a project that aims to develop an innovative and scalable process for the final stage of CF conversion by reaching sufficiently high coupling and temperature elevation of the material. This project is the continuation of a previous effort dedicated to LTC that will complete the portfolio of technologies developed by ORNL and 4XTechnologies, funded by DOE, which are intended to replace the conventional carbonization technology used in the CF industry. This is a joint development research project carried out by ORNL and 4XTechnologies (formerly RMX Technologies) that is fully funded by DOE. Preliminary work on EM carbonization was initiated at ORNL with the microwave assisted plasma project, and then jointly continued with 4XTechnologies since 2013. This report covers progress made on the project during FY 2022.

ORNL and 4XTechnologies recently completed the development of a new LTC technique for the manufacture of CF. This successful LTC project demonstrated that close proximity electromagnetic carbonization (CPEC)⁸ technology is feasible and scalable⁹ and produces CF with the tensile strength meeting or exceeding 500 kilopound per square inch (ksi) after subsequent conventional HTC processing. This novel technology has the potential to significantly reduce the cost of manufacturing CF by reducing energy consumption and processing time, while also decreasing maintenance, capital, and labor requirements. This new method utilizes an EM heating technique that operates at atmospheric pressure. Nevertheless, this process still requires a final HTC stage to produce completed CF, which itself is highly energy-intensive and high maintenance. The recent achievements and the need for cost reduction in CF production justifies the pursuit of this HTC project.

⁸ CPEC: Close Proximity Electromagnetic Carbonization is the given name to the technology developed for the EM-powered LTC stage.

⁹ The last prototype built with the CPEC technology (LTC project) was rated to 1.0 annual metric ton of CF.

EM processing is, in general, characterized by direct deposition of energy into the material by dielectric coupling. This leads to faster and more efficient energy deposition than conventional processing, provided the dielectric properties are adequately aligned with the coupling requirements. This was the case with the LTC project. However, with HTC, the feedstock material shows unfavorable dielectric properties, since the polymer has already been exposed to a thermal treatment, thus making the fiber electrically conductive. This critical difference must be considered in the design for the HTC process. The progress with EM LTC has already reduced the residence time to less than one minute as compared to 90 seconds or more for conventional processing). Fiber processed by EM LTC and then conventionally carbonized at high temperature produces CF with tensile properties above 500 ksi. Related to energy efficiency deposition per unit mass in the EM LTC, the experimental work showed it is possible to decrease the energy consumption compared to the lowest value of a benchmark¹⁰ by approximately 40% under certain conditions. These conditions include the limitation of the control volume to the applicator¹¹ only.

The goal of this new project is to develop an EM-based technology to replace the conventional HTC stage while producing CF with comparable mechanical properties. The scope of this project is limited to high-temperature carbonization and will capitalize on the knowledge and experience gained from former successful projects such as EM LTC and microwave assisted plasma. The HTC apparatus operates at a higher power density level compared to devices built for LTC. The primary mechanism for the HTC applicator is a hybrid of the two different configurations explored at LTC, thereby providing a novel pattern of radiation while still operating at atmospheric pressure. The ultimate goal is to make EM HTC technology more efficient than conventional technology and increase its scalability for use in industrial production lines.

Objectives

The objective of the HTC project is to develop a faster and more efficient carbonization process than the current conventional one. The concept is to focus the energy deposition on the material and limited parts of the furnace with the goal of reducing the unit energy consumption (in kWh/kg) by approximately 20%, while producing the same (or better) CF quality. This achievement would represent about a 5% cost reduction of the overall CF manufacturing process. The HTC furnace is designed to treat at least four tows of 24,000 filaments.

Approach

The HTC project is split into four phases over a two-year effort. The first three phases are dedicated to the design and construction of the experimental setup, which represents Year 1 of this HTC program. The second and final year will be dedicated to the experimental work, which will include testing, as well as all needed upgrades. The four phases are summarized and described in Table II.3.1.1.1. The HTC technology is co-developed by ORNL and 4XTechnologies.

¹⁰ Details about benchmarks can be found here: Ellringmann, T., C. Wilms, M. Warnecke, G. Seide, and T. Gries. 2016. "Carbon fiber production costing: a modular approach," *Text. Res. J.*, 86(2), 178–190. <https://doi.org/10.1177/0040517514532161>.

¹¹ If the controlled volume is extended to include the generator and its cooling system, the energy yield per unit mass of the experimental setup becomes greater than the lowest value of the benchmark; this is mostly because the generator has a low energy conversion yield, with only around 41% of consumed electric power being converted into EM energy.

Table II.3.1.1.1. Phased Approach to HTC Project

Phase	Name	Year	Status as of Sept. 2021	Description
1	Modeling and design	FY-21	Completed	Evaluation, modeling, design, sourcing.
2	Construction	FY-21	Completed	Construction of the setup with all subsystems.
3	Commissioning	FY-21	Completed	Performance test and adjustment of each subsystem. This phase includes the safety evaluation.
4	Operation	FY-22	Completed	Testing, upgrade, and energy evaluation of the setup.

Results

Summary of Previous Year

FY 2021 was the first year of the HTC project. As of September 30, 2021, design, procurement, construction, and commissioning were completed. The HTC applicator and all its ancillary equipment were declared ready for operation, validating milestone M3.¹² At this point, the project accrued approximately three months of delay compared to the initial schedule proposed in the DOE Annual Operating Plan (AOP) FY 2021, and the fourth milestone (M4)¹³ related to material production had to be rescheduled to FY 2022.

The three-month delay was due to the following factors:

- The project effectively began in the second half of November 2020 because of an administrative delay.¹⁴
- Some critical parts were delivered with a five-week delay in the final quarter.
- The research team had been contaminated by the COVID-19 virus in the final quarter.

Therefore, the milestone schedule in the AOP of FY 2022 was amended. In this new schedule, the production of fiber (e.g., Milestone M4) was set to 30 December 2021, and the three follow-on milestones were rescheduled, keeping the overall timeline and resources of the project unchanged. As of 1 October 2021, the project completion date remained 30 September 2022¹⁵ with the same budget.

Sourcing and Equipment and Its Impact on the Schedule

This project involves the construction of an experimental setup. The sourcing and equipment preparation is one of the major tasks of this HTC project. The effort dedicated to this task took the entire first year of this project and, due to a technical issue that arose during the experimental work, a substantial part of the second as well. Thus, some modifications and refurbishment were needed over FY 2022. The procurement phase for those refurbishments exceeded the scheduled time allocated to these circumstances. At the time of the conception of this project and based on the experience of the LTC project, the hardware sourcing was anticipated as one of the major risks. The reasons are:

8. This project is based on the construction of a prototype. This type of task requires a large number of custom parts from multiple suppliers.
9. The suppliers related to EM power equipment carry limited to no stock of their regular products, typically have a long lead time (months), and frequently exceed them (months).
10. Some parts are not readily available on the market, especially when purchased for research and development purposes; this is the case for the oxidized precursor fiber (OPF) feedstock material.

¹² Milestone M3: Commissioning of HTC hardware and demonstration of stable/proper operation of all subcomponents for 15 min.

¹³ Milestone M4: Successfully carbonize material on a continuous basis in the HTC process with carbonized material achieving a minimum density of 1.6g/cc, a minimum mechanical properties of 300 ksi tensile strength, and a 25 Msi modulus.

¹⁴ The contract between the two main project participants (ORNL and 4XTechnologies, LLC) was signed on November 18, 2020.

¹⁵ During FY 2022, this date will have to be changed to 30 June 2023.

This FY, some parts related to the EM transmission line failed during operation. Those parts needed either repair, replacement, or upgrade. The sourcing of those parts negatively impacted the project for the reason described in No. 2 in the list above.

In addition to the inerrant risks related to the sourcing of specific items to this project, the circumstances related to COVID-19 remained up to this FY. Over the past two years, supplier lead times have been impacted in a random manner; thereby increasing substantially on average.

Safety Management

The safety concerns remain identical to those encountered with the former LTC project and were addressed at that time. Aside from regular electrical hazards inherent to any equipment powered with high-power and high voltage (e.g., 480 VAC, 3 phases), the two additional concerns needing special care were:

- **Toxic Off-Gassing:** This hazard is a well-known and common to any work of CF carbonization. An appropriate ventilation system was available and gas detectors are connected to a control system.
- **EM Radiation:** The hazard related to the leakage of non-ionizing radiation is the most sensitive one since it is not perceptible by humans. The hardware is designed to limit any EM leakage, and mobile probes and fixed sensors connected to the control system ensure the exposure of operators never exceeds the limit of population exposure.¹⁶ [1]

The management of the hazards related to the current HTC project was substantially eased thanks to the legacy of the LTC project.

Experimental Work and Progress

Process with Material A: 300k Filament Ribbon¹⁷ from a Box

The experimental work began in September 2021 using a large ribbon of 300k filaments. This material is an oxidized polyacrylonitrile (PAN) fiber considered as ‘commodity grade’ industrially produced by a CF manufacturer. In this work, the OPF is fully carbonized in a single process, using two furnaces inline (e.g., LTC, HTC). Both furnaces are EM-powered. The configuration of the setup used for the carbonization, as shown in Figure II.3.1.1.1, is as follows: Feedstock Material—box of 180 kg of a continuous OPF ribbon of 300k filaments; Stretcher #1; LTC furnace (e.g., the EM power source which was built during the former LTC project); Stretcher #2; HTC furnace (e.g., the EM power source, which was built during the current HTC project); Stretcher #3; splitter; and the take-up winder (four positions).

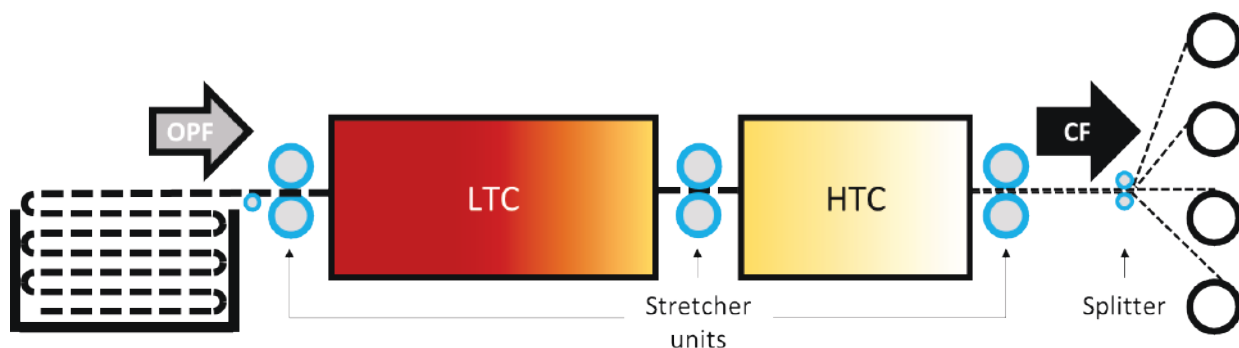


Figure II.3.1.1. Carbonization in one-step of a 300k ribbon of commodity grade OPF using two EM-powered furnaces set-up inline. Source: ORNL.

¹⁶ Based on International Commission on Non-Ionizing Radiation Protection (ICNIRP) recommendation.

¹⁷ A ribbon of fiber is defined as a large and flat band (belt) of filaments substantially wider than regular tows.

Continuous samples were collected following several attempts. The results in Table II.3.1.1.2 and Figure II.3.1.1.2 show:

- Mechanical properties that satisfy the criteria of the programmatic milestone M4
- Large deviation on the tensile strength (e.g., 30%–50%)
- Some deviation across the width of the process (e.g., the left side is less processed than the other parts of the tow)
- Some damage on the tow may happen.

Measured values are the first numbers and the standard deviations are in parentheses. Tensile strength is the value of primary importance. Its value on the left side of the sample is smaller than others and its standard deviation for the dataset is large (e.g., 30% or more). The modulus shows quite consistent values with a low standard deviation.

Table II.3.1.1.2. Mechanical Properties of a Continuous Sample Fully Carbonized with the LTC and HTC EM-Powered Furnaces

Four Sampling Locations on the 300k Filament Ribbon				
Sampling Location	Diameter [μm]	Tensile Strength [ksi]	Modulus [Msi]	Strain [%]
Off-Center	8.3 (0.4)	380 (156)	29.3 (1.2)	1.25 (0.45)
Central Zone (Damaged Area)	8.5 (0.2)	334 (123)	27.7 (0.9)	1.20 (0.40)
Right Side	8.0 (3.2)	327 (104)	29.5 (1.3)	1.08 (0.27)
Left Side	8.3 (0.3)	269 (134)	27.9 (0.9)	0.96 (0.44)

Note: Measured values are the first numbers and the standard deviations are in parentheses.



Figure II.3.1.2. Picture of a continuous sample of 300k filaments ribbon coming out of the HTC before the split. The yellow tags delimit the processing conditions. Minor damage can be noticed in the center left of the sample. Source: ORNL.

The density of the continuous sample, as shown in Figure II.3.1.1.2, was measured at $\rho = 1.7573 \text{ g/cc}$, which is typical¹⁸ for CF. Multiple basic electrical measurements showed the resistance of a $\sim 50 \text{ mm}$ length of material is in the 1Ω range, as shown in Figure II.3.1.1.3. This shows the material has been carbonized across the entire width of the ribbon and demonstrates the furnace can treat the full width. Finally, the mechanical properties of single filaments reported in Table II.3.1.1.2 confirm the material is fully carbonized.



Figure II.3.1.3. Random resistance measurements of the continuous batch sample. Most of the values are in the 1Ω range or below, as shown in the pictures. This value is typical of fiber that has been processed at 1200°C or higher. (Note: the unknown number of filaments between the probes is a limitation of the accuracy of this method.) Source: ORNL.

This configuration, using a large ribbon of OPF (e.g., Material A), provided results in accordance with the expectation of the first milestone involving mechanical properties. However, it quickly showed some limitations related to the overall processability of such a wide ribbon. Indeed, the ribbon exceeds the specification of some pieces of equipment. Both furnaces (e.g., LTC, HTC), as well as the take-up winder, were designed to handle four tows of 50k filaments.¹⁹ Two issues resulted:

1. The HTC furnace is too narrow to process such a wide ribbon. Indeed, the natural spread of the ribbon exceeds the opening of the entrance, and a set of nip rollers must be implemented to adjust its width. This results in a material accumulation on both edges of the ribbon, offering some disparity in its thickness. This may contribute to the deviation observed in the dataset.
2. The available take-up winder is limited to four individual tows of 50k filaments. By using a single ribbon of 300k filaments, this specification is largely exceeded, and the ribbon significantly overwhelms the pulleys. One solution consists of splitting the ribbon into four tows. Unfortunately, a split generates damage on the collected material as shown in Figure II.3.1.1.4(a). This non-ideal solution allows for the collection of continuous, but short samples. The process had to stop once the damage prevented proper operation, as observed in Figure II.3.1.1.4(b).

If the ribbon is pristine coming out of HTC, there is still a high probability of jamming the winder ($\sim 90\%$) after a few minutes of operation due to the splitting. If the material is already damaged coming out of HTC, the jamming happens even faster. This issue led to the following conclusions:

- The full carbonization of a 300k filament ribbon is possible with the applicator as designed.
- The 300k filaments overload the HTC applicator. This applicator was designed for a maximum 200k filament.
- The process of a large ribbon of fiber is not sustainable with the existing winding equipment, which is limited to 50k tows.

¹⁸ Most commercial CF have a density in the range of $1.74\text{--}1.80 \text{ g/cc}$.

¹⁹ Like for the LTC project, the commitments of all programmatic milestones of this project are based on the continuous processing of 4 tows of 24k filaments simultaneously. However, as a safety factor, all hardware was designed to process for tows of 50k filaments.

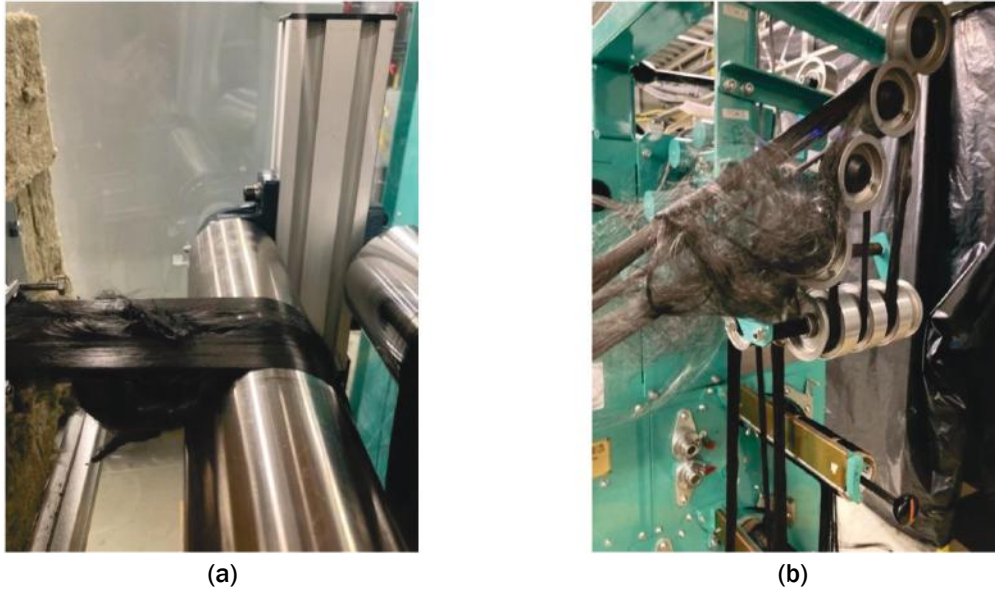


Figure II.3.1.4. (a) Damage of moderate importance coming out of the HTC furnace which might randomly create a filament jam in the cavity of the furnace. This damage is systematically exacerbated by the splitter (not shown) and (b) results in a ‘Gordian knot’ that fails to pass through the winder. Source: ORNL.

It was concluded that processing a 300k filament ribbon (e.g., ‘Material A’) with this hardware configuration was possible for shot runs, but not sustainable for production runs. Another OPF material (e.g., ‘Material B’) was also available in spools of 50k filaments, so it was decided to discontinue the work with Material A.

Processing of Two 50k Tows: Material B, in Spools

The available material in spool form is also an industrial product of the same nature as the ribbon of the 300k filament previously used—both are commodity grade OPF. Material B was purchased from another CF manufacturer and was a holdover from the previous LTC project. This material comes in spools of 50k filaments. Its usage with the HTC project began by the end of the second quarter of FY 2022. Material B was not used sooner due to its limited supply. The change of material resulted in immediate success. The use of Material B eliminated all failures caused by handling impairment (e.g., material overload and tow split). The amount of material to be processed was initially restricted to two tows to keep the process simple (one-step), as shown in Figure II.3.1.1.5 and to match the milestone requirements, all while limiting the material consumption.

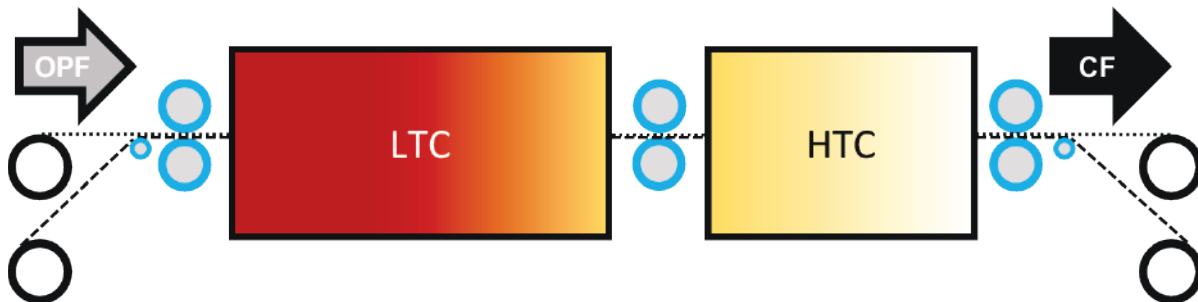


Figure II.3.1.5. Carbonization in one-step. Two tows of 50k filaments of commodity grade OPF using two EM-powered furnaces setup inline. Source: ORNL.

As of June 30, 2022, Milestone M6 and M7 were successfully completed. This was achieved with tests performed using two tows of 50k filaments each, for a total of 100k filaments. Mechanical properties²⁰ are presented in Table II.3.1.1.3 and Table II.3.1.1.4. In Table II.3.1.1.4, two outliers are observed on Tow #2 at 1.69 g/cc and 1.86 g/cc. A contributing factor to this large variation in density is the fact that the tows were not perfectly centered during the process in HTC only.

Table II.3.1.1.3. Mechanical Properties of Two Tows of 50k Filaments Simultaneously Processed with LTC and HTC Devices Inline That Are EM-Powered and Maintained Constant for All Samples with the Main Variable Among the Samples Being the Total Residence Time (LTC + HTC)

Tow	Fiber Type	Sample #	Diameter [μm]	Tensile Strength [ksi]	Modulus [Msi]	Strain at Breakage [%]
#1	LTC	1	8.32 (0.20)	198.44 (39.18)	8.07 (0.22)	2.46 (0.47)
	HTC	2	6.84 (0.36)	536.98 (124.27)	33.05 (1.32)	1.57 (0.33)
	HTC	3	6.99 (0.46)	514.92 (146.12)	31.05 (1.21)	1.60 (0.43)
	HTC	4	6.48 (0.61)	595.57 (88.31)	30.75 (1.21)	1.87 (0.25)
	HTC	5	6.92 (0.24)	514.88 (152.90)	29.32 (1.26)	1.68 (0.44)
#2	LTC	1	8.28 (0.40)	187.89 (54.99)	9.37 (1.76)	2.07 (0.71)
	HTC	2	6.80 (0.49)	512.48 (166.19)	32.15 (0.87)	1.55 (0.49)
	HTC	3	6.80 (0.52)	568.89 (105.15)	31.48 (0.67)	1.75 (0.32)
	HTC	4	6.58 (0.46)	559.88 (107.20)	31.06 (1.35)	1.72 (0.29)
	HTC	5	7.59 (0.29)	427.17 (139.50)	23.74 (2.17)	1.73 (0.50)

*Total residence time (LTC + HTC) color code: orange > red > 1 min > brown > green. Sample 1 (black) is LTC treated only.

Table II.3.1.1.4. Density of the Samples Reported In Table II.3.1.1.3 With an Average Density of the HTC Samples of ~1.76 g/cc

Sample	Carbonization	Tow #1 [g/cc]	Tow #2 [g/cc]	
1	Black	LTC	1.6211	1.6149
2	Orange	HTC	1.7580	1.7515
3	Red	HTC	1.7594	1.6842
4	Brown	HTC	1.7414	1.7704
5	Green	HTC	1.7775	1.8581

²⁰ These results were already presented during the last Vehicle Technology Annual Merit review 2022.

Table II.3.1.1.3 and Table II.3.1.1.4 show relevant mechanical properties in the 500–550 ksi range for the tensile strength and 30–31 Msi for the modulus for nearly the entire dataset. This example demonstrates the process is able to produce good CF (above 500 ksi) continuously with 100k filaments. Sample 4 (brown) exceeds the 550 ksi and 29 Msi required to validate milestone M7 for both tows. Furthermore, the final density of this sample is an average of ~ 1.76 g/cc and its residence time is observed being under 60 s for both LTC and HTC processes combined. Regarding this latter consideration, the performance of the HTC has the potential to process 100k filament fiber substantially faster than the initially expected residence time of 160 s. However, some discrepancies might be noted:

11. The deviation, specifically across the tensile strength dataset, is on the high-end of desired values.
12. Outlier (unusual data) points were observed among the densities and the tensile strength especially with sample #4 (green), which is the one that received the shortest treatment.
13. The HTC system shows a relatively high reflection level of 9dB.

Points 1 and 2 are not critical. However, Point 3 is of higher importance; see the section entitled, “System Failure and Damage.”

Processing of Four 50k Tows (Four Spools)

Based on the programmatic milestones, the goal of this HTC project is to carbonize continuously four tows of 24k filaments for a total of 98k filaments, as observed in Figure II.3.1.1.6. Despite some tests that have been successful with 100k filaments using two tows of 50k, it has been decided to continue the experimental work with four tows of Material B. These tests will allow the ability to assess the following aspects:

- Better assessment of the energy distribution across the entire width of the applicator: Two tows of 50k filaments do not spread as much as four tows of 24k filaments. The Addition of material will increase the width of the material to be processed.
- Evaluation of the processing performance as a function of the load: the material quantity increase might impact both residence time and processes. Those two characteristics of the HTC applicator must be known.
- The input material quantity has been a critical variable in the study of energy performance with the LTC applicator in the former project and is anticipated to be of similar importance with this HTC project.

At the time of the first attempt with four tows—9 June 2022—the operation was discontinued due to malfunction and system failure. No sample could be collected and no data is available with this amount of material. Another attempt has not been possible as of 30 September 2022. More details hereafter.

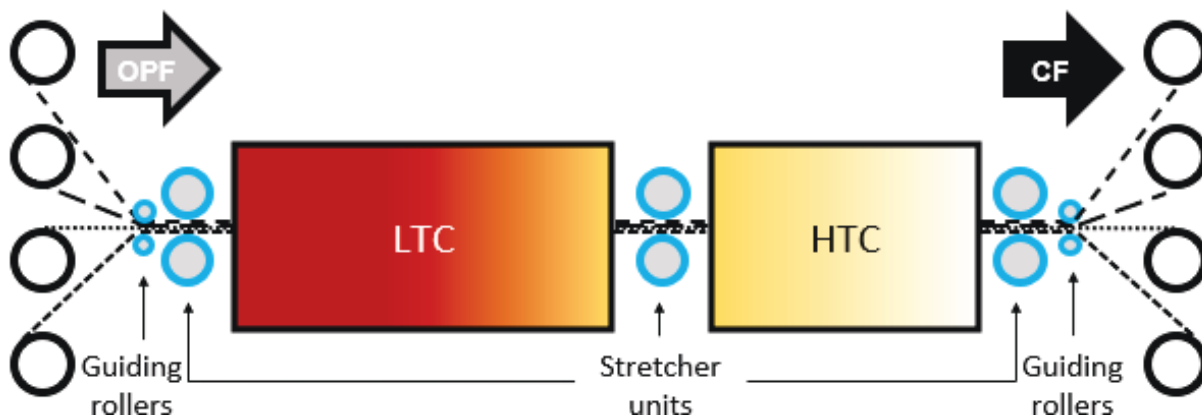


Figure II.3.1.6. Carbonization in one-step of four tows of 50k filaments of commodity grade OPF using two EM-powered furnaces set-up inline. Source: ORNL.

System Failure and Damage

On 9 June 2022, the system failed when the HTC system reached temperature, triggering the safety mode on the generator and the emergency stop automatically enabled when return loss was detected. The root cause of this failure was a poor tuning configuration, resulting in a -9dB return loss on average across all ports. The presence of a standing wave in the transmission line induces a derating of some components. A short degradation of the return loss on one port created a standing wave exceeding the rating capability of one piece of equipment. This piece melted and initiated a chain reaction of damage that impacted nearby components. The damage was substantial, as indicated by the examples shown in Figure II.3.1.1.7(a) and Figure II.3.1.1.7(b), thus requiring the ordering of new parts in late June and early July. However, most of this replacement equipment is custom-made and the parts of interest required several more months to acquire due to the limited supply. Most of the replacement parts had been delivered as of 30 September 2022, with the exception of one critical part, thereby allowing only very limited progress. These long lead times severely impacted the schedule. At the end of FY 2022, the programmatic milestone M8 and the follow-on efforts were not completed. An extension at no additional cost was agreed to by DOE to complete the project.

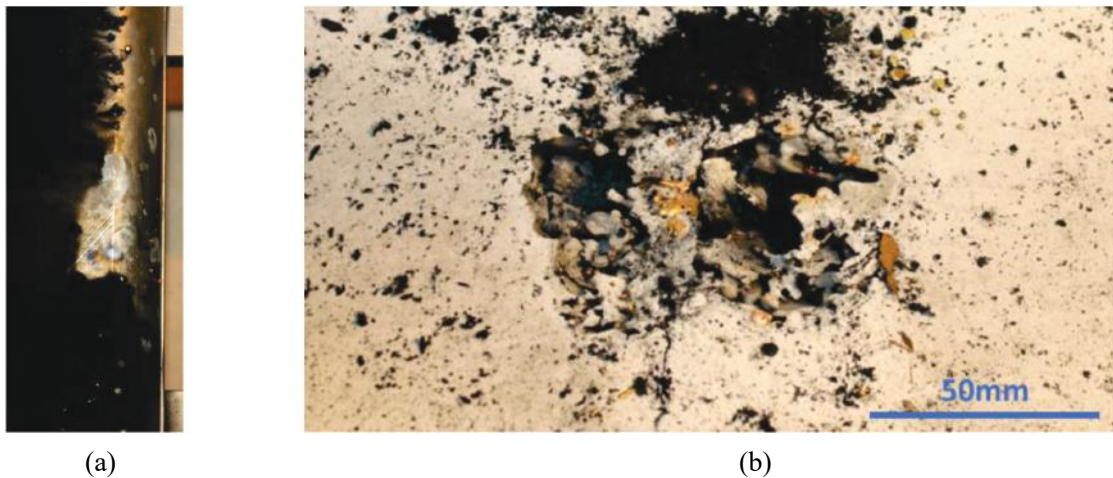


Figure II.3.1.7. Example of a damaged areas. (a) Metallic part of the cavity partially covered with dark soot showing obvious pitting and the signature of undesirable arcing. (b) Molten metal (in yellow) on top of damaged insulation. Source: ORNL.

Additional technical issues were encountered prior to the equipment failure shown in Figure II.3.1.1.7. Among the most significant is the one related to thermocouple failure. Thermocouple of Type K and, subsequently, Type B were tested and failed. An example this hardware failure is pictured in Figure II.3.1.1.8. Those thermocouples are essential to the process. Their failure had a moderate impact on the project, due to their long lead time to replace, especially for the Type B thermocouples.

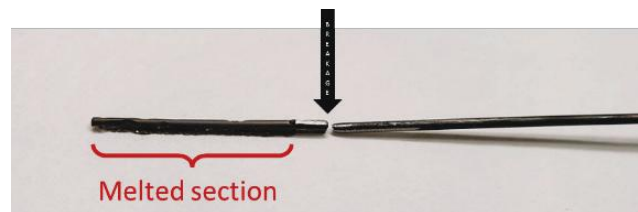
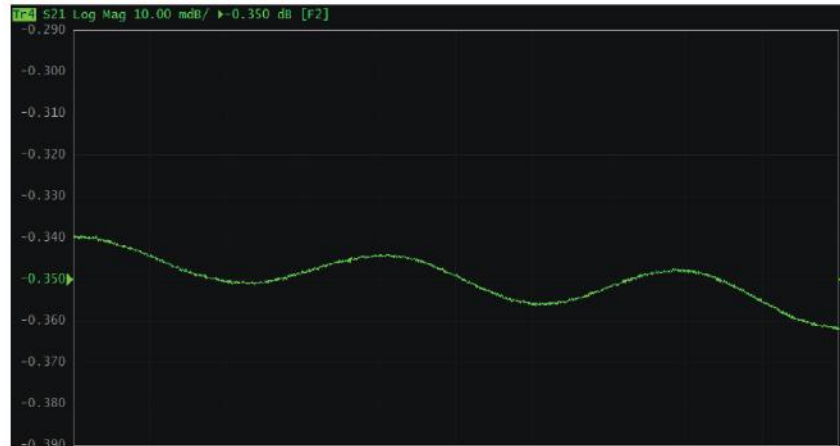


Figure II.3.1.8. Type K thermocouples of 1/16 in. (~1.6mm) were used to probe the process. This thermocouple experienced two levels of damage: (1) the tip melted during the process; and (2) the tip could no longer travel through the bore after the process cooled down and broke during the replacement procedure. The thermocouples in similar locations were replaced with Type B that failed in a comparable manner. Source: ORNL.

The full set of thermocouples eventually will be replaced. As of 30 September 2022, the new set was received, but was not tested at the operational temperature due to other backlogged parts.

The HTC Setup: Reconstruction and Testing (M9)

Some of the parts that were received had to pass through a series of tests—the most important of which was the measurement of the forward voltage gain, S_{21} . An example of those measurements are shown in Figure II.3.1.1.9. The scattering parameter is measured across the band of interest using a vector network analyzer and represents the attenuation of the signal across the component at the frequency of interest. The first component has the lowest attenuation of the set between -0.34 dB and -0.36 dB. The second component shows the strongest attenuation of the set, between -0.46 dB and -0.52 dB.



(a)



(b)

Figure II.3.1.1.9. Example of two custom components (from the same manufacturer) tested for their forward voltage gain (S_{21}) for (a) the first component and (b) the second component. Source: ORNL.

The inspection and measurements showed that the custom-made components do not have identical characteristics. The attenuation range is from 7.5%–11%. The component will be selected and installed on the setup according to performance as compared to other subsystems. Some modification on the setup was completed and tuning tests begun. Due to a critical missing part, those tuning tests cannot perform at full power, but are indicative of the tuning capability of the applicator.

Ancillary Tasks Not Directly Related to This Project

ORNL cannot currently produce quantities of the precursor autonomously, which represents ~50% of the cost of CF, at the level needed to demonstrate fully and cost-effectively new CF approaches in composite test articles. For multiple reasons, such as the restricted number of manufacturers, their fear of reverse engineering, etc., it is a real challenge to acquire a reliable supply of PAN precursors on the open market. ORNL encountered this difficulty multiple times over the past few decades, frequently delaying or even compromising some projects.

At the end of FY 2022, a spinning line is one of the final pieces of equipment ORNL needed to cover the entire production stream of PAN fiber. During FY 2022, a wet spinning line was identified that provides the appropriate scale to match the CF conversion development and demonstration capabilities already at ORNL. The acquisition of this industrial line at a reasonable cost is an exceptional opportunity, thus allowing ORNL to support multiple projects with custom material at different levels of processing without having to rely on external suppliers. This will significantly increase ORNL's capacity to develop new technologies of precursors for future materials. To expediently acquire this unique capability, ORNL worked with DOE to modify the AOP of the HTC project for FY 2022 by adding a task focused on the acquisition of the wet spinning line. The equipment will be supplied by Dienes Corporation (Mülheim, Germany). Some upgrades have been specified to meet ORNL's needs and upgrade the laboratory to the current state-of-the-art level. The specifications were submitted before 30 September 2022. The purchase order is expected to be issued in the first quarter of FY 2023 to complete milestone M8 of the most recent AOP.

Conclusions

The work conducted in FY 2022 led to the following achievements:

- Testing of equipment built the previous year.
- CF production from a 300k filament ribbon of commodity grade OPF, thus matching the property requirements of milestone M4 only. Mechanical properties achieved were: $260 \text{ ksi} \leq \text{tensile strength} \leq 380 \text{ ksi}$ and $27.5 \text{ Msi} \leq \text{modulus} \leq 29.5 \text{ Msi}$.
- CF production from tows of 50k filaments from spools of commodity grade OPF. All property requirements were exceeded (i.e., milestones M5, M6, and M7). The mechanical properties that were achieved were: $427 \text{ ksi} \leq \text{tensile strength} \leq 595 \text{ ksi}$ and $23.5 \text{ Msi} \leq \text{modulus} \leq 33 \text{ Msi}$.

These achievements demonstrated the relevance of the process. However, due to significant hardware failure, milestones M8 to M10 could not be completed by the end of FY 2022 as originally planned. Several parts of the system have been irreparably damaged and need to be replaced. Some replacement parts were already available, though others required months to order and acquire. Consequently, this project required an extension at no additional cost. A new milestone schedule, factoring potential delays from the suppliers, has been issued in the AOP for FY 2023. As such, the HTC project is currently set to end on 30 June 2023.

Key Publications

Based on the work accomplished during the previous LTC project, work at the foundation of the current project, two patents were submitted to the United States Patent and Trademark Office (USPTO) on 3 September 2022. The application numbers are 4XT-1 17/902,815 and 4XT-2 17/902,818.

References

1. International Commission on Non-Ionizing Radiation Protection (ICNIRP) Guidelines on Limiting Exposure to Electromagnetic Fields (100 kHz to 300 GHz), *Health Phys* 118(5): 483–524; 2020 <https://www.icnirp.org/cms/upload/publications/ICNIRPrfgdl2020.pdf>.

Acknowledgments

This research was sponsored by DOE-EERE VTO, performed at ORNL, and managed by UT-Battelle, LLC, for DOE under AOP project contract DE-AC05-00OR22725.

II.3.1.2 A Novel Manufacturing Process of Lightweight Automotive Seats – Integration of Additive Manufacturing and Reinforced Polymer Composite (Oak Ridge National Laboratory)

Vlastimil Kunc, Principal Investigator

Oak Ridge National Laboratory
2350 Cherahala Blvd.
Knoxville, TN 37932
E-mail: kuncv@ornl.gov

Rich Davies, Composites Core Program Manager

Oak Ridge National Laboratory
Materials Science and Technology Division
1 Bethel Valley Rd.
Oak Ridge, TN 37831
E-mail: daviesrw@ornl.gov

H. Felix Wu, DOE Technology Development Manager

U.S. Department of Energy
E-mail: felix.wu@ee.doe.gov

Start Date: February 1, 2020	End Date: September 30, 2022	
Project Funding (FY 2022): \$500,000	DOE share: \$500,000	Non-DOE share: \$0

Project Introduction

This project is aimed at developing a novel manufacturing technique to produce lightweight automotive seats by combining AM with the conventional manufacturing process. The car seatback frame will be designed via topology optimization and numerical simulations to minimize the overall weight while ensuring it meets all performance requirements. The optimization of the seatback will be based on a computational stress analysis to maximize stiffness and minimize weight. A novel manufacturing process integrating AM metal inserts with discontinuous reinforced composite through large-scale AM and compression molding (CM) will be developed. The seatback will be iteratively designed through numerical simulations to ensure it meets all performance requirements while also maintaining manufacturability via this novel AM-CM process. The composite and metallic materials along with the overmolded panels will be tested as a part of mechanical characterization. Furthermore, the optimized sub-components and seatback frame assembly are analyzed numerically to ensure they meet performance requirements.

Objectives

In collaboration with Ford Motor Company (Ford), the primary focus of this project is developing a novel manufacturing process for lightweight automotive seats in passenger vehicles—specifically a seatback frame.

First, the novel manufacturing process for lightweighting the automotive components will be developed by combining metal and reinforced composite parts with tailored mechanical properties. AM enables fabricating complex geometries of metal or polymer composite preforms with tunable mechanical properties. Hence, the AM metal inserts or lattice, as well as composite preforms with desired materials, will be used in this work. Subsequently, these elements can be combined through the CM process after preheating the preforms and placing the metal inserts within the mold. The fabricated hybrid panels can then be mechanically characterized to evaluate their performance. The aim for the automotive seat is to design the seatback frame to optimize weight while ensuring the seat meets all performance requirements. To achieve this, topology optimization will be performed on the seatback frame followed by numerical simulations for iteratively designing the seatback

frame. To simplify the design optimization process, the sub-components in high-stress regions will be first identified and optimized. Subsequently, all sub-components are assembled into the seatback frame and the entire seatback is optimized to minimize weight and resultant maximum displacement simultaneously. The optimized sub-component and seatback design are then compared with Ford's original design through numerical simulations, illustrating how the novel manufacturing process developed in this project enables the lightweighting of automotive seats.

Approach

The proposed work is divided into three major tasks. The first task involves developing the AM-CM process for fabricating hybrid metal composite panels. The second task deals with mechanical characterization of the overmolded hybrid panels. The third task will focus on optimizing the seatback frame with its sub-components to ensure the performance requirements are met while lightweighting the entire seatback. All of these tasks were performed in close collaboration with Ford in FY 2022.

1. Materials and manufacturing process:
 - 1.1. Additive manufacturing CM process.
 - 1.2. Investigation of mechanical interlocking.
2. Mechanical characterization:
 - 2.1. Base material characterization: Composites and metals.
 - 2.2. Overmolded hybrid specimens.
3. Lightweight seat design:
 - 3.1. Sub-component design.
 - 3.2. Seatback frame design.

Results

1. Materials and Manufacturing Process

1.1. Additive Manufacturing CM Process

The novel manufacturing process involves three major steps—namely, AM of metals, polymer composites, and compression overmolding. It has been shown that the compression overmolding on an AM part provides higher mechanical performances [1]. For metals, the binder jet AM process is chosen due to its cost-effectiveness for industrial applications. However, the process encounters difficulties in printing very thin features, which can be overcome by selecting appropriate feature sizes. 316L stainless steel infiltrated with bronze is used for the binder jetting. The process settings used in the binder jetting are a 100 mm, 1 g/ml binder density, and a 60% powder packing rate. The printed metal binder jet specimens are shown in Figure II.3.1.2.1(a).

Next, the polymer composite tailored preforms are fabricated using the big area additive manufacturing (BAAM) machine, manufactured by Cincinnati, Inc. The 40 wt.% CF to polyamide 66 (PA66) long-fiber reinforced thermoplastic (LFT) pellets from Techmer PM, TN were used as feedstock material in this work. Pellets were dried at 70°C for 8 h before use to remove moisture. A single-screw extruder mounted on the BAAM fitted with a 10.16 mm diameter nozzle was used to deposit 40 wt.% CF/PA66 in a rectilinear pattern to obtain composite preforms. The CF/PA66 pellets were fed to this single-screw extruder with five heating zones set at different temperatures (e.g., 250°C, 265°C, 280°C, and 280°C for Zones 1, 2, 3, and 4, respectively), and a nozzle temperature of 285°C. The material is deposited in a rectilinear pattern to form square preforms of different sizes (in inches)—10 × 10 and 18 × 18—and were subsequently machined to the mold sizes of 6 × 6 and 14 × 14, respectively, as shown in Figure II.3.1.2.1(b). The machined preforms would fit into the mold for compression overmolding on top of the metal inserts. In addition to the CF/PA66, 20 wt.% CF to acrylonitrile-butadiene-styrene (ABS) short-fiber reinforced thermoplastic (SFT) pellets were used as

feedstock material to produce the AM preforms. The feedstock material was then processed through a single-screw extruder mounted on a KUKA AG robotic arm fitted with a 0.3 in. diameter nozzle. The temperatures of three different zones within the extruder are set as 190°C, 230°C, and 250°C for Zones 1, 2, and 3, respectively, and a nozzle temperature of 250°C. The material is deposited in a rectilinear pattern into a 14 × 14 mold directly, and subsequently compression-molded to obtain square plaques of 14 × 14. The CF/ABS preforms would also directly fit into the mold for compression overmolding.

The metal inserts are first placed within the mold, as shown in Figure II.3.1.2.1(c). The AM composite preforms are preheated in a Protherm oven, which was first heated to 371°C and the AM preform was then placed inside for 7 min. Next, the preform was flipped over and heated for another 7 min. before moving it to the mold to be placed on top of the metal specimens. Once the AM preform was placed in the mold, the compression process was initiated to exert a 50-ton force for 1 min. The consolidated specimen was then removed from the press and is shown in the last insert of Figure II.3.1.2.1(c).

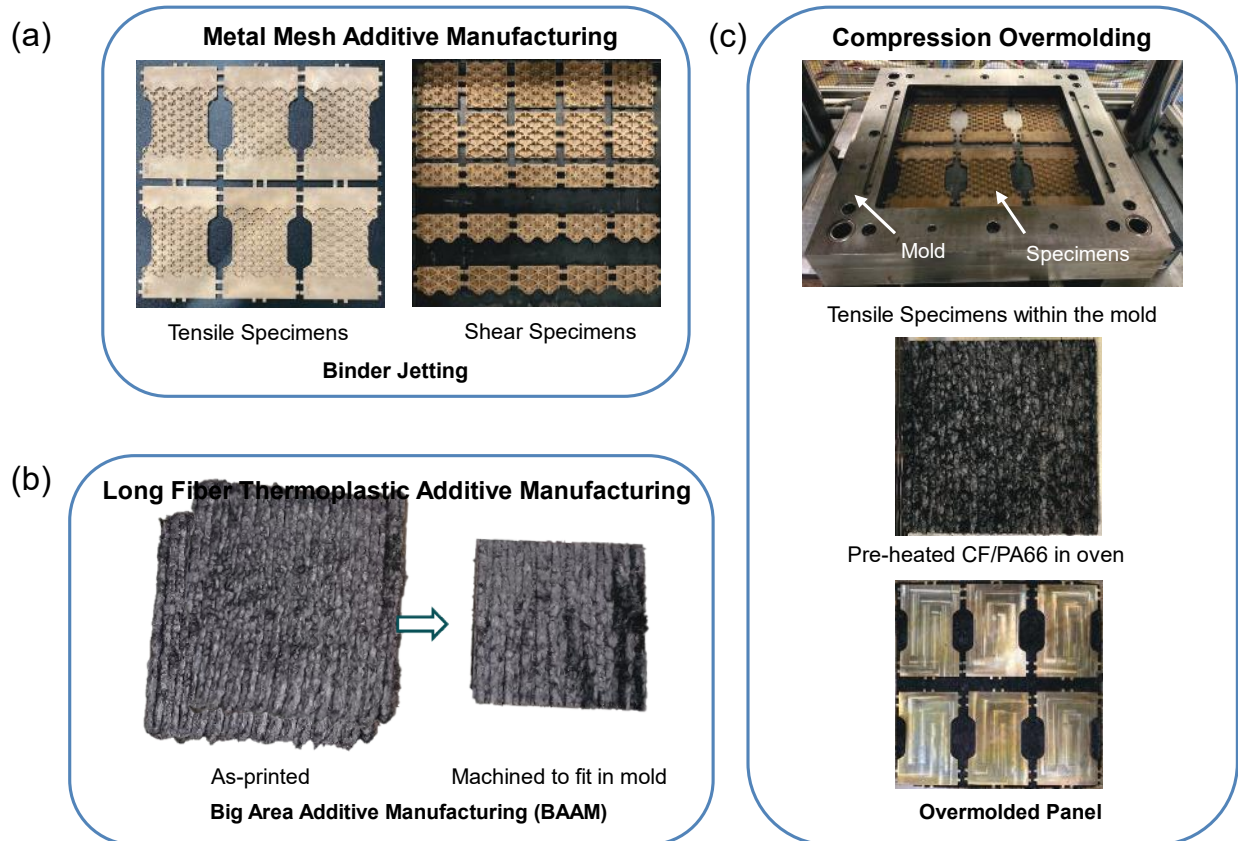


Figure II.3.1.10. The AM-CM process: (a) binder jetting of metal specimens with custom designs, (b) BAAM of composite preforms, and (c) compression overmolding of composite on top of the metal inserts to obtain the hybrid panels. Source: ORNL.

1.2. Investigation of Mechanical Interlocking

The hybrid panels are obtained after overmolding the CF/PA66 LFT onto various metallic designs. However, the flowability of polymer composite into the metallic lattice was very poor. The metal inserts can be easily peeled off the composite. The features of the metal insert are too small to allow the LFT to properly flow into the metal inserts, resulting in improper mechanical bonding. Since the 40 wt.% CF/PA66 LFT did not penetrate through the metal insert with the star-shaped hooks, 20 wt.% CF/ABS SFT was considered as an alternative to investigate the metal insert design. Using the CF/ABS preforms instead showed that good flowability and good mechanical interlocking can be obtained. The hybrid panels fabricated are then machined to obtain the tensile specimens for mechanical testing.

2. Mechanical Characterization

2.1. Base Material Characterization: Composites and Metals

In this study, two different polymer composite materials—namely 20 wt.% CF/ABS and 40 wt.% CF/PA66—were used for the compression overmolding on metal inserts. The panels composed of both these materials are individually tested under tension to determine the base material characteristics both along the bead and in perpendicular directions. Type 4 tensile specimens as per ASTM D638 were machined from the AM-CM panels and tested at 5 mm/min in a universal tensile testing machine with strain extensometers. The tensile characteristics of the 20 wt.% CF/ABS AM-CM panel are shown in Figure II.3.1.2.2(a). The average tensile strength along the bead is 63.35 +/- 9.44 MPa while the average tensile strength perpendicular to the bead is 33.77 +/- 8.3 MPa. The tensile characteristics of the 40 wt.% CF/PA66 AM-CM panel are shown in Figure II.3.1.2.2(b). The average tensile strength along the bead is 81.80 +/- 21.66 MPa while the average tensile strength perpendicular to the bead is 30.86 +/- 5.39 MPa.

Next, the metal cubes fabricated via the binder jetting process were machined to obtain SS-J3 tensile specimens. The SS-J3 tensile specimens were subsequently tested while monitoring with the DIC system, which was synchronized with the universal testing machine for the strain measurement. The stress-strain curves obtained from specimens of various batches are summarized in Figure II.3.1.2.2(c).

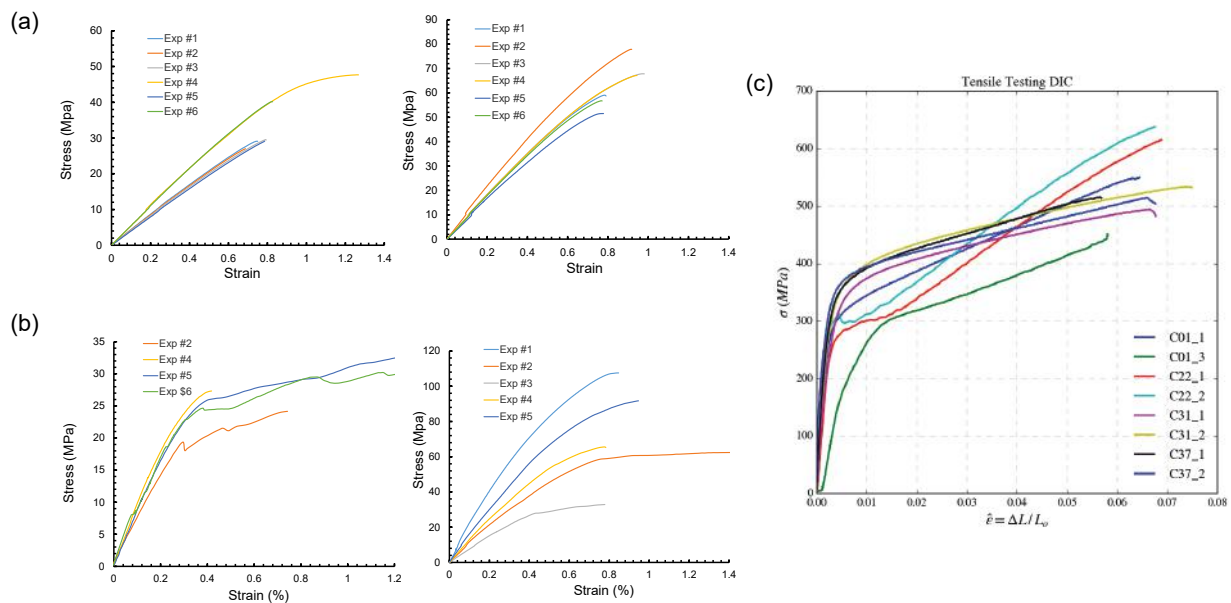


Figure II.3.1.11. Stress-strain characteristics of polymer composite perpendicular to the bead and along the bead directions: (a) 20 wt.% CF/ABS and (b) 40 wt.% CF/PA66. (c) Stress-strain characteristics of 316L stainless steel infiltrated with bronze. Source: ORNL.

2.2. Overmolded hybrid specimens

The tensile specimens obtained by overmolding CF/ABS onto stainless steel 316L were mechanically tested while monitoring using DIC synchronized with the tensile testing frame. Two different cameras were used to observe the polymer and metal sides of the overmolded specimens under tension. The initial and fracture images are shown in Figure II.3.1.2.3(a), while the stress-strain curves obtained from the analysis are shown in Figure II.3.1.2.3(b). The stress-strain curves reveal good agreement between tracking on either side of the specimens. The tensile strength thus achieved from the overmolding of polymer composites on metal specimens is 72 MPa.

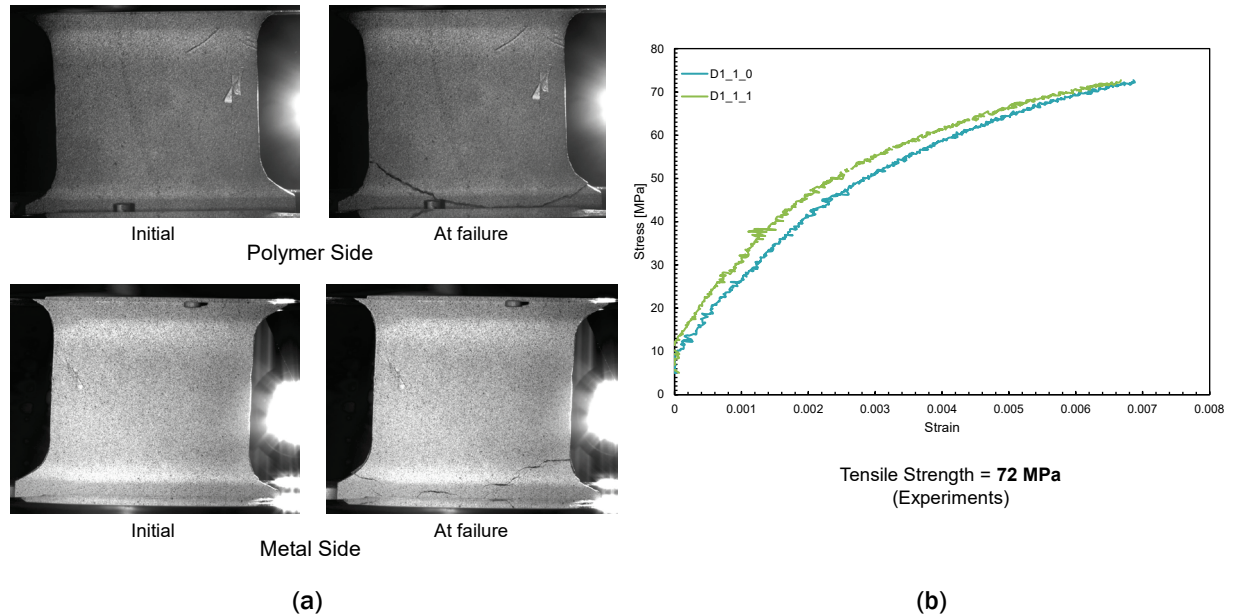


Figure II.3.1.12. (a) Tensile testing of metal composite overmolded specimens. (b) Stress-strain curves obtained from DIC. Source: ORNL.

3. Lightweight Seat Design

3.1. Sub-component Design

A sub-component is identified from the high-stress region of the seatback frame and design optimization is performed on this sub-component. The sub-component is made up of a 3D-printed metal bracket with mesh design and LFT reinforced with unidirectional fibers on either side. First, the metal bracket with the mesh design will be fabricated using the binder jet AM process. Next, this metal insert will be placed in a mold for AM and compression overmolding of LFT. The overmolded part will then be removed from the mold and cooled at RT before reinforcing with unitape on either side. Finally, the sub-component fabricated through this AM-CM process will be attached to the entire seatback frame with nuts and bolts.

The design iterations for the sub-component are shown in Figure II.3.1.2.4(a). The sub-component is optimized to minimize weight while also improving structural performance by reducing the maximum displacement and stress for an applied load of 3 kN. The optimized sub-component after multiple design iterations is shown in Figure II.3.1.2.4(b). The resultant Von-Mises stress and displacement contours are summarized in Figure II.3.1.2.4(b) as well. The weight of the sub-component is 1.22 kg and maximum displacement is 1.05 mm for an applied load of 3 kN. The weight of the sub-component is reduced by 27% as compared to the original Ford design and max displacement is reduced by 8 \times . Thus, the optimized sub-component that can be fabricated via the novel AM-CM process satisfies the performance requirements while lightweighting the seatback.

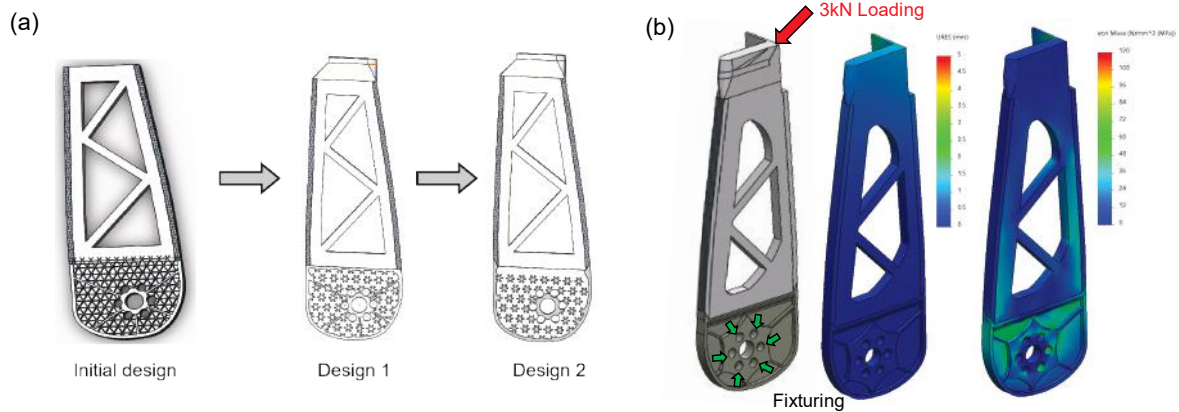


Figure II.3.1.13. (a) Sub-component design evolution through multiple iterations. (b) Optimized sub-component design, resultant displacement, and stress contours. Source: ORNL.

3.2. Seatback Frame Design

The entire seatback frame was optimized through multiple iterations to make it lightweight using a combination of metal parts overmolded with polymer composites. The seatback frame design that evolved through multiple iterations is shown in Figure II.3.1.2.5(a). Both the metal and polymer composites area are improved in subsequent design iterations to enable the low-weight and high mechanical performance requirement. The sub-component design in the previous section was redesigned to ensure the weight of the total seatback is optimized. Design 1, as shown in Figure II.3.1.2.5(a), consists of some of the original parts from the Ford design, while the rest of the polymer composite parts are designed to fit with the metal parts, thus enabling the lightweighting of the seatback frame. The polymer composite area in Design 1 is improved by structurally stiffening with the addition of the polymer composite material shown in Design 2. The high-stress area in Design 2 is replaced with a metal insert and polymer composite overmolded on top. Subsequently, the sub-component area is redesigned to obtain the final design. The redesign of the sub-component is performed to ensure the overall weight of the seatback frame is reduced, while ensuring the performance requirements are met. The optimized seatback frame design, along with the resultant displacement and Von-Mises contours, are shown in Figure II.3.1.2.5(b). The optimized design is 20% lighter than the original Ford design and weighs around 6.93 kg. The maximum displacement for the optimized design is 6.54 mm, which is 30% lower than the original Ford design for the same applied load of 3 kN. Overall, the optimized seatback design enabled by the novel AM-CM process is lightweight, while satisfying the performance requirements.

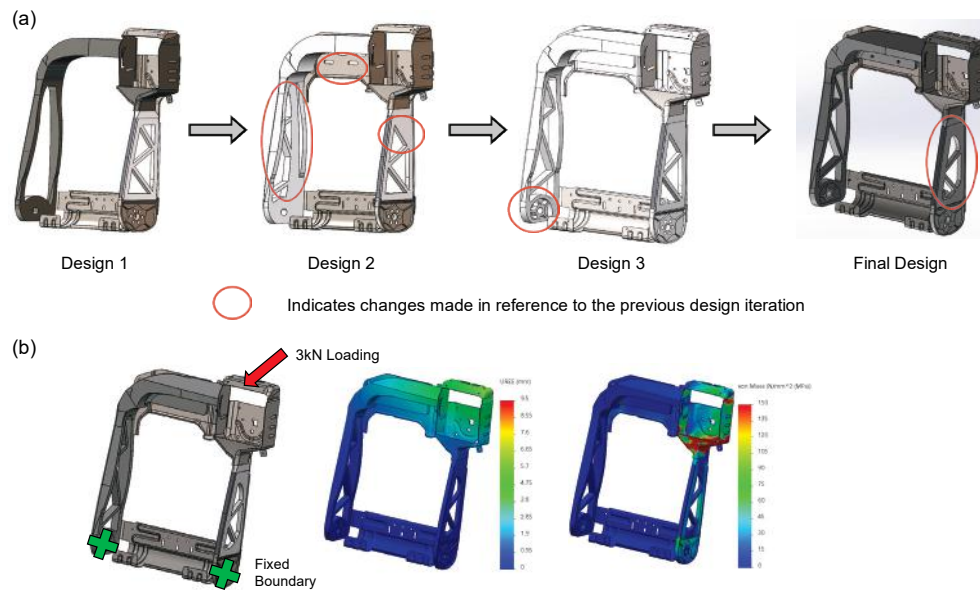


Figure II.3.1.14. (a) Design evolution of seatback frame through multiple iterations. (b) The optimized seatback frame design, resultant displacement, and stress contours. Source: ORNL.

Conclusions

In FY 2022, the novel AM-CM process was developed and tested for different materials in large size molds. Various metal insert designs were explored and fabricated via a binder jetting process. The SFT and LFT polymer composite preforms were obtained via BAAM. The preforms were then overmolded onto various metal designs and the hybrid panels obtained were investigated for mechanical interlocking and bonding properties. The mechanical characterization on the hybrid panels was performed to fully characterize the metal composite parts, revealing a good bond strength for the overmolded parts. Using the base material properties of composite and metal as input, numerical simulations were performed for the seatback design. A sub-component in a high-stress region is first identified and optimized through multiple iterations. Next, the entire seatback is designed through topology optimization and multiple iterations of numerical simulations to continually decrease the overall weight while satisfying the performance requirements. Finally, the optimized seatback design enabled by the novel process is lightweight while also satisfying the performance requirements.

Key Publications

1. Pokkalla, D. K., A. A. Hassen, D. Nuttall, N. Tsiamis, M. L. Rencheck, V. Kumar, P. Nandwana, C. B. Joslin, P. Blanchard, S. L. Tamhankar, P. Maloney, V. Kunc, and S. Kim, 2023, "A novel additive manufacturing compression overmolding process for hybrid metal-polymer composite structures," *Addit. Manuf. Lett.*, Vol. 5, Art. 100128. <https://doi.org/10.1016/j.addlet.2023.100128>.

References

1. Kumar, V., S. P. Alwekar, V. Kunc, E. Cakmak, V. Kishore, T. Smith, J. Lindahl, U. Vaidya, C. Blue, M. Theodore, S. Kim, and A. A. Hassen, 2021, "High-performance molded composites using additively manufactured preforms with controlled fiber and pore morphology," *Addit. Manuf.*, Vol. 37, Art. 101733. <https://doi.org/10.1016/j.addma.2020.101733>.

Acknowledgments

The work performed in this project in FY 2022 involved contributions from teams at ORNL and Ford. The key personnel who contributed to project progress include D. Pokkalla, S. Kim, A. Hassen, T. Smith, V. Kumar, M. Paramanathan, M. L. Rencheck, and V. Kunc from ORNL; and S. Tamhankar, P. Blanchard, P. Maloney, and A. Khan from Ford.

II.3.1.3 Additive Manufacturing for Property Optimization for Automotive Applications (Oak Ridge National Laboratory)

Seokpum Kim, Principal Investigator

Oak Ridge National Laboratory
2350 Cherahala Blvd.
Knoxville, TN 37932
E-mail: kimsp@ornl.gov

Rich Davies, Composites Core Program Manager

Oak Ridge National Laboratory
Materials Science and Technology Division
1 Bethel Valley Rd.
Oak Ridge, TN 37831
E-mail: daviesrw@ornl.gov

H. Felix Wu, DOE Technology Development Manager

U.S. Department of Energy
E-mail: felix.wu@ee.doe.gov

Start Date: October 1, 2020

End Date: September 30, 2023

Project Funding (FY 2022): \$500,000

DOE share: \$500,000

Non-DOE share: \$0

Project Introduction

This project is aimed at using advanced manufacturing for developing property-optimized structures for applications in passenger vehicles. The primary objective of this project is to develop lightweight structures with tailored mechanical responses by utilizing multiple technologies associated with polymer and composites AM. The primary AM technologies developed in this work include multimaterial printing using a material extrusion AM process, out-of-plane printing (OPP) using a multi-axis robotic arm printer, and toolpath optimization associated with printing systems. In addition to material selection and optimization, design flexibility offered by the AM process will be leveraged in this project by developing novel lattice structures with tailored responses in AM parts. Some of the key steps towards attaining these goals include lattice structure optimization, ML for design selection, toolpath optimization, multi-axis robot arm control, and part fabrication/testing.

Objectives

The primary focus of this project is the development of high-performance, tailored structures for applications in passenger vehicles. Two target parts/components have been chosen in collaboration with Ford Motor Company (Ford). The first part is a front bumper, while the second is a door panel arm rest. To develop a front bumper that meets the performance requirements, research will be conducted on fabricating parts with multimaterial printing. Therefore, our studies involve printable material properties and optimizing material combinations. In the design space, novel 2.5D lattice structures with tailored mechanical responses will be developed in collaboration with the University of California–Berkeley (UCB) using ML techniques. The final printed bumper will be aimed to incorporate both material and design optimized structures, thereby being a customized lightweight structure with high-performance.

In the case of a door arm rest, research will be conducted with the OPP technique using a robotic arm printer. Extrusion and control techniques in the OPP system require research and development in this project, including slicing technology development, toolpath planning and optimization, robotic arm control and extrusion control optimization, and material property evaluation and optimization. For OPP technology

development, a single material with optimized structures will be explored to obtain lightweight high-performance components.

Approach

The proposed work is divided into three major tasks, with various sub-tasks for each. Task 1 will provide a large-scale structure optimized for structural design and multimaterial placement printed in the BAAM system. In Task 2, a control technique for OPP will be developed, and the sub-component of a vehicle will be fabricated. Task 3 will focus on the ML algorithm development for a sub-component structure with tailored energy absorption characteristics in collaboration with Prof. R. Zheng at UCB. Below is the list of tasks and sub-tasks in FY 2022.

1. Multimaterial large-scale printing of optimized structures (bumper):
 - 1.1. Toolpath optimization for the lattice-based bumper designs.
 - 1.2. Printing demonstration of multimaterial lattice-based bumper design.
2. OPP of optimized structures (arm rest):
 - 2.1. Mechanical property evaluation for OPP.
 - 2.2. Design optimization and performance simulation on the armrest structure.
 - 2.3. Toolpath planning, robotic arm control, and OPP of armrest.
3. Tailored lattice structures using ML:
 - 3.1. ML framework: development, training data acquisition, and predictions.

Results

1. Multimaterial Large-Scale Printing of Optimized Structures (Bumper)

1.1. Toolpath Optimization for the Lattice-Based Bumper Designs

The large-scale automotive bumper can be printed using different lattice design and material combinations. Multiple-material blends can be obtained by mixing carbon fiber-reinforced acrylonitrile-butadiene-styrene (CF-ABS) and thermoplastic polyurethane (TPU) in different proportions where CF-ABS constitutes the stiffer material and TPU is the elastomeric, flexible material. The slicing of lattice-based designs using a commercially available software slicer, such as Cura, would lead to discontinuous paths causing multiple start and stops, as shown in Figure II.3.1.3.1(a). Thus, the toolpath for the lattice-based bumper is optimized using an ORNL slicer to obtain continuous paths that minimize print times and avoid non-uniform thickness of the struts, as shown in Figure II.3.1.3.1(b).

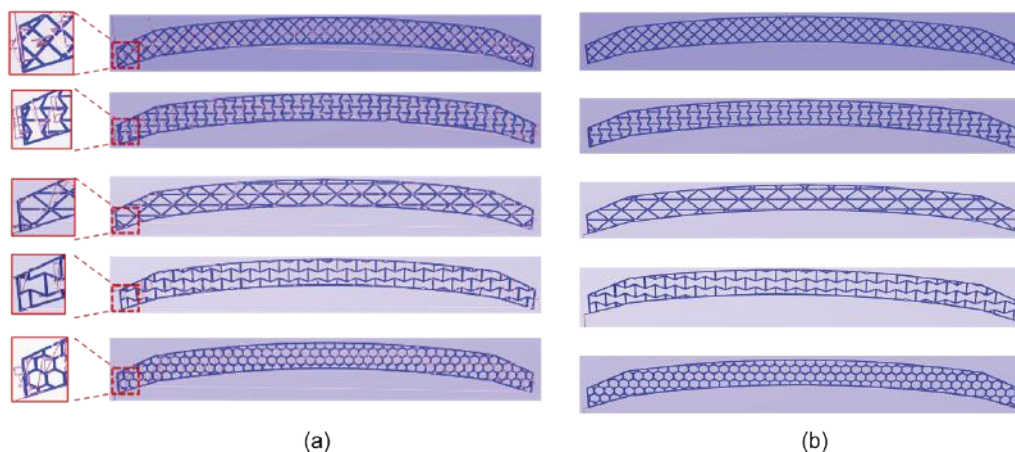


Figure II.3.1.15. Toolpaths for lattice-based bumper designs: (a) discontinuous toolpaths generated in Cura and (b) continuous toolpaths generated using an ORNL slicer. Source: ORNL.

1.2. Printing Demonstration of Multimaterial Lattice-Based Bumper Design

A full-scale lightweight, multimaterial bumper was printed, as shown in Figure II.3.1.3.2. First, 20 wt.% CF-ABS is used to print the lower portion of the bumper, while the top portion is printed using a CF-ABS/TPU custom material blend. The addition of TPU to CF-ABS in different proportions results in custom materials with tunable stiffness. Next, a triangular lattice structure was chosen, and a computer-aided design model was generated in SolidWorks. Subsequently, the model was sliced and a continuous toolpath was obtained using an ONRL slicer. Finally, the full-scale bumper was printed with an optimized continuous toolpath in a 3DP filament-based printer with CF-ABS and CF-ABS/TPU material blends, as observed in Figure II.3.1.3.2.



Figure II.3.1.16. Full-scale multimaterial lattice-based bumper. Source: ORNL.

2. OPP of Optimized Structures (Armrest)

2.1. Mechanical Property Evaluation for OPP

The mechanical property of polylactic acid (PLA) polymer was evaluated by performing tensile testing on the 3DP dog bone specimens. The tensile properties were evaluated in both the x-(print) and z-(perpendicular to print) directions to determine the elastic modulus and tensile strength. The average elastic modulus in the x- and z-directions was 2.93 GPa and 2.76 GPa, respectively. The average tensile strength in the x- and z-directions was 58.11 and 42.54 MPa, respectively.

2.2. Design Optimization and Performance Simulation on the Armrest Structure

A topology-optimized design was first obtained based on identification of load cases and deflection criteria. The topology-optimized design was modified into a shell-based design with a weight of 274 g. The shell-based design was further optimized to a strut-based design suitable for AM using a robotic arm printer. The strut-based optimized armrest design has a weight of 234 g. The entire design iteration process is shown in Figure II.3.1.3.3. Performance simulations were conducted using FEA simulation software, assuming the material is neat PLA. For given loading conditions, the maximum deflection was 5.1 mm, which satisfies the requirement of < 15 mm deflection. Load conditions are shown in Figure II.3.1.3.4.

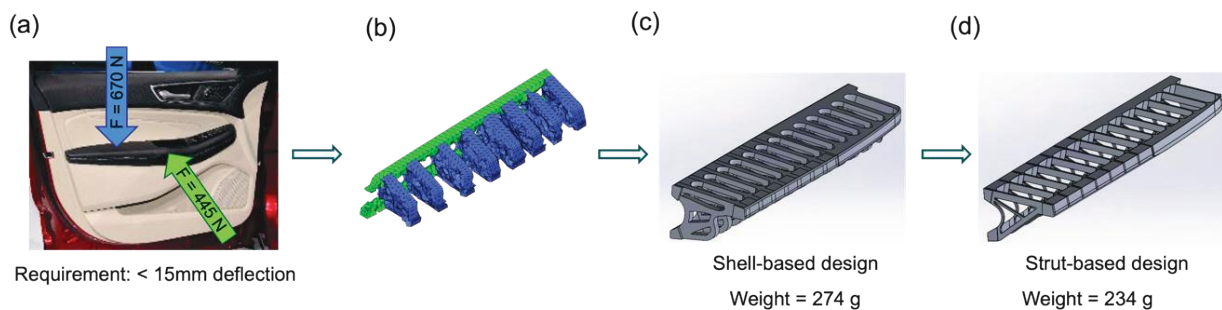


Figure II.3.1.17. (a) Load cases and deflection requirement for a door arm rest. (b) Topology-optimized design. (c) Shell-based design. (d) Strut-based design. Source: ORNL.

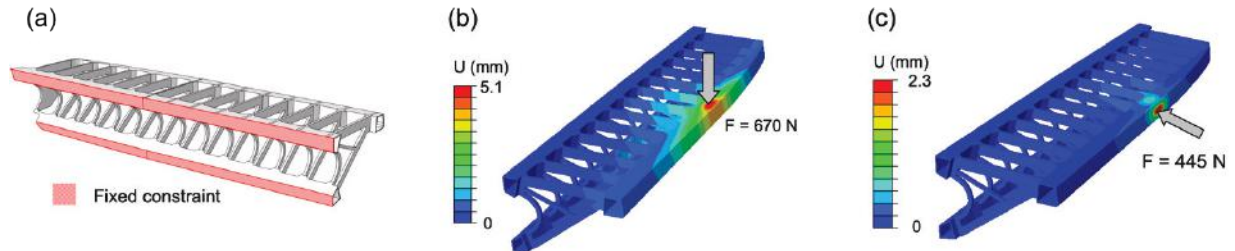


Figure II.3.1.18. (a) Boundary conditions applied on the armrest design, and resultant displacement via FEA for applied (b) vertical load and (c) horizontal load. Source: ORNL.

2.3. Toolpath Planning, Robotic Arm and Extrusion Control, and OPP of Armrest

The optimized strut-based design can be manufactured in a robotic arm 3D printer. First, in-plane slicing and toolpath optimization was performed. The armrest was printed in the vertical configuration shown in Figure II.3.1.3.5 using the Orbital Composites robotic arm-controlled system. The continuous OPP on the curved surface of the armrest will strengthen its load-carrying capacity and the wrapping on the surface of the armrest will improve its structural performance. The toolpath for the OPP on the curved surface was generated in HyperMill software. The generated toolpath was then imported into Octopuz software to obtain the robotic arm extrusion control through simulations. The optimized toolpath at various stages of printing on the curved surface and corresponding snapshots from the printing are provided in Figure II.3.1.3.6(a) and Figure II.3.1.3.6(b), respectively. The toolpath for the wrapping on the surface of the armrest is shown through a sequence of snapshots in Figure II.3.1.3.6(c) and Figure II.3.1.3.6(d), respectively.

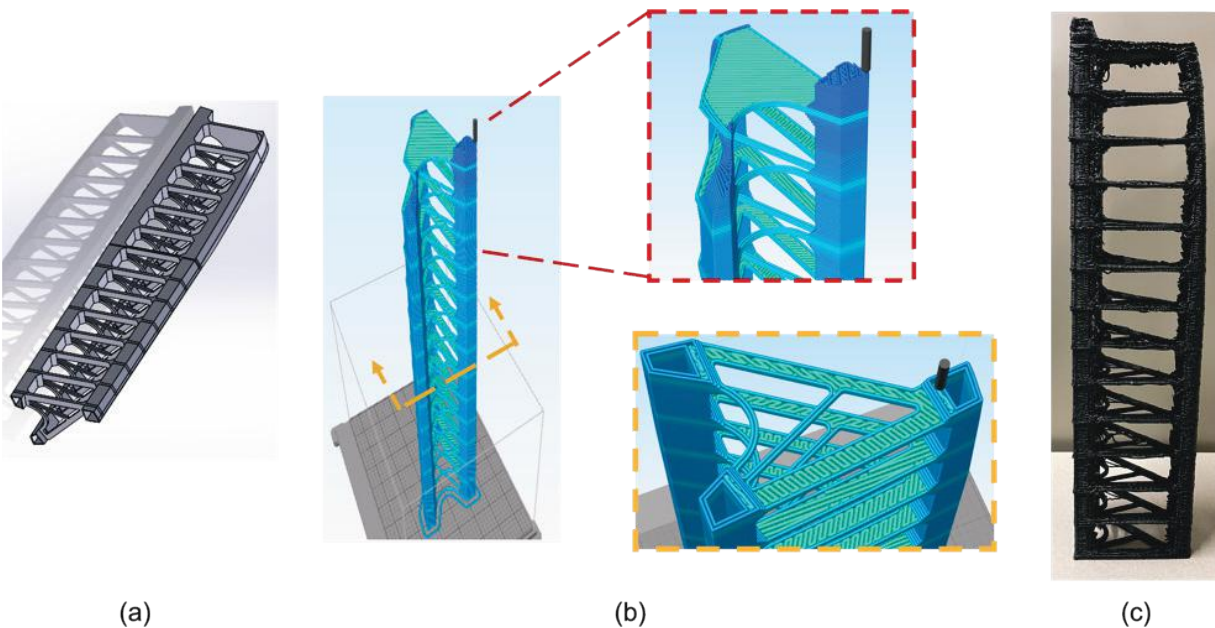


Figure II.3.1.19. (a) Strut-based armrest design. (b) In-plane slicing and toolpath for 3D printing. (c) In plane printed armrest design. Source: ORNL.

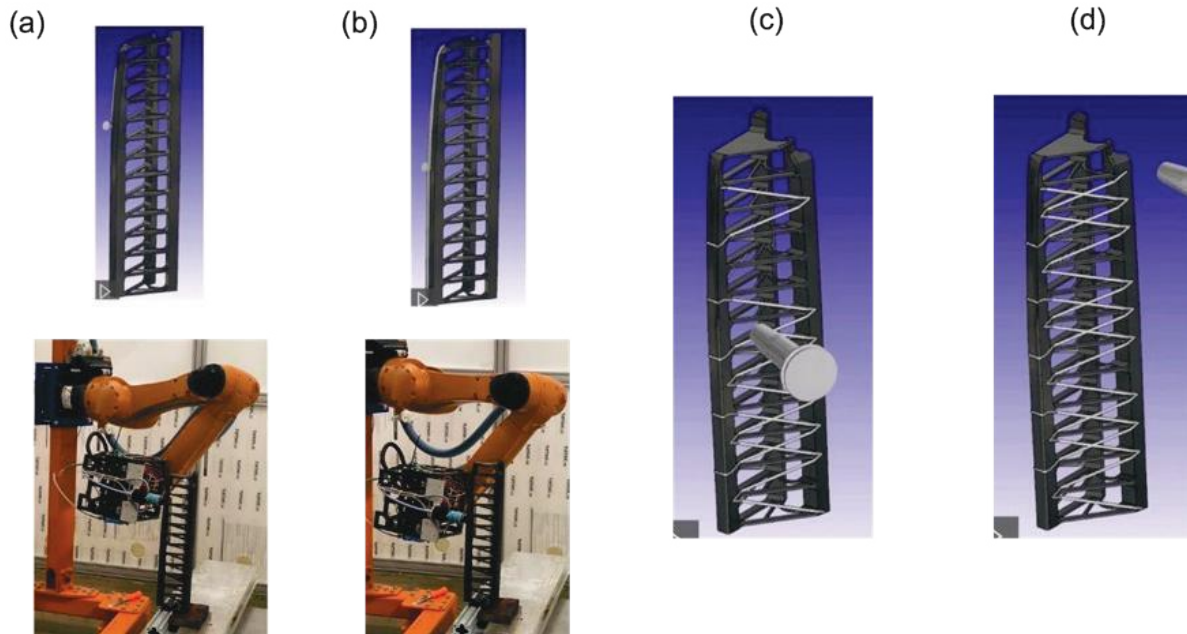


Figure II.3.1.20. (a) - (b) OPP of door armrest. (c) - (d) The toolpath planning for OPP wrapping. Source: ORNL.

3. Tailored Lattice Structures Using ML

3.1. ML Framework: Development, Training Data Acquisition, and Predictions

In the ML framework, the target mechanical properties are used as the input to inverse design lattices to satisfy the design requirements. Numerical simulations were performed via FEA on a representative volume element consisting of $3 \times 2 \times 2$ -unit cells using periodic boundary conditions. The workflow of the ML framework for the inverse design of lattices is shown in Figure II.3.1.3.7. The architectural genes consist of seven distinct types of unit cells based on internal strut member angles. Five different material blend ratios were also used for the choice of material. The full design space of attainable properties by combining lattice topologies and material combinations was first analyzed. The sequential integrated ML strategy takes mechanical properties as input and outputs the lattice gene type and material combinations. Once the tailored lattice was determined, a full-scale computer-aided design model was obtained followed by slicing, toolpath optimization using an ORNL slicer and 3D printing in a 3DP filament-based printer.

Coupon level mechanical tests were performed in two directions and anisotropic material properties were estimated using a dehomogenization technique [1]. The simulated response on various lattice genes using ABAQUS FEA simulation software was used to generate the training data after calibrating with experimental data. Mechanical tests of 3D printed lattices subjected to low- and high-strain rate were performed. A comparison between experiments and numerical responses for low- and high-strain rates are summarized in Figure II.3.1.3.8. The ML framework was tested on a limited set of data consisting of compliant and rigid genes. Using peak and valley stresses as targets, predictions were made for the inverse design of lattices, as shown in Figure II.3.1.3.9. The comparison between ML predictions and actual numerical responses are within 10% deviation, thus demonstrating the capability of ML framework on a limited set of training data.

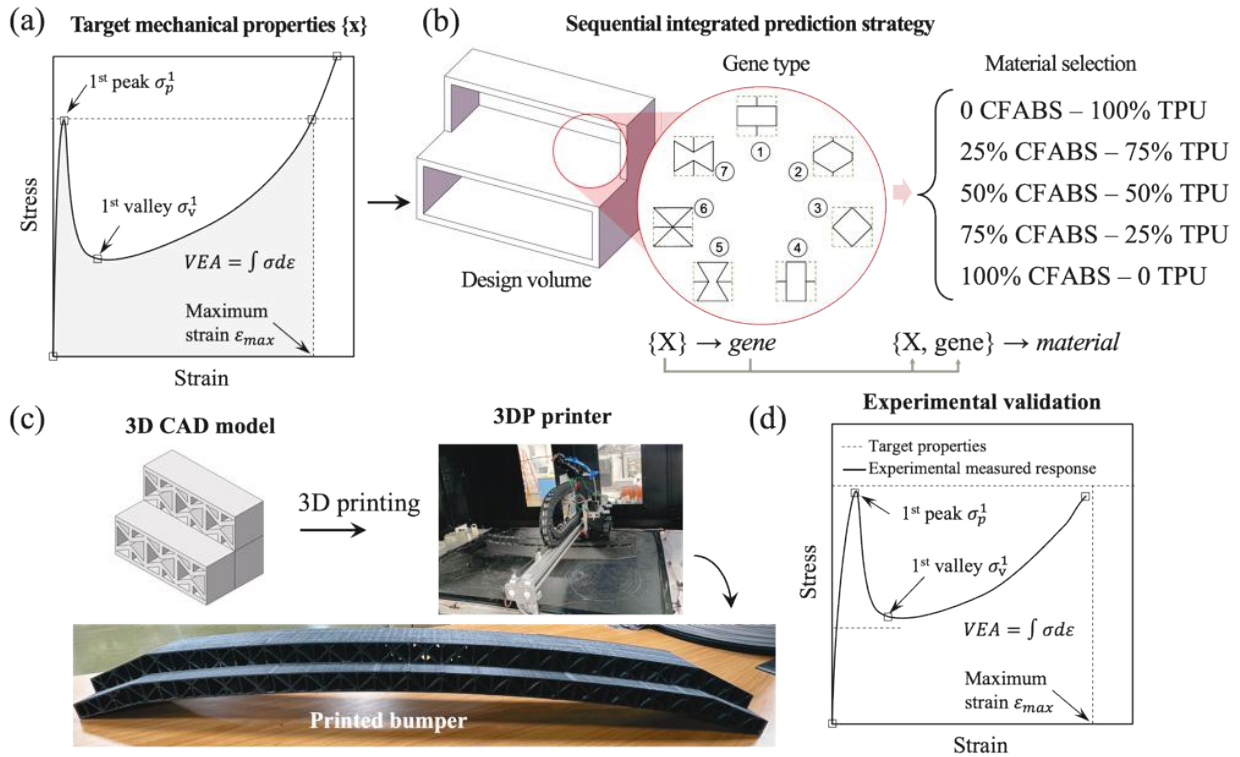


Figure II.3.1.21. Workflow of the ML-based inverse design framework. (a) Mechanical properties as inputs. (b) Design with lattice gene types and material combinations. (c) Computer-aided design model leading to the printed bumper. (d) Experimental validation of mechanical properties. Source: UCB.

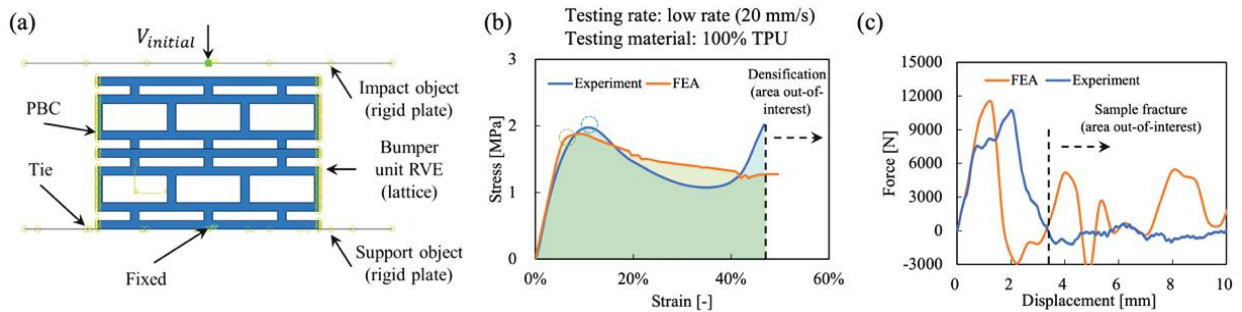


Figure II.3.1.22. Setup and benchmark of the simulation framework. (a) Configuration for test samples. (b) and (c) Comparison between experiments and numerical responses for low- and high-strain rates. Source: UCB.

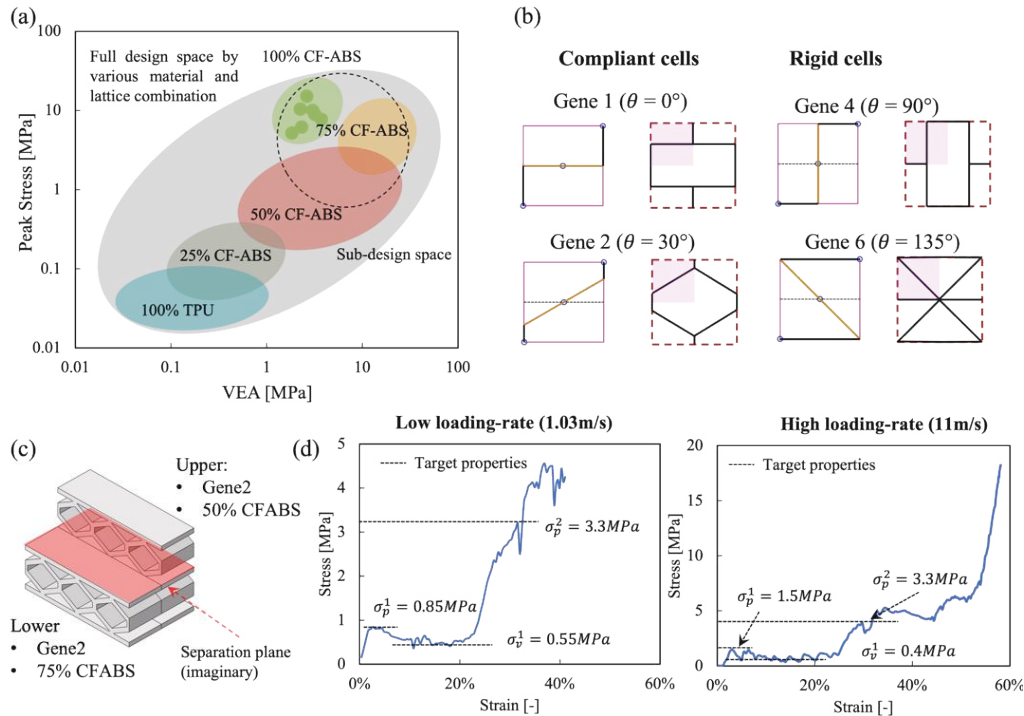


Figure II.3.1.23. Inverse design using ML. (a) Venn diagram showing the design space by materials and lattice combinations. (b) Configuration for compliant cells and rigid cells. (c) Isometric of the Gene 2 configuration. (d) Stress-strain curves for low and high loading rates. Source: UCB.

Conclusions

In FY 2022, the toolpaths of lattice-based bumper designs were optimized to eliminate start and stops and ensure high structure-performance through the ORNL slicer for Task 1. In addition, a multimaterial bumper made up of triangular lattice was printed in a 3DP mid-scale printer. In Task 2, PLA mechanical properties were evaluated, and the arm rest design was further optimized to a strut-based design with a lower weight. Performance simulations were performed on the optimized arm rest design followed by in-plane slice, toolpath planning, and printing using a robotic arm printer. The robotic arm and extrusion control for the OPP on the curved surface of the armrest was also performed. Task 3 involved the testing and design of tailored lattices. Selected lattice with different materials were tested for dynamic impacts. An ML framework was developed for multimaterial, lattice-based bumper design and training data was acquired. Preliminary predictions were made using a simple model, and the complete tailored lattice-based bumper design is in progress.

Key Publications

1. Kim, S., A. Nasirov, D. K. Pokkalla, V. Kishore, C. Duty, and V. Kunc, 2023, "Compression characteristics of additively manufactured lattice composite structures," Manuscript in review.

References

1. Kim, S., H. Baid, A. Hassen, and A. Kumar, 2019, "Analysis on part distortion and residual stress in big area additive manufacturing with carbon fiber-reinforced thermoplastic using dehomogenization technique," *The Composites and Advanced Materials Expo (CAMX 2019)*. TP19-0694. <https://doi.org/10.33599/nasampe/c.19.0694>.

Acknowledgments

The work performed in this project in FY 2022 involved contributions from teams at ORNL, UCB, and Ford. The key personnel who contributed to project progress in the past year include D. Pokkalla, V. Kishore, S. Simunovic, T. Smith, V. Kunc, and T. Feldhausen from ORNL; X. Zheng, and D. Yao from UCB; and E. Lee, I. Farooq, R. Baccouche, S. Chowdhury, Z. Pecchia, and M. Rebandt from Ford.

II.3.1.4 3D-Printed Hybrid Composite Materials with Sensing Capability for Advanced Vehicles (Oak Ridge National Laboratory)

Rigoberto C. Advincula, Principal Investigator

Oak Ridge National Laboratory
Materials Science and Technology Division
1 Bethel Valley Rd.
Oak Ridge, TN 37830
E-mail: advincularc@ornl.gov

Rich Davies, Composites Core Program Manager

Oak Ridge National Laboratory
Materials Science and Technology Division
1 Bethel Valley Rd.
Oak Ridge, TN 37831
E-mail: daviesrw@ornl.gov

H. Felix Wu, DOE Technology Development Manager

U.S. Department of Energy
E-mail: felix.wu@ee.doe.gov

Start Date: October 1, 2020	End Date: September 30, 2023	
Project Funding (FY 2022): \$500,000	DOE share: \$500,000	Non-DOE share: \$0

Project Introduction

Now on the third year of this project, ORNL and collaborators at the University of North Texas (UNT) have pursued research on 3D-printed CF composites for vehicle lightweighting with sensing functionality. The objectives for Year 3 are: (1) to enhance the organic-inorganic interface for long-term performance via covalent bonding between CF and a polymer matrix; and (2) to perform a real-time evaluation of material properties with embedded sensors. The group has targeted the use of AM and synchronous sensor fabrication/embedding towards next-generation vehicle structure and materials. This will require:

1. Synthesis, modification, and characterization of CF-polymer composites using low-cost CFs, surface modifiers, and optimized resin formulations and chemistry.
2. Dynamic studies of curing control and characterization guided by simulations on multifunctional polymer-based composites—feedback loop materials development protocol.
3. Advanced AM and 3D printing of continuous CF-polymer composite geometries.
4. The assembly of sensor-embedded CF-polymer composites via multimaterial 3D printing.

Specific developments for this period involved detailed studies on the following: (a) bonding-adhesion properties between CF and an epoxy matrix; (b) the use of plasma surface-treatment of fibers with extensive characterization; (c) the use of polyvinylidene fluoride (PVDF) as a host material for 2D nanomaterials and electrode development; and (d) the use of artificial intelligence (AI) and ML methods to predict behavior and optimize device fabrication. The team met twice a month and developed cohesive strategies for meeting the objectives and working with complementary capabilities, including the exchange of samples and writing manuscripts. There are several publications to report this year, including plans for several reporting and planned presentations.

Objectives

The overall objective of this project is to focus on enhancing the interfacial interaction between CF and polymer and enable monitoring of the materials performance [1]. To meet these objectives, the group has pursued the following specific objectives:

1. Investigated chemical reactions at the CF-polymer interface and long-term thermomechanical performance to achieve mechanical properties with Young's modulus > 15 GPa and tensile strength > 250 MPa.
2. Conducted simulation and computational studies to establish structure-process-property relationships and evaluate interfacial failure mechanisms with FEA.
3. Fabricated 3D-printed composite parts with controlled fiber orientation, multi-axis capabilities, and enhanced fiber-polymer interfacial adhesion at various test geometries and parts design.
4. Incorporated and tested sensor-embedded CF-polymer composites with 3D printing to embed piezoelectric sensor layers *in-situ* with designed vehicle component geometries that can be monitored for stress and fatigue over time.

Specifically in FY 2022, the group has pursued the following objectives: (a) to understand the effectiveness of the critical surface modification method (e.g., chemical, plasma); (b) to understand and simulate the properties of matrix/composite development with 2D materials (e.g., V₂O₅, MoS₂, graphene) and their dispersion towards piezoelectric and electrode behavior; and (c) to optimize the design of continuous fiber printing with epoxy and CF with the 3D printing machine.

Approach

ORNL brings strengths in synthetic chemistry, composite materials, and AM to the project. The UNT enables simulations and embedded sensors using nanomaterials and 3D printing capabilities. The project has been divided into the following four tasks:

Task 1. Precise chemical reaction control in resin materials:

Objective: Develop CF/polymer composites with enhanced inorganic-organic interface covalent interaction.

End-of-Project Goal: Composites with optimum chemistry, processability, and high-performance.

Task 2. Computational studies of interfacial interaction between polymer matrix and CF:

Objective: Simulation of interfacial properties and optimum reactive chemical species.

End-of-Project Goal: Achieve high correlation of printed components with predictive tools.

Task 3. 3D printing of continuous CF/epoxy composite with enhanced fiber-polymer adhesion:

Objective: 3D printing continuous CF-epoxy matrix with optimal fabrication parameters.

End-of-Project Goal: Achieve AM process and materials combination for high-performance.

Task 4. Continuous sensor-embedded polymer/CF composite 3D printing:

Objective: 3D print continuous CF/polymer composites with embedded sensor geometries and testing.

End-of-Project Goal: Achieve sensing capability in continuous CF/epoxy 3D-printed parts.

A focus for FY 2022 was to understand the importance of interfacial adhesion properties between the individual fiber and the polymer matrix in CF-based composite materials, as shown in Figure II.3.1.4.1. We have used mainly Bisphenol A diglycidyl ether resins and reactive silane-amine surface modifiers on model CF fillers. Systematic studies for characterization were made using: (a) spectroscopic imaging (e.g., nuclear magnetic resonance, infrared, Raman); (b) microscopic examination (e.g., SEM, energy-dispersive X-ray); (c)

rheology testing; (d) thermal scanning (e.g., DSC, TGA); and (e) thermomechanical investigation (dynamic mechanical analysis—tensile, modulus, compressive). To optimize resin composition, establish process parameters, predict structure-property relationships, and understand interfacial failure mechanisms, we also used FEA and density functional theory computational and simulation tools.

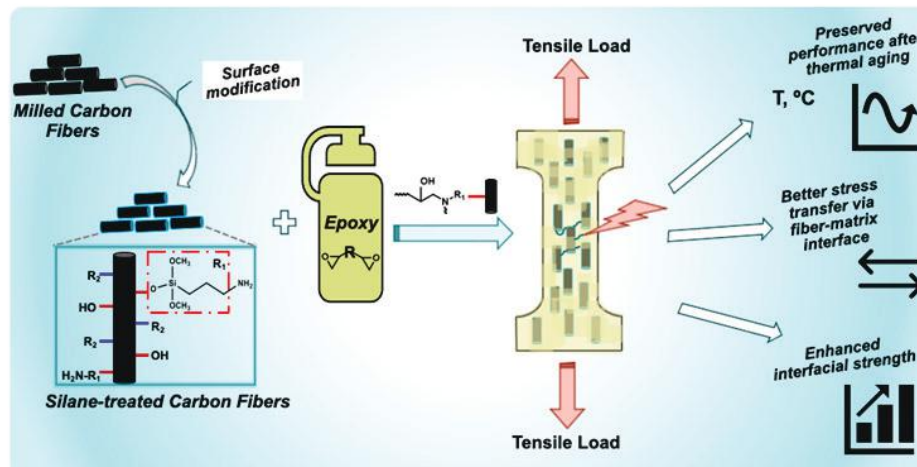


Figure II.3.1.24. Schematic modification of the fibers with silane treatment methods and the testing protocols for evaluating composite fabricated test samples to determine adhesion strength. Source: ORNL.

The 3D printing attempts are ongoing. We have demonstrated 3D printed chopped CF/epoxy composites with the project. The development of the continuous fiber printing attachment with either a double printing head or a single printing head loaded with viscosity-optimized epoxy resin is being pursued [2]. The printing geometries and materials dispensing has been programmed (G-code modification). Test bars and cubes (with control sample) is being prepared to be validated using tensile, compression, and flexural strength tests.

To demonstrate the embedment of a piezoelectric sensor with the ability to monitoring the health of the 3D-printed structure, we have designed and tested mechano-electric sensor layers of transition metal dichalcogenides (TMDs)/PVDF 3D-printed composite electrodes. The stacking of graphene and 2D TMD layers (e.g., MoS₂) are piezoelectric materials with broken inversion symmetry. These sensor layers convert stress-strain changes into electrical signals, sensing stress-strain distribution over a specific area of the 3D-printed structure over stress or time. High TMD/PVDF layered compositions have been 3D-printed and tested as specific patterns and electrode arrays with impedance/conductance characterization.

Results

Results and accomplishments for each task are described below:

Task 1. Precise chemical reaction control in resin materials:

- Demonstrated optimized silane modification method on CF, including amine and crown-ether amines with reproducible protocols. A fixed model epoxy resin composition was optimized for consistent formulation in subsequent studies, as shown schematically in Figure II.3.1.4.2(a).
- The target strength and tensile performance was achieved; strength of 10 GPa, tensile strength of 200 MPa, and a minimum of 1 wt.% CF.
- Phase separation was observed for samples with 5 wt.% CF; therefore, the uniform distribution of CFs into the system during the entire process is found to be critical, as tested over 12 thermal cycles as shown in Figure II.3.1.4.2(b), and deterioration of tensile strength of epoxy composites after thermal cycling occurred as observed in Figure II.3.1.4.2(c).

- Raman mapping results confirmed the presence of a notable interphase area between the amino-functionalized CF (s-CF) and epoxy, thus establishing the presence of strong interfacial adhesion.
- SEM imaging and FEA modeling also confirmed the effect of CF chemical treatment toward the formation of a strong s-CF/epoxy interface, with a higher toughness capable of withstanding higher loadings and providing better stress distribution across the composite.

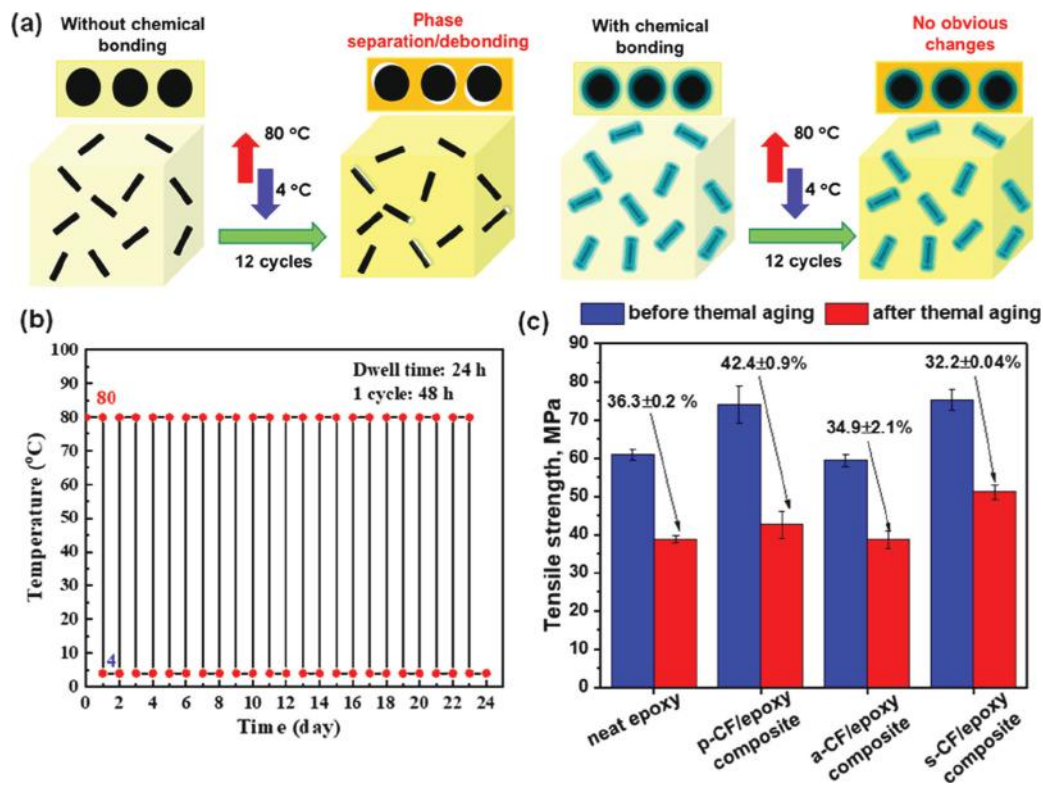
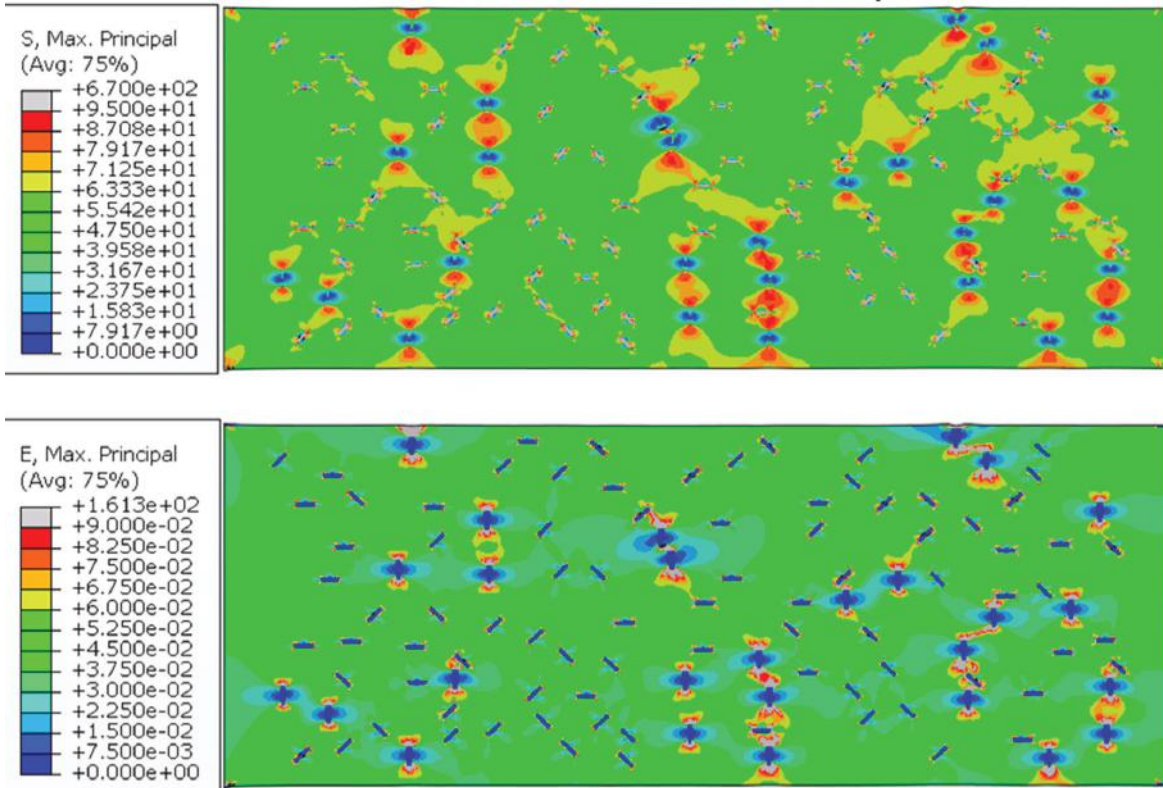


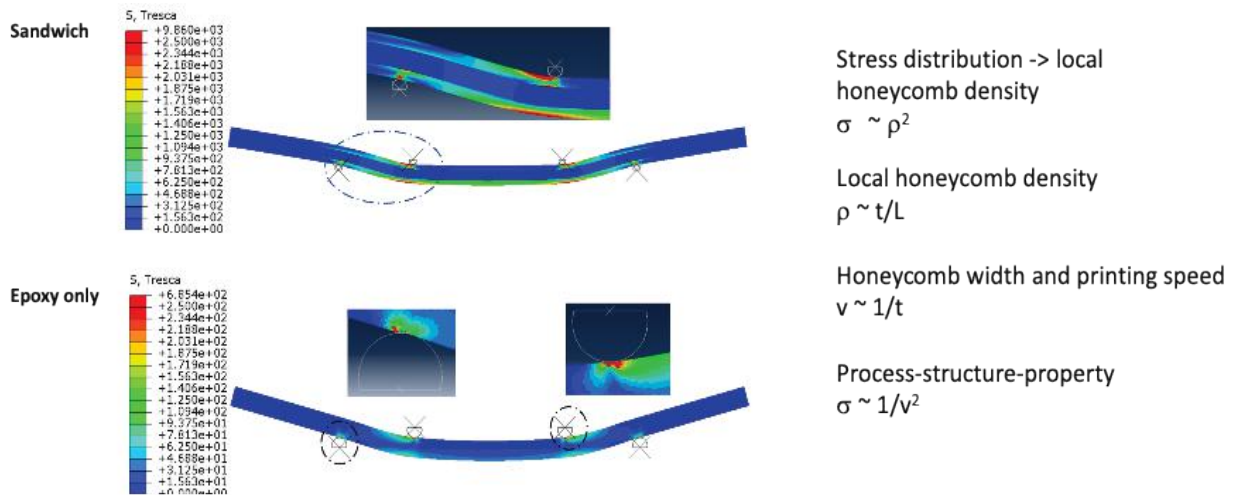
Figure II.3.1.25. (a) Schematic representation of the thermal aging process in CF-epoxy composites. (b) Thermal cycling protocol for CF-epoxy composites during the aging process. (c) Extent of deterioration of tensile strength of epoxy composites after thermal cycling. Source: ORNL.

Task 2. Computational studies of interfacial interaction between polymer matrix and CF:

- Utilized data-driven ML models to precisely predict the interface adhesion properties and identify imperfections along interfaces from FEA and standard experiments.
- Developed algorithms for material programming of crack design; however, algorithm development for high-toughness and high-strength composites is ongoing. Also, established genetic algorithm and FEA iterations for crack propagation simulations with designed composites.
- Established FEA models via a Python-Abaqus customized program. The interfacial strength and toughness were fitted with the experimental data. Figure II.3.2.1.3.(a) compares the collective stress-strain test results of 5 wt.% s-CF, acid-treated CF (a-CF), and pristine CF (p-CF) epoxy composites under tensile loads. By fitting the interfacial properties, the FEA results matched the initial stress-strain curves, stiffness, and ultimate strength of the experimental data. In addition, the silane treatment of CFs results in a substantial increase (e.g., > 1.6× higher) in interfacial toughness as compared to p-CF.
- Conducted modeling studies on sandwich structures of epoxy and various 3D-printed internal geometries, including variables such as printing speed and cell size, as shown in Figure II.3.2.1.3.(b).



(a)



(b)

Stress distribution -> local honeycomb density
 $\sigma \sim \rho^2$

Local honeycomb density
 $\rho \sim t/L$

Honeycomb width and printing speed
 $v \sim 1/t$

Process-structure-property
 $\sigma \sim 1/v^2$

Figure II.3.1.26. FEA simulations comparing the stress-strain test results and the interfacial strength and toughness measurement for 5 wt% p-CF, a-CF, and s-CF/epoxy composites. (a) First-principals stress (top image) and strain (bottom image) contours for the s-CF/epoxy composite. (b) The FEA simulation of a 3D-printed sandwich structure and epoxy only prepared for a piezoelectric sensor embedment protocol.

Source: ORNL.

Task 3. 3D printing of continuous CF/epoxy composite with enhanced fiber-polymer adhesion:

- Achieved 3D-printing of epoxy-CF composite using a viscous solution printing based method. The wt.% composition was studied from 1%–10%.
- Used rheology and mixing of commercial-based epoxy and chopped CF to demonstrate the upscalability of the process with Epon, Epikure, and silica nanoparticles added.
- Identified limitations of the current 3D printing methods/design as shown in Figure II.3.1.4.4(a). Only two CF/epoxy extrusions were successful because the continuous fiber was large enough to almost reduce backflow completely. Additionally, maintaining CF diameter was difficult with ~3–6 k tow CF spool. (Note: need to find smaller diameter fibers NOT in the form of tows.)
- Studied model of the thixotropic/viscoelastic fluid flow of epoxy resin within the coextrusion process to determine accurate pressure, viscosity, and shear stress/rate measurements at specific points within the extrusion process to optimize coextrusion design and ink rheology.
- The need exists to determine nozzle exiting deposition velocity experimentally AND theoretically, based on the simulation results.
- Designed a new coextrusion assembly, as shown in Figure II.3.1.4.4(b).
- Conducted early investigations into multilateral 3D printing with a CF mat pre-preg, as well as the development of a sandwich structure.



Figure II.3.1.27. (a) 3D-printing of epoxy and continuous CF was initially achieved with the modified Hyrel attachment; however, results were not ideal and backpressure flows are still a problem. (b) A new co-extrusion assembly was designed to have both the fiber and epoxy matrix under the same pressure environment. Source: ORNL.

Task 4. Continuous sensor-embedded polymer/CF composite 3D printing:

- Published results of a previously developed protocol and 3D printing inks for embedded sensors and a zinc-ion battery.
- Designed and fabricated porous structures of PVDF-MoS₂ and V₂O₅ composites. The MoS₂ is commercial and through hydrothermal reaction/synthesis for piezoelectric sensors.
- Demonstrated the electrode, piezo sensor, and diode properties.
- Used SEM, atomic force microscopy, EDS elemental mapping, XRD, and Raman mapping to characterize the PVDF test structures. Raman mapping revealed significant aggregation at higher than 8%, as shown in Figure II.3.1.4.5(a).

- Successfully performed multimaterial-layered 3D printing of epoxy and PVDF-MoS₂ sample sandwich structure. Prepared a sample with ~250 μm in thickness, 1 cm in length, and sandwiched between epoxy layers. Mechanical tapping or impact tests will be performed in preparation for use with future CF/epoxy composite printing.
- Demonstrated 3D printing with electric poling to orient the 2D nanomaterials/PVDF composite formulations, as shown in Figure II.3.1.4.5(b). Challenges in the rheology and reproducibility are still present, but promising results have been achieved.

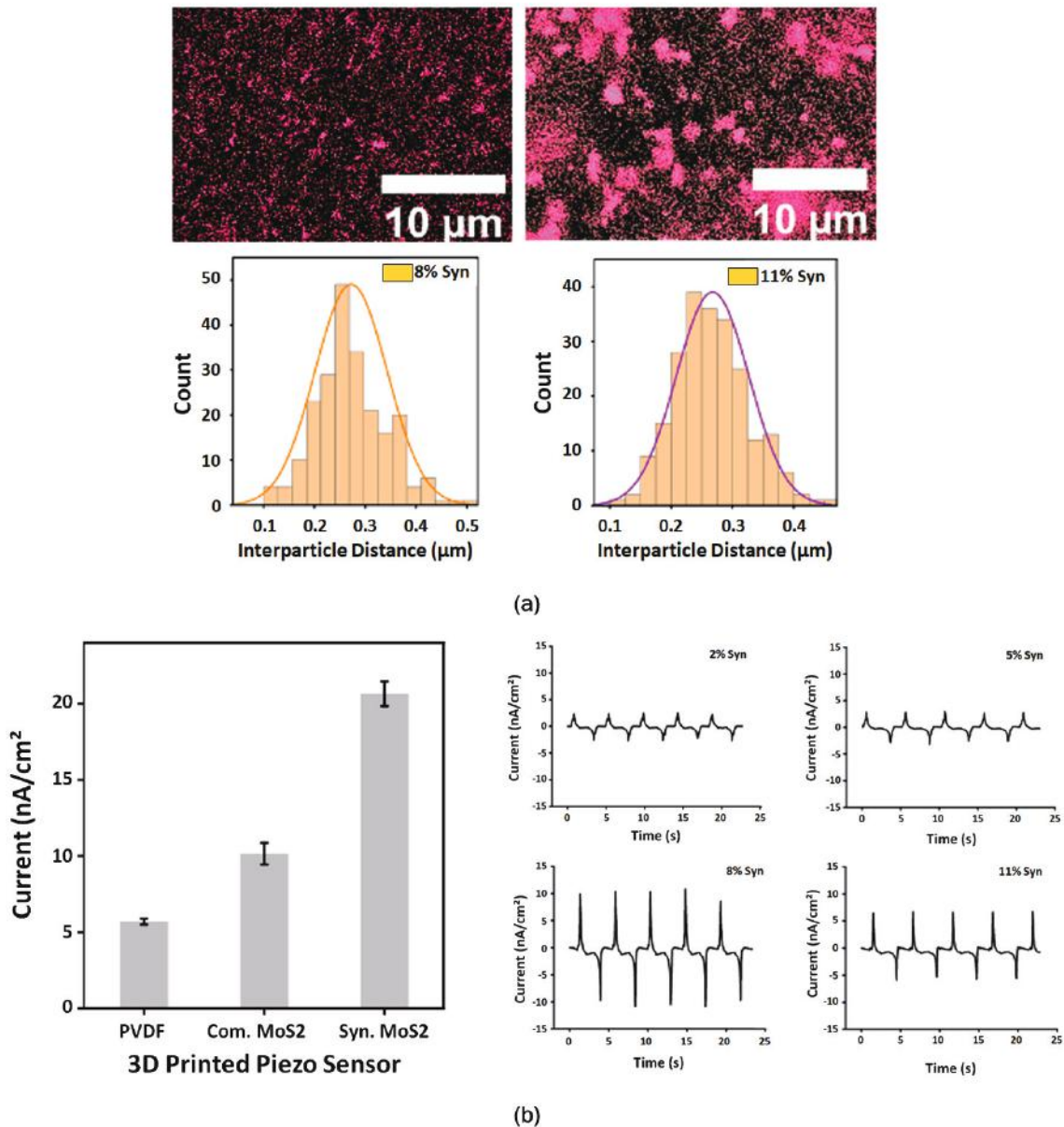


Figure II.3.1.28. (a) Raman mapping of MoS₂ distribution into PVDF at 8% and 11%. Note the poor distribution at higher concentrations of the 2D nanomaterial. (b) The properties of the 3D-printed PDF-MOS₂ piezoelectric sensors showing concentration-dependent differences between commercial and modified filler materials. Source: UNT.

Conclusions

- Demonstrated optimized silane modification method on CF, including amine and crown-ether amines with reproducible protocols. A fixed model epoxy resin composition was optimized for consistent formulation in subsequent studies.
- Utilized data-driven ML models to precisely predict the interface adhesion properties and identify imperfections along interfaces from FEA and standard experiments. Also established genetic algorithm and FEA iterations for crack propagation simulations with designed composites.
- Achieved 3D-printing of epoxy-CF composite using a viscous solution printing based methods, but limitations of the current printing methods/design have been identified and need to be mitigated. A new unibody design for controlled backflow pressure has been initiated.
- Designed and fabricated porous structures of PVDF-MoS₂ and V₂O₅ composites. The MoS₂ is commercial and used for hydrothermal reaction/synthesis for piezoelectric sensors. We have demonstrated their electrode, piezo sensor, and diode properties. Multimaterial and multilayer 3D printing will allow future embedment in epoxy-CF composite test structured.
- Reviewed the projects consistently in 2022 for end-goal objectives with bimonthly meetings and a cohesive team between ORNL and UNT for sharing results and joint publications.

Key Publications

1. Demchuk, Z., J. Zhu, B. Li, X. Zhao, N. M. Islam, V. Bocharova, G. Yang, H. Zhou, Y. Jiang, W. Choi, R. Advincula, and P.-F. Cao, 2022, “Unraveling the influence of surface modification on the ultimate performance of carbon fiber/epoxy composites,” *ACS Appl. Mater. Interfaces*, Vol. 14, No. 40, pp. 45775–45787. <https://doi.org/10.1021/acsami.2c11281>.
2. Jiang, Y., N. Islam, R. He, X. Huang, P.-F. Cao, R. C. Advincula, N. Dahotre, P. Dong, H. F. Wu, and W. Choi, 2022, “Recent advances in 3D printed sensors: Materials, design, and manufacturing,” *Adv. Mater. Technol.*, Vol. 8, No. 2, Art. 2200492. <https://doi.org/10.1002/admt.202200492>.
3. Stephen, A., S. Bhoyate, P. Cao, R. Advincula, N. Dahotre, Y. Jiang, and W. Choi, 2022, “3D-printed flexible anode for high-performance zinc-ion battery,” *MRS Commun.*, Vol. 12, pp. 894–901. <https://doi.org/10.1557/s43579-022-00267-5>.

References

1. Sun, J., F. Zhao, Y. Yao, Z. Jin, X. Liu, and Y. Huang, 2017, “Highly efficient and continuous surface modification of carbon fibers with improved tensile strength and interfacial adhesion,” *Appl. Surf. Sci.*, Vol. 412, pp. 424–435. <https://doi.org/10.1016/j.apsusc.2017.03.279>.
2. Hao, W., Y. Liu, H. Zhou, H. Chen, and D. Fang, 2018, “Preparation and characterization of 3D printed continuous carbon fiber reinforced thermosetting composites,” *Polym. Test.*, Vol. 65, pp. 29–34. <https://doi.org/10.1016/j.polymertesting.2017.11.004>.

Acknowledgments

The authors acknowledge technical support with Hyrel on the fabrication of the 3D printing attachment and the Sokolov Group at the ORNL Chemical Sciences Division.

II.3.1.5 New Frontier in Polymer Matrix Composites via Tailored Vitrimer Chemistry (Oak Ridge National Laboratory)

Tomonori Saito, Principal Investigator

Oak Ridge National Laboratory
Materials Science and Technology Division
1 Bethel Valley Rd.
Oak Ridge, TN 37831
E-mail: saitot@ornl.gov

Rich Davies, Composites Core Program Manager

Oak Ridge National Laboratory
Materials Science and Technology Division
1 Bethel Valley Rd.
Oak Ridge, TN 37831
E-mail: daviesrw@ornl.gov

H. Felix Wu, DOE Technology Development Manager

U.S. Department of Energy
E-mail: felix.wu@ee.doe.gov

Start Date: October 1, 2020

End Date: September 30, 2023

Project Funding (FY 2022): \$500,000

DOE share: \$500,000

Non-DOE share: \$0

Project Introduction

Manufacturing transformation towards a net-zero carbon society demands polymeric composite materials to be reprocessable in circularity in an energy-efficient and stable manner. Enabling recyclability and establishing circular manufacturing of currently non-recyclable polymers would significantly reduce global carbon intensity compared to traditional polymers. Carbon fiber-reinforced polymers (CFRPs) play a major role in enabling highly efficient energy usage in automobile and aerospace applications, because of their lightweight and robust mechanical properties. The rapid growth of CFRPs in various industries generates major environmental challenges in waste management. Most of the conventional CFRPs are very difficult to recycle and end up in the natural environment or a landfill because their resins are permanently crosslinked, preventing remolding, repairing, or recycling, as observed in Figure II.3.1.5.1(a). Moreover, CF production is energy-intensive (~198–595 MJ/kg) and causes large amounts of greenhouse gas emissions. Recycling CFs and CFRPs will significantly save energy consumption and reduce the manufacturing carbon footprint. While advances are made for recycling CFRPs, conventional recycling technologies are energy-intensive and the mechanical properties of the reprocessed material are typically much lower compared to the original product. As a consequence, recycling rates remain very low and the poor recyclability of CFRPs is the major bottleneck for the wider adoption of lightweight materials in contrast to traditional metals (e.g., steel) with established recycling paths. In addition, the current epoxy-based CFRP manufacturing process is time-consuming, not cost-effective, and not ideal for efficient mass production. In this project, novel vitrimer-based resins were designed and synthesized using a fast and robust dynamic exchange chemistry, enabling the crosslinked network to be fast, reprocessable, and repairable.

Vitrimers are crosslinked with dynamic covalent networks that can change their topology and decrease their viscosity upon heating, and they are an excellent candidate for enabling circular manufacturing of CFRPs. Similar to thermoplastics, vitrimers can be reshaped, reprocessed, and recycled at elevated temperatures, while maintaining the network integrity of crosslinked thermoset polymers. Various types of vitrimers have been developed to achieve recycling, reprocessing, and repairing of thermosets, including disulfide, ester, urea, imine amine, and hexahydro-s-triazine containing a dynamic covalent bond. Recent advancements in vitrimers have bestowed crosslinked polymers like epoxies with reprocessability, opening a path for the circular manufacturing of thermosets. However, (re)processing of mechanically robust vitrimers, such as a dynamic epoxy (DE), typically requires high temperatures and long processing times, which cause degradation and compromise efficient recyclability, as shown in Figure II.3.1.5.1(b). The simple strategy of a tailored resin combination presented here is effective in preparing mechanically strong and readily reprocessable vitrimers and their CFRPs as with a dynamic polyurea (PU)/epoxy (DPE), shown in Figure II.3.1.5.1(c) [1].

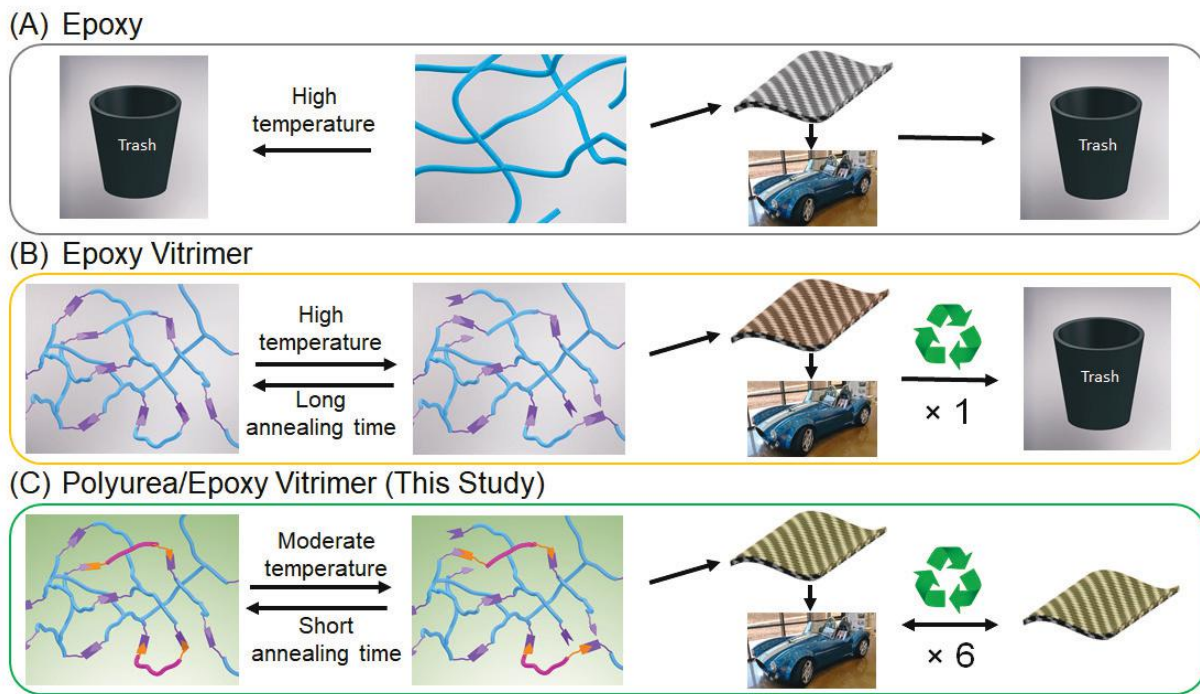


Figure II.3.1.29. Illustration of traditional processes for thermoset and dynamic vitrimers. (a) Conventional epoxy-based on permanently crosslinked networks cannot be reprocessed or recycled after cure. (b) DE consisting of dynamic covalent bonds, as part of the crosslinked network, can be reprocessed or recycled only at high temperatures and a long annealing time, but it lacks repeated recyclability. (c) DPE with exchangeable bonds has a controllable network reconfiguration, possesses a relatively low glass transition temperature, and can be reprocessed or recycled at least six times at a moderate temperature and short annealing time after curing. Source: ORNL.

Objectives

This project aims to develop fast-processable, repairable, recyclable, and affordable CFRPs while exhibiting superior mechanical properties by incorporating vitrimer chemistry into the fibers and resins. The use of CFRPs for vehicles is currently limited due to the high manufacturing cost of CFs, as well as the time-consuming curing process of manufacturing CFRP parts. CFRPs based on thermoset epoxy are widely utilized due to good thermal and mechanical properties; however, these epoxy resins require a long processing time and cannot be repaired, remolded, reprocessed, or recycled. To overcome the existing limitations of current CFRPs, we pursued three research objectives:

1. Develop next-generation affordable vitrimer-based resins and reinforce using CFs.
2. Optimize the manufacturing process (e.g., fast-curing) of CFRPs and improve fiber-matrix interfacial adhesion for achieving higher load transfer efficiency.
3. Generate fast-processable, repairable, and recyclable vitrimer-based CFRPs, while maintaining superior mechanical properties.

Developing novel vitrimer-based CFRPs will enable high-volume, high-performance, and affordable polymer composites with reprocessability/recyclability, repairability, and fast-processability; thus, significantly contributing to achieving the goals of the VTO for lightweight vehicles.

Approach

To achieve the project objectives, the project team tailored a resin combination for multicycle recyclability of robust dynamic CFRPs without deterioration of performance, as can be seen in Figure II.3.1.5.1(c), overcoming the limitation of various vitrimer systems. We chose disulfide dynamic bonds, since disulfide bonds are easily cleavable, and the cured thermoset materials become malleable and reprocessable under external stimuli (e.g., a moderate temperature). The mechanical properties can be easily recoverable due to the fast exchange of disulfide bonds. The strategy involves the incorporation of dynamic metathesis of aromatic disulfide bonds bridging between a ductile PU segment and mechanically robust epoxy network. Dynamic PU/epoxy (DPE) vitrimers were synthesized by reacting tailored ratios of aliphatic poly (hexamethylene diisocyanate) [HDI] prepolymer and diglycidyl ether of bisphenol A (DGEBA) using 4-aminophenyl disulfide (AFD) as dynamic crosslinks, as can be seen in Figure II.3.1.5.2(a). The incorporation of ductile PU not only improves the mechanical properties (e.g., toughness, resilience, ductility) but also decreases the processing temperature, which ultimately leads to improved recyclability. We have investigated the thermal, mechanical, and rheological properties of DPEs and compared them with the conventional epoxy thermosets and the DE vitrimer control. Because of the rapid exchange reactions and the efficient PU/epoxy chain rearrangement, the DPE resins exhibited superior reprocessability with a rapid processing rate and excellent recovery of mechanical strength compared to the DE. Furthermore, the DPE resins and their CFRPs displayed outstanding mechanical and chemical recyclability. These advanced properties highlight the great promise of tailored resin combination with dynamic disulfide crosslinkers for providing mechanically robust, rapidly processable, and chemically and mechanically recyclable CFRPs [1].

Results

The DPE vitrimers were prepared by the reaction of DGEBA and HDI aliphatic polyisocyanate prepolymer with disulfide-based dynamic crosslinker AFD, as observed in Figure II.3.1.5.2(a). To investigate the impact of PU, we synthesized different weight ratios of PU to epoxy resins at 1:0, 2:1, 1:1, 1:2, and 0:1. Three reference samples, including conventional epoxy, dynamic PU (i.e., 1:0), and DE (i.e., 0:1) networks, were prepared. The conventional epoxy was obtained via mixing DGEBA and 4,4'-diaminodiphenylmethane, while the DE network was prepared by mixing DGEBA with AFD, followed by an ultrasonic degassing procedure. Both conventional and DE resins were cured in the same condition in an oven at 120°C for 2.5 hours. For DPE vitrimers, tetrahydrofuran was used to dissolve AFD and then mixed with HDI prepolymer or HDI/epoxy resins. After solvent evaporation, both HDI and HDI/epoxy resins were cured at the same conditions as epoxy resins at 120°C for 2.5 hours. Fourier-transform infrared (FTIR) spectroscopy confirmed the formation of DPE vitrimers as observed in the amine-epoxy bond at ~1580 cm⁻¹ and urea peak at ~1680 cm⁻¹, respectively, as shown in Figure II.3.1.5.2(b) [1].

The thermomechanical properties as a function of different weight ratios of dynamic PU to epoxy resins were investigated by the typical temperature sweeps of dynamic mechanical analysis to record their storage modulus (E') and loss factor ($\tan \delta$) values. The storage modulus of the DPE sample with lower epoxy content starts to decrease at lower temperatures and turns into a constant rubbery plateau. The presence of constant storage moduli at their rubbery plateau state in all samples confirms the crosslinked nature of dynamic covalent networks. The glass transition temperature (T_g) was determined from the maximum of the $\tan \delta$. As shown in

Figure II.3.1.5.2(c), the dynamic PU shows a T_g at $\sim 88^\circ\text{C}$, while the DE has a T_g at $\sim 140^\circ\text{C}$, which agrees with previous reports. The DPE network exhibited a clear trend of decreasing T_g with an increasing concentration of PU. For example, T_g of DPE resin is $\sim 100^\circ\text{C}$ at a weight ratio of 1:1, which is much lower than that of the DE at $\sim 140^\circ\text{C}$.

To examine the mechanical properties of the dynamic resins, we first fabricated dumbbell-shaped specimens using a liquid solution-based method and cured them in an oven to obtain fully crosslinked dynamic networks. As shown in Figure II.3.1.5.2(d), the uniaxial tensile strength of samples increased with more loading of epoxy. In contrast, the fracture tensile strain (ductility) exhibited the opposite trend. For example, the tensile strength of the dynamic PU was 39.2 ± 1.7 MPa, while that of the DPE network with a weight ratio of 1:1 increased to 56.8 ± 3.8 MPa. The DE exhibited a tensile strength of 67.8 ± 4.6 MPa, which is similar to the tensile strength of conventional epoxy. Considering desirable strength, ductility, and T_g value for processing, we identified the DPE network with 1:1 as a well-balanced vitrimer, and therefore, we used this system as the baseline for other modifications and characterizations.

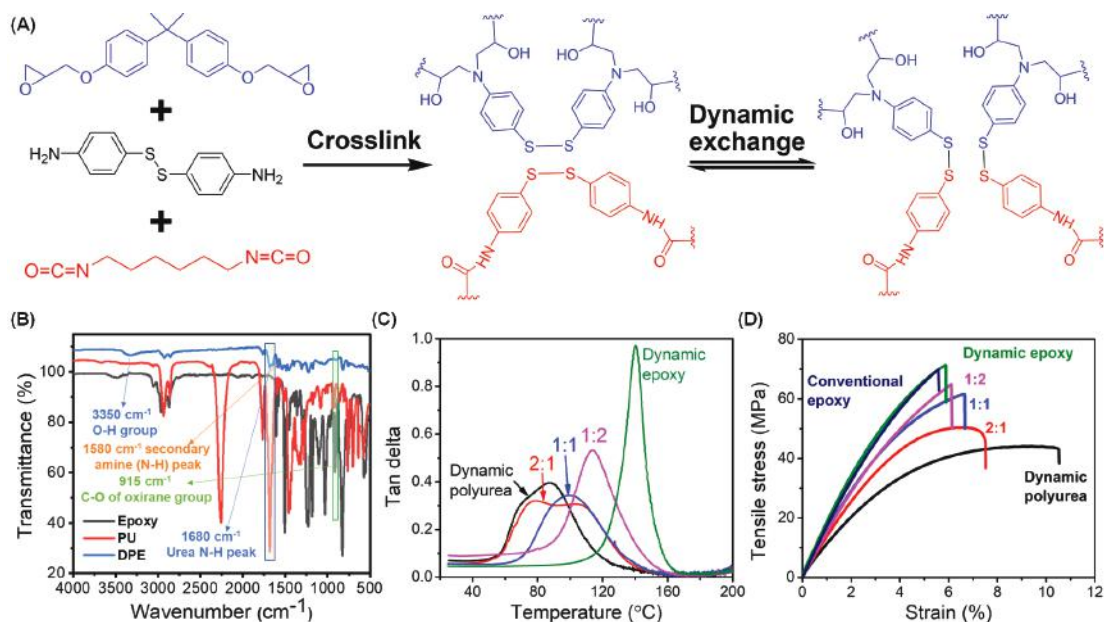


Figure II.3.1.30. Synthesis and thermomechanical properties of DE and DPE. (a) Synthesis of crosslinked DPE resin by reacting isocyanate and epoxy with AFD (each chemical structure is in red, blue, and black, respectively). (b) FTIR spectra of epoxy (black), PU (red), and DPE (blue) samples. (c) Dynamic mechanical analysis curves obtained for different weight ratios of PU to epoxy representing $\tan \delta$ versus temperature. (d) Representative tensile stress-strain curves for three different weight ratios of PU to epoxy resins for 1:2 (pink), 1:1 (blue), and 2:1 (red). Source: ORNL.

To illustrate the superior reprocessability of our dynamic vitrimers, we compared the traditional epoxy crosslinked with unexchangeable covalent bonds processed in a hot-press at 200°C and 500 psi for 5 min, resulting in broken pieces, as observed in Figure II.3.1.5.3(a), with the DE and DPE vitrimers having dynamic covalent crosslinks shown in Figure II.3.1.5.3(b) and Figure II.3.1.5.3(c), respectively. Due to the permanently crosslinked networks, the broken scraps of traditional epoxy specimens could not be reprocessed or recycled using hot-pressing at elevated temperatures of 200°C , and they remained broken after hot-pressing, as can be seen in Figure II.3.1.5.3(a). In contrast, owing to the exchangeable disulfide bonds, both the DE and DPE scraps were successfully hot-pressed and reformed into homogenous, compact films, as shown in Figure II.3.1.5.3(b) and Figure II.3.1.5.3(c), respectively. Importantly, the reprocessing of the DPE could be performed at a moderate temperature of 160°C , coupled with a short annealing time of 1 min.

The effectiveness on the recyclability of DPE and DE was evaluated by testing their mechanical properties after each reprocessing cycle. The reprocessing of the DE was conducted at 200°C and 100 psi for 5 min, while the DPE was reprocessed at 160°C and 100 psi for 1 min. As shown in Figure II.3.1.5.3(c), the broken pieces were successfully remolded into compact films and then cut into dumbbell-shaped specimens. The tensile behavior of both DE and DPE samples was evaluated after each of the six recycling cycles, as indicated in Figure II.3.1.5.3(d). The results demonstrate that both DE and DPE can recover their tensile strength. The tensile strength of the DE started to decrease from the second reprocessing and dramatically dropped after the sixth reprocessing to ~26 MPa, which is ~36% of the initial tensile strength, as seen in Figure II.3.1.5.3(d). This significant loss of tensile strength may be due to the degradation of disulfide bonds and oxidation of the epoxy network upon repeated exposure to the high processing temperature of 200°C. In contrast, the DPE maintained nearly 100% of the mechanical strength, ~61 MPa after the sixth reprocessing cycle, suggesting the DPE was readily reprocessed multiple times at 160°C without any considerable degradation. The FTIR spectra confirmed the stability of DPE resin, as shown in Figure II.3.1.5.3(e), as there is no obvious change observed in the disulfide bond (e.g., ~450-650 cm^{-1} for S-S bond stretching) owing to the moderate temperature and short annealing time. Stable multicycle reprocessability is crucial for practical deployment since multi-processes such as remodeling are necessary for the thermoformation of composites, as well as repeated mechanical recycling.

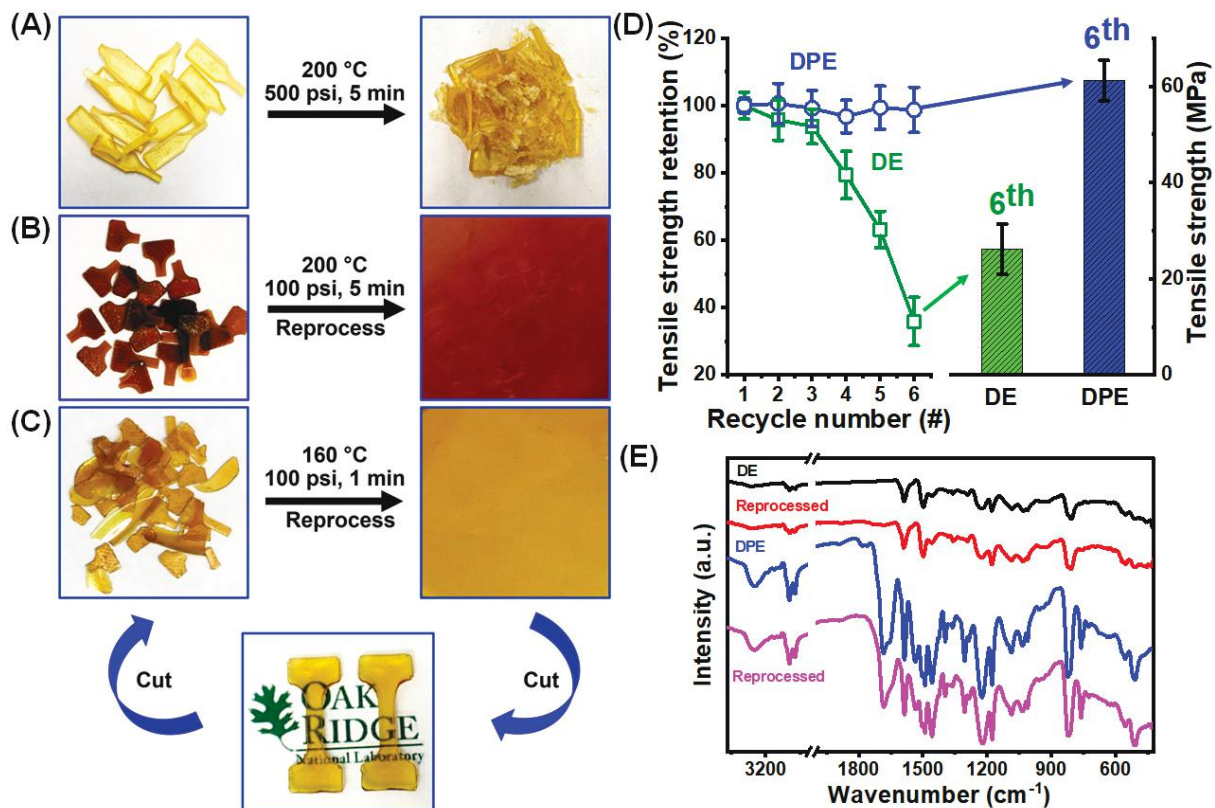


Figure II.3.1.31. Reprocessing by hot-pressing. (a) Traditional epoxy samples crosslinked by unexchangeable bonds resulting in broken pieces. (b) Tested DE specimens reprocessed at the same hot-pressing condition as traditional epoxy resulting in a compact film. (c) Pristine DPE samples after testing that were hot-pressed (reprocessed) to obtain a recycled compact film which was easily cut to dumbbell-shaped specimens. (d) Summarized tensile strength values of reprocessed DE (green) and PU/epoxy samples (blue) (data are represented as mean \pm SEM). (e) FTIR spectra of dynamic samples before and after reprocessing.

Source: ORNL.

The facile processability of the DPE is well-suited for (re)processing and fabrication of CFRPs. We followed conventional thermoforming of cured composite CFRP laminate, as shown in Figure II.3.1.5.4(a). First, three individual CF woven fabric composites with a dimension of 120×120 mm were soaked in a DPE resin solution with a weight ratio of 1:1 and cured in an oven at 120°C for 2.5 hours, as observed in Figure II.3.1.5.4(a). After curing, the three composite sheets were placed together and pressed in a hot-press. After hot-pressing at 160°C and 500 psi for 1 min, these three sheets were formed into a compact multilayer composite laminate sheet, also observed in Figure II.3.1.5.4(a), which further demonstrates the excellent processability of the DPE. The multilayered composite laminate was then placed inside a closed-cavity compression mold, as shown in Figure II.3.1.5.4(b), to quickly obtain a reshaped 3D composite. Such a fast-thermoforming process illustrates the great promise of the DPE for scalable, low-cost manufacturing of CFRPs.

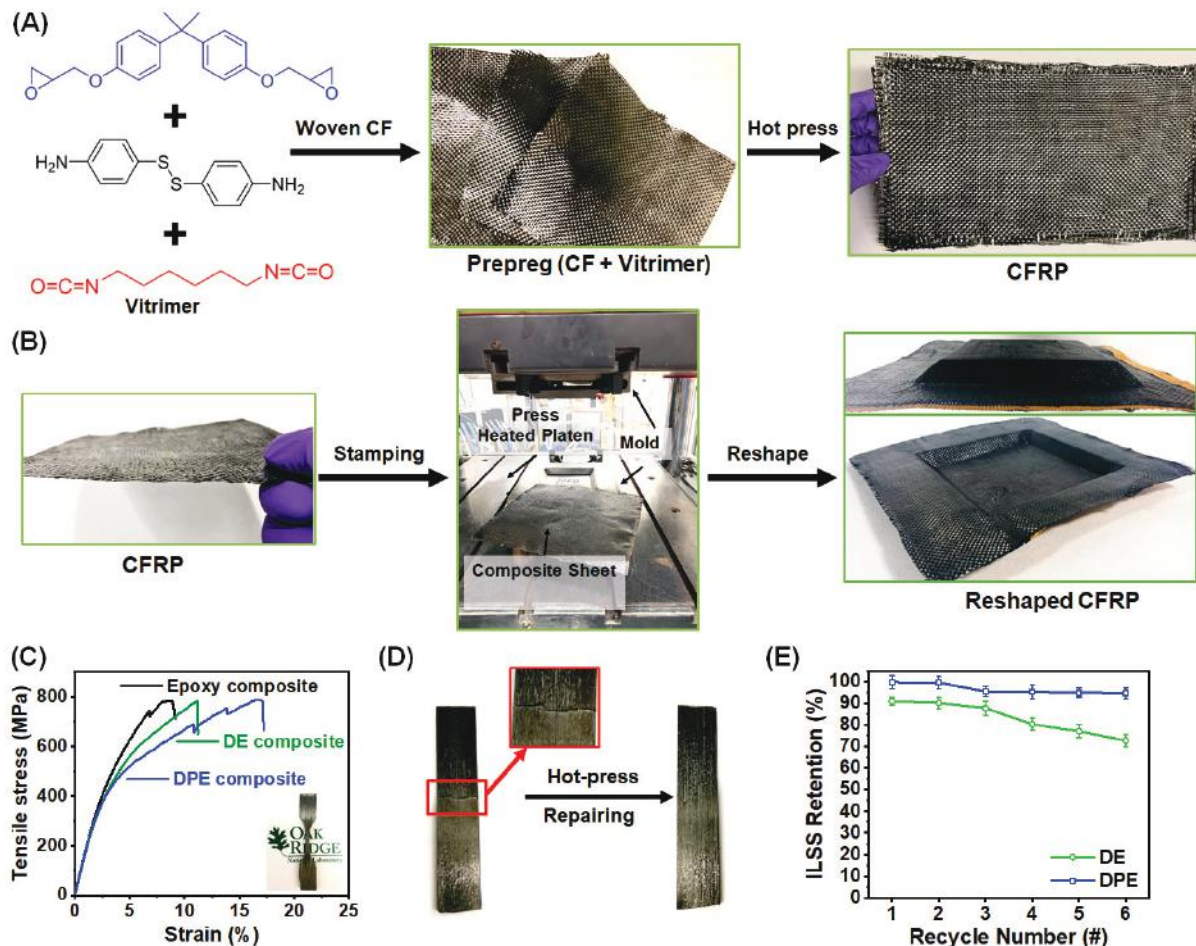


Figure II.3.1.32. Demonstration of CFRP manufacturing by both prepregs and stamping: (a) Preparation of CFRP from a vitrimer of DPE resin and (b) CM and stamping of the cured multilayered CFRP sheet via thermoforming technique reshaped to a 3D form (top and bottom views of the multilayered 3D composite sheet). (c) Representative stress-strain curves obtained from the tensile tests for conventional epoxy composites (black), DE composites (green), and DPE composites (blue), respectively. (d) A DPE composite with a crack in the middle after the flexural test and fully repaired after being hot-pressed at 160°C for 5 min. (e) Interlaminar shear strength (ILSS) retention measured after repairing the cracked sample from each cycle's short-beam shear tests for up to six cycles of both DPE and DE CFRPs. Source: ORNL.

Uniaxial tensile tests were performed on conventional epoxy, DE, and DPE composites with unidirectional CFs (Hexcel IM7, 12K) according to ASTM D638. Figure II.3.1.5.4(c) shows the representative tensile stress-

strain curves. The tensile strength of the DPE composite was found to be comparable to those of the DE and conventional epoxy composites, exhibiting a high-tensile strength of ~800 MPa. In addition, we used a short-beam shear test method following ASTM D2344 to characterize the apparent interlaminar shear strength (ILSS) of CFRPs and repaired CFRPs, as seen in Figure II.3.1.5.4(d). The DPE composite showed a crack in the middle after the flexural test, but after being hot-pressed at 160°C for 5 min, the crack in the sample disappeared and the matrix was fully repaired. The DPE composite exhibits a sufficient ILSS of 50 ± 1.2 MPa, which is ~67% of that of the DE composite. Furthermore, the repaired DPE composite exhibited only less than ~2% loss in the ILSS of the original sample, which is 4× smaller than the ~8% drop in the DE composite. Even after six cycles of repairing, the repaired DPE CFRP retained approximately 97% ILSS, whereas the DE CFRP lost almost 28% of initial ILSS, as indicated in Figure II.3.1.5.4(e). The mechanical property and reparability demonstrated here suggest the great potential of a tailored resin combination of DPE composite to design and prepare mechanically robust, readily reprocessable CFRPs.

Conclusions

We identified the tailored resin system with exchangeable disulfide bonds, DPE for CFRPs, to overcome two long-lasting challenges—simultaneously achieving high mechanical strength and facile multicycle reprocessability. The DPE vitrimer exhibited a 6× faster stress relaxation time at 160°C compared to the DE, which was enabled by the synergy of the rapid exchange reaction of disulfide metathesis and the efficient PU/epoxy chain rearrangement. Importantly, the DPE vitrimer retained the mechanical strength after many processing cycles thanks to the facile moldability at a moderate temperature with a short annealing time, in contrast to the dramatic decrease in the mechanical strength observed from DE after four cycles. Notably, the CFRPs with the DPE exhibited excellent reprocessability and reparability with near-complete preservation of mechanical strength. The DPE resins and their CFRPs also displayed chemical recyclability where CFs could be recycled while maintaining good chemical resistance to the common solvents. These findings thereby provide a solution to the fundamental challenges of high-energy/carbon-intensiveness and mechanical deterioration upon recycling of thermoset composites. Furthermore, the formulation of DPE is intentionally designed to be simple, meaning facile scaleup and rapid adoption in the industry is possible. The stable multicycle recyclability of the DPE composites and their design principle can promote the development of highly sustainable, efficient, and low carbon manufacturing of next-generation CFRPs, which can be widely adopted in lightweight materials for applications in various clean energy technologies.

Key Publications

1. Saito, T., M. A. Rahman, and Z. Zhou, 2022, “Unraveling a path for multicycle recyclability in robust dynamic fiber-reinforced vitrimer composites,” U.S. Provisional Patent Application, No. 63/334261.
2. Zhou, Z., S. Kim, C. C. Bowland, B. Li, N. Ghezawi, E. Lara-Curzio, A. Hassen, A. K. Naskar, M. A. Rahman, and T. Saito, 2022, “Unraveling a path for multicycle recyclability in robust dynamic fiber-reinforced vitrimer composites,” *Cell Rep. Phys. Sci.*, Vol. 3, No. 9, Art. 101036. <https://doi.org/10.1016/j.xcrp.2022.101036>.

References

1. Zhou, Z., S. Kim, C. C. Bowland, B. Li, N. Ghezawi, E. Lara-Curzio, A. Hassen, A. K. Naskar, M. A. Rahman, and T. Saito, 2022, “Unraveling a path for multicycle recyclability in robust dynamic fiber-reinforced vitrimer composites,” *Cell Rep. Phys. Sci.*, Vol. 3, No. 9, Art. 101036. <https://doi.org/10.1016/j.xcrp.2022.101036>.

Acknowledgments

This research was sponsored by the DOE-EERE VTO. We thank the team members of this project: A. Rahman, C. Bowland, A. Naskar, Z. Zhou, S. Kim, B. Li, and N. Ghezawi.

II.3.1.6 Adopting Heavy-Tow Carbon Fiber for Repairable, Stamp-Formed Composites (Oak Ridge National Laboratory)

Amit Naskar, Principal Investigator

Oak Ridge National Laboratory
Chemical Sciences Division
1 Bethel Valley Rd.
Oak Ridge, TN 37831
E-mail: naskarak@ornl.gov

Rich Davies, Composites Core Program Manager

Oak Ridge National Laboratory
Energy Science and Technology Directorate
1 Bethel Valley Rd.
Oak Ridge, TN 37831
E-mail: daviesrw@ornl.gov

H. Felix Wu, DOE Technology Development Manager

U.S. Department of Energy
E-mail: felix.wu@ee.doe.gov

Start Date: October 1, 2020

End Date: September 30, 2023

Project Funding (FY 2022): \$500,000

DOE share: \$500,000

Non-DOE share: \$0

Project Introduction

This research focuses on interface engineering and high-throughput manufacturing methods for heavy-tow CF having > 100 k filaments in a single bundle and tailoring its bonding and interactions with thermoplastic matrices to develop new stamp-formed layered structures. This involves the integration of fundamental understanding, the application of modern x-ray and neutron-based characterization tools, and high-performance computation to achieve the rational molecular level design and control of the mechanical properties in thermoplastic composites. State-of-the-art automotive parts produced from thermoplastic composites at a high production rate (> 250,000 parts/year) cost more than \$ 50/kg. We will develop technology that enables a 30%–50% cost reduction in composite parts, such as roofs, hood inner-liners, and inner door panels (\$20–\$30/kg in parts). This project will eliminate several processing steps, multiple shipments, and storage requirements for composite intermediates. In addition, it will deliver repairable low-cost thermoplastic composites with a multilayered stamp-formed structure containing 40%–60% by volume of fiber and outstanding mechanical performance (e.g., 0.8–1.4 GPa tensile strength, 50–100 GPa Young's modulus, and ~10% failure strain). We will use a high-temperature resistant polyamide (nylon), polyphenylene sulfide, and a low-cost commodity grade polypropylene (PP) plastic to develop automotive composite structures with broad end-use potentials. ORNL has successfully produced low-cost, heavy-tow CFs from textiles; however, the brittle nature of the carbonized fibers precludes complex handling. In addition, uniform application of sizing on such a large number of filaments following the application of proper surface chemistry remains a challenge. Current surface-treatment methods are developed for epoxy matrices and are not applicable for thermoplastics with less polarity than epoxies.

To address these challenges, this project envisions a sizing-free, direct-calendaring process for the surface activated fibers. With minimal unit operations, direct manufacturing of heavy-tow CFs into reinforced intermediates enables subsequent stamp-forming to a structure. Unlike thermosets, thermoplastic matrix infused intermediates are easy to store, enabling repair or remolding of the parts and restoration of the embodied energy in the structures after EOL.

Objectives

The objective of this research is to develop and commercialize new interfacial engineering methods for efficient reinforcement of thermoplastic matrices by heavy-tow CFs and demonstrate that the chemistry and processing allow the formation of multilayer laminate structures rivaling the rapid stamping rate of metals. The project will deliver repairable low-cost thermoplastic composites with a multilayered stamp-formed structure containing 30%–60% by volume of fiber and outstanding mechanical performance (e.g., 0.8–1.4 GPa unidirectional tensile strength, 50–100 GPa Young's modulus). High-throughput processing technologies for thermally recyclable or repairable CF composites of thermoplastic matrices will enable a new paradigm toward cost-competitive lightweight materials for automotive fuel efficiency without compromising their mechanical performance and crashworthiness.

Approach

The overarching goal of this research is to connect the key physicochemical relationships at different length scales (including surface adsorption or bonding, polymer interfacial dynamics, and fiber–fiber interactions) to the key process engineering considerations, along with macroscopic rheological and mechanical properties of thermoplastic polymer matrix composites. To this end, we combine polymer and interfacial chemistry, x-ray scattering, rheology, thermomechanical characterization of intermediates and formed samples and spectroscopy (on the experimental side) with molecular dynamics simulations (on the high-performance computation side). Specifically, the project team is (1) developing new interfacial chemistries under the guidance of a computationally defined framework to optimize polymer-fiber interaction, (2) revealing the interplay of the interfacial interactions on the processability and composites' response to load by using mechanical testing and in situ x-ray scattering, and (3) elucidating the relationship between fiber volume fraction, matrix morphology, and performance of the stamp-formed multilayered structures.

Results

The following summary includes the work performed in FY 2022 for the completion of project milestones listed in Table II.3.1.6.1 at ORNL.

Table II.3.1.6.1. FY 2022 Milestone Summary

Milestone Name/Description	Criteria	End Date
Demonstrate 10% immobilized PP on the CF by analytical methods	Analytical methods confirm that at least 10% matrix is bound to the fibers.	12/31/2021
Quantify effect of molding pressure and temperature on the properties of discontinuous preform laminate composites and show >100 MPa strength.	Processing data reported and mechanical testing of composites delivers the expected properties.	03/31/2022
Quantify activation energies for forming chemisorbed matrices and identify stabilized structures of polymer matrix attached to the CF surface.	Thermal analysis data confirms relaxation behavior of the bound matrix on the fibers.	06/30/2022
Demonstrate 500 MPa tensile strength in unidirectional intermediate.	Mechanical testing of fibers delivers the expected properties.	09/30/2022

A key design consideration in composite manufacturing is the interface, which serves to efficiently transfer the load between the reinforcing phase and the continuous matrix phase. In traditional composite formulations, surface treatments on the carbon or glass fibers are applied to produce reactive functional groups that have been carefully matched with the stoichiometry of the thermoset resin [1]. In this case of thermoplastic-based composites, the interfacial function is performed by physisorbed polymer chains [2]. To ascertain the robustness of the polymer adlayer, we developed a gravimetric-based analytical method. The CF-PP composites with 45 wt.% CF was cut into strips, and 1 g of composite sample was added to 20 ml of xylene for refluxing, as observed in Figure II.3.1.6.1(a). This implies that the PP content in the composite was 55 wt.%, which translates to 0.55 g of PP and 0.45 g of CF before the start of the reflux process, which was carried out for 2 hours to ensure xylene thoroughly infiltrates the composite and dissolves the PP chains that are not

strongly bonded to CF surfaces. Following the reflux process, the composite sample was removed from the reflux vessel and washed with hot xylene at 140°C to remove any traces of dissolved PP that might have settled on the composite surface, as found in Figure II.3.1.6.1(b). Finally, the composite sample was dried to remove the xylene solvent and weighed to obtain the remaining weight. The sample weight after reflux and solvent washing was found to be 0.53 g. This implies that 0.08 g of PP is retained in the composite since weight contribution from CF stayed constant (CF = 0.45 g). Hence, the remaining 0.08 g of the initial 0.55 g of PP indicates that 14.5% of PP was immobilized on the CF surface and did not get separated from the surface even after the xylene reflux, exceeding the preliminary goal of 10%.

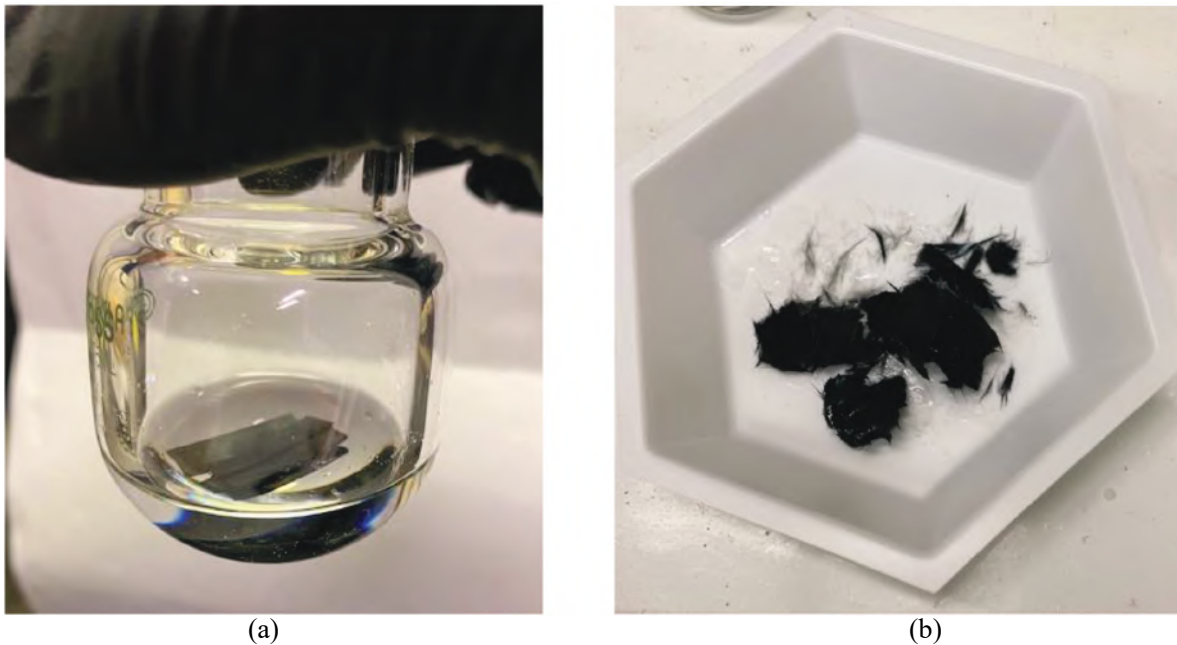


Figure II.3.1.33. Refluxing 45 wt.% CF-PP composite: (a) CF-PP strips in xylene solvent before refluxing; and (b) the remaining CF-PP sample after refluxing and washing with xylene solvent. Source: UNT.

To ascertain the effects of compaction pressure in isotropic composites, we utilized an air vortex channel to randomly distribute chopped fiber mats to form laminate composites, as observed in Figure II.3.1.6.2(a). The chopped fibers were fed through a feeder tube approximately 2 inches behind the air-blowing nozzle. Due to the low pressure created behind the air-blowing nozzle, the CFs are pulled into the hollow tube and dispersed randomly by the high-velocity air. In the second step of the fabrication process, alternate layers of PP films and chopped CF mats were stacked on top of each other and hot-pressed between steel plates at different pressures to investigate the effect of molding pressure on mechanical properties. Two different pressures of 5 tons and 10 tons were investigated for hot-pressing at 190°C for 30 mins, as can be seen in Figure II.3.1.6.2(b). Samples were cooled to RT in the press to prevent resin shrinkage.

A commonly employed melt-mixing process yielded an average tensile strength of 39.7 MPa and was used as the composite baseline. The mat-pressing method showed significant improvements in response to compaction pressure, increasing the strength of the laminate composite from 60 MPa to over 96 MPa, as shown in Figure II.3.1.6.3. The pressure and temperature profile were utilized on isotropic composites formed using a liquid-based fiber dispersion process composites to achieve an average of 115 MPa at just 20 vol.% fiber-loading to achieve the FY 2022 second quarter milestone, which aimed at > 100 MPa strength.

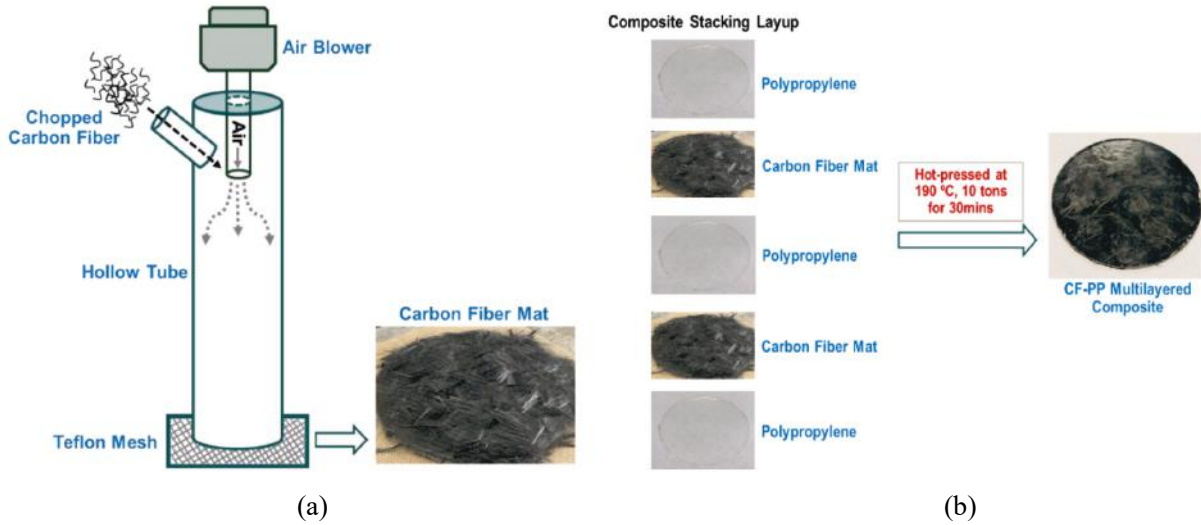


Figure II.3.1.34. Schematic of fabrication process for multilayered composite structures showing: (a) the air-blowing setup for preparing chopped CF mats; and (b) the hot-pressing process for fabricating multilayered CF-PP composite. Source: UNT.

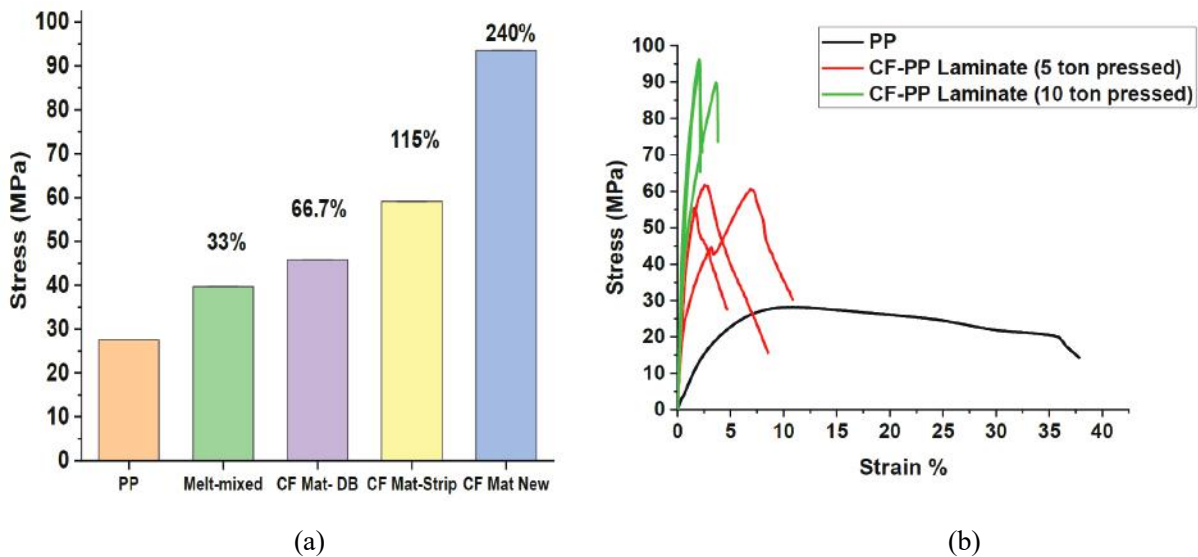


Figure II.3.1.35. Tensile test data for the CF-PP composites: (a) results for samples prepared using different fabrication techniques; and (b) stress-strain results for the novel multilayered CF-PP laminates that were hot-pressed at different molding pressures. Source: UNT.

The deployment of CF containing thermoplastic composites requires a precise understanding of the underlying morphology of the polymer matrix. In the case of semi-crystalline polymers, which are commonly desired for their toughness resulting from a deeply interconnected morphology of reinforcing high density crystalline regions and more mobile amorphous sections. Previously, the project aimed to better understand the morphology of polymer phases. Polarized optical microscopy revealed a distinct transcrystalline region directed at the fiber surface, which suggests that the CFs are acting as microscopic nucleating agents. PP spherulites grown near fibers are restricted to 10–30 micrometer radii with thinner lamellae (e.g., < 200 nm) as compared to those formed in bulk. The results suggest that PP crystal nucleation and growth on CF surfaces probably contributed to the enhancement of interfacial interactions between CFs and the PP matrix. Differential scanning calorimetry (DSC) was employed to understand crystal dimensionality and the modes of crystal nucleation utilizing the Avrami and Kissinger equations under isothermal and non-isothermal

conditions, respectively. Compacted CF composites of PP and nylon (N6,6) at fiber loadings of 10, 20, and 30 vol.% were prepared for these studies and sectioned into DSC samples. To determine the impacts of increased fiber-loading on the activation energy of crystallization (E_a) under non-isothermal conditions, ramp rates from 1 to 10°C/min were utilized to best represent practical thermoforming conditions. Utilization of the Kissinger equation allows for determination of a single E_a for a multi-stage process like crystallization and, thereby, qualitative comparisons for uniform processes. Briefly, for any reactive transition, the activation energy (E_r) can be determined from the reaction rate maximum, which is assumed as the peak heat flow value from the thermogram. With the peak reaction rate temperature (T_p) determined for several linear cooling rates, a linear form of the equation was used to determine the slope that delivered E_r , as given by Eq. 1.

$$\ln\left(\frac{\beta}{T_p^2}\right) = \ln\left(\frac{AR}{E_a}\right) - \frac{E_r}{RT_p} \quad (1)$$

DSC thermograms at three ramp rates for each N6,6 and PP composite formulations are shown in Figure II.3.1.6.4(a-f), respectively. Clearly resolved crystallization peaks are observed for each curve without evidence of a multistep phase change. In Figure II.3.1.6.5, the linearized Kissinger equation is plotted to extract the activation energy for each composite composition. From this data, it is clear that the nylon-based system requires a higher E_a at all compositions than the PP system, which is consistent with a higher requirement for chain folding due to the more rigid nature of the hydrogen bonded N6,6 backbone. Good agreement between each composition is observed in both systems, suggesting that the assumptions inherent to the Kissinger analysis are valid for the formulations and ramp rates used here. In addition to the apparent trends in activation energy, the PP compositions show monotonic increases in T_p with increasing fiber-loading. This suggests that the addition of fiber helps to stabilize the onset of crystal nuclei and leads to a maximum crystallization rate achieved at higher temperatures. The N6,6 -CF composites show a similar trend, although the 20 and 30 vol.% show nearly identical T_p trends, consistent with a less nucleation driven crystallization process from the melt. These details, alongside our previous work analyzing isothermal crystallization kinetics, and dimensionality through the Avrami equation, yields a clear picture of the morphological evolution of the polymer phase within these composites, which are modulated by the addition of CF (e.g., see the third quarter milestone in Table II.3.1.6.1). Additional studies will be performed to fully unravel the effects of polar vs. non-polar subunit chemistry on the polymer interaction in subsequent quarters to optimize the processing windows for these thermoplastic composite systems in the context of high-throughput manufacturing.

Fabrication of unidirectional specimens could also be used to interrogate the interfacial interactions in composites. The project developed a fabrication and testing route for multilayered CF-PP composites. The task utilized sequential stacks of five layers of CF fabric and seven bilayers of PP sheets to comprise a laminate composite preform, which is shown in Figure II.3.1.6.6. The stack was then consolidated under a constant pressure of 5000 psi and heated to melt the PP at 185°C. Following equilibration of the temperature in the composite, the part was cooled while under pressure to prevent shrinkage and delamination of the layers. A fiber volume fraction of approximately 40% was used to ensure proper full wetting of the fibers with the PP melt. The resulting laminate was sectioned into tensile specimens and tabs were affixed to pre-abraded regions of the composite to eliminate grip failure. Average tensile strength for the composites was approximately 1040 MPa, as observed in Figure II.3.1.6.7, achieving the targeted milestone for the last quarter (e.g., > 500 MPa). This project will continue to expand fabrication capabilities for thermoplastic composites and finalize the efforts on optimization of the polymer–CF interface through directed morphologies in the PP system.

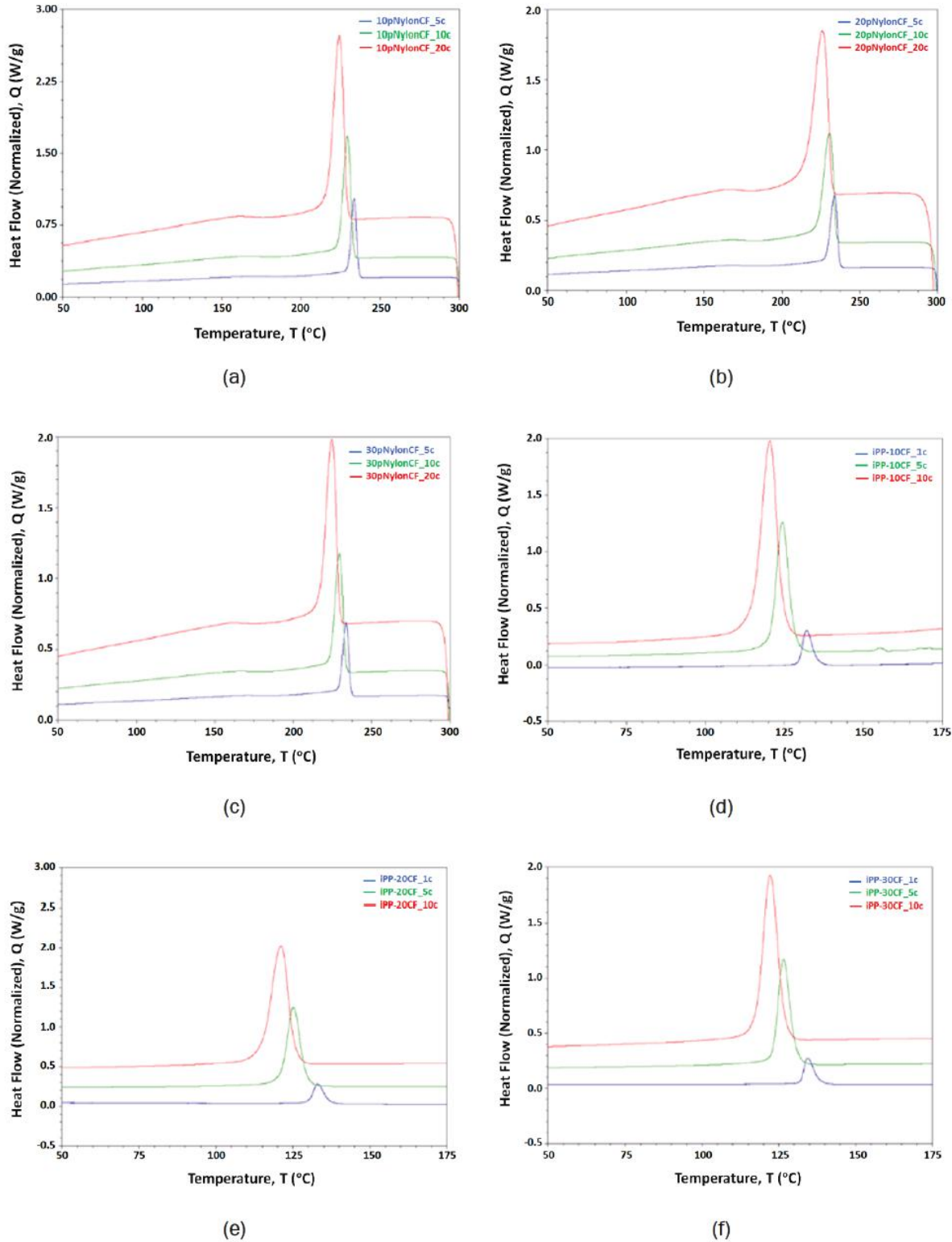


Figure II.3.1.36. DSC thermograms of (a-c) N6,6 and (d-f) PP-CF composites for fiber-loading ratios of 10, 20 and 30 vol.%. Source: ORNL.

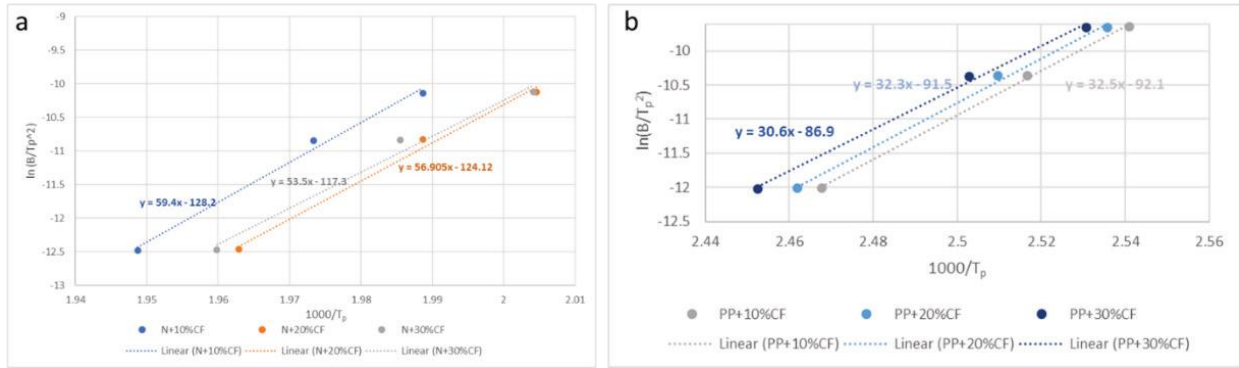
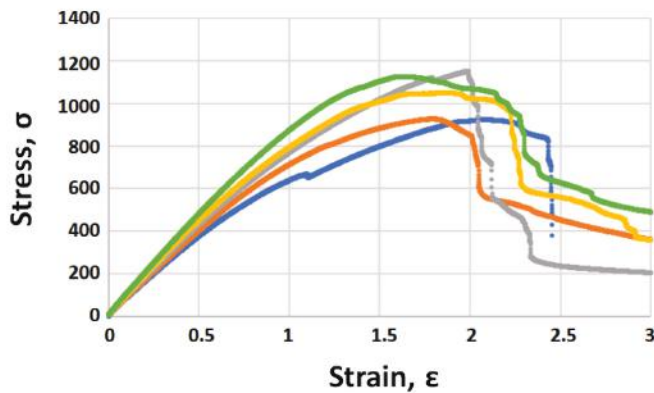


Figure II.3.1.37. Kissinger plot for the (a) N6,6-CF and (b) PP-CF composites. Source: ORNL.



Figure II.3.1.38. CF-PP laminate stack prior to consolidation. Source: ORNL.



(a)



(b)

Figure II.3.1.39. (a) Stress vs. strain plot summarizing the tensile properties of the uniaxial composite. (b) CF-PP composite laminate showing composite mode failure. Source: ORNL.

Conclusions

ORNL achieved all FY 2022 milestones toward the development of rapidly processable thermoplastic composites via processing of stamp formable or compression moldable laminates. The researchers developed a fiber processing method to engineer the interface in polymer matrix composites, observing significantly higher strength and stiffness compared to control composites. An in-depth study of the crystallization behavior, along with nano- and microscale morphology of the composites, revealed that crystallization rates increase with CF loading, as CF surfaces provide an abundance of nucleation sites for semi-crystalline matrix crystal growth. Researchers also observed that the matrix forms a transcrystalline region at the fiber surfaces with abundant individualized crystals on the surface since it offers an excellent nucleation site. In addition to understanding interfacial morphology, researchers developed a novel fabrication process and successfully fabricated multilayered composite structures with good fiber wetting and resin penetration and a void-free microstructure that delivered > 1 GPa tensile strength.

Key Publications

1. Allen, K., L. T. Kearney, S. Datta, and A. K. Naskar, 2023, “Tuning crystallization in isotactic polypropylene–carbon fiber composites for rapid composite manufacturing,” (in preparation).

References

1. Daniel, I. M., and O. Ishai, 2006, *Engineering Mechanics of Composite Materials*, Oxford University Press, Oxford, U.K.
2. Ghossein, H. K., 2019, “Novel wet-laid nonwoven carbon fiber mats and their composites,” Ph.D. Dissertation, University of Tennessee, Knoxville, TN, USA. Available at: https://trace.tennessee.edu/cgi/viewcontent.cgi?article=6883&context=utk_graddiss (last accessed 31 January 2023).

Acknowledgments

The authors would like to acknowledge K. Allen, S. Datta, L. Kearney, C. Bowland, Z. Yu, N. Kanbargi, and S. Gupta.

II.3.1.7 Multimaterial, Functional Composites with Hierarchical Structures (Oak Ridge National Laboratory)

Christopher Bowland, Principal Investigator

Oak Ridge National Laboratory
Materials Science and Technology Division
1 Bethel Valley Rd.
Oak Ridge, TN 37831
E-mail: bowlandcc@ornl.gov

Rich Davies, Composites Core Program Manager

Oak Ridge National Laboratory
Materials Science and Technology Division
1 Bethel Valley Rd.
Oak Ridge, TN 37831
E-mail: daviesrw@ornl.gov

H. Felix Wu, DOE Technology Development Manager

U.S. Department of Energy
E-mail: felix.wu@ee.doe.gov

Start Date: October 1, 2020	End Date: September 30, 2023	
Project Funding (FY 2022): \$500,000	DOE share: \$500,000	Non-DOE share: \$0

Project Introduction

This project is developing approaches to modify fiber surfaces with nanostructures and microstructures to improve composite strength through better fiber-matrix adhesion. Stronger composites require less material to meet strength specifications, thus leading to better vehicle efficiency. As reported by DOE, a 10% reduction in vehicle weight equates to a 6%–8% increase in vehicle efficiency [1]. To further enhance efficiency, this work is enhancing the mechanical properties of fiber-reinforced composites by at least 10%–20% using hierarchical structures with different fiber-matrix combinations. Based on DOE estimates, this 10%–20% increase of the composite strength-to-weight ratio leads to a 12%–16% increase in vehicle efficiency.

Fiber surface modification via added functional groups or nanomaterials has shown promising laboratory-scale results in the literature for enhancing the fiber-matrix interface, but few approaches have been successful in going beyond laboratory-scale demonstrations. Process scalability is one key aspect of fiber production and composites manufacturing that limits a good deal of research from making the transition from laboratory-scale demonstrations to commercial-scale applications. The fibers in this project are processed using different scalable methods and integrated into both thermosets and thermoplastics, covering a wide performance range to meet specifications for both semi-structural and structural automotive applications with added functional properties. Specifically, the structural automotive components of interest for the thermoset matrix are the frame components, such as A-, B-, and C-pillars and roof rails, where high-specific strength and stiffness are paramount. The thermoplastic composites will be used in semi-structural composites on the automobile's exterior, such as the door panels, bumpers, pickup truck bed, and trunk lid/deck lid.

Objectives

The tasks laid out for this research offer routes toward vehicle lightweighting by increasing the strength of the composites. The overall goal is to present versatile methods to deposit nanostructures and microstructures on the fiber surface for both high-performance structural composites and low-cost, high-volume semistructural composites. Beyond mechanical performance enhancements, the high-performance structural composites will

be capable of being embedded *in situ* sensing and structural health monitoring, owing to the design of the added structures. Even though the main focus of this research is to increase the strength of fiber-reinforced composites to meet the DOE's vehicle lightweighting goal, there are other functional properties that the surface-adhered structures can provide to the composites.

Approach

The processing routes developed for this project are versatile, as they offer compatibility with different fibers and a wide variety of nano- and micro-sized particles using a continuous feed-through process. Based on the type of sensor (i.e., passive or active), the electrical conductivity of the composite needs to match the requirements for that sensing system. Therefore, it is advantageous to have this continuous dip-coating technique that is compatible with different fibers to be able to change the electrical conductivity of the bulk composites. For the first part of the project, the focus of the work was on the dip-coating process. This technique was successful in depositing spherical particles on the fiber surface. An additional technique was required to deposit high aspect ratio particles onto the fiber surface. This alternative technique used electrospinning to deposit high aspect ratio polymer nanofibers onto the surface of different fibers. A specific polymer was selected to crosslink with the matrix material, resulting in enhanced mechanical properties when utilizing an optimized processing protocol.

Results

Prior work on this project established the continuous feed-through dip-coating process to deposit different concentrations of barium titanate (BaTiO_3) microparticles (200 nm diameter) on basalt fiber tows. The prior results showed that the BaTiO_3 coating was able to increase the mechanical performance of the composites by up to 20% using interlaminar shear strength testing. Recent research progress further investigated the electromechanical properties of the developed BaTiO_3 -coated basalt fiber composites. Unidirectional composites were fabricated into beams and electroded in a through-thickness configuration. These beams were mounted on a permanent magnet shaker, as shown in Figure II.3.1.7.1. This setup imparted varying input vibrations to the beam while measuring the output voltage from the beam generated by the piezoelectric behavior of the BaTiO_3 microparticles. As shown in Figure II.3.1.7.2, the root-mean-square output voltage is displayed as a function of BaTiO_3 concentration and acceleration. Using this data, the sensitivity of the composite was determined by averaging the output voltage over the entire acceleration range. The best performing composite was the 3.5 wt.% BaTiO_3 composite with the highest voltage output of 2.6 mV/g.

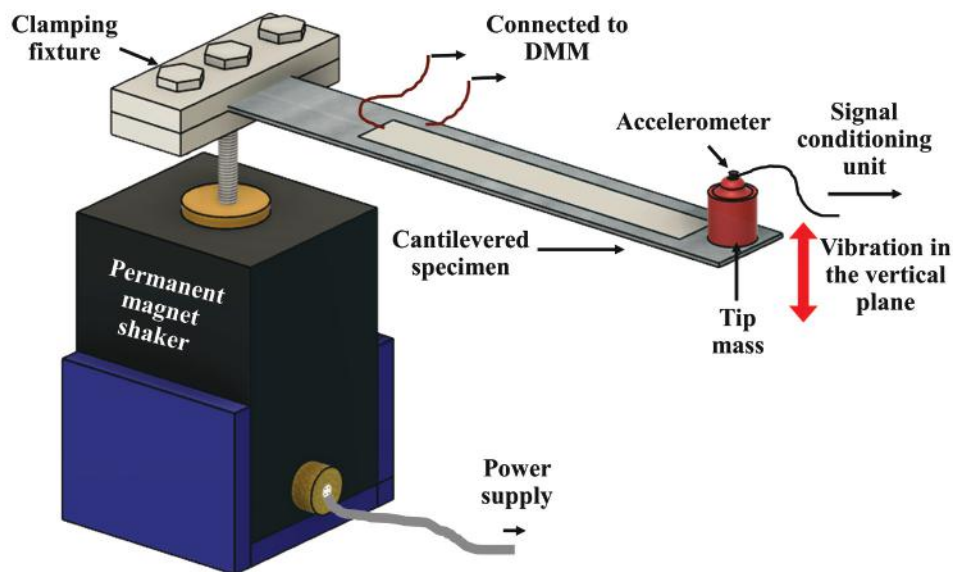


Figure II.3.1.40. Schematic illustrating the test setup for characterizing the electromechanical properties of the composite beams. A permanent magnet shaker was used to input vibrations at the base of the beams while the voltage was measured using a digital multimeter. Source: ORNL.

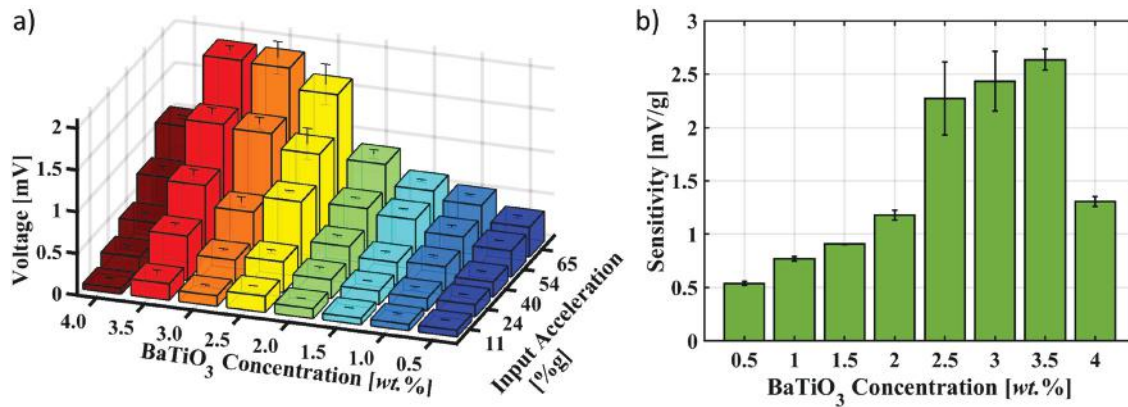


Figure II.3.1.41. (a) Output voltages of the composite beams with different concentrations of BaTiO₃ and different accelerations input. (b) The average sensitivity of the composites with different concentrations of BaTiO₃. Source: ORNL.

Additional analysis of the voltage signals revealed the resolution and power output of the composites with varying BaTiO₃ concentrations. The resolution results are shown in Figure II.3.1.7.3. The resolution was determined by measuring the noise floor of the composites with no input acceleration and plotting it against the generated voltage as a function of input acceleration. A linear regression was fit to the voltage output data, and the intersection of the regression line with the noise floor was determined to be the resolution of the beam. A lower resolution value represents a better performing composite in that it can detect smaller accelerations. The composite with the best resolution was the 3.5 wt.% BaTiO₃ composite with an acceleration resolution of 0.045 g.

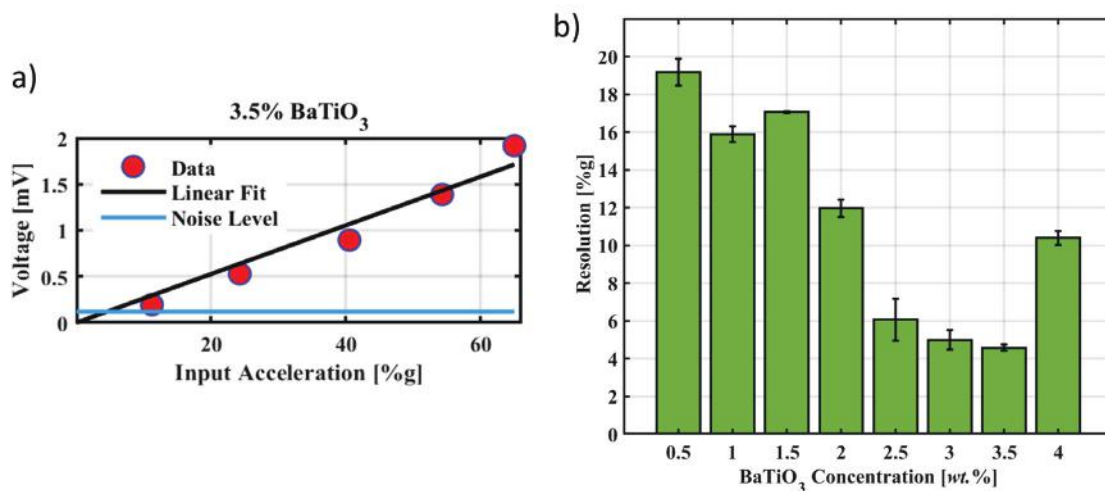


Figure II.3.1.42. (a) One representative sample illustrating the noise floor voltage and voltage outputs plotted as a function of acceleration for the 3.5 wt.% BaTiO₃ sample to calculate the resolution. (b) The resolution values calculated for all composites with varying BaTiO₃ concentrations. Source: ORNL.

For the power harvesting quantification, the composite beams were excited with a sinusoidal wave of constant acceleration, and the resulting voltage was measured over varying circuit resistances to calculate the power output. The composite samples were normalized by dividing the power output by the composite volume to give the power density. Representative plots of the voltage output and power densities as a function of circuit resistances for three selected samples are shown in Figure II.3.1.7.4. The best performing composite was the 3.5 wt.% BaTiO₃ composite with the highest power density of 0.69 nW/cc.

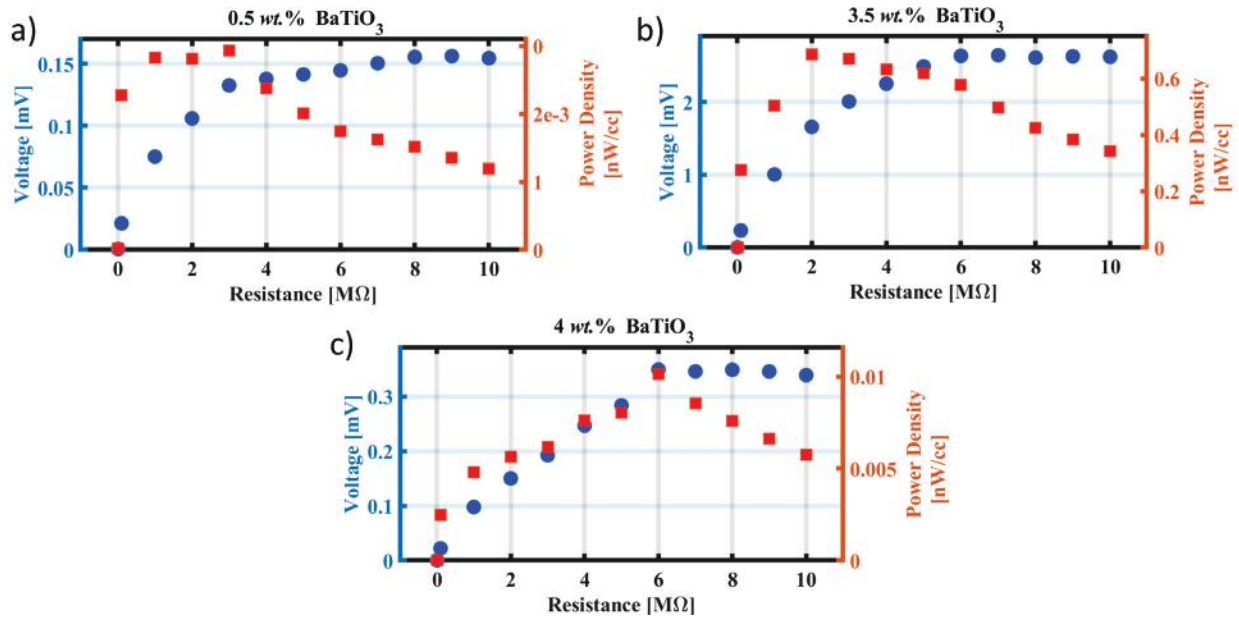


Figure II.3.1.43. Scatter plots showing the voltage generated and power density as a function of circuit resistance for (a) 0.5 wt.%, (b) 3.5 wt.%, and (c) 4 wt.% BaTiO₃ composites. Source: ORNL.

Utilizing these voltage signals generated by the composite, it was also demonstrated that the composites could detect crack formation during short-beam shear tests. During the test, the composite experiences a linear loading region on the stress-strain plot, and prior to failure, an inflection point was observed. It is at this inflection point where internal damage initiates in the composite. At this inflection point, the BaTiO₃-enhanced composites generated voltage. As shown in Figure II.3.1.7.5, a voltage spike of 1.175 mV was observed in the best performing 3.5 wt.% BaTiO₃ composite while the pristine composites (without BaTiO₃) revealed negligible generated voltage. All concentrations of BaTiO₃ were evaluated with this test, and the 3.5 wt.% BaTiO₃ performed the best. Therefore, the BaTiO₃-enhanced composites were able to reveal damage initiation using a self-generated voltage signal prior to failure.

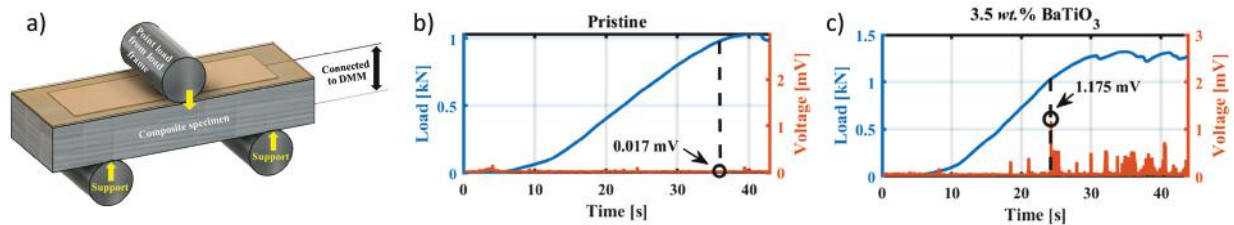


Figure II.3.1.44. Scatter plots showing the voltage generated and power density as a function of circuit resistance for (a) 0.5 wt.%, (b) 3.5 wt.%, and (c) 4 wt.% BaTiO₃ composites. Source: ORNL.

To deposit high aspect ratio nanofibers on the fiber surface, an electrospinning process was used, as opposed to the two-step dip-coating process used for the BaTiO₃ deposition. The electrospinning process shown in Figure II.3.1.7.6(a) utilized a polymer dissolved in a solvent that was ejected through a needle using a syringe pump. The polymer nanofibers were deposited on a grounded CF mat by applying a high voltage to the needle, which accelerated the nanofibers to the CFs and evaporated the solvent in an air gap. The resulting polymer nanofiber deposition on CFs is shown in Figure II.3.1.7.6(b). This process produced polymer nanofibers roughly 350 nm in diameter and homogeneously dispersed the fibers across the CF mat in a random orientation.

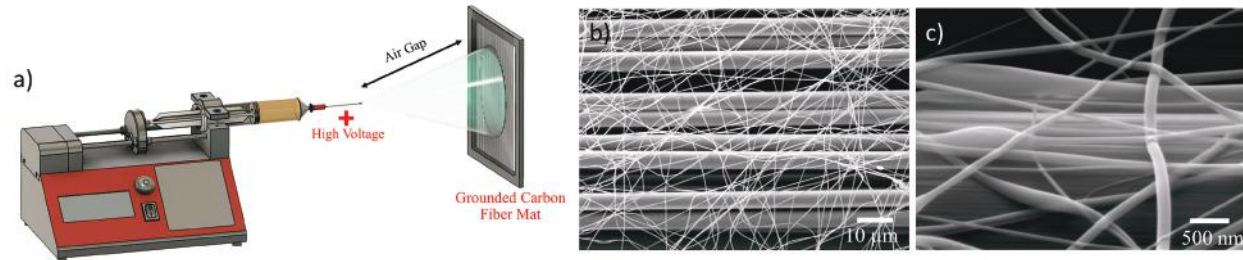


Figure II.3.1.45. (a) Schematic of the electrospinning process on a CF mat. (b) SEM image showing homogenous deposition of nanofibers in random orientations on the CFs. (c) A higher magnification SEM image of the nanofibers on the CF surface. Source: ORNL.

To test the mechanical performance of the nanofiber coated CFs, two coated mats were combined in a unidirectional configuration, infiltrated with a thermoplastic, and hot-pressed under various conditions, as shown in Figure II.3.1.7.7.(a). The interfacial adhesion of each composite was tested by performing tensile tests in the transverse direction to the CFs axial direction. Several different processing conditions were evaluated to optimize the mechanical performance. As compared to the bare CF composite, the nanofiber coated CFs under optimum processing conditions improved the transverse tensile strength by 430% and the Young's modulus by 416%, as shown in Figure II.3.1.7.7.(b). This electrospinning process demonstrated that high aspect polymer nanofibers could be deposited on CFs to significantly increase the mechanical performance when integrated into a thermoplastic matrix.

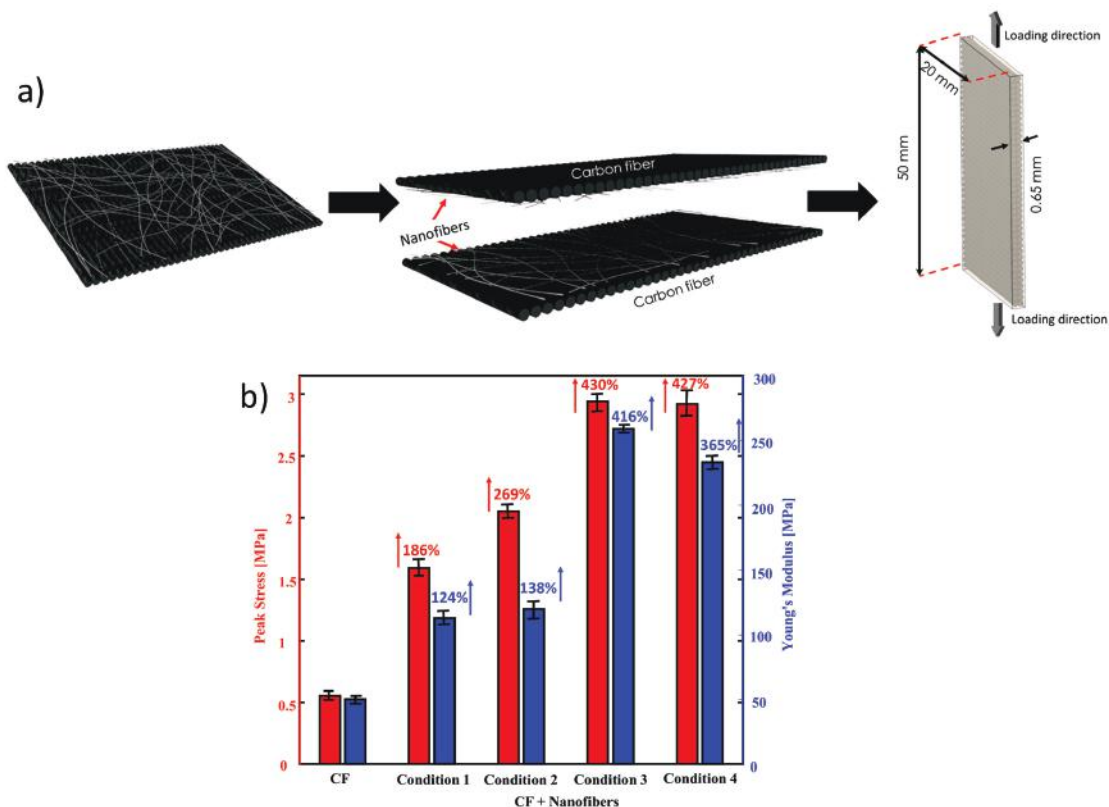


Figure II.3.1.46. (a) Schematic showing the fabrication process of combining two layers of nanofiber coated CFs and testing it in the transverse direction. (b) Transverse tensile test results comparing the bare CFs with nanofiber coated CFs under various processing conditions. Source: ORNL.

Conclusions

The developed dip-coating process for depositing BaTiO₃ microparticles on basalt fibers was successful in enhancing the composite's mechanical properties while offering self-sensing capabilities. The electromechanical properties of unidirectional composites with varying BaTiO₃ concentrations were characterized by fabricating the composites into cantilevered beams mounted on a shaker. This setup allowed for control over the mechanical input while monitoring the electrical output. The beam's electromechanical sensitivity, resolution, and power output were characterized using this beam excitation configuration. The best composite was the 3.5 wt.% BaTiO₃ composite that showed the highest sensitivity, resolution, and power output with values of 2.6 mV/g, 0.045 g, and 0.69 nW/cc, respectively. Utilizing the composite's ability to generate power in response to mechanical input, additional testing explored the ability of the composite to sense damage. The composites were short-beam shear tested while measuring the voltage output. The 3.5 wt.% composite revealed the best ability to sense cracks prior to catastrophic failure by producing mV-level voltage spikes corresponding to damage. Moving beyond the dip-coating process, electrospinning was used to deposit high aspect ratio polymer nanofibers on the surface of the CFs with the goal of significantly improving the composite's mechanical properties. By optimizing the processing conditions, initial transverse tensile tests of a unidirectional composite in a thermoplastic matrix revealed up to 430% and 416% increases in tensile strength and Young's modulus, respectively. Therefore, this work has established two separate paths to deposit hierarchical features onto the surface of fibers that improved the mechanical performance with the dip-coating process offering additional self-sensing attributes to the structure.

Key Publications

1. Bowland C. C., S. Gupta, and A. K. Naskar, 2022, "Passive Sensing Fiber-Reinforced Composite," U.S. Provisional Patent Application No. 63/158,921.
2. Bowland, C. C., S. Gupta, S. M. Rankin, and A. K. Naskar, 2021, "Passive sensing of a microparticle modified hybrid, fiber-reinforced composite," *Nondestructive Characterization and Monitoring of Advanced Materials, Aerospace, Civil Infrastructure, and Transportation XV*, Vol. 11592, 115920B. Preprint copy available at: <https://www.osti.gov/servlets/purl/1817516> (last accessed 1 February 2023).
3. Gupta, S., A. K. Naskar, and C. C. Bowland, 2022, "Multifunctional fiber-reinforced composites for passive sensing and energy harvesting with enhanced mechanical performance," *Nondestructive Characterization and Monitoring of Advanced Materials, Aerospace, Civil Infrastructure, and Transportation XVI*, Vol. 12047, 120470F. Preprint copy available at: <https://www.osti.gov/servlets/purl/1881133> (last accessed 1 February 2023).
4. Gupta, S., A. K. Naskar, and C. C. Bowland, 2022, "An engineered multifunctional composites for passive sensing, energy harvesting, and in situ damage identification with enhanced mechanical performance," *Adv. Mater. Technol.*, Vol. 7, No. 9, Art. 2101549. <https://doi.org/10.1002/admt.202101549>.

References

1. Joost, W. J., 2012, "Reducing vehicle weight and improving U.S. energy efficiency using integrated computational materials engineering," *JOM*, Vol. 64, No. 9, pp. 1032–1038. <https://doi.org/10.1007/s11837-012-0424-z>.

Acknowledgments

The authors would like to acknowledge S. Gupta, who is working as a postdoctoral research associate on this project. They would also like to thank A. K. Naskar for his supervision and assistance with this research and other members of the Carbon and Composites Group; as well as L. Kearney, N. Kanbargi, J. Damron, and S. Rohewal, for assisting with the nanofiber coated CF analysis.

II.3.1.8 Layer Time Control for Large-Scale Additive Manufacturing Using High-Performance Computing (Oak Ridge National Laboratory)

Seokpum Kim, Principal Investigator

Oak Ridge National Laboratory
Materials Science and Technology Division
2350 Cherahala Blvd.
Knoxville, TN, 37932
E-mail: kimsp@ornl.gov

Rich Davies, Composites Core Program Manager

Oak Ridge National Laboratory
Materials Science and Technology Division
1 Bethel Valley Rd.
Oak Ridge, TN 37831
E-mail: daviesrw@ornl.gov

H. Felix Wu, DOE Technology Development Manager

U.S. Department of Energy
E-mail: felix.wu@ee.doe.gov

Start Date: August 6, 2021	End Date: September 30, 2024	
Project Funding (FY 2022): \$300,000	DOE share: \$300,000	Non-DOE share: \$0

Project Introduction

We have developed a method to optimize a layer deposition time (i.e., layer time) for large-scale AM via physics-based simulations. A long layer time leads to an over-cooled surface on which a new layer is deposited resulting in a weak bonding or debonding between layers, cracking, or warping. A short layer time leads to a high temperature of the structure due to insufficient cooling, which leads to a structure that is not stiff enough and may collapse during manufacturing. Therefore, it is important to estimate the optimal layer time in AM for a high-quality product. The temperature of a top layer right before deposition is recommended to be slightly higher than the glass temperature of the material. A temperature cooling was approximated to an exponential function of time, and the optimized layer time was obtained based on a target temperature while maintaining a minimal printing time. The material used is carbon fiber-reinforced polycarbonate (CFR/PC), and the large-scale deposition system used is Large-Scale Additive Manufacturing (LSAMTM) from Thermwood Corporation. Three different layer time cases were used for experiments, and a series of thermal images were obtained via an infrared (IR) camera during the entire AM processes. AM process simulations were performed using a FEM and the temperature profiles from the simulation agreed with those from experiments. The layer time optimization was performed based on the temperature profiles from the simulations. A layer temperature with the optimal layer time was confirmed as the target temperature through simulation.

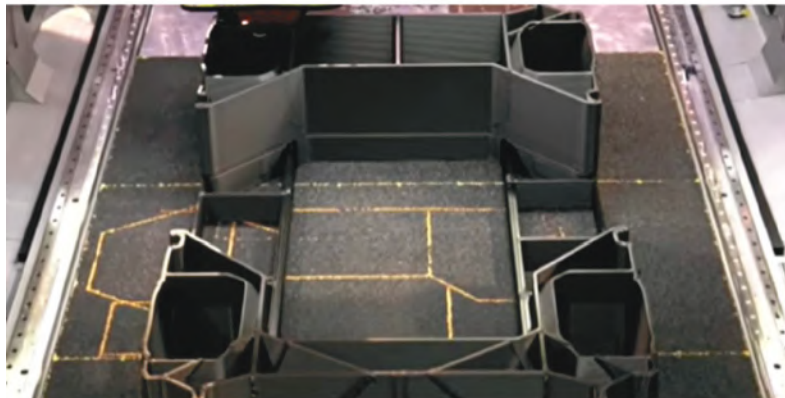
In addition to the development of a layer time optimization method, we have developed a numerical framework for AM simulation with element activations in synchronization with the toolpath, based on an open-source finite element framework called “deal.II.” AM technologies have shown a significant improvement in manufacturing processes in terms of design freedom and no requirement of a mold or die. AM processes incrementally deposit materials and build a product layer-by-layer. To develop a stable structure, each new layer should strongly bond to the previously deposited layer. At or near RT, certain AM processes rely on chemical bonding or crosslinking of molecules to join layers such as vat photopolymerization, material jetting, binder jetting, and direct-write. [1] In other procedures, such as DED, powder bed fusion, and thermoplastic material extrusion, heat is used to melt and fuse new layers of material to the previous layer. [1]

As the hotter top layer cools and shrinks against the constraint of the cooler rigid layers below, these approaches can cause considerable stresses within the printed artifact.

Large-scale AM approach using a thermoplastic material extrusion process can produce structures several meters in size at rates between 5 and 50 kg/hr, using a combination of extrusion and robotic deposition technologies. [2] LSAM™ by Thermwood Corporation is an example of a large-scale 3D printer, as shown in Figure II.3.1.8.1(a) and Figure II.3.1.8.1(b) (image adapted from www.thermwood.com). One of the major challenges is to predict the cooling behavior due to a large amount of extruded substance with an arbitrary shape and size; therefore, it is difficult to estimate an optimal layer time. A long layer time leads to an over-cooled surface on which a new layer is deposited, which leads to a weak bonding or debonding between layers, cracking, or warping. An example of debonding and warpage is shown in Figure II.3.1.8.2(a). Also, a short layer time leads to a surface temperature that is too high due to insufficient cooling, which may cause the structure to collapse due to the lack of stiffness during manufacturing, as shown in Figure II.3.1.8.2(b). Therefore, an optimal layer time should be determined that is directly related to the surface temperature of the previously deposited layer to prevent defects and reduce the failure costs of the AM process.



(a)



(b)

Figure II.3.1.47. (a) The LSAM™ and (b) 3D printing of a shuttle in process at Local Motors.
Source: Thermwood Corporation and ORNL.

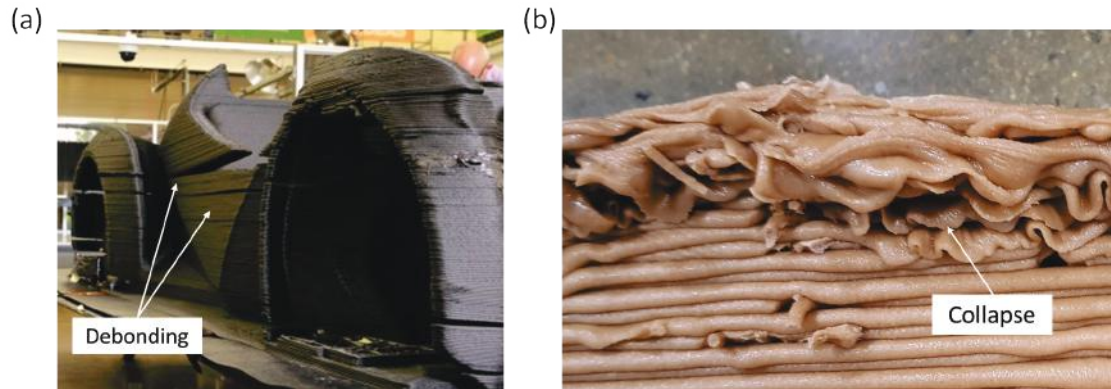


Figure II.3.1.48. Failures in large-scale 3D printing: (a) debonding between layers due to overcooling and (b) material collapse due to the too high temperature of layers. Source: Thermwood Corporation and ORNL.

Objectives

Current operation on 3D printing involves depositing each layer at its maximum speed and pausing the extruder for a certain time at the end of the layer. The layer time is determined based on an operator's intuitions and experiences. The objective of this project is to develop a framework of deposition time control for large-scale AM by combining an AM simulation technique, ML algorithms, and control methods. In the first year of the project, we will focus on layer time optimization using a temperature history profile predicted from simulation and real-time thermal images. Because the simulation-driven optimization often involves a large amount of resources for industrial application, we propose a ML approach (stretched goal for Year 1) based on the pair data between the toolpath designs and the optimal layer times. A full analysis on the ML framework will be proposed for the second year (Phase II). To meet our objective, the following three frameworks will be developed:

- **Integrated Framework for Layer Time Optimization:** An integrated framework will be developed including a high-fidelity temperature simulation, a layer time optimization, and a G-code generation with an updated layer time. The goal is to find an optimal layer time for each layer based on the thermal history from simulation. The simulation will account for heat transfer and the deposition process via element activation in sync with G-code. An AM feature will be developed in deal.II, and the development of software will have similar capabilities (e.g., AM process simulation), such as Abaqus from SIMULIA. To obtain an efficient optimization, multiple simulations with several layer time cases will be submitted simultaneously, so that only a few optimization iterations are required for each design. The framework developed here will be utilized for multiple design objects, and the pair data between the design objects and the corresponding optimal layer times will be used for AI training.
- **Online Layer Time Optimization Model:** An online optimization method using real-time thermal images will be developed to account for the difference from the offline model to improve printing efficiency and print quality. Using a thermal camera, the real-time temperature information for the current layer will be obtained and fed into the optimization model to determine the optimal layer time based on the optimal temperature.
- **Artificial Intelligence Surrogate Framework (Stretched Goal):** The layer time optimization is computationally expensive due to multiple iterations between the simulation and the optimization model. Therefore, we will develop a ML-based predictive stand-in framework with a convolutional neural network. The input data includes layer toolpath images with sequence information while the output target will be optimal layer time. The training data input-target pairs will be obtained from a large number of simulations running on a high-performance computer. In the first year of the project, simple geometries with various sizes will be used to develop an appropriate training methodology and select a network architecture.

Approach

This section explains the material and methods that were used. Experiments were conducted to investigate the relationship between the layer temperature and the interlayer bonding property. To make a different layer temperature condition, single bead wall structures were printed using the LSAMTM with four different layer times, and the material used in experiments was CFR/PC. A long layer time allowed the previously deposited substance to cool down for a long period, resulting in a low layer temperature in the case of the long layer time. The layer temperatures were 89°C, 104°C, 120°C, and 140°C, depending on the layer time. Test specimens were fabricated from the printed structures in the z-direction. Tensile tests were conducted with the test specimens, and the results are shown in Figure II.3.1.8.3. The results of our tests are consistent with findings from previous research considering the relationship between the strength of interlayer bonding properties and the layer temperature [3]. The z-direction tensile strength degrades by over 50% from 140°C to 89°C layer temperature, indicating a substantial association between layer temperature and z-direction tensile strength.

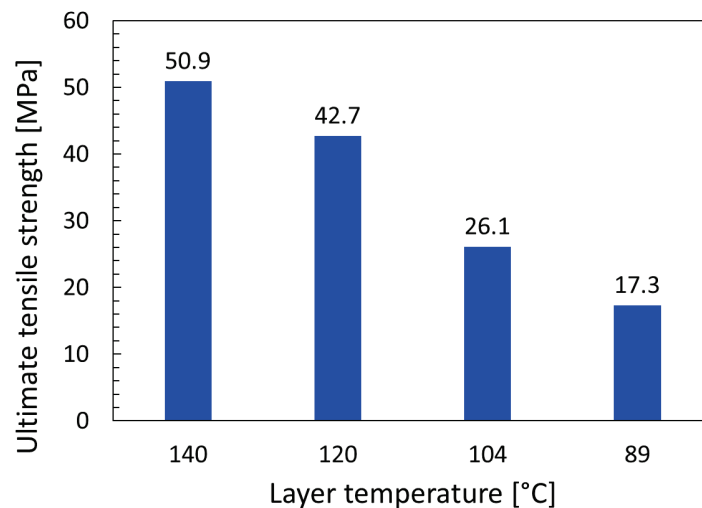


Figure II.3.1.49. Failures in large-scale 3D printing: (a) debonding between layers due to overcooling and (b) material collapse due to the too high temperature of layers. Source: Thermwood Corporation and ORNL.

The glass temperature of CFR/PC is 145°C and the z-direction ultimate strength of LSAMTM structures becomes higher as the layer temperature gets closer to the glass transition temperature. However, when the layer temperature exceeds the glass transition temperature, the influence of the temperature is not effective to the z-direction strength. [4] Therefore, the glass temperature can be a target layer temperature in the optimization process. Since the layer temperature of the substrate over 20°C above the glass transition temperature will cause material collapse due to the lack of stiffness, our upper limit of the layer temperature is set as 165°C. Also, the lower limit of the layer temperature is set as 125°C since below that temperature the property was rapidly decreased.

A hexagon geometry with single bead wall was designed and fabricated with different layer times. The hexagon geometry has 1,036 mm length and 304 mm height with 61 layers. A schematic of the hexagon model and a photograph of the fabricated hexagon structure are shown in Figure II.3.1.8.4. Three cases of 3D printing with the different layer times were conducted with the hexagon geometry, and the printing times are shown in Table II.3.1.8.1. To design a consistent print condition, the printing time is the same, 84 seconds in all cases with the only difference being the waiting time. The print conditions such as extrusion temperature, bed temperature, ambient temperature, printing speed, bead height, and bead width are shown in Table II.3.1.8.2.

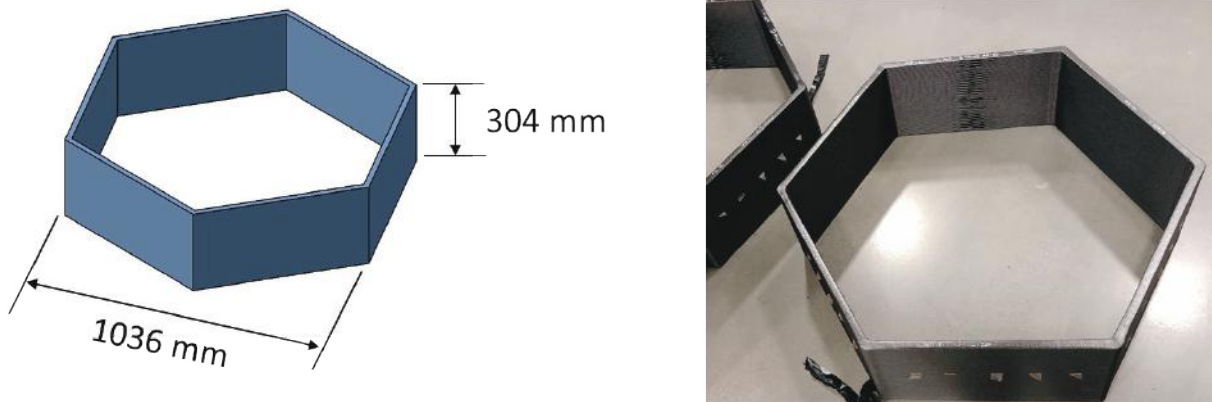


Figure II.3.1.50. Dimensions and the printed structure of a hexagon. Source: ORNL.

Table II.3.1.8.1. Three Cases with Different Layer Times.

Case	Printing Time (sec)	Waiting Time (sec)	Total Layer Time (sec)
Case 1	84	6	90
Case 2	84	58	142
Case 3	84	114	198

Table II.3.1.8.2. Experimental Conditions for 3D Printing.

Printing Conditions	Unit	Value
Extrusion Temperature	[°C]	265
Bed Temperature	[°C]	30
Ambient Temperature	[°C]	30
Printing Speed	[mm/min]	2540
Bead Height	[mm]	5.08
Bead Width	[mm]	20.32

Thermal images were gathered via two IR cameras during the full AM process. Figure II.3.1.8.5(a) shows a thermal image from an IR camera in the top view, while Figure II.3.1.8.5(b) shows a thermal image in the side view during the AM process. With the thermal images, temperature profiles and cooling behaviors for the three different layer time cases were investigated. Also, the temperature profiles throughout the part were used to verify the results of the AM simulation.

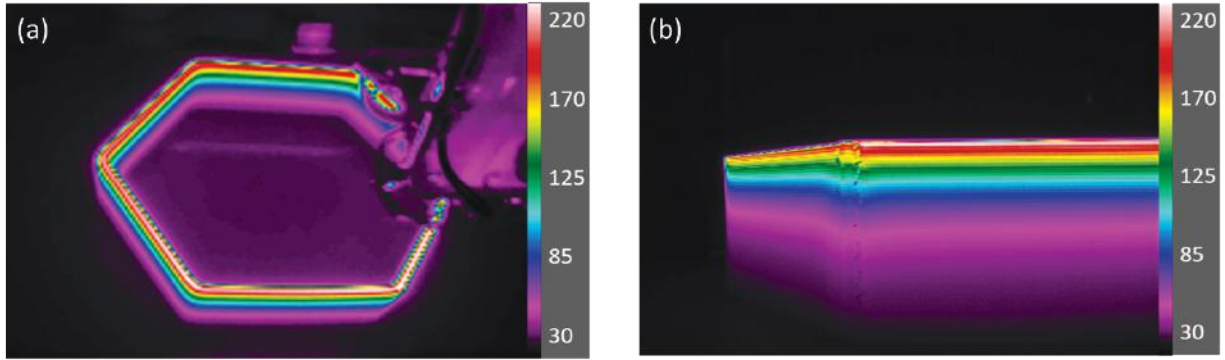


Figure II.3.1.51. Thermal images in °C of a hexagon from an IR camera during the 3D printing process. (a) Top view. (b) Side view. Source: ORNL.

Temperature Profile Prediction Via Finite Element Analysis (FEA) Simulation

FEA simulations were carried out to predict the temperature profiles and layer temperature of hexagon structures with different layer times. In the analysis, heat transfer occurs by thermal conduction, convection, and radiation. The CFR/PC material used in the experiments have an anisotropic thermal property due to the reinforced CF. The addition of CF may be expected to increase the thermal conductivity of the composite in the direction of the fiber. [5] Therefore, determining where the fiber will be directed is crucial to predict the temperature profile and layer temperature. Since the reinforced fiber in the extruded substance is aligned with the tool path direction, the deposited substance has a principal direction along with the tool path direction, and the z-direction is chosen as the stacking direction. Material property values for the analysis are summarized in Table II.3.1.8.3.

Table II.3.1.8.3. Parameters for Simulation

Printing Conditions	Unit	Value
Thermal conductivity, $\kappa_{11}, \kappa_{22}, \kappa_{33}$	$[W / (m \cdot K)]$	0.77, 0.35, 0.27
Specific heat capacity, C_p	$[J / (kg \cdot K)]$	1127
Density, δ	$[kg / m^3]$	1187
Emissivity, ε	-	0.9
Natural convection coefficient, h	$[W / (m^2 \cdot K)]$	5

For the analysis, progressive material activation was used to simulate the AM process. The tool paths used in the LSAM™ were converted as simulation code with a developed tool path converter. The converter changed G-code into an event series composed of time, deposition position, and extruder on-off information. To implement the layer-by-layer deposition, the elements were generated vertically with the stacking direction and height of a mesh was made in the portion of the height of a layer. When the tool path passed through the element, the element was activated and the boundary conditions continuously changed over the simulation. The process of progressive material activation of the AM process is shown in Figure II.3.1.8.6.

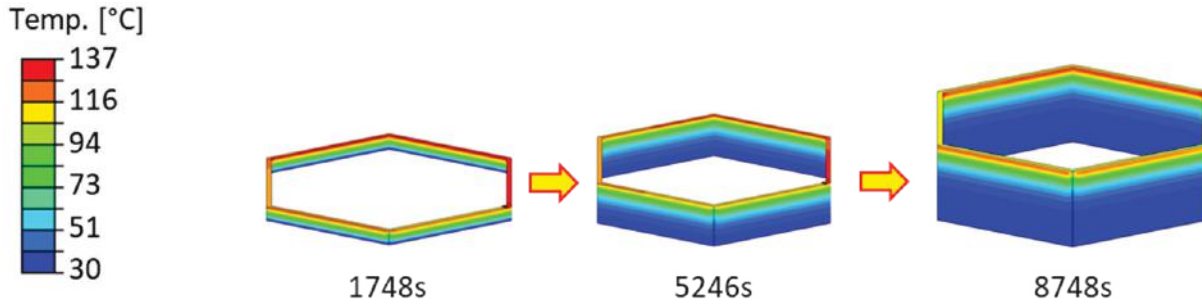


Figure II.3.1.52. Process of progressive material activation for the hexagon geometry (Case 2). Source: ORNL.

Regression Model for Temperature Profile Prediction in Optimization Algorithm

The simple linear regression model is used to predict the future surface temperature for each position on one layer. According to references [6, 7], the temperature change of a position follows the differential equation:

$$\frac{dT(t)}{dt} = \beta_0 + \beta_1(T(t) - T_{env}) \quad (1)$$

where $T(t)$ is the surface temperature at time t , T_{env} is the ambient temperature (30°C) and β_0 and β_1 are unknown parameters. The term $\frac{T(t+\Delta t)-T(t)}{\Delta t}$ is approximately equal to $\frac{dT(t)}{dt}$ when Δt is small enough, and Δt is known as the time between two timestamps. Thus, equation (1) can be rewritten as:

$$\frac{T(t + \Delta t) - T(t)}{\Delta t} = \beta_0 + \beta_1(T(t) - T_{env}) \quad (2)$$

where $\frac{T(t+\Delta t)-T(t)}{\Delta t}$ is the response variable y , and $T(t) - T_{env}$ is the predictor variable x . Then the intercept coefficient $\hat{\beta}_0$ and the slope coefficient $\hat{\beta}_1$ are found by fitting equation (2) in a position. Denote t_0 as current time, $T^k(t_0)$ as current layer temperature for location k , and $t \geq t_0$. By solving the given differential equation in equation (1), the future layer temperature $\hat{T}^k(t)$ for location k can be obtained as follows:

$$\hat{T}^k(t) = T_{env} - \frac{\beta_0^k}{\beta_1^k} + (T^k(t_0) - T_{env} + \frac{\beta_0^k}{\beta_1^k})e^{\hat{\beta}_1^k(t-t_0)} \quad (3)$$

Model For Layer Time Optimization

Based on references [6, 7], the number of positions in a layer surface are denoted by M . The temperature change of the k^{th} position, for $k=1, 2, \dots, M$, is modeled by equation (1); parameters β_0^k and β_1^k are obtained by regression. For the predicted layer temperature at the k^{th} position $\hat{T}^k(t)$, which is obtained by equation (3), the time t starts with 0 with the thermoplastic material deposited at the k^{th} position. Optimization model with decision variable t is built as follows:

$$\min f(t) = \sum_{k=1}^M \omega_k (\hat{T}^k(t) - T_b)^2 + \omega_0 t \quad (4)$$

$$\begin{aligned} \text{s. t. } & \hat{T}^k(t) \geq T_l, \text{ for } k = 1, 2, \dots, M \\ & \hat{T}^k(t) \leq T_u, \text{ for } k = 1, 2, \dots, M \end{aligned} \quad (5)$$

$$t \geq t_0$$

In equation (4), $f(t)$ is the objective function, which is a weighted summation with weight for each term denoted by ω_k , for $k = 0, 1, \dots, M$. The weight coefficient represents a tradeoff between the importance of different positions and layer time. The first term $\sum_{k=1}^M \omega_k (\hat{T}^k(t) - T_b)^2$ measures how much each position k has layer temperature close to the target temperature T_b (e.g., 145°C) at time t . The second term $\omega_0 t$ is the layer time t multiplied with a weight coefficient ω_0 . Therefore, getting the layer temperature of each position close to target temperature and minimizing layer time are considered simultaneously by minimizing the objective function.

In equation (5), there are three constraints. The first is set to ensure that no position can have a layer temperature lower than the predetermined lower temperature bound T_l (e.g., 125°C) at time t . Similarly, the second is constructed to ensure that no position can have a layer temperature greater than the predetermined upper temperature bound T_u (e.g., 165°C) at time t . The last constraint forces the layer time longer than t_0 . Reformulating the first two constraints by Eq. (3), the feasible region of layer time, denoted by $[t_l, t_u]$, can be found as follows:

$$t_l = \max_k \left\{ \frac{1}{\hat{\beta}_1^k} \ln \left(\frac{T_u - T_{env} + \frac{\hat{\beta}_0^k}{\hat{\beta}_1^k}}{T^k(t_0) - T_{env} + \frac{\hat{\beta}_0^k}{\hat{\beta}_1^k}} \right) \right\} + t_0 \quad (6)$$

$$t_u = \min_k \left\{ \frac{1}{\hat{\beta}_1^k} \ln \left(\frac{T_l - T_{env} + \frac{\hat{\beta}_0^k}{\hat{\beta}_1^k}}{T^k(t_0) - T_{env} + \frac{\hat{\beta}_0^k}{\hat{\beta}_1^k}} \right) \right\} + t_0 \quad (7)$$

Therefore, the optimal control model can be solved as minimizing the objective function $f(t)$ over bounded decision variable interval $[t_l, t_u]$ by using the sequential quadratic programming method [6].

Numerical Framework Development

A numerical framework for AM simulation, termed *adamantine*, is being developed to analyze the heat transfer behavior of anisotropic material deposition. We have used CF-reinforced polymer for large-scale printing, and the heat transfer behavior in one direction is different from that in another direction. The reinforced fibers are aligned along the printing direction and the reinforcements (i.e., fibers) have greater thermal conductivity than the polymer, so the heat transfer in the printing direction is dominant over the other direction (e.g., anisotropic behavior). The difference in heat transfer between isotropic material and anisotropic material is shown in Figure II.3.1.8.7. To develop the *adamantine* for the AM simulation with anisotropic material, it should contain (1) the calculation of the local direction of deposited material, (2) anisotropic thermal conductivity input parameters, and (3) thermal conductivity as a function of temperature.

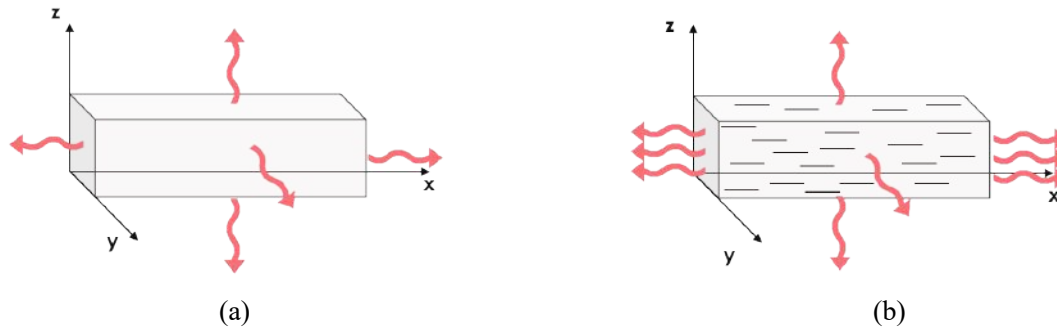


Figure II.3.1.53. Heat transfer behavior of (a) isotropic and (b) anisotropic materials. Source: ORNL.

For the local coordinate system update, we have improved the material deposition algorithm. The material is deposited in different directions during printing, so we used a toolpath direction from G-code to track the printing direction. The material local direction is aligned with the printing direction and the concept of tracking the local direction is shown in Figure II.3.1.8.8. The anisotropic material properties are defined in the local coordinate of each finite element where the material is deposited. To analyze the global heat distribution, the material properties assigned in the finite element in the local direction are rotated to the global coordinate and the global heat equation is solved.

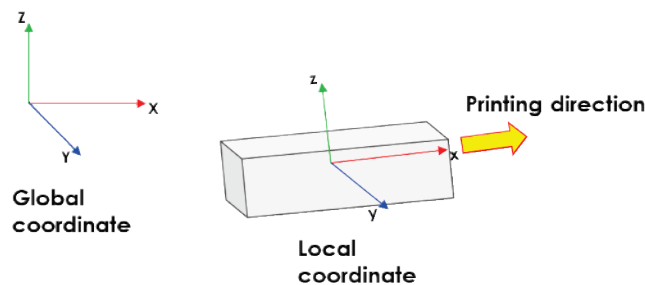


Figure II.3.1.54. Local coordinate system aligned with the printing (fiber) direction. Source: ORNL.

To extend the *adamantine* to solve the anisotropic heat equation, the core kernel of *adamantine* has been modified to support the anisotropic heat equation. The formulation of the anisotropic heat equation contains the capability of the material property class to allow heat conductivity to vary with the direction in the x, y, z-directions. Another feature of the development is that the *adamantine* contains the thermal conductivity input parameters as a function of temperature. Since thermal conductivity varies with different temperatures, the anisotropic conductivity changes should also be adjusted in the simulation. Figure II.3.1.8.9 shows the thermal conductivity change in the three directions of printed CFR/PC with different temperatures.

We have verified the anisotropic heat transfer behavior from *adamantine*. Figure II.3.1.8.10 shows the heat distribution field from the simulation. In this simulation, *adamantine* considers the local coordinate system, the additional input parameters for anisotropic thermal conductivity, and temperature-dependent thermal conductivity. As a result, in the isotropic material simulation, as shown in Figure II.3.1.8.10(a), the heat distribution in the transverse direction is big. However, in the anisotropic material, as observed in Figure II.3.1.8.10(b), the heat distribution, which is aligned with the printing direction, is dominant and the transverse directional heat distribution is small.

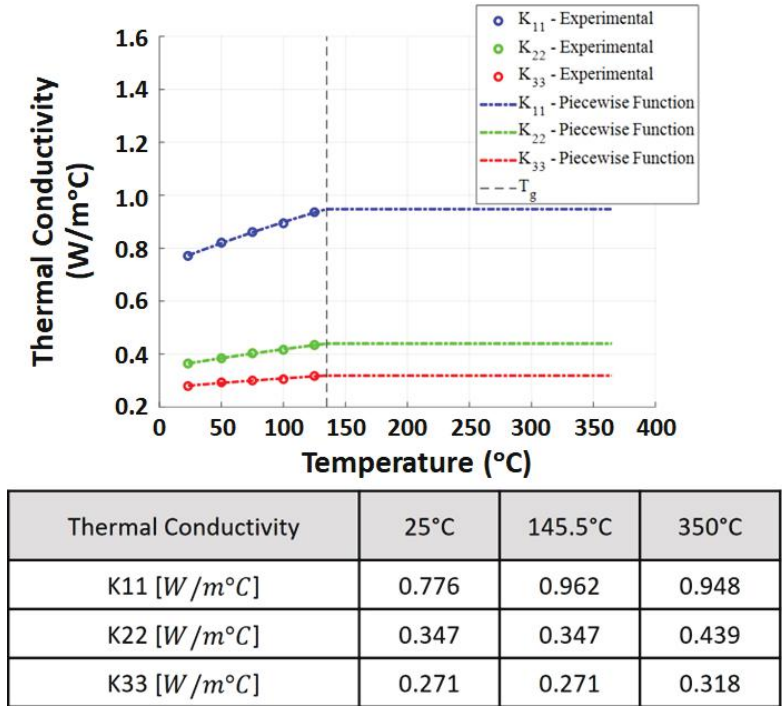


Figure II.3.1.55. Thermal conductivity in the three principal directions of printed CF-PC. Source: ORNL.

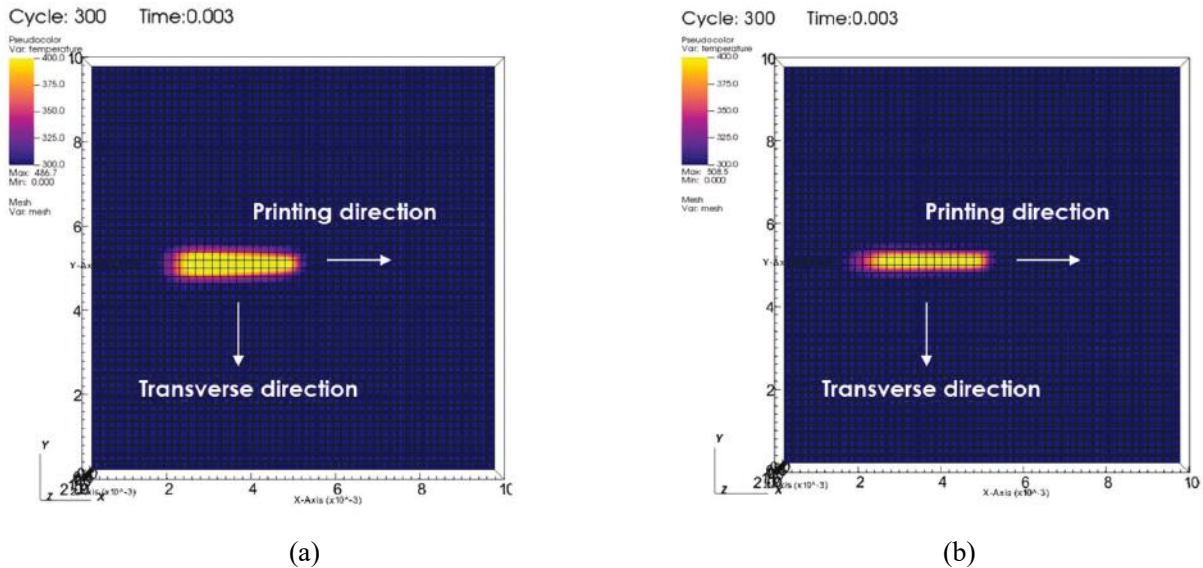


Figure II.3.1.56. Heat transfer behavior of (a) isotropic and (b) anisotropic materials. Source: ORNL.

Adamantine is based on open-source finite element framework, deal.II. So, our improved AM simulation framework will also be an open-source framework. With the increasing use of anisotropic materials for 3D printing, such as CF-reinforced polymer, industry partners can use *adamantine* for predicting heat distribution and will be able to improve the quality and design the manufacturing process more efficiently in terms of energy and cost.

Results

Temperature Prediction

Time-dependent temperature profiles were obtained from the AM simulation. The analysis lasted 5,515; 8,748; and 11,652 seconds for three different layer time cases, respectively, and the results were recorded at the time of dividing each experiment into five consistent intervals. The temperature graphs show the temperature profile from the base to the stacked layer over each time, which is produced to a height of 60 mm during each time interval. Since the base temperature and ambient temperature (e.g., 30°C) were set to the boundary condition, the final temperature of the deposited substance is 30°C.

Comparisons of temperature profiles in the simulations and experiments were conducted for the hexagon prints, and the results are shown in Figure II.3.1.8.11, where the dotted lines show the experimental results, and the solid lines show the simulation results. In each case, as printing progresses, the temperature of the previously deposited layers cools down to the base temperature and ambient temperature. The previous layers approach the final temperature in the later printing interval. In the case of a long layer time, there is a big temperature difference between the previous layer and the newly deposited layer. Therefore, the temperature is more sharply decreased in the longer layer time case (Case 3) than the temperature in the other cases. In all cases, the simulation results show good agreement with those from experiments. This proves that the results of the conducted simulations are reliable to predict the layer temperature.

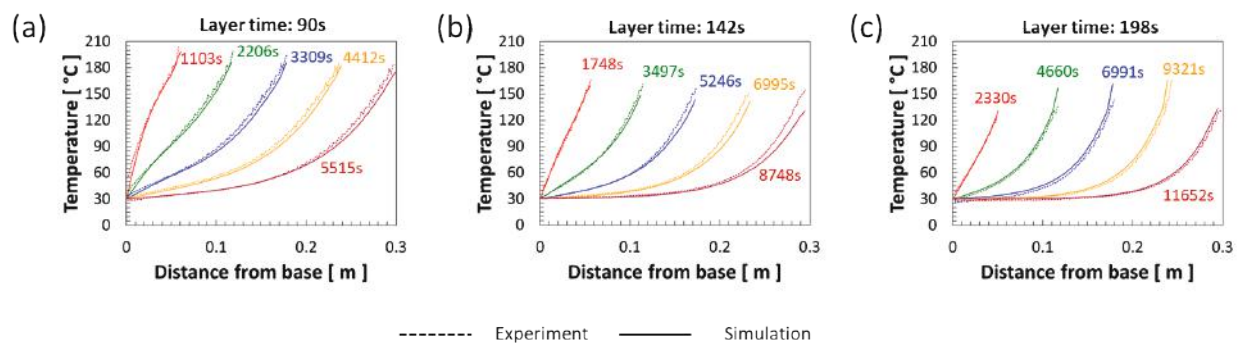


Figure II.3.1.57. Local coordinate system aligned with the printing (fiber) direction. Source: ORNL.

Layer Time Optimization: Trend of the Optimization Model

Optimized layer times for each layer were determined through the optimization algorithm based on the layer temperature predicted from the FEA simulation, and the results are shown in Figure II.3.1.8.12. The layers under the tenth layer were affected by the base temperature and showed a different tendency from the other part. These bottom layers were excluded so that the optimization process only considers the different cooling behavior due to the different layer times. Since the cooling pattern of the entire structure changed with the different layer times, different optimal layer times were calculated for each case. However, the results of the optimal layer time to meet the target temperature show a tendency to get close to one value. Therefore, the best optimal layer time for the hexagon geometry with a single bead wall could be found based on the optimization result's trend. The optimal layer time decreases as the layer time increase, and the trend is clearly shown in Figure II.3.1.8.13. With the correlation of the tested layer time and suggested optimal layer time, the best layer time was determined as a cross-section point, and the calculated layer time was 130 seconds for a layer.

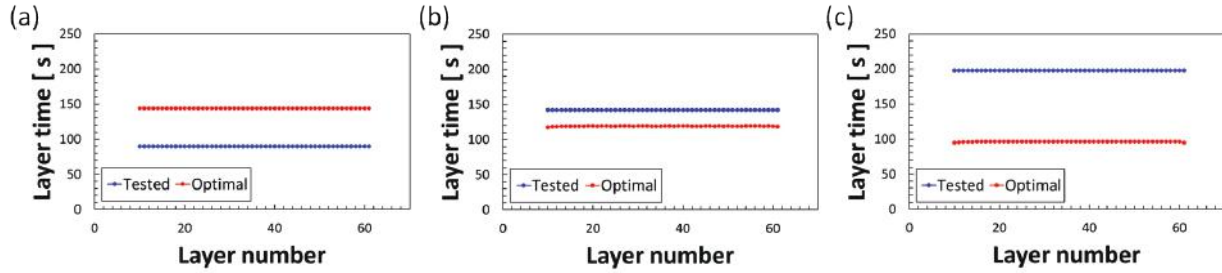


Figure II.3.1.58. Optimal layer time of each layer from the 10th layer to the 61st layer for (a) Case 1; (b) Case 2 and (c) Case 3. Source: ORNL.

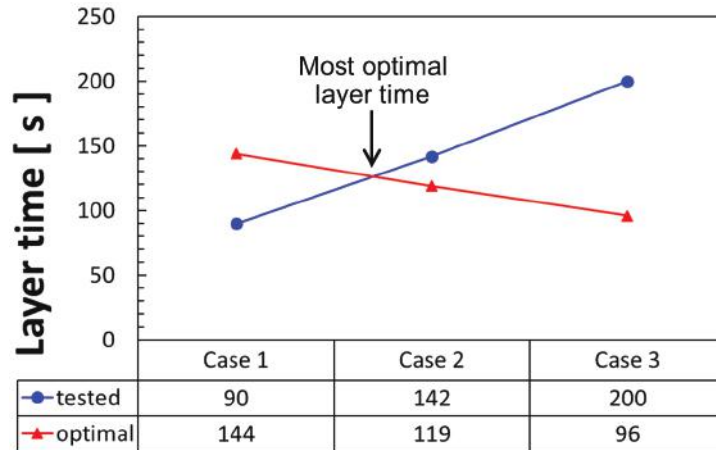


Figure II.3.1.59. Cross-section point presenting the most optimal layer time with the trend of optimization results. Source: ORNL.

Determination of an Optimal Layer Time

FEA simulation was conducted to predict the layer temperature for the 130 second layer time print, and the result is shown in Figure II.3.1.8.14. The previous layer temperature is exactly the same as the target temperature (e.g., 145°C) right before the extruder builds an additional layer. With the layer temperature from the simulation result, an additional optimization process was conducted to find a better optimal layer time. The result of the additional optimization process is shown in Figure II.3.1.8.15. The newly founded optimal layer time is 129 seconds for a layer, which is very close to the previously founded optimal layer time and means that the layer time optimization process is getting close to one value. Through this trial-and-error process, a very accurate optimal layer time can be found.

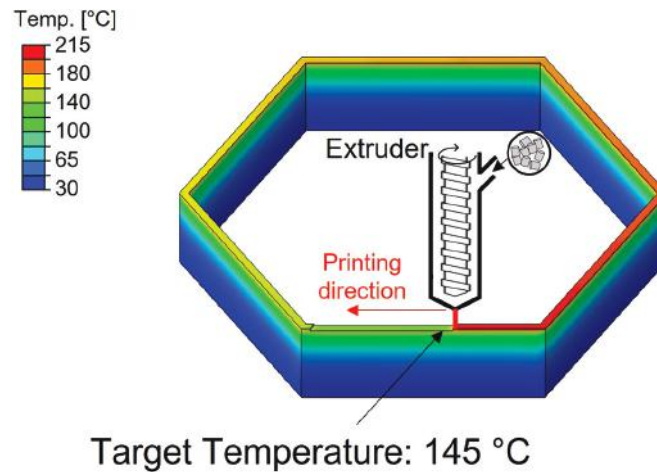


Figure II.3.1.60. Layer temperature prediction for the 130 seconds layer time case. Source: ORNL.

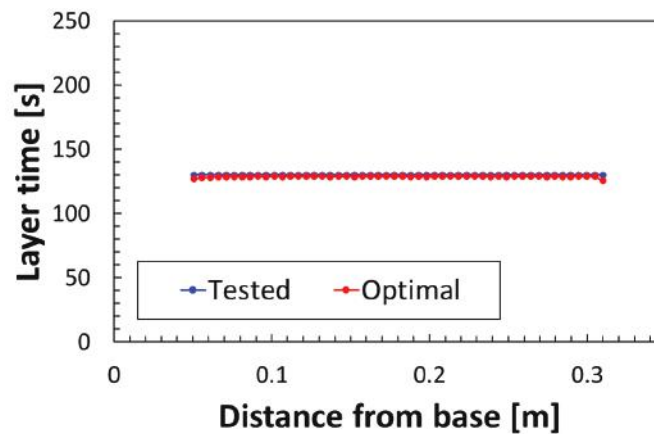


Figure II.3.1.61. Result of the additional optimization process for the 130 seconds layer time case. Source: ORNL.

Conclusions

We have shown the ability to predict the temperature profile for a single bead wall structure during AM and determined the optimized layer time with FEA simulation results with optimization algorithms. The optimization algorithm can find the optimized layer time, and it got closer to a certain value for the hexagon geometry. This optimization process can give a guideline and save the cost of failure to users of LSAMTM by suggesting the optimal layer time.

A numerical framework for AM simulation, termed *adamantine*, is being developed based on an open-source finite element framework, deal.II. To implement the local coordinate system update, we have improved the material deposition algorithm. The core kernel of *adamantine* has been modified to support the anisotropic heat equation. This improved *adamantine* can predict the heat distribution for an entire structure in the AM process using fiber-reinforced thermoplastic polymer.

Future work on this study will involve complex geometries, such as two bead wall, sharp corner, and round turn. Also, these complex geometries will contain different layer times for each layer. By using the optimization process, each optimized layer time will be found. The method developed in this study can be used to obtain an optimal layer time for extrusion-based 3D printing systems with thermoplastics. Furthermore, using the parameters and FEA *adamantine* program, we will generate a large number of simulation data, specifically temperature profiles with respect to printing time. The large data will be used for ML training.

Key Publications

1. Jo, E., L. Lui, F. Ju, D. Hoskins, D. K. Pokkalla, V. Kunc, U. Vaidya, and S. Kim, 2022, “Optimization of layer time in large-scale additive manufacturing with fiber-reinforced polymer composites,” *Society for the Advancement of Material and Process Engineering (SAMPE) 2022 Conference Proceedings*, 23–26 May 2022, Charlotte, NC, USA. Available at: <https://www.osti.gov/servlets/purl/1883859> (last accessed 1 February 2023).

References

1. ASTM International, 2012, *Standard Terminology for Additive Manufacturing Technologies*, ASTM Standard F2792-12a, ASTM International, West Conshohocken, PA, USA. Available at: <https://web.mit.edu/2.810/www/files/readings/AdditiveManufacturingTerminology.pdf> (last accessed 1 February 2023).
2. Talagani, M. R., S. DorMohammadi, R. Dutton, C. Godines, H. Baid, F. Abdi, V. Kunc, B. G. Compton, S. Simunovic, C. E. Duty, L. Love, B. Post, and C. A. Blue, 2015, “Numerical simulation of big area additive manufacturing (3D printing) of a full-size car,” *Sampe J.*, Vol. 51, No. 4, pp. 27–36. Available at: https://www.researchgate.net/profile/Saber-Dormohammadi/publication/279532514_Numerical_Simulation_of_Big_Area_Additive_Manufacturing_3D_Printing_of_a_Full_Size_Car/links/56d9c6bf08aee73df6cf6241/Numerical-Simulation-of-Big-Area-Additive-Manufacturing-3D-Printing-of-a-Full-Size-Car.pdf (last accessed 1 February 2023).
3. Nycz, A., V. Kishore, J. Lindahl, C. Duty, C. Carnal, and V. Kunc, 2020, “Controlling substrate temperature with infrared heating to improve mechanical properties of large-scale printed parts,” *Addit. Manuf.*, Vol. 33, Art. 101068. <https://doi.org/10.1016/j.addma.2020.101068>.
4. Turner, B. N., R. Strong, S. A. Gold, 2014, “A review of melt extrusion additive manufacturing process: I. Process design and modeling,” *Rapid Prototyp. J.*, Vol. 20, No. 3, pp. 192–204. <https://doi.org/10.1108/RPJ-01-2013-0012>.
5. Love, L. J., V. Kunc, O. Rios, C. E. Duty, A. M. Elliott, B. K. Post, R. J. Smith, and C. A. Blue, 2014, “The importance of carbon fiber to polymer additive manufacturing,” *J. Mater. Res.*, Vol. 29, No. 17, pp. 1893–1898. <https://doi.org/10.1557/jmr.2014.212>.
6. Wang, F., S. Fathizadan, F. Ju, K. Rowe, and N. Hofman, 2021, “Print surface thermal modeling and layer time control for large-scale additive manufacturing,” *IEEE Trans. Autom. Sci. Eng.*, Vol. 18, No. 1, pp. 244–254. <https://doi.org/10.1109/TASE.2020.3001047>.
7. Wang, F., F. Ju, K. Rowe, and N. Hofman, 2019, “Real-time control for large-scale additive manufacturing using thermal images,” *IEEE 15th International Conference on Automation Science and Engineering (CASE)*, 22–26 August 2019, Vancouver, British Columbia, Canada. pp. 36–41. <https://doi.org/10.1109/COASE.2019.8843264>.

Acknowledgments

This research was sponsored by the DOE-EERE VTO, and used resources at the Manufacturing Demonstration Facility, a DOE-EERE User Facility at ORNL. The author appreciates the contributions from E. Jo, B. Turcksin, and D. Rose of ORNL; K. Rowe and D. Hoskins of Local Motors; and F. Ju and L. Liu of Arizona State University.

II.3.1.9 Ultra-Lightweight, Ductile Carbon Fiber-Reinforced Composites (Oak Ridge National Laboratory)

Vlastimil Kunc, Principal Investigator

Oak Ridge National Laboratory
Materials Science and Technology Division
1 Bethel Valley Rd.
Oak Ridge, TN 37831
E-mail: kuncv@ornl.gov

Rich Davies, Composites Core Program Manager

Oak Ridge National Laboratory
Materials Science and Technology Division
1 Bethel Valley Rd.
Oak Ridge, TN 37831
E-mail: daviesrw@ornl.gov

H. Felix Wu, DOE Technology Development Manager

U.S. Department of Energy
E-mail: felix.wu@ee.doe.gov

Start Date: October 1, 2020	End Date: September 30, 2023	
Project Funding (FY 2022): \$500,000	DOE share: \$500,000	Non-DOE share: \$0

Project Introduction

CFRP composites are known for their high stiffness-to-weight ratio, and hence, are of great interest in diverse modern engineering fields. CFRP metamaterials with rationally designed architectures can be realized through AM technologies. Among many additive fabrication approaches, the light-based technique is most suitable for micro-architected metamaterials due to its high-resolution and robust mechanical properties of photopolymers. In the previous project phase, we developed a multimaterial optical AM technique for multiphase materials, which enabled the production of a group of CFRP microlattice that simultaneously exhibited high stiffness and high structural damping. Most high-precision AM techniques are limited by the tradeoff between printing area and resolution. The projection stereolithography process, in particular, is capable of achieving unmatched feature sizes below 100 microns, but the overall dimension is limited to a few centimeters. This limits their application to produce critical components that require high surface finish and precision multiscale feature sizes over large volumes.

This year, we designed and constructed a novel 3D printer capable of printing a large structure with a fine resolution and demonstrated a part with a 50-cm overall length and 50-micrometer minimum feature size. We also integrated a custom extrusion system with an optical scanning system for controlling fiber alignment. This work was performed in collaboration with the University of California–Los Angeles.

Objectives

This work aims to enable high-speed, large-area, and high-resolution printing of CFRP composites. The following milestones were proposed and accomplished:

- **Milestone 1.** Demonstrate a 3D printing system setup capable of printing a hierarchical CFRP lattice (Target: 50 micrometer feature sizes over ~50 cm printing areas).
- **Milestone 2.** Demonstrate hierarchical CFRP lattice materials (Target: 50 micrometer feature sizes for a high-resolution area with an overall size of over ~50 cm printing areas).

- **Milestone 3.** Assemble custom extrusion system and fiber alignment mechanisms.
- **Milestone 4.** 3D Print multimaterial CFRP samples with high-damping and stiffness.

The Go/No-Go milestone decision criteria was to demonstrate a lattice structure fabricated from the 3D printing system that should have the minimum feature size of 50 microns and the structural length of 50 cm.

Approach

This section documents the materials, methods, and system setup developed for this project.

A large-area high-resolution UV curing printer integrated with an infinity-corrected projection system was designed and constructed, as shown in Figure II.3.1.9.1. Figure II.3.1.9.1(a) and Figure II.3.1.9.1(c) show the basic working principle of the proposed infinity-corrected design. Here, light rays emitted from the light engine, which is equipped with a digital micromirror device chip, pass through a collimating lens and enter as an infinity parallel beam in the focusing lens, thus forming an intermediate image. The intermediate image is then relayed and forms an image with the prescribed resolution through a projection lens. In contrast to a conventional projection lens in digital light processing printing technology—where the focused image will be out of focus as soon as the lens moves—our infinity-corrected projection system allows the translation of a projected image over a large distance while keeping the focus and intensity. The image size stays constant even if the distance between the collimating lens and the focusing lens varies; thus, the projection images can be translated via a high-speed motion axis with high-resolution. A light engine equipped with a digital micromirror device chip of 1024×768 pixels was used in this work. Figure II.3.1.9.1(b) and Figure II.3.1.9.1(d) show the actual photos of the printer and the optical design. The light engine is fixed on the ground, while the scanning optics move along the x-y directions, sequentially projecting images onto extended areas of a large format resin vat, extending the build size to 20 cm and above. The scanning mirrors are mounted on two high-speed motion stages to provide a fast-scanning process. Except for the rapid translation of projection images, another advantage of such an infinity-corrected design is that the projection area/resolution can be adjusted easily by simply tuning the position of the projection lens (d_o). The overall magnification ratio can be adjusted as $M = (f_f/f_c) \cdot f_p/(d_o - f_p)$, where f_c , f_f and f_p are the effective focal length of the optics, d_o is the distance between the projection lens to the intermediate image, and M is the magnification ratio.

Our 3D printing method combines the advantage of direct ink writing (DIW) and projection stereolithography. The nozzle extrudes resin in the vat with predefined toolpaths, enabling localized 2D fiber alignment. Unlike regular DIW that uses extruded beads to compose the structure directly, our approach is to solidify the extruded resin onto the printing platform through moving optics. Therefore, the resolution of the printed feature depends on the optical system involved rather than the nozzle size, which makes the smallest printable feature size less than $50 \mu\text{m}$. The extrusion system consists of a plunger extruder providing external pressure using a motorized piston and an auger extruder that assists in extrusion from StoneFlower 3D, Inc. The motion axes carry the auger extruder to deliver the resin across the vat.

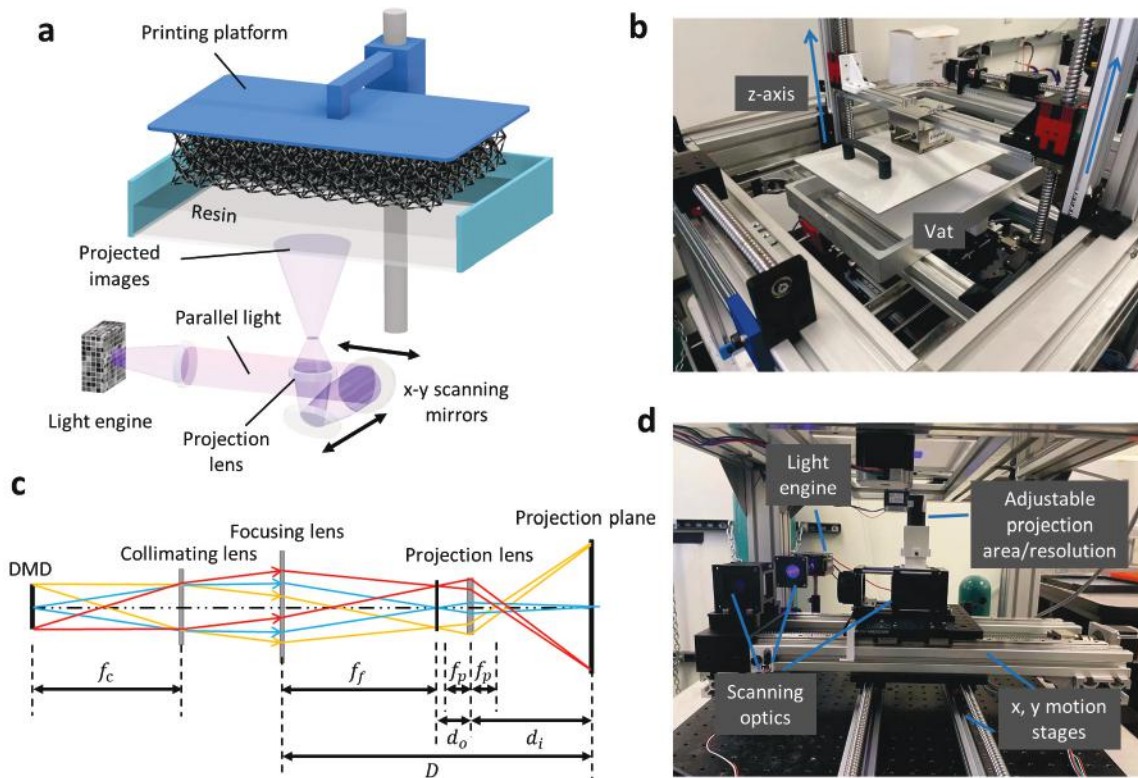


Figure II.3.1.62. (a) Schematic of the large-area high-resolution projection stereolithography system. (b) Large-area high-resolution projection stereolithography system with a large format printing vat. (c) Optical path diagram of the infinity-corrected projection design. (d) Current optical system setup with adjustable projection area/resolution. Source: ORNL.

System Setup

The diagram in Figure II.3.1.9.2(a) shows the processing and control schematic of the printing system. The process starts with a 3D model. Using a regular fused deposition modeling (FDM) printer slicer, the toolpath G-code for extruder movement and dispensing was generated. Using Netfabb and MATLAB, 2D images and G-code for curing were created. The extrusion G-code is saved into a secure digital card and read by microcontroller Duet 2 directly, while the sliced images and scanning G-code were entered into LabVIEW, which then sends commands to the microcontroller boards via universal serial bus to control all the motors. The different colors of the lines indicate the various controlling/processing signals (e.g., blue line – file processing; red line – 24V power circuit; green line – analog or digital signals; orange line – power circuit for motors). A custom LabVIEW program was developed to integrate all of these functions into one system.

The printing process begins with the delivery of printing ink over the entire printing area, allowing for localized fiber orientations. The platform then moves down, sandwiching the resin between the printing platform and the vat bottom, followed by optical system movement. The optical system cures resin onto the printing platform with specific patterns. Finally, the platform moves up, and the extruder delivers the resin for the next layer. The process was repeated layer-by-layer, combining them into a 3D structure. The process flow is shown in Figure II.3.1.9.2(b).

The adjustable projection area/resolution enables customization based on different designs. The minimum printable feature size (lateral resolution) of the developed system is $\sim 50 \mu\text{m}$ with a single projection area of $40 \times 30 \text{ mm}^2$. The layer thickness is set by the vertical motion axis to be $50\text{--}100 \mu\text{m}$. Currently, the overall printing area of the system is enlarged to $\sim 22.5 \times 20 \text{ cm}^2$, which is improved by a factor of 150 with respect to our previous study (e.g., $2 \times 1.5 \text{ cm}^2$).

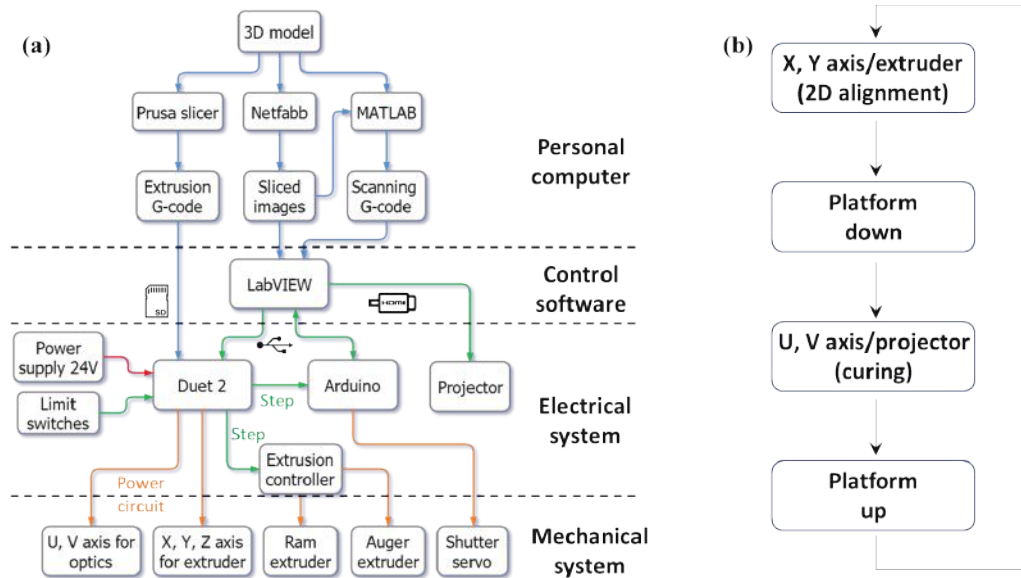


Figure II.3.1.63. (a) Block diagram of the processing and control schematic. Blue line: File processing; Red line: 24V power circuit; Green line: Analog or digital signals; Orange line: Power circuit for motors. (b) Diagram of the printing process. Source: ORNL.

Methods

To demonstrate large-area high-resolution printing, a vase that has a volume of $20 \times 20 \times 50 \text{ cm}^3$ with a minimal strut thickness of $50 \mu\text{m}$ was designed in nTopology software. To print the vase, the 3D model first was sliced into 2D images with predefined pixels, as shown in Figure II.3.1.9.3(a). Next, every single-layer is segmented into a set of sub-images, which will be sequentially projected onto the vat when the stage moves along x-y directions. Each sub-image represents a particular projection area. The projected UV images initiate the polymerization of the resin, converting it to a solid single-layer part. To ensure the bounding between neighbor sections, a small overlap area is introduced between sub-images (usually several pixels). For the vase, each sliced image was split into 35 ($m \times n = 5 \times 7$) sections to fulfill the printing resolution/area requirement.

An S-shape scan path is applied to cover the whole printing area (assuming each sub-section has an area of $40 \times 30 \text{ mm}^2$ and the scanning speed to be 80 mm/s , 60 mm/s for x, y directions). However, for hollowed structures or a more general case, as shown in Figure II.3.1.9.3(b), scanning dark sections where no exposure will take place is unnecessary and generate idle time. Here, we implemented an algorithm that finds the shortest scanning time. We developed a MATLAB code to plan the scan path for each layer. The code can identify sub-images with projection patterns and output the scanning route file for the stage motion control. As shown in Figure II.3.1.9.3(b), the blue dotted lines refer to the conventional S-shape scanning route, while the highlighted solid yellow line represents the shortest scan time path (using a traveling salesman problem (TSP) solver) among all possible routes that pass through necessary projection areas (e.g., we assume two motion stages simultaneously move when moving from one location to another, and the slower one is used to quantify the time cost). Changing the speed of linear stages might result in different optimized paths. It is worth noting that unlike the convention of the TSP, where the optimized path needs to be connected at the beginning and end, our scanning method has a fixed starting point and an open endpoint. As shown in Figure II.3.1.9.3(b), for layer n , the scanning starts from the green point and ends at the red dot. Then, the endpoint of layer n becomes the starting point of layer $n + 1$ and so on. This will further reduce unnecessary scan movements during layer changes. Figure II.3.1.9.3(c) compares the time cost of our TSP scanning method with the conventional S-shape scanning method. Specifically, when $k=20$ (e.g., one layer of the vase), the scanning speed can be improved by a factor of 1.75. For the case in Figure II.3.1.9.3(b) ($k=6$), the printing speed is three times faster than the S-shape method. This methodology highlights the printer's capability to print large-area high-resolution hollowed structures rapidly.

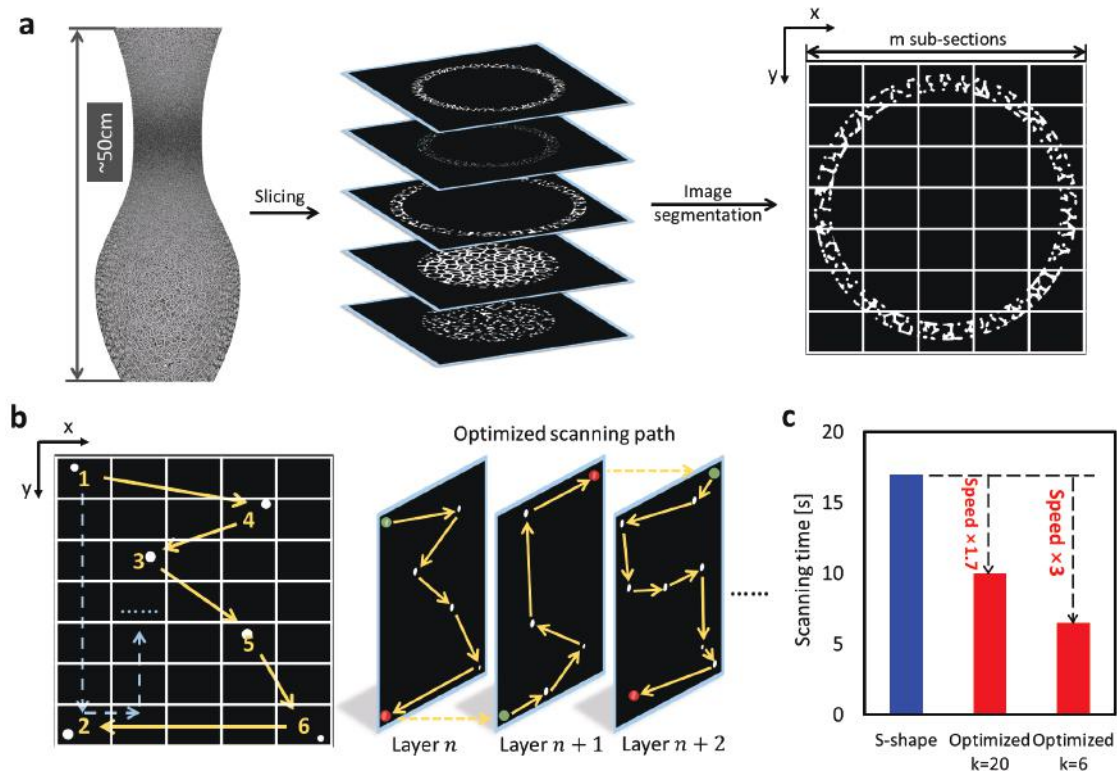


Figure II.3.1.64. (a) Schematic of the large-scale (50 cm), high-resolution (50 μm) vase designed in nTopology and sliced into layers with each layer split into 5×7 sub-sections. (b) An illustration outlining the optimization of the scan path. (c) Comparison of the scanning time cost between conventional and optimized paths, where $k=20$ refers to the circle pattern in (a), and $k=6$ refers to a more general pattern in (b). The scanning speed dramatically increases for the large volume structure with the hollowed inner. Source: ORNL.

The printing time of each layer follows this formula: $T_{\text{layer}} = T_{\text{coat}} + kT_{\text{exposure}} + \sum_{i=1}^k T_{i \rightarrow i+1}$, where T_{coat} is the recoating time, which is mainly determined by resin viscosity; k is the number of sub-images with pattern in one layer; T_{exposure} is the exposure time of a single projection area, which is related to the light intensity and resin property; and $T_{i \rightarrow i+1}$ is the movement time between positions. The proposed optical design has a high light flux density (e.g., $2.7 \pm 0.14 \text{ mW/cm}^2$ with a projection area of $100 \times 75 \text{ mm}^2$) over a long working distance. The optics are lightweight, making higher scanning speeds possible. All of these configurations ensure fast-scanning speeds, further increasing the throughput of the printer. As shown in Figure II.3.1.9.4, we summarize a chart that compares the resolution/throughput of different AM techniques for an hour of build time. This work exhibits a high printing resolution comparable to projection micro-stereolithography (P μ SL) and much higher throughput than FDM.

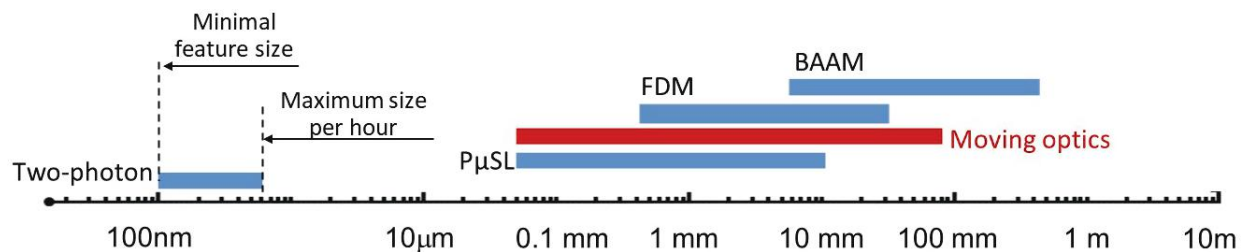


Figure II.3.1.65. Printable feature size range of different AM techniques in one hour. The maximum printable size is normalized according to the throughput of the methods. Estimated throughput: two-photon $0.22 \mu\text{m}^3/\text{h}$; moving optics: $500 \text{ cm}^3/\text{h}$, P μ SL $1 \text{ cm}^3/\text{h}$, FDM $30 \text{ cm}^3/\text{h}$, BAAM $45400 \text{ cm}^3/\text{h}$. Source: ORNL.

The fundamental reason that our technique enables superior throughput in parts requiring extensive spans of feature sizes is that our use of parallel, mobile optics causes the technique to follow a different fundamental scaling law for production time. In other techniques, to scale the size of a part while holding the resolution constant, the production time will increase with the cube of the increase in part size due to volumetric scaling. However, our approach effectively reduces the order of this time-scaling to a squared factor instead of a cubed factor. This is because when the build area increases in the lateral directions, an entire slice can be efficiently duplicated via optics while maintaining the same resolution, and therefore, the same minimal feature size. This means that the time to produce a part will only scale with two build volume dimensions, and will therefore, scale by a square law instead of a cube law.

The part size to minimum feature size ratio is also improved with our present technique. Conventional light-based 3D printers with only a single, stationary projector are fundamentally limited in this criterion by the resolution of the projector. For example, if a $50 \times 50 \text{ cm}^2$ part is desired, and the light engine has a 1000×1000 pixel resolution, then the projection resolution will be $500 \text{ }\mu\text{m}$, with even larger minimum feature sizes. By contrast, there is no such limit with our technique due to the mobility of the projectors. To increase the part size, the only requirement is to use a longer stroke motion stage for the optics and/or to increase the number of projectors in the projector array. With our technique, a higher projector resolution is not required to improve the ratio between the part size and minimum feature size, removing a fundamental limitation of conventional light-based 3D printing technology. This allows for scalability in the print volume of the technology without sacrificing minimum feature size.

Materials

The printing resins are prepared by mixing a UV-curable matrix (Rigid 10k from Formlabs, Inc.) with the appropriate amounts of milled short CFs (e.g., $7 \text{ }\mu\text{m}$ in diameter, $\sim 70/315 \text{ }\mu\text{m}$ mean length from E&L Enterprises, Inc.) and silica nanoparticles (TS 720 from Cabot, Inc.). Batches started with 100 g of Rigid 10k resin. Milled CFs are added in 2.5, 5, 10, or 15 g increments, followed by 1 hour of mixing on a roller from Fisher Development, Inc. Next, 3.5 g of silica nanoparticles are added, followed by manually mixing in a container. Finally, the resin is thoroughly mixed using the roller for 24 hours.

To fabricate composites with controlled fiber orientation, we first created printing inks that embody the essential rheological properties required for our 3D printing method. Specifically, we formulated the printing ink using a commercial UV-curable resin, Rigid 10k, short CFs, and silica nanoparticles as described in the previous section. The high aspect ratio CFs align under the shear and extensional flow field that develops within the nozzle during the printing, resulting in enhanced stiffening in the cured composite along the printing direction. The silica nanoparticles primarily serve as a rheology modifier that imparts shear-thinning behavior and a shear yield stress to the ink.

The rheological behavior of inks of varying compositions was measured using a TA Instruments AR-G2 rheometer. A parallel plate fixture with a diameter of 25 mm was used with a test gap of $500 \text{ }\mu\text{m}$ and a shear rate of 1 rad/s - 100 rad/s. The pure matrix resin exhibits a complex viscosity (η) of $\sim 1.8 \text{ Pa}\cdot\text{s}$ that is almost independent of the shear rate. As a result, the resin flows easily through the nozzle at moderate application pressure and immediately wets and spreads as it leaves the nozzle, unable to support itself. In contrast, the resin becomes a shear-thinning fluid with the addition of CFs and nanoparticles. The resulting resin has a low viscosity at high shear rates and high viscosity at low shear rates, making it flow only when extruded. Besides, given their solid-like nature in the quiescent state, the filler within the inks undergoes minimal aggregation or sedimentation, making them ideal for 3D printing that lasts for weeks.

Results

In this work, flat beads are preferred over oval beads because of less deformation upon compression. The shape of the extruded bead can be controlled by adjusting the flow rate and gap, as shown by the 'd' in Figure II.3.1.9.5(a), between the nozzle and the vat. To strictly control the spreading process and minimize the dislocation of the fibers, the bead's shape shall match the layer thickness (e.g., t, the distance between the vat

and the platform), as shown in Figure II.3.1.9.5(b). A compression speed of 0.5 mm/s and a layer thickness of 0.1 mm was applied during printing. Slow speed ensures the resin deforms at a low shear rate, keeping the fiber orientation constant during resin spreading. Selected small layer thickness ensures UV light penetrates the resin to be cured onto the platform.

Figure II.3.1.9.5(c) compares the fiber alignment quality with and without the compression process. The photos are captured using a regular optical microscope and processed using ImageJ. Herman's orientation parameter of the two cases was calculated accordingly. We found that the fiber orientation quality slightly deteriorated after compression due to lateral shear flow, but the difference is not significant ($f_p = 0.54$ vs. $f_p = 0.44$, both without and with compression). Using such a printing system, we first printed a small portion of a hollowed car bumper design, as shown in Figure II.3.1.9.5(d), and then printed a car bumper.

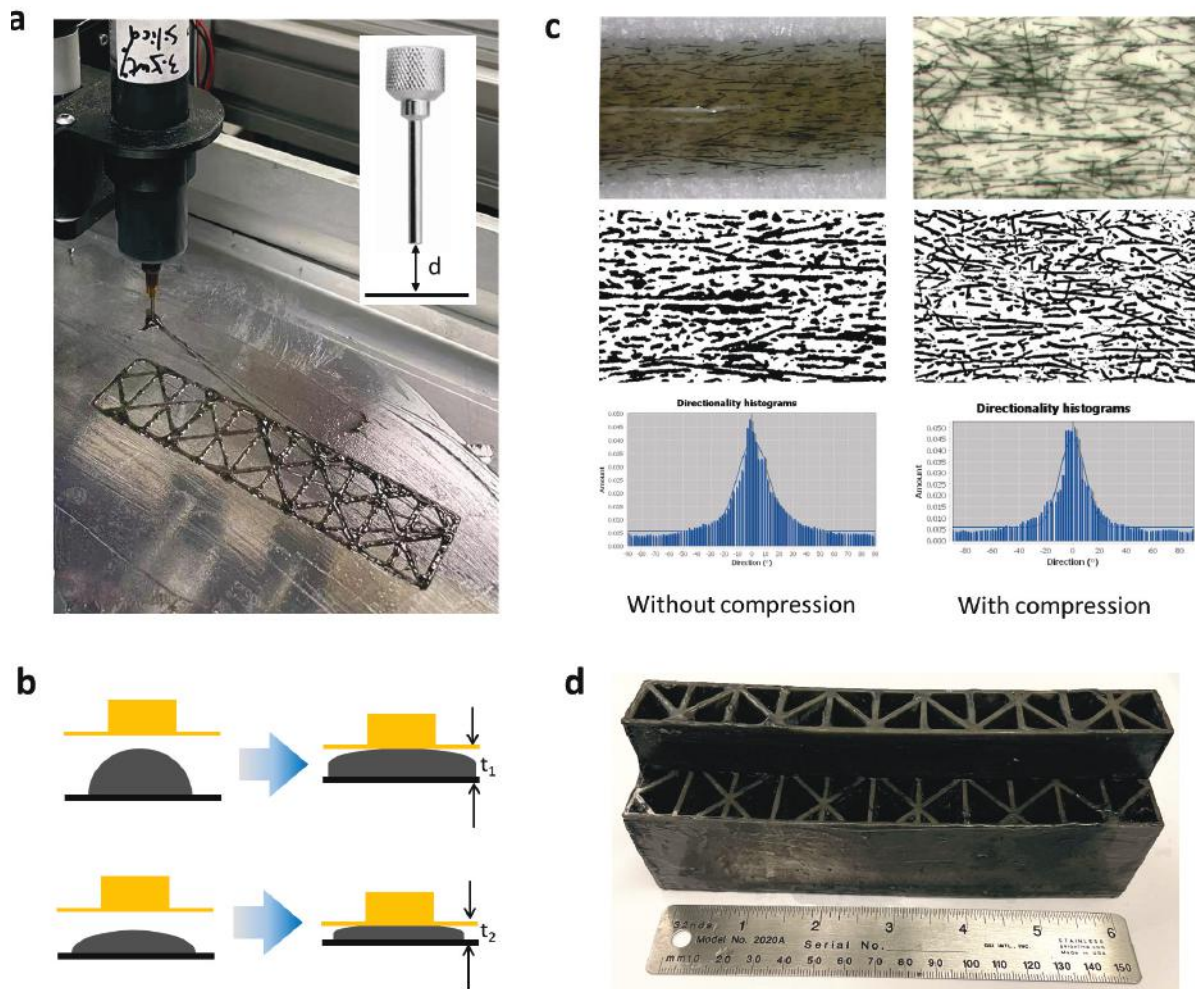


Figure II.3.1.66. (a) Extruded pattern with programmed fiber orientations. (b) The schematic of the compression process of beads with an oval and flat shape. (c) Captured images from cured beads before and after compression. The histogram shows the orientation distribution of the fibers. (d) Printed hollowed car bumper with localized fiber orientation. Source: ORNL.

Dogbone structures with a range of fiber-loading and fiber length were fabricated to experimentally characterize the mechanical performance of the base material. Unidirectional tensile tests were performed to capture the stress-strain curves of the samples, and their stiffness was measured accordingly, as shown in Figure II.3.1.9.6. We observed that the measured stiffness increases monotonically with an increase in fiber-

loading. Compared to the 70 μm , the 315 μm length fiber provides more reinforcement to the composite. Fibers within CFRP resin that contain over 10 wt.% 315 μm fibers tend to aggregate, making the resin extremely viscous so that it cannot be extruded. Therefore, there is no testing data for resins having fiber-loading greater than 10 wt.% with 315 μm fiber length. Moreover, the material shows higher stiffness and strength when alignment presents itself. Specifically, with aligned 315 μm fiber, the CFRP achieves a stiffness of 6.6 GPa, which is 85% higher than with a neat resin sample and is superior to other reported fiber-reinforced composites printed by SLA, as shown in Figure II.3.1.9.6(b). The stiffness was achieved not only by the nature property of the matrix material, but also by the reinforcement of the fibers. The literature reports that 3D printed CFRPs have a stiffness larger than 10 GPa, while those lattices usually have a low resolution (> 0.4 mm), depending on the nozzle size. Theoretically, the method proposed in this work can achieve a printing feature size of less than 50 μm .

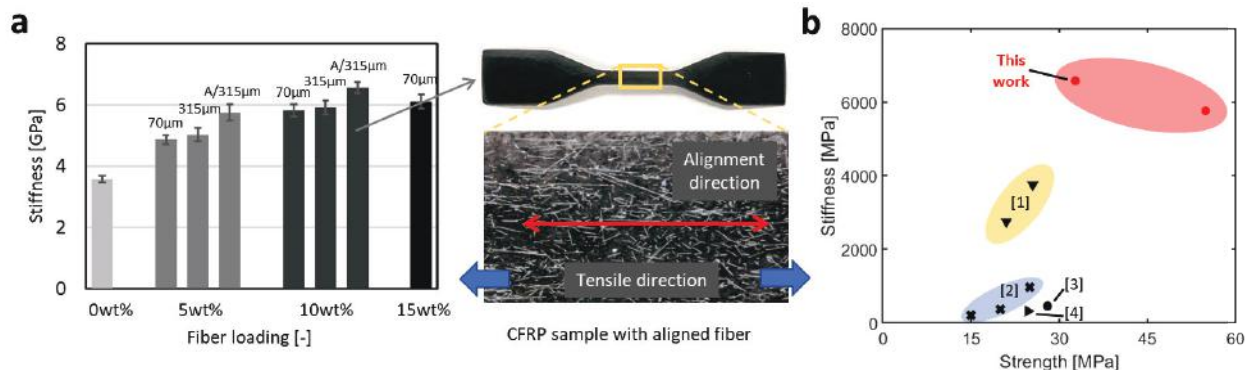


Figure II.3.1.67. (a) Measured stiffness of printed CFRPs with varying fiber-loading and lengths. (b) Mechanical property map of fiber-reinforced composites printed via SLA. Source: ORNL.

The proposed system provides a concurrent ability to print large-scale parts over 50 cm with features as small as 50 μm , thereby enabling the fabrication of metamaterials with features spanning over four orders of magnitude. With the developed printer, we achieved printing lattices with CFRP having an overall size of 10-50 cm, as shown in Figure II.3.1.9.7. Figure II.3.1.9.7(a) features a group of hierarchical CFRP lattice material, which is comprised of the octet of octahedral trusses. The overall size of the sample is as large as 18 cm, while the radius of the struts is as thin as 150 μm . Such a group of materials is nearly isotropic and has high structural connectivity within stretch-dominated architectures. Figure II.3.1.9.7(b) demonstrates the 3D printing of a group of plate-lattice materials using CFRP, which features a more efficient architecture with a higher energy absorption capability than truss-lattices. Figure II.3.1.9.7(c) shows a fabricated large size high-resolution Voronoi vase. The vase has a maximum length of 50 cm and a minimal strut thickness of 50 μm .

Benefiting from the advantages of AM for free forming, it is possible to manufacture components with complex internal structures to meet specific energy absorption requirements. In this work, a car bumper design was provided by Ford Motor Company initially (design not disclosed in this report). As shown in Figure II.3.1.9.8, using lattice design software (nTopology), we created a lattice design based on the outline profile of the bumper, filled with multiple blocks of architected unit cells. This design reduces the weight of the bumper while maintaining good structural rigidity. The total length of the bumper is ~ 110 cm, with a width of 13.3 cm and a height of 10.2 cm.

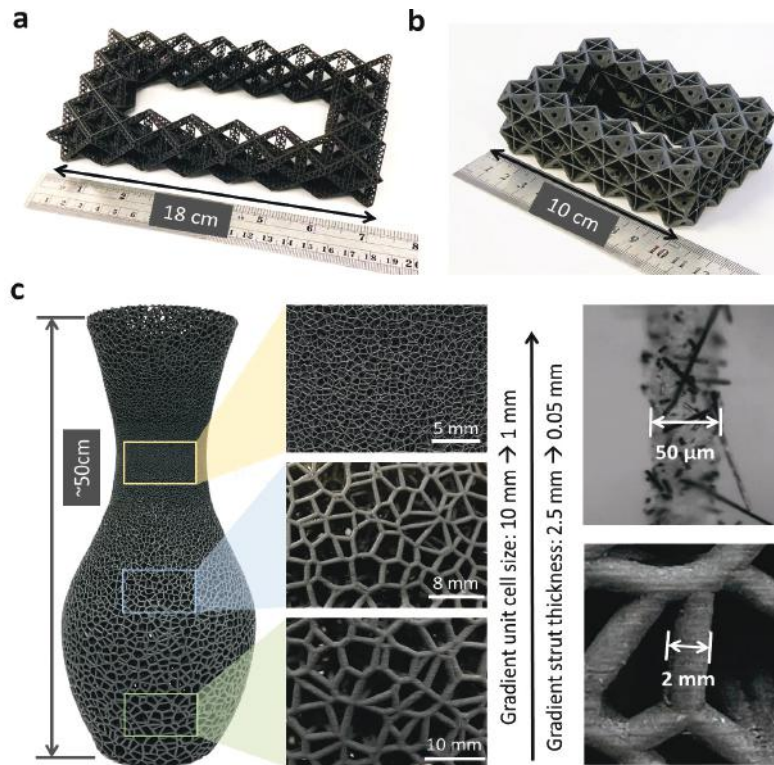


Figure II.3.1.68. (a) As-fabricated large-scale hierarchical CFRP truss-lattice materials (e.g., strut radius = 150 μm). (b) As-fabricated large-scale CFRP plate-lattice materials. (c) As-fabricated large size high-resolution Voronoi vase made of CFRP. The vase is designed to have gradient unit cell size and strut thickness along its height direction. Source: ORNL

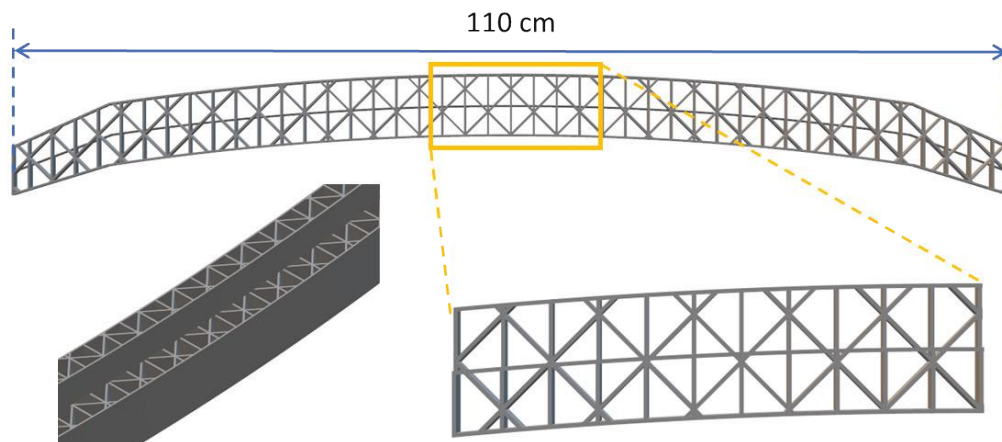


Figure II.3.1.69. Hollowed car bumper design with a lattice structure. Source: ORNL.

The printing of the proposed design is achieved by the large-area and high-resolution 3D printer. Firstly, the 3D model is converted into a .stl file, followed by splitting it into several parts to accommodate the size of the building plate. The segmented parts are then sliced into many layers in Netfabb software. Next, every layer is split into several sub-images, which are then sequentially projected onto the vat when the stage moves along the x-y directions. Polymerization initiates at the light-exposed areas, converting it into a solid single-layer part and sticking to the build platform. The build platform elevates to replenish resin and repeat the cycle. Two halves were printed separately and then assembled with an epoxy glue like J-B weld ClearWeld.

As shown in Figure II.3.1.9.9(a), with the developed printing technique, we have successfully printed the car bumper model with a size of 110 cm. We printed each half (~ 55cm) separately and bonded the two halves together. The printing resin of the bumper is formulated with a commercial UV-curable resin (Formlab Rigid 10k), with 2 wt% loading of short CFs (PC100 from E&L Enterprises, Inc). This resin shows good stiffness with the presence of fibers, reaching >4 GPa by tensile test. Figure II.3.1.9.9(b) shows detailed images of the bumper.

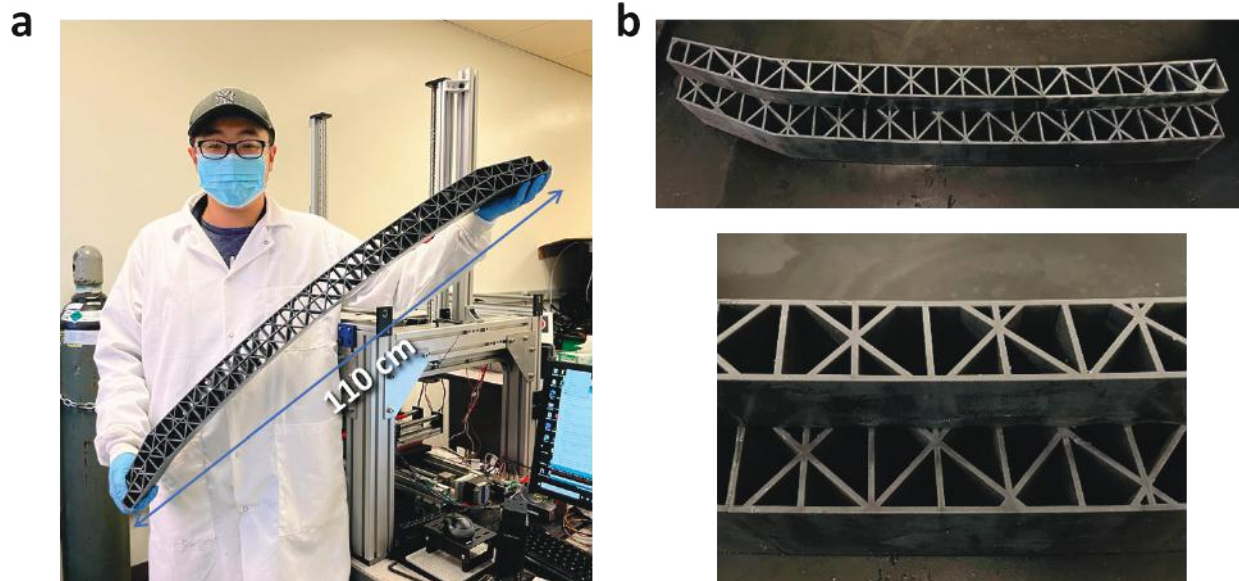


Figure II.3.1.70. (a) 3D printed hollowed car bumper with a length of 110 cm. (b) Each half (~55 cm) was printed separately and bonded together to make a full-size (110 cm) bumper. Source: ORNL.

Conclusions

In this report, we present a high-speed, large-area, and high-resolution projection SLA printer integrated with moving optics and a material extrusion system to print large-scale structures with tailored-fiber orientations aligned along the extrusion direction. The moving optical system consists of a light engine, lenses, mirrors, and a moving stage. The material extrusion system is based on a DIW technology in 3D printing. The printing is controlled by manually scripted MATLAB code with synchronization among the extrusion, nozzle movement, resin vat wetting control, light engine on/off control, slicing image projection from the light engine, and the stage movement. We have developed a moving stage optimization based on a math solution to a TSP and reduced the scanning time by nearly 1/2 to 1/3. We have conducted fiber alignment measurements and strength/stiffness measurements for the printed samples and obtained superior properties (strength and stiffness) as compared to samples from other SLA technologies. A vase with the length of 50 cm was 3D printed using the printer, and the minimum feature size printed in the vase was 50 μ m. We also 3D printed a car bumper with a lattice structure. Each half of the bumper was printed separately (size of ~55cm) and bonded together to make a 110 cm bumper.

Key Publications

1. Hsieh, M. T., C. S. Ha, Z. Xu, S. Kim, H. F. Wu, V. Kunc, and X. Zheng, 2021, "Stiff and strong, lightweight bi-material sandwich plate-lattices with enhanced energy absorption," *J. Mater. Res.*, Vol. 36, No. 18, pp. 3628–3641. <https://doi.org/10.1557/s43578-021-00322-2>.

References

1. Cheah, C. M., J. Y. H. Fuh, A. Y. C. Nee, and L. Lu, 1999, "Mechanical characteristics of fiber-filled photopolymer used in stereolithography," *Rapid Prototyp. J.*, Vol. 5, No. 3, pp. 112–119. <https://doi.org/10.1108/13552549910278937>.

2. Sano, Y., R. Matsuzaki, M. Ueda, A. Todoroki, and Y. Hirano, 2018, “3D printing of discontinuous and continuous fibre composites using stereolithography,” *Addit. Manuf.*, Vol. 24, pp. 521–527. <https://doi.org/10.1016/j.addma.2018.10.033>.
3. Xiao, R., M. Ding, Y. Wang, L. Gao, R. Fan, and Y. Lu, 2021, “Stereolithography (SLA) 3D printing of carbon fiber-graphene oxide (CF-GO) reinforced polymer lattices,” *Nanotechnology*, Vol. 32, No. 23, Art. 235702. <https://doi.org/10.1088/1361-6528/abe825>.
4. Zhang, X., W. Niu, Y. Zhang, X. Hu, J. Fang, L. Zuo, Y. Yin, and S. S. A. Shah, 2021, “Investigation of large-area sheet forming with laser shocking spot by spot,” *Mater. Des.*, Vol. 212, Art. 110279. <https://doi.org/10.1016/j.matdes.2021.110279>.

Acknowledgments

This work was performed in collaboration with the University of California–Los Angeles (UCLA), specifically Prof. R. Zheng’s group. Dr. Zheng is now a Professor in the University of California at Berkeley.

II.3.1.10 Low-Cost, High-Throughput Carbon Fiber with Large Diameter (Oak Ridge National Laboratory)

Felix Paulauskas, Principal Investigator

Oak Ridge National Laboratory
 Chemical Sciences Division
 1 Bethel Valley Rd.
 Oak Ridge, TN 37831
 E-mail: paulauskasfl@ornl.gov

Robert E. Norris, Co-Principal Investigator

Oak Ridge National Laboratory
 Chemical Sciences Division
 1 Bethel Valley Rd.
 Oak Ridge, TN 37831
 E-mail: norrisrejr@ornl.gov

Rich Davies, Composites Core Program Manager

Oak Ridge National Laboratory
 Materials Science and Technology Division
 1 Bethel Valley Rd.
 Oak Ridge, TN 37831
 E-mail: daviesrw@ornl.gov

H. Felix Wu, DOE Technology Development Manager

U.S. Department of Energy
 E-mail: felix.wu@ee.doe.gov

Start Date: October 1, 2020	End Date: September 30, 2023	
Project Funding (FY 2022): \$500,000	DOE share: \$500,000	Non-DOE share: \$0

Project Introduction

ORNL and its partners are demonstrating and evaluating the effects of combining textile PAN fibers produced via dry spinning at substantially larger diameters and oxidized with Atmospheric Plasma-Oxidation (APO) to produce CF that meets automotive requirements at significantly lower costs while also enhancing processing characteristics. CFCs have been gaining interest from automotive designers due to the potential benefits offered by their high stiffness and low-density. It has been projected that CFCs could possibly reduce the weight of vehicle structures by greater than 50% and that fuel economy can be increased by as much as half of the percentage of weight-savings. The high cost of the fiber remains the largest hurdle to production implementation of CFCs as a vehicle structural material. Automotive vehicle manufacturers have consistently indicated that fiber costs approaching \$5/lb. are necessary to achieve substantial inroads into automotive utilization in mass-marketed vehicles where fuel economy can significantly affect national petroleum usage. The costs to produce industrial grade CF with properties similar to those of interest to these automotive applications have been estimated at \$7–10/lb., almost equally split between the cost of the precursor itself and the cost of the conversion. To achieve the necessary cost reduction of 30% or greater, most industry insiders concede that a combination of precursor and conversion cost reductions must be implemented. Fortunately, automotive engineers indicate they are willing to give up some performance to get this cost reduction as well. This initiative intends to take advantage of all these factors to achieve the necessary cost reduction.

Essentially, all PAN-based CFs are currently produced from precursors manufactured expressly for CF production. While acrylic fiber produced for a CF precursor is similar chemically to acrylic fiber produced for textile applications, textile acrylics have not been involved in widespread CF manufacturing. ORNL has made significant progress in demonstrating pathways to CF production utilizing textile products, and that approach is being exploited further in this project. It is also worth noting that although PAN fibers are commonly utilized in textile applications worldwide, all acrylic fiber produced for CF conversion and the majority of PAN fibers produced for textiles are solution-spun. Dry spinning is a more challenging approach and an infrequently utilized variant, in textile acrylic fiber production. Dry spinning utilizes significantly less quantity of solvent in producing the fiber and requires less equipment and energy to extract and recover the solvents. These differences allow for greater production speeds as well, meaning this approach is less costly than wet spinning as described in the Institute for Advanced Composites Manufacturing Innovation (IACMI) Report #IACMI/R-0006-2020/6.061 [1]. The dry spinning process is also being demonstrated and exploited in this project.

Conventional oxidation takes place in large open chamber ovens that heat PAN in air. This process typically takes ~90 minutes (CF manufacturers do not allow their exact residence times to be published) for commercial CFs. The APO was jointly invented by ORNL and 4X Technologies (4XT) and is currently being scaled and commercialized by 4XT and its commercialization arm, 4M Carbon Fiber. The process involves the indirect exposure of PAN to atmospheric plasma in an oven at temperatures similar to conventional oxidation. This has been shown to enhance the oxidation process in CF conversion, especially since it has been shown to be at least three times faster than conventional approaches.

ORNL's acrylic fiber manufacturing partner, Dralon, has indicated that producing larger diameter fibers is not technically challenging and can significantly enhance production economics by up to 30% on their end. However, practical limitations in textile applications and/or the drastic time penalties associated with diffusion time requirements of large diameters in the oxidation process in CF conversion continue to be the limitations on acrylic fiber diameters until this approach is conclusively demonstrated for CFs. Success in our approach has the major benefit of dramatically increasing the throughput of both precursor production and CF conversion, leading to significant cost decreases in both stages.

Objectives

The objective of this work is to demonstrate the effects of combining (1) textile PAN fibers (2) produced via dry spinning (3) at substantially larger diameters and (4) oxidized with APO to produce lower cost CFs that meet automotive requirements at significantly lower costs while enhancing processing characteristics. While several of these factors have been considered individually or in combination with a single factor, in past DOE programs this is the first time that all four approaches have been combined. Ultimately, the team intends to demonstrate that this approach can produce CFs meeting mechanical performance minimums of 375 ksi, 30 Msi, and 1% strain, along with 25%–30% or greater savings. Scaled-up CF production at the ORNL for composite panel evaluation and/or demonstration part fabrication in the third year of this project will show the overall advantages of this approach, along with providing a more detailed assessment of cost/performance tradeoffs.

Approach

During Project Year 1, the team established a baseline for this approach with CFs converted from the dry-spun textile precursor from Dralon along with a fiber effectively at least 25% larger in diameter. Note that since the dry-spun fibers are not round, it is more appropriate to cite the fiber dtex (or mass per unit length in g/10,000 m) rather than diameter. For example, the fibers of focus in this study at 3.3 and 5 dtex would be similar in mass per unit length of 18.8 and 24.3 micron diameter, respectively, and round precursor fibers traditionally of 11 microns in diameter would be a little over 1.1 dtex. Thus, all of the fibers we are considering are at a significantly higher mass per unit length than the typical precursor. Performance of these fibers will be assessed utilizing single filament testing, such that cost information will be generated for inclusion into existing ORNL cost models. The cost of the project baseline fiber will be compared with modeled commercial industrial fiber cost data and preliminary cost projections for larger diameter fiber trends to demonstrate cost

savings for this approach. To meet the go/no-go decision point, baseline fiber must exceed performance of DOE minimum requirements established many years ago for the Low-Cost Carbon Fiber Program of 250 ksi strength, 25 Msi modulus, and 1% strain-to-failure. The ORNL team has actually established a higher requirement for this project go/no-go of 300 ksi strength, 30 Msi modulus, and 1% strain-to-failure, along with a projected cost-savings of 20% versus the modeled commercial fiber.

Year 2 has focused on producing fiber effectively at least 50% larger than the project baseline, along with performance minimums of 375 ksi, 33Msi, and 1% strain, while developing and scaling fiber post-treatment processes to pre-production level production. The cost target for Year 2 is to continue toward demonstration that 25%–30% or greater savings are potentially achievable with this approach and to project optimal diameter targets for scaled-up production in late Project Year 2 or early Project Year 3 for composite panel evaluation and/or demonstration part fabrication in order to demonstrate overall advantages of this approach.

Year 3 will focus on demonstrating and evaluating the attractiveness of the new CFs produced in late Project Year 2 and/or early Project Year 3. The majority of the effort will be expended on making and testing the composite articles required to fully evaluate and define the advantages of this approach. Cost models will be completed and utilized to evaluate the cost versus performance benefits in combining effects of the textile PAN fibers produced via dry spinning and at substantially larger diameters and oxidized with APO to produce significantly lower cost CFs.

Our project partner, Dralon, had earlier produced a variety of precursor fiber sizes in quantities largely commensurate with our needs for this project utilizing their well-established, world-class dry spinning process currently used commercially in producing acrylic fiber exclusively for textile applications. Steam-stretching is sometimes employed in CF production prior to either conventional or advanced oxidation processes to enhance precursor fiber orientation as desired going into conversion. ORNL was responsible for the steam-stretching processes utilized for some of the samples. 4XT is responsible for all of the advanced oxidative stabilization portion of the conversion of the dry-spun precursor. 4XT has been developing oxidation protocols specifically for the unique dry-spun precursors to oxidize the fiber and provide increments to ORNL for conventional oxidation utilized in some cases and carbonization of all samples along with test and evaluation of these variants in Years 1 and 2. To simplify effort for this project, we continue to focus on utilizing the most appropriate conversion capabilities in the middle of these production scales while acknowledging that the other capabilities might be beneficial in even better exploiting the approaches identified in this project in follow-on efforts. Similar to capabilities in conversion, ORNL has independently, and in collaboration with others, established post-treatment capabilities at a variety of scales. Oxidized fiber from 4XT was provided to ORNL in Years 1 and 2 (1) to develop appropriate carbonization and post-treatment protocols for completing the carbon fiber process; and (2) to produce larger quantities of completely converted and post-treated CF for the composite demonstrations in Year 3.

Initial fiber testing has been completed at the single filament level in Year 1 and Year 2 to provide basic strength, modulus, and strain data. Later in Year 3, fiber testing will transition to focus on impregnated strand testing, which allows for more direct comparison with commercial fibers and gives some insight into how well the fiber tows infuse and how the fiber performs due to compatibility with the ultimately intended composite resin system.

ORNL is generally considered as the preferred source for DOE technical modeling of CFCs for vehicle technologies applications. The project team will utilize the established results of this ongoing effort to evaluate what is expected to be a major impact in the approach for making lower cost CF.

Results

Due to a significant downturn in business conditions largely due to COVID-19 limitations, Dralon production over the last 2+ years was terminated pending potential sale of this unique capability. Fortunately, Dralon had already produced samples that were adequate for our initial needs for our other partner to utilize for other purposes. 4XT offered us access to materials they had in reserve that have attributes equivalent to those we were targeting for this work. We are now executing planned experimental activities. These plans include the experimental work to evaluate process conditions and associated economic/performance tradeoffs, as well as some equipment adaptations we believe will facilitate process control and overall production attractiveness.

As shown in Table II.3.1.10.1 and Table II.3.1.10.2, all of the 3.3 dtex Dralon fiber, stabilized using the advanced oxidation process conditions—regardless of whether it was steam-stretched or not—demonstrated tensile strength exceeding 375 ksi and achieved tensile modulus of 28-29 Msi. As observed in Table II.3.1.10.3, Table II.3.1.10.4, Table II.3.1.10.5, and Table II.3.1.10.6, respectively, the converted 5.5 dtex fiber averaged well over 300 ksi tensile strength. Tensile strength for conventionally oxidized 5.5 dtex fiber (steam-stretched or not) tended to be 25–50 ksi higher than for plasma oxidized fiber at that size, and modulus tended to be about 6–7 Msi higher as well.

Table II.3.1.10.1. Carbon Fiber from Plasma Oxidized Steam-Stretched Dralon 3.3 dtex Precursor*

Fv #	Diameter (µm)	Diameter Calculated	Density (g/cc)	Break Stress (Ksi)	Modulus (Msi)	Strain (%)
2872 Precursor	14.05 (0.60)	14.08	1.1787 (.0002)	75.29 (2.61)	1.80 (0.05)	11.26 (0.58)
3656	9.90 (0.61)	9.82	1.3536 (.0005)	41.79 (1.79)	1.22 (0.06)	22.40 (2.08)
3675	6.06 (0.28)	5.89	1.7904 (.0007)	393.15 (84.76)	29.16 (0.37)	1.31 (0.27)
3678	5.95 (0.22)			409.81 (63.31)	28.91 (0.38)	1.38 (0.20)
3677	6.12 (0.36)			443.49 (60.36)	28.49 (0.68)	1.51 (0.19)
3576	6.07 (0.43)	5.91	1.7934 (.0010)	434.17 (81.87)	28.68 (0.89)	1.48 (0.27)

* Please note that in all but Table II.3.1.10.6, the first data line is the property data for the precursor itself and, while the second line provides intermediate property data taken after oxidation is completed for either conventional or advanced oxidation. Other lines in the tables are for fully converted CFs with each line representing slightly different carbonization conditions. In Table II.3.1.10.6, one should refer to Table II.3.1.10.5 for precursor and oxidized fiber values. Fv is the Favimat number.

Table II.3.1.10.2. Carbon Fiber from Plasma Oxidized but Non-Steam-Stretched Dralon 3.3 dtex Precursor*

Fv #	Diameter (µm)	Diameter Calculated	Density (g/cc)	Break Stress (Ksi)	Modulus (Msi)	Strain (%)
2884 Precursor	17.40 (1.12)	16.91	1.1787 (.0002)	54.80 (2.38)	1.55 (0.05)	17.91 (1.71)
3634	12.03 (1.11)	11.32	1.3382 (.0003)	42.55 (1.59)	1.18 (0.02)	21.78 (1.93)
3644	7.00 (0.41)	6.99	1.7868 (.0007)	405.00 (57.66)	28.23 (0.90)	1.40 (0.19)
3645	6.81 (0.47)	6.80	1.7844 (.0004)	450.87 (51.94)	27.93 (0.63)	1.56 (0.18)

Table II.3.1.10.3. Carbon Fiber from Dralon 5.5 dtex Precursor Conventionally Processed*

Fv #	Diameter (µm)	Diameter Calculated	Density (g/cc)	Break Stress (Ksi)	Modulus (Msi)	Strain (%)
3153 Precursor	22.97 (0.79)		1.18	51.48 (1.92)	1.34 (0.02)	24.63 (1.23)
3811 Oxidation	19.32 (0.99)	18.47	1.3627 (.0002)	33.00 (2.88)	1.08 (0.02)	16.68 (4.10)
3812	11.43 (0.84)	11.75	1.7750 (.0003)	328.87 (87.34)	28.82 (1.30)	1.14 (0.31)
3813	11.46 (0.56)	11.44	1.7802 (.0003)	364.40 (53.92)	29.10 (0.40)	1.25 (0.18)
3814	11.28 (0.94)	11.46	1.7746 (.0004)	398.97 (74.49)	28.43 (0.55)	1.39 (0.25)
3821	11.40 (0.72)	11.42	1.7745 (.0011)	356.51 (73.37)	28.74 (0.54)	1.22 (0.24)
3827	11.44 (0.89)	11.41	1.7761 (.0002)	400.69 (74.26)	29.53 (0.84)	1.35 (0.27)
3828	11.37 (0.76)	11.28	1.7757 (.0003)	365.48 (66.51)	30.07 (0.39)	1.21 (0.21)
3829	11.24 (0.93)	10.99	1.7796 (.0004)	345.46 (58.96)	29.92 (0.86)	1.15 (0.19)
3833	11.21 (0.75)	11.30	1.7741 (.0005)	385.83 (58.92)	30.51 (0.54)	1.26 (0.19)
3834	11.64 (0.63)	11.30	1.7748 (.0005)	339.89 (64.18)	29.56 (0.47)	1.15 (0.21)

Table II.3.1.10.4. Carbon Fiber from Steam-Stretched Dralon 5.5 dtex Precursor*

Fv #	Diameter (µm)	Diameter Calculated	Density (g/cc)	Break Stress (Ksi)	Modulus (Msi)	Strain (%)
3916	20.15 (1.44)		1.18	63.94 (5.50)	1.52 (0.13)	14.37 (0.96)
3944	17.10 (0.96)	15.76	1.3557	36.09 (3.01)	1.14 (0.05)	17.91 (2.80)
3950	9.87 (0.50)	9.85	1.7959	379.55 (58.52)	29.18 (0.40)	1.29 (0.20)
3951	10.41 (0.87)	9.52	1.7926	410.90 (53.00)	29.26 (1.77)	1.39 (0.17)
3952	10.58 (0.51)	9.79	1.7871	326.29 (52.51)	28.73 (0.52)	1.13 (0.18)
3953	9.83 (0.47)	9.88	1.7963	407.95 (52.00)	29.92 (0.37)	1.35 (0.18)
3954	9.96 (0.59)	9.88	1.7778	359.84 (96.19)	29.22 (0.36)	1.22 (0.30)
3955	10.59 (0.49)	10.51	1.7769	379.78 (70.29)	28.02 (0.54)	1.34 (0.24)

Table II.3.1.10.5. MTR20798 Dralon 5.5 dtex Plasma Oxidized, Conventionally Carbonized Group 1*

Fv #	Diameter (µm)	Diameter Calculated	Density (g/cc)	Break Stress (Ksi)	Modulus (Msi)	Strain (%)
3153 Precursor	22.97 (0.79)		1.1800	51.48 (1.92)	1.34 (0.02)	24.63 (1.23)
3153 Oxidation	17.96 (0.97)		1.3508	31.38 (2.11)	0.94 (0.01)	19.75 (4.05)
3756	11.03 (0.56)			303.64 (74.53)	24.88 (1.45)	1.22 (0.34)
3759	11.59 (0.60)			256.07 (69.98)	22.23 (1.67)	1.14 (0.28)
3760	11.41 (0.68)		1.7737 (.0008)	325.35 (58.00)	22.22 (1.03)	1.44 (0.22)
3761	11.45 (0.57)		1.7763 (.0018)	333.76 (82.93)	22.88 (0.47)	1.44 (0.35)
3766	11.80 (0.82)		1.7664 (.0027)	295.09 (68.47)	22.54 (0.53)	1.29 (0.29)
3768	11.95 (0.55)		1.7666 (.0015)	305.67 (64.29)	22.08 (0.78)	1.37 (0.26)
3769	11.16 (0.93)		1.7642 (.0007)	341.97 (110.97)	22.18 (0.82)	1.52 (0.48)
3770	11.51 (0.42)		1.7673 (.0007)	365.67 (87.74)	21.98 (0.58)	1.63 (0.38)

Table II.3.1.10.6. MTR20798 Dralon 5.5 dtex Plasma Oxidized, Conventionally Carbonized Group 2*

Fv #	Diameter (µm)	Diameter Calculated	Density (g/cc)	Break Stress (Ksi)	Modulus (Msi)	Strain (%)
3771	11.28 (1.08)		1.7717 (.0008)	309.60 (79.48)	22.62 (0.92)	1.35 (0.32)
3772	11.54 (0.43)		1.7685 (.0056)	358.49 (74.47)	23.14 (0.23)	1.52 (0.31)
3773	11.59 (0.89)		1.7739 (.0009)	318.68 (83.60)	24.29 (0.92)	1.29 (0.33)
3774	11.28 (0.82)		1.7883 (.0545)	347.15 (74.04)	23.60 (0.40)	1.45 (0.31)
3775	10.75 (0.72)		1.7712 (.0049)	323.82 (75.16)	25.01 (0.50)	1.27 (0.29)
3776	11.09 (0.38)		1.7831 (.0006)	365.04 (88.40)	24.21 (0.40)	1.48 (0.33)

ORNL continues to develop a relationship with Sudamericana de Fibras (SDF) in Peru as an alternative supplier for the dry-spun PAN precursor should Dralon not be able to return to production. The SDF products are manufactured from essentially the same dry-spun process, but the PAN is co-monomered with vinyl acetate at SDF instead of methyl acrylate, which will not achieve the same tensile strength as the Dralon fiber. During the previous period, SDF has supplied a new variant that can be split more easily than in earlier forms and visually appears more robust in initial processing. Results from converting and testing this precursor show that, while not yet equivalent to the PAN / methyl acrylate precursor from Dralon, the SDF fiber is catching up and may indeed be a long-term alternative to Dralon should the Dralon precursor continue to be unavailable.

Since our objectives were to compare and contrast the unique opportunities presented by a dry-spun textile-based precursor produced with larger diameters and exploiting advanced conversion, our demonstration plan for FY 2023 has been tailored around making preforms and panels at the University of Tennessee with their wet-lay preform process and molding the panels. This approach utilizes a large-scale manufacturing-capable process of interest to the automotive industry, while working with the equipment and processes that can be rapidly tweaked to provide direct comparison to commercial CF products without requiring a very large amount of our extremely limited precursor supply. Our plan is to utilize two or more of our developmental products along with at least one commercially available variant. Due to the small amount of CF, we will be producing, this fiber can be fully and economically converted in the laboratory-scale facilities at ORNL while utilizing the specialized capabilities of our developmental partner at 4XT.

Conclusions

In FY 2022, significant technical progress has been achieved despite the severe impact of materials availability limitations due to COVID-19 and the resulting business impacts to our project partners. The project team has now largely caught up to schedules after more than six months of delay at project initiation and have identified both means for meeting our materials supply and composite article demonstration needs. Technically, the project team is very close to the project mechanical performance goals for the first year and anticipate being able to fully meet those goals during FY 2023.

The fiber data presented demonstrates that the textile-based, dry-spun precursor clearly has the potential for broad commercial application in vehicles as defined by the long-running VTO goals of performance exceeding minimum targets of 250 ksi tensile strength, 25 Msi tensile modulus, and 1% strain-to-failure. Although not required to meet these minimum requirements, the team feels that further property improvements are likely with better optimized precursor and conversion processes, especially in better tailoring the advanced oxidation to match the very large diameters of the 5.5 dtex fibers. One potential approach postulated for the larger diameter fiber is to develop and implement a plasma treatment that varies intensity as a function of the oxidation progression over time. In addition to making and testing composite articles during the final year of the project, areas needing more focus include modulus enhancement and completing more detailed techno-economic modeling. Typically, increasing modulus is accomplished much more easily than increasing tensile strength or strain, which already meet project targets, by increasing processing temperatures and/or conversion residence time. The techno-economic modeling has been delayed due to the uncertainty of materials availability and selection and, also, due to the larger width of the processing envelope than had been expected going into the project. However, the larger mass per unit length of the experimental product forms versus conventional CF precursors and the rapidity of conversion processes that are being employed to get the resulting CF still portend well for substantial economic advantages of this approach.

References

1. Wego, A. J., 2020 “Development of a Lower Cost, High Volume, Commercially Available, Precursor for Lower Cost Carbon Fiber for Automotive and Wind Blade Applications,” IACMI/R-0006-2020/6.06, Institute for Advanced Composites Manufacturing Innovation, Knoxville, TN, USA [Online]. Available at: <https://iacmi.org/wp-content/uploads/2022/01/IACMI-6.06-Final-Project-Report-for-Dralon-12.22.21-approved.pdf> (last accessed 2 February 2023).

Acknowledgments

The authors would like to recognize the technical contributions by A. Wego from Dralon; T. Bonds, D. Martin, and J. Nowak from 4XT; and F. Xiong and D. McConnell from ORNL.

II.3.1.11 Carbon Fiber Technology Facility (Oak Ridge National Laboratory)

Merlin Theodore, Co-Principal Investigator

Oak Ridge National Laboratory
1 Bethel Valley Rd.
Oak Ridge, TN 37831
E-mail: theodore@ornl.gov

Amit Naskar, Co-Principal Investigator

Oak Ridge National Laboratory
1 Bethel Valley Rd.
Oak Ridge, TN 37831
E-mail: naskarak@ornl.gov

Uday Vaidya, Governor's Chair for Composites MFG

Oak Ridge National Laboratory
1 Bethel Valley Rd.
Oak Ridge, TN 37831
E-mail: vaidyauk@ornl.gov

Rich Davies, Composites Core Program Manager

Oak Ridge National Laboratory
Materials Science and Technology Division
1 Bethel Valley Rd.
Oak Ridge, TN 37831
E-mail: daviesrw@ornl.gov

H. Felix Wu, DOE Technology Development Manager

U.S. Department of Energy
E-mail: felix.wu@ee.doe.gov

Start Date: March 1, 2011 End Date: Project continuation is evaluated annually
Project Funding (FY 2022): \$1,000,000 DOE share: \$1,000,000 Non-DOE share: \$0

Project Introduction

In March 2009, DOE-EERE issued a competitive call for proposals to construct and operate a highly flexible, highly instrumented, CFTF for demonstrating and evaluating LCCF and new low-cost manufacturing technologies at a pilot scale. Construction of the CFTF began in March 2011 and the facility was commissioned for operations in March 2013.

CFTF is a national treasure and the only open-access state-of-the art CF manufacturing research facility in the U.S. The CFTF offers a unique, highly flexible, highly instrumented CF and melt-spinning precursor processing line with a capacity of 25 and 65 tons per year, respectively. The facility is used for demonstrating advanced technology scaleup and for producing market development volumes of prototypical advanced fibers (e.g., CFs). The unique capabilities provided by CFTF, including the flexibility to process a range of feedstocks and product forms, are unmatched anywhere in the world. CFTF fills a critical need for supporting industrial competitiveness in the manufacture of advanced fibers in this nation by serving as a national resource assisting industry in overcoming the barriers associated with cost and technology scaling of low-cost advanced fibers and composites including product and market development. CFTF allows new advanced fiber-

related technologies to commercialize effectively by bridging R&D to demonstration, deployment, and validation of such technologies using low-cost precursors and energy-efficient advanced conversion processes at an industrial relevant scale. CFTF also serves as a conduit for testing and validating new technologies in digital and/or smart manufacturing.

ORNL operates the CFTF and works with leading companies to overcome technology barriers to reduce the cost and energy consumption of advanced fiber manufacturing to reveal the strength and energy saving benefits of these new materials. CF is one example of an advanced fiber. Due to its exceptional strength and low-density, CF is an enabling material for many applications, such as fuel-efficient automobiles, large wind-turbine blades, and lightweight compressed hydrogen or natural gas tanks. DOE is interested in increasing the availability and affordability of CF and CF composites to increase energy efficiency and product performance. The major obstacles to CF and other advanced fibers are the availability in high-volume industries at a high cost relative to materials currently used, limited availability or a lack of domestic sources, and the lack of compatible materials and processes for manufacturing its composites. For advanced fibers to achieve widespread use in vehicle and industrial markets, the cost of production of these advanced fibers must be reduced by 30% to 50%.

CF is a strong, stiff, and lightweight material used as a reinforcement for polymer-based composites to enable improved product performance in many applications. However, the use of CF in cost-sensitive, high-volume industrial applications is limited because of today's relatively high cost of production. Half of the cost in manufacturing lies in the precursor material, as seen in Figure II.3.1.11.1. Current methods for manufacturing CF and CF-reinforced composite structures are time-consuming and energy-intensive. New, innovative manufacturing processes for low-cost precursor development and conversion technologies hold the key to reducing CF cost for energy applications.

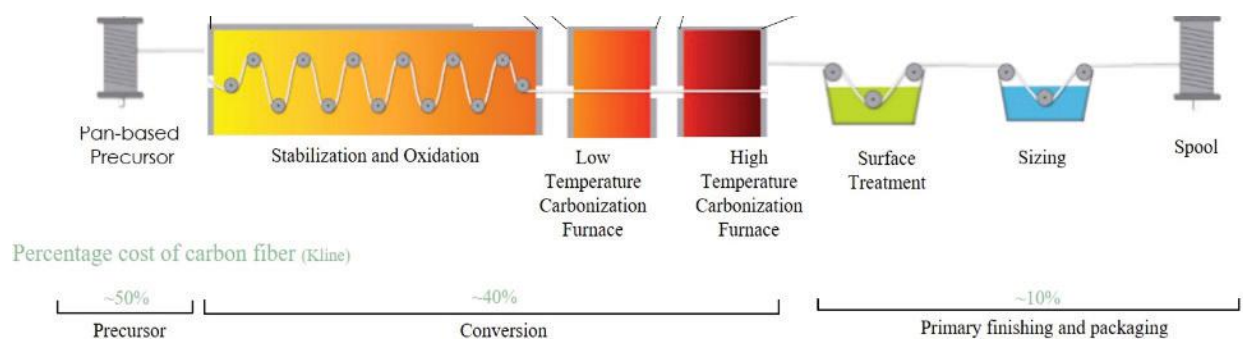


Figure II.3.1.71. CF manufacturing process and cost analysis. Source: ORNL.

The high cost of commercially available CF is due largely to the high cost of specialty precursor materials and the energy- and capital-intensive nature of the conversion process. ORNL was the successful proposer of a DOE-EERE competitive solicitation in 2009 for advanced research, development, and demonstration of CF production and build a semi-production-scale facility with capability to handle various feedstock materials, to integrate advanced energy-efficient conversion technologies, and to produce enough finished fiber to supply end users for R&D of improved composite manufacturing methods. The proposed capability was focused on four critical areas: (1) development of low-cost feedstocks (precursors); (2) development of more affordable feedstock conversion methods; (3) integration of developed technologies into an industry-scalable demonstration facility to reduce risk of investment; and (4) development of CF composite material and processing technologies. The project objective will be addressed through the third task in the CFTF AOP.

The objective of this project is to accomplish the safe and reliable operation of CFTF and to further DOE objectives for large-scale LCCF commercialization. ORNL's Advanced Fibers Manufacturing Group functioning at CFTF supports DOE-EERE's efforts toward transitioning technologies to industry by focusing on developing scaleup science and technologies for advanced fiber manufacturing and associated fabrication of functional components for high-volume energy applications at the CFTF.

In FY 2022, ORNL continued its R&D efforts to further reduce the cost of CF using other alternative precursors or advanced processes. Table II.3.1.11.1 depicts a list of alternative precursors and advanced processes, along with their advantage and disadvantage for use and the estimated reduction in cost and embodied energy.

Table II.3.1.11.1. Alternative Precursor and Advanced Conversion Processing Estimated Reduced Cost and Embodied Energy

Precursor/Process	Advantage	Disadvantage	Conversion Yield	Cost Reduction	Energy Reduction
Standard Polyacrylonitrile (PAN) Precursor (baseline)	Strength, elongation, knowledge base, and fiber architecture.	Feedstock price, volatility, capital cost, energy, yield, and processing.	50%	-	-
Textile PAN Precursor	Properties and knowledge base comparable to standard PAN. Energy consumption and cost reduced.	Capital cost and yield comparable to standard PAN precursor.	50%	*Theoretical ~25% Actual ~54%	Theoretical ~30 Actual ~41%
Polyolefin/Polyamide Precursor	Feedstock price and stability, spinning, yield, and fiber architecture.	Conversion process and equipment, knowledge base, and capital cost.	65%–75%	~20%	~50%
Pitch-Based Precursor	Feedstock price and stability, spinning, yield, knowledge base, properties develop w/o stretching, moderate capital. Pitch-based precursor offers the highest potential cost and energy reduction potential.	Elongation, compression strength, and fiber strength.	80%–85%	~70%	~70%

Preliminary estimations depicted in Figure II.3.1.11.2 show a significant reduction potential in coal pitch CF embodied manufacturing from a lower raw material embodied energy and a higher process yield. Additionally, pitch CF potentially offers the lowest cost/stiffness among CF; hence, a compelling value in cost-sensitive, stiffness-driven, and high-volume applications. ORNL will initiate R&D efforts in other advanced fibers in the near future.

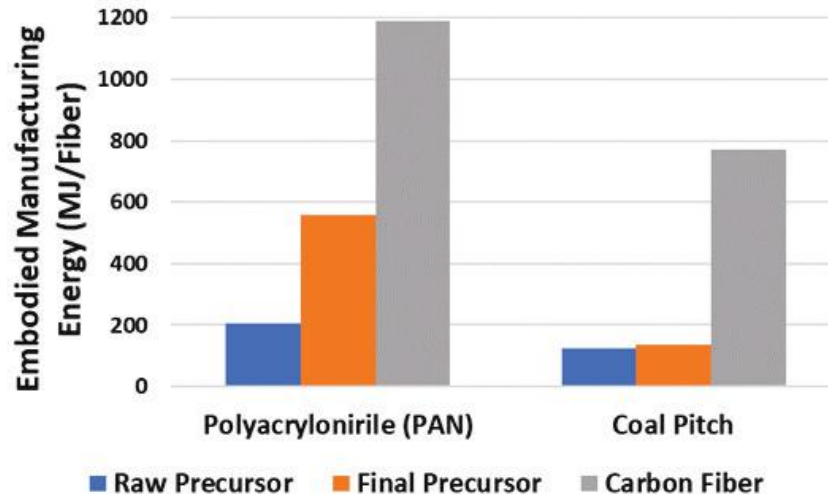


Figure II.3.1.72. Embodied energy for PAN and coal pitch precursor and CF manufacturing. Source: ORNL.

Objectives

The project's objective is to develop low-cost fibers from alternative precursors and accomplish safe and reliable R&D projects to further DOE objectives for large-scale LCCF commercialization. The tasks covered under these agreements are co-funded by the VTO and the AMMTO in support of the efforts by DOE-EERE in transitioning technologies to industry. The CFTF serves as a national resource to assist industry in overcoming the barriers of CF cost, technology scaling, and product and market development. The CFTF provides tours so that industry and others can see the technology and process science being developed to produce LCCF with industry-appropriate mechanical properties from alternative precursor materials.

Approach

The ORNL team recently modified their strategic planning that resulted in a diverse and comprehensive multiscale integrated plan delivering impactful research and development efforts from basic-to-applied technical readiness level research encompassing "conception to commercialization" or "precursor to part."

Currently, no commercial manufacturer exists for LCCF, therefore, the CFTF shall identify cost-effective alternative sources of precursors based on availability, carbon yield, cost, and spinnability. Once the chemistry of the precursor is developed and the baseline properties of 250 Ksi tensile strength and 25 Msi modulus are met, enough material will be produced for scaling up to the next level. Results generated from the bench scale studies are then used to develop a baseline condition or starting point for scaling to the next scale. The CFTF staff will then develop process conditions for converting the precursor material into LCCF that will exceed baseline properties. The fibers' performance will be characterized and evaluated in a variety of resins systems at a coupon level utilizing various compositing methods. Enough CF will be produced for deployment to industry to evaluate, thereby showcasing the quality of LCCF on a multitude of end-user platforms. This work is intended to produce industry demand for the technology. The CFTF staff continues to hold discussions with industrial partners that are interested in scaling the processes being developed at CFTF. The financial investment for industry to scaleup the technology is significant, and thus, not a subject for quick decision.

The CFTF's integrated CF and its composites research portfolio, within the intricate ORNL ecosystem as shown in Figure II.3.1.11.3, was developed to maximize the impact in the U.S. economy. ORNL is the only national laboratory in the United States that can deliver a multiscale strategic approach from precursor to part with TRLs ranging from TRL 1 through TRL 7 at handoff to our collaborating partners. The vision was developed to drive innovation in R&D from precursor to part for structural and non-structural applications across various technology areas, especially automotive.

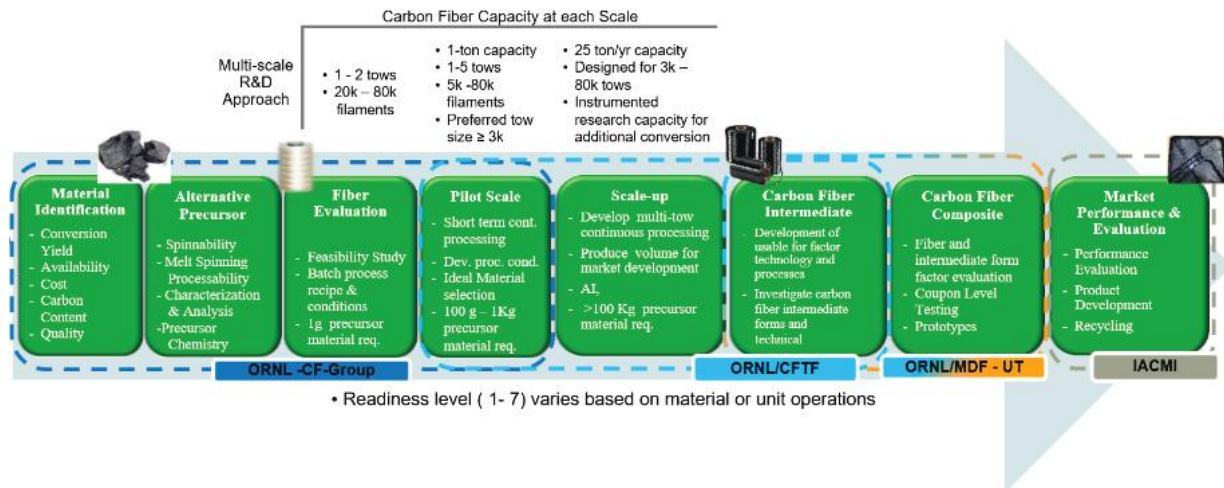


Figure II.3.1.73. Multiscale R&D approach. Source: ORNL.

CFTF’s mission is to transition technology to industry for scaling, but many technical challenges remain that must be overcome to further reduce the risk for industry to implement the technology. These technical challenges are being addressed in collaboration with industry to reduce uncertainties and implementation risks associated with scaling technologies. These challenges include handling the various form factors of fibers processed from the alternative precursors and developing appropriate sizing for LCCFs for specific composite applications. The CFTF continues to be a training ground for any technical staff involved in CF production. Key strategies implemented by the project and supported by VTO in FY 2022 were labeled under Task 3, entitled “Investigate Potential Alternative CF Precursors,” of the CFTF AOP with defined milestones. The milestones and their status at the end of FY 2022, as shown in Table II.3.1.11.2, were to investigate potential alternative CF precursors. This will allow for the selection of a candidate precursor not previously studied and an investigation of supplier-to-supplier variation effects in precursor chemistry, physical characteristics on product variability, and performance.

Table II.3.1.11.2. Task 3 Milestones, Task Descriptions, and Status

Milestone	Due Date	Type	Description	Status
3.1	12/31/2021	Regular	Develop process condition for spinning nylon precursor. \$300,000	Produce < 10 spools. Diameter: ~24.46 μ m Strain at Break (%): 85.7 Strength (GPa): 0.45 Modulus (GPa): 2.07
3.2	03/31/2022	Regular	The objective of this task is to demonstrate the feasibility of melt-blowing Participant's mesophase pitch using CFTF facilities. Participant will provide mesophase pitch pelletized to specifications agreed by Contractor/Participant, and in quantities needed for the melt-blowing trials. \$250,000	Feasibility study of melt-blowing Advanced Carbon Products, LLC mesophase pitch at scale Characterization and analysis of batch process samples report. Provide melt-spinning process condition, characterization analysis report, and video of demonstration.
3.3	06/30/2022	Regular	Evaluate the performance of low-cost advanced fiber in thermoplastic resin system. \$50,000	Characterization and Analysis report on thermomechanical, thermal, mechanical, and physical properties.
3.4	09/30/2022		Development of a new synthesis method for pitch material. ORNL will develop two pitch candidate material for later development of pitch precursor. \$400,000	Pitch material shall have a softening point >200 °C using feedstock not previously used internally.

Results

Visitors/Tours

During FY 2022, A total of 457 visitors from 193 organizations toured the CFTF.

Alternative Precursor and Carbon Fiber Development

Pitch CF

ORNL partnered with industry partners, who are in the process of developing and scaling a petroleum and/or a coal-based pitch material process for the purpose of producing pitch precursor for pitch CF production. Two kinds of pitch existing today are isotropic and anisotropic (mesophase). However, all pitch begins as isotropic that can be further processed through thermal processing to become a mesophase. The two resultant precursors and CFs produced from the aforementioned pitch material differ in their structure and properties. Mesophase pitch is favored over isotropic because it is possible to get a high degree of orientation of carbon hexagonal layers along the fiber axis during fiber processing, so it is not necessary to stretch the fibers during stabilization and carbonization [1]. The mesophase pitch has the potential to be an excellent precursor to produce high-quality CFs with a higher Young's modulus and a substantially lower cost than by using PAN.

Pitch material has various forms with inconsistent qualities, such as a varying concentration of volatiles, granules/particles size, as shown in Figure II.3.1.11.4, and texture within the same batch. Each source of pitch material poses different challenges with processability in the melt-blowing process.

The inconsistent particle size is not much of an issue at the bench scale but challenging in scaled-up processes. To address the inconsistent granule/particle size challenge, the team developed a pelletization process, as observed in Figure II.3.1.11.5(a), for producing a pelletized pitch chip, as shown in Figure II.3.1.11.5(b), with a consistent particle size.

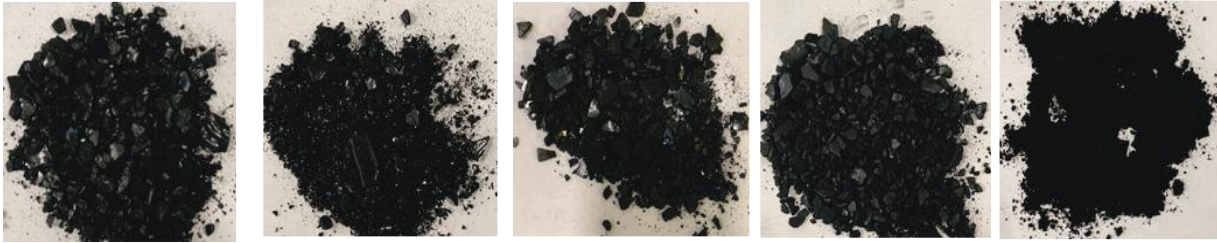


Figure II.3.1.74. Pitch material from different sources. Source: ORNL.

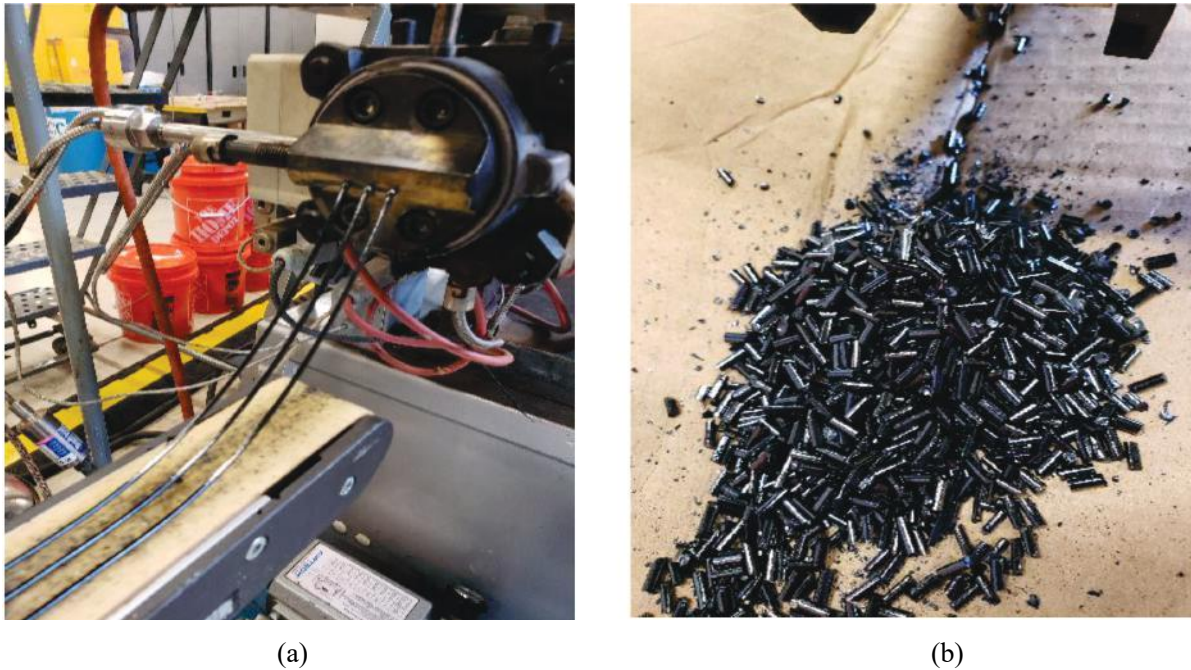


Figure II.3.1.75. (a) Pelletization process. (b) Pelletized pitch material. Source: ORNL.

One industry partner has developed several processes for the manufacturing of refinery oil into isotropic pitch, as well as a continuous process to convert this isotropic pitch into anisotropic mesophase pitch. ORNL tasks were to conduct spinning trials of the isotropic and mesophase pitch material, including developing the baseline and scaleup processing conditions for the conversion of the pitch material into pitch precursor fibers for further conversion into pitch CF. Thus, to demonstrate the large-scale production of pitch precursor fibers from a petroleum-based pitch material.

After a couple trials and addressing challenges at scale, the team was successful in melt-blowing the isotropic pitch material into precursor fibers, as observed in Figure II.3.1.11.6, for CF processing at the bench scale and at scaleup. In addition, the melt-blowing conditions were established. Examples of melt-blowing process challenges are the melt processing is not defined by one temperature and shear rate but by several scale effects due to temperature, residence time, shear rate, and volume of material impact. The factors influencing fiber production are known to be the content of mesophase (anisotropic) ratio (i.e., the percentage of optically anisotropic regions), softening point, degree of hydrogenation, and thermal history of the pitch, based on extensive works by various authors [2].

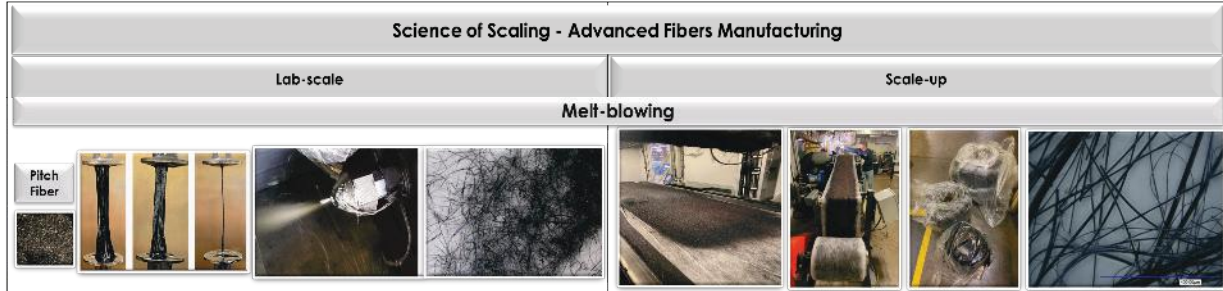


Figure II.3.1.76. Melt-blowing of pitch precursor at bench scale and scaleup including microscopy images of the produced fiber. Source: ORNL.

Nylon-6 Precursor Material

Research projects were established to support future potential work (e.g., the Hydrogen Tank Project was established for DE-FOA-0002229) jointly funded by VTO for hydrogen tank applications. In this AOP, the team must define baseline conditions at scale for melt-spinning/melt-blowing new material that was expected to be scaled at CFTF, if not done in the past. The team must determine and implement all modifications and/or requirements to the scaleup process prior to scaling. The team was provided the manufacturer/future project specification requirements for nylon-6 for use as a baseline material. The team was tasked with developing the process condition for scaling and spinning a minimum of ten nylon-6 precursor spools that meet the specifications.

The CFTF team successfully developed the spinning conditions and scaled the nylon-6 precursor fibers, as observed in Figure II.3.1.11.7. It took three spinning trials at scale to achieve the spools with the desired properties. In the trials, the team quickly realized the amount of moisture in the nylon pellets must be less than 0.01% prior to processing. The team surpassed the required number of spools desired and the expected properties. The tensile properties for the spools are listed in Table II.3.1.11.3. The team superseded the tensile property targets by achieving a 0.38 GPa, 2.13 GPa, and 94.4% for tensile strength, modulus, and strain at break (%), respectively. The target diameter requirements were 24 μm. The team also superseded that requirement and achieved an average diameter of 20 μm, as observed in Figure II.3.1.11.8 (images are for illustration only and details are not to be readable) . Thus, a smaller diameter precursor nylon-6 fiber is preferred for later applications.

Composite Studies with Textile CFs

The textile carbon fiber (TCF), previously developed at CFTF, was produced with a sizing coating that is compatible for thermoplastic polypropylene (PP) resin systems. Performance was evaluated on TCF using a thermoplastic resin system in a tape impregnation process. Then, the thermomechanical and physical properties were characterized and analyzed.

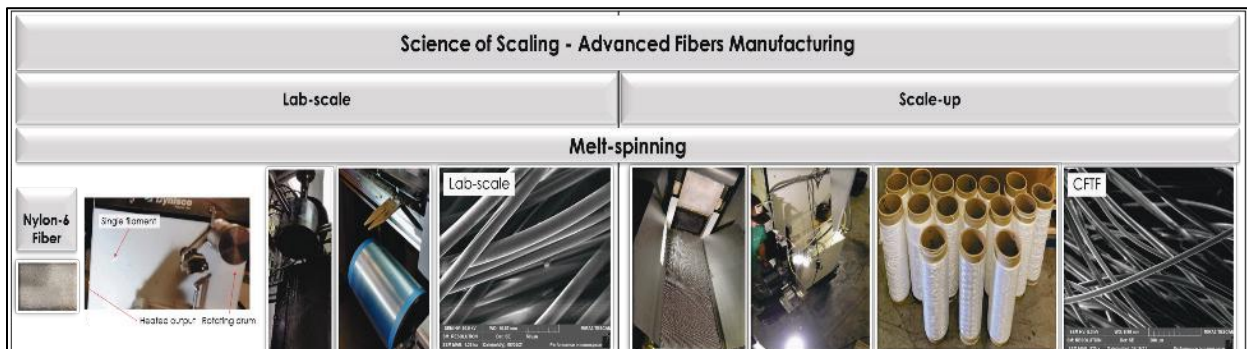


Figure II.3.1.77. Melt-spinning of pitch precursor at bench scale and scaleup including SEM images of the produced fiber. Source: ORNL.

Table II.3.1.11.3. Properties of Nylon-6 Precursor Spools

Property	Property Value
Diameter (μm)	20.52 +/- 1.82
Tensile Strength (GPa)	0.38 +/- 0.03
Tensile Modulus (GPa)	2.13 +/- 0.03
Strain at break (%)	94.4 +/- 14.42

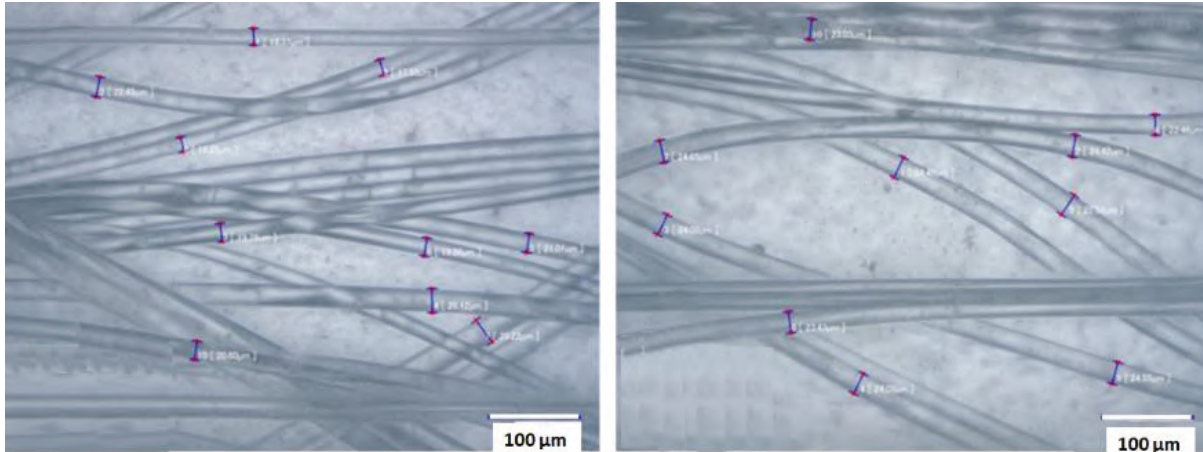


Figure II.3.1.78. Optical microscopy images of the nylon fiber samples (for illustration purposes only).
Source: ORNL.

Thermoplastic Tape Impregnation

This study is focused on developing a low-cost TCF thermoplastic impregnation tape line for laboratory-scale work that has implications for a broad application in parts and components for a wide range of sectors. There were two main considerations for the production quality of thermoplastic tape: (1) fiber weight (or volume) percentage; and (2) fiber wet-out. For fiber weight percentage, line speed and extruder speed are the main considerations. For fiber wet-out pin angle, fiber path and spreading have the largest effect on the production quality of tape. Development of this impregnation line was done in consideration of the previous development challenges by focusing on an open die process as compared to a traditional closed die system. This enabled an increased break angle and tension inside the die for optimal fiber wet-out. The properties of TCF-PP are compared to the literature for tensile, flexural, and interlaminar shear strength.

Thermoplastic Tape Production Process

This thermoplastic impregnation system at the FCMF consists of five modules. The fiber initially comes off a creel where the fiber is pre-tensioned, and then passed across a heated pin. This heated pin partially degrades and softens the sizing allowing the fiber to optimally spread. The fiber is then sent to an adjustable roller where the curvature of the roller can be changed to increase or decrease the amount of spreading. The optimal tow spread width for this system is four inches. The tow is then passed across a final heated pin where the fiber is heated up to match the temperature of the polymer. A coat hanger die is designed to spread the polymer into a flat sheet to match the width of the fiber tow. The fiber and polymer are then passed through a series of heated pins where induced tension and spreading on the fiber forces the polymer through the fiber medium, as shown in Figure II.3.1.11.9. The pin angle and fiber path has been optimized for complete fiber wet-out.

The composite tape was passed underneath an air knife attached to a vortex tube where approximately 0°C compressed air flash cools the composite. The composite is pulled with a pinch puller system that maintains the constant line speed for the system. A load cell and clutch then work in tandem to take-up the composite tape maintaining even tension insuring a neat roll of tape. Figure II.3.1.11.10 shows a visual representation of this hot melt thermoplastic impregnation system.

The die systems are modeled using Darcy’s law, which describes how a viscous fluid passes through a porous media where q represents the instantaneous flow rate of the through the fiber-matrix, k represents the permeability content of the reinforcement fibers, μ is the viscosity of the fluid, and ∇p describes the pressure drop through the media. Darcy’s law is a well-established model for calculating resin flow-through a fiber-matrix in composite manufacturing.

$$q = -\frac{k}{\mu} \nabla p \tag{1}$$

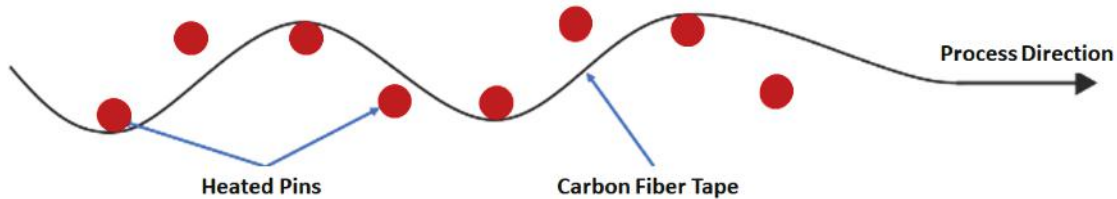


Figure II.3.1.79. Optimized pin configuration of the heated pin die system. Dual pin configurations were set to +45, -45, +45, and -45, respectively. Fiber was weaved through the pin system as shown. This pin configuration and weave pattern was found to optimally impregnate the CF tow. Source: FCMF.

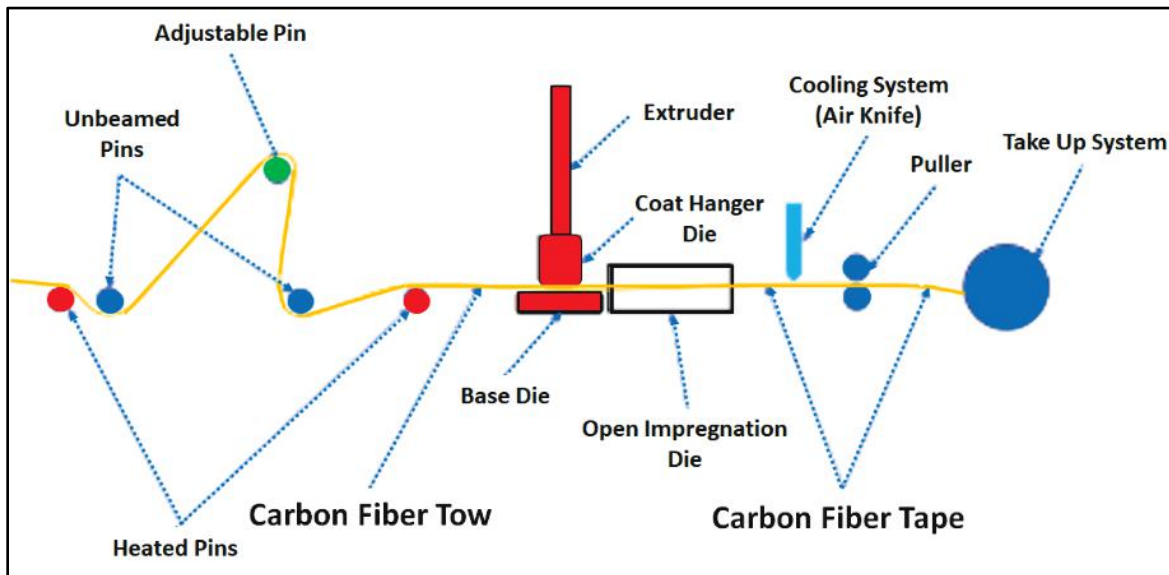


Figure II.3.1.80. Thermoplastic tape impregnation process. This system was designed for the impregnation of wide tow (+350K) TCF. Source: FCMF.

Material Constituents

Approximately 70 wt.% of textile-grade PAN from CFTF has a tensile strength of 2.2 GPa, a tensile modulus of 210 GPa, and a 1% elongation to failure. Table II.3.1.11.4 shows the relevant fiber properties.

Table II.3.1.11.4. Properties of Textile Carbon Fiber

Textile-Grade Carbon Fiber		
	International System of Units	U.S. System of Units
Tensile Strength	3000 MPa	335 Ksi
Tensile Modulus	275 GPa	40 Msi
Density	1.76 g/cc	0.0636 lb./in. ³
Fiber Diameter	7–10 μm	0.00027–0.00039 in.

The PP polymer used for this study was a homopolymer resin designed for spun bond nonwovens. This polymer has a density of 0.900 g/cm³ and a melt mass flow rate (e.g., 230°C/2.16 kg) of 36 g/10 min tested using ASTM standards D792 and D1238, respectively. The tensile strength and modulus of ExxonMobil PP3155 were 23.71 MPa and 1.25 GPa, respectively, as observed in Table II.3.1.11.5.

Table II.3.1.11.5. ExxonMobil™ PP3155 PP Homopolymer Properties

Property	S.I.	U.S.
Melt Mass Flow Rate	36 g./10 min	0.022 lb/10 min
Density	0.900 g/cc	0.0325 lb./in. ³
Tensile Strength	23.71 MPa	3.44 Ksi
Tensile Modulus	1.25 GPa	Msi

CF-PP Tape Production

All thermoplastic tape made in this study was produced on a hot melt thermoplastic impregnation line. A preliminary study was conducted on a Dyze Design extruder to determine polymer flow rate vs. motor speed. Results from this study showed a linear relationship between motor speed and PP flow rate. A similar study was conducted on the line speed vs. motor speed to determine how fast the line will run. These two preliminary studies were used to determine processing parameters (e.g., line speed, extruder speed) of the impregnation system to produce composite tape at a desired fiber weight fraction (FWF).

TCF was impregnated with ExxonMobil™ PP3155 PP homopolymer to produce composite tape (ZOLTEK tape [ZT]-PP and TCF-PP, respectively). ZT-PP and TCF-PP tape was produced with extrusion temperature for PP of 215°C and impregnation pin temperatures were set to 220°C. The intention for this study was to produce tape at a FWF of approximately 35%. To produce ZT-PP tape, two 50K tows were set-up and run at a line speed of 1.22 meters per minute with a polymer flow rate of 19 grams per minute. For TCF-PP tape production, a 363K tow of TCF was set-up and run at a line speed of 1 meter per minute with a polymer flow rate of 24 grams per minute. Figure II.3.1.11.11 and Figure II.3.1.11.12 illustrates the impregnated thermoplastic TCF tape (TTT) coming off the line.

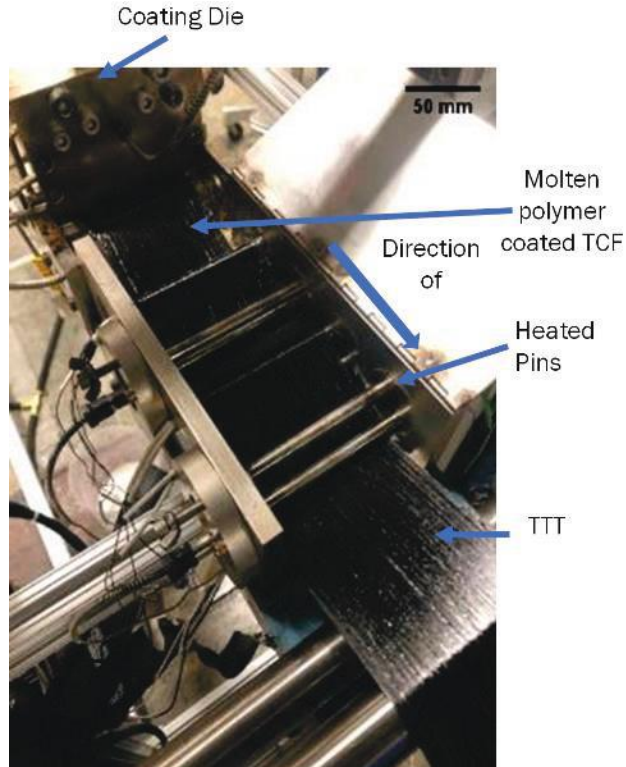


Figure II.3.1.81. Molten polymer coated TCF being kneaded in the pin/kneading die. Notice how the heated pins knead in the polymer into the TCF to completely impregnate it to make TTT. Source: FCMF.

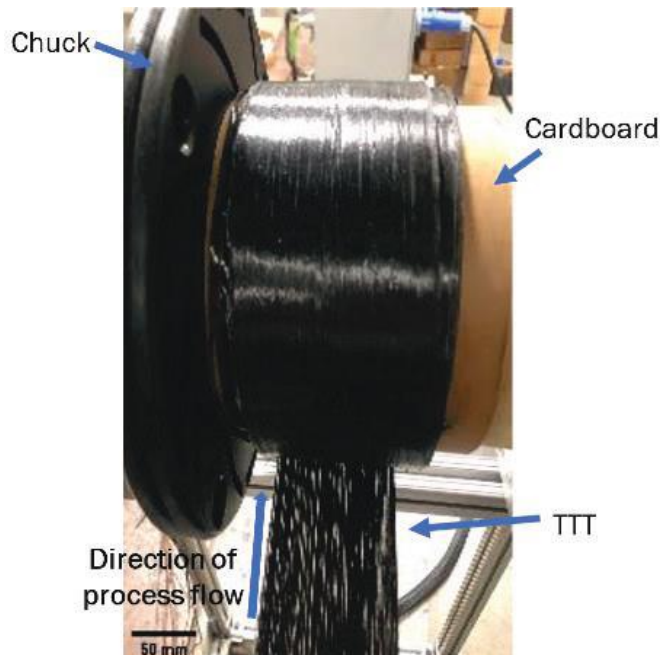


Figure II.3.1.82. Take-up system collecting the TCF thermoplastic impregnated tape. The TTT is wrapped about a cardboard tube clamped on a chuck to collect it. The chuck is further connected to a clutch that adjusts torque to maintain tension constant inline. Source: FCMF.

Composites Plate(s) Preparation

Composite plates were produced with the TCF thermoplastic tape. A 30-ton Wabash Carver press was used to produce all 6×6 plates. Flexural samples were produced with 77 grams of tape, which were used to make a 3-mm-thick plate. The tape was then placed into the mold with the desired fiber orientation and placed in a closed-cavity tool mounted in the Carver Press. The mold was then heated up to 175°C under 1.5 tons (e.g., 83.33 lb./in.^2). When the mold reached its desired temperature, the pressure was ramped up to two tons (e.g., 111.11 lb./in.^2). The sample was carefully observed for flow of polymer out of the mold. As soon as flow was observed on the edges of the mold both air and water cooling were started. Once cooled, the mold and plate were then taken out of the press and the mold was disassembled. Microscopy images were then taken of the entire cross-section where the images were stitched together. Stitched images were then modified to enhance the contrast between mounting resin, PP composite matrix, and voids. Each cross-section of tape was then analyzed to determine the void percentage of the sample. Figure II.3.1.11.13 shows the progression of image enhancement and image processing to determine void content.

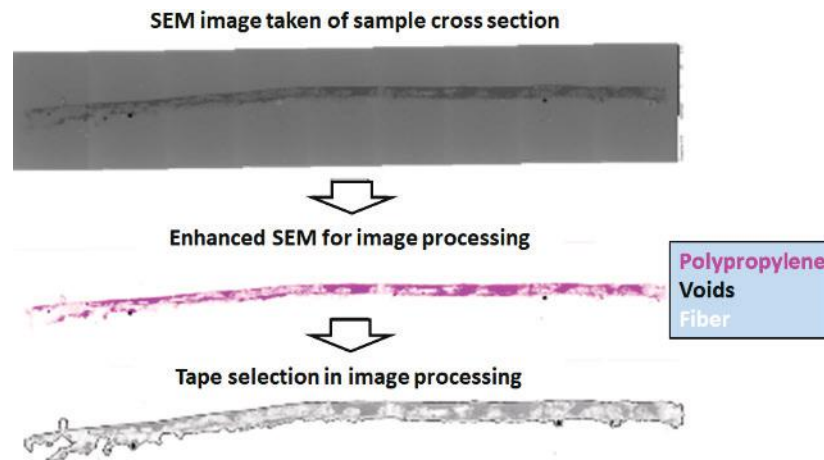


Figure II.3.1.83. Image enhancement for void analysis on two layers of *in-situ* consolidated CF-PP tape. Image processing program outlines edges of tape to exclude voids outside of the tape region. Source: FCMF.

Based on the preliminary studies of extruder flow rate and puller speed impregnation line, parameters were set to achieve a fiber weight of 35%. TGA was performed on the composite plate to confirm consistent FWF and fiber volume fraction (FVF). Multiple TGA samples were tested from each plate that was produced.

Table II.3.1.11.6 shows the average FWF and FVF for all materials that were produced. The average FWF and FVF were found to be 35.86% and 24.48%, respectively, with a 1.13 standard deviation. With the standard deviation well below 10% of average, this thermal analysis shows the produced material was consistent across all manufacturing cycles and within 1% of expected values. FWF confirmation was critical in determining the consistency of the processing line and to support the validity of experimental results.

Table II.3.1.11.6. Average Fiber Weight and Fiber Volume Percentages for All Material Plates Produced Where the Overall FWF Was 36.23% and FVF Was 24.74%

	TCF-PP 0/90 Flex	TCF-PP Uni Flex	TCF-PP Tensile
Average FWF	35.09%	37.93%	34.77%
Average FVF	24.49%	27.53%	24.26%

Mechanical Testing

Specimens from the consolidated thermoplastic TCF panels were tested for mechanical properties. Flexural, interlaminar shear strength (ILSS), and tensile testing was conducted according to relevant ASTM standards.

Flexural Testing

Three-point flexural testing was done on specimens taken from a consolidated panel. Flexural strength and modulus were found to be 242.01 ± 21.92 MPa and 37.98 ± 1.40 GPa for a FVF of 0.18. The flexural test data is shown in Table II.3.1.11.7.. The load/displacement curves for three tested specimens are shown in Figure II.3.1.11.14. The failure mode observed was typical for ductile CF-thermoplastic composites. The material exhibits a linear response until peak load, followed by a gradual load drop. There was no load recovery after the first drop from peak load until failure.

Table II.3.1.11.7. Flexural Testing Values for TCF Thermoplastic Tape

Type of Tape	Average Flexural Strength (MPa)	Average Flexural Modulus (GPa)	FVF
TTF	242.01±21.92	37.98±1.4	0.18

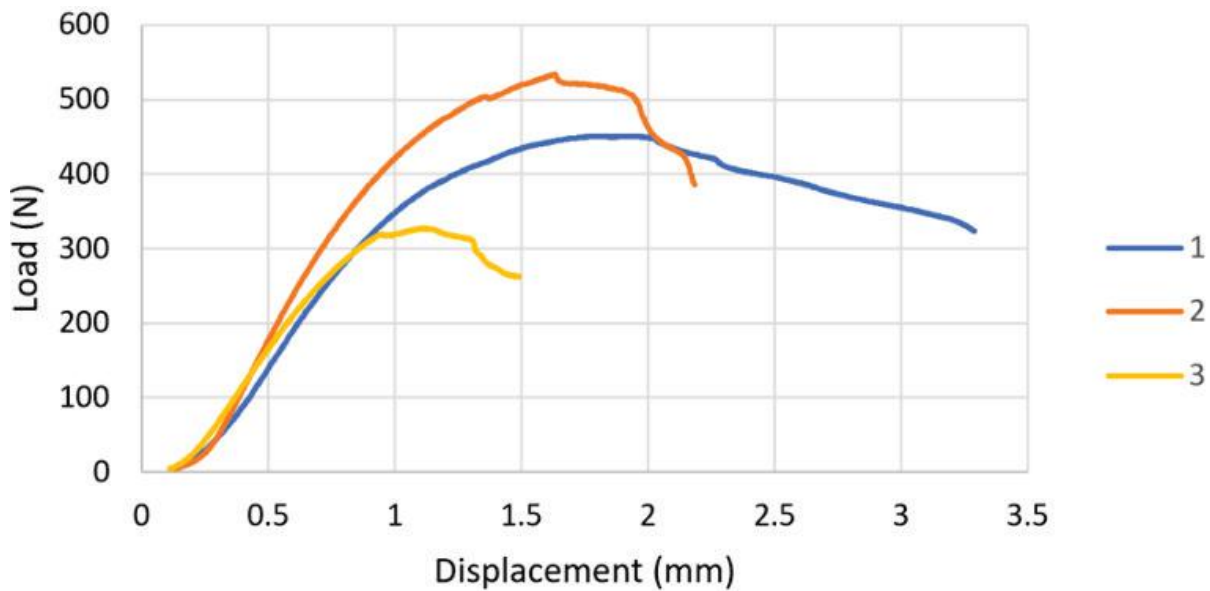


Figure II.3.1.84. Flexural load vs. displacement for TCF thermoplastic tape. Source: FCMF.

Figure II.3.1.11.15 shows the microscopic image of the failed sample. The crack initiated on the tension side but did not propagate through the thickness of the specimen. Figure II.3.1.11.16 and Figure II.3.1.11.17 show bar graphs comparing the flexural strength and modulus of the four samples, respectively.

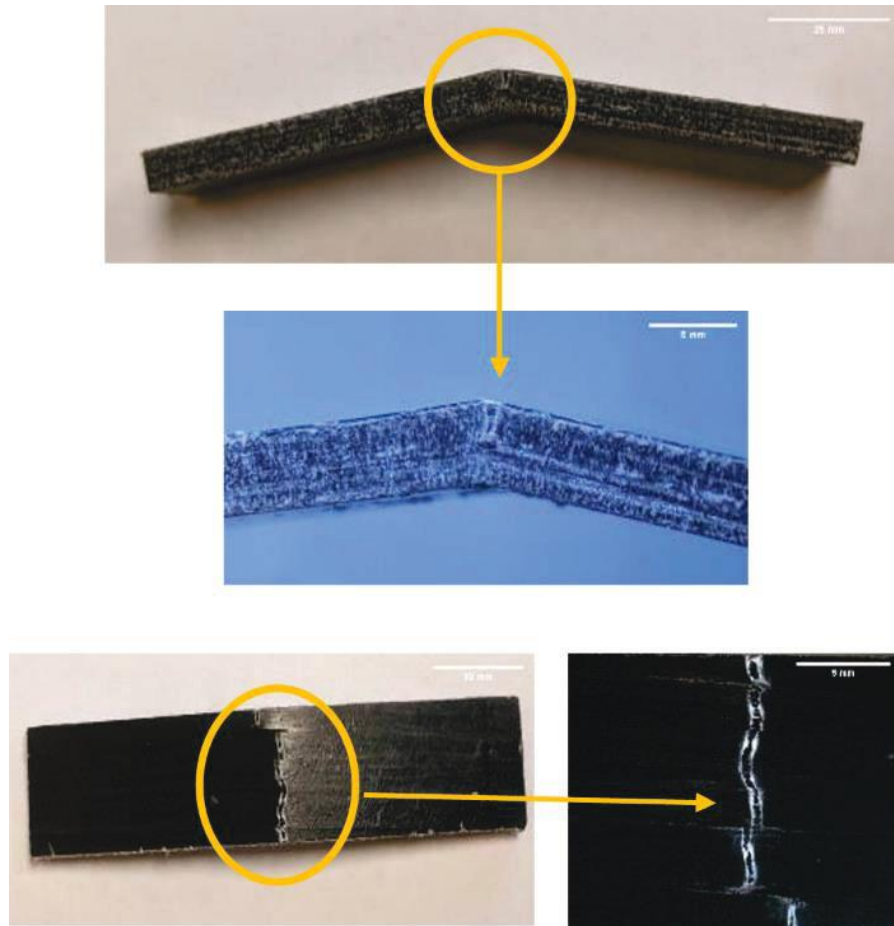


Figure II.3.1.85. Zoomed microscopic image of the failed sample demonstrating crack initiation on the thin side and along the tension surface. Source: FCMF.

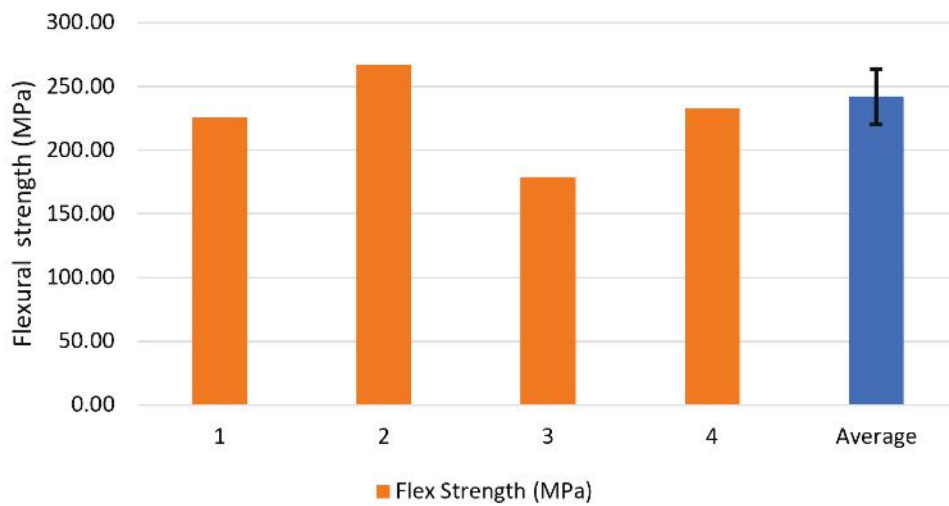


Figure II.3.1.86. Bar graph comparing flexural strengths of different samples. Source: FCMF.

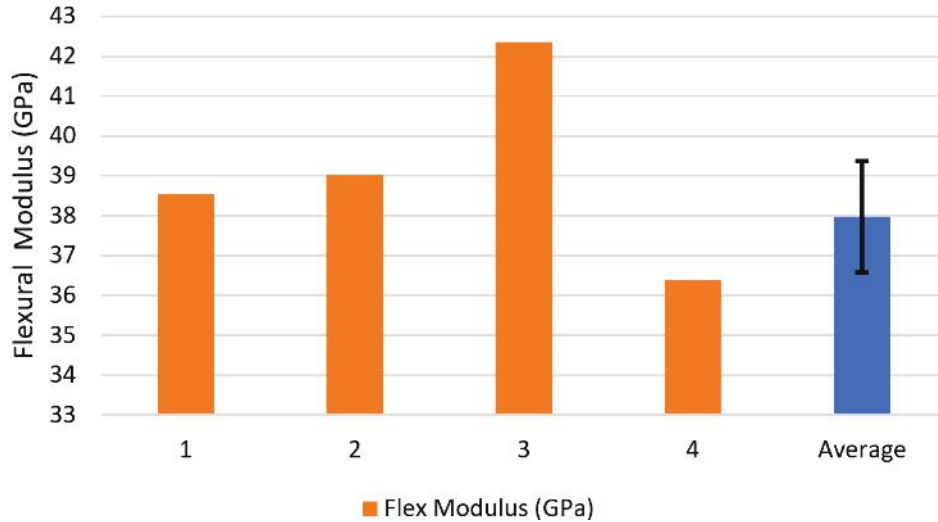


Figure II.3.1.87. Bar graphs comparing flexural modulus of different samples. Source: FCMF.

ILSS

An average ILSS value of 12 ± 1.37 MPa was found during experimental testing. Table II.3.1.11.8 summarizes the ILSS values from TCF-PP tape specimens. All the tested specimens showed plastic deformation, Figure II.3.1.11.18, instead of interlaminar shear failure. This is a commonly observed phenomenon in CF resin thermoplastic, where the matrix being more ductile, the mode of failure can be bottom surface fiber tension. Figure II.3.1.11.19 shows an optical microscopic image of the failed sample. No interlaminar failure or cracks were observed. The failure mode was bending and evident by the bottom surface fiber tension.

From open literature, ILSS values mainly depend on fiber-matrix interfacial strength and matrix characteristics more so than the fiber. ILSS is improved by increasing the matrix tensile properties and matrix volume fraction. A bar graph representing ILSS values for six specimens is shown in Figure II.3.1.11.20.

Table II.3.1.11.8. ILSS Values Obtained for TCF Thermoplastic Tape

Type of Tape	Average ILSS Strength (MPa)	FVF
Thermoplastic TCF Carbon Tape	12 ± 1.37	0.18

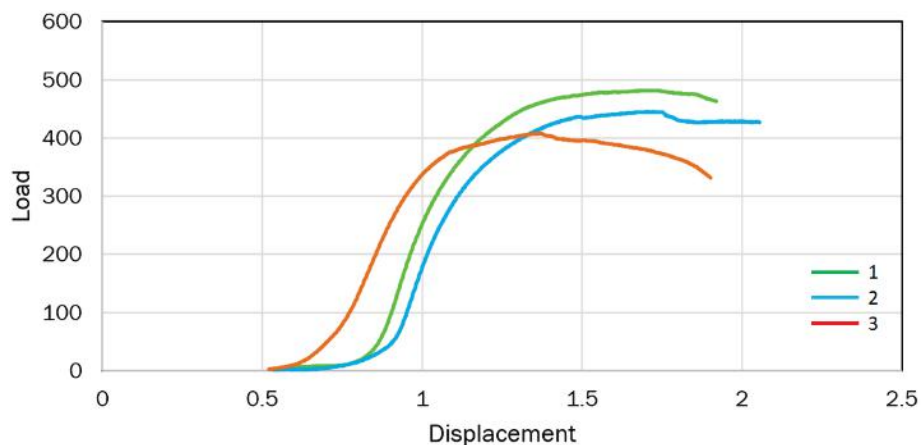


Figure II.3.1.88. Representative curves of load vs. displacement for ILSS of TCF thermoplastic tape. Source: FCMF.

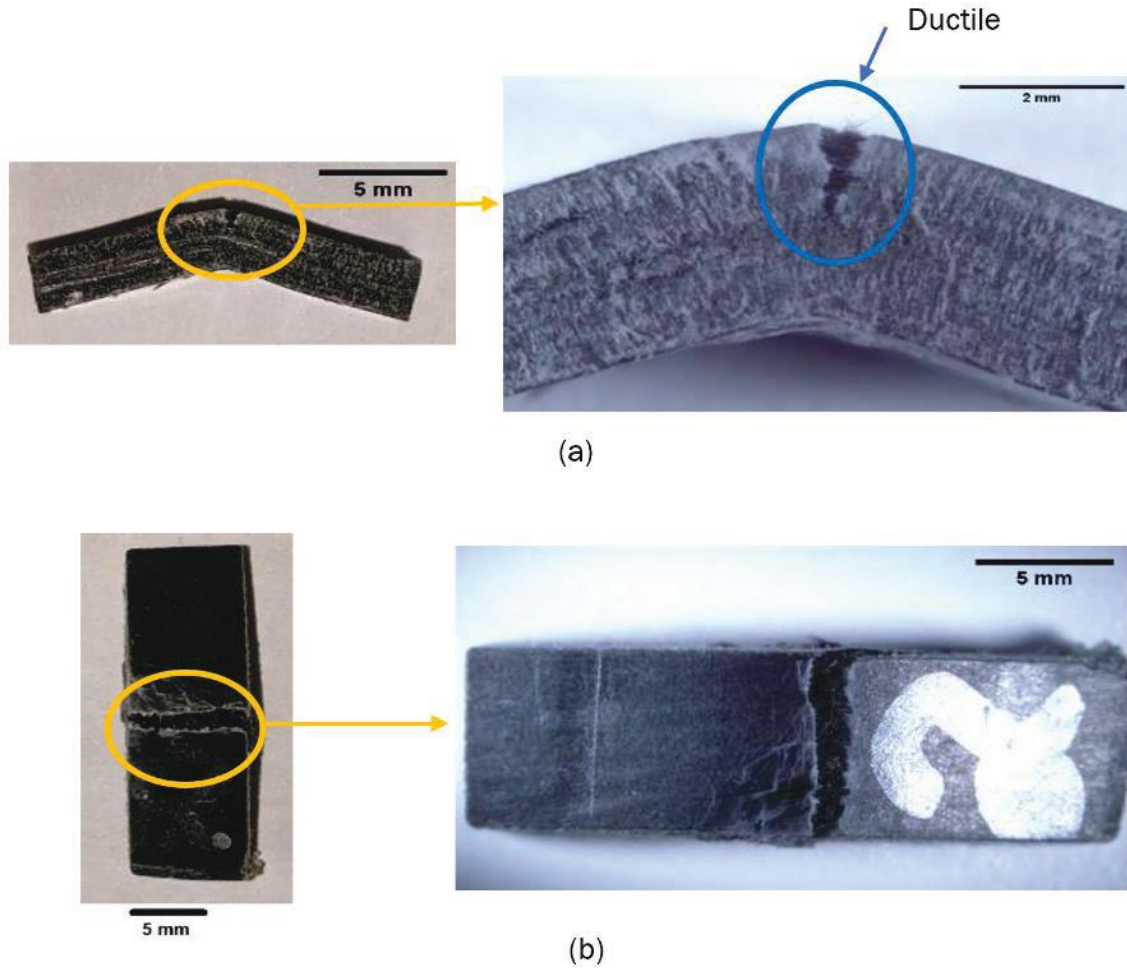


Figure II.3.1.89. (a) Side view of failed sample showing failure mode was ductile with crack initiation from the bottom side (tension). (b) Top view of bottom surface crack (tension side). Source: FCMF.

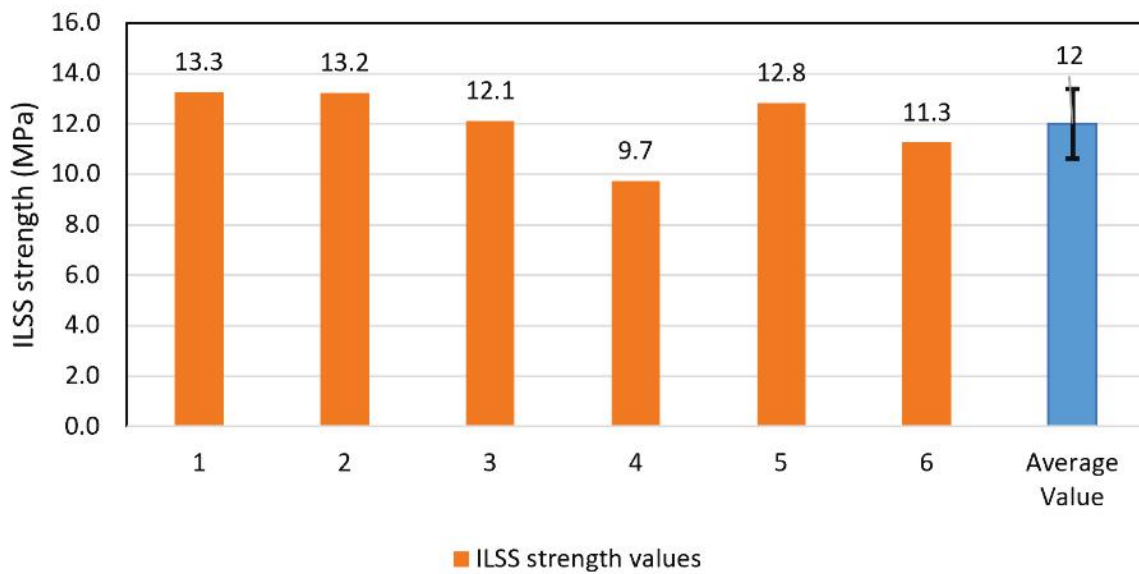


Figure II.3.1.90. Bar graphs comparing flexural modulus of different samples. Source: FCMF.

Tensile Testing

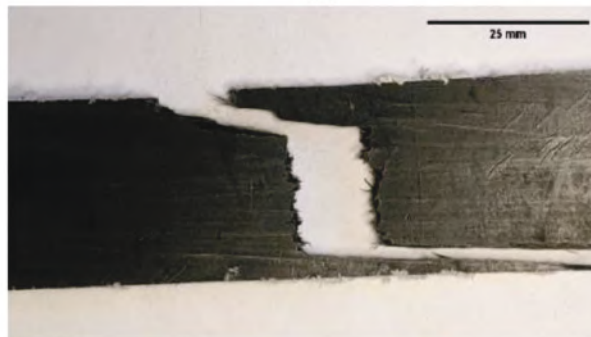
Tensile testing showed an average tensile strength of 150.6 ± 40.8 MPa and an average tensile modulus of 45 ± 10.3 GPa. The test data is represented in Table II.3.1.11.9. The specimens failed by tensile rupture and the failure mode was observed to be longitudinal splitting parallel to the fibers, which is typical of unidirectional laminates. Figure II.3.1.11.21 shows a photographic image of the failed tensile sample. Figure II.3.1.11.22 and Figure II.3.1.11.23 show bar graphs representing tensile modulus and strength, respectively. Figure II.3.1.11.24 shows representative curves for tensile load vs. displacement.

Table II.3.1.11.9. Tensile Strength and Modulus Values for TCF Thermoplastic Tape Composite

Sample Type	Average Tensile Strength (MPa)	Average Tensile Modulus (GPa)	Fiber Volume Fraction
TCF Thermoplastic Composite	150.6 ± 40.8	45.0 ± 10.3	0.18



(a)



(b)

Figure II.3.1.91. (a) Failed tensile sample specimen the failure can be due to crack propagation from matrix rich region. (b) Failed sample with the halves separated. Source: FCMF.

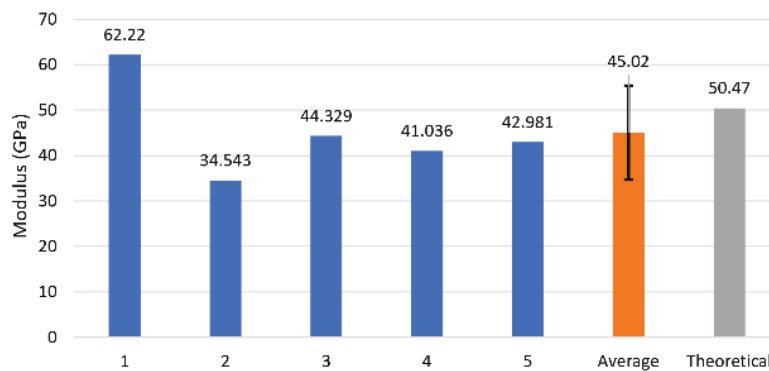


Figure II.3.1.92. Bar graph representing tensile modulus with the average value and standard deviation. Source: FCMF.

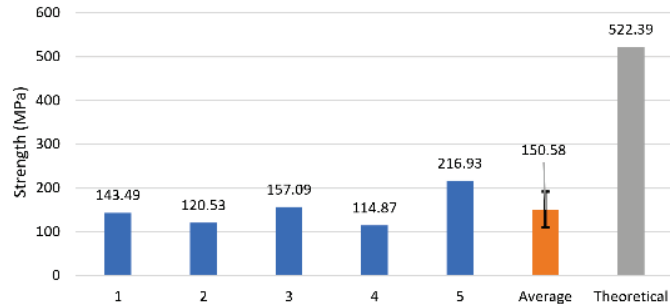


Figure II.3.1.93. Bar graph depicting tensile strength for tested specimen with the average value and standard deviation. Source: FCMF.

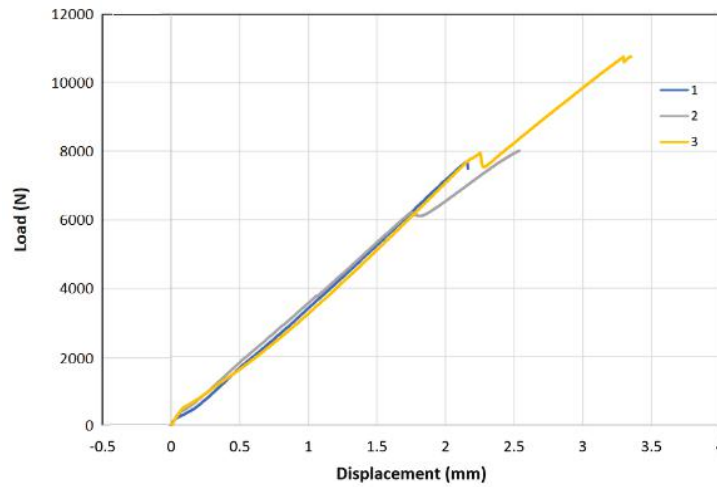


Figure II.3.1.94. Representative curves for tensile load vs. displacement for three samples. Source: FCMF.

The value for the tensile modulus and tensile strength is 11% and 71% less than the theoretical value. The tape has matrix rich and agglomerated fiber rich regions. The non-homogenous distribution of fiber in matrix can lead to lower tensile properties, due to crack initiation in the matrix rich regions. Matrix rich regions could behave like stress concentration points leading to premature failure. The effect of matrix rich regions on tensile strength is larger than tensile modulus. This could be because tensile modulus is calculated from the slope of the initial region of the tensile load vs. displacement curve. The presence of matrix rich regions could also be a reason for high standard deviation of the data. During the consolidated plate manufacturing, fiber washout due to polymer flow was observed. Fiber washout is the unintended movement of fibers due to excessive polymer flow. The misaligned fibers due to fiber washout could also be one of the reasons for lower value of tensile strength. Table II.3.1.11.10 summarizes rule of mixtures-based estimation of tensile properties.

Table II.3.1.11.10. Calculation of Theoretical Tensile Strength and Modulus Using Rule of Mixture

Material	Properties				
		Tensile Strength (MPa)		Tensile Modulus (GPa)	FVF
PP	σ_m	23.71		E_m	1.25
TCF	σ_f	2800		E_f	0.18
TCF Composite	σ_{Cl}	522.39		E_{Cl}	50.47

Comparison of Mechanical Test Data with Literature

Novo et al. [3] reported flexural, tensile, and ILSS test values for CF/PP tapes made using powder impregnation (PI) and crosshead melt (CHM) impregnation methods. The FVF for PI and CHM is 0.5 and 0.3, respectively. Matsuo et al. [4] reported an interlaboratory round robin tensile testing comparison of Tencate Cetex TC960 CF-PP tape. Tencate tapes were manufactured by a solvent impregnation process. The FVF of the tape in Matsuo's study was 0.23. Novo et al. [5] used PP powder ICORENE 9184B P[®] from ICO Polymers and 18K CF M30 SC[®] from TORAY for making PI CF-PP tapes. PP powder Moplen RP348U[®] from Basell and 18K CF M30 SC[®] from Toray was used to make the CHM impregnated tapes. Matsuo et al. analyzed commercially available Tencate Cetex TC960 CF-PP tape.

Microscopic analysis reported by Novo et al. showed all profiles have a reasonable distribution of the reinforcing fibers over the cross-sections. However, large differences in impregnation quality were found between the PI and CHM samples. The degree of impregnation of the PI tape was better than what was seen for the CHM tape, with almost all fibers enveloped by the matrix. But both PI and CHM had voids distributed throughout the tape, with the CHM having comparatively higher void content. The SEM images showed a reasonable degree of adhesion between the CF and the polymer powder particles. SEM images and analysis were only reported for the PI tapes.

Novo et al. reported flexural strength of 229 ± 7.3 MPa and 118.2 ± 6.9 MPa and a flexural modulus of 85.5 GPa and 37.7 GPa for PI and CHM impregnated tape, respectively. He et al. [6] claims that flexural properties are directly proportional to FVF up to 70% for CF unidirectional laminates. Hence, the flexural properties noted by Novo et al. should be greater than thermoplastic carbon tape. Hayashi et al. [7] observed that the flexural strength of CF/PP unidirectional composite specimens decreased drastically when their void content became higher than 1%. Hayashi et al. also found that, compared to the flexural modulus, flexural strength was influenced to a greater extent by voids under stress. Hayashi et al. claims value for flexural modulus saw only a gradual decrease because its value is calculated from the slope of the initial behavior in the bending test. This could be the reason the flexural strength of thermoplastic carbon tape equals the flexural strength observed by Novo et al. where the PI tape measured 34.4% greater than the CHM tape. But the flexural modulus of the Novo et al. PI tape is 130% greater than TTT, and the flexural modulus for the CHM tape equals the value of thermoplastic tape.

Matsuo et al. reported tensile strength of 445 ± 33.2 MPa and tensile modulus of 52 ± 5.7 GPa. Novo et al. reported PI and CHM impregnated tapes to have a tensile modulus of 106.1 ± 6.3 GPa and 63.5 ± 4.3 GPa, respectively. Novo et al. reported that the tensile strength for PI and CHM tape as 1060.8 ± 43.1 MPa and 636.9 ± 38.4 MPa, respectively. The tensile strength of the Novo et al. PI and CHM tape were 61% less than the theoretical tensile strength. The tensile modulus of the PI and CHM tape were 25% and 29% less than the theoretical tensile modulus, respectively.

Parallel-stacked fiber laminates directly oppose tensile loading, and hence, the tensile properties are a function of FVF. The FVF of the Novo et al. PI and CHM tape and the Matsuo et al. tape was 0.5, 0.3, and 0.23, respectively. Normalizing for FVF for comparison was not done due to the variety of CF and PP used by Novo et al. and Matsuo et al. A more logical comparison between thermoplastic carbon tape and Matsuo et al. can be made due to their closer FVF values. The tensile strength and tensile modulus for thermoplastic carbon tape was 66.2% and 11.11% lower than the properties reported by Matsuo et al. This was due to the non-homogenous distribution of fiber and matrix in TTT. The matrix rich regions can act as stress concentration points. Novo et al. reported that the PI and CHM impregnated CF-PP tapes to have ILSS values of 12.3 ± 0.3 MPa and 14 ± 0.2 MPa, respectively. This ILSS value matches the value for TTT. ILSS properties are highly dependent on the tensile strength of the polymer and the fiber-matrix interfacial shear strength rather than the fiber properties. This signifies that the fiber-matrix interfacial properties achieved by Novo et al. were very similar to the ones achieved in the thermoplastic carbon tape process.

Innovative Pitch Synthesis Method

The primary goal of this work is to devise a first-of-its-kind flow-through mesophase pitch reactor and characterize the resultant polymerized products to establish the key process-reactivity relationships. This groundbreaking concept is in its early stages. The envisioned system would bring isotropic-starting materials (e.g., mono- or poly-disperse) heated to melt flow conditions in contact with a supported metal catalyst bed positioned within the flow path of the molten reactant. This low TRL research can revolutionize pitch CF manufacturing dependence on the laborious, costly, and inconsistent production of mesophase pitch via slow (several hours or more) reactions in pressurized batch reactors. Circumvention of this process would enable the production of pitch from monodisperse feedstocks. The laboratory-scale concept reactor is designed, and the parts were procured. The team is awaiting delivery to initiate installation and commissioning of the reactor. In the interim period, thermophysical and spectroscopic characterization of potential feedstocks are underway.

Conclusions

The multiscale integrated strategy works seamlessly for scaling and reducing the energy and cost of advanced fiber production using new alternative precursor materials. The team was able to demonstrate successful melt-blowing and melt-spinning of isotropic pitch precursor and nylon-6 precursor, respectively, at CFTF using data generated from the R&D efforts at the bench scale. The process conditions were developed for compatibility within the processing envelope available at CFTF for future scaling. The next steps are to conduct R&D efforts to determine the ideal stabilization and carbonization process conditions for continuous processing at scale, minimize material and process variations, utilize advanced processes to further reduce cost, and evaluate the performance of the resulting fibers in a variety of resins systems at a coupon level. Mechanical properties of the nylon-6 precursor at the laboratory-scale show promising results for further treatment as a precursor for CF processing. Key highlights in FY 2022 include:

- A successfully scaled nylon precursor fiber that met the target properties requirements.
- A precursor spinning baseline for a potential phase 2 candidate hydrogen tank project was established.
- A pelletization process was developed for pitch material ensuring easier processability in melt-spinning/blowing process.
- A successfully scaled pitch material from industry source.
- A new innovative pitch processing unit was designed for development.
- The performance evaluation of TCF in PP resin was demonstrated. Key highlights include:
 - Significant advances made on TTT
 - TCF thermoplastic tape successfully used and demonstrated in overmolding
 - Laminates from the TCF thermoplastic tapes exhibited superior impact properties
 - Overmolding concepts included a sheet molding compound and an automated tape placement
 - Injection- and extrusion-CM being a focus of interest in this period.

Key Publications

1. Crabtree, J., P. Yeole, D. Nuttall, U. Vaidya, M. Theodore, V. Kunc, and V. Kumar, 2022, “The effect of nozzle size and print speed on the fiber orientation and porosity during large-scale additive compression manufacturing,” *Additive Manufacturing Benchmarks 2022 Congress*, 14–18 August 2022, Gaithersburg, MD, USA.
2. Kore, S., M. Theodore, and U. Vaidya, 2021, “Effect of the segmental structure of thermoplastic polyurethane (hardness) on the interfacial adhesion of textile-grade carbon fiber composites,” *ACS Appl. Polym. Mater.*, Vol. 3, No. 12, pp. 6138–6146. <https://doi.org/10.1021/acsapm.1c01001>.

3. Spencer, R., S. Wasti, S. Kim, M. Theodore, U. Vaidya, A. A. Hassen, V. Kunc, and V. Kumar, 2022, “Volumetric nondestructive evaluation for damage in CF-reinforced polymer panels subjected to artificial lightning strikes,” *Proceedings Volume 12047, Nondestructive Characterization and Monitoring Advanced Materials, Aerospace, Civil Infrastructure, and Transportation XVI*, Art. 1204705. <https://doi.org/10.1117/12.2614618>.
4. Spencer, R., S. Wasti, S. Kim, M. Theodore, U. Vaidya, A. A. Hassen, V. Kunc, V. Kumar, 2022, “Volumetric nondestructive evaluation for damage in CF-reinforced polymer panels subjected to artificial lightning strikes,” *SPIE Smart Structures + Nondestructive Evaluation 2022*, 6–10 March 2022, Long Beach, CA, USA.
5. Vaidya, U., M. Janney, K. Graham, H. Ghossein, and M. Theodore, 2022, “Mechanical response and processability of wet-laid recycled CF PE, PA66, and PET thermoplastic composites,” *J. Compos. Sci.*, Vol. 6, No. 7, Art. 198. <https://doi.org/10.3390/jcs6070198>.
6. Vaidya, U., M. Robinson, N. Hiremath, P. Yeole, M. Theodore, A. Hassen, and J. Unser, 2022, “Multi-process tooling for discontinuous carbon and hybrid glass fiber thermoplastics,” *Adv. Mech. Eng.*, Vol. 14, No. 7, Art. 16878132221113941. <https://doi.org/10.1177/16878132221113941>.
7. Vaidya, U., M. Theodore, and D. Penumadu, 2021, “Intermediates, processes and product routes for low-cost textile-grade carbon fiber into composites,” *SAMPE Journal*, March/April 2022, 44.

References

1. Inagaki, M., and F. Kang, 2014, “Engineering and applications of carbon materials,” in *Materials Science and Engineering of Carbon: Fundamentals (Second Edition)*, Elsevier, Portsmouth, NH, USA. pp. 219–525. <https://doi.org/10.1016/C2013-0-13699-9>.
2. Inagaki, M., and F. Kang, 2014, *Materials Science and Engineering of Carbon: Fundamentals (Second Edition)*, Elsevier, Portsmouth, NH, USA. <https://doi.org/10.1016/C2013-0-13699-9>.
3. Novo, P. J., J. P. Nunes, J. F. Silva, V. Tinoco, and A. T. Marques, 2013, “Production of thermoplastics matrix pre-impregnated materials to manufacture composite pultruded profiles,” *Ciênc. e Tecnol. dos Mater.*, Vol. 25, No. 2, pp. 85–91. <https://doi.org/10.1016/j.ctmat.2014.03.004>.
4. Matsuo, T., M. Hojo, and K. Kageyama, 2017, “Influence of gripping condition and matrix type on tensile properties of unidirectional carbon fiber reinforced thermoplastic composites,” 21st International Conference on Composite Materials (ICCM-21) 20–25 August 2017, Xi’an, China.
5. Novo, P. J., J. F. Silva, J. P. Nunes, and A. T. Marques, 2016, “Pultrusion of fibre reinforced thermoplastic pre-impregnated materials,” *Compos. B. Eng.*, Vol. 89, pp. 328–339. <https://doi.org/10.1016/j.compositesb.2015.12.026>.
6. He, H.-w., and F. Gao, 2015, “Effect of fiber volume fraction on the flexural properties of unidirectional carbon fiber/epoxy composites,” *Int. J. Polym. Anal. Charact.*, Vol. 20, No. 2, pp. 180–189. <https://doi.org/10.1080/1023666X.2015.989076>.
7. Hayashi, T., and J. Takahashi, 2017, “Influence of void content on the flexural fracture behaviour of carbon fiber reinforced polypropylene,” *J. Compos. Mater.*, Vol. 51, No. 29, pp. 4067–4078. <https://doi.org/10.1177/0021998317698215>.

Acknowledgments

The CFTF Team would like to acknowledge our DOE sponsor, H. F. Wu, DOE VTO Technology Development Manager. They would also like to thank the following members of the ORNL Management/Team: W. Peter, X. Sun, V. Kunc, U. Vaidya, N. Gallego, R. Paul, F. Vautard, J. Klett, A. Blankenship, F. Crowson, J. Carpenter, R. Strong, and R. Davies for their sponsorship, contributions, and/or support of the ORNL CFTF program.

II.3.1.12 Ultra-Lightweight Thermoplastic Polymer/Polymer Fiber Composites for Vehicles (Pacific Northwest National Laboratory and Oak Ridge National Laboratory)

Kevin Simmons, Co-Principal Investigator

Pacific Northwest National Laboratory
902 Battelle Blvd.
Richland, WA 99352
E-mail: kl.simmons@pnnl.gov

Amit Naskar, Co-Principal Investigator

Oak Ridge National Laboratory
1 Bethel Valley Rd.
Oak Ridge, TN 37831
E-mail: naskarak@ornl.gov

Rich Davies, Composites Core Program Manager

Oak Ridge National Laboratory
Materials Science and Technology Division
1 Bethel Valley Rd.
Oak Ridge, TN 37831
E-mail: daviesrw@ornl.gov

H. Felix Wu, DOE Technology Development Manager

U.S. Department of Energy
E-mail: felix.wu@ee.doe.gov

Start Date: August 17, 2020

End Date: September 30, 2023

Project Funding (FY 2022): \$375,000

DOE share: \$375,000

Non-DOE share: \$0

Project Introduction

PNNL and ORNL teamed to develop ultra-lightweight thermoplastic polymer fiber–thermoplastic polymer matrix composites to reduce vehicle component mass. The approach is built on the fact that mechanical properties of plastic materials such as polypropylene (PP) and polyethylene (PE) (density $\sim 0.9 \text{ g/cm}^3$) can be improved by introducing a structural alignment of polymer chains and crystals during solid-phase processes like uniaxial stretching. The resulting enhanced polymer fibers with highly oriented morphology can then be mixed with common thermoplastic polymers and formed into high-performance polymer-fiber-reinforced polymers (PFRPs) suitable for passenger vehicles. As a result, lightweighting and cost reduction can be attained due to the removal of higher density fibers (e.g., CFs $\sim 1.6 \text{ g/cm}^3$, glass fiber $\sim 2.6 \text{ g/cm}^3$) with lower density fibers and matrices. In addition, the use of PFRPs can have several advantages over traditional glass- and CF-reinforced thermoset and thermoplastic polymers due to their high-specific strength and stiffness ratios, impact performance, recyclability, and elimination of galvanic corrosion with Al and Mg joints.

Objectives

The project objective is to develop an all thermoplastic composite with polymer fibers that reduces weight by 30%, has a < 3-minute cycle time, meets the lower cost target (< \$15/kg of composite), and features higher specific properties. The research aims to exploit melt- and solution-spun high-performance polymer fibers that have unique mechanical properties, chemical resistance, and thermal stability. With a new composite that is more recyclable due to the use of polymer fibers, the project will also demonstrate a scalable, adaptable approach for recycling into new products with lower cost and higher manufacturing efficiency.

Approach

This project leverages existing processing methods and commercially available materials, promising low-cost and a short path to commercialization. The concept uses fiber spinning capabilities at ORNL for solid-phase uniaxial fiber processing to improve mechanical properties of performance polymers by inducing molecular alignment during the forming process. The project objectives will be met by developing ultra-high-strength, low-cost, lightweight polymer fibers from commodity plastics such as PP and polyester, and their highly drawn controlled crystallinity product with >700 MPa strength. A major challenge in manufacturing polymer-polymer composites is avoiding dimensional instability during fabrication caused by shrinkage force from misorientation/relaxation of fiber polymers. To achieve this, partial crosslinking in fibers will be induced and new chemistries will be developed.

PNNL will develop fabrication techniques with high-quality temperature controls for controlling the rheological behavior of the polymer matrix and cooling for development of polymer morphology to minimize void fractions and maximize material property performance while achieving continuous CM or injection-molding under three-minute cycle times.

Results

Summary of PNNL Results

The following summary includes the work for the completion of the project milestones for PNNL in FY 2022 listed in Table II.3.1.12.1.

Table II.3.1.12.1. FY 2022 PNNL Milestones

Milestone Name/Description	Criteria	End Date
PM1: Demonstrate fiber surface interfacial adhesion to thermoplastic matrix materials by evaluating the composite-fiber, strength, modulus, and thermal stability	Achieve a 10% increase over untreated baseline	12/31/2021
PM2: Demonstrate continuous compression molding	Show temperature of process can be controlled within 5 °C	06/30/2022
— Task1: Investigate mechanical behavior of PFRPs and the differences compared to CFRPs/glass fiber-reinforced polymers (GFRPs) (related to future milestones)	Quantify properties and identify failure mechanisms	N/A

Milestone PM1, entitled “Demonstrate fiber surface interfacial adhesion to thermoplastic matrix materials by evaluating the composite-fiber, strength, modulus, and thermal stability,” was achieved by 12/31/2021. The objective of this milestone was to identify an appropriate surface modification method to enhance the interfacial adhesion for a combination of a polymer fiber and polymer matrix (e.g., PP-PP, PE-PE, PP-PE), and quantify the increase in fiber-to-matrix adhesion and the improved mechanical properties of the composites.

A fiber pullout test method was used to evaluate the adhesion of a polymer fiber in a polymer matrix. Different material combinations (e.g., ultra-high molecular weight polyethylene [UHMWPE], high density polyethylene [HDPE], PP) were studied using this method. For a similar polymer fiber and matrix (PP-PP or PE-PE), plasma treatment (PT) (e.g., 25% oxygen, 75% Argon) provided the highest improvement (~25%) on the interfacial shear strength (IFSS) among different treatment methods, as indicated in Figure II.3.1.12.1(a-c). However, as shown in Figure II.3.1.12.1(d-f) for dissimilar combinations (PP-PE), an aerosol-based adhesion promoter provided the highest improvement (~122%) on the IFSS rather than just a PT.

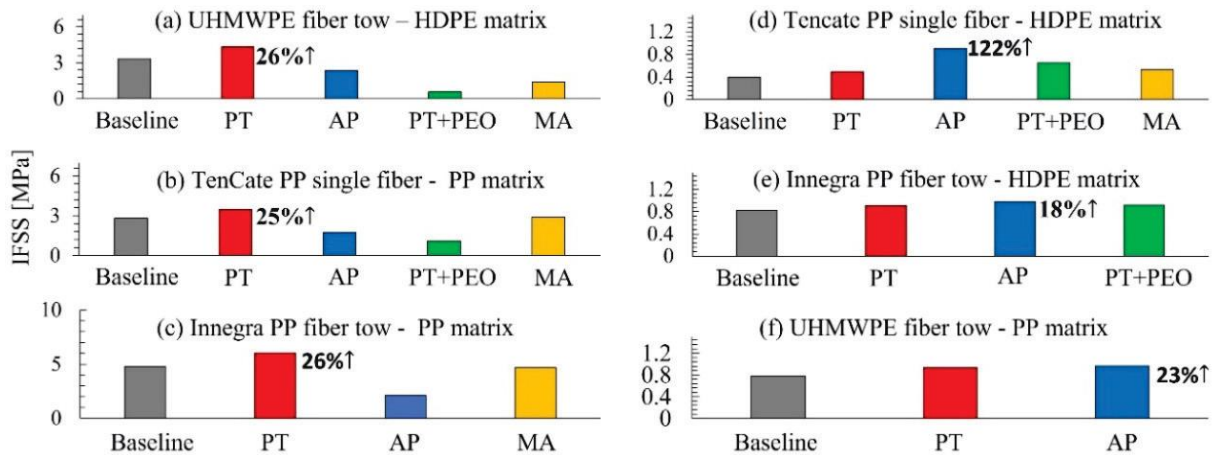


Figure II.3.1.95. Comparison on the IFSS of polymer matrix and polymer fiber with different treatment methods: (a-c) similar material system (e.g., PE-PE, PP-PP); (d-f) dissimilar material system (PP-PE). Note: PT means plasma treatment, AP means aerosol-based adhesion promotor, PT+PEO means grafting of polyethylene oxide after plasma treatment, and MA means maleic anhydride polypropylene sizing. Source: PNNL.

Uniaxial tensile tests were further conducted to evaluate the improved mechanical behavior of a composite with surface-treated polymer fibers. As exemplified in Figure II.3.1.12.2(a) for an HDPE matrix reinforced by 30 wt.% woven PP fabrics, the composite with surface-treated fabrics (e.g., aerosol-based adhesion) showed about 20% and 65% improvement on average tensile strength and toughness, respectively. This was due to the improved interfacial bonding between PP and HDPE, as can be seen from Figure II.3.1.12.2(b) and Figure II.3.1.12.2(c) for the comparison on the failure morphology between non-treated and fiber-treated specimens.

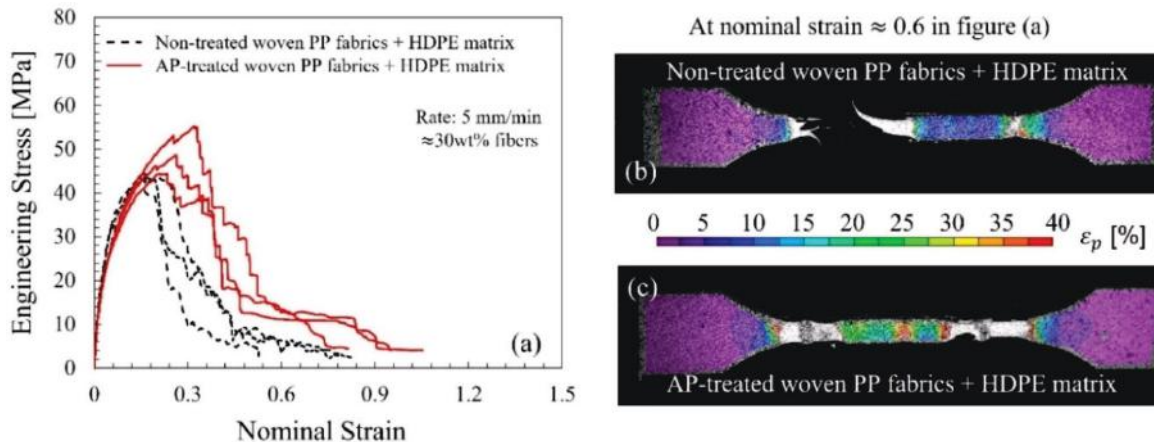


Figure II.3.1.96. (a) Stress-strain curves for non- and fiber-treated composites with PP fabrics and an HDPE matrix; and (b-c) maximum principal strain field and failure morphology at a nominal strain of 0.6. Source: PNNL.

Milestone PM2, entitled “Demonstrate continuous CM,” was achieved by 06/30/2022. The objective of this milestone was to develop a continuous CM process with an accurate temperature control of less than 5°C for the fabrication of the PFRP components. The process includes three steps: (1) press and heat a composite panel of a specified ply layup in a platen press with a temperature control; (2) transfer into an infrared (IR) equipment and heat the panel with a temperature control; and (3) press and heat into a desired part geometry via a press with a controlled heating and cooling. By taking the low-density polyethylene matrix reinforced by

woven UHMWPE fabrics as an example, three embedded thermocouples at different locations of the composite measured temperatures with standard deviation less than 2°C during the composite fabrication in the first step. The second step was the IR heating with the temperature control less than 4°C measured from the foregoing thermocouples. Finally, the pre-heated composite panel was then immediately transferred to a press for the forming of a hat-shaped geometry and cooling as exemplified in Figure II.3.1.12.3(a) and Figure II.3.1.12.3(b). The temperature history of three locations in the composite during the entire CM process was plotted in Figure II.3.1.12.3(c). All thermocouples are within 5°C with very little temperature excursion, as can be seen in Figure II.3.1.12.3(d), when the composite contacted the hat-shaped mold during the cooling and forming.

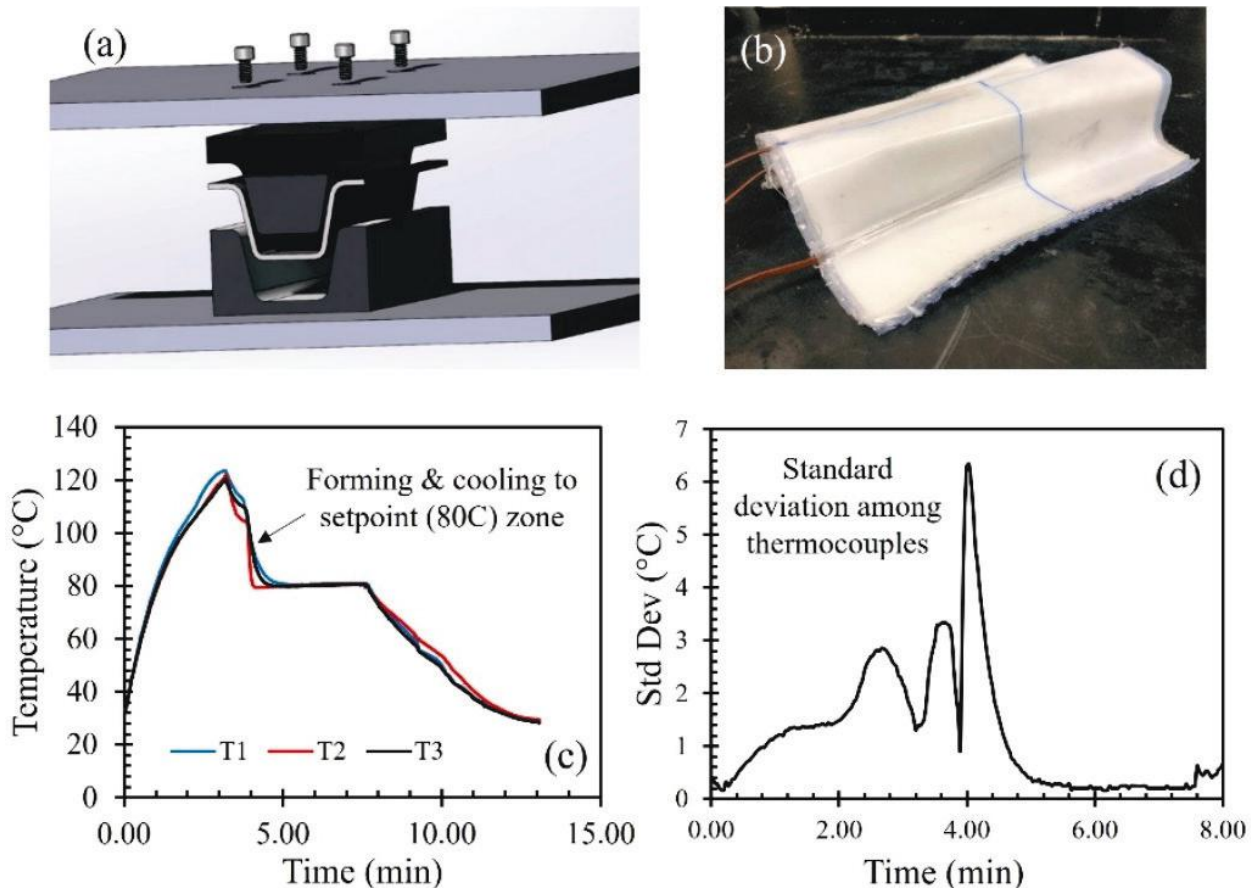


Figure II.3.1.97. (a-b) CM for the fabrication of hat-shaped low-density polyethylene reinforced by woven UHMWPE fabrics; (c) temperature profiles for the entire molding process measured from three embedded thermocouples; and (d) standard deviation of temperatures among thermocouples during molding.

Source: PNNL.

Task 1, “Investigate mechanical behavior of polymer/polymer composites and the differences compared to CFRP/GFRP (related to future milestones),” is currently in progress. This task was closely related to FY 2023 milestones and objective of this project. Three areas of focus were studied: (1) the longitudinal tensile behavior of an HDPE matrix reinforced by unidirectional (UD) UHMWPE fibers; (2) the failure behavior of pre-notched self-reinforced PP twill composite; and (3) the impact behavior of self-reinforced PP twill composites and the composites of PP woven fabric and HDPE matrix. For the first focus area, composites were fabricated by hot-pressing a filament-wound panel of UD UHMWPE fibers and HDPE films. A composite with 5 wt.% UD UHMWPE fibers were used to initially study their progressive failure mechanisms and the effects of processing temperature and pressure. As shown in Figure II.3.1.12.4(a) through Figure II.3.1.12.4(c),

respectively, for the failure morphology at the post-peak stage, the main failure characteristics include splitting cracks, significant polymer deformation and damage, and fiber breakage at the edge. The latter two failure behaviors were very different from CFRP composites, GFRPs, or other fiber-reinforced polymers where brush-type splitting failure in the entire gauge volume are common [1]. The effects of processing temperature and pressure on the strength and modulus of the composite with 5 wt.% UD UHMWPE fibers and the mechanical behavior of the composites with higher fiber volume fractions of up to 50% are in progress. The results will be reported in FY 2023. For the second focus area, the failure characteristics of pre-notched self-reinforced PP twill composites were also different from CFRP and GFRP composites, which feature a non-negligible damage zone embedded in a very large plastic zone ahead of the notch tip, as reported in the team's third publication in the section of key publications. For the third focus area, by taking an example of self-reinforced PP twill composites, the specific impact energy required to penetrate the composite plate was about 21 J/mm/g/cm³, which was nearly twice that of a twill CFRP (~12 J/mm/g/cm³). The increased impact resistance of PFRPs compared to CFRPs was confirmed by a comparison of the failure morphologies, as shown in Figure II.3.1.12.4(d) and Figure II.3.1.12.4(e).

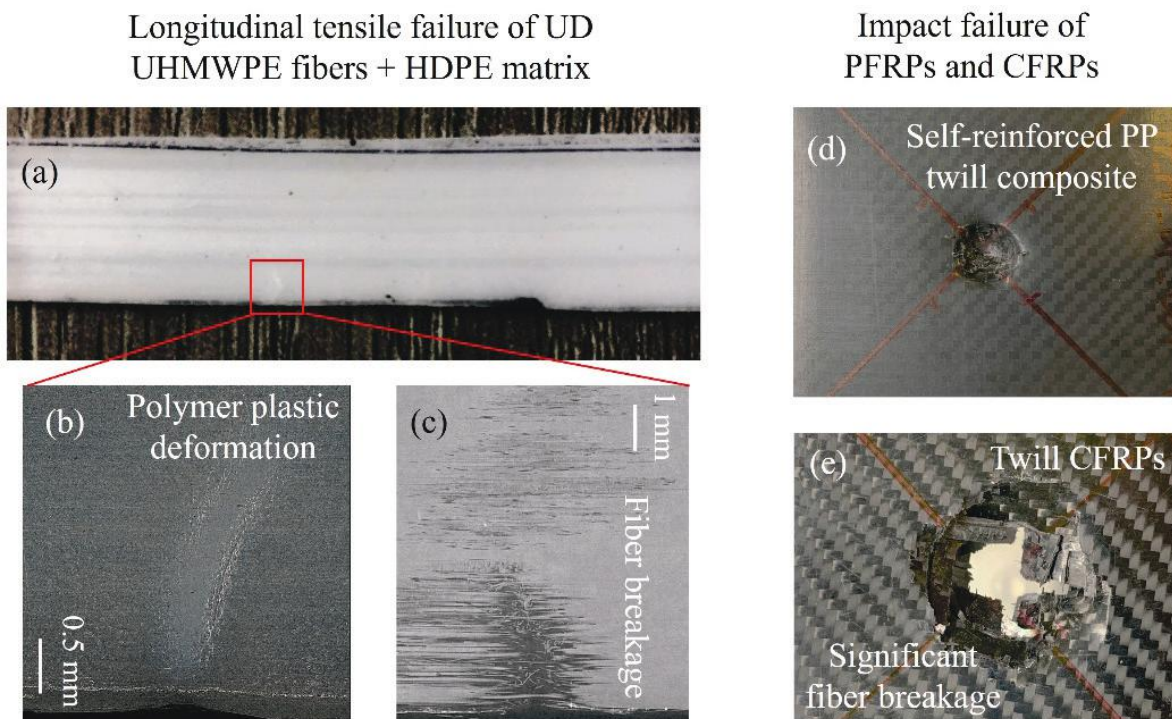


Figure II.3.1.98. (a) Morphology in the gauge area of an UHMWPE-HDPE composite after peak load, (b) plastic deformation and damage of HDPE matrix, (c) UHMWPE fiber breakage at edge, and (d-e) failure morphologies of penetrated self-reinforced PP twill composites and twill CFRPs after impact loading.

Source: PNNL.

Summary of ORNL Results

The following summary includes the work for the completion of the project milestones for ORNL in FY 2022 listed in Table II.3.1.12.2.

Table II.3.1.12.2. FY 2022 ORNL Milestones

Milestone Name/Description	Criteria	End Date
Develop heat setting conditions for fiber to avoid shrinkage force at molding conditions with a minimal temperature 150°C.	Developing methods for the crystallization or stress relaxation of an oriented amorphous phase in the fibers to enhance the dimensional stability of the fibers at molding temperatures.	12/31/2021
Demonstration of < 5% shrinkage of fibers after exposure at 150°C.	A demonstration of fiber shrinkage restriction to < 5% level after heat setting.	03/31/2022
Demonstrate successful preforming of the fibers for the development of a sandwiched structure. Characterize the interfacial bonding strength.	Developing methods to form a fibers assembly that can be molded to composite parts.	06/30/2022
Produce crosslinked PP Fiber with > 400 MPa strength and 5 GPa modulus. PP fibers are difficult to crosslink, but the success of < 5% shrinkage milestone will enable this.	Conducting mechanical testing of fibers that deliver the expected properties.	09/30/2022

The key milestone for ORNL in FY 2022 was to develop reinforced sandwiched composite structures using thermally stable high-performance polyolefin fibers in a suitable polyolefin matrix. The thermally stable reinforcing PP fiber was fabricated through a melt-fiber spinning and subsequent multiple fiber drawing process, resulting in the elevation of melting onset temperature from 130–160°C, as shown in Figure II.3.1.12.5.

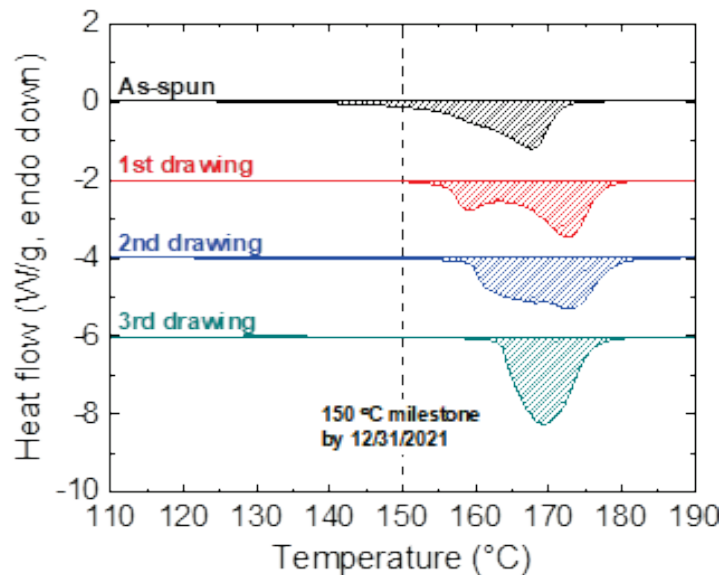


Figure II.3.1.99. Melting peaks for as-spun, 1st drawn, 2nd drawn, and 3rd drawn PP fibers. Source: ORNL.

According to the Gibbs-Thomson model, the melting temperature of polymer crystal is proportional to the lamellar thickness. As a polymer fiber is stretched, thin lamellar structures are rearranged into thicker structures. Thus, higher thermal stability could be achieved after the fiber drawing processes. The dimensional stability of the highly drawn PP fiber was evaluated after annealing the fiber at high temperatures as well, as shown in Figure II.3.1.12.6. First, the PP fiber was placed on a glass plate and two ends were fixed using tape. To mark the initial fiber length before annealing, 5 cm was painted using a black marker. Then, one end of the fiber was released to allow free shrinkage at the annealing temperature. To monitor the degree of shrinkage,

the setup was placed in an oven. The final fiber length after exposure at 150°C for 3 min was measured from the colored length. Finally, the degree of shrinkage (DS) was computed from the following equation:

$$DS(\%) = (IF-FL)/IL \times 100 \tag{1}$$

where IL and FL are the initial length and final length, which were 5 and 4.8 cm, respectively.

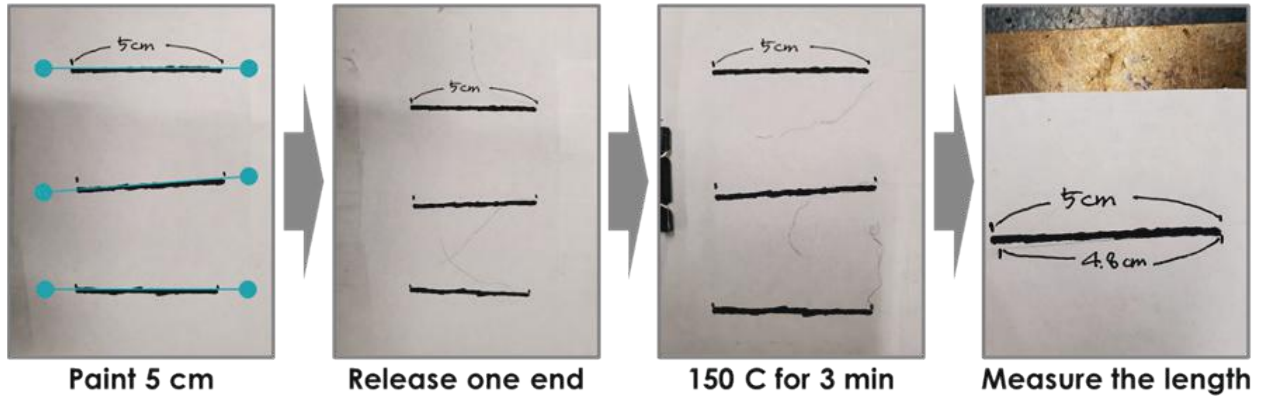


Figure II.3.1.100. Investigation of dimensional stability for polyolefin fibers at high temperatures. Source: ORNL.

In this study, the DS was determined to be ~4%, meeting the decision criteria (< 5%). Since the reinforcing PP fiber is required to have excellent mechanical properties, tensile testing was performed for the manufactured PP fiber with various draw ratios with results as shown in Figure II.3.1.12.7.

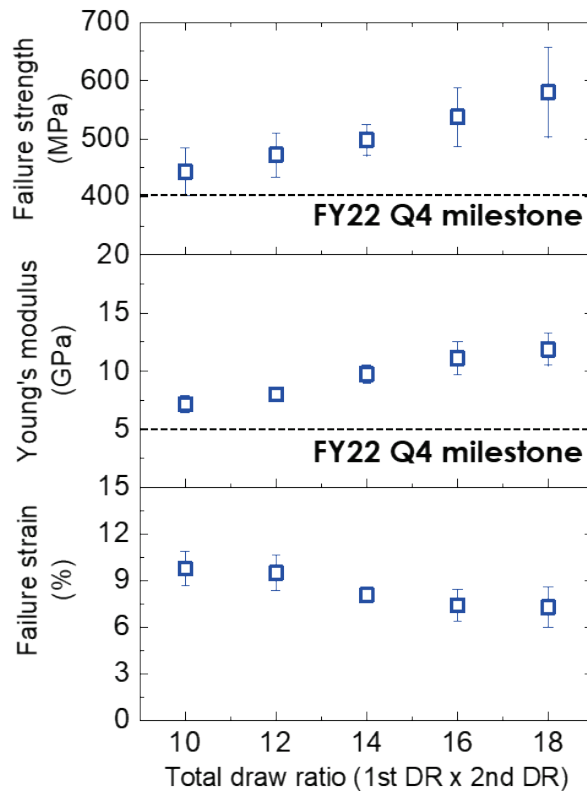


Figure II.3.1.101. Mechanical properties of reinforcing PP fibers drawn at various draw ratios. Source: ORNL.

As the total draw ratio increases from 10 to 18, both the tensile strength (440 → 580 MPa) and Young's modulus (7 → 12 GPa) increase, while the elongation at the break slightly decreases (10% → 7%). The excellent mechanical properties could be obtained from both high crystallinity and physical crosslinking, thus achieving the FY 2022 fourth quarter milestone. Eventually, the lightweight polymer composite laminate was fabricated by incorporating PP fiber reinforcements in a chemically modified PP derivative matrix through a hot-press, as demonstrated in Figure II.3.1.12.8.. The modified PP matrix was designed to suppress the melting temperature of the matrix to extend the processing temperature window, which is determined between two melting temperatures of the PP fiber and matrix. No visible delamination was observed when bending the tensile specimens, implying a good adhesion between the matrix and fiber reinforcements. The mechanical properties of the PFRP composites will be discussed in subsequent reports.

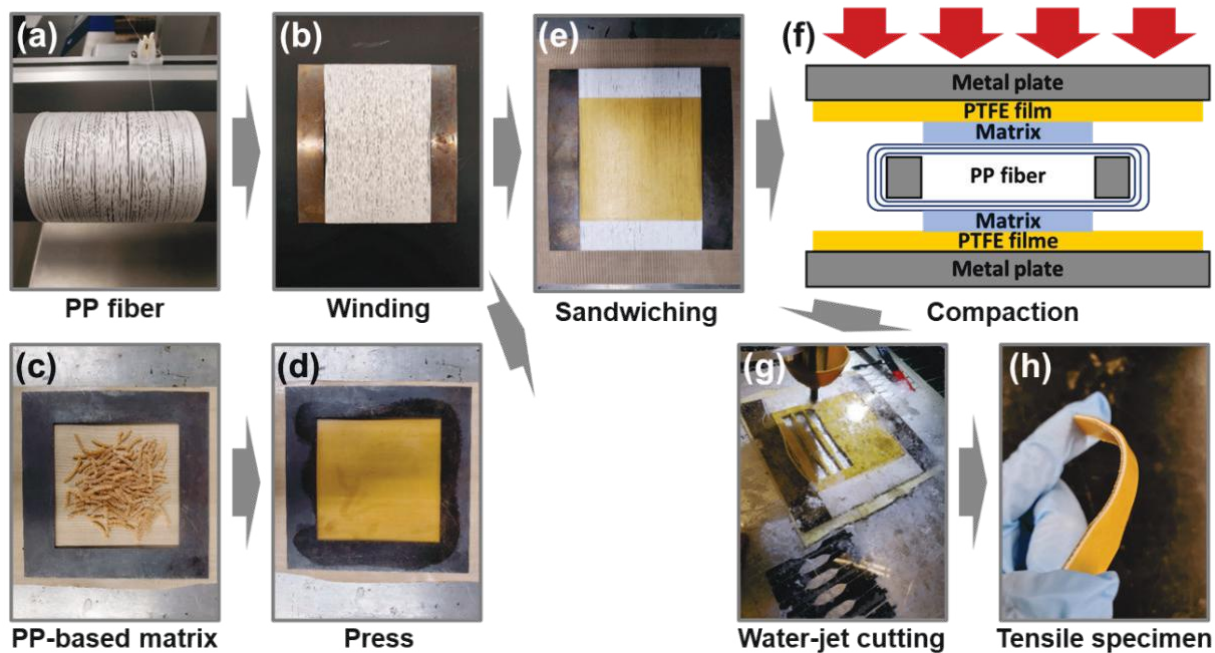


Figure II.3.1.102. The overall hot-press process to fabricate ultra-lightweight thermoplastic polymer/polymer fiber composites using PP fiber reinforcement and chemically modified PP matrix. Source: ORNL.

Conclusions

PNNL and ORNL achieved all FY 2022 milestones towards the development of an ultra-lightweight and high-performance thermoplastic polymer fiber–thermoplastic matrix composite system. In summary, our team achieved: (1) an interfacial bonding between a polymer fiber and polymer matrix via different surface modification methods; (2) a CM process with accurate temperature control to fabricate hat-shaped PFRP component; (3) mechanical behavior and failure morphology of different PFRPs under quasi-static and impact loads; (4) a manufacturing process to make high-performance polymer fibers; (5) the thermal and mechanical behavior of polymer fibers; and (6) the fabrication of PFRPs using developed polymer fibers.

Key Publications

1. Ko, S., Y. Qiao T. J. Roosendaal, J. L. Ramos, L. D. Fring, A. V. Rau, and K. L. Simmons, 2023, “Low-velocity impact performances of healed PFRPs,” *Society for the Advancement of Material and Process Engineering (SAMPE) 2023*, 17–20 April 2023, Seattle, WA, USA.
2. Qiao, Y., L. D. Fring M. R. Pallaka, and K. L. Simmons, 2022, “A review on the fabrication methods and mechanical behavior of thermoplastic polymer fiber – thermoplastic polymer matrix composites. polymer composites,” *Polym. Compos.*, Vol. 44, No. 2, pp. 694–733. <https://doi.org/10.1002/pc.27139>.

3. Qiao, Y., M. R. Pallaka, E. K. Nickerson, L. D. Fring, and K. L. Simmons, 2022, “Understanding the elastic, plastic, and damage features in fracturing of self-reinforced thermoplastic composites via nondestructive digital imaging correlation,” *Proc. SPIE 12047, Nondestructive Characterization and Monitoring of Advanced Materials, Aerospace, Civil Infrastructure, and Transportation XVI*, Paper No. 1204707, 18 April 2022, Long Beach, CA, USA. <https://doi.org/10.1117/12.2615378>.
4. Qiao, Y., M. R. Pallaka, Y. Shin, L. D. Fring, S. Ko, J. Ramos, A. V. Rau, H. F. Wu, and K. Simmons, 2023, “Enhanced interfacial bonding between polypropylene fiber and polyethylene matrix via different surface modifications for non-self-reinforced thermoplastic composites,” Journal manuscript in preparation.
5. Seo, J., L. T. Kearney, S. Datta, M. D. Toomey, J. K. Keum, and A. K. Naskar, 2022, “Tailoring compatibilization potential of maleic anhydride grafted polypropylene by sequential rheo-chemical processing of polypropylene and polyamide 66 blends,” *Polym. Eng. Sci.*, Vol. 62, pp. 2419–2434. <https://doi.org/10.1002/pen.26016>.

References

1. Daniel, I. M., and O. Ishai, 2006, *Engineering Mechanics of Composite Materials*, 2nd Ed., Oxford University Press, New York, NY, USA.

Acknowledgments

The authors would like to recognize the technical contributions by Y. Qiao, S. Ko, J. Ramos, M. R. Pallaka, L. Fring, Y. Shin, E. Nickerson, and D. Adam from PNNL; and J. Seo, L. Kearney, M. Toomey, and J. Keum from ORNL.

II.3.1.13 Efficient Synthesis of Kevlar and Other Fibers from Polyethylene Terephthalate (PET) Waste (Pacific Northwest National Laboratory)

Daniel R. Merkel, Principal Investigator

Pacific Northwest National Laboratory
908 Battelle Blvd.
Richland, WA 99354
E-mail: daniel.merkel@pnnl.gov

Rich Davies, Composites Core Program Manager

Oak Ridge National Laboratory
Materials Science and Technology Division
1 Bethel Valley Rd.
Oak Ridge, TN 37831
E-mail: daviesrw@ornl.gov

H. Felix Wu, DOE Technology Development Manager

U.S. Department of Energy
E-mail: felix.wu@ee.doe.gov

Start Date: July 1, 2020 End Date: September 30, 2023
Project Funding (FY 2022): \$300,000 DOE share: \$300,000 Non-DOE share: \$0

Project Introduction

Lightweighting of automotive components has become of paramount importance, not only to reduce the carbon footprint of final automotive products, but also to conserve valuable and depleting resources. The existing approaches of substitution and structure redesign with traditional materials have reached their limits. An urgent need exists to explore non-metallic—but equally functional—sets of materials to achieve more aggressive fuel savings targets. Lightweight fiber-reinforced plastics have become the material of choice due to their flexibility, functionality, and formability into intricate hybrid and multipart designs. CF is the reinforcement of choice for many applications in the aerospace industry, as CFCs have the most weight-reduction potential. However, CFCs have generally lower impact performance, so CF cannot be considered for applications in which impact performance is a principal design requirement [1]. Aramid fiber, such as Kevlar, fills this niche, providing superior impact performance while preserving the high-strength-to-weight ratio.

Carbon and aramid fiber composites have yet to be fully exploited in the automotive industry because of the high cost associated with the manufacture of such high-performance fibers. Presently, Kevlar fiber costs \$12/lb., which is comparable to the cost of CF. In the context of automotive parts, aramid fibers can improve the safety, performance, and durability of automotive components for a wide variety of vehicles, from passenger cars to light-duty trucks. Components of specific interest include those that demand excellent fatigue and impact performance. For example, belts, tires, and hoses that are subjected to continuous stress cycling require good fatigue properties, fore posts, hoods, and underbody components that are subject to rock impact require excellent impact properties. The replacement of metal components or glass fibers offers additional lightweighting opportunities, owing to the low-density of aramid polymers (e.g., 1.4 g/cm³ for aramid versus at least 2.5 g/cm³ for glass).

This project aims to fabricate Kevlar-like materials from waste PET. This methodology not only contributes to enabling an inexpensive starting material for fiber production, but also provides a means of addressing our plastic waste problem and a novel, exciting pathway to PET chemical upcycling. Various aramid polymers

have been synthesized from waste PET and will be spun into high-strength fibers, and then demonstrated in composite materials.

Objectives

The objective of this project is to demonstrate waste PET as an alternative source feedstock for poly(paraphenylene terephthalamide) (PPTA) (i.e., Kevlar), in addition to other aramid polymers and produce high-strength fiber at 40% reduced cost as compared to virgin feedstock fiber. The project will use waste PET sourced from used beverage bottles as a primary feedstock for aramid polymers that will be spun into high-strength fiber by standard fiber spinning methods. The project will target 25- μm fiber diameter, as well as tensile strength and modulus comparable to Kevlar 29. Fiber composite materials will be manufactured and mechanically characterized to demonstrate performance comparable to Kevlar and other high-performance fiber composites.

Approach

Before fibers and composites could be produced, we needed to identify suitable conditions to prepare aramid polymers made from PET waste, terephthalic acid derived from PET waste, or terephthaloyl chloride generated from terephthalic acid, a more reactive starting material. Our original aramid synthetic strategy involved the direct concerted depolymerization/repolymerization reaction, as illustrated in Figure II.3.1.13.1, via C-O bond cleavage and C-N bond formation. This methodology, if successful, was projected to provide a considerable advantage in the cost of aramid polymers, as the starting material is inexpensive PET waste.

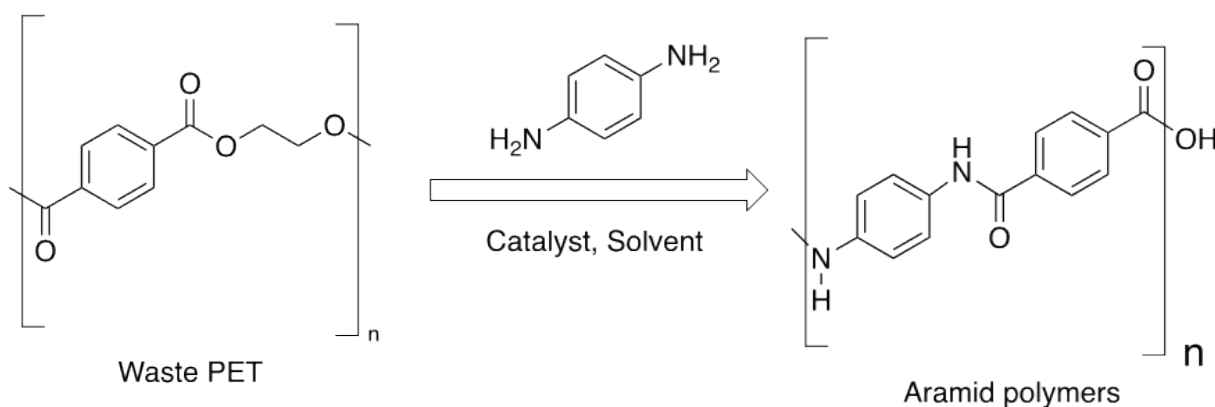


Figure II.3.1.103. Direct depolymerization of PET waste and concerted repolymerization. Source: PNNL.

The main challenge is PET insolubility in all non-reactive and relatively inexpensive organic solvents—such as N,N-dimethylformamide, dimethylsulfoxide, hexamethylphosphoramide, N-methylpyrrolidone (NMP), and dichlorobenzene—therefore making the solution chemistry difficult. Moreover, the reaction is unlikely to go to completion, and separation of insoluble starting materials (unreacted PET) from products (aramid) proved very challenging. Given these considerations, an alternative methodology was developed to deconstruct PET to a chemically functional intermediate and remove impurities, yielding a suitable feedstock for aramid synthesis. Then, a variety of polymerization procedures were developed and optimized to create aramid polymers with high molecular weights suitable for high-strength fibers. Polymer fibers will be spun via dry jet and wet spinning methods to fabricate high-strength fibers suitable for composites applications. Finally, polymer matrix composites will be formed and mechanically tested to demonstrate the utility of PET-derived fibers for automotive composites.

Results

The PET deconstruction, functionalization, and aramid polymerization reactions developed in FY 2021 were scaled-up and optimized to enable the production of high molecular weight polymers. Many conditions were applied to the generic reaction shown in Figure II.3.1.13.2 (e.g., temperature, concentration, addition of

solubility aids) and the resulting products assessed via gel permeation chromatography (GPC) to assess molecular weight.

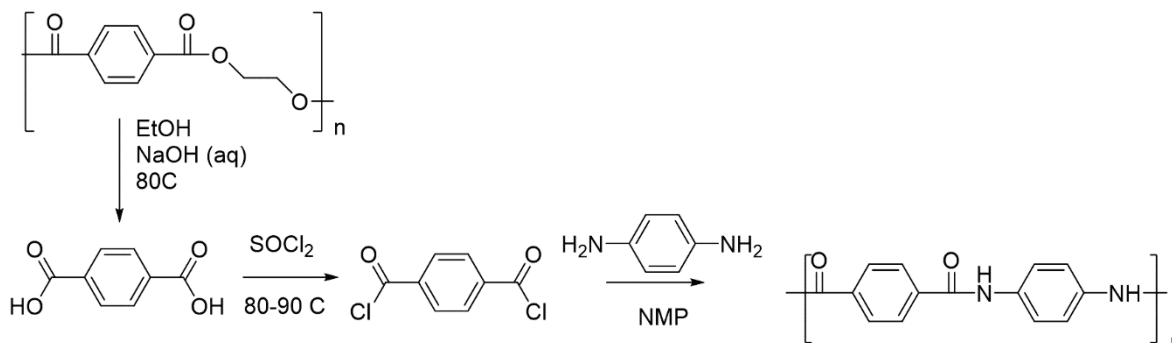


Figure II.3.1.104. Synthesis of PPTA through the acid chloride route, formed from terephthalic acid monomer obtained through PET hydrolysis. Source: PNNL.

The addition of CaCl_2 was found to be critical in promoting polymer solubility and chain growth for high molecular weight in the synthesis of PPTA. Initial investigations were performed at a 5-10 g scale with promising results. Reactions were scaled-up to ~25 g using similar procedures (e.g., Method 1) and resulted in polymers with molecular weights on the order of 10-20 kg/mol ($M_n = 5-9$ kg/mol) and inherent viscosity around 3.27 dL/g. However, industrial PPTA spinning operations typically require molecular weights of about 40 kg/mol and an inherent viscosity of 4-5 dL/g [2]. Thus, the 25 g scale procedure was optimized (e.g., Method 2) to improve molecular weight of the product with guidance from Dewilde et al. [3]. The most significant departure from the previously investigated method (e.g., Method 1) was complete dissolution of CaCl_2 in the NMP reaction solvent prior to introducing reactants. In this case, CaCl_2 is more efficient in disrupting hydrogen bonding between secondary amide groups, thereby promoting solubility and chain growth more efficiently. Trials were first carried out using commercially sourced terephthaloyl chloride (TCl) for proof-of-concept and repeated using PET-derived TCl. The improved method (e.g., Method 2) was most evident as the reaction neared completion, as shown in Figure II.3.1.13.3. The initial method (e.g., Method 1) reaction mixture maintained a brown color with low viscosity comparable to oil, whereas the improved reaction (e.g., Method 2) mixture developed a bright yellow color and high viscosity similar to baking batter.

Due to the cost and difficulty of performing GPC on PPTA, which is only soluble in specially developed solvents, inherent viscosity was used as a surrogate for characterizing molecular weight; higher inherent viscosity indicates higher molecular weight. After purifying and drying, the PPTA polymers synthesized by each method were dissolved at 0.5% w/v in 96.4% purity sulfuric acid, while inherent viscosity was measured by Ubbelohde viscometer at RT. Inherent viscosity of PPTA products of various reactions are shown in Figure II.3.1.13.4. Each reaction method was carried out at 25–30 g scale using either PET-derived TCl or commercially sourced TCl as a reactant. Reaction Method 1 using PET-derived and commercially sourced TCl produced PPTA with inherent viscosities of 3.27 dL/g and 3.01 dL/g, respectively. In comparison, PPTA produced by Method 2 yielded inherent viscosities of 4.12 dL/g using PET-derived TCl and 4.81 dL/g using commercially sourced TCl, both of which are within the range suitable for fiber spinning at the industrial scale. The apparent discrepancy between PPTA derived from PET and commercial TCl could be caused by the presence of impurities in the reaction. For example, NMP is hygroscopic; as such, water in the reaction is well-known to negatively affect molecular weight, which would result in lower inherent viscosity [3]. However, no chemical structural difference between PET-derived PPTA and commercial TCl-derived PPTA was detectable by either nuclear magnetic resonance or Fourier-transform infrared analysis.

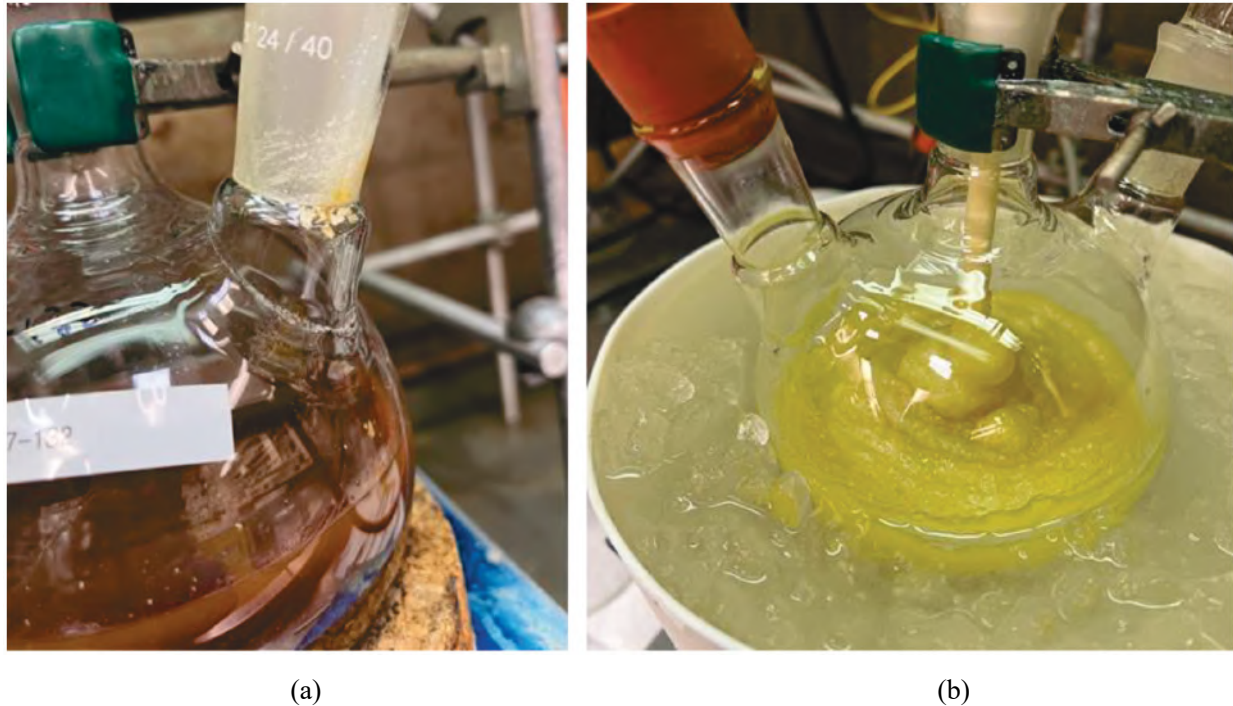


Figure II.3.1.105. (a) Initial reaction method (e.g., Method 1) near completion which yielded low molecular weight (inherent viscosity = 3.01 dL/g). (b) Improved reaction method (e.g., Method 2) near completion yielded higher molecular weight (inherent viscosity = 4.8 dL/g). Commercially sourced TCI was used in each case. Source: PNNL.

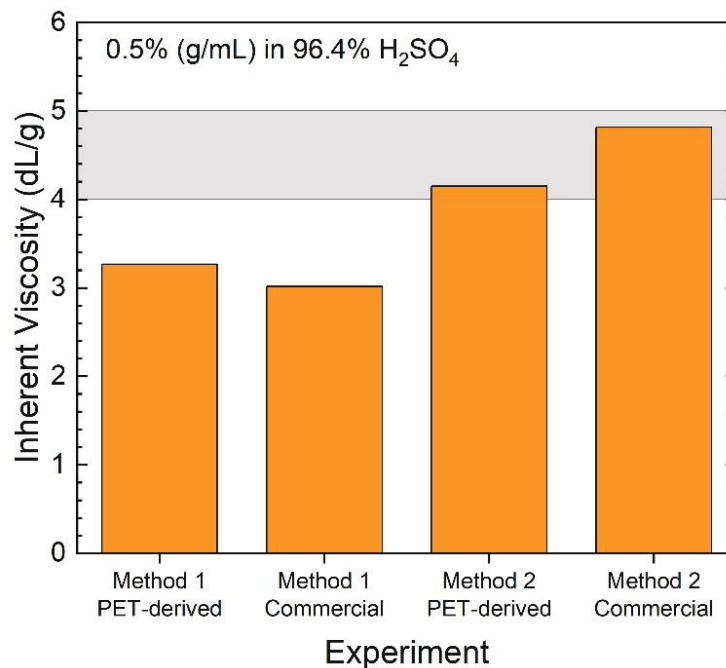


Figure II.3.1.106. Inherent viscosity of PPTA (0.5% w/v in sulfuric acid) synthesized by either Method 1 or Method 2 and using either PET-derived or commercially sourced TCI. The shaded zone (4-5 dL/g) represents inherent viscosity suitable for fiber spinning. Source: PNNL.

A similar synthesis strategy was developed for another PET-derived polymer referred to as poly(4,4'-oxydianiline terephthalamide) (PODA), as illustrated in Figure II.3.1.13.5, with potential use as high-strength fiber. This polymer contains an oxygenate in the backbone that aids solubility and eliminates the need for CaCl_2 in polymer synthesis and has similar implications in the fiber spinning process. Small-scale reactions (5-10 g) analyzed by GPC indicated that the largest molecular weight polymer was 78.9 kg/mol ($M_n = 35.6$ kg/mol). A large-scale reaction generated over 50 g of PODA at comparable molecular weights. While PODA is a useful high-temperature polymer (degradation temperature at least 475°C), it is commercially used as a high-strength fiber in copolymer form with PPTA, which will be investigated in FY 2023.

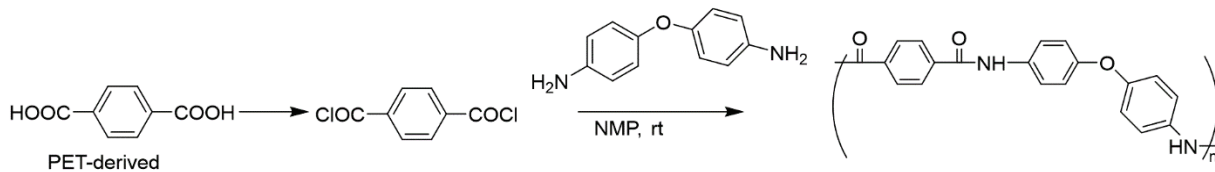


Figure II.3.1.107. Synthesis of PODA aramid polymer. Source: PNNL.

Washington State University (WSU) was contracted to spin PPTA fiber synthesized by PNNL. Spinning dopes were fabricated by dissolution of PPTA in 96.4%–99.9% purity sulfuric acid at polymer concentrations of 18%–20 wt.%. Dissolution was only possible at temperatures around 90°C or greater depending on acid purity and polymer concentration. Solidification occurred around the same temperature upon cooling, as shown in Figure II.3.1.13.6. Apparent viscosity was extremely high even at 120°C , which complicated the spinning process conditions requiring high-pressure to extrude fibers through the spinneret. The WSU spinning equipment had to be modified to provide adequate heating and pressure to the dope to facilitate spinning. The modifications required fabrication of an improved heater block which is underway.

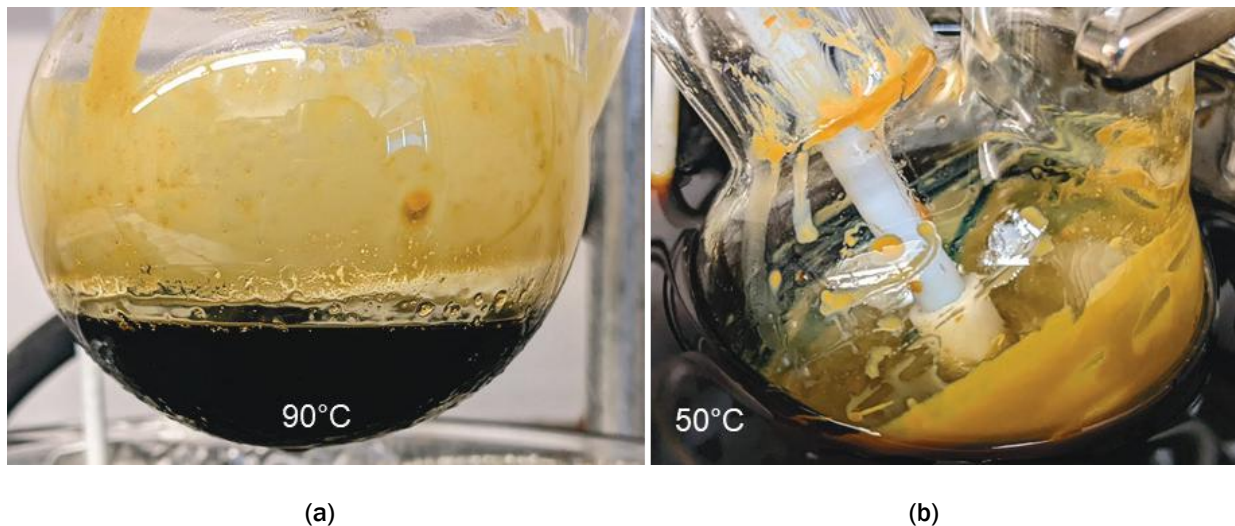


Figure II.3.1.108. (a) Liquid 18 wt.% PPTA dope solution in 99.9% purity H_2SO_4 at 90°C . (b) The same dope solidified at 50°C (in oil bath) upon cooling. Source: WSU.

Fuming sulfuric acid (e.g., 100% purity with additional SO_3 to maintain purity) was obtained to create dopes with expectedly lower melt temperature and viscosity. At 20 wt.% polymer concentration, melting temperature was found to be around 90°C with improved apparent viscosity compared to the 96.4%–99.9% purity sulfuric acid dopes. PNNL fabricated a bench scale fiber spinning setup with high-temperature and pressure capabilities to support the investigation. Alternative polymers, such as PODA-PPTA copolymer and meta-phenylene terephthalamide polymer that form fiber under more mild process conditions compared to PPTA, may be investigated as well.

Conclusions

In conclusion, the chemical reaction pathway from waste PET to aramid precursors, which was developed previously in FY 2021, was scaled-up to 60 g and optimized. PET-derived PPTA synthesis was improved to increase molecular weight and achieved inherent viscosity suitable for fiber spinning by industry standards. A bench scale fiber spinning apparatus was built in parallel to WSU fiber spinning activities. Spinning dopes of PPTA in concentrated and fuming sulfuric acid were characterized for thermal behavior at various concentrations. PODA was also synthesized from PET-derived reactants, providing an alternative pathway to high-performance polyaramids.

In FY 2023, the project will focus on spinning fibers in collaboration with WSU. Fibers will be characterized and incorporated into composites to demonstrate feasibility in engineering applications. A techno-economic analysis will be carried out in parallel to quantify cost-savings compared to fiber production from virgin feedstock.

Key Publications

1. Cosimbescu, L., D. R. Merkel, J. Darsell, and G. Petrossian, 2021, “Simple but tricky: Investigations of terephthalic acid purity obtained from mixed PET waste,” *Ind. Eng. Chem. Res.*, Vol. 60, No. 35, pp. 12792–12797. <https://doi.org/10.1021/acs.iecr.1c02604>.
2. Cosimbescu, L., D. Malhotra, M. R. Pallaka, and M. S. Swita, 2022, “Kevlar-like aramid polymers from mixed PET waste,” *ACS Omega*, Vol. 7, No. 36, pp. 32026–32037. <https://doi.org/10.1021/acsomega.2c03059>.

References

1. Kartal, İ., and H. Demirer, 2017, “Wear properties of hybrid epoxy composites reinforced with carbon/Kevlar/glass fabrics,” *Acta Phys. Pol. A*, Vol. 131, No. 3, pp. 559–562. <https://doi.org/10.12693/APhysPolA.131.559>.
2. Denchev, Z. Z., and N. V. Dencheva, 2012, “Manufacturing and properties of aramid reinforced composites,” in Bhattacharyya, D., and S. Fakirov (eds.), *Synthetic Polymer-Polymer Composites Manufacturing and Properties*. <https://doi.org/10.3139/9781569905258.008>.
3. Dewilde, S., J. Winters, W. Dehaen, and K. Binnemans, 2017, “Polymerization of PPTA in ionic liquid/cosolvent mixtures,” *Macromolecules*, Vol. 50, No. 8, pp. 3089–3100. <https://doi.org/10.1021/acs.macromol.7b00579>.

Acknowledgments

This work would not be possible without the efforts of L. Cosimbescu (former PI), J. Kothandaraman, D. Mayberry, Y. Ni, and S. Krishnamoorthy. Special thanks is also noted to D. Herling, K. Simmons, and A. Rau for their guidance.

II.3.1.14 Additively Manufactured, Lightweight, Low-Cost Composite Vessels for Compressed Natural Gas Fuel Storage (Lawrence Livermore National Laboratory)

James P. Lewicki, Principal Investigator

Lawrence Livermore National Laboratory
700 East Ave.
Livermore, CA 94550
E-mail: lewicki1@llnl.gov

Rich Davies, Composites Core Program Manager

Oak Ridge National Laboratory
Materials Science and Technology Division
1 Bethel Valley Rd.
Oak Ridge, TN 37831
E-mail: daviesrw@ornl.gov

H. Felix Wu, DOE Technology Development Manager

U.S. Department of Energy
E-mail: felix.wu@ee.doe.gov

Start Date: July 1, 2020	End Date: September 30, 2023	
Project Funding (FY 2022): \$460,000	DOE share: \$460,000	Non-DOE share: \$0

Project Introduction

CF/polymer composites are a transformative class of high-performance, lightweight material, where high aspect ratio CFs reinforce a polymer matrix and exceed the strength of steel alloys at a fraction of the density. Despite the advantages of such a class of material, the broader implementation of CF composites in a range of automotive, aerospace, and energy applications is hindered by limitations of current manufacturing methods. These current techniques (e.g., hand layup, wet filament winding) are costly and impose severe limitations on fiber placement, orientation, and angle, and thus the ultimate properties of a composite. Today's CF composites are expensive to manufacture, limited in form factor, and utilize costly and sub-optimal continuous filament CF. Advanced AM processes, combined with computational design optimization and new approaches to resin development, offer alternative design and manufacturing paradigms that have the realistic potential to lift these constraints. Such integrated AM approaches could thus help to realize the full potential of CFC materials.

One relevant application of CFC materials where manufacturing constraints limit the cost-benefit ratio is in the manufacture of high-performance composite pressure vessels for onboard CNG storage. Current CNG storage vessels (Types 3–5) are made from load-bearing filament-wound CFC and are ~3.5 times as expensive as an all-metallic Type-1 vessel. This cost is invariably tied to the complex and labor-intensive nature of conventional filament winding processes and the large volumes of expensive high-tensile-strength CF tow feedstock required in manufacture. Our proposed approach to CNG storage vessel manufacture is based on a combination of AM technologies for CFC printing and design optimization tools that were pioneered at Lawrence Livermore National Laboratory (LLNL) with advances in resin/composite formulation enabled by chemical and nanomaterial modification. Through the successful development of this technology, LLNL seeks to demonstrate the capability for advanced CNG storage vessel manufacture at reduced cost with no reduction in performance versus the most advanced, extant Type-5 CNG vessel designs.

Objectives

The proposed work addresses three objectives that are critical to the AM of next-generation CFCs:

- **Objective 1:** Enhance resin properties via chemical and nanomaterial modifications to yield an improved resin matrix with significantly increased mechanical performance over baseline winding resins. *(Enables reductions in CF content without detriment of performance.)*
- **Objective 2:** Realize compositionally graded CFCs. Apply novel AM and design methodologies to combine continuous and short-fiber structures in a graded, computationally optimized tank design, which maximizes performance while minimizing mass and cost. *(Hybrid, optimized design enables increased performance at lower relative volume fraction of expensive continuous CF filament.)*
- **Objective 3:** Additively manufacture and test a contoured hybrid CF vessel having all the major design elements of a Type-5 CNG vessel, providing validation of the materials and design concepts within a relevant laboratory-scale environment. *(Enables the development of a technology data package including a cost to benefit assessment for the demonstrated technology and will form a starting point for further maturation [post-project] at scale.)*

Approach

This project will develop a process to combine AM via DIW technology for CFC printing and use design optimization tools pioneered at LLNL, with advances in resin/composite formulation enabled by chemical and nanomaterial modification to produce lightweight low-cost CNG vessels. Our approach will yield sub-scale prototype composite pressure tanks equivalent to Type-5 CNG vessel designs that demonstrate a potential cost-benefit advantage. Central to our vision is using agile AM and design based on computationally informed DIW of both short and continuous CF, further coupled with high-performance thermoset polymer matrixes modified by emergent nanomaterials. Our single-stage, multimaterial AM technology, combined with a decreased volume fraction of CF and an increased proportion of economically advantaged short-fiber, all together drive the reduction in manufacturing time and overall cost. Importantly, reductions in continuous fiber and overall FVF will be achieved without detriment to the mechanical strength of the composite vessel. This will be achieved by employing a single process, multimaterials grading process involving the following: (1) a thermoset resin ‘ink’ modified with aligned nanoplatelets to leverage the efficient tortuous-path gas barrier effect, and (2) an inner flexible gas barrier printed as the initial stage in our manufacturing process before compositionally grading the AM feedstock in real-time to transition to a rigid, structural CF-filled resin. The proposed hybrid construction is projected to achieve pressure ratings (e.g., 2,900–3,600 psi service range with a 3× burst safety factor) comparable to conventional filament-wound composite tanks with an estimated 30–50% reduction in total manufacturing cost. The cost reductions are based on a reduction in the levels of CF required and process streamlining achieved via a hybrid DIW manufacturing method, as shown in Figure II.3.1.14.1.

A core advantage of our approach over existing technology lies within our high-performance thermosetting resins that are both ultraviolet (UV) gellable and thermally curable. They are specially formulated to be compatible with the DIW process and to engender enhanced gas barrier and mechanical performance in the final printed material. We will base our gas barrier resin technology on the development of a UV-gel/thermal-post-cure epoxy network that is chemically modified for flexibility and physically modified with two-dimensional graphene nanoplatelets. Our structural resin will be based on a family of LLNL high-performance polymers characterized by hybrids of cyanate ester and aromatic epoxy segments in a contiguous network. To overcome the ubiquitous challenges in CF composites relating to weak polymer matrices and fracturing at CF-matrix interfaces, we will introduce additional hierarchical reinforcement elements based on one-dimensional nanomaterials. Our non-acrylate-based, UV-gel/thermal-cure technology is found in both resin families. This similar chemistry enables a single-stage, multimaterials deposition process wherein one resin can be covalently blended into the next at a range of compositional gradients.

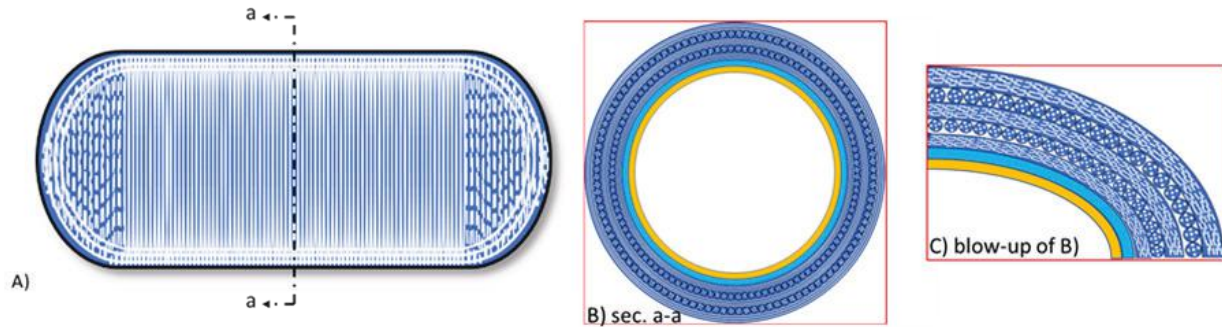


Figure II.3.1.109. Schematic of an AM-CNG storage vessel concept. (a) External rigid structural layers of the vessel: load-bearing resin filaments (blue) filled with short and continuous CF (white). (b) Continuous filament material is applied to the midbody yielding maximum hoop strength. (c) Short-fiber extrusion used to fabricate complex end caps. Flexible and cross-linkable polymer compositions reinforced with nanoplatelets shown in (b) and (c) will be printed to serve as the inner layers of a vessel (yellow and blue layers represent the inner gas barrier and transition to structural layers, respectively). Source: LLNL.

Through hybridizing continuous and short-fiber printing, we will enable the manufacture of novel graded composites. This will realize printing with tunable and enriched concentrations of continuous filament in the center of the vessel body to maximize radial hoop strength while minimizing the overall use of expensive continuous filament fibers. A unified resin deposition process seamlessly blends portions of the build requiring rich continuous filament with short-fiber material to accommodate conformal and open geometries problematic for standard continuous filament techniques (e.g., vessel endcaps). To realize this hybrid composite approach, a new print head is required to be developed, based on LLNL's patents and extant breadboard demonstrations in the area. The design, manufacture, and testing of a hybrid print head, which enables the laydown of both long-fiber tows and short-fiber 'ink' within a single AM structure will be carried out in collaboration with our industrial partner—Materials Sciences LLC, which will design and manufacture a practical hybrid head prototype, based on LLNL breadboard concepts that may be integrated into LLNL's current AM printing platform, participate in the integration and testing of the system, and execute any improvements/modifications that are necessary after completion of the prototype trials. They will also participate in the design of the hybrid test vessels under Task 3 of this project.

We will maintain optimal mechanical performance of our composite vessel walls using a multi-scaled, hybrid composite structure—realized in a rationally designed manufacturing form derived from DIW. Leveraging our advanced DIW printing technology for short and continuous fiber, we will develop unique capabilities to manufacture the main body of the vessel within one consolidated, cost-efficient process.

A series of burst and performance tests of manufactured articles will form the basis of the validation of our design and manufacturing approach. A breakdown of our project schedule at a task level is shown in Figure II.3.1.14.2.

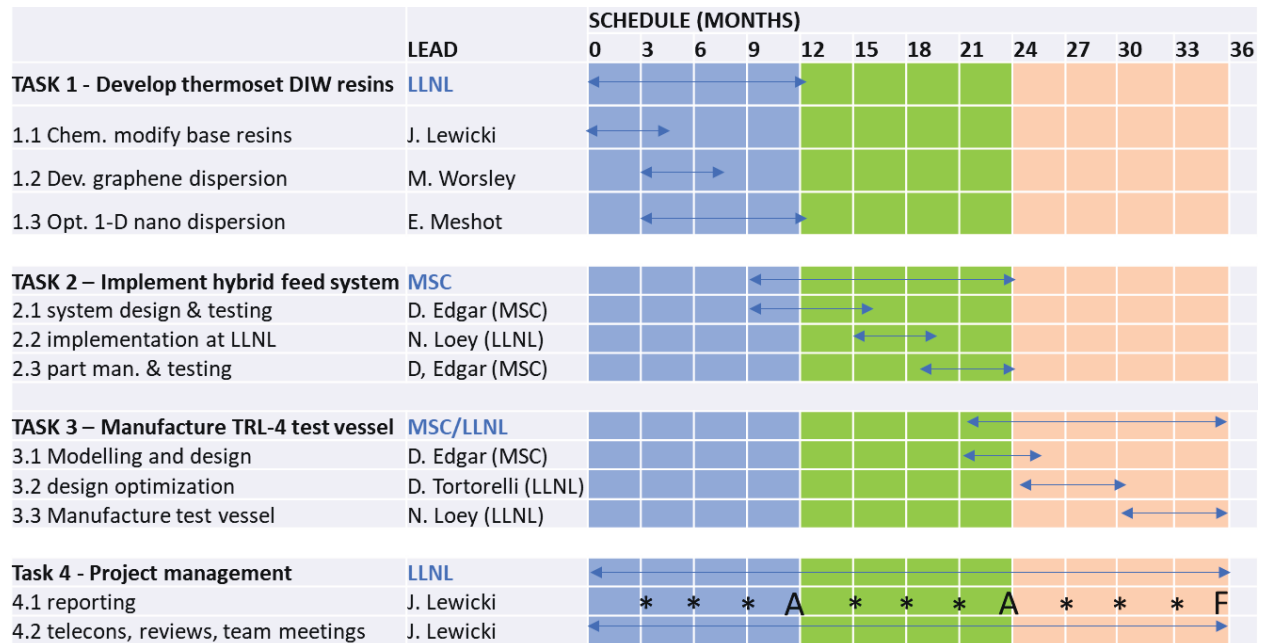


Figure II.3.1.110. Project schedule. Source: LLNL.

Results

Significant progress was made in FY 2022 towards meeting the technical goals of this project. Notably the overall design for the tank test articles was completed to high-fidelity, enabling test article manufacture activities to begin on schedule in FY 2023. A computer-aided drawing of the scaled test article tank design is provided in Figure II.3.1.14.3.

17-4PH steel boss,
AS 5202-10 port

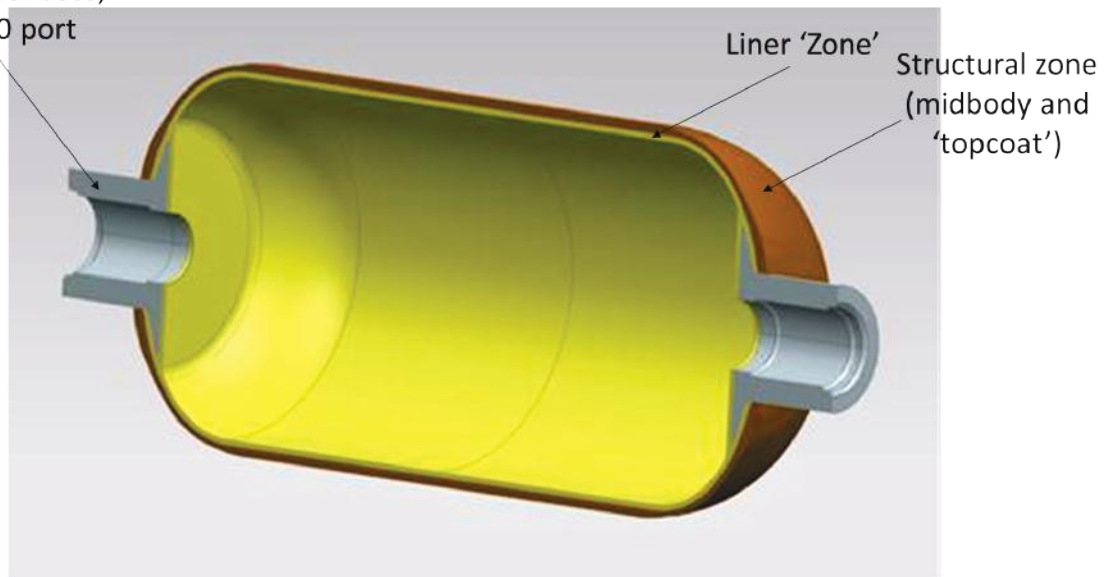


Figure II.3.1.111. Cutaway view of a 4-in. diameter by 6 in. long scaled CNG tank design that will be implemented in this project via an AM process. The tank consists of three material 'zones' (e.g., liner, midbody, topcoat) — all of which will be chemically contiguous and printed in the same process operation. Source: LLNL.

Our tank article design is finalized with the goal of making it both representative of Type-5 class vessels and an accurate platform from which to validate AM materials and process-performance. The tank is 4 in. in diameter with 0.12 in. average thickness walls having a 0.06 in. ‘liner’ region overwrapping 17-4PH steel bosses. Three compositional zones are defined: (1) liner zone, (2) midbody, and (3) outer ‘topcoat.’ In FY 2022, our team developed the ink for the liner zone in the form of a rubber-modified thermoset resin, filled with colloidal nano silica, nano clay, and carbon microfibers, and rendered thixotropic to enable application via DIW. The midbody structural region is a continuous filament fiber in a UV reactive Newtonian thermoset resin that will be applied using our now operational continuous filament 3D printing head. The outer ‘top coat’ resin has been formulated as a short fiber/ceramic nanofiber reinforced thixotropic composition with enhanced impact toughness, which will be applied via DIW. Each zone will be applied sequentially via the AM process with resin co-reactivity ensuring a continuum between zones.

In FY 2022, we also made significant progress in the application of computational design optimization approaches to define non-standard toolpaths/wind angles that enable enhanced performance at a low-volume fraction of CF. Figure II.3.1.14.4 provides an example of the optimized design solutions for four layers of the midbody region core.

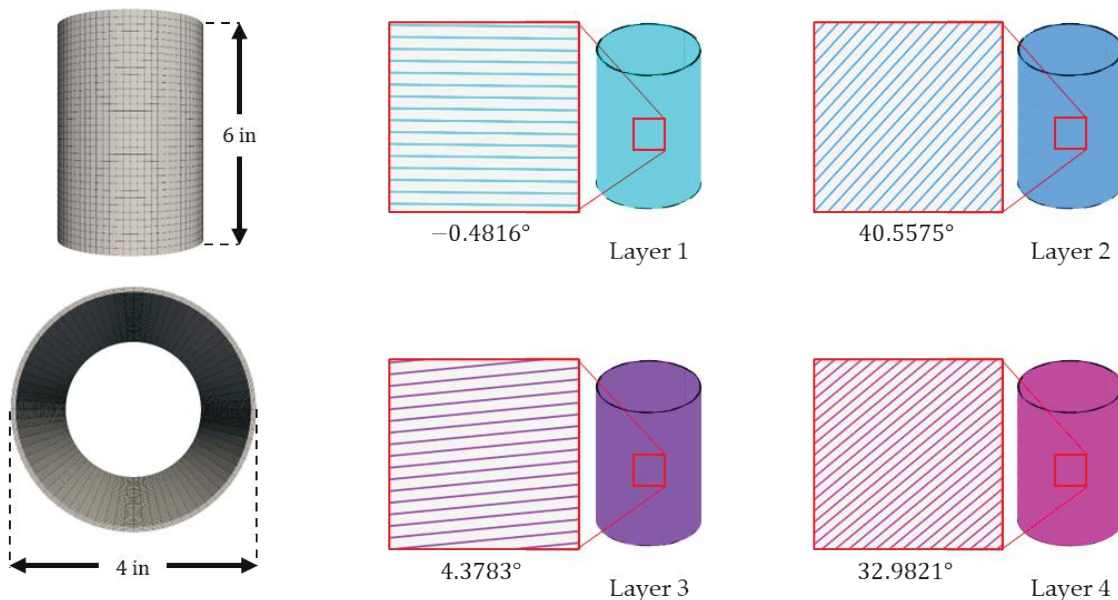


Figure II.3.1.112. Mathematically derived layer solutions for the cylindrical region of the midbody of the tank, which were generated using optimization tools in the LLNL Code NIKE-3D. These non-obvious solutions have been validated to show decreased compliance with decreased volume fraction fiber vs. standard wind geometries. Source: LLNL.

We have been successful in applying design optimization tools to the test article design to generate build/fiber laydown orientations that should deliver increased mechanical performance vs. conventional wind schedules (e.g., 2-helical layer, 3-hoop ply patterns). In the example given above, the brief was to minimize compliance of the cylinder under an internal pressure of 4500 psi while minimizing fiber volume. The 4-layer solution delivered a reduced FVF of six percent while reducing compliance under pressure by six percent also. These design solutions form the basis of computer-aided designs for wind-enabled toolpaths which will be employed in FY 2023 to fabricate articles that meet the maximum expected operating pressure performance criteria of 4500 psi for burst pressures greater than 14000 psi and 13,000 cycles or greater from 0-4500 psi without failing while minimizing continuous fiber usage in the design.

In FY 2022, we also successfully commissioned, tested, and validated our hybrid three dimensional printing head. In doing so, we validated the concept of a hybrid short-long-fiber printing system for tank manufacture. Parts were manufactured and characterized via microscopy and imaging—showing the successful incorporation of layered and adjacent zones of both short and continuous fiber within a single part, without defects, transition boundaries, or geometric disruption. This successful implementation will enable the manufacture of test articles meeting our design on all levels in FY 2023.

Conclusions

All major technical milestones were met in FY 2022 and the project is on track to complete manufacture and testing of CNG tank articles in FY 2023. Specifically, we finalized a high-fidelity structural design for the tank article and developed an in-depth manufacturing procedure to accompany the design. We successfully applied design optimization tools for the composite structure of the tank articles and demonstrated in-silico improvements in performance at reduced fiber fraction, using our computationally optimized approach. Finally, we completed hybrid short-long-fiber printing head deployment and testing, as well as validating the concept with test articles and enabling the manufacture of AM tanks in FY 2023.

Acknowledgments

The authors gratefully acknowledge P. Chastain of Aerojet-Rocketdyne for his consolation and assistance on gas bottle design and manufacturing methods; M. A. Worsley, S. Chandrasekaran, M. Tsurumoto, and E. Meshot of LLNL for their extensive scientific contributions to resin development and testing; and S. Mabery, T. Bryson, and K. Baron of LLNL are all greatly acknowledged for their technical support of the preparation, printing, testing, and characterization of the material. This work was performed under the auspices of DOE by LLNL under contract DE-AC52-07NA27344.

II.3.1.15 Biobased, Inherently Recyclable Epoxy Resins to Enable Facile Carbon-Fiber Reinforced Composites Recycling (National Renewable Energy Laboratory)

Nicholas A. Rorrer, Principal Investigator

National Renewable Energy Laboratory
15013 Denver West Parkway
Golden, CO 80401
E-mail: nicholas.orrer@nrel.gov

Gregg T. Beckham, Co-Principal Investigator

National Renewable Energy Laboratory
15013 Denver West Parkway
Golden, CO 80401
E-mail: gregg.beckham@nrel.gov

Rich Davies, Composites Core Program Manager

Oak Ridge National Laboratory
Materials Science and Technology Division
1 Bethel Valley Rd.
Oak Ridge, TN 37831
E-mail: daviesrw@ornl.gov

H. Felix Wu, DOE Technology Development Manager

U.S. Department of Energy
E-mail: felix.wu@ee.doe.gov

Start Date: October 1, 2020	End Date: September 30, 2023	
Project Funding (FY 2022): \$500,000	DOE share: \$500,000	Non-DOE share: \$0

Project Introduction

The use of carbon-fiber reinforced composites (CFRCs) in vehicles is a promising approach as CFRCs exhibit a superior strength-to-weight ratio and stiffness-to-weight ratio than that of steel at 60%–70% of steel's weight, thus increasing vehicle fuel efficiency. Despite this promising feature, CFRCs have currently not been widely implemented in vehicles because of the high cost of CF, as well as their inability to be repaired when damaged. To this end, we propose to develop biobased, inherently recyclable, high-performance resins for CFRCs using covalent adaptable networks (CANs), otherwise known as vitrimers. These covalent adaptable network-based carbon-fiber reinforced composites (CAN-CFRCs) will enable facile CF recycling and improve CFRC mechanical properties and performance.

Objectives

Overall, the proposed project aims to increase the use of reinforced composites in vehicles by enabling the recovery of CF via the use of CAN chemistry. We further aim to demonstrate that:

- The proposed chemistry can reuse CF in multiple-material lives without detriment to the performance of the CFRCs as measured by their thermomechanical properties
- The use of bioderivable building blocks can result in the requisite performance across multiple lives
- The use of bioderived building blocks can result in a cost-competitive resin while simultaneously lower the associated supply chain energy and GHG emissions [1]
- The reuse of CF across multiple lives can reduce the impacts associated with CF manufacture.

To accomplish these goals, the project work is divided into four tasks including:

- Synthesis of CAN-CFRC
- Sizing of fiber reinforcements for enhanced performance, reparability, and durability
- Validation and scaleup for manufacturing automobile parts
- Techno-economic analysis, life cycle assessment, and supply chain modeling of the materials relative to incumbent composite materials.

Approach

To accomplish our objectives, the first year of this project was aimed at initially demonstrating that our resin could be used alongside CFs to produce CFRCs with thermomechanical properties that are comparable to the industry standard epoxy-amine chemistries and could be depolymerized without damaging the fiber. Post-depolymerization, the fibers were reused alongside virgin resin to demonstrate that properties can be obtained across multiple lives and was complimented by techno-economic analysis and supply chain analysis focused on calculating the cost, supply chain energy, and GHG emissions of the resin and composites. This approach is summarized in Figure II.3.1.15.1.

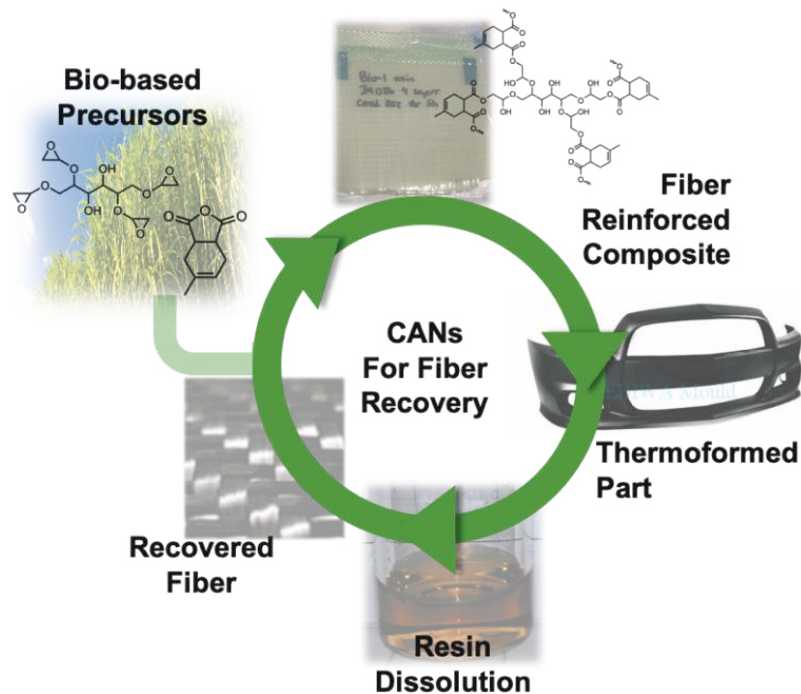
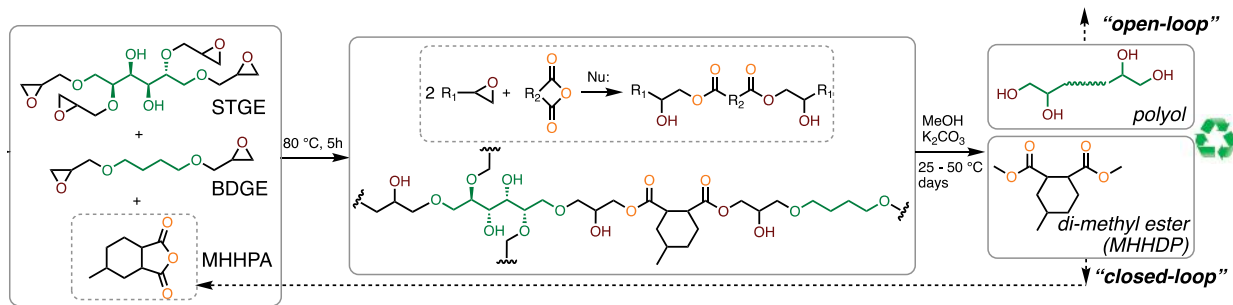


Figure II.3.1.113. Project overview. Source: NREL.

To demonstrate the reuse of the CF across multiple lives, it was necessary to develop a recyclable resin, unlike today's standard epoxy-amine resins. To these ends, we implemented a polyester-based covalently adaptable network (PECAN), which is comprised of both epoxy components and anhydride components. Akin to today's standard resins, PECAN possesses epoxies that enable quick reactivity; however, the PECAN uses an anhydride hardener, instead of an amine hardener, so the resultant chemical bonds are esters instead of amides. Esters can be recycled by hydrolysis or alcoholysis. The epoxy and hardener components are biobased and Figure II.3.1.15.2 provides chemical structures of the materials.



Note: STGE = sorbitol tetraglycidyl ether; BDGE = butanediol diglycidyl ether; MHPA = methylhexahydrophthalic anhydride; MHHDP = methylhexahydro dimethyl phthalic ester

Figure II.3.1.114. PECAN resin chemistry in which bioderived epoxies and anhydrides are combined to a crosslinked network and can be recycled with methanol. Source: NREL.

As outlined below, and demonstrated in our project milestones, the second year of this project built upon our previous year results and was overall successful. We demonstrated that (1) the PECAN-CFRCs can enable the reuse of CF over multiple lives, (2) the reuse of the CF can lead to decarbonization benefits, (3) formulation of the material for ideal properties was possible, and (4) the material could be thermoformed.

Results

All results that follow are covered by U.S. Provisional Patent Application No. 63/087,547. [2] Additionally, this project has experienced minimal delays due to the Covid-19 pandemic aside from limited lab time and space. The results summarized below were reflected in our peer review presentation and quarterly milestones. Some results are still preliminary and will be considered final when published in the peer review literature.

As outlined above, the PECAN resin is formed from bioderivable epoxies and anhydrides and can subsequently be depolymerized using low energy/temperature methanolysis. For the depolymerization, potassium carbonate (K_2CO_3) is used as a catalyst alongside methanol and a solvent (either acetone or dichloromethane) to break the resins bond and remove it from the CF. Post-depolymerization, the CF is left intact with its orientation substantially maintained. At the end of the last FY, we demonstrated that CF could be reused alongside virgin PECAN resin to exhibit comparable performance across three lives, as demonstrated in Figure II.3.1.15.3, for three CFRCs across multiple generations. Across all three generations, the storage moduli are within the measurement error, E' , of 30 ± 3 GPa and the glass transition temperature, T_g , as measured by the maximum of $\tan\delta$, is 80 ± 6 °C. Interestingly, the materials may exhibit enhanced performance on subsequent lives, but further investigation is needed into the mechanisms that may enable enhanced performance (e.g., residual resin acting as a fiber sizing and aiding compatibility). Supplemental studies were also conducted with virgin fibers and the depolymerization mixture to ensure that the depolymerization solution does not affect CFRCs properties. Demonstrating that PECAN could result in CFRCs with consistent properties ($< 20\%$ variation) across multiple lives.

Overall, the PECAN-CFRCs exhibit fantastic properties and are enhanced relative to their epoxy-amine counterpart. Figure II.3.1.15.4 provides a spider chart comparison of the properties of the base formulation PECAN-CFRCs relative to steel, the material they are ultimately aimed at replacing. On a volumetric basis, the PECAN CFRC outperform steel in terms of density and strength-to-weight ratios while possessing comparable GHG emissions, which are mainly driven by CF use and not by the resin itself. However, the elongation at the break is lower for the PECAN-CFRCs, indicating a more ductile material, and the cost is higher, once again driven by CF cost.

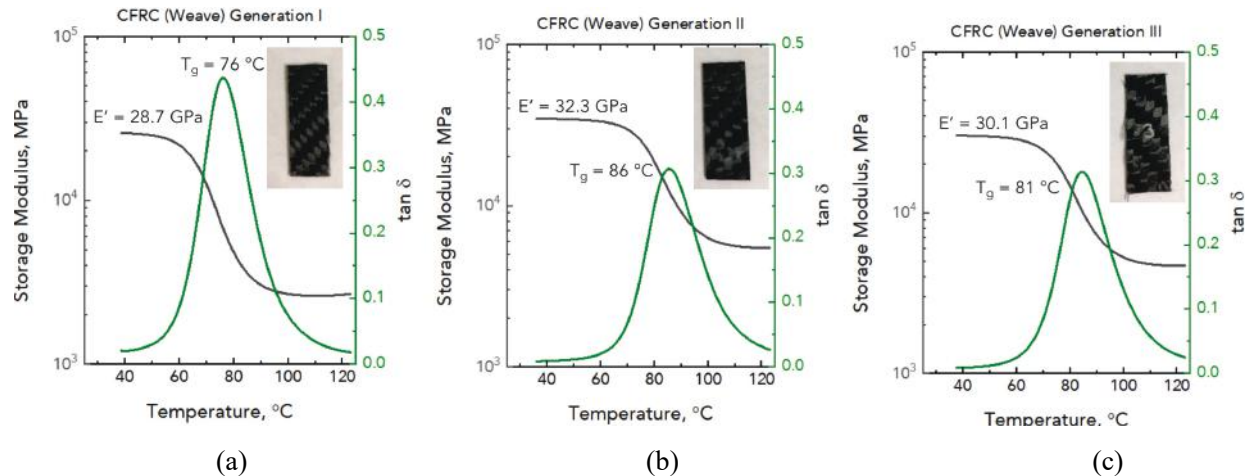


Figure II.3.1.115. Dynamic mechanical analysis results and coupons for the (a) first, (b) second, and (c) third lives of the PECAN-CFRCs demonstrating consistent or enhanced properties across lives.. Source: WSU.

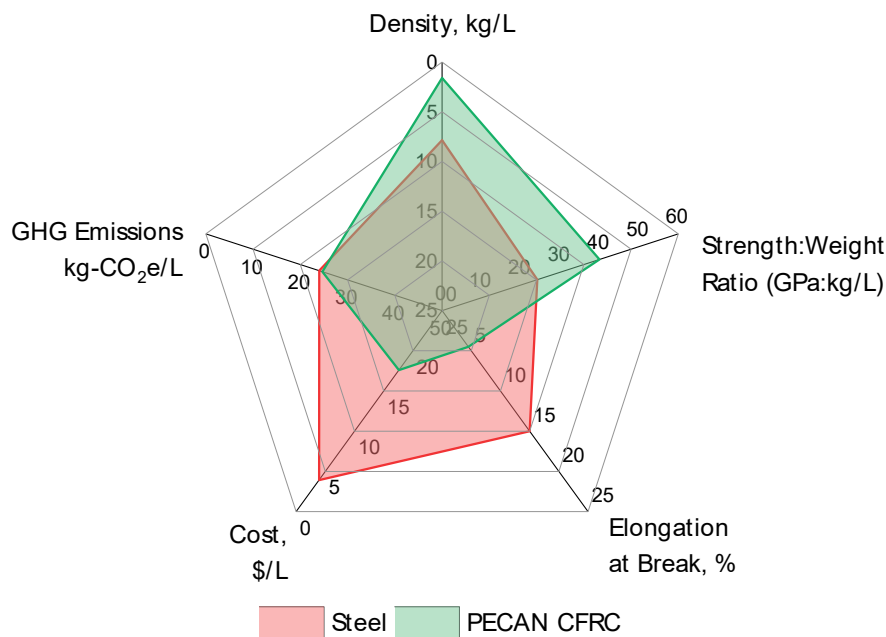


Figure II.3.1.116. Properties of the PECAN CFRC relative to steel. Source: NREL.

Despite the higher cost and GHG emissions of the first life of PECAN-CFRCs, their recyclable nature leads to a reduced cost and further GHG reductions in subsequent lives. Akin to our approach in modeling the production of CFRCs, techno-economic and supply chain analyses of the depolymerization were studied utilizing Aspen Plus and the Materials Flow-through Industry tool respectively. Table II.3.1.15.1 contains the results for the production of the first life of the resin, CF, and CFRC alongside the CF recovery and second plus life manufacture. As noted previously, CF drives the cost and GHG emissions of the first CFRC life while PECAN resin offers a 16% GHG reduction and the ability to reuse CFs across multiple lives relative to its petrochemical counterpart. Importantly, CFRC reclamation leads to a > 90% reduction in GHG emissions.

Table II.3.1.15.1. Techno-economic and Supply Chain Analyses Results for the PECAN-CFRCs Across Multiple Lives

Resin Components		Supply Chain Energy, MJ/kg	GHG Emissions, kg CO ₂ -e/kg	Minimum Selling Price, \$/kg
Petroleum-Based Resin	Overall	129	5.7	2.03
Biologically Derivable Resin (PE-CAN)	Overall	86	4.7	2.17
Carbon Fiber		467 [1]	29 [1]	21.50 (Variable) [1]
PECAN-CFRCs (First Life)		277	34	11.89
CF Recovery		71	4.4	1.70
PECAN-CFRCs (Second Plus Life)		79	4.6	1.94

Aside from demonstrating the multiple lives of the material, this past year we also investigated what materials phase space was accessible using our resin system by altering reinforcements layups, resin formulations, additives, and fiber sizing. Figure II.3.1.15.5 provides an overview and highlights of the results for the 12 different reinforcements. The use of different reinforcements, shown in the figure for polyethylene, demonstrates that different reinforcements could be used to augment the phase space of these materials to match or improve upon steel. When polyethylene is implemented, the elongation at break, cost, and density of the material could all be improved while the strength-to-weight ratio decreases. This implies that future research could target alternative fiber layups to balance properties for a given application. In consideration of post-processing—or necessity thereof—of recovered fibers, we investigated three industrially available fiber sizings, as well as four synthesized fiber sizings. With support from thermomechanical analysis and microscopy, we have shown evidence that the PECAN resin may be agnostic to fiber sizing. Additionally, we have found no changes in material properties with the application of three cost-savings and flame-retardant additives at our tested loadings. We also demonstrated that the materials can be reformulated by substituting the epoxy components to be more ductile and having a higher elongation at break. Overall, as also shown in Figure II.3.1.15.5, we have demonstrated the PECAN-CFRCs can be formulated to have properties that near-match steel while offering the potential decarbonization, motivating work beyond this initial project.

Finally, we also demonstrated that the PECAN-CFRCs can be thermoformed into a wide variety of shapes, which makes their applicability to the automotive industry even greater. As the PECAN resin chemically possesses ester linkages and hydroxyl groups, it can be subject to transesterification reactions to rearrange its chemical topology, unlike other chemestires used in CFRCs (e.g., epoxy amines) which enable it to be shaped. Here, we formed the CFRCs to shape by initially preparing a flat panel and pressing it into a custom-made aluminum mold. The mold and the thermoformed PECAN-CFRCs are shown in Figure II.3.1.15.6(a) through Figure II.3.1.15.6(c). Specifically, the PECAN CFRC was able to adopt multiple complex geometries of the mold including concave, convex, and linear deformations.

As these multiple features are often apparent on vehicle panels, this demonstrates the potential for these materials to be used in multiple vehicles applications. Future work should aim to increase cycle times of the material.

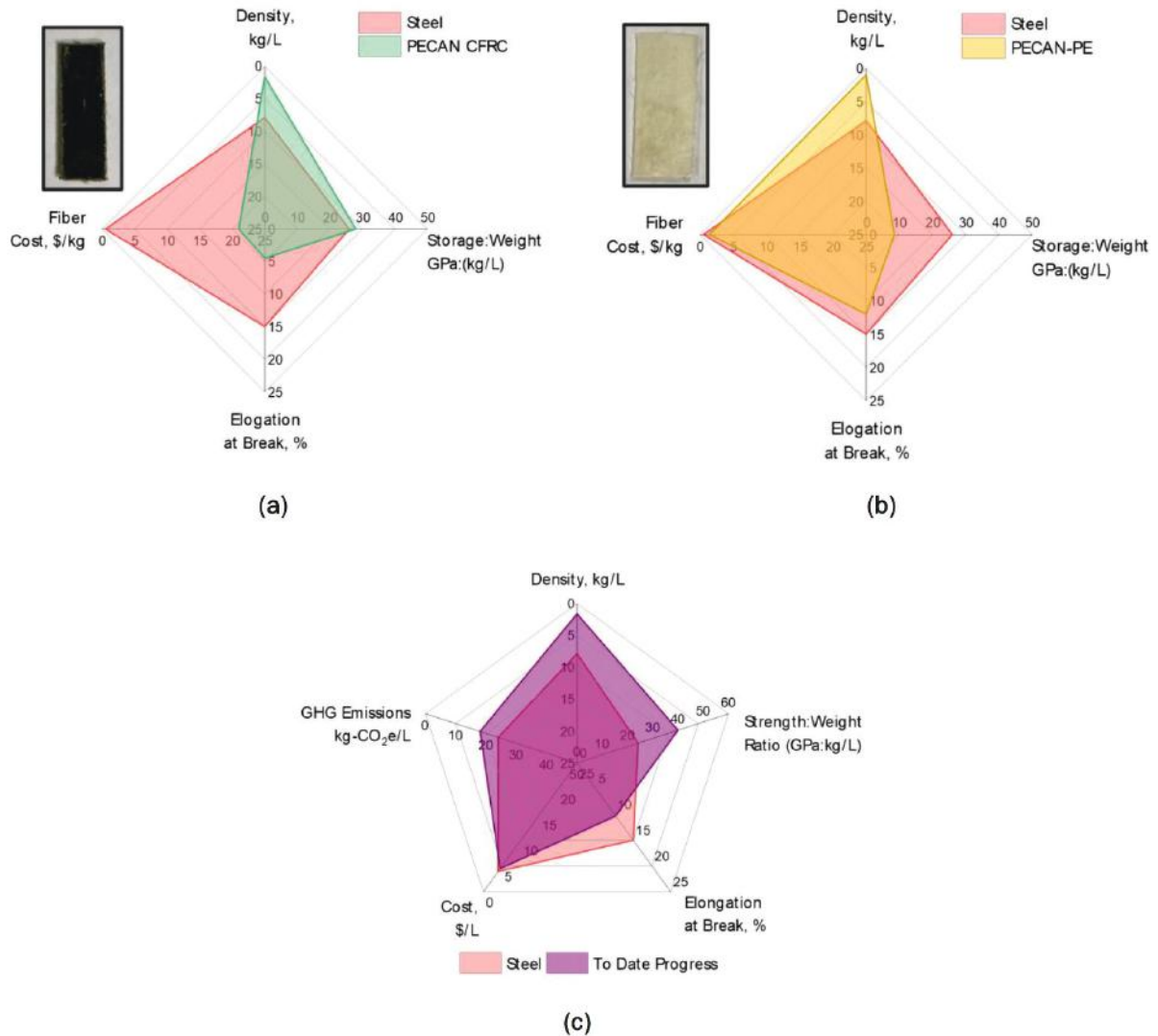


Figure II.3.1.117. A comparison of alternative fiber reinforcements for (a) a PECAN CFRC versus (b) a PECAN-based polyethylene reinforced composite. (c) Potential accessible phase space through reformulation of PECAN-CFRCs. Source: NREL.

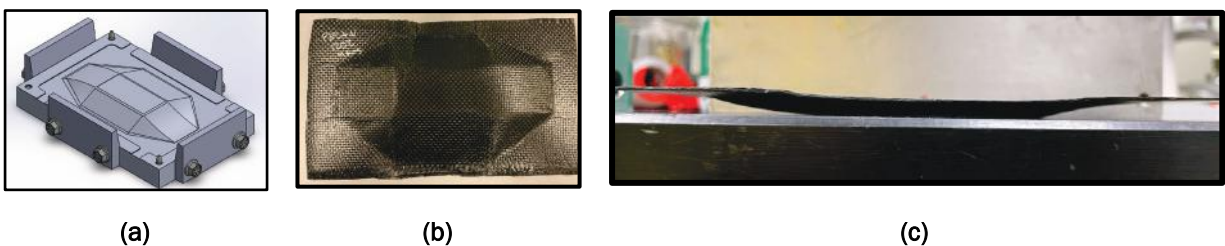


Figure II.3.1.118. PECAN CFRC thermoforming demonstration. (a) Digital drawing the thermoforming mold with multiple different geometries alongside the (b) top and (c) side view of the thermoformed CFRC. Source: NREL.

Conclusions

Across FY 2022, we have built upon our FY 2021 results to demonstrate the multiple benefits of bioderivable epoxy resins for CFRC applications. By implementing a bioderived and recyclable-by-design resin alongside a low energy depolymerization technique, it is possible to reuse the CF across multiple CFRC lives. The use of a bioderived resin results in comparable volumetric emissions to steel on the first life of the material while reclamation and reuse of the fibers leads to dramatic reductions (e.g., > 80%) in both the cost and GHG emissions of the subsequent life of these materials. Additionally, work across the year has demonstrated that PECAN-based composites can be formulated to have a performance that nearly matches steel while being thermoformable to a wide variety of shapes, making them ideal for application in vehicles, as well as a promising platform for continued research and investment. Future work can build upon the solid foundation to further tune PECAN-CFRCs for vehicle performance, enhance the manufacturing of the parts from PECAN-CFRCs, and enable recyclability at scale.

Key Publications

1. Rognerud, E. G., J. DeVeaux, G. T. Beckham, and N. A. Rorrer, 2023, “Towards a better steel replacement: Bioderivable carbon fiber composites across multiple lives,” in preparation.
2. Wang, C., R. Murray, A. Singh, G. Musgrave, E. G. Rognerud, M. Skala, P. Murdy, S. R. Nicholson, A. Shapiro, J. Miscall, R. Beach, R. D. Allen, N. A. Rorrer, and G. T. Beckham, 2023, “Polyester covalently adaptable networks for composite applications from sugar derived building blocks,” under review.

References

1. Nicholson, S. R., N. A. Rorrer, A. C. Carpenter, and G. T. Beckham, 2021, “Manufacturing energy and GHG emissions associated with plastics consumption,” *Joule*, Vol. 5, no. 3, pp. 673–686. <https://doi.org/10.1016/j.joule.2020.12.027>.
2. Wang, Chen; Murray, Robynne E.; Beckham, Gregg Tyler; Mauger, Scott; Rorrer, Nicholas A. “Bioderived recyclable epoxy-anhydride thermosetting polymers and resins,” Provisional Application No. 63/087,547, Publication No.: US 2022/0106442 A1, April 7, 2022.

Acknowledgments

The project PIs would like to thank the contributors to this work. E. Rognerud is the lead experimentalist on this work. A. Singh, J. DeVeaux, and S. Nicholson were instrumental in the analysis component of this work. R. Murray and her team were instrumental in demonstrating the scalability of the CFRCs using industrially relevant vacuum-assisted resin transfer molding techniques.

II.3.1.16 Soft Smart Tools Using Additive Manufacturing (Savannah River National Laboratory)

Jay Gaillard, Principal Investigator

Savannah River National Laboratory
Bldg. 999-2W
Aiken, SC 29808
E-mail: jay.gaillard@srnl.doe.gov

Srikanth Pilla, Co-Principal Investigator

Clemson University, International Center for Automotive Research
4 Research Dr.
Greenville, SC 29607
E-mail: spilla@clemson.edu

Richard Czerw, Co-Principal Investigator

Mainland Solutions, LLC
409 W. Maple St.
Yadkinville, NC 27055
E-mail: czerwr@mainlandsolutions.com

Rich Davies, Composites Core Program Manager

Oak Ridge National Laboratory
Materials Science and Technology Division
1 Bethel Valley Rd.
Oak Ridge, TN 37831
E-mail: daviesrw@ornl.gov

H. Felix Wu, DOE Technology Development Manager

U.S. Department of Energy
E-mail: felix.wu@ee.doe.gov

Start Date: October 1, 2022 End Date: September 30, 2023
Project Funding (FY 2022): \$500,000 DOE share: \$500,000 Non-DOE share: \$0

Project Introduction

Tooling is an integral part of composites manufacturing. Composite tools, also called ‘soft’ tools, are more easily constructed than ‘hard’ metal tools and, because they are made from materials similar to the manufactured composite part, they can be made in-house and have a good coefficient of thermal expansion match. However, as the ‘soft’ designation suggests, they are more vulnerable to wear and typically find application in relatively low-volume production. AM of thermoplastics has proven to be a lucrative option that can help improve the tooling functionalities, as it offers more design flexibility. Owing to the inherent nature of AM, the possibility of printing sensors within the tool material and at proximity to otherwise inaccessible areas of the tool become a reality. CCF-reinforced 3D printing of engineering thermoplastics has proven to be a viable option to strengthen a part well beyond the ideal moduli of unmodified thermoplastic. Furthermore, adding nanotubes or graphene to the thermoplastic matrix will also improve both the thermal conductivity and interlaminar shear strength within the tool. CNTs and CFs are microwave susceptors; exploiting the physics of Joule-heating to increase the energy efficiency of tool hardening and cure rates is a core goal of this project.

Because of the rapid volumetric heating enabled by the absorption of microwave or radio frequency energy and EM annealing presents an attractive opportunity to significantly reduce manufacturing cycle times while improving part performance.

The introduction of integrated sensors, such as thermocouples and strain gauges, allow for real-time feedback to the end-user, thus resulting in improved process controls, such as thermal management. Strain gauges provide valuable information about when the tooling becomes warped beyond tolerance and needs to be scrapped. Thermocouples help with reducing wasted processing time because the tooling temperature can be monitored for optimized cure schedules and out-of-tolerance thermal gradients. AM principles allow these integrated smart sensors to be printed simultaneously with production of the soft tool. Incorporation of integrated sensors into composite tools enables process controls that will further improve cycle times and reduce scrap rates.

Objectives

The goal of this Savannah River National Laboratory (SRNL) project is to develop high-toughness, wear-resistant CCF nanocomposite tooling with embedded sensors for vacuum bag molding or autoclaving of automotive parts. Using EM post-annealing of 3D-printed CCF and nanotube composite structures will improve the strength and thermal conductivity of the tooling as compared to traditionally annealed soft composite tools. AM allows for the integration of printable smart sensors to continuously monitor temperature, strain, and pressure within the tool itself, enabling improved process controls and lower inter-part variability. If successful, this technology will decrease soft-tooling costs by 30%, increase process throughput by 50%, and reduce failures in the molding process.

Approach

To increase process throughput, reduce scrap rates, and lower soft-tooling costs, the project is prototyping soft smart tooling using AM techniques incorporating the following concepts:

- Nanomaterial-filled thermoplastics to improve thermal conductivity with added tool strength in 3D continuous fiber printing. This allows for thinner tooling with less thermal gradient and thermal lag.
- Post-curing and post-annealing performed by coupling microwave or induction radio frequency energy directly to the susceptor-enhanced nanomaterials, resulting in reinforcement and improved polymer crystallinity for greater mechanical and thermal properties.
- Temperature, heat flux, strain, and pressure sensors printed into the tool to monitor cure kinetics, voids (especially for resin transfer molding), and spring-in.

Our approach seeks to 3D print nanomaterial enhanced CCF soft tooling with embedded sensors. Incorporating nanomaterials into the soft tooling adds toughness and improved thermal conductivity; EM annealing increases polymer crystallinity, further increasing mechanical and thermal properties; and adding sensors allows the user to monitor temperature and pressure during part manufacturing. Process controls implemented using sensor feedback allows the user to identify when a tool needs to be scrapped and replaced.

Figure II.3.1.16.1 provides a detailed schematic of our approach. The CCF tow, prepared with a thermoplastic prepreg containing our nanomaterials, is printed by the layup head. The nanomaterials incorporated within the prepreg, designed to be EM susceptors, are added at a concentration at which thermal conductivity between z-direction layers increases; this is a major challenge in AM. During printing of the layers using the CCF tow enhanced with nanomaterial-embedded thermoplastic substrate, secondary reservoir heads with conductive inks are used to print thermocouple and/or strain-gauge sensors in situ. Table II.3.1.16.1 provides the milestones and status for FY 2022.

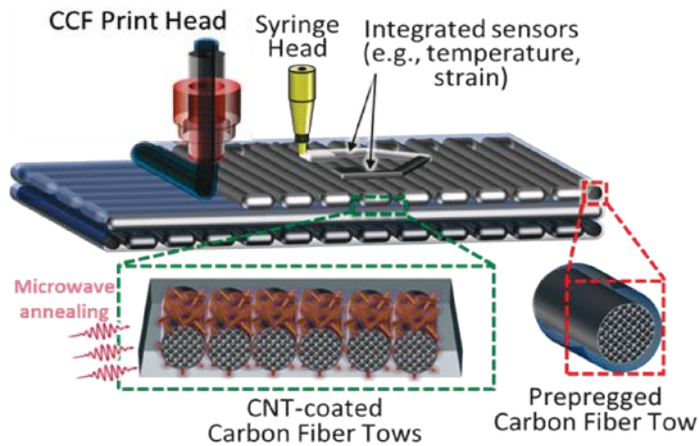


Figure II.3.1.119. Diagram of 3D printing equipment for CCF composites: Source: SRNL.

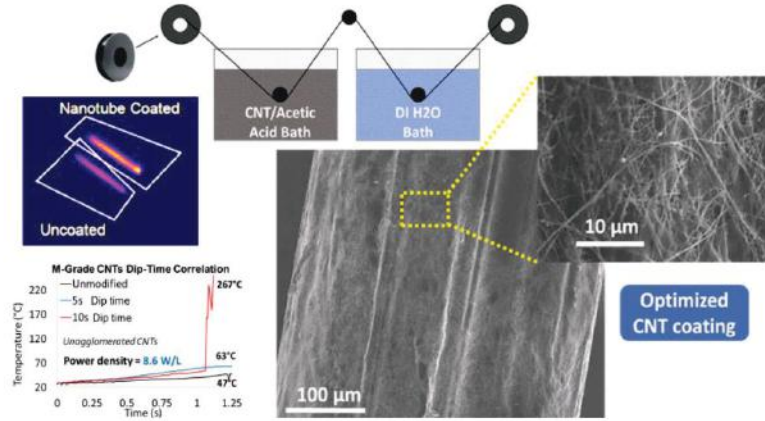
Table II.3.1.16.1. Project Milestones and Status

Milestone Name/Description	Milestone Status
M2.1 Demonstrate SMART sensor integration of at least two sensors into a test coupon.	Complete
M2.2 Optimize compounding, reduce agglomeration, improve filament tolerance. Produce filament.	Complete
M2.3 Demonstrate analytically the potential to reduce energy intensity by at least 40% by process heating	Complete
Year 2 Milestone: Demonstrate at least a 50% increase in throughput and a 20% increase in heat transfer	Complete

Results

The main project goals include increasing thermal conductivity, electrical conductivity, interlaminar shear strength, and other tensile properties. Maximizing the microwave absorption efficiency helps minimize the energy required to achieve these performance goals. CF tows themselves are moderate susceptors, though their susception capability still leaves room for improvement. By increasing the susception at the interface between CF layers, bonding (e.g., interfacial strength, z-directional thermal conductivity) between successive CF layers increases correspondingly. CCF tows are layered atop one another in our composite prints, bonded by a resin infill to form the backbone of tough composite parts. MarkForged CCF has a Nylon 6 sheath. SRNL devised a way to coat commercial CCF tow with a thin layer of carbon nanotubes to improve the microwave susceptibility. The carbon nanotubes were produced by a modified CVD process to obtain 800- μm -long nanotubes. The production line consists of a filament, passing first through a CNT/acetic acid bath at RT and then directly into a DI water bath to quench the reaction, then through a drying oven to remove all the moisture. CNTs were suspended in glacial acetic acid via a rotor stator homogenizer. CNT loading and bath residence time were optimized to produce a homogeneous CNT coating on the surface of the CCF filament, as seen in Figure II.3.1.16.2(a), and still maintain the diameter tolerance for acceptable printing. Mainland Solutions has developed a scaled-up, reel-to-reel, CNT coating line shown in Figure II.3.1.16.2(b) and Figure II.3.1.16.2(c). Initial production was for 300 ft. of test filaments, as shown in Figure II.3.1.16.3(a), but after scaleup, they have printed over 3,000 ft. of test filaments, as seen in Figure II.3.1.16.3(b). The coating line has the capability to coat full rolls of filament at a time.

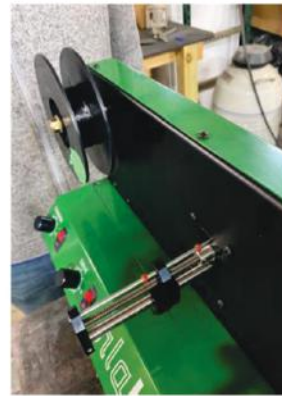
The diameter of the treated CCF filament should be roughly 380 microns to be printed successfully. Glacial acetic acid was chosen as the solvent as it dissolves Nylon 6. Improvements to the CNT coating line for the CCF filaments included a tensioner and lower friction tracking pulleys to ensure the filaments stayed on track without breaking.



(a)

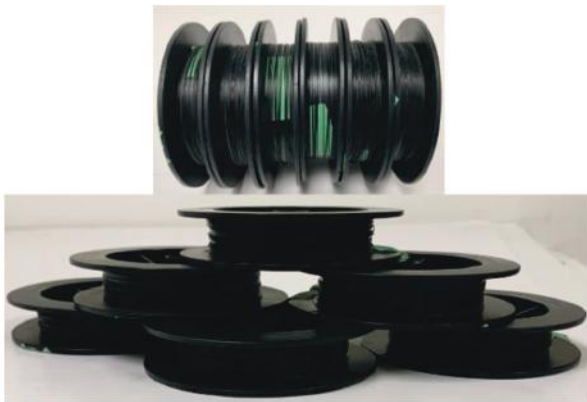


(b)

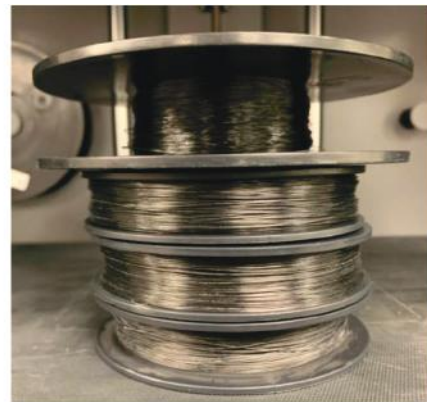


(c)

Figure II.3.1.120. (a) The process for coating the CNTs and micrographs of the CCF filament with an optimized homogeneous coating of CNTs; (b) the scaled-up CNT coating line; and (c) a close-up view of the fiber roller. Source: SRNL.



(a)



(b)

Figure II.3.1.121. (a) 300 feet of CNT-coated CCF filament on six rolls, and (b) larger rolls of 3,000 feet of CNT-coated CCF after scaleup. Source: SRNL.

As the next step, parts with the CNT-coated CCF were 3D-printed, utilizing the percolation of nanotubes to add strength and thermal conductivity. Short-beam shear, tensile dog bones, and thermal pucks were all printed with CNTs in FY 2022. Figure II.3.1.16.4 provides the results of the short-beam shear tests, while Table II.3.1.16.2 shows a comparison of the short-beam shear data. SRNL demonstrated that microwave annealing successfully improved the thermal conductivity and mechanical (tensile) strength of the tooling composites. This data represents a greater than 20% increase in shear strength for 30 minutes of microwave annealing.

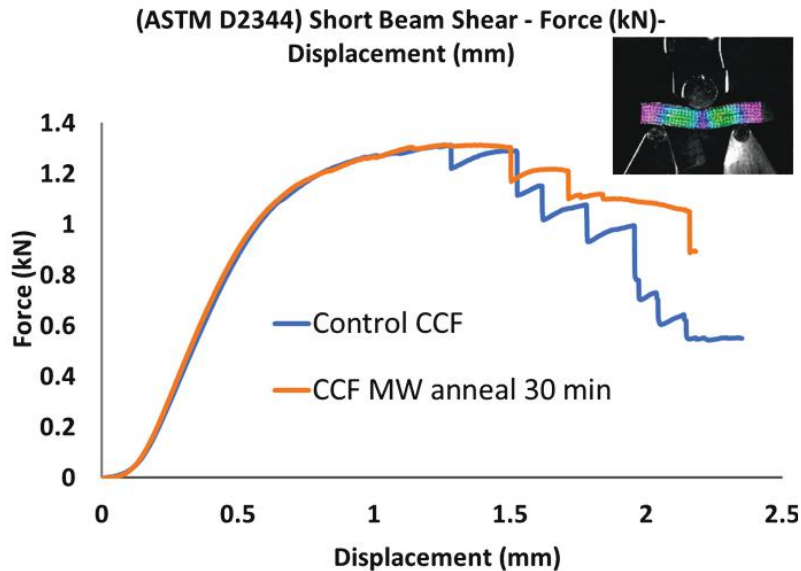


Figure II.3.1.122. Short-beam shear data showing a 20% increase in shear strength and 250 microns longer displacement for breakage with the microwave-annealed coupon. Source: SRNL.

Table II.3.1.16.2. Short-Beam Shear Data Comparison

Composition	Short-Beam Shear Force (MPa)
Nylon + CCF	27.08
Nylon + CCF + Microwave-annealed	32.62

The data shown in Figure II.3.1.16.5 depict the temperature change between a 3D-printed CNT-coated CCF thermal sample that was annealed for 30 minutes at 10.5 W/L power density in the MARS6 microwave versus a 3D-printed CCF sample that was thermally annealed at 120°C for 60 minutes. The thermal data was collected by placing the samples on a hot plate at 120°C and using an infrared camera to record the change in temperature of the thermal pucks versus time. A non-annealed control was also tested to verify the increase in thermal transfer. Figure II.3.1.16.5 shows the thermal transfer data collected over one minute of the three samples and illustrates the increase in heat transfer that the CNT-coated CCF, after being microwaved at a 10.5 W/L power density for 30 minutes, has over both the non-annealed sample, and the CCF sample that was thermally annealed at the same bulk temperature of 120°C for 60 minutes. The thermal transfer data represents an average of a 21%–24% increase in thermal transport of the CNT-coated sample over the control. Further, the CCF sample thermally annealed for twice the time as the CNT sample does not quite show the greater than 20% increase in thermal transfer indicating that even more time will be needed for the thermal annealing to achieve the same rate of thermal transfer as the CNT-coated samples. This represents a greater than 50% increase in throughput of the CNT-coated microwaved sample over the CCF thermally annealed sample.

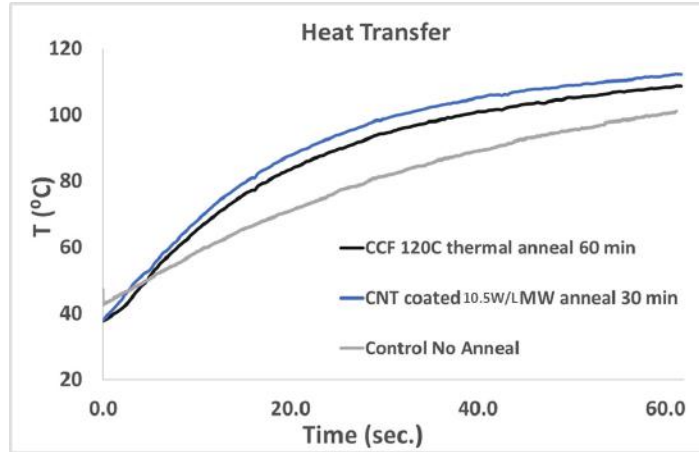


Figure II.3.1.123. Thermal transfer data of thermal pucks. Source: SRNL.

For this project, a prepreg composite material and process is being proposed for the prototype smart tool demonstration, as seen in Figure II.3.1.16.6(a) and Figure II.3.1.16.6(b). To understand the manufacturing process effects on the material system being used for the automotive component, a representative sub-component-level manufacturing study is often performed. For the proposed investigation, an axisymmetric tool profile—an asymmetric section extruded along the direction perpendicular to the cross-section plane—is being used. With a metal baseline tool already in use for research at Clemson University, this geometry can provide an objective comparison of the 3D-printed tool’s performance with the metal baseline and can also help improve the 3D-printed tools design to sustain the loads experienced during manufacturing. The end-use application of the proposed tool concept is for automotive components traditionally manufactured using thermoplastic prepreg preforms, thermoset prepreg vacuum bagging, or thermoset vacuum-assisted resin transfer molding with a moderate production-scale. Thus, the functional unit chosen for the LCA is ‘the number of tools required to produce 10,000 parts per year.’ This was done to account for the fact that the different material systems used for the tools will dictate the durability of the tool, and thus affect the number of CFRP components that can be produced for the tool. The study as mentioned above does not consider the EOL phase as the goal of the study is to demonstrate the advantages in the manufacturing of the tool.

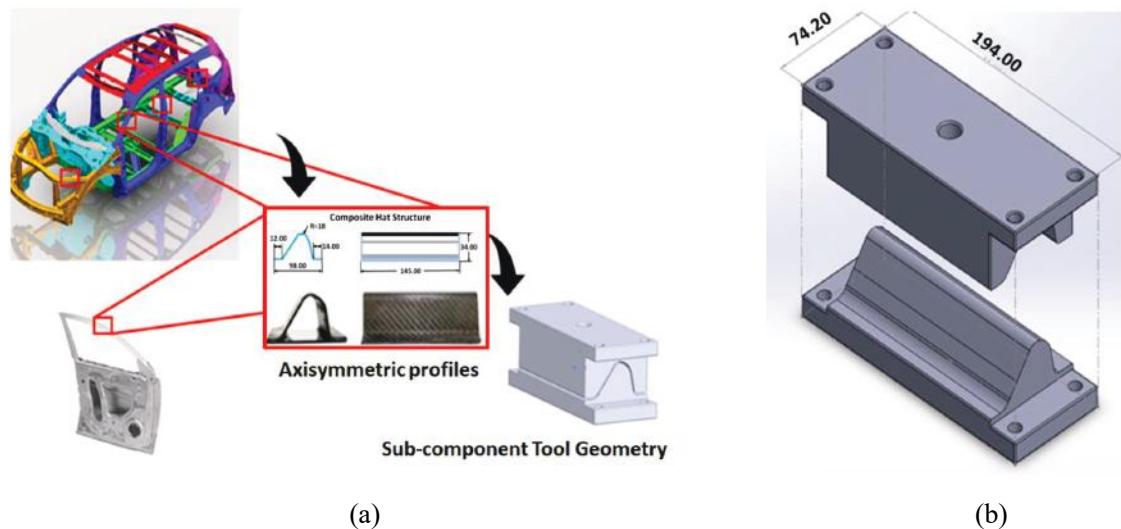


Figure II.3.1.124. (a) Thermoplastic prepreg forming tool geometry for concept demonstration and (b) sub-component tool parts geometry (dimensions in mm). Source: SRNL.

The techno-economic analysis (TEA) performed by Clemson University looked at a single score energy comparison to manufacture each part, whether it be the metal-machined tooling, the CFC tooling, or the 3D-printed CCF tool printed at SRNL, as seen in Figure II.3.1.16.7.

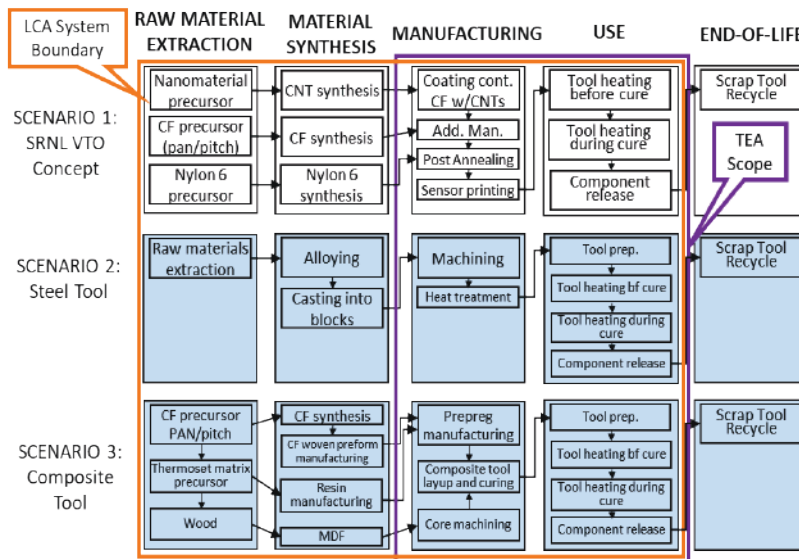


Figure II.3.1.125. TEA and LCA scenarios, processes, and identified scope. Source: SRNL.

Machined-metal tooling is 154% more energy-intensive to produce compared to SRNL’s tooling technology, and CFC tooling is 84% more energy-intensive. Figure II.3.1.16.8 demonstrates an argument about the total energy of production, Figure II.3.1.16.9 points to the reduction in the annealing energy used for microwave annealing versus convection oven annealing. This data shows a 927% increase in energy consumed per cubic meter of tooling part volume with the convection oven over the microwave. We believe that Clemson University’s TEA, guided by energy usage captured in tests at SRNL as well as their own market analysis of manufacturing expenses and energy envelopes, has provided an analytical basis to show that this technology has the potential to show greater than a 40% reduction in energy usage.

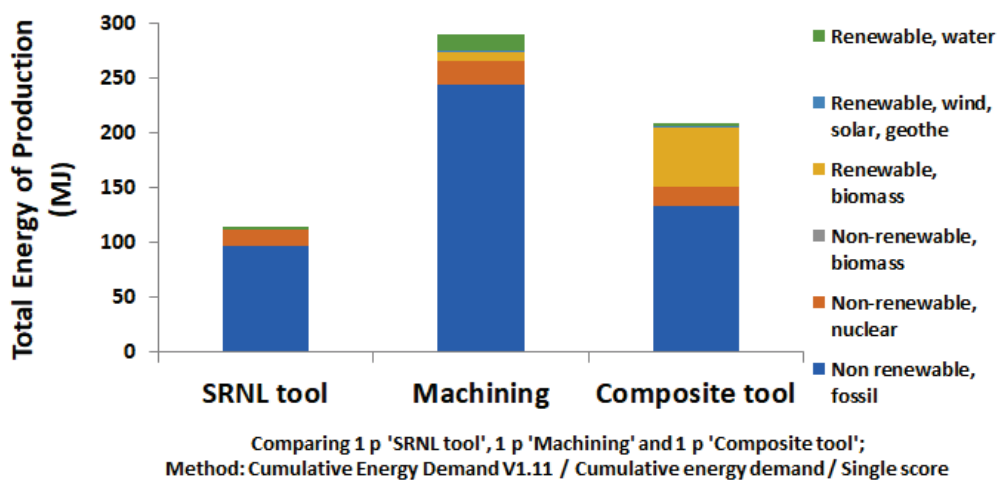


Figure II.3.1.126. Single score energy analysis comparing the three different tooling options. CFC and machined-metal tooling are 84% and 154% more energy-intensive to produce, respectively, over the SRNL 3D-printed CF tooling. Source: SRNL.

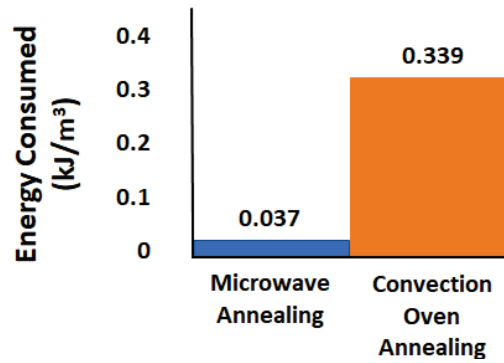


Figure II.3.1.127. Comparison of energy consumed per cubic meter for the annealing of CF soft tooling. SRNL's 3D-printed tooling shows an order of magnitude less energy usage per cubic meter. Source: SRNL.

Conclusions

In FY 2022, our team continued to make improvements to the 3D-printed sensor-integrated smart composite tooling to measure temperature, strain, and pressure during manufacturing processes, such as vacuum bag molding or autoclaving.

We have demonstrated that smart sensors can be successfully integrated onto 3D-printed test coupons by 3D-printing silver paint. More specifically, strain-gauge and thermocouple sensors were targeted and successfully printed onto the coupon. A comparison of the voltage response of the traditional thermocouple to a 3D-printed thermal sensor over a range of temperatures demonstrates a functional thermocouple. The strain response of the 3D-printed sensor has shown a 12% improvement in resistance compared to conventional strain sensors.

Filament productions have undergone significant improvements by suspending CCF in CNT/acetic acid bath at RT followed by placement into a water bath, and subsequent drying resulted in maximized strength and thermal conductivity compared to nylon. This treatment did not result in reduction of the filament diameter and filament thus produced was demonstrated to have minimal degradation to the surface and, therefore, to be suitable for 3D printing.

Comparative thermal studies of a microwave-annealed CNT-coated thermal coupon and a thermal-annealed CNT-coated coupon versus CF without any coating have shown a greater than 20% increase in thermal transport and greater than 50% increase in throughput for CNT-coated microwaved samples. Based on the TEA performed by our collaborators at Clemson University, we believe that 3D-printed tooling technology will result in 40% energy usage reduction compared to conventional machine tool manufacturing.

Acknowledgments

SRNL would like to acknowledge our sponsor, the DOE VTO, and Dr. H. F. Wu, the DOE VTO Technology Manager. This work was performed at SRNL and managed by Battelle Savannah River Alliance in collaboration with Clemson University's International Center for Automotive Research and Mainland Solutions, LLC. Key contributors include M. Craps, D. Digby, N. White, J. Meany, and A. Mullins of SRNL; and A. Deshpande and U. Lad of CU-ICAR.

II.3.1.17 Functionally Designed Ultra-Lightweight Carbon Fiber-Reinforced Thermoplastic Composites Door Assembly (Clemson University)

Srikanth Pilla, Principal Investigator

Department of Automotive Engineering
 Department of Materials Science and Engineering
 Clemson University
 4 Research Dr., Suite 340
 Greenville, SC, 29607
 E-mail: spilla@clemson.edu

Rich Davies, Composites Core Program Manager

Oak Ridge National Laboratory
 Materials Science and Technology Division
 1 Bethel Valley Rd.
 Oak Ridge, TN 37831
 E-mail: daviesrw@ornl.gov

H. Felix Wu, DOE Technology Development Manager

U.S. Department of Energy
 E-mail: felix.wu@ee.doe.gov

Start Date: December 1, 2015 End Date: November 30, 2021 (12-month no-cost extension)
 Project Funding (FY 2022): \$1,956,158 DOE share: \$1,956,158 Non-DOE share: \$0

Project Introduction

A promising route to achieve the 2025 Corporate Average Fuel Economy standards involves decreasing vehicular weight by incorporating lightweight materials—coupled with component redesign—to improve overall fuel efficiency. Indeed, one recent study indicates the simple replacement of current metallic doorframes with CF-reinforced plastic composites can reduce the overall weight of the component by nearly 58% [1]. The goals of this project are to achieve a weight-reduction of at least 42.5% as compared to a baseline door structure at the cost of less than \$5/lb., all while saving on energy metrics without compromising the fit, function, crash, and noise, vibration, and harshness requirements. The strategy for achieving these targets involves a holistic systems approach through the integration of unique designs, novel materials, manufacturing technologies, and joining/assembly of subsystems to ensure the developed technologies are ready for commercialization.

Objectives

The objective of this project is to reduce the weight of a door assembly by at least 42.5% as compared to a baseline driver's side front door with an expected cost increase of less than \$5/lb. in weight saved. The basis for design is a 2013 mid-sized sport utility vehicle's door from our OEM partner with an assumed production volume of 20,000 vehicles annually. These criteria will either meet or exceed the fit, function, crash, and noise, vibration, and harshness requirements of the baseline door.

The intent is to (1) enable the radical redesign of the baseline door via a holistic systems approach through the integration of unique designs, (2) use novel materials to render the door 100% recyclable, and (3) investigate manufacturing technologies and joining/assembly of subsystems to ensure the developed technologies are ready for commercialization. The partner organizations listed in Table II.3.1.17.1 are providing highly leveraged knowledge and expertise to ensure the success of this effort.

Table II.3.1.17.1. Project Participants

Universities	Industry Partners	Computation Partners
Clemson University	OEM	Altair Engineering
	Tencate, Lanxess	Core-Tech Systems (Moldex 3D)
University of Delaware	Krauss Maffei, Trexel Inc.	MSC Software (Digimat)
	Proper Tooling	LS-Dyna

Approach

The project entails the use of a systems-level approach that begins with systematic evaluation and benchmarking of the door and its subassemblies. In collaboration with our partnering companies and commercial suppliers, we are evaluating a variety of CF-thermoplastic material forms for structural components (i.e., novel unidirectional and fabric prepregs, co-mingled fabrics, high aspect ratio discontinuous fibers, performance thermoplastic resins, novel fiber architectures, and localized reinforcements) and alternative solutions for glazing, trim, and other sub-components. The initial focus involves creating the structural component and a materials database for all parts of the door structural assembly (i.e., outer shell, inner panel, carrier, and anti-intrusion beam[s]).

A two-phase integrated design and manufacturing optimization approach was adopted to obtain the optimal manufacturing process parameters of the thermoplastic materials and the optimal structural design parameters of the door. A top-level trade study was also conducted to determine at least two candidate designs for optimization. The design parameters include (a) thermoforming and injection-molding parameters (e.g., pressure and temperature), (b) fiber parameters (e.g., material, length, diameter, volume fraction), (c) matrix parameters (e.g., material, volume fraction), (d) structural wall thickness, and (e) material density distribution. The research team will use four analysis tools—Moldex3D, Digimat, and LS-DYNA Implicit and Explicit—to construct the manufacturing to response analysis pathway [2–4]. The team will fabricate a door based on this optimal design for testing in accordance with OEM performance requirements.

Results

Manufacturing of Structural Composite Components

The team's focus for FY 2022 was on manufacturing the thermoplastic door and its structural sub-components. To achieve this, extensive tooling and manufacturing trials were carried out for all structural components beginning with the inner beltline stiffener, as observed in Figure II.3.1.17.1(a) and Figure II.3.1.17.1(b).

The material handling frame was modified with line clamps to ensure a higher clamping area. Once the frame was modified, trials were carried out using appropriate safety attire and precautions. The trials consisted of three distinct steps as indicated in Figure II.3.1.17.2: (1) the heating of the blank, (2) the transport of the blank and frame to the press, and (3) the forming step, which consisted of holding the blank in the heated tool at a fixed consolidation pressure for a certain dwell time, and then releasing the pressure.

A total of 16 parts were made where tool temperature was gradually increased from 190–220°F, and finally 250°F. The parts at 190°F resulted in parts that had poor consolidation and several dry areas of exposed CF. Upon increasing the temperature, the part appearance improved, and further trials were carried out to decrease the areas that had dry and exposed CF, as shown in Figure II.3.1.17.3. Furthermore, upon reaching 250°F, the team still noticed a few areas of concern and realized the tool gap was larger in these regions. High-temperature aluminum tape was adhesively glued onto the tool surface to locally build-up material in areas of concern. The final part that was made had good consolidation and achieved final part thickness, the tool was sent back to be re-machined, which decreased the overall tool gap.

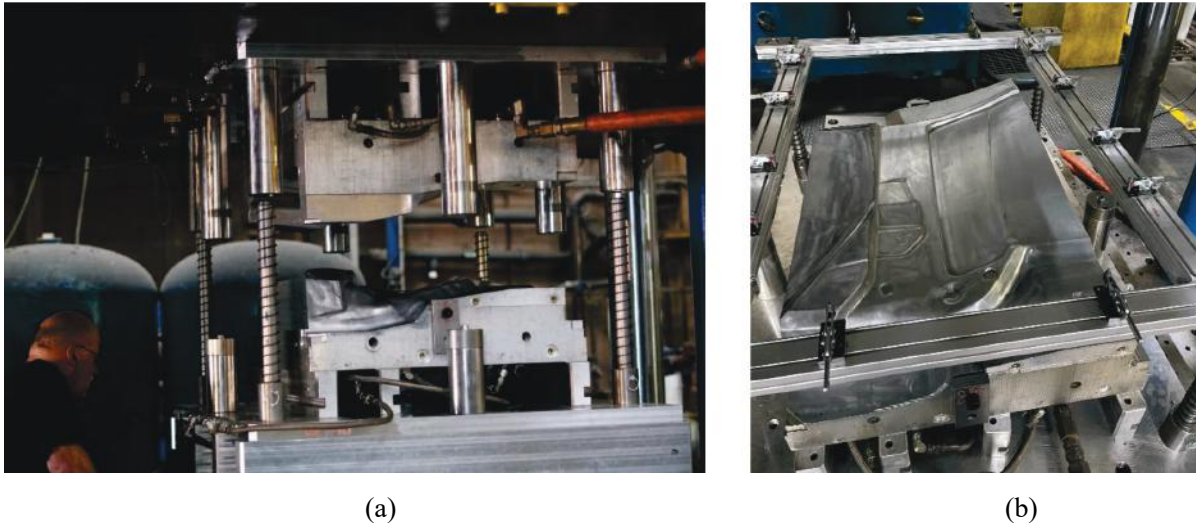


Figure II.3.1.128. Overview of (a) tooling installation trials for (b) inner beltline stiffener.
Source: Clemson University.



Figure II.3.1.129. Process flow for stamping: heating, transport and forming of material.
Source: Clemson University.

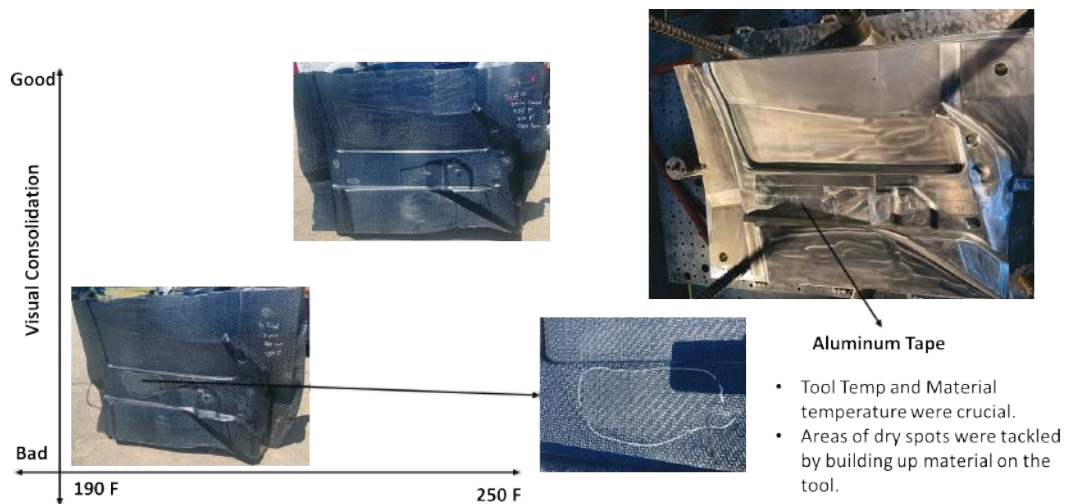


Figure II.3.1.130. Trials showing visual appearance of sample as a function of tool temperature.
Source: Clemson University.

Figure II.3.1.17.4(a) shows the formed part on the heated press, while Figure II.3.1.17.4(b) shows the post-processed parts that Clemson University is currently analyzing. The team is currently awaiting modification of

the tool and material handling frame in order to run the PA6 carbon material we have already received. Minor deviations were observed when the team compared the 3D scanned surfaces with the computer-aided drawing designs in features with a bend radius and in regions where there was significant overhang. However, the deviations in case of the bend radius were not as significant and were deemed to be good enough to be accommodated within the 1-mm-thick adhesive layer.



Figure II.3.1.131. (a) Formed inner beltline part on the heated tool. (b) Post-processed parts being evaluated. Source: Clemson University.

The manufactured belt line stiffener was scanned to study the differences obtained between the designed and manufactured part. The tolerance values were set between +6 mm to -6 mm for the analysis. The results that were obtained are being used to make further improvements that can be obtained for the manufactured part by altering the manufacturing process to obtain precise results.

As observed in Figure II.3.1.17.5, the manufacturing of the second CF-reinforced thermoplastic structural component of the proposed composite door design, the inner panel, required a custom material handling frame with spring-loaded clamps positioned at specific locations. The frame was loaded onto a custom-designed fixture to mount the frame and hold it inside the oven. The glass fiber and polypropylene material was heated up to 390°F, or an oven temperature of 415°F, which was measured using a temperature gun after heating for 9.5–10 minutes. The tool temperature was maintained at 250°F for both halves and a tonnage of 3000 tons proved sufficient to achieve the desired consolidation and finish. The end component was cut across to measure the thickness of the component at various deep draw locations to ensure that the thickness was uniform and within the desired range. The CF-PA6 material required additional metal rods across the frame to prevent excessive sag of the material when heated. The CF-PA6 material was heated up to 470°F, or an oven temperature of 485–490 F, with the tool temperature set at 325°F. However, due to the large volume of the convection oven, the heating rate was quite low, and it took close to 30 minutes for the CF-PA6 material to reach its processing temperature. Furthermore, a significant heat loss was observed in the time it took to transfer the material from the oven to the tool. The team is working on overcoming these challenges.

The door has three sheet metal components that have been stamped and welded, which are currently awaiting the inner frame to be fit-tested and then adhesively bonded. Lastly, the class A panel tool is ready and thermoforming trials are currently underway. Assembly of the door and its structural components is expected in January 2023.



Figure II.3.1.132. Overview of manufacturing progress on the inner panel part. Source: Clemson University.

Implement Static and Dynamic Tests on Prototype Composites Door

Static testing fixtures for the thermoplastic composite door assembly were manufactured with the specific goal to test two load cases, as shown in Figure II.3.1.17.6—namely door sag and door sash rigidity—which addresses the performance of the door assembly for loads typical of daily use and abuse. Furthermore, three dynamic tests have been scheduled at our OEM partner’s facility, which are a combination of Federal Motor Vehicle Safety Standards (FMVSS) and an internal OEM test geared for doors. An overview of these tests is outlined in Figure II.3.1.17.6. Testing was scheduled for the summer of 2022.

1. FMVSS 214s (Quasi-static pole test)

A cylindrical barrier is used to deform the door for 18 inches under quasi static loading condition.

2. ASIS Dynamic Door Test

Similar to QSP, but able to replicate dynamic impact. Tests the door in isolation for A-B comparison testing.

3. IISH SI MDB(DB)

A moving deformable barrier is impacted with a stationary vehicle at 50 km/h.

Note: FMVSS = Federal Motor Vehicle Safety Standards; ASIS = Advanced Side Impact System; IISH SI MDB(DB) – Insurance Institute for Highway Safety Side Impact Moving Deformable Barrier

Figure II.3.1.133. Overview of progress on static testing fixture and dynamic tests planned. Source: Clemson University.

Conclusions

The research focus during FY 2022 centered around completing manufacturing for all structural components, which included the large thermoplastic composite components and stamped sheet metal parts. The first set of thermoplastic composite beltline stiffeners and inner panels consisting of glass fiber and polypropylene were successfully manufactured. The team is currently focusing on completing manufacturing of PA6 and CF composite parts, and then focus on assembly and testing of the door in the first two months of next year.

Key Publications

1. Limaye, M., S. A. Pradeep, A. Kothari, S. Savla, A. Agha, S. Pilla, and G. Li, 2022, “Thermoforming process effects on structural performance of carbon fiber reinforced thermoplastic composite parts through a manufacturing to response pathway,” *Compos. B. Eng.*, Vol. 235, Art. 109728. <https://doi.org/10.1016/j.compositesb.2022.109728>.

References

1. Kelly, J. C., J. L. Sullivan, A. Burnham, and A. Elgowainy, 2015, “Impacts of vehicle weight-reduction via material substitution on life cycle greenhouse gas emissions,” *Environ. Sci. Technol.*, Vol. 49, No. 20, pp. 12535–12542. <https://doi.org/10.1021/acs.est.5b03192>.
2. Mi, H.-Y., X. Jing, J. Peng, L.-S. Turng, and X.-F. Peng, 2013, “Influence and prediction of processing parameters on the properties of microcellular injection-molded thermoplastic polyurethane-based on an orthogonal array test,” *J. Cell. Plast.*, Vol. 49, No. 5, pp. 439–458. <https://doi.org/10.1177/0021955X13488399>.
3. Chang, S. H., and S. S. Cheon, 2006, “In-plane directional mechanical properties of carbon fabric skins in sandwich structures after thermoforming,” *Compos. Struct.*, Vol. 75, Nos. 1–4, pp. 577–581. <https://doi.org/10.1016/j.compstruct.2006.04.033>.
4. Yu, Y., J. Ye, Y. Wang, B. Zhang, and G. Qi, 2013, “A mesoscale ultrasonic attenuation finite element model of composites with random-distributed voids,” *Compos. Sci. Technol.*, Vol. 89, pp. 44–51. <https://doi.org/10.1016/j.compscitech.2013.09.006>.

II.3.1.18 Multifunctional Smart Structures for Smart Vehicles (Ford Motor Company)

Patrick Blanchard, Principal Investigator

Ford Motor Company
2101 Village Rd.
Dearborn, MI, 48121
E-mail: pblanch3@ford.com

Rich Davies, Composites Core Program Manager

Oak Ridge National Laboratory
Materials Science and Technology Division
1 Bethel Valley Rd.
Oak Ridge, TN 37831
E-mail: daviesrw@ornl.gov

H. Felix Wu, DOE Technology Development Manager

U.S. Department of Energy
E-mail: felix.wu@ee.doe.gov

Start Date: October 1, 2020 End Date: December 31, 2023
Project Funding (FY 2022): \$9,021,422 DOE share: \$5,157,264 Non-DOE share: \$3,864,158

Project Introduction

It is always desirable to decrease vehicle mass while improving structural integrity. Development of a new class of multifunctional composite materials and processing technologies can lead to lightweight fully integrated smart structures and surfaces. These new materials and processing methods promise to have application to a broad range of automotive applications, thus magnifying the impact on the ability to achieve long-term improvements in fuel economy and/or vehicle range.

Objectives

This project will develop a new class of recyclable multifunctional composite materials to produce lightweight smart structures and surfaces. Functional high stiffness conductive composites will be processed using novel water assisted injection-molding, while integrating continuous fiber and additively manufactured hard points for optimized load transfer. Methods for integration of sensing functionality and controls will be developed to reduce system cost while providing a new capability for structural health monitoring. Final part performance and processing parameters will be optimized using AI/ML methods. This new class of composites is applicable to a broad range of vehicle interior, exterior, and battery enclosure systems. By way of demonstration, a vehicle instrument panel cross car beam will be developed to provide a 40% mass savings compared to steel while maintaining a cost penalty of less than \$3 per pound saved. These technologies will be validated for implementation by a uniquely qualified project team comprised of a U.S. automotive OEM, Tier 1 and Tier 2 suppliers, and key contributions coming from ORNL, Purdue University, and MSU.

Approach

The project covers three budget periods:

- Budget Period 1 was completed and focused on concept design and development
- Budget Period 2 is ongoing, covering design, materials and process optimization
- Budget Period 3 will demonstrate prototype validation and testing.

In the first year, a conceptual design for a new composite-based cross car beam was developed using CAD design and based on laboratory testing of candidate materials.

In the second year, the cross car beam design was further refined based on manufacturing feasibility trials and material and process optimization. Unit cell operations for integration of all overmolded structural inserts and sensors were demonstrated. A completed CAD design for the cross car beam was prepared and issued to a supplier for prototype tooling fabrication.

In the final year, the team will build prototype tooling to manufacture cross car beams for testing and validation. Materials and processing optimization will continue. Full-scale injection-molding will be demonstrated. The ability to fixture inserts and continuous fiber into the injection mold and retain them through the injection process will be demonstrated.

To manage all project objectives, 11 different working groups have been established in addition to Task 0 that encompasses project management related tasks, as indicated in Figure II.3.1.18.1. Task 1, “Component Design, Analysis and Prove-out,” is considered the lead work stream with Tasks 2 through 11 as dependents. Therefore, the reporting included in this annual report will highlight the continued work on the design concept out in FY 2022 followed by status on the supporting work streams.

RASIC Chart: Multi-Functional Smart Structures For Smart Vehicles					
R: Responsible: The Institute/Company Responsible for this task					
A: Approve: The company/institute giving the approval					
S: Supporting: The Company/Institute giving support for the completion of the task					
I: Informed: The Company/Institute to inform about this task					
C: Consulted: The company/institute that can act as expert in regard to the task					
Task 0. Program Management				R	
Task 1. Component Design, Analysis & Prove-Out	I	S	S	R, A	S
Task 2. Formulation/Compounding of novel materials	I	I	R	S, A	R
Task 3. Water-Assist Injection Molding (WAIM) Process Development	S	I	S	R	S
Task 4. Tow/Tape Placement of Continuous Fiber	I	R	S	S	S
Task 5. Sensor Integration	I	S	S	R	S
Task 6. Additive Manufactured Hardware Attachment Points	S	S	R	S	S
Task 7. High Volume Manufacturing Concept Feasibility Demonstration (sub-scale)	S	S	S	S	R
Task 8. Process Scale Up & Demonstration	S	S	S	S, A	R
Task 9. Additive Manufacturing of Segmented Tooling	I	S	R	S	I
Task 10. Artificial Intelligence/Machine Learning For Process Optimization		I	R	I	S
Task 11. Closed Loop Recycling		I	R	S	S

Figure II.3.1.134. Project task breakdown. Source: Ford Motor Company.

Results

Task 1. Component Design, Analysis, and Prove-Out

The design activities under Task 1 were broken down into sub-tasks 1.1 through 1.6, as shown in Figure II.3.1.18.2. The milestones scheduled in Budget Period 2 are also shown in Table II.3.1.18.1. The following sections describe ongoing studies in support of active work streams.

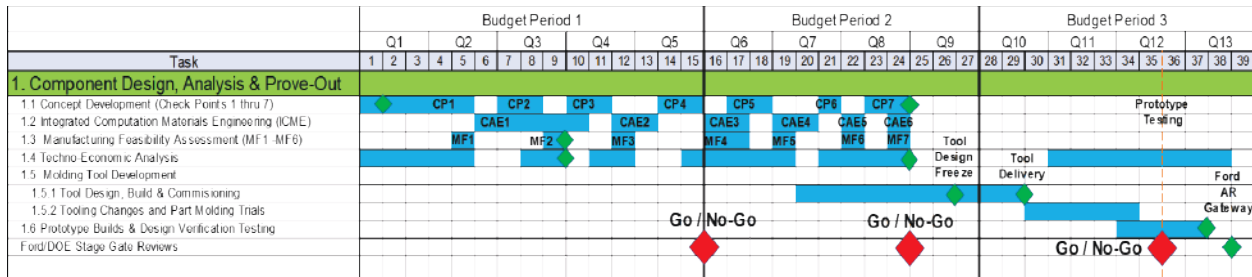


Figure II.3.1.135. Task list for component design work stream. Source: Ford Motor Company.

Table II.3.1.18.1. Milestones For Task 1 Work Stream Activities

Milestone (Project Month)	Lead Organization	Description
2.1.1 CAD Freeze (M24)	Ford	Complete CAD design freeze for cross car beam for tooling quote.
2.1.4 Cost Drivers (M24)	Purdue	Define and rank main cost drivers. Input is based on refined design and production alternatives, selected manufacturer, and input sensitivities.
2.1.5.1 Tool Design (M26)	Ford	Secure (3) tooling quotes for review. Complete tool design to accommodate materials/sensor handing and additively manufactured inserts.

Tasks 1.1 – 1.3

At the end of BP1, the concept design for the cross car beam was established. Therefore, BP2 focused on further refinement of this design to account for a more comprehensive set of load cases, system requirements, and manufacturing constraints. The bulletized list below highlights key work activities that have been ongoing over the past three-quarters:

- Refinement of geometry surfaces to resolve die lock and related manufacturing concerns
- Revision of the water channel to streamline the routing and geometry profile
- Finalizing the instrumental panel surface theme for Class A visible surfaces
- Manufacturing flow simulations in Moldflow/Moldex3D to set parameters and tooling assumptions in the injection-molding process
- Design revisions of AM inserts, sensor substrates, and multi-tow (M-Tow) materials
- Processing studies at Yanfeng to develop a final strategy for automated material handling and placement for all items to be incorporated in the cross car beam design
- Validation of material properties through testing of representative samples excised from plaques and components.

These work activities have led to the CAD rendering design of the beam shown in Figure II.3.1.8.3. This image shows the instrument panel cross car beam structure with the steering column sub-assembly in position. Based upon the status at the end of the Budget Period 2 gateway review, the weight and cost comparison to the steel baseline is shown in Figure II.3.1.8.4. Note that a weight optimization study will be performed in the first quarter of 2023 to achieve further mass efficiencies towards meeting the 40% mass savings target.

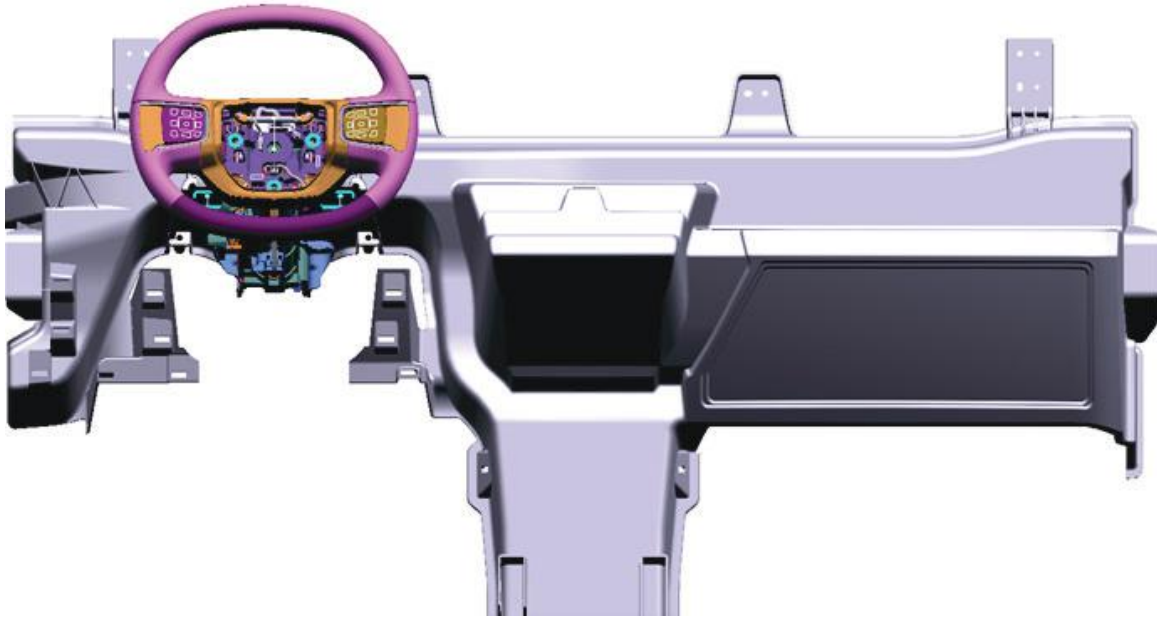




Figure II.3.1.136. CAD rendering of instrument panel cross car beam with relative placement of the steering column sub-assembly. Source: Ford Motor Company.

	Steel CCB	Next Generation	
			
	2022 Economics		
	Steel XCB Design	Composite IP-XCB	Target
Mass (kg)	15.00	7.942* - 8.642	
Over-molded items (kg)	-	0.673	
Steering column bracket	-	0.720	
Cost (\$)*	\$106.27	\$136.02	
Cost Premium	-	\$29.75	
Mass Savings (kg)	-	4.97 - 5.67*	
Mass Savings (%)		33.1% - 37.8%*	> 40%
Weight Buy (\$/kg)	-	\$5.25* - \$5.99	
Weight Buy (\$/lb)	-	\$2.38* - \$2.72	< \$5/lb per SOPO < \$3/lb in submission proposal

Based upon TCM output from Purdue model plus an inflation hedge for material cost

Figure II.3.1.137. Business and weight-savings assessment of the cross car beam design concept at the end of BP1. Source: Ford Motor Company.

Task 1.4: Techno-Economic Analysis

During BP1, the team at Purdue created a technical cost model to determine the commercial viability of the technologies under development. This led to the business case shown in Figure II.3.1.18.4 that was presented at the end-of-year gateway review. Since this time, the team has been updating the capabilities of the model to account sensitivity to input parameters plus the cost implications of the in-house versus sub-contracted sub-assembly manufacturing.

Task 1.5: Prototype Molding Tool Development

In preparation for Budget Period 3, an evaluation of prospective tooling suppliers was completed to determine sources capable of integrating the technology content of the multifunctional cross car beam. A request for a quote package was generated and issued to three tooling vendors for review, which are identified in the following list:

- Hi-Tech Mold & Engineering, Rochester Hills, MI, USA
- Cavalier Tool & Manufacturing, Windsor, ON, Canada
- Paragon, Grand Rapids, MI, USA.

As the timing chart in Figure II.3.1.18.2 indicates, tool design freeze was achieved in November 2022, just ahead of fabrication and delivery in 2023. This will support prototype part production throughout Budget Period 3.

Task 2. Formulation/Compounding of Novel Materials

The goal of the Task 2 work stream is to design a novel, multifunctional material that can replace a traditional steel substrate that is used in a conventional cross car beam design. However, this transition from steel to a CF-based material results in reduced conductive properties, which can negatively impact the grounding, static dissipation, and electromagnetic shielding that is offered with a metallic design. To improve conductive performance, the materials team has explored bulk modification of the polymer matrix using conductive fillers, as well as the local integration of conductive pathway through overmolding (e.g., Task 4). For Task 2, Budget Period 2 investigations extended the candidate list of fillers to determine the potential of three different variants of carbides and nitrides of transition metals (MXene) conductive filler (e.g., milled MAX, MXene powder, MXene aerogels) from its parent precursor $M_{n+1}AX_n$ (MAX) phase. The MXene conductive filler was compounded with neat polyamide 66 (PA66) using Brabender equipment to uniformly mix the fillers into the polymer system. The compounded material was further processed to create test samples using a mold and a hot-press and was tested for their electrical and mechanical properties.

Electrical and Mechanical Properties of MXene

The electrical conductivity of PA66/MXene was measured using a 4-probe method with an inductance, capacitance and resistance meter. Using silver epoxy, aluminum (Al) tape (electrodes) was attached to the end of the samples (measuring directions). The measured electrical resistances of all the samples showed very high (> 106 S/cm) indicating that the 5 wt.% MXene provided no further improvement over previous samples compounded with carbon nano tubes. It is believed that the lower aspect ratio of MXene and non-uniform dispersion of the MXene flakes are the main reasons for the low electrical conductivity of PA66/MXene composites. Samples used for the electrical conductivity were cleaned and reused for mechanical testing. Due to the size and material quantity restrictions, only flexural testing was conducted via a three-point bending method. The results are depicted in Figure II.3.1.18.5.

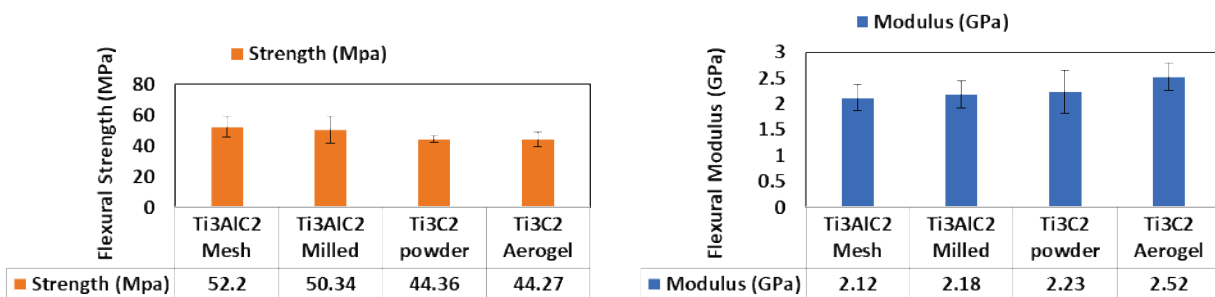


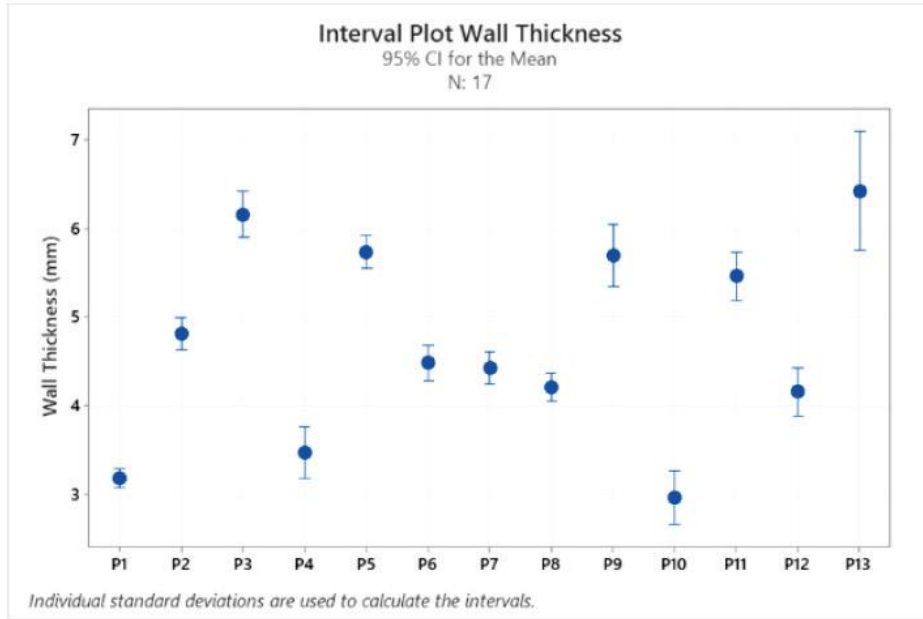
Figure II.3.1.138. Flexural strength and flexural modulus of PA66/MXene composites.
Source: Ford Motor Company.

The flexural strength of PA66/MXene was observed to reduce with an increased flake size. For example, the MAX phase (Ti_3AlC_2) had a particle size of 500–600 μm , while the milled MAX phase was 20–37 μm . The multilayer MXene powder and MXene aerogel also exhibited size reduction creating a larger surface area. The reduction in the flexural strength suggests that the surface of MXene did not bind with PA66 and created defects with an increased surface area. The flexural strength is dictated by the defects in the composites. On the other hand, increased flexural modulus with the increased surface area of the MXene flakes suggests that MXene possesses very high stiffness. MXene is a new type of two-dimensional material that have potential in improving the electrical and mechanical properties of the composites; however, additional studies are needed to investigate the surface chemistry of MXene to incorporate higher loadings of MXene in the matrix and also to enhance compatibility between polymers including PA66. Moreover, the raw material cost of MXene (\$200–400/g) is significantly higher than the conventional conductive fillers (\$200–600/kg), and thus, the team had decided not to include MXene in future investigations. However, from a research standpoint, the team believes that the study provides a valuable datapoint in identifying the most cost-effective options for near-term automotive applications.

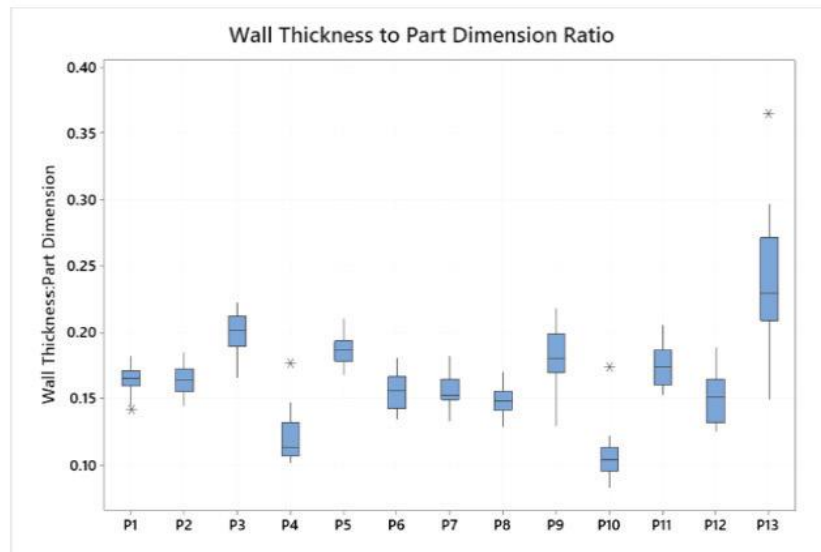
Task 3. Water-Assist Injection-Molding (WAIM) Process Development

To enhance structural design of the cross car beam, WAIM technology is being investigated to allow continuous closed sections within the finished component. Budget Period 2 has focused on further process development studies using a base polypropylene glass fiber material (PP45SGF). This allowed much of the process development to be completed on a commercially existing compound before transitioning over to the material designated for the cross car beam. During these studies, data collection for press-side quality and process design of experiments were collected to establish processing windows and troubleshoot molding defects.

An example of wall thickness data can be found in Figure II.3.1.18.6, which was taken from cross-sectioned parts produced during a molding trial. Wall thickness variation is observed as the cross-sectional area changes throughout the part with a wall thickness ratio of 15%–20% of the part cross-sectional area. It should be noted that a variation in wall thickness is expected as thickness is a function of overall section dimensions and the shape of the profile.



(a)



(b)



(c)

Figure II.3.1.139. (a) (b) Wall thickness variation along the length of the (c) demonstrator part used for process development. Source: Ford Motor Company.

The introduction of the water-assist cooling step helped reduce the sidewall warp/sink issues, but re-introduced thick-section voids into the parts, as can be seen in Figure II.3.1.18.7. A pack/hold study was then conducted to mitigate the thick-section voids by allowing for improved wall formation prior to the start of the water-assist coring phase.

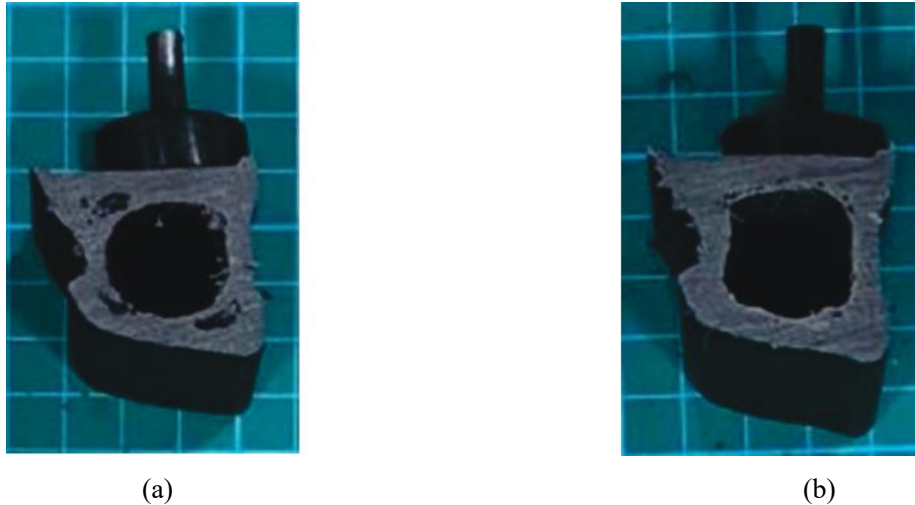


Figure II.3.1.140. Occurrence of thick-section voids in the corners of the demonstrator part (a) without added cooling and (b) with added cooling. Source: Ford Motor Company.

Figure II.3.1.18.8 shows the progression of a hot runner hollowing for the first five parts after the water-assist module is activated after switching from solid components for 7- and 10-second pack/hold time trials. The hot runner section appears to be a good indicator for overall quality of the water channel within the part and can be evaluated press-side via weight and quality of the channel opening. An optimized value for the hot runner weight is being determined for the PP45SGF material based on achieving approximately 50% hollow channel for the hot runner. As can be seen in Figure II.3.1.18.8, parts with a 7-second pack/hold time over-hollow the hot runner for parts 4 and 5. This introduces the risk of injecting water into the hot runner manifold, so the coring volume needs to be dialed back to avoid this error state. In future trials, active feedback based on hot runner weight will be used to dial in the correct coring volume.



Figure II.3.1.141. Progression of hot runner degree of hollow after water-assist is turned on. (a) A seven-second pack sample. (b) A ten-second pack sample. Source: Ford Motor Company.

Task 4. Tow/Tape Placement of Continuous Fiber

To support the Task 7, “High-Volume Manufacturing Concept Feasibility Demonstration (sub-scale)” work stream, the team at Purdue University has been working to supply M-TOW preforms for future partial cross car beam molding trials. To prepare for forming these preforms, the jig shown in Figure II.3.1.18.9 was designed to accommodate the M-TOW and AM attachment point designs provided by Yanfeng.

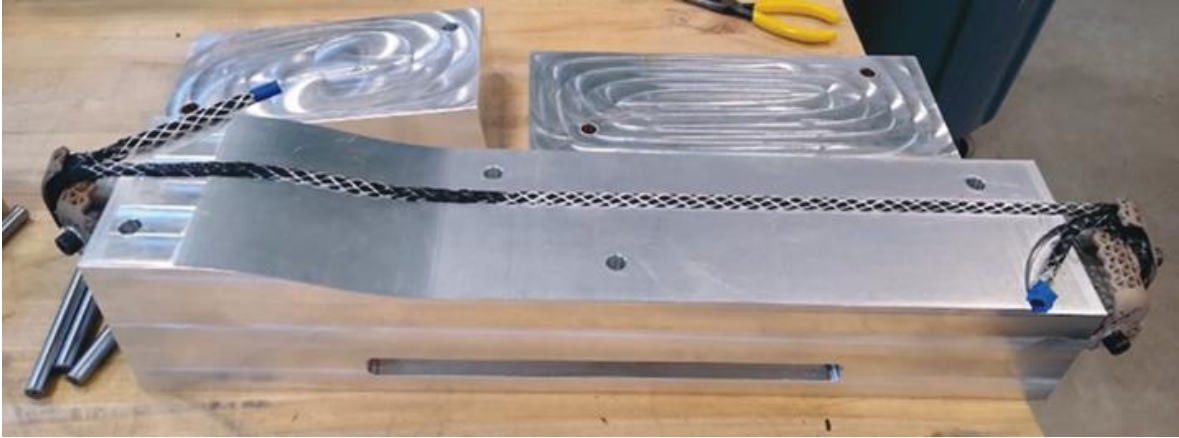


Figure II.3.1.142. Jig design to form M-TOW into AM attachment points. Source: Ford Motor Company.

Continued manufacturing of PA66+glass fiber M-TOW was completed to produce material for forming preforms for the partial cross car beam molding trials. By 1 July 2022, eight preforms with the design shown in Figure II.3.1.18.10 were sent to Yanfeng for subsequent molding.



Figure II.3.1.143. M-TOW preforms produced in support of injection overmolding studies. Source: Ford Motor Company.

Task 5. Sensor Integration

At the commencement of the project, a cross-functional skill team identified several sensing and integrated electrical system technologies to be investigated. With respect to sensors, strain sensing for various functions including component health monitoring and safety related actions were identified. Deadfront, capacitive switching, and swappable modular interfaces were technologies identified for other integrated functions. In these cases, the supporting electrical systems—including printed wiring and connector termination—are considered essentially common, and thus, enablers for integration of this capability into the cross car beam

structure. During Budget Period 2, printed circuitry on decorative film, such as those shown in Figure II.3.1.18.11, were produced for electrical testing.

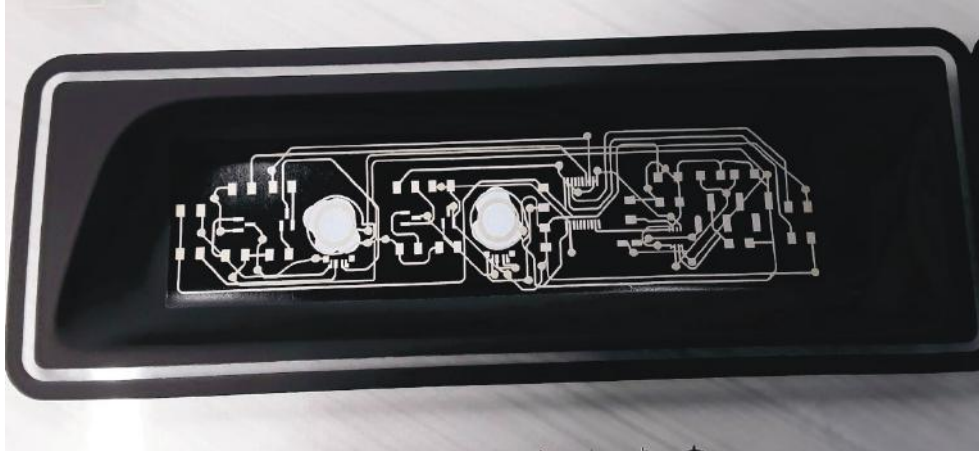


Figure II.3.1.144. Printed circuitry on decorative film. Source: Ford Motor Company.

These printed circuits with decorative films were over-injection molded without electronics to assess the viability of using this setup in the injection-molding process. It was quickly discovered that molding of films highlighted film distortion issues at the injection gate due to material flowing to the top side of the ink/film and folding it over, as can be seen in Figure II.3.1.18.12. However, this has been attributed to injection gate design on the molding tool and a modification is now planned to correct this condition. It was also decided to position the gating on the full cross car beam part to a non-visual locating post on the B side of the part to avoid disturbing the functional circuitry and decorative surface.

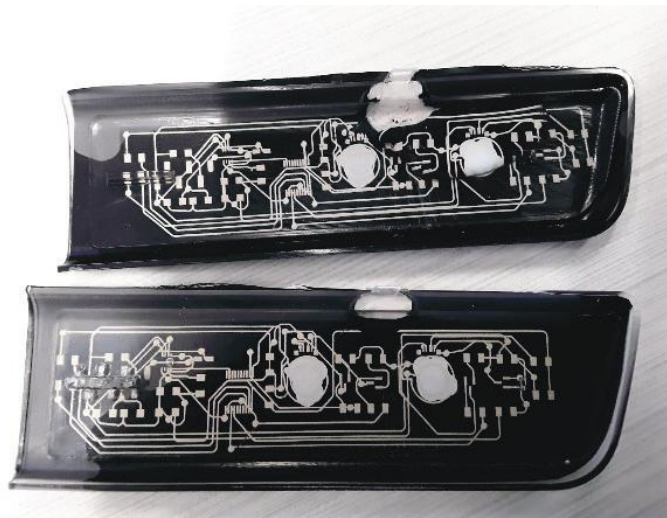


Figure II.3.1.145. Film distortion near the injection gate. Source: Ford Motor Company.

Based upon the current printed circuit issues and the lack of availability for several originally selected electronic components, a revised flat circuit was designed for surface mounting of electrical components, as shown in Figure II.3.1.18.13. A revised microprocessor was selected to ensure availability. The remaining original components were incorporated into the design with direct connections to each pin and traces for a ribbon connector. This allowed for direct electrical measurement of each component or ribbon connector via a breadboard.

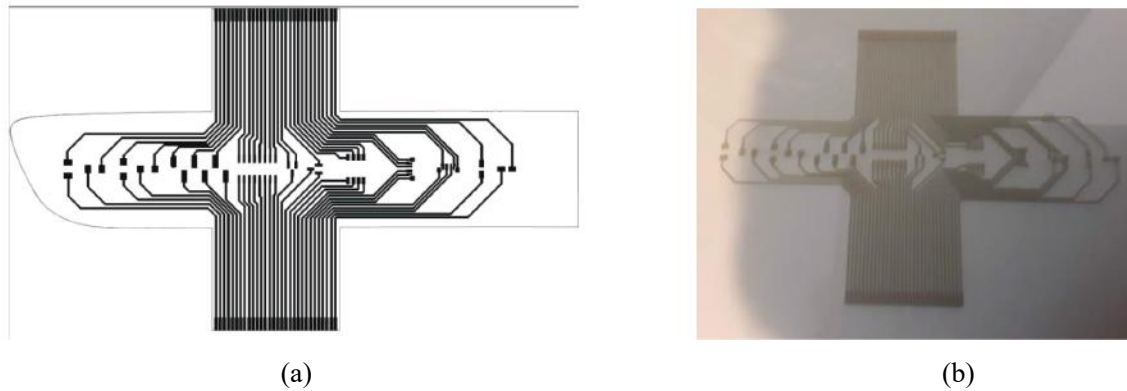


Figure II.3.1.146. (a) Revised printed circuit design and (b) physical prototype for surface mounting of electrical componentry. Source: Ford Motor Company.

To test the intended function within the cross car beam, the following electrical components were utilized for surface mounting on the film: resistors, capacitors, microprocessors, pin connectors, transistors, diodes, and red-green-blue light-emitting diodes. These components were manually mounted using conductive adhesive and potted prior to injection-molding trials. Injection-molding trials were conducted using a clarified antilock braking system material. Initial shots showed conductive ink washout near the injection gate area. In some instances, electrical components also became detached from the film near the injection gate. Various process modifications were performed in an effort to eliminate conductive ink washout and component debonding. In the end, a stable process was established with no ink washout or part debonding, as observed in Figure II.3.1.18.14.. Ultimately, it was noted that the injection gate design will be an important consideration moving forward.

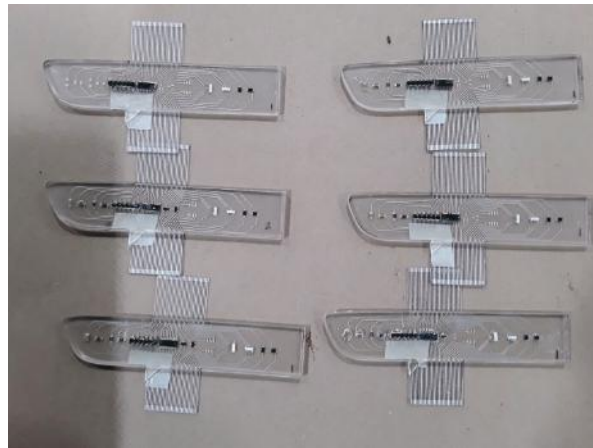


Figure II.3.1.147. Preliminary over-injection molding shots with no ink washout or electrical component debonding. Source: Ford Motor Company.

Task 6. Additive Manufactured Hardware Attachment Points

AM hardware attachment points were subject to several design iterations during 2022. Altogether, six sets (24 total) of initial prototypes were fabricated, followed by 15 sets (60 total) of a subsequent design iteration. Initial prototypes were produced successfully for the top brackets, as indicated in Figure II.3.1.18.10., which include the capability to accommodate the continuous fiber M-TOW reinforcements. Some early manufacturing issues were observed, such as warping. In addition, considerable breakage of the mesh, as well as difficulty cleaning out residual printing debris from the mesh in both the top and bottom brackets, was observed.

A second design iteration proved to be much more robust during processing and did not experience mesh failure. Warpage also decreased but was not eliminated. Additionally, there remain problems with the alignment holes fitting onto the tooling pins despite changes in hole size and draft angle from the first design. It is believed this is due to the warpage as well. However, overall, the team was successful in fabricating parts with these hardware attachment points. Figure II.3.1.18.15 shows the hardware attachments inside the tool prior to overmolding, while Figure II.3.1.18.16 shows a finished part after injection-molding. For the most part, the mesh within the hardware attachment point is fully filled with the injection material. There are a few areas in the bottom inserts that did not fill; however, the team will be developing resolutions for this.



Figure II.3.1.148. Close-up of inserts placed in the molding tool. Source: Ford Motor Company.



Figure II.3.1.149. Finished part after injection-molding showing the location of attachment points. Source: Ford Motor Company.

Task 7. High-Volume Manufacturing Concept Feasibility Demonstration

The team at Yanfeng has been continuing to develop the material handling and automation strategy in support of molding trials for the partial cross car beam shown above in Figure II.3.1.18.16. This work is intended to lay the groundwork for the full cross car beam that will be molded in BP3, as shown previously in

Figure II.3.1.18.3. Prior to the molding components, several iterations were completed to resolve geometric tolerancing issues with the additive manufacturer's hardware attachments. This has resulted in design modifications to the metal mesh design to increase tolerances and reduce warp during the 3D printing process. Following this, the team was successful in overmolding of metal mesh hardpoints, tow, and decorative functional film in a partial cross car beam tool. Initially, a glass/nylon material was used to assist with process setup before transitioning to the PA66 reinforced with the 30% CF/10% basalt fiber. The pick-and-place and end-of-arm design was completed with a subsequent fabrication. For the purpose of locating the AM inserts and M-TOW in the robot cell, AM fixtures matching the contour of the inserted components were fabricated. Figure II.3.1.18.17, Figure II.3.1.18.18, and Figure II.3.1.18.19, respectively, contain images of the automation cell and fixtures from these recent studies.

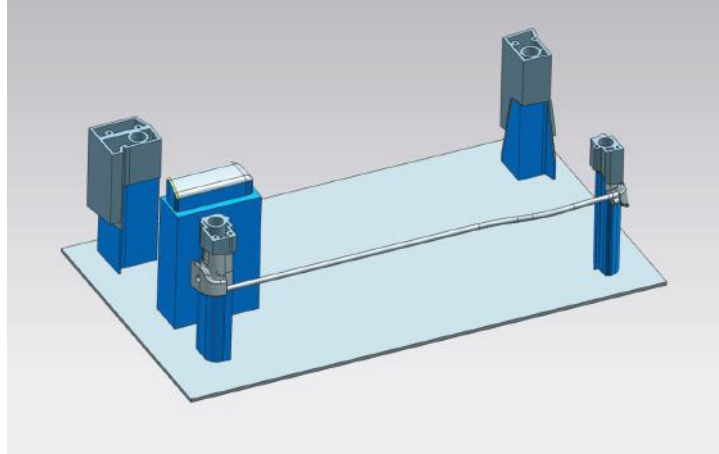


Figure II.3.1.150. Design of pick-and-place fixture (blue) and end-of-arm (dark grey).
Source: Ford Motor Company.

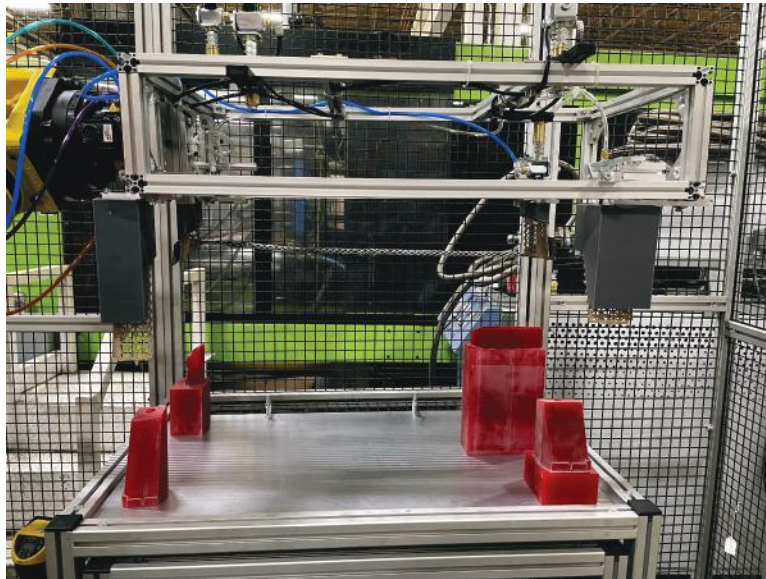


Figure II.3.1.151. The pick-and-place fixture and end-of-arm tooling picking up tow and hardpoints.
Source: Ford Motor Company.



Figure II.3.1.152. The pick-and-place robot automation cell. Source: Ford Motor Company.

Task 8. Full Process, Automation, Scaleup and Demonstration

As a continuation of the activities in Task 7, the team at Yanfeng has continued to trial material handling concepts to accommodate dimensional variation of all the inserted components to be overmolded.

AM fixturing, as shown in Figure II.3.1.18.17 above, has been fabricated to allow ‘layup’ of the inserted components in the correct orientation (shown in blue). Additively manufactured end effectors (shown in dark grey) match the geometry profile of the hardware attachment points (inserts) for accurate picking and placing. Each end-effector also includes a Gimatic expansion one-dimensional gripper that expands inside the locating hole of the metal mesh hardpoint allowing it to be transferred into the injection mold. Figure II.3.1.18.20 shows the operation of the end-of-arm tooling, whereby the M-TOW preform and the AM inserts are picked up from the fixture for transfer into the injection-molding tool.

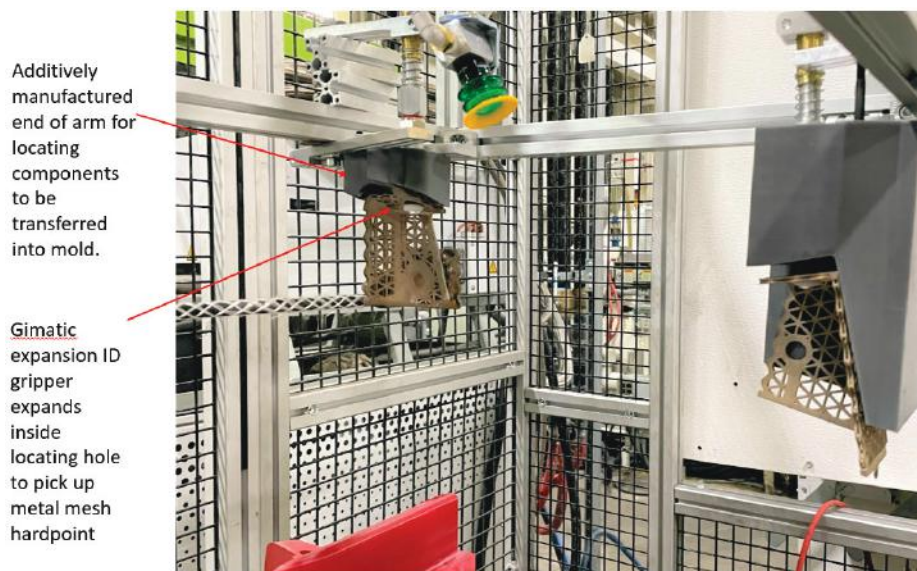


Figure II.3.1.153. Close-up of end-of-arm. Source: Ford Motor Company.

An initial design concept has also been completed for modification of the injection-molding cell at the MSU scaleup facility in Detroit, MI. This includes the transfer table design shown in Figure II.3.1.18.21(a) and the table setup shown in Figure II.3.1.18.21(b). The purpose of this work is to allow materials to be passed into the robotic cell for presentation to end-of-arm tooling. These design concepts will continue through the next quarter ahead of prototype tooling delivery in 2023.

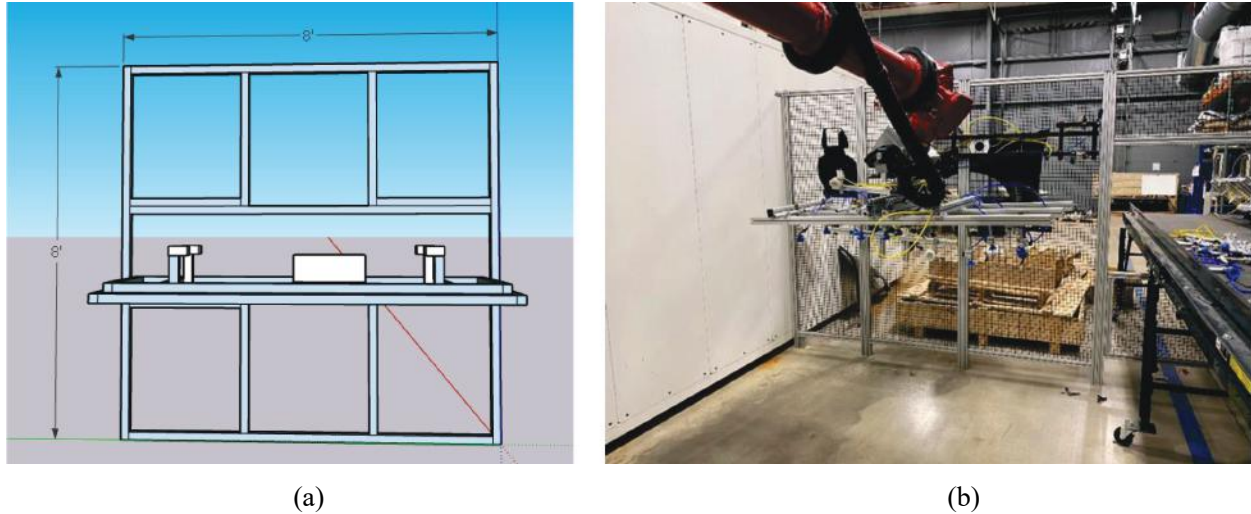


Figure II.3.1.154. (a) Initial design concept to retrofit existing robot cell with (b) the over-mold transfer table. Source: Ford Motor Company.

Task 9. AM of Segmented Tooling

Based upon access to AM printing facilities at Yanfeng, Budget Period 2 milestones for Task 9 were for the most part already integrated into Task 8 workstream activities. Therefore, a new set of milestones was proposed and accepted by the DOE contracting officer regarding deployment of AM printing facilities at ORNL. Specifically, results of material and handling and automation methods will be used to print fixtures at the MSU scaleup facility in Detroit. These location fixtures are to be used to align all inserts on the transfer table shown in Figure II.3.1.18.21. In support of this effort, CAD of the 3D fixtures is under development at MSU and Ford pending transfer to ORNL for printing on a filament printer. Based upon the revised workplan, the new tasks with corresponding milestones are shown in Figure II.3.1.18.22. ORNL will repeat these steps for the full cross car beam trials that will run at MSU’s scaleup facility to accomplish Milestone 3.9.3 in April 2023.

9.2 Cross Car Beam Corners for Attachments, Film placement, and stampings				
9.2.1 Design of negative hardpoint corners/Selection of Printing Materials and	Design due to ORNL			
9.2.2 Manufacturing of corners		Fabricate		
9.2.3 Dimensional validation		Validate		
9.2.4 Shipment to SuRF		Ship		
9.3 Fabricate and ship actual XCB corners to SuRF				Repeat

Figure II.3.1.155. Revised tasks and milestones for the AM tooling workstream. Source: Ford Motor Company.

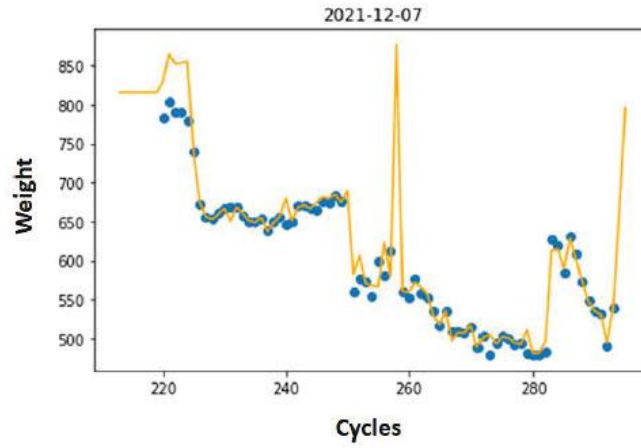
Task 10. AI/ML for Process Optimization

Task 10 will establish a digital thread to capture each step of part production, ranging from feedstock compounding, geometrical design, processing optimization, *in-situ* monitoring, and material characterization. During Budget Period 2, Task 10 has focused on training ML models to model the relationship between the WAIM processing parameters and component weight and part volume. For this work, XGBoost—an implementation of the Gradient Boosted ML model—was adopted. Initially, for each set of properties—‘weight’ and ‘part volume’—hyperparameter optimization was performed. This was accomplished using five-fold cross-validation. These optimal model parameters were then used to train a model that was subsequently used to predict the component characteristics—‘weight’ in Figure II.3.1.18.23 and ‘part volume’ in Figure II.3.1.18.24. These figures also show how the model predictions compare with the empirical data.

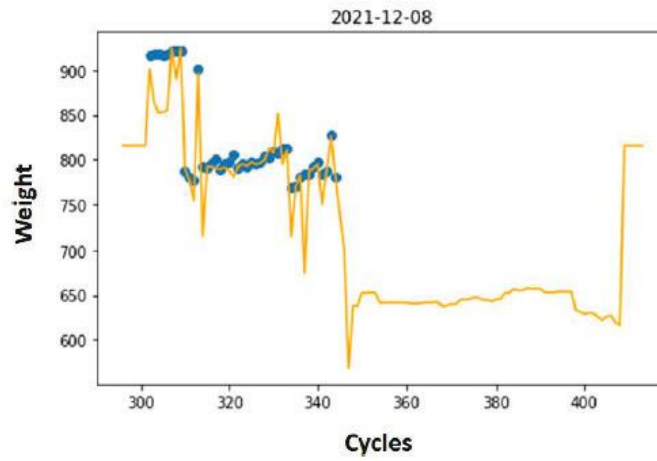
The models produce reasonably accurate predictions, so the important feature metrics may be used to analyze which input features have a salient role for producing the predictions for the respective component characteristics. Figure II.3.1.18.25 shows the rankings for the ‘weight’ predictions, while Figure II.3.1.18.26 shows the ranking for the ‘part volume’ predictions. For both characteristics, ‘partidor’ is the most salient input feature, which represents the cycle identifier as recorded by the injection-molding machine for each trial and holds important information about how long the machine has been running for a given trial when a cycle occurs. For ‘weight,’ the next important features are step five pressure, hose length, and step two volume. For ‘part volume,’ the other most salient features are step five pressure, step two volume, and step three volume. These rankings coincide with the hypotheses offered up by the WAIM team regarding which process steps and trial configurations are important for process stability.

The AI team has also been working with the process scaleup team working on Task 8 to outfit the partial cross car beam tool with two in-mold sensors. These sensors have been added to the tool. Some additional troubleshooting is being performed to ensure these sensors are operating for trials planned. Additionally, the ORNL team has completed exploratory work towards preliminary unsupervised modeling of historic process data provided by in-mold sensors. The goal of this work is to use this type of data in addition to process parameters and other process data to monitor process stability and predict component properties.

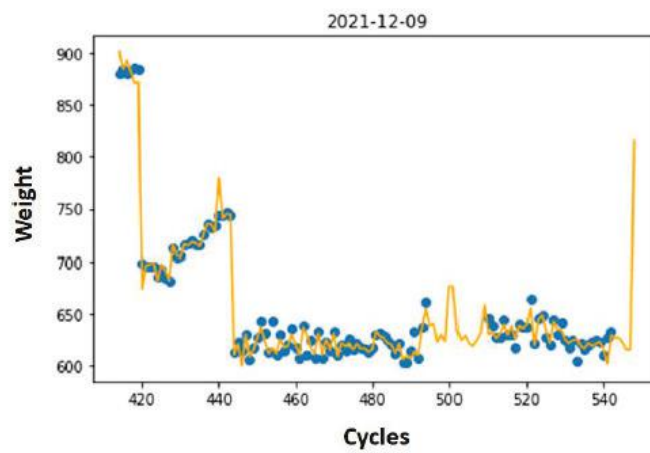
In summary, the AI team has worked to identify the various data streams that are available from injection-molding and auxiliary activities for this project and worked to adapt data collection, curation, and analysis paradigms currently employed at the ORNL Manufacturing Demonstration Facility for injection-molding. Meaningful relationships have been demonstrated between processing parameters and component characteristics for the WAIM process and show that data-based process models may be trained for eventual use in process optimization during fabrication of prototype cross car beams in BP3.



(a)

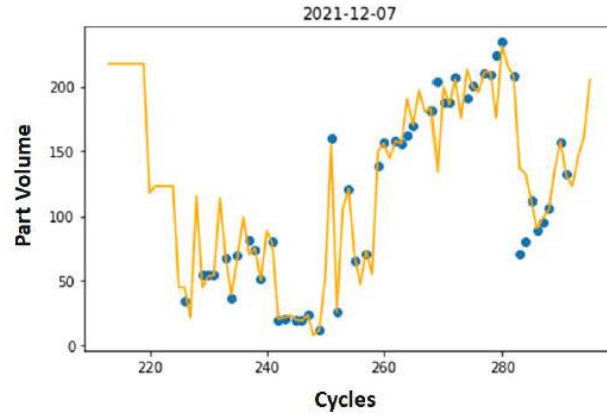


(b)

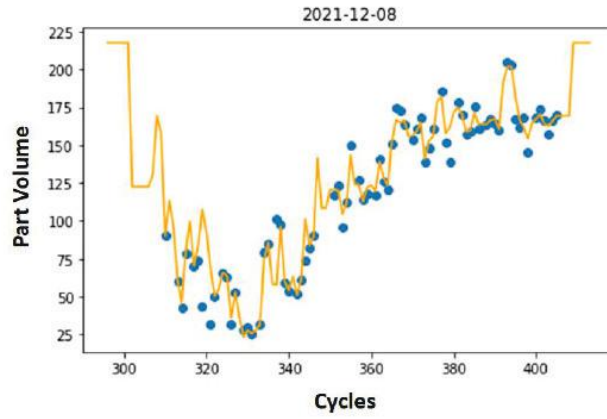


(c)

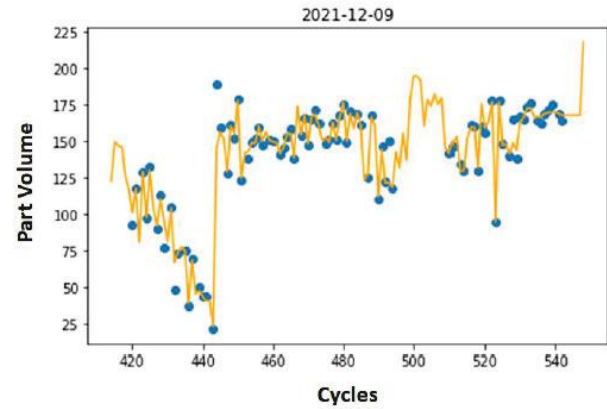
Figure II.3.1.156. XGBoost ‘weight’ predictions for individual cycles for three consecutive trials (orange line) and empirical data (blue dots). Source: Ford Motor Company.



(a)



(b)



(c)

Figure II.3.1.157. XGBoost 'part volume' prediction for individual cycles for three consecutive trials (orange line) and empirical data (blue dots). Source: Ford Motor Company.

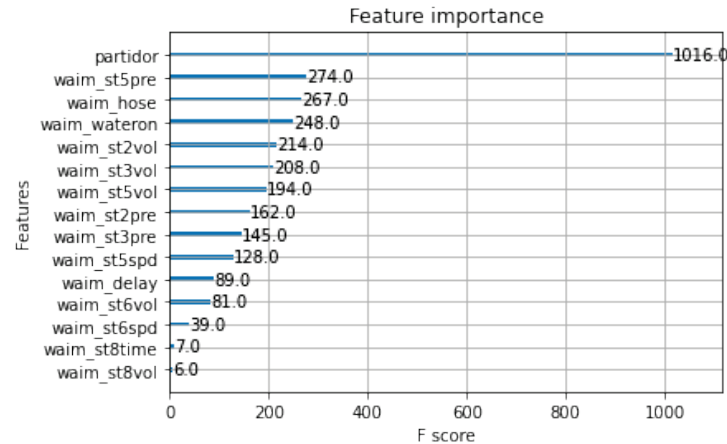


Figure II.3.1.158. Model input features ranked by importance for predicting 'weight.'
Source: Ford Motor Company.

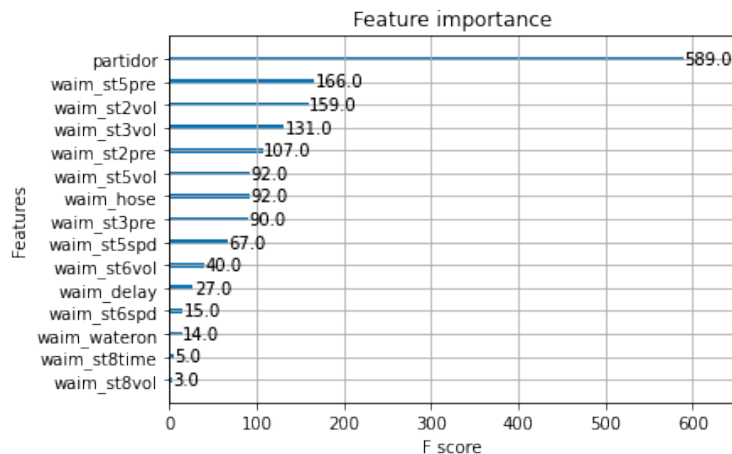


Figure II.3.1.159. Model input features ranked by importance for predicting 'part volume.'
Source: Ford Motor Company.

Task 11. Closed-Loop Recycling

This task will develop and demonstrate all compounds and materials in terms of circular economy with the demonstration of recycling materials specified for the cross car beam structure. During Budget Period 2, Task 11 focused on validation of the recycling strategy for the cross car beam assemblies. Material testing dog bone samples were produced through injection-molding of virgin 40CF/PA66 (e.g., 40% CF in a PA66 matrix). Subsequently, tensile test data was compared with PA66 compounded with a 40% blend of fiber (BF) reinforcement, as shown in Figure II.3.1.18.27. The 40% CF-reinforced specimens had a greater tensile modulus while the tensile strength remained statistically equivalent. The 40CF/PA66 tensile specimen scraps, runners, and sprues have been collected for shredding and granulating to create granulate for dry blending. Dry blended batches were produced with the RC of 33%, 67%, and 100% recycled materials. Fiber length distribution analysis was completed for samples containing 0 wt.%, 33 wt.%, 67 wt.%, and 100 wt.% RC, respectively, as shown in Figure II.3.1.18.28.

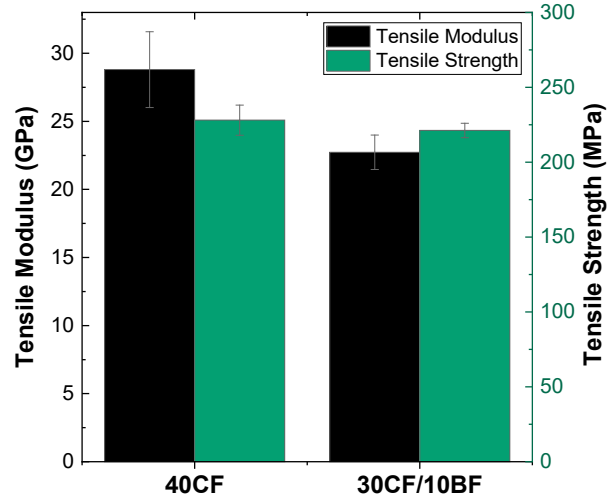


Figure II.3.1.160. Tensile testing results for 40CF/PA66 and 30CF/10BF/PA66 specimens
Source: Ford Motor Company.

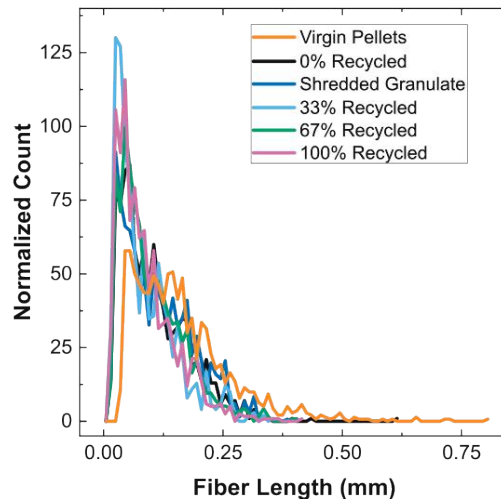


Figure II.3.1.161. The fiber length distribution for virgin pellets, 0 wt.% RC, shredded granulate, 33 wt.% RC, 67 wt.% RC, and 100 wt.% RC samples. Source: Ford Motor Company.

NMR spectroscopy was also employed to determine any degradation of PA66 as a result of recycling and re-manufacturing. The ^{13}C NMR spectra in Figure II.3.1.18.29 show many similarities between the structure of the neat PA66 and a 100% recycled sample at a lower parts per million (ppm). However, when examining the ^{13}C spectra at a higher ppm and ^1H spectra peaks arise detecting fragmented PA66 chains in the 100% RC samples, but not in the neat PA66 pellets. This indicates that during processing some polymer degradation is taking place, but further NMR analysis is required to determine which manufacturing processes are causing the degradation.

During the first quarter of BP3, the 40% CF-reinforced material (CF40/PA66) will be mechanically recycled, dry blended, and re-injection-molded to make 33, 67, and 100 wt.% RC samples. These samples will be tested to track the resultant tensile strength and modulus, the amount of fiber content remaining, fiber length distribution, and the extent of polymer degradation during processing.

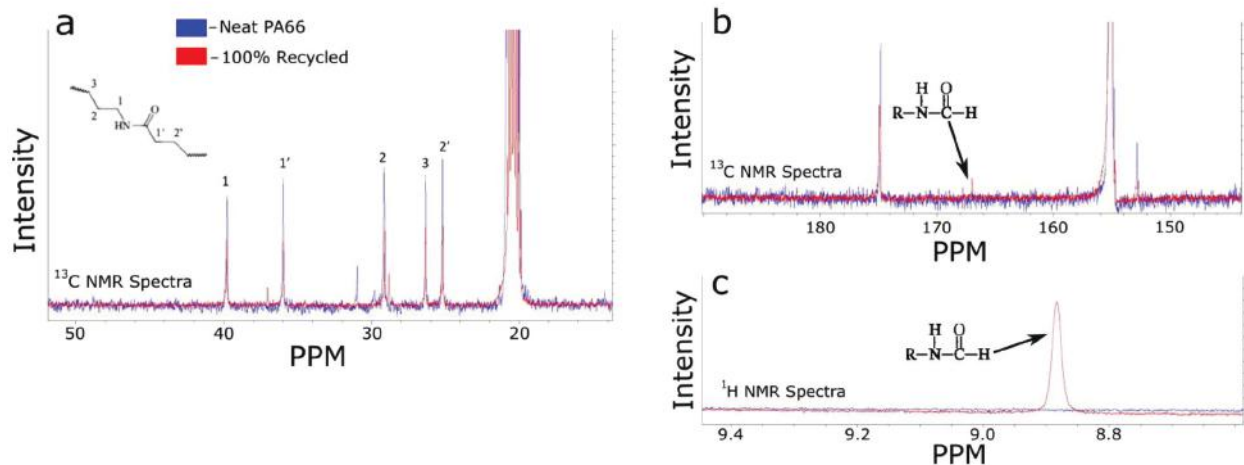


Figure II.3.1.162. NMR spectroscopy of neat PA66 pellets and 100% RC samples of 30CF/10BF/PA66 showing the ^{13}C spectra at (a) low ppm, (b) high ppm, and (c) the ^1H NMR spectra.

Source: Ford Motor Company.

Conclusions

During BP2, the project team was able to work collaboratively across the work streams to successfully complete design of the instrument panel cross car beam. Material and manufacturing validation studies were conducted in parallel to develop confidence ahead of issuing a purchase order for the prototype tooling needed to produce parts in 2023. Simulation studies show the composite structure was able to meet all performance targets while achieving a substantial mass reduction. From a commercial perspective, the Purdue team has also completed an analysis using a technical cost model to provide a revised assessment of the business case versus the steel base line. As in BP1, the projection is that the system cost targets continue to be met, which contributed to a successful gateway outcome during the Annual Project Review on 16 November 2022.

Key Publications

1. Blanchard, P., 2021. "Multifunctional smart structures for smart vehicles," 2022, U.S. Department of Energy 2022 Vehicle Technologies Office Annual Merit Review, 21 June 2022, Washington, D.C., USA.
2. Lavorata, J., and J.-A. E. Mansson, 2022, "Conductive multifunctional composite preform (M-TOW)," U.S. Provisional Patent 63/341,724.
3. Lavorata, J., P. Blanchard, and J.-A. E. Mansson, 2022, "High-rate manufacturing of thermoplastic composites with electrically conductive constituents," SPE-ACCE Conference Proceedings, Vol. 2022.
4. Rencheck, M., et al., 2022, "Utilizing recycled carbon fiber-based composites for sustainable manufacturing," SPE-ACCE Conference Proceedings, Vol. 2022.
5. Rencheck, M., et al., "Effect of mechanical recycling on carbon fiber based hybrid composites," CAMX Conference Proceedings, 30 October–2 November 2022, Atlanta, GA, USA.

Acknowledgements

The project team would like to recognize Chad Schell from the Advanced Manufacturing Office and Aaron Yocum from NETL for their continued support and guidance throughout BP2.

II.3.1.19 Development of Tailored-Fiber Placement, Multifunctional, High-Performance Composite Material Systems for High-Volume Manufacture of Structural Battery Enclosure (General Motors)

Venkateshwar Altharaju, Principal Investigator

General Motors Global R&D
 General Motors LLC
 30470 Harley Earl Blvd.
 Warren, MI 48092
 E-mail: venkat.altharaju@gm.com

H. Felix Wu, DOE Technology Development Manager

U.S. Department of Energy
 E-mail: felix.wu@ee.doe.gov

Start Date: April 1, 2021 End Date: June 30, 2024
 Project Funding (FY 2022): \$2,391,887 DOE share: \$1,736,510 Non-DOE share: \$655,377

Project Introduction

The automotive industry is currently in a major transition from internal combustion engines to a new era of EVs. Increasing the driving range of these vehicles, minimizing the cost of the battery system, and optimizing the vehicle architecture to meet new performance requirements imposed by electric propulsion, while meeting all safety criteria, are some of the new challenges posed during this significant transition. In this endeavor to meet the above challenges, lightweighting by using high-performance materials has become paramount. Composite materials, in addition to having lower densities, have significant benefits compared to metals. Despite these excellent benefits, composites still face significant challenges for large-scale implementation in automobile production. These challenges are (1) the inability to be truly multifunctional to stand apart from metals, (2) the lack of predictive tools to eliminate trial-and-error evaluations, (3) the inability to optimize the design parameters, and (4) the high cost of volume manufacturing. In this project, we will address the above challenges and develop game-changing multifunctional capabilities for composites to make a strong business case for large-scale implementation in automobiles.

Objectives

The objective of the project is to develop advanced composite materials systems with game-changing technologies, such as hybrid fiber systems at the lamina or tow level (commingled), strategic tailored-fiber placement (TFP), self-health monitoring (SHM), enhanced thermal and shielding capabilities, and high-volume manufacturing friendly production for the automotive industry. The material systems will be selected appropriately based on the structural requirements, and they will meet or exceed the performance metrics provided by DOE (e.g., fiber strength >25 ksi, fiber modulus >250 Msi, strain-to-failure >1%) to achieve the necessary weight-savings and cost targets. High-pressure resin transfer molding (HP-RTM) will be chosen as the high-volume manufacturing process for the components with fast-curing resins that can provide a cycle time lower than three minutes. Computational tools for both the manufacturing process and structural design based on an ICME approach will be developed and validated for the chosen material systems. Using these ICME tools, the project team will design, engineer, and build a structural composite battery enclosure as a baseline for GM's Cadillac Lyriq model vehicle. The composite battery enclosure structure will be tested to compare the performance with the baseline metallic assembly. The weight-savings, cost of materials, cost of components, and cycle times for a production volume of 85,000/year will be evaluated and compared with the DOE metrics.

Approach

Several key technology developments are proposed in this project under the following categories.

Materials

The newly developed TFP technology will be advanced to the next level in this project by creating hybrid fiber reinforcements (e.g., carbon, glass, other fibers) and using them in a single preform or commingled in the tow to enhance the material properties significantly. The material systems developed in the project will lower material and manufacturing costs significantly, meeting the DOE metric of a maximum increase of \$5 per pound saved compared to the steel baseline. Innovative sensor technologies will be embedded within the composite preforms for monitoring the structural health and environmental conditions (e.g., temperature, humidity) in self-sustained mode (energy harvesting).

Process/Design

Computational models will be developed to optimize the microstructure of composite preforms (e.g., tow size, tow spacing, stitch density) to maximize their drapability and permeability. The TFP technology explored in the project will provide greater flexibility to vary the geometry of the microstructure spatially, providing an opportunity for next-level optimization. HP-RTM is the chosen process in this project due to its advantages for volume manufacturing (notably fast cycle time) seen in our previous DOE-funded project (contract number DE-EE0006826). For the HP-RTM process design, we will develop enhanced simulation models to engineer the processing conditions (e.g., molding temperature, injection location, vent, injection pressure, flow rate profile) for a fast-curing resin with a cycle time of three minutes as was previously demonstrated. Variability in the preform material properties, preform placement, and process molding conditions are the major sources of defects and scrap in this process. To address this issue, we will develop models based on AI/ML to correlate the data from sensors embedded in the mold (resin arrival time, pressure, temperature, etc.) with the probability of dry spot occurrence in the manufactured parts.

Structure/Performance

Predictive tools for the structural performance of the hybrid carbon and glass composites will be enhanced by extending the ICME multiscale models developed previously in our project funded under DOE contract number DE-EE0006826. The models will be calibrated by using coupon level tests and validated by using component level tests. Further, a method will be developed to optimize the layup fiber directions and thickness of the lamina for minimal fiber mass. Using these ICME models, we will be able to exactly predict the optimum fiber makeup, fiber architecture, FVF, resin type, manufacturing process, and processing conditions to manufacture components that meet the required structural performance for the components of the composite battery tray.

Results

The project progress during the FY 2022 is provided in the following sections.

Task 1.2 Materials, Process Models, and Technology Development for Future Composite Assembly

Under this task, the development of materials, process simulation models, and structural design tools will be carried out for use in the design of future composite battery enclosures. Accomplishments under each of the development sub-tasks are provided below.

Task 1.2.1 Evaluate and Develop an Optimized Hybrid Material System

Optimum Hybrid System

Under this task, advanced hybrid materials proposed for the chosen battery enclosure components (e.g., CF, GF) were investigated to determine the optimum UD lattice hybrid ratios for maximizing the ratio of structural performance and material cost. Figure II.3.1.19.1 shows the test matrix developed for the study.

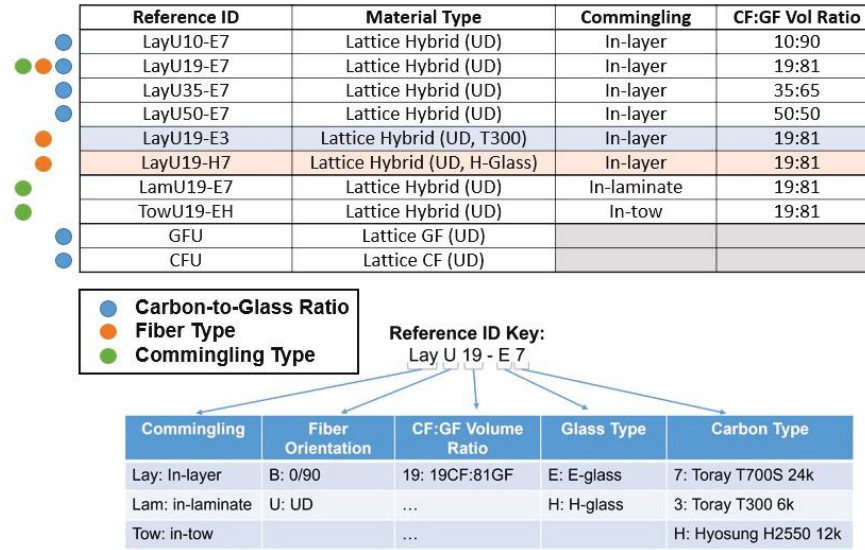


Figure II.3.1.163. Lattice materials included in this mechanical property study. Source: GM.

For brevity, we will focus on the carbon-to-glass hybrid ratio results only highlighted in blue and orange in Figure II.3.1.19.1. The tensile stress-strain curves for four of the fiber ratios along with curves for unidirectional CF and GF are shown in Figure II.3.1.19.2. The strength and modulus of the hybrid materials increase as the CF content increases, as would be expected. Hybrid materials show an “M” type behavior with a second peak corresponding to a delayed glass fiber failure. Further, the CF in the hybrid shows an increase in the failure strain compared to an all-carbon composite, a phenomenon of enhanced ductility. As the CF composition in the hybrid composite is increased in the range of 35% to 50%, we see a loss of M-shape behavior (i.e., the lack of a second peak for the glass fiber). Detailed experiments concluded that with a CF composition around 19%, the enhanced ductility of the hybrid composite is maximized.

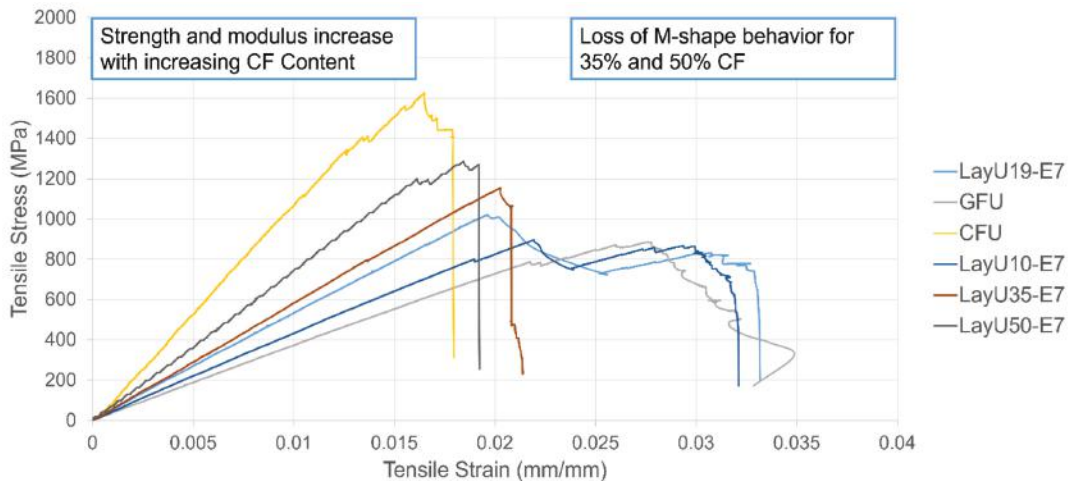


Figure II.3.1.164. Tensile stress-strain curves for Lattice materials at different carbon-to-glass fiber ratios. Source: GM.

Figure II.3.1.19.3 shows the stress-strain behavior of the hybrid system with different fiber grades. Using a lower strength CF, we were able to engineer the first and second peaks to be roughly at the same level, analogous to a metallic behavior. Thus, we were able to successfully engineer the hybrid systems to behave like a ductile behavior which was a crucial help for enhanced energy absorption.

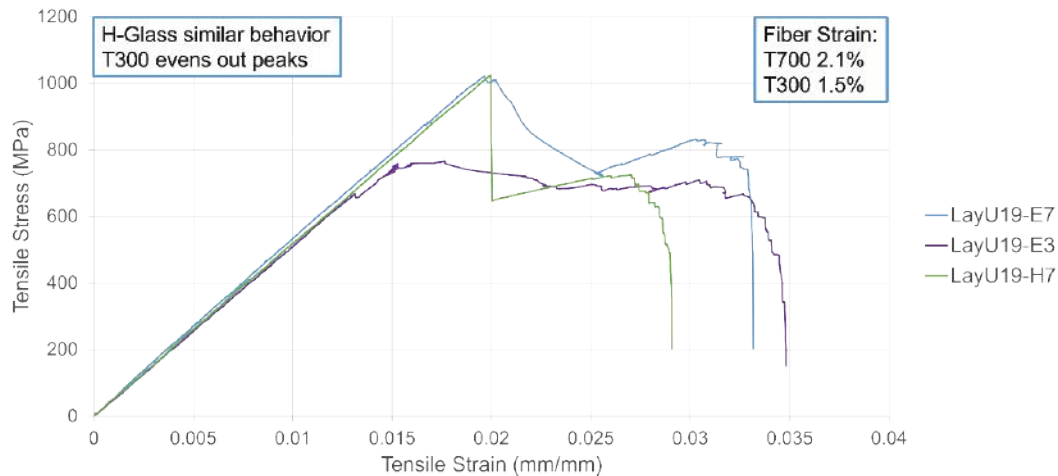


Figure II.3.1.165. Tensile stress-strain curves for hybrid materials at different types of carbon and glass fibers.
Source: GM.

Optimum Stitch Length

In this effort, the effect of stitch density on permeability was studied. A set of 12 GF lattice preforms were tested for permeability with four different stitch lengths: 2.0, 5.5, 8.0, and 11.0 mm. Experiments were performed with three replicates. The FVF for each stitch length varied from 40% to 55%. An analysis of variance study showed that the stitch length and fiber volume content are both significant influencers of permeability. The permeability decreased as fiber volume content increased. The effect of stitch length on the permeability was nonlinear, but generally indicated permeability increased with increasing stitch length (e.g., fewer stitches). This study is crucial to design the preform with appropriate stitch density to vary the permeability spatially, enabling a uniform flow front in the HP-RTM process for defect-free components.

Optimum Draping for One-Step Molding

The current production composite manufacturing process involves two steps: (1) preforming and (2) molding. During the preforming step, the 2D-shaped composite preform is draped into a 3D component shape. To remedy the wrinkles/splits, strategic slits are used to improve drapability as the component's geometric complexity increases. Thus, the process becomes mostly manual and becomes expensive. Furthermore, significant variability is introduced. In this project, we ambitiously aim to eliminate the preforming step and propose to combine the two steps under one tool by intelligently designing the preform for enhanced drapability. To investigate experimentally, we have designed and built a mold for conducting draping experiments. Figure II.3.1.19.4 shows the mold with a 2D preform and draped 3D preform. This mold features corners with differing complexity with different radius and height values allowing us to study diverse draping behaviors in a single mold.

Baseline experiments with commercially available Chomarat™ BT fabric were conducted using the new mold. Significant wrinkles were observed. Continuing the experiments with Chomarat™ fabric, strategic slits at the corners obtained from the developed computational models were created in the preform, and draping experiments were conducted. Figure II.3.1.19.5 shows the results. One can see a good correlation between the simulation and experimental results. However, the slits created in this exercise will adversely affect the strength of the manufactured component.

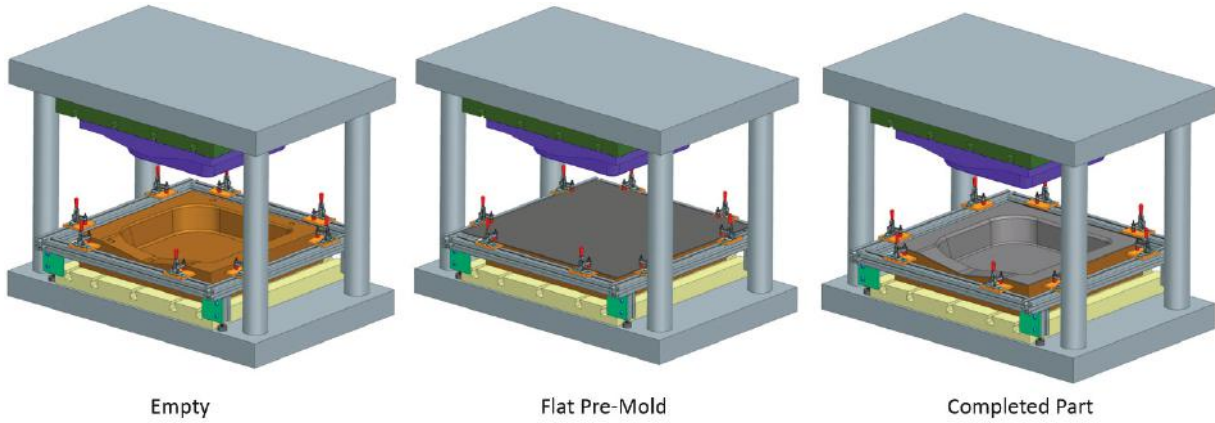


Figure II.3.1.166. Draping tool for experiments. Source: GM.

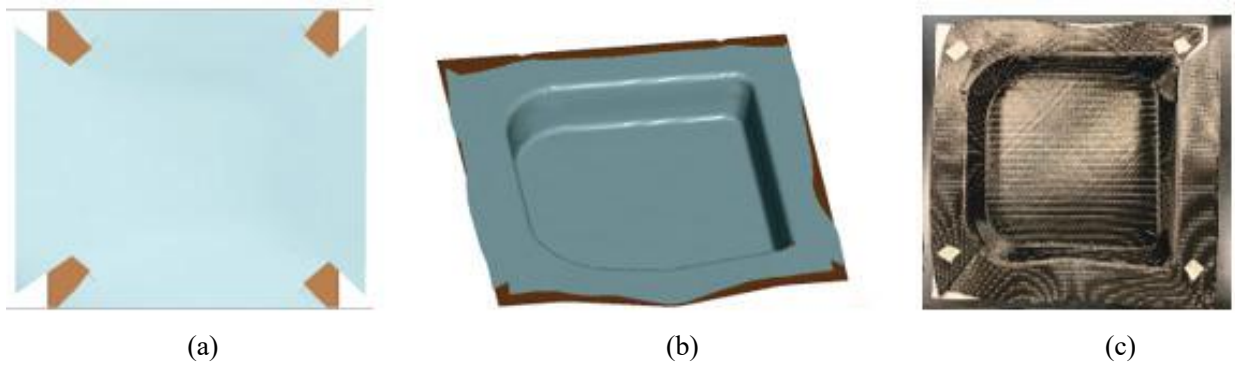


Figure II.3.1.167. (a) 2D fabric pattern. 3D draped geometry from (b) simulation and (c) experimental result. Source: GM.

In the current study, the parameters of the TFP preform, such as volume fraction, fiber angle, and stitch density, were strategically engineered to achieve a wrinkle-free draped preform. Figure II.3.1.19.6 shows the two designs of TFP Lattice preforms for which the experiments were conducted.

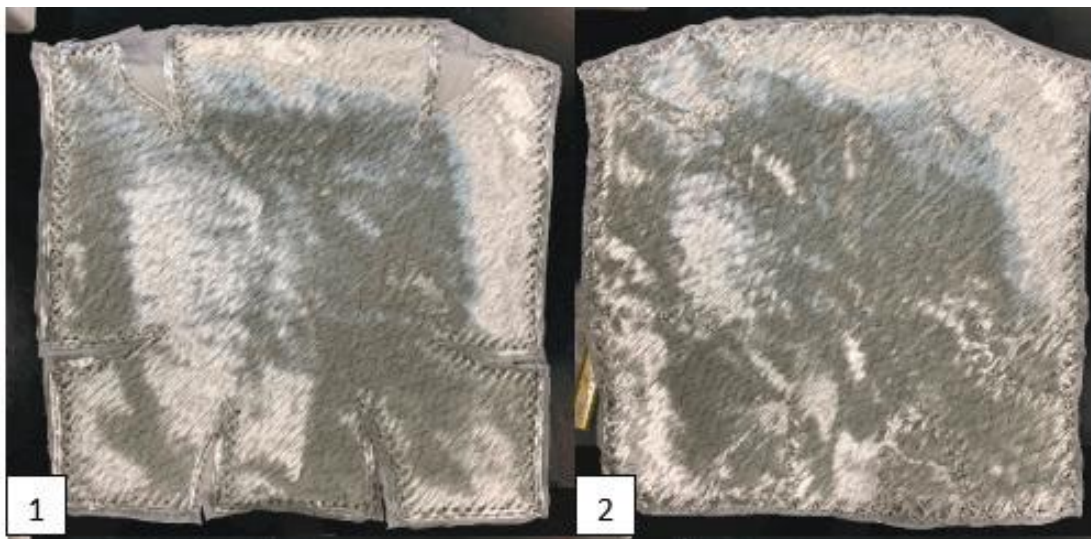


Figure II.3.1.168. Configurations studied using the lattice preform: (1) slits; and (2) no slits. Source: GM.

The slitted TFP preform replicates the results obtained with the Chomarat™ fabric studied previously. By engineering the volume fraction and fiber angles, the strategically designed no-slit TFP preform showed a successful draping of the preform without any wrinkles, as can be seen in Figure II.3.1.19.7. This development is crucial for future one-step molding planned for the tray component of the composite battery enclosure.

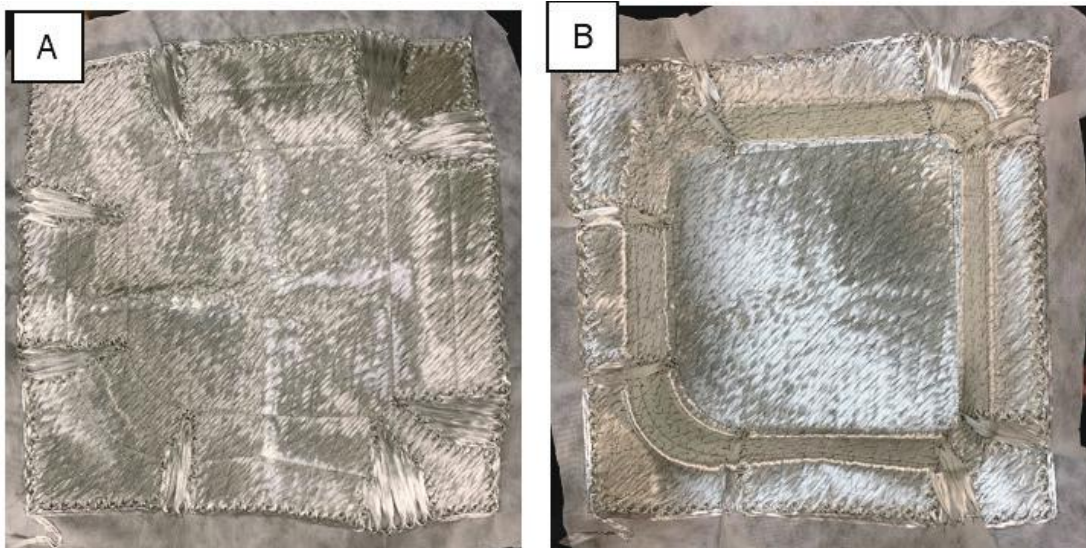


Figure II.3.1.169. (a) 2D preform design with no-slit and (b) the draped preform design with no-slit. Source: GM.

Task 1.2.2 Evaluate and Develop the Required Manufacturing Model

Under this task, the manufacturing models to design the HP-RTM process for battery enclosure components will be carried out. The computational model development involves solving complex coupled nonlinear differential equations modeling the heat transfer and fluid flow-through porous media [1]. We performed various experiments collecting the pressure profile, resin temperature evolution, and flow front progression during HP-RTM injection experiments with various flow rates. This data is used to develop the numerical model development, calibration, and validation. Figure II.3.1.19.8 shows the mold geometry used in the study. The mold has a center injection with a resin runner. Three pressure sensors are located in the mold to measure the pressure during the injection. One dielectric sensor measuring the temperature and ionic viscosity of the resin was included.

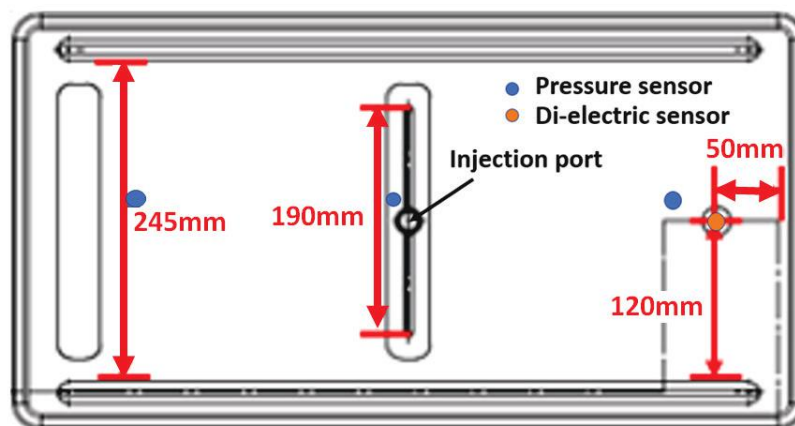


Figure II.3.1.170. Geometry of the HP-RTM mold used for experiments. Source: GM

The fluid flow-through the porous medium was modeled using Darcy's law, as indicated in Equation 1.

$$q = -\frac{K}{\mu L} \nabla P \quad (1)$$

where q represents the flow rate, K represents permeability of the preform, μ represents the viscosity of the resin, L is the length of the flow front, and ∇P represents the pressure gradient.

The simulation utilizes a 3D finite volume analysis methodology, utilizing material models consistent with state-of-the-art numerical constituent expressions for rheology and curing kinetics. Figure II.3.1.19.9 shows the comparison of the pressure profile measured in the HP-RTM experiment compared with the predictions. An excellent correlation between the developed model and experimental results was obtained, giving confidence in the process design of future battery enclosure components.

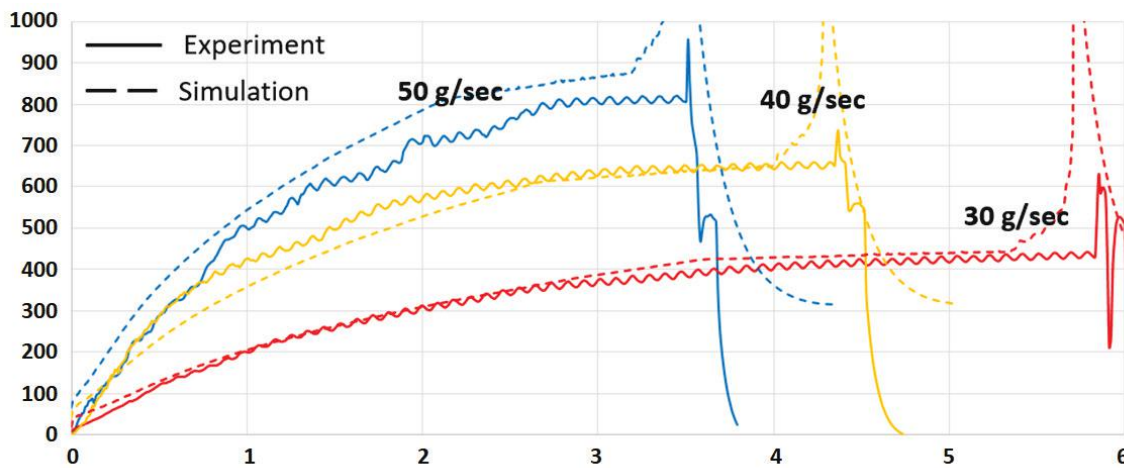


Figure II.3.1.171. Comparison of pressure profile from the experiments and simulations. Source: GM

Task 1.2.3 Evaluate and Develop the Required Structural Model

Under this task, we will develop state-of-the-art computational models to predict the performance of hybrid composites. Plaques were molded, as described under Task 1.2.1, to generate the experimental data to develop the structural performance model. Figure II.3.1.19.10 shows the framework of the multiscale structural model compared with the previous model developed under the DOE-funded project DE-EE0006826. In the present model, a neural network (NN)-based surrogate model will replace the representative volume element model for computational efficiency. The NN concept for multiscale modeling of composites is quite novel, and we believe that the technology will be game-changing in improving computational efficiency and accuracy of composite materials.

In this FY, the project team has further refined the representative volume element (RVE) model that was developed in the previous FY for improved predictability for the response of the hybrid fiber composite under multi-axial loading. Figure II.3.1.19.11 shows the RVE of the hybrid composite. A layer of cohesive elements was added on the surface of the fiber tow elements to represent the fiber and resin interface. Material model MAT_138, which is available in LS-DYNA, models a bilinear traction-separation law with a quadratic mixed mode delamination failure criterion that was used to model the adhesion between the fiber tow and the resin. In the new RVE model, the resin material was represented using a MAT_124 model in LS-DYNA representing an isotropic elastic-plastic behavior defined for tension and compression. Failure is initiated based on the plastic strain. Figure II.3.1.19.12 provides a comparison of the experimental and RVE results for the hybrid fiber composite.

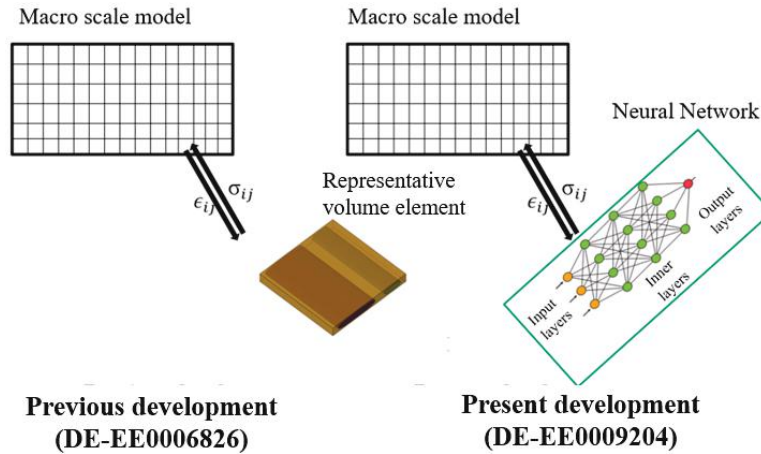


Figure II.3.1.172. Multiscale framework for structural performance of composites. Source: GM.

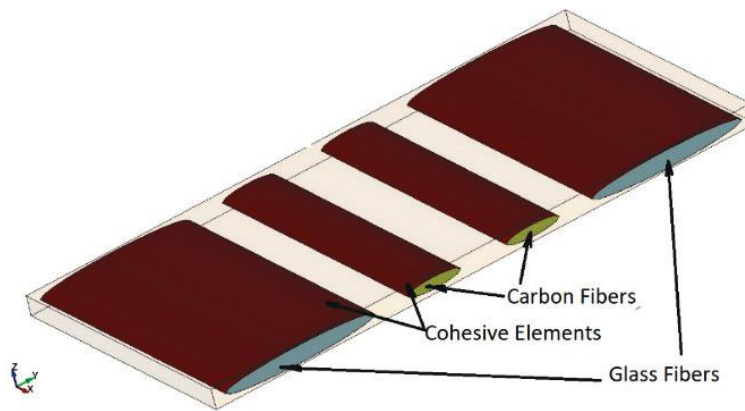


Figure II.3.1.173. Enhanced RVE model of hybrid fiber composite. Source: GM.

Hybrid Lattice (0/90/90/0, CF:GF 19:81) Tensile

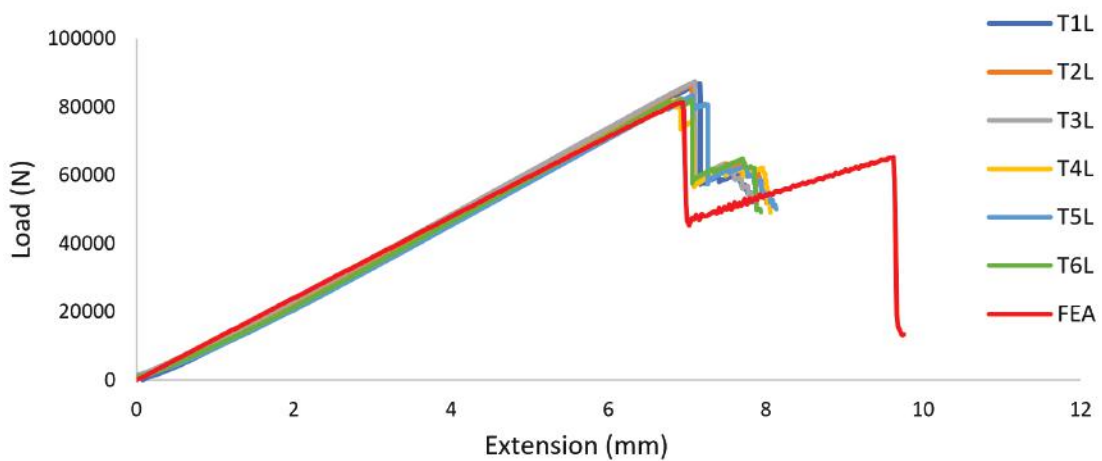


Figure II.3.1.174. Comparison of experimental and RVE results for the hybrid fiber composite. Source: GM.

These results provide confidence in designing the future composite battery enclosure to meet the critical crashworthiness performance. This RVE model was shared with the University of Southern California team in developing the RVE/ML component of the project.

Task 1.2.4 Evaluate and Develop SHM Technologies

Under this task, we will develop SHM technology by embedding electronic circuitry in the composites to detect and locate the damage. Further, a temperature/humidity sensor system will be developed to monitor the temperature of battery cells in the battery enclosure. For brevity, the accomplishments in the SHM sensor area are described below.

SHM Sensor

In this study, a novel CF tow sensor and its resistance property were utilized to sense the damage in the composite. The resistance of the CF tow sensor-embedded in the composite is measured by applying a small voltage and measuring the value of the resulting current caused by any stressor. Figure II.3.1.19.13 shows the plot of the change in resistance ($\Delta R/R_0$) versus strain in the composite. The implicit relationship between the strain and resistivity of the composite will be used to determine the strain state/damage in the composite. The following two approaches were pursued in designing a robust, low-cost, and high-volume manufacturing friendly SHM sensor: (1) optimize tow size for the sensor and (2) design of an electrical terminal.

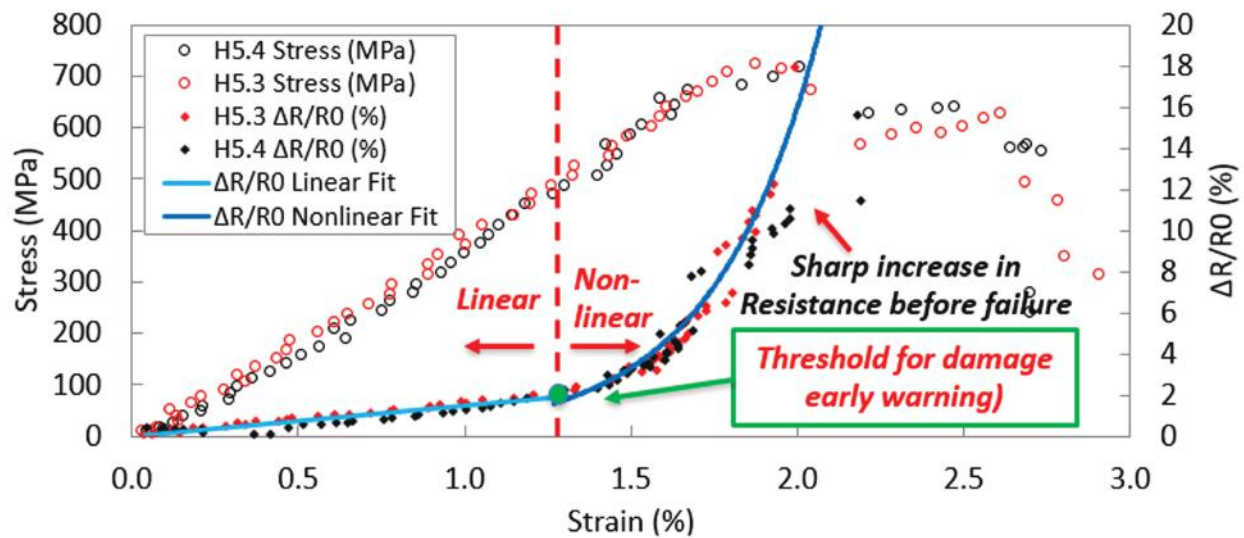


Figure II.3.1.175. Stress-strain and resistance relationship of a composite with an embedded carbon tow sensor. Source: GM

Optimum Tow Size for the Sensor

Eight self-SHM specimens with different fiber amounts, such as 3k and 24k, were designed, fabricated, and tested under tensile loading to determine the optimal tow count for the CF sensing tow. The testing results demonstrated better performance and higher accuracy for the 3k CF tow. Furthermore, the 3k tow showed a much better ability to characterize the resistance's nonlinear response to the composite strain, which is indicative of the non-reversible failure mechanisms, a critical feature for early damage warning strategies. Given the behavior, an early warning threshold can be established at the transition point from the linear to nonlinear range between the sensor resistance and the composite strain.

Impact Test Results

Several impact specimens using the 3k CF tow were designed, fabricated, and tested. The impact test results demonstrated a strong correlation between the impact energy and the change in the measured resistance of the CF tow, proving the high sensitivity of this sensor to impact and crush loadings as well. Figure II.3.1.19.14 shows the impact test setup and results of the resistance for undamaged and damaged samples.

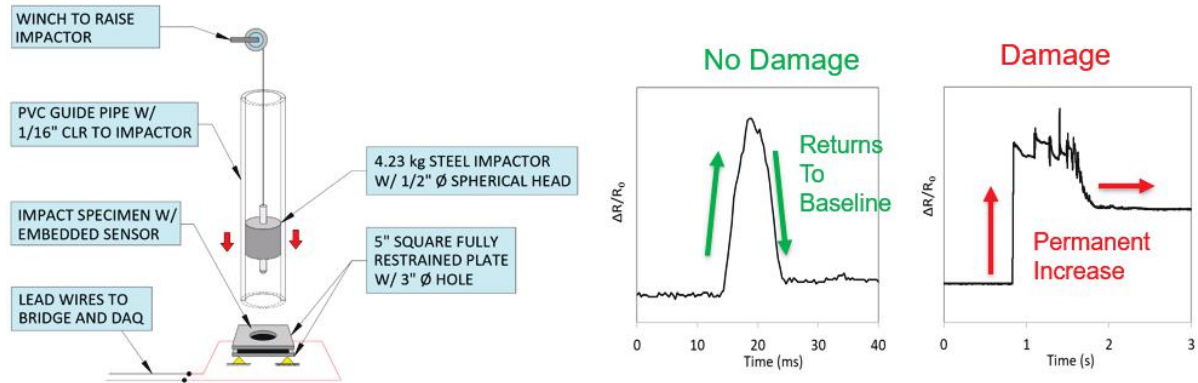


Figure II.3.1.176. Impact test setup and resistance results for undamaged and damaged samples.

Source: GM.

Electrical Terminal Design

The ability to connect the embedded sensors with the power supply to measure the resistance is challenging. In this project, the team developed a novel way to drill a copper rivet into the 3k sensor tow to access the sensor. Based on this concept, a total of 15 specimens were made with the 3k CF sensor tows electrically connected using copper rivet-based technology, as observed in Figure II.3.1.19.15.. This process is high-volume friendly. To study the sensitivity, sensor circuitry with a different number of loops was also studied. The results show an excellent performance of the copper rivet-based technology. Also, a 5-loop sensor tow showed the highest sensitivity as compared to the 3-loop and 1-loop specimens.

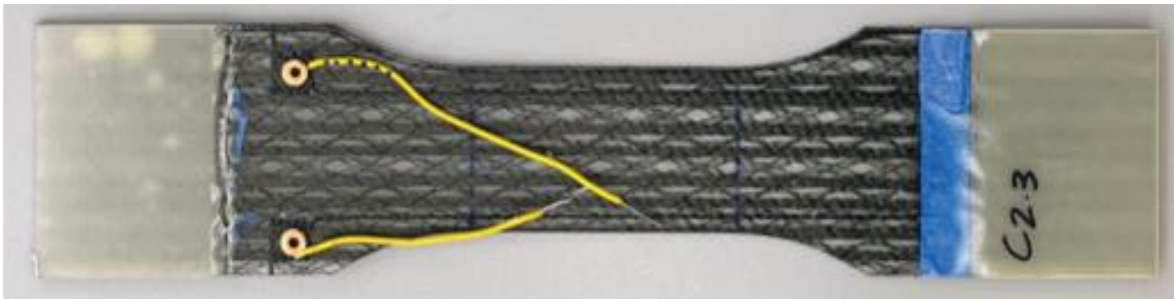


Figure II.3.1.177. Samples with embedded 3K sensor tow (copper rivets for electric terminals). Source: GM.

For damage detection and location identification, a novel multi-branch variable-resistance network was developed by optimizing the number and placement of the SHM sensor tows. This enables the use of a single resistance measurement circuitry to monitor a large area of the composite structure, substantially saving not only the overall sensor system cost, but also space for the sensor circuits. In the designed setup, the baseline resistance of each branch is designed to achieve a predetermined value by designing the length of the sensor tow branch or by adding a resistor. For 2D component domains, two sets of three-branch variable-resistance networks in the two cartesian coordinate directions (x and y) were designed. The sets were placed in two perpendicular directions forming a sensor grid that allow not only damage detection, but also the identification of the damaged location within the sensor grid.

For initial validation of the damage location technology, branched sensor circuits were designed and two impact specimens were prepared and tested. The trial panels demonstrated that the location of damage can be determined reliably using the three-branch variable-resistance network.

Finally, preparations have been made for investigating the potential usage of the above SHM technology for monitoring the composite structure's fatigue life. Fatigue specimens were designed, and a fatigue testing

regimen was determined that included at minimum three tests at four stress levels. Fatigue testing will be conducted in FY 2023 with fully reversible fatigue cycles.

Task 1.2.5 Evaluate and Develop AI/ML Technologies for Monitoring the Manufacturing Process

Under this task, we developed AI/ML technology for multiscale structural analysis and monitoring of the manufacturing process. In the multiscale analysis, computationally expensive representative unit cells are replaced with NN based surrogates. For the manufacturing process, in the event of any abnormalities noticed based on readings from the strategically located pressure sensors, the AI/ML system will automatically determine the required changes to the injection pressure and flow rate to mitigate the risk and produce a defect-free part. For brevity, AI/ML technology for multiscale analysis is discussed.

Multiscale NN Model

Utilizing the RVE model developed above, many simulations (~3,000) were conducted varying the strain values and recorded stress values to prepare the data for training the NN model. We explored the applicability of four different NN architectures. For brevity, only the final architecture yielding the best result is discussed here. The final NN consists of two subnetworks. The first part of the network has a layer with 50 neurons. It was trained with strain and material properties as input and energy density history of glass fiber tows as an output. The second part of the network has 50 neurons. It was trained with an energy density history of glass fiber tows as input and stress in the fiber direction as an output. The NN is shown in Figure II.3.1.19.16, while Figure II.3.1.19.17 shows a comparison of the NN predictions from the multiscale model against ground-truth experimental results of hybrid composite materials.

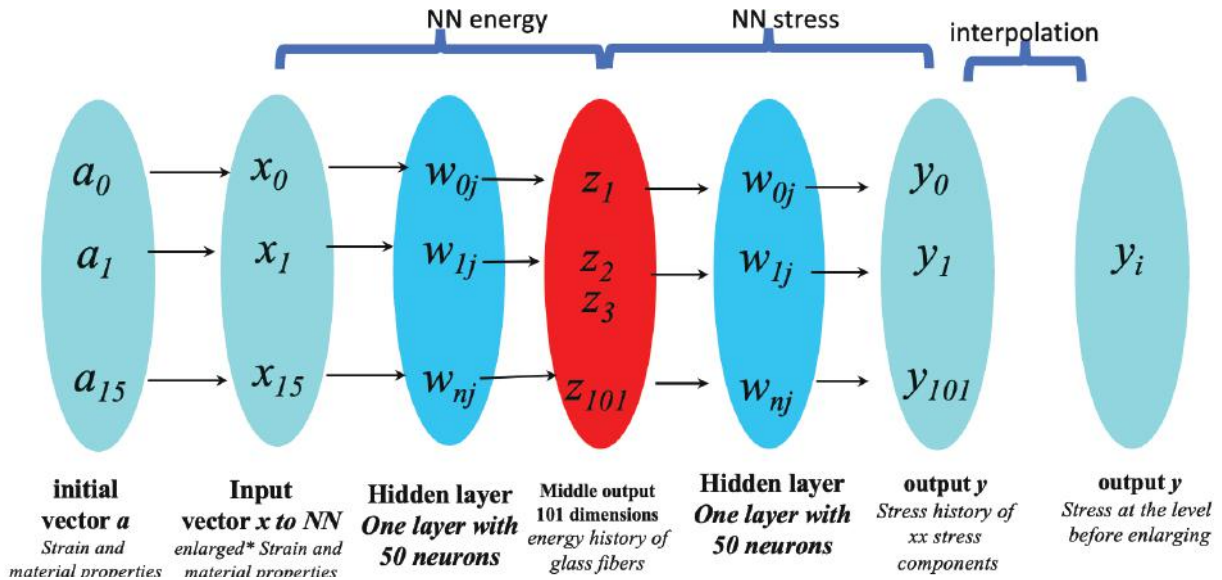


Figure II.3.1.178. Two-part NN. Source: GM.

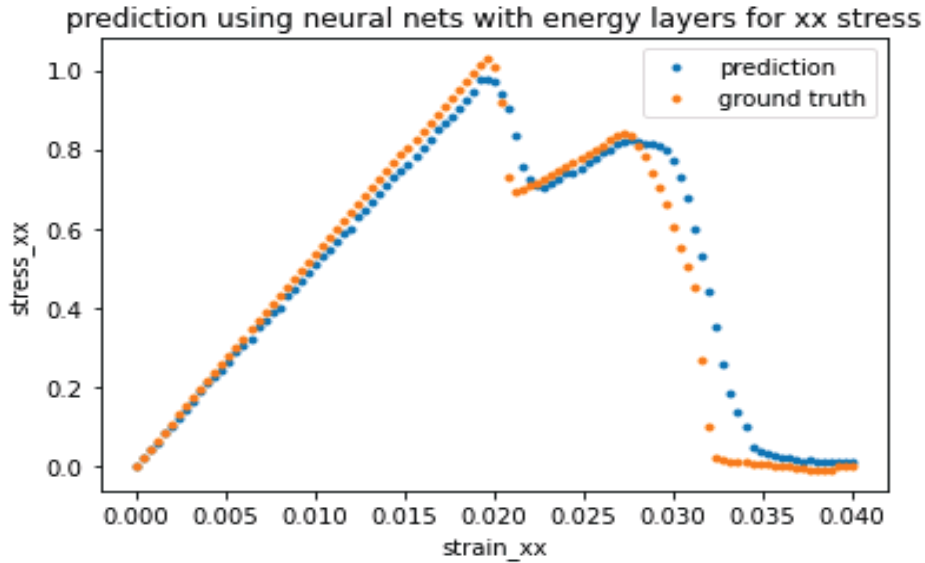


Figure II.3.1.179. Comparison of NN-based multiscale model with experimental results. Source: GM.

Task 2.1 Finalize the Structural Design of the Composite Battery Enclosure

The objective of this task is to design battery enclosure components using the manufacturing and structural models developed in this project. Figure II.3.1.19.18 shows the picture of the baseline metallic enclosure.

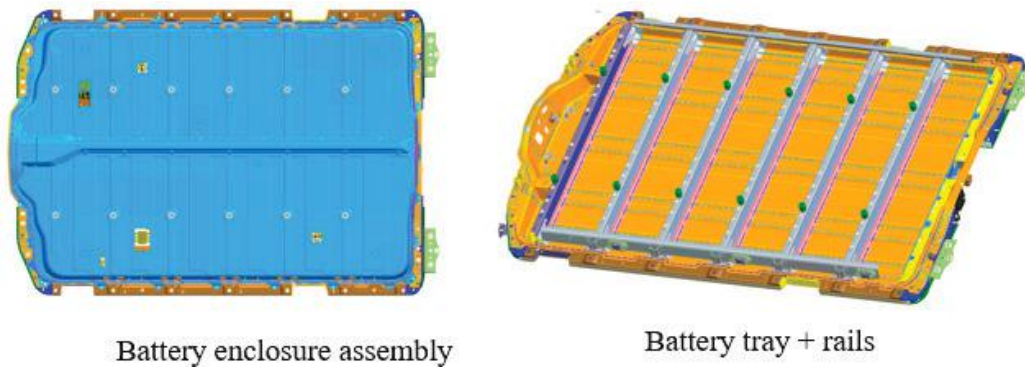


Figure II.3.1.180. Geometry of the baseline battery enclosure for the GM model Cadillac Lyriq. Source: GM.

Based on discussions with the project team, for each of the components, we have determined the materials, processes, and features for demonstration, which are shown in Table II.3.1.19.1.

Table II.3.1.19.1. Materials, Process, and Features for the Demonstration Battery Enclosure Assembly

Component	Materials	Process	Features for Demonstration
Cover	SMC intumescent material	Compression molding	Fire reatardancy, variable thickness
Tray	TFP hybrid fiber preforms	HP-RTM	Complex geometry, one-step moldable preforms, AI/ML strategy, SHM
Cross Rails	Continuous fibers	Pultrusion	
Side Rails	Continuous fibers	Pultrusion	

The reference battery enclosure design is available with 12, 8, and 6 battery modules. A few constraints, such as a tooling budget, platen size for molding the components, and the maximum TFP preform size, are used to determine the right baseline to design the future composite battery enclosure. Figure II.3.1.19.19 shows the final design after several iterations. The composite design of the battery enclosure was completed and a mass savings of 40% over the steel design was achieved. To gain additional confidence on the composite design, a mini-battery enclosure, also as shown in Figure II.3.1.19.19, will be built and tested before we finalize the manufacturing tool design.

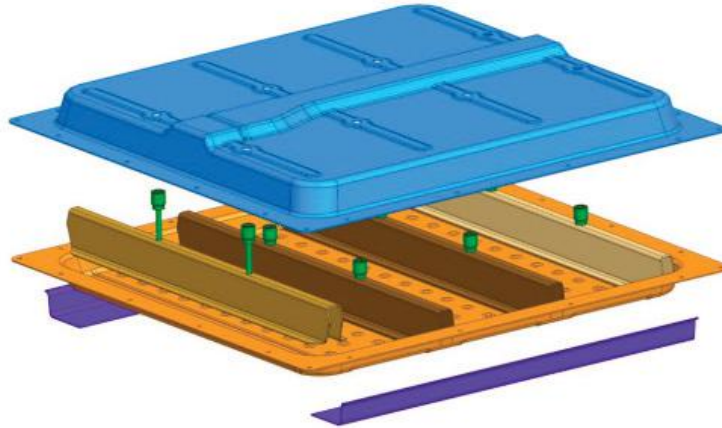


Figure II.3.1.181. Mini-battery enclosure design. Source: GM.

Conclusions

During FY 2022, the project team successfully investigated the ‘enhanced ductility of CF’ phenomenon in hybrid fiber composites and optimized the CF ratio for performance versus material cost. Utilizing different types of carbon and glass fibers, we have developed an innovative way to engineer the constitutive behavior to be “elasto-plastic” instead of a brittle, which is very helpful in designing high-specific energy absorption systems. Further, the design of the preforms obtained from the TFP process was optimized for improved permeability and drapability. Regarding the process modeling of HP-RTM, a new computational model was developed and successfully correlated with the pressure rise measurements in an HP-RTM injection experiment. For the structural performance side, an RVE model of hybrid fiber composite was developed and validated with experimental results. An NN-based surrogate model was developed by training the data from RVE results. This NN-based surrogate model was implemented as a user subroutine in the LS-DYNA computer program for multiscale structural simulations. A novel SHM technology utilizing a 3K CF tow as the sensor wire, and the property of resistance was used for damage detection of the composite. The developed SHM technology was of low-cost compared to state-of-the-art and is high-volume manufacturing friendly. A preliminary AI/ML technology for process monitoring was developed and implemented as add-on software to the HP-RTM system. This software is currently being validated. Finally, the assembly chosen for the demonstration of the technology is a battery enclosure of GM’s production vehicle (2022 Cadillac Lyriq model). The baseline assembly was made with high-strength steel. Using the baseline performance determined in the last year, we have designed a composite battery enclosure for the critical load case of side-pole impact using the structural models developed in the project. Overall, the second year of this project is very productive, and we believe our project outcome will be a significant benefit to the entire automotive industry and will accelerate the implementation of advanced composite materials for the next level of lightweighting of automobiles.

Key Publications

1. Burley, A., and V. Aitharaju, 2023, “Enhanced ductility in in-layer hybrid composites produced via tailored-fiber placement,” *Compos. - A: Appl. Sci. Manuf.* (in press, pre-proof). <https://doi.org/10.1016/j.compositesa.2023.107488>.

2. Patent Application #17/977,083. Preform with variable fiber density, forming and molding tool and method of forming of composite materials.
3. Patent Application #17/740,543. Carbon fiber composite panel with integrated fault detection and health monitoring.

References

1. Gauch, Z. G., V. Aitharaju, W. R. Rodgers, P. Pasupuleti, A. Dereims, and R. G. Ghanem, 2019, “Integrated stochastic analysis of fiber composites manufacturing using adapted polynomial chaos expansions,” *Compos. - A: Appl. Sci. Manuf.*, Vol. 118, pp. 179–193.
<https://doi.org/10.1016/j.compositesa.2018.12.029>.

Acknowledgments

The project team is extremely grateful for the valuable technical and administrative support from our DOE managers, H. Felix Wu, A. Yokum, and C. Schell.

II.3.2 Small Business Innovation Research (SBIR)

II.3.2.1 Sustainable Lightweight Intelligent Composites (SLIC) for Next-Generation Vehicles (Newport Sensors, Inc.)

Masato Mizuta, Principal Investigator

Newport Sensors, Inc.
 P.O. Box 174
 Newport Beach, CA 92625
 E-mail: info@newportsensors.com

Brandy Greenawalt, SBIR Program Manager

U.S. Department of Energy SC-29
 Small Business Innovation Research
 19901 Germantown Rd.
 Germantown, MD 20874
 E-mail: brandy.greenawalt@science.doe.gov

H. Felix Wu, DOE Technology Development Manager

U.S. Department of Energy
 E-mail: felix.wu@ee.doe.gov

Start Date: August 23, 2021 End Date: August 22, 2023
 Project Funding (FY 2022): \$1,100,000 DOE share: \$1,100,000 Non-DOE share: \$0

Project Introduction

Driven by zero-emission goals, the automotive industry is moving toward lightweight vehicles to improve fuel efficiency or battery mileages and reduce GHG emission. A 10% reduction in vehicle weight can improve fuel economy by 6%–8% [1]. Every 100-kilogram decrease in the weight of a vehicle is expected to cut emissions by 3%–5% [2]. With half of the weight and four times the strength, CFRP composites are an attractive alternative to the traditional steel used for vehicles. In addition to weight-reduction, CFRP composites offer several manufacturing advantages, such as design flexibility, lower tooling costs, and opportunities for part consolidation. However, wide deployment of CFRP composites is hindered by a few obstacles. A McKinsey study [3] identified the two most significant challenges. The first obstacle is the high cost of CFs, which is three times higher than the cost of steel. The high production demand and rising cost of petroleum feedstock have encouraged automakers to exploit plant-based natural fibers to maintain a competitive edge, but the relatively low mechanical property and moisture durability of natural fibers present a challenge. The second obstacle is structural reliability concerns and difficult damage inspection. Although CFRP composites have been widely studied for aerospace applications, their crashworthiness, which is uniquely critical for the safety of automotive vehicles, remains to be thoroughly investigated. Due to the brittle nature of the material, CFRP composites are susceptible to impact loads caused by debris and collisions, resulting in matrix cracks, fiber-matrix debonding, fiber breakages, and interlayer delamination. Such damage often cannot be seen by the naked eye but can propagate and suddenly and drastically reduce structural strength and stiffness. Additionally, the long-term aging effects of CFRP composites when used as automotive structural materials are unknown. Therefore, frequent inspection is required by trained technicians using expensive nondestructive testing and sub-surface imaging equipment, such as ultrasonic, infrared, and X-ray imaging. All these inspection technologies impose potential equipment and personnel investment costs on dealerships and workshops. Due to these obstacles, the use of CFRP composites has been mostly limited to high-end, low-volume racing cars.

Objectives

The objective is to develop a highly innovative multifunctional composite material that is embedded with five functionalities:

- The spatially distributed piezoelectric sensor-integrated into the composite structure shall continuously monitor the structural health and detect and locate any impact load and initiation/propagation of structural damage in real-time.
- The spatially distributed piezoresistive trace sensor on the structural surface shall continuously monitor strain and detect and locate an unusual change of strain in real-time.
- The piezoelectric energy harvester integrated into the composite structure shall harvest sufficient energy from vehicle vibration to power the above dual-sensing, SHM system, eliminating the requirement for an external power source.
- The fiber-hybridized structural composite shall achieve equivalent strength, stiffness, and crashworthiness as a steel baseline but at half of the weight.
- The economic competitiveness shall result from the sustainable supply of low-cost natural fibers.

Approach

The team focused on developing the multifunctional composite material using the following approaches:

- Natural fibers are incorporated to not only reduce material cost, but also substantially improve the crashworthiness. SLIC are an innovative, lightweight, low-cost, high-performance, sustainable structural composite integrated with self-powered, dual-sensing, and SHM intelligence to ensure structural safety and reliability.
- Structural materials, such as the CF and polymer matrix, are transformed into a spatially distributed piezoelectric transducer that serves as a sensor and vibration energy harvester.
- A novel design of the piezoelectric transducer electrodes creates an additional complementary sensor system to enhance the redundancy of damage detection and enable damage location.

The SLIC bumper beam illustrated in Figure II.3.2.1.1(a) will be designed and fabricated to demonstrate the SLIC technology. The bumper beam contains a softer natural fiber composite core concealed within a stiff CFRP external shell, which not only reduces CF cost, but also improves flexural strength and stiffness, as well as the impact energy absorption (i.e., the crashworthiness). In fact, the SLIC design overcomes the lack of impact energy absorption seen with CFRP. Furthermore, the external layer of the CF conceals the natural fiber, addressing the moisture durability concerns.

The external CF layer is bonded with a thin layer of polyvinylidene fluoride (PVDF) polymer, as shown in Figure II.3.2.1.1(b). This particular type of polymer can be made into a piezoelectric material upon permanent polarization. When deformed, a piezoelectric material will produce an electric signal, which can be measured by placing electrodes on both sides of the material. In this design, the CF layer, which is a structural material, doubles as an electrode on one-side of the PVDF. Thus, the integrated PVDF polymer and CF become a piezoelectric transducer that serves as a sensor. Impact load and initiation/propagation of any damage in the composites, such as fiber breakage, polymer cracking, and interlayer delamination, will generate elastic waves that cause deformation in PVDF, resulting in detectable electric signals. This piezoelectric transducer is also useful for harvesting energy. Vehicle vibration causes deformation of the piezoelectric transducer, generating electricity that will be stored in a capacitor to power the sensor system, which eliminates the requirement for an external source of power. Using the stored energy, the sensor system can stand by 24/7, even when the vehicle is not in operation, to ensure a damage event is not missed. Therefore, SLIC is a self-sustained intelligent system. While piezoelectric PVDF film sensors and energy harvesters have been studied, this SBIR project represents the first effort to turn CF and polymer structural materials into a piezoelectric transducer for simultaneous sensing and energy harvesting purposes.



Figure II.3.2.1. (a) SLIC bumper beam. (b) Cross section schematic of SLIC bumper beam.

Source: Newport Sensors, Inc.

The novel design of the electrodes for the piezoelectric PVDF transducer enables the new creation of a piezoresistive trace sensor. As depicted in Figure II.3.2.1.1(a), the PVDF polymer film is sandwiched between two layers of electrodes. As described above, the CF layer serves as an electrode on one-side of the PVDF. On the other side of the PVDF film (i.e., the external surface), the electrode is printed with electrically conductive ink in a specially designed trace pattern similar to a strain-gauge. Any change in the structural surface strain will cause a change in the electric resistance of these traces. Therefore, these traces can be referred to as piezoresistive sensors and used to monitor the structural strain. Damage can be determined when the strain exceeds a predetermined threshold.

These two types of sensor systems, the piezoelectric PVDF sensor and the piezoresistive trace sensor, complement each other and enhance the reliability of the SHM functionality of the SLIC. The piezoelectric PVDF sensor is suited for detecting dynamic signals caused by a dynamic event, such as an impact load, which automotive vehicles are often susceptible to, and the occurrence of structural damage induced by such loads or other reasons (e.g., aging). On the other hand, the piezoresistive trace sensor is suited for measuring the surface strain, a relatively static signal, which can be caused by material damage or deterioration. Combining the dynamic piezoelectric and the static piezoresistive sensors, SLIC provides unique, complementary dual-sensing functionality and system redundancy to enhance the reliability of the real-time damage detection and *in-situ* structural health monitoring. For example, if the SLIC bumper beam suffers damage from a collision, an elastic wave will be generated, causing the PVDF to produce a pulse signal that can be detected by the piezoelectric sensor. By measuring the surface strain with the piezoresistive trace sensor, the damage can be reliably detected.

Results

During the first year of Phase II, the team fabricated the composite specimen and the sensing system to conduct the material coupon test.

As shown in Figure II.3.2.1.2, the specimen panel is created with a CF shell and natural fiber core by vacuum bagging. Then, it is sliced and tabbed according to the tensile test ASTM D3039. For the sensing material, the PVDF piezoelectric polymer and strain-gauge conductive trace are attached to the CF surface. Three sensing sections can output three pairs of dynamic and static signals. The sensing system can measure these multiple sections simultaneously.

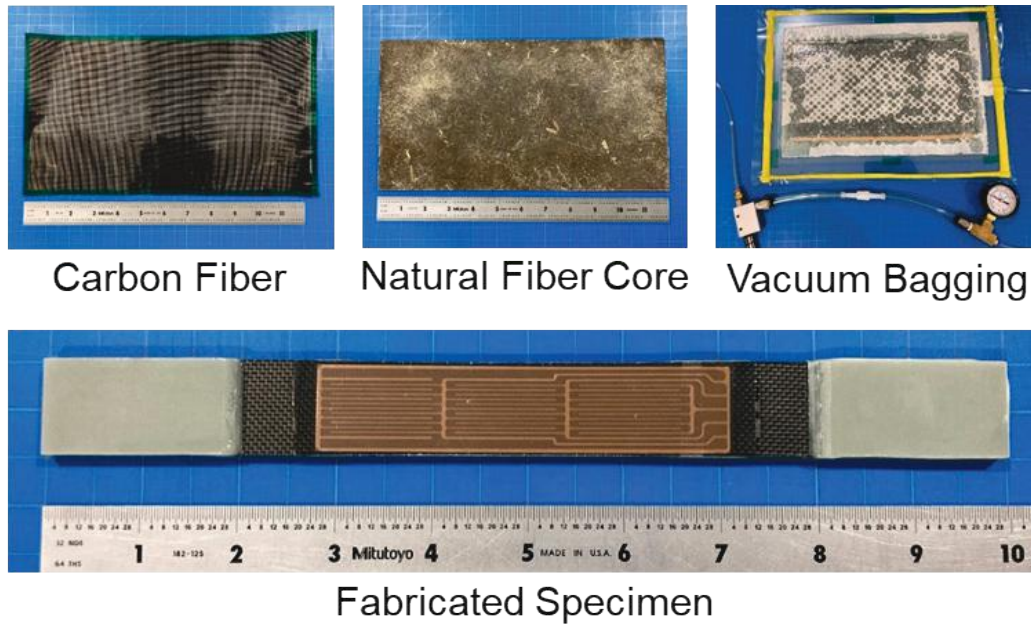


Figure II.3.2.2. Specimen fabrication. Source: Newport Sensors, Inc.

The team developed the piezo and strain amplifier, as shown in Figure II.3.2.1.3, which simultaneously converts the piezoelectric signal from the PVDF layer and the piezoresistive signal from the conductive trace to the voltage signal for the data acquisition (DAQ) system.



Figure II.3.2.3. The simultaneous piezo and strain amplifier. Source: Newport Sensors, Inc.

The team conducted the tensile test of the specimen with a universal testing machine. The test setup is shown in Figure II.3.2.1.4(a). The result shown in Figure II.3.2.1.4(b) shows that the conductive trace sensor can measure strain up to 0.4% with the common gauge factor around two. We will attempt to increase the maximum measurable strain by selecting other conductive trace materials.

After the tensile test, the specimen failed at the top portion, as shown in Figure II.3.2.1.5(a). The PVDF material detected the initialization of microcracks and identified their location 20 seconds before the failure shown in Figure II.3.2.1.5(b).

As a result, the team accomplished strain measurement, micro-crack detection, and location identification, which demonstrate efficacy for early warning of composite failure.

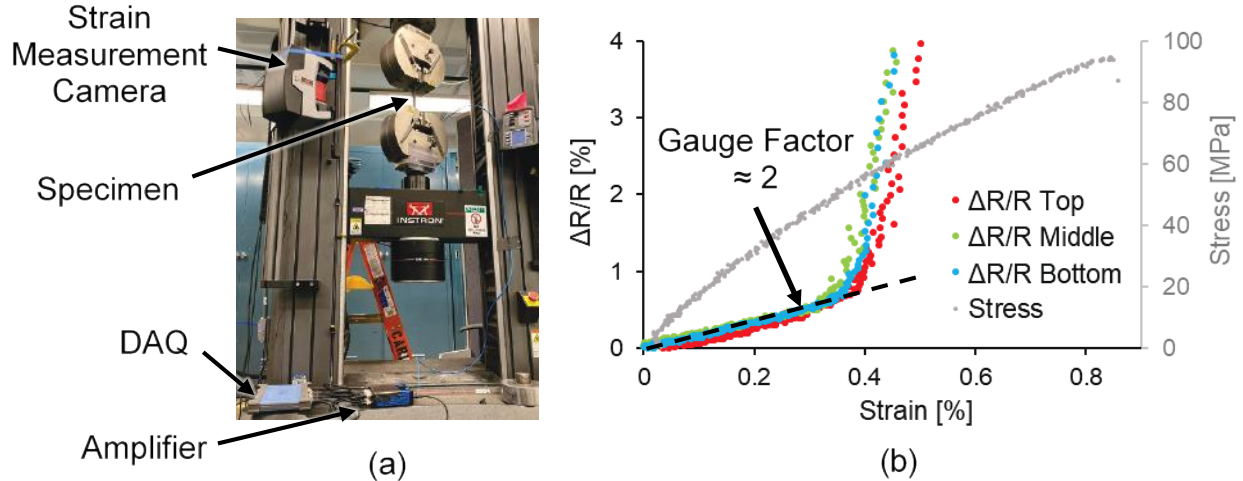


Figure II.3.2.4. (a) Experimental test setup showing the universal testing machine clamping the specimen. (b) Plots of strain-gauge resistance change vs. strain, and stress vs. strain. Source: Newport Sensors, Inc.

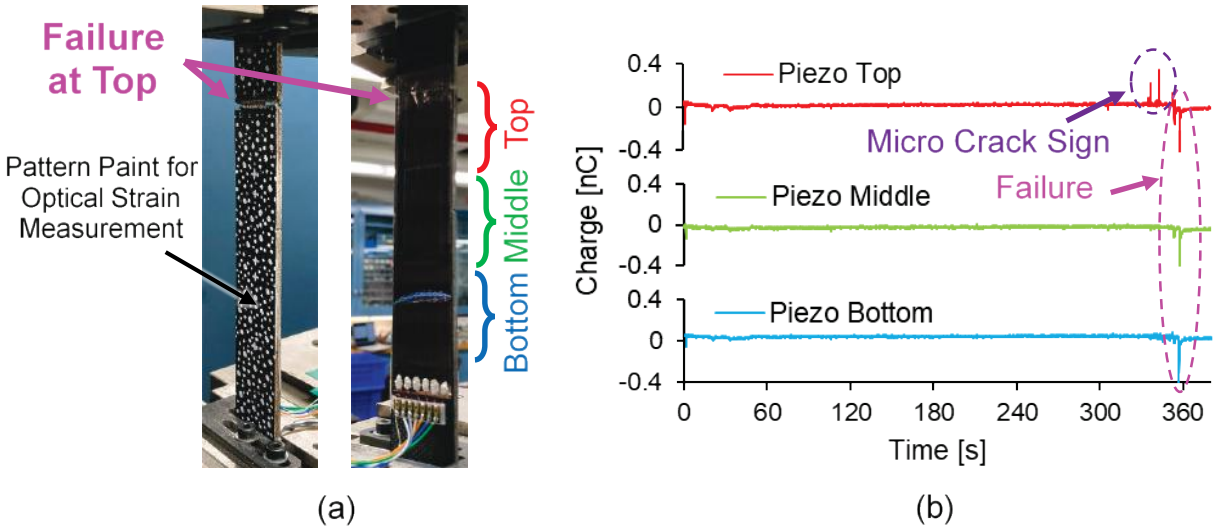


Figure II.3.2.5. (a) Specimen after tensile test showing failure at top. (b) Time history chart of piezoelectric charge showing micro-crack sign signal before failure at sensor located at top. Source: Newport Sensors, Inc.

Conclusions

During the first year of Phase II of the project, the team successfully created a multifunctional carbon/natural fiber-reinforced polymer composite specimen as a structural material vehicle that can be doubled as a distributed piezoelectric and conductive trace strain sensor.

The team also developed a novel dual-sensing system for simultaneous measurement of piezoelectric charge and conductive trace strain. The tensile testing of the specimen was conducted and demonstrated the following:

- Conductive trace sensor worked as a strain-gauge for strain monitoring.
- Disconnection of conductive trace sensor detected the damage.
- PVDF piezoelectric sensor detected microcracks prior to composite failure, demonstrating its efficacy for early warning.
- Multisectional sensor design enabled damage location capability.

Key Publications

1. Mizuta, M., 2022, “SLIC for Next-Generation Vehicles,” 2022 DOE Vehicle Technologies Office Annual Merit Review, 21 June 2022.
2. Mizuta, M., 2022, “An Integrated Strain and Piezoelectric Sensor System,” U.S. Patent Application No. 17/984,006, filed 09 November 2022.

References

1. U.S. Department of Energy–Energy Efficiency & Renewable Energy, Vehicle Technologies Office, 2014, “Lightweight Materials for Cars and Trucks,” DOE-EERE VTO website [Online]. Available at: <https://www.energy.gov/eere/vehicles/lightweight-materials-cars-and-trucks> (last accessed 15 February 2023).
2. Brooke, L., R. Gehm, and B. Visnic, 2016, “Lightweighting: What's next? Uncovering the next actions in the industry's grand mass reduction campaign,” *Automotive Engineering*, August 2016, pp. 16–25 [Online]. Available at: <http://www.nxtbook.com/nxtbooks/sae/16AUTP08/index.php> (last accessed 15 February 2023).
3. Heuss, R., N. Müller, W. Sintern, A. Starke, and A. Tschiesner, 2012, “Lightweight, heavy impact,” In: *How Carbon Fiber and Other Lightweight Materials Will Develop Across Industries and Specifically in Automotive*, McKinsey & Company, New York, NY, USA.

Acknowledgments

The author is grateful for the support provided by H. F. Wu from the DOE SBIR program under DOE Award No. DE-SC0020707. The author is also grateful for S. Shi from the UNT for his assistance with the natural fiber composite source and the material testing equipment.

II.3.2.2 Integrated Self-Sufficient, Structurally Integrated Multifunctional Sensors for Autonomous Vehicles (Acellent Technologies, Inc.)

Amrita Kumar, Principal Investigator

Acellent Technologies Inc.
835 Stewart Dr.
Sunnyvale, CA 94085
E-mail: akumar@acellent.com

Brandy Greenawalt, SBIR Program Office

U.S. Department of Energy SC-29
Small Business Innovation Research
19901 Germantown Rd.
Germantown, MD 20874
E-mail: brandy.greenawalt@science.doe.gov

H. Felix Wu, DOE Technology Development Manager

U.S. Department of Energy
E-mail: felix.wu@ee.doe.gov

Start Date: August 23, 2021	End Date: August 22, 2023	
Project Funding (FY 2022): \$1,149,997	DOE share: \$1,149,997	Non-DOE share: \$0

Project Introduction

DOE's VTO has identified the need for novel multifunctional composite materials and structures for the automotive industry with the capability to reduce weight, volume, and cost of 'conventional' structural components by performing engineering functions beyond load-carrying. The multifunctionality that couples structural performance and additional functionalities (e.g., electrical, magnetic, optical, thermal, chemical, biological) is critical to the growth of AI in the automotive industry. Multifunctional structures can sense, diagnose, and adapt to environmental changes with minimum external intervention; enable alternation of shape functionality and mechanical properties on demand; and support the structural integration of power harvest, storage, and transmission capabilities for 'self-sustaining' systems. Currently, the need exists to reduce the demands of a system as a whole. For example, for a city car, a pedestrian protection system (PPS) is of paramount importance; however, 98% of the required energy needs are associated with weight. Adopting composites provides the capability to integrate sensors needed by a PPS into the structure, as well as enabling significant weight-savings—especially with multifunctionality built in for electrical energy storage and to carry the mechanical load.

Objectives

Acellent Technologies Inc. proposes to develop an integrated AUTO-SMART sensor system for the automotive industry that can provide multifunctional capabilities and make the vehicles self-sufficient. The primary focus is on how multifunctionalities in composites can impact the design of automotive vehicles to provide increased pedestrian safety, weight-savings, and structural efficiencies. The proposed development will focus on two multifunctionalities: (1) a PPS and (2) a battery monitoring system (BMS).

Approach

The following developments are targeted in this program, with Phase II focusing on *developing a complete design for the AUTO-SMART sensor system*:

1. Develop the design for a pedestrian crash sensing system that has the capability to detect any impact event occurring on the front bumper of an automobile within a very short duration and generate the

proper response signal to a built-in protection system. A primary challenge in this effort was to design and develop an impact event detection technique that can work efficiently even for complex structures with local property variation. Conventional impact detection systems have long response times because of the slow response of traditional sensors. The proposed system utilizes lead zirconate titanate (PZT) sensors to generate the impact signal immediately after the impact event happens. By doing this, passive safety systems—such as air bags and pyrotechnic restraints—can be activated in time to save lives.

2. Develop the system design for monitoring the state of health (SOH) and state of charge (SOC) of a typical battery pack for automobiles. Key design features, such as sensor locations, will be developed for the battery.

Results

Pedestrian Protection System (PPS)

An automotive PPS is generally used for protecting pedestrians from harm caused by frontal collisions. In Phase II, the system is being developed on a stationary bumper. Methods for the design and installation of the sensors on the bumper are being developed. The work is being conducted in collaboration with Ford Motor Company, who is guiding development efforts.

Sensor Network Design for Pedestrian Crash Sensing

In Phase II, Acellent used its established SMART Layer sensors for installation in the bumper. The SMART Layer is well-established in the field and is currently known for its unique ability to provide a large structural coverage for gathering data with its network of sensors/actuators embedded on a layer, thus eliminating the need for each sensor to be installed individually, as shown in Figure II.3.2.2.1 [1–4]. The layer consists of a network of embedded, distributed PZT discs, which act as both sensors and actuators for monitoring structural conditions in real-time. The SMART Layer manufacturing process utilizes the printed circuit technique to connect sensors and actuators embedded in the layer. The SMART Layer is treated as an extra ply that can be embedded between composite plies during the composite layup process or be surface mounted on both metallic and composite structures using a secondary adhesive, such as epoxy.



Figure II.3.2.6. SMART layer sensors. Source: Acellent Technologies, Inc.

For this application, Acellent chose small, disc-shaped PZTs. The PZT sensors, capacitors, and wiring can all be embedded in a thin dielectric film, as shown in Figure II.3.2.2.1. Additional shielding layers and wiring are added to the sensor layer to minimize external electromagnetic interference (EMI) and crosstalk between sensors. All SMART Layer strips are EMI-shielded on one-side of the circuit by a copper layer. The small size

of the PZTs is important because they do not protrude from the bumper and can be embedded in the bumper during manufacturing.

To find an optimal sensor density and spacing for the sensor network, the team considered several factors. Speed and accuracy requirements play a critical role in making this determination. Ideally, the team would like sensors instrumented along the entire length of the bumper with minimal spacing between each sensor to account for impacts at every location as discussed in the requirements above. However, cost and practicality issues require us to set a minimum sensor density [5–6].

Many impact tests were performed on the bumper to determine the locations of the sensors. A total of 12 PZTs were installed on the bumper based on bumper size and test result. The SMART Layer sensor locations were designed based on the bumper.

A prototype PPS was tested by Acellent on a test car bumper provided by Ford from their EV collection. The bumper with the installed sensors was fastened securely to two concrete poles. The sensors were connected to the impact data collection hardware through cables. The data was sent to the laptop via Ethernet for analysis. Figure II.3.2.2 shows the test setup. To identify the impact signals due to different types of object impacts, impact tests were performed using various objects. For simulating the pedestrian impact on the bumper, a Hybrid II adult test dummy leg was used. This dummy leg represents the 50th percentile adult male, and the size and weight of the dummy leg represent the ‘average’ U.S. adult male population. To study the non-pedestrian impacts and the corresponding signals at the bumper, impacts were performed on the bumper using a polyvinyl chloride pipe, wooden dowel rod, wooden board chunk, golf club, stone, etc. The test results of the impact testing are presented in the next section.

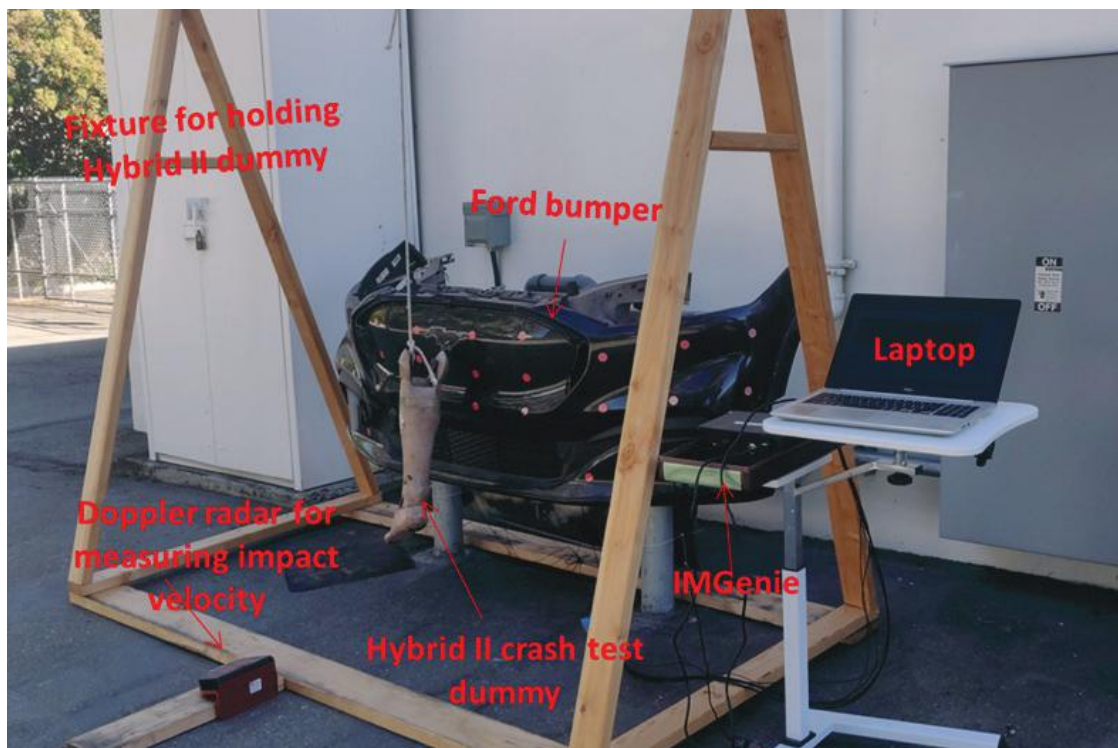


Figure II.3.2.7. System test setup. Source: Acellent Technologies, Inc.

Impact with a Golf Club

The car bumper was hit by a golf club at the front edge of the bumper. The impact triggered the system to collect data from the sensors. As shown in

(a)

(b)

Figure II.3.2.2.3, the SHM system successfully captured the impact.

(a)

(b)

Figure II.3.2.2.3(a) shows the golf club that was used for the impact tests, while

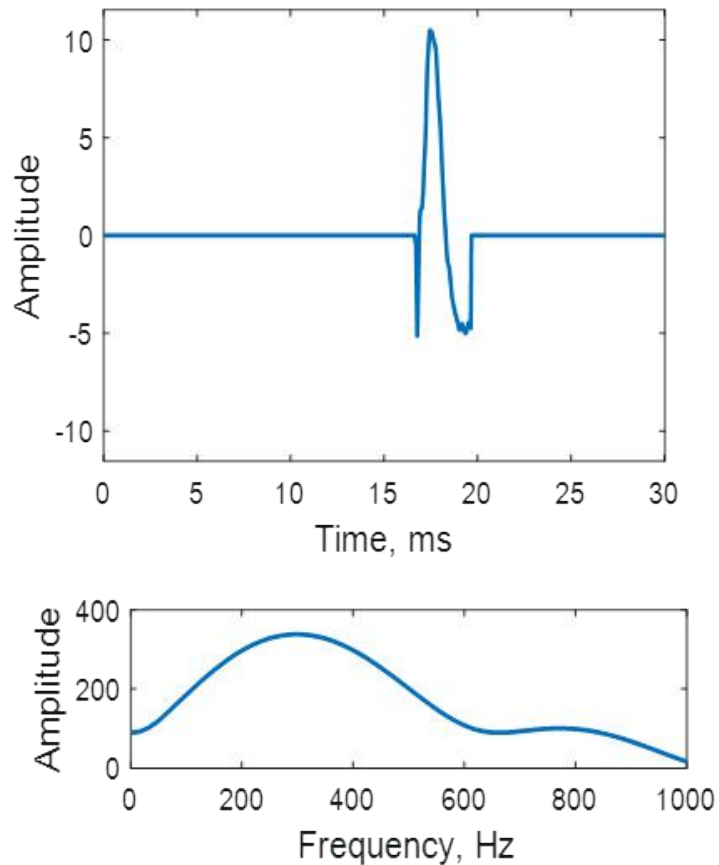
(a)

(b)

Figure II.3.2.2.3(b) shows the signal received from the sensors and the frequency spectrum of the signal. The initial 3ms part of the signal was used to identify the characteristics of the signal. Repeated impact tests were performed to test the repeatability of the signal. The frequency spectrum of the signals was calculated and studied. The peak frequency of the signals was obtained from the tests and observed as between 269–395 Hz. The golf club impact test results were found to be similar for repeated tests.



(a)



(b)

Figure II.3.2.8. Voltage impulse received upon an impact with a golf club: (a) golf club and (b) voltage impulse curves. Source: Accellent Technologies, Inc.

Impact with a Hybrid II Dummy Leg

In the second series of tests, the car bumper was hit by a Hybrid II dummy leg, as observed in Figure II.3.2.2.4(a), to simulate hitting a pedestrian. The impact triggered the system to collect data from the sensors. The signal received from the sensor and its frequency spectrum is presented in Figure II.3.2.2.4(b). The SHM system successfully captured the impact. The initial 3 ms of the signal was studied to identify the signal characteristics due to pedestrian impact. The frequency analysis was performed for the 3ms of the

signal, and the peak frequency of the signal was identified as <100 Hz. Repeated impacted tests were performed on the bumper and the Hybrid II impact signals were noticed as repeatable.

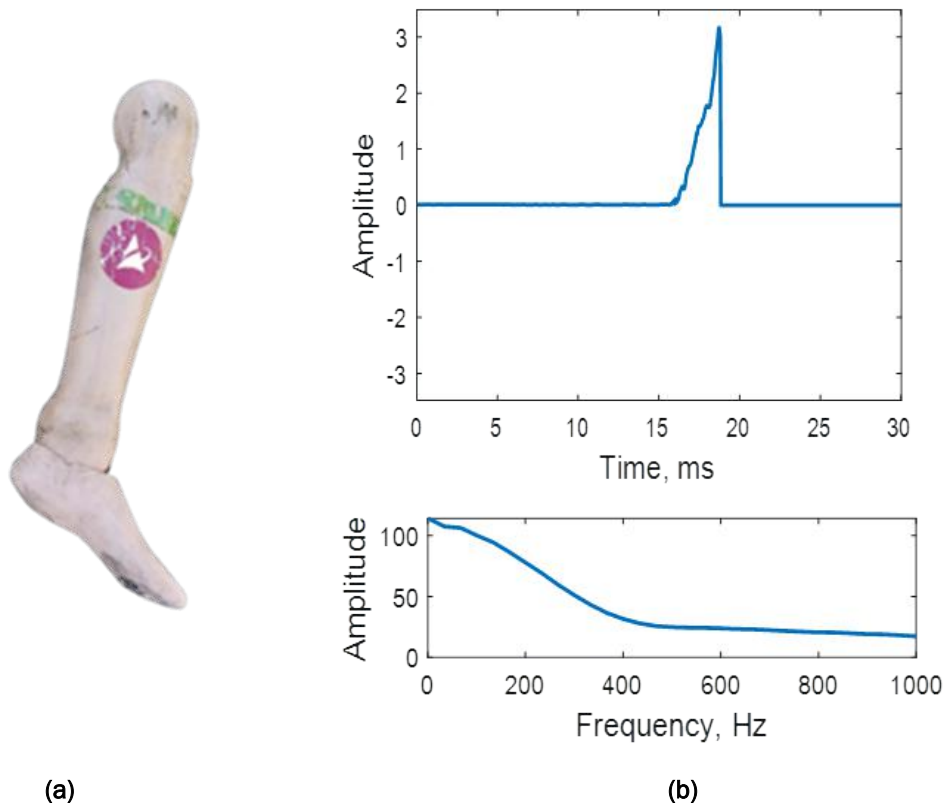


Figure II.3.2.9. Voltage impulse received upon an impact with a prosthetic leg: (a) prosthetic leg and (b) voltage impulse. Source: Accellent Technologies, Inc.

During Phase II, Accellent utilized data obtained from the tests to identify the frequency responses due to the impact of various objects on the bumper. The peak frequency due to diverse impact objects was studied from several repeated tests. A summary of the peak frequency study is presented in Table II.3.2.2.1. As the data demonstrates, the impact signals obtained from non-pedestrian objects vs. pedestrian objects are significantly different. Based on this discovery, the software was tweaked to meet the requirements for the detection of pedestrians. Extensive testing of the software will be performed in the next stage.

Table II.3.2.2.1. Peak Frequency due to Various Object Impacts

Component	Peak Frequency Range	Avg. Peak Frequency
Hybrid II Leg	< 100 Hz.	35.19 Hz.
Polyvinyl Chloride Pipe	285–363 Hz.	321.35 Hz.
Wooden Dowel Rod	269–363 Hz.	320.13 Hz.
Wooden Board Chunk	174–316 Hz.	264.54 Hz.
Golf Club	269–395 Hz.	314.35 Hz.
Stone	269–442 Hz.	358.70 Hz.

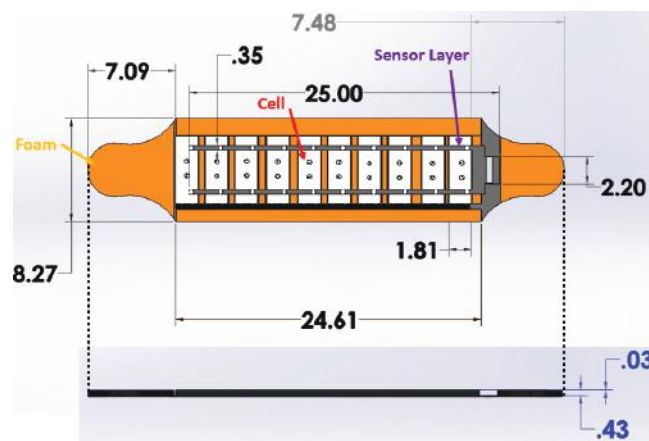
BMS

The BMS is used to monitor and control power storage systems, ensure the health of the battery cells and deliver power to the vehicle systems. The lithium ion (Li-ion) battery technology has performed magnificently and has improved over the last decade; however, the chemistry inside the battery is very susceptible to certain risks such as overheating, over-voltage, deep discharge, over-current, and pressure or mechanical stress. To prevent battery failure and to mitigate potential hazardous situations, there is a need for a BMS that ensures that batteries function properly in the final application. The BMS can provide SOC, SOH, and EOL of the battery. This work was completed in collaboration with Stanford University, which introduces multifunctional energy storage composite (MESC) structures as an alternative strategy towards structural load-bearing batteries fabrication—an intermediate, multidisciplinary strategy. MESC structures represent a novel form of multifunctional, structural battery enclosures that can carry mechanical loads while simultaneously providing energy storage capabilities. MESC structures provide a disruptive integration technique that enables high-energy Li-ion battery electrode materials to be embedded in high-strength CFRP composites. The novelty of MESC structures lies in their incorporation of through-thickness interlocking polymer rivets, which extend through carefully designed perforations in the battery stack to interlock the electrode layers and securely anchor these layers onto the structural CFRP face sheets. Standard industry electrodes can be adapted to function directly within this design without any requirement for battery chemistry modifications, which may be crucial for industry adoption.

Like sandwich structures, the comparatively stiff CFRP face sheets are placed on either side of the electrode stack, separated by the electrode core thickness, to carry the majority of the bending moment. This sandwich-style construction effectively increases the area moment of the laminate, giving it higher flexural rigidity. Without the interlayer shear resistance of the battery core, the thin CFRP face sheets will tend to bend around their individual neutral axis, and the structural contributions of the face sheets will be minimized. The interlocking rivets, therefore, act to inhibit interlaminar slippage between electrode layers, thus allowing effective transfer of the shear stress through the battery stack to the CFRP face sheets. This is analogous to the use of stud shear connectors in civil construction to enhance the shear interaction and the load transfer between concrete and steel sections. The shear transfer enables the battery laminate to bend around a common neutral axis, thus using the intrinsic mechanical properties of the electrode layers efficiently and making them a suitable sandwich structure core material.

Fabrication of the MESC Skateboard

As a demonstration for the MESC applications, the team made an MESC skateboard that is representative of an EV. The skateboard consists of 10 MESC cells between two CFRP boards. Figure II.3.2.2.5 shows the dimensions of board, battery cells, wiring, and sensor layers.



Note: Dimensions are in inches

Figure II.3.2.10. The dimension and design of the skateboard. Source: Accellent Technologies, Inc.

This skateboard has 10 MESC cells, which are connected in series style to generate 37 V, which is the required voltage for a BMS to be able to run a typical skateboard's motor and wheels. Figure II.3.2.2.6 shows the sketch for wiring and arrangements of the cells. The skateboard's electrical characteristics are tabulated in Table II.3.2.2.2. Skateboard testing is currently ongoing.

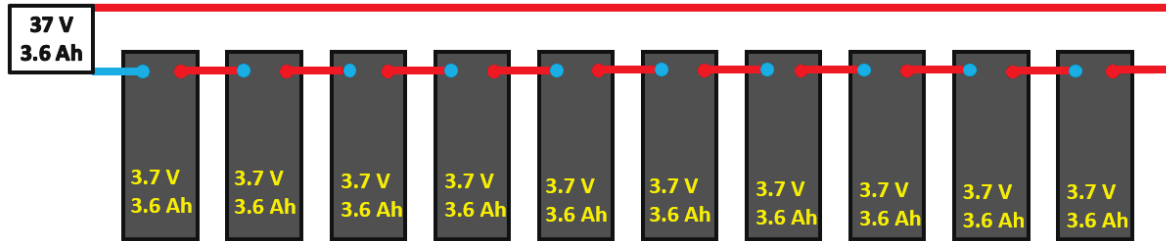


Figure II.3.2.11. MESC battery arrangement. Source: Accellent Technologies, Inc.

Table II.3.2.2.2. Important Characteristics of the Skateboard

Characteristics	Ampirus Cells
Number of Cells	10 cells
Charge Capacity of Each Cell	3.6 Ah
Charge Capacity of Whole System	3.6 Ah
Current Supplied	1.14 A
Battery Charging Time	3.2 h
Voltage of Each Cell	3.7 V
Voltage of Whole System	37 V
Energy Capacity	133 Wh
Range	13.3 miles
Weight	6.8 kg
Target Max Load	150 kg
Target Top Speed	30 mph
Weight (only CFRP board)	1.8 kg
Energy Density	73.88 Wh/kg

Conclusions

During the last year, Accellent has developed and tested two multifunctional applications, PPS and BMS, for vehicles. Algorithms required for the detection of pedestrians vs. non-pedestrians have been developed; testing is currently ongoing. In the coming year, detailed testing will be conducted with Ford’s guidance to ensure the requirements for the deployment of a safety mechanism are met.

For the BMS, a skateboard was manufactured using MESC technology, which includes composites, batteries, and sensors. This skateboard is representative of an EV. Testing is currently ongoing to see if the skateboard can be used effectively for monitoring the SOC and SOH of the batteries.

References

1. Accellent Technologies, Inc., 2020, “Accellent: Smarter structures, safer world,” Accellent website. [Online] Available at: www.acellent.com (last accessed 1 March 2023).

2. Chang, F.-K. (ed.), 2019, *Proceedings of the 12th International Workshop on Structural Health Monitoring, 10–12 September 2019, Stanford University, USA*. [Online] Available at: <https://www.dpi-proceedings.com/index.php/shm2019> (last accessed 1 March 2023).
3. Qing, X. P., S. J. Beard, A. Kumar, I. Li, M. Lin, and F.-K. Chang, 2009, “Stanford multiactuator–receiver transduction (SMART) layer technology and its applications,” in Boller, C., F.-K. Chang, and Y. Fujino (eds.), *Encyclopedia of Structural Health Monitoring*, John Wiley & Sons, New York. <https://doi.org/10.1002/9780470061626.shm098>.
4. Qing, X. P., S. J. Beard, R. Ikegami, F.-K. Chang, and C. Boller, 2009, “Aerospace applications of SMART layer technology,” in Boller, C., F.-K. Chang, and Y. Fujino (eds.), *Encyclopedia of Structural Health Monitoring*, John Wiley & Sons, New York. <https://doi.org/10.1002/9780470061626.shm152>.
5. Kim, A. C., and F.-K. Chang, 2015, “Rapid detection and identification of pedestrian impacts using a distributed sensor network,” in *Proceedings SPIE Smart Structures and Materials 2005: Smart Structures and Integrated Systems*, Vol. 5764. <https://doi.org/10.1117/12.600433>.
6. Kim, A. C., 2006, “A rapid method for identifying and characterizing structural impacts using distributed sensors: An application for automotive pedestrian protection,” Thesis (Ph.D.)--Stanford University, Stanford, CA, USA. Publication Number AAI3197453.

Acknowledgments

Accellent Technologies Inc. would like to acknowledge the guidance of DOE Program Manager H. F. Wu during the progress of this research.

Accellent Technologies Inc. would also like to acknowledge the support of Ford Motor Company in providing the test bumper and guidance for the PPS.

This work was conducted with support from DOE SBIR Phase II under Award # DE-SC0020714.

II.3.2.3 Short-Fiber Preform Technology for Automotive Part Production – Phase II (Composites Automation, LLC)

Roger Crane, Principal Investigator

Composites Automation, LLC
7 McMillan Way, Ste. #1
Newark, DE 19713
E-mail: roger.crane@compositesautomationllc.com

Dirk Heider, Co-Principal Investigator

Composites Automation, LLC
7 McMillan Way, Ste. #1
Newark, DE 19713
E-mail: dirk.heider@compositesautomationllc.com

Brandy Greenawalt, SBIR Program Manager

U.S. Department of Energy SC-29
Small Business Innovation Research
19901 Germantown Rd.
Germantown, MD 20874
E-mail: brandy.greenawalt@science.doe.gov

H. Felix Wu, DOE Technology Development Manager

U.S. Department of Energy
E-mail: felix.wu@ee.doe.gov

Start Date: September 30, 2020 End Date: February 23, 2023
Project Funding (FY 2022): \$1,100,000 DOE share: \$1,100,000 Non-DOE share: \$0

Project Introduction

CFCs exhibit superior properties and enable part consolidation, reduced system weight, and reduced emission benefits for automotive applications. A lack of affordable and high-rate-capable CFC materials and processes limit the widespread implementation of these materials. With participation from our academic partner, the University of Delaware Center for Composite Materials (UD-CCM) and vehicle OEM GM, studies during a Composites Automation (CA) project sponsored by DOE-EERE—the ‘Ultralight Composite Door’—have shown that a key obstacle to widespread CFC adoption is the ability to manufacture complex geometry CF preforms that meet performance, cost, and rate targets in infusion processes while minimizing scrap. Single-piece, continuous CF preforms are restricted to simple geometries, as the continuous CF layup cannot be easily and cost-effectively formed into doubly curved or complex geometry parts, limiting the application of CF preforms to a few components. Multi-piece preforms are complex to manufacture, require joining, are difficult to handle prior to molding, have inconsistencies in-mold filling, and have limited rate production, all of which increase part cost. Another challenge is the high cost and embodied energy of the CF material itself. With current composite processing approaches, lower cost recycled or waste stream short CFs, currently available only in discontinuous form, cannot be converted into high-fiber-volume and high-performance CFCs.

With the support of GM and the U.S. Automotive Materials Partnership (USAMP), our team, which is comprised of CA, UD-CCM, and Vartega, Inc. (Vartega), is addressing these shortcomings through a novel aligned, short-fiber material called ‘Tailorable universal Feedstock for Forming (TuFF).’ TuFF was developed in a four-year UD-CCM program that was sponsored by the Defense Advanced Research Projects Agency.

TuFF production uses low-cost short virgin, waste stream, or recycled fibers. The recycled CF is optimized and provided by Vartega. The material has significant in-plane extensibility and exhibits metal-like formability with full property translation, compared to continuous fiber composites. CA has produced composite panels with 46% FVF using \$11/kg (\$5/lb) CF from waste stream sources and wet compression processing that exhibited tensile properties sufficient for primary structural automotive applications.

The CF TuFF material has unique properties that make it amenable to the automotive stamp-forming typically used for metals. These properties include: (1) the ability to stretch up to 50% without losing material integrity, allowing net-shape preforming; (2) enabling a near-zero waste process with full recovery and reuse of CFs, as is possible with metals; and (3) the potential to use recycled/waste stream CFs to produce structural parts with reduced cost and embodied energy efficiency. One issue being addressed in this project is the ability to handle TuFF preforms in the mechanized material handling typically used in automotive part production. To address this challenge, CA has developed a method to automate the stabilization of the TuFF preforms. CA has also used recycled fibers in the TuFF process to further improve cost and embodied energy. Although the TuFF processing with the recycled fiber production has been demonstrated, there were issues with mechanical property translation, which will be presented later in this report. The ability to process short fiber into stretchable preforms with rapid conversion to high-performance, complex geometry, and low-cost CFC structures creates opportunities to replace automotive metal structures. To demonstrate high-rate production capability with TuFF, CA has prepregged TuFF preforms with a snap-cure resin system. Initial production using this combination demonstrated significantly reduced cycle times of minutes compared with hours for conventional thermoset prepreg systems.

Objectives

The objective of this SBIR Phase II effort is to evaluate the use of low-cost, discontinuous CFs from a variety of sources to produce TuFF preforms that can be used in high-rate formation of the TuFF material into composite automotive parts. The CF sources include virgin material from commercial and government sources, waste stream fibers, and recycled fibers from Vartega. The specific technical objectives of the Phase II SBIR are as follows:

- Identify low-cost short-fiber and resin systems that can be used to produce TuFF prepreg material that can be fabricated into components at production rates approaching those of metal stamping
- Evaluate and address challenges with recycled CF materials, such as entanglement, adhesion, resin residue, and fiber length distribution
- Develop and scale stabilization methods, such as electrospinning veil surfaces onto the TuFF preforms; methods must be compatible with resin systems, such as snap-cure resin systems, which have minimal or no effect on TuFF composite-FVF
- Demonstrate that the veil materials enable handling of blanks in automated processes (transfer to infusion line, placement in tooling, etc.)
- Fabricate TuFF preforms using low-cost (waste/recycled) fibers and stabilize the preforms using the electrospinning process for infusion processing
- Demonstrate formability of dry TuFF preforms for complex part production
- Demonstrate performance
- Meet automotive microstructure requirements, such as FVF (e.g., > 50%)
- Measure mechanical properties for a property database
- Demonstrate at-rate fabrication, performance, and cost for an automotive component (e.g., the intent is to leverage DOE-EERE door tooling and data)
- Evaluate insertion opportunities with GM and USAMP.

Approach

This effort is developing the requirements for fiber geometry (i.e., fiber length and distribution), demonstrating the ability to disperse the various fiber systems in water to produce TuFF preforms, developing an environmentally friendly electrospinning material and process that will allow for the TuFF preform to be handled without disrupting the fiber orientations, and developing resin process conditions that will allow for high-rate or snap curing of the TuFF composite material. To provide handleability, the project team is developing a system to apply an electrospun veil on the TuFF preform. An E-spin system has been designed and fabricated that can be integrated into the TuFF2-CA production line. This system allows for tailorable veil properties and will ensure compatibility with snap-cure resin chemistry being investigated with the TuFF preforms. The electrospun materials do not affect mechanical properties, are optimized to minimize areal weight using equipment tailored to match the TuFF sheet width. Compaction studies on TuFF preforms with the polyvinyl alcohol (PVA) veil were done to ensure 50% FVF is maintained. TuFF composite panels were produced with standard epoxy for mechanical property determination, showing near 100% property translation compared to continuous fiber composites. In addition, CA has investigated the use of snap-cure resins for the prepregging of the TuFF preforms. These systems will potentially enable high-rate production capability. CA will establish the process conditions that will produce the TuFF prepreg material with these snap-cure systems without advancing the cure. Process conditions that will allow for rapid curing of these prepreg materials will also be developed.

Mechanical properties of the TuFF material with the PVA veil and prepregged with the snap-cure resin will then be determined. Feature-based parts will be investigated for fabrication demonstration. The intent is to use the mechanical property database and apply it to the DOE-EERE door design to provide a TuFF solution that demonstrates weight, cost, and performance metrics comparable or superior to the continuous CFC. The team will conduct a trade study to assess the material and final part cost and compare the results to the DOE-EERE findings, as well as the current steel baseline. During this process, we will continue to brief our OEM partners, GM and USAMP, and expect to engage their supply chains throughout the effort to evaluate potential technology insertion opportunities.

Results

This SBIR project is working toward three advances to enable more general use of composite materials for general automotive structural applications: (1) low material costs; (2) material that can be compression- or stamp-formed, similar to metals; and (3) high-rate fabrication similar to metals. From the survey of sources of low-cost short fibers, CA has selected T-800 waste stream fibers from Barnett, T-800 recycled fibers from Vartega, and P35 low-cost commercial CFs from ZOLTEK. The cost of these fiber systems currently ranges from \$5–10/lb., but for large quantities, the cost has been projected to be as low as \$3/lb. To produce the highly aligned TuFF fiber preforms using the above-mentioned fibers, several attributes must be met. The fibers must (1) be a specific length with a narrow distribution, (2) have an aspect ratio between 600 and 1,000, and (3) be able to be well-dispersed in water. This project selected a fiber length of 3 mm. T-800 virgin fibers were cut to length by Engineered Fibers Technology. ZOLTEK was able to provide fibers of this length. The recycled and waste stream fibers were provided by our industry partner, Vartega.

Although the use of recycled fibers has numerous benefits such as reduced embodied energy costs, issues arose in their use in the TuFF processing. Specifically, although fiber length of the Vartega recycled fiber was well controlled, dispersion of these fibers was hindered by residue that remained on the cut fibers after the solvolysis process used by Vartega. Figure II.3.2.3.1(a) and Figure II.3.2.3.1(b) show two examples of SEMs of the as-received T-800 recycled fiber from Vartega. To produce TuFF material with these fibers, CA developed a pyrolysis process that removed this residue and enable the fibers to be dispersed in the TuFF processing. Figure II.3.2.3.1(c) shows a SEM of these pyrolyzed fibers.

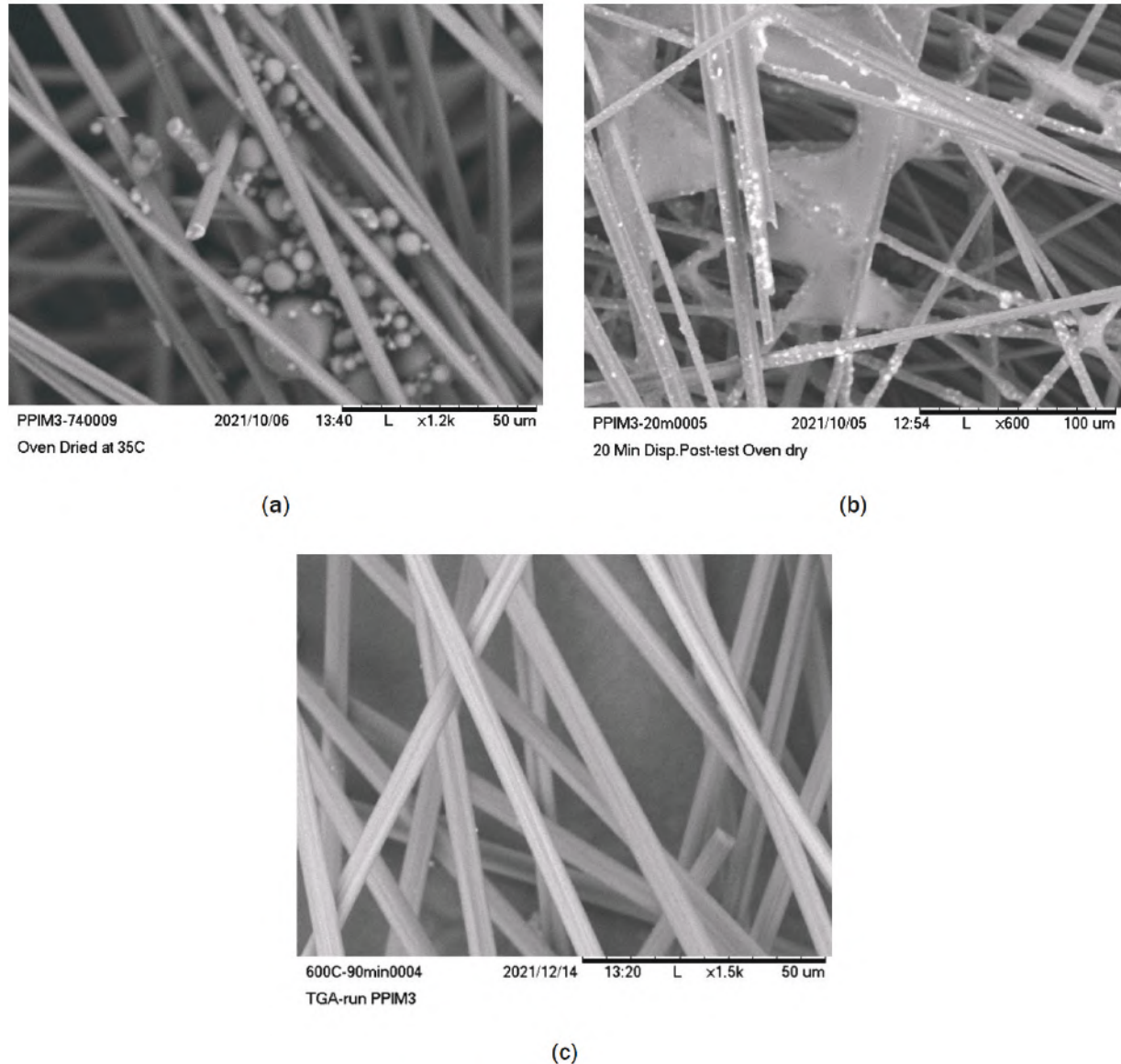
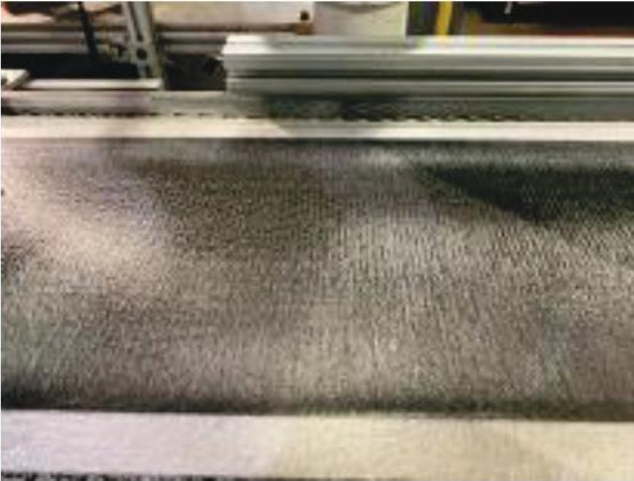


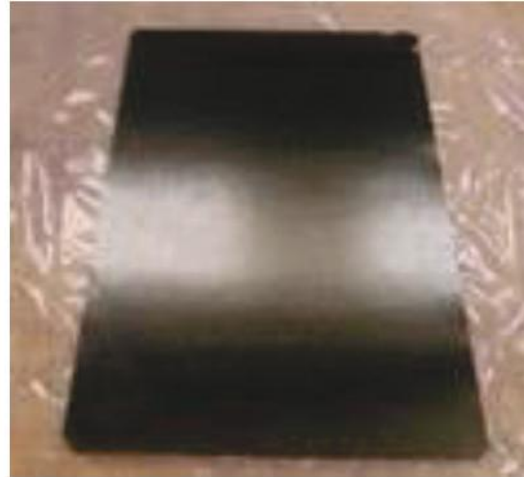
Figure II.3.2.12. SEM of T800 prepreg recycled fiber from Vartega: (a) and (b) as received; and (c) after additional pyrolysis process. Source: Composites Automation, LLC.

These pyrolyzed fibers were used to manufacture TuFF material. After processing, 24 plies of the TuFF material were laid up, prepregged using the Axiom epoxy film, cured using a bladder molding process, C-scanned to verify quality, and tensile tested to determine mechanical properties. These processes are shown in Figure II.3.2.3.2.

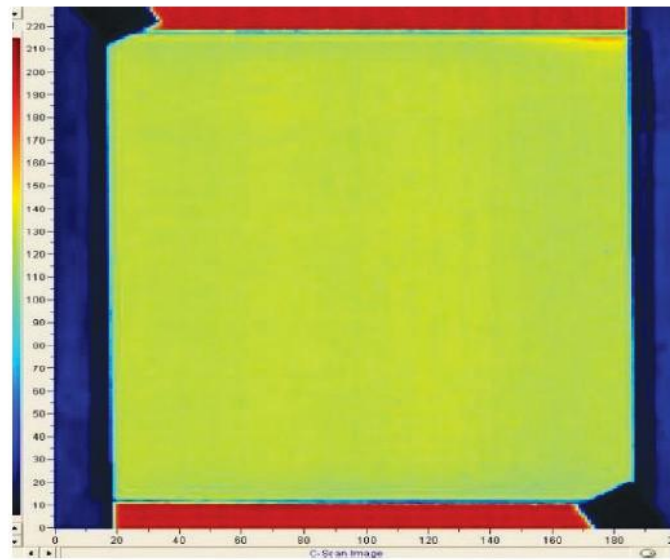
Table II.3.2.3.1 shows the tensile test results for the panel discussed above. It should be noted that the fiber volume fraction (FvF) of the TuFF panel was 48%. The TuFF material properties were compared with the material properties provided by Toray that were also normalized to a FvF of 48%. The modulus translation was shown to be 98% of the normalized value for a continuous T-800 fiber composite while the strength only had a strength translation of 54%. Inspection of the tensile failure surface revealed fiber clusters where tens of fiber appear to be adhered together with all the ends of the fibers in the bundle terminating at the same location thereby resulting in stress concentration and premature failure, as observed in Figure II.3.2.3.3.



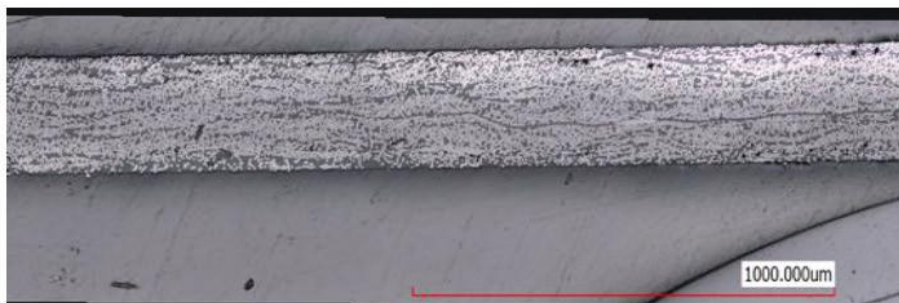
(a)



(b)



(c)



(d)

Figure II.3.2.13. TuFF processing using recycled T-800 from Vartega: (a) TuFF material processing; (b) 24 layer TuFF prepreg; (c) C-scan of bladder molded TuFF material; and (d) micrograph showing high-quality material for tensile testing. Source: Composites Automation, LLC.

Table II.3.2.3.1. Recycled T-800 TuFF Composite Comparison to Continuous Fiber Mechanical Properties

	Fiber Volume Fraction	Strength (ksi)	Modulus (Msi)
Toray T800H Datasheet	0.60	424	24
	0.48	339	19.2
Recycled T800H TuFF	0.48	184±18 COV = 9%	18.8±0.4 COV = 2%
Property Translation		54%	98%

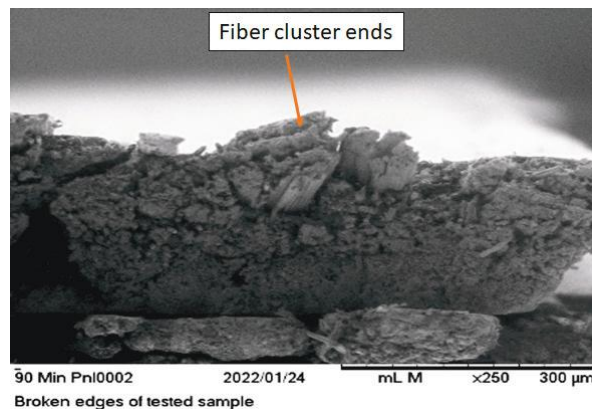


Figure II.3.2.14. SEM of recycled T-800 TuFF composite failed tensile surface showing fiber clusters. Source: Composites Automation, LLC.

To be able to handle the TuFF material for automotive like metal forming, the TuFF preform needs to be stabilized. Two processes have been investigated: (1) prepregging the TuFF preform and (2) applying a veil over the TuFF surface. Of the veil materials investigated, PVA was selected as the best solution. The PVA solution is water-based and therefore is environmentally friendly. In addition, the PVA can be obtained in various molecular weights, thereby enabling electrospun areal weights as low as 0.1 gram per square meter (gsm). Figure II.3.2.3.4(a) shows the full-scale production electrospinning apparatus designed for the TuFF2-CA process line. Figure II.3.2.3.4(b) shows a SEM of the 0.1 gsm PVA e-spun fibers on the T800 TuFF material. In addition to holding the TuFF fibers in place, the electrospun veil material allows the TuFF material to deform while keeping the preform fibers intact. Preliminary testing showed that the TuFF material stabilized with the 0.1 gsm PVA held the fibers in place while being stretched 50% transverse to the fibers.

To enable metal-like forming, prepregging T800 TuFF material with M77 fastcure resin film is being investigated. The focus of the current work is to characterize this resin system and determine the isothermal cure kinetics and rheology behavior as a function of temperature and time to determine an optimized impregnation and subsequent cure schedule for prepreg manufacture and composite consolidation. Figure II.3.2.3.5(a) shows the non-isothermal DSC heating ramps using ramp rates of 2, 5, and 10°C/min. This data was used as input for Netzsch Kinetics Neo software to determine the average energy of activation, E_a , and average pre-exponential factor, A , using the model-free Friedman analysis that is then used to fit the model to the DSC data. From this, simulation runs using the Netzsch Kinetics Neo software were done to determine the time to achieve 95% conversion using various isothermal temperatures, as shown in Figure II.3.2.3.5(b).

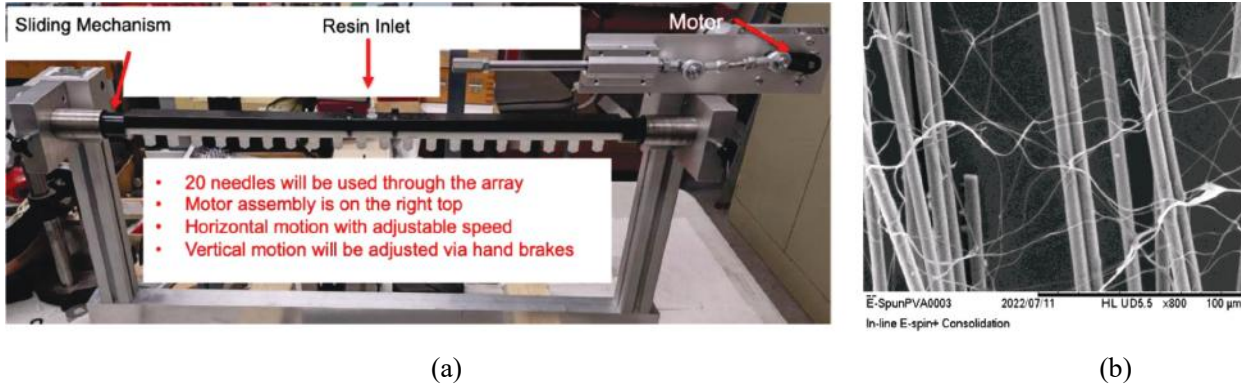


Figure II.3.2.15. (a) Electrospinning apparatus for the TuFF2-CA process line. (b) SEM of 0.1 gsm PVA e-spun fibers on T800 TuFF preform. Source: Composites Automation, LLC.

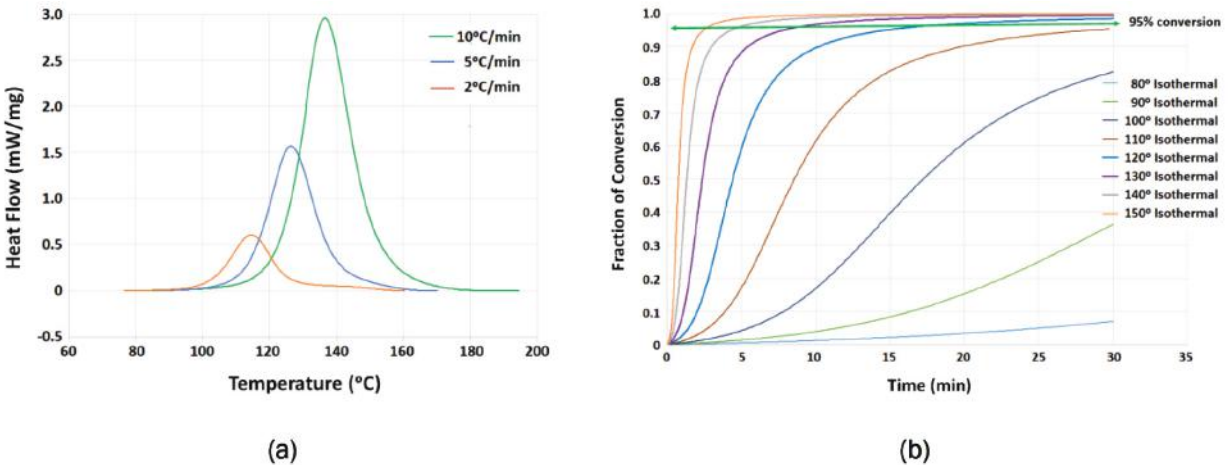
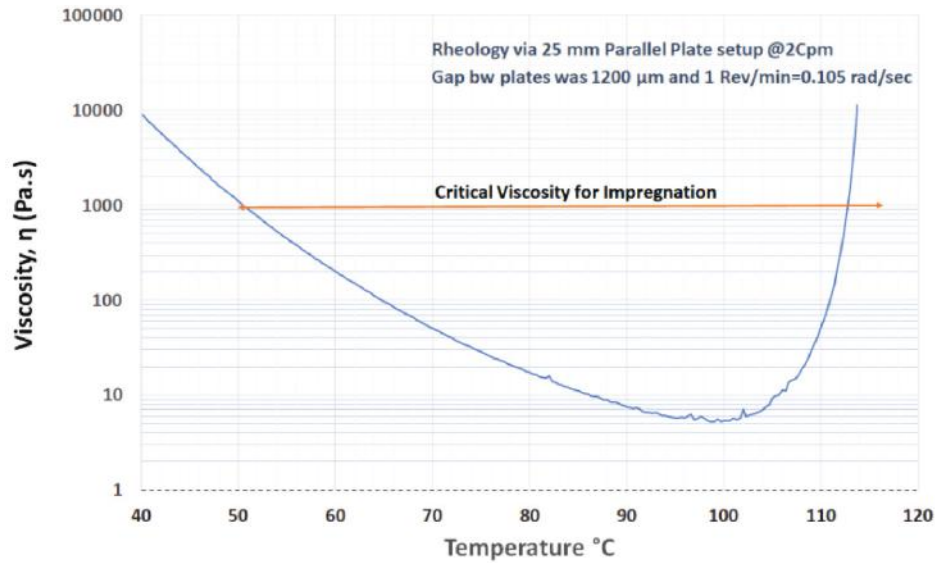


Figure II.3.2.16. (a) Non-isothermal DSC scans for different heating rate. (b) Fraction of conversion vs. time predictions for isothermal cure temperatures ranging from 80 °C to 150 °C. Source: Composites Automation, LLC.

To prepreg the TuFF material, the M77 resin needs to be heated high enough to reduce the viscosity to allow for resin to infuse the TuFF material while not advancing the cure. A non-isothermal Parallel Plate Rheology experiment was conducted using a heating rate of 2°C/minute to determine the viscosity as a function of temperature as shown in Figure II.3.2.3.6(a). It is possible to achieve complete infiltration of a dry TuFF preform for resins with viscosities <1000 Pa.S. Based on rheology and DSC analysis, the prepregging process was done by placing the TuFF material with the M77 resin film in a heated bladder mold at 80°C, applying a full vacuum and pressurizing to 100 psi. This was held for 5 minutes and was then removed from the bladder mold. This material can be stored in a freezer for processing at a later time. To snap-cure a part, the prepregged material is placed in a heated mold/tool at 150°C and full vacuum and 200 psi pressure is applied. The material is held at temperature for 90 seconds after which the cured material can be removed. Figure II.3.2.3.6(b) shows a micrograph of a TuFF T800/M77 snap-cure resin prepreg sample processed using these conditions. Test samples to determine mechanical properties are being processed and will be reported on in the final SBIR report.



(a)



(b)

Figure II.3.2.17. (a) Viscosity as a function of temperature for a heating ramp of 2 °C/minute and (b) micrograph of TuFF T800/M77 snap-cure resin. Source: Composites Automation, LLC.

Conclusions

Composite solutions for structural automotive applications require that the material be cost-competitive with metal, have mechanical properties similar to metals, be handleable for use with automated equipment and be processable using stamp-forming type processes at similarly high rates. All of these attributes are required to transition the TuFF material technology to the automotive production environment, and all are being addressed in this effort. Verification of mechanical performance of the TuFF material processed with the M77 snap-cure resin is still in process. The further scaleup and demonstration of repeatable material performance using a high-rate processing of relevant automotive component will require additional work.

Acknowledgments

The authors would like to acknowledge the support of A. Maxey and K. Van Aken from Vartega for their support in providing recycle and waste fiber for this project, and J. Dietzel from the University of Delaware for his support in developing the electrospinning of veil material for TuFF preform stabilization.

II.3.2.4 Low-Cost Resin Technology for the Rapid Manufacture of High-Performance Fiber-Reinforced Composites (Trimer Technologies, LLC)

Megan Dunn, Principal Investigator

Trimer Technologies, LLC
45800 Mast St.
Plymouth, MI 48170
E-mail: mdunn@trimer-tech.com

Henry A. Sodano, Co-Principal Investigator

Trimer Technologies, LLC
45800 Mast St.
Plymouth, MI 48170
E-mail: hsodano@trimer-tech.com

Brandy Greenawalt, SBIR Program Manager

U.S. Department of Energy SC-29
Small Business Innovation Research
19901 Germantown Rd.
Germantown, MD 20874
E-mail: brandy.greenawalt@science.doe.gov

H. Felix Wu, DOE Technology Development Manager

U.S. Department of Energy
E-mail: felix.wu@ee.doe.gov

Start Date: August 24, 2020 End Date: February 28, 2023
Project Funding (FY 2022): \$1,150,000 DOE share: \$1,150,000 Non-DOE share: \$0

Project Introduction

The lightweighting of vehicle structures clearly represent a significant opportunity for energy savings. However, traditional composite manufacturing technologies offer either high-volume or significant weight-savings—but not both. Over the past decade, automotive composites have focused on the sheet molding compound (SMC), which enables high-volume manufacturing, but is produced with chopped fibers, and therefore, inefficiently capitalizes upon the strength of the reinforcement, thus leading to materials with poor specific properties. For instance, AOC Aliancys' (now AOC) PALAPREG® P18-03 vinyl ester SMC with 30% glass fiber obtains a tensile strength of only 100 MPa, which is below most neat (e.g., without reinforcement) epoxies used in the aerospace industry. The tensile strength of CF SMCs can be double that of fiberglass SMCs but is still roughly four times lower than that of a composite using continuous CF reinforcement. Manufacturing processes using continuous fiber reinforcement would fully capitalize upon the greater cost and lightweighting potential of CF.

Recently, high-pressure resin transfer molding (HP-RTM) has emerged as an alternative approach to manufacture composite materials with continuous fiber reinforcement. HP-RTM was demonstrated to be cost-effective and compatible with high-rate manufacturing through BMW's i-series vehicle program, which achieved a 50% weight-reduction as compared to traditional steel designs. HP-RTM injects a catalyzed resin into a heated mold containing draped woven or non-crimp fabric at pressures as high as 200 bar. In the BMW i3 program, HP-RTM enabled cycle times of approximately five minutes versus several hours for standard RTM processes used in the fabrication of large components, such as wind-turbine blades. However, while a

five-minute cycle time is acceptable for lower volume production in high-performance vehicles, it is too slow to realize the use of low-cost composite materials required by the automotive industry for mass market vehicles.

DOE's VTO is targeting a 25% glider weight-reduction at less than \$5/lb. saved by 2030, which will require innovative new materials that achieve both rapid-cure and significantly improved mechanical properties. Current HP-RTM resins include polyesters, vinyl esters, snap-cure epoxies, and polyurethanes. However, the low-cost polymers employed for automotive parts have properties inferior to those employed in the aerospace industry. Trimer Technologies, LLC (Trimer), has identified the catalysts required to enable snap-cure (e.g., <45 seconds) while maintaining aerospace-grade performance. Furthermore, the resin has an infusion viscosity at 65°C of less than 25 cP, which will enable rapid infusion to further reduce manufacturing time. In addition to the manufacturing benefits and aerospace-grade strength, the cured polymer achieves a glass transition temperature (T_g) greater than 700°F (375°C) and is non-flammable without additives, providing unique commercialization opportunities. Table II.3.2.4.1 provides a comparison of the material properties for two snap-cure epoxies and two vinyl esters and demonstrates that the proposed Trimer polymer greatly outperforms state-of-the-art materials while simultaneously offering significantly reduced cost.

Table II.3.2.4.1. Comparison of Trimer's RTM Polymer with Current Low-Cost Rapid-Cure Resins

Material Property	Trimer RTM Resin	Dow Voraforce 5300	Huntsman Araldite LY 3585/ Aradur 3475	AOC VIPEL FO10 BIS-A VE	Reichhold DION IMPACT 9102-75
Polymer Type/Chemistry	-	Epoxy	Epoxy	Vinyl Ester	Vinyl Ester
Glass Transition (T_g) Dry (°C)	375	120	110	130	99
Tensile Strength (MPa)	105	68	77.5	88	79.2
Tensile Modulus (GPa)	4.0	2.8	2.8	3.2	2.9
Tensile Strain-to-Failure (%)	4.0	7	9	6.2	4.5
Compressive Strength (MPa)	149	-	-	121	108.9
Flexural Strength (MPa)	140	-	-	153	144
Fracture Toughness, K_{1c} (MPa/m ^{1/2})	1.03	1.22	0.85	0.6	-
Viscosity (cP at 23 °C)	200	500	1,000	3,200	170

Objectives

The objective of this SBIR Phase II project is to demonstrate the manufacture of high-strength CF composites with a full molding and injection cycle time below 60 seconds for thin parts and a cycle time under 120 seconds for thick chassis structures such as leaf springs. This aggressive goal is enabled by Trimer's patent-pending thermosetting resin, which has been shown to achieve aerospace-grade mechanical and thermal properties through a 30-second cure. The polymer is ideally suited for integration into the automotive industry since the raw material cost is below vinyl esters, and the polymer's high-strength and stiffness will enable further reduction of component weight. The high-performance-to-cost ratio of Trimer's resin is revolutionary and will drive its commercial adoption in an industry where value is critical. The product is non-flammable, with a T_g greater than 700°F (375°C) and mechanical properties that rival the highest-performance aerospace resins. No competing technology exists that can match the cure time, strength, and cost.

Approach

To achieve DOE's ambitious weight targets, a critical need to implement new resin technologies exists that are compatible with high-rate industrial manufacturing approaches yet provide the mechanical properties of aerospace resins. In this Phase II SBIR project, Trimer has demonstrated that its low-cost RTM resin exhibits high-strength and a cure time as fast as 23 seconds with a 3.5-mm-thick panel and under 60 seconds with a

10-mm-thick panel. These rapid-cure results were obtained through liquid CM with an unheated resin and unheated fiber preform, which indicates that significantly faster cure times should be achievable with an HP-RTM system. Cycle times under 60 seconds are possible because of the very low resin viscosity (e.g., 25 cP at 65°C), which reduces the infusion time, combined with preheating the resin, which quickens the cure. While other resin systems can cure in 60 seconds, they are compatible with only very thin parts. These systems exhibit a highly exothermic reaction that leads to thermal runaway and severe degradation of the cured polymer in parts thicker than a couple millimeters, or, in some cases, combustion. The Trimer resin can cure 28-mm-thick parts in 90 seconds, which is eight times faster than state-of-the-art epoxy resins. The proposed polymer will enable both high-volume manufacturing and significant weight-savings in vehicle structures through the realization of unprecedented low cycle times.

Trimer is working with the IACMI Scaleup Research Facility (SuRF) to demonstrate production-scale HP-RTM manufacturing with a focus on minimizing the cycle time. Trimer's efforts with the IACMI-SuRF used its Hennecke HP-RTM system and Schuler 4,000 ton press equipped with a Cannon dough molding compound flat plate mold to manufacture panels with non-crimp CF reinforcement for evaluation. The project is working with both high-pressure injection resin transfer molding and high-pressure compression resin transfer molding processes to optimize cycle time. Researchers are further characterizing the infusion process through the analysis of reinforcement wet-out, void content, and dimensional stability of the cured part.

Results

Trimer performed extensive mechanical testing to show that the resin performance greatly exceeds that of currently used resins. Test results were shown previously in Table II.3.2.4.1. This combination of properties exceeds many aerospace resins and greatly outperforms automotive epoxies. HP-RTM manufacturing is a cyclic process in which it is advantageous to avoid applying an external mold release through the use of internal mold release (IMR) agents that enable efficient removal of the cured part from the mold. Given the importance of the IMR for HP-RTM, Trimer spent considerable effort developing a suitable IMR. In addition to providing a weak adhesive strength, one of the critical IMR parameters is that it leaves the mold surface clean and without residue. The testing used a small pultrusion die fabricated such that an Instron could be used to pull a CF tow through the die while the pull force was measured. This methodology allowed Trimer to identify several effective IMRs and isolate one for production manufacturing. Trimer has also found the IMRs do not affect the tensile properties of the resin but lead to a significant improvement in the fracture toughness, K_{IC} , that increases by as much as 36% because of a plasticizing effect.

The project has also performed testing on composite panels manufactured using Trimer's RAPID infusion resin and Scott Bader's Crestapol 1250 resin, a low viscosity and fast-curing resin system that is currently used by Shape Corp. in the manufacture of the Chevrolet Corvette bumper. Composite panels were prepared using vacuum-assisted resin transfer molding and E-glass non-crimp fabric from Vectorply (weave ELA2412). Samples were cut and tested in accordance with ASTM standards for tensile strength (ASTM D3039), compressive strength (ASTM D6641), in-plane shear response (ASTM D3518), Mode I fracture toughness (ASTM D5528), Mode II fracture toughness (ASTM D7905), and tensile and compressive translaminar fracture toughness (ASTM E1922). The Crestapol 1250 resin was cured at a lower temperature but required a 60-minute cure time as compared to the 3-minute cure time of the RAPID parts, which would greatly reduce the cycle time in a production setting. The results, as indicated in Table II.3.2.4.2, show significant performance improvements (emphasized in red text) over the Crestapol 1250 resin, with notable improvement to compressive strength. The axial compressive strength of the Trimer RAPID resin was 966.02 MPa, compared to 568.71 MPa for the Crestapol 1250 resin. The transverse strength was 99.5 MPa for Crestapol 1250 and 184.3 MPa for Trimer's RAPID resin, which is 70% higher under axial loading and 85.2% under transverse loading. In addition to the compressive strength, RAPID performed extremely well in both Mode I and Mode II fracture toughness. The average Mode I interlaminar fracture toughness, G_{IC} of 0.473 kJ/m², is more than twice the value of Hexcel 8552, a toughened aerospace resin. The RAPID pre-cracked Mode II fracture toughness, a G_{IIC} value of 1.51 kJ/m², is nearly three times higher than Hexcel 8552. This testing was not only beneficial for highlighting the strength of the resin system being developed in this project, but also

allowed Trimer to further populate its data sheet for future commercial partners and benchmark a competing resin system.

Table II.3.2.4.2. Material Properties from Vacuum-Assisted Resin Transfer Molding E-Glass Composites

Property	Standard	Trimer RAPID	Crestapol 1250
0° Tensile Strength, MPa	ASTM D3039	1.04	1.03
0° Tensile Modulus, GPa	ASTM D3039	44.2	46.45
0° Compression Strength, MPa	ASTM D6641	966.0	568.70
0° Compression Modulus, GPa	ASTM D6641	47.2	43.90
90° Tensile Strength, MPa	ASTM D3039	36.4	19.50
90° Tensile Modulus, GPa	ASTM D3039	14.3	14.90
90° Compression Strength, MPa	ASTM D6641	184.3	99.50
90° Compression Modulus, GPa	ASTM D6641	31.0	12.90
In-Plane Shear Strength, MPa	ASTM D3518	64.7	57.77
In-Plane Shear Modulus, GPa	ASTM D3518	3.4	2.66
Mode I Fracture Toughness, J/m ²	ASTM D5528	437	809
Mode II Fracture Toughness, J/m ²	ASTM D7905	1,510	1,640
Translaminar Fracture Toughness, MPa-m ^{1/2}	ASTM E1922	60.64	51.87

To meet the project's Phase II objective for reduced manufacturing cycle time of composite parts in a production environment, we worked with an OEM to perform a series of RTM trials on thick chassis composites. State-of-the-art snap-cure epoxies require ~12 minutes to cure a 28-mm-thick composite because of the highly exothermic reaction, which, if pushed, will cause the resin to overheat and thermally degrade or even combust. Trimer's resin provides the ability to cure thick composites in under 120 seconds since the resin has very little exotherm. During our trials, a dielectric cure monitoring system was used to establish RTM composite panel cure times. The dielectric cure monitoring system measures the ion viscosity velocity, which increases as the press is closed and decreases back to baseline once the polymer is cured, stopping ion mobility. Figure II.3.2.4.1 shows the cure monitor data for injection into a production part, with a 60-second vacuum followed by a fast 23-second injection and a 90-second cure. The cycle time demonstrated in the RTM trials is faster than state-of-the-art epoxies for either times. Trimer is now working with IACMI-SuRF to demonstrate HP-RTM manufacturing in which higher injection pressure can be used to further reduce molding time. We will mold the same chassis component, which is a production part, and will evaluate the cycle time using production injection tooling. The initial trials will focus on cycle time reduction through optimization of infusion viscosity (controlled through temperature) and pressure. IACMI-SuRF's tooling does not have cure monitor hardware, so the degree of cure will be analyzed on molded parts. Because of delays at IACMI-SuRF, it is anticipated that the manufacturing trials will occur in the first quarter of FY 2023.

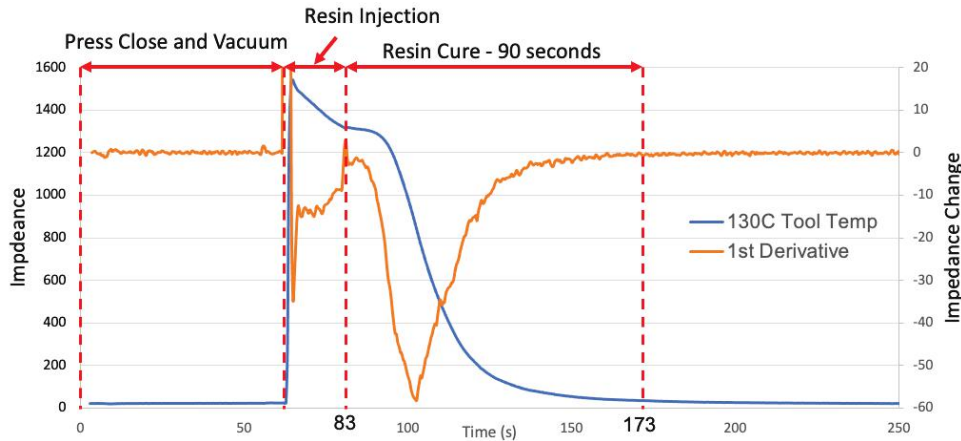


Figure II.3.2.18. Dielectric cure monitor data from the molding of a 28-mm-thick composite part demonstrating a 90-second cure time. Source: Trimer Technologies, LLC.

The composite panels molded during the trials were tested for both static and fatigue properties, with the results proving similar to or better than epoxies, yet with significantly improved cycle time. The fatigue testing specification required the part to exhibit less than 5% load loss after 200,000 cycles at 200 MPa; however, our composites were tested at 450 MPa, and after 8 million cycles, the composite exhibited only 2.1% load loss. Given that our specimens were tested at more than 100% higher load and a far greater cycle count, this result clearly demonstrates our resin is well within the range of acceptable fatigue for automotive chassis systems.

In addition to mechanical testing of the resin, the Phase II has also demonstrated the fire performance of our resin system [1]. Trimer has performed thermal analysis through the dynamic mechanical analysis to identify the T_g , which showed an extreme T_g of 707°F (375°C) with a high storage modulus of ~2.5 GPa at 300°C. While an extreme T_g such as that obtained here is not critical for automotive applications, the high T_g does enable the resin to be compatible with the E-coat process and potentially opens the door to under the hood applications, such as composite engine blocks. Furthermore, these extremely high thermal properties make the resin suitable for even faster cure since it does not degrade when heated to extreme temperatures and also expands the use in a broader range of commercial applications. This high T_g also contributes to the non-flammable nature of the resin, which is critical for vehicle applications, and a particular need for battery enclosures. Trimer's resin exhibits excellent fire, smoke, and toxicity (FST) properties without additives, so certain additives can be incorporated into the resin to affect the combustion cycle without changing the resin properties. Trimer worked with the University of Dayton Research Institute to perform oxygen consumption calorimetry under ASTM E-1354/ ISO 5660 to characterize the fire performance with results at a heat flux of 50 kW/m² with the data showing a very low average peak heat release rate of 16 kW/m², a long time to ignition of 156 sec and a low average heat release rate of 4.9 kW/m². Furthermore, Smoke Density and Toxicity (ASTM E662/E800) and Surface Flammability (ASTM E162) all exceed MIL-STD-2031, the U.S. Department of Defense's most stringent FST specification for submarine applications, therefore clearly demonstrating Trimer's FST performance. We have further performed testing according to ASTM D635 and the polymer passed the horizontal burning test after 30 sec exposure to flame; however, to further demonstrate the polymer's non-flammable properties, we have subjected the polymer to a 60-second burn time under significantly more intense flux than the ASTM method requires. Images of the results are provided in Figure II.3.2.4.2, where it is clear that the panel can effectively self-extinguish in under 10 seconds.

IACMI-SuRF has continued to have delays with their HP-RTM tooling, and therefore, Trimer has focused our recent efforts on the development of the resin for pultrusion with an emphasis placed on EV battery separators. We have worked with more than six pultruders and have successfully run a number of profiles using both carbon and fiberglass, as shown in Figure II.3.2.4.3(a) and Figure II.3.2.4.3(b), respectively. Our pultrusion runs were successfully processed using Axel Plastics INT-1230 IMR; however, this product is being

discontinued. Therefore, Trimer has run numerous IMR trials over the past several months in an effort to identify an alternative. Based on our successful pultrusions, Trimer is currently moving to prototype production for three separate OEMs with two manufacturers. We are also working towards the commercialization of wind-turbine spar caps with ZOLTEK and infrastructure with Strongwell. We will continue this development with an anticipated commercialization in 2023.

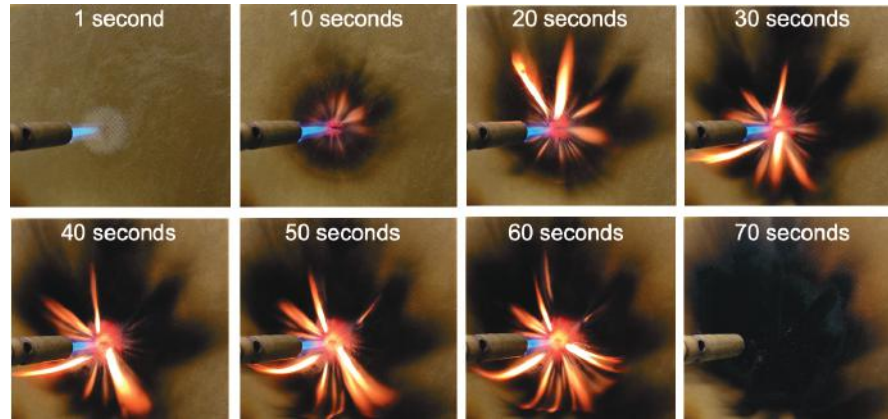


Figure II.3.2.19. Propane torch testing on a 3-mm-thick fiberglass composite panel with a 60-second flame exposure after which the composite was able to self-extinguish in under 10 seconds. Source: Trimer Technologies, LLC.



(a)



(b)

Figure II.3.2.20. Pultruded profiles using Trimer's resin system for (a) carbon and (b) fiberglass. Source: Trimer Technologies, LLC.

Conclusions

Trimer has developed a new resin system that can enable unprecedented cycle time while producing fire-resistant composites with the strength and stiffness of more costly aerospace-grade materials. Through the first year of this SBIR Phase II project, Trimer demonstrated RTM manufacture of composite structures and validated their fatigue performance while reducing the cycle time eight-fold. The next year of the project will focus on HP-RTM manufacturing of chassis components and further refinement of the fire-resistant properties.

References

1. "Compartment Interiors," 1991, Code of Federal Regulations, title 14 14 CFR § 25.853(d), Appendix F, Part V, at Amdt. 25–116.

Acknowledgments

Trimer Technologies would like to thank H. Felix Wu for his support of our efforts and the Ford Motor Company for providing access to facilities and personnel to support our efforts.

II.3.2.5 Flexible, Lightweight Nanocomposites for EMI Shielding Suppression in Automotive Applications (Applied Sciences, Inc.)

Carla Lake, Principal Investigator

Applied Sciences, Inc.
141 W. Xenia Ave.
Cedarville, OH 45314
E-mail: cleer@apsci.com

Brandy Greenawalt, SBIR Program Manager

U.S. Department of Energy SC-29
Small Business Innovation Research
19901 Germantown Rd.
Germantown, MD 20874
E-mail: brandy.greenawalt@science.doe.gov

H. Felix Wu, DOE Technology Development Manager

U.S. Department of Energy
E-mail: felix.wu@ee.doe.gov

Start Date: June 28, 2021	End Date: June 27, 2022	
Project Funding (FY 2022): \$533,984	DOE share: \$533,984	Non-DOE share: \$0

Project Introduction

As technology advances, the need to place larger numbers of electrical and electronic systems into automobiles has dramatically increased. Metals are best suited as EMI shielding materials, but their use comes with a weight penalty, lower flexibility, and lower corrosion resistance, which make them unattractive for use in under-hood EMI shielding applications. The emergence of flexible conductive polymer composites has enabled the use of these materials for EMI shielding applications in the automotive industry due to their unique features, such as their light weight, flexibility, strength, and corrosion resistance, as well as their high electrical and di-electrical performance [1, 2]. Traditionally, carbon black (CB) has been used to impart electrical conductivity and EMI shielding to polymer-based composites. However, the high loadings (e.g., 20 wt% - 30 wt.%) required to impart conductivity tend to degrade the overall mechanical properties of the composite. Several studies have shown that fiber-like materials, such as CF, carbon micro, and nanofibers—in addition to multiwalled carbon nanotubes—demonstrate superior EMI shielding capability than CB, at much lower loadings [2–5]. The ability to achieve equivalent or better electrical conductivity and EMI shielding at lower loadings enables preservation of mechanical durability and flexibility of the host polymer material, thereby yielding a superior conductive plastic. These emerging composite materials are ideal candidates to provide EMI shielding for vehicle applications, including but not limited to, under the hood electronics enclosures, cable/wire harnesses, and wraps [6].

Applied Sciences, Inc. (ASI) also fabricated several nonwoven hybrid composite veils comprised of CF and carbon nanofibers (CNF). These flexible, lightweight multiscale EMI shielding veils demonstrated a shielding effectiveness of up to 60 dBs. These developed composite materials represent a hybrid holistic solution to lightweight design, where they can be integrated directly or strategically placed where a particular performance needs to be met.

Objectives

The overall objective of this Phase I Small Business Innovation Research effort was to develop a flexible lightweight polymer composite for EMI shielding suppression for automotive applications.

Approach

During this period, ASI developed several non-metallic composite solutions with EMI shielding characteristics for under the hood electronics and battery enclosures, including a multiscale polyvinyl chloride (PVC) composite for cable/wire EMI shielding braid harness to replace heavy metal braid harness/wraps. This PVC carbon composite replaces metal harnesses, reducing the weight by as much as 40%, while maintaining a shielding effectiveness of 99.9%. This lightweight polymer solution comes with added flexibility, corrosion and chemical resistance, and increased ease of installation and durability. ASI used its multiscale image analysis (MSIA) method to tailor the structure-performance relationship of the multiscale hybrid composites to achieve the ideal dispersion state to accomplish the material property targets [7–9]. This approach has proven to be adaptable to multiple polymer chemistries, creating design freedom for various OEMs and component suppliers.

Results

Agglomeration is widely recognized as a problem when incorporating nanofillers in systems such as this, affecting the homogeneity of dispersion and formation of areas with high nanofiller concentrations, which act as stress concentrators instead [10]. Four different carbon additives were used in this study. Short carbon fibers (SCFs), CB, and structured carbon black (SCB) were used as received from the manufacturer. CNFs were sifted through a 297 μm mesh in order to remove larger diameter CNFs to ensure the percolation threshold is attained at lower loadings [11].

Processing methods and operating conditions used to compound fillers with polymers strongly influence the fiber dispersion/distribution, orientation, and aspect ratio. Twin screw extruders are very effective instruments for the distribution and dispersion of carbon nanomaterials into polymeric matrices; they are also very flexible in their design and capability to allow adjustments in residence time and dispersive and distributive mixing conditions. Compounding was done at ASI using a modular intermeshing co-rotating twin screw extruder to produce the different polymer compounds. Because this machine is equipped with a modular screw, the shear intensity and residence time conditions were tailored to yield the final properties desired in the produced compound. The screw configuration was designed taking in account the type of carbon-based filler used and the level of electrical conductivity that is required in the final compound. The processing conditions were varied to create different shear-mixing intensities. The dispersion quality of the developed polymer dispersions was monitored using the MSIA method, developed by Leer et al. to quantify dispersion in nanocomposites [8]. This method can be used to make quantifiable relationships between the CNFs used, the resulting dispersion, and the measured properties. This intermediate step is vital for the complete understanding of the relationships between the identified variables and the electrical performance of the fabricated composites. The MSIA was used as a performance development tool to determine if the processing conditions and/or loadings were adequate to create a conductive network microstructure in the composite. The electrical resistivity of the fabricated strands was measured using the four-point method. Table II.3.2.5.1 summarizes the different trial conditions and resulting electrical conductivity.

As can be observed from the data in Table II.3.2.5.1, the type of carbon additive and shear conditions resulting from the processing conditions have a major impact on the electrical conductivity of the composite. It was found that the CNFs and SCB are synergistic, when processed under mild shear conditions resulting in a very electrically conductive yarn, suitable for EMI shielding suppression. Figure II.3.2.5.1 compares the weights of an EMI shielding copper plated metal braided harness and the EMI shielding PVC/CNF composite braided harness developed by ASI. As can be seen, the composite EMI shielding harness is 40% lighter than its metal counterpart with the identical dimensions. Aside from lightweighting, the polymer composite harness brings the added benefits of flexibility, corrosion, and chemical resistance.

Table II.3.2.5.1. Effect of Carbon Loading and Shear Conditions on the Electrical Resistivity of a Hybrid PVC/Carbon Compound

Sample	SCF %	CB %	SCB %	CNF %	Shear Conditions	Electrical resistivity [Ohm.Cm]
2432-1	◇◇	-		◇	●	10 ¹²
2432-2	◇◇	-		◇	●●	10 ¹²
2432-3	◇◇◇	-		◇	●●	10 ¹²
2432-4	◇◇◇	-		◇	●●●	10 ¹²
2432-5		◇◇		◇	●	10 ¹²
2432-6		◇◇		◇	●●	10 ¹²
2432-7		◇◇◇		◇	●●	47
2432-8		◇◇◇		◇	●●	126
2432-9			◇	◇	●●●	10 ¹²
2432-10			◇◇	◇	●●	7

Legend: SCF – short carbon fibers; CB – carbon black; SCB – structural carbon black; CNF – carbon nanofiber. Additive loading: ◇ low; ◇◇ mild; ◇◇◇ high. Shear conditions: ● low; ●● mild; ●●● high.



Figure II.3.2.21. Weight comparison between two braided harnesses: (a) traditional copper plated metal harness and (b) 40% lighter PVC/CNF composite fabricated by ASI. Source: ASI.

EY Technologies at Fall River, MA tested the shielding effectiveness of the fabricated braid and reported the same shielding effectiveness as the metal braid harnesses. This PVC carbon composite replaces metal harnesses, thereby reducing the weight by as much as 40%, while maintaining a shielding effectiveness of 99.9%. This lightweight polymer solution comes with added flexibility, corrosion, and chemical resistance, as well as increased ease of installation and durability.

Several nonwoven polyacrylonitrile (PAN)/CNF 12 in. × 12 in. square veils were fabricated to evaluate the effect of nanofiber type and grade, binders, spray gun pressure, solvent/nanofiber ratios, deposition rate, and loading level on the material properties. For screening purposes, the direct current electrical resistivity of the fabricated PAN/CNF nonwoven veils was measured at ASI with a Jandel four-point probe in accordance with ASTM D257, which is reported as Ohm/square. Scanning electron micrographs of the different nonwoven veils are represented in Figure II.3.2.5.2. Notice the hybrid multiscale composite structure created by the PAN macroscopic CFs that are wrapped by CNF, which themselves are surrounded by nano-sized CB.

As can be seen from the results presented in Table II.3.2.5.2, the type of CNF and loading percentage has a critical impact on the shielding effectiveness of the nonwoven veils. The veils produced with various compositions of CNF at various areal weights reveal that the fiber type and aspect ratio of the nanofiber plays a crucial role in the shielding performance. Even at similar areal densities, the CNF nonwoven samples #3 and #5 exhibited vastly different attenuation values. The data suggests that blending in a small percentage of shortened CNFs boosts the attenuation from -40 dB to -66 dB.

A comparison of samples #5 and #4 once again show that the use of CNF-HHT, even in the shortened state and designated as CNF-HHT advanced manufactured (AM), provides superior performance over the CNF heat-treated at a lower temperature (CNF-PS). This effect is even more impressive given that sample #4 has a higher areal weight at the same thickness as sample #5. It is noteworthy to mention that when the formulation is optimized, to sample #6, with a thickness of only 0.1 mm and an areal weight of 23 gsm, is still testing at 27 dB in the frequency range of 30 MHz–18 GHz.

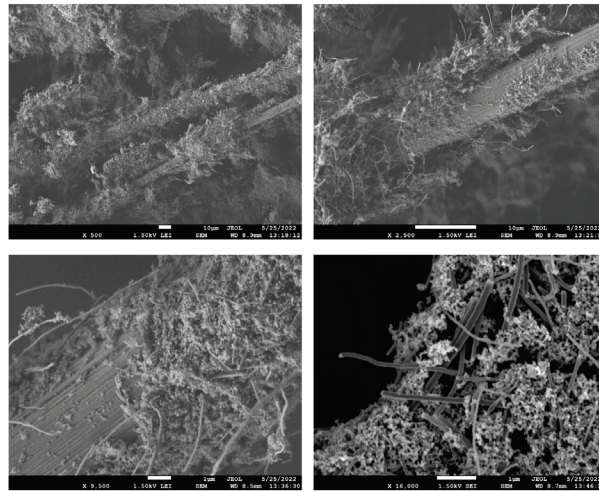


Figure II.3.2.22. SEM images of the PAN/CNF nonwoven veils. Notice the hybrid multiscale composite structure created by the PAN macroscopic CFs that are wrapped by CNF, which themselves are surrounded by nano-sized CB. Source: ASI.

Table II.3.2.5.2. Effect of CNF and Areal Weight on the Sheet Resistivity and Shielding Effectiveness of Nonwoven Samples

Sample ID	CNF-LHT	CNF-HHT	CNF-PS AM	CNF-HHT AM	Areal Weight (g/m ²)	Thickness (mm)	Sheet Res. (Ohms per square)	Attenuation (Avg. dB)
1	●●			●	35	0.25	4.3	-27
2	●●			●●	55	0.5	3.8	-29
3		●●●●			80	0.35	2.85	-40
4		●●	●●		100	0.35	5.2	-48
5		●●		●●	75	0.35	2.08	-64
6		●●	●●		23	0.1	7.23	-27

Legend: LHT – light heat-treated (1500°C); HHT – high-heat-treated (2800°C); PS – polymer shielded; and advanced manufactured (AM). Shear conditions: ● low; ●● mild; ●●● high; ●●●● ultra-high.

Conclusions

ASI demonstrated the Phase I proposed approach to produce multiscale, low-weight EMI shielding materials. ASI successfully demonstrated the ability to replace heavy metal braid harnesses by a lightweight conductive

PVC/CNF composite, which replaces metal harnesses, reducing the weight by as much as 50%, while maintaining a shielding effectiveness of 99.9%. This lightweight polymer solution comes with added flexibility, corrosion, and chemical resistance, as well as increased ease of installation and durability. The data and feedback received to date validate the proposed approach and demonstrate the feasibility for ASI to utilize this approach to accomplish the program goals and weight-reduction targets for under the hood electronics applications in vehicles. CNF is a highly graphitic and electrically conductive nanomaterial produced by ASI and is available in ton quantities at less than \$0.75 per gram. Several CNF product forms are available with an index of graphitization, surface state, and other properties that can be tailored to specific applications.

References

1. Kruželák, J., A. Kvasničáková, K. Hložeková, and I. Hudec, 2021, “Progress in polymers and polymer composites used as efficient materials for EMI shielding,” *Nanoscale Adv.*, No. 3, pp. 123–172. <https://doi.org/10.1039/D0NA00760A>.
2. Villet, M., 2020, “Tech talk: Sustainable mobility, connectivity, safety, and EMI shielding,” DSM, Heerlen, Netherlands. Available at: <https://youtu.be/I6CUsDODx-U> (last accessed 1 March 2023).
3. Chakradhary, V. K., S. Juneia, and M. J. Akhtar, 2020, “Correlation between EMI shielding and reflection loss mechanism for carbon nanofiber/epoxy nanocomposites,” *Mater. Today Commun.*, Vol. 25, Art. 1011386. <https://doi.org/10.1016/j.mtcomm.2020.101386>.
4. Mamunya, Y., L. Matzui, L. Vovchenko, O. Maruzhenko, V. Oliynyk, P. Slawomira, and U. Szeluga, 2019, “Influence of conductive nano- and micro-filler distribution on electrical conductivity and EMI shielding properties of polymer/carbon composites,” *Compos. Sci. Technol.*, Vol. 170, pp. 51–59. <https://doi.org/10.1016/j.compscitech.2018.11.037>.
5. Shakir, F. S., A. N. Khan, R. Khan, S. Javed, A. Tariq, M. Azeem, A. Riaz, A. Shafqat, H. M. Cheema, M. A. Akram, I. Ahmad, and R. Jan, 2019, “EMI Shielding properties of polymer blends with inclusion of graphene nano platelets,” *Results Phys.*, Vol. 14, Art. 102365. <https://doi.org/10.1016/j.rinp.2019.102365>.
6. Kittur, J., B. Desai, R. Chaudhari, and P. Loharkar, 2020, “A comparative study of EMI shielding effectiveness of metals, metal coatings, and carbon-based materials,” *IOP Conf. Ser.: Mater. Sci. Eng.*, Vol. 810, No. 1. <https://doi.org/10.1088/1757-899X/810/1/012019>.
7. Friedrich, K., and A. A. Almajid, 2013, “Manufacturing aspects of advanced polymer composites for automotive applications,” *Appl. Compos. Mater.*, Vol. 20, pp. 107–128. <https://doi.org/10.1007/s10443-012-9258-7>.
8. Spowart, J. E., B. Maruyama, and D. B. Miracle, 2001, “Multiscale characterization of spatially heterogeneous systems; implications for discontinuously reinforced metal matrix composite microstructures,” *Mater. Sci. Eng. A*, Vol. 307, p. 51–66. [https://doi.org/10.1016/S0921-5093\(00\)01962-6](https://doi.org/10.1016/S0921-5093(00)01962-6).
9. Leer, C., 2010, *Carbon Nanofibers Thermoplastic Nanocomposites: Processing – Morphology – Properties Relationships*, Ph.D. Thesis, University of Minho, Minho, Portugal.
10. van Hattum, F., C. Leer, and O. Carneiro, 2006, “Quantitative assessment of mixing quality in nanoreinforced polymers using a multiscale image analysis method,” in SAMPE Fall Technical Conference (38th ISTC), 6–9 November 2006, Dallas, TX, USA.
11. Stauffer, D., and A. Aharony, 1994, *Introduction to Percolation Theory*, 2nd Edition, Taylor & Francis, Milton Park, Oxfordshire, U.K.

Acknowledgments

The authors would like to thank H. Felix Wu for his technical guidance and program support.

II.3.2.6 Conductive Lightweight Hybrid Polymer Composites from Recycled Carbon Fibers (RockyTech Ltd.)

Yinghua Jin, Principal Investigator

RockyTech Ltd.
1111 Engineering Dr.
Boulder, CO 80305
E-mail: jin@rockytechs.com

Brandy Greenawalt, SBIR Program Manager

U.S. Department of Energy SC-29
Small Business Innovation Research
19901 Germantown Rd.
Germantown, MD 20874
E-mail: brandy.greenawalt@science.doe.gov

H. Felix Wu, DOE Technology Development Manager

U.S. Department of Energy
E-mail: felix.wu@ee.doe.gov

Start Date: June 28, 2021	End Date: August 21, 2024	
Project Funding (FY 2022): \$533,984	DOE share: \$533,984	Non-DOE share: \$0

Project Introduction

By replacing steel with CFRPs, the weight of an automobile body system can be reduced by over 20%, equivalent to a 12%–16% increase in fuel economy, per DOE guidelines. However, the production of virgin CF is energy-intensive and costly, and current CFRPs are generally not recyclable. The use of recycled carbon fibers (rCFs) improves the cost and environmental footprint of CFRPs, while closed-loop recycling of EOL CFRPs further increases their sustainability and reduces their overall cost, thereby making lightweight strategies affordable for mainstream vehicles.

Objectives

The overall objective of the project is to develop multifunctional, recyclable, nano- and micro-filler reinforced vitrimer composites made from recycled milled carbon fibers (NMVC-R²), which have combined lightweight, conductive, and electromagnetic shielding properties in addition to robust mechanical performance.

Approach

Lightweight polymer NMVC-R² possessing high-strength, conductivity, and by-design reprocessability and recyclability will be developed from low-value milled rCF micro-fillers and carbon-based nanofillers. Synergistic reinforcement of the composites with hybrid nano- and micro-fillers in a vitrimer matrix ensures efficient load transfer from the matrix to the fillers, prevents stress concentrations, and improves overall mechanical properties, specifically: (1) the interfacial adhesion between the fillers and polymer matrix can be improved through covalent surface modification of rCF micro-fillers with carbon-based nanofillers, (2) the conductivity of the NMVC-R² can be increased through the formation of an interconnected network of conductive hybrid nano- and micro-fillers, (3) the reprocessability and 100% recyclability of NMVC-R² can be accomplished by using vitrimers as the polymer matrix, and (4) malleable and fully cured NMVC-R² prepregs with infinite shelf-lives can be formed.

Results

Surface Modification of rCF

It is critical to control the interfacial properties of CFRPs to ensure efficient load transfer from the polymer matrix to the fillers. Poor adhesion between the fiber and the matrix creates an inherent weak zone that easily causes delamination and failure under stress. We developed a synthetic method to functionalize the surface of rCFs having an average length 100 μm with reactive groups to covalently link the vitrimer matrix and improve the interfacial interactions. We also covalently attached conductive carbon-based nanofillers onto the surface of rCF to increase the surface contact area of fillers with the polymer matrix and improve the conductivity of CFRPs. Such nano-, micro-combined fillers (NMCFs) show excellent stability over multistep chemical and physical processing (e.g., composite formation through polymerization and subsequent recycling through depolymerization). The recycled NMCFs show a similar grafting density of nanofillers on the surface to that of the as-prepared NMCF, indicating the stability of the covalently attached nano-micro hybrid fillers, as shown by the SEM images in Figure II.3.2.6.1.

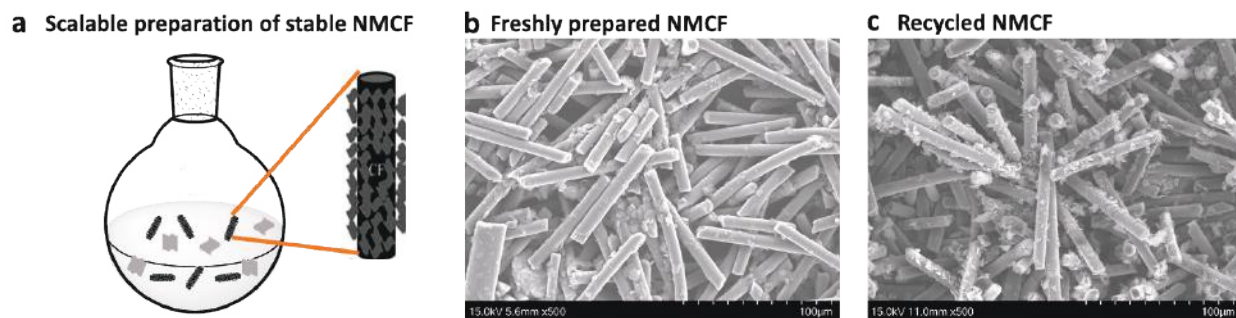


Figure II.3.2.23. (a) Covalent surface functionalization of rCF with carbon nanofiller to form highly stable NMCF. SEM images of (b) freshly prepared NMCF and (c) recycled NMCF from NMVC-R². Due to the strong covalent bonding between CF micro-fillers and carbon-based nanofillers, NMCF is stable even after a series of solution and solid-state processing under heat. Source: RockyTech Ltd.

Development of NMVC-R²

A series of NMVC-R² consisting of various vitrimers and surface-modified rCFs were prepared through CM and gel-impregnation methods. Since the properties of the polymer matrix play a critical role in the performance and processibility of CFRPs, we first developed a novel type of malleable thermoset, or vitrimer [1, 2]. However, there has been a critical tradeoff between mechanical properties and the malleability of vitrimers—combining high mechanical properties with malleability under mild conditions has been a grand challenge. By carefully choosing monomer compositions and reversible covalent crosslinks, we were able to effectively mitigate this tradeoff and obtain a vitrimer with tensile modulus up to 5.2 GPa and a processing temperature around 120°C, as indicated by V5 in Figure II.3.2.6.2(a).

NMVC-R² were then prepared through a solution-based gel-impregnation method or a solid-phase powder compression method. Unlike traditional plastic synthesis, we found that the formation of certain vitrimers is accompanied by a sudden increase in viscosity at the gel point, at which everything immobilizes and forms the bulk composite. Therefore, it is possible to disperse NMCF powders in the oligomer solution before the onset of gelation to achieve a homogeneous suspension. Using this strategy, we prepared composites with various compositions of NMCFs and vitrimers. We screened monomer combinations, reaction conditions, rCF and nanofiller loadings, and processing conditions. The gel typically forms within 3 min. once all the monomers are mixed. Through the gel-impregnation method, NMVC-R² with tensile moduli up to 15 GPa and electrical conductivity >2500 S/m could be obtained.

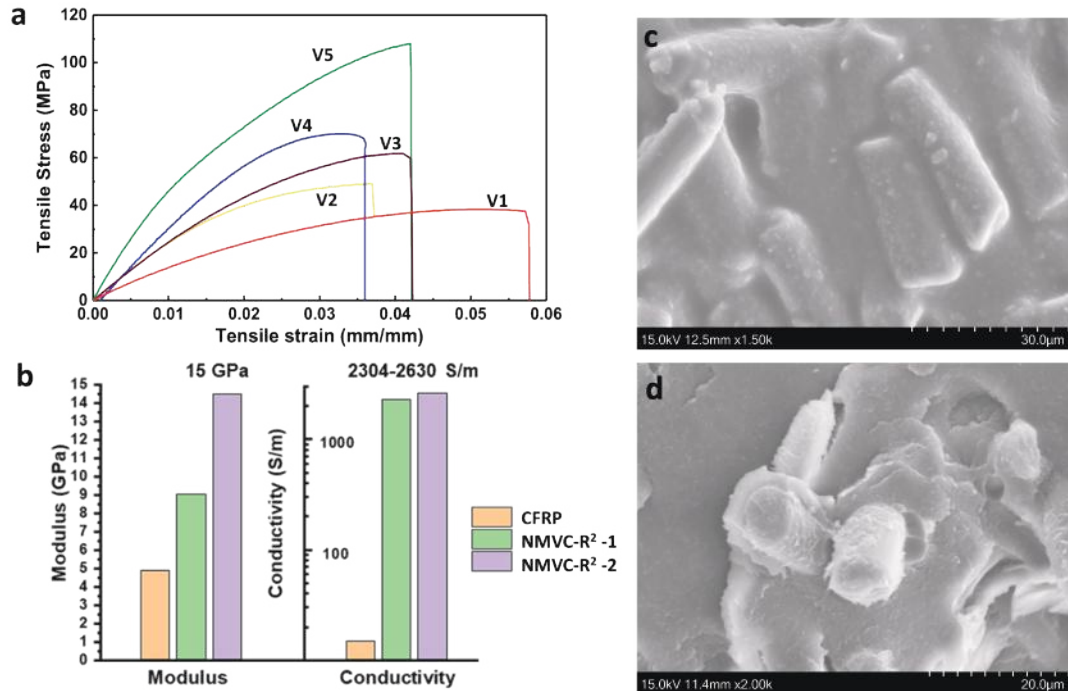


Figure II.3.2.24. (a) Tensile stress-strain curves of various vitrimers. (b) Tensile and conductive properties of NMVC-R² made of vitrimers and NMCs in comparison with CFRP made with unmodified rCF. SEM images of (c) the surface and (d) the cross-section of the NMVC-R². Source: RockyTech Ltd.

The unique advantage of a vitrimer matrix is the ability of particle deformation and interfacial healing, enabled by dynamic bond exchange reactions between polymer chains [3, 4]. During CM under heat, the vitrimer matrix undergoes thermally activated stress relaxation and large deformation, followed by contact and interfacial healing between neighboring particles. Such dynamic bonding-enabled malleability offers the opportunity for multiple reprocessing, lamination, and rapid fabrication of vitrimer-based CFRPs. As an alternative approach, we explored the solid-phase CM of a mixture of fine vitrimer particles and NMCs to form NMVC-R². We obtained composites with a tensile modulus up to 12 GPa and a conductivity of 1490 S/m, which are comparable to the properties of those prepared through the gel-impregnation method. The SEM images of the cross-section and surface of the composites show there are no obvious voids or defects between the polymer matrix and the NMCs, as shown in Figure II.3.2.6.2(c) and Figure II.3.2.6.2(d), respectively. These results clearly support the assumption that our powder-to-film design is a suitable manufacturing method for preparing NMVC-R².

We found that the surface modification of rCF micro-filler has a profound effect on the mechanical properties and electrical conductivity of CFRPs. NMCs can improve not only the mechanical properties, but also the conductivity of the composites when compared to the unmodified rCF. When NMCs were used as a filler, we observed nearly a 2-fold increase in the modulus and over a 50-fold increase in conductivity for the NMVC-R² as compared to the otherwise similar CFRP composite with unmodified rCF in Figure II.3.2.6.2(b). Another remarkable advantage of NMCs is the effective suppression of nanofiller self-aggregation during processing, achieving efficient dispersion with maximal surface area within the composite.

Recyclability of NMVC-R²

The reversibility of dynamic bonds also imparts vitrimers with full degradability and recyclability through depolymerization. When vitrimers are used as a matrix, closed-loop recycling of the composites, including all fillers and chemicals, is possible by converting the vitrimer matrix into soluble oligomers and monomers. Closed-loop recycling of NMVC-R² was achieved through depolymerization of the vitrimer matrix into short soluble oligomers by shifting the equilibrium toward network decomposition. The degradation and

solubilization of the vitrimer matrix release NMCs in their original form, which can directly re-enter the next production cycle after simple drying, as observed in Figure II.3.2.6.3(a). We demonstrated that the first generation recycled NMCs show a similar grafting density of nanofillers on the surface to that of the original fillers, and by removing all the volatiles from the recycled mixture, we formed second generation NMVC-R². The first and second generations of the recycled composites exhibit nearly 100% recovery of tensile modulus and strength as indicated by the stress-strain curves in Figure II.3.2.6.3(b). When the NMVC-R² were recycled the third time, there was a slight decrease in both the tensile strength and the modulus.

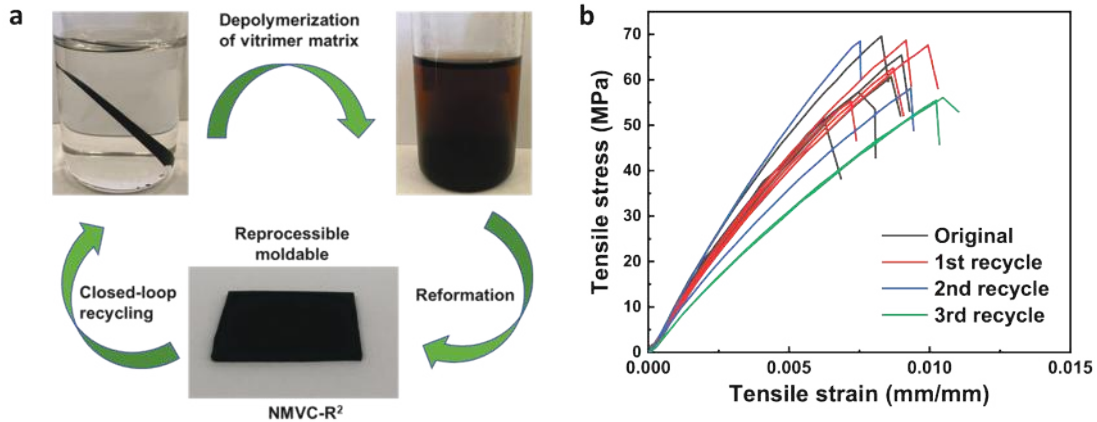


Figure II.3.2.25. (a) Closed-loop recycling of NMVC-R² through solution-phase depolymerization and repolymerization. (b) Tensile stress-strain curves of recycled NMVC-R² in comparison with the original sample. Source: RockyTech Ltd.

Flow-Induced Fiber Alignment

It has been long recognized that fiber alignment can substantially improve the mechanical properties (e.g., modulus and strength) of short-fiber composites along the fiber direction [5]. Recently, there have been emerging technologies to achieve high mechanical properties from discontinuous chopped CFs through fiber alignment. These include the High-Performance-Discontinuous Fiber alignment method developed by the University of Bristol in the United Kingdom [6] and Tailorable Universal Feedstock and Forming technology developed by the Center for Composite Materials of the University of Delaware [7]. A tensile modulus as high as 115 GPa could be obtained from chopped discontinuous CFs measuring 3–6 mm length in a thermoset matrix. In contrast to the great advances in chopped CF composites, the use of milled recycled CFs measuring 50–250 μm length is largely underdeveloped. In this project, we explored a wet process that relies on the shear stress generated by viscous flow to align the short fibers. Our preliminary results show that the flow-induced fiber alignment (FIFA) method is highly promising. The CFRP obtained through the FIFA method using unmodified CFs shows alignment of more than 80% of fibers, as shown in Figure II.3.2.6.4.

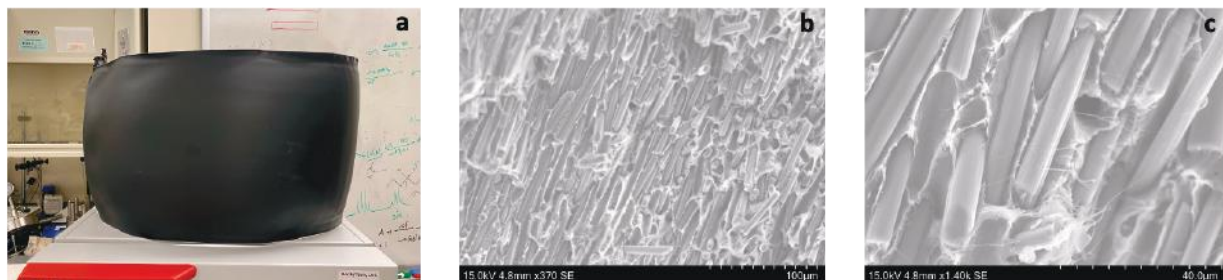


Figure II.3.2.26. Alignment of microscale rCF (unmodified) through FIFA: (a) The image of 1' x 3' panel of CFRP with aligned short carbon fibers; (b, c) SEM images of the CFRP along the fiber direction showing successful fiber alignment through the FIFA method. Source: RockyTech Ltd.

Investigation of EMI Shielding Effectiveness

EVs have become greener and cleaner with the continuous innovation of battery technology. EVs are packed with electronic components and systems, including batteries, power converters, and interconnectors, all of which are significant sources of EMI. These electromagnetic waves can lead to malfunction and even failure of nearby electronic systems. They also cause a serious threat to human health. Metals have been typically used as EMI shielding materials. However, they are heavy, easily corroded, and suffer from poor processability and sealing problems. Conductive NMVC-R² would serve as excellent EMI shielding materials in EV manufacturing given their lightweight density, corrosion resistance, and ease of fabrication. There are three EMI shielding mechanisms: (1) reflection, (2) absorption, and (3) multiple reflections. It is likely that the NMVC-R² combine all three shielding mechanisms. First, NMVC-R² is electrically conductive; therefore, electromagnetic waves striking conductive surfaces can be deflected. Second, it is possible that the combination of conductive microscale and nanoscale fillers creates highly conductive 3D network pathways, which will assist absorption and multireflection of the electromagnetic waves inside the materials, thus providing a superior shielding property at a low thickness. It has been reported that EMI shielding of ~45 dB in the X-band (e.g., 8.2–12.4 GHz) can be achieved when reduced graphene oxide (e.g., 7 wt.%) is dispersed in a polystyrene matrix having a 2.5 mm thickness [8]. In our preliminary study, we could obtain EMI-SE of ~30 dB with a single-layer CFRP composite having a 0.4-mm thickness made from unmodified milled rCF and a vitrimer, as shown in Figure II.3.2.2.5.(a). When a double-layer sample was used, EMI-SE of ~40 dB was achieved in the X-band region. Interestingly, the CFRP composite with aligned rCF showed frequency-selective shielding behavior, with more efficient shielding in the frequency range of 7.5–10 GHz, as observed in Figure II.3.2.6.5(b). The EMI shielding mechanism of these composite materials and the structure-property relationships are currently under investigation.

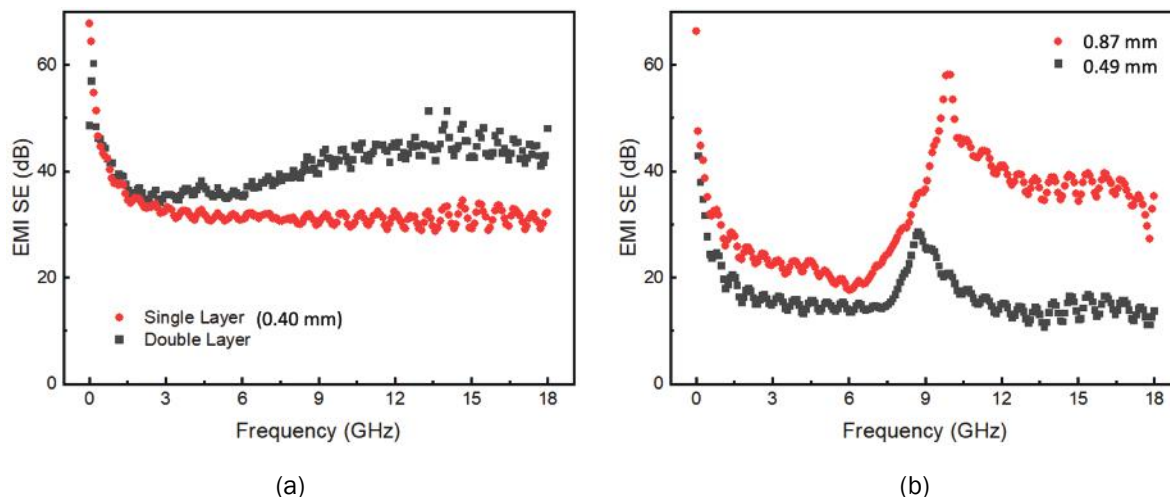


Figure II.3.2.27. EMI-SE of CFRP samples consisting of unmodified rCF: (a) without fiber alignment; and (b) with fiber alignment, as shown in Figure II.3.2.6.4(b). Source: RockyTech Ltd.

Conclusions

RockyTech has successfully developed conductive lightweight NMVC-R² from low-value rCF and carbon-based nanofillers through synergistic surface modifications to improve filler-matrix interface interactions. In fact, NMVC-R² has been shown to have a Young's modulus of up to 15 GPa and a conductivity of up to 2630 S/m, both of which represent the highest reported for milled CF composites. We also demonstrated a promising FIFA method of short CFs having an average length of ~100 μm . Additional advantages of NMVC-R² include: (1) excellent sustainability of the materials, made not only from recycled CFs but also from reprocessable and fully recyclable matrices over multiple processing cycles; (2) the use of vitrimers as a matrix, which offer excellent malleability through dynamic bond exchange reactions and nondestructive fiber

recycling method through depolymerization; (3) isotropic mechanical and electroconductive properties of the material; and (4) improved cost and environmental footprint of CFRPs.

Key Publications

1. Jin, Y., Y. Hu, and H. Yu, 2022, “Polyhydroxyurethanes and method of their use,” U.S. Patent Application #63/322,758.

References

1. Jin, Y., Z. Lei, P. Taynton, S. Huang, and W. Zhang, 2019, “Malleable and recyclable thermosets: The next-generation of plastics,” *Matter*, Vol. 1, No. 6, pp. 1456–1493. <https://doi.org/10.1016/j.matt.2019.09.004>.
2. Kloxin, C. J., and C. N. Bowman, 2013, “Covalent adaptable networks: Smart, reconfigurable, and responsive network systems,” *Chem. Soc. Rev.*, Vol. 42, No. 6, pp. 7161–7173. <https://doi.org/10.1039/C3CS60046G>.
3. Yu, L., Z. Lei, X. Sun, P. Ding, A. Wesche, Y. Jin, W. Zhang, and R. Long, 2021, “Rapid fabrication of fiber-reinforced polyimine composites with reprocessability, repairability, and recyclability,” *ACS Appl. Polym. Mater.*, Vol. 3, No. 11, pp. 5808–5817. <https://doi.org/10.1021/acsapm.1c01027>.
4. Taynton, P., H. Ni, C. Zhu, K. Yu, S. Loob, Y. Jin, H. J. Qi, and W. Zhang, 2016, “Repairable woven carbon fiber composites with full recyclability enabled by malleable polyimine networks,” *Adv. Mater.*, Vol. 28, No. 15, pp. 2904–2909. <https://doi.org/10.1002/adma.201505245>.
5. Paphthnasiou, T. D., and A. Benar (eds.), 2021, *Flow-Induced Alignment in Composite Materials, 2nd Edition: Woodhead Publishing Series in Composites Science and Engineering*, Elsevier, Sawston, U.K.
6. Yu, H., K. D. Potter, and M. R. Wisnom, 2014, “A novel manufacturing method for aligned discontinuous fibre composites (high-performance-discontinuous fibre method),” *Compos. Part A-Appl. Sci. Manuf.*, Vol. 65, pp. 175–185. <https://doi.org/10.1016/j.compositesa.2014.06.005>.
7. Tierney, J., A. Vanarelli, D. Heider, S. Yarlagadda, and J. W. Gillespie, Jr., at the University of Delaware, 2020, “Aligned discontinuous fiber preforms, composites and systems and processes of manufacture, U.S. Patent #US10,669,659 B2.
8. Yan, D.-X., H. Pang, B. Li, R. Vajtai, L. Xu, P.-G. Ren, J.-H. Wang, and Z.-M. Li, 2015, “Structured reduced graphene oxide/polymer composites for ultra-efficient electromagnetic interference shielding,” *Adv. Funct. Mater.*, Vol. 25, No. 4, pp. 559–566. <https://doi.org/10.1002/adfm.201403809>.

Acknowledgments

We would like to thank our collaborators, R. Long and W. Zhang, and their research teams at the University of Colorado–Boulder for their assistance and support throughout the project, and the University of Colorado–Boulder, Department of Mechanical Engineering for general support.

II.3.2.7 Game-Changing Resin/Coating/Adhesive Technology for Lightweight Affordable Composites (Structural Composites, Inc.)

Scott Lewit, Principal Investigator

Structural Composites, Inc.
360 East Dr.
Melbourne, FL 32904
E-mail: slewit@structuralcomposites.com

Brandy Greenawalt, SBIR Program Manager

U.S. Department of Energy SC-29
Small Business Innovation Research
19901 Germantown Rd.
Germantown, MD 20874
E-mail: brandy.greenawalt@science.doe.gov

H. Felix Wu, DOE Technology Development Manager

U.S. Department of Energy
E-mail: felix.wu@ee.doe.gov

Start Date: June 28, 2021	End Date: December 30, 2022	
Project Funding (FY 2022): \$199,256	DOE share: \$199,256	Non-DOE share: \$0

Project Introduction

The automotive industry is aiming to improve energy efficiency, fuel economy, and enable the United States to use less petroleum. Introducing lighter weight materials will improve fuel economy and environmental impact. The materials currently being used in the industry have adverse effects when compared to composites, which have been identified as a material with a high potential for application. This has led to many setbacks in the development of incorporating composites into the automotive industry due to industry leaders being unable to achieve material requirements with the primary goals of significant weight-savings of 60%–70%, while offering high-specific strength, stiffness, and excellent chemical/corrosion resistance. Composites would be a good replacement material to meet many of these goals because they represent a lightweight, cost-efficient key enabler for increasing fuel economy and reducing the environmental impact of vehicles, at a time in the automotive market when manufacturers are looking for increased performance and manufacturing optimization that may only be met by incorporating composites and their integrated out of paint booth (OOPB) finishes.

This program answers and exceeds OEM requirements for functional design features, exercising preliminary analyses of the automotive elements most suitable for composite fabrication using manufacturing methods adaptable to volumes ranging from 20,000 and above, annually. Structural Composites, Inc. (SCI), is focused on the development of advanced ultralight composite materials suitable for custom and fleet applications, as well as high-volume. These materials offer high-performance, economic vehicle applications, adaptation to modular soft rapid tooling with low capital ‘cost-of-entry,’ and compressed lead times. Phase II and III partners have been identified; some Phase III activities have already taken place.

Objectives

SCI developed objectives to facilitate sliding scales of volume with low-cost of entry for tools and processing that implement the many advantages of composites. This results from advanced development of novel materials, composite intermediate/preforms, innovative manufacturing approaches, and fortifying components.

The first objective was the development of relation-oriented tasks, including establishing key partners, conducting the kick-off meeting, and continuing discussions with key partners securing supply chain and project advancement. The second objective was the identification of raw materials and suppliers to create material and lamination matrices to reduce weight, achieve multiscale materials for reinforcing effects, and reduce environmental impact. From the material matrix, a third objective was identified for materials that will replace the need for the paint booth, thereby avoiding chemical and corrosion issues with the use of CoCure® coatings rather than paint, allowing composites to be incorporated into the automotive process and creating an OOPB finish. PRISMA® preforms were analyzed for conceptual design of structural panels and beams (parts) for automotive applications. Through fabricating composite samples of novel materials, testing and analyzing provided preliminary results for materials to be downselected for the best fit in the automotive industry. The leading materials can be integrated into manufacturing design and process for upscaling/commercialization leading into Phase II and III.

Approach

SCI established key partners and customer relations through weekly meetings, quarterly updates, and project planning. Alternative sources of raw materials were developed under this contract enabling program progress despite pandemic and supply chain complications. All materials were able to be sourced in a timely manner after receiving the no-cost extension for Phase I. The Phase I results have been disseminated to contributors and teammates who are expected to participate in Phases II and III. The SCI team researched materials, conceptualized structures, and analyzed manufacturing processes best fitting to the project scope. Materials were downselected to create a matrix for the project based upon lead time, cost, and innovative applications. Cost, performance, sustainability, and manufacturing volumes were considered in material selections.

SCI began sample fabrication and testing in the spring of 2022. Nano/micro/macro enhancements were tested to enhance resin/laminate performance through inter-mixed conventional nano-powders using sensitive precision measurement of percentages for additive content. SCI developed an innovative approach combining graphene and carbon nanotubes into thermoplastics. The thermoplastic precursor of unsaturated polyesters was compounded with a high level of graphene (e.g., 2% by weight) and carbon nanotubes (e.g., 5% by weight). Fiber-bridging additives of graphene and carbon nanotubes, environmentally friendly bio-fibers, and starches were dispersed in polyols, polyesters, and urethane resin blends for enhanced mechanical properties. The additive rich resins were used to fabricate sample panels to be sent for further testing and analysis. Other raw materials of focus include fiberglass, polyester wool, aluminum, hemp fiber, CoCure® coatings, adhesives, and putty.

Partnering with Interplastic Corporation, SCI developed CoCure® technology, which is a hybrid polymer that combines a resin (e.g., polyester or vinyl ester) and urethane that polymerize to cure in a crosslinked network. CoCure® coatings exhibited superior performance when tested to automotive paint standards. CoCure® offers the ability to integrate 'in-mold' finish-quality coatings without the use of a paint booth. CoCure® demonstrated promising applications in base resin for integrated/compound for adhesive and putty trials.

SCI developed a new formable composite called 'Metal Hybrid' using CoCure® combinations. The Metal Hybrid can be formed with sheet-stock uncured, partially, fully, or post-cured. Materials or parts can then be bonded together using CoCure®, adhesives, or stamped into shaped elements and bonded. CoCure® Metal Hybrids offer both the ability to function as an individual, integrated invested tool, as well as the ability to be formed using soft tooling, such as what may be produced using thermoplastic 3D printing. PRISMA® Preforms were analyzed for conceptual design for automotive applications. PRISMA® Preforms offer advanced structural properties while being low-cost and weight efficient. In addition to mechanical performance and cost, PRISMA® Preforms add a crush factor for safety and advanced thermal applications.

SCI fabricated a sample Ford battery box demonstrating commercial integration using CoCure® and Metal Hybrid technologies. Automotive applications were evaluated for suitable application of composite materials and combinations. Sample fabrication and large-scale prototype fabrication were completed. Test results

indicate high value opportunities in application of automotive composites, leading to discussions for Phase II and III.

Results

CoCure® was formulated at five different levels throughout the project for testing—CoCure® 0, 15, 20, 25, and 50 wt% polyurethane. Each level represents the polyurethane content for strain-tunable resin requirements. CoCure® hybrid thermoset resin/Metal Hybrid composite laminates offer high market impacts on numerous industries as a pre- and post-formable material with the unique ability to be married with alloys and thermoplastics, while retaining beneficial mechanical properties of metallic structures. Research revealed innovative new technologies advancing energy security, economic viability, and quality of life. Table provides a list of the objectives that were achieved with these new products.

Table II.3.2.7.1. Test Objectives and Summary of Most Promising Candidates

Objective	Most Promising Candidates
Toughness	CoCure® 25 Metal Hybrid, Applied Science Carbon Nanotube Resin Additive (0-50)
Strength	Standard CoCure® (0-50), Carbon Rivers Graphene Resin Additive (0-50), CoCure® Metal Hybrids (0-50)
Finish Quality	CoCure® Coatings 15 & 20
UV	CoCure® Coatings 15 & 20
Flexibility	Standard CoCure® (0-50), Carbon Rivers Graphene Resin Additive (0-50), CoCure® Metal Hybrids (0-50)
Adhesion	CoCure® Putty 15 & 25
Formability	CoCure® 25 & 50 Metal Hybrids

CoCure® coatings demonstrated higher performance in weathering, mechanical properties, material adhesion, 100% improved impact strength, gloss and color retention, and thermal performance compared to standard coatings and automotive paints. *Specific data for performance and properties cannot be presented in this report because they are proprietary.* Coatings yielded the highest strength at low temperatures and greatest elongation at high temperatures. Weathering test results show improvement in color and gloss retention with increasing CoCure® level. Gloss retention and color change for CoCure® 20 displayed the best results per ASTM G155. This system qualifies as a low hazardous air pollutant in-mold coating system. CoCure® in-mold coatings eliminate the need for a spray booth through the coating process, enabling OOPB composites in the automotive industry. Neat resin casting samples tested in accordance with ASTM D638 and ASTM D790 resulted in high modulus, high-temperature elongation, and high-strength at low temperatures. CoCure polyurethane content better resists fracture as compared to conventional polyester compositions. Additional improvement in resin performance through inter-mixed conventional nano-powders was also demonstrated. However, measurable improvement relies on precise percentage of additive content. Optimal mixtures of additives in resin improve micro/macro fracture toughness-resistance and fracture bridging. Project results indicate graphene additives can provide improved strength and impact resistance greater than standard polyester resin. Irrespective of the experimental findings with additives, CoCure® resins 15 and 25 resulted in consistent high-strength results and CoCure® 50 led in impact strength, as indicated in Figure II.3.2.7.1.

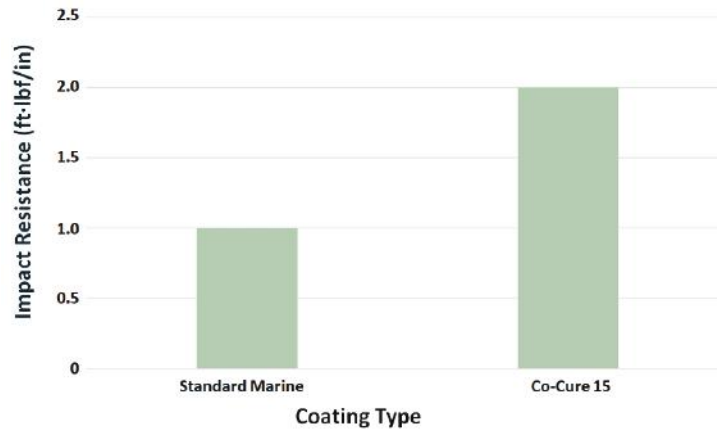


Figure II.3.2.28. Impact test results (ASTM D256). Source: SCI.

CoCure® Metal Hybrid is compelling to the automotive industry as a pre-formable, formable, and post-formable section-active structure, attained with low-cost rapid tooling processes. Initial Metal Hybrid composites provided high-strength and modulus with the best results exhibited by CoCure® 15 and 25. CoCure® putty adhesives show excellent structural properties compared to commonly available putty, such as methacrylate, silicone, polysulfide, and foaming adhesive. CoCure® putty adhesives using a standard DDM9 catalyst possesses the highest strength in CoCure® 15 and 25, thereby outlasting the threshold beyond the interlaminar failure of substrate structure, thus leading to a broader range of candidate solutions.

PRISMA® Preforms provide incomparable levels of specific strength (strength-to-weight ratio) resulting in lighter weight vehicle structures that reduce fuel consumption resulting in a smaller environmental impact. PRISMA® Preforms are customizable 3D shapes that are easily incorporated into complex geometries during (and alternatively after) the molding process. Testing verifies PRISMA® integrated composites are lighter weight and stronger alternative material for applications replacing aluminum and steel frame structures. *Test data is proprietary and cannot be presented in this report.* Strong commitments from teammates for Phase II initial opportunities have been established in accordance with high value test results that can be applied to composite automotive applications and key partners identified.

Conclusions

Project test results revealed a broader range of candidate solutions than first hypothesized. As a result, SCI developed CoCure® Metal Hybrid solutions, advanced CoCure® adhesives and coatings and established OOPB applications and PRISMA® Preform structural applications of significant potential to the automotive market. CoCure® coatings have returned promising results with higher values than standard coatings and gel coats to allow composites to be incorporated into OOPB manufacturing for both in-mold and after-mold processing. CoCure® resins and PRISMA® Preform structures introduce a cutting-edge capability for rapid manufacturing at a low-cost of entry for tooling and processing. These characteristics open new opportunities for manufacturing democratization and surge production. All results from Phase I returned with promising applications to automotive for Phases II and III.

Acknowledgments

SCI would like to acknowledge the following key teammates who made this project possible: H. Caldwell, project manager/engineer; B. Said and F. Em, subject matter expert- composite materials; and J. Unser, program manager. SCI would also like to acknowledge our Interplastic Corporation partners—especially C. Peickert and S. Crump for their efforts in CoCure research—and our Florida Institute of Technology research partner, Dr. Mirsayar.

II.3.2.8 Changing the Design Rules of Rubber to Create Lighter Weight, More Fuel-Efficient Tires (Molecular Rebar Design, LLC)

Kurt Swogger, P.E., Principal Investigator

Molecular Rebar Design, LLC
 13477 Fitzhugh Rd.
 Austin, TX, 78736
 E-mail: kswogger@molecularrebar.com

Brandy Greenawalt, SBIR Program Manager

U.S. Department of Energy SC-29
 Small Business Innovation Research
 19901 Germantown Rd.
 Germantown, MD 20874
 E-mail: brandy.greenawalt@science.doe.gov

H. Felix Wu, DOE Technology Development Manager

U.S. Department of Energy
 E-mail: felix.wu@ee.doe.gov

Start Date: June 28, 2021	End Date: March 27, 2022	
Project Funding (FY 2022): \$197,359	DOE share: \$197,359	Non-DOE share: \$0

Project Introduction

EV tire treads are wearing at a rate much faster (30%+) than their internal combustion engine counterparts [1]. This is primarily due to the heavier weight of the vehicle, near-instant torque, and urban-oriented driving. Typically, passenger car tires are produced with tread compounds utilizing a solution styrene-butadiene rubber (SSBR) and butadiene rubber (BR) polymer blend with silica bound by silane. This tread polymer composite is preferred for improved fuel economy and wet grip, typically termed a ‘green’ compound—referencing the fact that it has better fuel economy and less CB content than a typical tire. Sometimes, a higher portion of CB replaces some of the silica to create better wearing tire treads to improve wear—termed a ‘gray’ compound because of its higher content of CB. Figure II.3.2.8.1(a) shows typical ‘green’ and ‘gray’ compounds [2], while Figure II.3.2.8.1(b) shows the typical difference between a conventional tire tread compound and a ‘green’ one [3]. Molecular Rebar Design, LLC (MRD) seeks to improve the wear resistance and fuel efficiency of a state-of-the-art silica-silane tire tread composite using discrete molecular rebar (MR) carbon nanotubes (CNTs).

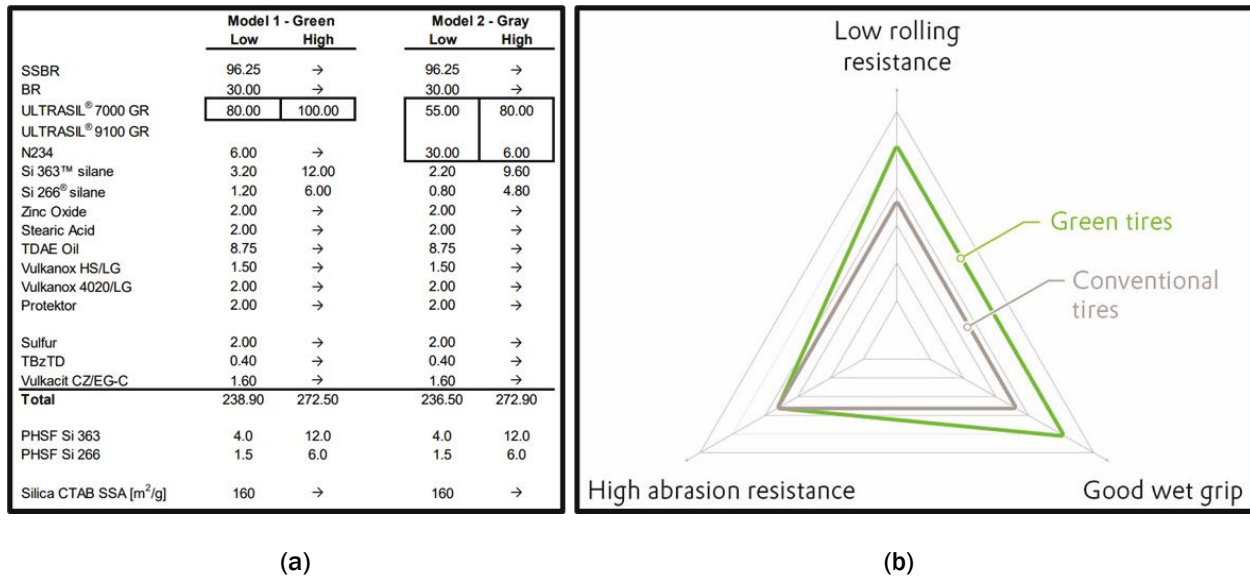


Figure II.3.2.29. (a) The basis from literature for the tested ‘gray’ and ‘green’ tire tread compounds. (b) A rendition of the differences between a conventional ‘black’ and high silica ‘green’ tire treads. Source: MRD.

Objectives

In Objective 1, the goal of MRD was to understand the changed structure-polymer relationships with available MR products for this application space, as well as the maximized benefits of the current MR technology when used as a CB replacement for a polymer composite formulation. MRD is familiar with various rubber compounds but was unfamiliar with the silica-silane in synthetic polymer composites used in this project.

Objective 2 builds upon the work performed in Objective 1, where MR was demonstrated to disperse well into a CB-silica-silane-SSBR ‘gray’ compound. The sufficient dispersion of MR, even without chemical functionalization, can improve wear resistance properties—such as the German Institute for Standardization, Deutsches Institut für Normung (DIN), abrasion resistance—by 20% without detrimentally effecting the dynamic, or hysteresis properties, of the compound. That improved ‘gray’ compound has a ratio of CB to silica of 30:55 parts per hundred resin (PHR). That was compared to the focus of Objective 2, wherein a ‘green’ compound is being improved, where the ratio of CB to silica is much lower at only 6:90 PHR.

The goal of Objective 3 is to replace the dominant silica filler in a ‘green’ tread compound and deliver both improved lifetime (abrasion) properties and improved energy efficiency (rolling resistance [RR]) properties. The likely scenario is not a total replacement of the silica, but some mixed composite of both fillers—nano and micro—where the silica and MR are coupled into the rubber, thereby providing mixed modes of reinforcement and improving those sought-after properties.

Approach

Figure II.3.2.8.2 is intended to help visualize how the results of each iteration of experimentation informed the design of the next experiment. Not all experimental results are included in this report, as many of them did not result in a conclusive step-change in properties. Nonetheless, those experimental results did inform and influence the pathway of the Phase I work.

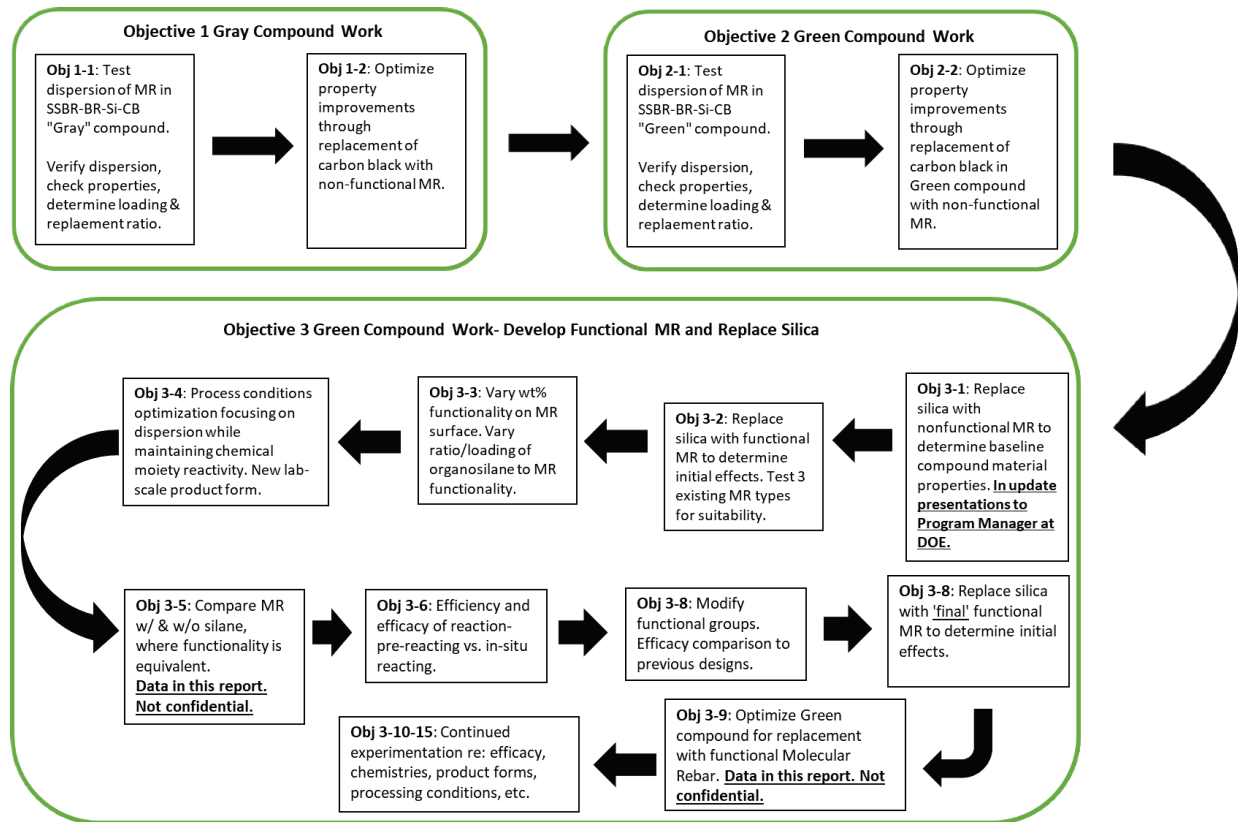


Figure II.3.2.30. Flow diagram of most experiments performed by MRD during the course of Phase I. Source: MRD.

Results

In Objective 1, it was shown that nonfunctional MR can be used to replace the less reinforcing N234 CB content in a 'gray' tread compound for silica-silane-SSBR tread compounds. However, if too much CB is removed, some of the overall baseline properties are substantially reduced—such as tensile strength. If a tensile strength sacrifice can be made, the nonfunctional MR can be utilized to achieve an improvement of 20% DIN abrasion resistance—20% constrained tear toughness—while maintaining RR. The dispersion of the non-functionalized MR in this system seemed to be unaffected by the presence of silica, in conjunction with the silane bonding system. A major concern was whether the MR nanotubes would appropriately disperse in (1) a new synthetic polymer system, (2) with silica fillers (different than previous CB systems), and (3) whether the silane would affect dispersion of the MR CNTs. Given the property improvements, with an optimal sample shown in Figure II.3.2.8.3 and transmission electron microscope images shown in Figure II.3.2.8.4, the nonfunctional MR is discrete, which is providing reinforcing benefits in the silica-silane-SSBR formula that can be used to some extent in place of CB.

In Objective 2, the use of chemically nonfunctional MR is also a substitute for CB in the 'green' compound, similar to its property improvements in the 'gray' compound, with one key difference: the high silica of the content and low CB content in the 'green' compound does not allow for quantities of MR greater than ~3 PHR with CB removal, or ~2 PHR without CB removal to be used as reinforcing aids. An optimized compound with the MR as a replacement for the 6 PHR CB content is shown in Figure II.3.2.8.5.

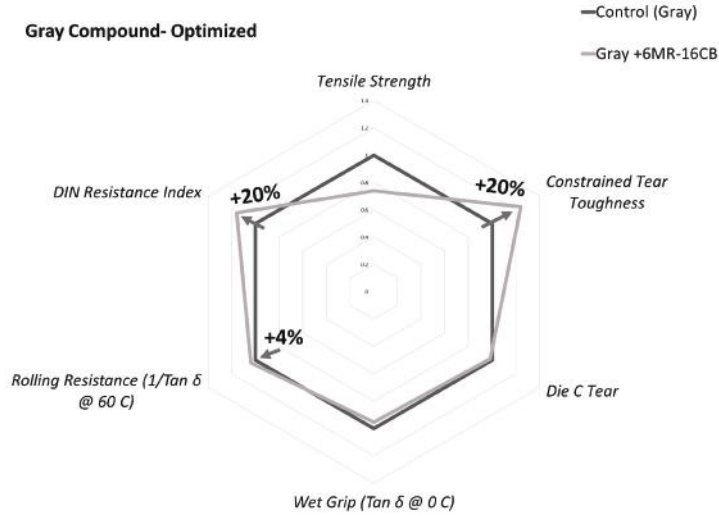


Figure II.3.2.31. Spider graph demonstrating materials property changes with nonfunctional MR in a ‘gray’ tire tread compound. Source: MRD.

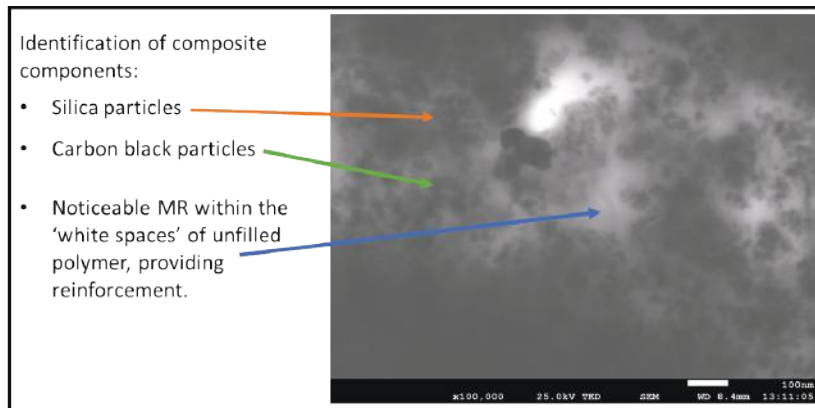


Figure II.3.2.32. Annotated transmission electron microscope image of MR dispersed in a ‘gray’ tire tread compound. Source: MRD.

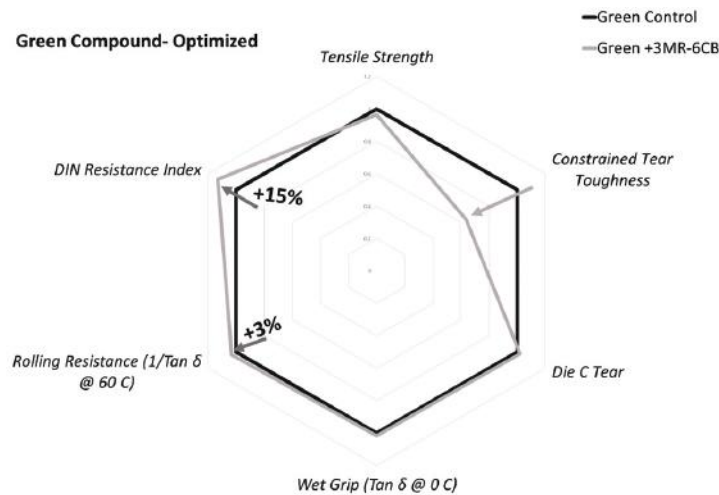


Figure II.3.2.33. Spider graph demonstrating materials property changes with nonfunctional MR in a ‘green’ tire tread compound. Source: MRD.

In the work to meet Objective 3 of Phase I, a chemically functional MR has been proven to increase binding with the polymer matrix, providing a unique combination of reinforcement and hysteresis property benefits. The mechanism of the MR functionalization is shown in Figure II.3.2.8.6, where the bis-(3-triethoxysilylpropyl) tetrasulphane (TESPT) organosilane bonds with the -OH (and maybe -COOH) groups on the outside of the carbon nanotubes (1) – (2), and then the TESPT bonds to the polymer matrix through sulfur-sulfur crosslinks during the curing process (3).

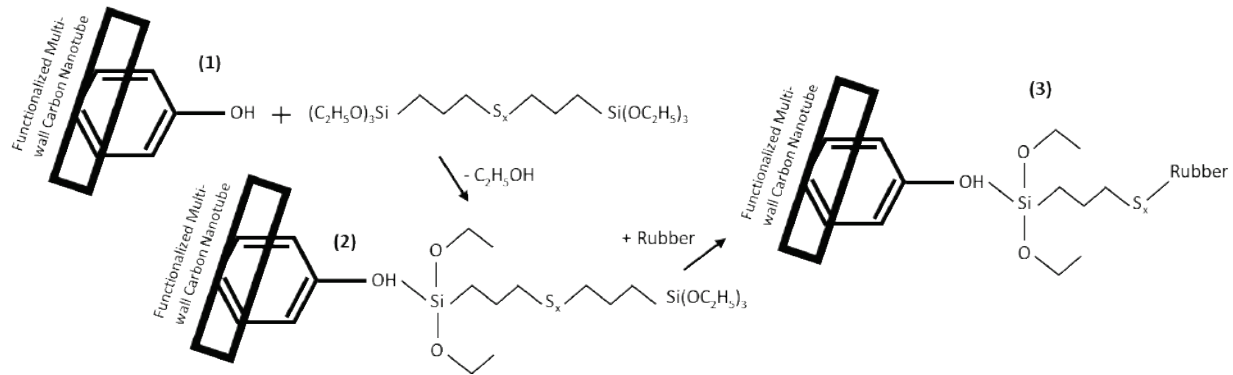


Figure II.3.2.34. Graphic showing theorized mechanism of organosilane bonding between MR and the polymer matrix. Source: MRD.

The graph shown in Figure II.3.2.8.7 demonstrates the unique materials' property changes with these functionalized carbon nanotubes, where the 100% modulus and tan delta at 60°C are simultaneously improved with two different weight loadings of the MR with silane (TESPT, i.e., Evonik Si69®) functionality.

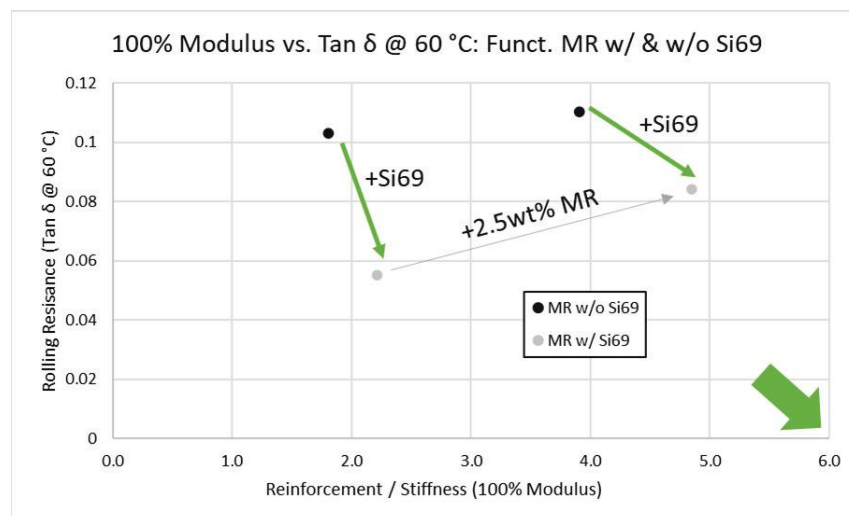


Figure II.3.2.35. Plot demonstrating simultaneous improvement in reinforcement (100% modulus) and RR (Tan δ at 60 °C). Source: MRD.

When used as a replacement for silica, with some adjustment to oil concentration, the functional MR with silane bonding provides needed property enhancements, such as improved DIN abrasion resistance and reduced RR, for a 'green' tread compound for EVs. These improvements were made and measured using commercial testing techniques, indicating that the commercial viability of this functional MR product is high. The 'rule set' to describe replacement of existing silica content with the functional MR is a work in progress, with the exact relationship being undefined, but this objective's work indicates that the relationship is a sliding scale, where the more silica is removed, the more MR must be added. MR is more reinforcing than current

state-of-the-art fillers, such as silica, wherein the MR is thrice as reinforcing as normalized by RR (e.g., three times the modulus for the same increase in RR) and ten times more reinforcing than silica on a PHR basis, as shown in Table. As MR increases from 13-26 PHR, 100% modulus and RR increases. As silica content increases from 45-90 PHR, the 100% modulus increases at a rate slower than the MR, and the RR increases at a higher rate than the MR. Thus, the MR is three times as reinforcing as silica on a 100% modulus per unit increase of RR (e.g., second column from the right) and is ten times as reinforcing as silica on a 100% modulus per PHR loading basis (e.g., right-hand column).

Table II.3.2.8.1. Changes in Reinforcement with Silane-Functionalized MR vs. Incumbent Reinforcing Filler Silica

31 PHR of Oil - Constant	13 PHR MR or 45 PHR Silica		26 PHR MR or 90 PHR Silica		Difference in PHR	Δ 100% Modulus / Unit RR	Δ 100% Modulus / PHR
	Initial 100% Modulus (MPa)	Initial RR	Final 100% Modulus (MPa)	Final RR			
MR 13-26 PHR (no silica)	2.6	0.074	7.7	0.1796	13	48.3	0.39
Silica 45-90 PHR (no MR)	2.4	0.061	4	0.1736	45	14.2	0.036

When dispersed and functional MR is used in conjunction with a significantly reduced quantity of silica, the lifetime and RR of a tire tread rubber composite can be improved simultaneously, as shown in the spider graph in Figure II.3.2.8.8.

Summarized Results- Optimized Compounds w/ Novel MR

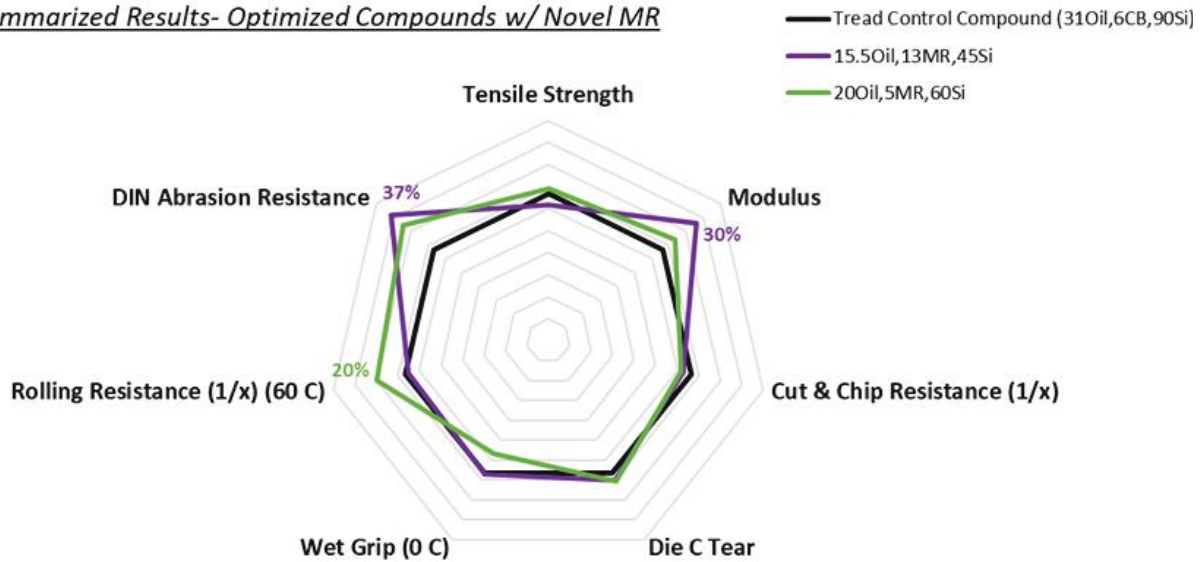


Figure II.3.2.36. Plot demonstrating simultaneous improvement in reinforcement (100% modulus) and R (Tan δ at 60 °C). Source: MRD.

Conclusions

The development for the use of MR in tire rubber composites changes the paradigm of wear, grip, and RR for tire compounds that have been used for decades, with the most recent shift being the adoption of silica bound by silane. With MR, particularly a functionalized version that covalently binds to the rubber composite structure, new rubber compounds can be designed to improve energy efficiency with a lower tire weight to improve a lifetime of tires for EVs and to maintain grip. Over time these improved composites will be used in various types of tires, regardless of power train source (e.g., internal combustion engine or EV).

Key Publications

1. Swogger, K., and A. Krupp, 2022, “Discrete and functional carbon nanotubes (Molecular Rebar) for improved tires in transportation,” *Proceedings of the SPIE Smart Structures + Nondestructive Evaluation, 7–9 March 2022, Long Beach, CA, USA*. Vol. 12047. [Online] Available at: <https://www.spiedigitallibrary.org/conference-proceedings-of-spie/12047/2615261/Discrete-and-functional-carbon-nanotubes-Molecular-Rebar-for-improved-tires/10.1117/12.2615261.full> (last accessed 1 March 2023).
2. Swogger, K., and A. Krupp, 2022, “Carbon nanotubes: The rapidly approaching future of tire reinforcement,” *Clemson University Global Tire Industry Conference, 19–21 April 2022. Hilton Head Island, SC, USA*.
3. Swogger, K., and A. Krupp, 2022, “Carbon nanotubes with organosilane functionalization improve abrasion and rolling resistance of silica-silane tire tread compounds,” *Rubber World Magazine*, Vol. 267, No. 1, pp. 14–16, October 18, 2022 [Online]. Available at: <https://mydigitalpublication.com/publication/?m=9911&i=765217&p=16&ver=html5> (last accessed 1 March 2023).
4. Swogger, K., and A. Krupp, 2022, “Discrete and chemically functional carbon nanotubes (molecular rebar) for improved EV tires,” *200th Technical Meeting of Rubber Division, American Chemical Society, 10–13 October 2022, Pittsburgh, PA, USA*.

References

1. Lambert, F., 2018, “Goodyear unveils new tire for electric cars to reduce wear from powerful instant torque.” *Electrek*, 8 March 2018. [Online]. Available at: <https://electrek.co/2018/03/08/goodyear-tire-electric-cars-reduce-wear-instant-torque/> (last accessed 1 March 2023).
2. Roben, C., A. Wehmeier, and L. Gatti, 2017, “Investigations into the optimization of Si 363™ and Si 266™ silane combinations across three differing tire tread formulation types,” *ITEC in Focus, 13–14 September 2017*. [Online]. Available at: <https://www.rubbernews.com/assets/PDF/RN112110915.PDF> (last accessed 1 March 2023).
3. Evonik website, 2022, “Keep on rolling! The green tire,” [Online]. Available at: <https://corporate.evonik.com/en/the-green-tire-1456.html> (last accessed 1 March 2023).

Acknowledgments

The authors acknowledge the contributions of A. Krupp (akrupp@molecularrebar.com), the Director of Rubber Development for MRD.

II.3.2.9 Hierarchical Micro/Nano Reinforced Multiscale Hybrid Composites for Vehicle Applications (Advent Innovations, Ltd.)

Shawn Beard, Principal Investigator

Advent Innovations Limited Company
1225 Laurel St., Ste. 213
Columbia, SC 29201
E-mail: shawnb@adventinnous.com

Brandy Greenawalt, SBIR Program Manager

U.S. Department of Energy SC-29
Small Business Innovation Research
19901 Germantown Rd.
Germantown, MD 20874
E-mail: brandy.greenawalt@science.doe.gov

H. Felix Wu, DOE Technology Development Manager

U.S. Department of Energy
E-mail: felix.wu@ee.doe.gov

Start Date: June 28, 2021	End Date: March 27, 2022	
Project Funding (FY 2022): \$98,625	DOE share: \$98,625	Non-DOE share: \$0

Project Introduction

In an effort to stimulate the economy of the United States and global competitiveness overall, there is currently a push to reduce dependence on foreign oil imports and establish a domestic energy industry utilizing fuel-efficient vehicles. Nearly all vehicle fuel consumption goes to vehicle acceleration (e.g., kinetic energy), climbing a hill (e.g., potential energy), and overcoming frictional forces, all of which are associated with vehicle body weight. To reduce the energy consumption in next-generation vehicles, it is essential to reduce the overall body weight of the vehicles. In addition to reducing dependence on foreign oil imports, this will have two major impacts. First, by reducing the weight of the constituent structural components, the fuel economy of the vehicles will be improved allowing longer travel distance, and second, by reducing fuel consumption, environmental impacts will be greatly reduced. In recent years, many industries have taken advantage of carbon fiber composite (CFC) to reduce the weight and maximize the performance. CFC materials offer high stiffness- and high-strength-per-weight ratios, which are desirable in weight-sensitive applications. Unfortunately, the U.S. automotive industry is far behind the aerospace industry in the adoption of CFCs [1]. This is partly due to the high cost of the fibers, the cost and source of fiber precursor materials, suitability of manufacturing processes, and the energy requirements for converting the precursors to the finished fibers. If fully realized and adopted by the industry, vehicles made of CFC have the potential to reduce the weight of their body structure by 60%. However, using CFC materials alone, without any other added reinforcements, may not be sufficient to meet DOE's goal of 75% reduction of composite body weight by 2050 [2].

The goals and metrics in DOE reports [2, 3] state that lightweighting of structures to improve fuel economy is one of the primary objectives of this century. One way to solve this challenge is to not only reduce the weight of the body structure using polymer composites, but to also add reinforcements, such as microfillers or nanofillers in a relatively soft matrix. Employing multiscale micro/nano hybrid reinforcements would result in an exceptional reinforcing effect that is currently not achievable using a single type of reinforcement. Such hierarchical reinforcements are necessary to enhance the filler/matrix interfacial load transfer while reducing the overall weight of the composite structure [4].

In this Small Business Technology Transfer (STTR) project, Advent Innovations Limited Company (Advent) teamed with Georgia Southern University (GSU) to develop and test high-performance, high-volume, and highly affordable hybrid structural nanocomposite fibers micro-coated with hybrid nanomaterial for composite materials shown conceptually in Figure II.3.2.9.1. The low-cost and significantly lightweight hybrid nanocomposite fibers (HyFi) will not only exhibit high-strength and toughness (e.g., increased crashworthiness), but coating of the HyFi fibers with hybrid nano materials will also increase the fiber/matrix bonding and enhance filler/matrix interfacial load transfer, which will be a game-changing performance indicator beyond the conventional single type of reinforcement. Furthermore, the energy absorbing, ductile nature of the material will help reduce noise, vibration, and harshness.

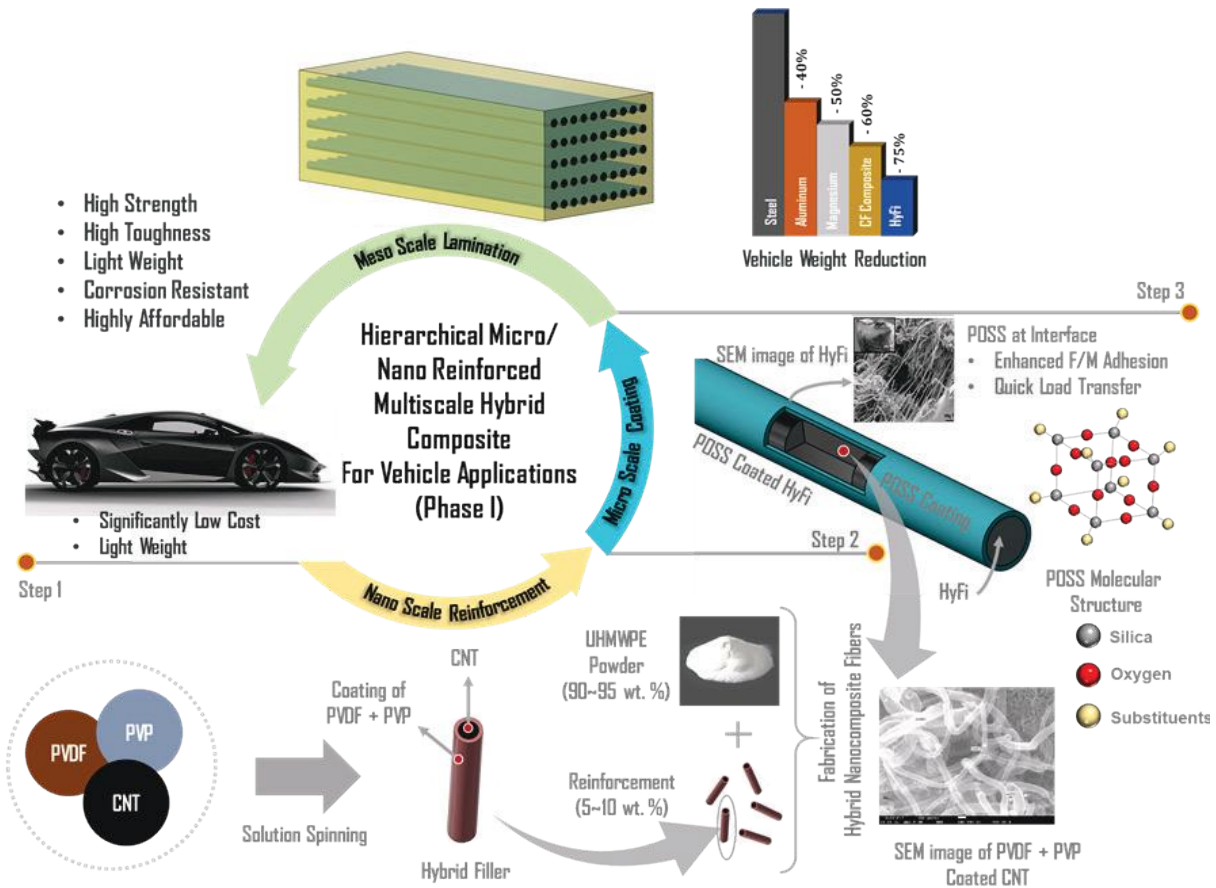


Figure II.3.2.37. Conceptual design of proposed multiscale hybrid composite for vehicle applications. Source: Advent.

The HyFi fibers are synthesized using ultra-high molecular weight polyethylene (UHMWPE) powder and carbon nanotubes (CNTs) that are coated with polyvinylidene fluoride (PVDF) and polyvinylpyrrolidone (PVP). This increases the fiber's strength- and toughness-to-weight ratios. The fibers are then coated with polyhedral oligomeric silsesquioxanes (POSS) to increase fiber/matrix bonding and enhance filler/matrix interfacial load transfer. The micro-architected reinforcements inherently create hierarchical fillers to result in higher strength than CF, Spectra/Dyneema, or Kevlar, and 75% lighter in weight than steel. The multiscale composite material will enable reduced weight and volume of structural components, resulting in increased vehicle energy efficiency and increased crashworthiness capabilities.

By virtue of the constituents of the HyFi and its hybrid coating, the manufactured composite system will have excellent chemical and corrosion resistance, in addition to high-strength and toughness, which are important for vehicle operational environment contributing to low-cost, secure, and clean energy environment, a technology aligned perfectly with the DOE vision for 2050.

Objectives

The POSS-coated HyFi development covered three overarching target areas:

- **Target 1:** Utilize UHMWPE fibers, reinforced with PVDF+PVP-coated CNTs, to increase strength and toughness and reduce the necessity of the cosmetic, ad-hoc, and non-load-bearing structures that are used to mitigate impacts.
- **Target 2:** Utilize POSS to coat the HyFi fibers to enhance the filler/matrix interfacial load transfer and increase the adherence to microfibrils resulting into augmented reinforcing capabilities.
- **Target 3:** Utilize high-performance resin in the vacuum-assisted resin transfer molding process to fabricate affordable high-performance laminated composite for the automotive industry.

Approach

Advent designed the multifunctional system architecture and conducted feasibility testing to quantify the functional parameters (e.g., specific strength, specific stiffness, toughness, strength-to-weight ratio, etc.), while GSU synthesized, processed, and characterized the hybrid fibers and nanofiber membranes, including reinforcements with PVDF and PVP-coated CNTs and POSS application. Advent used the fibers to fabricate composite specimens and conducted mechanical testing to provide feedback to GSU to optimize the process parameters. Multiple design iterations were required to maximize the fiber strength and toughness, while optimizing the fiber/matrix interfacial properties. The specific aims in Phase I were:

1. **Architecture Design:** To develop the requirements and specifications for each element of the HyFi material system to ensure compatibility and synergistic integration.
2. **Nanofillers Fabrication:** To synthesize and process PVDF+PVP-coated CNTs to enhance the dispersion and reinforcement of CNTs in microfibrils.
3. **Strong and Tough:** To synthesize and process UHMWPE fibers reinforced with PVDF+PVP-coated CNTs for enhanced strength and toughness.
4. **Fiber/Matrix Interface Modification:** To process POSS to disperse over the HyFi to add micro-reinforcements and enhance the filler/matrix interfacial load transfer.
5. **Composite Manufacturing:** To fabricate composite specimens using POSS-coated HyFi fibers in thermoset epoxy-based matrix for mechanical testing and architectural design optimization.
6. **Feasibility Testing & Design Recommendation:** To conduct testing of the manufactured composite specimens to demonstrate the feasibility of multiscale (both microscale and nanoscale) reinforcing effect simultaneously in the polymer composite. Determine the strength-to-weight and toughness-to-weight ratios. Based on results, generate design recommendations for multiscale reinforced hybrid composites for improvement.

Results

During this Phase I STTR project, 15 grams of HyFi fibers were synthesized and processed at GSU's Nanomaterial Research Laboratory. The fibers were produced using a solution-spinning machine, as shown in Figure II.3.2.9.2. The extruded fibers were then subjected to strain-hardening, which is the process to make a fiber harder and stronger through plastic deformation and aligning of the CNTs. As the strain increases beyond the elastic deformations, the fiber becomes stronger while permanent deformation is induced. In the case of a HyFi fiber, strain-hardening permanently elongates its length and reduces its diameter. Prior to strain-hardening, the average fiber diameter is approximately 100 micrometers. After strain-hardening, the average fiber diameter is reduced to approximately 22–30 micrometers as shown in Figure II.3.2.9.3.

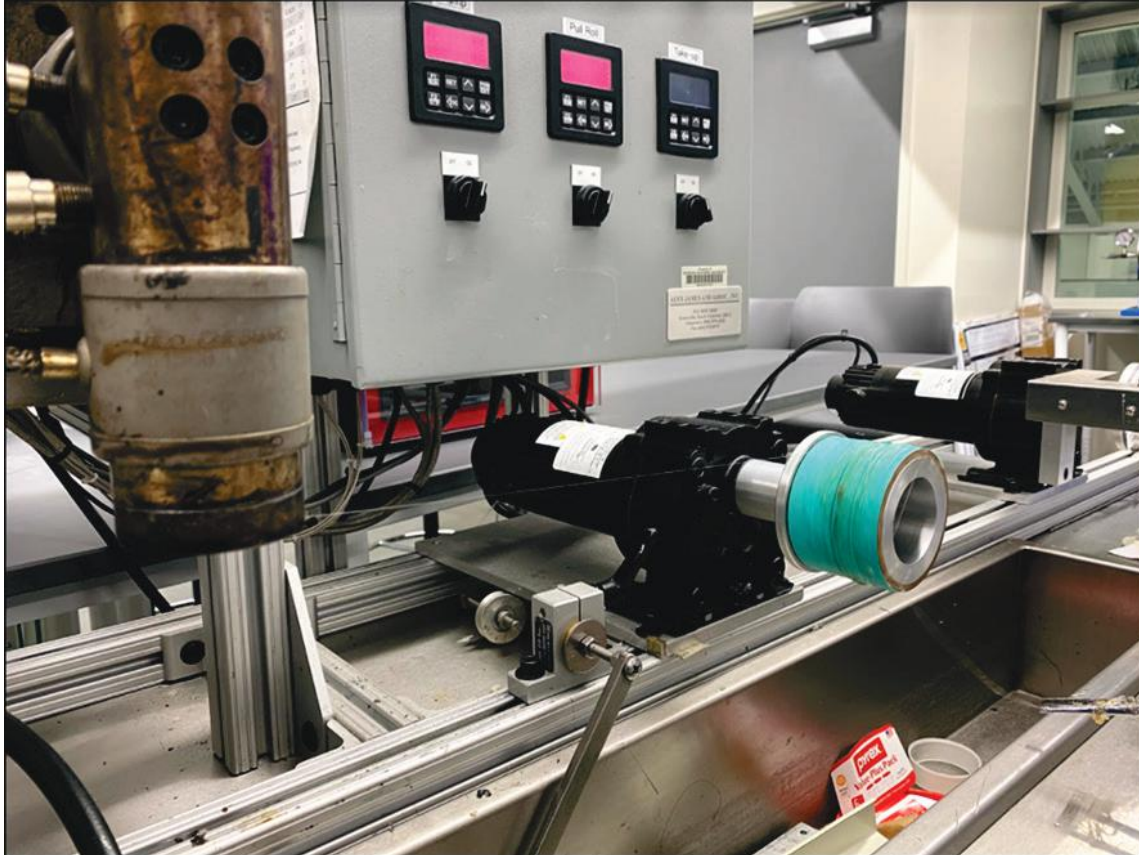


Figure II.3.2.38. Solution-spinning system. Source: GSU.

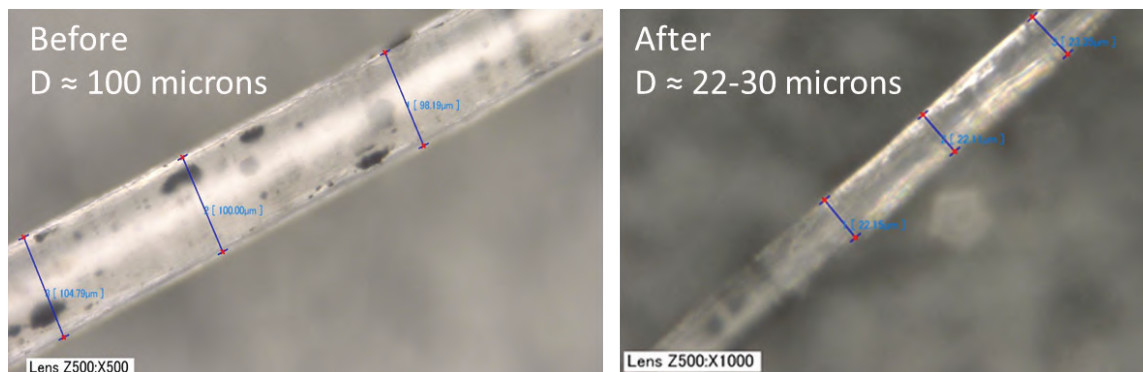


Figure II.3.2.39. Fiber diameter before and after strain-hardening. Source: GSU.

Following strain-hardening, the fibers were coated with POSS through an electro-spraying process to increase the fiber/matrix bonding and enhance filler/matrix interfacial load transfer. The POSS coating increased the fiber diameter between 4–10 microns, depending on the POSS concentration in the solution.

The fibers were then used to manufacture composite specimens. Multiple sets of composite architecture designs were prepared through a vacuum-assisted resin transfer molding process, as shown in Figure II.3.2.9.4. The architectures include both unidirectional, long-fiber composites and chopped, short-fiber composites. The architectures consist of HyFi fibers only and hybrid HyFi/carbon designs. For example, one set of designs of the unidirectional long-fiber designs utilized only HyFi layers, while another utilized multiple HyFi layers embedded in CF layers. All architecture designs were subjected to tensile testing, as observed in Figure II.3.2.9.5, and compared with traditional all-CF composite. The test results are summarized in Table II.3.2.9.1.

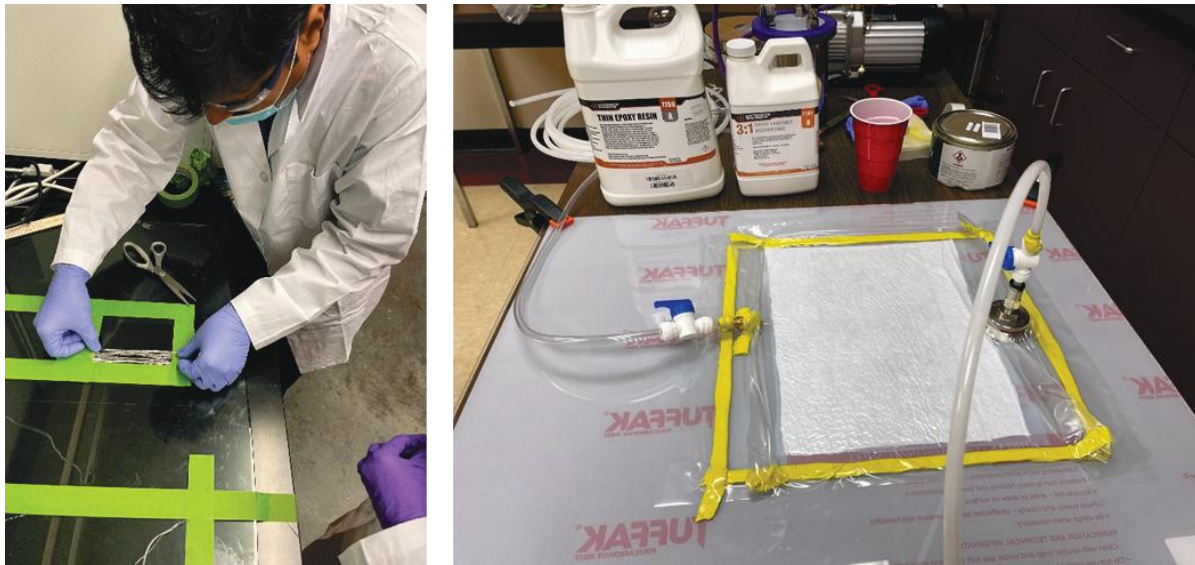


Figure II.3.2.40. Composite specimen manufacturing. Source: Advent.

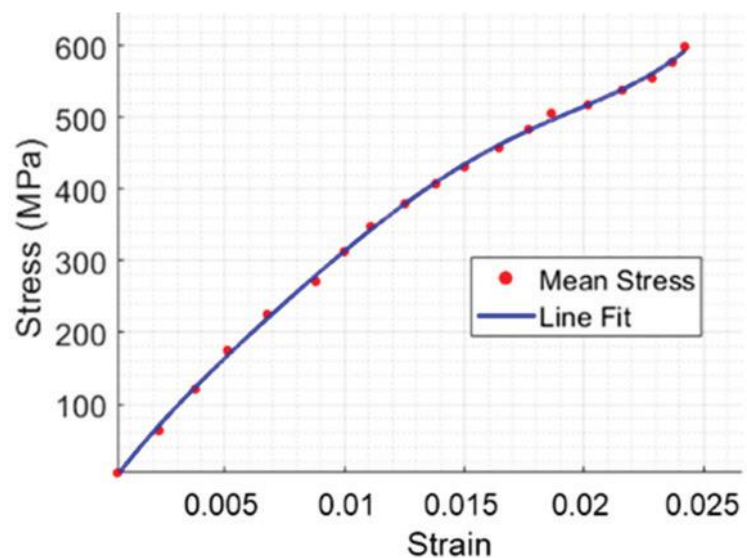
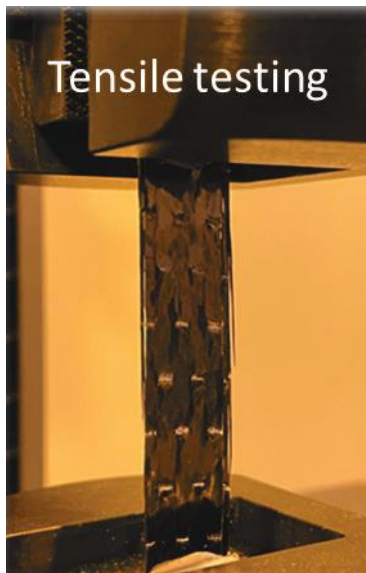


Figure II.3.2.41. Composite specimen tensile testing. Source: Advent.

Table II.3.2.9.1. Summary of Tensile Test Results

Specimen Type	Fibers	Number of Specimens	Fiber/Resin Ratio	POSS Coating of HyFi Fibers	Strain-Hardening of HyFi Fibers	Average Max Stress (MPa)	Average Max Strain
Unidirectional Long-Fiber	HyFi	2	30/70 by weight	Yes	No	6.89	0.034
	Carbon	2	30/70 by weight	-	-	489	0.009
	Hybrid Carbon-HyFi (50-50 by volume)	3	30/70 by weight	No	No	503	0.021
Chopped Short-Fiber	HyFi	2	20/80 by weight	Yes	Yes	6.6	0.035
		2	30/70 by weight	Yes	No	6.5	0.081
	Carbon	1	20/80 by weight	-	-	96	0.019
		3	30/70 by weight	-	-	142	0.015
	Hybrid Carbon-HyFi (50-50 by weight)	1	20/80 by weight	No	No	10	0.097

Conclusions

In this STTR project, a unique phase-enhanced hybrid nanocomposite fiber for composite materials called ‘HyFi’ was developed and tested. The hierarchical multiscale composite consists of macro-, meso-, and micro- as well as nano-features, all of which are responsible for imparting unique and mutually exclusive mechanical properties. The fibers were engineered with micro-architected reinforcements that inherently create hierarchical fillers for high-strength and toughness. An innovative synthesis and fiber spinning process was used to manufacture the HyFi fibers with increased strength-to-weight and toughness-to-weight ratios, and the ability to absorb and redistribute impact energy before local failure conditions are met. In addition, the HyFi fibers were coated with hybrid nano materials to increase fiber/matrix bonding and enhance filler/matrix interfacial load transfer. Both long-fiber and short-fiber (e.g., chopped) composite specimens were manufactured and subjected to mechanical testing to demonstrate the enhanced properties. Once fully developed, the multiscale composite material will enable reduced weight and volume of structural components, resulting in increased vehicle energy efficiency and increased crashworthiness capabilities. The energy absorbing nature of the material will not only increase crashworthiness and reduce impact intrusion, but it will also reduce noise, vibration, and harshness

Key Publications

1. Beard, S., 2022, “Hierarchical micro/nano reinforced multiscale hybrid composites for vehicle applications,” STTR Final Report Number DOE-AI-21754, 27 March 2022, Advent Innovations, Ltd., Columbia, SC, USA.

References

1. Gardiner, G., 2015, “Multifunctional composites: Past, present, and future,” *Composites World*, 2 November 2015. [Online] Available at: <https://www.compositesworld.com/articles/multifunctional-composites-past-present-and-future> (last accessed 1 March 2023).
2. U.S. Department of Energy–Office of Energy Efficiency and Renewable Energy, 2013, *Workshop Report: Light-Duty Vehicles Technical Requirements and Gaps for Lightweight and Propulsion Materials*, DOE/EE-0868, February 2013, DOE-EERE, VTO, Washington D.C., USA. [Online] Available at: <https://www.energy.gov/eere/vehicles/articles/workshop-reportlight-duty-vehicles-technical-requirements-and-gaps> (last accessed 1 March 2023).

3. U.S. Department of Energy–Office of Energy Efficiency and Renewable Energy, 2013, *Workshop Report: Trucks and Heavy Duty Vehicles Technical Requirements and Gaps for Lightweight and Propulsion Materials*, DOE/EE-0867, February 2013, DOE-EERE, VTO, Washington D.C., USA. [Online] Available at: <https://www.energy.gov/eere/vehicles/articles/workshop-report-trucks-and-heavy-duty-vehicles-technical-requirements-and> (last accessed 1 March 2023).
4. U.S. Department of Energy–Office of Energy Efficiency and Renewable Energy, 2021, . “Vehicle technologies office (webpage),” 16 February 2021, DOE-EERE, VTO, Washington D.C., USA. [Online] Available at: <https://www.energy.gov/eere/vehicles/vehicle-technologies-office>.

Acknowledgments

The authors gratefully acknowledge the financial support from the U.S. Department of Energy–Office of Energy Efficiency & Renewable Energy, under Award Number DE-SC0021754. The authors would also like to thank R. Banerjee, S. Salekin, S. Wilkes-Davis, and M. Flemming of Advent Innovations for their work on the project. Finally, the authors gratefully acknowledge the contributions from M. Khan and the Nanomaterial Research Laboratory at GSU and H. Ahmed and the Mechatronics Lab at GSU. A special thanks is extended to F. Wu for his helpful guidance during this development.

II.4 Joining of Dissimilar Materials

II.4.1 Joining Core Program (JCP)

II.4.1.1 Machine-Learning for Automated Weld Quality Control (Pacific Northwest National Laboratory and Oak Ridge National Laboratory)

Zhilli Feng, Co-Principal Investigator

Oak Ridge National Laboratory
1 Bethel Valley Rd.
Oak Ridge, TN 37831
E-mail: fengz@ornl.gov

Keerti Sahithi Kappagantula, Co-Principal Investigator

Pacific Northwest National Laboratory
908 Battelle Blvd.
Richland, WA 99352
E-mail: keertisahithi.kappagantula@pnnl.gov

Blair Carlson, Co-Principal Investigator

General Motors, LLC
30500 Mound Rd.
Warren, MI 48090
E-mail: blair.carlson@gm.com

Christopher Schooler, DOE Technology Development Manager

U.S. Department of Energy
E-mail: christopher.schooler@ee.doe.gov

Start Date: October 1, 2021 End Date: September 30, 2024
Project Funding (FY 2022): \$1,167,000 DOE share: \$1,167,000 Non-DOE share: \$0

Project Introduction

The use of lightweight material combinations has been highly demanded in manufacturing automotive structures. However, making robust dissimilar material joints of such lightweight materials is still challenging. A significant barrier to achieving high-quality and repeatable joint performance is a deficient understanding of the relationship between the welding process, joint attributes, and joint performance. In this context, welding factors refer to material, equipment, environment, and process parameters, while joint features comprise specific microstructural attributes of the weld—such as, but not limited to, nugget size, heat affected zone topology, intermetallic layer thickness, and sheet thickness reduction. Joint performance is quantified in terms of strength (e.g., tensile shear, coach peel, cross-tension), weld size, and hardness, among other factors. While there have been many attempts to establish this process-structure-property relationship by developing a model derived from the associated physics and first-principles, the complexity of the joining processes compounded by the complex interactions with different materials, in the context of an automotive assembly line environment, has hindered the usefulness of such attempts. The complexity is further exacerbated by the use of different stacking materials, especially comprising dissimilar material combinations. In practice, the common approach has been the laborious process of creating welds, characterizing them, and then physically testing them through the design of experiments. With the emergence of AI methods, an alternative pathway to eliciting the desired process-structure-property relationship at an accelerated pace is to use a data-driven approach by employing ML techniques. This approach is benefited by the availability of large streams of data,

generated through years of research and testing by OEMs, in the form of material, process, environmental, equipment, microstructural, and bulk-scale performance information from multimodal, multiscale sensors making measurements from laboratory-scale to production-scale processes.

In the Phase I efforts that were concluded in FY 2021, the ORNL/PNNL team has demonstrated the effectiveness of ML/AI frameworks in elucidating complex relationships between resistant spot-welding (RSW) process parameters, weld attributes, and joint properties using a subset of data from General Motors (GM), with different ML approaches at the two National Laboratories. In FY 2022, the project team further refined and expanded their respective ML models to analyze additional welds with new weld stack-ups and materials to enhance the ML model predictive capability. ORNL extended its unified deep neural network (DNN) ML training and prediction framework with new data streams of process parameters and PNNL extended its model describing the associations that RSW process parameters have with the weld attributes.

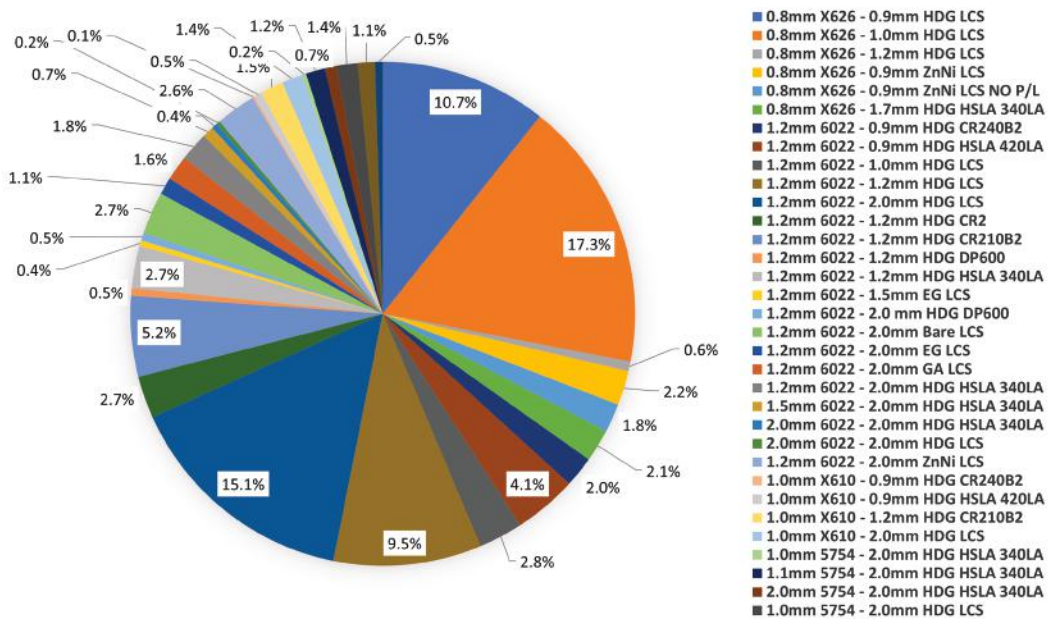
Objectives

Develop and apply a ML/AI-based model framework to analyze inline and post-processed joint data from existing and novel sensor streams to achieve automated weld quality monitoring and control. Specific goals include:

1. The identification of data streams with the greatest impact on joint performance by developing a data-driven understanding of process/structure/property associations.
2. The translation of ML/AI tools from a test case to parallel configurations/materials/processes using generalized learning methodologies.
3. The application of control programs to maintain process parameters within optimal limits for manufacturing joints with desired performance.

Approach

Project objectives will be achieved by demonstrating the application of a suite of ML and AI tools to analyze inline and post-processed joint data for manufacturing assemblies with optimal performance. Joints manufactured by the RSW of aluminum (Al) alloy sheets to different types of steels will be evaluated for applications in automotive manufacturing. Data being assessed, as well as the performance targets, were provided by GM, the industry partner of the project. The large GM data set covers a wide range of welding data associated with Al and steel RSW joints, comprised of material specifications, welding process parameters such as voltage, current, pressure, and duration; microstructural features such as hardness, interface topology and IMC; and bulk performance in terms of peak load, elongation, and energy under different loading/mechanical testing conditions (e.g., coach peel, lap-shear, cross-tension tests). Figure II.4.1.1.1 summarizes the weld data in terms of different materials, thicknesses, and surface treatments. Two different ML approaches are explored to establish associations among process parameters, weld attributes, and weld performance, as shown in Figure II.4.1.1.2. PNNL focused on using explainable, ML-based methods in Approach-I, while ORNL focused on flexible, expandable deep learning methods in Approach-II. This will lead to the construction of a cohesive model from the two different sets of findings from the two national laboratories collated with literature and physics-based model predictions. Finally, we predict the process conditions for making optimized RSW samples per GM's performance metrics using the cohesive set of findings.



Note: HDG = hot-dip galvanized, LCS = low carbon steel, HSLA = high-strength low alloy, CR = cold-rolled, DP = dual phase, LA = low alloy, EG = electrogalvanized, GA = galvanized.

Figure II.4.1.1. A summary of two sheet thick weld stack-ups in terms of materials, thicknesses, and surface treatments. Source: ORNL.

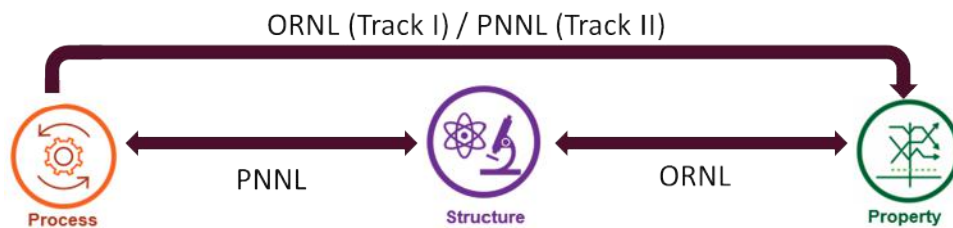


Figure II.4.1.2. Two approaches to establish associations among process parameters, weld attributes, and weld performance. Source: PNNL/ORNL.

Results

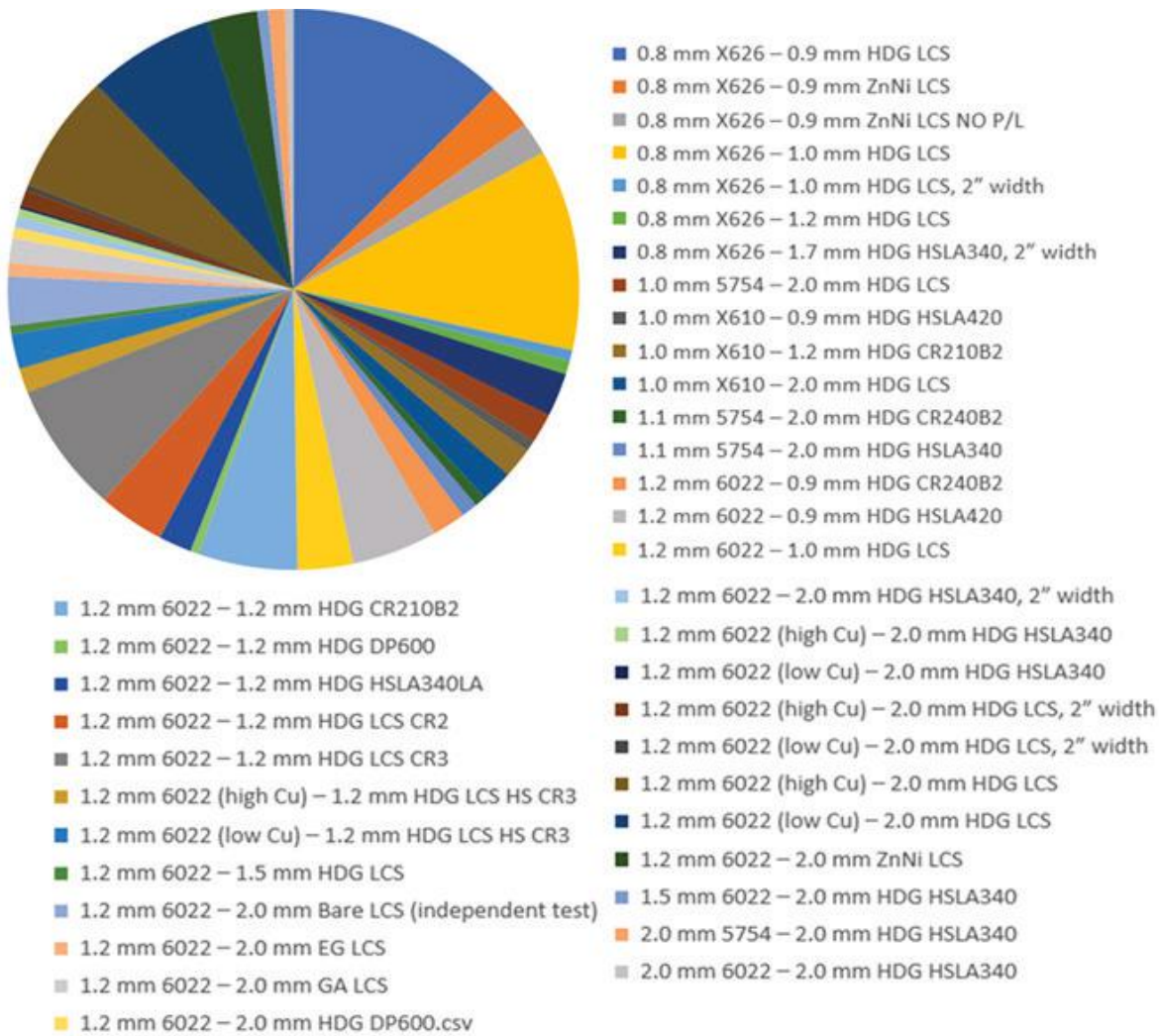
An Expandable ML with Unified Architecture of DNNs for Weld Performance Prediction (ORNL)

The research activities in FY 2022 were organized to achieve the following three major milestones:

- Extend the unified ML training and prediction framework to cover the entire usable 2-layer materials and stack-ups in GM’s data set.
- Testing and confirming the unified ML predictive capability to an independent material stack-up data set (i.e., not included in the training).
- Extend the input data stream to key process input variables into the unified ML training and prediction framework.

Our expendable unified ML model approach utilized one NN design and one training strategy for all material combinations and weld stack-ups. Such a unified strategy can benefit comprehensive learning as the model expanded to cover more weld stack-ups, base materials, welding conditions, etc.

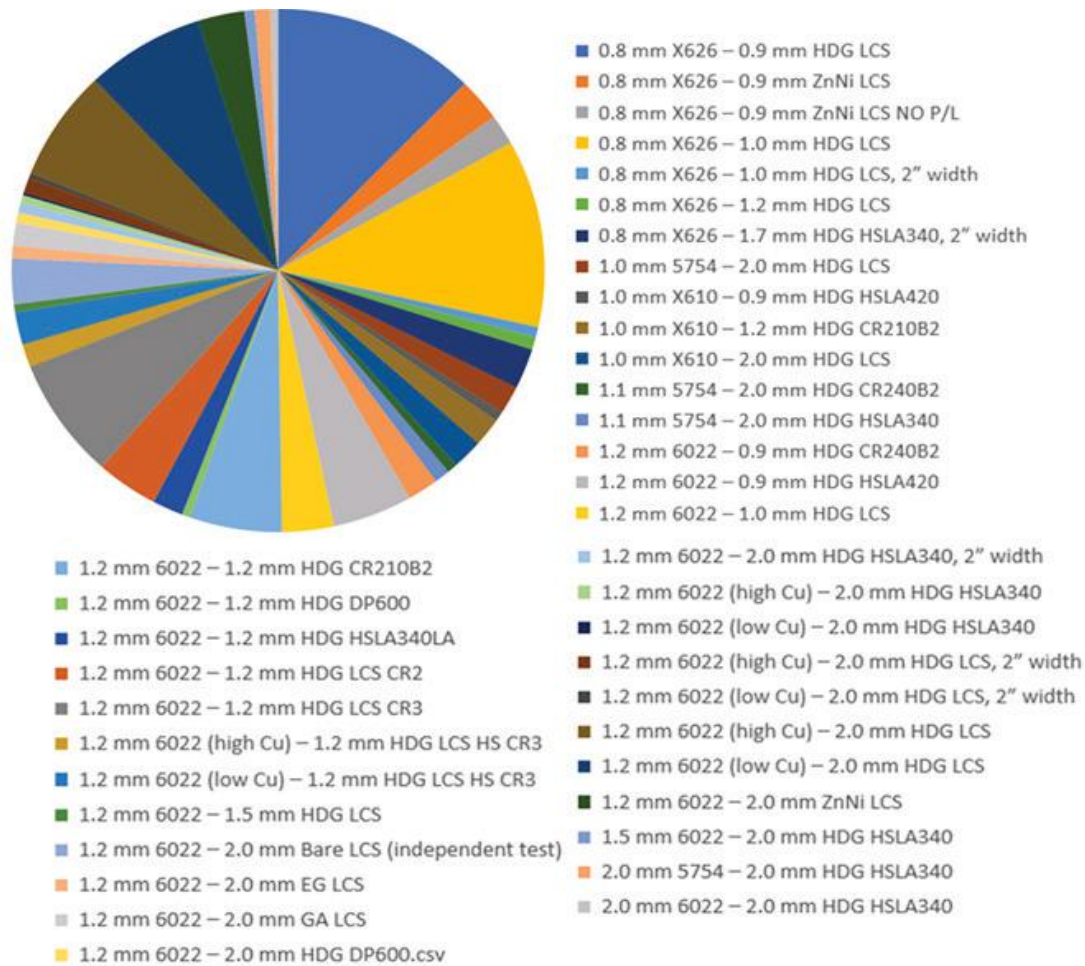
The unified model design strived to (1) improve the wisdom of welding engineering by designing data representation with support of welding physics knowledge and (2) use the ML analysis results to provide insights for RSW of Al and steel alloys. A supervised DNN regression approach was employed to establish the quantitative correlation between weld attributes, base materials, other weld conditions, and joint performance, referring to the model flowchart presented in Figure II.4.1.1.3. The independent data streams were classified into four major categories, which included the key weld quality attributes (e.g., weld button size, weld surface indentation, state of expulsion, weld nugget size, IMC thickness, hardness), material information (e.g., types of steel and Al alloys, surface coating conditions, stack-up conditions), weld coupon dimensions, and other conditions (e.g., post-weld baking, aging). The weld performance properties in the form of coach peel test metrics, such as peak load, extension at break, total energy, were the dependent variables and formed a triple-object DNN model. A summary list for the data distribution of the 40 weld stack-ups with ~99% of the usable Al-steel weld data set was received from GM is shown in Figure II.4.1.1.4.



Completed data analysis

- A total of 40 different material and thickness stackups (~99% of usable 2-layer Al-steel weld dataset from GM, over 800 separate weld conditions)
- An independent test dataset of 1.2 mm 6022 - 1.4 mm bare LCS, 2" width

Figure II.4.1.3. The expendable unified ML model. Source: ORNL.



Completed data analysis

- A total of 40 different material and thickness stackups (~99% of usable 2-layer Al-steel weld dataset from GM, over 800 separate weld conditions)
- An independent test dataset of 1.2 mm 6022 - 1.4 mm bare LCS, 2" width

Figure II.4.1.4. A summary list of data distribution of the 40 weld stack-ups (~99% of usable Al-steel weld data set from GM). Source: ORNL.

Extending ML Model to Cover 90% of GM Data Set (ORNL)

The welds were fabricated mostly from four types of Al alloys (e.g., X626, 6022, X610, 5754) and multiple types of steel alloys (e.g., low carbon steels (LCS), high-strength low alloy (HSLA) steels, dual phase (DP) steels) with various types of surface coatings (e.g., hot-dip galvanizing (HDG), ZnNi, electrogalvanized (EG), galvanized (GA), bare material). For notation, a weld stack-up was defined as a group of welds which were made by the same thickness combination of one Al alloy and one steel alloy. Each weld stack-up comprised tens to hundreds of welds that were fabricated through different process parameters resulting in a wide range of joint quality attributes and performance properties. In GM's experiments, each weld was fabricated with multiple replicates for characterization and testing, generally including seven repeats of a given type of mechanical property test (e.g., coach peel test). A total of 4756 labeled data sets for two-layer Al-steel welds were prepared for ML analysis. The labeled data sets were then randomly categorized into training and validation testing, with the ratio of 8:2 (training to testing). The training process of neural networks was conducted using Pytorch [1].

In FY 2022, the unified ML model has progressively expanded to a total of 40 different stack-ups, which covered ~90% of usable two-layer Al-steel weld data set from GM with over 800 separate weld conditions and ~4700 individual welds, as detailed in Figure II.4.1.1.4 above. A Python code was written and used to automatically standardize and transform the large amount of experimental data provided by GM into usable formats for ML analysis through knowledge-guided quality assurance and control.

The ML performance model is highlighted in Figure II.4.1.1.5(a)-Figure II.4.1.1.5(c), which includes an accuracy assessment of both the training data set and cross-validation data set that were not used in training. The accuracy assessment from the cross-validation provides a less biased estimate of the model skill by looping around the split fold data. Overall, the mean absolute accuracy for peak load, extension at break, and total energy were 89.2%, 85.6%, and 79.0% for the training data set. Our ML model maintained a prediction accuracy of 88.3%, 84.8%, and 77.4% for peak load, extension at break, and total energy, respectively, when applied to the validation testing data set. The above assessment was for a total of 40 different weld stack-ups, covering ~99% of usable two-layer Al-steel weld data set from GM. Furthermore, because of the comprehensive learning from our expendable unified ML training strategy, our ML model performed well for those weld stack-ups that had only a limited amount of training data. The consistent accuracy between training and validation testing suggested that the DNN model was appropriately designed and the quantitative correlations governing the weld quality was established through training over the comprehensive data set of dissimilar Al-steel RSWs.

Figure II.4.1.1.6(a) presents the comparison between the ML predictions and the measured peak loads for the mean value and standard deviation for each weld stack-up. It is evident that the ML predictions captured the mean value and variation behavior of peak load for the 40 different weld stack-ups (~90% of entire usable data). The plot is divided according to different material combinations. The effect of material thickness on the joint strength are evident in both the ML prediction and measurement. Figure II.4.1.1.6(b)-Figure II.4.1.1.6(e) are more detailed comparisons of the ML prediction against measured peak load of individual welds in different stack-ups of different types and thicknesses of Al and steel alloys. Overall, the predictions from our unified DNN model are within the measured data scatter range for all the data covered by our ML model, in terms of both mean values and standard deviations. Nevertheless, there were a few cases whose predictions deviated from the observed values, such as the welds made with adhesives (e.g., D114-2 and D116-2 in stack-ups of 1.0 mm AA X610 and 1.2 mm HDG CR210B2, respectively). This could be related to insufficient learning from the limited available data of welds with adhesives. Given enough training data, it is possible for the unified ML model to learn the underlying mechanism and predict the joint performance for the welds made with specific conditions.

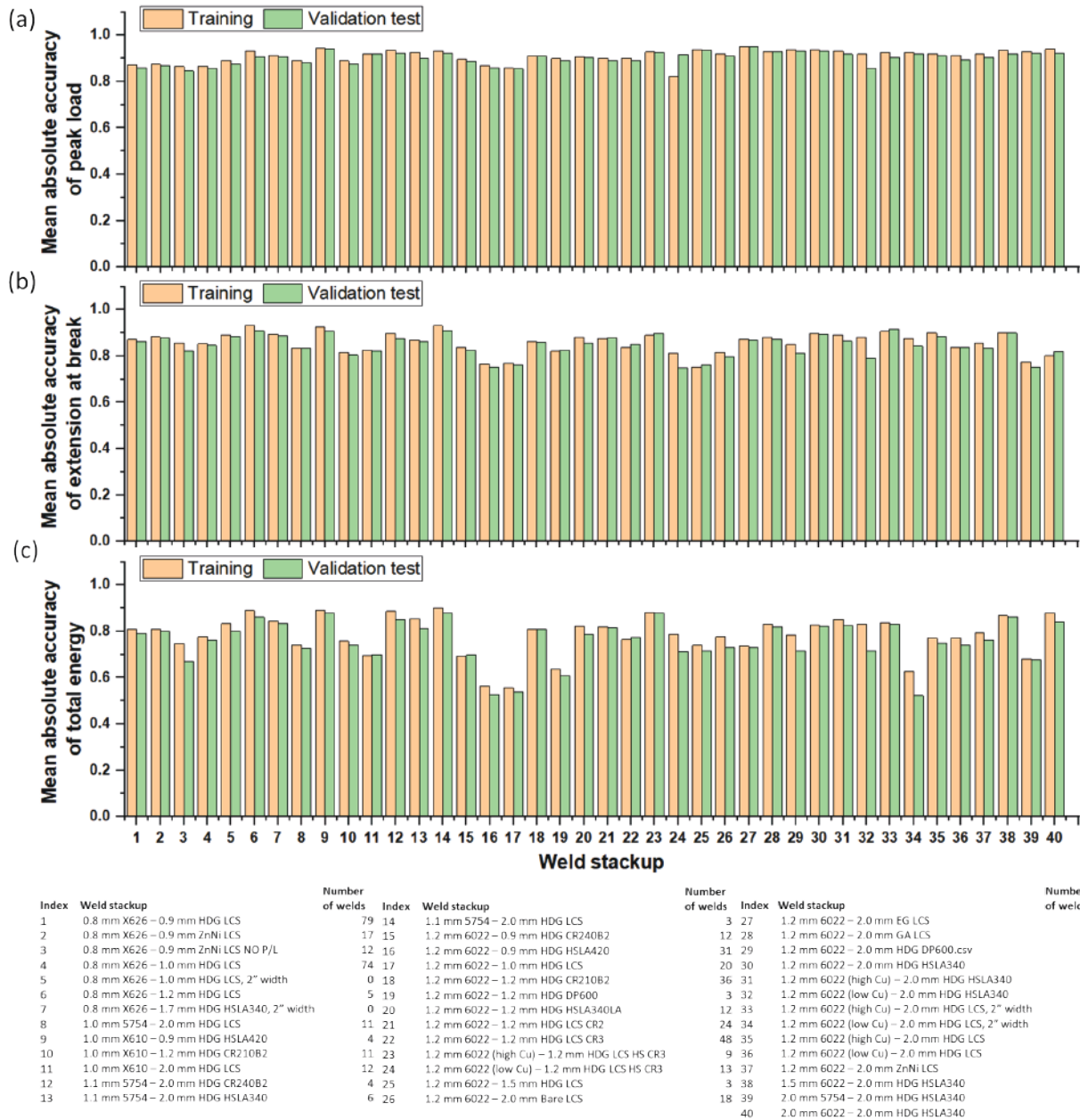


Figure II.4.1.5. Mean absolute accuracy of ML predicted (a) peak load; (b) extension at the break; and (c) total energy for all 40 Al-steel weld stack-ups. Source: ORNL.

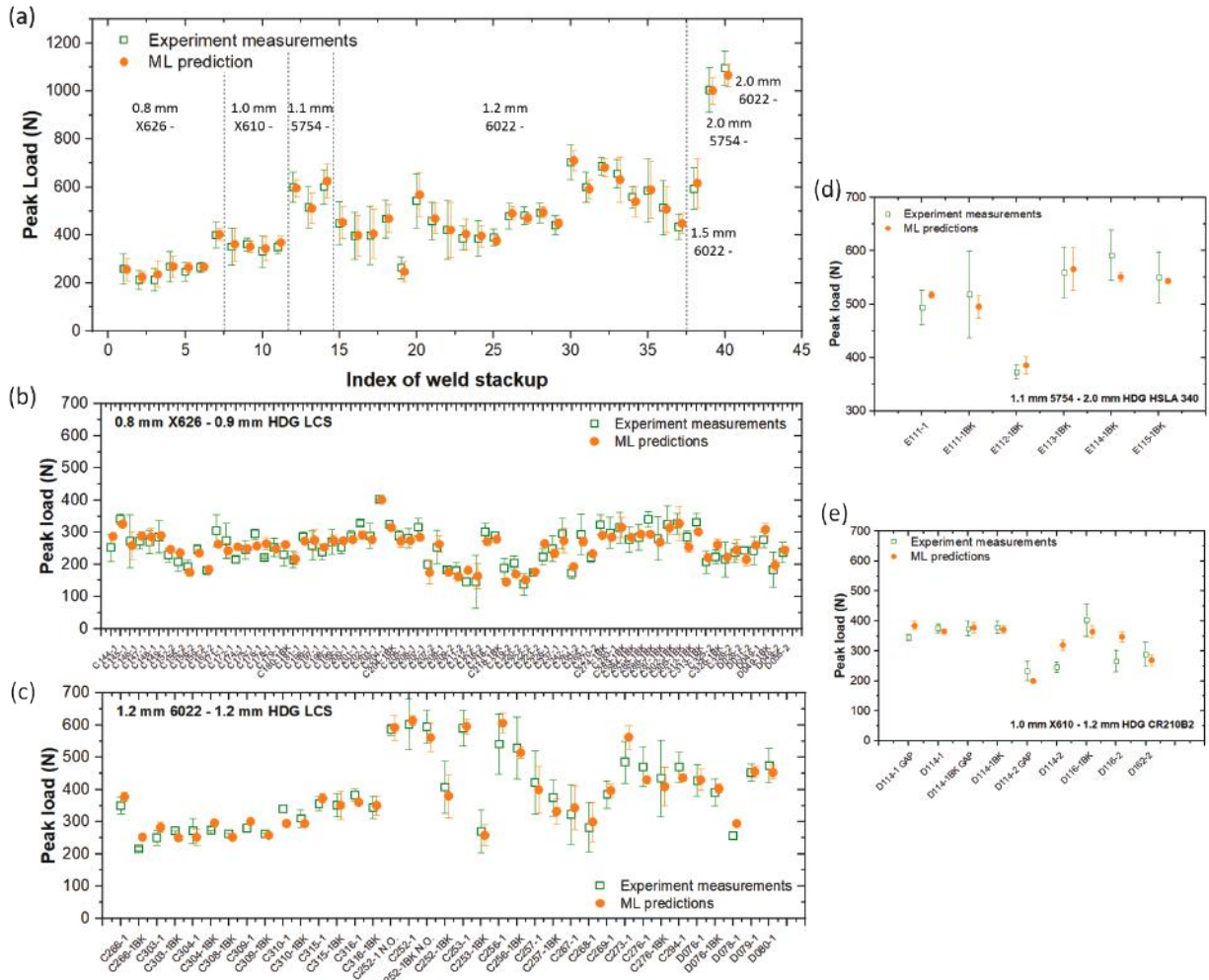


Figure II.4.1.6. A comparison between ML predictions and experimentally measured mean value and standard deviation of peak load for (a) GM’s 40 Al-steel weld stack-ups, as well as for individual welds of different weld stack-ups, including (b) 0.8-mm-thick AA X626 with 0.9-mm-thick HDG LCS, (c) 1.2-mm-thick AA 6022 with 1.2-mm-thick HDG LCS, (d) 1.1-mm-thick AA 5754 with 2.0-mm-thick HDG HSLA 340, and (e) 1.0-mm-thick AA X610 with 1.2-mm-thick HDG CR210B2. Source: ORNL.

Performance of ML Model Against an Independent Data Set (ORNL)

The performance of the unified ML modeling framework was further tested with an additional data set of ‘unseen or independent’ welds. These independent welds were from material/stack-up combinations that were never used, or unseen, in the development of the ML model. This would provide an unbiased assessment for the expandability of our ML model—to predict the weld properties of future material and stack-up combinations that were not part of the ML training.

For this purpose, GM provided the results of 1.2-mm-thick AA6022 and 1.4-mm-thick bare LCS with 2-in. width coupons. Compared to the data sets used in building our ML model, this stack-up is a challenging case—there was only one weld stack-up (e.g., 1.2-mm-thick 6022 and 2.0-mm-thick bare LCS with 1.5-in. width coupon) by the same material combination. In addition, the 2-in. width coupon accounted for only about 5% of the whole training data set (e.g., the majority of weld stack-ups have 1.5-in. coupon widths). Figure II.4.1.1.7 shows the comparison of the ML predictions of the peak load and the measured values for the independent test welds. Our ML model predicted the peak load with a greater than 80% accuracy for over 90% of the

independent testing welds. Overall, the unified ML framework exhibited its strong predictive and generalization capability when exposed to an unseen weld stack-up.

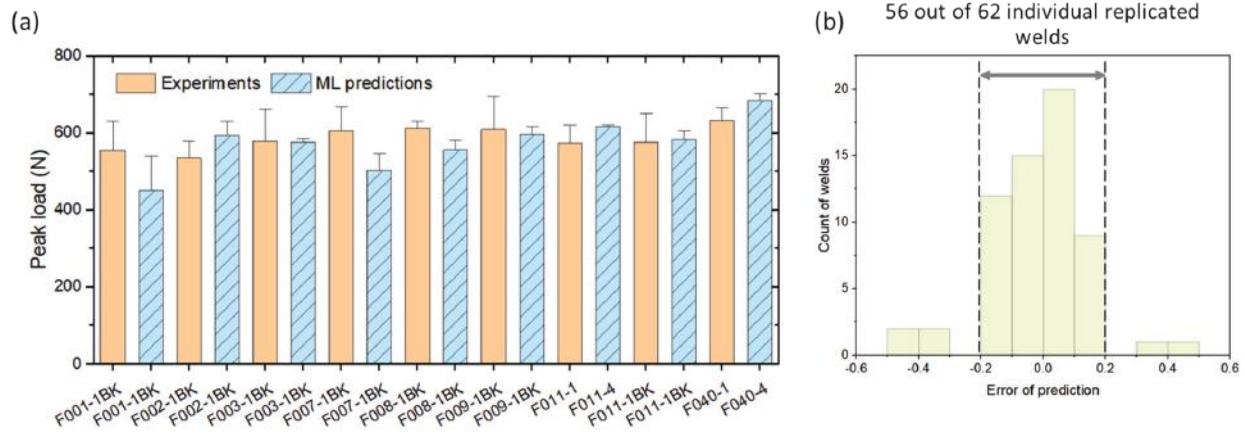


Figure II.4.1.7. ML model predicted the peak load of ~ 90% independent test welds on the 1.2-mm-thick AA6022 and 1.4-mm-thick bare LCS with a more than 80% accuracy. Source: ORNL.

Rank of Importance (ORNL)

With the unified ML model covering 90% of the usable data set with sufficient accuracy, it is now possible to use the ML model to identify and rank the relative importance of the weld attributes, base materials, and other conditions on the performance of Al-steel RSW welds. The results are presented in Figure II.4.1.1.8—the factor of importance for the independent predictors are arranged in decreasing order. The button sizes were identified to have the highest impact on joint performance, followed by base material thickness, IMC thickness, hardness, indentation, and expulsion, as determined from the comprehensive ML.

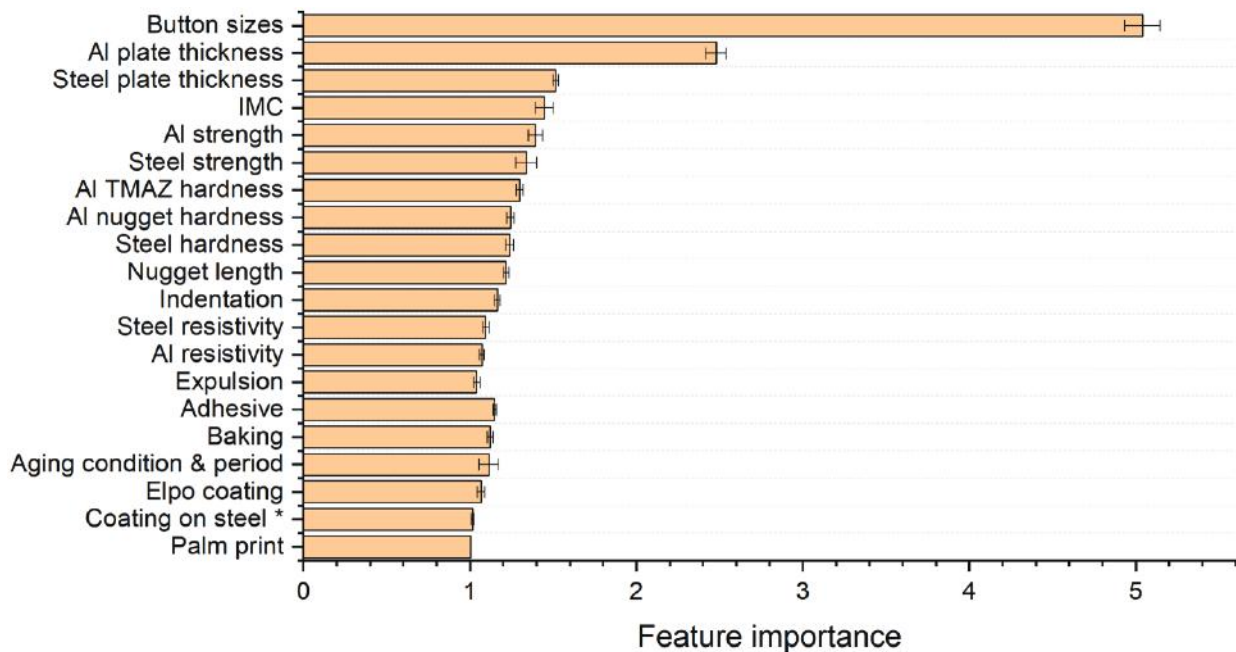


Figure II.4.1.8. Importance scores of the independent variables determined based on comprehensive ML analysis of 40 weld stack-ups. Source: ORNL.

Determination of Weld Conditions to Achieve Performance Target Through Unified ML Model (ORNL)

Our unified ML model was applied to determine the weld attributes meeting a specific target performance for a certain weld stack-up, as well as to search for possible optimal performance. This was done by utilizing an optimization scheme in connection with the fully trained ML framework, as indicated in Figure II.4.1.1.9(a). The weld attribute variables are searched within ranges in the training data sets and optimized in a way to minimize the difference between the ML predictions and targeted joint performances. The optimization algorithm of stochastic gradient descent with adaptive moments was adopted for its convergence capability, computational cost, and memory requirement in searching the high-dimensional weld variable spaces. Figure II.4.1.1.9(b1-b2) presents the identified ranges of weld attributes that are necessary to meet the target performance peak load ≥ 750.0 N and total energy ≥ 14.5 J, for two weld stack-ups: (b1) 1.2-mm-thick AA6022 and 2.0-mm-thick HDG LCS and (b2) 1.1-mm-thick AA6022 and 2.0 mm HDG LCS. Please note that the second stack-up was a material combination not yet tested experimentally. The ML results indicate that thicker sheet welds, a larger button and shallower indentation is required to achieve the high peak load and total energy. None or slight expulsion is always required to have high joint performance. This example demonstrates the feasibility to apply our unified ML framework to guide RSW development with ‘untested’ materials, thickness, and other conditions.

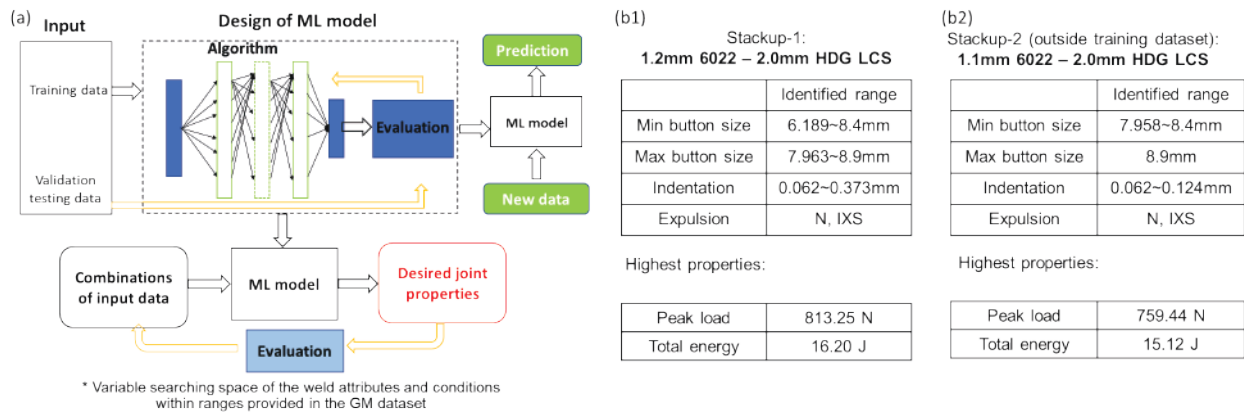


Figure II.4.1.9. (a) Flowchart showing the application of the fully trained ML model for weld design to identify weld attributes/conditions for meeting joint target performance. (b1) and (b2) Identification of a set of weld variables to achieve the performance target: peak load ≥ 750.0 N and total energy ≥ 14.5 J for welds made by 1.2-mm-thick 6022 with 2.0-mm-thick HDG LCS and 1.1-mm-thick 6022 with 2.0-mm-thick HDG LCS (e.g., a material combination not yet tested experimentally). Source: ORNL.

Interpretable ML Models for Process-Structure-Performance Relationships (PNNL)

PNNL developed process-structure-property relationships for the AA6022/LCS and X626/LCS RSW joints in FY 2022. Additionally, PNNL also adopted the process-performance model developed for AA6022/LCS in FY 2021 for RSW stack-ups comprising of AA6022 as one plate (with any thickness) and the second plate with different types of steels (with any thickness) to predict the process parameters required to manufacture RSW joints with desirable weld performance. The terminology used for the different stack-ups in this effort is listed in Table II.4.1.1.1.

Random Forest Regression Approach for Weld Process-Structure-Performance Relationship (PNNL)

In FY 2022, we developed a methodology for associating structure data, such as hardness at the interface and intermetallic thickness measured on the cross-sections of the welds, with coach peel performance metrics (such as peak load, load at failure, etc.). Principal components comprising the five dependent coach peel property variables (e.g., peak load, total energy, extension at break, extension at peak load, energy up to peak load) were constructed as shown in Figure II.4.1.1.10. Principal component analysis performs well in this case and explains nearly 90% of the variation in the coach peel performance metrics owing to the correlations between the variables. It is noted that high values of the principal component correspond to better weld performance. Following this, the k-means clustering method was used to divide the principal components of the coach peel

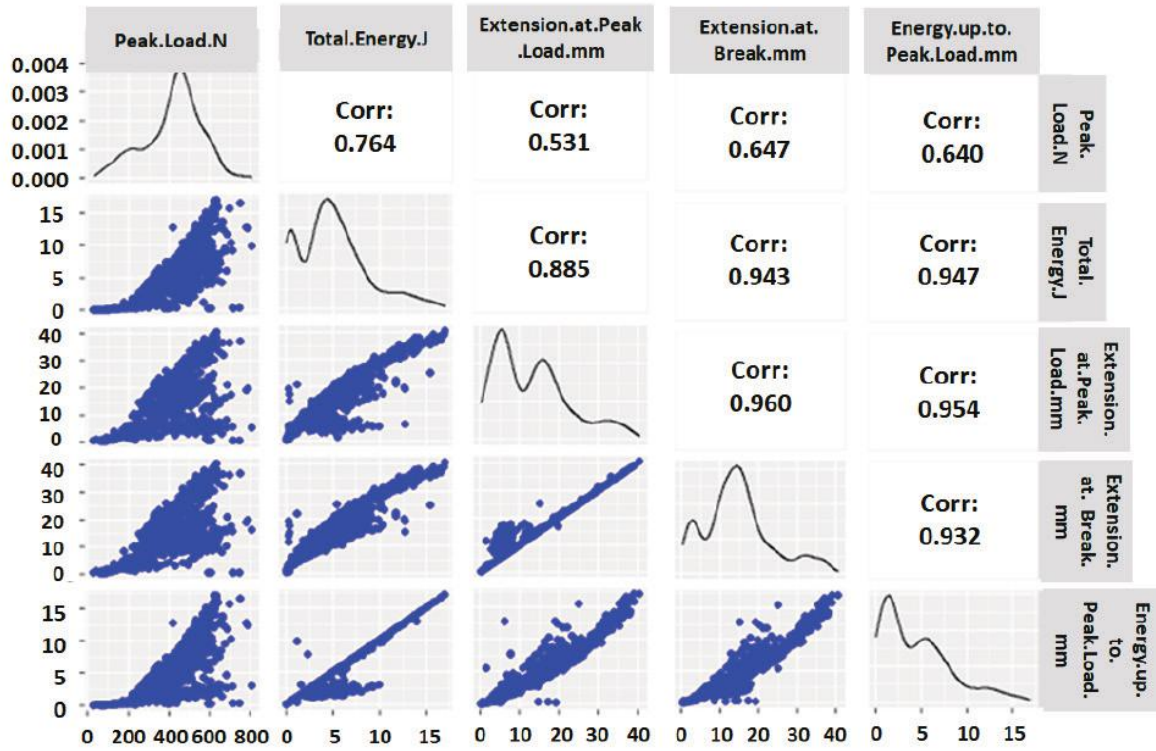
performance metrics into two clusters—one corresponding to values higher than a threshold value for the joint performance and one lower than the threshold. For this exercise, we used average performance as the threshold; but in operation, this threshold can be selected by the users preferentially. The result was two groups of samples, one with high coach peel performance metrics and one with low coach peel performance metrics.

Table II.4.1.1.1. Stack-up Nomenclature by PNNL Used with the Corresponding Materials (and Thicknesses) for Model Building

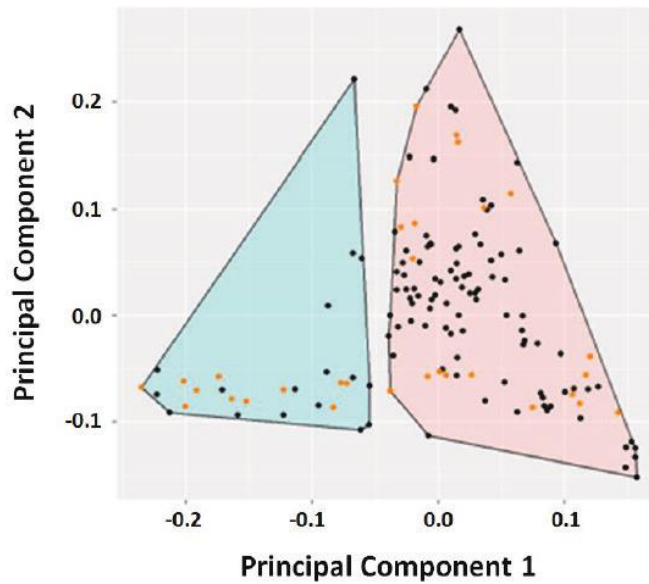
Stack-up Name	Material 1	Material 2
Stack-up 1	1.2-mm-thick AA6022	1.0-mm-thick HDG LCS
Stack-up 2A	0.8-mm-thick X626	1.0-mm-thick HDG LCS
Stack-up 2B	1.2-mm-thick AA6022	1.2-mm-thick HDG LCS
		2.0-mm-thick HDG LCS
Stack-up 2C	AA6022	CR2
		DP600
		HSLA 340LA
		HSLA 420LA

The weld structure data that was considered in this effort was the intermetallic hardness and intermetallic thickness. GM collected this data specific to certain locations at the interface of the two plates in the RSW joint. As such, the structure data is in the form of ‘curves’ along the RSW weld width or other relevant dimensions. Initially, hardness and intermetallic thickness curves were developed for all of the AA6022/LCS and X626/LCS joints using the GM structural data database. Subsequently, ‘ideal’ curves with desirable microstructure attributes were determined using graphical methods, as well as smoothing operations using the data from the ‘optimal’ samples, as determined from the k-means clustering method. For reference, the representative smoothed hardness curve is presented in Figure II.4.1.1.11.

Following this, the hardness and intermetallic thickness curves of the RSW joints were compared to the ‘ideal’ curve developed to identify which of the RSW joints had structural features that were ‘optimal.’ Five similarity metrics were used to make the assessments—namely, cosine similarity, Frechet distance, dynamic time warping, squared distance, and Hausdorff distance, each of which provided a similarity score. Based on the similarity analysis, RSW joints were classified as optimal and similar, non-optimal and similar, optimal and dissimilar, and non-optimal and dissimilar. Currently, efforts are underway to understand the distribution of process parameters across these four categories and identify any emerging trends to inform our fundamental understanding into the RSW process design for future experiments.



(a)



(b)

Figure II.4.1.10. Principal components of the five coach peel performance metrics (peak load, total energy, extension at break, extension at peak load, energy up to peak load) constructed for (a) AA6022/LCS and X626/LCS RSW joints, and (b) classification of RSW joints as optimal and non-optimal using the k-means clustering method. Source: PNNL.

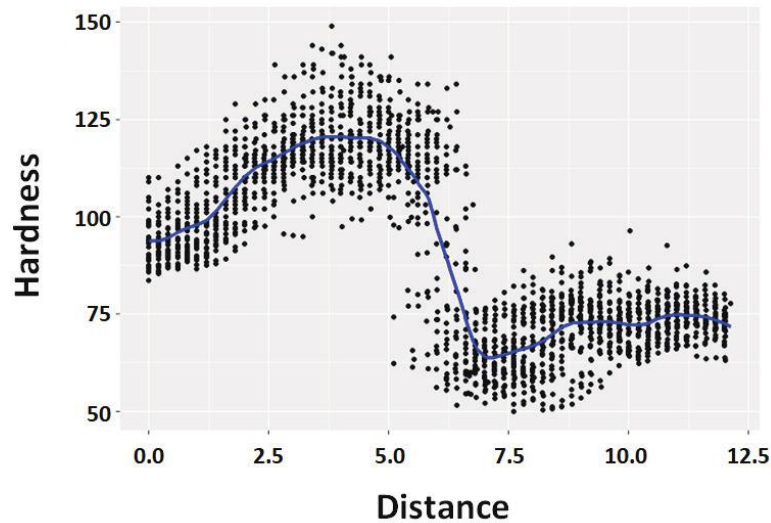
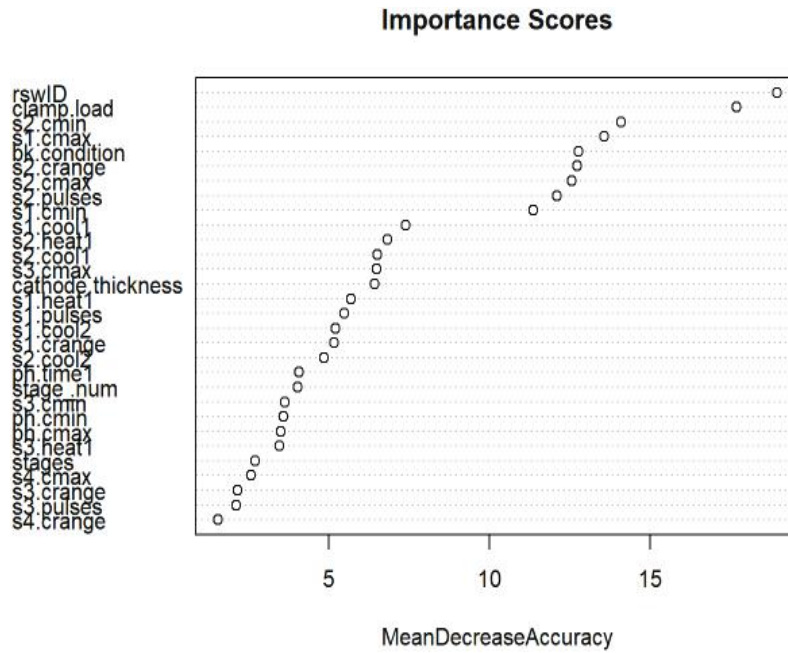


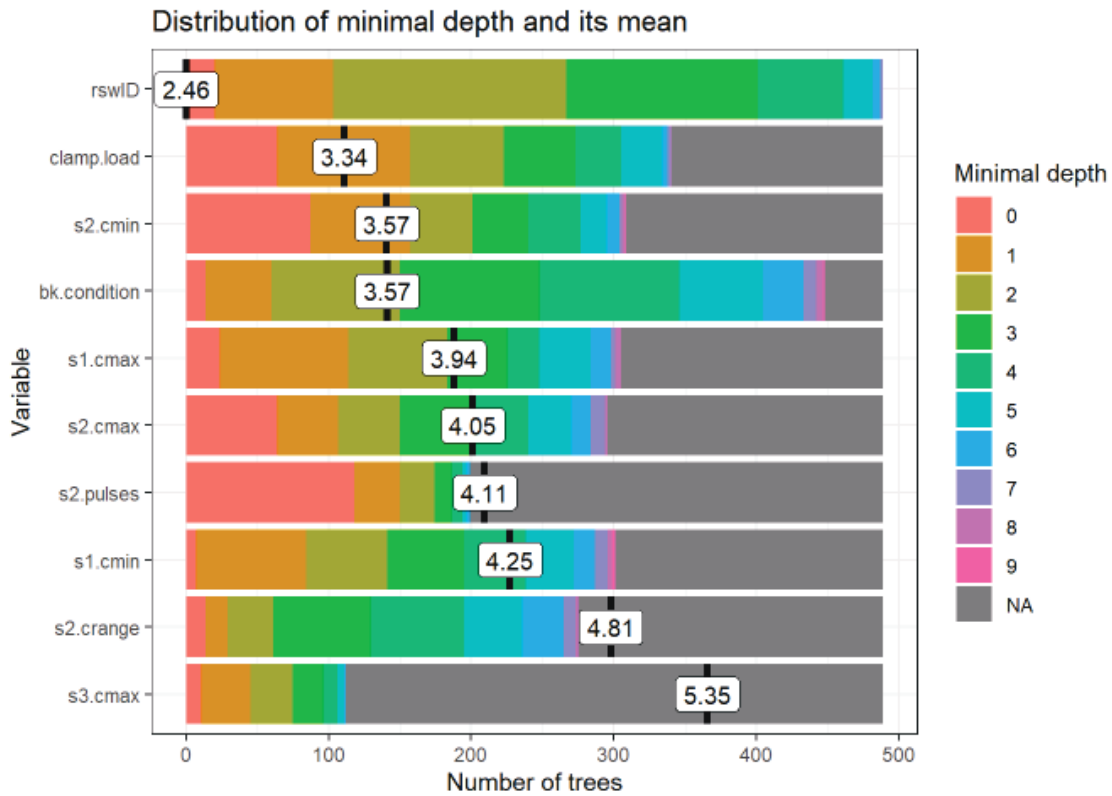
Figure II.4.1.11. The smoothened ‘ideal’ hardness curve demonstrating the ideal hardness distribution across the width of the RSW joints developed for comparison of RSW weld structure metrics. Source: PNNL.

Additionally, the average values of the weld structures, such as average hardness and average intermetallic thickness, across the measurement dimension corresponding to each process parameter set was determined from the GM data. This data column was also introduced into the ‘cause’ list (e.g., x-parameters), along with the process parameters, and their relationship with the principal components of the ‘effect’ parameters (e.g., coach peel performance metrics, described previously) was modeled using the Random Forest methodology developed in FY 2021. A series of experiments were conducted by constructing 500 trees accommodating 41 independent and correlated process variables, as well as the weld structure parameters—hardness and intermetallic thickness, referred to as predictors (43 in total), using the regression type of Random Forest where the number of variables at each split was 13. The data from GM was split into 60/40 training/testing portions. Subsequently, the model predicting the coach peel performance metrics for the AA6022/LCS and X626/LCS joints was developed and the importance of the predictors, as well as the distribution of variable minimal depth was determined. The Random Forest model had an accuracy of 73% on the data provided. Results are shown in Figure II.4.1.1.12 where process conditions such as clamp load, stage 2 variables such as minimum current and number of pulses, and baking condition can be seen playing a significant role in predicting coach peel performance metrics.

Additionally, a Random Forest model was developed to associate the process conditions used to manufacture AA6022/steel RSW joints, with their corresponding coach peel performance metrics. The methods used to develop the Random Forest models for Stack-ups 2A and 2B were also applied for Stack-up 2C. Here, the principal components for the five coach peel performance metrics (e.g., peak load, total energy, energy up to peak load, extension at peak load, and extension at break) were constructed and are shown in Figure II.4.1.1.13. The principal component explains ~80% of the variation in all five variables. One key difference in this Random Forest model development was that cathode-facing material was identified as a variable named ‘Material 2’ in the Stack-up 2C model. The model accuracy was seen to be ~81%, thus meeting the project milestone. It was interesting to note that the second material in the joint, corresponding to the different steels used, was seen to be the second most important variable in predicting joint performance. However, apart from that, the other process conditions of importance were still seen to be similar to what was observed in the Random Forest models for the AA6022/LCS and AAX626/LCS models.

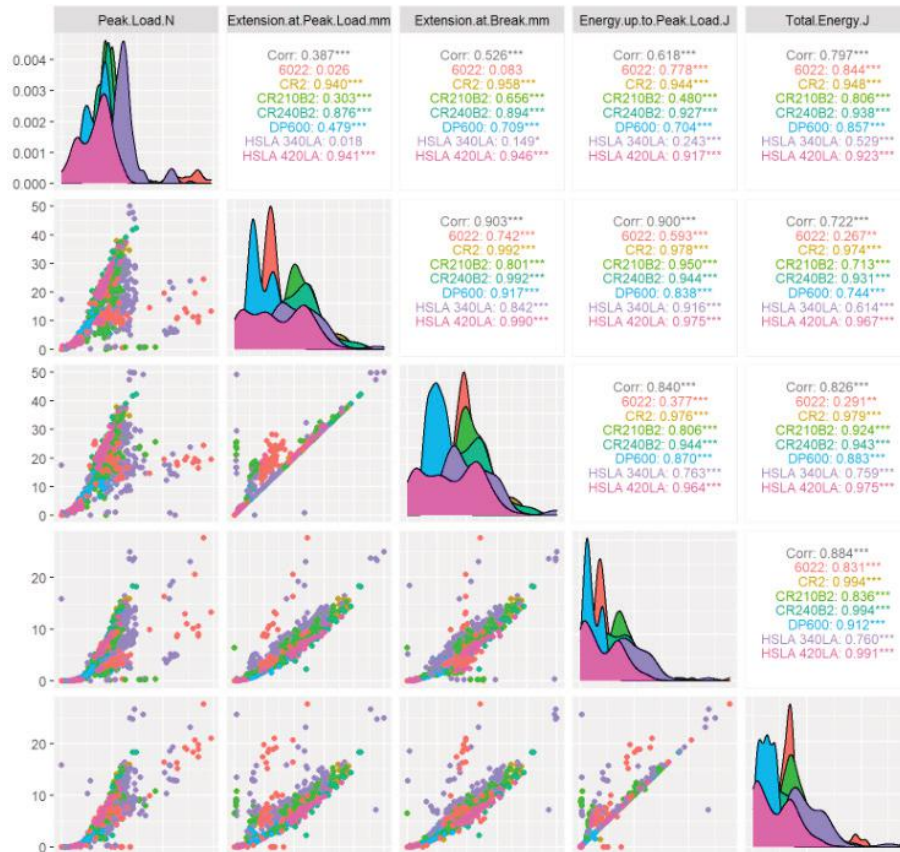


(a)

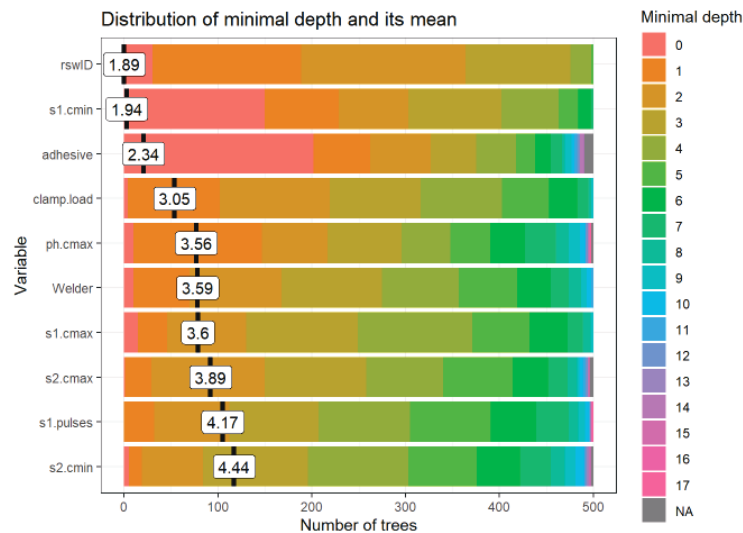


(b)

Figure II.4.1.12. The smoothed ‘ideal’ hardness curve demonstrating the ideal hardness distribution across the width of the RSW joints developed for comparison of RSW weld structure metrics. Source: PNNL.



(a)



(b)

Figure II.4.1.13. (a) Principal components of the five coach peel performance metrics (e.g., peak load, extension at peak load, extension at break, energy up to peak load, total energy) constructed for Stack-up 2C RSW joints, and (b) the distribution of variable minimal depth of the variables from the Random Forest model. Source: PNNL.

Deep Neural Networks Approach for High-Fidelity Process-Structure-Property Predictions (PNNL)

The accuracy of predictions of the Random Forest model was lower than the targeted 80% accuracy for the completion of the Go/No-go decision point for FY 2022; however, we explored other models that could be used for predicting coach peel performance metrics at a higher accuracy. Subsequently, associations between process-microstructure-property data streams were developed using deep learning models, namely ResNet50, in the fourth quarter of FY 2022. The association problem was recast as a classification problem to accommodate the small number of experiments available for the AA6022/LCS and X626/LCS RSW joint data sets. The ResNet50 architecture was parameterized and trained to classify process conditions and cross-sectional images of the RSW joints into two categories—one where the coach peel peak load was higher than the average of the data set and one where the peak load was over. It was interesting to note that the training and testing accuracy for predicting peak load using the new model was around 81% and 80%, respectively. However, as expected interpretability for this model is minimal. A lot of this understanding, on the other hand, was garnered through the interpretable Random Forest model developed previously.

Conclusions

Two classes of an ML modeling approach have been developed and used to investigate the relationships between the process parameter, weld attributes, and joint performances. ORNL focused on the development of “Expandable ML with Unified Deep Neural Networks Architecture” for weld performance prediction. PNNL focused on the development of “Interpretable Random Forest ML Models for Process-Structure-Performance Relationships.” The key findings and conclusions were:

3. Both the Random Forest and DNN models are capable of predicting the relationships between process parameter/weld attribute and performance with over 80% accuracy.
4. The Unified DNN ML model:
 - A. Capable to predict the joint performance based on the weld attributes, material stack-ups, and other welding conditions for over 40 unique material combinations and weld stack-ups representing ~90% of two-layer usable Al-steel RSW data set from GM.
 - B. Exhibited strong prediction and generalization capability when exposed to unseen independent weld stack-ups, with over 80% accuracy for ~ 90% of the test welds.
 - C. Identified the weld attributes, including button sizes, IMC thickness, hardness, material indentation, and expulsion, to have important effects on joint performance, from the comprehensive ML analysis of 40 Al-steel weld stack-ups.
 - D. Feasible to identify the weld variable ranges to achieve the specific joint performance target for Al-steel RSW joints.
5. The Random Forest model:
 - A. Provided an optimal balance between flexibility and interpretability to model the RSW process parameter and performance relationships in order to identify the parameters of interest.
 - B. Existing Random Forest model with the previously developed parameters could be adopted with ease for newer Stack-ups. Only the addition of weld structure data led to a decrease in accuracy, but still provided the advantage of interpretability.
 - C. It was possible to predict the process conditions necessary to be used in order to achieve the highest peak load and highest total energy in the RSW joints for AA6022/LCS two sheet thick stack-ups using the ML architecture developed in this project.

Key Publications

1. Feng, Z., D. Wang, J. Chen, W. Zhang, H. Ghassemi-Armaki, and B. Carlson, 2022, “Methods of determining weld quality and properties in resistance spot-welding process,” Invention Disclosure #202205121, Oak Ridge National Laboratory, Oak Ridge, TN, USA.

2. Zhang, W., D. Wang, J. Chen, H. Ghassemi-Armaki, B. Carlson, and Z. Feng, 2022, “Machine-learning modeling for relationship between joint attributes and weld performance in resistance spot-welding,” *Advances in Welding & Additive Manufacturing Research Conference*, 13–16 June 2022, Virtual.
3. Zhang, W., D. Wang, J. Chen, H. Ghassemi-Armaki, B. Carlson, and Z. Feng, 2023, “A new perspective of post-weld baking effect on Al-steel resistance spot weld properties through machine-learning and finite element modeling,” *J. Manuf. Mater. Process.*, Vol. 7, No. 1, Art. 6.
<https://doi.org/10.3390/jmmp7010006>.
4. Fagan, D., M. Obiri, A. Ojeda, K. Kappagantula, B. Carlson, and H. Ghassemi-Armaki, “Method for Identifying Resistance Spot-Welding Process Parameters Responsible for Generating Desirable Weld Features Using Weld Performance Metrics,” Invention Disclosure #32798-E, Pacific Northwest National Laboratory, Richland, WA, USA.

References

1. Paszke, A., S. Gross, F. Massa, A. Lerer, J. Bradbury, G. Chanan, T. Killeen, Z. Lin, N. Gimeshain, L. Antiga, A. Desmaison, A. Köpf, E. Z. Yang, Z. DeVito, M. Raison, A. Tejani, S. Chilamkurthy, B. Steiner, L. Fang, J. Bai, and S. Chintala, 2019, “Pytorch: An imperative style, high-performance deep learning library,” *Adv. Neural Inf. Process. Syst.*, Vol. 32, pp. 8026–8037.
<https://doi.org/10.48550/arXiv.1912.01703>.

II.4.1.2 Extending High-Rate Riveting to New Material Pairs (Pacific Northwest National Laboratory)

Kevin L. Simmons, Co-Principal Investigator

Pacific Northwest National Laboratory
902 Battelle Blvd.
Richland, WA 99352
E-mail: kl.simmons@pnnl.gov

Amit Naskar, Co-Principal Investigator

Oak Ridge National Laboratory
1 Bethel Valley Rd.
Oak Ridge, TN 37831
E-mail: naskarak@ornl.gov

Christopher Schooler, DOE Technology Development Manager

U.S. Department of Energy
E-mail: christopher.schooler@ee.doe.gov

Start Date: August 16, 2020

End Date: September 30, 2023

Project Funding (FY 2022): \$683,000

DOE share: \$683,000

Non-DOE share: \$0

Project Introduction

PNNL, ORNL, and ANL are teaming together to develop a combination of adhesive-based bonding and high-velocity mechanical joining methods for multimaterial systems to reduce vehicle component mass.

Objectives

This project aims to develop a hybrid adhesive-mechanical joining method to efficiently join two and three thickness configurations of multimaterials that exceed lap-shear strength by 50% and cross-tension strength by 30% beyond what is possible with adhesive bonding alone and demonstrate its effectiveness as a robust approach that has improved joint integrity. The project will combine state-of-the-art riveting techniques with adhesive bonding and focus on adhesive curing, thermal stability, and wettability issues both by experimental and modeling to enhance the performance of hybrid and non-hybrid joints. We will develop and demonstrate an adhesively bonded multimaterial joint that has high-velocity-formed rivets and high-friction rivets that will increase the performance and reliability of the joined dissimilar material sets.

Approach

The approach will investigate adhesively bonded and non-bonded joints with 2T and 3T material sets of high-strength steel (DP590), Al alloys (5052 and 6061), Al castings (<12 mm), and polyphthalamide (PPA), polyamide 66 (PA66) CFCs from sheets up to 3 mm in material thickness. These systems represent different combinations that could be used in different vehicle joints. The project will evaluate cured and uncured adhesively bonded joints to determine the effect of the riveting process on the adhesive. Modeling simulations will be performed to optimize rivet design and process parameters. The joints will be mechanically tested and characterized to develop both a physical and chemical understanding of bond strengths and external effects.

Results

Surface-Treatment for Adhesive Bonding (PNNL)

High-power plasma surface-treatment conditions were optimized for lap-shear performance of adhesively bonded and hybrid joints. Treatment parameters included plasma tip-to-surface distance (d), tip speed (v), and step-over distance. After plasma-treating, the rectangular samples were immediately bonded using epoxy-based YL230 adhesive produced by the L&L Company. As shown in Figure II.4.1.2.1(a), lap-shear strength of

Al5052/CFRP-PA66 joints (adhesive bond only) improved by up to 24% relative to the untreated material combination. Fracture morphology of the sheared joints was investigated after failure using a Keyence metrology microscope. For plasma-treating parameters $d=3$ mm and $v=30$ mm/s, damage occurred through the CFRP-PA66 substrate via tortuous crack growth initiated at the adhesive interface, as shown in Figure II.4.1.2.1(b). By reducing the speed of PT to 30 mm/s, the plasma effect coupled with a heating effect exposed fibers at the CFRP surface and further improved the bonding behavior. The damage progression throughout CFRP-PA66 thickness dissipated energy as matrix and fibers fractured leading to the maximum observed improvement of 24% in lap-shear strength. Further reducing the plasma-treating speed to $v=10$ mm/s caused the PA66 matrix to degrade due to high temperatures and damaged surface chemistry advantageous to bonding, resulting in only 19.7% improvement in lap-shear strength.

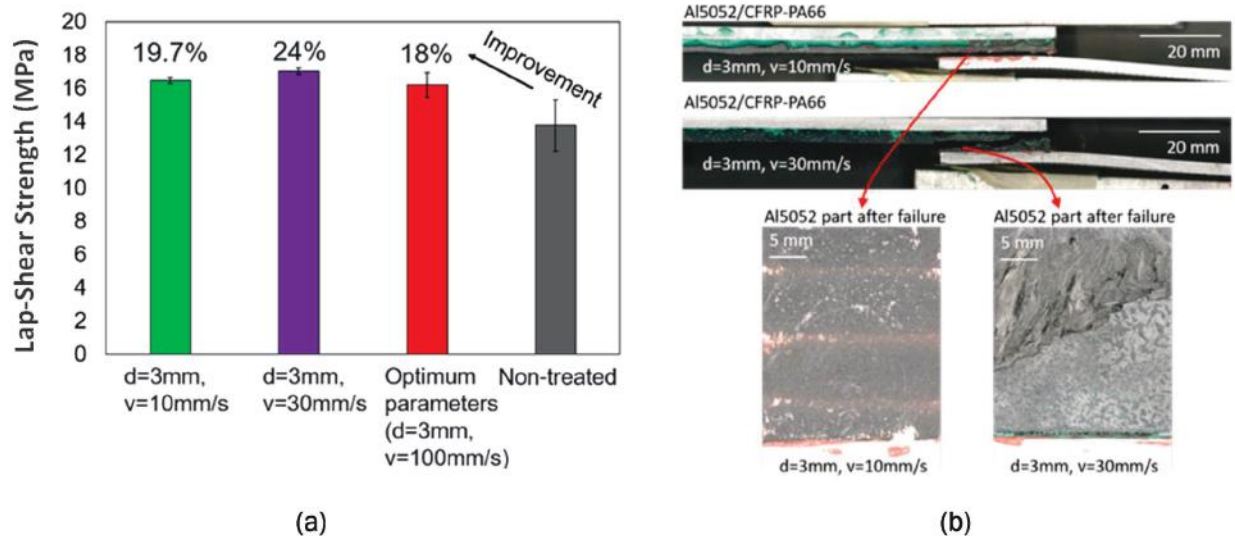


Figure II.4.1.14. (a) Lap-shear strength of Al5052/CFRP-PA66 combination with various PT parameters on CFRP-PA66. (b) Fracture morphology after the lap-shear failure showed residual black CFRP PA66 was evident on all failure surfaces. Source: PNNL.

Surface modifications of CFRP-PA66 using a CO₂ laser were also investigated. Several laser parameters were studied—including the power, frequency, speed, and spot spacing. The surface roughness of each surface modification was measured by profilometry. Surface roughness is plotted as a function of laser power intensity and spot spacing treatment parameters in Figure II.4.1.2.2(a). Surface roughness increased as the power intensity increased and spot spacing decreased. As observed in Figure II.4.1.2.2(b), a microscale computational model using real surface roughness data was established to study the effect of adhesive/adherend interfacial behavior on the adhesive bonding of different materials. It was found that the shear behavior of adhesively bonded metals generally increased and then saturated when the ratio of the interfacial strength to adhesive strength increased. The model will be used to inform laser treatment strategy to rapidly optimize lap-shear strength performance in adhesively bonded joints. A collaborative effort with GM was initiated to develop laser ablation strategies for AA380 substrates. In this arrangement, GM treated substrates under various ablation conditions and PNNL characterized the resulting surface chemistry and morphology by XRD, profilometry, Fourier-transform infrared, scanning electron microscopy-EDS, and XPS. An analysis showed significant removal of Si, Fe, Cu, and C from the surfaces, as well as an increase in surface roughness (Ra) from Ra = 1.74 μ m to Ra = 4.31 μ m. Al grains of 2–10 μ m were changed to a wave shape due to the Al melting by the laser heat, as observed in Figure II.4.1.2.2(c1-c2). XPS showed a significant Al oxidation and decrease in other alloy elements. Increased laser power caused a gradual change from Al(OH)₃ to Al₂O₃ to Al₂O₃·3H₂O. The remaining Si and C residues changed to SiO₂ and oxidized carbons (C-O/C(=O)-O/CO₃²⁻) as shown in Figure II.4.1.2.2(c3).

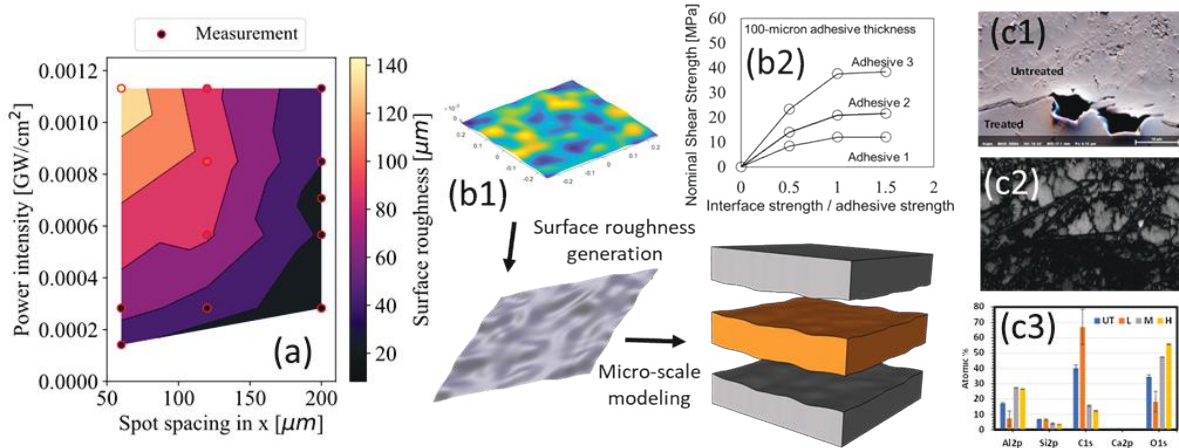


Figure II.4.1.15. (a) Average surface roughness vs. laser treatment parameters. (b1) Microscale computation with the consideration of real material surface morphology. (b2) Nominal shear strength vs. interfacial strength/adhesive strength for an adhesively bonded metal joint. (c1) SEM of AA380. (c2) Al grains of laser-ablated AA380. (c3) Atomic percentage of surfaces treated with different laser powers from GM.

Source: PNNL.

Novel Adhesive Development (ORNL)

Because of growing environmental and health concerns, improving the sustainability of adhesives and production processes have inspired efforts to incorporate renewables into petroleum-based products. A thermoplastic acrylonitrile-butadiene-lignin (ABL)-based multiphase polymer developed at ORNL [1-2] was tested for adhesive performance. This work investigated the effect of acrylonitrile content in nitrile rubber fraction and lignin loading (e.g., 40 wt.% - 80 wt.%) on the adhesion properties. Among them, the adhesive with 60% lignin concentration presented the highest lap-shear strength (LSS) and was selected for further study. The composition was further modified by the addition of an adhesive matrix thickening agent (TA) during the shear-mixing process to adjust viscosity. The goal was to improve the dispersion of lignin—and simultaneously modify the surface energy of the adhesives. With the optimal loading of the TA, as shown in Figure II.4.1.2.3(a), tensile strength can be increased by ~95% as compared to the base ABL (control). The surface energy values shown in Figure II.4.1.2.3(c) further improved with the addition of TA—especially the one with 5 wt.% filler content shows the highest polar component. Attributed to the enhancements from both mechanical properties and surface energy, the LSS that was obtained measured ~18 MPa, which was 100% higher than the neat ABL control sample shown in Figure II.4.1.2.3(b). The glass transition (T_g) temperature of the adhesive films was also raised up to 52°C compared to the 41°C of the control sample when the optimal amount of TA was added. Digital images of the debonded surfaces are presented in Figure II.4.1.2.3(d); all of the samples still show adhesive failure. Surface modifications on the adhesive layer and substrates are under investigation to further improve the LSS. Figure II.4.1.2.3(e) compares the morphology of the ABL adhesive with and without TA. Using TA as the filler improved the dispersion of lignin particles, which resulted in a harder and smoother surface.

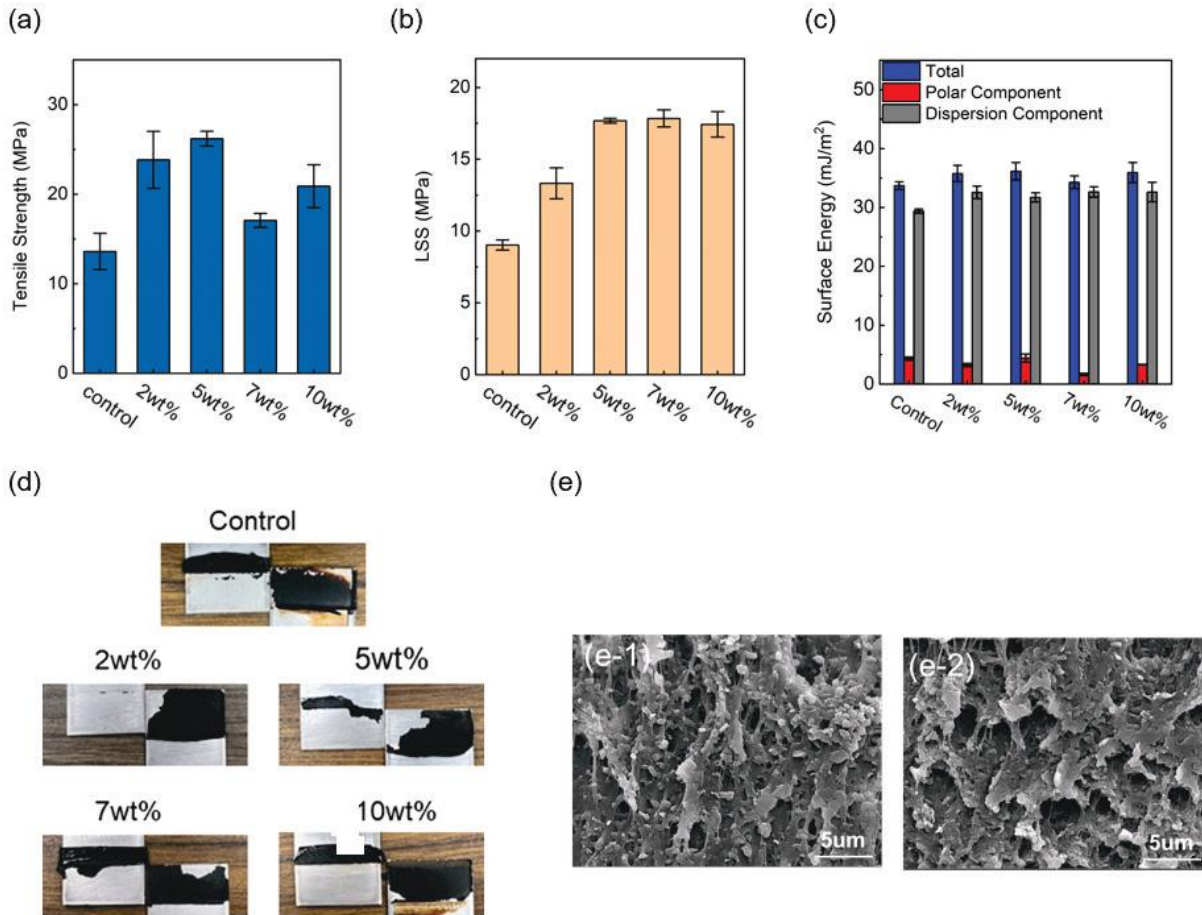


Figure II.4.1.16. The properties of ABL-based adhesives: (a) tensile strength of adhesive films; (b) LSS results with Al 6061 as the substrate; (c) surface energy for adhesive films; (d) fracture surface for lap-shear samples; (e) SEM of adhesives; (e-1) control sample; and (e-2) with addition of TA. Source: ORNL.

High-Velocity Riveting (PNNL)

Dissimilar Metal Joints

Trials for high-velocity riveting (HiVe) of dissimilar joints were completed using a commercially available steel rivet with a powder-actuated device. Multiple stack combinations were successfully joined between Al steel and an Al composite. Steel-composite combinations proved elusive due to catastrophic failure in the CFRP composite as a result of large deformation incurred in the steel sheets during riveting.

Figure II.4.1.2.4(a) shows the respective load-displacement curves from the lap-shear tests of the Al steel and Al composite stack-ups. The steel rivet used in this work had an ogival tip shape, which promoted gradual deformation of the plates during the quick rivet process, contrary to the flat-head type rivets that either deformed without penetrating through the plates or induced significant cracking in the plates—particularly the CFRP materials. In Figure II.4.1.2.4(b), the effect of adhesive and PT application on the maximum lap-shear is highlighted. PT of the interfacing surfaces prior to adhesive and riveting application showed a significant increase over non-plasma-treated surfaces. Even in cases where no adhesive application was done, higher strength was observed in Al-Al joints due to a metallurgical bond formation at the mating interfaces after riveting.

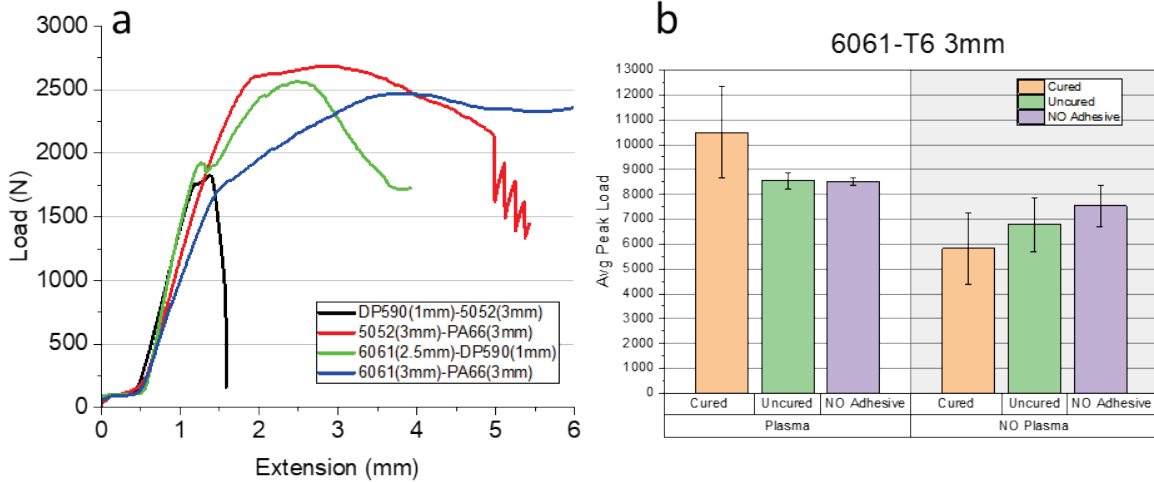


Figure II.4.1.17. (a) Lap-shear load-displacement curves of DP590 steel plates to AA5052-H32 and AA6061-T6 plates along with AA5052-H32/AA6061-T6 to PA66 composite plates. (b) Testing results for the various surface treatments on lap-shear loading in the AA6061-T6 joints. Source: PNNL.

HiVe – Al-Al Joint Performance vs. Flow-Drill Screw

Proving the HiVe capability over other joining methods, such as the flow-drill screw, can be seen in Figure II.4.1.2.5 where all combinations of adhesive applications and PT conditions showed a significant improvement over the flow-drill screw (FDS) stack-ups of similar geometry. In Al-Al joints, the application adhesive provided the largest improvement in lap-shear loads up to 160% increase in maximum load as compared to FDS. The processing time of HiVe is in the millisecond regime, whereas the flow-drill process extends in to the 12-15 second range of processing time; therefore, the HiVe is two to three orders of magnitude faster than the FDS process.

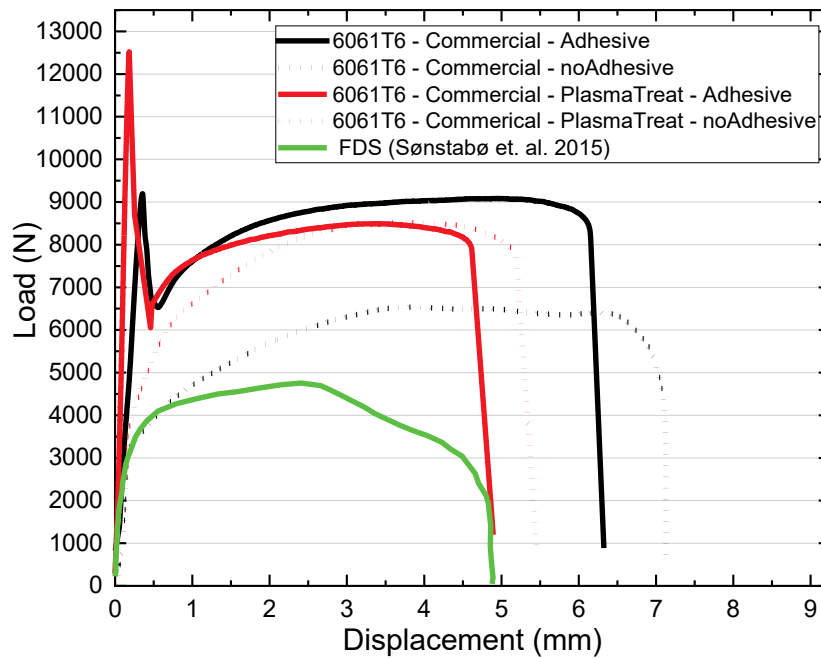


Figure II.4.1.18. Load-displacement curves for AA6061-T6 joints with and without adhesive/plasma application. Source: PNNL.

Optimization of Die Design using Finite Element Modeling

A 3D adiabatic thermal-stress finite element model was created to understand the HiVe process, particularly plastic deformation, temperature generation, pressure, and joint integrity, and how they are affected by variations in the processing conditions. Due to the symmetry of the problem, a wedge model was selected to reduce the computational cost by simulating only 1/360 of the complete model, as observed in Figure II.4.1.2.6.

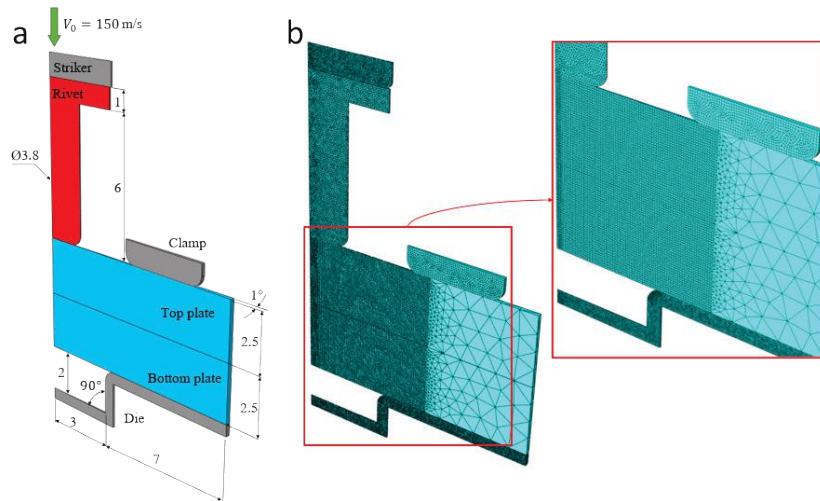


Figure II.4.1.19. (a) Schematic of HiVe process set-up and dimensions. (b) Finite element mesh for HiVe simulations. Source: PNNL.

The effects of varying the die design (e.g., depth, radius, angle) on the HiVe joint were analyzed through a parametric study, which helped develop an optimized die geometry, as observed in Figure II.4.1.2.7(a). Figure II.4.1.2.7(b) shows the resulting cross-section obtained using the new die. Figure II.4.1.2.7(c) compares the load-displacement curves obtained during a lap-shear test for the baseline and new die designs. As observed in these images, the maximum load is increased by 40% when using the new die. These results prove the new die design improves the strength of the metallurgical bond due to two factors: (1) increased interfacial temperature; and (2) providing enough and quick support to the bottom plate to achieve the pressure threshold early during the HiVe process.

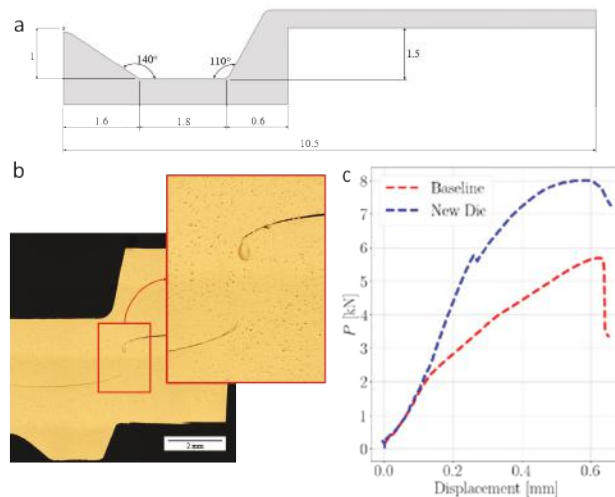


Figure II.4.1.20. (a) Optimized die design. (b) Corresponding experimental cross-section. (c) Comparison of load-displacement curves. Source: PNNL.

High-energy XRD Mapping of HiVe Rivets

To better understand the microstructural features responsible for the favorable properties obtained in the Al 6061/DP590 and Al/Al joints, ANL conducted a diffraction mapping of the joined region in transmission geometry at beamline 1-ID-E through the APS. An x-ray beam measuring $100\ \mu\text{m} \times 100\ \mu\text{m}$, with an energy of 71.676 keV and an exposure time of 0.2 s per point, was used to collect two-dimensional (2D) diffraction patterns for an array of points (e.g., $\sim 30 \times 20$) spaced out regularly to cover the joined region and substrates. The objectives of this characterization were to obtain site-specific microstructural information (e.g., crystal structures and lattice strains of the phases present) in the joined and substrate regions, as well as to further use this information to better understand the phase evolution and stresses imparted into different regions of material during the riveting process.

Figure II.4.1.2.8 shows the experimental setup at the beamline. The total scan area covered by the measurement array—an example 2D diffraction pattern in the substrate away from the joined region in the Al/Al rivet and the corresponding one-dimensional (1D) diffraction pattern obtained by integrating along the azimuth/circumference of the ‘rings’ using the General Structure Analysis System (GSAS)-II software—is shown in Figure II.4.1.2.9. The 2D pattern is spotty due to the grain size of the Al in the substrate being large and the probed diffraction volume having insufficient grains to result in continuous rings. Further, the 1D pattern shows that the microstructure consists mainly of the Al- FCC phase.

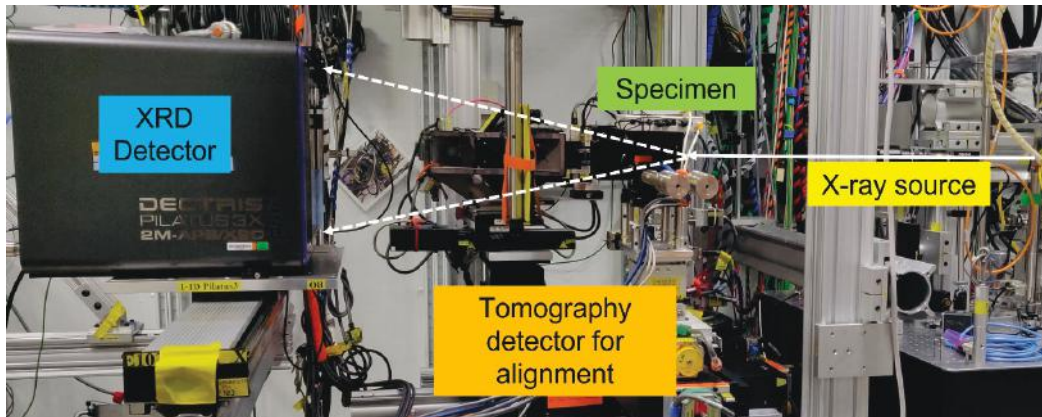


Figure II.4.1.21. Experimental setup showing the diffraction geometry in transmission mode at beamline 1-ID through APS. The x-ray beam path is marked in white with a solid line showing the incident beam and dashed line showing two diffracted beams. Source: ANL..

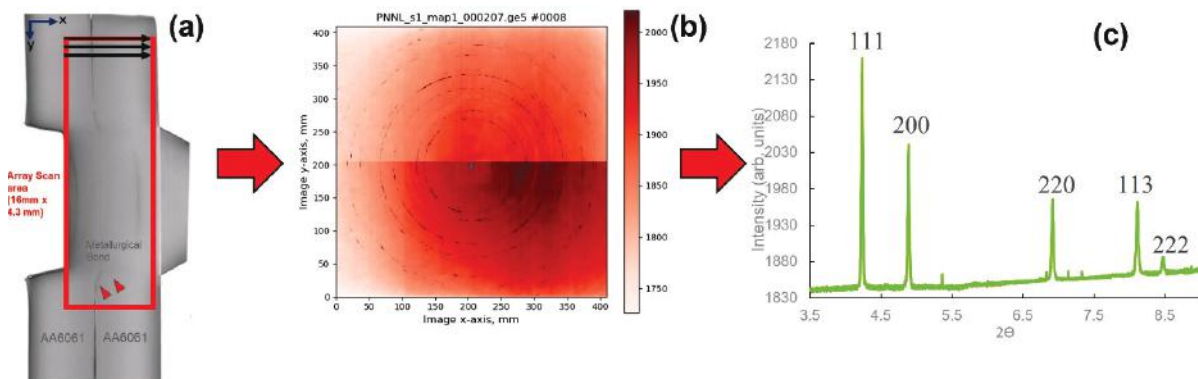


Figure II.4.1.22. (a) Total scan area covered by the measurement array of spots (e.g., ~ 30 rows along x and ~ 20 columns along y) marked in red. Note that it covers both the joined and substrate areas. (b) 2D diffraction pattern acquired from the substrate region of the Al/Al joint. (c) Corresponding 1D diffraction pattern obtained by azimuthally integrating the 2D pattern in (b). Source: ANL.

Further, GSAS-II software was then used to perform a Rietveld refinement of the 1D diffraction pattern to obtain an average lattice parameter value of the Al - FCC phase for a given diffraction volume/measurement spot. This procedure was repeated for all the points in the array (e.g., $\sim 30 \times 20$) to obtain a colormap consisting of lattice parameters for all the spots in the array. This ‘lattice parameter map’ overlaid on the optical micrograph of the Al/Al rivet can be seen in Figure II.4.1.2.10, which shows the lattice parameter is lower (red regions) in the joined areas than the ‘strain-free’ lattice parameter of Al (blue/yellow regions) in the substrate areas, implying the metallurgically bonded region is being subject to a compressive strain. The results from this study will help validate the finite element simulations being conducted at PNNL.

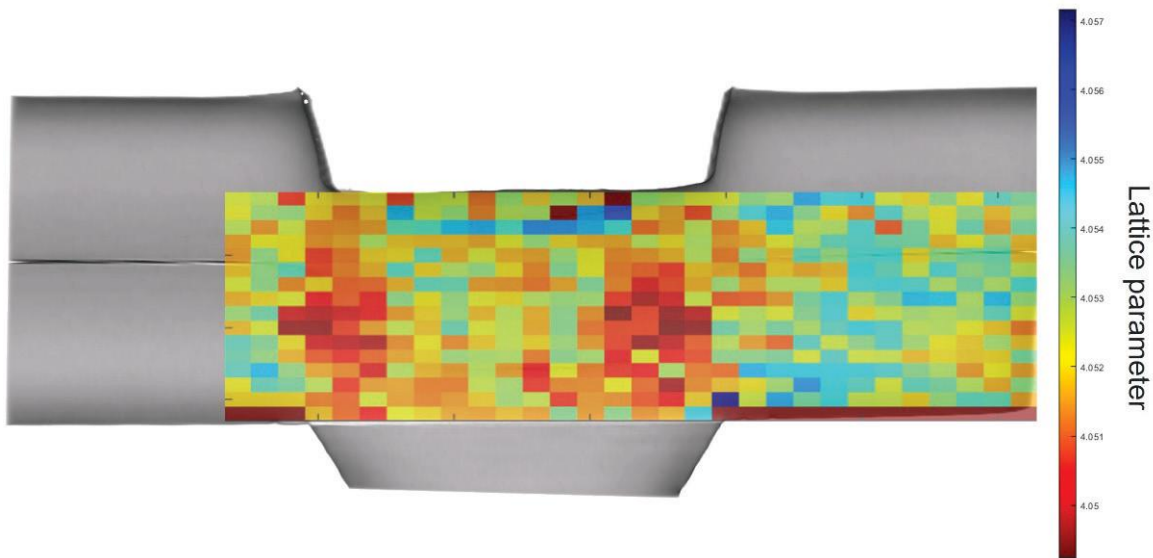


Figure II.4.1.23. Lattice parameter map from the measurement array overlaid on an optical micrograph of the Al/Al rivet. Source: ANL.

As a next step, dissimilar material joints made of Al/steel and Al/CFRP were received from PNNL and will be characterized using diffraction mapping using the 1-ID beamline in the upcoming APS run. Additionally, to probe the site-specific deformation during the high-velocity joining process, *in-situ* high-speed radiography experiments are planned. The fundamental insights of the high-velocity riveting process obtained from the above *ex-situ* and *in-situ* means will be a key step in helping the scaleup and commercializing of this joining process.

High-Rate Friction Riveting (PNNL)

High-rate friction riveting (HFR) is a multimaterial joining method where a rotating cylindrical rivet is driven into a joint assembly, typically in an overlap configuration to produce mechanical interlocking and metallurgical bonding simultaneously. It is predicated on the FricRiveting process developed by Helmholtz Zentrum Geesthacht [3]. Existing methods, such as self-piercing riveting [4] and friction-bit joining [5], would require a separate joining tool and a consumable part where the part is inserted into the joint assembly while the tool is retracted after the joining process. In contrast, HFR offers benefits similar to those of FricRiveting, but CP off-the-shelf rivet materials are driven into a joint assembly with no need for a separate tool or any modification to the rivet. In FY 2022, HFR work was focused on the joining of dissimilar materials combinations—including but not limited to—dissimilar Al alloys, Al-steel, etc. The HFR process was applied to: (1) AA6061-T6 sheets (e.g., 3-mm-thick) with DP 590 (e.g., 1-mm-thick) using a commercially available advanced alloy steel (M42) rod as the rivet material and (2) AA6061-T6 and AA5052-T32 sheets (e.g., both 3-mm-thick) with a low strength steel threaded rod. After achieving the optimum processing parameters, surface modification by PT was implemented to evaluate influence on bond strength. For brevity, this report is limited to Al-steel joining only.

Dissimilar Metal Joining (Al to Steel)

Figure II.4.1.2.11(a) shows the AA6061-DP590 joint processed via HFR. Figure II.4.1.2.11(b) shows the optical microscopy image of the cross-section of AA6061-DP590 HFR joint with an M42 rivet. The tip of the rivet diameter expands from 6.35 mm to 8.4 mm. This tip deformation behavior is a desirable feature for improvement in the strength of the joints by providing metallurgical bonding, as well as mechanical interlocking, through the mushrooming effect. Interestingly, the rivet was broken inside the Al sheet and a second mushrooming at 1.9 mm from the top surface of Al was revealed in Figure II.4.1.2.11(b). Figure II.4.1.2.11(c) and Figure II.4.1.2.11(d) present the lap-shear performance of the joints; the results are compared with the FDS method.

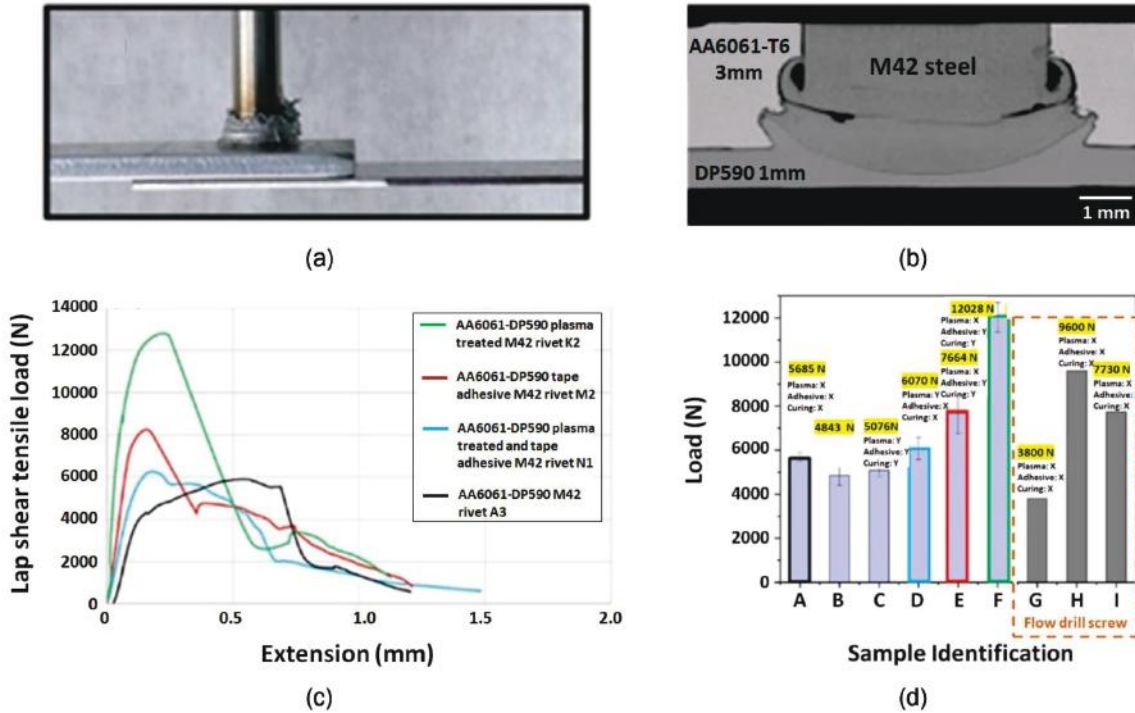


Figure II.4.1.24. (a) The AA6061-DP590 joint processed via HFR. (b) Optical microscopy image of the cross-section of AA6061-DP590 HFR joint with an M42 rivet. (c) The smoothed ‘ideal’ hardness curve demonstrating the ideal hardness distribution across the width of the RSW joints developed for a comparison of RSW weld structure metrics. (d) Lap-shear performance comparison of the joints. Source: PNNL.

While Figure II.4.1.2.11(c) shows the load vs. the extension of selected lap-shear joints—meaning the color of the flow curves match with the color of the corresponding sample shown in the bar graph in Figure II.4.1.2.11(d)—with various surface modifications. Figure II.4.1.2.11(d) presents the peak load for the AA6061-DP590 joints and different surface-modified configurations:

- A. AA6061-DP590 joint with no surface modification
- B. AA6061-DP590 joint with paste adhesive (with glass beads) + HFR + curing
- C. AA6061-DP590 joint with PT + paste adhesive (with glass beads) + HFR + curing
- D. AA6061-DP590 joint with PT + HFR
- E. AA6061-DP590 joint with tape adhesive + HFR + curing
- F. AA6061-DP590 joint with PT + tape adhesive+ HFR + curing.

These data are compared with FDS joint lap-shear performance:

- A. Average LSS of joints SABC1470 steel (1 mm) – A6014 (1.2 mm) and SABC1470 steel (1 mm) – A5182 (1.2 mm) formed via the FDS method as reported in [6]
- B. Average LSS of stacking of two steel (1 to 1.6-mm-thick on top) and Al alloys (3-mm-thick on bottom) joint formed using the FDS method as reported in [6]
- C. AW-5083 H111 (2 mm) – steel HC340LA (1.5 mm) joint formed using the FDS method as reported in [7].

The Al and steel joints formed via HFR on average perform better than those formed via FDS. As seen in Figure II.4.1.2.11(d), the surface-modified HFR joint (F) shows a peak load that is 25% higher than the peak load obtained via FDS in the (H) samples and 55% higher than that of the FDS-processed (I) samples.

Joint Performance Prediction using Finite Element Analysis

A computational model was also developed for quantitative prediction of maximum joint load, ductility, and capture failure mechanisms for different interfacial configurations. The 3D FEM was created using digital images of the cross-section presented in Figure II.4.1.2.11(b) after the friction riveting process has taken place. Figure II.4.1.2.12 shows the experimental and simulated load vs. displacement curves for the lap-shear test and corresponding failure morphologies. As shown in Figure II.4.1.2.12(a), the presence of the metallurgical bond results in a higher peak load of the joint when compared to the case without a bond. Figure II.4.1.2.12(a) also shows a comparison of the computational load-displacement curves obtained from cases with and without a metallurgical bond against the experimental results, which agrees well with the experimental results. The failure morphologies are shown as equivalent plastic strain (e.g., PEEQ) distributions in simulation, as observed in Figure II.4.1.2.12(c), with metallurgical bonding as compared to without metallurgical bonding, as indicated in Figure II.4.1.2.12(b). Figure II.4.1.2.12(d) shows a bonded rivet after testing.

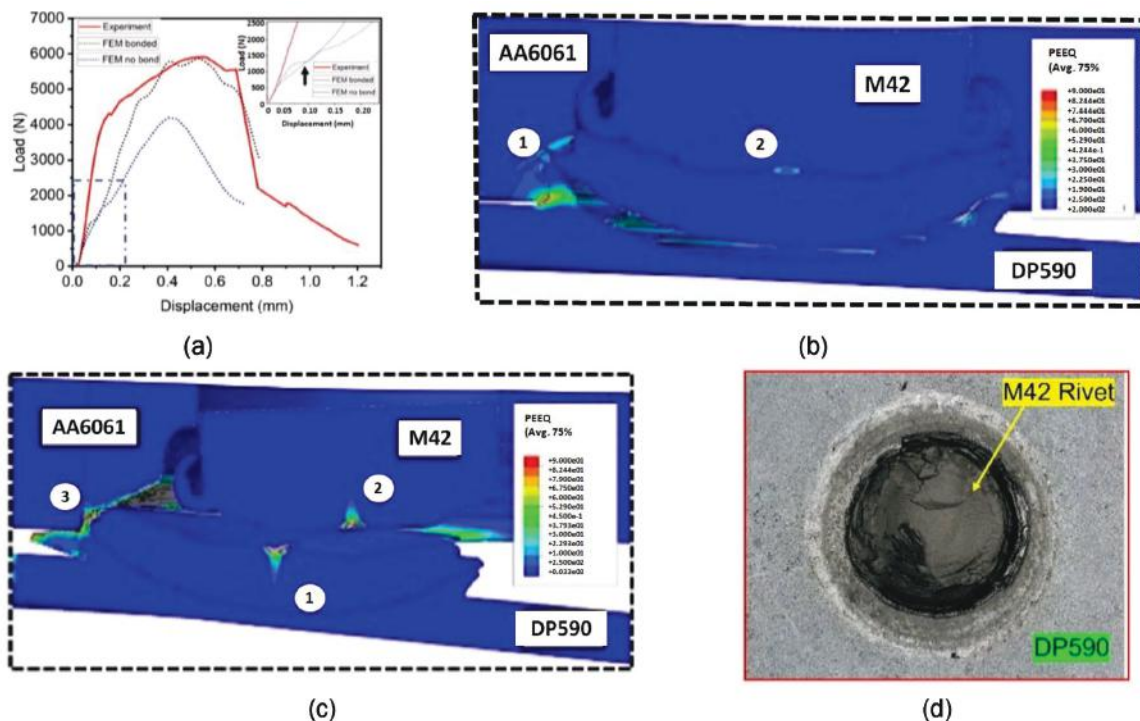


Figure II.4.1.25. (a) Experimental and simulated load vs. displacement lap-shear test results. (b, c) Equivalent plastic strain distributions at peak load for the case: (b) without bonding; and (c) with a metallurgical bonded interface. (d) Experimental failure morphology showing a rivet bonded with DP590. Source: PNNL.

Conclusions

Plasma surface modifications optimized for lap-shear performance achieved a 24% increase in LSS in Al5052/CFRP adhesive joints. Laser surface modifications were developed for the CFRP substrates and the relationship between laser power, spot spacing, and surface roughness was determined. A microscale computational model was developed for surface characteristics as they relate to lap-shear performance, which will assist in optimizing laser treatment parameters. Laser ablation of AA380 substrates was characterized in collaboration with GM and caused an increase in oxidized species at the surface.

The incorporation of a TA in the ABL matrix was needed to adjust the viscosity of the multiphase composite adhesive, which increased the shear stress during the mixing process. As a result, the dispersion of the lignin was improved, which led to an enhanced surface energy and significantly reinforced adhesive behavior with approximately 95% increase tensile strength of the thermoplastic adhesive. When this stronger adhesive layer was applied, the LSS of the adhesively bonded Al 6061 joints improved 100% compared to equivalent joints from the control adhesive. Other adhesive modifications and surface-treatment conditions are being evaluated to further improve the adhesion performance.

HiVe of dissimilar metals exhibited large improvements in lap-shear strengths in AA6061-T6 as compared to the FDS techniques—upwards of 160% in max loading when coupled with plasma treatments and an adhesive. Riveting of dissimilar metals of Al-Al, Al-steel, and Al-CFRP were successful, and the combinations of plasma treatments + adhesives on joint strength were explored. The effect of the die geometry on the HiVe process was explored utilizing FEA where an optimized die was isolated, which provided the ideal pressure and temperature conditions for the bonding of AA6061-T6 joints.

HFR demonstrated that the metallurgical bonding and mechanical interlock that formed between the rivet and the sheets resulted in improved joint mechanical properties, providing an advantage over other metal joining processes. The computational model matched the behavior of lap joints observed experimentally when a perfect bond was assumed between the rivet and the bottom plate. It was found that the peak load of the joint increased by 39% due to the presence of a metallurgical bond at the rivet/bottom plate interface.

Key Publications

1. Das, H., K. S. Kappagantula, A. Srivastava, P. Upadhyay, J. F. Dos Santos, Md. Reza-E-Rabby, 2023, “Embedded anchoring of multimaterial assemblies by friction riveting process,” in Hovanski, Y., Y. Sato, P. Upadhyay, A. A. Naumov, and N. Kumar (Eds.), *TMS 2023: Friction Stir Welding and Processing XII*. The Minerals, Metals, & Materials Series, Springer, Cham. pp. 149–156. https://doi.org/10.1007/978-3-031-22661-8_14.
2. Kanbargi, N., D. Hoskins, S. Gupta, Z. Yu, Y. Shin, Y. Qiao, D. R. Merkel, C. C. Bowland, N. Labbé, K. L. Simmons, and A. K. Naskar, 2023, “A renewable lignin-based thermoplastic adhesive for steel joining,” *Eur. Polym. J.*, Vol. 189, Art. 111981. <https://doi.org/10.1016/j.eurpolymj.2023.111981>.
3. Qiao, Y., Y. Shin, M. R. Pallaka, E. K. Nickerson, D. R. Merkel, R. J. Seffens, A. Ortiz, J. L. Ramos, and K. L. Simmons, 2022, “Plasma surface modification coupled with thermal and step-over distance effects on significant fracture improvement of adhesively bonded metal-CFRTP dissimilar materials,” *Compos. Sci. Technol.*, Vol. 232, Art. 109833. <https://doi.org/10.1016/j.compscitech.2022.109833>.
4. Qiao, Y., D. R. Merkel, E. K. Nickerson, Y. Shin, R. J. Seffens, A. Ortiz, and K. L. Simmons, 2022, “Mode I tensile fracture behavior of adhesively bonded metal-metal, metal-CFRP, and CFRP-CFRP bi-material combinations analyzed by size effect method,” *Compos. A: Appl. Sci. Manuf.*, Vol. 160, Art. 107025. <https://doi.org/10.1016/j.compositesa.2022.107025>.
5. Shin, Y., Y. Qiao, N. Canfield, Z. Yu, H. M. Meyer III, D. R. Merkel, E. K. Nickerson, N. S. Kanbargi, A. Ortiz, A. K. Naskar, and K. L. Simmons, 2022, “Significant slowdown of plasma-optimized surface energy deactivation by vacuum sealing for efficient adhesive bonding,” *Compos. B: Eng.*, Vol. 240, Art. 110001. <https://doi.org/10.1016/j.compositesb.2022.110001>.

References

1. Tran, C. D., J. Chen J. K. Keum, and A. K. Naskar, 2016, “A new class of renewable thermoplastics with extraordinary performance from nanostructured lignin-elastomers,” *Adv. Funct. Mater.*, Vol. 26, No. 16, pp. 2677–2685. <https://doi.org/10.1002/adfm.201504990>.
2. Kanbargi, N., M. Goswami, L. Collins, L. T. Kearney, C. C. Bowland, K. Kim, K. Rajan, N. Labbé, and A. K. Naskar, 2021, “Synthesis of high-performance lignin-based inverse thermoplastic vulcanizates with tailored morphology and properties,” *ACS Appl. Polym. Mater.*, Vol. 3, No. 6, pp. 2911–2920. <https://doi.org/10.1021/acsapm.0c01387>.
3. Amancio-Filho, S. T., and J. F. dos Santos, 2008, “Development of FricRiveting as a new joining technique for polymer and lightweight alloys,” *Mater. Werkst.*, Vol. 39, No. 11, pp. 799–805. <https://doi.org/10.1002/mawe.200800369>.
4. Settineri, L., E. Atzeni, and R. Ippolito, 2010, “Self-piercing riveting for metal-polymer joints,” *Int. J. Mater. Form.*, Vol. 3, pp.995–998. <https://doi.org/10.1007/s12289-010-0937-3>.
5. Miles, M., S.-T. Hong, C. Woodward, and Y.-H. Jeong, 2013, “Spot-welding of aluminum and cast iron by friction-bit joining,” *Int. J. Precis. Eng. Manuf.*, Vol. 14, No. 6, pp. 1003–1006. <https://doi.org/10.1007/s12541-013-0133-8>.
6. Kim, J., H. Lee, H. Choi, B. Lee, and D. Kim, 2020, “Prediction of load-displacement curves of FDS and RIVTAC joints between dissimilar materials using artificial neural networks,” *J. Manuf. Process.*, Vol. 57, pp. 400–408. <https://doi.org/10.1016/j.jmapro.2020.06.039>.
7. Graf, M., S. P. Sikora, and C. S. Roeder, 2018, “Macroscopic modeling of thin-walled aluminum-steel connections by flow-drill screws,” *Thin-Walled Struct.*, Vol. 130, pp.286–296. <https://doi.org/10.1016/j.tws.2018.02.023>.

Acknowledgements

The authors from PNNL recognize Y. Qiao, Y. Shin, A. Ortiz, J. Ramos, E. Nickerson, S. Ko, A. Samanta, and D. Merkel for the surface-treatment work; Z. Yu and N. Kanbargi for the novel adhesive work; B. Schuessler, M. Rhodes, R. Seffens, S. Niverty, A. Guzman, and V. Joshi for the HVR/HiVe work; M. Rabby, A. Srivastava, H. Das, M. Pole, and K. Kappagantula for the HFR work; A. Soulami, L. Li, D. Ramirez-Tomayo for the computational simulations.

The co-PI at ANL would like to acknowledge J. Thomas, R. Kamath, and A. Chuang for their assistance in conducting the APS experiments and data analysis. This research used APS resources; a U.S. Department of Energy–Office of Science (DOE-SC) User Facility operated for the DOE-SC by ANL under Contract No. DE-AC02-06CH11357.

II.4.1.3 Solid-State Joining of Multimaterial Autobody Parts Toward Industry Readiness (Pacific Northwest National Laboratory and Oak Ridge National Laboratory)

Piyush Upadhyay, Co-Principal Investigator

Pacific Northwest National Laboratory
900 Battelle Blvd.
Richland, WA 99352
E-mail: piyush.upadhyay@pnnl.gov

Yong Chae Lim, Co-Principal Investigator

Oak Ridge National Laboratory
One Bethel Valley Rd.
Oak Ridge, TN 37831
E-mail: limy@ornl.gov

Christopher Schooler, DOE Technology Development Manager

U.S. Department of Energy
E-mail: christopher.schooler@ee.doe.gov

Start Date: October 1, 2020 End Date: September 30, 2023
Project Funding (FY 2022): \$3,500,000 DOE share: \$3,500,000 Non-DOE share: \$0

Project Introduction

PNNL and ORNL are teaming to further advance and mature friction-based solid-state joining technologies toward industry readiness for the high-volume production of multimaterial autobody structures. Two solid-state joining technologies—F-SPR and FSLW—have been under development at the two national laboratories and have been proven to apply to a wide range of material stack-ups at the laboratory coupon level. We intend to overcome identified technical barriers related to robustness, joint function to process correlation, and equipment scaleup to sufficiently advance joining technologies for industry adoption with support from a partnering OEM, Honda R&D Americas; and a material supplier, Arconic Inc.

The ability to join dissimilar materials with specific properties is critical for lightweight multimaterial design. In a BIW construction, replacing the steel passenger cage with an appropriately designed stamped Al assembly and using CFRCs to stiffen AHSS in front/rear end sections is an approach to achieving this goal. This approach comes with two joining challenges: (1) the ability to effectively assemble dissimilar stamped Al subassemblies and (2) the ability to join the Al sub-assembly to the AHSS/CFRC sub-assembly.

This need requires the development of technologies that can join different material sets in a cost-effective, robust manner, in addition to minor modifications to assembly lines that can meet high-volume demands. Friction stir derived linear and spot-joining technologies provide solutions.

In FY 2022, we further developed baseline joints from the previous year in dissimilar Al combinations—Al-Steel and Al-CFRP. FSLW was successfully transferred from a gantry-based machine to a robotic platform at a higher welding speed in two alloy systems. Three sheet (3T) stack-ups of Al FSLW joints produced in the robot exceeded the coupon level strength target up to a welding speed of 2 m/min. Fabrication on a larger 3T joint beyond coupon level commenced this year with the production of lap-shear test, cross-tension (KSII) and crush test samples. As a single joining process, the F-SPR process was refined for different material combinations to achieve high joint strength in lap-shear and cross-tension testing in the laboratory coupon level.

Objectives

The goal of this multi-lab, multiyear project is to mature two friction-based joining technologies and to demonstrate the joining of dissimilar Al components and Al to steel/CFRC subassemblies. The outcomes of this effort will include process parameters, machine control strategies, and a clamping and fixturing design, which are all necessary to advance the FSLW and F-SPR joining methods from the laboratory-scale plaque and coupon levels to component level demonstrations geared toward high-volume production.

Approach

Two friction stir-based joining processes—FSLW and F-SPR—at two national laboratories are being leveraged to develop and demonstrate multimaterial joining in a relevant automotive component. The material stacks to be joined and characterized in this project for both processes are shown in Figure II.4.1.3.1. The materials, as well as their temper and thicknesses, were established in consultation with the industry.

FSLW-stack 1	FSLW stack 2	FSPR	FSPR
7075-T6 – 2.5 mm	6111-T4 – 2.5 mm	CFRP- 1.9 mm to 3.2 mm	7055 – 2.5 mm
7075-T6 – 2.5 mm	6111-T4 2.5 mm	6111-T4 7055-T76 – 2.5 mm	AHSS – 1.2 mm to 1.6 mm
6022-T4 – 1 mm	6022-T4 – 1 mm		

Figure II.4.1.26. Material arrangements for the four material stacks to be joined and characterized. Source: PNNL.

The overall tasks to be performed each year and their interactions, as illustrated in Figure II.4.1.3.2, are:

- Linear (short stitches and long continuous welds): FSW of dissimilar Al alloys
- Spot-welding: spot/tack welding for Al structures before FSLW
- F-SPR: spot-welding of Al-CFRC and Al to AHSS.

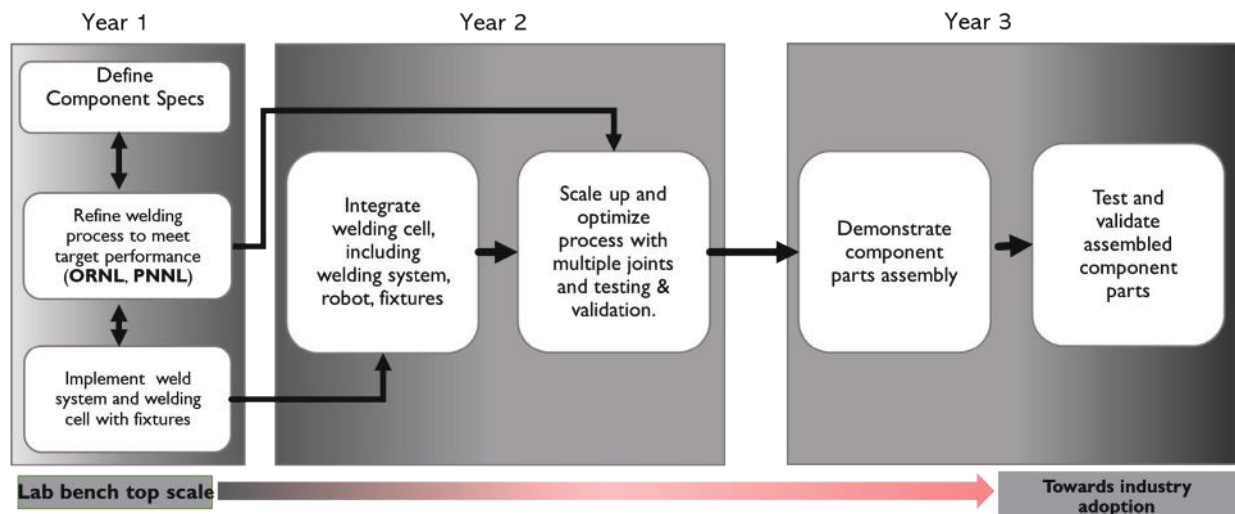


Figure II.4.1.27. Overview of project approach. Source: ORNL.

The R&D activities during this first FY were to define material stack-up and refine joining processes to meet target performance by implementing welding system and fixtures at each national laboratory.

Results

After several rounds of process development and over 800 weld trial runs, we were able to identify the welding parameters to produce 3T FSLW joints at a welding speed of 1 m/min for Stack 1, and 2 m/min for Stack 2 that exceeded the minimum strength requirements stipulated by our collaborating OEM (viz. 375 N/mm for the

lap-shear and 112.5 N/mm for the T-peel). This was demonstrated for both the 3T multi-alloy Al combinations being developed in this project:

- Stack 1: 7075-T6 (2.5 mm) - 7075-T6 (2.5 mm) - 6022 (1.0 mm)
- Stack 2: 6111-T4 (2.5 mm) - 6111-T4 (2.5 mm) - 6022 (1.0 mm).

Note that there is a change in alloy used for Stack 1. Thus far, developmental work has been performed on 7055-T6. Due to the lack of material availability and industry preference, developmental work has been moved to 7075-T6. Most of the work reported herein are for the 7075-T6 material set. This material will be used for the developmental work on the remainder of the project. For Stack 1, an average LSS of 747 ± 25 N/mm, as observed in Figure II.4.1.3.3(a), and T-peel strength of 140 ± 10 N/mm, as shown in Figure II.4.1.3.3(b), were achieved. For Stack 2, an average LSS of 545 ± 8 N/mm and a T-peel strength of 131 ± 8 N/mm was achieved at 2 m/min welding speed. For Stack 2, the LSS measured 630 ± 6 N/mm at 1 m/min welding speed and the sample fractured at the base metal. This was despite the presence of a small void on the advancing side root. It indicates that there is more room for improvement in LSS for Stack 2 with 2 m/min welding speed. The lap-shear tests were performed on 1 in. wide samples extracted from the long linear welds. The T-peel samples were tested in the form of a 50-mm long stitch weld. The bar charts in Figure II.4.1.3.3(c) and Figure II.4.1.3.3(d) show the average strength values, deviations, crosshead displacement, and number of samples tested. Earlier this year, a repeatability study was conducted on 7055-T6 (2.5 mm) - 7055-T6 (2.5 mm) - 6022 (1.0 mm) in Stack 2 at a welding speed of 1 m/min. The results of the repeatability study were reported in our annual merit review. Having achieved this milestone, our team has now changed our focus towards generating and further developing the welding process for our final FSLW demonstration in a representative stamping part.

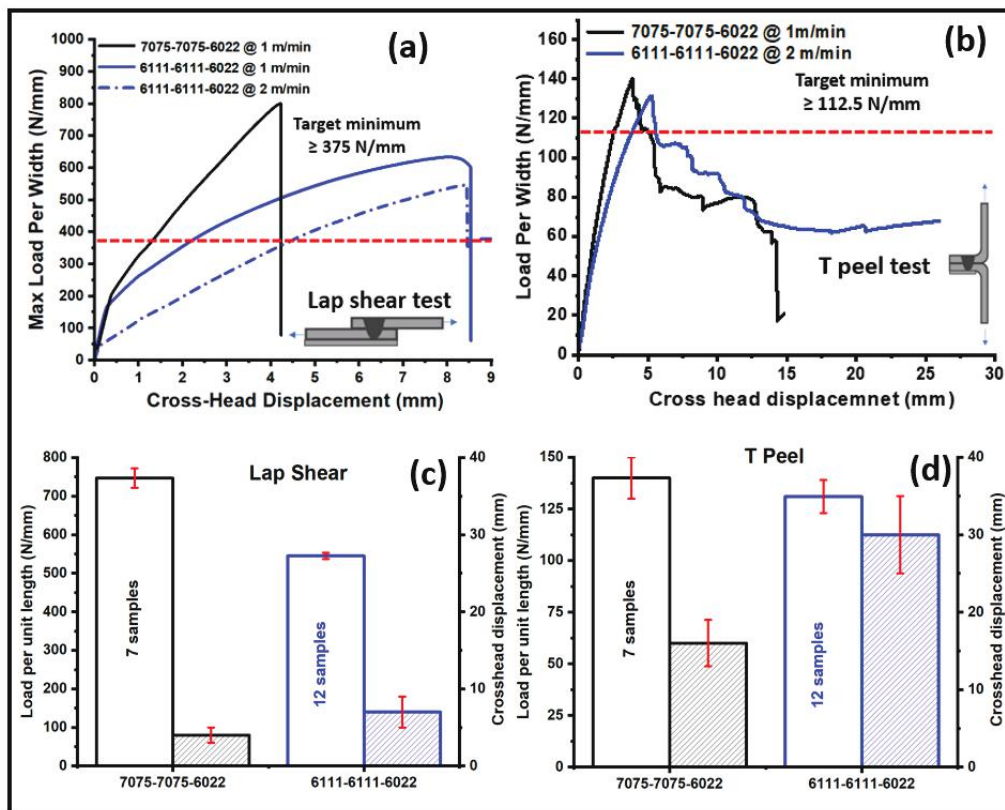


Figure II.4.1.28. Load per unit width vs. crosshead displacement plot for 3T FSLW joints: (a) lap-shear, (b) T peel, and (c)-(d) bar chart compilation of several tested samples. Source: PNNL.

It is well demonstrated in the literature that the FSW exit hole is considered as a weak point during loading [1]. Our modeling efforts have indicated that dwelling at the exit hole (i.e., keeping the tool rotating at the exit hole location for a limited amount of time) may strengthen the area around the exit hole. This will have a beneficial effect on the overall strength of the weld. With this notion, several welds with varying dwell times were made and tested. Figure II.4.1.3.4(a) shows the load per width vs. displacement curves for two different welds: one with no dwelling and one with 5 secs of dwelling time at the exit hole. Clear differences in the peak load values can be observed for both conditions, with the peak load for 5 secs exit dwell time reaching well beyond the same of the no dwell weld.

Furthermore, the feasibility of a pilot hole at the location of tool plunge-in was investigated this year. There are two reasons to have a pilot hole in assembly sheets. A pilot hole can minimize inevitable flash at the tool plunge-in location. A pilot hole can also serve as a locating point for a robot in an automatic manufacturing step. The diameter of the pilot hole is smaller than the tip diameter of the FSW tool. In the present study, the pilot hole diameter is 4 mm and was only present on the top sheet. With the pilot hole, a higher plunging revolutions per minute of the tool was employed to generate enough frictional heat, which can plasticize the material around the plunge location prior to traverse. Figure II.4.1.3.4(c) shows the top view of one sheet with the pilot hole with a 4-mm diameter. Some of the benefits observed with the pilot hole are an increase in the plunge-in speed, reduced flash around the plunge-in location, and reduced tool walking during the plunge, as shown in Figure II.4.1.3.4(b) and Figure II.4.1.3.4(c).

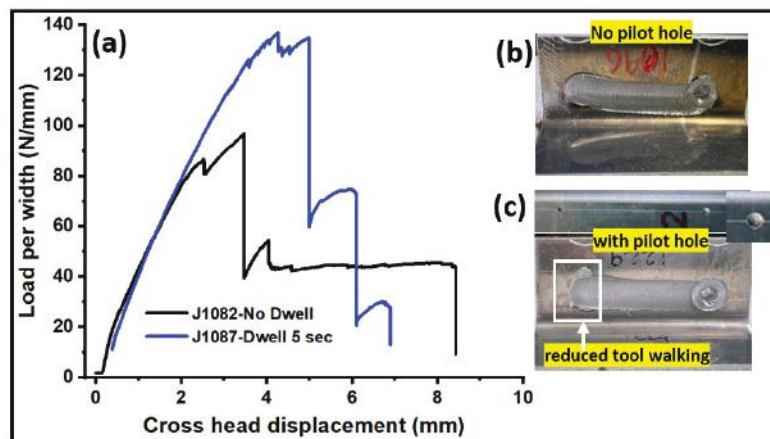


Figure II.4.1.29. (a) Load per width vs. crosshead displacement plot for 3T FSLW joints showing the effect of the dwell on joint strength. (b) Top view of the weld without the pilot hole. (c) Top view of the plate with the pilot hole. Source: PNNL.

Total weld time—including the plunge-in, ramp, and traverse time—is an important criterion for large volume productions. During FSW, the plunge can be the most time-consuming part of the overall welding cycle. A detailed effect of the pilot hole on the plunge-in time and overall weld time is shown in Figure II.4.1.3.5. For instance, a plunge-in velocity of 0.5 m/sec shows a plunge-in time of 34 seconds, as observed in Figure II.4.1.3.5(a), whereas a plunge-in velocity of 4 mm/sec results in 6 sec. of plunge-in time, which is more than five times faster. This certainly reduces the overall weld time to make a 50 mm stitch weld from 39 secs to 11 secs, thus making the whole weld ~3.5 times faster. However, the plunge-in sequence facilitates shoulder/tool seating and mixing of the cold material during the start of the welding affecting the overall strength of the T-Peel joints. Figure II.4.1.3.5(b) shows the effect of the plunge-in speed on the strength of the joint. Evident is the reduction in joint strength when the plunge-in velocity is increased from 1 mm/s to 4 mm/s (e.g., 141 N/mm to 115 N/mm). Note that the strength values for the joints with pilot holes and higher plunge speeds are still above the required threshold values. Hence, the pilot hole in conjunction with dwell time can be the path forward to optimize the tradeoff between plunge-in speed/plunge revolutions per minute combination for each material without compromising the mixing required.

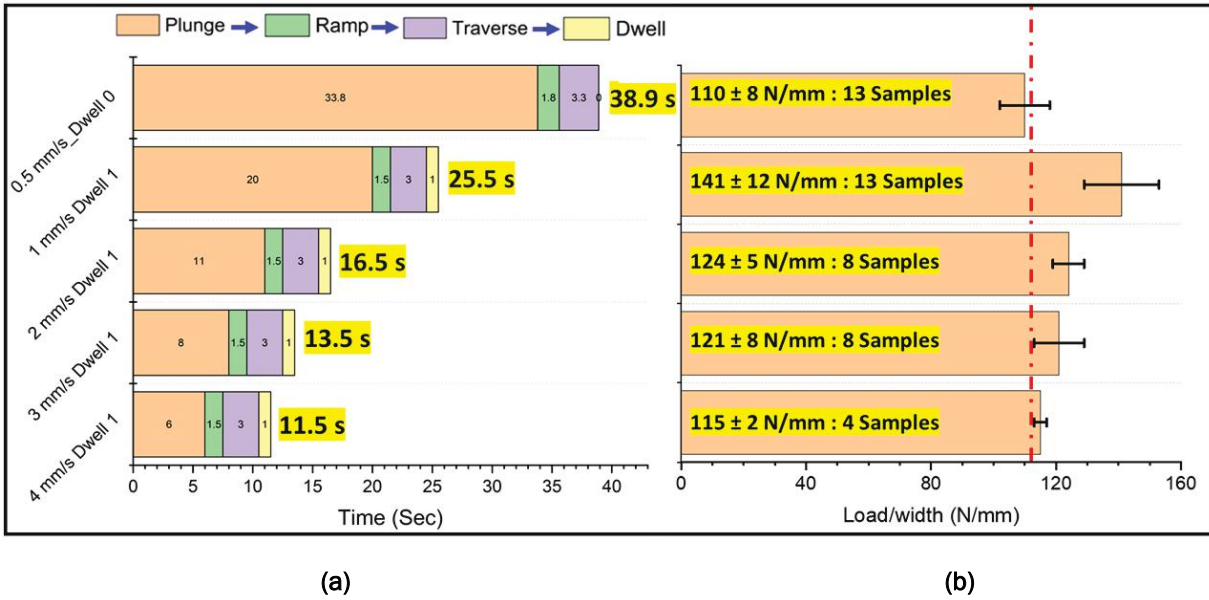


Figure II.4.1.30. Comparison of welding time (including plunge-in and traverse time) per plunging speed for (a) plunge-in time and (b)“strength of joint. Source: PNNL

We have performed U-shaped 3T joints at 1 m/min welding speed with different configurations of short stitches (30 mm) and point stitches (10 mm) to explore the impact of weld length and numbers of exit holes on joint performance. This kind of study is unique in its way and will provide baseline information to design engineers. Typically, this type of study is used to qualify spot-welded and adhesive joints. KSII samples employ symmetric loading to test similar or dissimilar joints. A tailored clamping and fixture arrangement was designed and set-up to U-shaped samples for KSII testing, as shown in Figure II.4.1.3.6(a). Three different seam configurations were designed hierarchically to understand the scenario of load-bearing capacity and stiffness behavior with an increasing number of stitches:

- Seam A: 4 stitches: 2 × 30 mm stitch in the transverse direction and 2 × 30 mm stitch in the longitudinal direction, as shown in Figure II.4.1.3.6(b)
- Seam B: 6 stitches: 2 × 40 mm stitch in the transverse direction and 4 × 10 mm stitch in the longitudinal direction, as shown in Figure II.4.1.3.6(b1)
- Seam C: 8 stitches: 4 × 10 mm stitch in the transverse direction and 4 × 10 mm stitch in the longitudinal direction, as shown in Figure II.4.1.3.6(b2).

The loading direction is shown in Figure II.4.1.3.6(c). The load-bearing capacity of three different seam designs is shown in Figure II.4.1.3.6(d). It is observed that Seam C shows higher strength and stiffness compared to Seam A and Seam B. It should be noted that an increase in the number of stitches introduces more plunge-in and exit holes in Seam C. The plunge-in and exit holes can act as crack closure and opening locations and in this way inhibit the sudden movement of the crack as well as the change in the crack path. This effect results in a higher joint strength and stiffness in the seam C. Furthermore, the time required to finish Seam A, Seam B, and Seam C are approximately 130 secs, 190 secs, and 250 secs. The reported time only includes the time required for the tool tip touchdown, plunge, traverse, and the extract sequences.

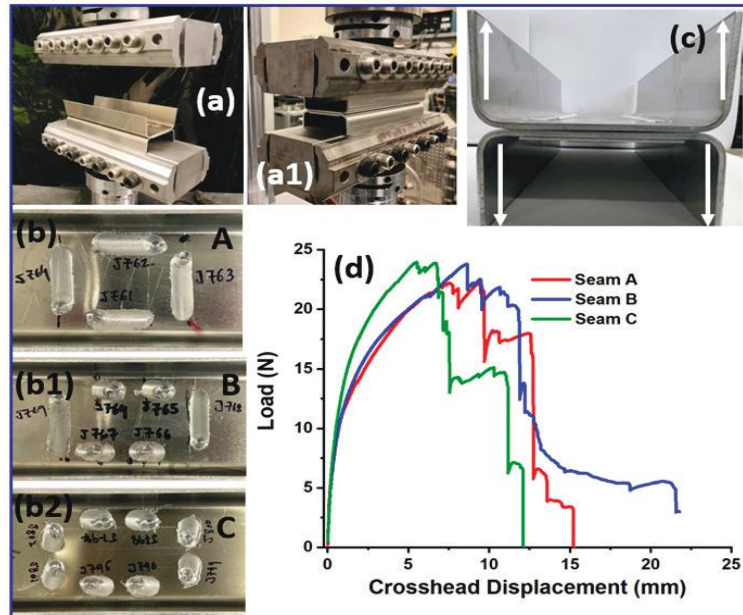


Figure II.4.1.31. 6111-6022 stack FS welded U-Peel (a) and (a1) testing set-up, welding scheme (b) Seam A, (b1) Seam B, (b2) Seam C, (c) loading direction, (d) load vs. displacement plot. Source: PNNL.

To prepare for FSLW demonstration on stamping parts, curved welding parameters were developed and executed for 7055 stacks with a radii of 50 mm and a 6111 stack with a radii of 10 and 20 mm at 1 m/min. Optical macrograph of cross-sections from locations across the welds for both the 7055 and 6111 stack show sound welds without any visible defects, as observed in Figure II.4.1.3.7(a) and Figure II.4.1.3.7(b). Honda R&D Americas provided a few developmental research stamping parts. Trial 3T welding was performed on one of the stampings for initial feasibility study, as shown in Figure II.4.1.3.7(c). The stamping contained some wrinkles on both sides. Nevertheless, welds without any surface defects, as observed in the inset of Figure II.4.1.1.7. (c), were made on stack consisting of 2.5 mm 7055 stamped part-2.5 mm 7055 flat sheet and 1 mm 6022 flat sheet in select areas. However, it is clear that excessive wrinkling on stamping will result in significant flashing and defects. Preliminary observation suggests FSLW can tolerate Z surface variation under ± 0.5 mm with a minimal flash. This can serve as an input to verify the quality of stamping needed for FLSW demonstration later this year.

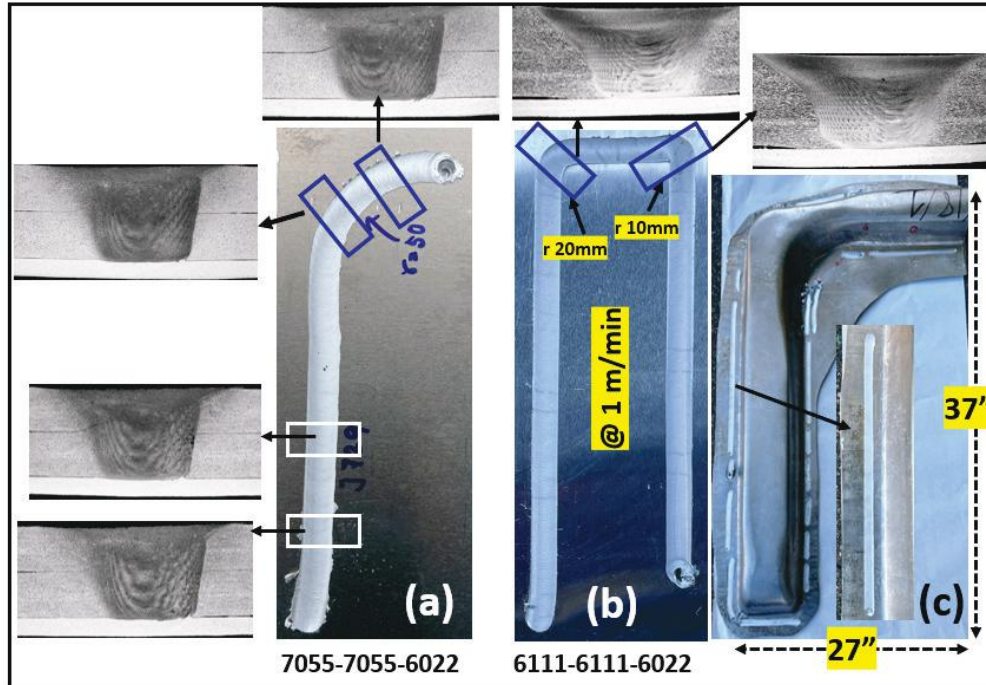


Figure II.4.1.32. Curve welding on (a) 7055-7055-6022 stack and (b) 6111-6111-6022 stack with a macrograph of cross-sections. (c) FSLW of demonstration stamped part (inset: ~ 500 mm long weld without any surface defect). Source: PNNL.

Friction Stir Welded Joint Strength Modeling (PNNL)

FSW joints contain microstructural features that may be responsible for reduced joint performance, such as voids and oxide layers. In addition, the material properties near the weld are heterogeneous. FEA simulation studies were carried out in this project to determine the role of each aspect of the joint's structure on its strength (i.e., structure-property relationships). In this report, the effect of fracture property variation was determined.

Specially designed single-edge notch bending coupons, which are shown in Figure II.4.1.3.8(a), were prepared by cutting out the top sheet of the three sheet AA7055 joint. A notch and a fatigue-induced pre-crack were made in the center of the sample such that the crack tip lies in the weld's stir zone. The same test coupon was made for the base metal too. These samples were bent until fracture to determine their fracture strengths. The parameters of the FEA simulations for the fracture model were determined by calibrating the strength of these tests. Subsequently, lap-joint strength simulations were carried out using these parameters. Figure II.4.1.3.8(b) shows that the simulation predicted the experimental strength with an error of less than 10%. The simulation strength when using base metal fracture properties was much higher, indicating that fracture property variation in the weld is critical in determining the joint strength of an FSLW joint.

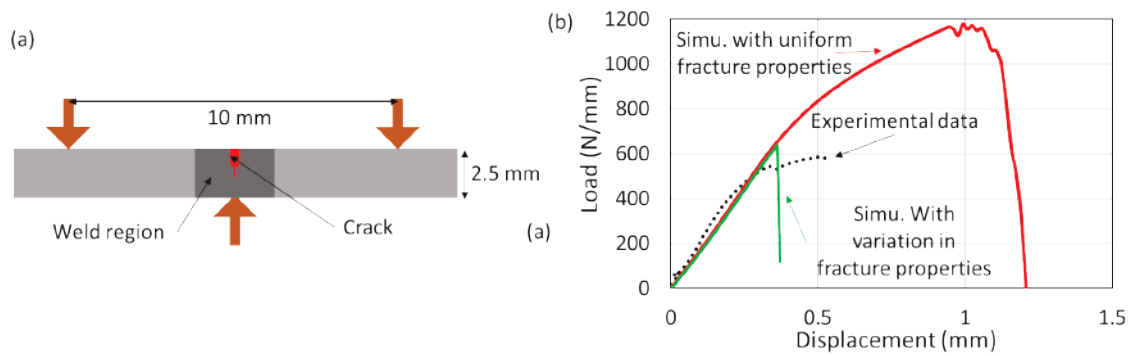


Figure II.4.1.33. (a) A schematic of the test sample used for the single-edge notch bending fracture tests. (b) Lap-joint load-displacement plots from the two simulations, with and without the weld fracture test data, as compared to the lap-shear test data. Source: PNNL.

Good prediction accuracy was also obtained for the T-Peel joint cut sections. This completes the structure-property relationship study of the FSW Lap and T-Peel joints. Process-property optimization can now improve efficiency by using this knowledge and focusing only on the influential aspects of the joint's structure.

Joints in real-life components would contain the whole weld of a finite length. In such cases, aspects of the three dimensional features of a joint, such as the exit location, could influence its strength. Cross-sections of the weld near the exit location indicate minimal joining around the hole, as indicated by limited mixed volume of material next to the exit hole. Simulations of a three sheet AA7075 T-Peel joint were used to determine the role of this ineffective joining around the exit hole on the joint's strength. The simulations considered were a base case with the ineffective joint and a case with an ideal joining around the exit hole. Using an extra dwell time at the exit location before the tool exits was expected to lead to an ideal joint. The material properties were determined through the characterization and calibration of the base joint's strength with the test data. The results in Figure II.4.1.3.9 show that calibration works, and the strength of the joint with ideal joining at the exit hole is larger by 18%. Experimental testing of joints with different dwell times at the exit hole showed that the strength increases by around 20–40%, thereby validating the simulation predictions.

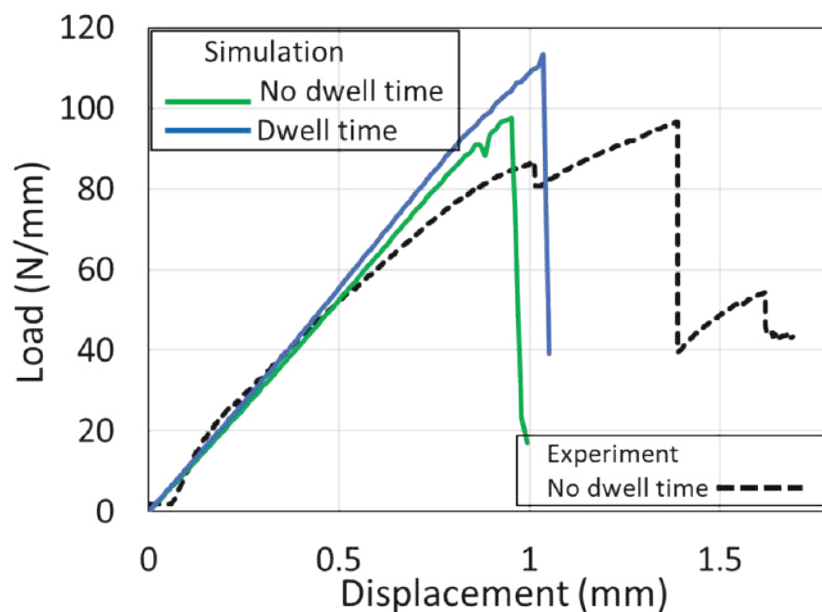


Figure II.4.1.34. The T-Peel load-displacement plots from the two simulations, with and without dwell time at the exit hole, as compared to the experimental data from a sample with no dwell time. Source: PNNL.

A 3T FSLW configuration that provides adequate crash performance with minimal cycle time in component is required. For instance, simulations need to determine the strength of various weld seams with a different number of welds and weld length combinations in a U-Peel joint. Figure II.4.1.3.10 shows the simulation results for a U-Peel joint under KSII-type loading. The simulation relied on the structure-property relationships determined earlier in this study to predict the strength of the joint with an error of less than 15% for this particular weld seam. Simulations for different weld seams predicted the experimentally observed trends, but the error was larger. In the future, simulations will incorporate the fracture test data in various other regions of the weld and improve meshing near the exit and plunge location to reach the targeted error of less than 20%.

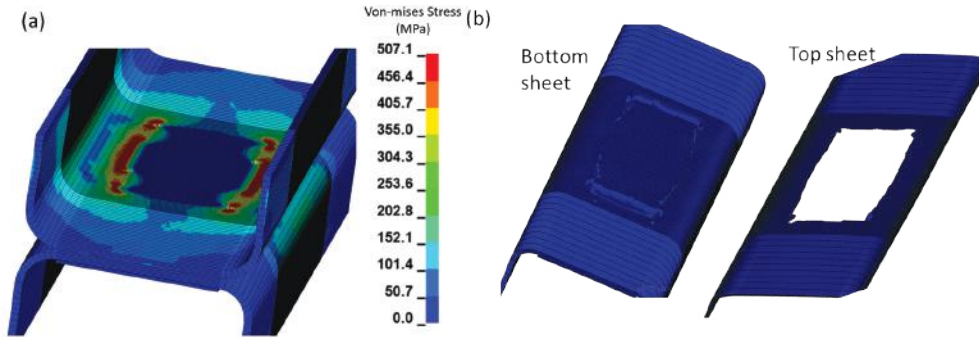


Figure II.4.1.35. Simulation results of U-Peel joint under KSII-type loading. (a) Von-Mises stress distributions just before fracture. (b) Bottom and top sheets after complete fracture of the joint. Source: PNNL.

F-SPR Process Development for Various Material Combinations (ORNL)

As a collaboration effort with PNNL for FSLW in Al-Al, ORNL refined the F-SPR process for spot-joining of high-strength Al7055 to Al7055. For the F-SPR joints, the mechanical interlocking distance between the flared rivet and bottom sheet is critical for performance. In addition, frictional heating is important to prevent Al7055 cracking due to low ductility at RT. Frictional heat and axial plunge force will also promote solid-state joining between the rivet and the surrounding material if they are metallurgically compatible. This solid-state bonding will add to the mechanical strength. With support from numerical modeling, we were able to refine designs of rivets and the back support die to achieve good mechanical joint performances, as summarized in Table II.4.1.3.1. Averaged lap-shear fracture was 11.31 ± 0.4 kN, while averaged cross-tension failure load was 5.82 ± 1.35 kN, thus achieving 51.9% of lap-shear failure load. Cross-tension fracture load exceeded the evaluation criteria suggested by our industry partner (e.g., 30% of LSS). All tested lap-shear and cross-tension coupons showed a fracture at the bottom of the Al7055 sheet, indicating strong mechanical interlocking between the flared rivet leg and the bottom sheet.

Table II.4.1.3.1. Summary of Mechanical Joint Performances for F-SPR Al7055-Al7055 Joints

Joint Configuration	Avg. Peak Failure Load (kN)	Avg. Elongation at Failure (mm)	Failure Location
Lap-Shear Coupon	11.31 ± 0.4	4.78 ± 0.34	Bottom Al pullout
Cross-Tension Coupon	5.82 ± 1.35	10.16 ± 2.41	Bottom Al pullout

As illustrated in Figure II.4.1.3.11(a) and Figure II.4.1.3.11(b), we are trying to avoid excessive clamps for FSLW by using F-SPR spot tack joint. This will help to reduce the number of clamping needs for 3T FSLW. In addition, the F-SPR joint can provide additional mechanical strength along with FSLW joint strength. Therefore, this unique and hybrid approach will be more beneficial to industry readiness for high-volume production, as well as to further improve joint strength by combining strength from both F-SPR and FSLW. After we achieved good mechanical joint strength for Al7055-Al7055, we made two F-SPR tack joints on scaleup Al7075 coupons measuring 3 in. wide \times 4 in. long for FSLW at PNNL. Four Al7055 tack joints were made and shipped to PNNL for FSLW trial.

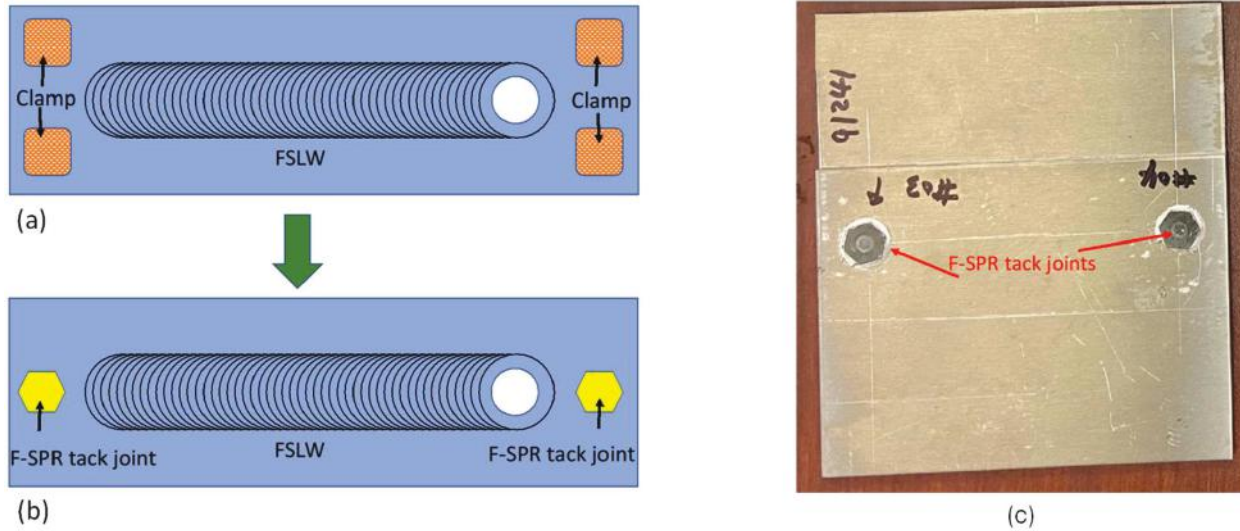


Figure II.4.1.36. (a) Experimental and simulated load vs. displacement lap-shear test results. (b, c) Equivalent plastic strain distributions at peak load for the case: (b) without bonding; and (c) with a metallurgical bonded interface. (d) Experimental failure morphology showing a rivet bonded with DP590. Source: PNNL.

After successful F-SPR process development for the Al-Al coupons, we moved to Al7055-thermoset CFRC process development and evaluated mechanical joint performances of metal-polymer F-SPR joints from lap-shear tensile, cross-tension, and fatigue testing. In particular for fatigue testing, we were suggested to study how piercing a rivet into CFRC will affect CFRC performance. Figure II.4.1.3.12 summarizes the (a) lap-shear tensile (e.g., four samples), (b) cross-tension (three samples), and (c) fatigue testing of the TS for the CFRC-Al7055 joint. For fatigue testing, different peak loads (i.e., 2.63, 1.75, and 1.1 kN) were examined as suggested by our industry partner. An R ratio of 0.1 and a frequency of 20 Hz were used for fatigue testing using lap-shear coupons. When the sample reached 1 million cycles, testing was stopped to save testing time for other samples. Three samples were then used for each peak load for statistical study. The average fracture load from the lap-shear tensile testing process was 5.33 kN, exceeding the milestone target strength of 5 kN. Failure mode was shear out of CFRC. The average fracture load for the cross-tension coupons was 3.12 kN, higher than the target milestone value of 30% of LSS. Failure mode for cross-tension tested samples was rivet pullout. For fatigue testing, the fracture location for all fatigue-tested samples was the bottom Al sheet, showing typical eyebrow crack, rather than CFRC. This eyebrow crack failure occurred due to fretting wear and this failure mode is widely observed for self-piercing riveted joints from the open literature. From the fatigue testing, it can be concluded that CFRP damage caused by rivet piercing does not significantly affect fatigue performance, which is important for automotive applications in real-life. We evaluated the LSS for 1 million cycles tested Al-CFRC joint and the retained lap-shear failure load (5.38 kN) is similar to the average lap-shear fracture load (5.33 kN) of pre-fatigue-tested joints.

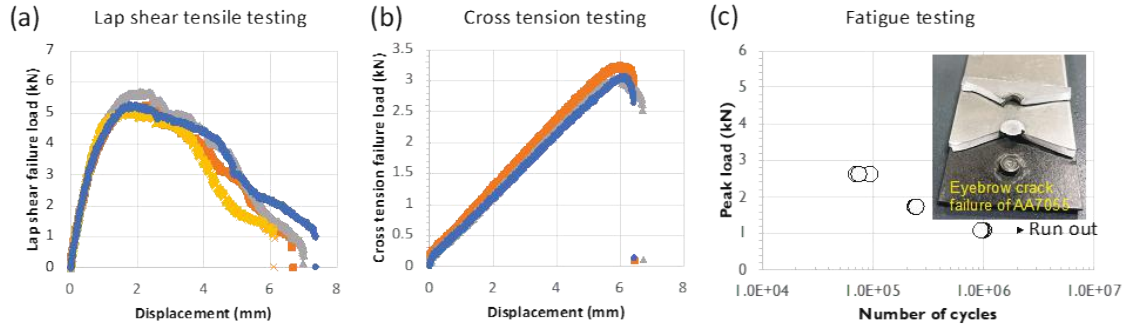


Figure II.4.1.37. Summary of mechanical joint performances for Al7055-CFRC F-SPR joints. (a) Load vs. displacement curves from lap-shear tensile testing. (b) Load vs. displacement curves from cross-tension testing. (c) S-N curve from fatigue testing, showing Al fracture after fatigue testing. Source: ORNL.

In general, it is difficult for the conventional rivet from the self-piercing riveting process to pierce into steels where the TS of target steel substrate is greater than 780 MPa. Also, it always produces a crack on steel substrate [2]. This is because advanced/ultra-high strength steels have low ductility and formability at RT. Therefore, an auxiliary heating system is required to increase ductility and formability at elevated temperature prior to joining step, leading to additional time, cost, and complex joining steps. To overcome such technical challenges, the F-SPR process was further applied for 7055 and DP 980 steel consisted of ferrite and martensite (TS=1060 MPa) [3]. It also has low ductility and formability at RT. Again, frictional heat generated during the joining step can improve local ductility and formability of DP980 at elevated temperature, so a crack-free joint can be achieved. F-SPR process parameters, such as spindle speed, axial plunge speeds, and axial plunge depths, were varied to achieve the highest lap-shear tensile failure load and crack-free joints.

The high-fidelity model was used to guide the experiment design toward improved joint quality and strength. Both the interface temperature and pressure between dissimilar material have critical factors in selecting the appropriate rivet material and heat-treatment method. In addition, the maximum principal stress and strain determines whether the sheet will crack depending on the material property of base material and compatibility of die and rivet design. Through the numerical simulation of the F-SPR process, such factors can be optimized to accelerate the process development cycle.

The process parameter, including spindle rotation speed and plunging depth, can affect the interface temperature and mechanical interlocking behavior. Through a case study by numerical model, the optimum plunging speed can be identified to provide initial processing parameters for the experimental trials. Figure II.4.1.3.13 is a plot of interlocking distance at different plunging depths. It is clear that the interlocking distance is positive before reaching a plunging depth of about 0.2 in. and then becomes negative due to large hydrostatic pressure from the bottom of the die cavity. Such prediction is consistent with the experimental observation and the processing window of UHSS to an Al alloy F-SPR joining is found to be narrow compared with that of the Al-Al similar material joining.

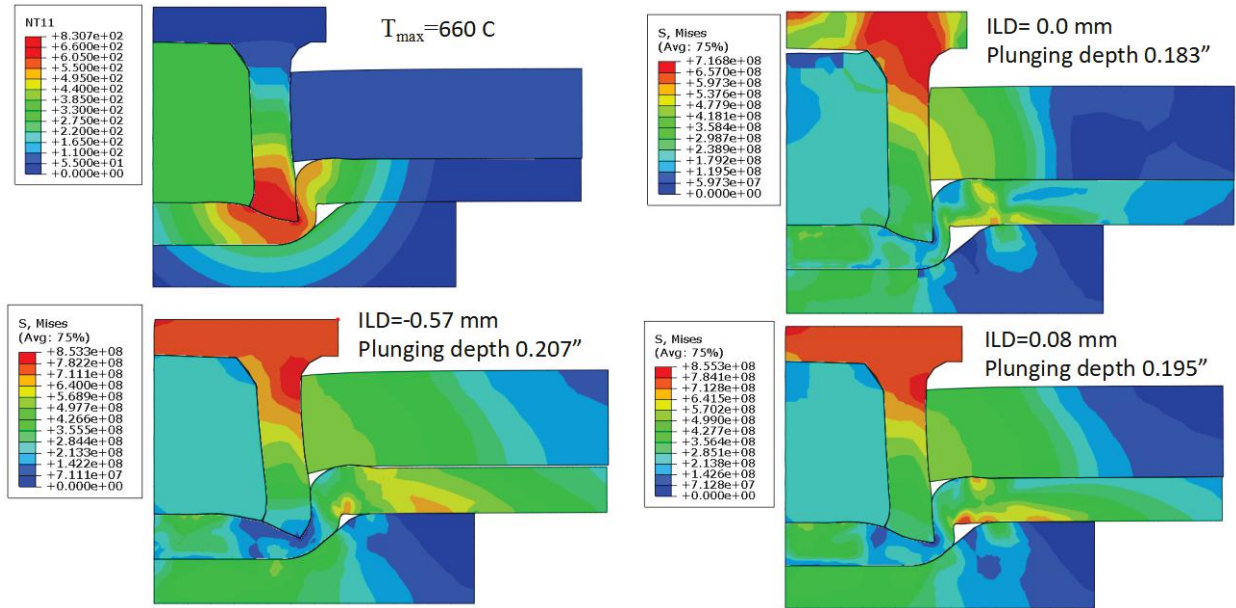


Figure II.4.1.38. Temperature distribution for a two-dimensional axisymmetric model and Mises stress plot showing the rivet shape under different plunging depths. ILD stands for interlocking distance. Source: ORNL.

The die geometry feature, such as cavity depth and fillet size, has considerable influence on joint quality. Figure II.4.1.3.14 shows the interlocking distance in the case of die design with a smooth transition and a steep transition. At a similar plunging depth of 0.2 in., the interlocking distance is 0.08 mm and 0.25 mm, respectively; thus, the mechanical strength will be improved in the steep transition case. In addition, the die cavity depth can enable large interlocking, but it can induce cracking on the bottom of the steel sheet.

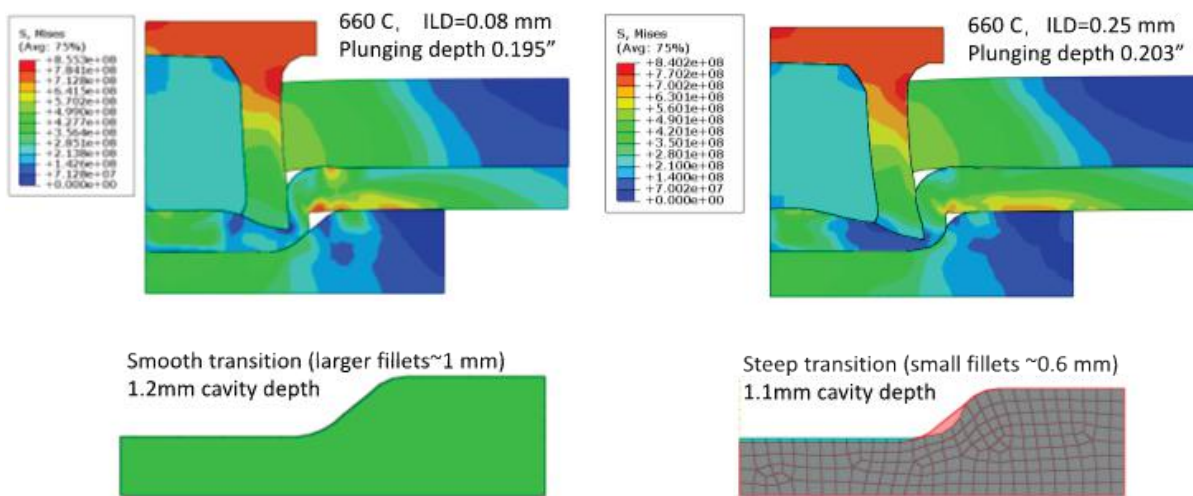


Figure II.4.1.39. The stress plot for different die shapes. ILD indicates the interlocking distance between the rivet and the bottom sheet. Source: ORNL.

Based on guidance from numerical modeling of Al-steel combination, F-SPR process for Al-DP980 was refined. Based on visual inspection and cross-sectional analysis, no crack on DP980 was observed. This is because frictional heat improves local ductility and formability of steel substrate. Figure II.4.1.3.15 presents load and displacement curves from (a) lap-shear and (b) cross-tension testing for Al7055 and DP980 material combination. Averaged lap-shear and cross-tension fracture loads are 9.83 ± 0.3 kN and 5.3 ± 0.77 kN,

respectively. Similar to Al-Al and Al-CFRC material combinations, cross-tension failure load exceeds the 30% of lap-shear fracture load as evaluation criteria. The failure location for lap-shear tensile-tested samples is consistently found at the fracture of the rivet, while rivet pullout of DP980 was found for cross-tension tested samples. Before the rivet pulled out of the DP980, deformation of steel substrate occurred ranging from 5–10 mm elongation at failure, as shown in Figure II.4.1.3.15(b), indicating a strong joint between the rivet and the bottom steel sheet.

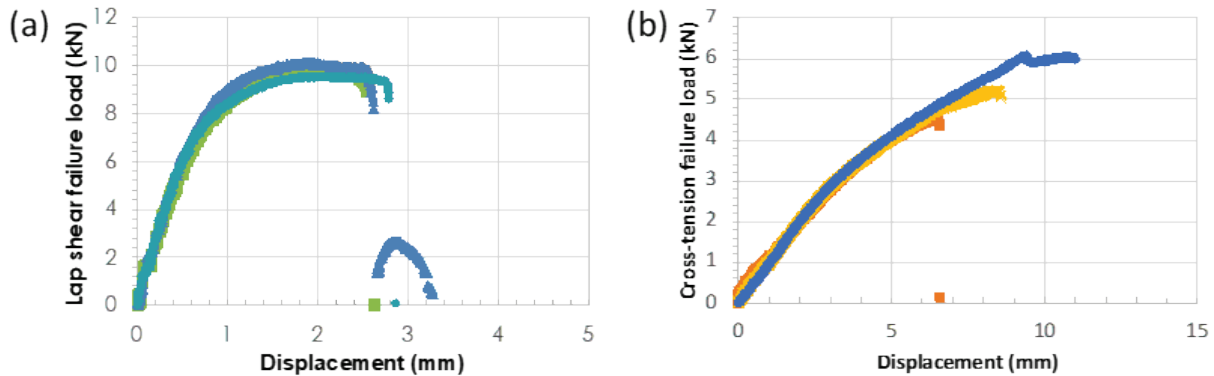


Figure II.4.1.40. Summary of mechanical joint performances for Al7055-DP980 F-SPR joints. (a) Load vs. displacement curves from lap-shear tensile testing. (b) Load vs. displacement curves from cross-tension testing. Source: ORNL.

The F-SPR technique has been developed and refined for various higher specific strength materials (e.g., Al, CFRC, UHSS), which are mostly low ductility materials at RT. Therefore, the cracking issue is a great technical challenge to make sound joints. With an aid from frictional heat generation during joining, crack-free joints were produced, while strong mechanical joint performances were achieved without an auxiliary heating system. A single class joining process with or without minimal modification for lightweight dissimilar materials in BIW automotive structures is highly desired for wide applications in automotive industries. During the project period, we were able to successfully demonstrate a single class F-SPR joining process for different materials combinations in a laboratory coupon-scale by using a bench-top machine at ORNL. To scaleup joining process and join demonstration parts, a C-frame type welding head system was developed and fabricated by the equipment manufacturer, as shown in Figure II.4.1.3.16. This new system has an automated clamping and automated rivet feeding system, which is more suited for a high-volume production environment and is more relevant to industrial readiness of multimaterial joining in automotive applications. We evaluated the functionality of this new joining system by using a vendor's equipment for our selected materials and found that mechanical joint performances were comparable to our results. This new system will be further validated and refined for repeatability of multiple joints at scaleup coupons and joining of prototype demonstration parts for the rest of the project period.

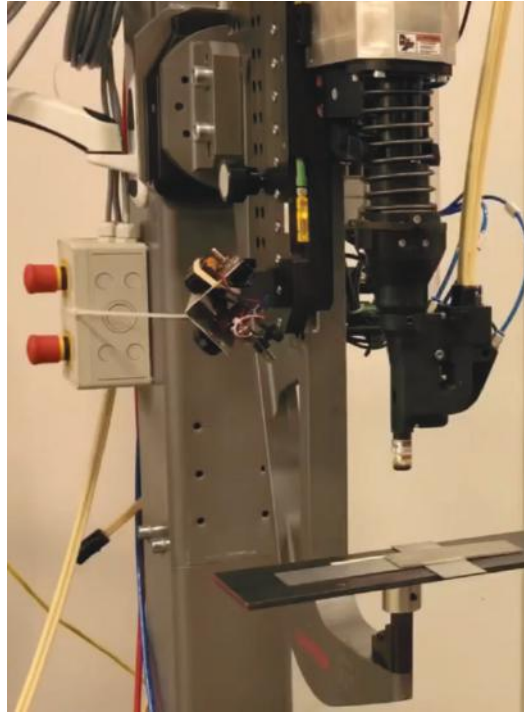


Figure II.4.1.41. New F-SPR weld system with C-frame for joining of demonstration parts. Source: ORNL.

Conclusions

This multi-laboratory project is aimed at maturing two solid-phase joining techniques to overcome several identified technological barriers towards enabling dissimilar Al assembly with Al/CFRC and Al/Steel joining in high-volume applications. In FY 2022, the project team at PNNL (developing FSLW for 3T Al joints) and ORNL (developing F-SPR for 2T/3T material stacks) focused on refining the joining technology, demonstrating higher coupon level mechanical joint performance on industry-selected material stack-up.

FSLW was successfully transferred to a robotic platform at a commercially viable welding speed of 1 m/min for the 7xxx stack and 2 m/min for the 6xxx stack. A coupon level milestone set by our OEM collaborator for lap-shear and T-Peel strength for both 3T stack of 7075-7075-6022 and 6111-6111-6022 has been achieved in the robotic platform along with a repeatability study showing strength variation within $\pm 10\%$. Two-dimensional curve welding for 3T 7055 and 6111 stack have successfully been demonstrated. Our team is now working towards the goals of the third year of the project, which includes the ability to make a 3T welding demonstration of a prototype stamped part and reducing cycle time for stitch welding. The structure to property model has been improved to include fracture properties of the joint obtained from experimental measurements. Component level modeling has been initiated after attaining the milestone of predicting coupon level joint strength.

With computational modeling support, the F-SPR process was further refined for spot-joining of various material combinations high-strength Al-Al, CFRC-Al, and Al-UHSS as a single class joining process. Friction heat generated during the joining process suppresses the formation of cracking for high-strength and low ductility on Al and UHSS sheets. Superior mechanical joint properties from lap-shear and cross-tension testing also were achieved in the laboratory coupon level. A new welding system has been developed and fabricated from the equipment manufacturer for joining of demonstration parts for the rest of the project period.

Key Publications

1. Li, Y., Y. C. Lim, H. Huang, J. Chen, and Z. Feng, 2022, “The role of rotational speed on the joint strength of frictional self-piercing riveting of AA7055-T76/AA7055-T76,” *Advances in Welding and Additive Manufacturing Research Conference*, 12–17 June 2022, Virtual.
2. Lim, Y. C., J. Jun, H. Huang, J. Chen, Y. Li, Y. Wang, J. K. Keum, Y. F. Su, D. N. Leonard, and Z. Feng, 2022, “Recent progress in multimaterial joining for lightweight vehicle application,” *International Welding and Joining Conference*, 4–7 October 2022, Jeju Island, Republic of Korea (**Invited**).
3. Lim, Y. C., H. Huang, Y. Li, Y. Wang, and Z. Feng, 2022, “Joining of carbon fiber reinforced composite to lightweight metals by friction self-piercing riveting,” *Advances in Welding and Additive Manufacturing Research Conference*, 12–17 June 2022, Virtual.
4. Upadhyay, P., Y. C. Lim, et al., 2022, “Solid-state joining of multimaterial autobody parts toward industry readiness,” DOE Vehicle Technology Offices Annual Merit Review, 21–23 June 2022, Washington, D.C., USA.

References

1. Meng, X., Y. Huang, J. Cao, J. Shen, and J. F. dos Santos, 2021, “Recent progress on control strategies for inherent issues in friction stir welding,” *Prog. Mater. Sci.*, Vol. 115, Art. 100706. <https://doi.org/10.1016/j.pmatsci.2020.100706>.
2. Sakiyama, T., G. Murayama, Y. Naito, K. Saita, Y. Miyazaki, H. Oikawa, and T. Nose, 2013, “Dissimilar metal joining technologies for steel sheet and aluminum alloy sheet in auto body,” *Nippon Steel Technical Report*, No. 103, May 2013. Available at: <https://www.nipponsteel.com/en/tech/report/nsc/pdf/103-14.pdf> (last accessed 31 March 2023).
3. Taniguchi, K., Y. C. Lim, A. Flores-Betancourt, and Z. Feng, 2020, “Transient microstructure evolutions and local properties of DP 980 MPa grade steel via friction stir spot processing,” *Materials*, Vol. 13, No. 19, Art. 4406. <https://doi.org/10.3390/ma13194406>.

Acknowledgements

At PNNL, H. Das and S. Shukla performed the welding and data analysis; K. Balusu and A. Soulamani performed and supervised the modeling work; C. Smith provided robotic welding guidance and support; T. Roosendaal, R. Seffens, and E. Nickerson performed the mechanical testing; and A. Ortiz, A. Guzman, and M. Blazon performed the metallography and hardness testing. At ORNL, R. Davies, Z. Feng, and A. Hayes are recognized for their leadership and technical guidance, while H. Huang is acknowledged for the modeling work and Y. Li and Y. Wang for characterization. Technical guidance and material support from E. Boettcher at Honda R&D America and R. Long at Arconic are also acknowledged.

II.4.1.4 Surface Modifications for Improved Joining and Corrosion Resistance (Pacific Northwest National Laboratory, Oak Ridge National Laboratory, and Argonne National Laboratory)

Yong Chae Lim, Co-Principal Investigator

Oak Ridge National Laboratory
One Bethel Valley Rd.
Oak Ridge, TN 37831
E-mail: limy@ornl.gov

Vineet V. Joshi, Co-Principal Investigator

Pacific Northwest National Laboratory
900 Battelle Blvd.
Richland, WA 99352
E-mail: vineet.joshi@pnnl.gov

Dileep Singh, Co-Principal Investigator

Argonne National Laboratory
9700 S. Cass Ave.
Lemont, IL 60439
E-mail: dsingh@anl.gov

Christopher Schooler, DOE Technology Development Manager

U.S. Department of Energy
E-mail: christopher.schooler@ee.doe.gov

Start Date: October 1, 2020 End Date: September 30, 2023
Project Funding (FY 2022): \$1,000,000 DOE share: \$1,000,000 Non-DOE share: \$0

Project Introduction

PNNL, ORNL, and ANL are teaming to develop a combination of adhesive-based bonding and high-rate mechanical hybrid joining methods (i.e., utilizing adhesives along with mechanical fastening joining techniques) for multimaterial systems to reduce vehicle weight. Specifically, this project will demonstrate the potential of laser or atmospheric plasma surface treatments to achieve high-quality aluminum (Al) alloy-galvanized steel and Al-CFC joints that also offer improved bulk substrate and galvanic corrosion resistance. We will utilize several joining techniques, including ultrasonic spot-welding, friction-based fastener joints, and adhesive bonding, which were developed as a part of the first phase of the Joining Core Program, for this effort. The team will also collaborate with other projects in Phase 2 of the project to leverage the understanding of the surfaces and improve joint performance.

Corrosion mitigation (e.g., general and galvanic corrosion) in the joints of dissimilar materials is a key technical challenge that must be overcome to successfully integrate candidate lightweight autobody structures from materials such as Al alloys, CFRP composites, magnesium (Mg) alloys, and steels [1–3]. Galvanic couples forming at the joint interface of two different materials can greatly accelerate the corrosion of the more anodic material (i.e., Al alloys can suffer from accelerated corrosion when coupled with steels and stainless steels) [4]. If a mechanical fastener is utilized in the joining process, additional galvanic coupling interfaces can be formed [5]. Surface modification strategies can potentially be used to enhance the general corrosion resistance of the bulk substrate [6], as well as to form the electrical isolation between the joint materials to minimize the galvanic effects [7]. However, surface modifications change the surface chemistry and surface

morphology of the substrates. These chemical and/or morphological changes on the surface influence the surface energy affecting adhesive wetting and bonding performance. The key challenge is to define the extent to which corrosion protection and galvanic isolation can be achieved without compromising joint quality utilizing surface modification processes that are also amenable to high-volume vehicle production.

Laser and atmospheric plasma (AP) surface treatments are being investigated as an effective way to clean local surfaces for improved joining performance as compared with conventional chemical cleaning. Additionally, these methodologies can be scaled-up for high-volume automotive production through integration with automatic translation stages or a robotic system. These treatments are also capable of controllably growing oxide and related ceramic phases on alloy substrates that can offer enhanced corrosion protection. Three key aspects will be addressed: (1) how the chemistry, morphology, and thickness of these surface-modified layers evolve on selected Al alloys (or galvanized steel) and CFRP composite surfaces; (2) how they impact joining processing and adhesive adherence; and (3) if they can significantly increase bulk corrosion resistance and also mitigate galvanic coupling effects between the Al and the galvanized steel by electrically insulating the interface(s).

Objectives

In this project, we will specifically focus on optimizing the treatment/modification of different faying surfaces to improve the corrosion resistance, as well as adhesion. The surface optimization techniques being utilized are laser- and AP surface treatments. These techniques are becoming established as an effective way to clean local surfaces for improved joining characteristics as compared with conventional chemical cleaning and can also offer enhanced corrosion protection as aforementioned. The project will also evaluate the effect of the riveting process on cured and uncured adhesively bonded joints.

Approach

The surface optimization techniques being utilized are laser and AP surface treatments. Corrosion properties of metal surfaces are being evaluated in post-laser- and AP-treated Al alloys and steel using both macroscopic and microscopic electrochemical measurement techniques. SEM with EDS is used to characterize the sample morphology and chemical element distribution before and after surface modification. Tafel and EIS are recorded in the bulk and locally modified regions. Advanced characterization techniques including optical profilometry, XPS, Fourier-transform infrared spectroscopy (FTIR), STEM, and contact angle measurement are used to study pre- and post-surface-modified samples. Experimental data will be compared to corrosion modeling and joint strength simulations to improve the model prediction to allow for optimum conditions to reach the fullest potential of the joint strength.

Corrosion properties of metal surfaces are being evaluated in post-laser- and AP-treated Al alloys and steel using macroscopic and microscopic electrochemical measurement techniques. Scanning electrochemical cell microscopy (SECCM) is being employed to probe the microscopic corrosion response of pre- and post-treated surfaces. A micron-sized theta probe with $\sim 10\ \mu\text{m}$ diameter and 0.01 M sodium chloride (NaCl) solution was used for localized electrochemical measurement. Multiple point analyses were carried out on top of the flat sample surfaces at multiple locations. Measurements were also performed successfully immediately after PT. Tafel and EIS were recorded at each location. Long-term corrosion tests were conducted on rivet samples with combinations of PT and adhesives. Finally, to understand the role of rivet geometry on corrosion performance, COMSOL multiphysics modeling was performed and combined with sensitivity analysis for pre- and post-plasma-treated samples.

Results

Surface-Treatment on 7xxx Al by Laser and AP Processes (ORNL)

The control of surface chemistry is critical to achieve high-quality, adherent joints and minimize the impacts of galvanic coupling of dissimilar materials on corrosion susceptibility. In this project, we focused on Al-CFRP and Al-steel joints to further optimize joining and mitigate galvanic corrosion risk. First, the cleaning of Al surfaces, as well as controlled growth of aluminum oxide (Al_2O_3) and related oxides for improved corrosion

resistance were pursued by laser and AP techniques, with benchmarking to anodized Al surfaces. We used a pulsed Nd:YAG (wavelength of 1064 nm) laser system at ORNL for Al7075-T6 and found improvement of corrosion resistance by EIS measurement [8]. Unfortunately, the pulsed laser system experienced a controller failure, which we were not able to fix due to the pandemic. For this reason, we used a continuous wave laser at ORNL, as shown in Figure II.4.1.4.1(a) to continuously investigate surface modification to improve corrosion resistance of Al7075-T6. Because Al7075-T6 is well-known for hot-cracking, crack-free surface-treatment conditioning was studied by varying laser power, scan speed, and focal spot size. Finally, downselected process parameters were used for scanned surface-treatment as a next step. Al coupons measuring 1 in. \times 1 in. were cut and cleaned with alcohol to remove any dirt or oil residue. Then, laser surface-treatment was applied in a 1 in. \times 1 in. scan area that is large enough for EIS measurement to study the effectiveness of corrosion improvement. The EIS technique in 3.5 wt.% NaCl solution at RT was used to access the macroscopic corrosion behavior of the Al7075-T6 with and without laser surface-treatment. The impedance data from the measurements were fitted using equivalent circuit models to determine corrosion reaction resistance, R_2 or $R_2 + R_3$. In the two equivalent circuits, R_1 indicates solution resistance, R_2 and R_3 are charge transfer resistance in single and double Resistance-Constant Phase Element models, respectively, where R_2 indicates film resistance. Figure II.4.1.4.1(b) presents the Nyquist impedance plot of the baseline 600-grit silicon carbide finish and 75, 100, and 150W laser power treated Al7075-T6. The impedance spectra of the laser-treated Al7075 exhibited two arcs, unlike the baseline Al7075 with one depressed semi-circles, suggesting that the laser-treated samples had both a corrosion interface and film resistance elements, while the resistance of baseline samples was primarily from corrosion interface without any effective film resistance. The impedance scales were greater in laser-treated Al7075 due to the presence of the second arcs associated with film resistance.

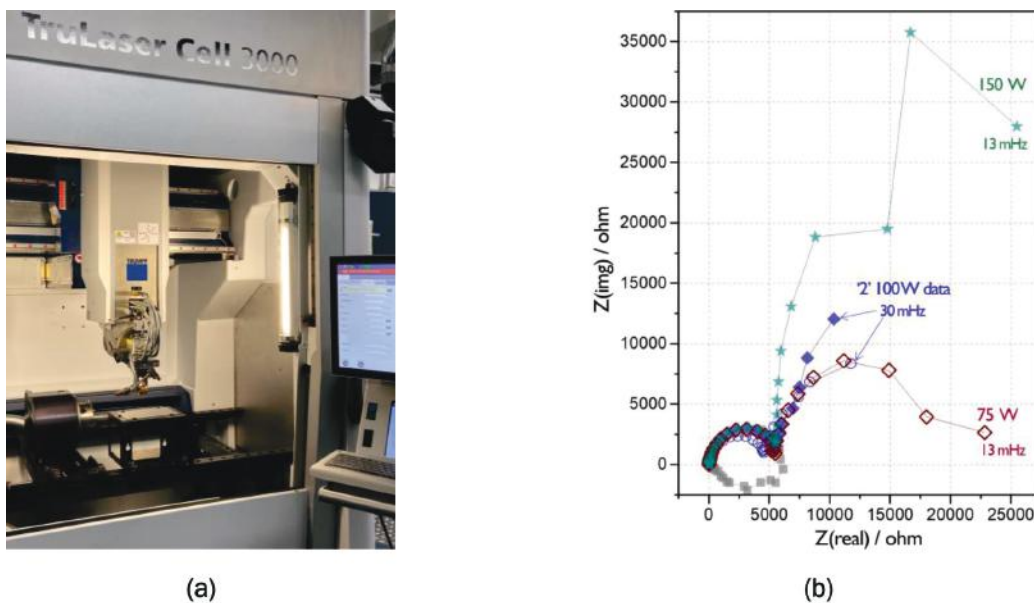


Figure II.4.1.42. (a) Continuous wave laser system at ORNL. (b) A Nyquist impedance plot of baseline 600 grit finish (grey squares) and 75, 100, and 150W laser-treated Al7075. Source: ORNL.

Impedance data fitting was performed to determine R_2 for the baseline and $R_2 + R_3$ for the laser-treated samples as their corrosion reaction resistance values. These resistance values of the baseline, pulsed laser, and continuous wave laser-treated Al7075 samples under different energy and power inputs are summarized in Table II.4.1.4.1. The average resistance values of all laser-treated samples were greater than the values of baseline Al7075. In addition, the pulsed laser-treated samples (e.g., 1.2J) shows a higher impedance than the 150W laser power case because the higher energy pulsed laser beam created more effective cleaning of the natural oxide and allowed the growing of a fresh oxide after local melting. However, it should be noted that a more statistical study should be conducted for the pulsed laser.

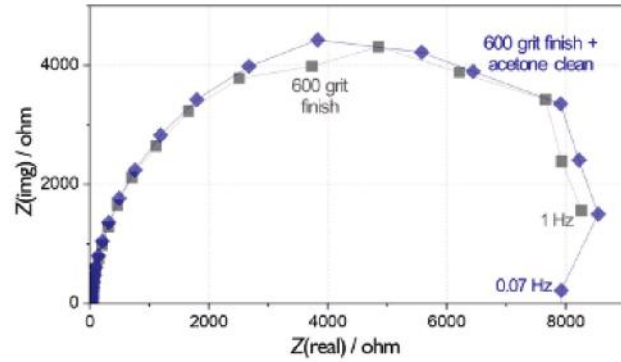
Table II.4.1.4.1. Summary of EIS Impedance for Baseline, Laser-treated, and Open-air Plasma-treated Al7075

Sample Condition	Average Corrosion Reaction Resistance ($\Omega \text{ cm}^2$)	Improvement
Baseline, 600-grit (control)	6500 \pm 1600	--
Pulsed Laser (1.2J)	30801.5	4.63 \times
Continuous Laser (150W)	17320	2.6 \times
Open-air PT #12	506500	76 \times
Open-air PT #14	934500	140 \times

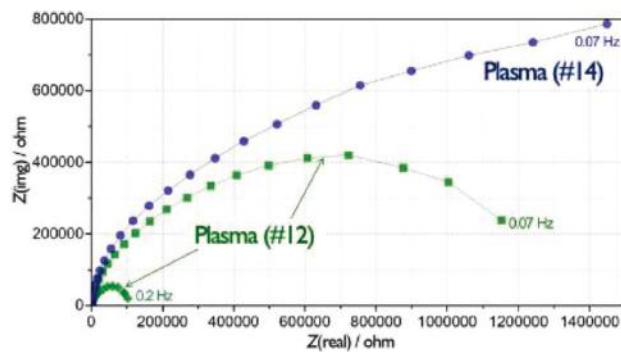
In parallel to the laser surface modification studies, AP surface treatments were evaluated as a second method for surface-cleaning and oxide growth on the Al alloy surface. During our FY 2021 and FY 2022 efforts, we discovered some corrosion resistance improvement for Al7075 by using this AP system. However, we faced a repeatability issue due to nozzle degradation and unstable power during surface modification. For this reason, we employed a new AP system from a new manufacturer to further develop and improve Al7075 corrosion resistance. Below, we report new results for open-air plasma-based Al7075 surface modification, as well as its corrosion improvement. Recently, we completed the integration of this new technique with a robotic system, as shown in Figure II.4.1.4.2(a), for more 3D part treatment to be relevant to industrial application. All open-air PTs were conducted on the same size coupons with the same scan area used for laser surface modification. Based on initial EIS results and assessment on sample deformation, open-air plasma processing conditions were downselected and a summary of Nyquist plots for baseline Al7075 and open-air plasma-treated Al7075 are presented in Figure II.4.1.4.2(b) and Figure II.4.1.4.2(c). The Al7075 sample with a 600-grit silicon carbide finish, with and without acetone wash, showed similar impedance spectra, indicating there was no impact of acetone rinse (i.e., a pre-cleaning step for plasma-oxidation) on corrosion behavior, as observed in Figure II.4.1.4.2(b). Note that these untreated Al7075 samples showed impedance values that were lower than $1 \times 10^4 \text{ ohm}\cdot\text{cm}^2$ in Z(real) axis. However, when two different plasma-oxidations were applied on Al7075, the impedance spectra of plasma-oxidation treated Al7075 showed distinctively higher values (e.g., greater than $1 \times 10^6 \text{ ohm}\cdot\text{cm}^2$ in Z(real) axis) in #12 and #14 samples, as well as a higher value (e.g., greater than $1 \times 10^5 \text{ ohm}\cdot\text{cm}^2$ in Z (real) axis) for another #12 sample, indicating that these plasma-oxidation treated samples were more resistant to corrosion.



(a)



(b)



(c)

Figure II.4.1.43. (a) New AP system integrated with a robotic system at ORNL. (b) A Nyquist impedance plot for baseline Al7075. (c) A Nyquist impedance plot for AP-treated Al7075. Source: ORNL.

Changes of chemical element/groups for baseline Al7075 (control) and representative open-air plasma-treated Al7075 samples were analyzed by XPS with Ar-ion beam etching. For the control sample, the total etch time was 1275 seconds, while the total etch time for the open-air plasma-treated sample was 2685 seconds. The equivalent depths (assuming that the 12 nm/min etch rate was accurate for Al7075) would be 255 nm and 537 nm, respectively. This was an initial attempt to investigate chemical element change in thickness direction, so the total etch time may be longer for much deeper depth for future characterization efforts. Figure II.4.1.4.3 summarizes the depth profiles for both cases. Figure II.4.1.4.3(a) presents a full depth profile for the controlled sample with the Al 2p peak fit to show both the Al-metal and the Al oxide (native oxide), while Figure II.4.1.4.3(c) shows a close-up of the Mg, Zn, and Cu signals. The surface of the control shows that it is enriched in Mg (~3-4 at.%) as compared to the Mg-bulk value. The Mg profile continually decreases with further etching until it reaches its bulk value at ~500 sec of etching. The initially small Zn and Cu signals increase while the Mg is decreasing and eventually reach near their bulk values by ~500 sec. of etching. Figure II.4.1.4.3(b) depicts the depth profile for the open-air plasma-treated Al7075 sample, while Figure II.4.1.4.3(d) shows the Al-metal, Mg, Cu, and Zn at a finer scale. The Al oxide and O signals do not change much during the depth profile, indicating the formation of thick Al₂O₃ oxide (> 500 nm) as compared with the control case (2~3 nm). This may be the reason why EIS impedance for the open-air plasma-treated sample is much higher than observed in the control case, as previously summarized in Table II.4.1.4.1. At the 500 sec. point, the Al-metal emerges, but this is likely due to thin spots and pinholes and not the removal of the outer Al oxide layer. In Figure II.4.1.4.3(d), the initial surface again shows enrichment of Mg and Zn, and that as etching continues, the signals decrease. The Cu remains very low throughout the profile but is present.

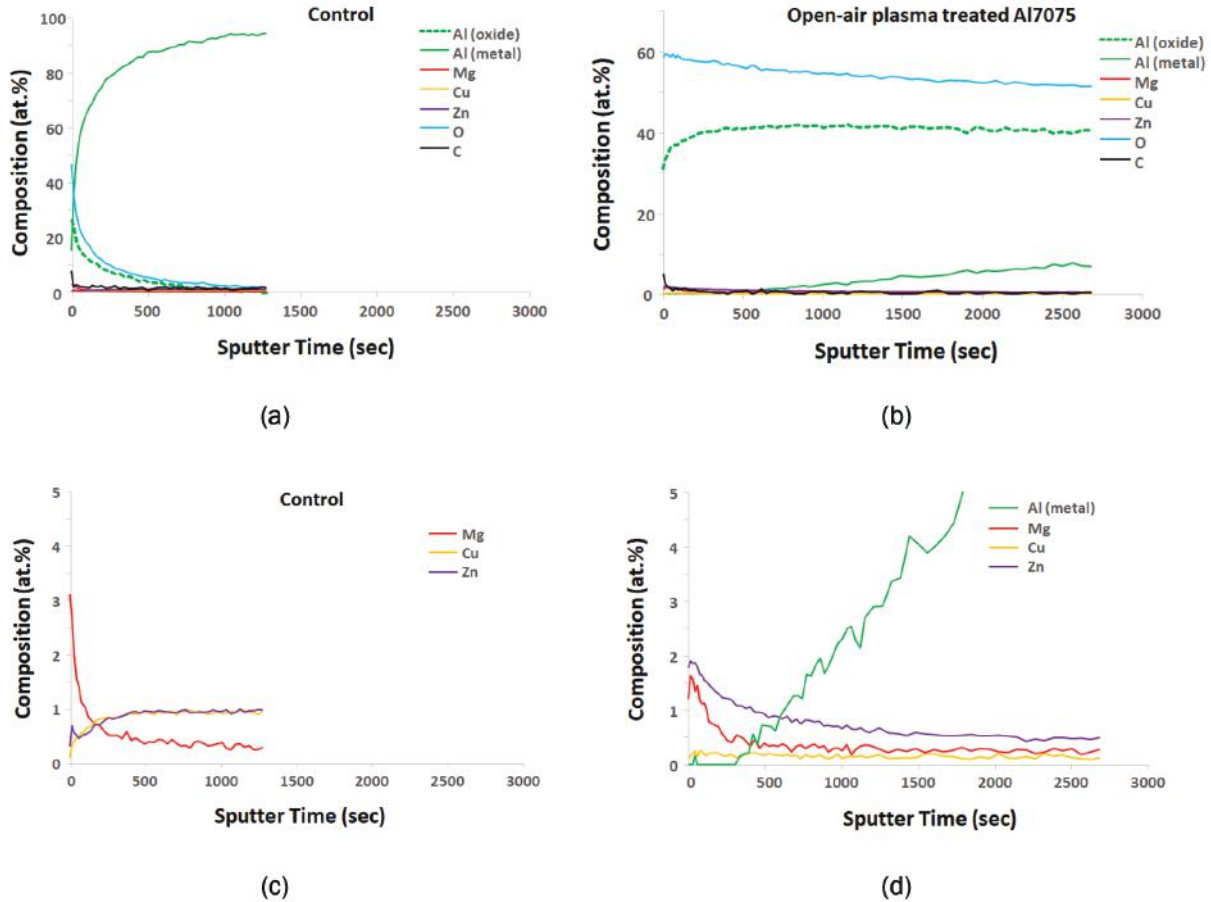


Figure II.4.1.44. Depth profiles by XPS: (a) and (c) show the baseline Al7075 (control); (b) and (d) show the open-air plasma-treated Al7075. Source: ORNL.

Figure II.4.1.4.4 presents SEM images with EDS chemical element maps and a depth profile for cross-sectioned open-air plasma-treated Al7075. Thick, globular, and continuous Al and O distribution can be seen on the top surface. Due to low magnification SEM analysis, it is not possible to differentiate other oxide formation, such as Mg or Zn. Therefore, a much higher magnification analysis, such as STEM, is required. From a SEM depth profile, Al₂O₃ thickness is approximately 1 μm, which is a comparable result from the initial XPS depth profile (> 500 nm).

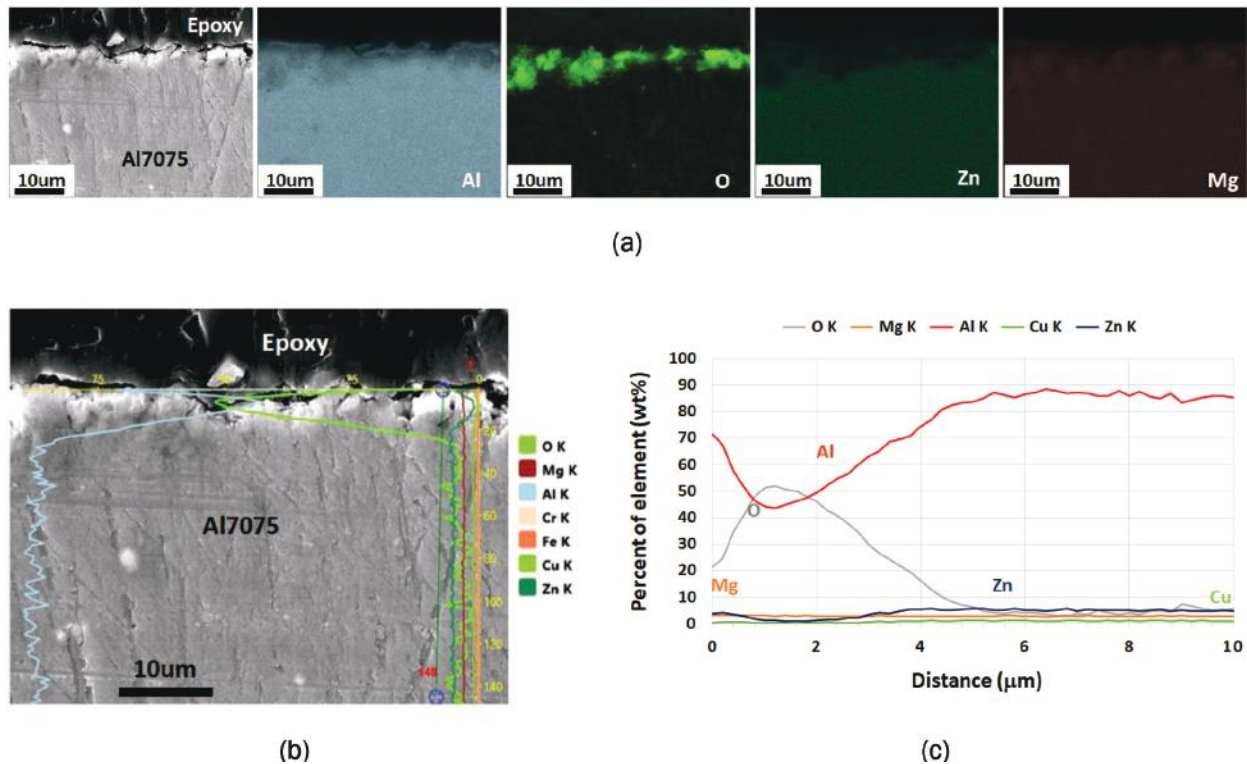


Figure II.4.1.45. (a) SEM image with chemical element maps. (b) Cross-section SEM image for open-air plasma-treated Al7075. (c) Elemental depth file. Source: ORNL.

Figure II.4.1.4.5 shows a high-magnification STEM image with EDS chemical element maps for a cross-sectioned open-air plasma-treated Al sample. The formation of Al, Mg, and Zn oxide can clearly be seen on the surface. Porous Al oxide is found on the top layer where dense and continuous Al oxide is observed. Next, below the porous Al oxide, thin layers of Mg and Zn are shown to have formed as a result of the oxidation process from open-air plasma. Al7075 is a multi-element alloy with multiple phases, such as η -phase ($MgZn_2$) (main precipitate strength hardening phase), $AlZnMgCu$, Al_2CuMg , and even Al_2Cu phases reported in the literature [9], so it is possible that multiple oxides can form. To identify what oxides form from open-air PT, we collaborated with ANL using micro-beam XRD, as provided in the following section.

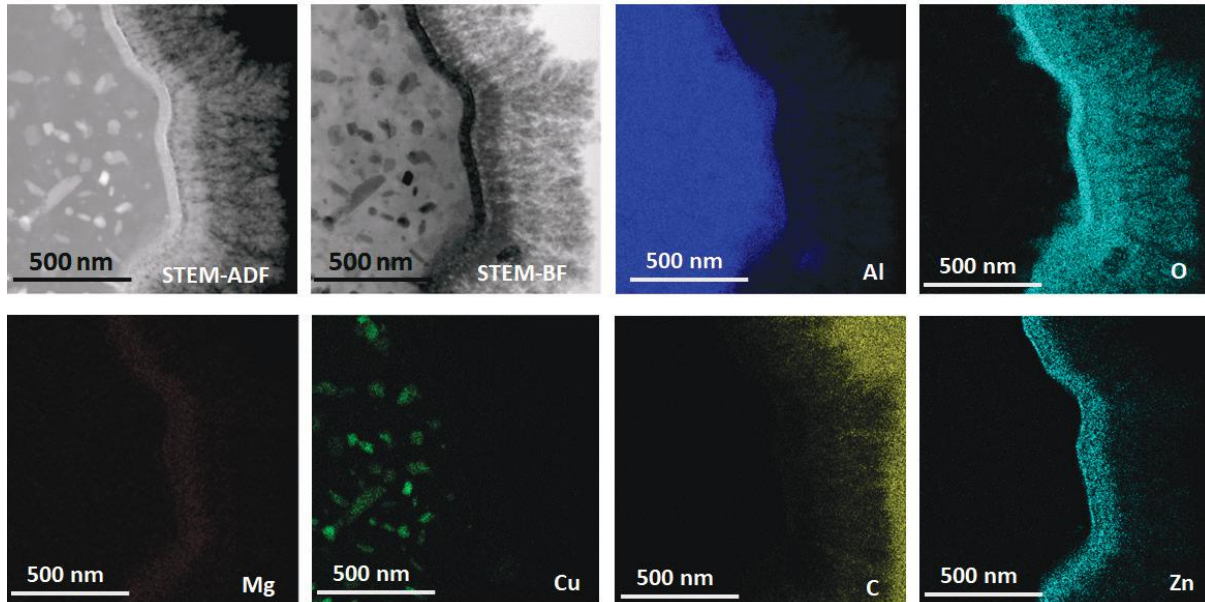
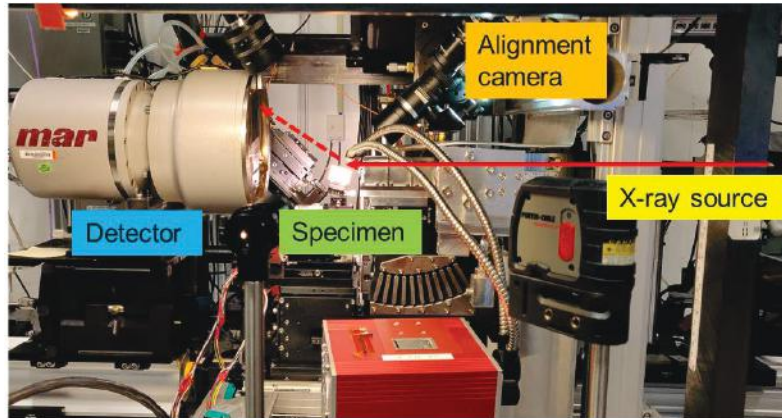


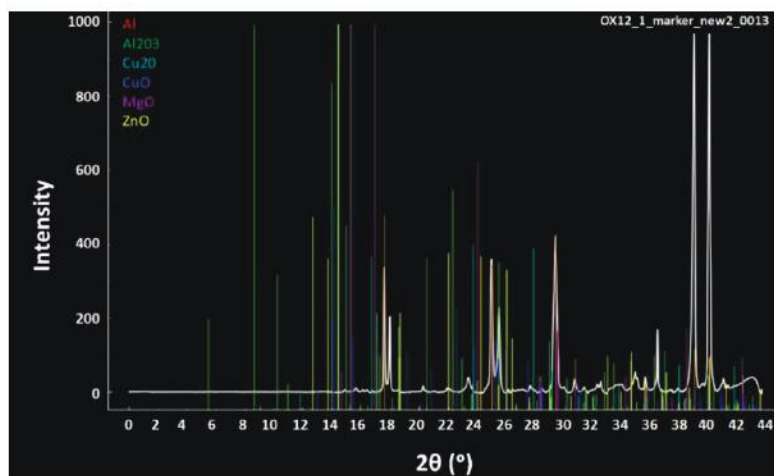
Figure II.4.1.46. High-magnification STEM image for open-air plasma-treated Al7075 with chemical element maps. Note: ADF = annular dark field; BF = bright field. Source: ORNL.

Micro-beam XRD Characterization of Open-air Plasma-treated Al7075 (ANL)

Al-7075 alloy plates were open-air plasma-treated at ORNL with the aim of improving corrosion resistance. Preliminary EDS characterization at ORNL showed a nearly uniform distribution of constituent elements (e.g., Al, Mg, Zn, Cu) at all locations and a high O content about 30 μm in-depth on the side of the treated surface, which was an oxide layer. To further characterize the oxide layer, micro-beam XRD measurements were conducted in a reflection geometry at beamline 34-ID-E in the Advanced Proton Source at ANL. An x-ray beam measuring $1\ \mu\text{m} \times 1\ \mu\text{m}$ with an energy of 20 keV and an exposure time of 60 sec. was used to collect two-dimensional diffraction patterns along the depth for each sample. Figure II.4.1.4.6(a) shows the characterization setup at the beamline. The aim of the characterization was twofold: (1) identify the various oxides along the depth of the oxide layer; and (2) obtain a more accurate depth of the oxide layer that formed. Figure II.4.1.4.6(b) presents the one-dimensional diffraction patterns, showing peaks corresponding to Al, Al_2O_3 , CuO , and ZnO in the oxide layer, which is expected based on the alloy composition. Peaks corresponding to other expected phases— Cu_2O and MgO —were not observed. Additional peaks were seen in the diffraction pattern and are suspected to be from mixed oxides, such as MgAl_2O_4 spinel.



(a)



(b)

Figure II.4.1.47. (a) Characterization setup showing the diffraction geometry in reflection mode. The x-ray beam path is marked in red with a solid line showing the incident beam and a dashed line showing the diffracted (reflected) beam. Note that the sample is inclined at an angle of 75 degrees to the beam direction. (b) An example of a one-dimensional diffraction pattern for the oxide layer shown in white along with the stick patterns/peak positions of various expected oxide species. Source: ANL.

The above data was collected during a limited beamtime (< 0.5 day) at beamline 34-ID-E. As a next step, oxide layers on samples with different surface-treatment variables will be sourced from ORNL and characterized along the depth using micro-beam XRD. General user proposals have been submitted with the aim of acquiring more time for the same. Further, analysis will be conducted in conjunction with the STEM-EDS results obtained at ORNL to identify site-specific variation of oxide species along the depth of the oxide layer. This knowledge will be used to hypothesize the possible formation mechanisms of the oxide species during the surface-treatment and explain the observations made in the post-treatment corrosion behavior tests performed at ORNL.

Bulk Corrosion Measurement of Plasma-treated Samples (PNNL)

Macroscopic electrochemical characterizations were performed on pre- and post-atmospheric plasma-treated Al5052. Electrochemical measurements were performed on the optimized PT condition. An Ag/AgCl reference system and a 3.5% NaCl solution was used for the electrochemical measurements. Open circuit potential (OCP), Tafel, and EIS were recorded before and after PT. Measurements were performed

immediately after PT or samples were vacuum-sealed and opened at the time of the electrochemical measurements. For the vacuum-sealed samples, measurements were performed within 48 hours of PT. Figure II.4.1.4.7(a) shows the OCP and Tafel data both before and after the PT, respectively. The serrations in the OCP and Tafel data indicates pitting corrosion occurs in the ‘without plasma-treated’ sample. However, serrations not observed in the ‘plasma-treated’ sample indicates surface stability improvement after PT. Figure II.4.1.4.7(b) shows the Nyquist data fitted with an equivalent circuit diagram to obtain the impedance values. The total resistance (R2+R3) after PT is increased by appropriately 2500% in Al5052 sample compared with starting material. The impedance values for both pre-and post-plasma-treated samples are shown in Table II.4.1.4.2.

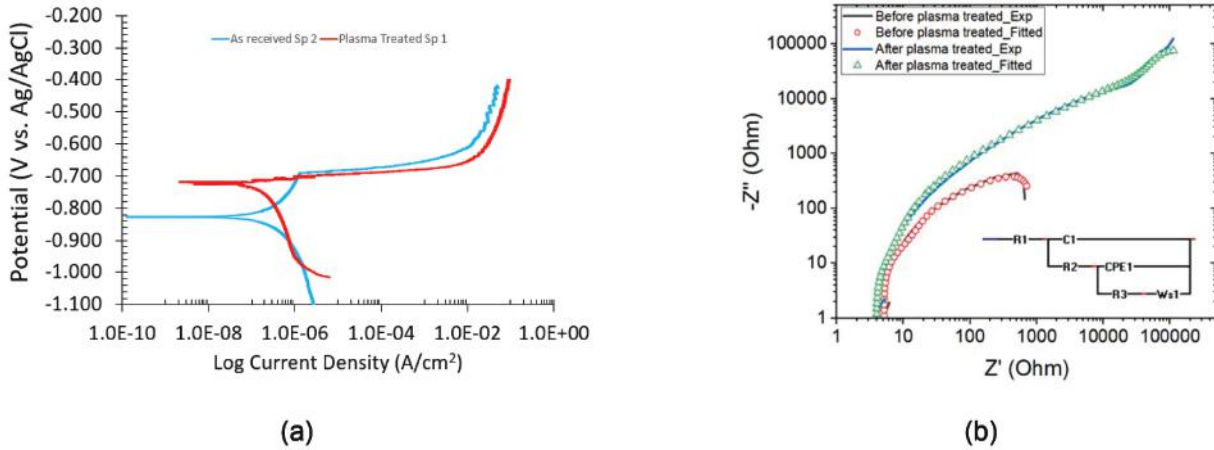


Figure II.4.1.48. (a) SEM image with chemical element maps. (b) Cross-section SEM image for open-air plasma-treated Al7075. (c) Elemental depth file. Source: ORNL.

Table II.4.1.4.2. Impedance Values on the Before and After Plasma-treated Al5052 Alloy

Al5052							
As-received	R1 (Ω)	C1 (F)	R2 (Ω)	R3 (Ω)	P1	n1	
	5.1	1.9E-6	69.5	728.1	1.8E-6	0.95	
Plasma-treated	R1 (Ω)	C1 (F)	R2 (Ω)	R3 (Ω)	P1	n1	Wsr1 (Ohm S-0.5)
	3.9	1.1E-5	45.4	21033	1.1E-5	0.87	12070

Two dissimilar material configurations were explored: (1) AA6061 and AA6061 joints formed using high-velocity riveting (e.g., without a rivet) both with and without adhesives in between the plates; and (2) DP590 and AA6061 plates joined using high-velocity riveting both with and without a steel rivet, as well as with and without adhesives in between the plates. The samples in configuration #1 were corroded in a salt fog chamber for a duration of 200 hours and 800 hours. The samples in configuration #2 were corroded in a salt fog chamber for a duration of 200 hours. The salt fog chamber was maintained at 35°C with an NaCl concentration of 5 wt.%. Prior to and after salt fog corrosion, images of the sample were acquired, and their weights recorded to compare the surface corrosion and weight change due to corrosion.

Figure II.4.1.1.8.(a) provide images of a representative sample from configuration #1 both before and after 200 h and 800 h of corrosion. Figure II.4.1.1.8.(b) provides a representative sample from configuration #2 both before and after corrosion. Adhesives prevent the flow of corrosive fluid to regions between the plates in the joints, thereby preventing localized corrosion in the form of galvanic and crevice corrosion. This shows that the presence of adhesives between the joining plates is beneficial for corrosion protection of the joints.

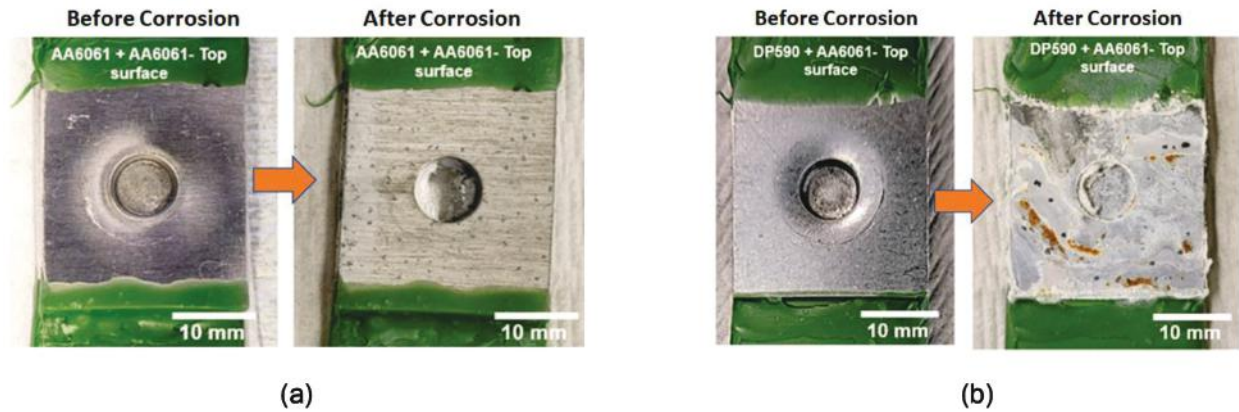


Figure II.4.1.49. (a) Comparison of a representative joint of AA6061 plate joined to AA6061 plate before and after corrosion. (b) Comparison of a representative joint of DP590 plate joined to AA6061 plate (without a rivet) before and after corrosion showing white corrosion product on the surface. Source: PNNL.

Microscopic Corrosion Measurement of HVR Samples (PNNL)

SECCM characterization was performed on two different rivet configurations: (1) an Al6061-Al6061 steel rivet and (2) an Al6061-Al6061 Al7075 sacrificial rivet. SECCM was performed only on the rivet samples with an optimized processing condition. Measurements were made on the cross-section of the rivets. OCP, Tafel, and EIS data were recorded across lines between the rivet-to-sheet metals for the ramset rivet and the sheet metal to sheet metal for the sacrificial Al7075 rivet. An Ag/AgCl reference system and 0.01 M NaCl solution were used for the electrochemical measurements. Figure II.4.1.4.9 shows the pre- and post-SECCM images of the rivet samples. Measurements were performed across four lines. Ten measurements were carried out across a line with a step size of 50 μm . For representative purposes, data from a single line is shown in this figure. Figure II.4.1.4.10 shows the corrosion potential (E_{corr}) values across an interface for the two rivet samples. The data shows very small variation of E_{corr} potential across the interface (e.g., steel-Al6061 and Al6061-Al6061 joint interface), which indicates the interface regions are not very anodic compared with the base materials.

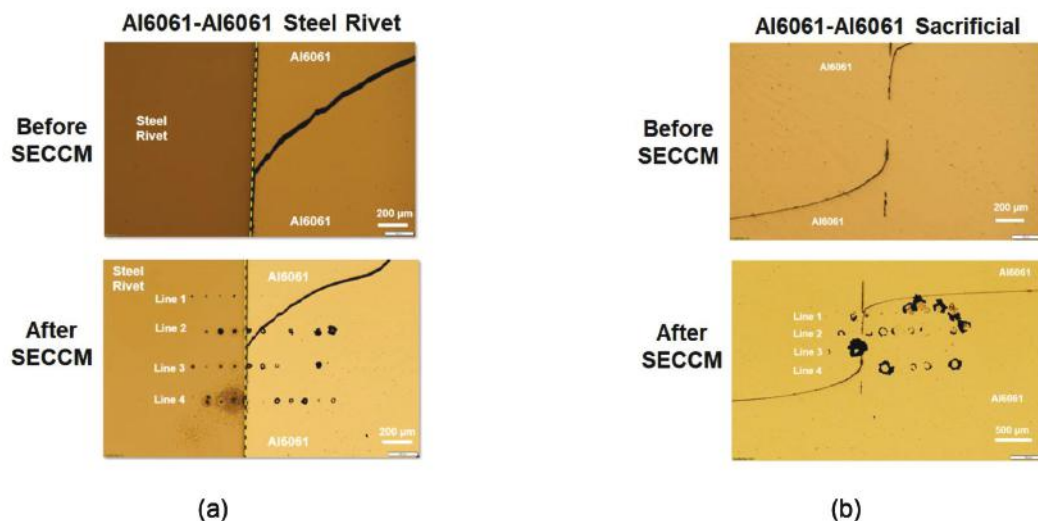


Figure II.4.1.50. Pre- and post-SECCM measurements showing cross-sectional optical images of two different rivet samples: (a) Al6061-Al6061 with a steel rivet and (b) Al6061-Al6061 with an Al7075 sacrificial rivet. Source: PNNL.

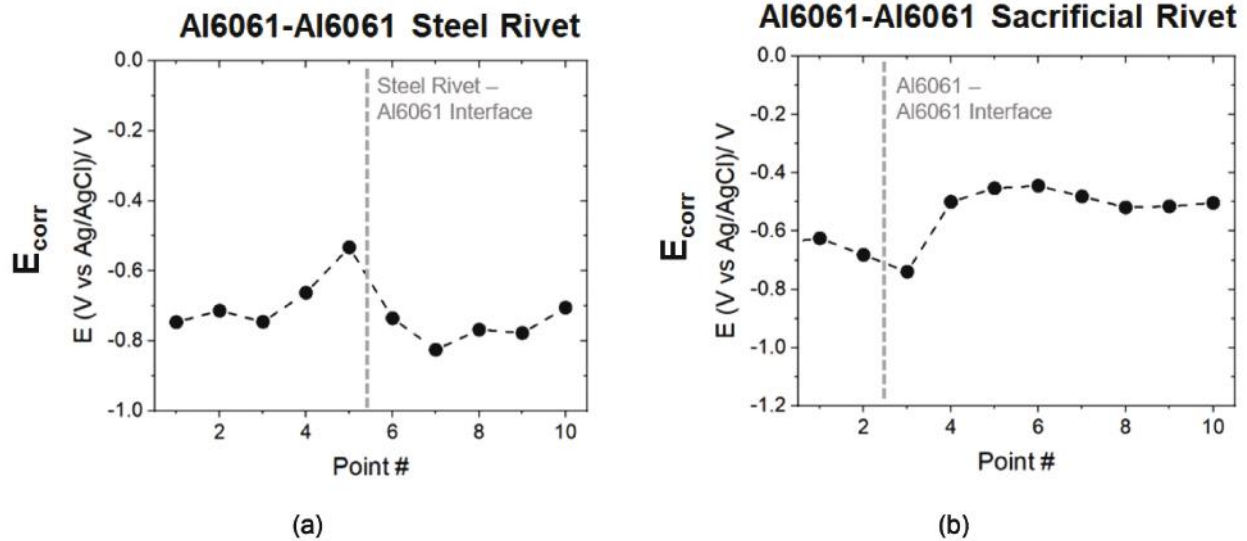
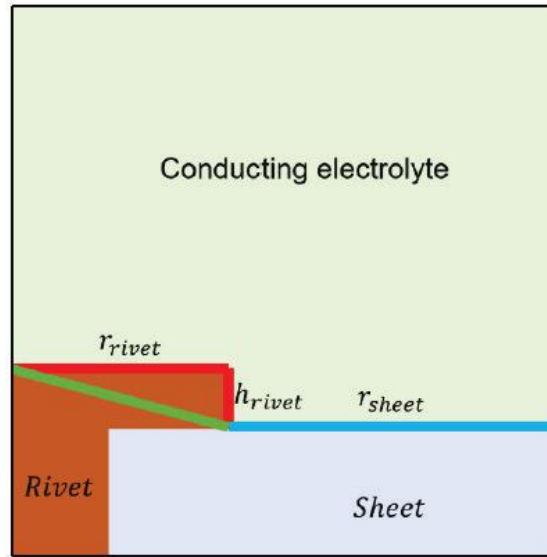


Figure II.4.1.51. Corrosion potential values across an interface for (a) Al6061-Al6061 steel rivet (dotted line) and (b) Al6061-DP590 steel rivet. Source: PNNL.

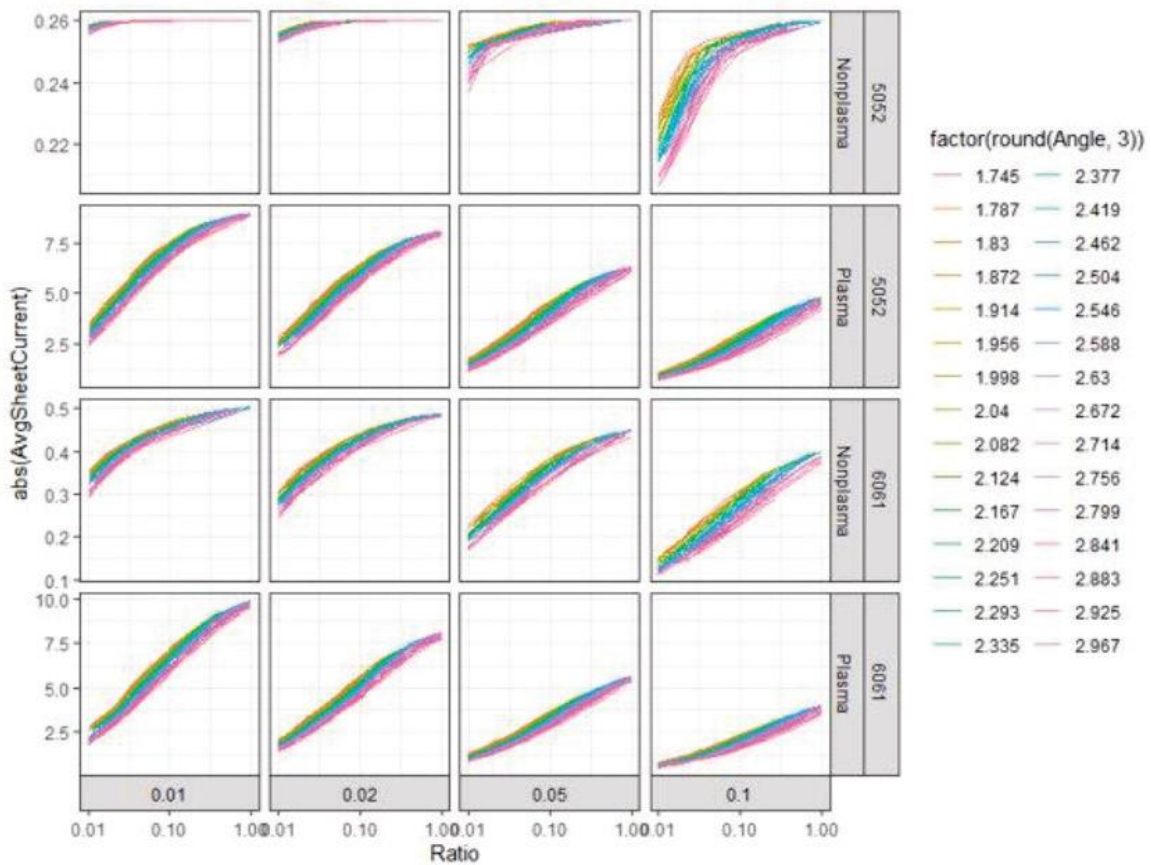
Corrosion Modeling (PNNL)

The COMSOL multiphysics modeling tools are being used to predict the maximum current density and understand the role of rivet geometry in corrosion performance. Current density was calculated on pre- and post-plasma-treated Al6061 and Al5052 sheets. The rivet was made from Zn-coated steel. Figure II.4.1.4.11(a) shows the simple rivet geometry and Figure II.4.1.4.11(b) shows the current density values calculated for a range of rivet-to-sheet area ratios and with varying angles. The data indicates a higher surface current density in the plasma-treated surface for both the Al6061 and Al5052 alloys.

A sensitivity analysis was performed to understand the role of sheet-rivet geometry on corrosion current density. Galvanized steel was used as a ramset rivet. Factorial design, where each input parameter has four or more discrete level of values all combined, was used to select all input parameter combinations for simulation inputs. To analyze the importance of those parameters on the rivet or sheet current, a Multivariate Adaptive Regression Splines surrogate model was built to predict the current distribution with the input of (r_{sheet} , ratio and θ). The sensitivity score of those input parameters can be calculated based on the sensitivity score (0-1 score), which is calculated by removing a specific variable x^i in the surrogate model one at a time: $s_i = GCV(M \setminus x^i) - GCV(M)$, where GCV stands for the Generalized Cross-Validation (GCV) score for the surrogate model. Figure II.4.1.4.12 shows the sensitivity scores of the input parameters for both pre- and post-plasma-treated samples. With plasma treatment, the three studied input parameters did not show a significant difference in terms of affecting the results. The r_{sheet} and ratio are the two most important factors affecting the averaged i_{sheet} current, while the ratio is the most dominant factor for the averaged i_{rivet} current.



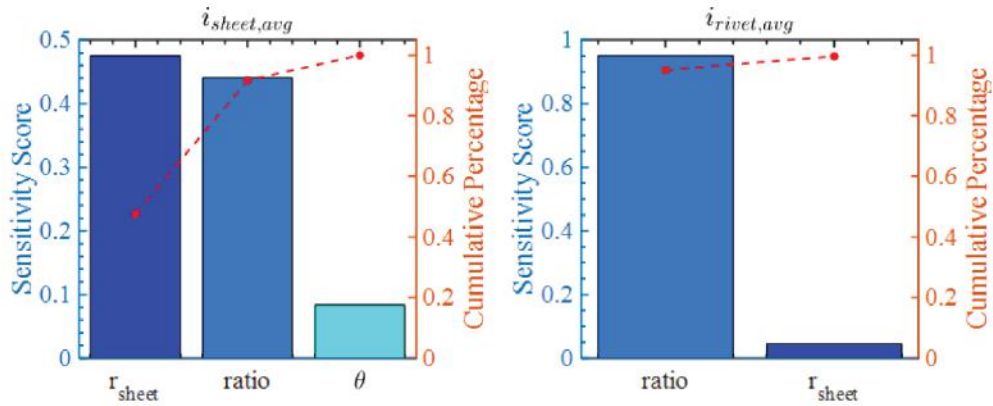
(a)



(b)

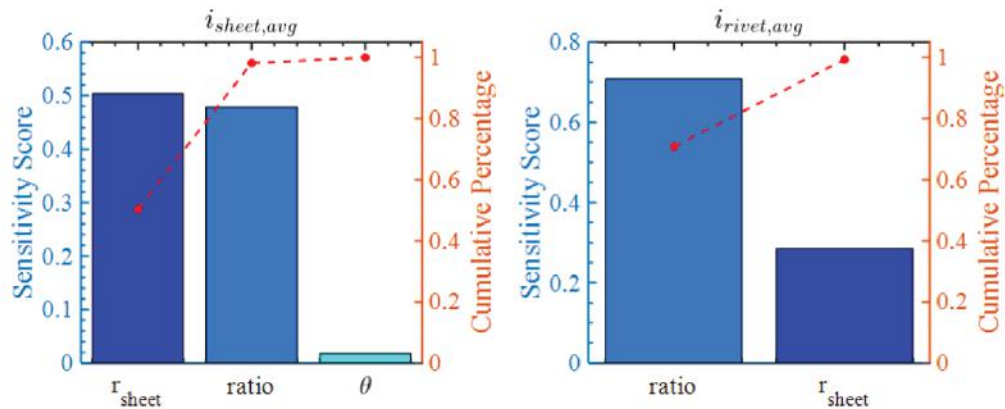
Figure II.4.1.52. (a) Simple rivet geometry and (b) pre- and post-plasma-treated surface current density of Al6061 and Al5052 sheet for a range of rivet-to-sheet ratio. Source: PNNL.

Sensitivity score for pre-plasma treated samples



(a)

Sensitivity score for post-plasma treated samples



(b)

Figure II.4.1.53. (a) Simple rivet geometry and (b) pre- and post-plasma-treated surface current density of Al6061 and Al5052 sheet for a range of rivet-to-sheet ratio. Source: PNNL.

Interfacial Adhesive Bonding Chemistry (PNNL)

Chemical bonding of three adhesives, XP0012 (thermoset paste), XP5005 (thermoset tape), and nitrile butadiene rubber (NBR)-Lignin (thermoplastic film) at the interface between Al6061 and CFRP-PA66 was characterized. Al6061 and CFRP-PA66 surfaces were plasma-treated to optimize their surface energies. XP0012 and XP5005 were provided from L&L Products and their main components are epoxy resin and dicyandiamide (curing agent); XP5005 contains extra polymers including polyphenol and polyacrylate to control curing speed, as observed in Figure II.4.1.4.13.

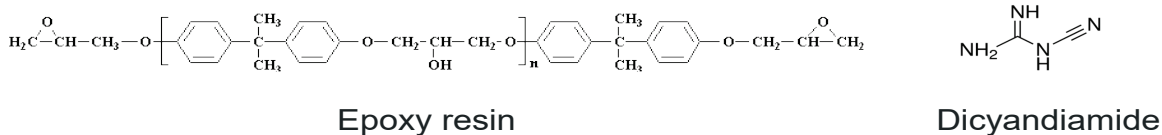


Figure II.4.1.54. The main components of XP0012 and XP5005 adhesives. Source: PNNL.

Thermoplastic NBR-lignin adhesive was developed by the ORNL adhesive team, which contains 51% acrylonitrile. Interfacial characterization was performed by the attenuated total reflectance-Fourier-transform infrared (ATR-FTIR) spectroscopy with 0.964 cm^{-1} resolution and 128 scans in the range of $500\text{--}4000\text{ cm}^{-1}$. First, XP0012 (paste) adhesive was cured at 150°C for 40 min to understand how each component of the adhesive interacted with each other, as shown in Figure II.4.1.4.14(a). Epoxy ring opening polymerization was dominant by decreasing the bending vibration peak at 914 cm^{-1} and the primary and secondary amines in dicyandiamide were developed into a broad peak around 3400 cm^{-1} associated with OH group formation. This can be explained by two different epoxy ring opening polymerizations that would occur concurrently in XP0012: (1) primary and secondary amine-initiated polymerization and (2) hydroxyl group-initiated polymerization. At the interface of the XP0012/CFRP-PA66, the nitrile ($\text{C}\equiv\text{N}$) group gradually decreased while the epoxy group stayed the same, which did not occur with the XP0012 curing. This indicated that the surface hydroxyl groups on CFRP-PA66 reacted with nitrile groups of dicyandiamide and formed linear amide bonding, as can be seen in Figure II.4.1.4.14(b). At the interface of XP0012/Al6061, amine- and hydroxyl-initiated epoxy ring opening polymerization and some ester bonds formed, as observed in Figure II.4.1.4.14(c). The crosslinking polymerization between XP0012 and Al6061 would be much stronger than the linear amide bonds of XP0012/CFRP-PA66.

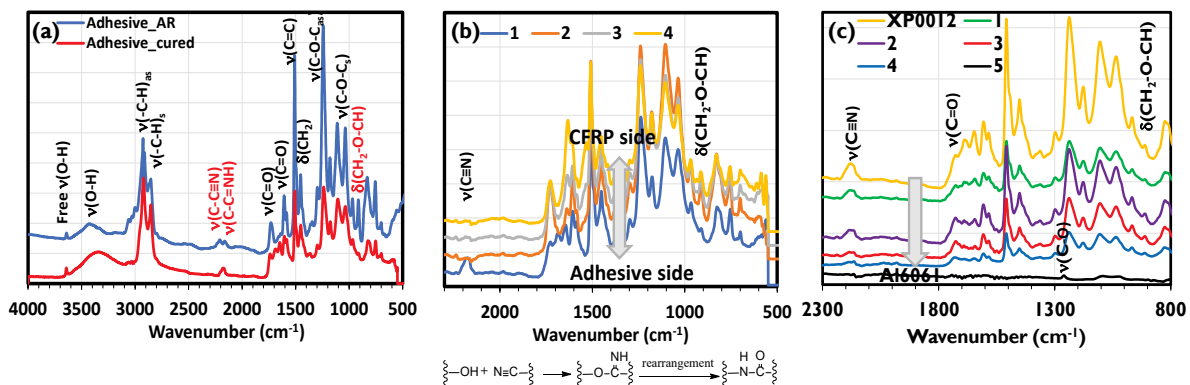


Figure II.4.1.55. (a) Vibrational peak assignment of uncured and cured XP0012 adhesive. Peak change at the interface of (b) XP0012/CFRP-PA66, and (c) XP0012/Al6061. Source: PNNL.

Second, XP5005 (tape) adhesive showed slight differences compared to the reaction of XP0012. Near the CFRP-PA66 surface, the nitrile peak remained constant. Amine peaks of dicyandiamide were also maintained at 3360 and 3330 cm^{-1} , as indicated in Figure II.4.1.4.15(a). This indicated that only OH-initiated epoxy polymerization occurred at the interface of XP5005/CFRP-PA66. However, near the Al6061 surface, nitrile and epoxy peaks were gradually reduced, as shown in Figure II.4.1.4.15(b), which is similar to XP0012/Al6061.

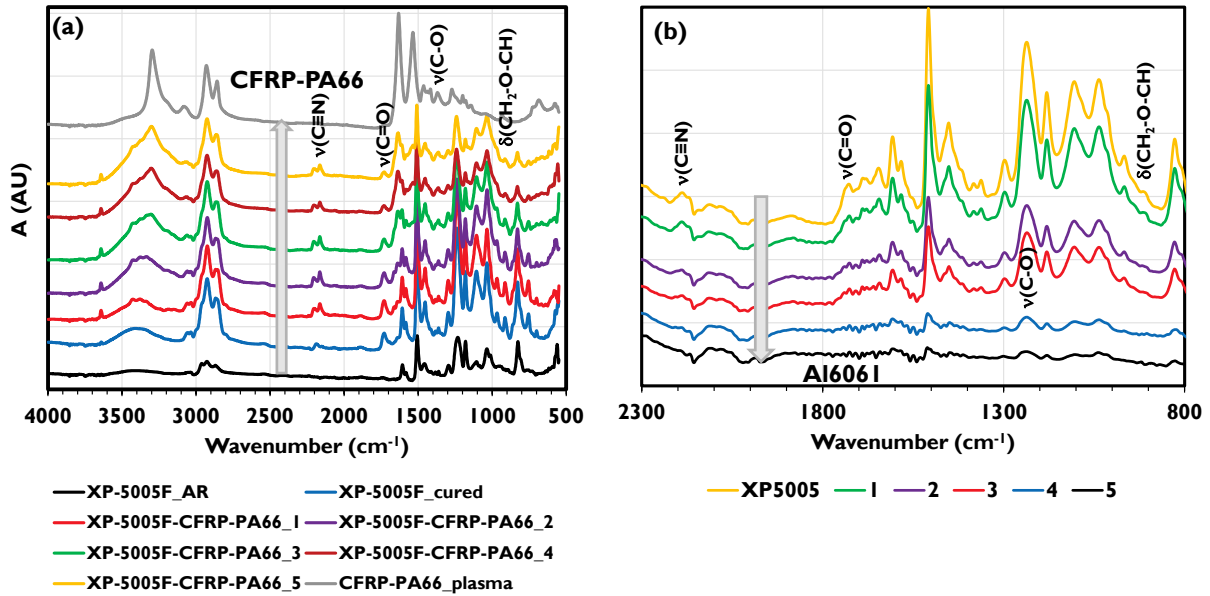


Figure II.4.1.56. XP5005 adhesive on (a) CFRP-PA66 and (b) Al6061 surfaces. Source: PNNL.

Third, the thermoplastic NBR-lignin adhesive did not show noticeable bonding during the curing at 180°C for 1 hour when no pressure was applied. However, when 51.7 MPa pressure was applied, all strong vibrational peaks were gradually decreased nearer to the CFRP-PA66 and Al6061 surfaces and only small C=O and C-O peaks remained. This strongly supports a linear ester (-C(=O)O-) bond formation by pressure-driven thermal dehydration at the interface of NBR-lignin/surfaces, as indicated in Figure II.4.1.4.16.

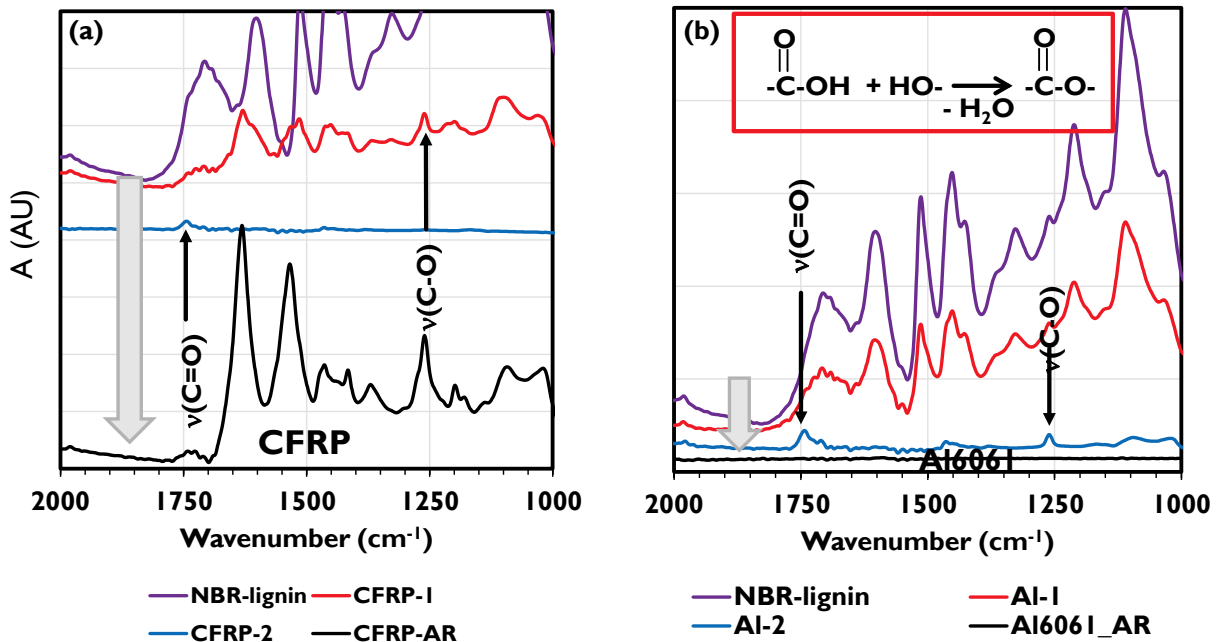


Figure II.4.1.57. NBR-lignin adhesive on (a) CFRP-PA66 and (b) Al6061 surfaces. Source: PNNL.

In summary, the XP0012 and XP5005 adhesives were found to react similarly on Al6061, but differently on CFRP-PA66 because XP5005 contains extra components including polyphenols and polyacrylate copolymers, as illustrated in Figure II.4.1.4.17(a) and Figure II.4.1.4.17(b), respectively. This made strong crosslinking networks at the interface of XP5005/CFRP-PA66 and a simple linear amide bonding at the interface of XP0012/CFRP-PA66. NBR-lignin provided C=O and -OH to form ester linkages to Al6061 and CFRP-PA66 surfaces, as observed in Figure II.4.1.4.17(c).

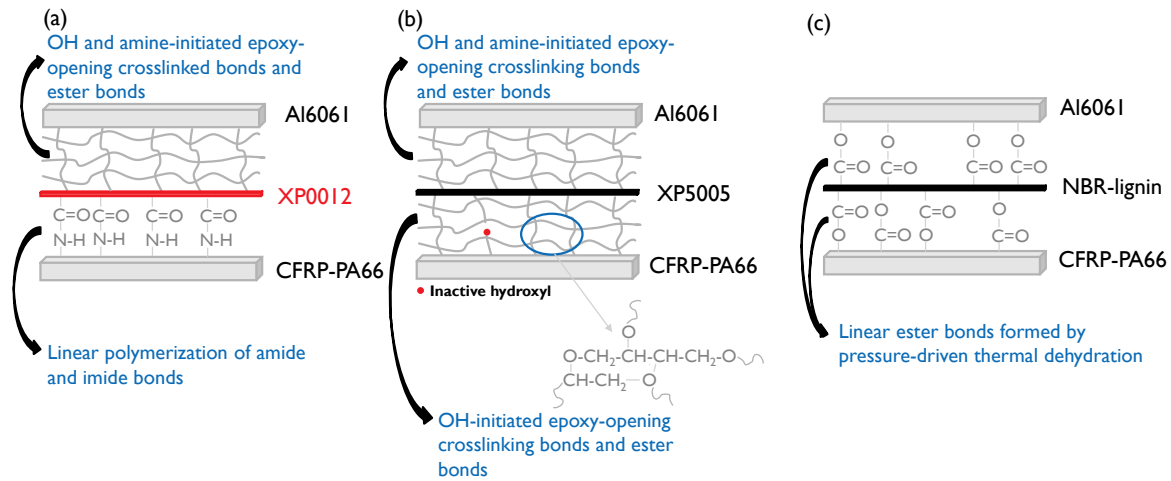


Figure II.4.1.58. Chemical interaction diagram of (a) XP0012, (b) XP5005, and (c) NBR-lignin adhesives on CFRP-PA66 and Al6061 surfaces. Source: PNNL

Surface Characterization of Laser-ablated Al380 (PNNL)

GM provided laser-ablated Al380 samples and PNNL characterized them using XRD, ATR-FTIR, Keyence optical metrology microscopy, SEM-EDS, XPS, and electron backscatter diffraction (EBSD) techniques. Typically, a die-casted Al380 contains Al, Si, Cu, Zn, Fe, and other traces. The laser-ablated Al380 surface was rougher than the as-received Al380 surface, as shown in Figure II.4.1.4.18(a). XRD showed that non-treated Al380 contained Al, Si, Al₂O₃, and some alloys, but all alloys and oxides were removed from the laser-ablated surface. Only dominant Al peaks with small amounts of Si were detected, as indicated in Figure II.4.1.4.18(b).

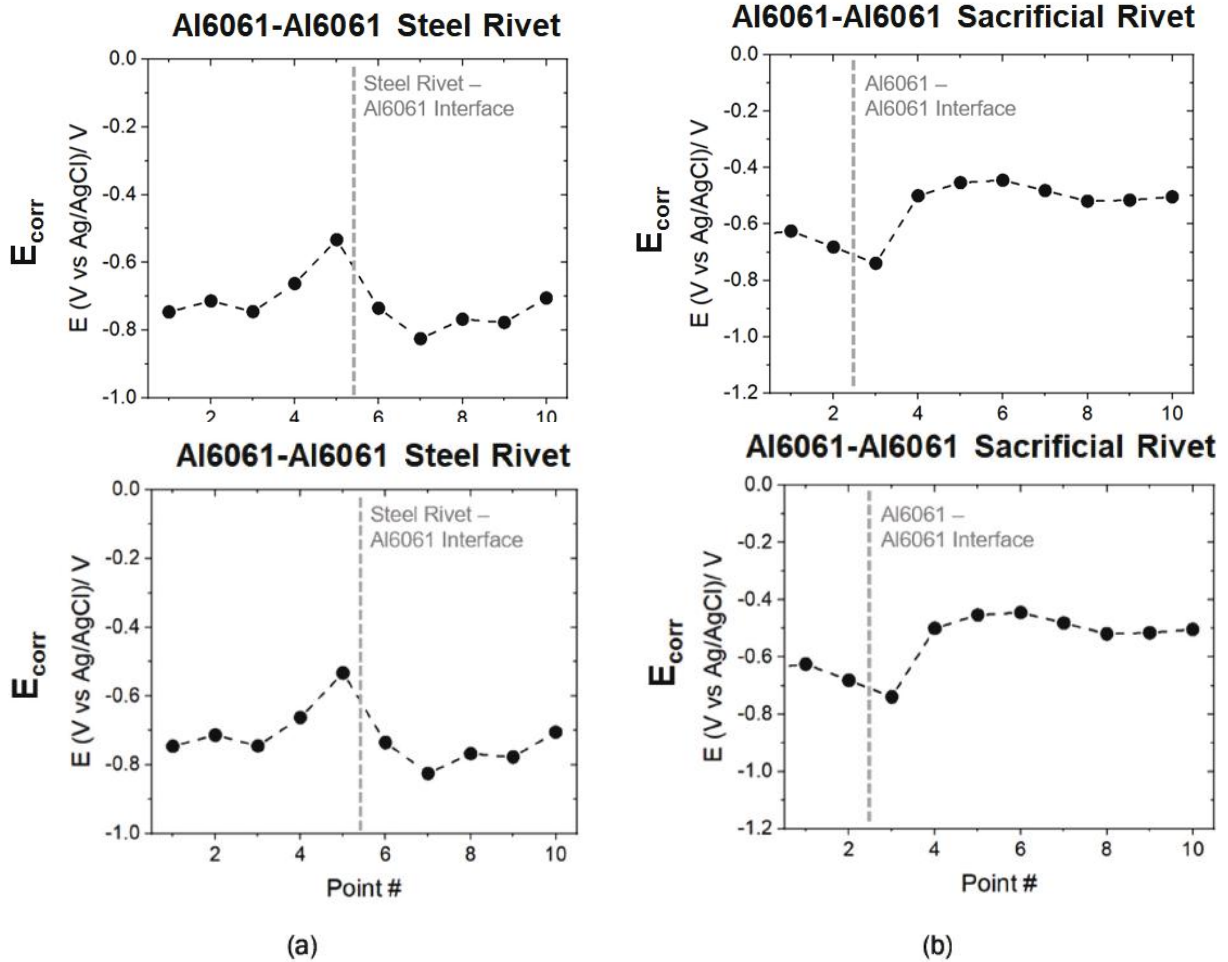


Figure II.4.1.59. Corrosion potential values across an interface for (a) Al6061-Al6061 steel rivet (dotted line) and (b) Al6061-DP590 steel rivet. Source: PNNL.

SEM investigation of sample cross-sections showed that laser ablation generated rough surfaces and cavities near the surface. Surface grains changed from small and granular to a wave-shaped Al layer. Cu, Fe, and Si particles were mainly removed, while the surface was more oxidized due to air contact, as observed in Figure II.4.1.4.19. A crack between the bulk material and the ablated surface layer was observed and measured by nano-EBSD after separating the section by PFIB, as indicated in the bottom right of Figure II.4.1.4.19.

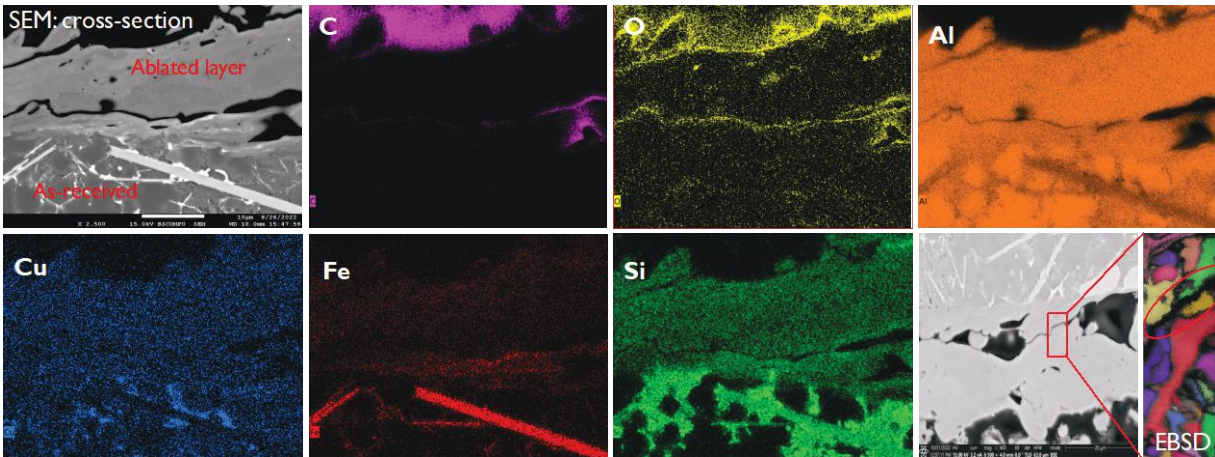


Figure II.4.1.60. SEM, atomic map, and EBSD images of laser-ablated Al380 cross-section. Source: PNNL.

Conclusions

Several conclusions can be drawn from these experiments:

- Both laser and open-air plasma surface treatments on AA7075 showed improved corrosion resistance as compared to the base material. For the continuous laser treatments, the increase of corrosion reaction resistance was significant for laser power input conditions of 150 W. For the atmospheric PTs, a much higher EIS impedance than the baseline 7075 is achieved by forming a thick, dense, and continuous oxide layer. From the impedance spectra data, it is considered that both the laser and atmospheric plasma treatments can promote the formation of resistive surface film contributing to improved corrosion resistance. XPS and advanced electron microscopy characterizations show the formation of multiple oxides including Al, Mg, and Zn after surface-treatment.
- Bulk electrochemistry data indicates the plasma-treated sample showed an improvement of surface stability after plasma treatment by reducing pitting corrosion. A salt fog test showed the weight change observed in the samples with an adhesive is notably lower than those without an adhesive. Adhesives prevent the flow of corrosive fluid to regions between the plates in the joints, thereby preventing localized corrosion in the form of galvanic and crevice corrosion. SECCM data show a very small variation of E_{corr} potential across the interface (e.g., steel-Al6061 and Al6061-Al6061 joint interface), which indicates interface regions are not very anodic compared with the base materials. COMSOL modeling combined with sensitivity analysis shows the r_{sheet} and ratio are the two most important factors affecting the averaged i_{sheet} current, while the ratio is the most dominant factor affecting the averaged i_{rivet} current.
- Adhesive-substrate interfacial chemistry was characterized for two thermoset adhesives and one thermoplastic film. Thermosetting XP0012 (paste) and XP5005 (tape) adhesives were found to react similarly with Al6061 substrates. However, the extra polyphenol and polyacrylate copolymers in XP5005 promoted a slightly different interfacial chemistry with CFRP-PA66. This resulted in strong crosslinking networks at the XP5005/CFRP-PA66 interface and a simple linear amide bonding at the XP0012/CFRP-PA66 interface. Thermoplastic NBR-lignin adhesive provided C=O and -OH to form ester linkages to Al6061 and CFRP-PA66 surfaces only when substantial pressure was applied during thermal curing.
- Laser ablation of Al380 formed surfaces dominated by Al with small amounts of Si. The surface was substantially rougher than the as-received Al380 and mainly oxidized only by exposure to air. Ablated surfaces appeared as a distinct layer segregated from the bulk material with extensive voids located at the interface.

Key Publications

1. Jun, J., V. V. Joshi, A. Crawford, V. Viswanathan, D. N. Leonard, J. Chen, P. Updadyay, Y. C. Lim, and Z. Feng, 2023, “Galvanic corrosion of AZ31B joined to DP steel with and without Zn layer by ultrasonic and friction stir welding,” *J. Magnes. Alloy.*, Vol. 11, No. 2, pp. 462-479. <https://doi.org/10.1016/j.jma.2023.01.016>.
2. Lim, Y. C., V. V. Joshi, D. Singh, K. Simmons, R. Kalsar, V. Viswanathan, V. Prabhakaran, A. Crawford, D. N. Leonard, A. Naskar, J. Jun, M. P. Brady, D. Hoskins, and N. Kanbargi, 2022, “Surface modification for improved joining and corrosion resistance,” DOE Vehicle Technology Offices Annual Merit Review, 21–23 June 2022, Washington, D.C., USA.
3. Lim, Y. C., J. Jun, D. N. Leonard, H. Meyer III, J. K. Keum, M. Brady, and Z. Feng, “Atmospheric plasma surface processing of a 7xxx Al alloy surface to improve corrosion resistance,” *TMS 2022 Annual Meeting & Exhibition*, 23–27 February 2022, Anaheim, CA, USA.
4. Lim, Y. C., J. Jun, Y. F. Su, H. M. Meyer III, J. K. Keum, B. Lokitz, A. Sy, R. Robinson, D. Pappas, and Z. Feng, 2023, “Open-air plasma surface processing of Al alloy 7075 surface to form oxide-based corrosion barrier layer,” *TMS 2023 Annual Meeting & Exhibition*, 19–23 March 2023, San Diego, CA, USA.
5. Lim, Y. C., N. Kanbargi, Z. Yu, B. Lokitz, J. Jun, Y. F. Su, A. Naskar, and Z. Feng, 2023, “Adhesive bonding of lightweight multimaterials with surface modifications,” *TMS 2023 Annual Meeting & Exhibition*, 19–23 March 2023, San Diego, CA, USA.
6. Su, Y. F., Y. C. Lim, K. M. Faraone, D. A. Frederick, J. Jun, H. Meyer, J. K. Keum, and Z. Feng, 2022, “Laser surface processing on 7075 Al alloys to improve corrosion resistance,” *International Materials Applications & Technologies Conference and Exposition (IMAT) 2022*, 12–15 September 2022, New Orleans, LA, USA.

References

1. Lim, Y. C., J. Chen, J. Jun, D. N. Leonard, M. P. Brady, C. D. Warren, and Z. Feng, 2021, “Mechanical and corrosion assessment of friction self-piercing rivet joint of carbon fiber-reinforced polymer and magnesium alloy AZ31B,” *J. Manuf. Sci. Eng.*, Vol. 143, No. 3, Art. 031106. <https://doi.org/10.1115/1.4048378>.
2. Lim, Y. C., H. Park, J. Jang, J. W. McMurray, B. S. Lokitz, J. K. Keum, Z. Wu, and Z. Feng, 2018, “Dissimilar materials joining of carbon fiber-polymer to DP 980 by friction-bit joining, adhesive bonding, and weld-bonding,” *Metals*, Vol. 8, No. 11, Art. 865. <https://doi.org/10.3390/met8110865>.
3. Lim, Y. C., L. Squires, T.-Y. Pan, M. Miles, G.-L. Song, Y. Wang, and Z. Feng, 2015, “Study of mechanical joint strength of aluminum alloy 7075-T6 and DP steel 980 welded by friction-bit joining and weld-bonding under corrosion medium,” *Mater. Des.*, Vol. 69, pp. 37–43. <https://doi.org/10.1016/j.matdes.2014.12.043>.
4. Mansfeld, F., and J. V. Kenkel, 1976, “Laboratory studies of galvanic corrosion of aluminum alloys,” In: Baboian, R., W. France, L. Rowe, and J. Rynewicz (eds.), *Galvanic and Pitting Corrosion—Field and Laboratory Studies*, ASTM International, West Conshohocken, PA, USA. pp. 20–47. <https://doi.org/10.1520/STP41395S>.
5. Mandel, M., and L. Kruger, 2013, “Determination of pitting sensitivity of the aluminum alloy EN AW-6060-T6 in a carbon-fiber-reinforced plastic/aluminum rivet joint by finite element simulation of the galvanic corrosion process,” *Corros. Sci.*, Vol. 73, pp. 172–180. <https://doi.org/10.1016/j.corsci.2013.03.033>.
6. Liu, Z., Y. Dong, Z. Chu, Y. Yang, Y. Li, and D. Yan, 2013, “Corrosion behavior of plasma sprayed ceramic and metallic coatings on carbon steel in simulated seawater,” *Mater. Des.*, Vol. 52, pp. 630–637. <https://doi.org/10.1016/j.matdes.2013.06.002>.

7. Lim, Y. C., J. Jun, M. P. Brady, and Z. Feng, 2021, “Methodology to avoid accelerated corrosion of dissimilar material fastener joints using alloys forming surface oxides,” ORNL invention disclosure No. 202004631, Oak Ridge National Laboratory, Oak Ridge, TN, USA.
8. Lim, Y.C., V. V. Joshi, 2021, “Surface modifications for improved joining and corrosion resistance,” Vehicle Technologies Office Materials 2021 Annual Progress Report.
9. Gharbi, O., S. K. Kairy, P. R. De Lima, D. Jiang, J. Nicklaus, and N. Birbilis, 2019, “Microstructure and corrosion evolution of additively manufactured aluminum alloy AA7075 as a function of aging,” *NPJ Mater. Degrad.*, Vol. 3, Art. 40. <https://doi.org/10.1038/s41529-019-0101-6>.

Acknowledgements

The co-PI at PNNL would like to acknowledge Y. Shin, D. Merkel, K. Simmons, Y. Qiao, B. Schuessler, L. Strange, R. Kalsar, A. Guzman, M. Rhodes, V. Prabhakaran, V. Viswanathan, and A. Crawford for the surface processing, characterization, and modeling activities for this project. The co-PIs at ORNL would like to acknowledge R. Davies, Z. Feng, and A. Hayes for their leadership and technical guidance. In addition, the co-PIs recognizes the great efforts from the project team members at ORNL are acknowledged as well, including J. Jun, A. Frederick, D. Kyle, H. Meyer III, J. K. Keum, M. Brady, N. Kanbargi, Z. Yu, and A. Naskar are greatly appreciated. Finally, the co-PIs at ORNL show their appreciation for L&L Products for their providing adhesives for this project.

II.4.1.5 Extending Ultrasonic Welding Techniques to New Material Pairs (Oak Ridge National Laboratory)

Jian Chen, Principal Investigator

Oak Ridge National Laboratory
1 Bethel Valley Rd.
Oak Ridge, TN 37831
E-mail: chenj2@ornl.gov

Zhilli Feng, Co-Principal Investigator

Oak Ridge National Laboratory
1 Bethel Valley Rd.
Oak Ridge, TN 37831
E-mail: fengz@ornl.gov

Christopher Schooler, DOE Technology Development Manager

U.S. Department of Energy
E-mail: christopher.schooler@ee.doe.gov

Start Date: October 1, 2020	End Date: September 30, 2023	
Project Funding (FY 2022): \$584,000	DOE share: \$584,000	Non-DOE share: \$0

Project Introduction

Modern multimaterial vehicles require joining of various lightweight materials, such as aluminum (Al) and magnesium (Mg) alloys and CFRP, with advanced high-strength steels together to form a high-performance and lightweight body structure. A variety of joining methodologies (e.g., resistance spot-welding, adhesive bonding, linear fusion welding, hemming, clinching, bolting, riveting) have been attempted by the automotive industry to join different materials. Often, these joining techniques are limited to only certain material combinations. For capital and operational cost, automobile OEMs need to limit the number of joining technologies implemented on an assembly line.

In Phase I of the Joining Core Program, we investigated the versatility of ultrasonic-based spot-joining (UJ) processes to join different material combinations [1, 2]. Ultrasonic spot-welding (USW) is one of the major UJ processes which is a solid-state joining method that produces weld joints by localized high-frequency tangential vibration under moderate clamping pressure. The temperature rise during a USW process is generally not sufficient to melt the material. Instead, the high-temperature and pressure at the interface induce rapid diffusion between the substrates to form the joint. In Joining Core Program Phase I, we successfully demonstrated the ability of joint DP590 steel and AZ31B Mg alloys with a reasonably high-strength, including bare steel to Mg that were considered to be unweldable as they are metallurgically immiscible, through USW process innovations assisted by extensive physics-based process modeling.

However, a number of technical challenges still remain in the prevention of successful application of USW for automotive body structures. They include challenges to produce consistent joint quality for many welds to assemble large metal body structures. This is particularly challenging due to the lack of understanding of complex ultrasonic wave propagation and interaction with other spot welds in a large structural assembly. In addition, further research is required to extend the USW to other material combinations for further lightweighting of multimaterial autobody structures.

Objectives

The primary objective of this project is to further explore, understand, and extend the unique characteristics of UJ—the ability to metallurgically bond immiscible material pairs and the acoustic softening phenomenon—to various lightweight material combinations in an assembly of a lightweight multimaterial vehicle. The targeted outcomes will be a versatile, ultrasonic-based solid-state spot-joining technology to join representative component level coupons in which multiple UJs are required. The outcome will include extending the joining technology to join a variety of lightweight dissimilar material stack-ups including Al, CFRP, Mg, and steel.

Approach

The project is divided to three major tasks to ensure risk mitigation and successful completion. These main tasks are:

- **FY 2021:** Making multiple USW joints in large steel-Mg coupons and obtaining an average joint strength at least 80% of that is obtained in single-joint coupons.
- **FY 2022:** Extending USW method to join large Al-steel and Al-Mg coupons consisting of multiple joints and obtaining an average joint strength at least 80% of that is obtained in single-joint coupons.
- **FY 2023:** Using one UJ variant to join polymer-metal structural stack-ups.

The following sub-tasks were planned to meet FY 2022 milestones:

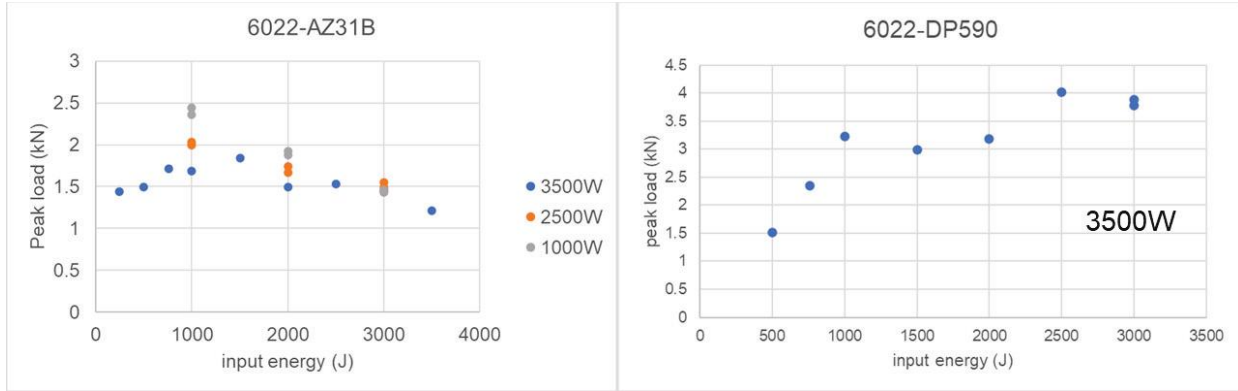
- **Sub-Task 1:** Feasibility study to extend USW to join Mg-Al and Al-steel in single-joint lap-shear coupons.
- **Sub-Task 2:** Perform microstructural analysis and mechanical tests on single Mg-Al and Al-steel coupons.
- **Sub-Task 3:** Apply thermal-mechanical and model-based numerical tools to assist the process development to join multiple Mg-Al and Al-steel joints in component level structures.

Results

In Phase II, we developed an innovative strategy to join large coupons with consistent weld quality and strength. We identified that different welding energy levels were required depending upon the part geometry and joint location. Hence, a wide range of welding energy was systematically investigated to join single-joint lap-shear Al-steel and Al-Mg coupons in FY 2022. For the study, Al was 1-mm-thick 6022, steel was 1-mm-thick DP590 with a galvanized surface coating, and Mg was 2-mm-thick AZ31B.

Plots of the peak lap-shear tensile strength as a function of ultrasonic energy for the single-joint Al-Mg and Al-steel coupons are shown in Figure II.4.1.5.1(a) and Figure II.4.1.5.1(b), respectively. Al-Mg USW coupons were made using three welding power levels (e.g., 1000W, 2500W, 3500W). The welding energy varied from 250–3500 joules (J). The maximum value of the peak strength occurred at ~1000J welding energy regardless of which power was used. On the other hand, for Al-steel USW coupons, only one welding power was used, where the welding energy varied from 500–3000J. The peak LSS monotonically increased from 1.6–4kN.

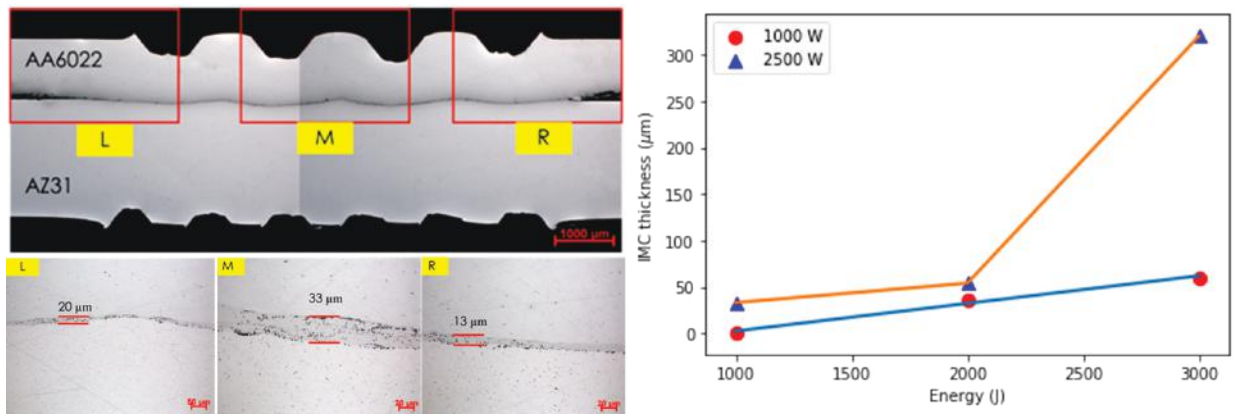
Figure II.4.1.5.2(a) shows the optical micrograph of a representative Al-Mg USW joint interface. A layer of Al/Mg IMC was formed at the faying surface. The average thickness of the IMC layer for USW joints made with different energy under 1000W and 2500W was compared as shown in Figure II.4.1.5.2(b). These results suggest that a thin layer of an Al-Mg IMC layer is critical to obtain a strong LSS. Overgrowth of the IMC layer would deteriorate the mechanical performance. Figure II.4.1.5.3 shows the micrographs of the Al-steel USW joint interface and the chemical composition at the center of the joint interface. A layer of Al-Fe-Zn ternary phase was observed.



(a)

(b)

Figure II.4.1.61. Peak lap-shear tensile load as a function of ultrasonic energy on single-joint (a) Al-Mg and (b) Al-steel coupons. Source: ORNL.



(a)

(b)

Figure II.4.1.62. (a) Representative microstructure at the Al-Mg USW joints showing IMC at the interface. (b) The average IMC thickness as a function of welding energy of Al-Mg USW joints. Source: ORNL.

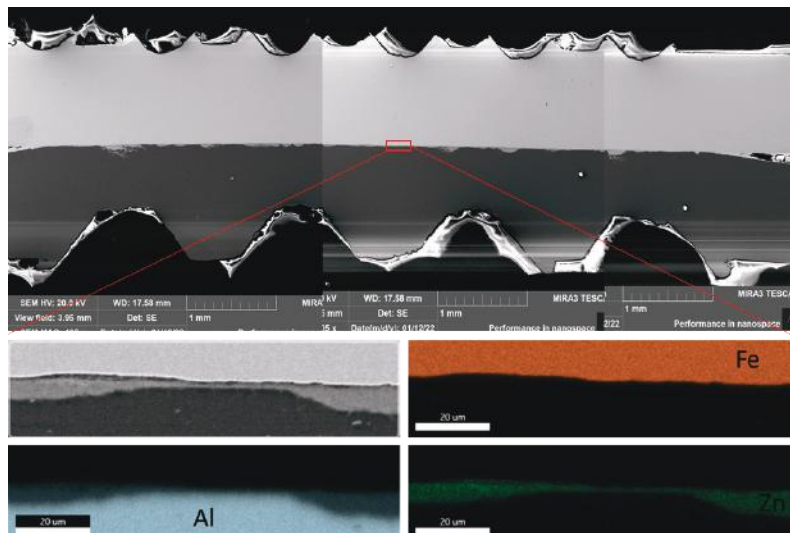


Figure II.4.1.63. Chemical composition of Al-steel joint interface at the center of the joint. Source: ORNL.

Computational modeling of ultrasonic wave propagation in a metal sheet were utilized to assist the process development for joining large coupons consisting of five USW joints. Both elastic linear modal and thermal-mechanical finite element analyses suggest that the mechanical and thermal responses are different when making joints at different locations. The linear modal analysis suggests that the amplitude of actual contact force between the sonotrodes and metal sheets varied with joint locations, even though a constant static clamping force (i.e., 1000N) was applied when making all five joints. For instance, they were 1748N versus 1530N for the first and third Al-Mg USW joint. As a result, the resistance force at the first joint was higher, while the actual sonotrode vibration amplitude was smaller, which is consistent to the experimental measurement using a vibrometer, as shown in Figure II.4.1.5.4(a) and Figure II.4.1.5.4(b). Further nonlinear thermal-mechanical modeling shows a higher heat generation when making the first USW joint versus the third joint, as observed in Figure II.4.1.5.5(a), which is also consistent with the experimental measurements using an infrared camera shown in Figure II.4.1.5.5(b).

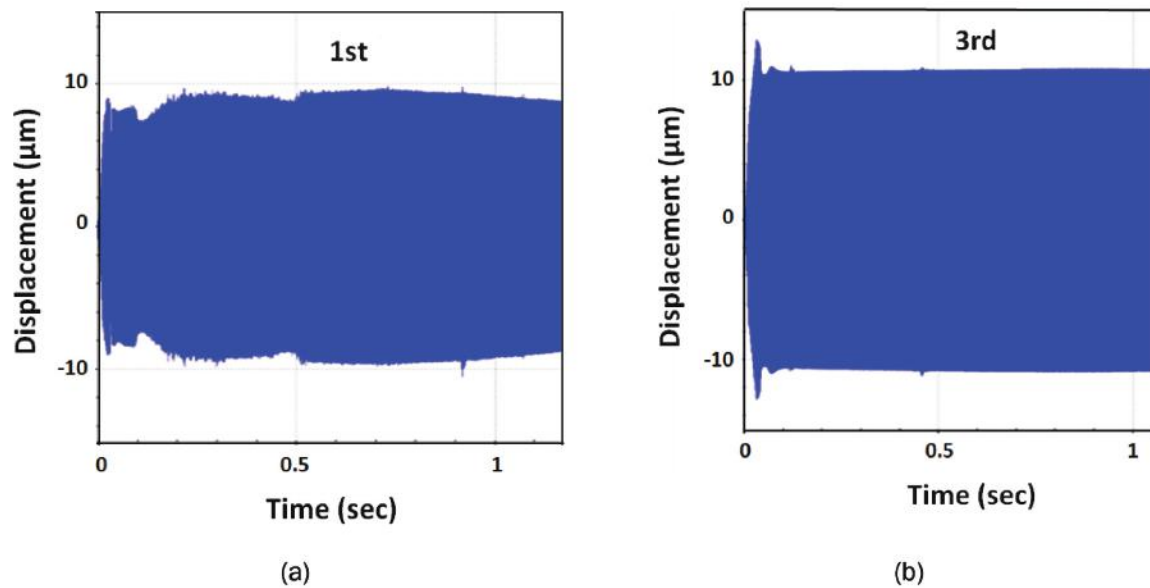


Figure II.4.1.64. Measured sonotrode vibration amplitude during the (a) first and (b) third USW although the power setting was identical. Source: ORNL.

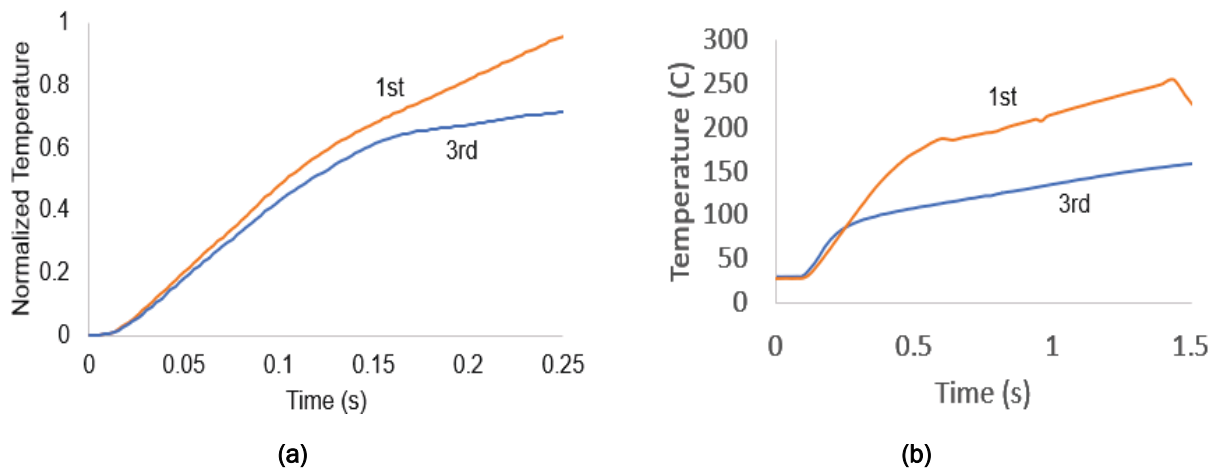


Figure II.4.1.65. (a) Predicted and (b) measured temperature history showing a higher temperature occurred when making the first USW joint. Source: ORNL.

Before utilization of the model, the trial-and-error experimental processes resulted in inconsistent weld quality at different weld locations for joining large coupons. Particularly for Mg-Al coupons, no effective joint was formed in the middle of the coupons (e.g., third joint). Great success has been achieved after adoption of the numerical models for better design and optimization of the process parameters. Figure II.4.1.1.7. and Figure II.4.1.1.8., respectively, plot the lap-shear mechanical strength results for each joint in the large coupons and the comparison with the reference joint strength obtained from the single-joint coupons. For Al-Mg, an overall average strength of 1.92 kN of the large coupons was achieved, which was 83.5% of the reference strength 2.3 kN obtained on the single-joint coupon. For Al-steel, the average joint strength of the large coupons was almost identical to what was obtained on the single-joint coupons.

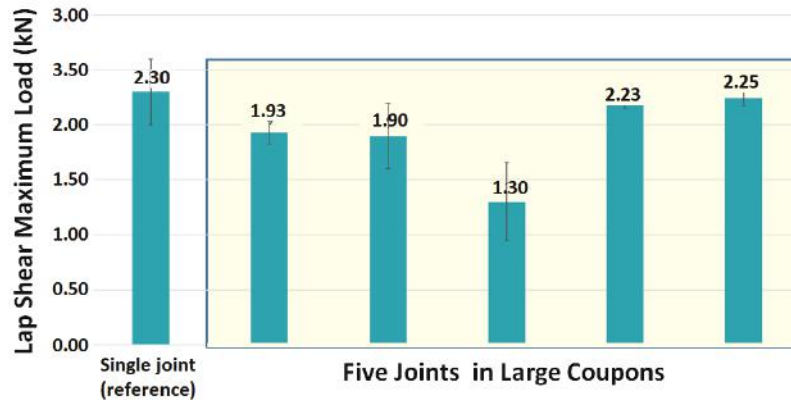


Figure II.4.1.66. Reference single-joint strength and strength of each joint in large coupons of Al-Mg.
Source: ORNL.

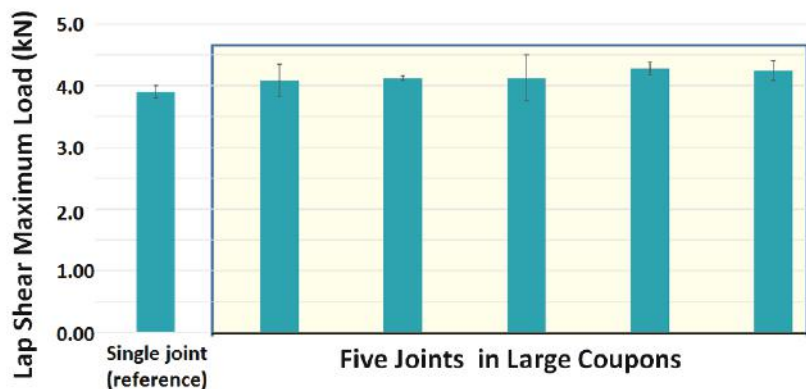


Figure II.4.1.67. Reference single-joint strength and strength of each joint in large coupons of Al-steel.
Source: ORNL.

Conclusions

The research and development in FY 2022 led to the following major achievement and findings:

- USW process is not only material-dependent, but also geometry-dependent. A process parameter set developed on single-joint small coupons cannot be readily applied to join large structures consisting of multiple joints.
- Numerical models can be adopted for better design and optimization of the process parameters.
- USW is feasible to join large dissimilar metal coupons (e.g., Mg-steel, Al-steel, Mg-Al).

Key Publications

1. Chen, J., Y.-C. Lim, H. Huang, Z. Feng, and X. Sun, 2019, “Ultrasonic welding of AZ31B magnesium alloy,” *MRS Bull.*, Vol. 44, No. 8, pp. 630–636. <https://doi.org/10.1557/mrs.2019.182>.
2. Chen, J., Y.-C. Lim, H. Huang, and Z. Feng, 2019, “Ultrasonic welding of AZ31B magnesium and DP590 steel,” *American Welding Society Annual Conference*, 11–14 November 2019, Chicago, IL, USA.
3. Chen, J., Y. C. Lim, D. N. Leonard, H. Huang, Z. Feng, and X. Sun, 2020, “In situ and post-mortem characterizations of ultrasonic spot-welded AZ31B and coated DP 590 steel joints,” *Metals*, Vol. 10, No. 7, Art. 899. <https://doi.org/10.3390/met10070899>.
4. Chen, J., R. W. Davies, Z. Feng, X. Hu, H. Huang, and X. Sun, 2020, “Ultrasonically assisted self-piercing riveting,” U.S. Patent Application No. 16/585,754, filed 2 April 2020, UT-Battelle, LLC.
5. Chen, J., Y. Li, H. Huang, J. Cheng, Y.-C. Lim, X. Hu, Z. Feng, 2022, “Ultrasonic spot-welding of immiscible mg/steel: bonding mechanisms and approach to weld multi-joint components,” *Advances in Welding and Additive Manufacturing Research (AWAMR) Conference*, 13–16 June 2022, Virtual (Invited).
6. Huang, H., J. Chen, Y.-C. Lim, X. Hu, J. Cheng, Z. Feng, and X. Sun, 2019, “Heat generation and deformation in ultrasonic welding of magnesium alloy AZ31,” *J. Mater. Process. Technol.*, Vol. 272, pp. 125–136. <https://doi.org/10.1016/j.jmatprotec.2019.05.016>.
7. Huang, H., J. Chen, Y.-C. Lim, Z. Feng, and X. Sun, 2019, “Enhance heat generation and joint strength in dissimilar metal ultrasonic welds by surface engineering,” *American Welding Society Annual Conference*, 11–14 November 2019, Chicago, IL, USA.
8. Jun, J., J. Chen, Y.-C. Lim, M. Brady, D. N. Leonard, and Z. Feng, 2020, “Corrosion behavior of ultrasonic-welded AZ31B and DP steel with and without galvanize layer,” *TMS Coatings and Surface Engineering for Environmental Protection II Conference*, 23–27 February 2020, San Diego, CA, USA (Invited).
9. Lim, Y.-C., Z. Feng, J. Chen, X. Sun, and R. W. Davies, 2022, “Ultrasonic rivet joining of dissimilar materials,” U.S. Patent 11,253,908 B2, Awarded 22 February 2022. Available at: <https://www.osti.gov/servlets/purl/1892631> (last accessed 17 March 2023).
10. Xiong, L., A. Chuang, D. Singh, J. Chen, Y.-C. Lim, and Z. Feng, 2020, “Synchrotron XRD and CT studies of ultrasonic welding dissimilar Mg-Fe metals,” *TMS Coatings and Surface Engineering for Environmental Protection II Conference*, 23–27 February 2020, San Diego, CA, USA.
11. Pending patent: Chen, J., Y.-C. Lim, H. Huang, Z. Feng, A method to consistently produce high-quality ultrasonically welded spot joints in large metal structures. (US Patent application. 63/358,250, July 5, 2022). Invention Reference # 202104997. <https://www.ornl.gov/technology/202104997>

References

1. Upadhyay, P., H. Das, J. Chen, Z. Feng, H. Huang, Y. C. Lim, Y. Li, D. N. Leonard, X. Sun, L. Xiong, C. A. Chuang, and D. Singh, 2021, *Solid-State Joining of Magnesium Sheet to High-Strength Steel*, ORNL/SPR-2021/1836, Oak Ridge National Laboratory, Oak Ridge, TN, USA. <https://doi.org/10.2172/1772623>.
2. Chen, J., R. W. Davies, Z. Feng, X. Hu, H. Huang, and X. Sun, 2020, “Ultrasonically assisted self-piercing riveting,” U.S. Patent Application No. 16/585,754, filed 2 April 2020, UT-Battelle, LLC.

Acknowledgments

The authors acknowledge the contributions from the following ORNL team members: Y. Li, H. Huang, Y. C. Lim, Y. Wang, J. Cheng, and D. Kyle.

II.4.2 Multi-Material Joining

II.4.2.1 A Hybrid Physics-Based, Data-Driven Approach to Model Damage Accumulation in the Corrosion of Polymeric Adhesives (Michigan State University)

Roozbeh Dargazany, Principal Investigator

Michigan State University
428 S. Shaw Ln., Rm. #3567
East Lansing, MI 48824
E-mail: roozbeh@msu.edu

Christopher Schooler, DOE Technology Development Manager

U.S. Department of Energy
E-mail: christopher.schooler@ee.doe.gov

Start Date: October 1, 2018 End Date: December 31, 2022
Project Funding (FY 2022): \$1,345,954 DOE share: \$944,202 Non-DOE share: \$401,752

Project Introduction

The degradation of polymeric adhesives in dissimilar joints is a menace to electric and structural components of the automotive industry. In polymeric adhesives, failure often occurs due to damage accumulated from discrete environmental sources—thermal degradation, oxidation, hydrolysis, radiation, and moisture—that are combined with progressive damage mechanisms, such as aging and fatigue. Because most damage mechanisms that lead to degradation act in parallel, the estimation of the lifetime of a polymeric material becomes a significant reliability issue. No study currently exists that can simultaneously consider even two of these phenomena. Most current efforts are directed toward a single-phenomenon, single-model approach in which a model is developed to cover one specific damage mechanism. While this approach is advantageous in exploring single mechanisms, it is strongly inconclusive for degradation that occurs by multiple damage mechanisms. Our team plans to take a fresh perspective by designing a hybrid constitutive/data-driven approach that allows models of different damage mechanisms to be integrated into one model and then used to explore the degradation-induced failure of polymeric adhesives. The theoretical-computational part of this work is divided into four research components, as discussed in the ‘Approach’ section.

Objectives

This project aims to develop and validate a model to predict degradation-induced failure in polymeric adhesives with respect to damage accumulated by different degradation and fatigue mechanisms within 10% of the measured performance. Models of different damage mechanisms will be integrated into one platform and used to explore the degradation-induced failure of polymeric composites. Initially, the focus will be on modeling and coupling of viscoelasticity, thermo-oxidation, photo-oxidation, and moisture degradation. The platform output will be given to a NN engine to calculate the remaining service life. Using the NN, a new fatigue-failure model will be developed that considers the degradation effect.

Approach

This report covers our results for FY 2022, where the focus was on understanding, characterizing, and modeling individual degradation mechanisms. The modeling task consists of ten major parts, each focusing on multiscale modeling of individual damage mechanisms based on sub-structural changes associated with them:

- **Thermo-oxidative model:** Modeling and validation finished in FY 2020
- **Vibration-induced model:** This has been developed based on Michigan State University’s (MSU’s) quasi-static [1] and viscoelastic [2] models in FY 2020
- **Thermo + Vibration + Mechanical:** Modeling and validation finished in FY 2021
- **Thermo + Fatigue + Mechanical:** Modeling and validation finished in FY 2022

- **UV + Thermal + Mechanical:** Modeling and validation finished in FY 2021
- **Hydrolysis + Mechanical:** Modeling and validation finished in FY 2020
- **Hydrolysis + Thermal (hygrothermal) + Mechanical:** Modeling and validation finished in FY 2021
- **Hydrolysis + Thermal (hygrothermal) + UV + Mechanical:** Modeling and validation finished in FY 2022
- **Machine-learned (ML) Engine:** Implementation and validation will be finished in FY 2022
- **Software Implementation and Release to Endurica:** The framework is implemented in a user-defined mechanical material behavior subroutine (UMAT) code, which will be a separate product for Endurica commercial software.

Results

Thermo + Vibration + Mechanical

The proposed model should be able to capture the constitutive behavior of polymers in both thermo- and vibration-scenarios simultaneously. In this study, we limit our discussion to the coupling of thermo-oxidative and environmental/mechanical effects.

Damage Quantification

The main goal is to find a generic damage parameter, \mathcal{D} , which is a macroscopic quantity representing all micromechanical damages due to mechanical and environmental loading. The damage indicator is considered as the amount of energy that the material can absorb before the failure point, λ_f , which is regarded as the toughness of the material. The damage, \mathcal{D} , can be defined as $\mathcal{D} = 1 - J/J_0$, where J_0 is the virgin specimen toughness, and J is the aged material toughness. The environmental damage is $\mathcal{D}_{ev} = 1 - \exp(\gamma \exp(-E_a/RT)t)$, while the mechanical damage, \mathcal{D}_{me} , is formulated for the change of maximum stress, and can be written as $\mathcal{D}_{me} = 1 - j^{-\xi}$. In the presence of two mechanical and environmental loadings, the damage can be split up into mechanical and environmental damages and can be written as $\mathcal{D} = d_1 \epsilon^{d_2} \mathcal{D}_{me}^{d_3} + \mathcal{D}_{ev}^{d_3}$, where d_1, d_2, d_3 are constant parameters that can be achieved by fitting through experimental results.

Experimental Status

The dumbbell-shaped material specimens that are in accordance with ASTM D412-C used in this study are shown in Figure II.4.2.1.1(a). The experimental characterizations are briefly summarized here and shown in Figure II.4.2.1.1(b) through Figure II.4.2.1.1(d). In this respect, a uniaxial universal testing machine (e.g., Test Resources 311 series frame) was used for the quasi-static tensile tests. All tests were displacement controlled, the extensometer grips holding each specimen were 25.4 mm apart, and all experiments were performed at average RT. Mechanical characterization of material during aging was categorized as intermittent, where material samples were kept in an air convection oven for designed durations at a constant temperature and with ambient oxygen.

To induce thermal aging damage: The aged samples were removed from the medium at predefined intervals and submitted to a short-term test at RT. Then, the specimens were stored in a stress-free state at 60°C or 80°C with 0%RH for 10 or 20 days.

To induce cyclic fatigue damage: Aged and unaged samples were exposed to uniaxial tensile cycles under displacement control settings with a certain amplitude, as shown in Figure II.4.2.1.1(c). In this respect, cyclic fatigue was induced by non-relaxing cyclic loads with different amplitudes of 10% or 20% with a crosshead speed of 50 mm/min. Accumulated damage was characterized after a certain number of cycles—namely 5, 50, 100, and 500—by measuring the changes in constitutive behavior under uniaxial loading, as shown in Figure II.4.2.1.1(d).

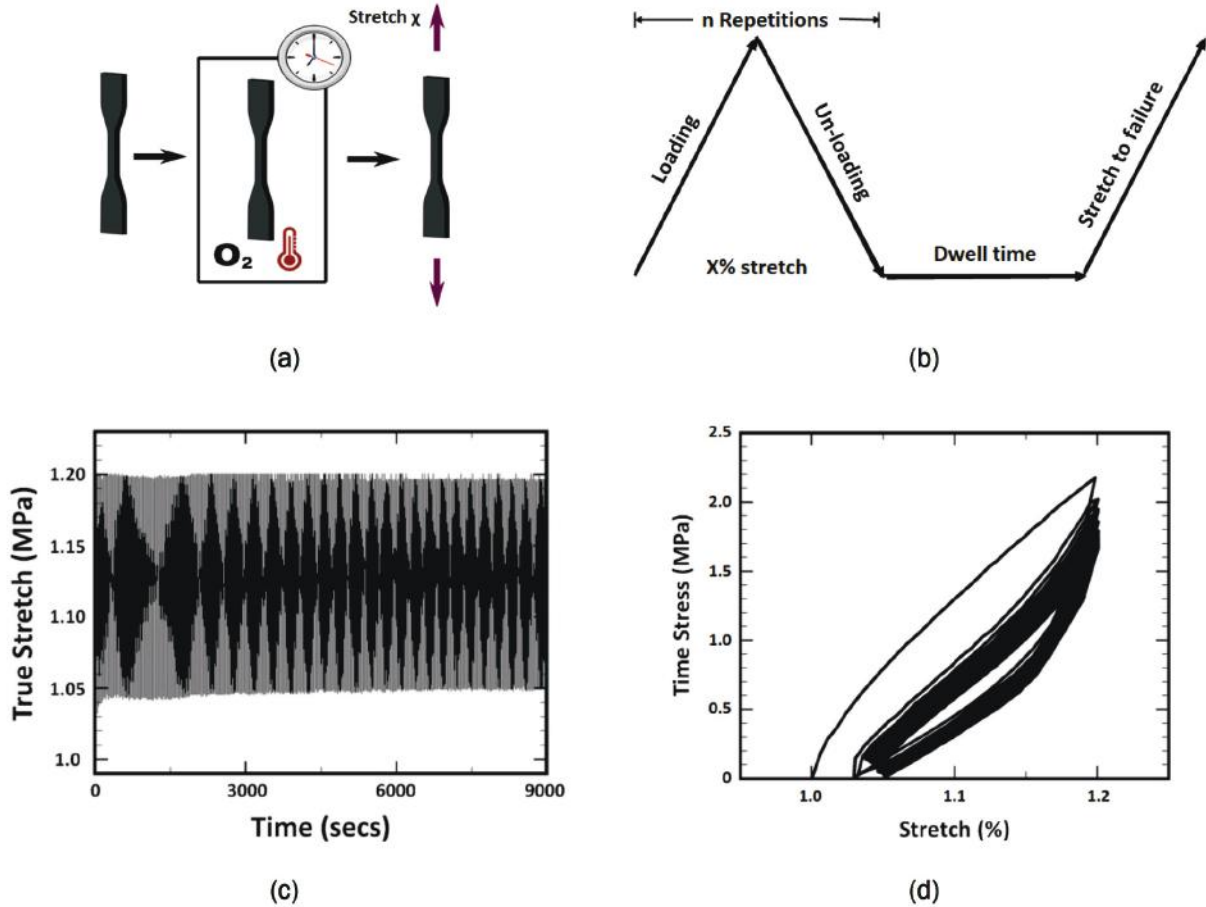


Figure II.4.2.1. Details for the thermo- and vibration experiment: (a) sample treatment, (b) loading profile, (c) example of loading test results, and (d) changes in constitutive behavior under uniaxial loading. Source: Michigan State University.

Experimental Validation

Results for the validation of the modeling against the experimental data for the thermo + vibration + mechanical testing are shown in Figure II.3.2.1.2..

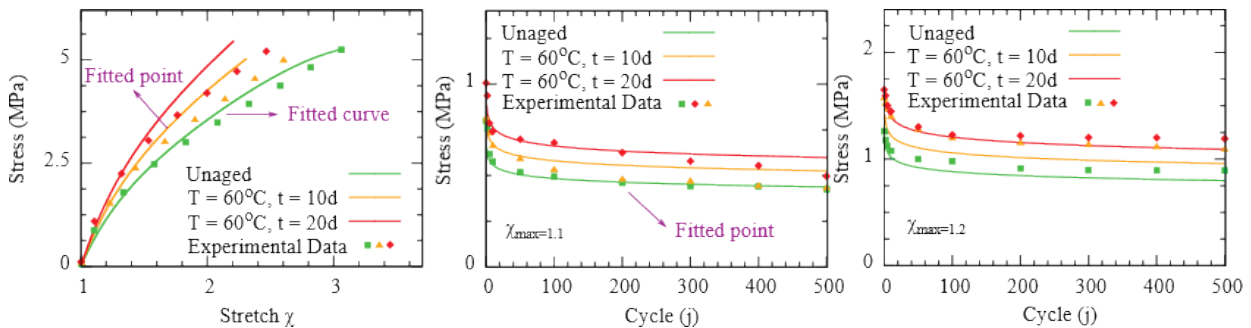


Figure II.4.2.2. Validation of the model outputs to experimental data for the thermo + vibration + mechanical testing for tensile and cyclic conditions. Source: Michigan State University.

Thermo + Fatigue + Mechanical

Aged and virgin samples were exposed to uniaxial tensile cycles under displacement control settings under designed amplitudes. Different sub-structural phenomena, such as chain scission or crosslink formation, are

responsible for the damage accumulation in various mechanical (e.g., chain breakage) [3][4] conditions and environmental degradation (e.g., chain scission + crosslink formation). Experimental data suggests the evolution of σ_{max}^j in quasi-static cyclic tests depends mainly on the number of cycles, j , and the status of thermal damage (e.g., aging time and temperature). Due to fatigue-induced damage, the stress-stretch curves of elastomers soften in each cycle toward a steady-state value often known as the fatigue limit. The peak stress level σ_{max}^1 is at its maximum in the first cycle and continuously decreases with the number of cycles toward a steady-state σ_{max}^∞ . By normalizing the peak stress value to that of the first cycle, σ_{max}^1 , one can define a dimensionless, strain-independent function,

$$\hat{\sigma}^j = \sigma_{max}^j(\lambda_i) / \sigma_{max}^1(\lambda_i) \approx j^\xi \quad (1)$$

where ξ is a material parameter.

Experimental Validation

Results for the validation of the modeling against the experimental data for the thermo + fatigue + mechanical testing are shown in Figure II.4.2.1.3.

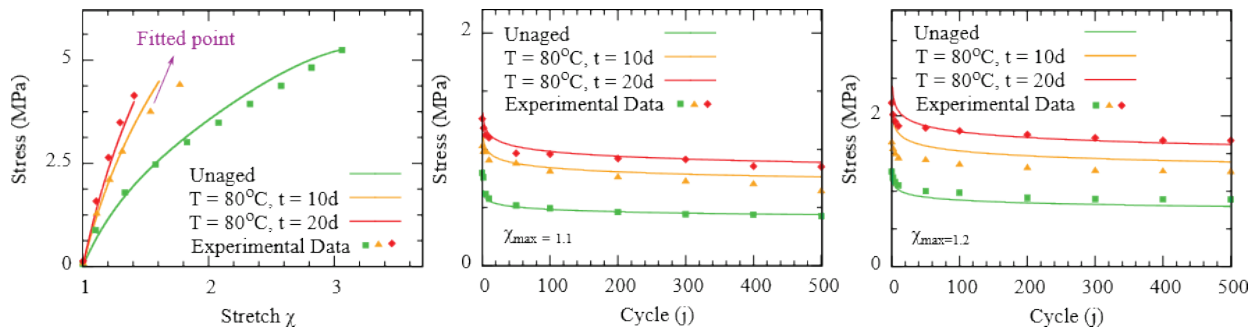


Figure II.4.2.3. Validation of the model outputs to experimental data for the thermo + fatigue + mechanical testing for tensile and cyclic conditions. Source: Michigan State University.

Thermo + Hydrolysis + Ultraviolet (UV) + Mechanical

The synergized effects of diverse environmental conditions, such as humidity, temperature, UV, and oxygen, are considered through a generic model by combining network alteration, hygrothermal, and photothermal oxidation models [5].

The strain energy of the polymer matrix, $\Psi(\mathbf{F}, t, T, RH, \iota)$, could be considered as a nonlinear interpolation of two reference states of the polymer matrix, namely initial Ψ_0 and infinity Ψ_∞ [6], where

$$\Psi(\mathbf{F}, t, T, RH, \iota) = N(t, T)\Psi_0 + N'(t, T)\Psi_\infty \quad (2)$$

$N(t, T)$ is the interpolation function that could be considered an Arrhenius decay function and rewritten as: $N(t, T) = \exp(-\gamma_1 \exp(-E_1/RT)t)$, where γ_1 is the underlying degradation rate, E_1 the activation energy, and R the universal gas constant. With the synergized effect of UV radiation, which could be written as

$$N(t, T, \iota) = \exp(-[\gamma_2 \iota^\kappa \exp(-\frac{E_2}{RT}) + \gamma_1 \exp(-\frac{E_1}{RT})]t) \quad (3)$$

where ι is the radiation dose rate, and γ_2 and κ are adjustable empirical parameters. The synergism rate is independent of the aging time at a given dose rate and temperature and should be considered as the weakness of this shape function. The network decomposition theory is utilized to describe the infinity reference state. The assumption is made that there is competition between two networks—namely, hydro, Ψ_h , and photo-

thermo networks, Ψ_{pt} —to lead the main role of the damage mechanism. The contribution of the hydro network in constructing the infinity state is assumed to have the same form as water uptake, which can be written as:

$$\Psi_{\infty} = (1 - \beta)\Psi_{pt} + \beta\Psi_h, \text{ where } \beta(t, T, RH) = \text{erf}(RH/Q) \sqrt{\gamma_3 \exp[-E_3/RT]t} \quad (4)$$

where Q and γ_3 are adjusting parameters between the value of β between 0 and 1.

Experimental Validation

For this aging study, we utilized the Q-lab accelerated weathering testers to age the specimens at 45°C and 60°C. In both temperatures, UV exposure cycles have been combined with 10% relative humidity (RH) (thermo-oxidation) and 100% RH (condensation) cycles for an aging duration of 6, 10, 20, 30, 50, and 80 days. After completing trio-aging, a backward validation approach was performed to characterize material response in isolated environments (i.e., UV, condensation, and thermo-oxidation). Those data were required to validate individual damage models by knowing the exact contribution of each environment towards the net degradation resulting in the trio-aging conditions. Aging and testing have been completed for up to 80 days, which was the maximum designed condition for this experiment. Results for the validation of the modeling against the experimental data for the thermo + hydrolysis + UV + mechanical testing are shown in Figure II.4.2.1.4.

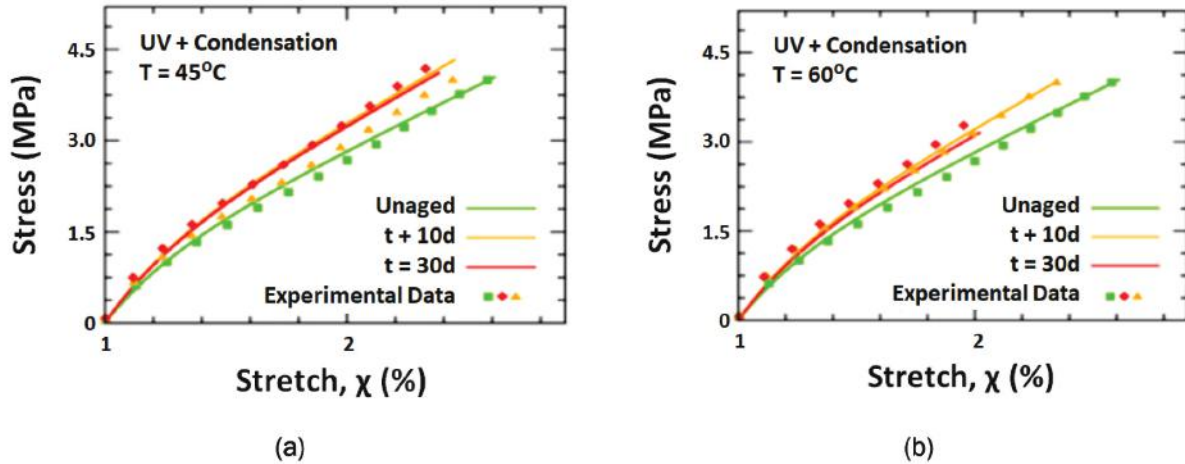


Figure II.4.2.4. Validation of trio-aging against experimental data for the thermo + hydrolysis + UV + mechanical testing at (a) 45°C and (b) 60°C. Source: Michigan State University.

ML Model

Our previous work on physics constrained NNs inspired the concept of the ML model. The model is defined by a simple deep-learned NN, which is super-constrained by laws derived from physics, thermodynamics, and continuum mechanics. To estimate the simultaneous impacts of environmental and mechanical aging on the constitutive and failure behavior of adhesives, a physics-informed data-driven constitutive model is provided. Individually, each of such degradation damages has received in-depth research. Here, simulating the loss that results from those systems operating simultaneously is the main objective. In this regard, using their respective aging mechanisms, we individually model the effects of each aging state before coupling them using the idea of the conditional NN. As a result, the physics-informed ML approach couples kinetic equations representing damage of each damage process to enable the consideration of mechanical and environmental damage synergy on the constitutive response of the polymer matrix. A model is built based on the entire independence of mechanical and environmental effects, following our recent models of thermal-oxidative aging and hydrolytic aging. The developed model is evaluated against a wide range of experimental data for validation. The suggested model offers encouraging findings with satisfactory precision. For the ML model validation, we incorporated data sets from silicone- and polyurethane-based adhesives aged in thermo-oxidative (0%RH) and

hydrolytic aging (submerged in distilled water) conditions for 1, 10, and 30 days at 60°C, 80°C, and 95°C, respectively, as shown in Figure II.4.2.1.5.

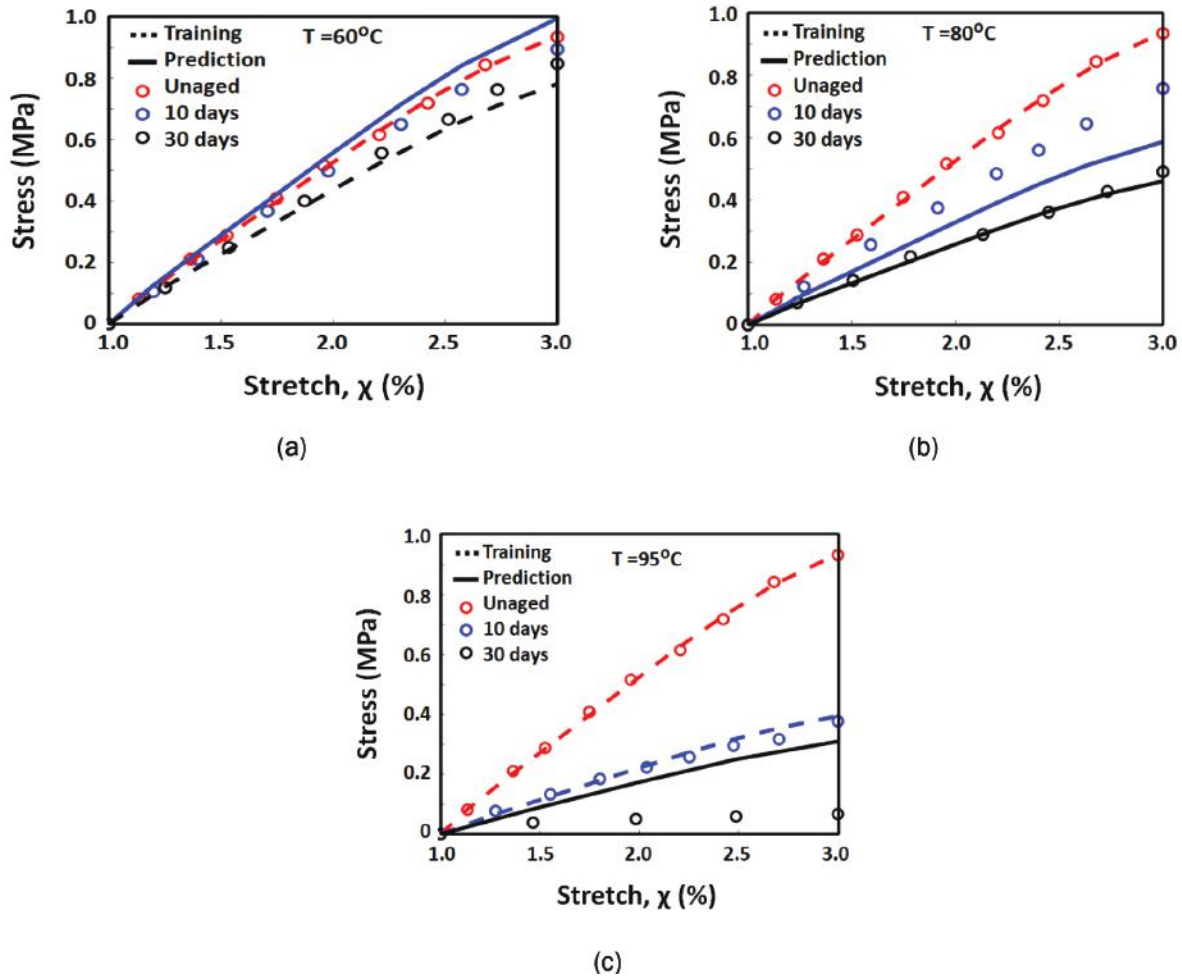


Figure II.4.2.5. V Validation of model prediction for hydrolysis experimental data at (a) 60°C, (b) 80°C, and (c) 95°C. Source: Michigan State University.

Software Implementation and Release to Endurica

At Endurica, the aging model is described using a scaling factor. They set reference lines based on virgin material, then linearly scaled the stiffness using Arrhenius equations. The aging model developed at MSU will be a stand-alone product line in the Endurica software environment. The MSU model is achieved in UMAT, a user subroutine in Abaqus. After deriving the 2nd Piola-Kirchhoff stress and tangent modulus, the total Lagrangian finite strain is formulated under the in-compressible plane stress condition. The Newton-Raphson method is applied to solve these nonlinear equations.

Advantages of using UMAT:

1. High accuracy of prediction, same as the constitutive model.
2. Versatile to different geometry and different materials.

The disadvantage of using UMAT:

1. Job creation in Abaqus needs multiple input files.
2. Material parameters need to be fitted before simulation.

Conclusions

We developed an integrated experimental, computational, and analytical approach to creating a modular theoretical platform to predict the concurrent degradation of polymeric adhesives through multiple environmental and mechanical stressors. An extensive set of experimental tests validates our platform. The proposed model provides, for the first time, the capability to predict damage accumulation in real-time service through any loading scenario that may be induced by multiple parallel mechanical and environmental loads.

The proposed platform can also guide the design, maintenance, selection, and reliability monitoring of different adhesives. The micromechanical concepts and modeling strategies employed in this project are evolving to reflect best practices to provide the most confidence in the predicted results. By performing experimental validation against different adhesive types, the proposed platform is relevant for all thermoset/elastomeric adhesives with crosslinked networks, which are highly susceptible to damage when environmental loads are combined with mechanical loads.

Key Publications

1. Alazhary, S., H. Mohammadi, and R. Dargazany, 2020, "Thermo-oxidation analysis of structural adhesives: An experimental study," in *ASME 2020 International Mechanical Engineering Congress and Exposition (IMECE2020)*, 16–19 November 2020, Virtual, American Society of Mechanical Engineers, Paper No. IMECE2020-24323, Art. V012T12A003. <https://doi.org/10.1115/IMECE2020-24323>.
2. Bahrololoumi, A., V. Morovati, M. Shaafaey, and R. Dargazany, 2021, "A multiphysics approach on modeling of hygrothermal aging and its effects on constitutive behavior of crosslinked polymers," *J. Mech. Phys. Solids*, Vol. 156, Art. 104614. <https://doi.org/10.1016/j.jmps.2021.104614>.
3. Bahrololoumi, A., Shaafaey, M., Ayoub, G., & Dargazany, R. (2022). A failure model for damage accumulation of crosslinked polymers during parallel exposure to thermal aging & fatigue. *International Journal of Nonlinear Mechanics*, 146, 104142. <https://www.sciencedirect.com/science/article/pii/S0020746222001482>.
4. Mohammadi, H., V. Morovati, A.-E. Korayem, E. Poshtan, and R. Dargazany, 2021, "Constitutive modeling of elastomers during photo- and thermo-oxidative aging," *Polym. Degrad. Stab.*, Vol. 191, Art. 109663. <https://doi.org/10.1016/j.polymdegradstab.2021.109663>.
5. Morovati, V., A. Bahrololoumi, and R. Dargazany, 2021, "Fatigue-induced stress-softening in crosslinked multi-network elastomers: Effect of damage accumulation," *Int. J. Plast.*, Vol. 142, Art. 102993. <https://doi.org/10.1016/j.ijplas.2021.102993>.
6. Shaafaey, M., A. Bahrololoumi, H. Mohammadi, S. Alazhary, and R. Dargazany, 2021, "Investigation of hygrothermal aging on the polyurethane-based (PUB) adhesive: Substantiating competition scenario between sub-aging thermo-oxidation and hydrolytic phenomena," *J. Polym. Res.*, Vol. 28, Art. 453. <https://doi.org/10.1007/s10965-021-02718-4>.
7. Bahrololoumi, A., Shaafaey, M., Ayoub, G., & Dargazany, R. (2022). Thermal aging coupled with cyclic fatigue in crosslinked polymers: Constitutive modeling & FE implementation. *International Journal of Solids and Structures*, 252, 111800. <https://www.sciencedirect.com/science/article/pii/S0020768322002864>.

References

1. Dargazany, R., and M. Itskov, 2009, "A network evolution model for the anisotropic Mullins effect in carbon black filled rubbers," *Int. J. Solids Struct.*, Vol. 46, No. 16, pp. 2967–2977. <https://doi.org/10.1016/j.ijsolstr.2009.03.022>.
2. Khalili, L., V. Morovati, R. Dargazany, and J. Lin, 2017, "Micromechanical modeling of visco-elastic behavior of elastomers with respect to time-dependent response of single polymer chains," *Constitutive Models for Rubber X, 28–31 August 2017, Munich, Germany*, Vol. 10, Art. 523. <https://doi.org/10.1201/9781315223278-94>.

3. Mohammadi, H., and R. Dargazany, 2019, “A micromechanical approach to model thermal-induced aging in elastomers,” *Int. J. Plast.*, Vol. 118, pp. 1–16. <https://doi.org/10.1016/j.ijplas.2018.12.009>.
4. Mohammadi, H., and R. Dargazany, 2018, “Micromechanical model for thermo-oxidative aging of elastomers,” in *ASME 2018 International Mechanical Engineering Congress and Exposition (IMECE2018)*, 9–15 November 2018, Pittsburgh, PA, USA, American Society of Mechanical Engineers, Paper No. IMECE2018-88109, Art. V009T12A028. <https://doi.org/10.1115/IMECE2018-88109>.
5. Khalalili, L., A. I. Azad, J. Lin, and R. Dargazany, 2019, “Modular platform to model parallel inelastic mechanisms in rubber-like materials,” *Rubber Chem. Technol.*, Vol. 92, No. 1, pp. 51–68. <https://doi.org/10.5254/rct.19.82669>.
6. Morovati, V., and R. Dargazany, 2019, “NET v1.0: A framework to simulate permanent damage in elastomers under quasi-static deformations,” *SoftwareX*, Vol. 10, Art. 100229. <https://doi.org/10.1016/j.softx.2019.04.001>.

Acknowledgments

The authors would like to thank S. Kleinbaum, and C. Schooler, DOE-EERE VTO Technology Managers, for their comments and suggestions on the experimentation procedure and continuous feedback, as well as J. Terneus from the National Energy Technology Laboratory (NETL) for managing the progress of the project. This material is based on work supported by DOE-EERE under Award Number DE-EE0008455. This report was prepared as an account of work sponsored by an agency of the U.S. Government. The views and opinions of authors expressed herein do not necessarily state or reflect those of the U.S. Government or any agency thereof.

II.4.2.2 High-Strength Steel-Aluminum Components by Vaporizing Foil Actuator Welding (The Ohio State University)

Glenn Daehn, Co-Principal Investigator

Department of Materials Science and Engineering
The Ohio State University
295 Watts Hall, 2041 College Rd. N.
Columbus, OH 43210
E-mail: daehn.1@osu.edu

Anupam Vivek, Co-Principal Investigator

Department of Materials Science and Engineering
The Ohio State University
348 MacQuigg Labs, 105 W. Woodruff Ave.
Columbus, OH 43210
E-mail: vivek.4@osu.edu

Christopher Schooler, DOE Technology Development Manager

U.S. Department of Energy
E-mail: christopher.schooler@ee.doe.gov

Start Date: October 1, 2016

End Date: March 31, 2022

Project Funding (FY 2022): \$50,000

DOE share: \$0

Non-DOE share: \$50,000

Project Introduction

This project aims to address the challenge of effectively welding dissimilar materials—high-strength steel and high-strength Al for creating lightweight, multimaterial automotive components. Traditional fusion-based welding between dissimilar combinations of Al and steel is difficult due to starkly disparate melting points, which usually leads to the formation of brittle IMCs at the weld interface. Such joints are weak and cannot be implemented in crash-sensitive components. Structural adhesives and mechanical fasteners of various types including self-piercing rivets, flow-drilled screws, friction element welds, and RIVTAC® are currently being utilized to address this issue. Solid-state welding techniques, like friction stir and impact welding, offer an elegant alternative solution for joining dissimilar metals without the use of a third body, such as rivets. This project utilizes Vaporizing Foil Actuator Welding (VFAW), an impact welding method developed at OSU [1]. Details on this process can be found in the Materials 2017, 2018, 2019, 2020, and 2021 Annual Progress Reports [2-6], as well as several journal articles published on this technology.

VFAW has demonstrated much success in welding a wide range of alloys, including Mg-Al, Al-Cu, Ti-Cu, bulk metallic glass-Cu, and Ni-Ti. In this project, the focus is on welding specific grades of steel and Al that are relevant to automotive sub-frames and developing the technology to a level where it can be transitioned to an automotive supplier or an OEM. Besides the research on weldability of different material combinations and determining the ideal parameters through experiment and simulation, the project also includes design, production, and testing of a prototype sub-frame component, as well as the production equipment. Fully automated VFAW joints were achieved with the automation work cell. Construction, assembling, testing, and optimizing of the prototype weld head was complete. The work completed in FY 2022 was focused on the manufacture and characterization of the prototype sub-components produced in FY 2021. Two sets of engine cradles were completed and tested at OSU.

Objectives

This project accelerated and focused the development of VFAW to produce an automotive component. At project completion, the technology will be ready for adoption within the research and development groups of Tier 1 and OEMs for assembly of any mixed/advanced material bodies.

The overall objectives of the project are:

- To provide a 20% weight-reduction of the current all steel automotive component from a 2017 mid-size sedan at a cost premium of \$3/lb. saved by developing a mixed material joining technology capable of high-volume production
- To produce a component that should meet or exceed the strength and durability of the incumbent component
- To develop a predictive modeling capability for relating process, structure, and property of VFAW joints.

The specific objective for FY 2022 was:

- To evaluate the quality and performance of the VFAW engine cradle products via sub-component-level testing and characterization.

The overall approach for this project was to perform coupon-scale testing at OSU, develop welding systems and part fixtures at OSU and Coldwater, conduct prototype-scale manufacture and testing at Magna, and complete process simulation at PNNL. Ashland, Arconic, Hydro, Novelis, and Magna all provided material. The pre-prototype welding heads and final welding head were fabricated at Coldwater and tested at OSU. Coupon data were imported into the design of the prototype component, while simulated testing and design iterations led to the final part. After the prototype design was released, OSU produced sub-components and Magna performed the assembly at its prototype facility. The assembled prototypes were tested at OSU.

Approach

Prototype Production of Engine Cradles

Using the developed prototype welding head, Al-steel prototype engine cradles were produced. The discharge current from the capacitor bank was monitored by an oscilloscope during the welding process to ensure the weld quality. To better apply VFAW into the production, sub-assembly fixing was used. VFAW production was divided into three batches: (1) all the interlayer welds, (2) part of the Al-steel welds joining the sub-components, and (3) the rest of the Al-steel welds. The sub-assembly fixing was performed by Magna before production of each batch. After welding process, coating was applied to the components by Magna.

Component-Scale Testing

Prototype-scale testing of the produced prototype components could not be performed due to delays. However, to ensure that the welds in the component were sound, they were cut from various regions of welded sub-components and tested.

Results

The final prototype product, a high-strength Al-steel engine cradle that was constructed via VFAW, is shown Figure II.4.2.2.1. All of the tested welds cleared the minimum failure load requirement of 2.5 kN as set by Magna's simulation of the extreme abuse loading on the component, as shown in Figure II.4.2.2.2(d).



Figure II.4.2.6. Final prototype component with Al painted gray and steel black.
Source: The Ohio State University.

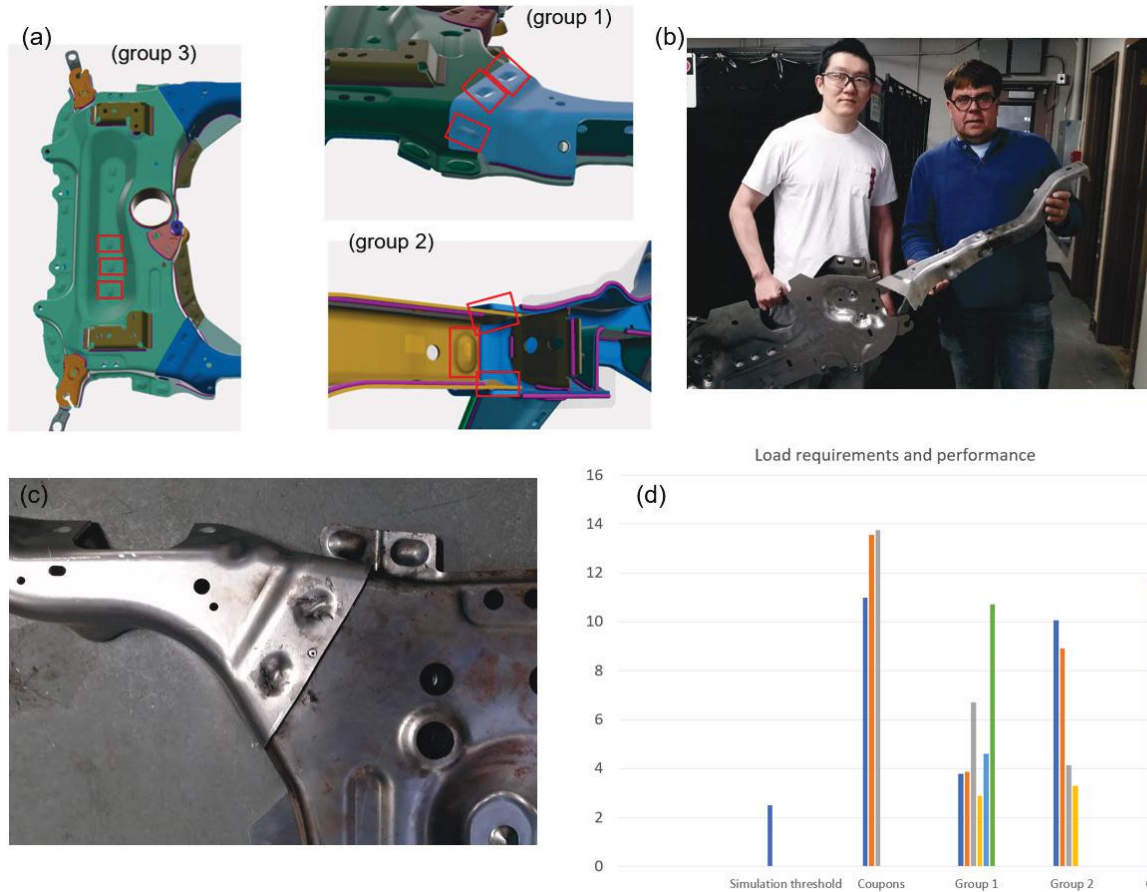


Figure II.4.2.7. Testing of prototype welds: (a) the regions where welds were cut, (b) project participants Y. Mao and J. Wright holding the welded sub-components, (c) a VFAW sub-component, and (d) the failure loads of prototype welds compared to the baseline. Source: The Ohio State University.

A final cost analysis was conducted by OSU and Magna to assess the premium that producing this component design will incur with the currently used VFAW method (i.e., double shot). For reference, the initial target set by DOE for the premium on weight-savings was \$5/lb. saved or \$11/kg saved. The costs were estimated for the process flowchart shown in Figure II.4.2.3. The material cost premium itself when using the Al-steel hybrid material designed turned out to be \$8.68/kg saved. Additionally, a cost premium of \$13.44/kg saved was incurred due to material and process costs related to assembly capital (\$3.9M) and assembly tooling (\$3.2M) required for manufacturing 255,000 units with the demonstrated process. The VFAW component of the process is still manual for the most part. These costs include the use of nine capacitor banks and attached welding heads at \$100,000 per combined unit. Therefore, the total cost premium for weight-reduction came out to be \$22.12/kg saved or \$10.03/lb. saved. The cost premium for weight-savings could have been lower, and the overall weight-savings could have been higher if a different design was chosen for prototype production.

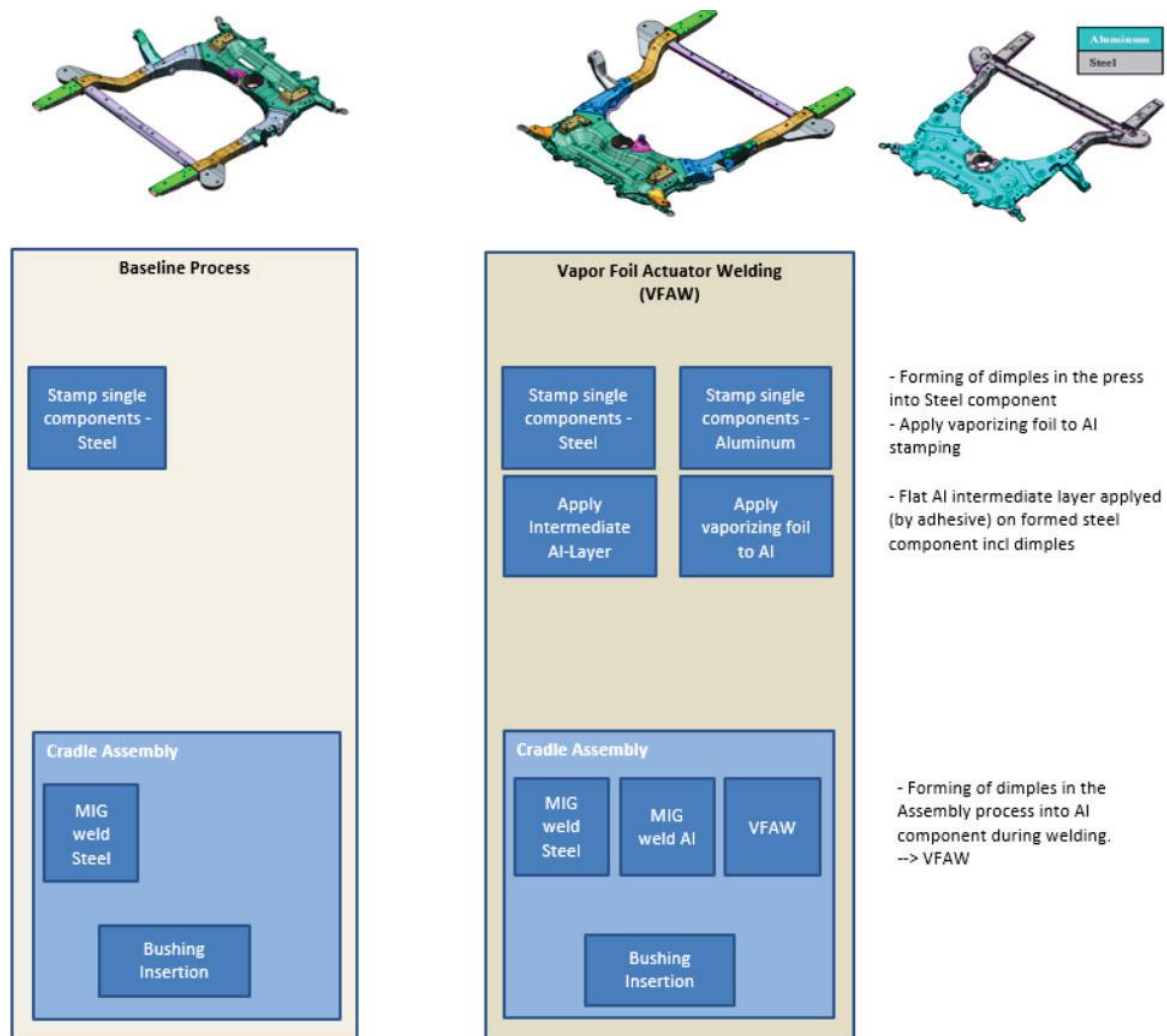


Figure II.4.2.8. A process flow for manufacturing the baseline and prototype components.
Source: The Ohio State University.

Conclusions

VFAW prototype production was complete. The prototype components were mechanically tested and met the strength requirement. The cost analysis shows the process spends more than the initial target, but the cost-efficiency can be further improved.

Key Publications

1. Gupta, V., X. Sun, K. Choi, A. Vivek, Y. Mao, and G. Daehn. 2017, “A computational modeling approach to predict the interfacial characteristics obtained in high-velocity impact welding of metals,” *Materials Science & Technology 2017*, October 8–12, 2017, Pittsburgh, PA, USA.
2. Gupta, V., K. Choi, A. Vivek, Y. Mao, X. Sun, and G. Daehn, 2018, “Prediction of joint properties obtained in the high-velocity impact welding of dissimilar metals,” *TMS 2018 Annual Meeting & Exhibition*, March 11–15, 2018, Phoenix, AZ, USA.
3. Gupta, V., T. Lee, A. Vivek, K. S. Choi, Y. Mao, and X. Sun, 2019, “A robust process-structure model for predicting the joint interface structure in impact welding,” *J. Mater. Process. Tech.*, Vol. 264, pp. 107–118. <https://doi.org/10.1016/j.jmatprotec.2018.08.047>.
4. Mao, Y., “Systematic optimization of vaporizing foil actuator welding and dynamic science,” OSU Thesis, 2021
5. Mao, Y., V. Gupta, B. Ufferman, A. Vivek, K. S. Choi, X. Sun, and G. S. Daehn, 2018, “On process, structure, property relationships in impact welding of Aluminum 6061 and Steel 4130,” *Eighth International Conference on High-Speed Forming*, May 14–15, 2018, Columbus, OH, USA.
6. Sridharan, N., J. Poplawsky, A. Vivek, A. Bhattacharya, W. Guo, H. Meyer, Y. Mao, T. Lee, G. Daehn, 2019, “Cascading microstructures in aluminum-steel interfaces created by impact welding.” *Mater. Charact.*, Vol. 151, pp. 119–128.
7. Thurston, B.P., Vivek, A., Nirudhoddi, B.S. and Daehn, G.S., 2019. Vaporizing foil actuator welding. *MRS Bulletin*, 44(8), pp.637-642.
8. Ufferman, B., “Process Development of the Vaporizing Foil Actuator Welding Technique,” OSU Thesis, 2020

References

1. Vivek, A., S. R. Hansen, B. C. Liu, and G. S. Daehn, 2013, “Vaporizing foil actuator: A tool for collision welding,” *J. Mater. Process. Tech.*, Vol. 213, No. 12, pp. 2304–2311. <https://doi.org/10.1016/j.jmatprotec.2013.07.006>.
2. DOE Vehicle Technologies Office, 2018, “FY 2017 Materials Annual Progress Report,” DOE-EERE VTO Report No. DOE/EE-1711, May 2018. <https://doi.org/10.2172/1439271>.
3. DOE Vehicle Technologies Office, 2019, “FY 2018 Materials Annual Progress Report,” DOE-EERE VTO Report No. DOE/EE-1827, April 2019. <https://doi.org/10.2172/1525365>.
4. DOE Vehicle Technologies Office, 2020, “FY 2019 Materials Annual Progress Report,” DOE-EERE VTO Report No. DOE/EE-1990, May 2020. <https://doi.org/10.2172/1637437>.
5. DOE Vehicle Technologies Office, 2020, “FY 2020 Materials Annual Progress Report,” DOE-EERE VTO Report No. DOE/EE-2236, June 2021. <https://doi.org/10.2172/1826270>.
6. DOE Vehicle Technologies Office, 2021, “FY 2021 Materials Annual Progress Report,” DOE-EERE VTO Report No. DOE/EE-2615, August 2022. Available at: https://www1.eere.energy.gov/vehiclesandfuels/downloads/VTO_2021_Materials_Consolidated_Report_FINAL_2022-09-14_compliant_v2.pdf (last accessed 15 March 2023).

II.4.2.3 Manufacturing Demonstration of a Large-scale, Multi-Material Passenger Vehicle Sub-system (Clemson University)

Srikanth Pilla, Principal Investigator

Department of Automotive Engineering
 Department of Material Science and Engineering
 Clemson University
 4 Research Dr., Ste. #340
 Greenville, SC 29607
 E-mail: spilla@clemson.edu

Christopher Schooler, DOE Technology Development Manager

U.S. Department of Energy
 E-mail: christopher.schooler@ee.doe.gov

Start Date: October 1, 2021

End Date: June 30, 2024

Project Funding (FY 2022): \$3,805,511

DOE share: \$1,570,596

Non-DOE share: \$2,234,915

Project Introduction

Transportation accounts for 26.9% of all energy consumption in the United States [1], which results in nearly one-third of all CO₂ emissions [2]. Furthermore, recent global energy markets and supply chain disruptions have given impetus towards developing cost-effective lightweighting utilizing materials, such as aluminum (Al), magnesium (Mg), and fiber-reinforced polymer (FRP) composites as they have the potential to reduce the weight of a vehicle's body-in-white (BiW) by up to 50% [3]. It is estimated that for every kilogram of weight-reduction, approximately 20 kg CO₂ emissions reduction is achievable [4]. However, lightweighting approaches that leverage a single material system do not present a cost-effective solution. Further, conceptual redesigning and optimization to suit the lightweight material system often result in tradeoffs in cost, increased manufacturing complexity and higher cycle times. Thus, a multimaterial lightweighting approach, capitalizing on the progress made in multiple domains is necessary. Despite an increasing trend in the sales of sport utility vehicles and trucks, no previous studies specifically address their lightweighting through a systemic multimaterial redesign of the vehicle structure using FRP composites.

Objectives

The goal of this project is to employ a systems approach to redesign, manufacture, and validate the glider system (e.g., BiW) of a 2019 mid-size sport utility vehicles (e.g., Honda Pilot) to achieve cost-effective and sustainable lightweighting of 160 lbs. This will be achieved by aligning with the U.S. DRIVE roadmap to leverage component consolidation, state-of-the-art design optimization tools, multimaterial transition and joining technologies, industry standard manufacturing processes, and proprietary recycling technologies. The final design will meet or exceed benchmark structural requirements, crash performance, and noise, vibration, and harshness requirements while preserving the OEM's existing factory assembly process. To meet the objectives, the team proposes to evaluate new multimaterial designs via a clean-sheet redesign approach to use novel, lightweight, and low-cost composite materials, multimaterial design optimization, patented CFRP-metal transitions, and state-of-the-art composites manufacturing technologies. The project partner organizations, as indicated in Table II.4.2.3.1, have significant expertise in the above core methodologies and the ability to provide expert opinions and guidance to ensure success in achieving the project goals.

Table II.4.2.3.1. Project Partner Organizations

Universities	Automotive OEM Partners	Computer-Aided Engineering Partners	Materials and Sustainability Partners
CU	Honda	Moldex3D	ZOLTEK
		Altair Engineering	Huntsman
OSU		Siemens	Carbon Conversions, Inc.
		Hexagon (Digimat®)	

Approach

DOE’s project objectives clearly define the scope for lightweighting and structural performance requirements, established through benchmarking of the baseline BiW by performing structural analyses for several load cases. The overall technical approach follows the automotive industry’s standard practice of product development based on the V-diagram. Because manufacturing processes play a very significant role in the end properties achieved, multiple simulation-validation loops have been incorporated into the approach at the coupon level, sub-component level, and assembly level as illustrated in Figure II.4.2.3.1 (for illustration only). The subsequent sections elaborate on efforts made on the design and simulation fronts to develop feasible multimaterial lightweighting concepts for the baseline steel intensive BiW of the 2019 Honda Pilot.

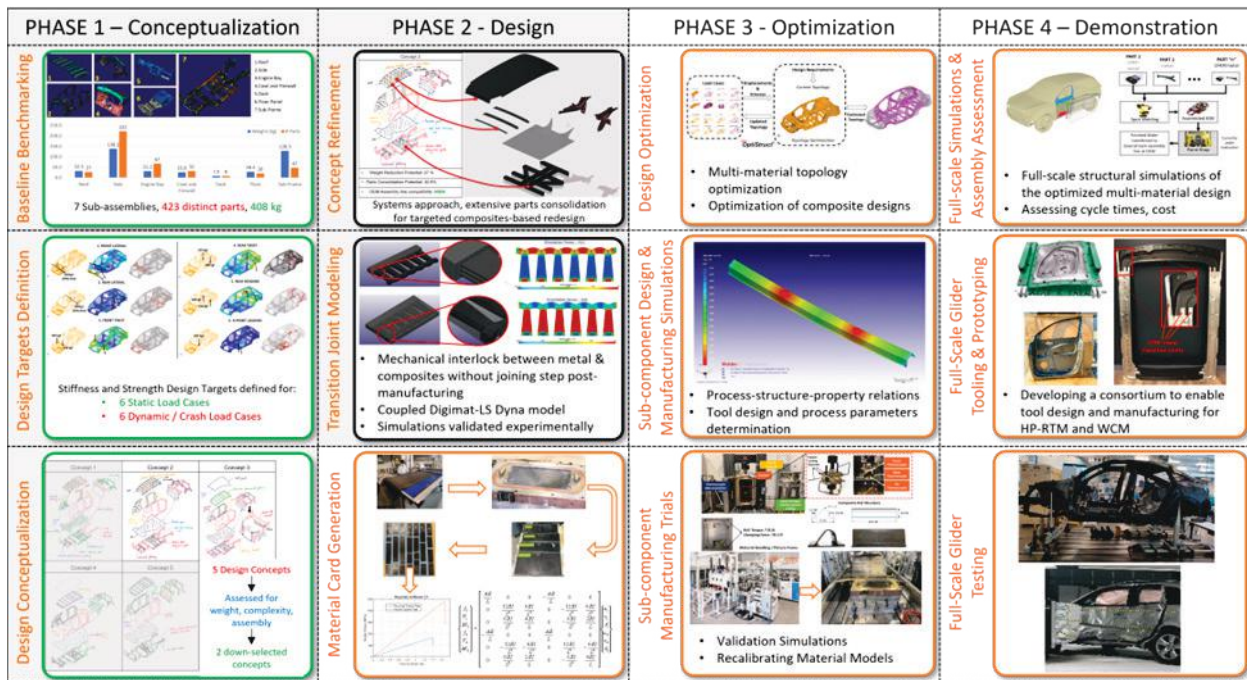


Figure II.4.2.9. Systems approach with multiple simulation-validation loops at various component scales. (For the purpose of illustration only; details not intended to be readable) Source: Clemson University.

Results

Design Assessment Criteria, Requirements and Validation Plan

Six design assessment criteria were identified based on the project objectives—lightweighting potential, parts consolidation potential that allows for secondary savings in terms of cost and cycle times, compatibility with the assembly and joining infrastructure at the OEM’s site, and the ability to meet structural design targets and scope to utilize sustainable recycled CF to enable circularity. These criteria will be used to assess different concept designs. Selection/refinement will be completed based on the matrix that is built using these criteria.

To validate the structural requirements, relevant FMVSS and Insurance Institute for Highway Safety (IIHS) dynamic testing standards were considered. Since the scope of the project is limited to the glider system, dynamic crash tests that can realistically be performed without the presence of other vehicle subsystems, such as the powertrain and transmission, were specifically identified to be performed on the full-scale prototype. Other dynamic tests, such as frontal crash and rear crash, were not considered for actual physical testing as the significant inertial mass associated with the powertrain and transmission would not be present. Instead, these tests will be simulated virtually and a FEA will be performed to ensure they meet or exceed simulated baseline performance, as summarized in Table II.4.2.3.2.

Table II.4.2.3.2. Planned Full-scale Glider Structural Validation Plan

Concern	Requirement	Description	Validation Plan
Static	Front lateral loading	Lateral loading at front suspension points	FEA simulation
	Rear lateral loading	Lateral loading at rear suspension points	FEA simulation
	Front axle twist loading	Torsional loading at front suspension points	Torsion Test at Clemson University International Center for Automotive Research (CUICAR)
	Rear axle twist loading	Torsional loading at rear suspension points	Torsion Test at CUICAR
	Driver H-point loading	Loading at seat mounting points	H-point Test at CUICAR
	Front axle longitudinal bending	Bending load at front suspension points	Bend Test at CUICAR
	Rear axle longitudinal bending	Bending load at rear suspension points	Bend Test at CUICAR
Dynamic	Front wheel loading	Loading on front left wheel well	FEA simulation
	Front Crash @ 40 mph (IIHS – small overlap impact)	Small overlap front impact	FEA Simulation
	Rear Crash @ 11 mph (IIHS – small overlap impact)	Small overlap rear impact	FEA Simulation
	Side Impact Test @ 55kmph (IIHS Moving deformable barrier test)	Side Impact Crashworthiness Evaluation (IIHS)	Physical testing at Transportation Research Center, Inc. (TRC)/ Virtual Testing at Clemson Composites Center
	Side-Pole Impact Test @75 deg angle, 32 kmph (FMVSS 214)	Side-pole impact loading near occupant	Virtual Testing at Clemson Composites Center
	Roof Crush Test (FMVSS 214)	Loading on the roof	Physical testing at TRC

Baseline Benchmarking

The first step in developing new design concepts was to perform detailed benchmarking of the baseline. Parts serving as vital structural components were identified by studying the baseline performance under various load cases in conjunction with the OEM's recommendations. Small components, such as local reinforcing plates, brackets, and fasteners, were identified as potential components that could be eliminated through parts consolidation. The glider assembly was divided into seven distinct subassemblies to be evaluated individually for different conceptual designs. The number of parts and their overall weight were assessed for each of the subassemblies for use as a benchmark to compare the lightweighting and parts consolidation achievable in the proposed designs, as illustrated in Figure II.4.2.3.2 [5]. The parts and weights associated with the subassemblies were used to identify focus areas for lightweighting and parts consolidation using composites. The rationale behind this approach was that the cost of more expensive composite materials would be offset by

less parts to be manufactured and assembled. This helped the design team identify conceptual designs that do not result in an overwhelming increase in the cost and assembly complexity, while also ensuring that the OEM’s joining and assembly infrastructure is still useful.

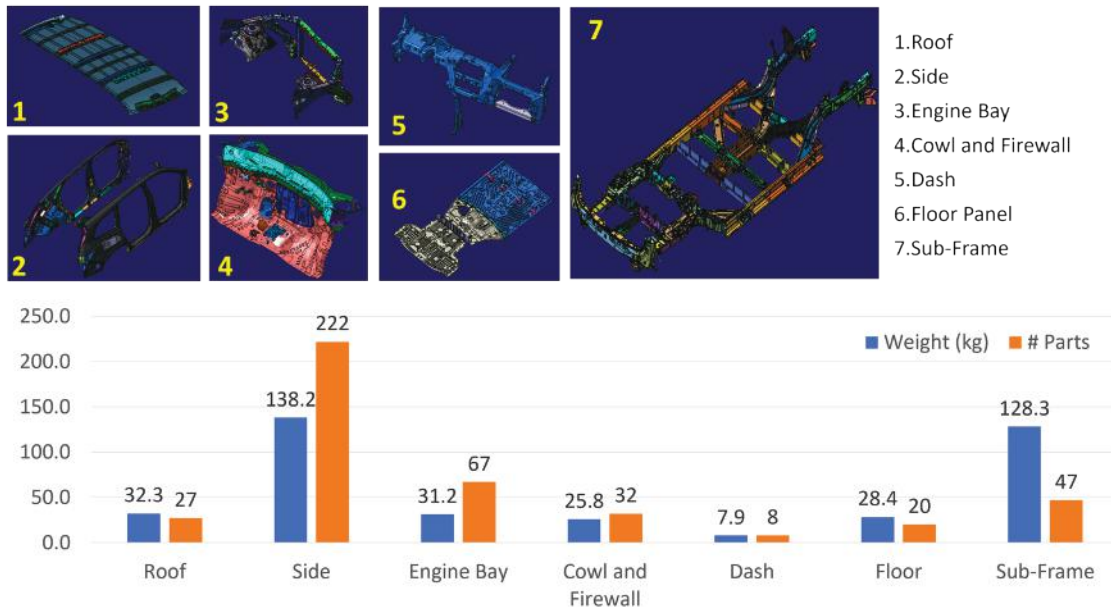


Figure II.4.2.10. Baseline BiW breakdown by sub-assembly. Source: Clemson University.

Based on Federal standards and discussions with our OEM partner, 12 global load cases were established and classified as static or dynamic. These load cases and their descriptions are explained in Figure II.4.2.3.3 [5]. Altair Optistruct is used to solve for deformation for each of the load cases. The finite element model provided by the OEM includes stiffness induced due to adhesives, glasses, and welds to accurately determine the deformations in the baseline BiW. For static load cases, the analysis is linear static using the inertia relief method to account for rigid body motion. For dynamic/crash load cases the analysis is implicit dynamics with contacts. For each static load case, stiffness is defined as the ratio of applied force to resultant deformation.

The baseline performance metrics (i.e., stiffness and peak Von Mises stresses) for both static and dynamic load cases was used to establish design development targets for the proposed design concepts. Note that this analysis assumes a linear material behavior; therefore, while it can approximate the values of stiffness, the stress and deformation results may not be accurate. The results shown here are sufficient to establish the constraints for the topology optimization problem. After discussions with the OEM, we established that the standard practice is to solve the dynamic cases under a linear assumption for initial design assessment and optimization purposes. Once a design concept is developed in detail, it will be analyzed for crash under a full elastic-plastic and damage analysis. The team also intends to go further than the OEM standards and attempt topology optimization that includes plastic deformation and damage analysis.

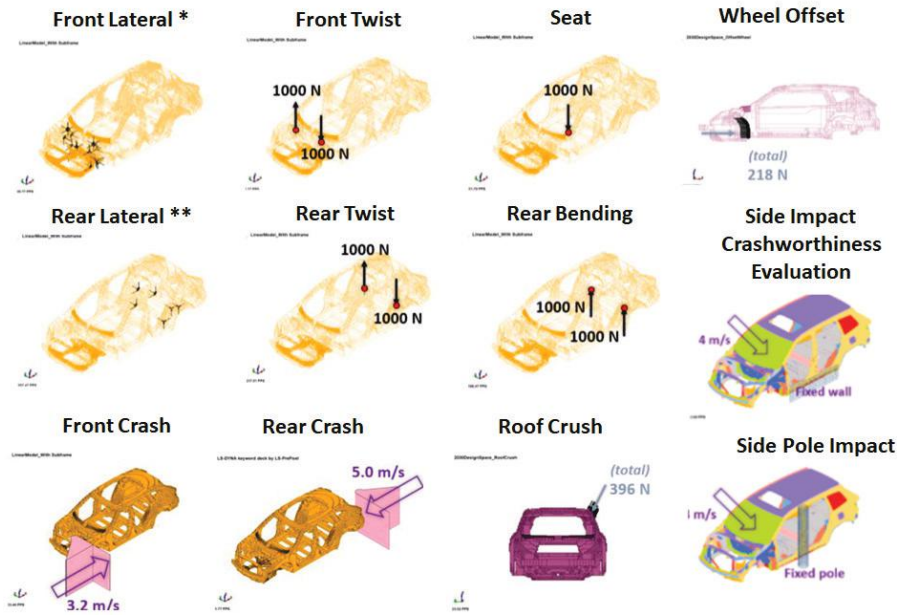


Figure II.4.2.11. Baseline BiW breakdown by 12 global load cases. Source: Clemson University.

Conceptual Designs, Design Downselection, Refinement, and Structural Assessment

Following the benchmarking study and review of feasible manufacturing and joining processes, brainstorming was initiated to develop conceptual designs that would align with the project objectives. While conceptualizing designs, it was assumed that any baseline steel component replaced with an equivalent composite or Al part would have twice the thickness of the baseline steel component. Lightweighting estimates were then calculated based on commonly available densities for a typical Al and CF-epoxy composite. Five design concepts, as illustrated in Figure II.4.2.3.4, were proposed and reviewed in detail during a team-wide design brainstorming and assessment meeting where industry experts from the OEM provided their valuable feedback.

Concept 1	Concept 2	Concept 3	Concept 4	Concept 5
<ul style="list-style-type: none"> Carry-over steel parts major replacement with aluminum selective parts consolidation with composites 	<ul style="list-style-type: none"> Carry-over steel parts major parts consolidation with composites for sub-frame and side-assembly 	<ul style="list-style-type: none"> CFRP-steel construction with transition joints CFRP-aluminum-steel transition joints for roof Subframe outer members and mid-rails retained, composite cross members 	<ul style="list-style-type: none"> Welded Aluminum sections as frames for composite panels use of basalt fibers/GFRP for panels Side panel and stiffener sub-assembly consolidated into single composite design 	<ul style="list-style-type: none"> Spaceframe with metal nodes Adhesive bonding RSW + transition joints leveraged Favorable for prototype technology demonstrator glider
Weight Reduction Potential: 17.4%	Weight Reduction Potential: 27%	Weight Reduction Potential: 30%	Weight Reduction Potential : 43%	Weight Reduction Potential: 39%
Parts Consolidation Potential: 21.75%	Parts Consolidation Potential: 32.8%	Parts Consolidation Potential: 30.5%	Parts Consolidation Potential: 39.5%	Parts Consolidation Potential: 41%
OEM Assembly line compatibility: LOW	OEM Assembly line compatibility: HIGH	OEM Assembly line compatibility: MODERATE	Assembly compatibility: MODERATE to LOW	OEM Assembly line compatibility: LOW

Figure II.4.2.12. Conceptual designs – summary, assessment, and downselection. Source: Clemson University.

Following the downselection process, the proposed design concepts 2 and 3 were translated to computer-aided drawings and subsequently evaluated for their performance under the identified load cases to verify that the concepts also meet the design targets. The first developed concept was analyzed against the same load cases. Like the baseline evaluation, the analysis was performed on Altair Hyperworks. The first nine load cases are solved under an assumption of linear static analysis, while the last four cases, referred to as ‘dynamic’ cases, are solved under a linear material implicit dynamic analysis.

The parts that were replaced with composites use a MAT8 material card for Altair Hyperworks. For the preliminary results, it is assumed that the parts are connected to the rest of the BiW using the same connections as the baseline. When material cards for the transition joints are developed, these will be updated. The composite parts were considered twice as thick as the baseline parts. Initial results showed these designs to be within 5% of the baseline, a difference small enough to be addressed by further optimization. However, to show that the concept can satisfy the baseline requirements, the thicknesses were adjusted to 3 mm for all composite parts. The results shown in Table II.4.2.3.3 are for these updated thicknesses. The concept satisfies all static requirements for the updated thicknesses, which is desired, and can be further optimized in the future.

Table II.4.2.3.3. Stiffnesses for Concept 1 vs. Baseline Performance

Load Case	Percent (%) Difference Between the Baseline and the Conceptual Designs
Front Lateral	+0.00
Rear Lateral	+17.06
Front Twist	+5.52
Rear Twist	+15.77
Rear Bending	+59.66
Driver H-point Bending	+4.93
Roof Crush	+8.27
Wheel Offset	+3.64
Small Overlap Front Crash	In progress
Small Overlap Rear Crash	In progress
Side Impact Crashworthiness Evaluation	In progress
Side-Pole Impact	In progress

Metal Composite Transition Joint Development

A framework to create a computationally friendly, yet highly accurate, model of the metal composite transition joint has been developed to capture the mechanical performance of the transition joints in the BiW simulations. The framework reduces computational costs by capturing the mechanical performance of a detailed coupon level transition joint and passing those performance matrices to a simplified, solid cuboid representation of the transition joint. The basic process modeling framework can be seen in Figure II.4.2.3.5. This framework can account for any metal composite combination, but initial validation work has targeted an Al-CF joint.

The modeling framework segments the detailed coupon level sample of the transition joint into three critical regions: (1) metal-only, (2) hybrid, and (3) composite-only. The hybrid region represents the connection between the composite loops that have been impeded into metal channels and secured using ultrasonic additive manufacturing (UAM). The metal- and composite-only regions can be modeled as simple cuboid bodies, while the hybrid region must account for the interaction between the composite loops and metal channels. The mechanical performance for each region could be determined by running a series of loading simulations in all three axes. To run these simulations, the constitutive properties of the UAM metal-only, composite-only, and hybrid fibers needed to be determined.

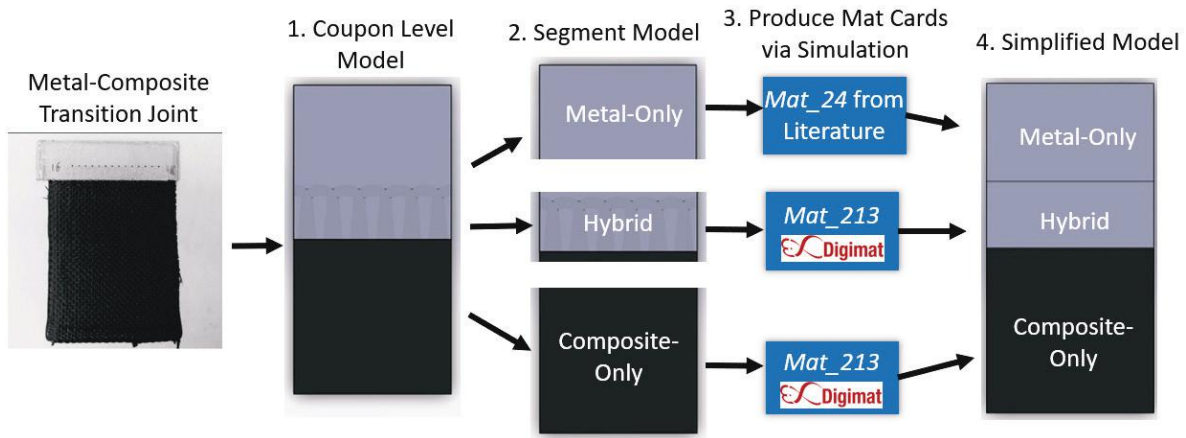


Figure II.4.2.13. Process for modeling metal composite transition joints. Source: Clemson University.

A MAT_24 (*Mat_Piecewise_Linear_Plasticity*) material card taken from Guo 2021 [6] was used to define the mechanical performance of the UAM metal regions. Therefore, a series of simulations is not needed to capture the mechanical performance of the UAM metal. However, the mechanical performance of any composite regions does require additional simulations. Digimat was called upon to define the constitutive properties in these composite simulations. Digimat used the mean-field homogenization technique to find the mechanical performance of a composite according to the microscopic interactions and volume fraction of its constituents, such as fiber and epoxy. Additionally, the strength of the composites is dependent on the orientation of its fibers. Therefore, a fiber orientation algorithm was developed to determine fiber orientation for each element in the composite loops. Composite elements in the composite-only region are treated as a woven-composite.

Currently, mechanical testing is underway to obtain experimental results to calibrate the constitutive properties of the composite material model in Digimat. Upon calibration, series stress-strain analyses will be run to determine the mechanical performance of the composite regions to populate MAT_213 (*Composite_Tabulated_Plasticity_Damage*) material cards. These cards, along with the MAT_24 card for the UAM metal, will define the mechanical performance of the simplified cuboid model of the transition joint. However, a series of initial simulations with composite regions defined by simplified material cards were run to show the simulations capture the appropriate failure modes. These results focus on a three-layer transition joint, as indicated in Figure II.4.2.3.6, which is designed for fiber failure and pullout. These results do not serve as a comparison point for experimental results but do capture the appropriate failure modes and ensure they are appropriately set-up.

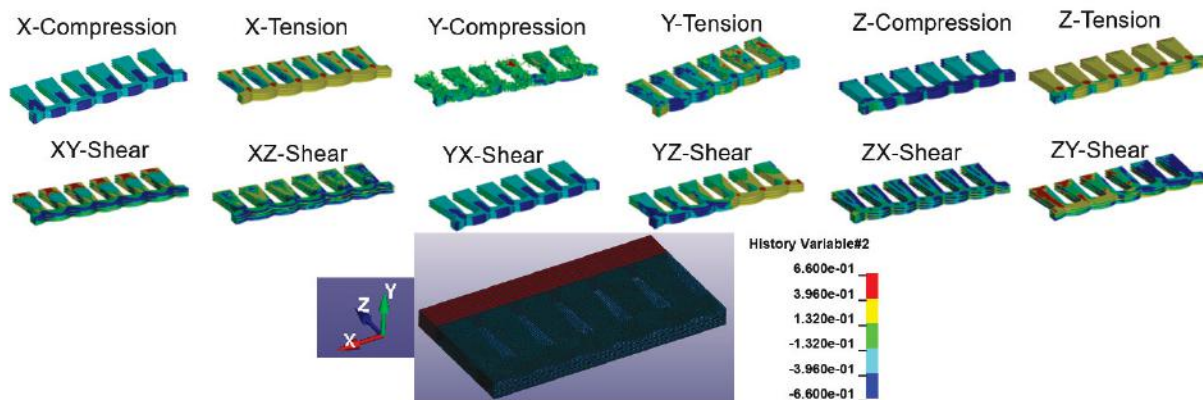


Figure II.4.2.14. Stress distributions of composite-fiber loops for three-layer transition joint. Source: Clemson University.

To calibrate the FEA model, experimentally determined mechanical properties of the CFRP-AA (CFRP-aluminum alloy) transition joint and pure CFRP are required. For the three-layer CFRP-AA transition joints, five sets of mechanical tests are planned, including longitudinal tensile testing, transverse tensile testing, longitudinal compression testing, shear testing, and the three-point bending test. For CFRP alone, three types of samples were designed: (1) woven CFRP, (2) 0-degree unidirectional CFRP, and (3) 90-degree unidirectional CFRP. For each type of CFRP sample, three mechanical tests are planned, including tensile, shear, and compression testing, as illustrated in Figure II.4.2.3.7 and Figure II.4.2.3.8, respectively. Meanwhile, Table II.4.2.3.4 and Table II.4.2.3.5 show the current state-of-the-sample building and testing results, respectively.

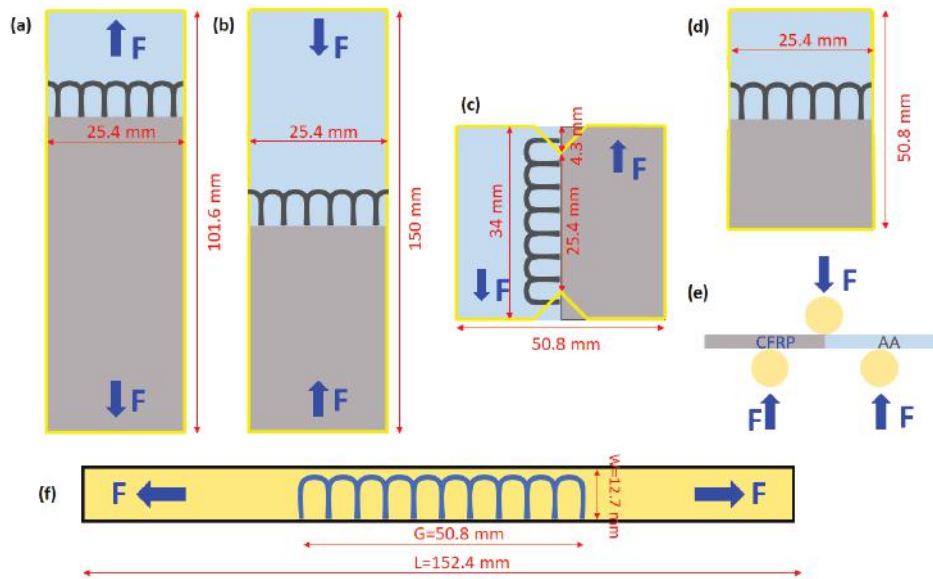


Figure II.4.2.15. CFRP-AA samples: (a) longitudinal tensile sample; (b) longitudinal compression sample; (c) shear sample; (d) and (e) three-point bending sample; and (f) transverse tensile sample. Source: The Ohio State University.

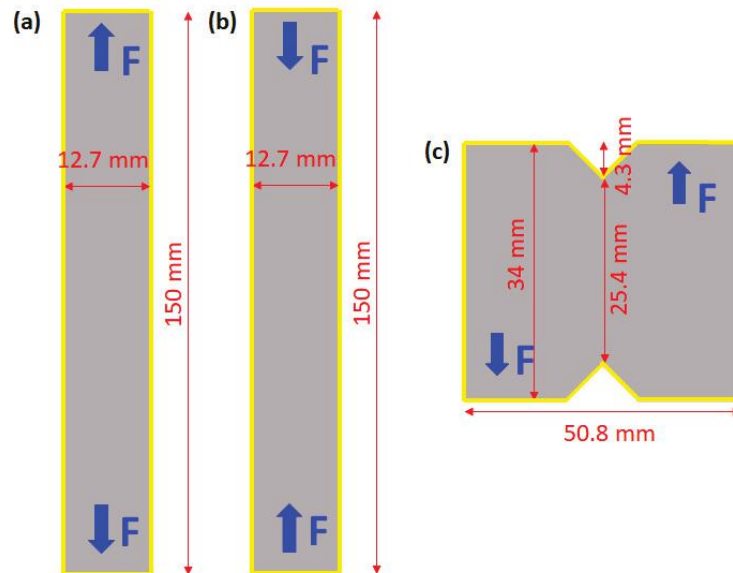


Figure II.4.2.16. Schematics of pure CFRP samples: (a) longitudinal tensile sample; (b) longitudinal compression sample; and (c) shear sample. Source: The Ohio State University.

Table II.4.2.3.4. Experimental Data from CFRP-AA Testing

Three-layer CFRP-AA	Longitudinal Tensile Test	Transverse Tensile Test	Compression Test	Shear Test	Three-Point Bending Test
Mechanical Properties	Peak load = 3315.56 N	Samples to be built	Samples built, to be tested	Peak load = 655.3 N	Samples to be built

Table II.4.2.3.5. Experimental Data from CFRP Testing

	Woven CFRP	0-Degree Unidirectional CFRP	90-Degree Unidirectional CFRP
Tensile Test	UTS=638.55 MPa	To be tested	To be tested
Shear Test	USS=74.37 MPa	USS=18.99 MPa	Failure mode unexpected
Compression Test	To be tested	To be tested	To be tested

Metal Composite Transition Joint Manufacturing Scalability

Three modifications have been made to target three primary bottlenecks in the UAM process to reduce the cycle time of metal composite transition joint fabrication. The first modification is the addition of a speed increaser to the UAM machine’s computer numerically controlled system. A speed increaser has been procured that allows for faster machining of the metal matrix channels embedded with the fiber material. The speed increaser is shown in Figure II.4.2.3.9(a). The second modification is the development of a fiber alignment device for placement of the fibers in the metal matrix channels. Three fiber alignment device prototypes have been developed that have identified the primary issue of fibers sticking to the device upon removal from the sample. A code to machine prototype-4 has been completed and simply needs to be run on the UAM machine’s computer numerically controlled system to complete the prototype. The piston-guide fit of prototype-4 is to be machined incrementally to ensure the closest possible fit. A representative graphic of the fiber alignment device assembly is shown in Figure II.4.2.3.9(b). The third modification involves the addition of a runway welding surface to the UAM machine’s table, as shown in Figure II.4.2.3.9(c). The runway increases the maximum possible transition joint length from 14 in. to 52 in. The runway is also targeted to reach a baseplate preheat temperature of 500–600°F, more than 100°F higher than the current welding surface. A higher temperature allows for easier welding of stiff materials like steel. Extensive thermal and structural finite element models have been used to determine a design capable of reaching the temperature target.

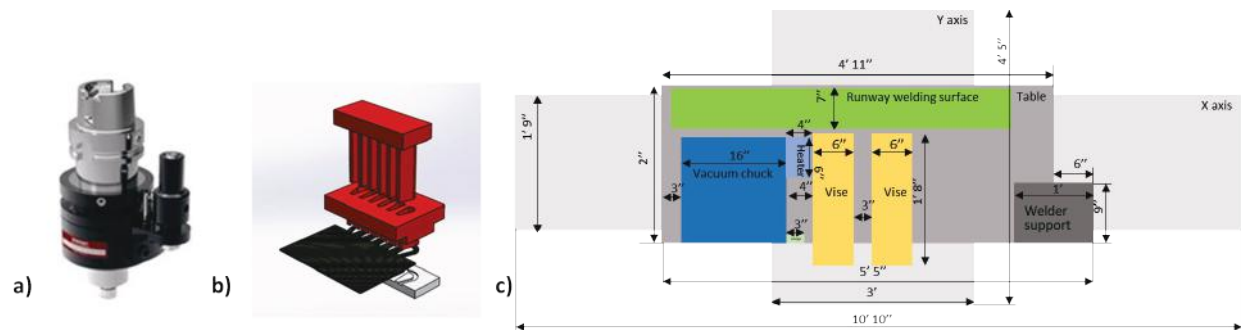


Figure II.4.2.17. UAM process modifications: (a) spindle speed increaser; (b) fiber alignment device; and (c) runway welding surface. Source: The Ohio State University.

Conclusions

In conclusion, major efforts for the first year have been dedicated to systematic benchmarking, establishing design targets, and developing solutions that utilize proposed composite manufacturing methods and multimaterial joining techniques. A holistic approach was developed for redesigning a pre-existing BIW design and incorporating composite structures without significant costs incurred. A detailed simulation and

experimental validation strategy was established to gauge performance at component, sub-assembly, and BIW system level. Development of various parametric assessment tools using the geometric features of the baseline and proposed designs enabled assessment of the proposed designs based on the design criteria and objectively downselect suitable designs for further development. The selected concepts were further developed and assessed for structural performance as compared to the baseline. To ensure the competitiveness of the proposed multimaterial designs, various machine modifications are being implemented for the metal composite transition joint fabrication setup for faster cycle times, higher repeatability, and scalability.

Key Publications

1. Deshpande, A. M., R. Sadiwala, N. Brown, S. A. Pradeep, L. M. Headings, N. Zhao, B. Losey, R. Hahnlén, M. J. Dapino, G. Li, and S. Pilla, 2022, “Design and Development of a Multimaterial, Cost-competitive, Lightweight Mid-size Sports Utility Vehicle’s Body-in-White,” *CAMX 2022 Conference Proceedings*.

References

1. Lawrence Livermore National Laboratory, 2021, “Flowcharts,” [Online] Available at: <https://flowcharts.llnl.gov/> (last accessed 15 March 2023).
2. Lawrence Livermore National Laboratory, 2021, “Carbon flow charts | Flowcharts,” [Online] Available at: <https://flowcharts.llnl.gov/commodities/carbon> (last accessed 15 March 2023).
3. U.S. Department of Energy, n.d., “Lightweight materials for cars and trucks,” [Online] Available at: <https://www.energy.gov/eere/vehicles/lightweight-materials-cars-and-trucks> (last accessed 15 March 2023).
4. Bhardwaj, B. P., 2014, *The Complete Book on Production of Automobile Components & Allied Products*. NIIR Project Consultancy Services, Delhi, India.
5. SAMPE, 2022, “Design and development of a multimaterial, cost-competitive, lightweight mid-size sports utility vehicle’s body-in-white,” [Online] Available at: <https://www.nasampe.org/store/viewproduct.aspx?ID=21248166> (last accessed 15 March 2023).
6. H. Guo, M.B. Gingerich, L.M. Headings, R. Hahnlén, and M.J. Dapino, “Seamless joining of carbon fiber and aluminum using ultrasonic additive manufacturing (UAM),” *Composite Structures*, Vol. 208, pp. 180-188, 2019. <https://doi.org/10.1016/j.compstruct.2018.10.004>.

III Crosscutting Activities

III.1 Lightweight Materials Crosscutting

III.1.1 Updated Analysis of the Relationship Between Light-Duty Vehicle Mass, Footprint, and Societal Fatality Risk per Vehicle Mile of Travel (Lawrence Berkeley National Laboratory)

Tom Wenzel, Principal Investigator

Lawrence Berkeley National Laboratory
Environmental Technologies Area
90R2002
1 Cyclotron Rd
Berkeley, CA 94720
E-mail: tpwenzel@lbl.gov

Sarah Ollila, DOE Program Manager

U.S. Department of Energy
E-mail: sarah.ollila@ee.doe.gov

Start Date: October 1, 2021

End Date: September 30, 2022

Project Funding (FY 2022): \$73,871

DOE share: \$73,871

Non-DOE share: \$0

Project Introduction

One approach to reduce fuel consumption in LD vehicles is to reduce their mass while maintaining their footprint (i.e., track width times wheelbase). However, there is concern that lightweighting vehicles will reduce their ability to protect their occupants in a crash and may lead to an increase in fatalities. This project will explore whether the relationship between vehicle weight/size and societal fatality risk in LD vehicles has changed since the previous analysis completed in 2018 [1]. This information will be critical to the NHTSA and EPA when they consider whether to change the current fuel economy/GHG emission standards for model year (MY) 2027 and later LD vehicles.

Objectives

The objective of the study is to use recent historical data to better understand the relationship between vehicle weight and size (i.e., footprint, or track width times wheelbase) and societal fatality risk (i.e., risk to occupants of the subject vehicle and other crash partners) per mile driven, after accounting for other vehicle attributes, such as four-wheel drive, antilock braking, electronic stability control systems, number and type of airbags, driver characteristics (i.e., gender and age), and crash circumstances (i.e., in rural counties, high-speed roads, high fatality states) that can influence crash frequency and severity.

Approach

The 2018 Phase 1 study [1] conducted by Lawrence Berkeley National Laboratory (LBNL) was used to estimate the percentage of mass reduction that can be considered without compromising occupant safety in the 2018 Final Determination/Rule. The results of the updated analysis can be applied in the NHTSA Volpe Model and EPA OMEGA Model to estimate the percentage of mass reduction that can be considered without compromising occupant safety as a part of future rulemaking. The 2018 Phase 1 study included MY 2004 to 2011 vehicles between calendar years 2006 and 2012; the current project will update the analysis to include 2010 to 2017 vehicles between calendar years 2012 and 2018. The methodology used to conduct the analysis is complicated and makes use of data from several sources. LBNL will seek to collaborate with NHTSA staff to update the data used for the revised analysis. However, if collaboration is not possible, LBNL will undertake additional steps to create the two databases required for the update.

Results

While the current project began in March 2021, an update on the project was not included in the FY 2021 Annual Progress Report. In FY 2021, LBNL downloaded and analyzed the national Fatality Analysis Reporting System database of all fatal crashes in the United States between 2012 and 2018, which will be used to identify case vehicles from MYs 2010 to 2017 that were involved in fatal crashes. LBNL used the Fatality Analysis Reporting System data to conduct a preliminary analysis of trends in crash fatalities to inform the detailed regression analyses to be conducted later in the project. Figure III.1.1.1 indicates that while total fatalities had stabilized between 2009 and 2014, they increased in 2015 and 2016, and then fell slightly through 2019. Compared with the previous analysis of calendar years 2006 to 2012, which are outlined in green, the fraction of fatalities in 2012 to 2018, which are outlined in blue, decreased by 10%. While the fraction of fatalities in non-collisions (mostly rollovers) decreased from 12% to 10%, pedestrian/cyclist fatalities increased from 13% to 16% between 2006 to 2012 and 2012 to 2018.

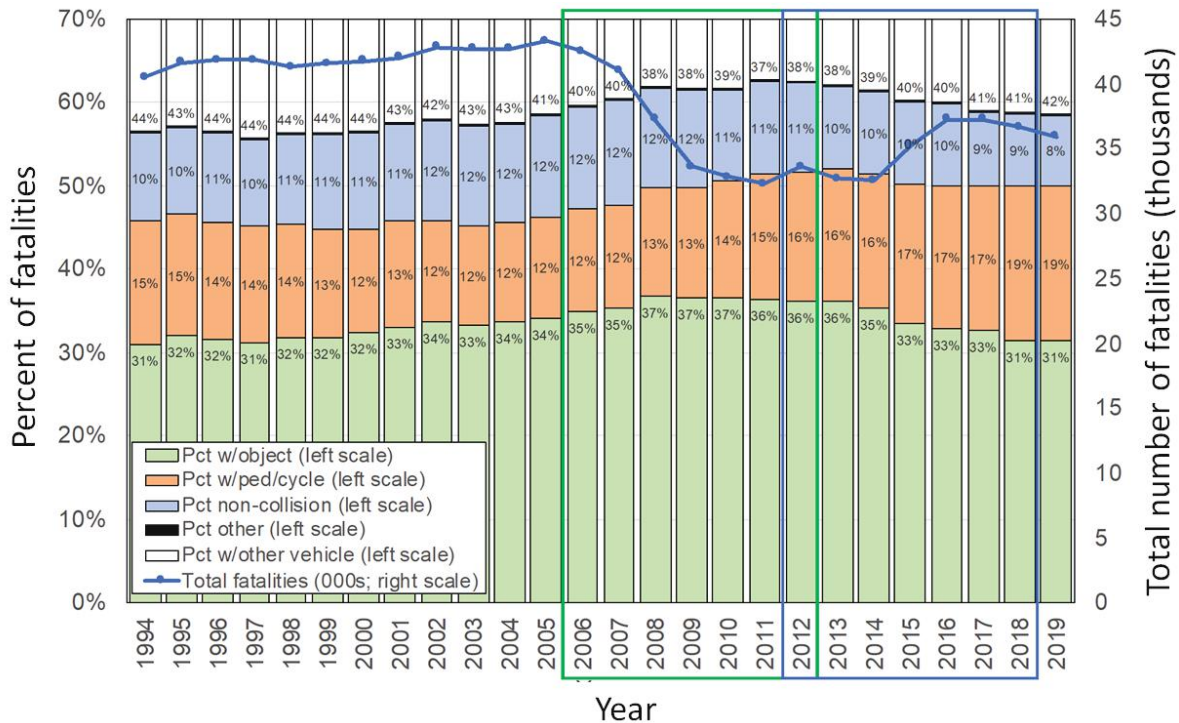


Figure III.1.1.1. Total number of U.S. crash fatalities, and distribution by crash type, by year.
 Source: NHTSA Fatality Analysis Reporting System.

Figure III.1.1.2 compares the fraction of all fatal crashes, as well as the fraction of pedestrian fatal crashes, by vehicle type and year. For cars, small pickups, and sport utility vehicles (SUVs), the trends in fraction of all pedestrian fatal crashes are similar; however, for crossover utility vehicles (CUVs), the fraction of pedestrian fatal crashes has been increasing at a faster rate than the fraction of all fatal crashes, suggesting that CUVs are responsible for the overall increase in pedestrian fatalities. For consistency with previous safety analyses, all car-based utility vehicles (i.e., those with unibody construction) are considered CUVs, whereas all truck-based utility vehicles (i.e., those with a body on frame rails) are considered SUVs, regardless of curb weight, drive type (i.e., 2-wheel drive vs. 4-wheel drive), number of seat rows, or ground clearance parameters, which determine the regulatory class of individual models for fuel economy/GHG emission standard purposes.

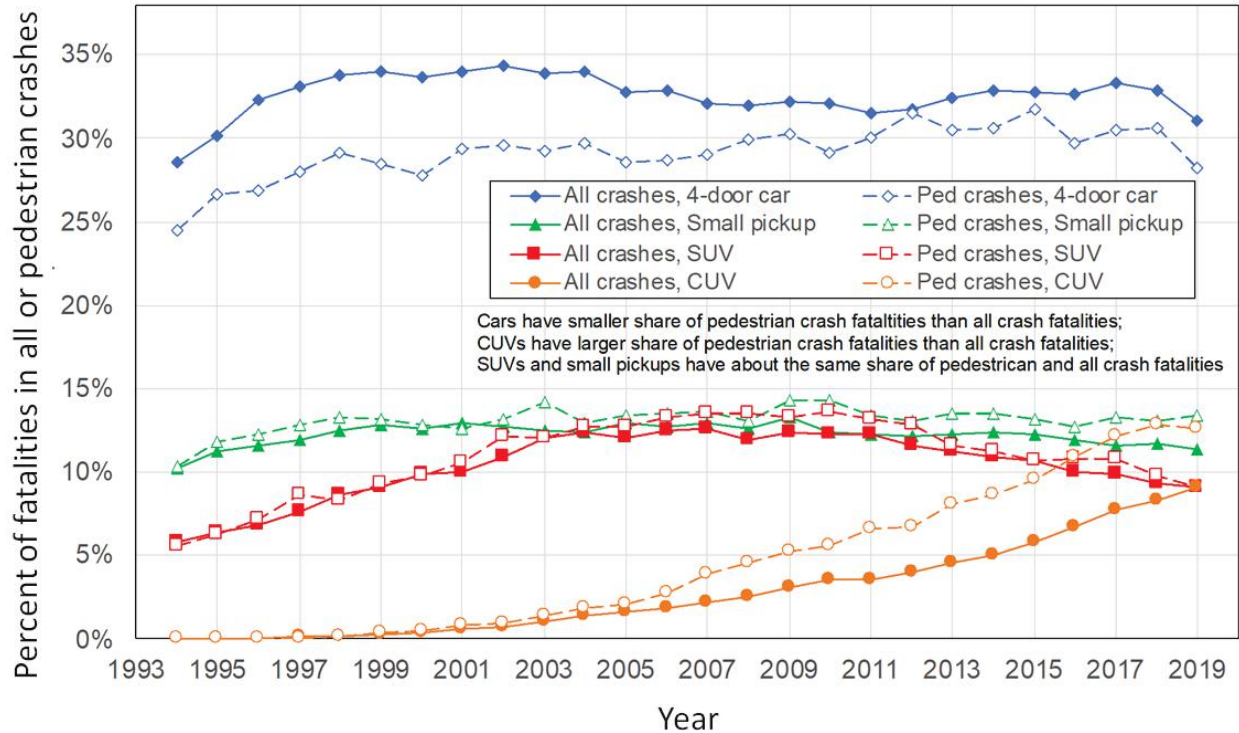


Figure III.1.1.2. Percent of fatalities in all crashes and pedestrian crashes, by vehicle type and year.
 Source: NHTSA Fatality Analysis Reporting System.

In FY 2021, NHTSA informed LBNL that it would not provide police-reported crash data that states provide to NHTSA’s State Data System. This required LBNL to contact each state directly to request the crash data necessary to conduct the analyses for this project. In FY 2021, LBNL obtained data on all police-reported crashes from several states, which will be used to develop the induced exposure dataset of non-culpable vehicles and their drivers and used to estimate the number of miles driven by vehicle/driver combinations. LBNL obtained and processed the data for ten states (i.e., Florida, Kansas, Maryland, Michigan, Missouri, New Jersey, Pennsylvania, Washington, Wisconsin, and Wyoming), which were used in the previous analyses; two states from the previous analyses (i.e., Alabama and Kentucky) no longer provide crash data including the Vehicle Identification Number (VIN). LBNL obtained data on police-reported crashes from two new states (i.e., Georgia and Texas), which now provide crash data including the VIN. LBNL is still awaiting data from the last state used in the previous analysis (i.e., Nebraska).

In FY 2021, LBNL also analyzed annual vehicle miles of travel (VMT) by vehicle type, MY, and model, using annual odometer readings between 2012 and 2018 from the Texas Department of Public Safety and Texas Council of Environmental Quality. These data will be used to develop the VMT schedules by vehicle type (i.e., passenger cars and light-duty trucks) and age, as well as the relative weights for specific vehicle models, for the current project.

In FY 2022, LBNL entered discussions with Experian to obtain vehicle registrations by calendar year, vehicle year, and model for the 13 states to be used in the analyses. These data will be used to assign national vehicle registration weights to each induced exposure vehicle in the police-reported crash data from the 13 states. LBNL also negotiated an amendment to an existing interagency agreement with the EPA to purchase national vehicle registration data at the county level from Experian for 2012 through 2021. Figure III.1.1.3 shows the distribution of vehicle registrations in an example state by vehicle type and MY as of December 2021. Figure III.1.1.3 indicates that when compared with the previous analysis of MY 2004 to 2011 vehicles, which are outlined in green, the fraction of MY 2010 to 2017, which are outlined in blue, CUVs nearly doubled from 15% to 29%, while the fraction of cars decreased slightly from 36% to 32% but continued to decrease substantially after MY 2017. The fraction of small and large pickups held fairly constant, but the fraction of SUVs decreased substantially from 14% to 8% between MYs 2004 to 2011 and MYs 2010 to 2017. Note that these registration trends are merely suggestive, as they are for a small state that is relatively rural.

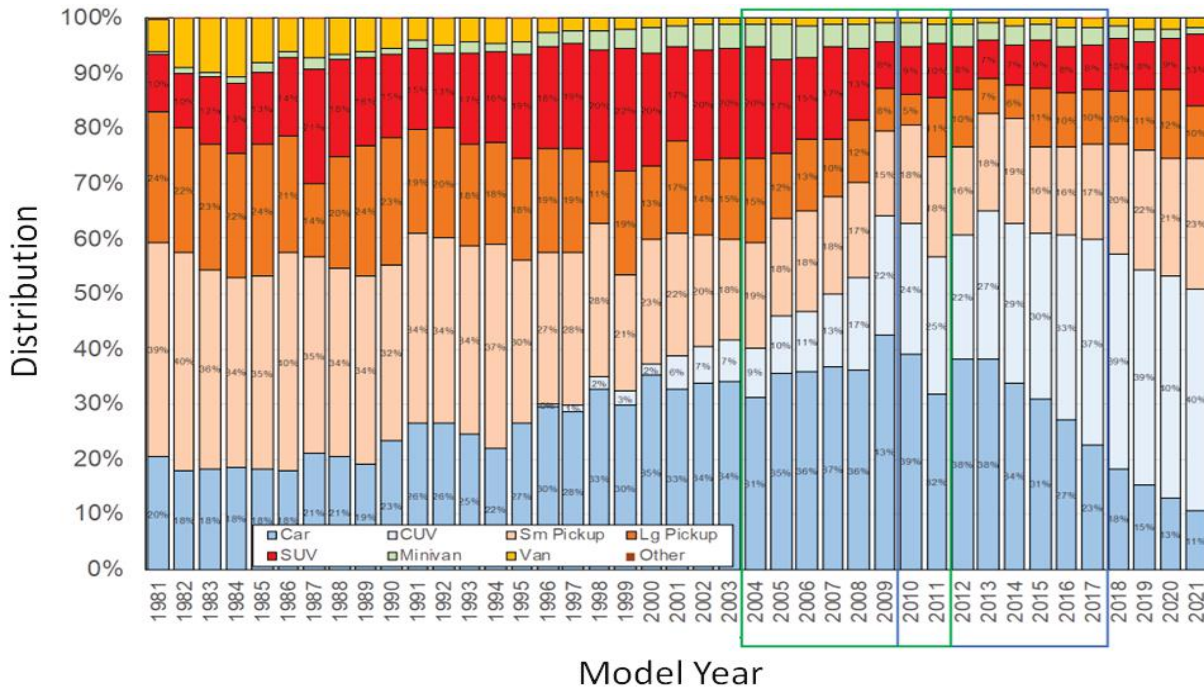


Figure III.1.1.3. Distribution of registered vehicles from a sample state by vehicle type and year. Source: Experian Vehicles in Operation.

Also, in FY 2022, LBNL began discussions with the EPA to obtain certification data on vehicle attributes, including curb weight, wheelbase, track width, drivetrain, engine characteristics, and safety features, for MYs 2010 through 2017. These data will be merged with the registration, crash, and VMT data to assign vehicle characteristics by VIN to individual vehicles in each of those datasets. The EPA provided LBNL with a dataset of attributes for MY 2019 vehicles, which LBNL analyzed. Figure III.1.1.4 indicates that MY 2019 2-door cars have a higher average mass than 4-door cars, and the heaviest SUVs have a higher mass than the heaviest small pickups. Figure III.1.1.5 shows the production-weighted footprint by vehicle type. Cars and CUVs have a similar footprint (i.e., median 46.6 square feet), but small pickups have a substantially larger footprint (i.e., median 68.2 square feet) than SUVs (i.e., median 53.3 square feet). The EPA data does not include pickup trucks with a rated capacity higher than 1/2-ton (i.e., 3/4- and 1-ton pickups), which in the previous analysis NHTSA included in a 'large pickup' category. As such, LBNL is in current discussions with the EPA to obtain data on the characteristics of large pickup models, as well as all vehicles back to MY 2011, from their compliance data.

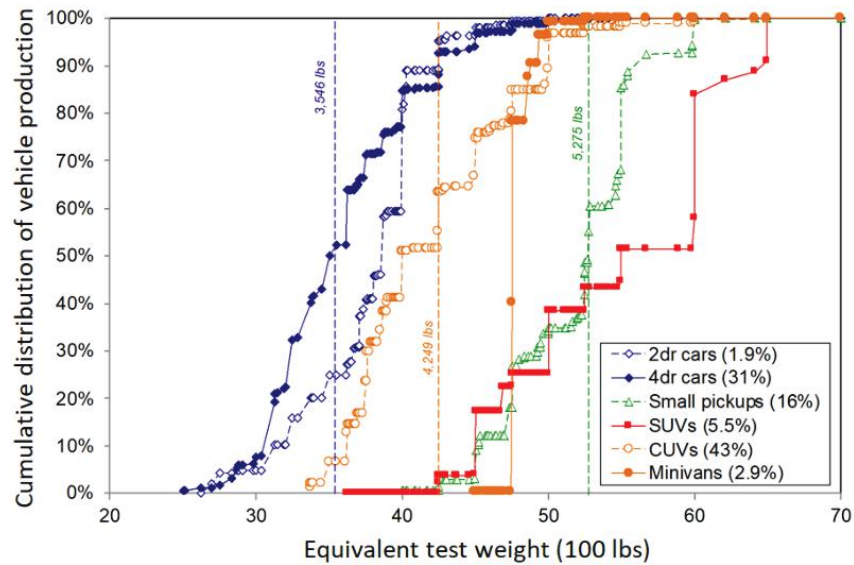


Figure III.1.1.4. Distribution of production-weighted estimated test weight of MY 2019 LD vehicles by vehicle type. Source: U.S. EPA.

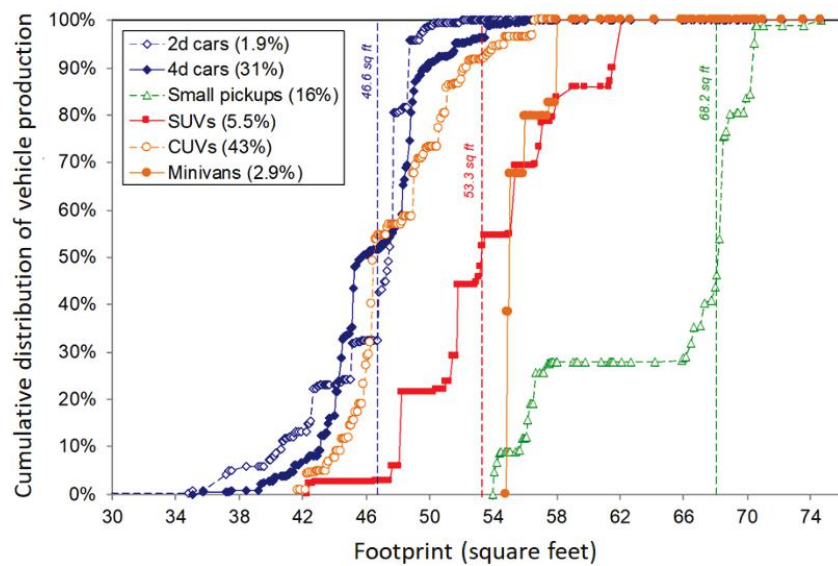


Figure III.1.1.5. Distribution of production-weighted footprint of MY 2019 LD vehicles by vehicle type. Source: U.S. EPA.

Conclusions

Data are still being gathered to update the analysis of the relationship between vehicle weight/footprint and societal fatality risk. Substantial changes in the composition of the on-road fleet by vehicle type, as well as the number of fatalities by crash type, suggest that the relationship between vehicle weight/footprint and safety may have changed since the previous analysis.

References

1. Wenzel, T. P., 2018, *Assessment of NHTSA’s Report “Relationships Between Fatality Risk, Mass, and Footprint in Model Year 2004-2011 Passenger Cars and LTVs” (LBNL Phase 1)*. LBNL-2001137, Lawrence Berkeley National Laboratory, Berkeley, CA, USA.

(This page intentionally left blank)

U.S. DEPARTMENT OF
ENERGY

Office of
**ENERGY EFFICIENCY &
RENEWABLE ENERGY**

For more information, visit:
energy.gov/eere/vehicles

DOE/EE-2731 August 2023